AUSTRALIAN
JNL. OF
PHYSICS

VOL. 21
1968

P

G. K. V.

गुरुकुल कांगड़ी विश्वविद्यालय, हरिद्वार
पुस्तकालय

R
विषय संख्या 530.5
पुस्तक संख्या M48A
V.21
आगत पंजिका संख्या 7794

पुस्तक पर किसी प्रकार का निशान लगाना वर्जित है। कृपया १५ दिन से अधिक समय तक पुस्तक अपने पास न रखें।

GULZAR BOOK BINDING HOUSE
ROORKEE

7797

COMPIL

सन्दर्भ ग्रन्थ
REFERENCE BOOK

यह पुस्तक वितरित न की जाय
NOT TO BE ISSUED

Stock Verification-2024

स्टाक प्रमाणीकरण १९८४-१९८५

R530.5, M48A V.21
7794

CHECKED 1973

AUSTRALIAN JOURNAL OF PHYSICS

UNIVERSITY OF KALYANI
LIBRARY

VOLUME 21, NUMBER 1, FEBRUARY 1968

REGISTERED IN AUSTRALIA FOR TRANSMISSION BY POST AS A PERIODICAL

AUSTRALIAN JOURNAL OF PHYSICS

Published by the Commonwealth Scientific and Industrial Research Organization. Issued six times a year, $A4 per annum.

BOARD OF STANDARDS

The Board of Standards for this Journal is appointed by the Commonwealth Scientific and Industrial Research Organization and the Australian Academy of Science and consists of Professor J. S. Turner (Chairman), Mr. A. E. Scott (Editor-in-Chief), Professor C. W. Emmens, Dr. S. D. Hamann, Professor C. B. O. Mohr, and Professor G. H. Satchell.

ADVISORY COMMITTEE

Acceptance of papers for this Journal is in the hands of an Advisory Committee appointed by the Board of Standards in consultation with the Australian Institute of Physics and consisting of Mr. A. E. Scott (Editor-in-Chief and Chairman), Professor A. J. F. Boyle, Dr. J. L. Farrands, Dr. C. H. B. Priestley, Professor R. Street, and Dr. J. P. Wild.

OTHER JOURNALS PUBLISHED BY CSIRO

Australian Journal of Agricultural Research	Issued six times a year, $A4 per annum
Australian Journal of Biological Sciences	
Australian Journal of Chemistry	Issued monthly, $A4 per annum
Australian Journal of Botany	Not issued at regular intervals, $A1 per issue
Australian Journal of Marine and Freshwater Research	
Australian Journal of Soil Research	
Australian Journal of Zoology	

The Organization is a signatory to the Fair Copying Declaration, details of which may be obtained from the office of the Royal Society, London.

All enquiries and manuscripts should be forwarded to:

The Editor-in-Chief,
Editorial and Publications Section, CSIRO,
Sixth Floor,
372 Albert Street,
East Melbourne, Victoria 3002

Printed by CSIRO, Melbourne

7794

AUSTRALIAN JOURNAL OF PHYSICS

VOLUME 21, NUMBER 1, FEBRUARY 1968

CONTENTS

CORRIGENDUM

VOLUME 20, NUMBER 5

"A survey of the southern sky at 85 MHz." By K. W. Yates, R. Wielebinski, and T. L. Landecker. pp. 595–607

Page 606, Section VII, second paragraph:

The coordinates of the features should read

$$l^{\mathrm{II}} = 320°,\ b^{\mathrm{II}} = -45° \qquad \text{and} \qquad l^{\mathrm{II}} = 250°,\ b^{\mathrm{II}} = -35°.$$

Accurate positions of 210 radio sources. By A. J. Shimmins 65

Identification of radio sources between declinations +27° and −30°. By J. G. Bolton, A. J. Shimmins, and Jeannette Merkelijn 81

Observations of 31 radio sources between 40 and 130 MHz. By R. F. Haynes and P. A. Hamilton 87

High resolution observations of the Orion Nebula at 408 MHz. By B. Y. Mills and P. A. Shaver 95

Short Communications

A search for a 5·5 MeV level in ^{7}Li. By P. J. Harvey 103

AUSTRALIAN JOURNAL OF PHYSICS

Published by the Commonwealth Scientific and Industrial Research Organization.
Issued six times a year, $A4 per annum.

BOARD OF STANDARDS

The Board of Standards for this Journal is appointed by the Commonwealth Scientific and Industrial Research Organization and the Australian Academy of Science and

	$A4 per annum
Australian Journal of Botany Australian Journal of Marine and Freshwater Research Australian Journal of Soil Research Australian Journal of Zoology	Not issued at regular intervals, $A1 per issue

The Organization is a signatory to the Fair Copying Declaration, details of which may be obtained from the office of the Royal Society, London.

All enquiries and manuscripts should be forwarded to:

The Editor-in-Chief,
Editorial and Publications Section, CSIRO,
Sixth Floor,
372 Albert Street,
East Melbourne, Victoria 3002

Printed by CSIRO, Melbourne

7794

AUSTRALIAN JOURNAL OF PHYSICS

Volume 21, Number 1, February 1968

CONTENTS

PAGE

The ground state of the $(p–\mu–p)^+$ molecule ion. By L. M. Delves and T. Kalotas 1

The Akhieser–Pomeranchuk–Blair model analysis for elastic scattering of deuterons. By M. Rahman, A. H. Khan, and H. M. Sen Gupta .. 7

The collision broadening of spectral lines. By R. W. Parsons, V. I. Metchnik, and R. J. Dyne 13

Calculation of surface energy as a function of orientation for cubic crystals. By J. F. Nicholas 21

Electromagnetic diffraction by a plane slit aperture. By H. S. Tan 35

Electron transport coefficients in hydrogen and deuterium. By R. W. Crompton, M. T. Elford, and A. I. McIntosh 43

Accurate positions of 210 radio sources. By A. J. Shimmins 65

Identification of radio sources between declinations +27° and −30°. By J. G. Bolton, A. J. Shimmins, and Jeannette Merkelijn 81

Observations of 31 radio sources between 40 and 130 MHz. By R. F. Haynes and P. A. Hamilton 87

High resolution observations of the Orion Nebula at 408 MHz. By B. Y. Mills and P. A. Shaver 95

Short Communications

A search for a 5·5 MeV level in ^{7}Li. By P. J. Harvey 103

AUSTRALIAN JOURNAL OF PHYSICS

VOLUME 21, NUMBER 2, APRIL 1968

CONTENTS

PAGE

Angular distributions in the giant resonance of ^{16}O. By R. J. J. Stewart .. 107

Trial of a numerical method for solving the Schrödinger wave equation in several variables. By I. M. Bassett 113

A quantum mechanical calculation of the radial distribution function for a plasma. By A. A. Barker 121

Compressional Alfvén wave propagation below ion cyclotron frequency. By R. C. Cross and J. A. Lehane 129

Astrophysical consequences of the existence of charged intermediate vector bosons. By J. A. Campbell 139

The excited atomic hydrogen lines 126α and 127α in HII regions. By R. X. McGee and F. F. Gardner 149

An interpretation of the distribution of metre wavelength radio emission. By K. W. Yates 167

A survey of the galactic plane at 85 and 150 MHz. By R. Wielebinski, D. H. Smith, and X. Garzón Cárdenas 185

Radio emission of 158 galaxies. By H. M. Tovmassian 193

Radio emission from the supernova remnant Vela-X. By D. K. Milne .. 201

Accurate right ascensions of selected southern radio sources. By J. M. Sutton 221

Short Communications

Inelastic scattering of deuterons from ^{56}Fe. By A. R. Majumder and H. M. Sen Gupta 235

AUSTRALIAN JOURNAL OF PHYSICS

Volume 21, Number 3, June 1968

CONTENTS

PAGE

0^+ states of ^{8}Be. By F. C. Barker, H. J. Hay, and P. B. Treacy 239

The ray theory of Doppler frequency shifts. By J. A. Bennett 259

Finite sample correlations of quantized Gaussians. By T. Cole 273

Structure of polytropes with purely toroidal magnetic fields. By Narendra K. Sinha 283

Equilibrium poloidal magnetic fields in rotating stars. By G. F. Davies .. 293

Gamma radiation from the reactions ^{20}Ne$(\alpha,\alpha'\gamma_{1\cdot63})^{20}$Ne and ^{20}Ne$(\alpha,p\gamma_{0\cdot44})^{23}$Na. By R. H. Spear and I. F. Wright 307

Directional correlation of gamma rays in the decay of 2·3 d ^{115}Cd. By M. M. Bajaj, S. L. Gupta, and N. K. Saha 317

Computed electron micrographs for tilted foils containing dislocations and stacking faults. By P. Humble 325

The linear polarization of radiation from Jupiter at 6 cm wavelength. By D. Morris, J. B. Whiteoak, and F. Tonking 337

The solar wind and Jovian decametric radio emission. By O. B. Slee and C. S. Higgins 341

A catalogue of galactic radio sources. By M. J. L. Kesteven 369

The Parkes catalogue of radio sources, declination zone +20° to +27°. By A. J. Shimmins and G. A. Day 377

Short Communications

A study of the 3·00 MeV level of ^{27}Al via ^{24}Mg$(\alpha,p\gamma)^{27}$Al. By D. C. Kean, R. V. Elliott, and R. H. Spear 405

Interpretation of the radio rotation period of Jupiter in terms of the cyclotron theory. By P. M. McCulloch 409

AUSTRALIAN JOURNAL OF PHYSICS

VOLUME 21, NUMBER 4, AUGUST 1968

CONTENTS

PAGE

R-matrix fit to ${}^9\mathrm{Be}(\gamma, \mathrm{n})^8\mathrm{Be}$ cross section near threshold. By F. C. Barker and B. M. Fitzpatrick 415

The behaviour of DWBA stripping amplitudes near the Butler pole. By M. Andrews, W. K. Bertram, and L. J. Tassie 423

Variational calculations for three-body S-states with Coulomb interactions. By L. M. Delves and T. Kalotas 431

Dielectric saturation in ionic crystals. II. Deformable ions. By J. Oitmaa .. 439

Multipole analysis. I. Theory, and geomagnetic multipoles 1965·0. By R. W. James 455

Nonlinear adiabatic pulsations of massive stars. By J. O. Murphy 465

The distribution of linear polarization over 13 extended sources at 21·2 cm wavelength. By D. Morris and J. B. Whiteoak 475

Observations of the linear polarization of radio sources at 6 cm wavelength. By D. Morris and J. B. Whiteoak 493

The optical spectrum of Vela X. By D. K. Milne 501

Radio sources in clusters of galaxies. By B. Y. Mills, R. R. Shobbrook, and D. Stewart-Richardson 511

Accurate positions and some optical identifications for 67 radio sources between declinations +20° and +27°. By Jeannette K. Merkelijn, A. J. Shimmins, and J. G. Bolton 523

Short Communications

Observations of 11 radio sources near 55 MHz. By R. F. Haynes, P. A. Hamilton, and P. M. McCulloch 539

AUSTRALIAN JOURNAL OF PHYSICS

VOLUME 21, NUMBER 5, OCTOBER 1968

CONTENTS

PAGE

An exact solution of Boltzmann's equation for a rigid sphere gas. By P. I. Brooker and H. S. Green 543

Ornstein–Zernike relation for a disordered fluid. By R. J. Baxter 563

The interaction energy of an ion pair with overlapping hydration shells. I. A truncated spheres model. By D. K. Ross and S. Levine .. 571

The interaction energy of an ion pair with overlapping hydration shells. II. A spheroidal cavity model. By D. K. Ross 587

The interaction energy of an isolated monovalent ion. By D. K. Ross .. 597

The formal nonequilibrium theory of partially ionized and/or nonuniform gas mixtures. By E. L. Bydder and B. S. Liley 609

Electron drift and diffusion in parahydrogen at 77°K. By R. W. Crompton and A. I. McIntosh 637

Directional correlations of gamma rays in the decay of 36 hr ^{82}Br. By S. L. Gupta and M. M. Bajaj 649

Diffraction by a slit aperture formed by two inclined surfaces. By H. S. Tan 661

The origin and propagation of acoustic-gravity waves ducted in the thermosphere. By A. F. Wickersham 671

Propagation of shock waves in a polytrope with a poloidal magnetic field. By Narendra K. Sinha 681

The nature of spread-F irregularities in Antarctica. By G. G. Bowman .. 695

Observations of Cen XR-2, Sco XR-1, and terrestrial X-rays. By J. R. Harries and R. J. Francey 715

PAGE

Optical and radio observations of the flare star UV Ceti in Australasia during September–October 1967. By C. S. Higgins, L. H. Solomon, and F. M. Bateson 725

A continuum survey of the Southern Milky Way at 1410 MHz. By E. R. Hill 735

Supernova remnants as radio sources. By M. J. L. Kesteven 739

Short Communications

Cosmic ray intensity increase on January 28, 1967. By L. V. Sud 755

The properties of a drifting and diffusing pulse of electrons and Townsend's coefficient of ionization α_T. By L. G. H. Huxley 761

The (γ, p) and (γ, n) reactions in molybdenum. By R. W. Gellie 765

AUSTRALIAN JOURNAL OF PHYSICS

VOLUME 21, NUMBER 6, DECEMBER 1968

CONTENTS

PAGE

Application of reaction matrix theory to meson processes. By J. L. Cook .. 769

On the problem of unresolved resonances in neutron spectroscopy. By A. R. de L. Musgrove 779

Charge exchange collisions involving multielectron atoms (lithium and sodium). By J. G. Lodge and R. M. May 793

States in ^{27}Al and ^{89}Y using high resolution surface barrier counters. By G. M. Crawley, D. L. Powell, and B. V. Narasimha Rao 803

The characteristic loss spectra of the second and third series transition metals. By M. J. Lynch and J. B. Swan 811

The potential due to two point charges each at the centre of a spherical cavity and embedded in a dielectric medium. By D. K. Ross 817

The shape and energy of a revolving liquid mass held together by surface tension. By D. K. Ross 823

The stability of a rotating liquid mass held together by surface tension. By D. K. Ross 837

On the relationship between recent measurements of cosmic ray electrons, nonthermal radio emission from the Galaxy, and the solar modulation of cosmic rays. By W. R. Webber 845

Study of a complete sample of cosmic radio sources. By W. Davidson .. 871

5 GHz continuum radiation from southern hemisphere galactic HII regions. By F. F. Gardner and M. Morimoto 881

Observations of the southern sky at 10·02 MHz. By P. A. Hamilton and R. F. Haynes 895

Accurate positions and identifications of 75 radio sources between declinations +20° and +27°. By Jeannette K. Merkelijn 903

Effect of horizontal and vertical magnetic fields on Kelvin–Helmholtz instability. By R. C. Sharma and K. M. Srivastava 917

PAGE

Effect of horizontal and vertical magnetic fields on Rayleigh–Taylor instability. By R. C. Sharma and K. M. Srivastava 923

Short Communications

Study of combined effect of Kelvin–Helmholtz instability and gravitational instability on a self-gravitating fluid layer. By C. Uberoi and R. Jayakaran Isaac 931

The temperature at 120 km altitude in April–May 1965. By L. M. Sheppard 939

The determination of stacking fault energy by the tetrahedron method. By P. Humble and C. T. Forwood 941

Corrigendum 944

Index to Volume 21 945

NOTICE TO AUTHORS

AUSTRALIAN JOURNAL OF PHYSICS

Papers will be considered for publication in the Journal if they make an original contribution to any branch of experimental or theoretical physics.

Two categories of articles are published. *Papers*—critical accounts of original work. *Short Communications*—scientifically complete accounts of work of limited scope; no summary is required.

Reviews of published work are not accepted unless they are interpretative in character and present new ideas that advance the state of knowledge of the subject.

Descriptions of techniques and equipment should generally be included in the experimental section of a paper. However, they are acceptable for separate publication if they are novel and are of evident importance to research in physics.

Submission of a paper implies that the results reported have not been published or submitted for publication elsewhere.

General presentation.— The work should be presented concisely and clearly in English. Introductory material, including a review of the literature, should not exceed what is necessary to indicate the reason for the work and the essential background. Generally, results and discussion should not be intermingled; the discussion should be restricted to logical interpretation as a basis for conclusions supported by the results. Some speculation is allowable but this should be restrained. Some types of work require special methods of presentation.

Authors are advised to note the typographical conventions and layout of headings, tables, and illustrations exemplified in recent issues of the Journal. Strict observance of these and the following requirements will shorten the interval between submission and publication.

Manuscripts.—Typescripts on good quality paper with double spacing (3 lines to the inch) throughout, and one copy, should be submitted. All pages of the manuscript must be numbered consecutively, including those containing references, tables, and captions to illustrations, which are to be placed after the text.

The title should be informative of the content of the paper. A running title not exceeding 50 characters in length should be added.

If the paper is one of a numbered series, a reference to the previous part should be given as a footnote on the first page. If it is necessary for a proper understanding of the paper to refer to an earlier part, it will assist referees if the author can provide a copy.

The summary should be brief; it is seldom necessary to exceed 200 words to indicate the scope of the work and the principal findings.

Footnotes within the text should be used only when essential. They should be placed within horizontal rules immediately under the line to which they refer.

References are cited in the text by the author and date and are not numbered. Authors are referred to recent issues for the style used in the Journal for citing references to books, periodicals, and other literature. Authors may include all titles or none, but the reference to any paper accepted for publication but not yet published must include the title. No editorial responsibility can be taken for the accuracy of the references; authors are requested to check these. All references in the text must be listed, with the names of authors arranged alphabetically; all entries in this list must correspond to references in the text. Sources indicated in the text as "personal communication", "in preparation", or similar phrases should not be listed as references. Abbreviations of titles of periodicals should conform to those used in *World List of Scientific Periodicals*, 4th Edition.

Mathematical formulae should be very carefully set out, preferably handwritten, in the exact form in which they are to be printed; even with a typewriter having appropriate symbols it is often difficult to indicate the required layout. Greek letters and special symbols should be indicated by marginal annotations. For typographical conventions, authors are referred to recent issues of the Journal. Two-line mathematical expressions should be avoided in the running text.

Tables should be numbered with arabic numerals and be accompanied by a title and by sufficient explanatory information to make them self-contained. They should be arranged having regard to the dimensions of the printed page, and the number of columns should be kept to a minimum. Long headings to columns should be avoided by the use of explanatory footnotes indicated in the table by superscript letters. Each table must be referred to in the text and its approximate location indicated in the margin. Only in exceptional circumstances will presentation of the same data in tabular and graphical form be permitted; where adequate, the latter form should be used. Vertical tables should not exceed 80 characters and spaces in width if they are to be set in 8 point type, the size generally used in tables in the Journal. Smaller type can be used if necessary, but the number of characters and spaces should not exceed 110. For very large tables with their width along the length of the page, the corresponding figures are 120 and 160.

Illustrations.—*Figures* must be drawn with black ink on board, drawing or tracing paper, coordinate paper with *faint blue* rulings, or plastic sheet (using the appropriate ink). Care should be taken to ensure that each line is of uniform width and density. Drawings should be about 2½ times the width of comparable diagrams reproduced in the Journal. Only in exceptional circumstances are drawings more than 12 inches wide acceptable. Good photographic prints may be submitted.

In graphs the axes and grid lines should be thinner than the "curves". In drawings 2½ times the final printed size no lines should be more than 0·8 mm or less than 0·25 mm wide; symbols should be 3–4 mm across and for typographical reasons should be restricted to crosses and open or solid circles, squares, or triangles. Allowance must also be made for the effect of reduction on dots and stipples.

All lettering on original figures should be in soft lead pencil or indicated on a transparent overlay. Copies should be lettered with ink.

The originals and two copies of each are required. The title of the paper and the name of the author must appear on each sheet. Figures must be numbered consecutively in the order in which they are mentioned in the text and their approximate position should be indicated in the margin. A typed list of captions must be supplied.

Photographic prints must be of the highest quality with a full range of tones and good contrast. They should be trimmed to exclude features not relevant to the paper. Three copies, identified on the back by the title of the paper and the name of the author, are required; one set should be without lettering.

All plates should be numbered consecutively. Where several figures are grouped on one plate, they should be given letter designations. A typed list of captions is required.

Details in a photograph which must be most clearly shown should be indicated on an overlay for the guidance of the blockmaker: this is particularly important with photo- and electron-micrographs.

Reprints.—Reprints are supplied free to authors as follows: one author, 40; two authors, 30 each; three or more authors, 20 each. Additional reprints may be obtained if ordered no later than when the galley proofs are returned.

पुस्तकालय
गुरुकुल कांगड़ी विश्वविद्यालय
हरिद्वार

THE GROUND STATE OF THE $(p\text{–}\mu\text{–}p)^+$ MOLECULE ION

By L. M. DELVES* and T. KALOTAS*

[*Manuscript received July* 31, 1967]

Summary

This paper gives the results of a variational calculation using a 100-term wavefunction on the ground (para) state of $(p\text{–}\mu\text{–}p)^+$, including the effects of the finite proton mass. The energy found is sensitive to the muon mass; with $m_\mu = 206\cdot77\ m_e$, we find $(\mathrm{B.E.})_{p\mu p}$ to be $253\cdot14\pm0\cdot01$ eV. Results are also given for the muon–proton overlap, and for a number of other geometric averages of the wavefunction.

I. INTRODUCTION

The stable Coulombic bound system $(p\text{–}\mu\text{–}p)^+$ is of some importance in the analysis of muon capture experiments and a number of calculations have previously been performed on both the ground state ($L = 0$) and first excited state ($L = 1$). The earlier calculations (Cohen, Judd, and Riddell 1960; Ta-You Wu, Rosenberg, and Sandstrom 1960) were limited in accuracy by their use of the Born–Oppenheimer approximation, while later calculations (Kalos, Roothaan, and Sack 1960; Halpern 1964; Wessel and Phillipson 1964; Kabir 1966) have retained the full (non-relativistic) Hamiltonian. We discuss here a series of variational calculations on the ground state using the full Hamiltonian and retaining up to 100 terms in the wavefunction. Values are given for the energy, for the muon–proton overlap γ (which is of interest in non-capture), and for some 50 other geometric averages over the p–μ–p wavefunction. The results are in agreement where applicable with those of Wessel and Phillipson (1964).

II. METHOD

Let $\mathbf{r}_1$ and $\mathbf{r}_2$ be the position vectors of the two protons relative to the muon and let $r_1 \equiv |\mathbf{r}_1|$, $r_2 \equiv |\mathbf{r}_2|$, and $r_{12} \equiv |\mathbf{r}_1 - \mathbf{r}_2|$. We then define the operators

$$T_0 \equiv \nabla_1^2 + \nabla_2^2, \qquad T_{12} \equiv \nabla_1 . \nabla_2, \qquad T_\infty \equiv T_0 + 2T_{12}.$$

Then the total kinetic energy operator T becomes

$$T = -(\hbar^2/2m_{\mathrm{red}})T_0 - (\hbar^2/m_\mu)T_{12}$$

$$= -(\hbar^2/2m_\mu)T_\infty - (\hbar^2/2m_p)T_0,$$

with

$$m_{\mathrm{red}} \equiv m_\mu m_p/(m_\mu + m_p).$$

---

* School of Mathematical and Physical Sciences, University of Sussex, Falmer, Brighton, Sussex, England.

Aust. J. Phys., 1968, 21, 1–6

The ground state wavefunction of $(p\text{-}\mu\text{-}p)^+$ is a function only of the interparticle distances r_1, r_2, and r_{12}. We take a trial function of the form

$$\psi_T = \sum_{i=1}^{N} a_i(1+P_{12})\exp[-\alpha^{-1}\{Z^*(l_i r_1+m_i r_2)+n_i r_{12}\}], \tag{1}$$

where P_{12} is the permutation operator, the a_i are a set of linear parameters, α and Z^* are nonlinear parameters, and (l_i, m_i, n_i) are a triplet of integers that are ordered in a systematic way such that the following conditions are all satisfied:

$$\left.\begin{array}{ll} \text{(i)} & l_i \geqslant m_i, \\ \text{(ii)} & n_i \geqslant n_{\min}, \\ \text{(iii)} & \text{the Hamiltonian is Hermitian with respect to } \psi_T, \\ \text{(iv)} & \text{the possible values of } q\ (= l_i+m_i+n_i) \text{ are} \\ & \text{successively exhausted.} \end{array}\right\} \tag{2}$$

Condition (iii) merely excludes values of l, m, and n for which the wavefunction is not normalizable.

The programme incorporating this wavefunction will be described in detail elsewhere (Delves and Kalotas, in preparation) together with the reasons for the above choice of basis functions; here we quote only the results obtained for the system p–μ–p. For these calculations we have set

$$Z^* = 1, \qquad n_{\min} = -1, \tag{3}$$

and have varied the scale factor α for values of N up to 100.

The energy E depends on the value assumed for the muon mass m_μ. We shall quote results in muon atomic units and in electron-volts. We take

$$m_\mu = 206\cdot77\,m_e, \qquad m_p = 1836\cdot12\,m_e. \tag{4}$$

We have 1 $(\text{a.u.})_e = 27\cdot2098$ eV and hence

$$1\ (\text{a.u.})_\mu \equiv a_\mu = 5626\cdot1703\ \text{eV}. \tag{5}$$

III. Results

The dependence of the upper bounds $E(N)$ on α for various values of N is shown in Figure 1, while optional values of α and energies E are given in Table 1. In this table the binding energy is the energy by which the last proton is bound

$$\begin{aligned} \text{B.E.} &= -\{E-E(p\mu)\} \\ &= -E-0\cdot5(m_{\text{red}}/m_\mu)\,a_\mu = -E-2528\cdot360\ \text{eV}, \end{aligned} \tag{6}$$

with m_{red} defined as above. The best result from Table 1, B.E. $\geqslant 253\cdot133$ eV, should be compared with the value B.E. $\geqslant 254\cdot3$ eV obtained by Wessel and

Phillipson (1964). Their assumed value for the muon mass, although not stated explicitly, appears from the value for $E(\mathrm{p}\mu)$ quoted there to be

$$m_\mu = 206\cdot8\, m_\mathrm{e}\,. \tag{7}$$

The mass m_μ affects the quoted energy not only through the conversion constant from muon atomic units to electron volts, but also through the term in the Hamiltonian coming from the finite size of m_μ/m_p (see Section II).

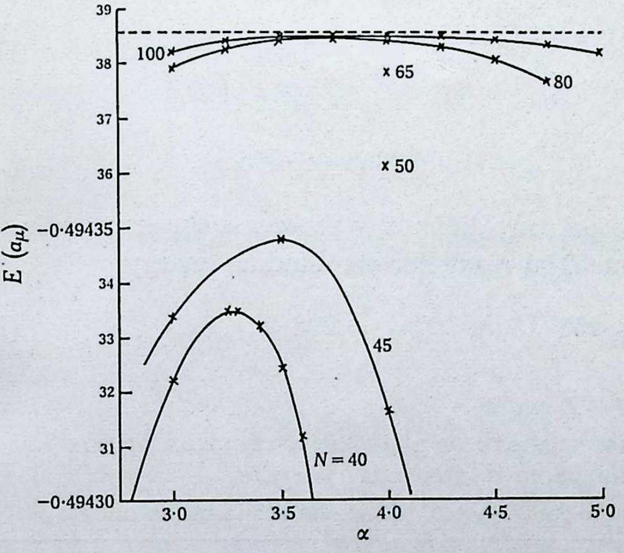

Fig. 1.—The dependence on the scale parameter α of the upper bounds $E(N)$ for various numbers of terms N. The dashed line is the estimated limit for $N \to \infty$.

TABLE 1

OPTIONAL VALUES OF SCALE FACTOR α AND ENERGY E FOR VARIOUS NUMBERS OF TERMS N IN THE WAVEFUNCTION (1)

N	α	Energy		
		E (a_μ)	E (eV)	B.E. (eV)
40	3·3	−0·49433500	−2781·2129	+252·853
45	3·5	−0·49434780	−2781·2849	+252·925
80	3·75	−0·49438441	−2781·4909	+253·1306
100	3·75	−0·49438482	−2781·4932	+253·1329

We have evaluated the expected values of the operators T_0 and T_{12} separately (see Section IV) and hence can correct for the effect of small changes in the assumed muon mass. Using the expected value of T_∞ $(=T_0+2T_{12})$ from Section IV we find

$$\mathrm{B.E.}\{m_\mu(1+\delta)\} = \mathrm{B.E.}(m_\mu) + [\{m_\mathrm{p}/(m_\mathrm{p}+m_\mu)\}E(\mathrm{p}\mu) - \tfrac{1}{2}T_\infty]\delta \quad \mathrm{a}_\mu$$

$$= \mathrm{B.E.}(m_\mu) + 145\cdot67\,\delta \quad \mathrm{eV}\,. \tag{8}$$

This yields, for comparison with Wessel and Phillipson, the value

$$\mathrm{B.E.} = 253\cdot15\ \mathrm{eV}\,, \qquad m_\mu = 206\cdot8\,. \tag{9}$$

We are unable to explain this discrepancy. We have analysed the rate of convergence of our expression by taking runs for a fixed value of $\alpha = 4\cdot0$. The result of these runs is shown below:

N	40	45	50	65
E	$-0\cdot49420763$	$-0\cdot49431666$	$-0\cdot49436131$	$-0\cdot49437836$

N	80	100	∞
E	$-0\cdot49438403$	$-0\cdot49438480$	$-0\cdot4943855$

If we assume the convergence to be of the form (Schwartz 1963)

$$E(N) = E_\infty + AN^{-p}, \tag{10}$$

then these results imply that

$$p = 8 \qquad \text{and} \qquad E_\infty = 0\cdot4943855 \pm 0\cdot075\,. \tag{11}$$

Since extrapolation of this kind is notoriously difficult, we increase the error estimate by a factor of three and quote as our final result for the binding energy

$$253\cdot13 \leqslant \text{B.E.} \leqslant 253\cdot15\ \text{eV} \quad (m_\mu = 206\cdot77)\,. \tag{12}$$

TABLE 2

RESULTS FOR OPERATORS IN THE GROUND STATE OF p–μ–p AS A FUNCTION OF THE NUMBER OF TERMS RETAINED IN THE TRIAL FUNCTIONS

The last column gives the estimated value for $N \to \infty$. All results are in muon units a_μ

	Number of Terms N					
Operator	40	50	65	80	100	∞
T_0	$-1\cdot144820$	$-1\cdot145259$	$-1\cdot146442$	$-1\cdot146982$	$-1\cdot147014$	$-1\cdot1470$
T_{12}	$-0\cdot142563$	$-0\cdot142969$	$-0\cdot143453$	$-0\cdot143688$	$-0\cdot143706$	$-0\cdot1437$
T_∞	$-0\cdot859695$	$-0\cdot859320$	$-0\cdot859536$	$-0\cdot859606$	$-0\cdot859603$	$-0\cdot85960$
$r_1^{-1}+r_2^{-1}$	$1\cdot340478$	$1\cdot340244$	$1\cdot340491$	$1\cdot340603$	$1\cdot340602$	$1\cdot3406$
r_{12}^{-1}	$0\cdot351835$	$0\cdot351737$	$0\cdot351793$	$0\cdot351832$	$0\cdot351831$	$0\cdot35183$
r_1+r_2	$4\cdot773050$	$4\cdot773697$	$4\cdot772134$	$4\cdot771302$	$4\cdot771331$	$4\cdot7713$
$r_1^2+r_2^2$	$15\cdot547886$	$15\cdot555133$	$15\cdot543640$	$15\cdot538348$	$15\cdot538789$	$15\cdot5385$
r_{12}	$3\cdot301826$	$3\cdot301657$	$3\cdot300229$	$3\cdot299493$	$3\cdot299494$	$3\cdot2995$
$\delta(r_1)+\delta(r_2)$	$0\cdot264562$	$0\cdot262824$	$0\cdot262840$	$0\cdot262859$	$0\cdot263041$	$0\cdot2628$
$\delta(r_{12})$	$10\cdot83\times10^{-5}$	$8\cdot22\times10^{-5}$	$4\cdot62\times10^{-5}$	$3\cdot86\times10^{-5}$	$3\cdot96\times10^{-5}$	$4\cdot0\times10^{-5}$

IV. EXPECTED VALUES OF OPERATORS

We have also calculated the expected values of a number of simple operators. These operators include:

(1) the delta function operators $\delta(r_1)+\delta(r_2)$ and $\delta(r_{12})$;

(2) the three kinetic energy terms T_0, T_{12}, and T_∞ defined in Section II;

(3) the potential terms $(r_1^{-1}+r_2^{-1})$ and r_{12}^{-1}, and mean radii r_1+r_2, $r_1^2+r_2^2$, and r_{12}.

The results found for these operators are given in Table 2 as a function of the number of terms N retained. All values are expressed in muon units a_μ. The last column in this table gives an estimate of the extrapolated value for $N \to \infty$.

The estimated accuracy is shown by the number of digits retained; in each case, the last digit shown may be in error by one or two units. Especially noteworthy is the result obtained for $\delta(r_{12})$. The expected value of this operator is zero in the Born–Oppenheimer approximation, and the small value and slow convergence obtained is a consequence of this.

We have also calculated the expected values of various powers of the interparticle distances

$$\langle l, m, n\rangle = \langle \psi \mid (r_1^l r_2^m + r_2^l r_1^m) r_{12}^n \mid \psi\rangle .$$

The extrapolated results for these operators are given in Table 3; again, the estimated accuracy is indicated by the number of digits retained.

TABLE 3

EXPECTED VALUES OF POWERS OF THE INTERPARTICLE DISTANCES

Extrapolated results are for operators of the form $(l, m, n) \equiv (r_1^l\, r_2^m + r_2^l\, r_1^m) r_{12}^n$.
All values are in muon units a_μ

l	m	n	Value	l	m	n	Value	l	m	n	Value
−1	−1	−1	0·33116	−1	1	0	3·5684	1	1	1	39·248
−1	0	−1	0·50982	−1	2	0	12·2001	−1	−1	2	6·5302
−1	1	−1	1·17052	−1	3	0	49·972	−1	0	2	14·7993
−1	2	−1	3·4930	0	3	0	63·09	−1	1	2	50·929
−1	3	−1	12·651	1	1	0	10·342	−1	2	2	221·67
0	1	−1	1·51753	1	2	0	31·71	0	0	2	24·7808
0	2	−1	4·4328	−1	−1	1	2·05008	0	1	2	70·645
0	3	−1	16·171	−1	0	1	4·15208	−1	−1	3	23·8050
1	1	−1	3·1146	−1	1	1	12·6270	−1	0	3	59·801
1	2	−1	8·869	−1	2	1	48·905	−1	1	3	231·3
1	3	−1	32·31	−1	3	1	224·5	0	0	3	104·54
2	2	−1	24·776	0	1	1	17·261				
−1	−1	0	0·75094	0	2	1	62·306				

Results for the operators $\delta(r_1)+\delta(r_2)$ and r_{12} have been given previously by Wessel and Phillipson (1964), who calculated the muon–proton overlap γ defined by

$$\gamma = \tfrac{1}{2}\pi\langle\delta(r_1)+\delta(r_2)\rangle . \tag{13}$$

In terms of the units used by them ($m_{\text{red}} = 1$) we find

$$\left.\begin{aligned} \gamma &= 0\cdot5686 \quad (0\cdot5733), \\ \langle r_{12}\rangle &= 2\cdot9655 \quad (2\cdot973), \end{aligned}\right\} \tag{14}$$

where the results of Wessel and Phillipson are given in parentheses. In both cases, the present results agree within the accuracy (~1%) claimed by Wessel and Phillipson.

V. ACKNOWLEDGMENTS

These calculations were made on the Atlas computer of the Computer Laboratory, Scientific Research Council, Chilton. The authors are grateful to Dr. Howlett,

the Director of the Laboratory, for the excellent facilities provided and for machine time; and to the staff of the Laboratory for their help and advice.

This work was carried out during the tenure of a Commonwealth Scholarship (T.K.) and an S.R.C. research fellowship (L.M.D.). It was partly financed by a grant from the Shell Petroleum Company to the University of Sussex.

VI. References

Cohen, S., Judd, D. L., and Riddell, R. J. (1960).—*Phys. Rev.* **119**, 384, 397.

Halpern, A. (1964).—*Phys. Rev. Lett.* **13**, 660.

Kabir, P. K. (1966).—*Z. Phys.* **191**, 447.

Kalos, W., Roothaan, C. C. J., and Sack, R. A. (1960).—*Rev. mod. Phys.* **32**, 178.

Schwartz, C. (1963).—*Computl Meth. phys. Sci.* **2**, 257.

Ta-You Wu, Rosenberg, R. L., and Sandstrom, H. (1960).—*Nucl. Phys.* **16**, 432.

Wessel, W. R., and Phillipson, P. (1964).—*Phys. Rev. Lett.* **13**, 23.

THE AKHIESER–POMERANCHUK–BLAIR MODEL ANALYSIS FOR ELASTIC SCATTERING OF DEUTERONS*

By M. Rahman,† A. H. Khan,† and H. M. Sen Gupta‡

[*Manuscript received September* 7, 1967]

Summary

Angular distributions of deuterons elastically scattered from Mg, Fe, Cu, and Zn have been analysed in terms of the smoothed Akhieser–Pomeranchuk–Blair model and reasonable agreement was obtained in each case up to about 90°. The interaction radius R and the surface thickness ΔR were obtained from the best-fit parameter values.

I. Introduction

The phenomenon of elastic scattering of a strongly absorbing particle can be described without detailed knowledge of the exact absorption mechanism. The small-angle diffraction model proposed by Akhieser and Pomeranchuk (1945) for the elastic scattering of high energy charged particles was extended by Blair (1954) to explain the experimental α-scattering data from a number of medium weight and heavy nuclei. The model is termed the Akhieser–Pomeranchuk–Blair (APB) model. In this semiclassical approach, the nuclear interaction zone is represented by a totally absorbing spherical region with a well-defined boundary. According to the model all incident waves up to a certain critical orbital angular momentum l_A are completely absorbed while those with higher momenta suffer scattering that is characteristic of the Coulomb potential of the target nucleus. These assumptions, however, underwent various modifications in subsequent years (McIntyre, Wang, and Becker 1960; Frahn and Venter 1963, 1964).

McIntyre, Wang, and Becker (1960) replaced the sharp cutoff assumption in angular momentum by a gradual transition from complete absorption to no absorption over a width Δl_A in l-space, corresponding to the diffuseness of the nuclear surface, and further introduced a real nuclear phase shift.

The APB model thus improved upon has been used in analyses of elastic scattering of α-particles and to some extent of heavy ions; the present authors applied the model to other projectiles such as deuterons (Sen Gupta, Rahman, and Khan 1967; henceforth referred to as paper I). Since these preliminary works gave quite encouraging results, further analyses were carried out on elastic scattering of deuterons. Results are presented here for scattering from Mg at 21·6 MeV, Fe at 11·8 and 13·6 MeV, Cu at 15·0 and 21·0 MeV, and Zn at 21·6 MeV. The various experimental data were taken from Yntema (1959), Cindro and Wall (1960), Gofman and Nemets (1961), Igo, Lorenz, and Schmidt-Rohr (1961), and Jolly, Lin, and Cohen (1963).

---

* Part of this work was presented by the authors at the International Seminar on Low Energy Nuclear Physics, Dacca, East Pakistan, 1967.

† Atomic Energy Centre, Dacca, East Pakistan.

‡ Department of Physics, University of Dacca, Dacca, East Pakistan.

II. Theoretical Calculations

Details of the analyses and procedure of calculations have been given in paper I. The adjustable parameters of the model are l_A, Δl_A, δ, and Δl_δ, where l_A is the critical angular momentum, Δl_A defines the width of the transition region (as mentioned above), δ is the real nuclear phase shift, and Δl_δ carries a meaning similar to Δl_A. The parameters are adjusted systematically one after another in order to minimize the root-mean-square difference between the measured cross sections and the calculated ones at the respective angles.

Table 1

PARAMETERS OF THE APB MODEL

The parameters for the nuclei Ni, Zr, Ag, and Er are taken from paper I

Target Nucleus	Beam Energy (MeV)	Parameter				R (fm)	ΔR (fm)
		l_A	Δl_A	δ (rad)	Δl_δ		
Mg	21·6	6·7	0·6	0·3	2·2	5·87	0·47
Fe	11·8	5·9	0·4	0		8·40	0·39
Fe	13·6	5·9	0·35	0		7·69	0·32
Ni	12·8	6·0	0·4	0·1	2·0	7·90	0·36
Cu	15·0	7·2	0·5	0		8·21	0·42
Cu	21·6	9·1	0·7	0·1	0·5	8·34	0·47
Zn	21·6	9·1	0·6	0·3	1·0	8·43	0·40
Zr	11·8	4·75	0·3	0·1	1·0	8·11	0·27
Ag	21·6	9·3	0·6	0·1	1·0	8·67	0·43
Er	15·0	7·0	0·5	0		10·44	0·38

III. Results

The best-fit parameter values of the model are given in Table 1 and the corresponding results are shown in Figures 1(*a*)–1(*c*). Agreement is reasonably good in all cases up to about 90° and in some cases beyond this angle. The predicted curves at large angles show a well-defined diffraction oscillation in contrast to the rather damped structure of the experimental angular distribution. This disagreement should not, however, be counted against the APB model since this is a small-angle approximation and is expected to be particularly valid in medium weight and heavy nuclei (Blair 1954; Khan, Rahman, and Sen Gupta 1967). Further, the deuteron data at large angles (i.e. for small impact parameters) are somewhat difficult to analyse in view of the loosely bound structure of the deuteron.

IV. Discussion

From the parameters l_A and Δl_A the interaction radius R and the surface diffuseness ΔR were obtained respectively from the semiclassical relations given by McIntyre, Baker, and Wang (1962), namely

$$l_A(l_A+1) = kR(kR-2\eta) \tag{1}$$

and

$$(2l_A+1)\Delta l_A = 2kR(kR-\eta)\Delta R/R\,, \tag{2}$$

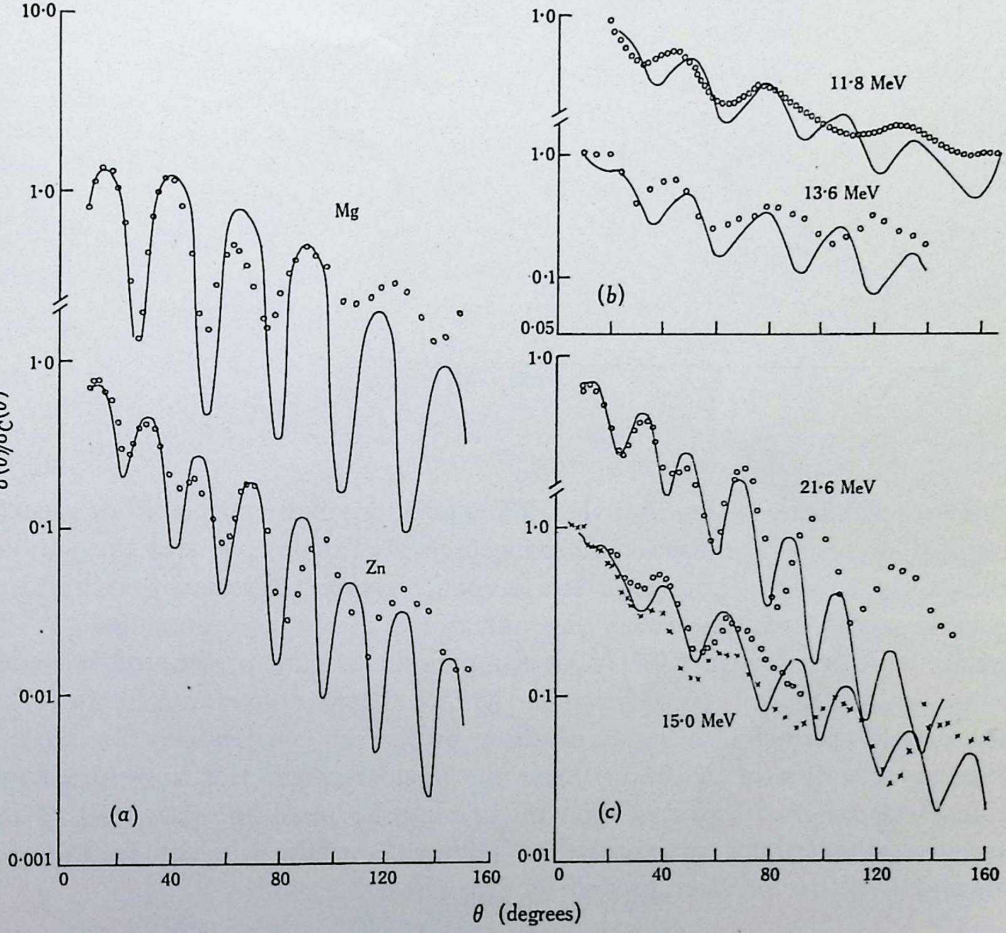

Fig. 1.—Ratio of differential cross section $\sigma(\theta)$ to Coulomb cross section $\sigma_C(\theta)$ plotted against the c.m. angle θ for experimental points and predicted curves from an APB model analysis of elastic scattering of (a) 21·6 MeV deuterons from Mg and Zn, (b) 11·8 and 13·6 MeV deuterons from Fe, and (c) 15·0 and 21·6 MeV deuterons from Cu.

where k is the c.m. wave number of the system and η is the Coulomb parameter. These quantities were calculated also for the nuclei Ni, Zr, Ag, and Er from the parameter values given in paper I and are included in Table 1. Figure 2 gives a plot of R against $A^{\frac{1}{3}}$, using the values obtained from equation (1). The errors shown in this figure are not exact but are estimated from the range in which l_A appears to lie; the straight line is the least-squares fit given by the relation

$$R = r_0 A^{\frac{1}{3}} + R_d\,,$$

with $r_0 = 1\cdot53$ fm and $R_d = 1\cdot84$ fm, which are quite reasonable values. The surface diffuseness obtained for the nuclei studied lies around $0\cdot4$ fm, being slightly less than that given by the optical model. This difference may well be attributed to the slightly different ways in which ΔR is defined in the two models. The value of δ is small in all cases whereas Δl_δ does not show any systematic change with target variation (the effect of this parameter is small, however; see paper I).

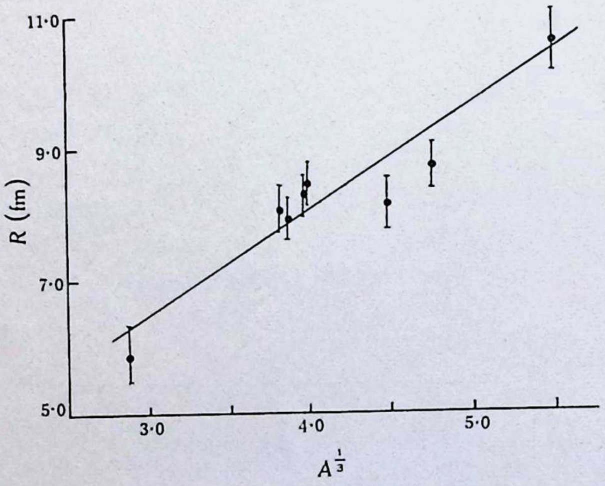

Fig. 2.—Plot of interaction radius R against $A^{\frac{1}{3}}$. The straight line is the least-squares fit given by the relation

$$R = 1\cdot53\,A^{\frac{1}{3}} + 1\cdot84\,.$$

We conclude by saying that the APB model, originally proposed for α-particles, can equally describe the elastic scattering process of deuterons and the parameters of the model seem to be more or less uniquely given. Agreement with this four-parameter model (sometimes only two parameters l_A and Δl_A are sufficient; Khan, Rahman, and Sen Gupta 1967) is of comparable quality to that of the complex potential optical model. In addition to the fact that deuterons are likely to be lost in the elastic channel as a result of being broken up, particularly for large-angle scattering, reflection of deuterons from the nuclear interaction zone (i.e. from the so-called "illuminated" part of the nuclei) should also be incorporated in the scattering process; this is expected to fill up the valleys in the backward-angle diffraction oscillations, as suggested by Dar (1964).

V. ACKNOWLEDGMENTS

The authors wish to thank Professor Innas Ali, Dr. A. M. Chaudhury, and Dr. A. Hossain for their interest in the work.

VI. REFERENCES

Akhieser, A., and **Pomeranchuk, I.** (1945).—*Fiz. Zh.* **9**, 471.
Blair, J. S. (1954).—*Phys. Rev.* **95**, 1218.
Cindro, N., and **Wall, N. S.** (1960).—*Phys. Rev.* **119**, 1340.
Dar, A. (1964).—*Nucl. Phys.* **55**, 305.
Frahn, W. E., and **Venter, R. H.** (1963).—*Ann. Phys.* **24**, 243.
Frahn, W. E., and **Venter, R. H.** (1964).—*Ann. Phys.* **27**, 135.

Gofman, Y. V., and Nemets, O. F. (1961).—*Soviet Phys. JETP* **12**, 1035.
Igo, G., Lorenz, W., and Schmidt-Rohr, U. (1961).—*Phys. Rev.* **124**, 832.
Jolly, R. K., Lin, E. K., and Cohen, B. L. (1963).—*Phys. Rev.* **130**, 2391.
Khan, A. H., Rahman, M., and Sen Gupta, H. M. (1967).—*Nuovo Cim.* B **48**, 13.
McIntyre, J. A., Baker, S. D., and Wang, K. H. (1962).—*Phys. Rev.* **125**, 584.
McIntyre, J. A., Wang, K. H., and Becker, L. C. (1960).—*Phys. Rev.* **117**, 1337.
Sen Gupta, H. M., Rahman, M., and Khan, A. H. (1967).—*Aust. J. Phys.* **20**, 265.
Yntema, J. L. (1959).—*Phys. Rev.* **113**, 261.

THE COLLISION BROADENING OF SPECTRAL LINES

By R. W. Parsons,* V. I. Metchnik,* and R. J. Dyne*

[*Manuscript received July* 14, 1967]

Summary

The shape of a collision-broadened spectral line depends on the assumptions made about the collision processes involved. If the collision cross section varies inversely as the relative speed of the colliding molecules, the half-width to the half-power points and to the points of steepest slope should be $1/2\pi\bar{\tau}$ and $1/(2\surd 3)\pi\bar{\tau}$ respectively, where $\bar{\tau}$ is the mean interval between line-broadening collisions. It is shown that, in a gas of "hard-sphere" molecules, the shape of the line is modified and the above half-widths are reduced by 6·4 and 9·7% respectively. While it is not suggested that gas molecules behave entirely as hard spheres, it is suggested that some deviations from the Van Vleck–Weisskopf–Lorentz shape may occur, and that it may be possible to detect these deviations experimentally.

I. Introduction

The shape of collision-broadened spectral lines was considered by Lorentz (1915). He assumed that molecules perform internal forced oscillations under the influence of an applied oscillating electromagnetic field, and that these oscillations are interrupted by collisions. If x represents the amplitude of the molecular oscillation, Lorentz assumed that immediately following a collision the mean values of x and $\dot{x}$, averaged over a sufficiently large number of molecules, are zero; it follows from this that oscillation energy is dissipated and distributed among the various degrees of freedom available, so that energy is absorbed from the applied electromagnetic field. Lorentz then deduced an expression for the power absorption coefficient α in terms of the frequency of the applied field ν and the natural frequency of molecular oscillation ν_0.

The Lorentz expression was modified by Van Vleck and Weisskopf (1945). They pointed out that if ν_0 approaches zero, the absorption coefficient should approach the expression found by Debye (1925) for non-resonant absorption. The Lorentz expression does not do this, and Van Vleck and Weisskopf showed that the discrepancy could be removed by assuming that the mean values of x and $\dot{x}$ immediately following a collision are not zero but are related to the instantaneous value of the applied field by a Boltzmann factor.

In both formulations, an expression for x at time t is found for those molecules that experienced their last collisions at time $t_0 = t-\theta$; it is then assumed that collisions occur completely at random, so that the probability that the last collision before t occurred in $(t-\theta-\delta\theta, t-\theta)$ is

$$\tau^{-1}\exp(-\theta/\tau)\,\delta\theta\,,$$

---

* Department of Physics, University of Queensland, St. Lucia, Brisbane, Qld. 4067.

Aust. J. Phys., 1968, **21**, 13–20

where τ is the mean interval between collisions and is assumed to be constant for a given gas at a constant pressure. On integrating with respect to θ, it then follows that the absorption coefficient α at frequency ν is given by

$$\alpha(\nu) = \frac{Ne^2}{mc}\left(\frac{\nu}{\nu_0}\right)^2 f(\nu,\nu_0)\,\Delta\nu\,, \tag{1}$$

where

$$f(\nu,\nu_0) = \left(\frac{1}{(\nu-\nu_0)^2+(\Delta\nu)^2}+\frac{1}{(\nu+\nu_0)^2+(\Delta\nu)^2}\right) \tag{2}$$

and $\Delta\nu = (1/2\pi\tau)$ is the line-width parameter.

Van Vleck and Weisskopf showed that this result can be generalized to a quantum mechanical form in which the shape factor $f(\nu,\nu_0)$ is preserved. If, as is frequently the case, $\nu_0 \gg \Delta\nu$ the second term in the parentheses in equation (2) may be neglected; for such a spectral line the half-widths to the half-power points and to the points of steepest slope are $\Delta\nu$ and $\Delta\nu/\sqrt{3}$ respectively.

This has formed the basis for much of the interpretation of experimental measurements of the widths of spectral lines in the microwave region; selected references will be found in the paper by Rinehart, Legan, and Lin (1965). Either the width between the half-power points, or, in the case of the work of Rinehart, Legan, and Lin, the width between the points of steepest slope, is measured for various gas pressures and the mean intervals between collisions are calculated from the results; these are then discussed in terms of collision processes. Microwave spectral lines are particularly suitable for this type of investigation since, at the comparatively low frequencies involved, natural or radiation broadening is negligible and, at pressures above a few millitorr, collision broadening is far greater than the only other significant mechanism, namely Doppler broadening (Parsons and Roberts 1965).

The mean intervals between collisions are usually interpreted in terms of equivalent "hard-sphere" collision diameters, and these are significantly greater than the corresponding diameters deduced from transport phenomena. As an example, the collision diameter of methyl chloride deduced from viscosity data is 5 Å, while that deduced from the self broadening of the $J = 0 \rightarrow 1$ line in the rotational spectrum is 15·9 Å (Roberts and Parsons 1966). This is presumably because in transport phenomena the energy of interaction on collision must be of the order of kT, while for the interruption of radiation it is of the order of $h\nu$, and in the microwave region for gases at room temperature $h\nu \ll kT$.

The purpose of this paper is to point out that the expression (2) for the shape factor is valid only if τ is constant for all the molecules in a gas at a given pressure. This will be so if the collision cross section is inversely proportional to the relative speed of the colliding molecules and, under the assumption of weak collisions such that the interacting molecules pass along straight line paths with constant velocities, this will be true (Anderson 1949; Tsao and Curnutte 1960). It will not be so for hard-sphere molecules, since those moving with high speeds will on the average experience more collisions per second than the slower ones, and the following analysis shows that under these circumstances the line shape is modified so that the half-width between the half-power points is $5\cdot4\%$ less than $\overline{\Delta\nu}$, while between the points of steepest slope it is $9\cdot7\%$ less than $\overline{\Delta\nu}/\sqrt{3}$, where $\overline{\Delta\nu}$ is the mean value of $\Delta\nu$ averaged over all the molecules. Since half-widths may be determined experimentally to an accuracy of 2%, the effect may be significant; and if the shape of a complete spectral line can be measured to an accuracy of this order, it may be necessary to interpret the results in terms of collisions between molecules that behave as hard-sphere cores (possibly with diameters of the order of those deduced from transport phenomena) surrounded by "soft-sphere" regions for which the collision probability is inversely proportional to the relative speed of the colliding molecules.

II. Calculation of Line Shape

(a) *Hard-sphere Molecules*

The calculation of the mean interval between collisions $\bar{\tau}$ averaged over all the molecules may begin from the expression

$$\bar{v}_{\mathrm{r}}\,\bar{\tau}\sigma N = 1\,, \tag{3}$$

where $\bar{v}_{\mathrm{r}}$ is the mean relative speed of the molecules, σ the cross section, and N the number of molecules per unit volume (Present 1958); for a Maxwellian distribution of particles of mass m at a temperature T

$$\bar{v}_{\mathrm{r}} = 4(kT/\pi m)^{\frac{1}{2}}\,. \tag{4}$$

Now, however, consider those molecules whose speeds, relative to the laboratory frame of reference, lie in the range $(v, v+\delta v)$. It is shown in the Appendix that the mean speed of these molecules relative to the remainder is

$$v_{\mathrm{r}} = 4(kT/\pi m)^{\frac{1}{2}}F(\beta)\,,$$

where

$$F(\beta) = \frac{1}{\sqrt{2}}\left(\tfrac{1}{2}\exp(-\beta^2) + (\beta + 1/2\beta)\int_0^\beta \exp(-y^2)\,\mathrm{d}y\right)$$

and

$$\beta = v(m/2kT)^{\frac{1}{2}}.$$

It follows from (3) that, if τ_v is the mean interval between collisions involving at least one molecule whose speed lies in the range $(v, v+\delta v)$, then

$$\tau_v/\bar{\tau} = \bar{v}_{\mathrm{r}}/v_{\mathrm{r}}\,, \tag{5}$$

and hence the corresponding line-width parameter is

$$\begin{aligned}\Delta\nu_v &= \overline{\Delta\nu}(v_{\mathrm{r}}/\bar{v}_{\mathrm{r}})\\ &= \overline{\Delta\nu}F(\beta)\,, \qquad \text{where} \qquad \overline{\Delta\nu} = 1/2\pi\bar{\tau}\,.\end{aligned}$$

The contribution $\delta\alpha$ to the absorption coefficient is then found from (1) on replacing N. by

$$\delta N_v = 4\pi N\left(\frac{m}{2\pi kT}\right)^{3/2} v^2 \exp\left(-\frac{mv^2}{2kT}\right)\delta v\,; \tag{6}$$

and hence, on integrating over all values of v and making the assumption $\nu_0 \gg \overline{\Delta\nu}$ so that the second term in equation (2) may be neglected, it follows that

$$\alpha(\nu) = A\left(\frac{\nu}{\nu_0}\right)^2 \overline{\Delta\nu} \int_0^\infty \frac{\beta^2 F(\beta)\exp(-\beta^2)}{(\nu-\nu_0)^2+\{\overline{\Delta\nu}\,F(\beta)\}^2}\,\mathrm{d}\beta\,, \tag{7}$$

where $A = 4Ne^2/mc\pi^{\frac{1}{2}}$. The quantum mechanical expression for A may be found from equation (2) of Van Vleck and Weisskopf (1945), but the dependence of α on ν is still described by the above equation (7). In this equation, it is convenient to introduce the dimensionless parameter $u = (\nu-\nu_0)/\overline{\Delta\nu}$; it then becomes

$$\alpha(u) = (A/\overline{\Delta\nu})(\nu/\nu_0)^2 G(u)\,.$$

where the shape function $G(u)$ is given by

$$G(u) = \int_0^\infty \frac{\beta^2 F(\beta)\exp(-\beta^2)}{u^2+\{F(\beta)\}^2}\,\mathrm{d}\beta\,. \tag{8}$$

This was evaluated numerically for a series of values of u with the aid of a GE225 computer, and the results are plotted in Figure 1. It has a maximum when $u = 0$, and falls to half the maximum value when $u = \pm 0\cdot 946$.

The points of steepest slope, which are of particular interest since their frequency separation may be measured directly, are given by the solutions of

$$\mathrm{d}^2G/\mathrm{d}u^2 = 0\,.$$

This equation was solved numerically and the result was $u = \pm 0\cdot 521$. The term $(\nu/\nu_0)^2$ in the expression for α may be equated to unity without significant error provided $\nu_0 \gg \Delta\nu$; thus if a spectral line of frequency $\nu_0 = 30$ GHz and width $\overline{\Delta\nu} = 500$ kHz is to be studied in the frequency range $\nu_0 \pm 3\overline{\Delta\nu}$, for example, $(\nu/\nu_0)^2$ will not differ from unity by more than 1 part in 10^4.

(*b*) *"Soft" Molecules*

If the result of Anderson (1949) that $\sigma \propto v_r^{-1}$ is assumed to be valid for all collisions, irrespective of the distance of closest-approach of the molecules, it follows from equation (3) that $\tau_v = \bar{\tau}$ and hence that τ_v is independent of v. The absorption coefficient is then given directly by equation (1), and may be expressed in the form

$$\alpha(u) = \frac{A}{\overline{\Delta\nu}}\left(\frac{\nu}{\nu_0}\right)^2 \tfrac{1}{4}\pi^{\frac{1}{2}}\left(\frac{1}{u^2+1}\right). \tag{9}$$

In order to facilitate comparison with equation (8), the shape function

$$H(u) = \tfrac{1}{4}\pi^{\frac{1}{2}}\left(\frac{1}{u^2+1}\right)$$

is also plotted as a function of u in Figure 1. It has a maximum when $u = 0$ but falls to half the maximum value when $u = \pm 1$; this implies a half-width of $\overline{\Delta\nu}$, as has been already stated. The points of steepest slope are given by the solutions of

$$\mathrm{d}^2H/\mathrm{d}u^2 = 0\,,$$

which are $u = 0\cdot 577\overline{\Delta\nu}$.

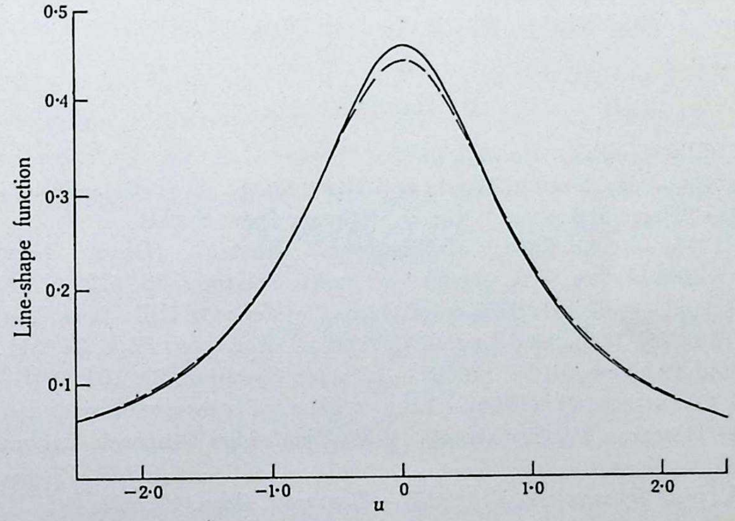

Fig. 1.—The line-shape function $G(u)$ for hard-sphere interactions (full curve) is compared with the Lorentz shape $H(u)$ (dashed curve). The abscissa u represents the dimensionless parameter $(\nu-\nu_0)/\overline{\Delta\nu}$.

III. Conclusions

It has been shown that the predicted shape of a collision-broadened spectral line depends on the assumptions made about the nature of the collision processes involved. If the cross section for line-broadening collisions varies inversely as the relative speed of the colliding molecules, the line shape is described by the Van Vleck–Weisskopf modification of the Lorentz theory; if not, departures from the Van Vleck–Weisskopf shape may be expected, and in the limiting case of hard-sphere collisions, these departures are of the order of several per cent. While it is not for a moment suggested that molecules do, in fact, behave entirely as hard spheres, it is suggested that some deviations from the Van Vleck–Weisskopf shape may occur, and hence it would be of interest if the shape of a collision-broadened line could be measured to an accuracy of, for example, 1%. A line in the microwave region of the spectrum appears most suitable for such an investigation, since at pressures above a few millitorr collisions provide the only line-broadening mechanism of significance. A line broadened by non-polar foreign gas collisions would be more appropriate for study than a self-broadened line, since in the former case the collision diameters for line broadening are not greatly in excess of those deduced from transport phenomena (Burton *et al.* 1965; Roberts and Parsons 1966), and hence the effect of a "hard-sphere core" may be more apparent. This may not now be beyond the range of possibility, since existing microwave line-width spectrometers are capable of an accuracy of better than 2%. However, such instruments merely measure one parameter of a spectral line (the half-width); the development of an instrument for measuring the complete line shape presents difficult experimental problems but these appear worthy of investigation.

IV. ACKNOWLEDGMENT

This investigation was performed as part of the microwave research programme of the University of Queensland, which receives support from the Australian Research Grants Committee.

V. REFERENCES

ANDERSON, P. W. (1949).—*Phys. Rev.* **76**, 647.

BURTON, C. H., NOON, J. H., LASICH, W. B., and PARSONS, R. W. (1965).—*Aust. J. Phys.* **19**, 283.

DEBYE, P. (1925).—"Polar Molecules." Ch. 5. (Dover: New York.)

LORENTZ, H. A. (1915).—"The Theory of Electrons." Note 57. (Dover: New York.)

PARSONS, R. W., and ROBERTS, J. A. (1965).—*J. molec. Spectrosc.* **18**, 412.

PRESENT, R. D. (1958).—"Kinetic Theory of Gases." (McGraw Hill: New York.)

RINEHART, E. A., LEGAN, R. L., and LIN, C. C. (1965).—*Rev. mod. Phys.* **36**, 511.

ROBERTS, J. A., and PARSONS, R. W. (1966).—*J. molec. Spectrosc.* **20**, 195.

TSAO, C. J., and CURNUTTE, B. (1960).—Line widths of pressure broadened spectral lines. Geophysical Research Papers No. 69, A. F. Cambridge Research Laboratories, U.S. Air Force, Bedford, Mass.

VAN VLECK, J. H., and WEISSKOPF, V. (1945).—*Rev. mod. Phys.* **17**, 227.

APPENDIX

Consider first a problem in geometry. Suppose that a sphere of radius a has a large number of points uniformly distributed over its surface and that one of these points is P. Suppose further that a second sphere, concentric with the first but of radius a_1, has points, one of which is Q_t, uniformly distributed over its surface, there being a large number n of points per unit surface area. It is required to find the mean distance PQ_t averaged over all the points Q_t. Using the nomenclature of Figure 2, this mean distance $\bar{s}$ will be defined as

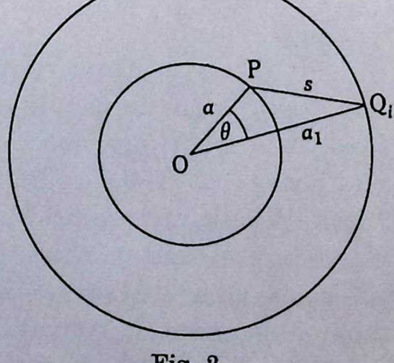

Fig. 2

$$\bar{s} = \lim_{n\to\infty} (4\pi a_1^2 n)^{-1} \sum PQ_t$$

$$= (4\pi a_1^2)^{-1} \int_0^\pi 2\pi a_1^2 s \sin\theta \, d\theta .$$

On writing $s^2 = a^2+a_1^2-2aa_1\cos\theta$, this becomes

$$\bar{s} = (2aa_1)^{-1}\int_{s_1}^{s_2} s^2\,\mathrm{d}s\,,$$

where the limits of integration are

$$s_1 = a_1-a \qquad \text{and} \qquad s_2 = a_1+a \qquad \text{if} \quad a < a_1\,,$$

or

$$s_1 = a-a_1 \qquad \text{and} \qquad s_2 = a+a_1 \qquad \text{if} \quad a > a_1\,.$$

Hence

$$\bar{s} = a_1+a^2/3a_1 \qquad \text{if} \quad a < a_1$$

and

$$\bar{s} = a+a_1^2/3a \qquad \text{if} \quad a > a_1\,.$$

Now consider a large number of molecules whose speeds are distributed according to the Maxwellian function, equation (6). It follows from the above analysis that the mean speed of all those molecules whose speeds are v in the laboratory frame relative to those whose speeds are v_1 in the same frame will be $v_1+v^2/3v_1$ if $v < v_1$ and $v+v_1^2/3v$ if $v > v_1$. On averaging over all values of v_1, the result is

$$v_{\mathrm{r}} = \frac{1}{N}\left(\int_0^v (v+v_1^2/3v)\,\mathrm{d}N_{v_1} + \int_v^\infty (v_1+v^2/3v_1)\,\mathrm{d}N_{v_1}\right),$$

where

$$\mathrm{d}N_{v_1}/\mathrm{d}v_1 = 4\pi N(m/2\pi kT)^{3/2}\exp(-mv_1^2/2kT)\,.$$

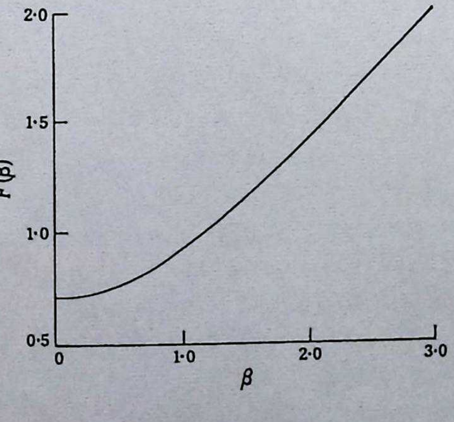

Fig. 3.—Relative speed distribution function $F(\beta)$ plotted as a function of the dimensionless parameter $\beta = v(m/2kT)^{\frac{1}{2}}$.

Successive integration by parts then gives the expression for v_{r} used in the text, namely

$$v_{\mathrm{r}} = 2\left(\frac{2kT}{\pi m}\right)^{\frac{1}{2}}\left(\tfrac{1}{2}\exp(-\beta^2)+(\beta+1/2\beta)\int_0^\beta \exp(-y^2)\,\mathrm{d}y\right)$$

$$= 4(kT/\pi m)^{\frac{1}{2}}F(\beta)\,, \qquad \text{(A1)}$$

where $\beta = v(m/2kT)^{\frac{1}{2}}$.

In Figure 3, $F(\beta)$ is plotted as a function of β. When $v = 0$, $v_r = 2(2kT/\pi m)^{\frac{1}{2}}$, and this is the mean speed relative to the laboratory frame of reference; for very large values of v, $v_r \rightarrow v$ and this also is as expected. As a further check of the validity of equation (A1), the quantity

$$\int_0^\infty \beta^2 F(\beta) \exp(-\beta^2)\, \mathrm{d}\beta$$

was evaluated numerically, and gave a result equal to $\frac{1}{4}\pi^{\frac{1}{2}}$; this then yields the value $4(kT/\pi m)^{\frac{1}{2}}$ for the mean relative speed averaged over the whole distribution, in agreement with equation (4).

7794

R
530.5
M48A
V. 21

CALCULATION OF SURFACE ENERGY AS A FUNCTION OF ORIENTATION FOR CUBIC CRYSTALS

By J. F. Nicholas*

[*Manuscript received August* 9, 1967]

Summary

The surface energies of face-centred and body-centred cubic crystals have been calculated on the assumption that the atoms interact with pairwise potentials of either Morse or Mie type. The calculations take into account interactions between all neighbours and have been carried through for about 50 crystallographically distinct orientations of the surface. No allowance has been made for relaxation of the surface atoms. Stereographic contour plots of the surface energy are presented for four Morse and six Mie potentials in each structure. It is shown that, for all these potentials, a good approximation to the results can be obtained by *counting* only the numbers of nearest and next-nearest neighbour bonds that are broken and associating empirically determined energies with each of these.

I. Introduction

In principle, if the atoms in a crystal can be regarded as interacting with a particular pairwise potential, then it is possible to calculate the energy involved in creating particular surfaces by summing the energies associated with all atomic pairs that are split up in this creation. The literature contains many calculations of this type, most of which have been limited to a few different surfaces (e.g. Stranski and Suhrmann 1947; Benson and Claxton 1964; Drechsler and Liepack 1965) and/or to an interatomic potential that has been neglected for all but the nearest few shells of neighbours (e.g. Stranski and Suhrmann 1947; Mackenzie, Moore, and Nicholas 1962; Drechsler and Liepack 1965).

The present paper reports calculations of the surface energy for 50–60 crystallographically distinct orientations in face-centred (f.c.c.) and body-centred (b.c.c.) cubic crystals, using potentials of both Mie (Lennard–Jones) and Morse types, and taking account of the interactions of *all* neighbours. No allowance has been made for any relaxation that may occur among the surface atoms to minimize the surface energy, but a study of this effect will be reported later.

II. Method of Calculation

With pairwise interactions, it is convenient to say that each atom is linked to each other atom by a "bond" and to associate an energy with each such bond. When an infinite crystal is divided into two parts, a number of these bonds will be "broken", i.e. will be increased to infinite length, and the energy associated with each new surface can be computed as one-half of the increase in energy associated with the breaking of these bonds. If $\phi(r)$ is the chosen interaction potential for two atoms separated by a distance r and a particular bond is specified by the interatomic vector

---

* Division of Tribophysics, CSIRO, University of Melbourne, Parkville, Vic. 3052.

Aust. J. Phys., 1968, **21**, 21–34

$\mathbf{u}_i$ of magnitude u_i, then the breaking of this bond will contribute to each surface an energy

$$E_i = \tfrac{1}{2}\{\phi(\infty)-\phi(u_i)\}. \tag{1}$$

It is customary to choose the origin of ϕ so that $\phi(\infty) = 0$ and we then have

$$E_i = -\tfrac{1}{2}\phi(u_i). \tag{1a}$$

In the present work, the division is assumed to occur along a mathematical plane of a particular orientation specified by the normal vector $\mathbf{h}$ of magnitude h, and the energy computed is then treated as the surface energy $\gamma(\mathbf{h})$ for this orientation. If $n(\mathbf{u}_i)$ is the number of bonds with original vector $\mathbf{u}_i$ that are broken per unit area of surface, then

$$\gamma(\mathbf{h}) = \sum E_i\, n(\mathbf{u}_i), \tag{2}$$

where the summation is over all interatomic vectors within the crystal. Following Mackenzie, Moore, and Nicholas (1962), we can write

$$\left.\begin{aligned} n(\mathbf{u}_i) &= \mathbf{h}.\mathbf{u}_i/\Omega h && \text{if } \mathbf{h}.\mathbf{u}_i \geqslant 0, \\ &= 0 && \text{if } \mathbf{h}.\mathbf{u}_i \leqslant 0, \end{aligned}\right\} \tag{3}$$

where Ω is the volume of crystal per atom. Thus equation (2) can be rewritten as

$$\gamma(\mathbf{h}) = (1/\Omega h)\sum E_i\,\mathbf{h}.\mathbf{u}_i, \tag{4}$$

where all terms are calculable for any given interaction potential and the sum covers all $\mathbf{u}_i$ with positive $\mathbf{h}.\mathbf{u}_i$.

(*a*) *Potentials Used*

The interacting potentials used, all having a minimum of $-\phi_0$ at a distance r_0, have been either

(1) of Morse type, that is,

$$\phi(r) = \phi_0[\{1-\exp a(1-r/r_0)\}^2-1], \tag{5}$$

where a is the dimensionless Morse constant, or

(2) of Mie (Lennard–Jones) type, that is,

$$\phi(r) = \phi_0\{n(r_0/r)^m - m(r_0/r)^n\}/(m-n), \tag{6}$$

where m and n ($> m$) are the exponents of the attractive and repulsive parts of the potential.

As is usual in these calculations, the constants in the potential are adjusted in all cases to minimize, for a perfect infinite crystal, the total lattice energy computed as a sum of pairwise interactions. This means that for a given a or (m, n) the ratio of r_0 to the lattice parameter is determined by calculations of lattice energy. This is discussed in some detail in Drechsler and Nicholas (1967*a*), where values of this ratio are given for a variety of Morse and Mie potentials.

Figure 1 shows some of the potentials considered, plotted against the positions of various neighbours. This figure is drawn exactly for the f.c.c. structure, but the scale added for b.c.c. is still accurate to within 0·5% for the potentials considered here, since, if we write r_1^* for the nearest neighbour distance in the perfect crystal,

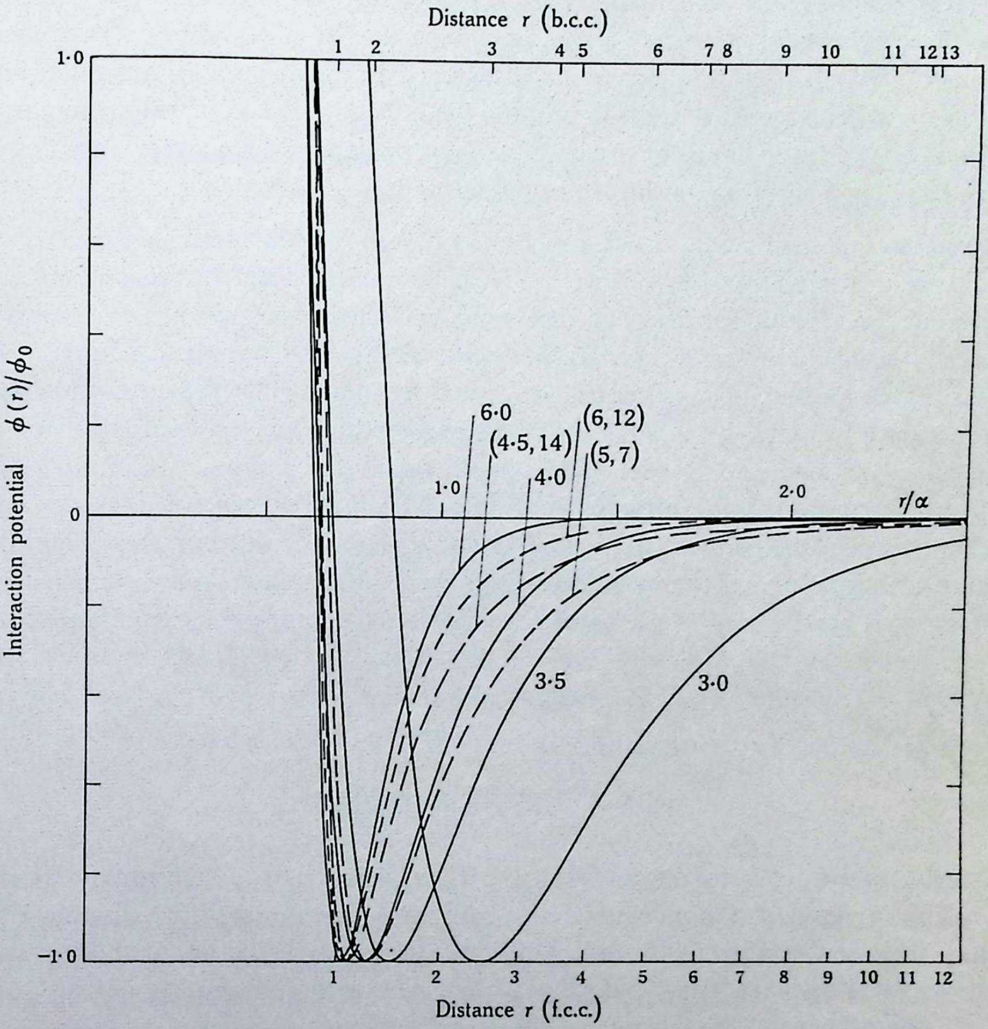

Fig. 1.—Plots of some Morse potentials (full lines labelled with Morse constants) and some Mie potentials (dashed lines with (m, n)). Plots of the (6, 10) and (6, 14) potentials would lie to the right and left of the (6, 12) plot; the (4·5, 8) potential is almost coincident with the (5, 7) potential, being one linewidth to the right for most of its length. The linear scale across the centre of the figure has a unit equal to the lattice parameter α of an f.c.c. crystal and the values of r_0 (the minimum of the interaction potential) have been chosen so as to minimize the lattice energy of such a crystal. The numbers at the bottom of the figure indicate the distances to the first 12 shells of neighbours in such an f.c.c. crystal and those at the top show the positions of the first 13 shells in a b.c.c. crystal.

we find, for example, that

$$\frac{(r_1^*/r_0)_{\text{f.c.c.}}}{(r_1^*/r_0)_{\text{b.c.c.}}} = \left.\begin{array}{ll} 1\cdot 029 & \text{for } a = 3\,, \\ 1\cdot 026 & \text{for } a = 5\,, \\ 1\cdot 025 & \text{for } (m, n) = (5, 7)\,, \\ 1\cdot 019 & \text{for } (m, n) = (6, 14)\,. \end{array}\right\} \qquad (7)$$

The b.c.c. scale is drawn for a value of this ratio of 1·024.

The constants ϕ_0 and either a or (m, n) can be chosen in two ways. In the first, the surface energies are computed for a whole range of values of these constants and these are then compared with some experimental data to determine the appropriate values for a particular material. This approach has been adopted in Drechsler and Nicholas (1967*b*), where measurements of the equilibrium shape of annealed crystals have been used to predict possible values for a or (m, n). Naturally, an approach based on equilibrium shapes or any other property dependent only on relative values of surface energy can give no information about the scale factor ϕ_0.

The second approach, which has been adopted in this paper, is to select appropriate values for the constants on the basis of other data before calculating the surface energy. Thus, for Mie potentials the calculations reported are those for the commonly used Lennard–Jones $(6, 12)$ form of the Mie potential, for the closely related $(6, 10)$ and $(6, 14)$ potentials, and for a few potentials whose significance has been suggested elsewhere (Fürth 1945; Drechsler and Nicholas 1967*b*). For Morse potentials, Girifalco and Weizer (1959) have calculated values of ϕ_0 and a (D and αr_0 in their notation) for a variety of metals using experimental values of sublimation energy and compressibility. Surface energy calculations have been carried through for all values of the constants given by Girifalco and Weizer, and a selection is reproduced here. In all these cases, the Morse constant is between 3 and 5.

(*b*) *Method of Summation*

Equation (4) can be rewritten as

$$\gamma(\mathbf{h}) = (1/\Omega h)\sum_j E_j(\mathbf{h}.\sum_k \mathbf{u}_k), \tag{8}$$

where the sum over k covers all bonds, with positive $\mathbf{h}.\mathbf{u}_k$, that have a particular magnitude u_j, and the sum over j covers all possible interatomic distances in the crystal. Physically, this means first summing (with k) over all bonds linking an atom to the atoms in a particular shell of neighbours and then summing (with j) over all shells. For later use, it is convenient to rewrite equation (8) as

$$\gamma(\mathbf{h}) = \sum_j \mu_j(\mathbf{h})\, E_j, \tag{9}$$

where

$$\mu_j(\mathbf{h}) = (1/\Omega h)\mathbf{h}.\sum_k \mathbf{u}_k \tag{9a}$$

is a "multiplicity factor" for the surface energy term associated with a broken bond from the jth shell.

For Morse potentials, the sums were evaluated directly using 300 shells of neighbours, which is sufficient to ensure that the neglected terms, even in the worst case of $a = 3$, have no effect on the eighth significant digit in the energy values. This number of shells corresponds to considering all bonds whose length is less than 17–18 times the distance between nearest neighbours.

For Mie potentials, the sums were evaluated directly for the first 500 shells of neighbours, i.e. for bond lengths up to 22–23 times the interatomic distance. The contribution from more distant neighbours was then estimated as an integral and added to the direct sum. For the exponent 6, this integral correction was of the order of 10^{-3} of the direct sum but rapidly became negligible for higher exponents. In all cases, the sums including the integral correction may be expected to be accurate to at least four digits.

Some of the calculations were checked by evaluating the sums of type (4) in the order adopted by Benson and Claxton (1964), i.e. in the order of increasing size of $\mathbf{h}.\mathbf{u}_i$. This method is slower than that generally adopted here since it involves more frequent evaluation of $\phi(u_i)$, but it does provide the additional information that is essential for calculations in which the surface atoms are allowed to relax. It also allows the Mie sums to be transformed into rapidly convergent series for small exponents and for orientations where the lattice planes parallel to the surface are densely packed, namely (100), (110), and (111). However, since the convergence of the transformed series falls off seriously for surfaces with higher indices, direct summation has been preferred in the present work.

(*c*) *Consideration of Oscillatory Potentials*

Friedel (1962), Harrison (1963, 1964, 1965), Johnson, Hutchinson, and March (1964), and Enderby and March (1965) have suggested that the real interatomic potential is described better by an oscillatory function rather than by one of either a simple Morse or Mie type. Although potentials proposed for solids are in general not available in a convenient analytic form, Johnson, Hutchinson, and March prescribe for liquid metals a pair potential of the form

$$\phi(r) = A(r_0/r)^3 \cos\{2k(r+\beta)\} \exp(-\alpha r)\,, \tag{10}$$

where A, r_0, k, β, and α are constants. They further specify the values of these constants for Li, Na, K, Rb, Cs, Al, and Pb, thus making it formally possible to calculate surface energies by use of equations (8) or (9). However, such calculations showed that γ would always be negative for Li, that α was negative for Na thus making all sums divergent, and that the ratio $\gamma_{\max}/\gamma_{\min}$ would be more than 3 for Rb. Since such results appear physically unreasonable, no further calculations were carried out with oscillatory potentials. In fact, it would seem unprofitable to pursue such calculations further until much better forms for the appropriate interatomic potential in the solid are available.

III. RESULTS

The results of the calculations are most conveniently displayed as contour plots of γ within a unit stereographic triangle. A selection of such plots is shown in Figure 2 for f.c.c. crystals and in Figure 3 for b.c.c. crystals. All results have been normalized to unity at (111) in Figure 2 and at (110) in Figure 3, the necessary normalization factors being shown in the tables to the figures.

Figures 2(*j*) and 3(*j*) show the orientations for which calculations were, in general, made and these give an indication of the accuracy with which the contours can be drawn. In order to define γ more clearly near the corners of the triangle, subsidiary calculations were carried out for sets of 25 extra orientations within some 7° of each corner. Such orientations are not marked on Figures 2(*j*) or 3(*j*), nor are the results used in the calculations described in the next section.

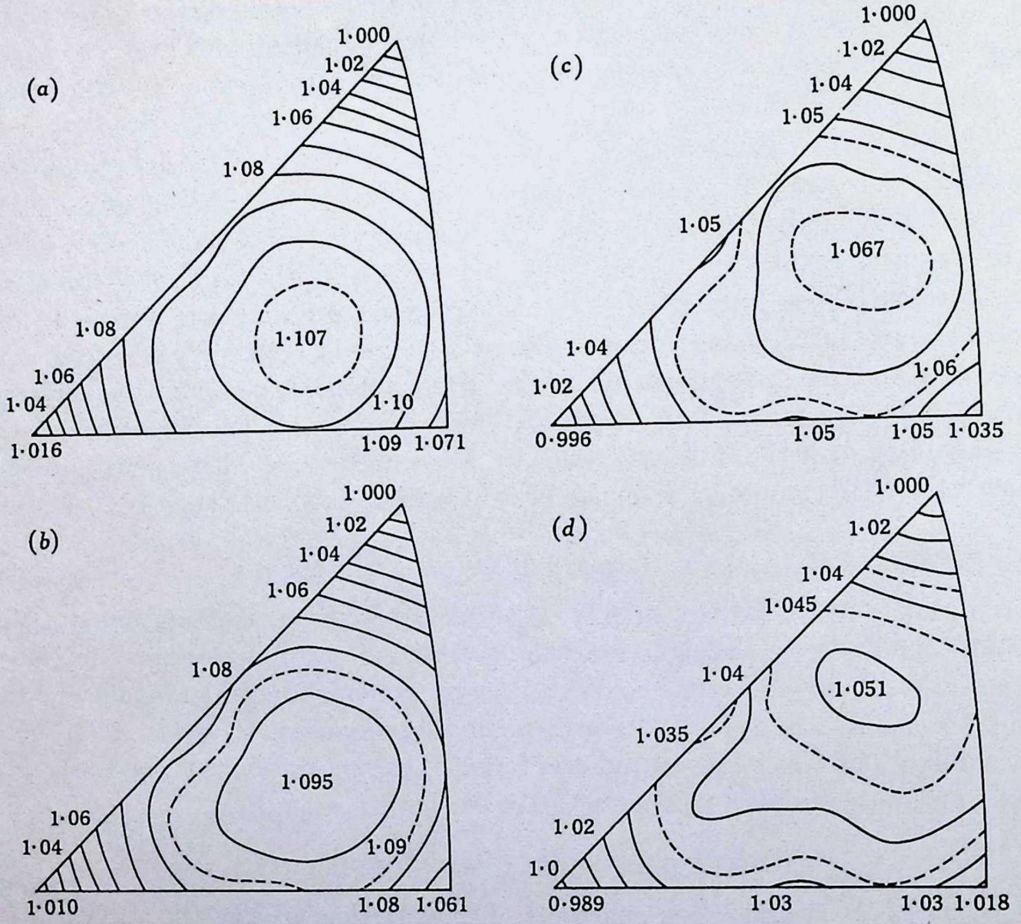

Plot	Symbol	$\frac{\gamma(111)}{\phi_0/\alpha^2}$	ϕ_0/α^2 (erg/cm^2)	Plot	Symbol	$\frac{\gamma(111)}{\phi_0/\alpha^2}$
(*a*)	F 4·419 (Pb)	7·1447	154·2	(*e*)	(4·5, 8) F	43·294
(*b*)	F 4·265 (Ag)	7·7902	320·1	(*f*)	(4·5, 14) F	23·203
(*c*)	F 3·894 (Cu)	10·092	422·0	(*g*)	(5, 7) F	26·861
(*d*)	F 3·680 (Ca)	12·453	83·96	(*h*)	(6, 10) F	8·4533
				(*i*)	(6, 12) F	7·4309
				(*j*)	(6, 14) F	6·8778

Figs. 2(*a*)–2(*j*).—Contour plots of surface energy for f.c.c. crystals using (*a*)–(*d*) Morse potentials and (*e*)–(*j*) Mie potentials. The full contours are drawn at intervals of 0·01 in $\gamma(\mathbf{h})/\gamma(111)$, dashed contours at intervals of 0·005, and dotted contours at intervals of 0·0025. Where a maximum occurs other than at a corner of the triangle, the value shown represents the highest value found in this region. The dots in (*j*) show the particular orientations for which calculations were made. The above table gives for each plot (1) a symbol for the potential (Drechsler and Nicholas 1967*b*) consisting of the value of either *a* or (m, n) together with F to denote f.c.c. and, for Morse potentials, the metal for which this value of *a* is appropriate (Girifalco and Weizer 1959), (2) a normalization factor in which α is the lattice parameter of the crystal, and (3) for the Morse potentials, the value of ϕ_0/α^2 given by Girifalco and Weizer (1959).

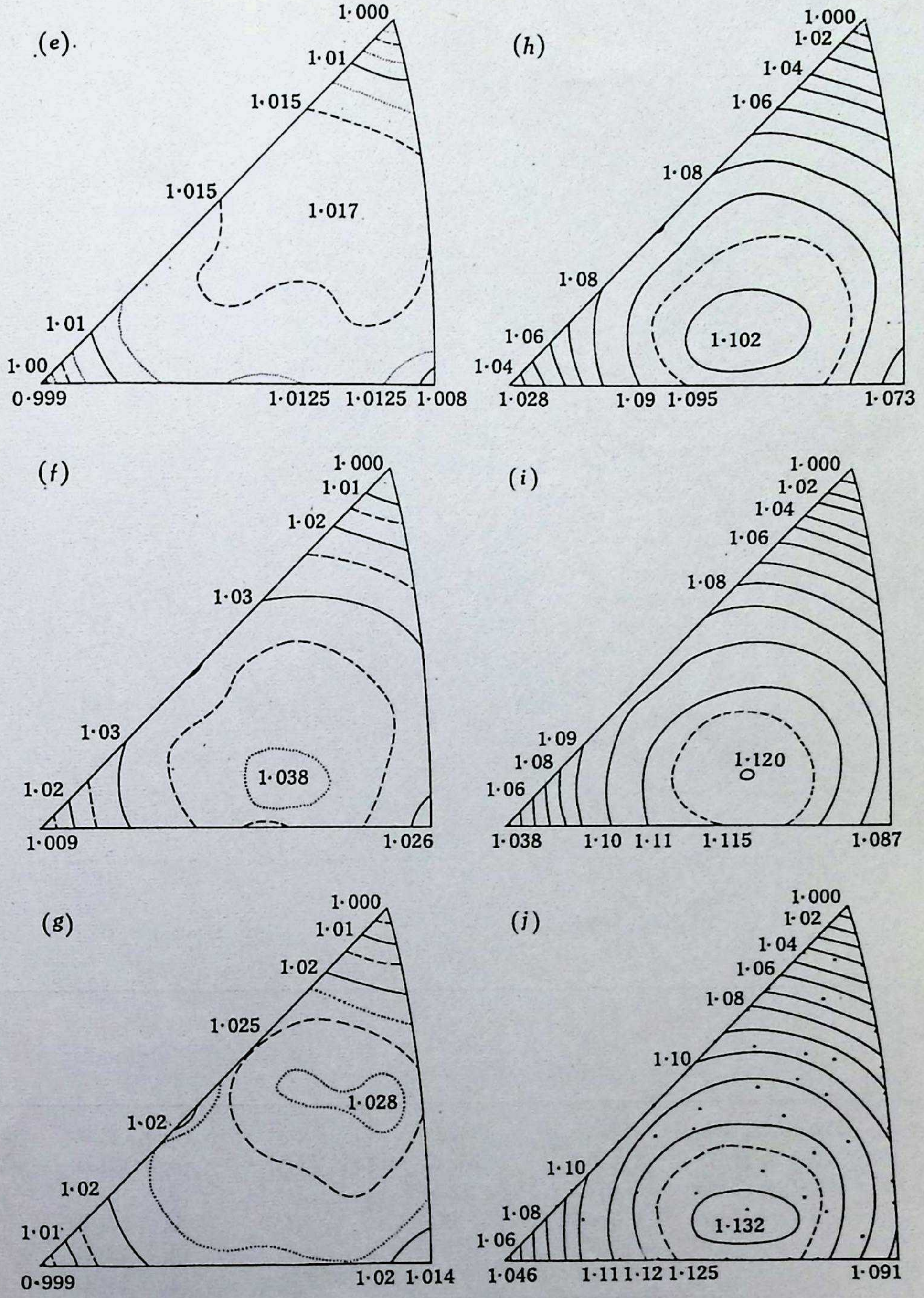

Figs. 2(*e*)–2(*j*)

IV. A Two-term Approximation

As Herring (1951) has pointed out, if the surface energy is calculated by the broken-bond method for any finite set of bonds, a polar plot of the energy will consist of portions of spheres through the origin. Since the present calculations involve the contributions from some thousands of different bonds, the final plots of energy will consist of small portions of so many spheres that the identity of each will be lost.

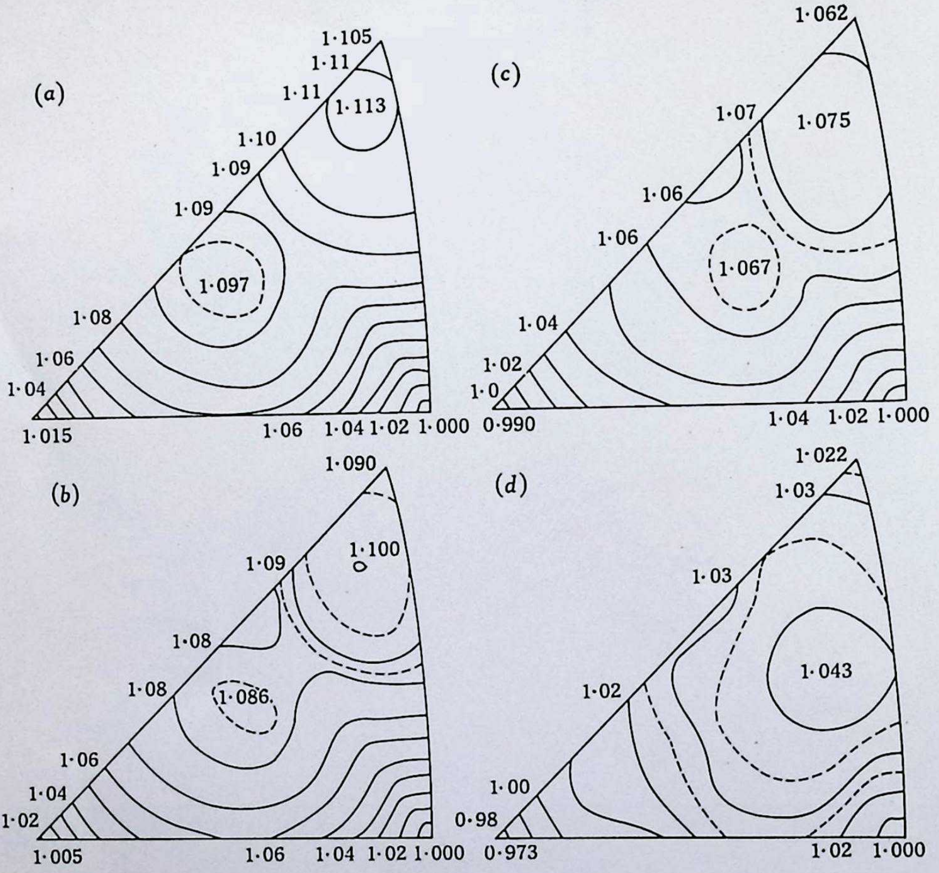

Plot	Symbol	$\frac{\gamma(110)}{\phi_0/\alpha^2}$	ϕ_0/α^2 (erg/cm^2)	Plot	Symbol	$\frac{\gamma(110)}{\phi_0/\alpha^2}$
(*a*)	B 4·488 (Mo)	4·3620	1304	(*e*)	(4·5, 8) B	26·894
(*b*)	B 4·279 (W)	4·8611	1591	(*f*)	(4·5, 14) B	14·155
(*c*)	B 3·951 (Fe)	6·0708	817·1	(*g*)	(5, 7) B	16·722
(*d*)	B 3·530 (Ba)	9·4451	90·41	(*h*)	(6, 10) B	5·2246
				(*i*)	(6, 12) B	4·5602
				(*j*)	(6, 14) B	4·1868

Figs. 3(*a*)–3(*j*).—Contour plots of surface energy for b.c.c. crystals using (*a*)–(*d*) Morse potentials and (*e*)–(*j*) Mie potentials. The full contours are drawn at intervals of 0·01 in $\gamma(\mathbf{h})/\gamma(110)$, dashed contours at intervals of 0·005, and dotted contours at intervals of 0·0025. Where a maximum occurs other than at a corner of the triangle, the value shown represents the highest value found in this region. The dots in (*j*) show the particular orientations for which calculations were made. The above table gives for each plot (1) a symbol for the potential (Drechsler and Nicholas 1967*b*) consisting of the value of either a or (m, n) together with B to denote b.c.c. and, for Morse potentials, the metal for which this value of a is appropriate (Girifalco and Weizer 1959), (2) a normalization factor in which α is the lattice parameter of the crystal, and (3) for the Morse potentials, the value of ϕ_0/α^2 given by Girifalco and Weizer (1959).

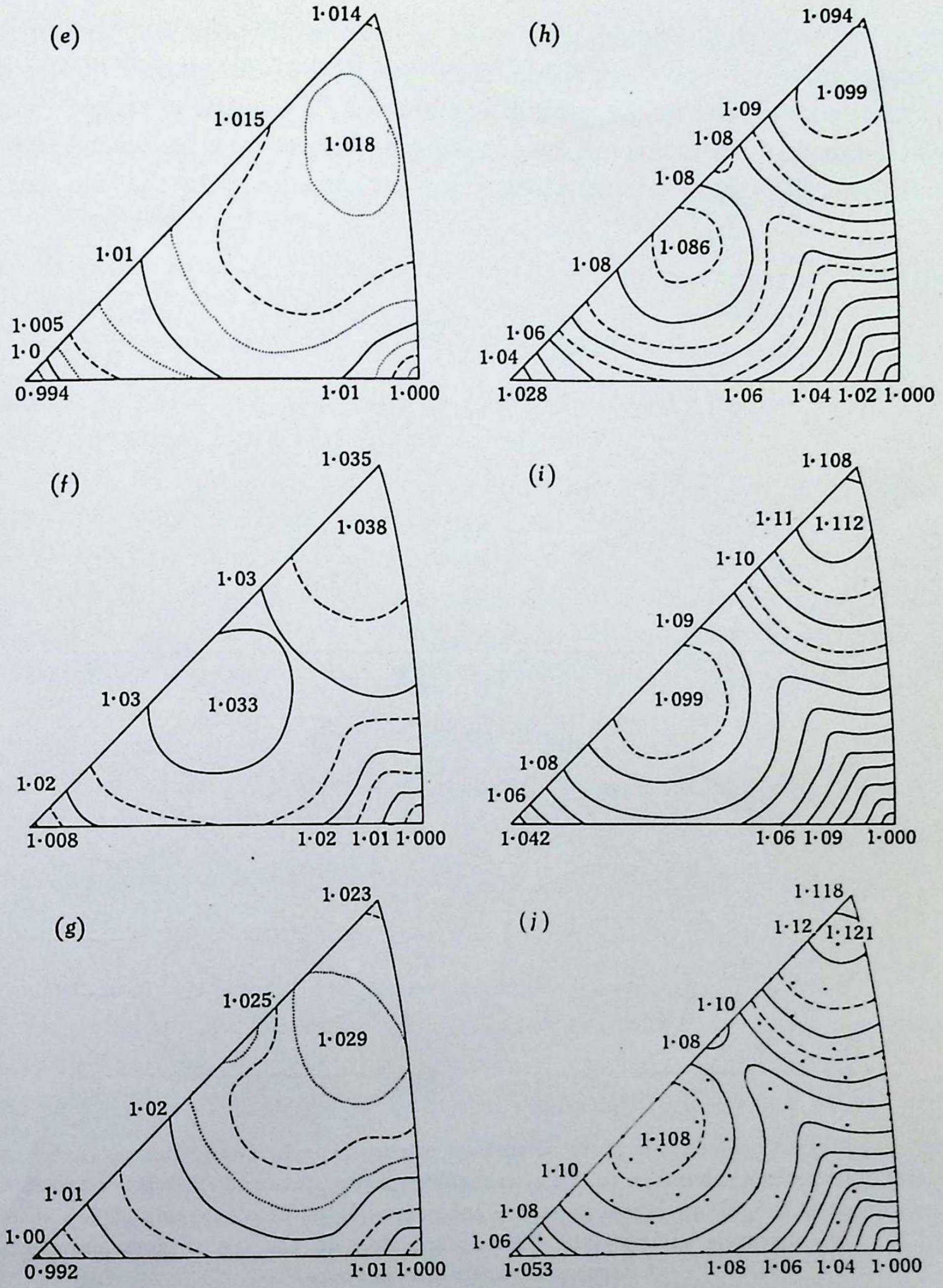

Figs. 3(*e*)–3(*j*)

However, in practice, it appears that the final plots can usually be approximated, within one stereographic triangle, as portions of one sphere for f.c.c. or two spheres for b.c.c. crystals. The implications of this are discussed below.

In broken-bond calculations the first approximation is to assume that only nearest neighbour interactions are significant, i.e. that

$$\phi(r) = \left.\begin{array}{ll} \infty & \text{for } r < r_0, \\ -\phi_0 & \text{for } r = r_0, \\ 0 & \text{for } r > r_0. \end{array}\right\} \qquad (11)$$

In this case, r_0 is both the spacing between nearest neighbours and the position of the minimum interaction energy, while the value of ϕ_0, the energy of the nearest neighbour interactions, is irrelevant for calculations of relative energies. This case has been discussed in some detail by Mackenzie, Moore, and Nicholas (1962), and Figures 4(*a*) and 4(*b*) show contour plots of the surface energy for the two structures.

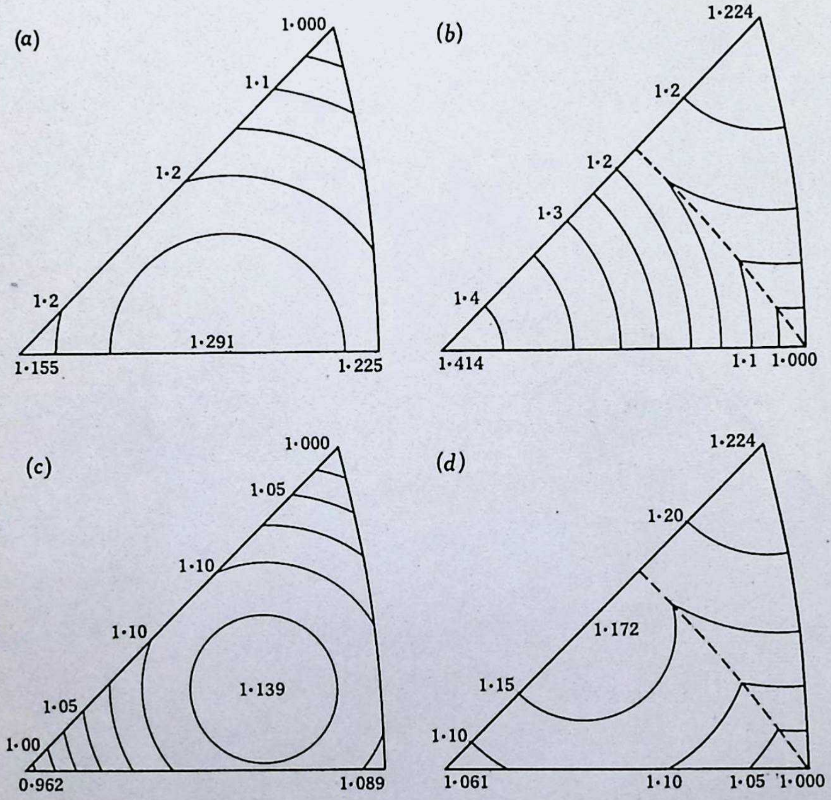

Fig. 4.—Theoretical contour plots of surface energy (1) when only nearest neighbour interactions are considered in (*a*) f.c.c. and (*b*) b.c.c. crystals and (2) when nearest and second-nearest neighbour interactions are considered in (*c*) f.c.c. crystals with $\rho = 0\cdot5$, and (*d*) b.c.c. crystals with $\rho = 1$. The dashed lines in the b.c.c. plots show where corners occur in the contours.

The next approximation is to include second-nearest neighbour interactions as well, i.e. to use a potential of the form

$$\phi(r) = \left.\begin{array}{ll} \infty & \text{for } r < r_1, \\ -\phi_1 & \text{for } r = r_1, \\ 0 & \text{for } r_1 < r < r_2, \\ -\rho\phi_1 & \text{for } r = r_2, \\ 0 & \text{for } r > r_2, \end{array}\right\} \qquad (12)$$

where r_1 and r_2 are the distances between nearest and second-nearest neighbours and ρ measures the relative strengths of the two interactions. This case is also treated by Mackenzie, Moore, and Nicholas (1962),† where it is shown that

(1) for f.c.c. crystals, the polar plot within the unit triangle for which $h \geqslant k \geqslant l \geqslant 0$ consists of portion of the sphere through the origin O with diameter from O along $[2+\rho\ 1+\rho\ \rho]$; and

(2) for b.c.c. crystals, this plot consists of portions of two spheres through O with diameters from O along [111] and $[2+\rho\ \rho\ \rho]$, the intersection of the spheres being along the zone from (110) to (211), that is, the $[1\bar{1}\bar{1}]$ zone.

Figures 4(*c*) and 4(*d*) show contour plots of γ calculated from such potentials with $\rho = 0\cdot 5$ for f.c.c. and $\rho = 1$ for b.c.c. crystals.

A striking feature of the results shown in Figures 2 and 3 is that, although all are markedly different from the nearest neighbour plots in Figures 4(*a*) or 4(*b*), many bear a strong similarity to the appropriate plot in Figures 4(*c*) or 4(*d*), or to a similar plot for a different value of ρ. Thus, it looks as if a good approximation to the results could have been obtained from some treatment involving nearest and second-nearest neighbours only. In other words, a good approximation to $\gamma(\mathbf{h})$ should be given by

$$\gamma^*(\mathbf{h}) = \mu_1(\mathbf{h})\, E_1^* + \mu_2(\mathbf{h})\, E_2^*, \tag{13}$$

with E_1^* and $\rho = E_2^*/E_1^*$ appropriately chosen and $\mu_1(\mathbf{h})$ and $\mu_2(\mathbf{h})$ defined as in equation (9a).

This approximation has been investigated by minimizing the sum

$$S = \sum \{\gamma(\mathbf{h}) - \gamma^*(\mathbf{h})\}^2, \tag{14}$$

taken over all $\mathbf{h}$ in the present set of orientations, by variation in E_1^* and ρ. Table 1 lists the values found for E_1^* and ρ for the same potentials that were considered in Figures 2 and 3.

Figure 5 shows plots of the error in the approximation for two Morse and two Mie potentials. This figure and the errors listed in the last four columns of Table 1 indicate the accuracy of the approximation. For the steep Mie potentials with $m = 6$ and Morse potentials with $a \gtrsim 3\cdot 6$, the maximum error is of the order of 5%, but for the shallower potentials with $m \leqslant 5$ or $a < 3\cdot 6$ the maximum error can rise to 10–12%. However, in all cases, this maximum occurs only in very restricted regions near one or two corners of the stereographic triangle and the average error over the whole triangle is always less than 3%.

Table 1 also lists values of E_1, E_2/E_1, and, for the simplest planes, the fractional contribution to γ that arises from the first two terms in equation (9), namely

$$\{\mu_1(\mathbf{h})\, E_1 + \mu_2(\mathbf{h})\, E_2\}/\gamma(\mathbf{h}).$$

As the influence of second neighbours (measured by E_2/E_1) decreases, this contribution from the first two terms increases and, as would be expected, the errors in the

---

† The final paragraph of the Appendix to this paper contains an error that is most easily corrected by replacing the definition $E_2 = \rho E_1$ by $E_2 = 2\rho' E_1$, and then replacing ρ by ρ' throughout the rest of the paragraph.

TABLE 1

ENERGY RELATIONS FOR POTENTIALS USED IN FIGURES 2 AND 3, TOGETHER WITH PARAMETERS OF THE TWO-TERM APPROXIMATIONS

The last four columns show the percentage error in the approximation at various orientations, the first of these being the largest negative error and the last the largest positive error that is found

Potential	$\{\mu_1(\mathbf{h})E_1+\mu_2(\mathbf{h})E_2\}/\gamma(\mathbf{h})$			E_1	E_2/E_1	ρ	E_1^*	Error (%) in Approximation at:			
	(100)	(111)	(110)					(100)	(111)	(110)	~(531)
					Face-centred Cubic Crystals						
$(m,n)=(4{\cdot}5,\ 8)$	0·078	0·093	0·092	0·2687	1·1546	0·5680	4·2326	−11·6	−6·6	−0·2	3·8
$(4{\cdot}5, 14)$	0·184	0·189	0·203	0·4418	0·4336	0·5000	2·1013	−10·3	−5·9	−0·2	3·3
$(5,\ 7)$	0·134	0·155	0·156	0·2952	1·0409	0·5662	2·3306	−10·8	−5·8	0·1	3·7
$(6,\ 10)$	0·508	0·519	0·542	0·4700	0·3484	0·3843	0·8543	−6·3	−3·1	0·4	2·3
$(6,\ 12)$	0·571	0·578	0·603	0·4817	0·2862	0·3390	0·7794	−5·5	−2·7	0·4	2·0
$(6,\ 14)$	0·610	0·613	0·639	0·4875	0·2488	0·3083	0·7400	−5·0	−2·5	0·3	1·8
$a=4{\cdot}419$ (Pb)	0·606	0·636	0·649	0·4443	0·4771	0·4218	0·7092	−5·3	−2·2	0·8	2·1
4·265 (Ag)	0·555	0·590	0·601	0·4278	0·5452	0·4559	0·7508	−6·0	−2·5	0·8	2·3
3·894 (Cu)	0·402	0·450	0·451	0·3564	0·8385	0·5493	0·9091	−7·8	−3·3	0·9	3·0
3·680 (Ca)	0·291	0·346	0·339	0·2731	1·2792	0·6102	1·0724	−9·1	−3·9	0·9	3·5
	(110)	(100)	(111)					(110)	(100)	(111)	
					Body-centred Cubic Crystals						
$(m,n)=(4{\cdot}5,\ 8)$	0·066	0·057	0·080	0·1280	3·9056	0·7824	4·6707	−12·4	−2·8	5·8	
$(4{\cdot}5, 14)$	0·164	0·167	0·194	0·3732	1·1944	0·7656	2·5185	−11·1	−2·4	5·2	
$(5,\ 7)$	0·113	0·101	0·135	0·1671	2·9925	0·8170	2·8765	−11·6	−2·3	5·8	
$(6,\ 10)$	0·462	0·474	0·517	0·4193	1·0353	0·8162	0·9460	−7·0	−0·8	4·2	
$(6,\ 12)$	0·525	0·542	0·581	0·4407	0·9221	0·7860	0·8470	−6·2	−0·7	3·7	
$(6,\ 14)$	0·565	0·585	0·619	0·4529	0·8467	0·7565	0·7950	−5·7	−0·6	3·4	
$a=4{\cdot}488$ (Mo)	0·561	0·566	0·621	0·3887	1·2243	0·9110	0·7598	−5·9	0·0	4·4	
4·279 (W)	0·493	0·494	0·554	0·3596	1·3560	0·9217	0·8346	−6·7	−0·2	4·9	
3·951 (Fe)	0·369	0·358	0·425	0·2813	1·7767	0·9324	1·0195	−8·2	−0·6	5·8	
3·530 (Ba)	0·152	0·119	0·182	0·04076	11·4476	0·9229	1·5509	−10·7	−1·3	7·1	

approximation decrease. However, the approximation is still remarkably good even when the first two terms account for less than 10% of the total surface energy.

The accuracy of the approximation has implications for those problems where it is desired to calculate energies of particular atomic configurations in a semi-quantitative way. The most common procedure is to take account of nearest neighbours only, despite the large errors that are introduced thereby. The present results suggest that the inclusion of second neighbours can lead to significantly more reliable results, provided the energies associated with the interactions are treated as adjustable parameters. The differences found here between E_1 and E_1^* and between E_2/E_1 and ρ show that it is profitless to calculate these energies from a given potential function. However, when only relative energy values are needed, Table 1 suggests that a good estimate should be obtained by taking ρ between $\frac{1}{3}$ and $\frac{1}{2}$ for f.c.c. and between $\frac{3}{4}$ and 1 for b.c.c. crystals.

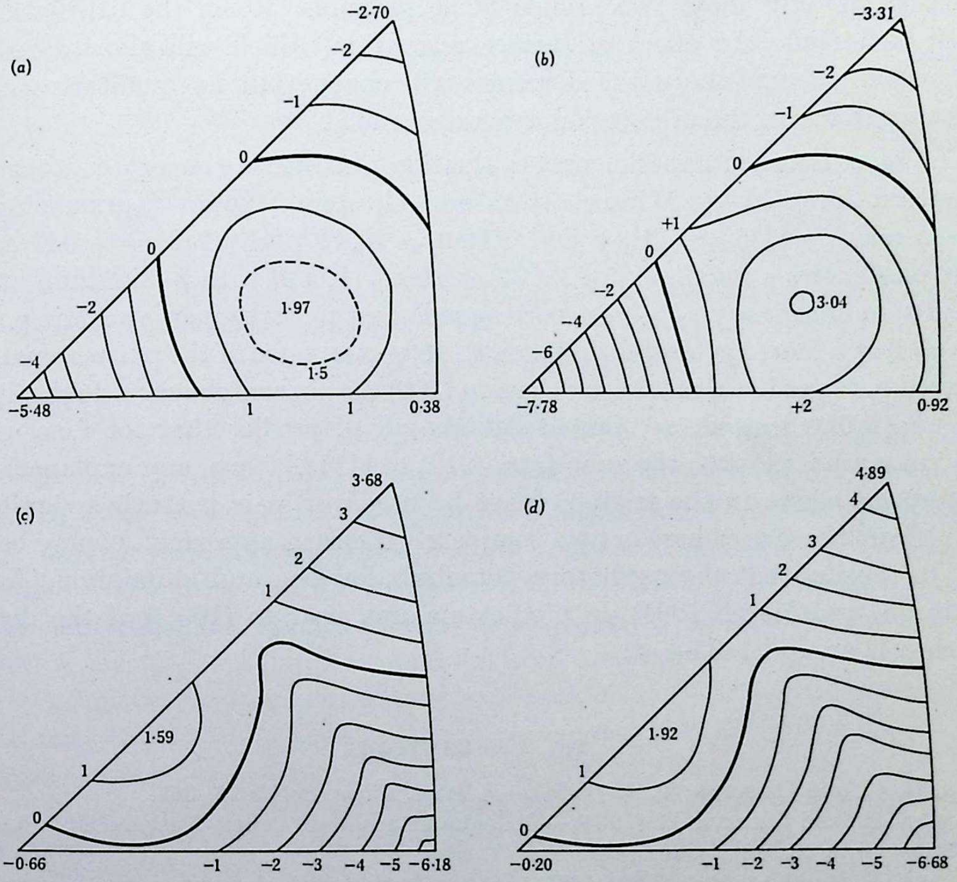

Fig. 5.—Contour plots of the percentage error in the two-term approximation for (*a*), (*b*) f.c.c. and (*c*), (*d*) b.c.c. crystals. The heavy contour is the zero error and others are drawn at intervals of 1% (full lines) or 0·5% (dashed lines). The symbols for the plots as defined for Figures 2 and 3 are

(*a*) (6, 12)F, (*b*) F 3·894,
(*c*) (6, 12)B, (*d*) B 4·279.

V. Discussion

The present work has shown how the surface energy will depend on orientation if a pairwise potential of a given form operates in an unrelaxed crystal. The calculations are exact within the limits of this assumption and the results in Table 1 show that the effects of distant neighbours can be highly significant. However, for potentials of the type considered, quite a good approximation can be obtained by *counting* only first and second neighbours and associating empirically determined energies with each of these. This may account for the success of various arguments (e.g. Sundquist 1964) based on only these two groups of neighbours. When the calculations are extended to include the effect of surface relaxation, which will allow a reduction in the surface energy, the detailed results will change but no qualitative changes are to be expected in the orientation dependence of γ.

The most detailed experimental evaluation of a surface energy contour plot is that derived for gold by Winterbottom and Gjostein (1966). Normalizing their results to make $\gamma(111) = 1$, they find $\gamma(100) = 1\cdot072$ and $\gamma(110) = 1\cdot047$ and the contour plot shows a maximum of $1\cdot077$ at about (10 1 0) with a minimum at (111). The degree of anisotropy $\gamma_{\max}/\gamma_{\min}$ corresponds best to that given by a Mie potential with $m = 6$ or a Morse potential with $a \simeq 4$. However, none of the pairwise potentials considered here predict a maximum close to (100) nor, in consequence, do they predict $\gamma(100) > \gamma(110)$. Indeed, as pointed out above, all predict that for f.c.c. crystals the maximum lies close to the zone from (210) to (111). Thus, any explanation of a maximum elsewhere in the triangle must be based on pair potentials significantly different from those used here or on a completely different approach. It may be worth noting in passing that the oscillatory potentials for lead and aluminium (Johnson, Hutchinson, and March 1964) do predict maxima near to (100) but the degree of anisotropy is around $1\cdot35$–$1\cdot4$.

VI. References

Benson, G. C., and Claxton, T. A. (1964).—*J. Phys. Chem. Solids* **25**, 367.

Drechsler, M., and Liepack, H. (1965).—Colloque Internat. du Centre National de la Recherche Scientifique No. 152, p. 49. (Paris.)

Drechsler, M., and Nicholas, J. F. (1967*a*).—Distribution of the lattice energy in cubic crystals and its variation with compression or expansion. *J. Phys. Chem. Solids* **28** (in press).

Drechsler, M., and Nicholas, J. F. (1967*b*).—On the equilibrium shape of cubic crystals. *J. Phys. Chem. Solids* **28** (in press).

Enderby, J. E., and March, N. H. (1965).—*Adv. Phys.* **14**, 453.

Friedel, J. (1962).—*J. Phys. Radium, Paris* **23**, 501.

Fürth, R. (1945).—*Proc. R. Soc.* A **183**, 87.

Girifalco, L. A., and Weizer, V. G. (1959).—*Phys. Rev.* **114**, 687.

Harrison, W. A. (1963).—*Phys. Rev.* **129**, 2512.

Harrison, W. A. (1964).—*Phys. Rev.* **136**, A1107.

Harrison, W. A. (1965).—*Phys. Rev.* **139**, A179.

Herring, C. (1951).—*Phys. Rev.* **82**, 87.

Johnson, M. D., Hutchinson, P., and March, N. H. (1964).—*Proc. R. Soc.* A **282**, 283.

Mackenzie, J. K., Moore, A. J. W., and Nicholas, J. F. (1962).—*J. Phys. Chem. Solids* **23**, 185.

Stranski, I. N., and Suhrmann, R. (1947).—*Annln Phys.* **1**, 153.

Sundquist, B. E. (1964).—*Acta metall.* **12**, 67.

Winterbottom, W. L., and Gjostein, N. A. (1966).—*Acta metall.* **14**, 1041.

ELECTROMAGNETIC DIFFRACTION BY A PLANE SLIT APERTURE

By H. S. Tan*

[*Manuscript received September* 21, 1967]

Summary

An asymptotic solution of the integral equations for diffraction by an E-polarized slit aperture is given. The results for the diffracted field are in excellent agreement with the exact solution and compare favourably with the results given by other approximate solutions.

I. Introduction

The problem of diffraction by a slit aperture in a plane screen has been the subject of many investigations in the past. It is well known that a rigorous solution can be found in terms of eigenfunction series of Mathieu functions (Morse and Rubenstein 1938; Hsu 1959), but its usefulness is limited to $ka \leqslant 10$ (where k is the wave number and a the half-aperture width in wavelengths) because of the difficulty of tabulating the Mathieu functions and the poor convergence of the series. Solutions as series of increasing powers in ka, also restricted to small slit widths, have been given by Groschwitz and Honl (1952), Honl and Zimmer (1953), Muller and Westpfahl (1953), and Bouwkamp (1954). For large slit widths, Clemmow (1956) used the concept of edge currents, while Millar (1958) presented an asymptotic solution of the integral equations by successive iteration. Grinberg (1958), using the concept of shadow currents, showed how the integral equations for the shadow currents may also be solved iteratively. A Wiener–Hopf treatment of the integral-equation approach was given by Levine (1959). More recent papers on this topic include those of Kleinman and Timman (1961), Stockel (1962), Khaskind and Vainshteyn (1964), Kieburtz (1964), and Popov (1965). Much of this previous work has been concerned with evaluating the transmission coefficient and the far-field patterns, and relatively little attention has been given to the near field. Only a few measurements have been reported (Hadlock 1958; Hsu 1959).

It is the purpose of the present paper to give an asymptotic solution of the integral equations for the screen currents, using a new approach. The near field is calculated and compared with the rigorous solution, and also with the Karp and Russek (1956) and second Rayleigh integral methods.

---

* Department of Physics, University of Malaya, Kuala Lumpur, Malaya.

II. Solution of Integral Equations

With an E-polarized plane wave incident on the slit aperture of width $2a$, the integral equations for the induced currents are (see Fig. 1)

$$j_{\mathrm{A}}(r) = j_{\mathrm{A0}}(r) + \int_0^\infty j_{\mathrm{B}}(\rho)\left(-\frac{\exp\{-ik(r+\rho+2a)\}}{\pi r^{\frac{1}{2}}(r+\rho+2a)}(\rho+2a)^{\frac{1}{2}}\right)\mathrm{d}\rho\,, \tag{1}$$

$$j_{\mathrm{B}}(r) = j_{\mathrm{B0}}(r) + \int_0^\infty j_{\mathrm{A}}(\rho)\left(-\frac{\exp\{-ik(r+\rho+2a)\}}{\pi r^{\frac{1}{2}}(r+\rho+2a)}(\rho+2a)^{\frac{1}{2}}\right)\mathrm{d}\rho\,, \tag{2}$$

where j_{A0} and j_{B0} are the half-plane currents on screens A and B respectively. These equations have been derived by Baker and Copson (1950) and Millar (1958) using Fox's formula, and also by Skal'skaya (1963) and Tan (1966) using integral transforms. The usual procedure is to solve (1) and (2) by a straightforward iterative method, but this is cumbersome because of the difficulty of evaluating the integrals in each iteration. The present treatment shows how this iteration scheme can be carried out more conveniently using Karp and Zitron's (1964) theorem.

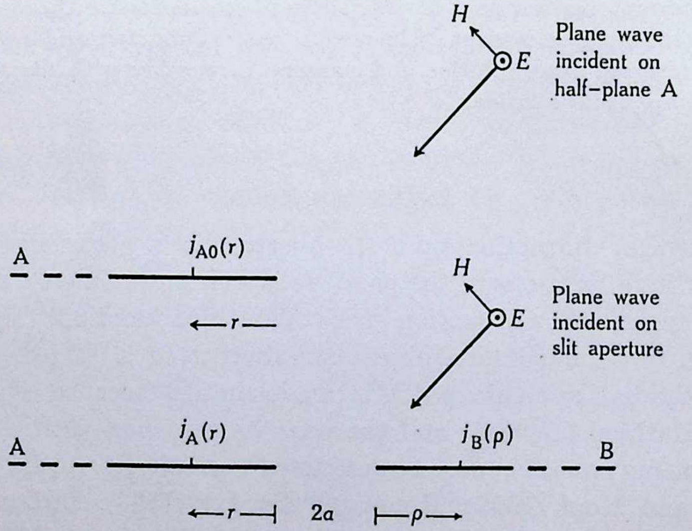

Fig. 1.—Schematic diagrams for diffraction by a slit aperture.

The form of equations (1) and (2) shows that the interactions between the two half-planes are represented by the integral terms. The kernel in each integral $G(r,\rho)$ is exactly the current induced at r on one half-plane due to the presence of a unit line current at ρ on the other half-plane. This interpretation of $G(r,\rho)$ then makes the form of equations (1) and (2) intuitively obvious, i.e. by superposition, the total induced current j_{A} is the sum of the unperturbed half-plane current j_{A0} and the currents induced in A by the presence of j_{B}. Each of the line currents j_{B} radiates a cylindrical wave that can be developed in an expansion of plane waves and derivatives of plane waves with respect to their angles of incidence (Karp and Zitron 1964). The currents induced on half-plane A by j_{B} are therefore equivalent to those induced by a series of plane waves and their derivatives. These induced currents can then be calculated from the half-plane solution and from the fact that the current induced by a derivative of a plane wave is the derivative of the current induced by a plane wave.

Writing $j_{\mathrm{A}0}$ and $G(r,\rho)$ as

$$j_{\mathrm{A}0}(r,\gamma) = -\frac{c}{\pi k}\sum_{n=0}^{\infty}\frac{\mathrm{i}}{2r}(2n+1)\,\mathrm{i}^{n+\frac{1}{2}}\,\mathrm{J}_{n+\frac{1}{2}}(kr)\sin\{(n+\tfrac{1}{2})\gamma\}\,, \tag{3}$$

$$G(r,\rho) = \sum_{n=0}^{\infty}\frac{\mathrm{i}}{2r}(2n+1)\,\mathrm{J}_{n+\frac{1}{2}}(kr)\,\mathrm{H}^{(2)}_{n+\frac{1}{2}}(k(\rho+2a))\sin\{(n+\tfrac{1}{2})\gamma\} \qquad r<2a\,, \tag{4}$$

and using the Karp and Zitron theorem, we obtain

$$G(r,\rho) = \mathrm{H}_{\mathrm{op}}(\rho,\mathrm{d}/\mathrm{d}\gamma)\,j_{\mathrm{A}0}(r,\gamma) \qquad r<2a\,, \tag{5}$$

where the operator $\mathrm{H}_{\mathrm{op}}(\rho,\mathrm{d}/\mathrm{d}\gamma)$ contains the series of plane waves and their derivatives. The expression for H_{op} follows from the expansion of the Hankel function in the following way

$$\mathrm{H}^{(2)}_{n+\frac{1}{2}}(kb) = \left(\frac{2}{\pi kb}\right)^{\frac{1}{2}}\exp\left(-\mathrm{i}kb+\tfrac{1}{4}\mathrm{i}\pi+\tfrac{1}{2}\mathrm{i}(n+\tfrac{1}{2})\pi\right) \times\left(\sum_{m=0}^{\infty}\frac{\{1+4\,\mathrm{d}^2/\mathrm{d}\gamma^2\}\{9+4\,\mathrm{d}^2/\mathrm{d}\gamma^2\}\ldots\{(2m-1)+4\,\mathrm{d}^2/\mathrm{d}\gamma^2\}}{m!\,(-8\mathrm{i}kb)^m}\right)g(\gamma)\,, \tag{6}$$

where $g(\gamma)$ represents a plane wave with angle of incidence γ. Hence

$$\mathrm{H}_{\mathrm{op}}(\rho,\mathrm{d}/\mathrm{d}\gamma) = \left(\frac{2}{\pi k(\rho+2a)}\right)^{\frac{1}{2}}\exp\left(-\mathrm{i}k(\rho+2a)+\tfrac{1}{4}\mathrm{i}\pi\right)\left(1+\mathrm{i}\frac{1+4\,\mathrm{d}^2/\mathrm{d}\gamma^2}{8k(\rho+2a)}-\ldots\right). \tag{7}$$

Equation (1) then becomes

$$j_{\mathrm{A}}(r) = j_{\mathrm{A}0}(r)+\left(\int_0^{\infty} j_{\mathrm{B}}(\rho)\,\mathrm{H}_{\mathrm{op}}(\rho,\mathrm{d}/\mathrm{d}\gamma)\,\mathrm{d}\rho\right)j_{\mathrm{A}0}(r,\gamma)\,, \tag{8}$$

where $j_{\mathrm{A}0}$ has been taken outside the integral because γ is independent of ρ. Equation (2) takes the same form. A solution by successive iteration is now easily carried out because each iteration yields the same type of integral. For example, if the incident plane wave makes an angle θ with the half-plane A, the third iteration gives

$$\begin{aligned} j_{\mathrm{A}}(r,\theta) = j_{\mathrm{A}0}(r,\theta) &+\{C_{\mathrm{B}}(\pi-\theta,\mathrm{d}/\mathrm{d}\gamma)+C_{\mathrm{A}}(\theta,\mathrm{d}/\mathrm{d}\gamma_1)\,C_{\mathrm{B}}(\gamma_1,\mathrm{d}/\mathrm{d}\gamma) \\ &+C_{\mathrm{B}}(\pi-\theta,\mathrm{d}/\mathrm{d}\gamma_1)\,C_{\mathrm{A}}(\gamma_1,\mathrm{d}/\mathrm{d}\gamma_2)\,C_{\mathrm{B}}(\gamma_2,\mathrm{d}/\mathrm{d}\gamma)\}j_{\mathrm{A}0}(r,\gamma)\,, \end{aligned} \tag{9}$$

where

$$\left.\begin{aligned} C_{\mathrm{A}}(\theta,\mathrm{d}/\mathrm{d}\gamma) &= \int_0^{\infty} j_{\mathrm{A}0}(\rho,\theta)\,\mathrm{H}_{\mathrm{op}}(\rho,\mathrm{d}/\mathrm{d}\gamma)\,\mathrm{d}\rho\,, \\ C_{\mathrm{B}}(\gamma_l,\mathrm{d}/\mathrm{d}\gamma) &= \int_0^{\infty} j_{\mathrm{B}0}(\rho,\gamma_l)\,\mathrm{H}_{\mathrm{op}}(\rho,\mathrm{d}/\mathrm{d}\gamma)\,\mathrm{d}\rho\,, \end{aligned}\right\} \tag{10}$$

and γ_l is to be put equal to π after all the differentiations have been carried out. The integral C_{A} or C_{B} can be evaluated in an asymptotic series by means of Erdelyi's

(1956) theorem, if we express the half-plane current j_{A0} or j_{B0} in closed form

$$j_0(r,\gamma) = \frac{c}{\pi^{3/2}}\left(\frac{\exp(-ikr-\frac{1}{4}i\pi)}{(2kr)^{\frac{1}{2}}}\sin\tfrac{1}{2}\gamma + \exp(\tfrac{1}{4}i\pi)\sin\gamma\exp(-ikr\cos\gamma) \times \int_0^{(2kr)^{\frac{1}{2}}\cos\frac{1}{2}\gamma}\exp(-it^2)\,dt\right). \tag{11}$$

The part of the integral containing the Fresnel integral can also be developed in series form by repeated integration by parts. The details of these calculations are tedious and are found in Tan (1966).

Because of the restriction on the expression for $G(r,\rho)$ in equation (4), equations (8) and (9) converge only for $r < 2a$. However, this is not a very severe restriction on the method because it is known (Moullin and Phillips 1952) that the currents j_A and j_B approach their respective half-plane values j_{A0} and j_{B0} when r is greater than a small fraction of $2a$. Thus, for any but the smallest apertures, this method would yield good results.

III. THE APERTURE FIELD

The diffracted electric and magnetic field everywhere in space can be calculated from the screen currents. For our purpose, to derive the aperture electric field for comparison with other theories and with experiment, it is more convenient to start from equations (1) and (2). We confine ourselves to the case of normal incidence and, multiplying both sides of equation (1) or (2) by

$$-(\pi k/c)\,H_0^{(2)}(k(r+x))$$

and integrating with respect to r, we have

$$E_d(x) = E_0(x) + \int_0^\infty j(\rho)\,E_s(\rho,x)\,d\rho, \tag{12}$$

where E_0 is the half-plane field, $E_s(\rho,x)$ is the field diffracted by one half-plane due to a unit line current at ρ on the other half-plane, and x in the aperture is measured from the aperture edge. Then

$$E_0(x) = -2\pi^{-\frac{1}{2}}\exp(\tfrac{1}{4}i\pi)\int_{(kx)^{\frac{1}{2}}}^\infty \exp(-it^2)\,dt \tag{13}$$

and

$$E_s(\rho,x) = \frac{4ik}{c}\exp\{-ik(\rho+2a-x)\}\int_{(2kx)^{\frac{1}{2}}}^\infty \frac{\exp(-it^2)}{t^2+2k(\rho+2a-x)}\,dt. \tag{14}$$

The integral in E_s can be approximated by a Fresnel integral to a degree of accuracy that is inadequate only if both x and $2a$ are very much smaller than one wavelength (Clemmow 1950). Thus

$$E_s(\rho,x) \simeq \frac{4ik}{c}\frac{\exp\{-ik(\rho+2a-x)\}}{\{2k(\rho+2a)\}^{\frac{1}{2}}}\int_{(2kx)^{\frac{1}{2}}}^\infty \exp(-it^2)\,dt. \tag{15}$$

Using for the first iteration

$$j(\rho) \simeq j_0(\rho, \tfrac{1}{2}\pi)$$

from equation (11), we have that

$$\begin{aligned} E_1(x) &= \int_0^\infty j_0(\rho, \tfrac{1}{2}\pi)\, E_{\mathrm{s}}(\rho, x)\, \mathrm{d}\rho \\ &= \frac{2}{\pi}\frac{\exp(-2\mathrm{i}ka)}{(2ka)^{\frac{1}{2}}}\int_{(2kx)^{\frac{1}{2}}}^{\infty} \exp(-\mathrm{i}t^2)\,\mathrm{d}t + \frac{5\mathrm{i}}{4\pi}\frac{\exp(-2\mathrm{i}ka+\mathrm{i}kx)}{(2ka)^{3/2}}\int_{(2kx)^{\frac{1}{2}}}^{\infty} \exp(-\mathrm{i}t^2)\,\mathrm{d}t \\ &\quad + O\{(ka)^{-5/2}\}, \end{aligned} \tag{16}$$

TABLE 1

COMPARISON OF SOLUTIONS FOR E-POLARIZED PLANE SLIT APERTURE ELECTRIC FIELD VECTOR

Halfwidth of slit $a = 0\cdot72$ cm ($ka = \sqrt{2}$)

η (degrees)	Distance from Aperture Centre $\bar{x} = a\cos\eta$ (cm)	Solutions			
		Exact* (Mathieu Fns.)	Integral Eqn. (Eqn. (19))	Rayleigh Integral Approximation†	Edge Current Approximation‡
10	0·709	0·209+i0·146	0·199+i0·136	0·726−i0·027	−1·490+i3·680
20	0·677	0·420+i0·292	0·411+i0·287	0·764+i0·051	0·073+i1·838
30	0·624	0·635+i0·433	0·627+i0·433	0·823+i0·145	0·675+i1·282
40	0·552	0·850+i0·566	0·845+i0·569	0·898+i0·243	1·045+i1·048
50	0·463	1·057+i0·688	1·054+i0·693	0·981+i0·338	1·319+i0·940
60	0·360	1·243+i0·790	1·242+i0·798	1·063+i0·444	1·533+i0·890
70	0·246	1·392+i0·871	1·392+i0·878	1·133+i0·487	1·691+i0·870
80	0·125	1·489+i0·921	1·490+i0·929	1·179+i0·545	1·791+i0·863
90	0·000	1·522+i0·938	1·524+i0·947	1·195+i0·564	1·825+i0·861

* Hsu (1959).

† Tan (1966).

‡ Karp and Russek (1956).

where we have used integration by parts and also Erdelyi's theorem. For the first iteration, the current induced on one half-plane by j_0 on the other half-plane is

$$j_1(\rho) = \int_0^\infty j_0(\eta, \tfrac{1}{2}\pi)\left(-\frac{\exp\{-\mathrm{i}k(2a+\rho+\eta)\}}{\pi\rho^{\frac{1}{2}}(2a+\rho+\eta)}(2a+\eta)^{\frac{1}{2}}\right)\mathrm{d}\eta\,. \tag{17}$$

j_1 in turn gives rise to a diffracted field $E_2(x)$ given by

$$\begin{aligned} E_2(x) &= \int_0^\infty j_1(\rho)\, E_{\mathrm{s}}(\rho, x)\,\mathrm{d}\rho \\ &\simeq -(2/\pi)^{\frac{1}{2}}\exp(-\tfrac{1}{4}\mathrm{i}\pi)\frac{\exp(-4\mathrm{i}ka+\mathrm{i}kx)}{2\pi ka}\int_{(2kx)^{\frac{1}{2}}}^{\infty}\exp(-\mathrm{i}t^2)\,\mathrm{d}t\,. \end{aligned} \tag{18}$$

E_2 is thus the result of two iterations of the integral equation. This iterative process can be carried further, but the approximation made in equation (15) would have to be improved. Thus, to an order of $(2ka)^{-3/2}$ the electric field in the aperture is given by

$$E(x) = 1+E_0(x)+E_0(2a-x)+E_1(x)+E_1(2a-x)+E_2(x)+E_2(2a-x)\,. \qquad (19)$$

IV. Results and Conclusions

Table 1 gives a numerical comparison of the aperture field as calculated by the various methods for $ka = \sqrt{2}$. It is seen that with only two iterations the results of equation (19) give very good agreement with the exact solution, even for this small slit width. The accuracy is even better for larger slit widths (Tan 1966). The two approximation methods are rather poor, especially near the aperture edge, where even the phase is incorrect. To indicate the range of accuracy of equation (19), Figure 2 compares a number of methods of calculating the electric field at the centre of the slit aperture for various slit widths. It is seen that results from equation (19) are accurate for slit widths larger than one-fifth of a wavelength. The relative performances of the approximate theories (curves 1, 2, and 4) are evident from Figure 2.

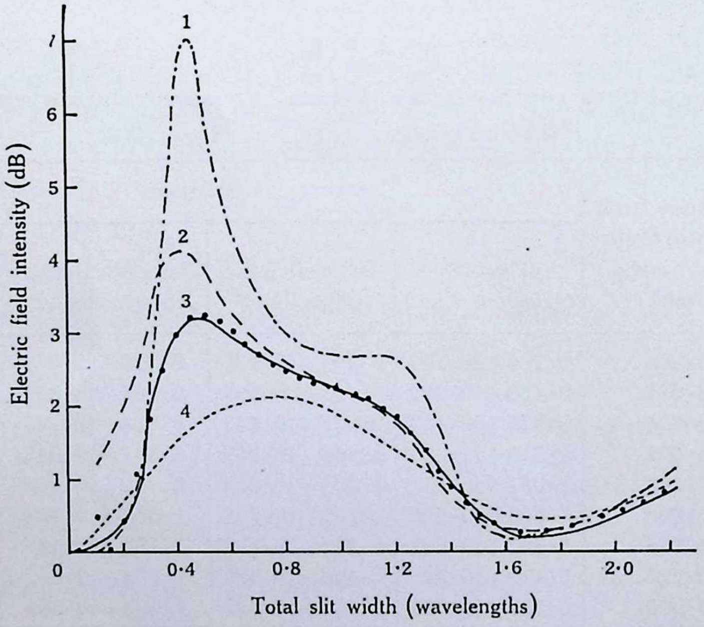

Fig. 2.—Comparison of methods of calculating electric field intensity at the centre of the slit aperture for various slit widths: curve 1, Hadlock's approximation (Hsu 1959); 2, Karp and Russek's (1956) approximation; 3, Mathieu function series (Hsu 1959); 4, second Rayleigh integral approximation. The points (●) lying close to curve 3 are the values obtained from equation (19).

V. References

Baker, B. B., and **Copson, E. T.** (1950).—"The Mathematical Theory of Huygen's Principle." 2nd Ed. (Oxford Univ. Press.)

Bouwkamp, C. J. (1954).—*Rep. Prog. Phys.* **17**, 35–100.

Clemmow, P. C. (1950).—*Q. Jl Mech. appl. Math.* **3**, 241–56.

CLEMMOW, P. C. (1956).—*I.R.E. Trans. Antennas Propag.* AP-4, 282–7.

ERDELYI, A. (1956).—"Asymptotic Expansions." (Dover: New York.)

GRINBERG, G. A. (1958).—*Soviet Phys. tech. Phys.* **3**, 509–19.

GROSCHWITZ, E., and HONL, H. (1952).—*Z. Phys.* **131**, 305.

HADLOCK, R. K. (1958).—*J. appl. Phys.* **29**, 918–22.

HONL, H., and ZIMMER, E. (1953).—*Z. Phys.* **135**, 196.

HSU, H. P. (1959).—Scient. Rep. No. 5, Case Inst. Technol., Ohio.

KARP, S. N., and RUSSEK, A. (1956).—*J. appl. Phys.* **27**, 886–94.

KARP, S. N., and ZITRON, N. (1964).—Res. Rep. EM-199, Courant Inst. Math. Sci., New York University.

KHASKIND, M. D., and VAINSHTEYN, L. A. (1964).—*Radio Engng electron. Phys.* **9**, 1492–1501.

KIEBURTZ, R. B. (1964).—*Appl. scient. Res.* B **12**, 221–34.

KLEINMAN, R. E., and TIMMAN, R. (1961).—Res. Rep. 3648-3-T, Radiation Lab., University of Michigan, Ann Arbor.

LEVINE, H. (1959).—*J. appl. Phys.* **27**, 1673.

MILLAR, R. F. (1958).—*Proc. Camb. phil. Soc. math. phys. Sci.* **54**, 479–96.

MORSE, P. M., and RUBENSTEIN, P. J. (1938).—*Phys. Rev.* **54**, 895–8.

MOULLIN, E. B., and PHILLIPS, F. M. (1952).—*Proc. Instn elect. Engrs* (4) **99**, 137–44.

MULLER, R., and WESTPFAHL, K. (1953).—*Z. Phys.* **134**, 245.

POPOV, G. YA (1965).—*Soviet Phys. tech. Phys.* **10**, 305–9.

SKAL'SKAYA, I. P. (1963).—*Soviet Phys. tech. Phys.* **8**, 179–81.

STOCKEL, H. (1962).—*Ann. Phys.* **9**, 242–51.

TAN, H. S. (1966).—Dissertation, McGill University, Montreal.

ELECTRON TRANSPORT COEFFICIENTS IN HYDROGEN AND DEUTERIUM

By R. W. Crompton,* M. T. Elford,* and A. I. McIntosh*†

[*Manuscript received August* 31, 1967]

Summary

Measurements have been made of the drift velocity W and the ratio of diffusion coefficient to mobility D/μ for low energy electrons in deuterium at 77°K, and of D/μ in hydrogen at 77 and 293°K. Tabulated data are given for D/μ within the range $2\times10^{-20} \leqslant E/N \leqslant 1\cdot2\times10^{-16}$ V cm^2 and for W within the range $8\times10^{-20} \leqslant E/N \leqslant 9\cdot5\times10^{-17}$ V cm^2. The low temperature results show a considerably reduced scatter when compared with previously published data and are of an accuracy comparable with the results of recent measurements made at room temperature. The data obtained complement those of Lowke and of McIntosh thus completing a set from which a more accurate determination of low energy elastic and inelastic cross sections can be made.

I. INTRODUCTION

Measurements of the drift velocity W and the ratio of diffusion coefficient to mobility D/μ for electrons moving through a gas under the influence of a uniform electric field have been used for many years to estimate the energy dependence of the momentum transfer cross section for collisions between electrons and gas molecules (see, for example, Crompton and Sutton 1952). Until recently, experiments of this type were subject to considerable experimental error and, moreover, the data obtained from them could be interpreted only in terms of various mean quantities (Crompton and Sutton 1952; Huxley and Crompton 1962). With the use of improved techniques and a better understanding of the factors limiting the accuracy of experiments of this kind, experimental data with an error of less than 1% can now be obtained (Crompton and Jory 1962; Crompton and Elford 1963; Lowke 1963). Furthermore, the use of computers has enabled these data to be analysed to determine the energy dependence of the cross sections for both elastic and inelastic processes without resorting to the less satisfactory averaging procedures. Analyses of this type (Frost and Phelps 1962; Engelhardt and Phelps 1963; Crompton, Elford, and Jory 1967) show that the techniques are capable of yielding results of reasonable energy resolution and therefore, in certain circumstances, allow a direct comparison to be made with the results of single scattering experiments. However, not all of the data on which these analyses have been based have been sufficiently accurate to allow maximum use to be made of the analytical techniques.

---

* Ion Diffusion Unit, Australian National University, Canberra, A.C.T. 2600.

† Present address: Department of Pure and Applied Physics, Queen's University, Belfast, Northern Ireland.

Aust. J. Phys., 1968, **21**, 43–63

In the inert gases at energies well below the first excitation threshold it is possible to infer the momentum transfer cross section directly from the experimental data. In such cases the cross section found is unique and its accuracy depends ultimately only on the precision of the experimental data (Crompton, Elford, and Jory 1967). On the other hand, in the molecular gases, where both elastic and inelastic collisions must be taken into account at all energies, the results obtained have been less satisfactory (Frost and Phelps 1962; Engelhardt and Phelps 1963). While this situation is largely due to the difficulties in obtaining a unique set of elastic and inelastic cross sections that are consistent with the experimental data, it may in part be attributed to the inadequacy of some of these data. Since any spread in the data leads to ambiguity in determining the cross sections, it is clearly desirable to achieve the greatest possible accuracy in the experimental measurements.

In experiments of the type described in this paper, the mean electron energy, as well as the distribution of electron energies, is controlled by the electric field strength and the nature, temperature, and number density of the gas. At a given gas temperature, the mean electron energy can be varied by varying E/N, the ratio of the electric field strength to the gas number density. If this ratio is large, the mean electron energy is well above the thermal energy of the gas molecules. On the other hand, if the field strength is small and the gas number density is large the rate at which energy is gained from the field is small while the frequency of the collisions in which excess energy is transferred to the gas molecules is large. In this case the energy balance may be achieved with the mean electron energy exceeding that of the gas molecules by only a few per cent and the electron energy can be controlled by varying the gas temperature.

Although the temperature of the gas may be lowered simply in order to extend the lower energy limit of the experiments, this procedure may have an additional advantage in that the subsequent analysis of the data to determine the cross sections may be simplified. For example, in hydrogen and deuterium at 77°K only the two lowest rotational levels are populated significantly and the electron energy distribution is therefore controlled by the cross sections for momentum transfer and for two rotational transitions only.

The electron transport coefficients measured in the present investigation were the drift velocity W and the ratio of diffusion coefficient to mobility D/μ, since these are the transport coefficients that can be measured with the greatest accuracy using existing techniques (Crompton, Elford, and Jory 1967). The measurements of W were made using the Bradbury–Nielsen method while the measurements of D/μ were made using the Townsend–Huxley lateral diffusion technique. Both types of experiments have been the subject of critical analyses (Crompton and Jory 1962; Lowke 1962; Crompton, Elford, and Gascoigne 1965) and their reliability is well established. Data for D/μ in hydrogen at 293 and 77°K, and for W and D/μ in deuterium at 77°K are contained in the present paper. These data complement the drift velocity data in hydrogen of Lowke (1963) and the data for W and D/μ in deuterium at 293°K of McIntosh (1966). A preliminary account of the measurements of D/μ in hydrogen at 293°K was given by Crompton and Elford (1963).

II. Apparatus and Experimental Techniques

(*a*) *Lateral Diffusion Experiments*

The method of measuring D/μ has been described in detail elsewhere (e.g. Crompton and Jory 1962) and will be considered only briefly here.

Electrons enter the diffusion chamber through a small hole in the cathode and then drift and diffuse under the influence of the uniform electric field E towards the anode, which is divided into a central disk of radius b and a surrounding annulus. The ratio R of the electron currents received by the segments of the anode is measured. It may be shown (Huxley and Crompton 1955; Crompton and Jory 1962; Hurst and Liley 1965) that the values of D/μ are related to the measured current ratios by the expression

$$R = 1-(h/d)\exp\{-\lambda(d-h)\}, \tag{1}$$

where h is the distance between the cathode and anode,

$$d^2 = h^2+b^2, \qquad \text{and} \qquad 2\lambda = E/(D/\mu).$$

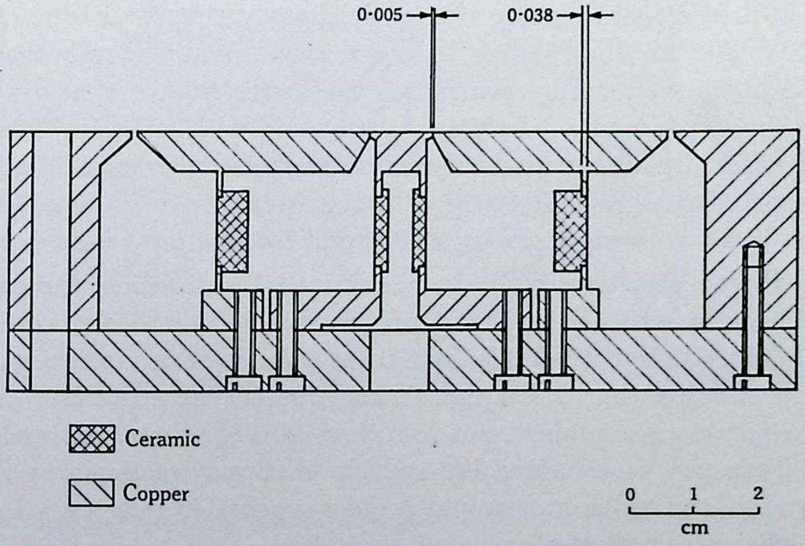

Fig. 1.—Schematic section through the lower electrode assembly of the lateral diffusion apparatus.

The apparatus and some of the experimental details and techniques used in the present investigation have been described in detail by Crompton, Elford, and Gascoigne (1965). The only major change in the apparatus was the replacement of the collecting electrode by one that was suitable for use at 77°K. The earlier collecting electrode, which consisted essentially of a disk and surrounding annulus mounted rigidly on a glass backing plate, proved unsatisfactory below 90°K when differential contraction of the components caused the disk and annulus, separated by an annular gap of 0·005 cm, to touch. In the collecting electrode used for most of the present investigation (see Fig. 1) the disk and annulus are supported by thin-walled copper cylinders 0·3 cm long which are vacuum brazed to concentric ceramic cylinders.

The cylinders are supported on the base plate in a similar way. The success of this design is due to the effectiveness of the copper cylinders, whose wall thickness is only 0·04 cm, in uniformly absorbing the differential contraction between the copper and ceramic components as the electrode is cooled to 77°K, thus ensuring that the disk and annulus do not touch and that the whole electrode remains flat at this temperature. An optical test at both 293 and 77°K showed that the disk and annulus remained undistorted and coplanar over this temperature range. The resistance to ground of each component was greater than 10^{14} ohms.

The experimental equipment used was identical to that described by Crompton, Elford, and Gascoigne. Each experimental observation, made with an accurately known field E established in the diffusion chamber, consisted of the measurement of the gas temperature and pressure together with the ratio R of the currents received by the disk and annulus, each of which was of the order of 10^{-12} A. This information, together with the dimensions of the apparatus, enabled the value of E/N and the corresponding value of D/μ to be determined.

Calculations show that impurity levels of up to 50 p.p.m. have a negligible effect on the measured transport coefficients in hydrogen and deuterium. Experience has shown that the level of impurity as a result of outgassing of the tube can be kept well below this value without baking the apparatus providing the outgassing rate is reduced to an adequate level by evacuating the apparatus for a long period before commencing the experiments. Isolation tests made without using liquid nitrogen traps showed that the rate of rise of pressure was of the order of 5×10^{-6} torr/hr, which corresponds to a gas influx rate of 8×10^{-9} torr litre/sec. The rate of rise of impurity level in a 500 torr sample of gas at 293°K is therefore 1 part in 10^8 per hour.

The hydrogen and deuterium were obtained by diffusion through a silver–palladium alloy osmosis tube using the apparatus and technique described by Crompton and Elford (1962). This method is known to be capable of producing hydrogen with an impurity level of less than 0·1 p.p.m. (Young 1963). The deuterium (from General Dynamics Corporation) contained not less than 99·9% of the isotope. The small amounts of hydrogen and deuterium hydride that may have been admitted by diffusion through the palladium would have a negligible effect on the measured transport coefficients in deuterium.

Two pressure gauges were used: a 0–500 torr capsule gauge of the type described by Crompton and Elford (1957), and a 0–250 torr fused quartz spiral gauge, manufactured by Texas Instruments Ltd. Both gauges were calibrated against a C.E.C. type 6–201 primary pressure standard. Using the capsule gauge the pressure could be measured with an error of less than 1% at 500 torr, the greater part of this error being due to hysteresis effects in the capsule. Fortunately, high pressures are needed only for the measurements at very low values of E/N. In this region D/μ varies slowly with E/N and hence errors in pressure measurement are relatively unimportant. The quartz spiral gauge was used to measure all pressures in the range 5–250 torr with an error of less than 0·1%.

The temperature at which the measurements are made can affect the value of D/μ either directly or indirectly through its effect on the gas number density, since the gas pressure rather than N is measured to determine E/N. An error of 1 degK leads to an error of 0·3% in N at 293°K and of more than 1% at 77°K, and it is therefore necessary to control the temperature closely and to measure it accurately. For the room temperature experiments the temperature of the laboratory was controlled to ±1 degK and the heat generated by the filament was removed by a water jacket through which distilled water was circulated by a small pump. At 77°K the apparatus was immersed in a liquid nitrogen bath, the level of the liquid nitrogen being controlled automatically to within 0·5 in. by a device based on the design of Pursar and Richards (1959). For the experiments at both temperatures the gas temperature was measured using two fine-wire copper–constantan thermocouples, one attached to the cathode and the other to the earthed ring surrounding the collecting electrode.

To obtain reproducible calibration values for the thermocouples at 77°K it was found necessary to use fully annealed copper wires. The thermocouples were calibrated against the boiling point of liquid nitrogen, care being taken to ensure that the liquid nitrogen was not super-heating. The purity of the liquid nitrogen was determined and the boiling point corresponding to the atmospheric pressure found. The same calibration values were obtained for many thermocouples prepared from different lengths of the same wire. During the assembly of the apparatus the calibration of the actual thermocouples used was confirmed after their installation in the vacuum envelope. The sensitivity of the thermocouples was approximately 16 μV/deg at 77°K, which, with the potentiometer used, enabled the temperature to be determined to better than 0·2 degK.

A possible source of error in lateral diffusion experiments is the presence of contact potential differences in the chamber (Crompton, Elford, and Gascoigne 1965). Despite the attention given to this problem, small contact potential differences remained in the apparatus, but these were eliminated, or compensated for, by the application of a small potential in the manner described by Crompton, Elford, and Gascoigne. For the measurements at 293°K the value of this potential was adjusted until the observed value of D/μ for K^+ ions was equal to the expected value of kT/e.

(b) *Additional Experimental Problems in Lateral Diffusion Experiments at 77°K*

When measurements of D/μ were first made at 77°K, several sources of error in addition to those investigated at 293°K were encountered. Although it was not always possible to eliminate these sources of error, methods of overcoming or avoiding them were developed. The investigation of one of these difficulties, the current dependence of the results at low E/N, led to the discovery of the extreme sensitivity of the experiments to oxygen in concentrations several orders of magnitude smaller than the limit of detection of any other known method.

(i) *Compensation for Contact Potential Differences*

At 77°K it was found that the use of the positive ion test to adjust the contact potential compensation (Crompton, Elford, and Gascoigne 1965) led to large errors in the observed values of D/μ, the errors increasing as the test proceeded. Over a period of several hours, the measured value of D/μ for the positive ions increased by more than 10% from a value that was initially only 1% above the expected value of kT/e. Electron results taken at intervals during the same period showed a similar, but smaller, increase. It should be noted that this does not correspond to a change in the contact potential differences within the apparatus, since this would have resulted in errors of different signs in the two cases. When measurements were taken only with electrons, i.e. the positive ion test was not used, the values obtained were consistent and did not vary with time. In subsequent experimental runs measurements were taken only with electrons and the compensation for contact potential differences was adjusted until for any given value of E/N the same value of D/μ was obtained when results were taken with a wide range of electric field strengths.

In previous papers (Crompton, Elford, and Gascoigne 1965; McIntosh 1966; Crompton, Elford, and Jory 1967) it has been stated that, to keep errors from contact potential differences within acceptable limits, the lowest value of the electric field strength used should be $3\cdot0$ V/cm. In the present apparatus, a stream of near-thermal electrons is not sufficiently divergent at 77°K to allow accurate measurements of the current ratios when field strengths of greater than $2\cdot5$ V/cm are used (Crompton, Elford, and Gascoigne 1965) and therefore field strengths of as little as $1\cdot0$ V/cm were used to obtain the values of D/μ at values of E/N of the order of 10^{-20} V cm^2. Provided the compensating potential was correctly adjusted at 293°K with $E = 3\cdot0$ V/cm, and was left at this setting when the apparatus was cooled to 77°K, it was found that errors that could be attributed to contact potential differences were generally less than $0\cdot5\%$ at $E = 1\cdot0$ V/cm. An error of this magnitude would not have been acceptable for the experiments at 293°K, but was less significant at 77°K when other experimental difficulties caused the error limit placed on the final data to be increased to $\pm2\%$. When errors due to incorrect compensation were observed at low field strengths, only data taken at field strengths sufficiently high to reduce these errors to less than $0\cdot25\%$ were included in the final data.

(ii) *Surface Effects*

After measurements had been taken at high values of E/N at 77°K, the measured values of D/μ at low E/N increased (e.g. by about 3% at $E = 1\cdot0$ V/cm), especially if the measurements at high E/N were not made until several days after cooling the apparatus to 77°K. Although the size of the error did not exactly halve as the value of E was doubled (as would be expected if the error were due to a contact potential difference in the apparatus; Crompton, Elford, and Gascoigne 1965), it did decrease with increasing electric field strength and was always negligible for results taken with $E \geqslant 10\cdot0$ V/cm. The error could not be eliminated as long as the apparatus was maintained at 77°K, but could be eliminated by warming the apparatus to room temperature for several days before resuming the low temperature measurements. It therefore seems probable that an insulating layer is formed when the somewhat more energetic electrons in the swarm at high E/N bombard an adsorbed layer on the surface of the collecting electrode.

Fortunately, although the effect was inconvenient, it could always be eliminated and the final data were not subject to errors from this source. At low values of E/N, only those results taken when no effect was observed were included in the final data. At higher values of E/N, when larger electric field strengths were used, the values of D/μ were always in agreement whether or not the effect was present. All the data obtained at high E/N and high field strengths were therefore included in the final analysis.

(iii) *Current Dependence of Results at Low* E/N

Crompton and Elford (1963) reported a slight dependence of the divergence of the electron stream on the total current received by the anode. The same phenomenon occurred in the present experiments. When such a dependence was observed, it was found that the apparent values of D/μ were linearly dependent on the current; the true value of D/μ was therefore found by extrapolating to zero current from values recorded at 1×10^{-12} and 2×10^{-12} A. The difference between the extrapolated value of D/μ and the value recorded at the lowest current was nearly always less than 1% for the room temperature experiments and always decreased rapidly with increasing E/N.

The slope of the D/μ against current graph increased progressively with time for a given gas sample. When a high current dependence was found in a particular sample of gas, a moderately high dependence was found in the next sample used, even though the apparatus was evacuated to a pressure of less than 10^{-6} torr between experimental runs. Both of these effects indicated that the phenomenon was associated with the outgassing of the apparatus, although the level of contamination from this source was known to increase at a rate less than 0·1 p.p.m./hr for a 500 torr sample of gas. The gases most likely to be present from outgassing were oxygen, carbon dioxide, and water vapour. Known proportions of these gases were added to the hydrogen in concentrations of a few p.p.m. In other tests carried out at room temperature, small amounts of the solvents used during the assembly of the apparatus (hexane, acetone, and isopropyl alcohol) and excessive amounts of the tap grease and the wax used for the demountable seal of the apparatus were also added. With the exception of the oxygen, all of the impurities added produced no observable current dependence of the results. In the case of oxygen, the slope of the D/μ against current curve was approximately linearly dependent on the amount of oxygen added.

Since attachment of thermal electrons to oxygen is known to be appreciable (Chanin, Phelps, and Biondi 1962), it was suggested that negative ions were present in the electron stream and that these ions led to space charge repulsion. At sufficiently low values of E/N, both the ions and the electrons are in thermal equilibrium with the gas and therefore the current distribution at the anode is the same for both species. Thus, if space charge effects were negligible, the current ratios would not be affected by the presence of a small number of negative ions in the stream and there would be no current dependence of the results. On the other hand, if space charge repulsion does affect the stream, a small number of ions will have a large effect, since, at low E/N, their drift velocity is of the order of 1000 times smaller than the corresponding drift velocity of electrons.

In the experiments at 77°K, the current dependence was found to be about five times greater than it had been at 293°K and to increase as the gas number density N increased. The increase with N can be qualitatively explained in terms of the hypothesis proposed above. For a given value of the electric field strength E, as N is increased the effective E/N is decreased and the drift velocities of the electrons and ions decrease; thus, for a given attachment rate, the effect of space charge on the stream is increased. Secondly, since the attachment of thermal electrons to oxygen is a three-body process, the rate of attachment depends on the square of the number density; an increase in N again leads to a larger current dependence.

Although the current dependence of the results at low E/N could be reasonably explained in terms of space charge repulsion enhanced by the presence of negative ions, the proportion of oxygen molecules present in the experiments at 77°K was expected to be very much less than 0·1 p.p.m. (see Section II(a)) owing to the reduced outgassing rate, so that some doubt was cast on the validity of the explanation. To confirm that such a small proportion of oxygen could lead to the large effects observed, mixtures of known concentrations of oxygen in hydrogen were made and the current dependence in these mixtures examined.

Mixtures with oxygen concentrations ranging from 0·5 p.p.m. to 3 parts in 10^{10} were prepared. In the most contaminated of these mixtures (0·5 p.p.m. of oxygen) the current ratio was immeasurably small, i.e. the space charge repulsion in the stream was so great that only a negligible fraction of the electron current fell on the central disk of 1 cm diameter. In the mixture containing 3 parts in 10^{10} of oxygen, the current dependence of the results approached, but was still greater than, that observed in the normal experimental runs.

The data obtained in these deliberately contaminated gas samples is in semi-quantitative agreement with the theory of Liley (1967), a more exact comparison being difficult in view of the uncertainty of some of the quantities required for the calculations.

Since the experimental conditions at 293°K could always be arranged to ensure that the difference between the extrapolated value of D/μ and the value measured at the lowest current was less than 1%, no attempt was made to reduce the oxygen content of the gas samples. After prolonged periods of pumping the difference was often reduced to as little as 0·25% at $E/N = 2\times10^{-19}$ V cm^2 and was too small to detect at higher values of E/N. All the 293°K data presented in Section III(a) were obtained under these conditions. Although the current dependence at 77°K was considerably larger, any errors incurred by the extrapolation of the values of D/μ to zero current were negligible compared with the errors from other sources.

(c) *Drift Velocity Experiments*

The method used to measure the electron drift velocities, that of Bradbury and Nielsen (Nielsen 1936), has been described by Lowke (1963). The apparatus used in the present investigation maintains the essential features of the one described by Crompton, Elford, and Jory (1967), but differs from their apparatus in several important details.

The present apparatus was designed primarily for the measurement of electron drift velocities in ultra-pure gases at low temperatures. The drift tube was therefore made as small as possible and was constructed in a form suitable for relatively high temperature baking to achieve the required low outgassing rates. These restrictions made it difficult to use the guard electrode structure used in the apparatus of Crompton, Elford, and Jory and in the lateral diffusion apparatus described in Section II(*a*), and also made it impossible to use a demountable seal as had been done in both of the earlier apparatuses.

The form of the guard electrode structure used can be seen in Figure 2. The electrodes, machined from copper and lapped and polished to a high degree of flatness and surface finish, were separated by ground glass spacers and mounted on ceramic tie-rods. Field plots for the electrode structure showed that a field which was virtually free of distortion over the important central region could be produced and that the system effectively prevented field distortion within the chamber from external sources.

A comparison of results obtained using the present apparatus with those obtained using the drift velocity apparatus of Crompton, Elford, and Jory, which was known to yield highly accurate data, showed that there was a systematic error of approximately 0·3% in the present apparatus. If the distance between the planes of the shutters was taken to be 5·014 cm instead of the measured value of 5·008 cm, the agreement between the two sets of data was to within 0·2% for all electric field strengths greater than 8·0 V/cm. The empirical distance was used in subsequent measurements and and no further discrepancies between the measured values and the results of Crompton, Elford, and Jory or Lowke (1963) were observed.

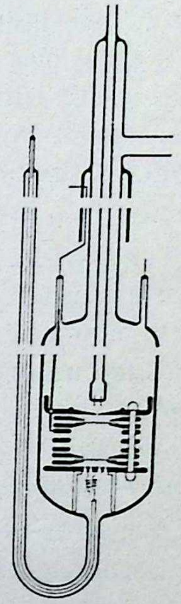

Fig. 2.—Drift tube.

The shutters were constructed of 0·08 mm diameter nichrome wires separated by 0·4 mm and sealed under tension on ceramic rings of internal and external diameters 3·0 and 5·5 cm respectively.

Figure 2 shows the apparatus mounted inside the Pyrex glass envelope. Kovar tube seals were used to bring the electrical leads through the glass. Unlike the lateral diffusion apparatus described above, the entire apparatus was immersed in liquid nitrogen to a depth just above the bottom of the glass skirt on the filament stem (see Fig. 2). Total immersion of the apparatus reduced the pressure variations caused by oscillations in the level of the refrigerant and also helped to reduce the temperature gradient between the top and bottom of the apparatus. The electrical leads through the glass skirt were sealed with silicon rubber, thereby ensuring that the space between the filament stem and the glass skirt was sealed off from the atmosphere. This arrangement prevented condensation and ice formation on the leads.

The potentials applied to the electrodes of the drift tube were similar in accuracy and stability to those applied to the lateral diffusion apparatus. The voltage between the planes of the electrode shutters was measured to within 0·05%.

The determinations of the frequencies of the maxima in the current–frequency curves were made using the equipment and techniques described by Elford (1966). The vacuum and gas handling techniques were essentially similar to those used in the lateral diffusion experiments, but the rate of rise of pressure in the drift tube was at least four times smaller than in the lateral diffusion apparatus.

Unlike the ratio of diffusion coefficient to mobility, the drift velocity is strongly dependent on E/N even at very small values of this parameter. As a result, the gas pressure must be measured as accurately as possible over the entire pressure range. To obtain the desired accuracy it was therefore necessary to use the quartz spiral gauge for the measurement of all pressures. Since this instrument is essentially a null manometer with a range of a little over 250 torr, pressures in the range 250–500 torr were measured by operating the gauge with its reference pressure held accurately at 250 torr. Stability of the pressure in the reference volume was improved by the addition of a 5 litre ballast volume immersed in a water bath.

The single thermocouple in the drift tube was attached to the electrode adjacent to the top shutter. Since the lower half of the apparatus was in good thermal contact with the liquid nitrogen bath, the existence of any temperature gradients could still be detected using this thermocouple, provided it was assumed that the lower end of the apparatus was at the bath temperature. Only very small temperature gradients were observed, the details of which are given in Section III(*c*) below. The thermocouple was prepared and calibrated and its e.m.f. measured in the manner described above.

Lowke (1963) showed that the measured drift velocities in a Bradbury–Nielsen experiment are relatively insensitive to distortion of the electric field. The primary effect of contact potential differences within the drift chamber is therefore to falsify the total potential difference between the planes of the shutters. The shutter wires were gold coated by vacuum deposition to minimize errors from this source, but in the present apparatus it was not considered necessary to coat the whole interior with gold. The results presented below show no effects of contact potential differences when the electric field strength is $8 \cdot 0$ V/cm or greater.

Each experimental observation consisted of the determination of the transit time of the electron pulse and the temperature and pressure of the gas. These data, together with the electric field strength and the distance between the shutters, enable the value of W and the corresponding value of E/N to be calculated.

III. RESULTS

(*a*) *Values of* D/μ *in Hydrogen at 293°K*

In the experiments at 293°K both the gas pressure and temperature could be accurately controlled. It was therefore possible to measure the value of D/μ at predetermined values of E/N corresponding to values of E/p_{293} (p is the gas pressure) chosen to facilitate comparison with earlier work, and no corrections resulting from departures of the actual values of E/N from the chosen values were necessary.

Results were taken using the collecting electrode and experimental techniques described by Crompton, Elford, and Gascoigne (1965) and with the collecting electrode and techniques described in Section II(*a*). These two sets of data were in agreement with each other to within $0 \cdot 5\%$ and their averages are presented in the final column of Table 1. An error limit of $\pm 1\%$ is placed on the average values in this table.

(*b*) *Values of* D/μ *in Hydrogen and Deuterium at 77·3°K*

A temperature gradient of approximately 0·3 degK appeared between the cathode and anode of the diffusion chamber as the pressure was lowered from 500 to 5 torr over a period of several hours. A corresponding change in the mean temperature of the apparatus from 77·3 to 77·4°K was observed. This temperature rise results from the fact that the top section of the apparatus becomes less effectively coupled thermally to the liquid nitrogen bath as the gas pressure is decreased. The temperature rise was taken into account in its effect on the value of E/N, but no corrections were made for the direct influence on the values of D/μ.

Table 1

EXPERIMENTAL VALUES OF D/μ FOR ELECTRONS IN HYDROGEN AT 293°K

10^{17} E/N (V cm^2)	E/p_{293} (V cm^{-1} torr^{-1})	D/μ (volt) at p (torr) of: 500	400	300	200	150	100	Average
0·01821	0·006	0·0258(1)						0·0258(1)
0·02428	0·008	0·0261(7)	0·0261(6)					0·0261(7)
0·03035	0·010	0·0265(3)	0·0265(1)	0·0265(0)				0·0265(1)
0·04553	0·015	0·0275(1)	0·0275(2)	0·0275(1)	0·0274(2)			0·0274(9)
0·06071	0·020	0·0286(1)	0·0285(8)	0·0285(9)	0·0285(2)	0·0284(7)		0·0285(5)
0·07589	0·025		0·0297(3)	0·0297(1)	0·0296(6)	0·0296(2)		0·0296(8)
0·09106	0·03			0·0308	0·0308	0·0308	0·0307	0·0308
0·1214	0·04				0·0330	0·0330	0·0330	0·0330
0·1518	0·05				0·0352	0·0353	0·0353	0·0353
0·1821	0·06					0·0374	0·0375	0·0375
0·2125	0·07					0·0396	0·0396	0·0396
0·2428	0·08					0·0418	0·0418	0·0418
0·2732	0·09						0·0439	0·0439
		p = 100	40	20	10			
0·3035	0·10	0·0461	0·0458					0·0459
0·3643	0·12		0·0500					0·0500
0·4553	0·15		0·0563	0·0561				0·0562
0·5464	0·18		0·0629	0·0621				0·0625
0·6071	0·20		0·0671	0·0664				0·0668
0·7589	0·25		0·0781	0·0776				0·0779
0·9106	0·3		0·0892	0·0884	0·0887			0·0888
1·214	0·4		0·1116	0·1109	0·1111			0·1112
1·518	0·5		0·1338	0·1331	0·1334			0·1334
1·821	0·6			0·1548	0·1554			0·1551
2·125	0·7			0·1758	0·1763			0·1761
2·428	0·8			0·1960	0·1963			0·1962
2·732	0·9			0·215(0)	0·215(0)			0·215(0)
3·035	1·0			0·232(9)	0·232(9)			0·232(9)
3·643	1·2				0·266(5)			0·266(5)
4·553	1·5				0·310			0·310
5·464	1·8				0·350			0·350
6·071	2·0				0·374			0·374

As described in Section II(*a*), each experimental observation resulted in a value of E/N and a corresponding value of D/μ. With the exception of data excluded for the reasons given in Section II(*b*), the results for hydrogen were plotted on a graph with scales sufficiently large to allow the values of D/μ to be read off at the required values of E/N with an error of no more than 0·3%. Almost 250 individual data points fairly evenly distributed over the whole range of E/N were plotted and every point lay within ±1% of the line of best fit drawn through the data. The results obtained in this manner are given in Table 2 and are considered to be in error by no more than ±2%.

A similar procedure was followed with the raw data for deuterium. Almost 300 individual data points were plotted and only three of these did not lie within ±1% of the line of best fit drawn through the remainder. The values of D/μ read from this graph at the required values of E/N are shown in Table 3. An error limit of ±2% is placed on the data in this table.

TABLE 2

EXPERIMENTAL VALUES OF D/μ FOR ELECTRONS IN HYDROGEN AT 77·3°K

E/N (V cm^2)	D/μ (V)	E/N (V cm^2)	D/μ (V)	E/N (V cm^2)	D/μ (V)	E/N (V cm^2)	D/μ (V)
$2{\cdot}0\times10^{-20}$	0·00676	$2{\cdot}0\times10^{-19}$	0·00986	$2{\cdot}0\times10^{-18}$	0·0294	$2{\cdot}0\times10^{-17}$	0·159(5)
2·5	0·00681	2·5	0·0108(4)	2·5	0·0329	2·5	0·192(9)
3·0	0·00685	3·0	0·0117(9)	3·0	0·0364	3·0	0·224
3·5	0·00690	3·5	0·0126(8)	3·5	0·0398	3·5	0·252
4·0	0·00696	4·0	0·0135(3)	4·0	0·0433	4·0	0·278
4·5	0·00702	4·5	0·0143(2)	4·5	0·0467	4·5	0·302
5·0	0·00709	5·0	0·0150(8)	5·0	0·0502	5·0	0·325
6·0	0·00723	6·0	0·0164(9)	6·0	0·0572	6·0	0·366
7·0	0·00738	7·0	0·0177(7)	7·0	0·0642	7·0	0·405
8·0	0·00755	8·0	0·0189(3)	8·0	0·0713	8·0	0·440
9·0	0·00772	9·0	0·0200	9·0	0·0786	9·0	0·474
1×10^{-19}	0·00790	$1{\cdot}0\times10^{-18}$	0·0210	$1{\cdot}0\times10^{-17}$	0·0860	$1{\cdot}0\times10^{-16}$	0·506
1·2	0·00827	1·2	0·0229	1·2	0·100(8)	1·2	0·565
1·4	0·00867	1·4	0·0247	1·4	0·115(7)		
1·6	0·00907	1·6	0·0263	1·6	0·130(6)		
1·8	0·00946	1·8	0·0278	1·8	0·145(3)		

The raw data in both hydrogen and deuterium showed some evidence of a plateau in the D/μ against E/N curve at about $E/N = 2{\cdot}5\times10^{-20}$ V cm^2, but since the maximum divergence from the smooth curves drawn through the data points given in Tables 2 and 3 was only 0·5% for hydrogen and 0·8% for deuterium, no firm conclusions about the existence of the plateau could be reached.

(c) *Values of* W *in Deuterium at 77·0°K*

In the Bradbury–Nielsen method of measuring drift velocities a graph of the transmitted current as a function of the frequency applied to the shutters, shows a series of maxima and minima whose amplitude decreases with increasing frequency. At constant E/N these maxima and minima should occur at integral multiples of a characteristic frequency f_0 such that $1/2f_0$ is the transit time of the electrons between the shutters. For each determination of the transit time, the frequencies corresponding to the first two maxima were determined. In the results presented below, the two values of f_0 obtained in this way were always in agreement with each other to within

0·2%; in about 90% of the observations the agreement was to within 0·1%. The cases where the agreement was not to within 0·1% were in either of two categories:

(1) at the lowest values of E/N, where the current was small and electrometer noise made accurate estimation of the current peaks more difficult, or

(2) at the lowest pressures used when the current pulses were greatly broadened by the effects of diffusion.

TABLE 3

EXPERIMENTAL VALUES OF D/μ FOR ELECTRONS IN DEUTERIUM AT 77·3°K

E/N (V cm^2)	D/μ (V)	E/N (V cm^2)	D/μ (V)	E/N (V cm^2)	D/μ (V)	E/N (V cm^2)	D/μ (V)
$2{\cdot}0\times10^{-20}$	0·00680	$2{\cdot}0\times10^{-19}$	0·00866	$2{\cdot}0\times10^{-18}$	0·0234	$2{\cdot}0\times10^{-17}$	0·199(7)
2·5	0·00682	2·5	0·00916	2·5	0·0278	2·5	0·237
3·0	0·00685	3·0	0·00962	3·0	0·0323	3·0	0·270
3·5	0·00688	3·5	0·0100(7)	3·5	0·0371	3·5	0·302
4·0	0·00692	4·0	0·0104(9)	4·0	0·0421	4·0	0·331
4·5	0·00697	4·5	0·0109(0)	4·5	0·0471	4·5	0·358
5·0	0·00702	5·0	0·0113(1)	5·0	0·0521	5·0	0·385
6·0	0·00712	6·0	0·0121(1)	6·0	0·0627	6·0	0·435
7·0	0·00722	7·0	0·0128(9)	7·0	0·0737	7·0	0·484
8·0	0·00733	8·0	0·0136(6)	8·0	0·0848	8·0	0·527
9·0	0·00744	9·0	0·0144(3)	9·0	0·0957	9·0	0·570
$1{\cdot}0\times10^{-19}$	0·00756	$1{\cdot}0\times10^{-18}$	0·0152(1)	$1{\cdot}0\times10^{-17}$	0·106(6)	$1{\cdot}0\times10^{-16}$	0·612
1·2	0·00778	1·2	0·0168(1)	1·2	0·127(9)	1·2	0·694
1·4	0·00801	1·4	0·0184(0)	1·4	0·147(6)		
1·6	0·00824	1·6	0·0200	1·6	0·166(2)		
1·8	0·00846	1·8	0·0217	1·8	0·183(6)		

When the apparatus was filled with gas to a high pressure and cooled to 77°K, the thermocouple attached to the electrode adjacent to the top shutter agreed with the liquid nitrogen bath temperature to within 0·1 degK. At all pressures in excess of 100 torr, the temperature rise as recorded by the thermocouple was negligible; at pressures of 50 torr and below, a temperature rise of as much as 1 degK was observed. This temperature rise results from heating of the gas by the filament and is greater in the drift tube than in the lateral diffusion apparatus because the open structure of the drift tube is less effective in thermally coupling the apparatus to the liquid nitrogen bath.

For the data given below it was assumed that the lower half of the apparatus was always maintained at the temperature of the liquid nitrogen, an assumption that was reasonable in the light of experience gained with the D/μ apparatus. The gas temperature used to calculate the values of E/N was therefore taken to be the average of this temperature and the temperature recorded by the thermocouple. On the other hand the temperature to which the drift data refer may be taken as 77·0°K throughout. For pressures greater than 100 torr the deviations from this temperature were less than 0·15 degK, i.e. the temperature fluctuations were small during the measurement of those values of W that are appreciably temperature dependent. Although deviations of the mean temperature of as much as 0·5 degK were observed at 20, 10, and 5 torr, the values of E/N used at these pressures were sufficiently high for W to be substantially independent of the gas temperature. Thus, provided the correct temperature was used to calculate the values of E/N, no significant errors were introduced by these more significant departures from the standard temperature.

Three experimental runs were made in deuterium, the measurements of W being made at predetermined values of E/N. Deviations of the actual values of E/N from the chosen values were always less than 1%, most being less than 0·5%. As a consequence of the small pressure-dependent diffusion error (see below), it is not possible to obtain a curve of best fit to represent the data simply by plotting all the experimental points. As described above, this procedure was followed for the D/μ data, since there is no corresponding difficulty in this case. In order to make a correct comparison of the drift data, on the other hand, it is necessary to present the raw data as a function of both E/N and N as in Table 4. This has been effected by applying to each observed value W' the appropriate small correction arising from the departure of the actual value of E/N from the nominal value, thereby obtaining the values of W' corresponding to the values of E/N in the table.

Results obtained at $E = 3\cdot0$ V/cm showed variations of as much as $\pm0\cdot75\%$, whereas the experimental scatter at high values of E was only 0·2%. It was concluded that the scatter at low field strengths was due to variations in the contact potential differences within the chamber; results taken with field strengths less than 5·0 V/cm were therefore not included in the final table of results.

Lowke (1962) investigated the effects of diffusion on drift velocity measurements and found that the observed drift velocity W' was related to the true drift velocity W through the relation

$$W' = W\{1+C/(hW/D)\}, \tag{2}$$

in which h is the distance between the planes of the shutters. The constant C depends on a number of factors including the mode of operation of the shutters, the ratio of the shutter open time to the transit time, and the relative sizes of the source and the collecting electrode (Burch, in preparation). It has been found (Elford 1966; Crompton, Elford, and Jory 1967) that the results are generally consistent with a value of C of 1·5 and this is the value used throughout the present investigation.

The measured values W' are shown in Table 4.* Each entry is the average of at least two results differing by no more than 0·3%, a large proportion of the differences between the sets of results being only 0·1–0·2%. The "best estimate" values of W in Table 4 were obtained by applying the correction implied by equation (2) and weighting the results in favour of those taken at higher pressures (Elford 1966; Crompton, Elford, and Jory 1967). The corrections made were less than 0·2% for $3\cdot985\times10^{-18} \leqslant E/N \leqslant 3\cdot985\times10^{-17}$ V cm^2 and less than 0·35% at higher values of E/N. An error limit of $\pm2\%$ is placed on the best estimate values in Table 4. This limit is conservative but takes account of uncertainty in the gas number density arising from the temperature rise at lower pressures described above.

---

* Allowance was made for a reduction of 0·1% in the drift distance due to contraction at 77°K.

Below $E/N = 3{\cdot}985 \times 10^{-18}$ V cm² the values of W' increase more rapidly as the pressure is lowered than can be accounted for by the influence of diffusion, and consequently no best estimate values of W are given. For example, the increase in W' at $E/N = 9{\cdot}564 \times 10^{-19}$ V cm² ($\sim 1{\cdot}5\%$) is more than 10 times greater than that expected from the effects of diffusion. Similar behaviour, but on a larger scale, was observed by Lowke (1963) in his measurements in nitrogen at 77·6°K. However, Lowke did not observe any unexpected pressure dependence of his results in hydrogen at low temperature. To check that the pressure dependence in deuterium was genuine and not instrumental, results were taken in hydrogen at $E/N = 7{\cdot}970 \times 10^{-19}$ V cm²

TABLE 4

EXPERIMENTAL VALUES OF DRIFT VELOCITY FOR ELECTRONS IN DEUTERIUM AT 77°K

E/N (V cm²)	W' (cm/sec) at p (torr) of: 500	400	300	200	100	50	Best Estimate, W (cm/sec)
$7{\cdot}970 \times 10^{-20}$	$2{\cdot}69(7) \times 10^{4}$						
9·564	3·19						
$1{\cdot}195 \times 10^{-19}$	3·90	$3{\cdot}91 \times 10^{4}$					
1·435	4·58	4·58	$4{\cdot}61 \times 10^{4}$				
1·594	5·01	5·02	5·04				
1·992	6·07	6·07	6·09	$6{\cdot}14 \times 10^{4}$			
2·391	7·07	7·08	7·10	7·16			
3·188	8·95	8·97	9·00	9·06			
3·985	$1{\cdot}072 \times 10^{5}$	$1{\cdot}072 \times 10^{5}$	$1{\cdot}077 \times 10^{5}$	$1{\cdot}083 \times 10^{5}$	$1{\cdot}090 \times 10^{5}$		
4·782	1·237	1·239	1·243	1·250	1·257		
5·579	1·393	1·395	1·400	1·407	1·414		
6·376	1·540	1·543	1·548	1·555	1·563		
7·173	1·681	1·682	1·687	1·697	1·704		
7·970	1·814	1·816	1·820	1·831	1·838	$1{\cdot}846 \times 10^{5}$	
9·564	2·06(1)	2·06(2)	2·06(7)	2·07(6)	2·08(5)	2·09(4)	
$1{\cdot}195 \times 10^{-18}$		2·39(1)	2·39(6)	2·40(6)	2·41(5)	2·42(4)	
1·435			2·69(5)	2·69(5)	2·70(4)	2·71(4)	
1·594			2·86(0)	2·86(5)	2·87(6)	2·88(7)	
	p = 200	100	50	20	10	5	
1·992	$3{\cdot}25 \times 10^{5}$	$3{\cdot}25 \times 10^{5}$	$3{\cdot}26 \times 10^{5}$	$3{\cdot}29 \times 10^{5}$			
2·391	3·56	3·57	3·58	3·59			
3·188		4·06	4·07	4·08			
3·985		4·43	4·44	4·45	$4{\cdot}46 \times 10^{5}$		
4·782		4·72	4·73	4·74	4·74		$4{\cdot}72 \times 10^{5}$
5·579			4·96	4·97	4·98		4·96
6·376			5·16	5·17	5·19		5·16
7·173			5·34	5·35	5·36		5·34
7·970			5·50	5·51	5·52		5·50
9·564			5·79	5·79	5·81		5·78
$1{\cdot}195 \times 10^{-17}$				6·20	6·21		6·19
1·435				6·59	6·61		6·58
1·594				6·85	6·87	$6{\cdot}88 \times 10^{5}$	6·84
1·992				7·51	7·52	7·54	7·50
2·391				8·15	8·16	8·19	8·14
3·188					9·36	9·39	9·34
3·985					$1{\cdot}044 \times 10^{6}$	$1{\cdot}047 \times 10^{6}$	$1{\cdot}042 \times 10^{6}$
4·782					1·146	1·148	1·144
5·579						1·244	1·240
6·376						1·331	1·326
7·173						1·416	1·411
7·970						1·497	1·492
9·564						1·651	1·646

and $9 \cdot 565 \times 10^{-19}$ V cm^2 over the same range of pressures as in deuterium. These were in good agreement with those of Lowke (1963), but once again W' was found to increase more rapidly with decreasing pressure than could be accounted for by diffusion. However, at $E/N = 7 \cdot 970 \times 10^{-19}$ V cm^2, the increase was only three times that predicted by equation (2) and, since the discrepancy not accountable for by diffusion was only $0 \cdot 5\%$, it is doubtful that Lowke, using a smaller range of pressures and less accurate pressure gauges, would have detected so small a difference. If account is taken of the non-ideal behaviour of hydrogen and deuterium, the unexplained discrepancies are reduced by no more than $0 \cdot 1$–$0 \cdot 2\%$.

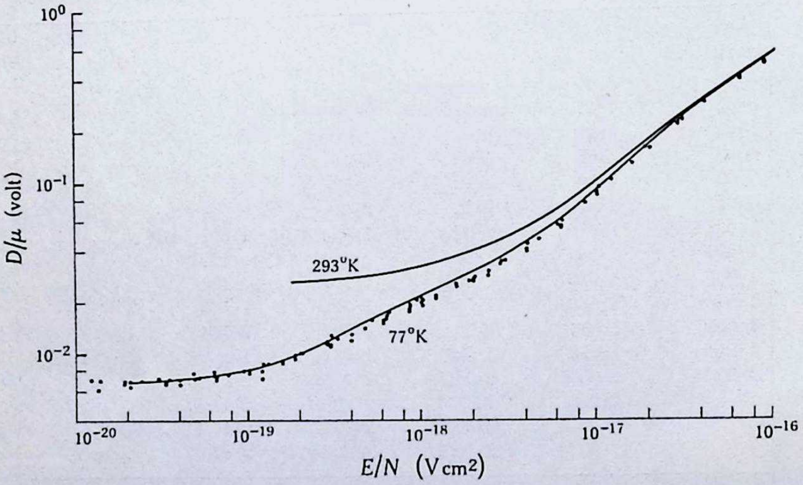

Fig. 3.—Variation of D/μ with E/N for electrons in hydrogen at 77 and 293°K: — present results; ● Warren and Parker.

IV. Discussion

Other results for the values of D/μ in hydrogen have been reported by Townsend and Bailey (1921), Crompton and Sutton (1952), Cochran and Forrester (1962), Crompton and Jory (1962), and Crompton and Elford (1963). Warren and Parker (1962) have reported values of D/μ in hydrogen at 77°K.

With the exception of Crompton and Elford, whose results were presented only in a graphical form, none of the other workers have obtained accurate values of D/μ in the near thermal region. The agreement with Crompton and Elford's results is to within $0 \cdot 5\%$ over the common range of E/N ($1 \cdot 82 \times 10^{-19} \leqslant E/N \leqslant 3 \cdot 03 \times 10^{-18}$ V cm^2 corresponding to $0 \cdot 006 \leqslant E/p_{293} \leqslant 0 \cdot 100$ V cm^{-1} torr^{-1}). The agreement with the results of Crompton and Jory (1962) is well within the combined experimental error.* If a temperature of 15°C is assumed for the work of Townsend and Bailey (1921), their results are also in fair agreement with the present data. Above $E/N = 3 \cdot 03 \times 10^{-17}$ V cm^2 ($E/p_{293} = 1 \cdot 0$ V cm^{-1} torr^{-1}) there is also fair agreement with the results of Crompton and Sutton (1952). The possible sources of error in Crompton and Sutton's data below this value of E/N and the large discrepancy between the data of Cochran and Forrester (1962) and the remaining sets of data have been discussed by Crompton and Jory (1962).

---

* A small correction must be made to the data of these workers. This correction results from the $0 \cdot 37\%$ difference between the torr and the 20°C mmHg used by them.

In Figure 3 the present results in hydrogen at 77°K are compared with those of Warren and Parker (1962), the only other data available for this temperature. All the present experimental points lie within the thickness of the plotted lines. Warren and Parker made no compensation for contact potential differences within their apparatus and used field strengths which, at times, were as little as one-tenth of the smallest used in the present experiments. Thus it would be expected that errors from contact potential differences and other surface effects would be much larger in their results than they are in the present results. The lack of self-consistency of Warren and Parker's data forced them to use an empirical calibration of the apparatus to obtain meaningful results. Even with this calibration, the scatter in the tabulated data supplied by them is still often in excess of 5% and the agreement with the present data is only to within 15–20%. By using low electric field strengths Warren and Parker extended their data to values of E/N approximately an order of magnitude lower than the present results. However, the scatter in their data at these very low values of E/N, and the fact that the present data extend to mean energies that exceed thermal energy by less than 2%, suggest that such a step is neither justified nor essential.

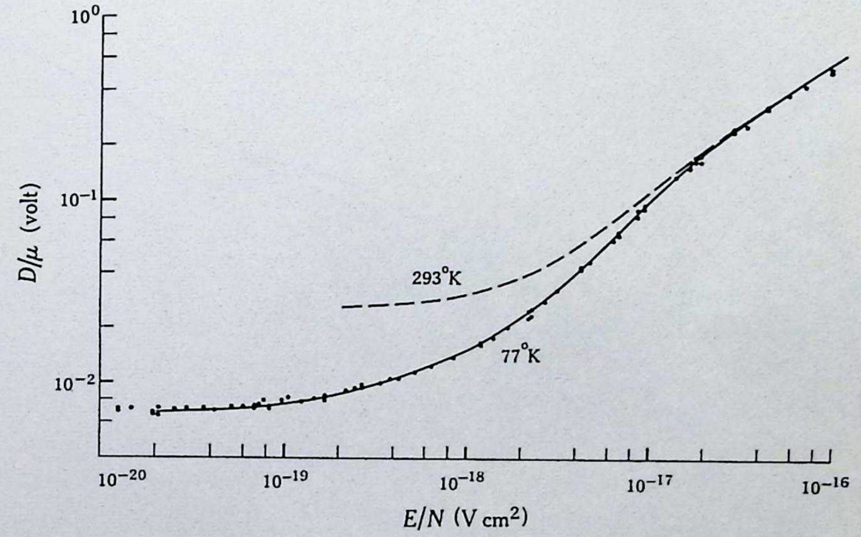

Fig. 4.—Variation of D/μ with E/N for electrons in deuterium at 77°K: — present results; ● Warren and Parker; – – – McIntosh (293°K).

A comparison between the values of D/μ measured at 293 and 77°K is also shown in Figure 3. As expected, the curves at both temperatures extrapolate to the corresponding thermal values of kT/e. As E/N is increased, the energy supplied by the field increases and the effect of the thermal motion of the gas molecules becomes less important. Thus the D/μ curves at the two temperatures gradually merge and the value of D/μ is virtually independent of the gas temperature for $E/N > 4\times10^{-17}$ V cm^2.

The present results for D/μ in deuterium at 77°K are shown in Figure 4. This figure also shows a comparison with the 77°K data of Warren and Parker (1962) and the 293°K data of McIntosh (1966). From the figure it can be seen that the agreement between Warren and Parker's data for deuterium and the present results is considerably better than the corresponding agreement for the hydrogen data, although the scatter in Warren and Parker's data is often in excess of 5%. As in hydrogen, the values of D/μ at the two temperatures gradually merge and the value of D/μ is virtually independent of the gas temperature for $E/N > 4\times10^{-17}$ V cm^2.

The only other results for the drift velocity of electrons in deuterium at 77°K are those of Pack, Voshall, and Phelps (1962). A comparison of the present results with their data and with the 293°K data of McIntosh (1966) is shown in Figure 5. The individual data points for the present 77°K data are not shown since they all lie within the thickness of the plotted line. On the log–log graph shown, the observed pressure dependence below $E/N = 3\cdot985\times10^{-18}$ V cm^2 cannot be seen. The agreement between the present results and those of Pack, Voshall, and Phelps is only fair; their values are approximately 7% above the present data over the whole range of E/N studied. The values of W are independent of temperature for $E/N > 4\times10^{-17}$ V cm^2, this observation agreeing well with the temperature independence of the values of D/μ noted in Figure 5.

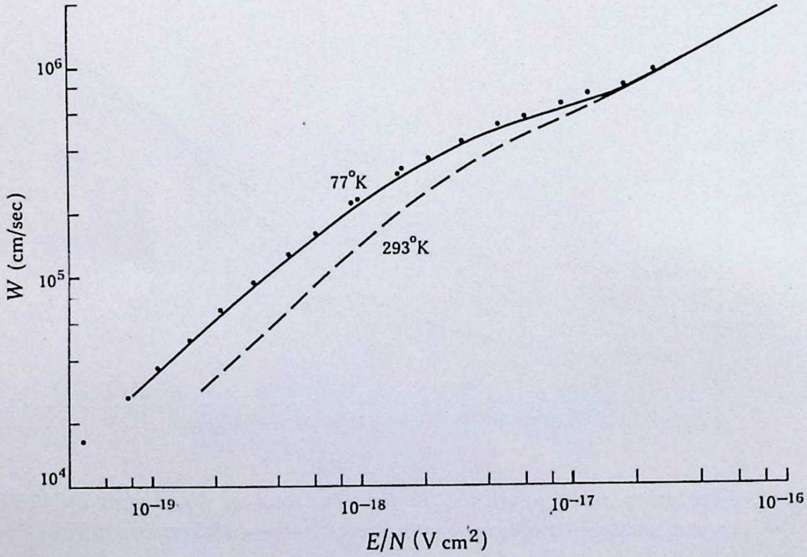

Fig. 5.—Electron drift velocities in deuterium at 77°K: — present results; ● Pack, Voshall, and Phelps; ---- McIntosh (293°K).

A comparison of the values of W and D/μ in hydrogen and deuterium at 77°K is shown in Figure 6. The values of the drift velocities in hydrogen are those of Lowke (1963). From the figure it is seen that:

(1) significant differences between the drift velocities in the two gases appear only for values of E/N greater than the value at which the values of D/μ depart significantly from each other and from the thermal value,

(2) the drift velocity curves for hydrogen and deuterium cross at very nearly the same value of E/N as that at which the D/μ curves cross, and

(3) the fractional differences between the values of W in the two gases are about half those between the values of D/μ at the same value of E/N.

Since the momentum transfer cross section is the same in the two gases, the drift velocity would be expected to be the same in those situations in which the energy distribution functions in the two gases are the same. This situation is realized in the thermal region; the agreement between the measured drift velocities for E/N less than about 10^{-19} V cm^2 thus provides confirmation of the self-consistency of the measurements in the two gases.

The second and third results can be accounted for as follows. For the case of constant momentum transfer cross section q_{m}, it can be shown (e.g. Crompton, Elford, and Jory 1967, equation (A9)) that

$$W = \tfrac{1}{3}(2\,e/m)^{\frac{1}{2}} F\,(E/N)/q_{\mathrm{m}}\,(D/\mu)^{\frac{1}{2}}\,. \tag{3}$$

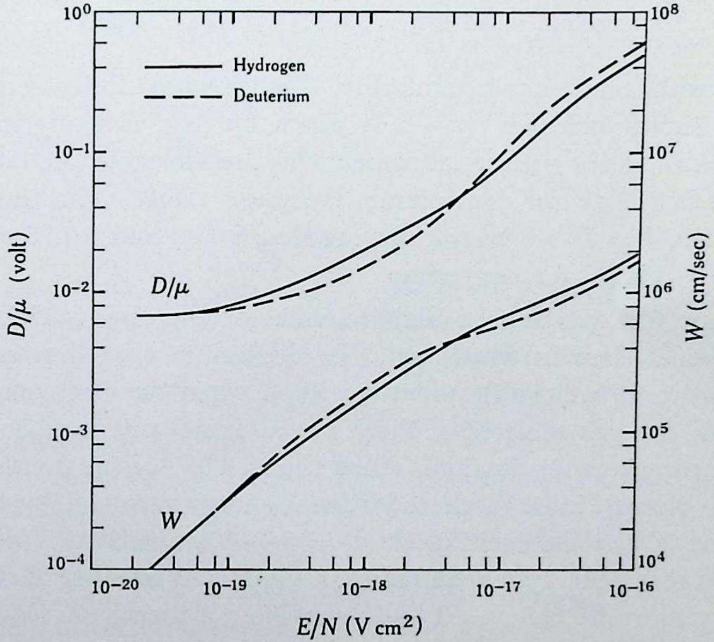

Fig. 6.—A comparison of the variation of W and D/μ with E/N for electrons in hydrogen and deuterium at 77°K.

In this formula e and m are the electronic charge and mass and the factor F is a dimensionless quantity, close to unity, which depends only on the functional form of the energy distribution but is not particularly sensitive to that form. For example, F differs by less than 5% for the Maxwellian and Druyvesteyn distributions. Frost and Phelps (1962) found that their calculated energy distribution functions in hydrogen were intermediate between the Maxwellian and Druyvesteyn forms over the important range of energy, despite the fact that their calculations were carried out over a range of values of D/μ in which the various inelastic processes would assume different degrees of importance. It may therefore be inferred that the energy distributions in hydrogen and deuterium are similar when the values of D/μ are equal, notwithstanding the differences between the inelastic cross sections in the two gases. It follows that, since hydrogen and deuterium have the same, slowly varying, momentum transfer cross section, the values of W should be approximately equal in the two gases for those values of E/N for which D/μ is the same. Furthermore, since the functional forms of the energy distributions never differ greatly, equation (3) shows that, for any value of E/N, the fractional difference between the drift velocities in the two gases should be half the fractional difference between the corresponding values of D/μ. Figure 6 shows that the experimental results are consistent with these conclusions.

The relatively simple situation that exists in hydrogen and deuterium at 77°K makes it possible to give a qualitative explanation of the shape of the curves in Figure 6. It may be shown (e.g. Farkas 1935) that the percentage populations of the rotational levels in these gases at 77°K are:

	$J = 0$	1	2	3
Hydrogen	24·9%	75·0%	0·1%	—
Deuterium	57·2%	33·1%	9·5%	0·3%

in which J is the rotational quantum number. The threshold for each of the rotational transitions in which J changes by $+2$ is given by (e.g. Gerjuoy and Stein 1955) $(4J+6)B_0$, where B_0 is the rotational constant of the molecule ($B_0 = 0{\cdot}00754$ eV for hydrogen and $0{\cdot}00377$ eV for deuterium; Herzberg 1950). The thresholds for the $J = 0 \rightarrow 2$ and the $J = 1 \rightarrow 3$ transitions are thus 0·045 and 0·075 eV for hydrogen and 0·023 and 0·038 eV for deuterium.

From Figure 6 it can be seen that the value of D/μ rises initially more rapidly in hydrogen than it does in deuterium. In deuterium the threshold for the first rotational transition is sufficiently low that, even when the electrons are in thermal equilibrium with the gas molecules, there are a significant number with sufficient energy to cause rotational excitation. Since almost 60% of the deuterium molecules occupy the $J = 0$ level, most of the additional energy received by the electrons as E/N is increased is used in exciting the $J = 0 \rightarrow 2$ transitions. Moreover, only a slight increase in mean energy is required for a significant number of electrons to have sufficient energy to excite the $J = 1 \rightarrow 3$ transition, a transition that is possible for a further 30% of the molecules. As a result the mean electron energy rises only slowly initially. In the case of hydrogen, not only does the first rotational transition have its threshold at the higher value of 0·045 eV, but only 25% of the hydrogen molecules occupy the $J = 0$ level. The energy of the swarm therefore rises more rapidly until a considerable proportion of the electrons have an energy in excess of 0·075 eV, corresponding to the threshold of the $J = 1 \rightarrow 3$ transition. At higher energies the rise is less rapid and, in fact, above $E/N \sim 4 \times 10^{-18}$ V cm^2 it can be seen that the values of D/μ in hydrogen are less than the corresponding values in deuterium. This results from the fact that electrons lose twice as much energy in exciting a transition in hydrogen as they do in exciting the same transition in deuterium, so that, when rotational transitions play a significant role in determining the energy distributions in both gases, the power loss from these collisions may be greater in hydrogen than in deuterium.

At still higher energies significant numbers of electrons have enough energy to cause vibrational excitation of the molecules, the thresholds for this process being 0·516 and 0·360 eV in hydrogen and deuterium respectively (Herzberg 1950). The vibrational excitation process absorbs the additional energy supplied as the value of

E/N is increased and therefore causes a decrease in the slope of the D/μ against E/N curve. A similar explanation can be applied to the drift velocity curves shown in Figure 6.

Although this simple qualitative interpretation is possible, best use can be made of the data only by applying an analysis of the type described by Phelps and co-workers (e.g. Frost and Phelps 1962; Engelhardt and Phelps 1963) from which the energy dependence of the cross sections can be found. Such an analysis of the present data and of the data obtained in pure para-hydrogen (Crompton and McIntosh 1967) is being carried out.

V. ACKNOWLEDGMENTS

The authors wish to thank Mr. J. Gascoigne for invaluable technical assistance throughout the whole of this project and Mr. K. W. Goggin for perfecting the technique for making the shutters in the drift tube. One of us (A. I. McI.) wishes to acknowledge gratefully the financial assistance of an A.N.U. research scholarship during the tenure of which this work was carried out.

VI. REFERENCES

CHANIN, L. M., PHELPS, A. V., and BIONDI, M. A. (1962).—*Phys. Rev.* **128**, 219.
COCHRAN, L. W., and FORRESTER, D. W. (1962).—*Phys. Rev.* **126**, 1785.
CROMPTON, R. W., and ELFORD, M. T. (1957).—*J. scient. Instrum.* **34**, 405.
CROMPTON, R. W., and ELFORD, M. T. (1962).—*J. scient. Instrum.* **39**, 480.
CROMPTON, R. W., and ELFORD, M. T. (1963).—Proc. 6th Int. Conf. on Ionization Phenomena in Gases, Paris, 1963. Vol. 1, p. 337.
CROMPTON, R. W., ELFORD, M. T., and GASCOIGNE, J. (1965).—*Aust. J. Phys.* **18**, 409.
CROMPTON, R. W., ELFORD, M. T., and JORY, R. L. (1967).—*Aust. J. Phys.* **20**, 369.
CROMPTON, R. W., and JORY, R. L. (1962).—*Aust. J. Phys.* **15**, 451.
CROMPTON, R. W., and MCINTOSH, A. I. (1967).—*Phys. Rev. Lett.* **18**, 527.
CROMPTON, R. W., and SUTTON, D. J. (1952).—*Proc. R. Soc.* A **215**, 467.
ELFORD, M. T. (1966).—*Aust. J. Phys.* **19**, 629.
ENGELHARDT, A. G., and PHELPS, A. V. (1963).—*Phys. Rev.* **131**, 2115.
FARKAS, A. A. (1935).—"Ortho–hydrogen, Para–hydrogen and Heavy Hydrogen." (Cambridge Univ. Press.)
FROST, L. S., and PHELPS, A. V. (1962).—*Phys. Rev.* **127**, 1621.
GERJUOY, E., and STEIN, S. (1955).—*Phys. Rev.* **98**, 1848.
HERZBERG, G. (1950).—"Spectra of Diatomic Molecules." (D. Van Nostrand: Princeton.)
HURST, C. A., and LILEY, B. S. (1965).—*Aust. J. Phys.* **18**, 521.
HUXLEY, L. G. H., and CROMPTON, R. W. (1955).—*Proc. phys. Soc.* B **68**, 381.
HUXLEY, L. G. H., and CROMPTON, R. W. (1962).—*In* "Atomic and Molecular Processes" (Ed. D. R. Bates.) p. 335. (Academic Press: New York.)
LILEY, B. S. (1967).—*Aust. J. Phys.* **20**, 527.
LOWKE, J. J. (1962).—*Aust. J. Phys.* **15**, 39.
LOWKE, J. J. (1963).—*Aust. J. Phys.* **16**, 115.
MCINTOSH, A. I. (1966).—*Aust. J. Phys.* **19**, 805.
NIELSEN, R. A. (1936).—*Phys. Rev.* **50**, 950.
PACK, J. L., VOSHALL, R. E., and PHELPS, A. V. (1962).—*Phys. Rev.* **127**, 2084.
PURSAR, K. H., and RICHARDS, J. R. (1959).—*J. scient. Instrum.* **36**, 142.
TOWNSEND, J. S., and BAILEY, V. A. (1921).—*Phil. Mag.* **42**, 873.
WARREN, R. W., and PARKER, J. H. (1962).—*Phys. Rev.* **128**, 2661.
YOUNG, J. R. (1963).—*Rev. scient. Instrum.* **34**, 891.

ACCURATE POSITIONS OF 210 RADIO SOURCES

By A. J. Shimmins*

[*Manuscript received September* 14, 1967]

Summary

The right ascensions and declinations of 210 radio sources have been determined. For most of the sources the estimated error is less than 16″ arc in each coordinate. The sources were selected from the Parkes catalogue of radio sources and are between declinations +27° and −33°.

I. Introduction

This paper is a supplement to a previous paper giving the accurate positions of 644 radio sources (Shimmins, Clarke, and Ekers 1966; subsequently referred to as SCE). The positions of an additional 160 sources are given, and the positions of 50 sources in SCE have been redetermined more accurately.

The sources were selected from the Parkes catalogue of radio sources (Bolton, Gardner, and Mackey 1964; Day *et al.* 1966; Shimmins *et al.* 1966; Shimmins and Day 1968).

The aim has been to extend the declination limit from +20° to +27° (the maximum declination obtainable with the Parkes radio telescope) and the minimum flux density of a complete sample from 1·0 to 0·8 f.u.† at 2650 MHz. It is thought that all catalogue sources in the declination range +27° to −33° (the latitude of Parkes) down to a flux density of 0·8 f.u. at 2650 MHz have now been accurately positioned. In addition, a number of weaker sources were included either because they have flat spectra or because they were identifications that had been suggested on the basis of their catalogue positions. A few very weak sources were included because one of their coordinates was almost identical to that of a stronger source in the programme and accurate relative positions could be measured.

The sources are thought to be mainly extragalactic, although a number of them are within ±10° of the galactic plane.

The positions have been determined to an average accuracy of ±16″ in both coordinates and as such are useful for identification of optical counterparts as faint as 19th magnitude.

The sources were positioned with the 210 ft radio telescope of the Australian National Radio Astronomy Observatory at Parkes, N.S.W., the observations being restricted to a range of ±10 min in hour-angle about the northern meridian, so that the significant errors are a simple function of zenith angle only.

---

* Division of Radiophysics, CSIRO, University Grounds, Chippendale, N.S.W. 2008.

† 1 flux unit = 10^{-26} W m^{-2} Hz^{-1}.

Aust. J. Phys., 1968, **21**, 65–79

The errors were determined empirically each day by including in the observations approximately 12 calibration sources whose radio positions are accurately known. An additional correction as a function of time of transit (i.e. of right ascension) was applied to correct for diurnal temperature effects on the pointing of the telescope.

TABLE 1

POSITION CALIBRATORS NORTH OF DECLINATION −33°

(1)	(2)	(3)				(4)				(5)	(6)	(7)
Parkes Catalogue Number	Other Catalogue Numbers	Right Ascension				Declination				S_{2650}	Remarks*	References†
		h	m	s	s	°	′	″	″			
0021−29	M 00−*29*	00	22	00·59	(±0·05)	−29	45	27·4	(±1·0)	1·5	19^{m} QSO	9
0051−03	3C 26	00	51	35·3	(±0·07)	−03	49	51	(±1·0)	1·1	19^{m} g	7
0157−31	M 01−*315*	01	57	58·3	(±0·4)	−31	07	54	(±12)	2·1	19^{m} QSO	1
0222−23	M 02−*27*	02	22	46·2	(±0·4)	−23	26	12	(±12)	1·3	18^{m} QSO	1
0240−00	3C 71	02	40	07·10	(±0·03)	−00	13	31·5	(±0·4)	3·1	$9{\cdot}8^{\mathrm{m}}$ SO	4
0316+16	CTA 21	03	16	09·11	(±0·2)	+16	17	40·3	(±10)	4·7	Occultation	2
0451−28		04	51	14·0	(±0·5)	−28	12	36	(±12)	2·2	19^{m} QSO	1
0518+16	3C 138	05	18	16·5	(±0·06)	+16	35	30	(±1)	6·4	18^{m} QSO	8
0855+14	3C 212	08	55	55·7	(±0·3)	+14	21	23	(±2)	1·4	Occultation	5
0915−11	Hydra A	09	15	41·2	(±0·03)	−11	53	04·4	(±0·4)	23·5	16^{m} E	4
1040+12	3C 245	10	40	05·89	(±0·06)	+12	19	17·6	(±1)	2·0	Occultation	5
1226+02	3C 273	12	26	33·0	(±0·1)	+02	19	38	(±2)	40·4	Occultation C	6
1327−21		13	27	23·7	(±0·1)	−21	26	34·1	(±1)	1·1	17^{m} QSO	3
1416+06	3C 298	14	16	38·82	(±0·03)	+06	42	21·6	(±0·4)	2·6	18^{m} QSO (*d*)	4
1453−10	14−*121*	14	53	12·3	(±0·5)	−10	56	30	(±10)	2·4	Occultation C	5
1648+05	Herc A	16	48	40·0	(±0·8)	+05	04	35	(±12)	21·9	19^{m} g	11
2115−30	M 21−*34*	21	15	11·1	(±0·1)	−30	31	50·1	(±0·7)	1·3	17^{m} QSO	3
2230+11	CTA 102	22	30	07·71	(±0·05)	+11	28	22·8	(±1·0)	5·3	17^{m} QSO	10

* C indicates that an estimated centroid at 2650 MHz has been used (quoted errors include errors in this estimation); (*d*) indicates object (*d*) in the list of Griffin (1963); other abbreviations are as for Table 2 (see text, Section VII).

† References to positions used are: 1, Bolton, Clarke, and Ekers (1965); 2, Clarke and Batchelor (1965); 3, Ekers and Bolton (1965); 4, Griffin (1963); 5, Hazard, Mackey, and Nicholson (1964); 6, Hazard, Mackey, and Shimmins (1963); 7, Sandage (personal communication); 8, Sandage, Véron, and Wyndham (1965); 9, Véron (personal communication); 10, Véron (1965); 11, Williams, Dewhirst, and Leslie (1961).

II. EQUIPMENT USED

The same equipment was used as for the previous measurements, and it is described in SCE. Briefly, observations were made at 2650 MHz using a degenerate parametric switched radiometer (Cooper, Cousins, and Gruner 1964) with a system temperature of 150°K and an i.f. bandwidth of 40 MHz. With an output time constant of 2 sec, the peak-to-peak noise fluctuations were approximately 0·2 degK, and short-term receiver instabilities were of the same order. The beam was approximately Gaussian with a width of 8′·0 arc at half-intensity points.

III. EXPERIMENTAL PROCEDURES

Calibration sources that were used during the measurements and their positions are given in Table 1. Observations were carried out between June 1966 and June 1967. The period of observation for each source is shown in Table 2 (column 14). The gain of the system was calibrated at intervals of approximately 15 min throughout the 24 hr period of observations by injecting a noise signal into the line between the feed and the r.f. switch.

(*a*) *Right Ascension Measurements*

The telescope was set, under master equatorial control, to the declination of the source, and the hour-angle was set in turn to a number of fixed values (within 10 min of the meridian). Thus a number of drift scans, usually four to six, were obtained for each source. Receiver output was recorded on a paper chart running at 3 in/min. Sidereal time markers were recorded at 10 sec intervals on the same trace. Each right ascension run lasted 24 hr, during which approximately 12 calibration sources were included. In the June 1966 observations a larger number of calibrators (approximately 40) were used in order to define more closely the calibration curve. The feed was set at a position angle of zero during the right ascension measurements.

(*b*) *Declination Measurements*

All the declination measurements were made under master equatorial control, again keeping within an hour-angle of ±10 min from the northern meridian. The telescope was set to the right ascension of the source, and from four to six scans in declination were made at 0·25 deg/min through the source position. Receiver output and declination markers at 5′ arc intervals were recorded on a paper chart running at 3 in/min. During the declination observations the feed was set at a position angle of 90°.

IV. Analysis of Observations

The records were analysed by hand. The apparent right ascension or declination of a source was determined from the centre of symmetry of the drift curve or the declination scan, and an average value obtained for each source. These observed right ascensions and declinations were precessed to epoch 1950·0. The flux density was obtained by measuring the peak amplitude of the record relative to the baseline. An average amplitude of the scans through the source was calculated, and converted into flux units by comparison with the amplitude of adjacent noise calibrations. The value of the noise calibration was obtained from measurements of Hydra A, which was taken as 23·5 f.u. at 2650 MHz. The effects of polarization were removed by taking the mean of the flux densities obtained during the right ascension (position angle 0°) and declination runs (position angle 90°).

V. Calibration of Position Measurements and Errors in Position

The calibration was carried out for both right ascension and declination runs as described in SCE. It was found that for each observing session the diurnal variation in pointing, $g(t)$, was approximately 15″ shift over the 24 hr observing period, and, after correcting for this, the scatter of the calibration sources about the calibration line was 5″ arc. As in the previous observations, it was found that the position errors are due mainly to receiver noise. Such errors were estimated by calculating the r.m.s. scatter between repeated scans (for declination) or successive drifts (for right ascension). These scatters are shown in Figure 1, which is identical to that obtained in previous measurements (SCE, Fig. 4).

VI. Optical Identification

The optical fields of all the sources in this paper have been examined by J. G. Bolton, using the prints of the Palomar Sky Survey. Brief optical data are included in Table 2 (column 13) and full details of the optical search are given in Bolton, Shimmins, and Merkelijn (1968; present issue pp. 81–6).

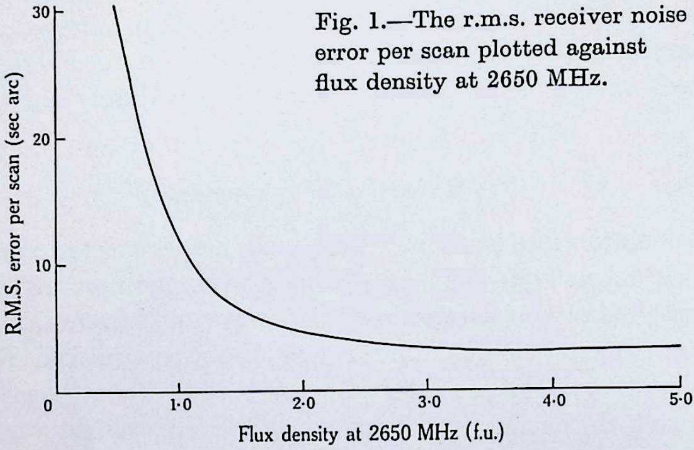

Fig. 1.—The r.m.s. receiver noise error per scan plotted against flux density at 2650 MHz.

VII. Tabulation of Results

The results of the work described in the present paper are contained in Table 2. Information concerning the use of this table is given below.

Column 1. Source number from the Parkes catalogue of radio sources.

Column 2. R means the source is a repeat of a measurement given in SCE.

Column 3. Other catalogue numbers.

Column 4. Measured right ascension (epoch 1950·0).

Column 5. Estimated r.m.s. error in right ascension, given in both seconds of time and seconds of arc.

Column 6. Number of days on which right ascension measurements of the source were made.

Column 7. Total number of drift scans used in deriving the final measurement of right ascension.

Column 8. Measured declination (epoch 1950·0).

Column 9. Estimated r.m.s. error in declination, given in seconds of arc.

Column 10. Number of days on which declination measurements of the source were made.

Column 11. Total number of scans used in deriving the declination.

Column 12. Measured flux density at 2650 MHz in flux units.

Column 13. Classification of optical field within $\pm 1'\cdot 0$ arc from the position of the source and the suggested optical identification. The numerals I–IV are defined as follows:

Class I. Error rectangle includes one or more galaxies brighter than $m_{\mathrm{pg}} = 17$.

Class II. Error rectangle includes one or more galaxies brighter than $m_{\mathrm{pg}} = 19\cdot 5$ and fainter than $m_{\mathrm{pg}} = 17$.

Class III. Error rectangle includes no galaxies above the plate limit.

Class IV. Field is heavily obscured.

The type and estimated photographic magnitude for optical identifications are as follows: E, elliptical galaxy; D, spherical galaxy with extended envelope; SO, spherical system with dust lane; db, dumb-bell or double system; N, compact galaxy with very bright nucleus; g, galaxy too faint for identification; QSO, confirmed quasi-stellar object; QSO?, suspected quasi-stellar object.

Column 14. Period of observation: T9, June 16–19, 1966; T10, October 8–11, 1966; T11A and T11B, February 1–4, 1967; T12, June 26–27, 1967.

Column 15. Remarks and miscellaneous data: S, spectra; Ext, extended.

For two sources measurements were made in one coordinate only. The other coordinate, taken from the Parkes catalogue, has been included and is in parentheses to distinguish it from the present observations.

VIII. Corrections to Previous Paper (SCE)

Since publication of SCE a number of errors have been found. These are given below.

(*a*) *Changes in Positional Data*

Table 1(*a*). The position of 1416+06 (3C 298) as given by Griffin (1963) is R.A. $14^{\mathrm{h}}\,16^{\mathrm{m}}\,38\cdot 82^{\mathrm{s}}$ ($\pm 0\cdot 03^{\mathrm{s}}$).

Table 2(*a*). The positions of a number of sources in Table 2(*a*) have been repeated here. The new measurements given in the present Table 2 should replace those given in SCE. These sources are indicated in the present Table 2 by an R in column 2.

In particular it should be noted that source 2154—18 has been resolved into two sources, 2154—18·4 and 2154—18·3, and the present paper gives the positions of both components.

Table 2(*b*). Correct values for source positions that contain an error in either right ascension or declination as published in Table 2(*b*) in SCE are given in the present Table 3.

TABLE 2

POSITIONS OF RADIO SOURCES NORTH OF DECLINATION −33°

(1) Parkes Catalogue Number	(2) Repeat Obs.	(3) Other Catalogue Numbers	(4) Right Ascension h m s	(5) Error in R.A. s	(5) Error in R.A. ″	(6) No. of Days Obs.	(7) No. of Scans	(8) Declination	(9) Error in Dec. ″	(10) No. of Days Obs.	(11) No. of Scans	(12) S_{2650}	(13) Identification	(14) Period of Obs.	(15) Remarks
0005−06		4C −06·1	00 05 55·4	1·3	19	1	3	−06 15 29	17	1	4	0·6	II g 19^{m}	T11A	
0010+20		(4C 20·1)	00 10 42·4	1·4	20	2	16	+20 30 27	30	1	4	0·5	III	T10 T12	
0011+20		(4C 20·1)	00 11 18·9	1·4	20	2	16	+20 28 27	28	1	7	0·3	III QSO? 18^{m}	T10 T12	
0013−00			00 13 37·2	0·9	14	1	5	−00 31 53	16	1	4	0·7	III QSO? $19{\cdot}5^{m}$	T11A	
0023−26	R	00−*210*	00 23 17·8	0·3	4	3	10	−26 18 46	4	2	10	5·6	III g 0·2min foll.	T9	
0035+13	R	3C 16 4C 13·05	00 35 07·1	0·9	12	2	4	+13 03 35	8	2	7	1·0	III	T11A	
0036+03		00+*010* 4C 03·1	00 36 43·8	1·1	17	1	2	+03 03 21	15	1	2	1·3	I E $14{\cdot}3^{m}$	T11B	
0038+08		4C 08·5	00 38 17·0	1·5	23	1	2	+08 37 07	20	1	2	0·8	II E 17^{m}	T11B	
0042+13		4C 13·6	00 42 45·6	0·9	13	1	4	+13 23 41	13	1	3	0·8	III	T11A	
0047−02		00−*014*	00 47 11·5	1·9	28	1	2	−02 58 43	25	1	2	0·6	III	T11B	
0048−09			00 48 09·3	0·7	10	1	3	−09 45 31	10	1	4	1·4	II blue g $18{\cdot}5^{m}$	T11A	Odd S
0053+26		3C 28 4C 26·2	00 53 10·8	1·0	14	2	9	+26 08 32	15	1	6	0·6	II E $17{\cdot}5^{m}$	T10	
0106+01	R	4C 01·2	01 06 03·6	0·5	8	4	12	+01 19 06	7	2	10	1·1	III QSO $18{\cdot}5^{m}$	T10	
0109+14		4C 14·5	01 09 25·4	1·0	15	1	3	+14 27 39	15	1	3	0·8	III	T11A	
0115+02		4C 02·4	01 15 42·6	1·5	22	1	2	+02 42 42	19	1	2	0·8	III QSO? $17{\cdot}5^{m}$	T11B	
0119+11			01 19 00·6	1·0	15	1	3	+11 34 00	16	1	4	0·8	II g $19{\cdot}5^{m}$	T11A	
0125−14	R	01−*111*	01 25 02·5	0·4	6	2	9	−14 18 28	6	2	14	1·5	III	T9	
0127+23		3C 43 4C 23·6	01 27 15·0	0·6	8	2	8	+23 22 50	9	1	4	1·9	III QSO 19^{m}	T10	
0128+06	R	3C 44 4C 06·7	01 28 43·2	0·7	10	3	10	+06 08 19	5	4	16	0·8	III	T11A T10	
0128+25		4C 25·7	01 28 32·9	0·9	12	1	4	+25 05 02	12	1	4	1·0	III	T10	
0135+22		4C 22·2	01 35 26·4	1·9	26	1	4	+22 46 17	26	1	4	0·4	III	T10	
0156−14			01 56 17·3	0·9	13	1	3	−14 27 38	13	1	4	0·9	III	T11A	
0202+14	R		02 02 07·1	0·3	4	5	20	+14 59 49	5	3	17	2·9	III	T9	
0204+06		4C 06·9	02 04 28·6	0·9	13	1	3	+06 44 38	12	1	3	1·0	III QSO? 16^{m}	T11A	
0207+09		02+*02* 4C 09·8	02 07 07·3	0·9	14	1	4	+09 35 43	15	1	4	0·8	II N 17^{m}	T11A	Odd S

0207−11		02−*13*	02 07 38·4	1·1	17	1	4	−11 12 11	15	1	3	0·9	III			T11B	
0208+21		4C 21·9	02 08 23·3	0·9	12	1	5	+21 05 11	10	2	10	0·9	III			T10	
0216−25	R	02−*215*	02 16 26·6	1·3	18	3	4	−25 02 02	8	3	12	0·7	III			T10	
0229+13		4C 14·13	02 29 02·3	0·8	12	1	2	+13 09 36	10	1	4	1·4	III	QSO	18^{m}	T11A	
0230−06			02 30 23·0	1·7	25	1	2	−06 59 12	22	1	2	0·7	III			T11B	
0231−23	R	02−*211*	02 31 07·1	0·7	10	3	7	−23 34 08	13	2	6	0·6	III			T9	
0232−04	R	4C −04·6	02 32 36·1	0·5	8	2	12	−04 15 06	7	2	13	0·9	III	QSO	$16{\cdot}5^{m}$	T9 T11B	
0235−19	R	02−*110*	02 35 25·2	0·4	5	3	6	−19 45 30	5	3	16	2·8	III			T9	
0237−23			02 37 52·1	0·4	5	2	8	−23 22 08	5	3	14	5·0	III	QSO	$16{\cdot}6^{m}$	T10 T11A	
0253+13			02 53 49·6	1·6	23	1	3	+13 22 29	21	1	4	0·5	III–IV			T11A	
0304−12			03 04 35·7	1·6	23	1	2	−12 17 24	18	1	3	0·8	I	SO	15^{m}	T11B	
0312+10		4C 10·10	03 12 37·4	0·8	12	1	4	+10 01 36	13	1	3	0·9	II	g	$19{\cdot}5^{m}$	T11A	
0312−03		03−0*1* 4C −03·11	03 12 52·1	1·9	28	1	2	−03 27 57	21	1	3	0·6	III	QSO?	$18{\cdot}5^{m}$	T11B	
0338+07		4C 07·13	03 38 12·2	1·0	15	1	4	+07 26 05	15	1	4	0·7	III			T11A	
0349+26		4C 26·12	03 49 01·7	0·9	12	1	9	+26 15 20	10	2	17	0·7	III–IV			T10	
0356+14		3C 96 4C 14·10	03 56 11·8	1·2	17	1	4	+14 27 24	17	1	4	0·7	III			T11A	
0404+03	R	3C 105 4C 03·8	04 04 45·2	0·3	5	5	8	+03 33 11	5	2	10	3·4	III			T9	
0406−18	R		04 06 52·0	0·5	7	2	11	−18 05 04	7	2	12	1·3	III			T9	
0408+07		4C 07·14	04 08 32·1	0·8	12	1	4	+07 00 08	12	1	4	0·9	III	QSO?	18^{m}	T11A	
0417+15		4C 15·13	04 17 30·9	1·2	17	1	3	+15 09 51	15	1	3	0·7	III			T11A	
0417+25		4C 25·14	04 17 46·1	1·1	15	1	9	+25 19 06	12	2	20	0·5	III–IV			T10	
0421+00		4C 00·15	04 21 15·5	1·5	22	2	4	+00 23 51	15	1	4	1·1	III			T11B T12	
0422+00		(04+0*5*)	04 22 11·8	1·5	22	1	4	+00 29 18	15	2	6	0·7	III	QSO	17^{m}	T11B T12	Odd S
0422+08		4C 08·14	04 22 55·0	1·4	21	1	2	+08 26 20	18	1	2	0·9	III			T11B	
0425+17		4C 17·26	04 25 04·2	1·2	17	1	4	+17 46 24	15	1	4	0·6	III			T12	
0428+01		3C 118 4C 01·10	04 28 31·1	1·0	14	1	3	+01 06 30	14	1	3	0·9	III			T11A	
0431−02	R	3C 121 4C 02·17	04 31 23·0	0·4	6	3	15	−02 36 03	6	3	22	1·0	III			T9	
0453+22		3C 132 4C 22·11	04 53 42·4	0·6	8	1	6	+22 44 40	7	2	20	2·1	II	g	19^{m}	T10	

TABLE 2 (*Continued*)

(1) Parkes Catalogue Number	(2) Repeat Obs.	(3) Other Catalogue Numbers	(4) Right Ascension h m s	(5) Error in R.A. s ″	(6) No. of Days Obs.	(7) No. of Scans	(8) Declination	(9) Error in Dec. ″	(10) No. of Days Obs.	(11) No. of Scans	(12) S_{2650}	(13) Identification	(14) Period of Obs.	(15) Remarks
0454+06	R	04+012	04 54 20·9	0·9 14	3	9	+06 39 58	9	3	11	0·5	III QSO? 17·5^{m}	T11A T11B	
0459+25		3C 133 4C 25·16	04 59 54·7	0·5 7	1	4	+25 12 01	7	1	4	3·6	III–IV	T11A	
0508−22	R	05−23	05 08 53·4	0·4 6	4	18	−22 05 24	5	3	20	0·9	III	T9	
0512+24		3C 136·1 4C 24·10	05 12 58·3	0·9 12	1	3	+24 55 13	7	2	12	1·6	II D 17^{m}	T10	
0541−24	R	05−27	05 41 04·0	1·2 17	3	7	−24 22 25	8	2	10	0·5	III	T11A	
0545+26		4C 26·18	05 45 36·5	1·4 19	1	4	+26 35 06	13	2	12	0·6	III–IV	T10	
0601+20		3C 152 4C 20·17	06 01 30·0	1·1 15	1	4	+20 21 26	16	1	3	0·7	IV	T11A	
0601+24		4C 24·11	(06 01 50·8)	— —	0	0	+24 29 38	19	1	4	0·7	III	T10	
0610+26		3C 154 4C 26·20	06 10 43·2	0·4 6	1	9	+26 05 25	6	2	14	3·4	III	T10	
0615+22		3C 157 4C 22·15	06 15 00·7	0·5 7	1	4	+22 40 49	8	1	3	(6·6)	IC 443	T11A	Ext α, δ size 24′
0628+25		4C 25·18	06 28 19·9	1·3 18	1	4	+25 02 44	18	1	5	0·6	II E 18^{m}	T11A	
0640+23		3C 165 4C 23·17	06 40 06·3	0·7 9	1	5	+23 21 59	8	2	10	1·4	III	T10	
0642+21		3C 166 4C 21·21	06 42 25·6	0·7 9	1	4	+21 25 01	7	2	10	1·8	II g 19^{m}	T10	
0649+22		4C 22·18 NRAO 249	06 49 45·1	1·6 21	1	3	+22 36 07	15	2	8	0·6	II g 19^{m}	T10	
0659+25		3C 172 4C 25·19	06 59 04·3	0·8 10	1	2	+25 18 05	7	2	9	1·7	III	T10	
0710+11	R	3C 175 4C 11·26	07 10 15·4	0·8 12	2	2	+11 51 23	5	3	14	1·3	QSO 17·5^{m}	T10	
0711+14	R	3C 175·1 4C 14·21	07 11 15·4	0·4 7	3	8	+14 41 15	13	1	4	1·2	III	T10	
0721+16		(3C 177) 4C 16·21	07 21 58·3	0·8 11	1	8	+16 07 35	14	1	5	0·8	II D 17·5^{m}	T11A	
0725+14	R	3C 181 4C 14·24	07 25 20·4	0·7 10	4	4	+14 43 57	8	4	14	1·2	QSO 19^{m}	T10	

0736+21		4C 21·23	07	36	49·1	1·6	21	1	6	+21	01	36	15	2	17	0·4	III			T10	
0741−06	R	4C −06·18	07	41	54·6	0·3	5	2	9	−06	22	20	4	3	17	4·9	III			T9	
0802+24		3C 192 4C 24·16	08	02	36·6	0·4	6	1	7	+24	18	24	6	2	16	3·3	II	D	15^{m}	T10	Odd S
0805−07			08	05	50·0	0·7	11	1	5	−07	42	30	11	1	5	1·1	III	QSO?	19·5^{m}	T11A	
0812+13		4C 13·37	08	11	57·7	0·7	11	1	5	+13	07	07	12	1	3	1·1	II	E	18^{m}	T11A	
0819+06	R	3C 198 4C 06·30	08	19	51·1	0·7	10	2	5	+06	06	24	10	2	5	0·9	I	E	17·5^{m}	T11A	Ext δ
0827+07		4C 07·25	08	27	24·3	1·4	20	1	3	+07	55	52	19	1	2	0·8	III	QSO?	20^{m}	T11B	
0829+18·7			08	29	25·0	1·0	14	1	2	+18	42	41	13	1	4	0·9	II	N	18^{m}	T11A T12	
0829+18·5			08	29	33·0	1·5	23	1	4	+18	30	15	23	1	4	0·2	III			T11A T12	
0834−19	R		08	34	55·7	0·4	5	3	16	−19	41	35	5	3	14	2·6	III			T9	
0835+25		4C 25·22	08	35	53·4	1·1	15	1	8	+25	37	23	12	2	16	0·5	III			T10	
0837−12		3C 206 NRAO 299	08	37	29·5	0·7	10	1	4	−12	03	33	9	1	6	1·0	III	QSO	15·7^{m}	T9	
0845+09		(4C 09·30)	08	45	24·8	2·0	28	1	3	+09	49	52	25	1	4	0·4	III			T11A	
0850−03		4C −03·34	08	50	56·6	1·4	21	1	3	−03	29	36	17	1	4	0·7	III			T11B	
0855−19	R	08−*119*	08	55	48·9	0·7	10	3	9	−19	39	04	7	4	20	1·0	III	QSO?	19·5^{m}	T10 T11B	
0906+01		(4C 01·24)	09	06	35·7	0·7	10	1	4	+01	33	53	11	1	4	1·2	III	QSO?		T11A	
0909+16	R	4C 16·27	09	09	15·7	2·1	30	2	2	+16	30	55	17	1	4	0·6	III	E	18·5^{m}	T12A	
0911+17		4C 17·48	09	11	17·0	1·0	15	1	4	+17	28	30	20	1	4	0·8	III			T12A	
0915+22		4C 22·23	09	15	38·4	1·6	22	1	4	+22	45	00	22	1	4	0·4	III			T10	
0940+00		4C 00·30	09	40	45·5	1·0	15	1	5	+00	09	24	15	1	6	0·7	III			T11A	
0947+14	R	3C 228 4C 14·34	09	47	28·2	0·3	5	5	15	+14	34	02	5	3	12	1·9	III			T9	
0949+24		3C 229	09	49	10·6	0·7	10	1	6	+24	36	27	9	1	8	1·2	II	db	18^{m}	T10	
0955−01		4C −01·20	09	55	55·4	1·1	17	1	4	−01	26	05	17	1	4	0·7	III			T11A	
1004+13		4C 13·41	10	04	44·0	0·9	13	1	5	+13	03	28	13	1	5	0·8	III	QSO?	16^{m}	T11A	
1015−31	R	10−*35*	10	15	54·4	0·5	6	4	7	−31	29	30	5	2	8	3·0	III			T9	
1019+22		3C 241 4C 22·28	10	19	09·2	1·0	14	1	4	+22	14	21	14	1	4	0·8	III			T10	
1022+20	R	3C 242 4C 20·22	10	22	36·3	1·1	15	3	9	+20	25	37	10	2	8	0·7	III	QSO?	18·5^{m}	T10	
1027+00		4C 00·35	10	27	34·3	1·7	26	1	2	+00	52	59	15	1	6	0·5	III			T11A	
1055+20		4C 20·24	10	55	36·3	2·1	30	1	2	+20	08	14	8	1	4	1·9	III	QSO?	18·5^{m}	T10	
1103−20	R	11−*22*	11	03	55·1	0·4	6	5	8	−20	52	46	6	2	11	1·3	III			T9	

TABLE 2 (*Continued*)

(1) Parkes Catalogue Number	(2) Repeat Obs.	(3) Other Catalogue Numbers	(4) Right Ascension			(5) Error in R.A.		(6) No. of Days Obs.	(7) No. of Scans	(8) Declination			(9) Error in Dec. ″	(10) No. of Days Obs.	(11) No. of Scans	(12) S_{2650}	(13) Identification			(14) Period of Obs.	(15) Remarks
			h	m	s	s	″														
1103−24		11−21	11	03	45·9	1·4	19	1	3	−24	28	25	17	1	5	0·6	II	D	17·5$^{\rm m}$	T11A	
1106+25		3C 250 4C 25·34	11	06	10·6	1·6	21	1	3	+25	17	21	19	1	4	0·6	III			T10	
1107+10	R		11	07	09·9	0·4	6	4	18	+10	59	58	7	3	15	0·8	III	QSO?	18·5$^{\rm m}$	T9	
1110−01		11−05 4C −01·25	11	10	58·4	0·8	12	1	4	−01	56	10	12	1	4	0·9	III			T11A	
1118+23		3C 256 4C 23·27	11	18	04·8	1·0	14	1	5	+23	44	24	14	1	5	0·7	II	D	17·5$^{\rm m}$	T10	
1131−17		(11−17)	11	31	52·7	1·0	14	1	4	−17	11	12	14	1	4	0·8	III	QSO?	19$^{\rm m}$	T11A	
1137+12		4C 12·42	11	37	53·6	0·8	12	1	4	+12	19	41	13	1	5	0·9	I	E	16·5$^{\rm m}$	T11A	
1138+01	R	11+08 4C 01·32	11	38	34·3	0·5	7	3	6	+01	30	51	6	3	10	1·4	III			T9	
1140+22		3C 263·1 4C 22·30	11	40	48·4	0·8	11	1	4	+22	23	36	8	1	8	1·6	III			T10	
1210+20		4C 20·27	12	10	23·2	1·2	16	1	4	+20	49	28	14	1	6	0·8	III			T10	
1212−00		12−07 4C −00·48	12	12	13·6	1·2	18	1	5	−00	43	23	17	1	6	0·6	III			T11A	
1222+21		4C 21·35	12	22	24·0	0·7	10	1	5	+21	39	33	13	1	4	1·1	III	QSO	18$^{\rm m}$	T10	
1226−21		12−26	12	26	08·1	1·4	20	1	4	−21	09	44	17	1	4	0·7	II	db	20$^{\rm m}$	T11B	
1232+21		3C 274·1 4C 21·36	12	32	57·6	0·7	10	1	7	+21	37	10	10	1	7	1·6	III			T10	
1245−19	R		12	45	44·8	0·3	4	4	9	−19	42	55	4	2	9	3·5	III			T9	
1251+15		3C 277·2 4C 15·40	12	51	03·3	0·8	11	1	4	+15	58	40	11	1	6	1·0	III			T11A	
1254−30		12−38	12	54	37·0	2·2	28	1	2	−30	05	35	21	1	3	0·6	I	db	16$^{\rm m}$	T11B	
1318+11	R	4C 11·45	13	18	49·0	0·4	6	3	10	+11	22	16	6	2	14	1·2	III			T9 T10	
1328+25·4		3C 287 4C 25·43	13	28	16·6	0·8	11	1	3	+25	24	30	8	1	3	5·1	III	QSO	17·7$^{\rm m}$	T11B	
1328−25A			13	28	21·8	1·2	16	2	8	−25	44	26	17	2	10	0·7	III	QSO?	20$^{\rm m}$	T11A T12	
1328−25B			13	25	57·6	2·0	28	1	4	−25	42	36	25	1	3	0·2				T12	
1329−25			13	29	45·0	1·0	14	2	8	−25	44	24	16	2	8	0·8	II	g	19·5$^{\rm m}$	T11A T12	
1340−17			13	40	51·8	1·0	15	1	4	−17	33	36	15	1	4	0·7	III			T11A	Odd S

1347+21		3C 291 4C 21·40	13	47	15·4	1·2	17	1	6	+21	22	24	15	1	5	0·5	III	QSO?	16^{m}	T10 T12	
1352+16	R	3C 293·1 4C 16·38	13	52	13·9	0·8	11	3	21	+16	29	33	12	3	19	0·4	I	g	20^{m}	T9	
1355+01			13	55	19·6	0·8	11	1	4	+01	01	06	11	1	4	1·0	III			T11A	
1404−01	R		14	04	14·9	1·7	25	1	2	−01	40	07	13	2	8	0·6	III	QSO?	19·5^{m}	T10	
1410−06			14	10	56·8	1·3	18	1	4	−06	56	29	18	1	4	0·6	II	E	19^{m}	T11A	
1423+24		4C 24·31	14	23	34·8	0·7	9	2	9	+24	17	13	11	1	4	1·0	III	QSO?	18^{m}	T10	
1434+03	R	14+0*10* 4C 03·30	14	34	25·5	0·3	4	8	22	+03	37	10	5	3	23	1·8	III			T9	
1445−16	R	14−1*18*	14	45	28·6	0·5	7	2	9	−16	08	02	7	2	9	1·1	III			T9	
1449−13·0		14−1*19*	14	49	52·4	1·0	15	1	3	−12	59	10	14	1	6	0·8	II	E	18^{m}	T11A T12	
1449−13·1		14−1*19*	14	50	13·0	1·0	15	1	4	−13	06	52	25	1	6	0·6	III			T11A T12	
1504−16·4		15−1*3*	15	04	03·9	1·5	23	1	2	−16	25	50	20	1	4	0·4	III			T12	
1504−16·7	R		15	04	16·0	0·4	6	2	5	−16	40	51	6	3	15	2·3	II	g	18·5^{m}	T10	Odd S
1505+01		4C 01·41	15	05	55·5	1·1	17	1	4	+01	13	38	18	1	4	0·6	III	QSO?	17·5^{m}	T11A	Odd S
1508−05	R	15−0*5* 4C −05·64	15	08	13·9	0·3	4	2	8	−05	31	43	7	2	6	2·8	III			T9	
1514+00		15+0*6* 4C 00·56	15	14	06·2	1·0	15	1	4	+00	25	58	9	1	5	1·7	II	E	16·5^{m}	T11A	
1520+24		3C 321 4C 24·34	15	20	39·1	0·5	7	2	8	+24	13	20	8	1	5	2·2	III			T10	
1532+01			15	32	19·3	0·7	11	1	4	+01	41	07	11	1	4	1·1	III			T11A	
1535+13		4C 13·56	15	35	11·1	1·2	17	1	3	+13	54	37	14	1	3	1·0	III			T11B	
1539−09	R		15	39	25·8	0·6	9	2	10	−09	18	17	11	1	4	1·0	III			T11A	
1545+21		3C 323·1 4C 21·45	15	45	30·7	0·6	9	2	6	+21	01	37	9	1	5	1·6	III	QSO	16^{m}	T10	
1547+21		3C 324 4C 21·46	15	47	36·0	0·6	8	2	4	+21	34	39	9	1	4	1·5	III			T10	
1553+20	R	3C 326·1 4C 20·38	15	53	57·4	0·4	6	5	8	+20	12	55	10	1	4	1·3	III			T10	
1556−21	R	15−2*13*	15	56	09·5	0·4	6	5	26	−21	31	32	6	4	28	0·9	III			T9	
1606+10		4C 10·45	16	06	22·7	0·8	11	1	4	+10	36	38	11	1	4	1·1	III	QSO?	18·5^{m}	T11A	Ext
1610+22		3C 331 4C 22·43	16	10	08·7	1·0	14	2	5	+22	29	36	15	1	4	0·7	III			T10	
1615+21		3C 333 4C 21·47	16	15	04·5	0·8	11	1	4	+21	14	46	11	1	4	1·0	III			T10	
1622+23		3C 336 4C 23·43	16	22	32·7	0·7	9	1	4	+23	52	04	9	1	4	1·5	III	QSO	17·5^{m}	T10	
1622−31			16	22	44·1	1·2	16	1	1	−31	01	38	13	1	3	1·1	III	QSO?	19·5^{m}	T11A	

TABLE 2 (*Continued*)

(1) Parkes Catalogue Number	(2) Repeat Obs.	(3) Other Catalogue Numbers	(4) Right Ascension h m s	(5) Error in R.A. s ″	(6) No. of Days Obs.	(7) No. of Scans	(8) Declination	(9) Error in Dec. ″	(10) No. of Days Obs.	(11) No. of Scans	(12) S_{2650}	(13) Identification	(14) Period of Obs.	(15) Remarks
1623−22			16 23 18·4	1·3 18	1	3	−22 49 04	17	1	3	0·7	IV	T11A	
1625+21		4C 21·48	16 25 20·7	1·3 18	1	4	+21 19 47	20	1	3	0·6	III	T10	
1627+23		3C 340 4C 23·44	16 27 29·7	0·7 10	1	3	+23 26 48	10	1	4	1·4	III	T10 T12	
1634+26		3C 342 4C 26·49	16 34 33·7	0·9 12	2	6	+26 54 03	13	1	4	0·8	III QSO 18^m	T10	
1645+17		(3C 346) 4C 17·71	16 45 28·0	0·7 10	1	3	+17 25 22	10	1	4	1·4	III QSO 19^m	T11A T12	
1712−03		4C −03·62	17 12 23·6	1·0 14	1	6	−03 17 45	16	1	4	0·7	III–IV	T11A	
1730+20		3C 359 4C 20·42	17 30 39·7	1·0 14	2	11	+20 39 54	17	1	6	0·5	III	T10	
1732−08		NRAO 532	17 32 38·7	1·1 16	1	4	−08 00 38	16	1	4	0·6	III	T11A	
1741−03			17 41 20·4	0·5 8	1	4	−03 48 35	8	1	4	2·4	III	T11A	Odd S
1744+23		4C 23·45	17 44 25·0	0·7 10	2	11	+23 43 49	12	1	6	0·8	III	T10	
1801+01			18 01 44·3	0·7 11	1	5	+01 01 25	12	1	4	0·9	III QSO 19^m	T11A	
1810+26		4C 26·55	18 10 29·0	1·0 13	2	12	+26 28 26	16	1	6	0·5	II g $19·5^m$	T10	
1819+22		4C 22·47	18 19 07·9	1·0 13	2	11	+22 49 35	16	1	6	0·6	III	T10	
1821+10			18 21 41·2	0·9 13	1	4	+10 43 12	15	1	5	0·8	III–IV	T11A	
1834+19			18 34 31·2	0·8 11	1	7	+19 39 12	15	1	4	0·8	I E 14^m	T11A	Ext α
1837+23		4C 24·46	18 37 57·3	0·8 10	2	12	+23 59 08	13	1	6	0·7	III	T10	
1859−23			18 59 47·0	0·7 9	1	3	−23 34 00	9	1	4	1·7	IV	T11A	
1915−12		19−15	19 15 06·4	0·9 13	1	4	−12 09 19	15	1	4	0·9	II db 18^m	T11A	
1921+14		3C 400	19 21 21·7	0·6 8	2	8	+14 24 00	30	1	2	108·0	IV	T10	Ext α, δ size <3′
1929−19		19−18	19 29 12·3	1·1 16	1	5	−19 38 01	17	1	4	0·6	III–IV	T11A	
1945−09			19 45 16·2	1·0 15	1	4	−09 27 52	15	1	4	0·8	III–IV	T11A	
2005−04		4C −04·76	20 05 46·0	1·2 18	1	4	−04 27 17	16	1	6	0·6	III QSO 18^m	T11A	
2012+23		3C 409 4C 23·53	20 12 18·1	0·4 6	2	14	+23 25 35	6	1	7	7·1	IV	T10	
2023−07			20 22 58·7	0·7 11	1	5	−07 45 23	14	1	4	1·1	III	T11A	
2031+21		4C 21·55	20 31 19·2	0·6 8	2	11	+21 35 58	9	1	7	1·4	II D $18·5^m$	T10	
2039−29			20 39 38·0	1·5 20	1	3	−29 06 37	18	1	3	0·6	III QSO? $19·5^m$	T11A	
2051+26		4C 26·58	20 51 07·8	1·0 13	2	13	+26 01 35	15	1	7	0·6	III	T10	
2121+24	R	3C 433 4C 24·54	21 21 30·8	0·4 5	3	14	+24 51 20	6	2	8	7·0	I D 17^m	T10	Ext α, δ

2127+04	R		21	28	02·8	0·3	4	5	19	+04	49	01	4	3	19	2·9	III			T9	Odd S
2138+14		4C 14·78	21	38	24·0	1·0	14	1	3	+14	25	00	15	1	3	0·9	III			T11A	Odd S
2144−17	R		21	44	17·1	0·7	10	3	16	−17	54	05	14	2	11	0·6	III	QSO	19·5^{m}	T10	
2149+17			21	50	01·1	0·9	13	1	3	+17	20	22	15	1	2	1·0	III			T11A	
2149−20	R	21−1*21*	21	49	04·4	0·4	5	3	19	−20	00	13	6	3	18	1·3	III			T9	
2154−01		4C −01·57	21	54	12·3	1·2	18	1	4	−01	40	06	15	1	4	0·8	III			T12	
2154−18·4	R	21−1*23*	21	54	10·3	1·2	17	1	4	−18	28	06	18	1	5	1·2	III			T12	
2154−18·3	R	21−1*23*	21	54	43·2	1·2	17	1	5	−18	21	48	18	1	3	0·9	III			T12	
2201+04		4C 04·77	22	01	43·6	1·1	17	1	3	+04	25	52	17	1	4	0·7	III	QSO?	16^{m}	T11A	
2203+05		4C 05·82	22	03	49·2	1·5	22	1	4	+05	41	36	20	1	4	0·6	III			T12	
2210−25			22	10	11·9	1·4	20	1	4	−25	44	00	18	1	4	0·9	III			T12	
2215+02			22	15	15·7	1·1	17	1	4	+02	05	19	18	1	3	0·6	III			T11A	
2227−08			22	27	01·1	0·9	13	1	3	−08	48	12	7	1	6	2·0	IV	QSO?	18^{m}	T11A T11B	
2229−17			22	29	38·5	1·2	17	2	6	−17	14	12	15	1	4	0·6	III			T11A T12	
2234−17			22	34	54·2	1·2	17	1	4	−17	27	36	17	1	4	0·7	III			T12	
2247+13		4C 13·84	22	47	15·0	1·1	15	1	4	+13	15	36	15	1	4	0·8				T12	
2305+18·8		4C 18·68	23	05	18·0	1·4	20	1	4	+18	45	28	17	1	6	0·5	III			T11A	
2313+10		4C 10·71	23	13	03·0	1·2	17	1	4	+10	11	18	17	1	4	0·7	III			T12	
2318+07			23	18	09·7	1·5	22	2	7	+07	55	12	18	2	4	0·4	I	E NGC 7626	13·8^{m}	T12	Ext δ
2318+23		3C 460 4C 23·58	23	18	58·7	0·7	10	2	8	+23	30	31	12	1	4	0·9	III			T10	
2319+07			23	20	05·4	1·5	22	2	4	+07	55	56	15	2	8	0·7	III	QSO?	17·5^{m}	T11A T12	
2322−12	R	23−1*12*	23	22	42·5	0·6	9	6	10	−12	23	58	9	2	6	0·8	I	E5	17^{m}	T10	
2328+10	R	(4C 10·73)	23	28	07·8	0·7	10	2	5	+10	43	53	8	2	6	0·9	III	QSO	18^{m}	T11A	Odd S
2329−10	R	23−1*18*	23	29	50·0	0·4	6	4	29	−10	14	35	6	4	31	0·7	III			T9	
2335+03		4C 03·59	23	35	34·1	1·2	18	1	3	+03	10	21	15	1	3	0·9	III			T11B	
2335+26		3C 465 4C 26·64	23	35	57·4	0·5	6	2	7	+26	44	15	7	1	4	4·0	I	D	12^{m}	T10	Ext α, δ
2337+22		4C 22·63	23	37	52·6	1·0	14	1	2	+22	04	15	14	1	2	1·4	III			T10	
2338+04		4C 04·81	23	38	24·1	0·8	12	1	6	+04	14	31	15	1	4	0·8	III	QSO?	19·5^{m}	T11A	
2349−01	R	23−0*20* 4C −01·61	23	49	22·5	1·0	15	1	4	−01	26	03	9	2	6	0·9	II	N	17·5^{m}	T10	

(*b*) *Changes in Optical Identification*

The following suspected quasi-stellar object identifications given in SCE have been optically confirmed: 0119−04, 0736+01, 0812+02, 0859−14, 1127−14, 1148−00, 1229−02, 1354+19, 1420−27, 1422−29, 1454−06, 1510−08, 2120+16, 2135−14, 2145+06, 2146−13, 2249+18, 2251+11, 2344+09, 2345−16, 2354+14.

Table 3

CORRECTIONS TO SOURCE POSITIONS IN SCE

Source	Right Ascension				Declination			
	h	m	s	″	°	′	″	″
0202−76	02	02	04·4	±15	−76	34	41	±14
0842−75	08	41	58·1	±13	−75	29	55	±14
1547−79	15	47	38·9	±13	(−79	32	36)	
2006−56	20	06	23·9	±19	−56	39	58	±17
2354−35	23	54	26·2	±16	−35	01	19	±15

A number of changes in identifications have been made, with some additional identifications. These are given in Table 4.

Table 4

MODIFICATIONS AND ADDITIONS TO OPTICAL IDENTIFICATIONS GIVEN IN SCE

Abbreviations used as for Table 2 (see text, Section VII)

Source	Identification given in SCE	New Identification	Source	Identification given in SCE	New Identification
0231−23	15$^{\mathrm{m}}$ QSO	Nil	1107+10	18·5$^{\mathrm{m}}$ QSO?	Nil
0319+12	—	18$^{\mathrm{m}}$ QSO?	1502+26	—	16$^{\mathrm{m}}$ db
0413−21	—	19·5$^{\mathrm{m}}$ QSO?	1511+26	—	17·5$^{\mathrm{m}}$ db
0453−30	—	19$^{\mathrm{m}}$ E	2128−12	—	19$^{\mathrm{m}}$ QSO (confirmed)
0456−30	—	17·6$^{\mathrm{m}}$ E3			
0508−22	18·5$^{\mathrm{m}}$ QSO?	19$^{\mathrm{m}}$ galaxy	2149−20	—	19$^{\mathrm{m}}$ QSO?
0539−01	—	HII region	2154−18	16·5$^{\mathrm{m}}$ QSO?	Nil
0834−20	—	18·5$^{\mathrm{m}}$ QSO?	2216−28	18$^{\mathrm{m}}$ E	19$^{\mathrm{m}}$ QSO?
0949+00	18·5$^{\mathrm{m}}$ QSO?	18·5$^{\mathrm{m}}$ N galaxy	2221−02	—	15·3$^{\mathrm{m}}$ N
1049−09	—	16·8$^{\mathrm{m}}$ QSO (confirmed)	2251+15	—	18$^{\mathrm{m}}$ QSO (confirmed)
1103−20	—	18·2$^{\mathrm{m}}$ E	2322−05	N	18·5$^{\mathrm{m}}$ N

IX. Comparison with Other Positions

Twenty-one of the sources listed in Table 2 have been measured by Adgie and Gent (1966) using the interferometer at the Royal Radar Establishment, Great Malvern. Three of these sources have also been measured by Parker, Elsmore, and Shakeshaft (1966). These measurements are about five times more accurate than the positions given in the present paper, but the latter have been retained for completeness. In general the present positions are in agreement with those of Adgie and Gent within the quoted errors. Two exceptions are 0404+03 (3C 105) and 0725+14, which differ by several times the estimated errors.

X. Acknowledgments

Thanks are due to Dr. J. Whiteoak and Mr. G. A. Day for assistance with the observations and to Mr. D. Gill for assistance with the observations and for checking some of the calculations.

XI. References

Adgie, R. L., and Gent, H. (1966).—*Nature, Lond.* **209**, 549.
Bolton, J. G., Clarke, Margaret E., and Ekers, R. D. (1965).—*Aust. J. Phys.* **18**, 627.
Bolton, J. G., Gardner, F. F., and Mackey, M. B. (1964).—*Aust. J. Phys.* **17**, 340.
Bolton, J. G., Shimmins, A. J., and Merkelijn, J. (1968).—*Aust. J. Phys.* **21**, 81.
Clarke, R. W., and Batchelor, R. A. (1965).—*Nature, Lond.* **207**, 511.
Cooper, B. F. C., Cousins, T. E., and Gruner, L. (1964).—*Proc. Instn Radio Engrs Aust.* **25**, 221.
Day, G. A., Shimmins, A. J., Ekers, R. D., and Cole, D. J. (1966).—*Aust. J. Phys.* **19**, 35.
Ekers, R. D., and Bolton, J. G. (1965).—*Aust. J. Phys.* **18**, 669.
Griffin, R. F. (1963).—*Astr. J.* **68**, 421.
Hazard, C., Mackey, M. B., and Nicholson, W. (1964).—*Nature, Lond.* **202**, 227.
Hazard, C., Mackey, M. B., and Shimmins, A. J. (1963).—*Nature, Lond.* **197**, 1037.
Parker, E. A., Elsmore, B., and Shakeshaft, J. R. (1966).—*Nature, Lond.* **210**, 22.
Sandage, A., Véron, P., and Wyndham, J. D. (1965).—*Astrophys. J.* **142**, 1307.
Shimmins, A. J., Clarke, Margaret E., and Ekers, R. D. (1966).—*Aust. J. Phys.* **19**, 649.
Shimmins, A. J., and Day, G. A. (1968).—The Parkes catalogue of radio sources, declination zone +20° to +27°. *Aust. J. Phys.* **21** (in press).
Shimmins, A. J., Day, G. A., Ekers, R. D., and Cole, D. J. (1966).—*Aust. J. Phys.* **19**, 837.
Véron, P. (1965).—*Astrophys. J.* **141**, 332.
Williams, P. J. S., Dewhirst, D. W., and Leslie, P. R. R. (1961).—*Observatory* **81**, 64.

IDENTIFICATION OF RADIO SOURCES BETWEEN DECLINATIONS +27° AND −30°

By J. G. Bolton,* A. J. Shimmins,* and Jeannette Merkelijn*

[*Manuscript received July 24, 1967*]

Summary

Seventy-four identifications have been made from inspection of the 48 in. Sky Survey prints in positions of 150 sources measured with the 210 ft telescope. Thirty-seven of the identified sources are galaxies and 37 possible quasi-stellar objects. In 26 cases previously suggested identifications are confirmed. Finding charts are given for the remainder.

Introduction

Shimmins (1968; present issue pp. 65–79) has recently measured positions of 150 sources between declinations +27° and −33°. These positions have an average accuracy of 15″ arc in both coordinates. We have searched the 48 in. Palomar Sky Survey prints in these positions for identifications.

The selection list for the position measurements comprised all sources in the Parkes catalogue for declinations +20° to +27° (Shimmins and Day 1968) with flux densities at 2650 MHz $\geqslant 0\cdot 8$ flux units and all sources north of −33° in the more southerly zones of the Parkes catalogue with flux densities at 2650 MHz $\geqslant 0\cdot 8$ flux units that had not been previously measured by Shimmins, Clarke, and Ekers (1966). In addition, some sources with spectral indices flatter than $-0\cdot 5$ and flux densities between $0\cdot 5$ and $0\cdot 8$ flux units were included.

The result of the search for identifications is as follows:

15 of the fields were heavily obscured,
1 contained a known supernova remnant,
60 contained only stars of normal colour,
37 contained blue stars that could be quasi-stellar objects,
37 contained galaxies.

North of declination +20° many of the sources are in the 3C or revised 3C catalogues, and identifications for 18 have been previously given by Wyndham and others. For the sake of completeness these identifications are repeated with references to both the original identification and to finding charts. South of +20° eight of the identifications have been previously suggested from this observatory on the basis of the Parkes catalogue positions. Here again the confirmations are listed and references given to finding charts. Finding charts for 49 new identifications are given in the present paper.

---

* Division of Radiophysics, CSIRO, University Grounds, Chippendale, N.S.W. 2008.

Aust. J. Phys., 1968, **21**, 81–6

TABLE 1

LIST OF IDENTIFICATIONS

(1) Parkes Cat. No.	(2) Position (1950·0) R.A. h m s	(3) Dec. ° ′	(4) Flux Density at 1410 MHz	(5) Spectral Index	(6) Type	(7) Magnitude	(8) Galactic Coordinates l^{II}	(9) b^{II}	(10) Ref. to Identification*	(11) Ref. to Finding Chart*	(12) Remarks†	(13) Other Cat. Nos.
0005−06	00 05 56·0	−06 15·5	1·3	−0·8	g	19	95	−67				4C −6·1
0011+20	00 11 18·5	20 29·0		−1·0	QSO?	18	111	−41			S_{2650} = 0·3	4C 21·2
0013−00	00 13 37·5	−00 32·0	0·8	−0·5	QSO?	19·5	104	−62		1	12	
0036+03	00 36 43·8	03 03·4	1·6	−0·7	E2	14·3	117	−59	2	2		
0038+08	00 38 17·0	08 37·5	1·5	−0·9	E3	17	119	−54			13	4C 8·5
0048−09	00 48 09·0	−09 45·4	1·1	+0·3	g	18·5	122	−72	1	1	Very blue	
0053+26	00 53 09·1	26 08·4	1·8	−1·2	E	17·5	124	−36	3	4		3C 28
0115+02	01 15 42·8	02 42·5	1·5	−0·7	QSO?	17·5	136	−59				4C 2·4
0119+11	01 18 59·5	11 34·2	1·2	−0·6	g	19·5	135	−50				
0127+23	01 37 15·0	23 22·9	3·0	−0·7	QSO	19	134	−38	5	5		3C 43
0133+20	01 33 39·8	20 42·2	3·5	−1·0	QSO	17·6	137	−41	6	6		3C 47
0204+06	02 04 28·0	06 44·8	1·4	−0·6	QSO?	16	154	−51				4C 6·9
0207+09	02 07 07·5	09 35·8	1·2	−0·7	N	17	153	−48	2	2		4C 9·8
0312+10	03 12 37·9	10 01·7	1·5	−0·7	g	19·5	171	−39				4C 10·10
0312−03	03 12 52·0	−03 27·8	1·3	−0·9	QSO?	18·5	185	−48				4C −3·11
0408+07	04 08 32·2	07 00·3	1·6	−0·6	QSO?	18	185	−31				4C 7·14
0422+00	04 22 12·2	00 29·2	1·4	−0·5	QSO	17	194	−35			14	
0453+22	04 53 42·4	22 44·7	3·4	−0·8	g	19	176	−15	4	4		3C 132
0512+24	05 12 59·3	24 55·2	3·0	C	D	17	180	−8	4	4		3C 136·1
0628+25	06 28 18·7	25 02·8	1·2	−0·7	E	18	188	7			Brighter galaxy 0′·8 n.p.	3C 162
0642+21	06 42 25·0	21 25·1	2·7	−0·8	g	19	193	8	4	4		3C 166
0649+22	06 49 45·5	22 36·4	1·0	−0·9	g	19	193	10				4C 22·18
0710+11	07 10 16·0	11 51·4	2·7	−1·0	QSO	17·5	205	10	4	4		3C 175
0721+16	07 21 59·2	16 07·7	1·5	−0·9	D	17·5	202	14				4C 15·21
0802+24	08 02 35·5	24 18·5	5·0	−0·6	D	15	198	26	7	4		3C 192
0805−07	08 05 49·1	−07 42·4	1·2	−0·4	QSO?	19·5	229	13				
0812+13	08 11 57·0	13 07·4	1·7	−0·8	E	18	210	24	2	2		4C 13·37
0827+07	08 27 23·0	07 55·7	1·3	−0·9	QSO?	20	217	25				4C 7·25
0829+18	08 29 25·0	18 42·4	1·1	−0·4	N	18	206	30			Possible jet in p.a. 180°	

0906+01	09 06 35·5	01 33·9	1·4	−0·3	QSO?	17·5	229	31				
0949+24	09 49 09·5	24 36·6	1·9	−0·7	db	18	206	50				3C 229
1004+13	10 04 44·0	13 03·5	1·3	−0·8	QSO?	16	225	49				4C 13·41
1022+20	10 22 34·5	20 25·6	0·9	−0·8	QSO?	18·5	217	56				3C 242
1055+20	10 55 37·0	20 07·8	2·2	C	QSO?	18·5	222	63				4C 20·24
1103−24	11 03 45·7	−24 28·5	1·3	−0·9	D	17·5	274	32	8	8		11−21
1118+23	11 18 04·0	23 44·2	1·2	−1·0	D	17·5	218	69	4	4		3C 256
1131−17	11 31 52·5	−17 11·2	1·5	−0·8	QSO?	19	278	42				11−17
1137+12	11 37 53·0	12 19·7	1·6	−0·8	E3	16·5	252	68	2	2		4C 12·42
1222+21	12 22 22·7	21 39·4	1·5	−0·6	QSO	18	255	82				4C 21·35
1226−21	12 26 08·5	−21 09·8	1·3	−0·8	db	20	296	41				12−41
1254−30	12 54 37·0	−30 05·6	1·3	−1·0	db	16	304	33				12−38
1328+25	13 28 16·0	25 24·6	7·0	−0·5	QSO	17·5	23	81	9	9		3C 287
1328−25	13 28 22·0	−25 44·4	1·5	−0·9	QSO?	20	314	36				
1329−25	13 29 45·0	−25 44·5	1·3	−0·7	D	19·5	315	36			Or db galaxy	
1347+21	13 47 15·5	21 25·2	1·1	C	QSO?	16	12	75				4C 21·40
1404−01	14 04 14·5	−01 39·9	1·2	−0·8	QSO?	19·5	337	55				4C −1·31
1410−06	14 10 57·0	−06 15·3	1·1	−0·7	E	19	336	50				
1423+24	14 23 35·2	24 17·2	1·5	−0·9	QSO?	18	30	69				4C 24·31
1449−13	14 49 51·5	−12 59·0	1·3	−0·8	E	18	343	40				14−19
1502+26	15 02 47·5	26 12·5	7·1	−1·0	db	14	39	60	10			3C 310
1505+01	15 05 56·0	01 13·4	1·3	C	QSO?	17·5	0	48				4C 01·41
1511+26	15 11 30·8	26 18·6	4·0	−0·8	db	16	39	58	10			3C 315
1514+00	15 14 05·0	00 26·0	2·5	−0·6	E3	16·5	1	46			15	4C 0·56

* References to original identifications or finding charts are: 1. Bolton and Ekers (1967); 2. Clarke, Bolton, and Shimmins (1966); 3. Mathews, quoted from Schmidt (1965); 4. Wyndham (1966); 5. Sandage, Véron, and Wyndham (1965); 6. Schmidt and Mathews (1964); 7. Longair (1965); 8. Bolton, Clarke, and Ekers (1965); 9. Sandage and Wyndham (1965); 10. Dewhirst (1959); 11. Wyndham (1965).

† Notes on individual sources:

12. Object is 0′·6 north preceding the original object suggested by Bolton and Ekers (1967).
13. The radio and optical positions differ by 0′·4. However, unpublished interferometry results by D. J. Cole and D. K. Milne indicate that the radio source is 2′ arc in extent.
14. Identification is confirmed on a two-colour (blue and u.v.) 48 in. plate.
15. This source was originally identified by Clarke, Bolton, and Shimmins (1966) as a possible quasi-stellar object on the basis of an incorrect catalogue right ascension. This object was shown to have an ultraviolet excess by Bolton and Kinman (1966). The source is extended in right ascension at 11 cm. The position of the peak given by Shimmins agrees with the galaxy. However, a weak confusing source towards later right ascension may be the quasi-stellar object (shown by an arrow on the finding chart). The identification with the galaxy has been given by Caswell and Wills (1967).

TABLE 1 (*Continued*)

(1) Parkes Cat. No.	(2) Position (1950·0) R.A. h m s	(3) Dec. ° ′	(4) Flux Density at 1410 MHz	(5) Spectral Index	(6) Type	(7) Magnitude	(8) Galactic Coordinates l^{II}	(9) b^{II}	(10) Ref. to Identification*	(11) Ref. to Finding Chart*	(12) Remarks†	(13) Other Cat. Nos.
1517+20	15 17 50·0	20 26·9	2·3	−0·8	g	19·5	30	55	11	11		3C 318
1545+21	15 45 30·5	21 01·4	2·3	−0·7	QSO	16	34	49	4	4		3C 323·1
1550+20	15 50 13·0	20 14·5	2·2	C	g	18·5	33	48	4	4		3C 326
1606+10	16 06 23·5	10 36·8	1·6	−0·4	QSO?	18·5	23	41				4C 16·45
1622+23	16 22 32·5	23 52·0	2·7	−0·8	QSO	17·5	41	42	5	5		3C 336
1622−31	16 22 43·5	−31 01·7	1·6	−0·7	QSO?	19·5	348	13			Highly reddened field	
1634+26	16 34 21·5	26 54·3	1·3	−0·8	QSO?	18	46	40				4C 26·49
1645+17	16 45 28·5	17 25·4	1·9	−0·3	QSO?	18·5	35	34				4C 17·71
1801+01	18 01 43·5	01 01·3	1·4	−1·0	QSO?	19	28	11				
1810+26	18 10 29·8	26 28·2	1·1	−1·0	D	19·5	53	20				4C 26·55
1834+19	18 34 29·0	19 41·0	1·8	−0·7	E	14	12	2			16	
1915−12	19 15 07·5	−12 09·4	1·5	−1·0	db	18	25	−11				19−15
2005−04	20 05 46·0	−04 27·3	1·0	−1·0	QSO?	18	38	−19				3C 407
2031+21	20 31 18·7	21 26·0	2·2	−0·6	D	18·5	64	−11				4C 24·50
2039−29	20 39 38·5	−29 06·8	1·3	−1·0	QSO?	19·5	16	−36			Galaxy 0′·2 n.f.	
2121+24	21 21 30·0	24 51·3	12·4	−0·8	D	17	74	−18	10	11		3C 433
2201+04	22 01 43·5	04 25·9	1·0	−0·4	QSO?	16	65	−39			17	4C 04·77
2227−08	22 27 02·1	−08 48·3	1·1	C	QSO?	18	55	−52	1	1	Odd spectrum $S_{2650} = 2\cdot0$ f.u.	
2319+07	23 20 02·5	07 55·8	1·1	−0·3	QSO?	17·5	88	−49				
2335+26	23 35 57·0	26 45·3	6·9	−0·8	D	12	103	−33	10			3C 465
2338+04	23 38 24·0	04 14·6	1·6	−0·9	QSO?	19·5	92	−54				4C 04·81

* For explanation of numbering of references, see corresponding footnote on previous page.

† Notes on individual sources are:

16. Radio position is about 2′ arc south of the optical centre. However, unpublished interferometry results by D. J. Cole and D. K. Milne suggest that the radio source may have an angular extent of 7′.
17. On the basis of the catalogue position the source was originally identified by Clarke, Bolton, and Shimmins (1966), as the galaxy 0′·6 south preceding the blue object. Interferometry shows that the angular size of the source is < 1′. The 0′·6 discrepancy is thus rather high. The accurate position by Shimmins is a good fit for the blue object suggested as a quasi-stellar object. However, the galaxy is not completely excluded.

IDENTIFICATION PROCEDURE

The regions of interest on the 48 in. Sky Survey print were examined with the aid of transparent overlays containing the error rectangle of the source position and the positions of 10 reference stars from the Yale catalogue. Positions of the suggested optical counterparts for the sources can be estimated with the aid of the overlay to 0′·2 arc, or better, where the reference stars are close to the object. Their estimated positions are given in Table 1, columns 2 and 3. Except where noted, identifications were made only if the radio position and the estimated optical position for a source agreed to within 0′·25 arc in both coordinates. The possibility of a chance coincidence with either a galaxy or a blue stellar object of magnitude 19·5 is about 1 in 10.

TABLE OF IDENTIFICATIONS

The identifications are listed in Table 1. Column 1 contains the Parkes catalogue number and column 13 the equivalent number in the 3C, 4C, or MSH catalogues. Columns 4 and 5 contain the flux density at 1410 MHz and the spectral index taken from the Parkes catalogue (C indicates a curved spectrum). Column 6 gives the type of object, as follows:

E	elliptical galaxy,
D	elliptical galaxy with diffuse outer envelope,
S	spiral galaxy,
SO	spherical system with a possible dust lane,
db	dumb-bell or double galaxy,
N	compact galaxy with starlike nucleus,
QSO	quasi-stellar object,
QSO?	possible quasi-stellar object.

Galaxies that are too faint to classify are denoted by g.

Estimates of the photographic magnitude for galaxies and visual magnitude for quasi-stellar objects are given in column 7. Columns 8 and 9 contain the new galactic coordinates of the object. References to prior identifications and to published finding charts are given in columns 10 and 11 and footnotes, and remarks or additional references to footnotes in column 12.

FINDING CHARTS

Finding charts for the identifications are given in Plates 1–6. These were prepared from the Sky Survey prints and the contrast has been increased slightly over that of the original prints. The finding charts for the galaxies were made from the "E" or red print and those for the quasi-stellar objects from the "O" or blue print, except for 0408+07, where the blue print contains flaws near the source. The scale is approximately 5 mm = 1′ arc, and north-east is at the top left-hand corner.

Note added in Proof

Dr. T. D. Kinman (personal communication) has kindly informed us that he has obtained confirmation of some of the suggested quasi-stellar objects through two-colour photography. These are 0115+02, 0312−03, 1634+26, 1645+17, 1801+01, and 2005−04. He found no ultraviolet excess for 0204+06, 0408+07, and 2201+04.

Image tube spectra obtained by Dr. Leonard Searle and Bolton with the Mount Stromlo 74 in. telescope also indicate that 0204+06 is not a quasi-stellar object. Spectroscopic confirmation has been obtained for 0115+02 and 2319+07.

References

Bolton, J. G., Clarke, Margaret E., and Ekers, R. D. (1965).—*Aust. J. Phys.* **18**, 627.

Bolton, J. G., and Ekers, Jennifer (1967).—*Aust. J. Phys.* **20**, 109.

Bolton, J. G., and Kinman, T. D. (1966).—*Astrophys. J.* **145**, 951.

Caswell, J. L., and Wills, D. (1967).—*Mon. Not. R. astr. Soc.* **135**, 231.

Clarke, Margaret E., Bolton, J. G., and Shimmins, A. J. (1966).—*Aust. J. Phys.* **19**, 375.

Dewhirst, D. W. (1959).—*In* "Paris Symposium on Radio Astronomy". (Ed. R. N. Bracewell.) p. 507. (Stanford Univ. Press.)

Longair, M. S. (1965).—*Mon. Not. R. astr. Soc.* **129**, 419.

Sandage, A. R., Véron, P., and Wyndham, J. D. (1965).—*Astrophys. J.* **142**, 1307.

Sandage, A. R., and Wyndham, J. D. (1965).—*Astrophys. J.* **141**, 328.

Schmidt, M. (1965).—*Astrophys. J.* **141**, 1.

Schmidt, M., and Mathews, T. A. (1964).—*Astrophys. J.* **139**, 781.

Shimmins, A. J. (1968).—*Aust. J. Phys.* **21**, 65.

Shimmins, A. J., Clarke, Margaret E., and Ekers, R. D. (1966).—*Aust. J. Phys.* **19**, 649.

Shimmins, A. J., and Day, G. A. (1968).—The Parkes catalogue of radio sources, declination zone +20° to +27°. *Aust. J. Phys.* **21** (in press).

Wyndham, J. D. (1965).—*Astr. J.* **70**, 384.

Wyndham, J. D. (1966).—*Astrophys. J.* **144**, 459.

Plates 1–6.—Finding charts for the identifications (marked between the bars). Scale is 5 mm = 1′ arc. North-east is at the top left-hand corner of each chart.

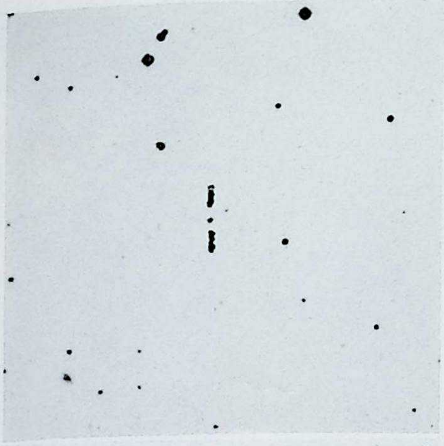

0115 + 02

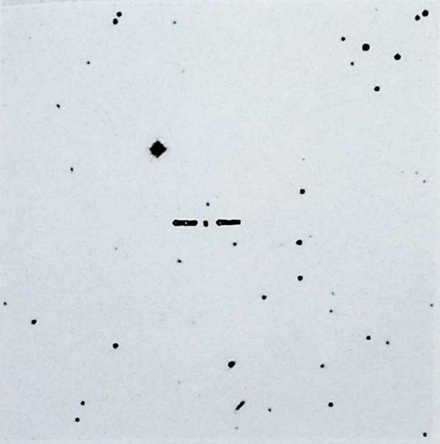

0038 + 08

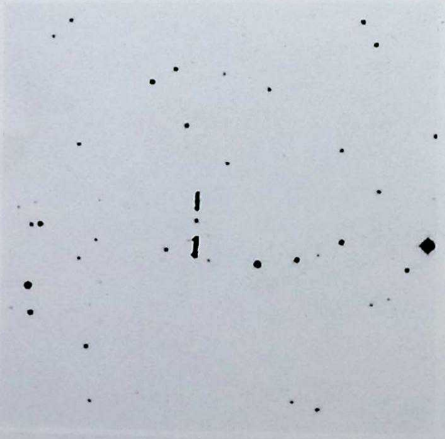

0011 + 20

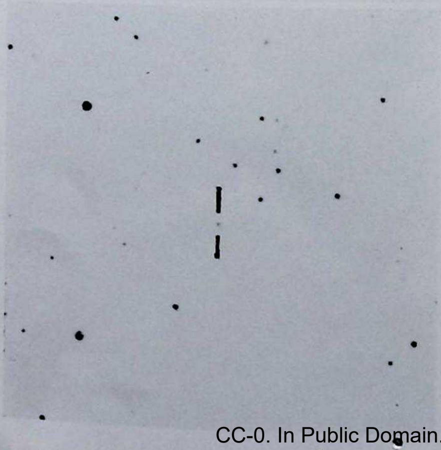

0005−06

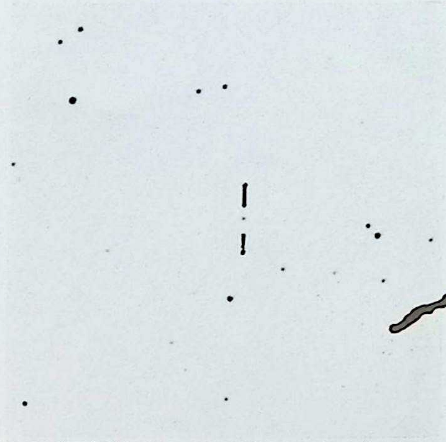

0312 − 03

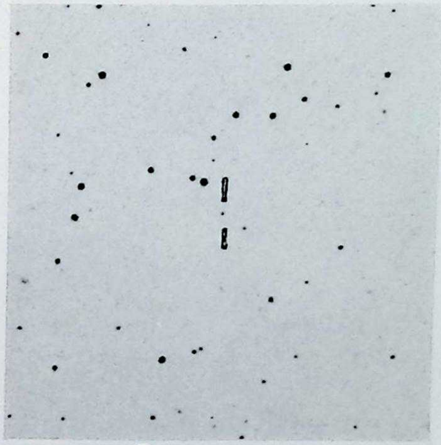

0312 + 10

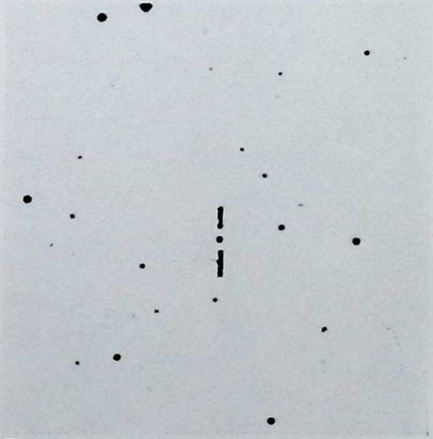

0204 + 06

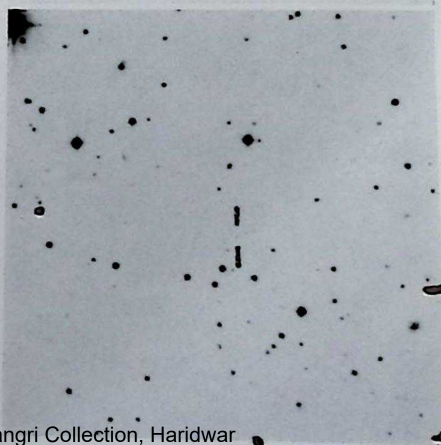

0119 + 11

Aust. J. Phys., 1968, **21**, 81–6

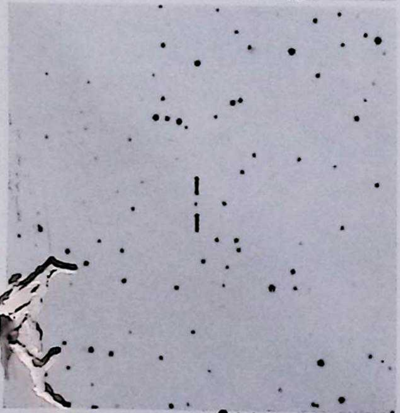

0408 + 07

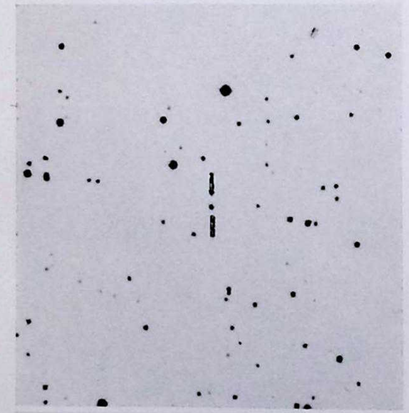

0422 + 00

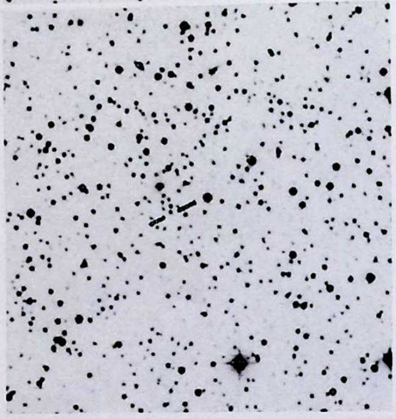

0628 + 25

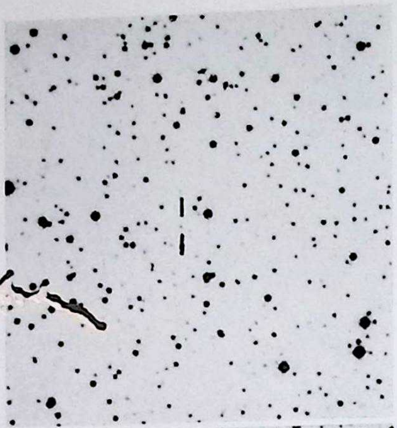

0649 + 22

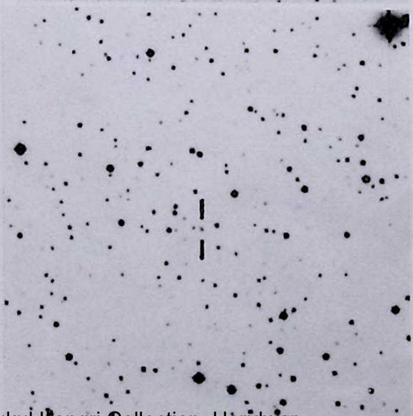

0721 + 16

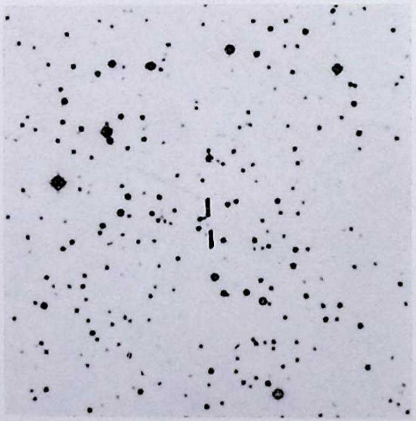

0805 − 07

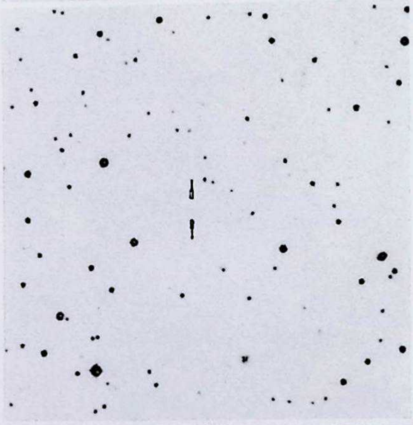

0827 + 07

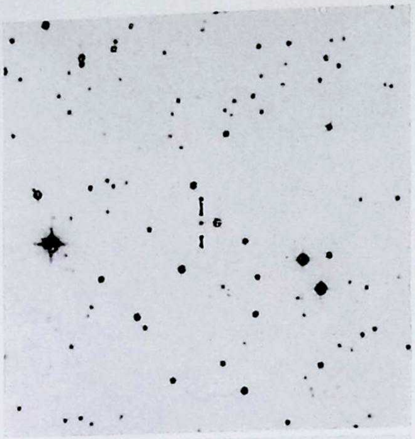

0829 + 18

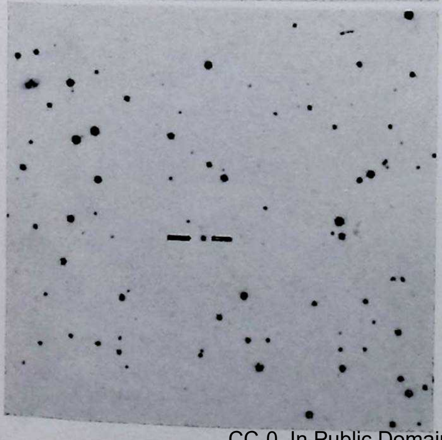
0906 + 01

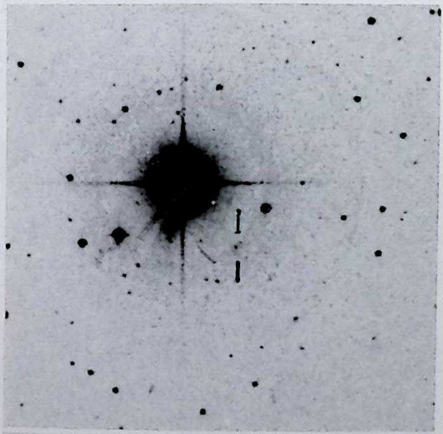
0949 + 24

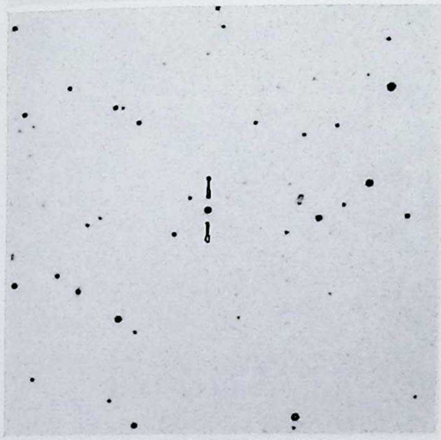
1004 + 13

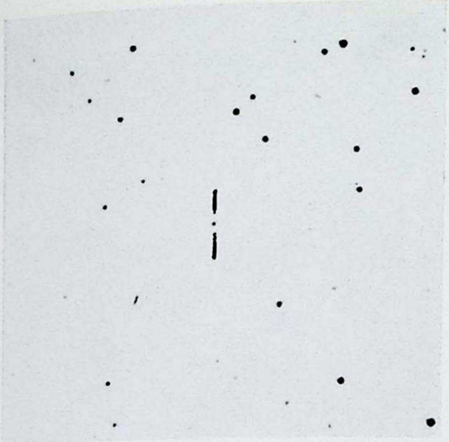
1022 + 20

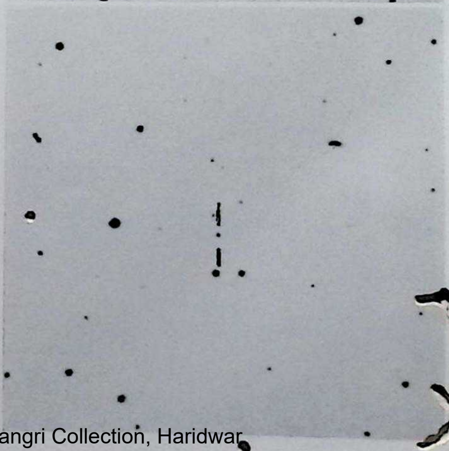
1055 + 20

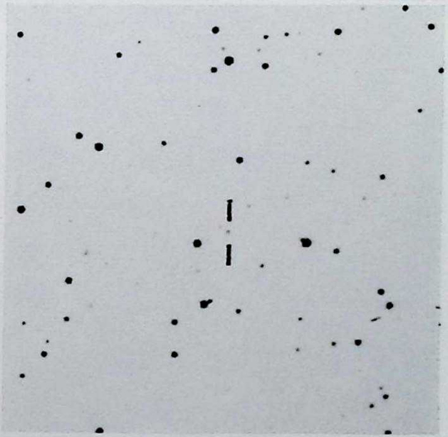
1131−17

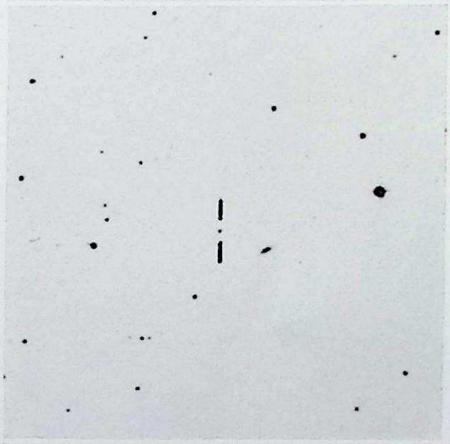
1222 + 21

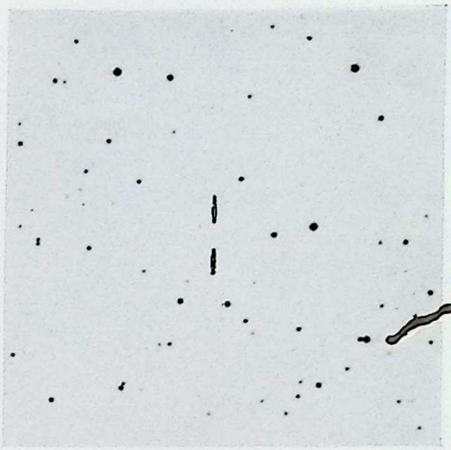
1226−21

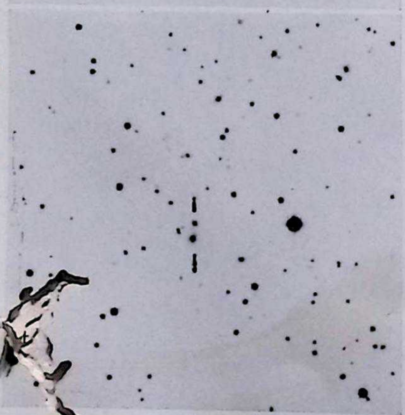
1254—30

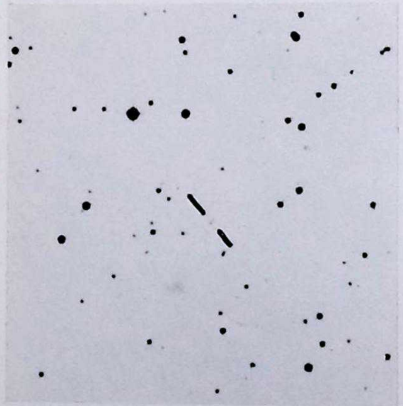
1328—25

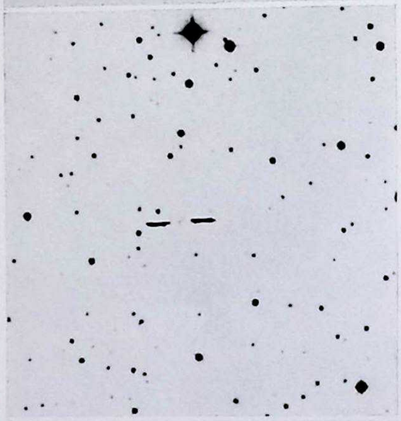
1329—25

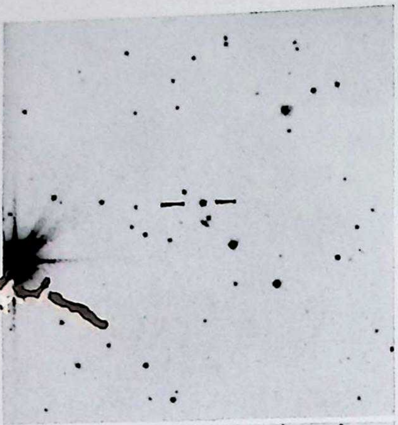
1347 + 21

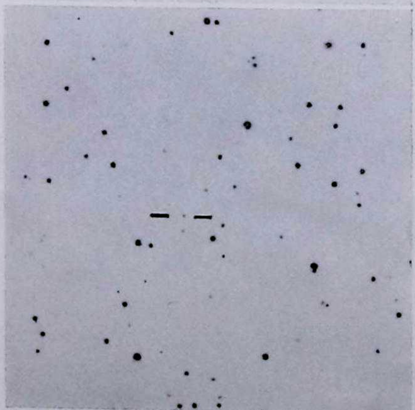
1404—01

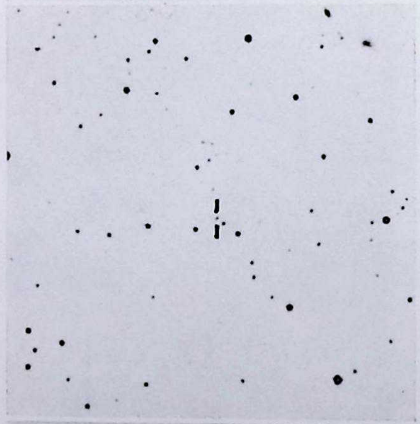
1410—06

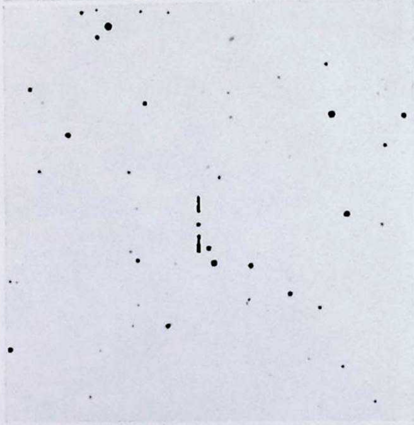
1423 + 24

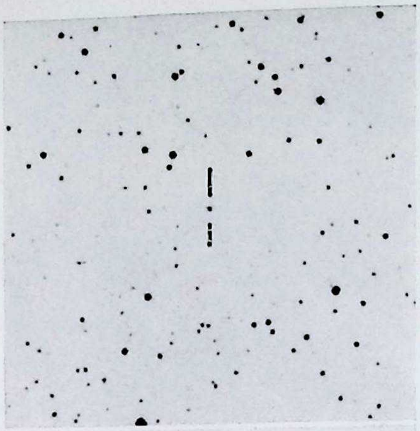
1449 − 13

Aust. J. Phys., 1968, **21**, 81–6

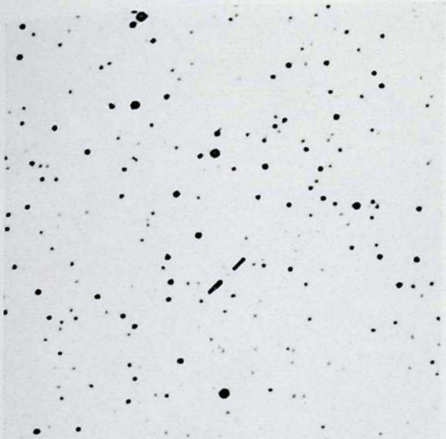
1622—31

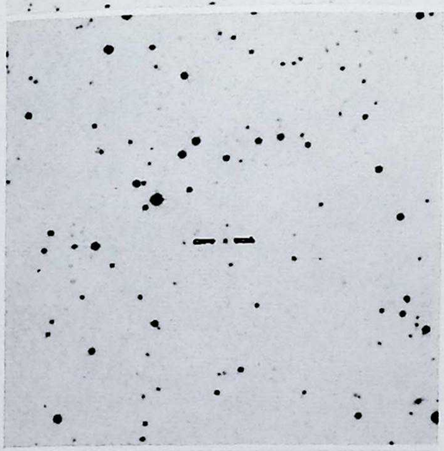
1606+10

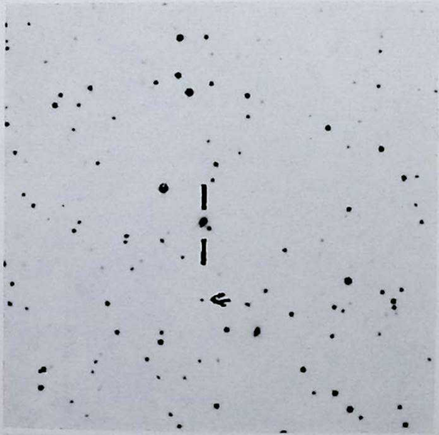
1514+00

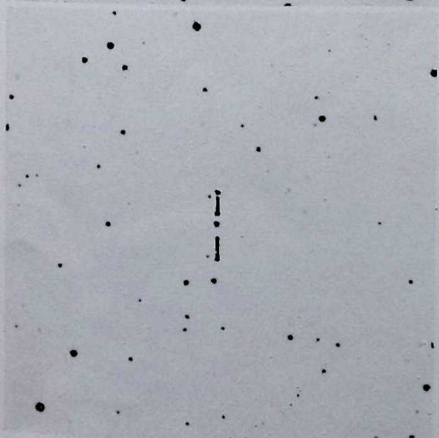
1505—01

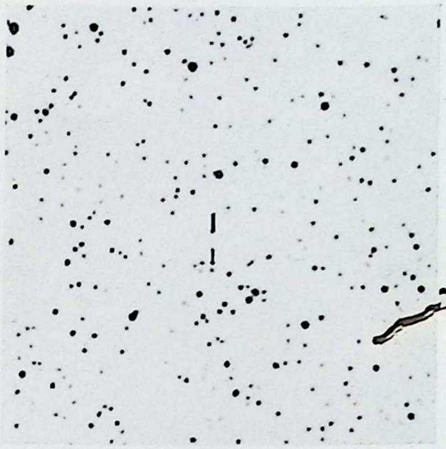
1810+26

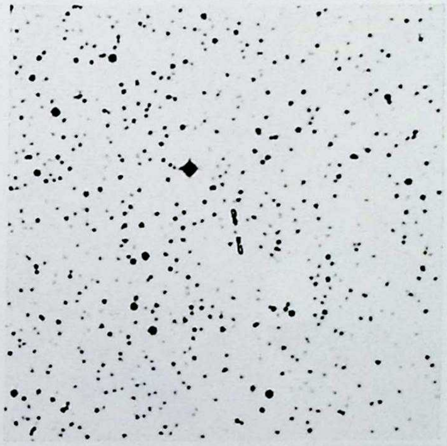
1801+01

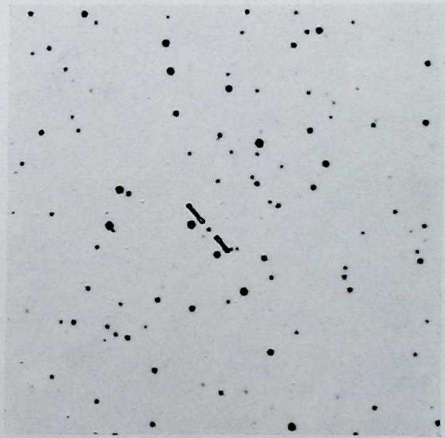
1645+17

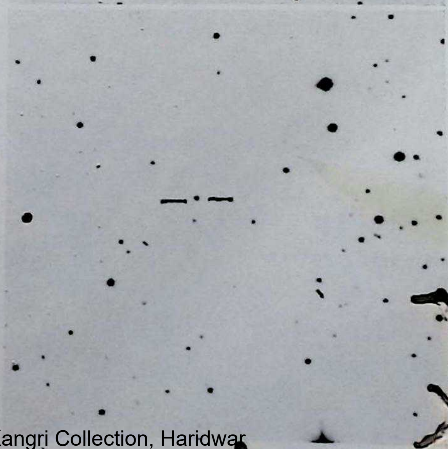
1634+26

Aust. J. Phys., 1968, **21**, 81–

PLATE 6

BOLTON, SHIMMINS, AND MERKELIJN

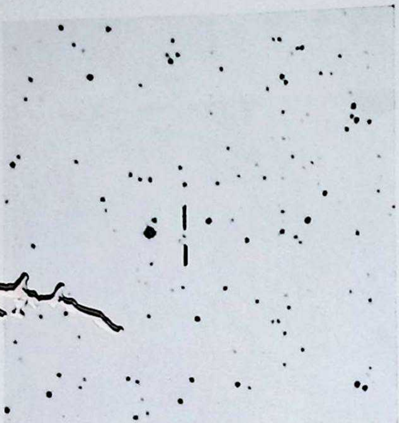

2039−29

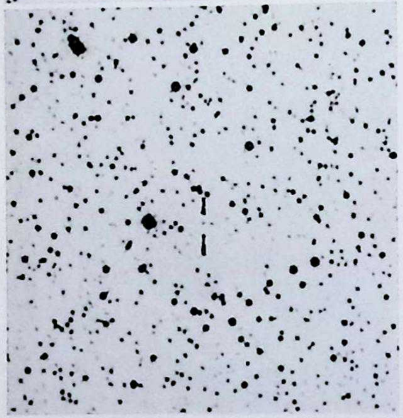

2031+21

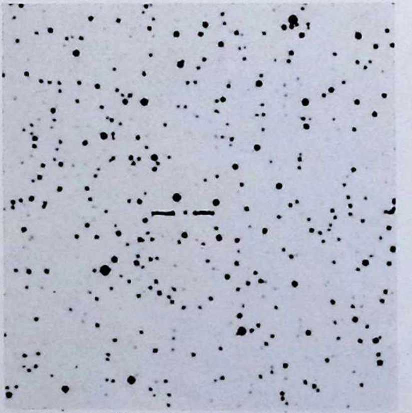

2005−04

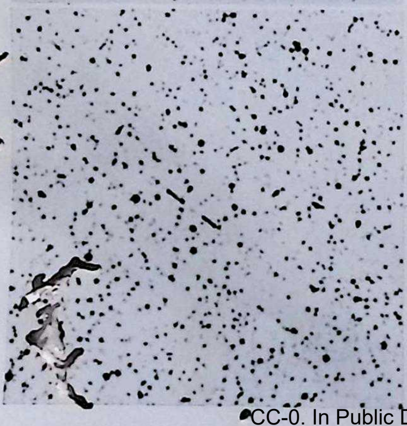

1915−12

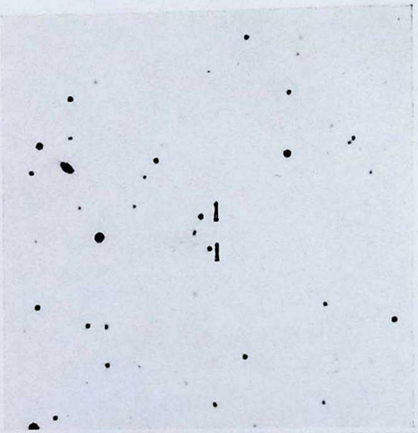

2338+04

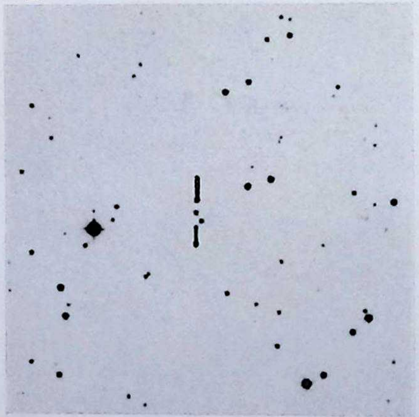

2319+07

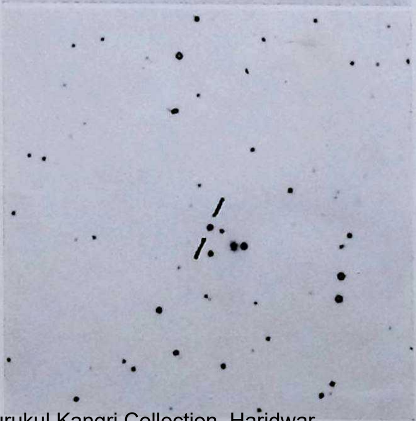

2201+04

Aust. J. Phys., 1968, **21**, 81–6

OBSERVATIONS OF 31 RADIO SOURCES BETWEEN 40 AND 130 MHz

By R. F. Haynes* and P. A. Hamilton*

[*Manuscript received October* 4, 1967]

Summary

Recent observations of 31 radio sources in the frequency range 40–130 MHz obtained at the Australian National Radio Astronomy Observatory, Parkes, N.S.W., are reported in this paper. The results obtained show that some useful information about source emission mechanisms may be deduced.

I. Introduction

Observations of radio sources in the southern sky at 85·5 MHz (Mills, Slee, and Hill 1958), 153 MHz (Hamilton and Haynes 1967), and in the Parkes catalogue at 408, 1410, and 2650 MHz (Bolton, Gardner, and Mackey 1964; Price and Milne 1965; Day *et al.* 1966) have shown that there are quite a number of sources with spectral curves that deviate significantly from a simple power law spectrum of the form $S \propto f^{-a}$, where S is the observed flux density, f is the frequency, and a is the spectral index.

Although a number of these sources have been studied in detail by Broten *et al.* (1965) and Kellermann (1966) at higher frequencies, many have not been investigated in detail below 408 MHz. A number of different theoretical mechanisms can produce curvature in a spectrum, and differentiation between models is not possible unless the shape of the spectrum in the curved region is well defined. Recent results by the authors and by Mills, Slee, and Hill at 85·5 MHz, together with the results in the present paper, have made it possible to define the spectra, at least down to 80 MHz, of 31 radio sources with reasonable accuracy. Of these 31 radio sources, 6 have also been measured down to 42 MHz.

II. Observations

(a) Equipment

Receivers. In order to make observations over the frequency range 40–130 MHz, it was found necessary to use two total-power transistorized receivers that were tuned over the ranges 43–63 and 84–125 MHz. Each receiver had a bandwidth of 2·1 MHz and with a final detection time constant of 3 sec the peak-to-peak noise fluctuations were found to be 1·5 and 2·2 degK for the low and high frequency receivers respectively. The system was tuned remotely using a synchronous motor to drive the ganged condensers on the input stages of each receiver.

---

* Department of Physics, University of Tasmania, Hobart, Tas. 7001.

Aust. J. Phys., 1968, **21**, 87–94

Feed System. The feed system that was designed to work over the required frequency range consisted of a pair of broadband "cage" dipoles mounted at the focus of the 210 ft telescope. Tests of the dipoles for matching efficiency into a load of 100 ohms showed that they were better than 50% efficient from 43 to 160 MHz. Observations showed that the telescope beamwidth at 44 MHz was 7·6°.

(*b*) *System Calibration*

Using the results of Conway, Kellermann, and Long (1963), the source Hydra A (with Parkes catalogue number 0915−11) was taken as a standard reference source. Measurements of this source were used to calibrate a noise signal from a temperature-saturated noise diode. The diode signal was calibrated at close intervals of frequency across both pass bands of the receiver system.

Prior to the observations, the receivers were calibrated for the operating frequency using a d.c. monitoring voltage obtained from a potentiometer mounted on the front-end tuning gang of each receiver. This monitoring voltage was continuously recorded together with the antenna temperature on chart recorders during the source scans.

Because of the possibility of interference during the observations, source identifications were made with two of the standard receivers in use at Parkes (20 cm and 50 cm).

(*c*) *Suitable Sources for Observation*

At frequencies below 120 MHz the possible sources that may be successfully observed with the 210 ft dish at Parkes are limited by the following factors.

(1) *Resolution.* For reliable measurements of the flux density, a source must be separated from nearby sources according to the beamwidth of the telescope at the operating frequency, i.e. for measurements down to 44 MHz the source must be separated from nearby sources by 7·5°.

(2) *Background Emission.* Emission from the galaxy was found to be the chief factor limiting the observations, especially within 10° to 15° of the galactic plane. Away from the galactic plane the source was confused by background fluctuations in only three cases.

(3) *Source Strength.* Owing to the high background temperature, only in exceptional cases were sources observed with a flux density < 20 f.u.* at 85 MHz.

(4) *Interference.* Observations over the whole of the desired frequency band were not possible owing to regions of man-made interference. Such interference was especially intense near 50 and 80 MHz.

Taking into consideration the above limitations, the published catalogues of radio sources in the southern sky were used to locate suitable sources for observation. With the assumption that the telescope has a Gaussian beam, the background flux due to nearby sources in the vicinity of each source was deduced. As a result 45 suitable sources were found where the background was small compared with the source strength.

---

* 1 flux unit = 10^{-26} W m^{-2} Hz^{-1}.

III. RESULTS

Of the 45 selected sources, 8 were found to be too weak to measure, either because the background emission was rapidly varying or because the source intensity was much smaller at these frequencies than previous observations at higher frequencies had indicated. After analysis, 6 of the source measurements were found to be confused due to interference. The results for the remaining sources are summarized in Table 1.

(*a*) *Errors in the Flux Density Measurements*

The flux densities listed in Table 1 are thought to be accurate to within 17% ±2 f.u. for the high frequency receiver, and 21%±6 f.u. for the low frequency receiver. The chief source of error in the measured results was due to the method of frequency-sensitivity calibration using the standard source Hydra A. Variations in the calibration signal from the saturated noise diode were found to be not greater than 7%. However, repeated scans of the calibration source over the frequency band showed variations in source intensity of up to 10% for the high frequency receiver and 14% for the low frequency receiver. Such fluctuations in source strength were probably due to small amounts of interference not detected at the time of observation.

Noise fluctuations from the receivers were less than 4 and 2 f.u. for the high and low frequency receivers respectively.

Any errors due to polarization of either the source or the background emission have been ignored since the polarization is probably small at these frequencies.

(*b*) *Notes on Table 1*

Table 1 contains a summary of the observations that have been completed for 31 radio sources at various frequencies between 43 and 130 MHz. Details of the columns of Table 1 are:

Column 1. Source catalogue number from the Parkes catalogue.

Columns 2 and 3. Frequency and flux density results between 43 and 130 MHz.

Columns 4–9. Flux densities (in f.u.) at frequencies of 85·5, 153, 159 (or 178), 408, 1410, and 2650 MHz respectively. Observations at 85·5 MHz are from the Mills, Slee, and Hill (1958) catalogue; at 153 MHz from Hamilton and Haynes (1967); at 159(178) MHz from the 3C catalogue; and at 408, 1410, and 2650 MHz from the Parkes catalogue.

Column 10. Comments and identifications. The abbreviations used are: P, polarization; ext, source extended at high frequencies; M, magnitude of galaxy; EW, east–west angular size. Other notation indicating the type of optical identification (I, II, III, E, N, D, db, QSO) follows that of Bolton, Gardner, and Mackey (1964) and Bolton, Clarke, and Ekers (1965).

TABLE 1

FLUX DENSITIES OF OBSERVED SOURCES

(1)	(2)	(3)	(4)	(5)	(6)	(7)	(8)	(9)	(10)
	Present	Results	Other Flux Density Measurements at a Frequency (MHz) of:						
Parkes Cat. No.	Frequency (MHz)	Flux Density (f.u.)	85·5	153	159(178)	408	1410	2650	Remarks
0123−01	82·7	59·6	88	25·1	26·0	16·4	4·5	(1·9)	I db 13·2M NGC545/7
	84·0	69·3							
	88·2	63·0							
	94·0	61·2							
	99·2	71·7							
	99·2	68·1							
	112·9	53·6							
	112·9	54·6							
	113·0	56·6							
0252−71	99·0	9·1	7·0			14·0	5·9		
	86·1	11·15							
0320−37	42·7	1255	950	474		249		89	NGC1316 P12%
	46·3	1532							Fornax A
	58·0	1309							
0349−27	86·5	50·1	53			15·8	5·2	3·1	P3·3% ext
	91·0	42·0							
	95·0	47·0							
	95·0	46·8							
	103·0	44·0							
	108·0	42·6							
	112·5	41·7							
0408−65	49·2	33·0	36·0			45·0	15·0		
	87·5	32·5							
	108·5	35·9							
	109·0	43·2							
0410−75	46·0	91·7	87·0	(55·3)		40·0	13·5	7·5	P<1%
	109·0	89·4							
0442−28	82·8	129·8	82·0	(66·0)		22·0	7·1	3·9	P3·7% ext
	86·2	95·5							
	91·5	86·1							
0518−45	44·0	774·2	570	343·0		166	66	30	Pictor A 19M P3%
0521−36	43·9	49·14	66	54·5		37	18·6	11·4	P3·5% N 16·8M
	46·3	45·5							(QSO)
	46·3	55·0							(Westerlund and Stokes 1966)
	88·0	55·3							
	88·0	51·3							
	93·2	47·4							
0522−69	102·2	5490	400			1100	620		L.M.C.
0532−05	42·2	73·7	(69)	41·6	45·0	(213)	(289)	(49)	HII Orion nebula
	47·3	89·0							
0634−20	88·0	71·8	67			21	7·0	2·8	P6% ext at 11 cm
	93·8	67·7							
	105	54·0							
1226+02	99·2	134·0	167·0		72	55·1	41·2	37·3	QSO 3C273

TABLE 1 (*Continued*)

(1)	(2)	(3)	(4)	(5)	(6)	(7)	(8)	(9)	(10)
	Present Results		Other Flux Density Measurements at a Frequency (MHz) of:						
Parkes Cat. No.	Frequency (MHz)	Flux Density (f.u.)	85·5	153	159(178)	408	1410	2650	Remarks
1416+06	100·0 116·0	96·2 91·0	114		48·0	24·4	6·2	2·7	III QSO
1459−41	87·0 105·2	60·9 40·7	55		32·9	17·4	4·7	1·4	ext at 11 cm
1602−63	109·0 112·0	36·5 35·7				14·6	5·4		
1648+05	98·0 113·0	695·6 627·0	890		350	161	46·0	24·6	18M P1% Herc. A
1717−00	98·0 111·0 113·2	417·2 327·6 383·4	475		180	138	50·2	27·5	16·8M P3%
1754−59	93·2	39·14	25			15·0	3·9	1·5	P3·2%
1814−51	113·2	28·4	27·0			14·4	4·2	1·6	P2·6%
1814−63	94·0 108·0 113·2	74·6 80·0 86·4	71·0			34·0	14·2	7·5	<20″ EW
1827−36	111·8 112·0	35·9 42·2				23·0	7·4	3·2	
1836+17	Flux at 80 MHz <40 f.u.				26	15·9	7·6	(4·0)	I 16M ext
1932−46	89·0 115·8 97·0	136·0 111·8 124·0	141			39	13·4	6·9	P1·2%
1938−15	93·2	44·4	(39)			16·5	6·9	3·8	III–IV
1949+02	93·2	70·7	64		28	15·4	5·1	3·6	I E 16·5M (QSO)
1954−55	93·6 113·2	54·7 62·3	54			14·8	7·0	4·0	P<1·5%
2104−25	99·0	109·0	100	54·1		31·0	12·0	7·3	16M E P<1%
2152−69	89·0 99·0 112·5 113·2	218·7 198 160·7 168·9	253			80·0	32·0	17·5	25″ EW P2–3%
2211−17	85·0 101·0 106·0 112·9	147·1 126·4 113·2 95·81	127		49·0	31·3	7·9	4·2	II D 19M P1%
2356−61	84·0 98·0 99·0 109·0 109·0 115·0	254·8 214·2 208·4 190·3 194·4 165·0	296·0			66·0	23·7	10·4	P5% 40″ EW

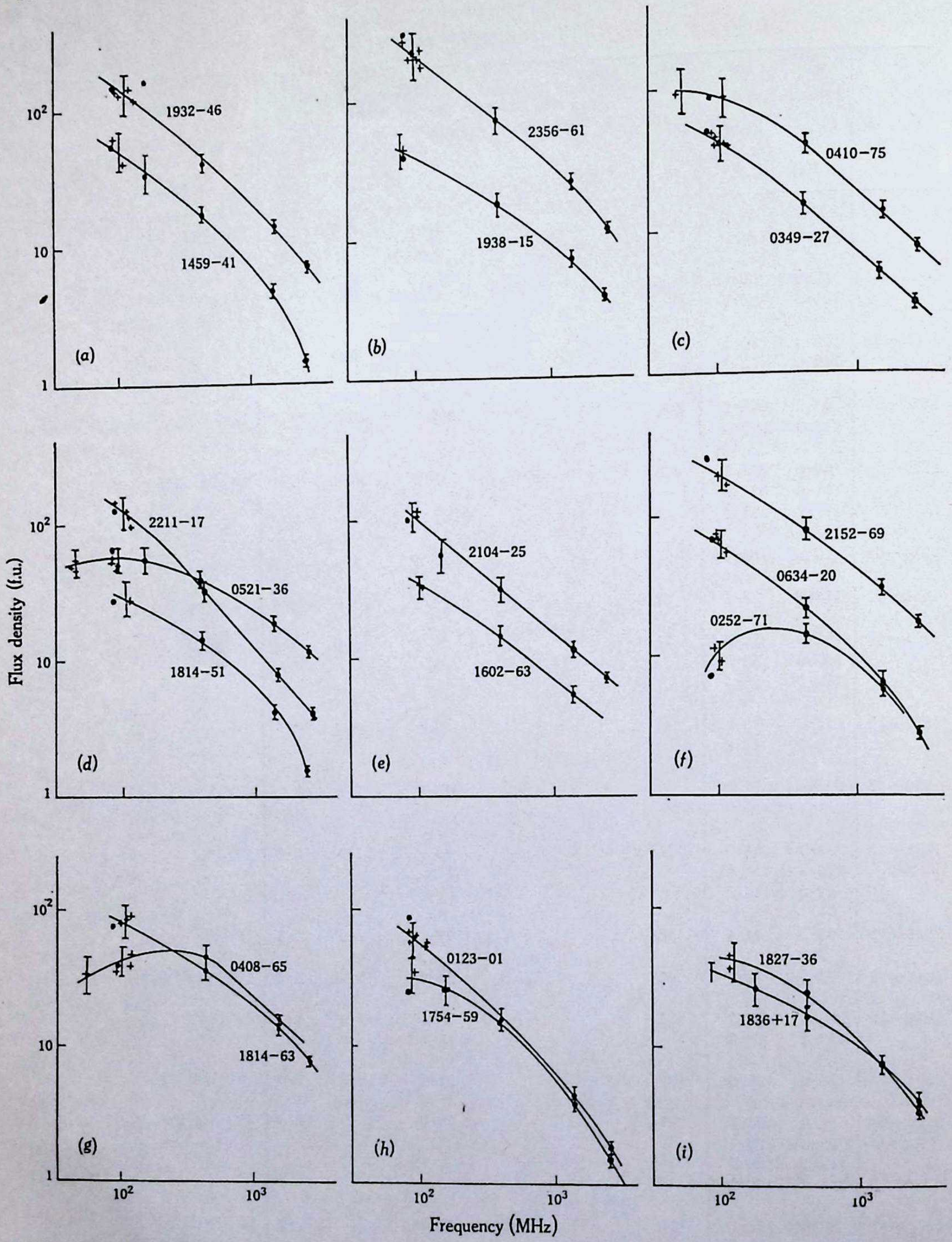

Figs. 1(*a*)–1(*i*)

(c) *Source Spectra*

The new observations of 31 radio sources have shown that 26 have distinct curvature in their emission spectra. Measurements near 40 MHz for those sources that were not observed would be useful but, nevertheless, the results are adequate to determine the spectra of all 31 radio sources down to 80 MHz. Following the

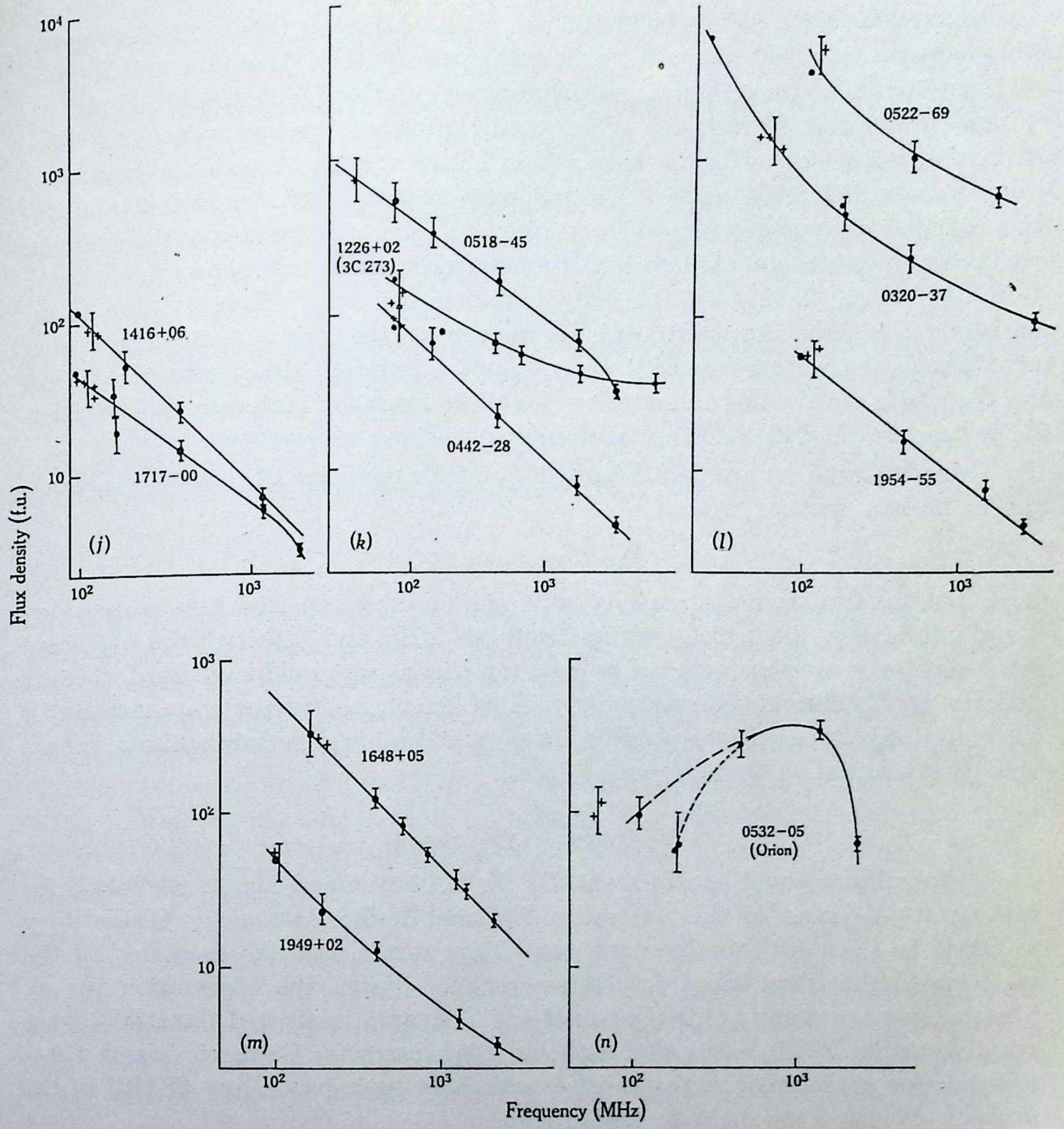

Figs. 1(*a*)–1(*n*).—Spectral curves of all sources studied. The present observations (+, with standard deviations as indicated) are shown together with previous observations (●) at: 85·5 MHz by Mills, Slee, and Hill (1958); 153 MHz by Hamilton and Haynes (1967); 159 MHz by Edge *et al.* (1959); 178 MHz by Bennett (1962); 408, 1410, and 2650 MHz by Bolton, Gardner, and Mackey (1964), Price and Milne (1965), Day *et al.* (1966), and Shimmins, Clarke, and Ekers (1966).

notation of Bolton, Gardner, and Mackey, sources with curved spectra may be classified as follows.

Positive Curvature Sources: 0123−01, 0252−71, 0349−27, 0408−65, 0410−75, 0521−36, 0532−05, 0634−20, 1459−41, 1602−63, 1754−59, 1814−51, 1814−63, 1827−36, 1836+17, 1932−46, 1938−15, 2152−69, 2211−17.

Negative Curvature Sources: 0320−37, 0522−69, 1226+02, 1949+02.

Positive Curvature Sources at High Frequencies: 0518−45, 1717−00, 2356−61.

In particular, the source 0532−05 (Orion nebula) is obviously one that needs more investigation. Measurements by the authors at 153 MHz (Hamilton and Haynes 1967) were in excellent agreement with the results of Edge *et al.* (1959). However, the new results near 45 MHz are higher than expected to be consistent with these previous observations, although they are in better agreement with the results of Mills, Slee, and Hill (1958) at 85·5 MHz. Spectral measurements between 40 and 180 MHz would accurately determine the spectrum and give a better idea of the emission mechanism in the source. At intermediate frequencies this source shows the features of an HII region, having a black body radiation spectrum. However, due to inconsistencies in the measurements at lower frequencies, the optical depth and emission temperature of the source cannot be readily determined. Measurements at 1410 and 2650 MHz are also not accurate because of the extension of the source in relation to the beamwidth of the telescope at these frequencies.

Figures 1(*a*)–1(*n*) give the observed spectral shapes for all sources considered in the present paper.

IV. Conclusions

The flux density measurements of 31 radio sources reported here have added useful information about these sources below 408 MHz, and, although the frequency intervals of measurement were not as close together as we would have liked, there is perhaps now sufficient information available on these sources to undertake a theoretical investigation into possible emission and absorption mechanisms. These will be considered in a subsequent paper.

V. Acknowledgments

The authors would like to thank Dr. E. G. Bowen and Mr. J. G. Bolton for making the facilities of the Australian National Radio Astronomy Observatory available to them for these observations. They would also like to thank all the members of the Observatory for their assistance during the observation period. The radiophysics group at the University of Tasmania is assisted financially by a grant from the Radio Research Board and the Australian Research Grants Committee. One author (R.F.H.) is assisted financially by a grant from CSIRO in the form of a Senior Post-graduate Studentship.

VI. References

Bennett, A. S. (1962).—*Mem. R. astr. Soc.* **68**, 163.

Bolton, J. G., Clarke, Margaret E., and Ekers, R. D. (1965).—*Aust. J. Phys.* **18**, 627.

Bolton, J. G., Gardner, F. F., and Mackey, M. B. (1964).—*Aust. J. Phys.* **17**, 340.

Broten, N. W., *et al.* (1965).—*Aust. J. Phys.* **18**, 85.

Conway, R. G., Kellermann, K. I., and Long, R. G. (1963).—*Mon. Not. R. astr. Soc.* **125**, 261.

Day, G. A., Shimmins, A. J., Ekers, R. D., and Cole, D. L. (1966).—*Aust. J. Phys.* **19**, 35.

Edge, D. O., Shakeshaft, J. R., McAdam, W. B., Baldwin, J. E., and Archer, S. (1959).—*Mem. R. astr. Soc.* **68**, 37.

Hamilton, P. A., and Haynes, R. F. (1967).—*Aust. J. Phys.* **20**, 697.

Kellermann, K. I. (1966).—*Aust. J. Phys.* **19**, 195.

Mills, B. Y., Slee, O. B., and Hill, E. R. (1958).—*Aust. J. Phys.* **11**, 360.

Price, R. M., and Milne, D. K. (1965).—*Aust. J. Phys.* **18**, 329.

Shimmins, A. J., Clarke, Margaret E., and Ekers, R. D. (1966).—*Aust. J. Phys.* **19**, 649.

Westerlund, B. E., and Stokes, N. R. (1966).—*Astr. J.* **145**, 354.

HIGH RESOLUTION OBSERVATIONS OF THE ORION NEBULA AT 408 MHz

By B. Y. Mills* and P. A. Shaver*

[*Manuscript received August* 30, 1967]

Summary

The Orion Nebula has been observed at 408 MHz with the 1 mile Cross radio telescope at the Molonglo Radio Observatory. NGC 1976 and NGC 1982 were observed separately and the former was well resolved. Comparison with high frequency results shows that the central region is optically thick; the electron temperature was measured directly at 7 600°K ± 800 degK. Both nebulae are strongly concentrated towards their exciting stars.

I. Introduction

Recent observations of the Kardashev lines have indicated that electron temperatures in emission nebulae are considerably lower than the 10 000°K conventionally assumed. One might query this result because quite small departures from a thermal population of the highly excited hydrogen levels would have very marked effects on emission of the lines at radio wavelengths, where absorption and stimulated emission are nearly equal (Goldberg 1966). Similarly the much higher temperatures derived from measurements of the forbidden line spectrum undoubtedly suffer from selection effects favouring regions of high ionization. It is therefore very important to explore other methods of observation that are not subject to these criticisms.

The recently completed 1 mile cross-type radio telescope at the Molonglo Radio Observatory allows direct measurement of electron temperatures for those nebulae possessing regions of large optical depth more than a few minutes of arc in size. At the present operating frequency of 408 MHz, emission measures in excess of 10^5 are necessary for reasonably accurate measurements. The Orion Nebula has been investigated initially as it is in a region of low and uncomplicated background temperatures unlike those near the galactic centre; it is also very suitable for observation with the 3′ beam of the radio telescope. A recently completed map at $\lambda 2\cdot85$ cm ($10\cdot5$ GHz) (Macleod and Doherty 1967) with similar resolution allows a direct comparison of spectra in different regions. In particular, both instruments separate NGC 1982 from the Orion Nebula proper (NGC 1976).

It is found that the resolved central region of NGC 1976 has an optical thickness considerably more than 5 at 408 MHz and so radiates effectively as a black body. The antenna beam temperature is therefore closely equal to the electron temperatures (T_e) averaged over the nearer parts of the nebula. After making the necessary small corrections for optical thickness and finite resolution, T_e is found to be 7 600°K,

---

* Cornell–Sydney University Astronomy Centre, School of Physics, University of Sydney, N.S.W. 2006.

Aust. J. Phys., 1968, **21**, 95–102

with a standard error estimated to be about 800 degK. This result is approximately 1 200 degK higher than values deduced from measurements of the Kardashev lines (Dieter 1967; Mezger and Höglund 1967). While the difference is not inconsistent with the combined errors, the most natural conclusion is that there is a real discrepancy.

In addition to the temperature measurements, the observations have clearly shown a low level emission more or less coinciding with the tenuous outer regions of the nebula. It is evident that the optical appearance is largely dictated by the emission regions rather than by the disposition of obscuring clouds.

An estimate of electron temperature in the neighbouring NGC 1982 has also been made and a value of the order of 8 000°K obtained. This nebula is not completely resolved by the telescope so that the result is very uncertain.

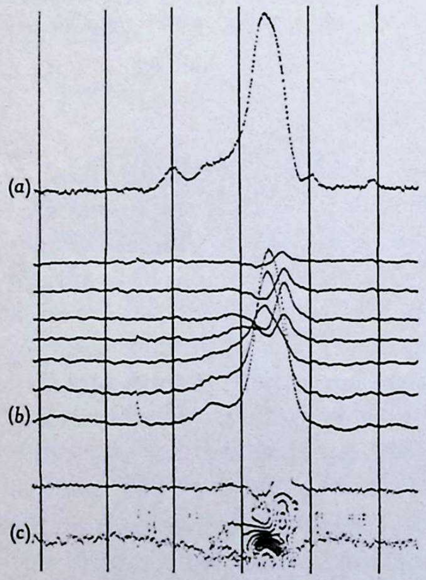

Fig. 1.—A reproduction of one of the Faximile records used in the analysis showing (*a*) the total power fan beam of the east–west antenna, (*b*) the seven independent pencil beams of the Cross, and (*c*) a rough contour map produced in real time. The vertical lines are the 1 min time marks.

II. Observations

During the last two years the east–west arm of the Molonglo radio telescope has been operating as a fan-beam total power instrument; the present results are the first to be described using the completed Cross. A certain amount of adjustment and calibration work remains to be carried out and consequently the initial programmes are rather limited in their scope. Nevertheless, it is considered that the present imperfections are of little consequence in the work described here. The chief difficulties are the presence of unnecessarily large sidelobe responses, which distort the contours in places, and the lack of a simple and accurate temperature calibration procedure. The temperature scale had to be derived indirectly, as described below, with a consequent loss in accuracy.

The output of the telescope may be recorded digitally on magnetic tape but the computer programmes are not yet fully operational, so that for the present observations the Faximile analogue output was employed (Mills *et al.* 1963).

A sample record is reproduced in Figure 1. Seven independent beams (*b*) are recorded simultaneously (finally 11 such beams will be available), together with the output of the east–west arm (*a*). Beneath these individual scans a crude contour map (*c*) is reproduced, in real time, as an aid to interpretation. In order to cover the complete range of declinations at which emission was detectable, three other such records were necessary, the coverage being so arranged that the outer scans overlapped.

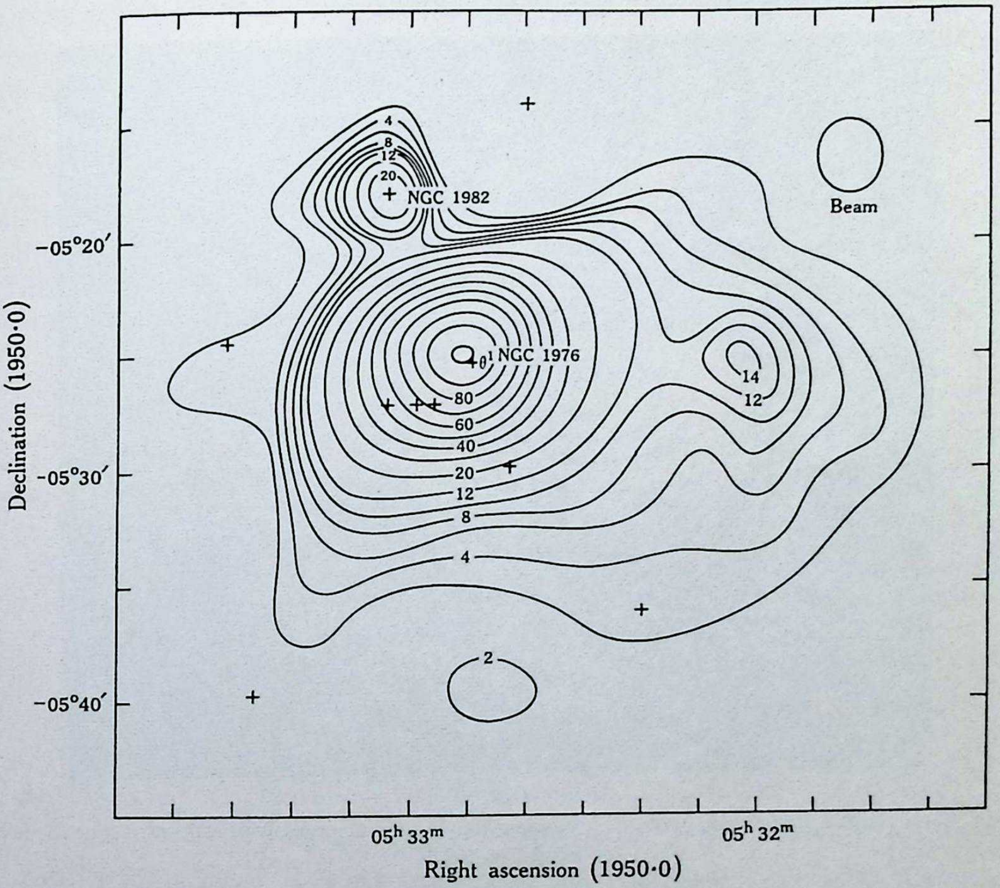

Fig. 2.—Derived beam temperature contour map of the Orion source complex. The contour unit is 66 ± 7 degK and the peak beam temperature for NGC 1976 is 6 700°K and for NGC 1982, 1 590°K. The positions of some bright stars are indicated by crosses, while the exciting star θ^1 Orionis is separately marked. For contour levels less than 30 the contour interval represents an emission measure of 2 360.

The relative calibrations of each of the scans in a single record were determined by injecting a reference noise signal simultaneously into each of the independent beam systems. The calibration between different records was obtained by matching overlapping scans. A set of corrected scans was then prepared from which the contour map shown in Figure 2 was drawn. This map represents the relative antenna beam temperatures and therefore adequately describes the shape of the nebula, as smoothed by the beam, which measures 2′·8 east–west by 3′·2 north–south to half-response points. A small negative sidelobe appears immediately north of the main peak, probably causing some distortion of the contours on the western side of NGC 1982;

the distribution of low level emission south of the peak may be similarly distorted. A simplified set of contours is superimposed on a photograph of the nebula in Figure 3, where the general correspondence between the radio and optical appearance is well demonstrated.

Conversion of the relative temperature scale in Figure 2 to an absolute scale has been carried out via the fan-beam observations. This has proved necessary because the sensitivity of the Cross system varies with declination in a way that has not yet been adequately determined, whereas the east–west antenna gain is practically independent of declination. Scans were made through the Orion region and two reference sources of small angular size (MSH 06−*04* and MSH 12+*08* (3C 273)) using high sensitivity and a normal paper chart recorder for improved accuracy. The integrated emission of the Orion complex was then obtained relative to the reference sources by intercomparison of the areas under the response curves, after correction for the relative gains of the receiver. These were established for each source by injection of a standard signal from a noise diode.

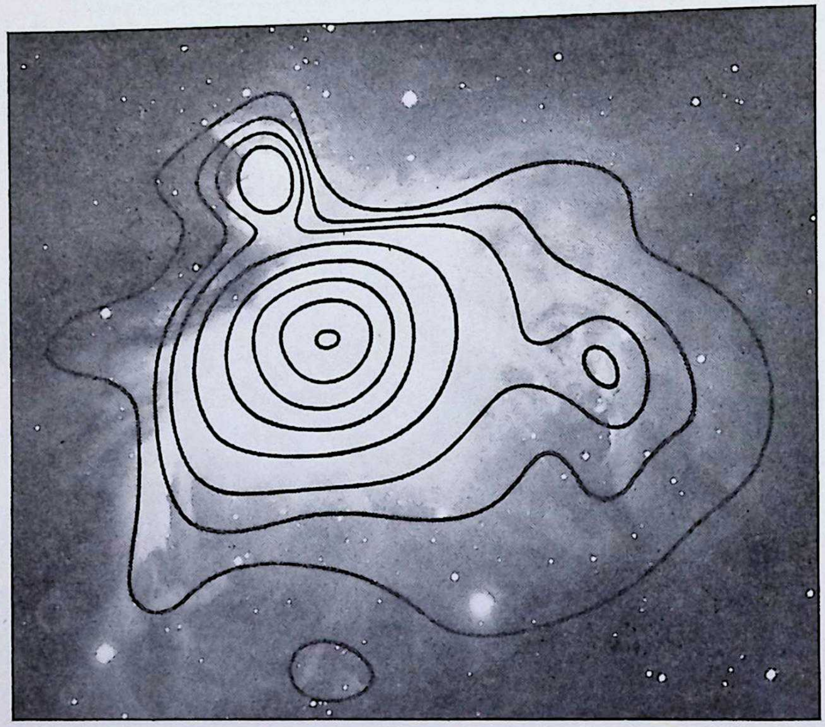

Fig. 3.—A simplified version of the contours of Figure 2 superimposed on a photograph of the nebula.

Unfortunately, an acceptable *absolute* standard of flux density does not exist at the lower frequencies. The common and useful CKL scale (Conway, Kellerman, and Long 1963) is basically a *relative* flux scale in which several low frequency absolute determinations have been adjusted to fit an assumption that Cassiopeia A has a simple power law spectrum. Most absolute determinations at metre wavelengths fall above this scale, particularly for the southern sources. More than a year ago a programme of absolute flux determinations was instituted at the Molonglo Radio Observatory and the values used for our reference sources have been supplied by D. Wyllie (personal communication), who has now established a preliminary scale at 408 MHz with a standard error of 6%. It falls approximately 15% above the CKL scale when averaged over the sources common to both.

The flux densities of the reference sources MSH 06−*04* and 3C 273 are 44·5 and 65·1 f.u.* respectively on Wyllie's scale. The derived flux density of the whole Orion complex is 213 f.u., with an estimated standard error of 8%. In obtaining this value a small reduction of 5 f.u. was made to allow for the expectation value of weak sources within the area of the fan beam; it was derived from a study of neighbouring regions.

The pencil-beam temperature scale was obtained by fitting the integrated flux from Figure 2 to that derived above. The contour unit was thus found to be 66±7 degK (standard error). The corresponding peak beam temperatures for NGC 1976 and NGC 1982 are 6 700 and 1 590°K respectively.

III. Discussion

It is evident from Figure 3 that qualitative features of the emission nebulae are reproduced well in the radio isophotes. The maximum in the radio emission also occurs very close to the exciting stars: θ^1 Orionis is approximately 30″ from the peak in NGC 1976; BD−5°1325 is approximately 15″ from the peak in NGC 1982. The radio peaks are believed to be positioned with a standard error of about 5″ arc.

It is clear that, while the central region of the Orion nebula appears to be quite symmetrical, there is a marked asymmetry in the brightness distribution of the extended component; the assumption that has been made in the past that the Orion nebula is spherical, centred on the Trapezium, with a radius of 22′ arc (Osterbrock and Flather 1959; Menon 1961; Vandervoort 1964) is therefore incorrect.

Both nebulae show very strong central concentrations, which are much more evident when the 10·5 GHz observations of Macleod and Doherty (1967) are taken into account. The nebulae are everywhere optically thin at this frequency so that the surface temperature is equal to τT_{e}. We may scale the results to 408 MHz on multiplication by the ratio of optical depths.

Taking

$$\tau = \frac{3\cdot02\times10^{16}EM}{\nu^2 T_{\mathrm{e}}^{3/2}}\left(19\cdot8+\ln(T_{\mathrm{e}}^{3/2}/\nu)\right),$$

where the emission measure $EM = \int N_{\mathrm{e}}^2\,\mathrm{d}s$ and the electron temperature $T_{\mathrm{e}} = 7\,600$°K, as derived below, we find

$$\tau_{400}/\tau_{10\,500} = 875\,.$$

---

* 1 flux unit = 10^{-26} W m^{-2} Hz^{-1}.

In Figure 4 we have plotted temperatures along a section taken through the centre of both peaks. The observed beam temperature at 408 MHz (curve 1) is plotted, along with the corresponding beam temperature at 10·5 GHz multiplied by the ratio of optical depths (2). A small zero adjustment (200 degK) has been made to the high frequency result to bring the outer skirts into coincidence with the 408 MHz beam temperatures. The effect on the 408 MHz temperatures of the large optical depth in the centre of NGC 1976 is very evident.

The electron temperature must be slightly higher than the observed peak temperature at 408 MHz both because of resolution effects and the finite value of τ (> 5). The correction, however, is not great and need not be known accurately.

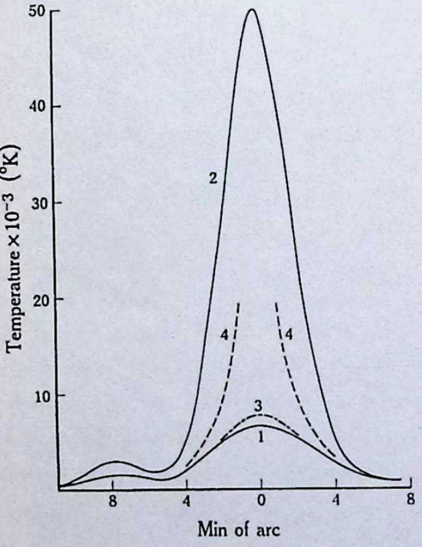

Fig. 4.—Temperatures plotted along a section through the peaks of NGC 1982 and NGC 1976:

1, present 408 MHz observations
2, 10·5 GHz observations of Macleod and Doherty multiplied by $\tau_{408}/\tau_{10\,500}$
3, 408 MHz distribution partially corrected for resolution of antenna beam
4, τT_e derived directly from 408 MHz observations

We have used the chord construction described by Bracewell (1955) to correct partially for the finite resolution, as shown by curve 3 in Figure 4. The nearly flat top of the restored distribution suggests that the degree of restoration is adequate and that the further correction due to finite optical depth is negligible. We adopt an electron temperature of 7 600°K ± 800 degK, which adequately fits the observations.

With this value of electron temperature, which will be assumed constant throughout the nebula, it is possible to obtain τ directly from the brightness temperature at 408 MHz, which is equal to $T_e(1-e^{-\tau})$. Curves 4 of Figure 4 show the quantity τT_e derived from our restored beam temperatures. As the uncertainty increases rapidly near the centre, the plot is continued only to a radius of 1′ arc. It should be emphasized that both this result and that obtained at 10·5 GHz are affected by the finite resolution of the antenna beams and the actual distribution is likely to be considerably more peaked at the centre than either result. An estimate of the actual shape can best be derived from the high frequency results, but as this requires detailed knowledge of the antenna response it has not been attempted here. A very rough estimate of the central optical depth suggests that it is at least double that indicated, i.e. about 10 or more at 408 MHz, corresponding to an emission measure of the order of 3×10^6.

Emission measures over the remainder of the nebula, where optical depths are small and the nebula well resolved, may be readily obtained. Thus, for surface brightness temperatures less than about 2 000°K (i.e. contour levels less than 30) the contour interval corresponds to an emission measure of 2 360.

NGC 1982 is much less amenable to analysis because of its small size. The measured distribution at 408 MHz is only slightly wider than the antenna beam, so that actual brightness temperatures are considerably higher than beam temperatures. The ratio of the solid angle of the observed distribution to that derived for the actual distribution is approximately 3·6, whence the brightness temperature at 408 MHz is, very roughly, 6 000°K. If it is assumed that the high frequency temperature is increased in the same ratio, we find that the central optical depth is 1·4 and the electron temperature is of the order of 8 000°K. However, this is a very uncertain estimate.

To conclude, we would emphasize that, because of the high optical depth, the present work is a direct measurement of electron temperature in NGC 1976 and is not dependent on any theory for the population of excited levels. The only significant uncertainties arise in correcting the result for finite resolution, and in the absolute temperature scale. The former uncertainty is quite small and may be ignored in comparison with the latter, which depends critically on the absolute flux scale derived by Wyllie and on evaluation of the relative response of the Orion complex using a fan beam. Wyllie's work has not yet been published and, in fact, further observations are planned to decrease the error. However, we believe that his derived flux densities for the reference sources are the best available absolute determinations at 408 MHz and that the quoted standard error of 6% is realistic. Nevertheless, it cannot be overlooked that the CKL scale lies 15% below Wyllie's when averaged over the southern sources common to both and would yield an electron temperature of 6 600°K. It is not unreasonable to suppose that, within the errors, our assumed flux densities of the reference sources are more likely to be high than low, but we find that there are too many unknowns to assign a weight to the CKL scale and use it to improve our estimate of the temperature.

In evaluating the relative flux density of the Orion complex we have made an allowance of 5 f.u. for the integrated effect of weak sources within the response of the fan beam. No sources are listed in the region in any catalogue, so that this uncertainty should be adequately covered by our estimate of the error. One possible source of excess emission is the NGC 1973, 5, 7 complex, half a degree to the north.

Both the above uncertainties should be reduced by future work, allowing more reliable estimates. At present we conclude that the electron temperature is very significantly less than 10 000°K, but probably slightly more than the 6 400°K obtained from Kardashev line measurements. The derived temperature refers to the nearer region of the nebula in front of the central concentration around θ^1 Orionis, whereas the Kardashev lines are derived from the emission over the whole nebula; because of the nonlinear dependence on T_e, the line results tend to be weighted towards regions of lower temperature.

A further interesting result is the demonstration that obscuring clouds have little effect on the overall appearance of the nebula. The sharp cutoff in the north-following sector is real and implies that the ionized gas does not extend in this direction. Likewise, the nebula NGC 1982 is a separate entity, with a strong central concentration around the exciting star BD−5°1325. Taken in conjunction with a similar concentration around θ^1 Orionis in NGC 1976, the implication is that both nebulae are very new formations resulting from the gravitational contraction and fragmentation of a gas cloud. This view is supported by the evidence for new star formation in NGC 1976 (e.g. Becklin and Neugebauer 1967).

IV. ACKNOWLEDGMENTS

This work was supported by grants from the U.S. National Science Foundation and the Australian Grants Committee. We are indebted to Dr. L. H. Doherty for making available his measurements at λ2·85 cm and to Mr. D. Wyllie for providing the absolute flux densities of the reference sources. The photograph for Figure 3 was supplied by Dr. R. R. Shobbrook.

V. REFERENCES

BECKLIN, E. E., and NEUGEBAUER, G. (1967).—*Astrophys. J.* **147**, 799.
BRACEWELL, R. N. (1955).—*Aust. J. Phys.* **8**, 200.
CONWAY, R. G., KELLERMAN, K. I., and LONG, R. J. (1963).—*Mon. Not. R. astr. Soc.* **125**, 261.
DIETER, N. H. (1967).—*Astrophys. J.* **150**, 435.
GOLDBERG, L. (1966).—*Astrophys. J.* **144**, 1225.
MACLEOD, J. M., and DOHERTY, L. H. (1967).—URSI Spring Mtg, Ottawa.
MENON, T. K. (1961).—*Publ. NRAO* **1**, No. 1.
MEZGER, P. G., and HÖGLUND, B. (1967).—*Astrophys. J.* **147**, 490.
MILLS, B. Y., AITCHISON, R. E., LITTLE, A. G., and MCADAM, W. B. (1963).—*Proc. Instn Radio Engrs Aust.* **24**, 156.
OSTERBROCK, D. E., and FLATHER, E. (1959).—*Astrophys. J.* **129**, 26.
VANDERVOORT, P. O. (1964).—*Astrophys. J.* **139**, 869.

SHORT COMMUNICATIONS

A SEARCH FOR A 5·5 MeV LEVEL IN ^{7}Li†

By P. J. HARVEY‡

A level at about 5·5 MeV excitation energy in ^{7}Li has been predicted theoretically on the basis of a number of models (Balashov 1959; Clegg 1962; Chesterfield and Spicer 1963) but the only one of these that also accounts for the other levels below 8 MeV, with correct spin and parity, is a rotational model put forward by Chesterfield and Spicer.

The experimental evidence for this 5·5 MeV level comes from electron scattering, proton scattering, and photonuclear studies. Inelastic electron scattering from ^{7}Li has been performed by Bernheim and Bishop (1963) using an incident energy range of 100–180 MeV. They report a level at 5·7 MeV of spin and parity $\frac{5}{2}^-$ or $\frac{3}{2}^-$, with slight preference for $\frac{5}{2}^-$. Chesterfield and Spicer predicted spin and parity $\frac{3}{2}^-$ for their 5·5 MeV level. In a later paper, Bernheim and Bishop (1964) refer to the difficulty of accounting for a second $\frac{5}{2}^-$ state in this region, and suggest that their 5·7 MeV level may be due to direct disintegration into triton and an α-particle.

In high energy (185 MeV) inelastic proton scattering, Hasselgren *et al.* (1965) have reported a small peak at 5·5 MeV in ^{7}Li, but say that its existence is uncertain because it was not clearly resolved.

Erdos *et al.* (1954) used the reaction $^7\mathrm{Li}(\gamma,\alpha)^3\mathrm{H}$ to study energy levels in ^{7}Li and reported a clear level at 5·5 MeV. Shevchenko and Yur'ev (1961) performed a similar experiment and reported a level at 5·3 MeV.

The present experiment was undertaken firstly in an attempt to observe this level in the $^7\mathrm{Li}(\mathrm{n,n'})$ reaction and, secondly, to verify the results of Regis *et al.* (1966), who report a level at 5·7 MeV in a similar experiment.

Neutrons from the $\mathrm{T(d,n)^4He}$ reaction were scattered from ^{7}Li and their energies measured by a time-of-flight spectrometer. The associated α-particle was used for the time reference of the spectrometer, which had a flight path of 6 m and a time resolution of 2·5 nsec under experimental conditions.

In the spectrum obtained (Fig. 1) the unresolved ground and 0·48 MeV states and the 4·63 MeV state stand out clearly, but there is no evidence for any level at higher energies. This conflicts with the results of Regis *et al.*, who report levels in this region.

The two spectra were taken under similar conditions; 14 MeV neutrons were used in both experiments and the ratios of flight path to time resolution were comparable. The main difference in the conditions for the spectra was the scattering

---

† Manuscript received November 9, 1967.

‡ School of Physics, University of Melbourne, Parkville, Vic. 3052.

angle, which was 12° lab. (13·4° c.m.) for Regis *et al.* and 20° lab. (22·3° c.m.) for the results in Figure 1. Little difference in cross section would be expected between these angles, and this is supported by examination of a compilation of neutron angular distributions (Brookhaven National Laboratory 1962). (Where angular distributions for inelastic scattering of 14 MeV neutrons were included, the differential cross sections did not vary by more than 7% between the angles of interest.) Thus it was considered that valid comparisons could be made between the spectra.

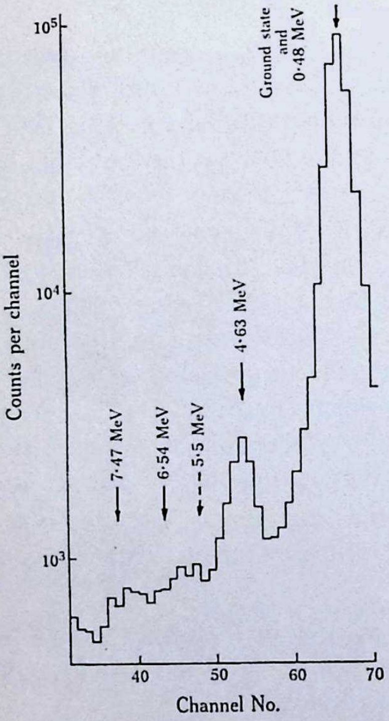

Fig. 1.—Inelastically scattered neutron spectrum from the reaction ^{7}Li(n, n′) at a laboratory scattering angle of 20° and an incident neutron energy of 14 MeV. The solid arrows indicate the expected positions of peaks due to levels in ^{7}Li for which adequate experimental evidence exists. The broken arrow indicates where a peak would appear due to a level at 5·5 MeV.

There is some evidence in the spectrum of Regis *et al.* for peaks at 5·7, 6·3, and 7·47 MeV excitation, but the number of counts in this region is small and the error bars are comparatively large. The 6·3 MeV level is assigned a spin and parity of $\frac{3}{2}^{+}$, which means it is not the generally accepted level at 6·54 MeV ($\frac{5}{2}^{-}$). This $\frac{5}{2}^{-}$ level was said to be weakly excited at 120°.

There is no evidence in Figure 1 for any levels higher than the 4·63 MeV level, despite extended experimental running time. (The 4·63 MeV peak in Figure 1 contains three times the number of counts in the corresponding peak of Regis *et al.*) This indicates that the levels of excitation higher than 4·63 MeV in the spectrum of Regis *et al.* may well be caused by statistical fluctuations and should not be regarded as firm evidence for the less generally accepted levels.

As no 5·5 MeV level was observed in the present work (Fig. 1), its cross section for inelastic scattering of 14 MeV neutrons must be markedly less than the value of $1 \cdot 9 \pm 0 \cdot 5$ mbn/sr estimated by Regis *et al.*, but this does not provide evidence against its existence, since the known higher energy levels were not seen.

The author would like to thank Dr. C. D. McKenzie for his guidance and encouragement, and Professor B. M. Spicer for his interest and useful advice. The assistance of the members of the Statitron electrostatic accelerator research group has been greatly appreciated. A University Research Grant was held throughout this work.

References

Balashov, V. V. (1959).—*Zh. éksp. teor. Fiz.* **36**, 1123.
Bernheim, M., and Bishop, G. R. (1963).—*Phys. Lett.* **5**, 294.
Bernheim, M., and Bishop, G. R. (1964).—*Phys. Lett.* **8**, 48.
Brookhaven National Laboratory (1962).—BNL 400, 2nd Ed., Vol. 1. $Z = 1$ to 22.
Chesterfield, C. M., and Spicer, B. M. (1963).—*Nucl. Phys.* **41**, 675.
Clegg, A. B. (1962).—*Nucl. Phys.* **33**, 194.
Erdos, P., Stoll, P., Wachter, M., and Wataghin, V. (1954).—*Nuovo Cim.* **12**, 639.
Hasselgren, D., Renberg, P. U., Sundberg, O., and Tibell, G. (1965).—*Nucl. Phys.* **69**, 81.
Regis, V., Ngyen Van Sen, Fiore, A., Pham Dinh Lien, and Bouchez, R. (1966).—*J. Physique*, Suppl. Fasc. 3–4, C1–84.
Shevchenko, V. G., and Yur'ev, B. A. (1961).—*Izv. Akad. Nauk. SSSR* **25**, 1269.

NOTICE TO AUTHORS

AUSTRALIAN JOURNAL OF PHYSICS

Papers will be considered for publication in the Journal if they make an original contribution to any branch of experimental or theoretical physics.

Two categories of articles are published. *Papers*—critical accounts of original work. *Short Communications*—scientifically complete accounts of work of limited scope; no summary is required.

Reviews of published work are not accepted unless they are interpretative in character and present new ideas that advance the state of knowledge of the subject.

Descriptions of techniques and equipment should generally be included in the experimental section of a paper. However, they are acceptable for separate publication if they are novel and are of evident importance to research in physics.

Submission of a paper implies that the results reported have not been published or submitted for publication elsewhere.

General presentation.— The work should be presented concisely and clearly in English. Introductory material, including a review of the literature, should not exceed what is necessary to indicate the reason for the work and the essential background. Generally, results and discussion should not be intermingled; the discussion should be restricted to logical interpretation as a basis for conclusions supported by the results. Some speculation is allowable but this should be restrained. Some types of work require special methods of presentation.

Authors are advised to note the typographical conventions and layout of headings, tables, and illustrations exemplified in recent issues of the Journal. Strict observance of these and the following requirements will shorten the interval between submission and publication.

Manuscripts.—Typescripts on good quality paper with double spacing (3 lines to the inch) throughout, and one copy, should be submitted. All pages of the manuscript must be numbered consecutively, including those containing references, tables, and captions to illustrations, which are to be placed after the text.

The title should be informative of the content of the paper. A running title not exceeding 50 characters in length should be added.

If the paper is one of a numbered series, a reference to the previous part should be given as a footnote on the first page. If it is necessary for a proper understanding of the paper to refer to an earlier part, it will assist referees if the author can provide a copy.

The summary should be brief; it is seldom necessary to exceed 200 words to indicate the scope of the work and the principal findings.

Footnotes within the text should be used only when essential. They should be placed within horizontal rules immediately under the line to which they refer.

References are cited in the text by the author and date and are not numbered. Authors are referred to recent issues for the style used in the Journal for citing references to books, periodicals, and other literature. Authors may include all titles or none, but the reference to any paper accepted for publication but not yet published must include the title. No editorial responsibility can be taken for the accuracy of the references; authors are requested to check these. All references in the text must be listed, with the names of authors arranged alphabetically; all entries in this list must correspond to references in the text. Sources indicated in the text as "personal communication", "in preparation", or similar phrases should not be listed as references. Abbreviations of titles of periodicals should conform to those used in *World List of Scientific Periodicals*, 4th Edition.

Mathematical formulae should be very carefully set out, preferably handwritten, in the exact form in which they are to be printed; even with a typewriter having appropriate symbols it is often difficult to indicate the required layout. Greek letters and special symbols should be indicated by marginal annotations. For typographical conventions, authors are referred to recent issues of the Journal. Two-line mathematical expressions should be avoided in the running text.

Tables should be numbered with arabic numerals and be accompanied by a title and by sufficient explanatory information to make them self-contained. They should be arranged having regard to the dimensions of the printed page, and the number of columns should be kept to a minimum. Long headings to columns should be avoided by the use of explanatory footnotes indicated in the table by superscript letters. Each table must be referred to in the text and its approximate location indicated in the margin. Only in exceptional circumstances will presentation of the same data in tabular and graphical form be permitted; where adequate, the latter form should be used. Vertical tables should not exceed 80 characters and spaces in width if they are to be set in 8 point type, the size generally used in tables in the Journal. Smaller type can be used if necessary, but the number of characters and spaces should not exceed 110. For very large tables with their width along the length of the page, the corresponding figures are 120 and 160.

Illustrations.—*Figures* must be drawn with black ink on board, drawing or tracing paper, coordinate paper with *faint blue* rulings, or plastic sheet (using the appropriate ink). Care should be taken to ensure that each line is of uniform width and density. Drawings should be about 2½ times the width of comparable diagrams reproduced in the Journal. Only in exceptional circumstances are drawings more than 12 inches wide acceptable. Good photographic prints may be submitted.

In graphs the axes and grid lines should be thinner than the "curves". In drawings 2½ times the final printed size no lines should be more than 0·8 mm or less than 0·25 mm wide; symbols should be 3–4 mm across and for typographical reasons should be restricted to crosses and open or solid circles, squares, or triangles. Allowance must also be made for the effect of reduction on dots and stipples.

All lettering on original figures should be in soft lead pencil or indicated on a transparent overlay Copies should be lettered with ink.

The originals and two copies of each are required. The title of the paper and the name of the author must appear on each sheet. Figures must be numbered consecutively in the order in which they are mentioned in the text and their approximate position should be indicated in the margin. A typed list of captions must be supplied.

Photographic prints must be of the highest quality with a full range of tones and good contrast. They should be trimmed to exclude features not relevant to the paper. Three copies, identified on the back by the title of the paper and the name of the author, are required; one set should be without lettering.

All plates should be numbered consecutively. Where several figures are grouped on one plate, they should be given letter designations. A typed list of captions is required.

Details in a photograph which must be most clearly shown should be indicated on an overlay for the guidance of the blockmaker: this is particularly important with photo- and electron-micrographs.

Reprints.—Reprints are supplied free to authors as follows: one author, 40; two authors, 30 each; three or more authors, 20 each. Additional reprints may be obtained if ordered no later than when the galley proofs are returned.

ANGULAR DISTRIBUTIONS IN THE GIANT RESONANCE OF ^{16}O†

By R. J. J. Stewart‡

[*Manuscript received December* 19, 1967]

Summary

The $^{16}O(\gamma, p_0)^{15}N$ reaction has been studied in the region of excitation in ^{16}O from 20·5 to 25·6 MeV. Angular distributions on the resonances observed were extracted from the spectra, which were taken at 20° intervals from 30° to 150°. The results are compared with other related work.

I. Introduction

The giant resonance region of ^{16}O has been the subject of much theoretical and experimental attention over the past 10 years. The reason is that ^{16}O is a light, doubly-closed shell nucleus, and so is particularly suited to calculations based on the shell model; in fact it has become a yardstick against which the success of such calculations may be gauged. The stage has now been reached at which efforts are being made to account for more than just the gross overall shape of the giant resonance (Greiner 1963; Gillet, Melkanoff, and Raynal 1967) and it has become important to obtain more detailed experimental information than has so far been available, in order to test the validity of the predictions of the theories.

In particular, a knowledge of the spin and parity of all the observed states in the vicinity of the giant resonance of ^{16}O would be of great value. There is at present only indirect evidence for the spin and parity of the state at 21·0 MeV and very little is known about the smaller resonance at 23·1 MeV. Further, there is contradictory evidence regarding the state at 24·3 MeV, since Dodge and Barber (1962), using the (e, pe′) reaction, found $J^{\pi} = 1^{-}$, whereas the electron scattering measurements of Isabelle and Bishop (1963) indicated $J^{\pi} = 2^{+}$ for this resonance.

The present paper presents the results of measurements of the angular distribution of protons on the peaks in the ground state cross section from 20·5 to 25·6 MeV. Proton angular distributions from the $^{16}O(\gamma, p)$ reaction have been studied previously by Johannson and Forkman (1957), Milone *et al.* (1958), and Brix and Mascke (1959), but these works all suffered from poor resolution and so were able to give only very general information. The most detailed photoproton work is that of Dodge and Barber (1962), who established the electric dipole nature of the strong state at 22·3 MeV. Recently a detailed study of angular distributions in the inverse $^{15}N(p, \gamma_0)^{16}O$ reaction was published (Earle and Tanner 1967). This work covers the energy region examined in the present study, and is discussed further in Section IV.

---

† This work was supported by the United States Army Research Office.

‡ School of Physics, University of Melbourne, Parkville, Vic. 3052; present address: Iowa State University, Ames, Iowa, U.S.A.

II. EXPERIMENTAL DETAILS

The first excited state of ^{15}N lies at 5·3 MeV, and it follows that only the highest 5·3 MeV of each proton spectrum can be assumed to contain purely ground state protons. With a bremsstrahlung end-point energy of 25·6 MeV this means that the region above 20·3 MeV excitation in ^{16}O can be examined. This lower limit corresponds to an emitted proton energy of 7·7 MeV.

Protons were detected in silicon surface barrier detectors 1000 μ deep (Ortec type SBEI 200–1000) that were placed in a 24 in. diameter scattering chamber, which featured a table mounted on tapered roller bearings that enabled it to be rotated under vacuum. This table had tracks cut into it radially at 20° intervals in which the detector mounts were positioned. Up to four spectra could be accumulated simultaneously. The pulses from each detector were fed via a preamplifier to a discriminator stage that biased out the low energy electrons, and then after further amplification and shaping were presented to one quadrant of a 512-channel pulse height analyser. The time duration of the γ-ray pulse was lengthened to about 150 μsec to reduce electron pile-up.

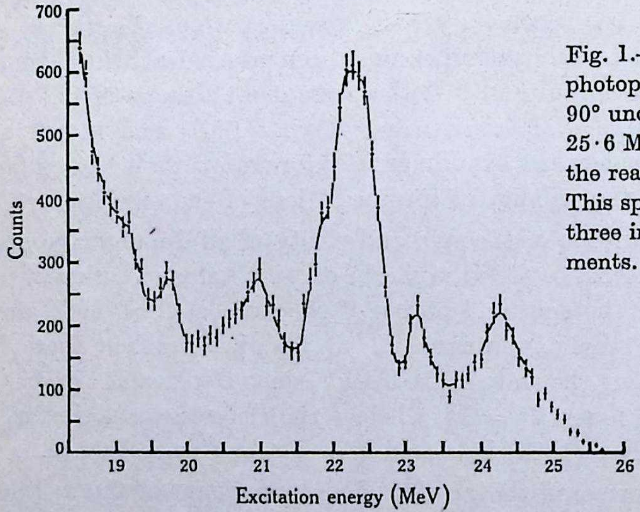

Fig. 1.—The spectrum of photoprotons from oxygen at 90° under bombardment by 25·6 MeV bremsstrahlung in the reaction $^{16}O(\gamma, p_0)^{15}N$. This spectrum is the sum of three independent measurements.

The chamber was filled with 1 atmosphere of oxygen gas and the collimated γ-ray beam passed axially through it, so that the target was that cylinder of irradiated gas seen by the detectors. The detectors were each collimated to an acceptance angle of ±10° by two parallel, vertical, aluminium plates mounted on a base that ran in the tracks cut into the turntable. Measurements were taken at 20° intervals from 30° to 150°. The detectors were situated 16·0 cm from the chamber centre; the beam diameter was 3·4 cm and did not change significantly over the region viewed by the detectors. Corrections for geometric factors (e.g. variation of detection efficiency over the face of each detector and variation in the amount of target seen by detectors at different angles) were made using the calculations of Silverstein (1959). It was found to be unnecessary to correct for variations in cross section over the acceptance angle of a detector.

Detectors were positioned at 90° on either side of the beam line in each run, and the total counts above a particular energy in these spectra were used to normalize the runs. The two independent normalizations obtained from these data agreed to within $\pm 0\cdot 5\%$.

The stability of each system was checked at two-hourly intervals using a mercury relay pulser; the energy calibration was determined using the known energies of the main resonances in ^{16}O, since an independent calibration using α-particle spectra from ThC+C′ showed some variation from detector to detector. The overall energy resolution was about 200 keV. The spectrum obtained by summing the three 90° runs is shown in Figure 1.

III. Analysis of Data

Despite the high initial proton energy of interest, Figure 1 shows that electron background is still evident at energies of 6 MeV and above. However, exponential fits showed that in almost all cases it is zero for proton energies corresponding to an excitation energy above 21·5 MeV, and has very little effect on the lowest peak of interest, namely that centred at 21·0 MeV.

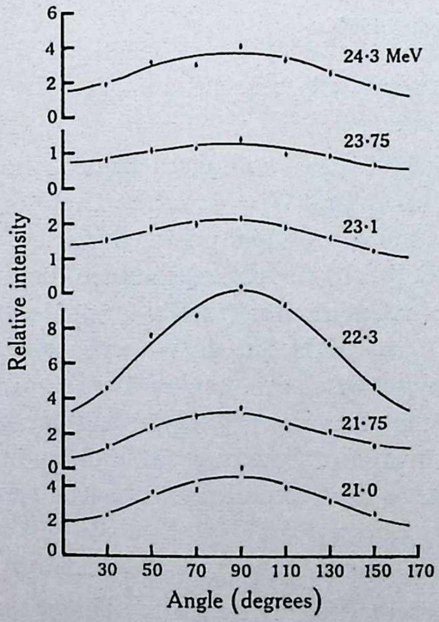

Fig. 2.—The measured photoproton angular distributions in the reaction ^{16}O(γ, p_0)^{15}N and the fits to them using the sum of Legendre polynomials with coefficients as given in Table 1. Note the changes in the vertical scale.

Angular distributions were extracted from the data both by summing total counts within particular energy bins and by fitting a series of Lorentz curves to each spectrum.

The distributions obtained were fitted by the least squares method to an equation of the form

$$W(\theta) = A\left(1 + \sum_{i=1}^{n} a_i P_i(\cos\theta)\right),$$

where the $P_i(\cos\theta)$ are Legendre polynomials. The programme gave fits for all values of n from 1 to 4. The variances given for each fit showed that in all cases except one the best fit was obtained by only retaining terms up to P_2. In the higher order fits the coefficients a_3 and a_4 were generally indistinguishable from zero, indicating that they were too small to be measured by this experiment. The data and Legendre fits are shown in Figure 2, and the coefficients a_i are listed in Table 1.

TABLE 1

EXPERIMENTAL ANGULAR DISTRIBUTION COEFFICIENTS FOR THE REACTION $^{16}O(\gamma, p_0)^{15}N$

In the form $W(\theta) = A\left(1 + \sum_{i=1}^{n} a_i P_i(\cos\theta)\right)$

E_γ (MeV)		a_1	a_2	a_3
21·00	(20·25–21·45)	0·04±0·07	−0·53±0·10	
21·75	(21·45–22·00)	0·06±0·08	−0·68±0·10	−0·21±0·15
22·30	(21·45–22·90)	0·00±0·02	−0·65±0·02	
23·10	(22·95–23·65)	0·12±0·02	−0·36±0·03	
23·75	(23·50–24·00)	0·14±0·06	−0·43±0·09	
24·30	(23·70–25·60)	0·10±0·08	−0·58±0·10	

IV. DISCUSSION

The features of the spectra that are of particular interest are the resonances centred at 21·0, 22·3, 23·1, and 24·3 MeV.

Previous evidence on the state at 21·0 MeV indicates that it has $J^\pi = 1^+$. Tanner, Thomas, and Earle (1964) concluded that $J = 1$, while the $^{16}O(\gamma, n)$ work of Caldwell *et al.* (1965) indicated that the state had positive parity. However, the present experiment gives $a_2 = -0·53 \pm 0·10$ for this resonance, compared with the expected value of −0·5 for pure d-wave emission from a 1^- state. This result cannot exclude the possibility that the a_2 value is due to p-wave proton emission from a 1^+ state with just the right proportion of channel spins 0 and 1 contributing, but the former explanation must be regarded as more likely. Angular distribution data on the $^{16}O(\gamma, n)^{15}O$ reaction by Verbinski and Courtney (1965) also indicate a 1^- state emitting d-wave neutrons, although in that experiment spectra were taken at only three angles.

Earle and Tanner (1967) give values of $a_1 = 0·13$, $a_2 = -0·17$, and $a_3 = -0·10$ at 21·0 MeV. This may be interpreted as evidence for the presence of the basic shell model state composed predominantly of the $(1p_{3/2})^{-1}(2s_{1/2})$ configuration and predicted to lie at 19·6 MeV (Gillet and Vinh-Mau 1964), since a state emitting s-wave neutrons will lead to an essentially zero value for the a_2 coefficient. If this interpretation is correct, then the upper portion of the averaging interval used in the present work at this energy will be influenced strongly by interference between that state and the state at 22·3 MeV. Earle and Tanner (1967) do not make this interpretation, but conclude that the states seen by them at 18·97 and 19·48 MeV are probably connected with the shell model state in question.

The value of a_2 found for the 22·3 MeV resonance $(-0·65 \pm 0·02)$ is in excellent agreement with the value obtained by Dodge and Barber (1962), namely $a_2 = -0·68$.

The mean value of a_2 given by Earle and Tanner in this energy region is $-0\cdot6$. The simplest hypothesis is again that the resonance is formed by predominantly d-wave protons emitted from a 1^- state in ^{16}O. A small s-wave component is then sufficient to give agreement with experiment. This conclusion agrees with the one-particle–one-hole shell model calculation of Gillet and Vinh-Mau (1964), which predicts a state at 22·2 MeV with 73% of the dipole strength and composed predominantly of the configurations $(1p_{3/2})^{-1}1d_{5/2}$ and $(1p_{1/2})^{-1}1d_{3/2}$.

The smaller resonance at 23·1 MeV shows forward peaking and is more isotropic than the other resonances, as reflected by the smaller a_2 coefficient. Dodge and Barber (1962) quote $a_2 = -0\cdot36$ at 23·3 MeV, again in excellent agreement with the present work. Earle and Tanner (1967) do not cover the resonance fully, but give values of $a_1 = 0\cdot19$ and $a_2 = -0\cdot25$ at 22·9 MeV. The a_1 coefficient indicates the presence of two states of opposite parity, though only a small admixture of a positive parity state underlying a predominantly 1^- state is required to give an a_1 value of the observed magnitude. The simplest explanation of the data again appears to be in terms of a 1^- state emitting both s- and d-wave protons, with a small underlying positive parity component causing the odd polynomial coefficient, although again other combinations cannot be excluded.

The data from the resonance at 24·3 MeV are also most simply explained as due to a 1^- state emitting predominantly d-wave protons, and agree very well with the work of Dodge and Barber, who quote $a_2 = -0\cdot68$. Earle and Tanner (1967) show values of a_2 of about $-0\cdot6$ in this energy region. It is concluded that no evidence is found for the 2^+ state reported by Isabelle and Bishop (1963) at this energy (this would require a positive a_2 coefficient).

The data show little evidence for the presence of other than 1^- states, although the a_1 coefficient tends to increase towards higher energies. However, a_2 never becomes positive and seldom varies far from the one-particle–one-hole model prediction in this energy region of predominantly d-wave emission from a 1^- state. More recent calculations, which include effects of the continuum (Buck and Hill 1967; Wahsweiler, Greiner, and Danos, personal communication), still seem unable to significantly improve upon this description.

V. ACKNOWLEDGMENTS

The author wishes to acknowledge assistance from Miss J. M. Dixon, Mr. P. H. Cannington, and Mr. D. Holmes, and would like to thank Professor B. M. Spicer for helpful discussions. Financial assistance in the form of a CSIRO Senior Post-graduate Studentship is also acknowledged.

VI. REFERENCES

BRIX, P., and MASCKE, E. R. (1959).—*Z. Phys.* **155**, 109.

BUCK, B., and HILL, A. D. (1967).—*Nucl. Phys.* A **95**, 271.

CALDWELL, J. T., BRAMBLETT, R. L., BERMAN, B. L., HARVEY, R. R., and FULTZ, S. C. (1965).—*Phys. Rev. Lett.* **15**, 976.

DODGE, W. R., and BARBER, W. C. (1962).—*Phys. Rev.* **127**, 1746.

Earle, E. D., and Tanner, N. W. (1967).—*Nucl. Phys.* A **95**, 241.

Gillet, V., Melkanoff, M. A., and Raynal, J. (1967).—*Nucl. Phys.* A **97**, 631.

Gillet, V., and Vinh-Mau, N. (1964).—*Nucl. Phys.* **54**, 321.

Greiner, W. (1963).—*Nucl. Phys.* **49**, 522.

Isabelle, D. B., and Bishop, G. R. (1963).—*Nucl. Phys.* **45**, 209.

Johannson, S. A. E., and Forkman, B. (1957).—*Ark. Fys.* **12**, 359.

Milone, C., Milone-Tamburino, S., Rinzivillo, R., Rubbino, A., and Tribuno, C. (1958).—*Nuovo Cim.* **7**, 729.

Silverstein, E. A. (1959).—*Nucl. Instrum. Meth.* **4**, 53.

Tanner, N. W., Thomas, G. C., and Earle, E. D. (1964).—*Nucl. Phys.* **52**, 45.

Verbinski, V. V., and Courtney, J. C. (1965).—*Nucl. Phys.* **73**, 398.

TRIAL OF A NUMERICAL METHOD FOR SOLVING THE SCHRÖDINGER WAVE EQUATION IN SEVERAL VARIABLES

By I. M. Bassett*

[*Manuscript received September* 21, 1967]

Summary

A numerical method previously described for the solution of eigenvalue–eigenfunction problems in several variables has been applied to the Schrödinger wave equation for the lithium atom. The method employs an expansion of the wavefunction in terms of Slater determinants. Some information is obtained about the convergence behaviour of such expansions, the convergence being too slow in this instance to yield an energy of useful accuracy.

I. Introduction

A numerical method (Bassett 1959*a*, 1959*b*, 1959*c*) for the solution of eigenvalue–eigenfunction problems in several variables has been applied to the Schrödinger wave equation for the lithium atom. The lithium atom is a three-particle system (assuming that its nucleus is fixed) and so is a problem in nine variables; the fundamental eigenfunction (i.e. ground state wavefunction) was sought. In order to provide the method with a reasonably stiff test, no use was made of the spatial symmetry of this ground state wavefunction. The results constitute some evidence about the rate of convergence of series expansions of wavefunctions in terms of the class of Slater determinants employed. The rate of convergence in this case was too slow to yield an energy of useful accuracy but the results seem worth reporting briefly, together with some details of the computational method. The basic method may yet be useful in some form.

The wave equation for the electrons in a lithium atom, in atomic units (Hartree 1957), is

$$\left(\sum_{j=1}^{3}\left(-\tfrac{1}{2}\nabla_j^2-3r_j^{-1}\right)+r_{12}^{-1}+r_{23}^{-1}+r_{31}^{-1}\right)\psi=E\psi, \tag{1}$$

where $\psi=\psi(\mathbf{r}_1,\mathbf{r}_2,\mathbf{r}_3)$ is the wavefunction, E the energy, r_{ij} the distance between electrons i and j, r_j the distance between electron j and the nucleus, and ∇_j^2 the Laplacian operator on $\mathbf{r}_j$, the position vector of the jth electron.

The wavefunction is expressed as a sum of Slater determinants built from one-electron functions, which in this calculation were taken in the form

$$F(r_i)\,G(\theta_i)\,H(\phi_i)\,\sigma(s_i)\,,$$

where r_i,θ_i,ϕ_i are the spherical polar spatial coordinates of the ith electron with s_i its spin coordinate. To obtain the lowest *doublet* state, the spin wavefunctions were

---

* Department of Theoretical Physics, University of Sydney, N.S.W. 2006.

Aust. J. Phys., 1968, **21**, 113–19

chosen to be α, α, and β, i.e. two the same. The method imposes no other restriction on the form of the one-electron functions, and the results suggest that for the ground state of the lithium atom 35 Slater determinants (the maximum number taken) when constructed in this way cannot give an eigenvalue estimate in error by less than about 0·1%, or about 0·01 atomic units. Further, the successive eigenvalue estimates that the method generates do not lie on a smooth curve (Fig. 1). It follows that only the roughest estimate of the error resulting from terminating the series can be made by extrapolation, in contrast to Pekeris's solutions of the wave equation for the helium atom, where the eigenvalue estimates change smoothly enough to permit extrapolation (Pekeris 1958; Frankowski and Pekeris 1966).

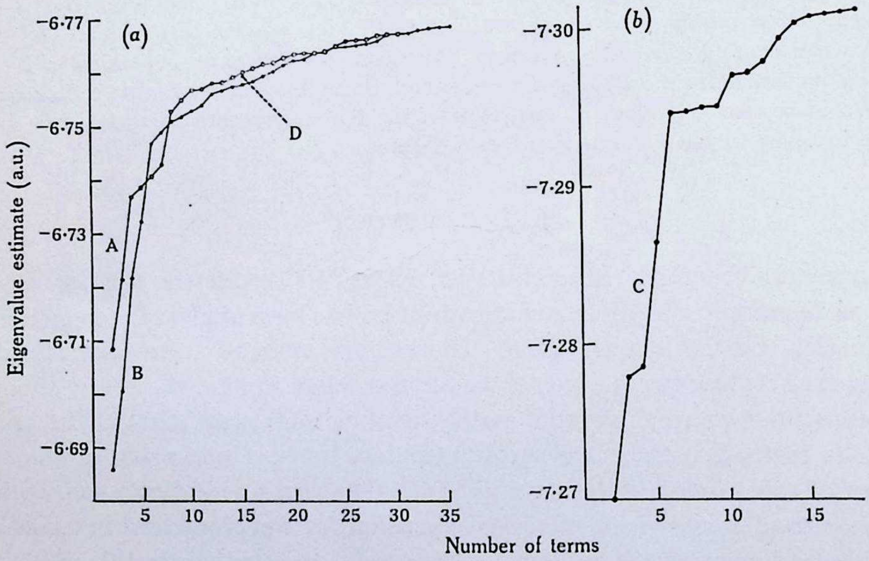

Fig. 1.—Eigenvalue estimates in atomic units plotted against number of terms (Slater determinants) of some series approximations to the eigenvectors. The results of three separate calculations, wavefunctions A, B, and D (the last being represented by the isolated point at 15 terms), for a mesh size determined by $n = 6$ are shown in (a), while the result of a further calculation, wavefunction C, using a finer mesh size ($n = 14$) is shown in (b). The eigenvalue–eigenvector problem concerned may be regarded as a model problem that approximates the wave equation for the lithium atom, the closeness of approximation being determined by the mesh size.

II. Aspects of the Method of Calculation

A very coarse mesh was used for the finite difference operations. That results obtained on such a coarse mesh can be meaningful has been illustrated in the application of the method to a simple problem (Bassett 1959a, p. 434; 1959b, p. 447). There the rate of convergence and other features of the solution were found to be obtainable on a very coarse mesh, provided formulae for numerical integration and differentiation are chosen in a particular way, namely, so that the sequence of estimates of the solution converges (exactly) to the solution of an eigenvalue–eigenvector problem, which is itself an approximation, in the sense of finite differences, to the eigenvalue–eigenfunction problem.

This technique has been used in the present calculation. It permits separation of the error arising from termination of the series of Slater determinants from that which depends on the size of the mesh. The eigenvalue–eigenvector problems for which the successive eigenvalue estimates are illustrated in Figures 1(*a*) and 1(*b*) might be described as *models* of the wave equation for the lithium atom, that shown in Figure 1(*b*) (wavefunction C) using a finer mesh and therefore being a more accurate model. The eigenvalue estimate based on this 18-term wavefunction is $-7\cdot30$ a.u., which may be compared with the experimental energy of $-7\cdot48$ a.u. This error of $0\cdot18$ a.u. undoubtedly is due mainly to the size of the mesh, not to the termination of the series. It is the author's contention that the convergence behaviour shown in Figure 1 would be exhibited on an arbitrarily fine mesh.

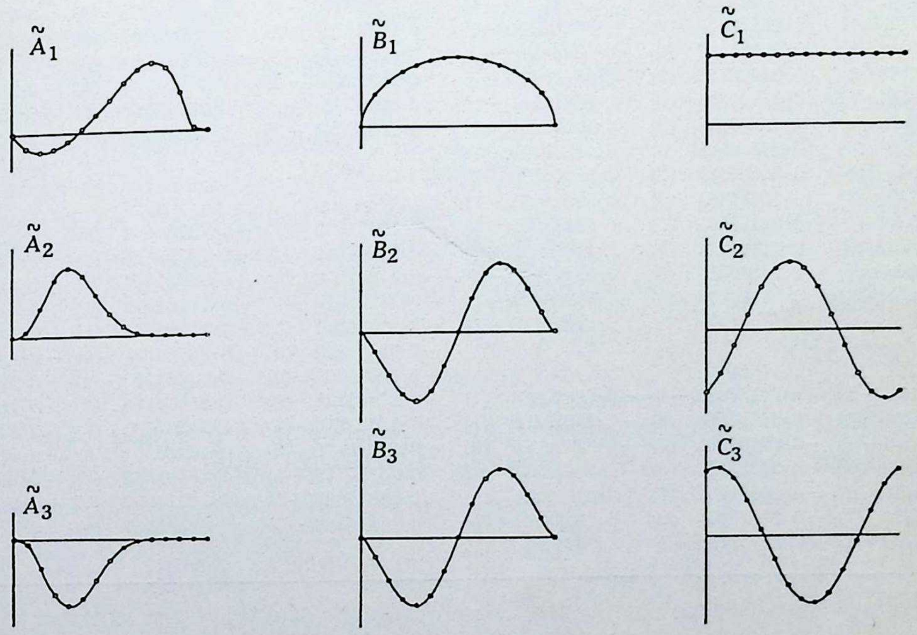

Fig. 2.—Typical term (i.e. Slater determinant) obtained in the series expansion. (The figure represents the ninth Slater determinant of wavefunction C.) The Slater determinant is built from three one-electron functions, each having the spatial dependence

$$\sin^{-1}\rho\,\sin^{-\frac{1}{2}}\theta\,A_i(\rho)\,B_i(\theta)\,C_i(\phi)\qquad(i=1,2,3),$$

where $r=\tan^{-1}\rho$, θ, and ϕ are the spherical polar coordinates of an electron. The functions $\tilde{A}_i$, $\tilde{B}_i$, and $\tilde{C}_i$ shown in the figure are normalized versions of A_i, B_i, and C_i; $\tilde{A}_i$ is obtained from A_i by dividing each element of A_i by the modulus of its largest element, and $\tilde{B}_i$ and $\tilde{C}_i$ are similarly related to B_i and C_i. The functions A_i, B_i, and C_i themselves are given in Table 1.

The terms r_{ij}^{-1} in equation (1), i.e. the Coulomb repulsion terms, were replaced in these calculations by the first four terms of the standard series expansion in Legendre polynomials (Hartree 1957, p. 46), i.e. the terms up to and including Legendre polynomials of order four. In this respect also, the problem tackled was only an approximation to the differential equation (1). However, it seems unlikely that this truncation of the series expression for r_{ij}^{-1} affected the results appreciably; the dependence on azimuthal angle of the terms actually obtained suggests low order trigonometric functions (Fig. 2) and so the matrix elements of the neglected terms in the series for r_{ij}^{-1} are probably very small. A typical term obtained in the series expansion is represented in Figure 2, in which the $\widetilde{A}_i$, $\widetilde{B}_i$, and $\widetilde{C}_i$ shown are normalized versions of the values given in Table 1 and are further explained in the caption to the figure.

TABLE 1

FUNCTIONS $A_i(\rho)$, $B_i(\theta)$, AND $C_i(\phi)$ SHOWN (IN NORMALIZED FORM) IN FIGURE 2

Values are given of the functions at the interior mesh points of the domains in which they are defined. Each function value F is represented by a decimal fraction a followed by an integer n in parentheses, where $F = a \times 10^n$

A_1	B_1	C_1	A_2	B_2	C_2
−0·48400974(−1)	0·18634528 (0)	0·58246334(−1)	0·62290119(−2)	0·17217258 (0)	0·35884824 (1)
−0·63965057(−1)	0·26020265 (0)	0·58248314(−1)	0·16704225(−2)	0·29902595 (0)	0·24827574 (1)
−0·55788281(−1)	0·31191417 (0)	0·58254585(−1)	0·25805055(−3)	0·34913594 (0)	0·87811397 (0)
−0·29985636(−1)	0·34928732 (0)	0·58260443(−1)	0·16182795(−4)	0·31507891 (0)	−0·90655550 (0)
0·90689929(−2)	0·37497006 (0)	0·58261503(−1)	0·19835345(−6)	0·21673553 (0)	−0·25070044 (1)
0·57688385(−1)	0·39007213 (0)	0·58256993(−1)	0·10867061(−9)	0·98236185(−1)	−0·36027028 (1)
0·11189613 (0)	0·39506368 (0)	0·58250353(−1)			−0·39857160 (1)
0·16627940 (0)	0·39007518 (0)	0·58246629(−1)			
0·21239215 (0)	0·37497465 (0)	0·58248655(−1)	A_3	B_3	C_3
0·23641524 (0)	0·34929095 (0)	0·58254907(−1)	−0·10655063 (0)	−0·48586652 (0)	0·35917097 (1)
0·21670403 (0)	0·31191434 (0)	0·58260672(−1)	−0·59667442 (0)	−0·10718196 (1)	0·37452092 (1)
0·12930864 (0)	0·26019813 (0)	0·58261579(−1)	−0·11642276 (1)	−0·15581524 (1)	0·31646253 (1)
0·79151293(−2)	0·18633772 (0)	0·58256904(−1)	−0·14118070 (1)	−0·17266828 (1)	0·19548870 (1)
		0·58250138(−1)	−0·12519251 (1)	−0·14790433 (1)	0·34926701 (0)
			−0·85571349 (0)	−0·85184018 (0)	−0·13270780 (1)
A_2	B_2	C_2	−0·45069335 (0)	−0·54365768(−4)	−0·27325790 (1)
0·36878363(−2)	−0·98187280(−1)	−0·35876873 (1)	−0·17482144 (0)	0·85174178 (0)	−0·35916615 (1)
0·20659705(−1)	−0·21663983 (0)	−0·24820589 (1)	−0·44627719(−1)	0·14789700 (1)	−0·37451153 (1)
0·40343695(−1)	−0·31497303 (0)	−0·87776963 (0)	−0·53683178(−2)	0·17266364 (1)	−0·31645543 (1)
0·48986350(−1)	−0·34907462 (0)	0·90655528 (0)	0·35117172(−3)	0·15581252 (1)	−0·19548906 (1)
0·43525947(−1)	−0·29904702 (0)	0·25069316 (1)	0·13867882(−3)	0·10718036 (1)	−0·34934101 (0)
0·29848112(−1)	−0·17227203 (0)	0·36028823 (1)	0·11216488(−5)	0·48585857 (0)	0·13269911 (1)
0·15818520(−1)	−0·65737158(−4)	0·39862806 (1)			0·27325469 (1)

The process of successive approximation by which the one-electron functions are determined requires a starting point, and as this point, for each Slater determinant except the first, a set of more or less random numbers was used, prepared by shuffling a deck of cards on which were punched an assortment of numbers of reasonable magnitude. These form acceptable initial functions, since, as remarked above, the arithmetical procedure can be regarded as solving a finite eigenvector problem and it will work even if the intermediate approximations to the eigenvector do not represent smooth functions.

Before introducing finite difference approximations, the wavefunction ψ in equation (1) was replaced by χ, defined by

$$\chi = \sin\rho_1 \sin^{\frac{1}{2}}\theta_1 \sin\rho_2 \sin^{\frac{1}{2}}\theta_2 \sin\rho_3 \sin^{\frac{1}{2}}\theta_3 \psi\,, \tag{2}$$

where

$$r_i = \tan\rho_i\,. \tag{3}$$

The equation, equivalent to (1), satisfied by χ is

$$\mathscr{H}\chi = E\,W(\rho_1)\,W(\rho_2)\,W(\rho_3)\,\chi\,, \tag{4}$$

$$W(\rho) = \cos^{-4}(\rho)\,, \tag{5}$$

where

$$\begin{aligned}\mathscr{H} = {} & W(\rho_2)\,W(\rho_3)\,T(\rho_1,\theta_1,\phi_1) + W(\rho_1)\,W(\rho_3)\,T(\rho_2,\theta_2,\phi_2)\\ & + W(\rho_1)\,W(\rho_2)\,T(\rho_3,\theta_3,\phi_3) + W(\rho_1)\,W(\rho_2)\,W(\rho_3)\,V\,,\end{aligned} \tag{6}$$

V, the potential energy, is given by

$$V = -\sum_{j=1}^{3} 3r_j^{-1} + r_{12}^{-1} + r_{23}^{-1} + r_{31}^{-1}\,, \tag{7}$$

and T, the kinetic energy operator for one electron, is given by

$$\begin{aligned}T(\rho,\theta,\phi) = {} & -\tfrac{1}{2}(\partial^2/\partial\rho^2) + \cos^{-2}\rho\,\sin^{-2}\rho\,\{-\tfrac{1}{2}(\partial^2/\partial\theta^2) - \tfrac{1}{8}\sin^{-2}\theta\}\\ & + \cos^{-2}\rho\,\sin^{-2}\rho\,\sin^{-2}\theta\,\{-\tfrac{1}{2}(\partial^2/\partial\phi^2)\} - \tfrac{1}{8}\cos^{-2}\rho\,\sin^{-2}\rho - \tfrac{1}{2}\,.\end{aligned} \tag{8}$$

As a result of these transformations the differential operator T is Hermitian with weight factor unity, in contrast to the Laplacian operator in spherical polar coordinates, which is Hermitian with weight factor $r^2 \sin\theta$. It is easy to obtain a finite difference representation of (6) that is a strictly symmetric matrix. (The second derivatives were represented by the second central difference δ^2 divided by the square of the mesh size, that is, δ^2/h^2.) It follows (Bassett 1959*c*) that the numerical procedure produces a solution of the eigenvalue–eigenvector problem for this matrix.

III. Results

The mesh points were chosen so as to divide the ranges of the variables ρ, θ, and ϕ into the same number n of equal intervals. An approximate solution to 30 terms (Slater determinants) was obtained (wavefunction A) with $n = 6$. Another solution (using reshuffled cards as starting point) with $n = 6$ was carried to 35 terms (wavefunction B). The eigenvalue estimates as a function of the number of terms in the corresponding approximate eigenfunctions are shown in Figure 1(*a*). The first term in the series was rather arbitrarily taken to be the Slater determinant formed from two hydrogen-like unscreened 1S functions and one 2S function. The terms other than the first were determined one by one in accordance with the procedure described previously (Bassett 1959*a*, 1959*b*, 1959*c*) by cyclically varying their nine functions of one variable. Ten such cycles were nearly always sufficient to produce satisfactory convergence from the initial functions determined by the shuffled decks. A variant of this procedure was used to obtain another solution with $n = 6$ (wavefunction D). First a two-term wavefunction was obtained by varying the two terms alternately (in this case, therefore, the first term was not the $(1\mathrm{S})^2 2\mathrm{S}$ Slater determinant). Then, leaving these first two terms fixed, another 13 terms were added and varied cyclically, i.e. instead of building up a wavefunction term by term and varying only the last term at each stage, the last 13 terms were varied in cyclic order (so that they were all roughly on an equal footing). This procedure seems more flexible than the other, but led to no improvement in the eigenvalue estimate (see the isolated point at 15 terms in Figure 1(*a*) labelled wavefunction D). A third approximate solution (wavefunction C, Fig. 1(*b*)) was obtained with $n = 14$. This was carried to 18 terms and shows slow and fitful convergence like cases A and B.

IV. HANDLING SINGULARITIES OF THE TRANSFORMED HAMILTONIAN

The transformation (2) results in some singular terms in the kinetic energy operator (8). The only one that gives any trouble is the term containing the factor

$$-\tfrac{1}{2}(\partial^2/\partial\theta^2)-\tfrac{1}{8}\sin^{-2}\theta. \tag{9}$$

Among the class of functions $f(\rho)\,g(\theta)\,h(\phi)$ that must contribute to the wavefunction are functions whose θ-dependence is $\sin^{\frac{1}{2}}\theta$. For example, if an S wavefunction is transformed in accordance with (2) it has this θ-dependence. Now

$$\begin{aligned}\{-\tfrac{1}{2}(\partial^2/\partial\theta^2)-\tfrac{1}{8}\sin^{-2}\theta\}\sin^{\frac{1}{2}}\theta &= +\tfrac{1}{8}\sin^{-3/2}\theta\cos^2\theta+\tfrac{1}{4}\sin^{\frac{1}{2}}\theta-\tfrac{1}{8}\sin^{-3/2}\theta\\ &= \tfrac{1}{8}\sin^{\frac{1}{2}}\theta,\end{aligned} \tag{10}$$

which is finite at $\theta=0$ and π. Thus, although both the terms $-\frac{1}{2}(\partial^2/\partial\theta^2)\sin^{\frac{1}{2}}\theta$ and $-\frac{1}{8}\sin^{-2}\theta\sin^{\frac{1}{2}}\theta$ have non-integrable singularities at 0 and π, their sum is well behaved. It is not obvious how to achieve this cancellation of singularities in a numerical calculation in which $\partial^2/\partial\theta^2$ is replaced by a finite difference operator. There is a second difficulty which arises from the fact that the operator $-\frac{1}{2}(\partial^2/\partial\theta^2)-\frac{1}{8}\sin^{-2}\theta$ does not have a fundamental eigenvalue, except in a representation based on a restricted class of functions. For example, the average value

$$\int_0^\pi g(\theta)\,\{-\tfrac{1}{2}(\partial^2/\partial\theta^2)-\tfrac{1}{8}\sin^{-2}\theta\}\,g(\theta)\,\mathrm{d}\theta\div\int_0^\pi g^2\,\mathrm{d}\theta$$

is $-\infty$ for a function $g(\theta)$ that approaches zero like $\theta^{\frac{1}{4}}$, so that such functions have somehow to be excluded. Both difficulties can be overcome by adopting an appropriate numerical representation for the function $\sin^{-2}\theta$ occurring in the transformed kinetic energy operator (8). We adopt $S(\theta)$ as the finite vector representing $\sin^{-2}\theta$, where

$$\{-\tfrac{1}{2}(\delta^2/h^2)-\tfrac{1}{8}S(\theta)\}\sin^{\frac{1}{2}}\theta=\tfrac{1}{8}\sin^{\frac{1}{2}}\theta. \tag{11}$$

Equation (11) is a finite difference analogue of (10). Thus

$$S(\theta)=-1-4\sin^{-\frac{1}{2}}\theta\,(\delta^2/h^2)\sin^{\frac{1}{2}}\theta. \tag{12}$$

$S(\theta)\to\sin^{-2}\theta$ in any prescribed interval *inside* $(0,\pi)$ as $h\to 0$. This choice of $S(\theta)$ achieves by construction the desired cancellation of singularities. Furthermore, the fundamental (i.e. one-signed) eigenvector of

$$-\tfrac{1}{2}(\delta^2/h^2)-\tfrac{1}{8}S(\theta)$$

is $\sin^{\frac{1}{2}}\theta$ and accordingly there are no eigenvalues lying below that which is associated with the eigenvector $\sin^{\frac{1}{2}}\theta$. The numerical vector space therefore contains nothing corresponding to the unwanted functions like $\sin^{\frac{1}{4}}\theta$.

V. CONCLUSIONS

Inspection of the sequences of eigenvalue estimates in Figure 1 suggests that the error in the eigenvalue at 30 or 35 Slater determinants, arising from termination of the series, is not less than about 0·1% or 0·01 a.u. Because of the way in which these sequences of eigenvalue estimates were obtained, it is the author's opinion that they probably exhibit the most rapid possible convergence of a series expansion of the ground state lithium wavefunction, using these coordinates. This rate is too slow with existing computers to yield wavefunctions and total energies of useful accuracy.

Variants of the basic method are possible. For example, it would be possible to represent the one-electron functions by a three-dimensional table (most simply using Cartesian coordinates). A series expansion in Slater determinants constructed from such one-electron functions might converge rapidly enough to yield useful results. Further, the basic method can certainly be adapted to determine low lying excited states. It is possible that the energy *differences* between such low lying excited states and the ground state would be approximately equal to the corresponding eigenvalue differences of the finite matrix approximating the physical problem, even on a mesh on which the truncation error of the numerical integration is greater than the energy differences in question.

VI. ACKNOWLEDGMENTS

The author wishes to acknowledge the help and hospitality of the IBM Watson Laboratory at Columbia University, where most of this work was done, and the National Institute for Research in Nuclear Science (U.K.) and the Deutsches Rechenzentrum, Darmstadt (West Germany), where it was finished. The author also wishes to thank Professor F. T. Wall, Professor Martin Karplus, Professor M. H. L. Pryce, and Dr. John Malos for encouragement and assistance.

VII. REFERENCES

BASSETT, I. M. (1959*a*).—*Aust. J. Phys.* **12**, 430.
BASSETT, I. M. (1959*b*).—*Aust. J. Phys.* **12**, 441.
BASSETT, I. M. (1959*c*).—*Aust. J. Phys.* **12**, 449.
FRANKOWSKI, K., and PEKERIS, C. L. (1966).—*Phys. Rev.* **146**, 46.
HARTREE, D. R. (1957).—"The Calculation of Atomic Structures." (Chapman & Hall: London.)
PEKERIS, C. L. (1958).—*Phys. Rev.* **112**, 1649.

A QUANTUM MECHANICAL CALCULATION OF THE RADIAL DISTRIBUTION FUNCTION FOR A PLASMA

By A. A. Barker*

[*Manuscript received December* 22, 1967]

Summary

A quantum mechanical calculation of the radial distribution function $g_{\text{q.m.}}(r)$ for unlike particles in a hydrogenous plasma is presented. Results for a neutral plasma over a range of temperatures show that $g_{\text{q.m.}}(r)$ differs significantly from the corresponding classical distribution function $g_{\text{c}}(r) = \exp(\beta e^2/r)$ when r is less than a chosen distance r_1, the value of which is temperature dependent. The effect of shielding, the relative contribution from scattered and bound states, and the relation to percentage ionization are discussed.

I. Introduction

In solving a modified Percus–Yevick integral equation for a hydrogenous plasma to find the radial distribution function for unlike particles for temperatures near 10^4 °K, it was found (Barker 1966) that the efficiency of the numerical iterative procedure used was very sensitive to the initial form assumed for the radial distribution function. If a classical or Debye–Hückel form was used, the cutoff point as r became small was of critical importance to the solution. This reflects the fact that at these temperatures an appreciable number of particles of opposite charges are bound, and the classical theory does not adequately describe the bound states. To overcome this difficulty a quantum mechanical expression for the radial distribution function at low radii has been evaluated, the results of which are presented in this paper.

II. Quantum Mechanical Expression for $g_{ab}(r)$

The radial distribution function $g_{ab}(r)$ is usually defined by $D_{ab}(r) = D_b\, g_{ab}(r)$, where $D_{ab}(r)$ is the number density of particles of type b at a distance r from a particle of type a, and D_b is the average number density of type b particles throughout the fluid. It is proportional to the conditional probability of finding particle b in volume element $\mathrm{d}x(2)$ given particle a in volume element $\mathrm{d}x(1)$, and, for a neutral plasma of electron number density D_{e}, the distribution function between protons and electrons can be expressed as

$$g_{\text{q.m.}}(r) = \frac{\sum_n \exp(-\beta E_n)\,\psi_{nlm}\psi^*_{nlm} + \sum_{\mathbf{k}} \exp(-\beta \mathbf{k}^2\hbar^2/2m)\,\psi_{\mathbf{k}}\psi^*_{\mathbf{k}}}{\sum_{\mathbf{k}} \exp(-\beta \mathbf{k}^2\hbar^2/2m)\,\psi_0\psi^*_0}, \tag{1}$$

where the summation over n sums over the bound states of energy E_n of the hydrogen atom, and ψ_{nlm} are the wavefunctions normalized so that $\int \psi_{nlm}\psi^*_{nlm}\,\mathrm{d}V = 1$. The

---

* Department of Mathematical Physics, University of Adelaide, S.A. 5000.

Aust. J. Phys., 1968, **21**, 121–7

summation over **k** sums over scattered states of the hydrogen atom and $\psi_{\mathbf{k}}$ are the wavefunctions normalized so that $\int \psi_{\mathbf{k}} \psi_{\mathbf{k}}^* \, \mathrm{d}V = 1$. ψ_0 is the wavefunction of an electron without a proton present, that is, a plane wave, but normalized so that $\int \psi_0 \psi_0^* \, \mathrm{d}V = 1$. Substituting the wavefunctions as given by Pauling and Wilson (1935) and Schiff (1955), replacing the summation over **k** by an integral, and removing the angular dependence, we have

$$g_{\mathrm{q.m.}}(r) = \left\{ \sum_{n=1}^{\infty} \exp(-\beta E_n) \sum_{l=0}^{n-1} \frac{2l+1}{4\pi} \left(\frac{2Z}{na_0}\right)^3 \frac{(n-l-1)!}{2n\{(n+l)!\}^3} \exp(-\rho)\, \rho^{2l} \{\mathrm{L}_{n+l}^{2l+1}(\rho)\}^2 \right.$$

$$\left. + \frac{2}{(2\pi)^2} \int_0^\infty \exp(-\beta k^2 \hbar^2/2m) \sum_{l=0}^{\infty} \frac{2l+1}{k^2 r^2} \{\mathrm{F}_l(\alpha, kr)\}^2 \, k^2 \, \mathrm{d}k \right\}$$

$$\div \frac{4\pi}{(2\pi)^3} \int_0^\infty \exp(-\beta k^2 \hbar^2/2m) \, k^2 \, \mathrm{d}k \,. \tag{2}$$

where $\rho = 2rZ/na_0$ (a_0 being the first Bohr radius, Z the atomic number, and n the principal quantum number), L_{n+l}^{2l+1} are the associated Laguerre polynomials, and $\mathrm{F}_l(\alpha, kr)$ are the Coulomb wavefunctions with $\alpha = Zme^2/\hbar^2 k$. Evaluating the denominator directly gives $(2\pi\beta\hbar^2/m)^{-3/2}$ cm^{-3}, which can be conveniently expressed in units of (Bohr radii)$^{-3}$, and we have

$$g_{\mathrm{q.m.}}(r) = \left(\frac{2\pi\beta\hbar^2}{m}\right)^{3/2} \left\{ \frac{Z^3}{\pi} \sum_{n=1}^{\infty} \frac{\exp(-\beta E_n - \rho)}{n^4} \sum_{l=0}^{n=1} \frac{(2l+1)(n+l+1)!}{\{(n+l)!\}^3} \, \rho^{2l} \{\mathrm{L}_{n+l}^{2l+1}(\rho)\}^2 \right.$$

$$\left. + \frac{1}{2\pi^2 r^2} \int_0^\infty \exp(-\beta k^2 \hbar^2/2m) \sum_{l=0}^{\infty} (2l+1) \{\mathrm{F}_l(\alpha, kr)\}^2 \, \mathrm{d}k \right\}. \tag{3}$$

III. EVALUATION OF $g_{\mathrm{q.m.}}(r)$ AND RESULTS

The associated Laguerre polynomials were generated by two methods, one using recurrence relations and the other using a power series, so providing a consistency check. The zero and first-order Coulomb functions were similarly generated by two methods, one using a power series and the other using an asymptotic expansion, depending on the range of α and ρ; the recurrence relation technique of Abramowitz and Stegun (1964) was then used to generate the functions of higher order. A computer programme was written for a C.D.C. 6400 computer to evaluate $g_{\mathrm{q.m.}}(r)$ from equation (3), for r varying from 0 to 150 Bohr radii. The sums were terminated when the last term became less than one ten-thousandth part of the sum, and the integral was evaluated using a trapezoidal rule with upper and lower limits, which, when doubled and halved respectively, failed to alter the value of the integral by more than one ten-thousandth of its value.

Figure 1 shows plots of $\log_{10}(g_{\mathrm{q.m.}}(r))$ versus r (Q curves) calculated for three temperatures: 10^4, 2×10^4, and 4×10^4 °K. The curves show that the bound state contribution is quite large, especially at low temperatures, and for 10^4 °K even at 50 Bohr radii the bound states contribute 18% of $g_{\mathrm{q.m.}}(r)$, and still contribute 11% at 100 Bohr radii. The value of n at which the sum of the bound states is terminated is also of interest, and for 10^4°K at 10 Bohr radii 26 terms were needed, at 50 Bohr radii 84 terms, and at 100 Bohr radii 110 terms contributed. In a similar manner the number of terms contributing to the scattering states increased as the radii increased.

The figure shows that $g_{\mathrm{q.m.}}(r)$ runs smoothly onto the classical radial distribution function $g_{\mathrm{c}}(r)$ (C curves) at a certain joining radius r_{j}, which has been chosen such that the ratio $\{g_{\mathrm{q.m.}}(r)-g_{\mathrm{c}}(r)\}/g_{\mathrm{c}}(r)$ is less than $0\cdot05$ for $r > r_{\mathrm{j}}$. It can be seen that below r_{j} there is a marked difference between $g_{\mathrm{q.m.}}(r)$ and $g_{\mathrm{c}}(r)$. At $r = 0$ the quantum mechanical curve tends to a constant (approximately equal to the first bound state contribution of

$$(2\pi\beta\hbar^2/m)^{3/2}\exp(15\cdot780/T\times10^{-4})/\pi$$

for temperatures T below 4×10^4), while the classical curve approaches infinity. For small r and low temperatures the quantum mechanical curve lies close to the first bound state contribution, i.e.

$$(2\pi\beta\hbar^2/m)^{3/2}\exp\{(15\cdot780/T\times10^{-4})-2r\}/\pi$$

(where r is in Bohr radii), whilst the classical curve

$$g_{\mathrm{c}}(r) = \exp\{63\cdot156/(T\times10^{-4}\times2r)\}$$

falls away much more sharply. As the radii increase, other bound states and scattered

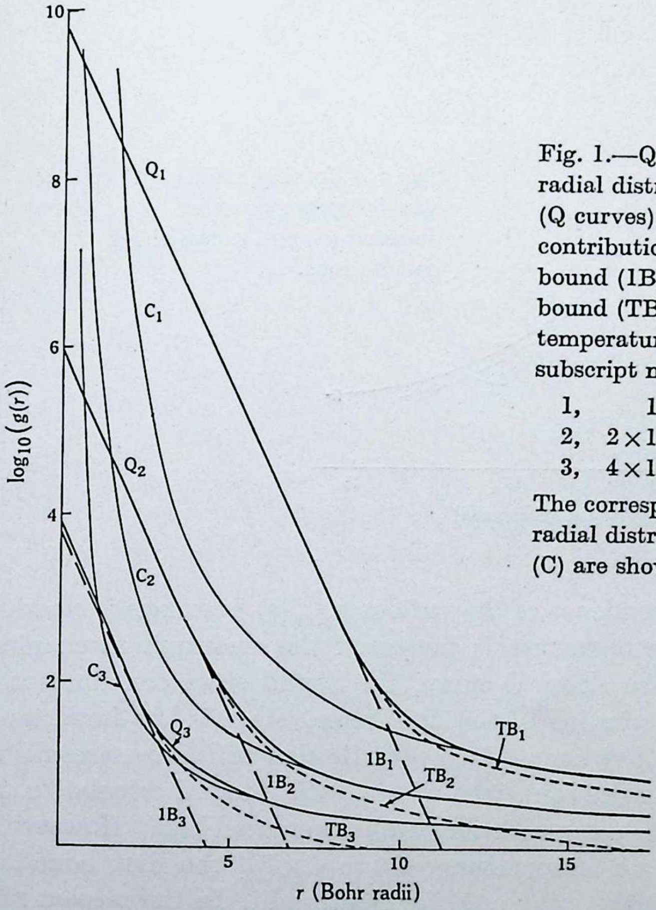

Fig. 1.—Quantum mechanical radial distribution functions (Q curves) showing contributions from the first bound (1B) state and total bound (TB) states for three temperatures indicated by subscript numbers:

1, 10^4 °K,
2, 2×10^4 °K,
3, 4×10^4 °K.

The corresponding classical radial distribution functions (C) are shown for comparison.

states start making an appreciable contribution to $g_{\text{q.m.}}(r)$, until at r_j it effectively joins the classical curve.

So far no allowance has been made for the effects of other particles present in the plasma, equation (3) being valid for a two-particle system just as the classical distribution function is valid for a proton–electron system. To take account of this shielding effect is more difficult and, as the procedure is discussed fully in Section IV, it will only be mentioned here that curves are presented below in which an attempt has been made to include the shielding effect approximately.

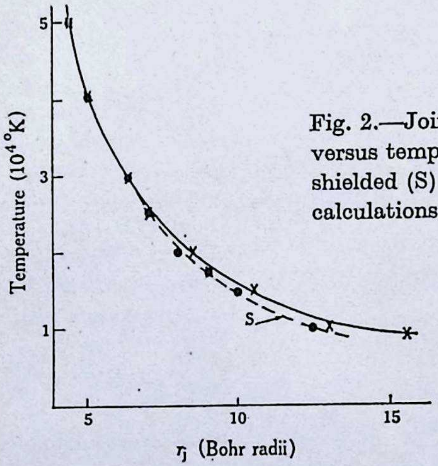

Fig. 2.—Joining radius r_j versus temperature for shielded (S) and nonshielded calculations.

The temperature dependence of the various $g_{\text{q.m.}}(r)$ functions is clearly evident from Figure 1. As the temperature is increased the quantum mechanical curve becomes much closer to the classical curve, the bound state contribution falls off much faster, and the contribution of the first bound state is less important. Comparison of $g_{\text{q.m.}}(r)$ and the first bound state contribution with recent results obtained by Storer (personal communication), who uses a path integral calculation to obtain $g_{\text{q.m.}}(r)$, indicates close agreement with the results presented here. However, Storer's results clearly show that at temperatures above 4×10^4 the first bound state no longer contributes nearly 100% of $g_{\text{q.m.}}(r)$ for small radii. In the present results the divergence of $g_{\text{q.m.}}(r)$ from the first bound state contribution at $r = 0$ is only just apparent at 4×10^4 °K.

Figure 2 shows that the joining radius r_j falls off sharply as the temperature increases from $0\cdot9\times10^4$ to 3×10^4 °K but that at higher temperatures it varies only slightly. There is no obvious analytical dependence of r_j on temperature.

IV. EXTENSION TO ALLOW FOR SHIELDING

To include the effects of other particles in the quantum mechanical distribution function to a high degree of accuracy it is necessary to use $g_{\text{q.m.}}(r)$ as a first approximation in a modified Percus–Yevick equation, and the author hopes to present results using this approach in the near future. However, in the present paper an approximate estimate of the shielding effect of other particles is obtained by including a Debye–Hückel shielding factor on the charge of the hydrogen atom, and Z in equation (3) is replaced by $Z\exp(-r/\lambda_D)$, where λ_D is the Debye shielding distance. This involves the approximation that the wavefunctions obtained by solving the Schrödinger equation for a Debye–Hückel shielded potential are equal to the wavefunctions obtained by solving the usual hydrogen atom wave equation, but now weighting these wavefunctions by a Debye–Hückel shielding factor.

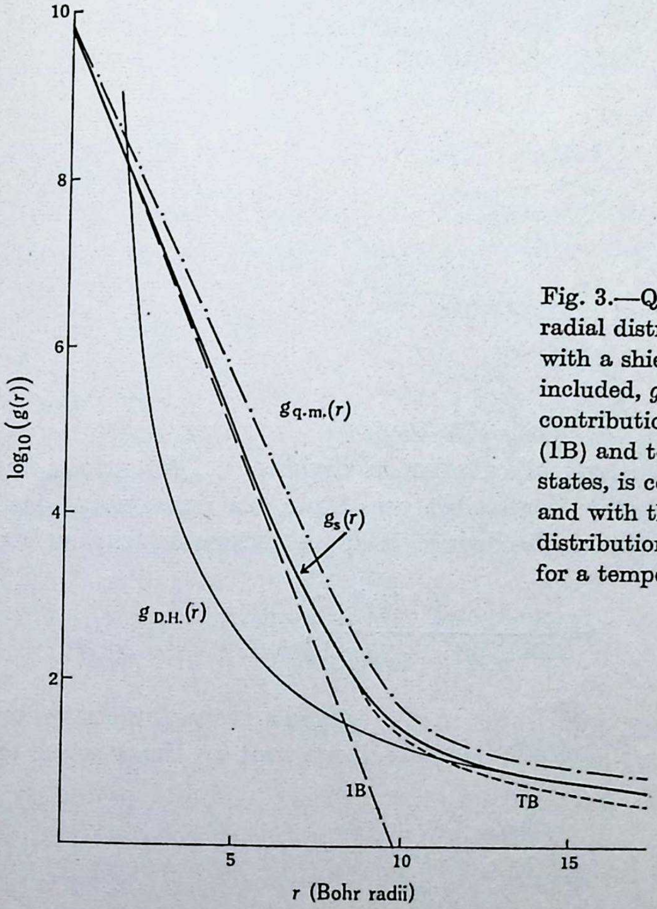

Fig. 3.—Quantum mechanical radial distribution function with a shielding factor included, $g_s(r)$, showing contributions from first bound (1B) and total bound (TB) states, is compared with $g_{q.m.}(r)$ and with the Debye–Hückel distribution function $g_{D.H.}(r)$ for a temperature of 10^4 °K.

Figure 3 shows the radial distribution function including this shielding factor, $g_s(r)$, at 10^4 °K, and comparing it with $g_{q.m.}(r)$ it can be seen that the inclusion of shielding has little effect on the general shape of the curve but lowers it by an appreciable factor, so that now $g_s(r)$ joins the Debye–Hückel curve ($g_{D.H.}(r)$) above a certain radius. From Figure 2 it can be seen that this joining radius (defined as before, except now the criterion is that $g_s(r)$ approaches within 5% of $g_{D.H.}(r)$, not $g_c(r)$ as before) only differs from the nonshielded case at temperatures below 3×10^4 °K. The effect of the shielding is more pronounced on the bound state and first bound state contributions, and Figure 3 shows that these fall off appreciably faster than the nonshielded case.

Figure 4 continues Figure 3 to much higher radii showing that the difference in bound state contribution continues, becoming negligible for the shielded case beyond the Debye shielding distance λ_D. The classical curve is almost identical to $g_{\text{q.m.}}(r)$ and so is not shown, and similarly $g_{\text{D.H.}}(r)$ remains so close to $g_s(r)$ that it also is not shown.

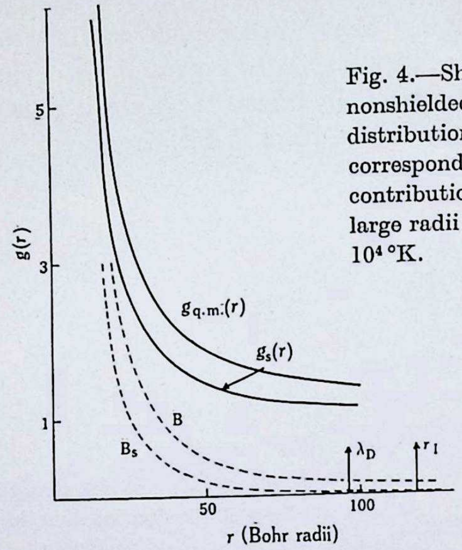

Fig. 4.—Shielded ($g_s(r)$) and nonshielded ($g_{\text{q.m.}}(r)$) distribution functions with the corresponding bound state contributions (B_s and B) for large radii at a temperature of 10^4 °K.

V. IONIZATION

Since the quantum mechanical calculation divides $g_{\text{q.m.}}(r)$ into bound and scattered state contributions, it is possible to obtain the percentage ionization present in the hydrogen gas. From the definition of percentage ionization I we have

$$I = \frac{\int_0^{r_I} g_{\text{scatt.}}(r)\,4\pi r^2\,\mathrm{d}\boldsymbol{r}}{\int_0^{r_I} g_{\text{q.m.}}(r)\,4\pi r^2\,\mathrm{d}r}, \tag{4}$$

where $g_{\text{scatt.}}(r)$ is the scattering contribution to $g_{\text{q.m.}}(r)$ and r_I is a radius chosen such that $3/4\pi r_I^3$ is the number density (i.e. $4\pi r_I^3/3$ is the volume that on the average contains one electron). Figure 4 shows that r_I is 117·2 Bohr radii for an electron number density of 10^{18} electrons/cm³, and is larger than the Debye shielding distance.

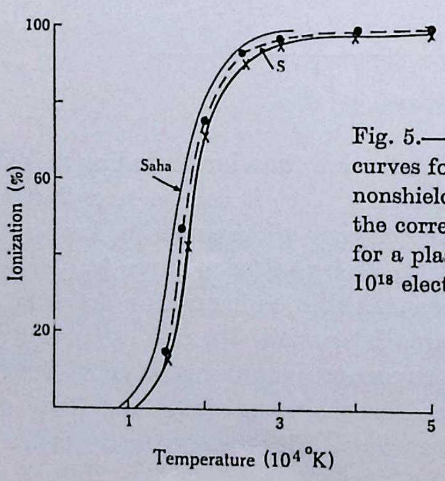

Fig. 5.—Percentage ionization curves for shielded (S) and nonshielded calculations with the corresponding Saha curve for a plasma of density 10^{18} electrons/cm³.

Figure 5 presents the results of calculations of I by equation (3) using both shielded and nonshielded distribution functions and compares them with Saha's theory (Saha and Saha 1934). The effect of shielding is to increase the ionization some 2 or 3%, which is to be expected, as the shielding precludes some of the bound states. The results agree quite closely with those of Saha, the main disagreement being just above $1\cdot5\times10^4$ °K, where the nonshielded ionization value is only half the Saha value and even the shielded value is 15% below. Also by Saha's theory, between $1\cdot5\times10^4$ and 2×10^4 °K, 48% of the ionization occurs, while the quantum mechanical calculation gives 59% without shielding and 60% with shielding. At $2\cdot5\times10^4$ °K the nonshielded theory implies that there are twice as many neutral particles as the number predicted by Saha's results.

VI. CONCLUSIONS

The results are of interest in showing that there are rather large deviations from classical theory at short interparticle distances and that below r_1 quantum mechanical effects become important, especially at low temperatures. An approximate allowance for shielding indicates that results are essentially the same for this case, the main difference being in the degree of ionization present. The existing theory in current use is one due to Saha and Saha (1934) and this takes account of the spectrum of bound states in only an approximate way, with no allowance for shielding effects. Nevertheless from the results it can be seen that, by fully taking account of the bound states and also by attempting to allow for shielding, the degree of ionization is surprisingly close to the values obtained by Saha. Also from the results it can be seen that there is some justification in the approach of considering the first bound state as the major contribution to the bound states, especially at temperatures below 3×10^4 °K with a density of 10^{18} electrons/cm^3.

VII. ACKNOWLEDGMENTS

This work has been carried out with the help of a generous grant from the Australian Institute of Nuclear Science and Engineering for computing. The author wishes to thank Dr. R. G. Storer for informing him of his similar results obtained by a path integral technique. The author is also indebted to Professor H. S. Green for many constructive discussions on the above material and to Dr. P. W. Seymour for helpful advice.

VIII. REFERENCES

ABRAMOWITZ, M., and STEGUN, I. A. (1964).—"Handbook of Mathematical Functions." Ch. 14. (National Bureau of Standards: Washington.)

BARKER, A. A. (1966).—*Phys. Fluids* **9**, 1590.

PAULING, L., and WILSON, E. B. (1935).—"Introduction to Quantum Mechanics." Ch. V. (McGraw-Hill: New York.)

SAHA, M. N., and SAHA, N. K. (1934).—"A Treatise in Modern Physics." p. 793. (The Indian Press: Calcutta.)

SCHIFF, L. I. (1955).—"Quantum Mechanics." Ch. V. (McGraw-Hill: New York.)

COMPRESSIONAL ALFVÉN WAVE PROPAGATION BELOW ION CYCLOTRON FREQUENCY

By R. C. CROSS* and J. A. LEHANE*

[*Manuscript received November 20, 1967*]

Summary

When the compressional wave cutoff frequency is below ion cyclotron frequency both compressional and torsional Alfvén waves may be present simultaneously. Compressional wave measurements in this regime are particularly important because of their relevance to certain ion cyclotron resonance heating experiments. This paper extends the work of others in this important regime.

The measurements deal mainly with the dispersion of the azimuthally symmetric wave and the radial variation of its magnetic field components. The observed radial variation agrees with that expected theoretically, as does the change in the relative amplitudes of the field components with frequency. The dispersion relation measurements, made in a decaying plasma, yield values of the plasma parameters that change with time after breakdown in a way consistent with spectroscopic observations. These measurements bring out the importance of ion–neutral coupling and yield a value of the ion–neutral momentum transfer cross section of $7 \cdot 5(\pm 2 \cdot 5) \times 10^{-15}$ cm^2, which is consistent with estimates made from torsional wave studies.

I. INTRODUCTION

The dispersion relation for hydromagnetic waves propagating parallel to a magnetic field in a cylindrical plasma has two branches, one corresponding to what is generally known as the torsional or slow wave and the other to the compressional or fast wave. The torsional wave, whose electric vector rotates in the same direction as the ions, propagates only for frequencies below the ion cyclotron frequency where there is a resonance. The compressional wave propagates for frequencies below the electron cyclotron frequency and has a wave-guide cutoff, the frequency of which is proportional to the Alfvén velocity and to the radial wave number. The cutoff may thus be either above or below the ion cyclotron frequency depending on the plasma parameters.

The case where the cutoff frequency is above the ion cyclotron frequency and the torsional wave is not propagating has been extensively studied by Kovan *et al.* (1961), Hooke *et al.* (1962), and Jephcott and Malein (1964).

When the cutoff frequency is below the ion cyclotron frequency both waves may be present; there has been considerable interest in this laboratory and elsewhere in the use of the torsional wave resonance at the ion cyclotron frequency for plasma

---

* School of Physics, University of Sydney, N.S.W. 2006.

Aust. J. Phys., 1968, **21**, 129–38

heating, where any energy fed into the compressional wave is lost unproductively in wave rather than particle energy. It has been necessary therefore to extend the work of Gould, Swanson, and Hertel (1964) and Malein (1965) in this important regime of compressional wave propagation.

II. THEORY

The theory of the propagation of magnetohydrodynamic waves in a uniform partly ionized plasma has been fully developed by a number of workers (e.g. Woods 1962; Brown 1965; Sodek and Willett 1967). In each of these treatments the equations of motion for ions, electrons, and neutral particles are obtained by linearizing the Boltzmann equation and then applying the conservation and Maxwell's equations to obtain the dispersion relation. Brown (1965) considers the propagation of azimuthally symmetric ($m = 0$) waves of angular frequency ω that are travelling in the z direction with a propagation constant p such that all wave variables vary as $\exp \mathrm{i}(pz-\omega t)$ and obtains the dispersion relation

$$ap^4+bp^2+c = 0\,, \tag{1}$$

where a, b, and c, are algebraic functions of the plasma parameters and are given in the Appendix to his paper. The real and imaginary parts of p are respectively the wave number k and the attenuation constant ϵ, that is,

$$p = k+\mathrm{i}\epsilon\,. \tag{2}$$

The attenuation constant ϵ is just the reciprocal of the attenuation length L.

The numerical evaluation of equation (1), which is quadratic in p^2, gives the velocity and attenuation length of both the torsional and compressional waves as a function of frequency. These depend on the axial magnetic field B_0, total particle density n, percentage ionization P, electron temperature T_{e}, and cross section for ion–neutral momentum transfer σ, as well as the radial wave number ν, which is determined by the boundary conditions.

The radial variations of the wave magnetic field components are also obtained. These are given by

$$b_\theta = A\,\mathrm{J}_1(\nu r)\,, \qquad b_r = B\,\mathrm{J}_1(\nu r)\,, \qquad b_z = C\,\mathrm{J}_0(\nu r)\,,$$

where J_0 and J_1 are Bessel functions of the first kind of order zero and one respectively. The amplitude constants A, B, and C depend on the frequency, the wave type, and the radial mode in addition to the plasma characteristics listed above. Their relative amplitudes are given by (see Spillman 1963)

$$C/B = \mathrm{i}\nu/p\,,$$

$$B/A = -\mathrm{i}\Omega U^2/\{\beta^2-(1-\alpha_\perp)(1+U^2)\}\,,$$

where $U = p/\nu$, $\beta = \omega/V_{\mathrm{A}}\nu$, $\Omega = (\rho_1/\rho_1)(\omega/\omega_{\mathrm{ci}})$ and $\alpha_\perp = \omega\eta_\perp/\mu_0 V_{\mathrm{A}}^2$. Here ω_{ci} is the ion cyclotron frequency, $\eta_\perp$ is the plasma resistivity perpendicular to the axial magnetic field B_0, and V_A is the Alfvén velocity given by $V_A = B_0/(\mu_0 \rho_1)^{\frac{1}{2}}$. In these expressions ρ_1 is a complex mass density, the modulus of which is the effective mass density determining the wave velocity. It is given by

$$\rho_1 = \rho_i + \rho_n(1+i\tau)/(1+\tau^2),$$

where the subscripts i and n refer to ions and neutral particles respectively and $\tau = \omega/\nu_{ni}$, ν_{ni} being the ion–neutral collision frequency. In the work to be described ν_{ni} is approximately 11 MHz and thus, at frequencies appreciably less than 1 MHz, ρ_1 is the total density (the sum of the ion and neutral mass densities) whereas, at frequencies comparable with 11 MHz, it is approximately the ion mass density.

III. EXPERIMENTAL METHOD

(a) *Plasma Source*

The measurements to be discussed were made in the Supper II machine, which is described in detail by Brennan *et al.* (1963). This machine consists basically of a stainless steel vessel 170 cm long and 21·5 cm in diameter which is immersed in an axial magnetic field that is variable up to 13 kG. One end of the machine is sealed with a quartz plate to which is attached a central molybdenum electrode of diameter 7·6 cm and length 7·6 cm. The other end is sealed with a Pyrex glass plate to which is attached on the inside an earthed stainless steel wire mesh. Hydrogen, purified by a palladium filter, is continuously circulated through the machine.

The plasma was prepared by the hybrid method discussed by Brown *et al.* (1967), whereby an initial ionizing front is followed by an axial discharge of peak current 45 kA decaying to zero in 200 μsec. Most of the measurements were made for the same conditions used by the above authors, namely a magnetic field of 7 kG and a filling pressure of 70 mtorr. These authors give the radial and axial distributions of both ion density and electron temperature in the decaying plasma. They find that these parameters have no axial variation but do have some variation with radius. Near the vessel wall there is a region of low ion density that extends radially inwards as the plasma decays, and for times up to 350 μsec there is also a region of low ion density at the centre of the plasma column. For comparison with the wave results to be presented here, average values of ion density and electron temperature were calculated from these distributions. As typical values, the average ion density and electron temperature 200 μsec after breakdown are $2 \cdot 4 \times 10^{15}$ cm^{-3} and 12 000°K respectively.

(b) *Wave Excitation and Detection*

Azimuthally symmetric waves were excited by discharging appropriate capacitors through a quartz-sheathed 11·6 cm diameter loop, which was placed in the plasma 30 cm from the plasma preparation end of the vessel with its axis along the vessel axis. The diameter was chosen to minimize the second radial mode. Frequencies used ranged from 2 to 8 MHz and the quality factor Q in the presence of the plasma ranged from 20 at 2 MHz to 10 at 8 MHz, the wave launched being thus essentially monochromatic.

The waves were detected via their perturbation magnetic fields by using small calibrated magnetic probes. These consisted of 30-turn coils wound on 0·2 cm diameter formers. The coils were centre-tapped, the signals from the two sides being subtracted using a differential amplifier to remove capacitive pickup. The probes were inserted into the plasma through re-entrant quartz tubes. The signals from the probes were transmitted via double-screened coaxial cable to oscilloscopes that were operated in a screened room.

The radial distributions of the field components were measured by a probe that could be moved along a diameter of the vessel. Two probes were used, one to measure either b_θ or b_z and the other to measure b_r. Measurements were made at a distance of 30 cm from the launcher. The field profiles were determined by making a series of six shots for each component at several radial positions and averaging.

The velocity and attenuation of the wave were determined using a probe that was moved longitudinally through the plasma. Measurements were made over a distance of 50 cm starting at the wave exciter. Six shots were taken every 5 cm. The wave component used in these measurements was the b_z component and it was detected on the vessel axis. This component and radial position were chosen to minimize interference from the torsional wave.

IV. RESULTS

The results fall into three groups. Measurements were made of (1) the cutoff frequency as a function of both magnetic field and original neutral particle density, (2) the wave magnetic field components as a function of radius for two different frequencies, and (3) the velocity and attenuation length as a function of frequency for several different times after breakdown.

Those in the first and second groups are important in showing that it is the compressional wave that is being studied and, to a good approximation, that it is only the $m = 0$ mode with the lowest radial wave number.

(a) *Variation of Cutoff Frequency*

The compressional wave cutoff frequency ω_c is given by the expression

$$\omega_c = \nu V_A ,$$

where ν is the radial wave number and V_A the Alfvén velocity. It thus depends on the plasma conditions and, providing all other parameters are held fixed, should be proportional to the magnetic field B_0 and inversely proportional to the square root of the particle density.

The cutoff frequencies for various conditions were measured using the method suggested by Gould, Swanson, and Hertel (1964). A pulse of width 0·3 μsec was launched by critically damping the wave excitation circuitry. This pulse contains a spectrum of frequencies and so a group of waves is excited. Of these, the high frequency waves have the largest group velocity and reach the magnetic probe first. The last frequency to appear is just above the cutoff frequency, which is hence determined. This method enables the cutoff frequency to be determined rapidly and in those cases where both measurements were made it was found that the frequency obtained by this method agreed well with that obtained from the complete dispersion relation.

The variation of cutoff frequency with (1) magnetic field for three different filling pressures and (2) filling pressure for two different magnetic fields are given in Figures 1 and 2 respectively. All the measurements were made 200 μsec after breakdown of the gas. As indicated by the straight lines that have been fitted to them, the

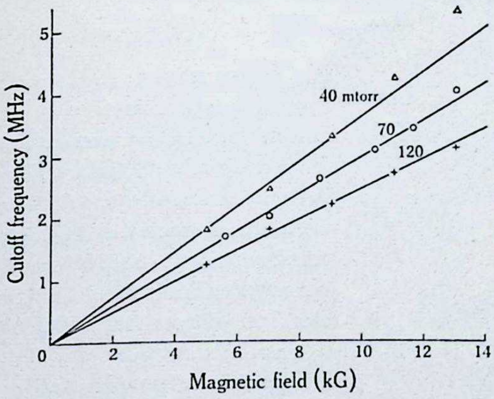

Fig. 1.—The $m = 0$ compressional wave cutoff frequency as a function of magnetic field for gas-filling pressures of 40, 70, and 120 mtorr.

results in Figure 1 show in general that the cutoff frequency varies with magnetic field in the expected way. There is, however, some tendency for the cutoff frequency to increase more rapidly than expected, particularly at low pressures. This is probably due to an increased radial wave number arising from the more peaked radial density distribution that occurs at high magnetic fields. The effect, however, is also to be expected since decoupling of the neutral particles from the ions is taking place.

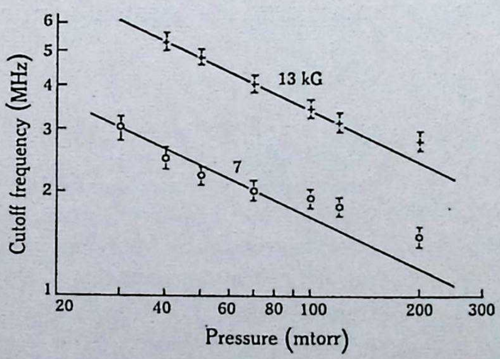

Fig. 2.—The $m = 0$ compressional wave cutoff frequency as a function of gas-filling pressure for magnetic fields of 7 and 13 kG.

The results in Figure 1 also indicate that the cutoff frequency decreases with increasing pressure. A comparison of the slopes of the fitted lines shows, however, that the variation is not as the inverse of the square root of the pressure. This is shown further by the results presented in Figure 2. The implication is that the percentage ionization decreases as the neutral pressure increases, an effect independently observed by Millar and Watson-Munro (1965) of this laboratory.

Finally it should be noted that the absolute values of the cutoff frequencies imply that the densities determining the Alfvén velocities are significantly less than the original filling densities down to the lowest pressures used. Impurities are thus not important in determining the wave propagation.

(b) *Radial Variation of Wave Magnetic Field Components*

To check that basically only one azimuthal mode (the $m = 0$ mode) is being propagated and that radial modes other than the first are insignificant, it is important to make measurements of the radial variation of the wave field components. Such measurements were made at 2·8 and 6·1 MHz using a field of 7 kG and a filling pressure of 70 mtorr, for a time after gas breakdown of 200 μsec. For such conditions the cutoff frequency is 2 MHz. The radial variation at 2·8 MHz is presented in Figure 3 for the three components b_r, b_θ, and b_z. The theoretical curves given are for the $m = 0$ mode with the lowest radial wave number and for plasma parameters determined from the 200 μsec dispersion results, as discussed in the next section. The fit was made by normalizing to the b_z component and retaining the relative amplitudes. The agreement is quite good.

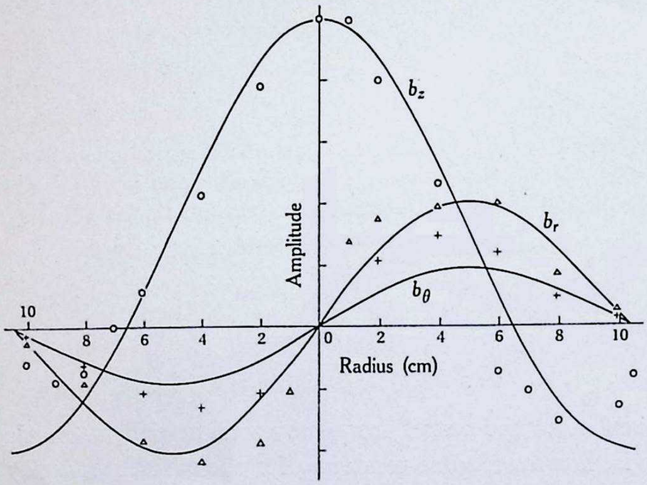

Fig. 3.—Radial variation of the $m = 0$ compressional wave magnetic field components at a frequency of 2·8 MHz. The theoretical curves are for a plasma with axial magnetic field 7 kG, total density $1 \cdot 8 \times 10^{15}$ cm^{-3}, percentage ionization 71%, and electron temperature 10 500°K. For such conditions the compressional wave cutoff frequency is about 2 MHz.

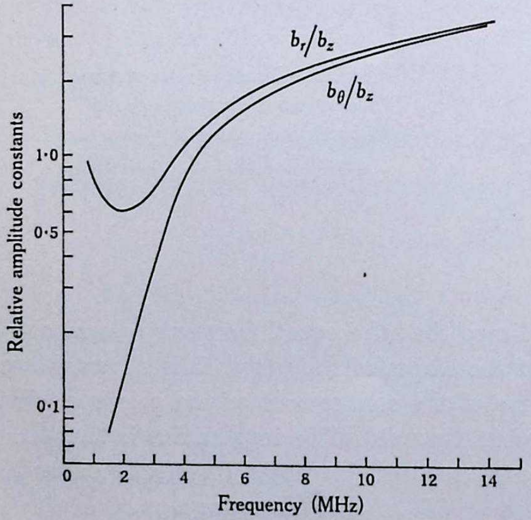

Fig. 4.—Theoretical relative amplitudes of the $m = 0$ compressional wave magnetic field components as a function of frequency for the following values of the relevant parameters: total particle density $1 \cdot 7 \times 10^{15}$ cm^{-3}, percentage ionization 70%, electron temperature 10 000°K, axial magnetic field 7 kG, radial wave number 0·365 cm^{-1}, ion–neutral momentum transfer cross section 5×10^{-15} cm^2. For such conditions the cutoff frequency is about 2 MHz.

As indicated in Section II, an interesting feature of the wave field components is that the relative amplitudes of the components should change with frequency. This is shown in Figure 4, where the theoretical ratios b_r/b_z and b_θ/b_z are plotted as a function of frequency, 200 μsec after breakdown, for the plasma produced at 7 kG with a filling pressure of 70 mtorr. In Table 1 the maximum values of the three components at 6·1 MHz together with those at 2·8 MHz obtained from Figure 3 are compared with the theoretical values obtained from Figure 4. The amplitudes are given relative to the b_z component.

It is clear that the relative amplitudes change in the expected way. For the b_r and b_z components there is good numerical agreement between the observed and calculated relative amplitudes. The disagreement for the b_θ component is due to interference from the azimuthal magnetic field of the torsional wave, which was observed to be propagating with small amplitude, by making measurements of b_θ below cutoff frequency.

TABLE 1

COMPARISON BETWEEN EXPERIMENTAL AND THEORETICAL VALUES OF WAVE MAGNETIC FIELD COMPONENTS AT TWO FREQUENCIES

Wave Field Component	2·8 MHz Experimental Value	2·8 MHz Theoretical Value	6·1 MHz Experimental Value	6·1 MHz Theoretical Value
b_z	1·00	1·00	1·00	1·00
b_r	0·42	0·41	1·02	1·05
b_θ	0·30	0·19	0·64	1·04

(c) *Wave Velocity and Attenuation*

The velocity and attenuation length of the wave were determined as a function of frequency for a field of 7 kG and a filling pressure of 70 mtorr for four different times after breakdown (200, 250, 300, and 350 μsec). The results are given in Figure 5 together with theoretical curves that have been fitted to them. For each time the velocity and attenuation results were simultaneously fitted. In making the fit the magnetic field was taken as known but all the other parameters (total density, percentage ionization, electron temperature, ion–neutral momentum transfer cross section, and radial wave number) were taken as variables, although ν was not allowed to be less than the value $0\cdot365\ \mathrm{cm}^{-1}$, which is expected for a plasma of diameter 21·5 cm bounded by a conducting wall. The amount of information contained in the velocity and attenuation results is such that all of the parameters are well determined by the fitting process. The curves giving velocity and attenuation length as a function of frequency depend quite differently on the different parameters, as shown in Figure 6. It will be noted for example, that, whereas the total particle density n affects both the cutoff frequency and the value of velocity at the higher frequencies, the percentage ionization P has an appreciable effect only on the latter. The values of the parameters obtained by the fitting process are given in Table 2. The curves shown in Figure 5 correspond to these best-fit values.

The results in Table 2 show well the changes that take place in the plasma as it decays. Whereas the total density remains approximately constant, the temperature and ion density decrease and do so at a rate that is consistent with a three-body recombination model. Further, the radial wave number increases as the plasma decays. This is in accord with spectroscopic and framing camera observations, which show that the radius of the plasma column decreases as the plasma decays.

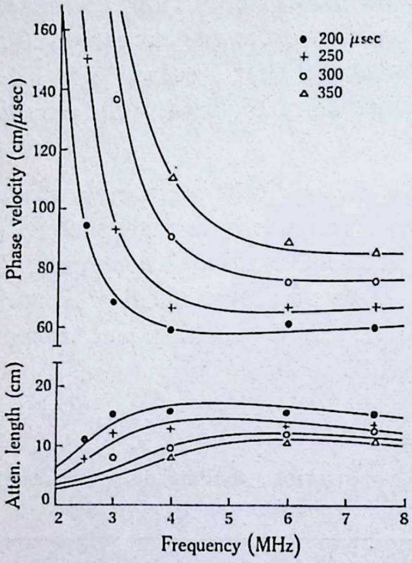

Fig. 5.—Velocity and attenuation length of the $m = 0$ compressional wave as a function of frequency for four different times after plasma preparation. The curves shown are the best-fit theoretical curves.

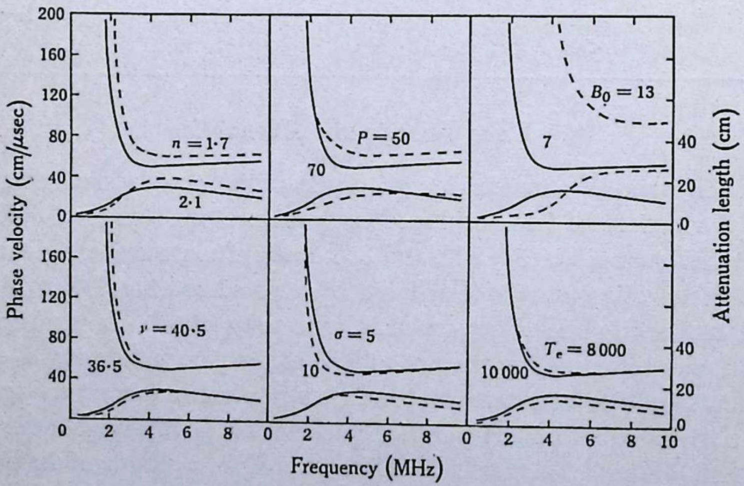

Fig. 6.—Dependence of the velocity versus frequency and attenuation length versus frequency curves on the various plasma parameters. The solid curves are for plasma parameter values of total particle density $n = 2{\cdot}1 \times 10^{15}$ cm^{-3}, percentage ionization $P = 70\%$, magnetic field $B_0 = 7$ kG, radial wave number $\nu = 0{\cdot}365$ cm^{-1}, ion–neutral momentum transfer cross section $\sigma = 5{\cdot}0 \times 10^{-15}$ cm^2, and electron temperature $T_e = 10^4$ °K. The dashed curves show, in turn, the effect of changing each of these parameters to the new values indicated on the figures.

It is of interest to compare the values of the various parameters deduced here with the corresponding values deduced from spectroscopic observations. As discussed in Section III, average values of ion density and temperature were determined from the distributions given by Brown *et al.* (1967). These are given in Table 3.

Comparison of the values given in Tables 2 and 3 shows that there is good agreement at all times between the spectroscopically and wave determined temperatures. There is, however, disagreement between the two estimates of ion density, though the relative values agree well. This discrepancy is due in part to the difficulty of obtaining reliable averages from the spectroscopically determined distributions. These have to be extrapolated to the wall and there is hence significant error since the ion densities are weighted proportionately to their distances from the centre.

The dispersion results are of further interest as they show that a considerable change in ion–neutral coupling is taking place over the frequency range used. Figure 5 shows that at the highest frequencies used the velocity increases as the time after breakdown increases. Since the total particle density is expected to remain constant with time, this change must be associated with a decrease in ion density and hence in percentage ionization (see Fig. 6). It is thus apparent that at these frequencies the velocity is determined essentially by the ion density. Indeed the theoretical calculations show, for example, that for a time of 200 μsec after breakdown the effective number density determining the wave propagation (the absolute value of ρ_1 divided by the ion mass) is $1 \cdot 28 \times 10^{15}$ cm^{-3} at $7 \cdot 5$ MHz, which is approximately equal to the ion density $1 \cdot 25 \times 10^{15}$ cm^{-3}. At the cutoff frequency (2 MHz), however, this effective number density is $1 \cdot 60 \times 10^{15}$ cm^{-3}, which is closer to the total particle number density $1 \cdot 80 \times 10^{15}$ cm^{-3}.

TABLE 2

VALUES OF PLASMA PARAMETERS DEDUCED FROM COMPRESSIONAL WAVE STUDIES

Time (μsec)	n (10^{15} cm^{-3})	P (%)	T (°K)	ν (cm^{-1})	σ (10^{-15} cm^2)	Ion Density (10^{15} cm^{-3})
200	$1 \cdot 8 \pm 0 \cdot 1$	71 ± 5	$10\,500 \pm 1500$	$0 \cdot 365 \pm 0 \cdot 01$	$7 \cdot 5 \pm 2 \cdot 5$	$1 \cdot 25 \pm 0 \cdot 1$
250	$1 \cdot 6 \pm 0 \cdot 1$	68 ± 5	$7\,000 \pm 1000$	$0 \cdot 375 \pm 0 \cdot 01$		$1 \cdot 1 \pm 0 \cdot 1$
300	$1 \cdot 6 \pm 0 \cdot 1$	55 ± 5	$6\,000 \pm 1000$	$0 \cdot 395 \pm 0 \cdot 01$		$0 \cdot 8 \pm 0 \cdot 1$
350	$1 \cdot 6 \pm 0 \cdot 1$	45 ± 5	$4\,500 \pm 500$	$0 \cdot 395 \pm 0 \cdot 01$		$0 \cdot 7 \pm 0 \cdot 1$

TABLE 3

VALUES OF PLASMA PARAMETERS DEDUCED FROM SPECTROSCOPIC OBSERVATIONS

Time (μsec)	Average Ion Density (10^{15} cm^{-3})	Average Electron Temperature (°K)
200	2·4	12 000
250	1·9	7 500
300	1·5	6 000
350	1·2	4 500

V. Conclusions

Measurements dealing with the azimuthally symmetric compressional wave have been presented. These deal in the main with the dispersion of the wave and the radial variation of the wave magnetic field components. The observed radial variation agrees quite well with that expected theoretically, as does the change in the relative amplitudes of the field components with frequency.

The dispersion relation measurements, made at various times in a decaying plasma, result in estimates of the plasma parameters at these times. They have the expected trend in that the total density stays approximately constant whereas the ion density and electron temperature decrease with time after breakdown. Though there is some disagreement in absolute values, the relative changes with time of the parameters are in agreement with those determined spectroscopically. Some evidence for the contraction of the plasma as it decays is also given.

The dispersion relation measurements are also of importance in that they clearly show the effect of ion–neutral coupling on the wave propagation. The value of the ion–neutral momentum transfer cross section that is obtained ($7 \cdot 5 \pm 2 \cdot 5 \times 10^{-15}$ cm^2) is the same as the value determined by Brown (1965) from torsional wave studies.

VI. Acknowledgments

The authors are grateful to the Australian Institute of Nuclear Science and Engineering, the Australian Research Grants Committee, and the University of Sydney Research Committee for financial support, and to Professor H. Messel for provision of facilities in the School of Physics. Thanks are due to Mr. N. Lowe for maintaining the apparatus and for his assistance in taking the measurements.

VII. References

Brennan, M. H., Lehane, J. A., Millar, D. D., and Watson-Munro, C. N. (1963).—*Aust. J. Phys.* **16**, 340.

Brown, I. G. (1965).—*Aust. J. Phys.* **18**, 437.

Brown, I. G., Lehane, J. A., Potter, I. C., and Watson-Munro, C. N. (1967).—*Aust. J. Phys.* **20**, 47.

Gould, R. W., Swanson, D. G., and Hertel, R. H. (1964).—*Phys. Fluids* **7**, 269.

Hooke, W. M., Rothman, M. A., Avivi, P., and Adam, J. (1962).—*Phys. Fluids* **5**, 864.

Jephcott, D. F., and Malein, A. (1964).—*Proc. R. Soc.* A **278**, 243.

Kovan, I. A., Patrushev, B. I., Rusanov, V. D., Smirnov, V. P., and Frank-Kamenetsky, D. A. (1961).—I.A.E.A. Conf. Plasma Physics and Controlled Nuclear Fusion Research, Salzburg. Paper 205.

Malein, A. (1965).—*Nucl. Fusion* **5**, 352.

Millar, D. D., and Watson-Munro, C. N. (1965).—Proc. 7th Int. Conf. on Ionised Gases. Paper 47.

Sodek, B. A., Jr., and Willett, J. E. (1967).—*Plasma Phys.* **9**, 113.

Spillman, G. R. (1963).—Univ. California Lawrence Radiation Lab. Rep. No. UCRL-10990.

Woods, L. C. (1962).—*J. Fluid Mech.* **13**, 570.

ASTROPHYSICAL CONSEQUENCES OF THE EXISTENCE OF CHARGED INTERMEDIATE VECTOR BOSONS

By J. A. Campbell*

[*Manuscript received November* 16, 1967]

Summary

Two-photon annihilation into a neutrino–antineutrino pair, which is forbidden to the lowest order in the coupling constant for weak interactions if the conventional form of weak interaction is assumed, is permitted at that order if it is supposed that the reaction is carried by a charged intermediate vector boson (W). The rate of loss of energy in stellar evolution through this process is calculated. Evolutionary time scales derived with and without this rate are compared with results from astronomical observations. Comparisons with present data are inconclusive, but further observations and calculations that may give more accurate information concerning the question of the existence of charged W mesons are suggested.

I. Introduction

The present status of weak interactions in elementary particle physics differs from that of the strong and electromagnetic interactions, in that experimental results for weak processes involving four fermions can still be treated adequately by a theory in which the four particles are assumed to interact strictly locally, at one point. By contrast, the simplest pictures of electromagnetic and strong interactions require the exchange of one photon and one pion respectively between the interacting particles. Each of these processes is therefore nonlocal, having a scale of range equal to the Compton wavelength of the exchanged particle. As a means of bringing weak-interaction theory into line with theories for the stronger interactions, Lee and Yang (1960*a*) have proposed the existence of a particle, the W meson or intermediate boson, which can be exchanged between weakly interacting particles. To account for the weak interactions that have been observed, it is necessary to postulate only two states of charge, W^+ and W^-, and to suppose that this intermediate boson is a vector particle, having a spin of 1. Varieties of neutral W mesons have been suggested (Lee and Yang 1960*b*; Marshak 1966) on additional theoretical grounds, but in the present paper only the implications of the original proposal are considered.

Since the range of an interaction is inversely proportional, through the Compton wavelength, to the mass of the exchanged particle, a strictly local interaction is one in which a particle of infinite mass is "exchanged". Therefore any theoretical description of a weak process involving W mesons must reproduce exactly the results of the point-interaction theory in the limit that the mass of the W meson tends

---

* School of Physical Sciences, Flinders University of South Australia, Bedford Park, S.A. 5042.

Aust. J. Phys., 1968, **21**, 139–48

to infinity. This requirement provides a condition of consistency on the nonlocal theory, and in practice it relates the square of the coupling constant of W mesons with other weakly interacting particles to the known coupling constant for beta decay.

Laboratory experiments that seek to observe W production by proton beams explore progressively shorter ranges of interaction as the proton energy increases. If the W meson is not observed when the experiment measures a given transfer of four-momentum, a lower limit for the W mass can therefore be set. It has been reported, by means of an argument of this type, that the mass must be greater than 2 GeV (Burns *et al.* 1965) and that it is unlikely that a W meson with mass between 2 and 3 GeV exists (Lamb *et al.* 1965). Recently Glashow, Schnitzer, and Weinberg (1967) have found that certain amplitudes for the decays of K mesons, which are divergent if the local weak interaction is used, become convergent if a W meson is assumed to take part in the decays. The convergent theoretical calculation contains the W mass as a free parameter. From a comparison with the experimentally determined rate of decay of the state K_1^0, they conclude that the mass is approximately 8 GeV. This value is exceptionally large by the standards of the elementary particles that have been detected in past experiments.

Without positive evidence of the W meson (which is of crucial interest for the structure of weak interaction theory) from the laboratory, one may still turn to astrophysics to see what effects the existence of the particle implies in stellar evolution and to compare these effects with what is observed astronomically. Moreover, since the numerical limits quoted above are appreciably higher than the mass of the heaviest meson detected to date, any astrophysical test that can in principle distinguish merely between the existence and non-existence of the W meson (and not make stronger statements about limits in mass) is welcome. In Section II are listed several neutrino-producing reactions that are the most efficient mechanisms for loss of energy from stars at central temperatures above about 5×10^8 °K. One of these reactions, neutrino–antineutrino production by the annihilation of pairs of photons, depends critically on the existence of the W meson. Quantitative estimates of the effect of that reaction in stars are made in Section III, and are compared with the consequences of the other neutrino processes in Section IV.

II. ASTROPHYSICAL NEUTRINO PROCESSES AND W MESONS

The present theoretical description of weak interactions is based in effect on the current–current hypothesis of interaction put forward by Feynman and Gell-Mann (1958). In this theory, a vertex of interaction is predicted at which an electron and a positron can annihilate to give an electron neutrino and an electron antineutrino. That interaction has not yet been seen in the laboratory, but Chin, Chiu, and Stothers (1966) conclude from astrophysical evidence that the vertex actually occurs, and that its coupling constant is probably about the same as the coupling constant for other observed vertices permitted by the theory of Feynman and Gell-Mann. That value for the coupling constant is assumed in equation (4) below.

Existence of the $(e\nu_e)(e\nu_e)$ local interaction allows three astrophysically important reactions involving neutrinos to take place: the pair-annihilation process,

$$e^+ + e^- \rightarrow \nu_e + \bar{\nu}_e\,, \tag{1}$$

the photoneutrino process,

$$\gamma + e^- \rightarrow \nu_e + \bar{\nu}_e + e^-\,, \tag{2}$$

and the plasma process,

$$\gamma \rightarrow e^+ + e^- \rightarrow \nu_e + \bar{\nu}_e\,. \tag{3}$$

The process (3) is forbidden by gauge invariance for a free photon, but is permitted in the degenerate electron gas that occurs in the core of a star at some stages of stellar evolution. There, the symmetrical disposition of filled and unfilled electron states about an energy of zero in the basic Dirac theory is removed by the filling of all states between an energy of $+mc^2$ (where m is the mass of the electron and c the velocity of light) and a Fermi energy E_F. Photons propagating through the electron gas are not free photons and the process (3) takes place.

Chiu (1966) has summarized the expected rates of loss of energy in stars for each of the three processes listed above. Generally, the summary shows that the plasma process is the most important mechanism for loss of energy in degenerate material, while in nondegenerate matter the photoneutrino process is most important below about 7×10^8 °K and pair annihilation is the dominant process above that temperature.

If the coupling constant for interactions of W mesons with leptons is f, the condition of consistency (mentioned in Section I) on the weak interaction in the limit of a strictly local four-fermion process implies (Lee and Wu 1965) that:

$$f^2/W^2 = G/\sqrt{2}\,, \tag{4}$$

where W is the mass of the W meson and G is the coupling constant for beta decay. A practical consequence of equation (4) is that, if the cross section σ_W for a weak four-fermion reaction mediated by a W meson and the cross section σ_0 for the corresponding local reaction are calculated separately, they can be related by the equation

$$\sigma_W \approx \sigma_0(1 + 2q^2/W^2)\,, \tag{5}$$

where q is the four-momentum transferred in the process and terms containing higher powers of q^2/W^2 have been neglected. Since an energy of 1 MeV is associated with a temperature of $1 \cdot 16 \times 10^{10}$ °K (temperatures reached in stars during ordinary stellar evolution scarcely attain this value) and the experimental lower limit quoted for W in Section I is 2 GeV, it is not possible to measure any significant astrophysical differences between σ_W and σ_0 for the processes (1), (2), and (3).

However, there is a fourth process,

$$\gamma + \gamma \rightarrow \nu + \bar{\nu}\,, \tag{6}$$

which is not subject to the limitations of equation (5). Both σ_W and σ_0 for the process of two-photon annihilation can be calculated by an application of the conventional rules that relate Feynman diagrams to matrix elements, but Gell-Mann (1961) has shown separately, in the lowest order of G, that reaction (6) cannot proceed through a local interaction. His argument uses invariance under charge conjugation, the inability of a pseudovector particle to decay into two photons, and the fact that $\gamma . p\, v(p)$ and $\bar{v}(p)\, \gamma . p$ are zero from the Dirac equation, where $v(p)$ is an antineutrino spinor and γ represents a Dirac matrix. Nevertheless, as Gell-Mann himself has pointed out, this argument does not hold if the reaction is mediated by a W meson, as in the Feynman diagram in Figure 1. Therefore the presence or absence of the process (6) in stellar evolution depends on the existence of charged W mesons. The question of their existence may be examined by comparisons of predictions about stellar evolution with and without (6) to actual astronomical observations.

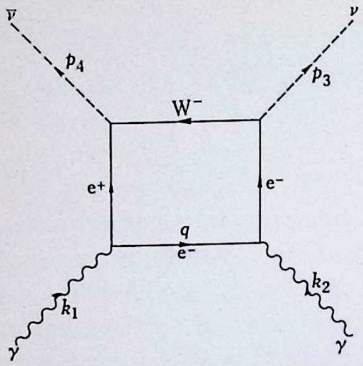

Fig. 1.—Feynman diagram for the process of two-photon annihilation, with the inclusion of a virtual charged W meson.

III. Quantitative Results for the Two-photon Reaction

For the reaction illustrated by the Feynman diagram in Figure 1, the matrix element is

$$\frac{\mathrm{i}}{(2\pi)^6}\frac{e^2 f^2}{(16E_1 E_2 E_3 E_4)^{\frac{1}{2}}}\,\delta(p_3+p_4-k_1-k_2)$$

$$\times\int \mathrm{d}^4 q\, \bar{v}(p_4)\, \gamma_\mu(1+\gamma_5)\frac{\gamma . (k_1-q)+m}{q^2-2k_1 . q-m^2}\,\gamma . e_1\frac{\gamma . q+m}{q^2-m^2}\,\gamma . e_2\frac{\gamma . (k_2+q)+m}{q^2+2k_2 . q-m^2}$$

$$\times\gamma_\nu(1+\gamma_5)\, v(p_3)\,\frac{\delta_{\mu\nu}-W^{-2}(q+k_2-p_3)_\mu\,(q+k_2-p_3)_\nu}{q^2+2(k_2-p_3) . q-W^2}. \tag{7}$$

In (7), which results from a straightforward application of Feynman's rules, e_1 and e_2 are polarization four-vectors for the photons, δ is the four-dimensional Dirac delta function, and natural units with $\hbar = c = 1$ are used. Diagrams with γWW vertices are ignored because of the extra factors of W^{-2} that they contribute to (7). For the parts of (7) in which five factors of q occur in the numerator of the integrand, the integral over q is zero because a function that is odd about $q = 0$ is involved. In each of the five possible combinations of four factors of q, the integral is logarithmically divergent and may be expressed in terms of a cutoff Λ with the dimension of a mass. The introduction of a cutoff is somewhat artificial, but it is usually justified by the statement that Λc^2 is the highest energy for which the theory is valid. In this example, uncertainties introduced into the calculation by the different possible numerical choices of Λ are not important on an astrophysical scale.

The dominant terms in the cross section derived from (7) contain the logarithmic dependence on Λ. If only these terms are retained, scalar products of q with four-momenta for external lines of Figure 1 are neglected in the denominator of (7) (because they are considerably smaller than W^2 for small q, and smaller than q^2 for large q), and factors of $\hbar$ and c are re-introduced, the cross section σ for the process is given by

$$\sigma \approx \frac{811G^2M^4}{262\,144}\frac{\alpha^2}{\pi^5}\left(\frac{11}{6}+\log\frac{\Lambda^2}{W^2}\right)^2\left(\frac{\hbar}{mc}\right)^2\left(\frac{m}{M}\right)^4\frac{E_1E_2}{(mc^2)^2} \qquad \mathrm{cm}^2, \tag{8}$$

where α is the fine-structure constant and M is the mass of the proton. To obtain equation (8), sums over final-state quantities and averages over all initial-state quantities except the photon energies E_1 and E_2 have been performed. Further, the coupling constant f has been replaced in terms of G from equation (4). The derivation of equation (8) has been carried out by computer programmes (Hearn 1966; Campbell 1967) designed for such an application, and checked by hand.

The cross section in equation (8) is an integral of a differential cross section with respect to the momenta $\mathbf{p}_3$ and $\mathbf{p}_4$. The energy lost per event of the type (6) can be calculated if the differential cross section is multiplied by (E_3+E_4) prior to the integration. Then, if this energy loss is represented by $E(\mathbf{p}_1, \mathbf{p}_2)$, the total rate of loss of energy through (6) in a star is given by the integral of $E(\mathbf{p}_1, \mathbf{p}_2)$ with respect to the differentials of the number densities of the particles with momenta $\mathbf{p}_1$ and $\mathbf{p}_2$. In general, it is possible to write (Chiu and Stabler 1961)

$$-\rho\,\mathrm{d}E/\mathrm{d}t = \int |\mathbf{v}|\,E(\mathbf{p}_1,\mathbf{p}_2)\,\mathrm{d}n(\mathbf{p}_1)\,\mathrm{d}n(\mathbf{p}_2)\,, \tag{9}$$

where $\mathbf{v}$ is the relative velocity of particles 1 and 2 and ρ is the density of material in which the reaction takes place. Because both particles are photons, $|\mathbf{v}| = c$ and the number densities refer to particles that obey Bose–Einstein statistics. For dimensional consistency in equation (9), $\mathrm{d}n$ must have the dimension of a number per unit volume. The correct substitution for inclusion in equation (9) is therefore

$$\mathrm{d}n(\mathbf{p}) = \mathrm{d}n(E) = \{\pi^2(\hbar c)^3\}^{-1}\{\mathrm{e}^{E/kT}-1\}^{-1}E^2\,\mathrm{d}E\,. \tag{10}$$

The neutrinos in Figure 1 and the process (6) may equally well be muon neutrinos as electron neutrinos, provided that the electron and positron lines in Figure 1 are replaced by negative and positive muon lines in the first case. In this respect, the process (6) is unlike the reactions (1), (2), and (3), which involve only electrons and positrons, because stellar temperatures below about $1{\cdot}2\times10^{12}$ °K are insufficient for the production of appreciable concentrations of muons. Muons may still make virtual contributions to (6) at lower temperatures by their presence as internal lines in Figure 1. Admittedly electrons and positrons occur only as internal lines in the Feynman diagram for the plasma process (3), but these virtual particles accompanying photon propagation come from the degenerate electron gas that supports it. There is no corresponding "muon gas". Therefore, in the evaluation of equation (9), $E(\mathbf{p}_1, \mathbf{p}_2)$ should include contributions from both the processes

$$\gamma+\gamma \rightarrow \nu_\mathrm{e}+\bar{\nu}_\mathrm{e} \qquad \text{and} \qquad \gamma+\gamma \rightarrow \nu_\mu+\bar{\nu}_\mu.$$

Both contributions are covered adequately if the differential cross section that leads to equation (8) is multiplied by a factor of two.

The expression for the rate of loss of energy when equation (10) is substituted into equation (9) is then

$$-\frac{\mathrm{d}E}{\mathrm{d}t}=\frac{811}{131\,072}\left(\frac{kT}{\pi c}\right)^{9}\frac{G^{2}\alpha^{2}}{\hbar^{4}\rho}\left(\frac{11}{6}+\log\frac{\Lambda^{2}}{W^{2}}\right)^{2}\int_{0}^{\infty}\mathrm{d}x\int_{0}^{\infty}\mathrm{d}y\,\frac{(x+y)x^{3}y^{3}}{(\mathrm{e}^{x}-1)(\mathrm{e}^{y}-1)}$$

$$=\frac{811}{40\,960}\left(\frac{kT}{c}\right)^{9}\frac{G^{2}\alpha^{2}}{\pi^{5}\hbar^{4}\rho}\left(\frac{11}{6}+\log\frac{\Lambda^{2}}{W^{2}}\right)^{2}\zeta(5)\qquad \mathrm{ergs\,g^{-1}\,sec^{-1}}, \qquad (11)$$

where k is Boltzmann's constant and ζ is the Riemann zeta function. If it is supposed that $\Lambda \approx 50W$ in equation (11), the rate of loss in terms of the two variables ρ and T_9 ($= T/10^9$) is

$$-\mathrm{d}E/\mathrm{d}t \approx 2\cdot 5\times 10^{9}\,T_{9}^{9}/\rho \qquad \mathrm{ergs\,g^{-1}\,sec^{-1}}. \qquad (12)$$

This rate is independent of both the degeneracy of the material in which it occurs and any approximations concerning nonrelativistic or extreme-relativistic kinematics. Moreover, it agrees with the rate calculated approximately by Boccaletti, de Sabbata, and Gualdi (1964) for annihilation of pairs of optical photons.

Chiu and Morrison (1960) have estimated losses of energy in the additional astrophysical process $\gamma+\gamma \rightarrow \gamma+\nu+\bar{\nu}$. If the subscript B is used for this reaction and A for the process (6), an order-of-magnitude calculation based on equations (8) and (11) and Feynman diagrams suggests that

$$\left(-\frac{\mathrm{d}E}{\mathrm{d}t}\right)_{\mathrm{B}} < \frac{2\pi\alpha(4a+1)^{2}}{9a^{2}}\left(-\frac{\mathrm{d}E}{\mathrm{d}t}\right)_{\mathrm{A}}, \qquad (13)$$

where

$$a = 11/6+\log(\Lambda^{2}/W^{2}).$$

The inequality (13) implies an insignificant rate of loss of energy for the reaction B, which is not examined further. The results of the examination of a three-photon astrophysical process by de Graaf and Tolhoek (1966) also satisfy the inequality.

IV. DISCUSSION

Rates of loss of energy for the processes (1), (2), and (3) have been presented collectively, in forms suitable for comparison with equation (12), by Chiu and Stabler (1961), Zaidi (1965), and Chiu (1966). Provided that charged W mesons exist, examination of these results shows that, as a medium of loss of energy in stars, the process of two-photon annihilation is competitive with:

(i) The plasma process, when the quantity $\hbar\omega_{\mathrm{p}}/kT$ (where ω_{p} is the plasma frequency) is either less than 0·01 or greater than 50. The first case corresponds to an extremely high temperature, and the second to an extremely high degree of degeneracy. Although either of these conditions may be realised in an exceptional situation such as the gravitational collapse of a star, it is unlikely that they can be the subjects of widespread observation.

(ii) All photoneutrino processes except those taking place in degenerate matter at nonrelativistic energies.

(iii) Pair annihilation in degenerate matter, provided either that the energies involved are nonrelativistic or that $T_9 \geqslant 3$. The definition of degeneracy used in this example is that the Fermi energy E_F should be greater than about $5mc^2$.

Chiu (1966) and Chin, Chiu, and Stothers (1966) have considered altogether six situations in astrophysics in which neutrino production may have a significant influence. Of these, the behaviour of intergalactic neutrinos is not notably affected by the reaction (6) because of low temperature, and the evolution of degenerate white dwarf stars and semidegenerate "ultraviolet" dwarf stars is believed to depend only on details of the plasma process. Two-photon annihilation may be expected to have an important place in models describing supernovae or gravitational collapse, but in these cases there is no chance that astronomers can make a sufficient number of observations to provide indirect evidence of the existence of charged W mesons.

In the two remaining examples, counts of numbers N of stars in different regions of colour–magnitude diagrams are used to determine characteristic evolutionary time scales for the different regions, according to relations of the form

$$\tau_A/\tau_B = N_A/N_B \tag{14}$$

Overall normalization of times is provided by relevant models that describe stellar evolution. The time scale for any one region is connected with the output of energy from a star by the relation

$$\tau \propto \int \left(\sum_i L_i(T) \right)^{-1} \mathrm{d}T\,, \tag{15}$$

where each $L_i(T)$ is the luminosity contributed by one mechanism for loss of energy which assists the evolution of the star through that region. Luminosity is given in terms of the rate of loss of energy per unit volume by

$$\mathrm{d}L_i/\mathrm{d}r = 4\pi r^2(-\mathrm{d}E/\mathrm{d}t)_i\,. \tag{16}$$

The rate on the right-hand side of equation (16) is a function of r to the extent that stellar models usually divide a star into a core and a small number of outer shells, the material in each section having a different temperature, density, and chemical composition. The integral over r in equation (15) can thus be written as a sum of integrals over different ranges of r, $\mathrm{d}E/\mathrm{d}t$ being constant within each range.

Central stars of planetary nebulae occupy a well-defined region on a colour–magnitude diagram. Calculations (Seaton 1966) based on observations by O'Dell (1963) indicate that the time scale for their contraction to the limiting or Chandrasekhar radius lies between 3×10^4 and 5×10^4 years. Hayashi, Hōshi, and Sugimoto (1962) have calculated that model central stars of 0·6 and 0·4 solar masses go through the contraction in 10^6 years if neutrino processes are not taken into account. From other model calculations, Chin, Chiu, and Stothers (1966) find that this time is reduced to about 10^4 years if the effect of the photoneutrino process is included.

An approximate analysis based on equations (15) and (16) suggests that their estimate is not reduced by more than 5% for central stars with masses less than one solar mass, but that the difference may be increased in heavier stars. It is therefore desirable to have much more astronomical information on the heavier central stars of planetary nebulae to clarify this point.

The most promising situation for discussion concerns the evolution of stars through the stages of helium and carbon burning in their cores after they have left the main sequence on a colour–magnitude diagram. It should be possible to make observations on many more stars in this situation than in any other of the cases mentioned above. With the help of a model for the evolution of stars of 15·6 solar masses, Hayashi and Cameron (1962) have analysed a diagram prepared from observations by Johnson and Morgan (1955) on the star clusters h and χ Persei. Time scales for evolution through various regions of the diagram are computed from the model and compared with "experimental" times obtained from equation (14). The scales disagree only for the region occupied by stars at the stage of carbon burning in their cores. With limited data, the measured time for this stage is between 7×10^5 and 10^6 years, while the theoretical time is $2 \cdot 5 \times 10^5$ years when neutrino processes are neglected. However, the disagreement becomes worse if neutrino production is also considered. During carbon burning, cores are nondegenerate and at temperatures where the photoneutrino process (2) is important. With the luminosity (Chiu and Stabler 1961) for this process included in equation (15), the time becomes 2×10^4 years (Chiu 1966).

Let $\tau_{12 \ldots n}$ be the time scale calculated through equation (15) when luminosities for n different reactions are considered. Let $L_1(T)$ be the luminosity obtained from the burning of ^{12}C in nuclear reactions, $L_2(T)$ be the luminosity accompanying the burning of the oxygen isotope ^{16}O (which is also present in stellar cores after the end of the helium-burning stage), $L_3(T)$ be the luminosity for the photoneutrino process, and $L_4(T)$ be the luminosity obtained from equations (12) and (16) for the two-photon reaction (6). Then $\tau_{12} = 2 \cdot 5 \times 10^5$ years and $\tau_{123} = 2 \times 10^4$ years.

It has been suggested that the mismatch between τ_{12} and the observed result is due to uncertainties about the relative concentrations of ^{12}C and ^{16}O present at the beginning of the carbon-burning stage. The concentration of carbon (and therefore the overall luminosity) decreases as the rate for the reaction

$$^{12}\mathrm{C} + \alpha \rightarrow {}^{16}\mathrm{O} + \gamma \qquad (17)$$

increases, which allows τ_{12} to increase. In the present work a calculation of Hayashi, Hōshi, and Sugimoto (1962) on the rates of reactions contributing to $L_1(T)$ and $L_2(T)$ has been repeated with different reduced widths for the nuclear reaction (17), and a match between τ_{12} and the result of observations has been found for reduced widths in the range from 0·23 to 0·32. This adjustment is nevertheless not very plausible, because the most recent experimental information about the reduced width (Loebenstein *et al.* 1967) is that it lies between 0·06 and 0·14, in agreement with a detailed theoretical estimate by Stephenson (1966). It may be possible to obtain values inside the experimental range if the square-well potential used by Hayashi, Hōshi, and Sugimoto is replaced by a more realistic optical potential, as is implied by Stephenson and by Vogt, Michaud, and Reeves (1965). However, $L_3(T)$ is notably larger than either $L_1(T)$ or $L_2(T)$ at the temperatures of interest, so that no new description of the reaction (17) is likely to alter greatly the result that $\tau_{123} = 2\times10^4$ years.

When $L_4(T)$ is included in equation (15), the calculated time scale for carbon burning in stars in the clusters h and χ Persei becomes $\tau_{1234} = 1\cdot75\times10^4$ years. Therefore at present both τ_{123} and τ_{1234} disagree with observations. It is necessary to have a much greater quantity of astronomical data in the form of colour–magnitude diagrams for star clusters to determine whether the disagreement for h and χ Persei is merely accidental, or whether the coupling constant for the local $(e\nu_e)(e\nu_e)$ interaction is up to an order of magnitude smaller than the coupling constant for other vertices in the current–current theory of weak interactions. The question is further complicated by Iben's (1967) summary of objections to the identification of carbon-burning stars (and therefore to the estimate of the carbon-burning lifetime) in h and χ Persei. Iben has suggested that the identified stars may be recently formed objects in the process of gravitational contraction onto the main sequence, that it is difficult to choose one definite direction of evolution in the colour–magnitude diagram for stars in relatively young clusters, and that the position of helium-burning stars on the main sequence can vary considerably according to their chemical composition. Therefore, in order to isolate the effect of two-photon annihilation as well as possible, calculations bearing on all of these points are needed. To assist the calculations, observational colour–magnitude diagrams for a large number of clusters like h and χ Persei are also required.

V. Conclusions

In equation (12) is presented an expression for the rate of loss of energy in stars from the process of two-photon annihilation into neutrino–antineutrino pairs. The circumstances under which this reaction is competitive with other neutrino-producing processes are indicated in Section IV. The inclusion of equation (12) in astrophysical models, followed by comparisons of the models with astronomical observations, constitutes a test of the existence of charged W mesons. The present observational evidence quoted in Section IV is questionable because it seems to exclude not only the annihilation process but also the existence of other processes of loss of energy in neutrino reactions which occur either with or without mediation by charged W mesons. Although it is unlikely that the effects due to two-photon annihilation can be separated beyond doubt from the other effects mentioned in the last paragraph of Section IV, calculations concerning these effects are necessary for an understanding of the role of neutrino processes in general in stellar evolution. It is desirable to have more than the present limited amount of observational data on evolution in stellar clusters in support of these calculations.

VI. Acknowledgments

The author wishes to thank Dr. M. Nakagawa for a discussion, and Professor F. C. Barker, Professor R. H. Dalitz, and Professor I. Iben for drawing various references to his attention.

VII. References

Boccaletti, C., de Sabbata, V., and Gualdi, C. (1964).—*Nuovo Cim.* **33**, 520.

Burns, R., *et al.* (1965).—*Phys. Rev. Lett.* **15**, 42.

Campbell, J. A. (1967).—*Nucl. Phys.* B **1**, 283.

Chin, C-W., Chiu, H-Y., and Stothers, R. (1966).—*Ann. Phys.* **39**, 280.

Chiu, H-Y. (1966).—*Ann. Rev. nucl. Sci.* **16**, 591.

Chiu, H-Y., and Morrison, P. (1960).—*Phys. Rev. Lett.* **5**, 573.

Chiu, H-Y., and Stabler, R. (1961).—*Phys. Rev.* **122**, 1317.

Feynman, R. P., and Gell-Mann, M. (1958).—*Phys. Rev.* **109**, 193.

Gell-Mann, M. (1961).—*Phys. Rev. Lett.* **6**, 70.

Glashow, S. L., Schnitzer, H. J., and Weinberg, S. (1967).—*Phys. Rev. Lett.* **19**, 205.

de Graaf, T., and Tolhoek, H. A. (1966).—*Nucl. Phys.* **81**, 596.

Hayashi, C., and Cameron, R. C. (1962).—*Astrophys. J.* **136**, 166.

Hayashi, C., Hōshi, R., and Sugimoto, D. (1962).—*Prog. theor. Phys., Kyoto* Suppl. No. 22.

Hearn, A. C. (1966).—*Communs Ass. comput. Mach.* **9**, 573.

Iben, I. (1967).—*Ann. Rev. Astr. Astrophys.* **5**, 571.

Johnson, H. L., and Morgan, W. W. (1955).—*Astrophys. J.* **122**, 429.

Lamb, R. C., *et al.* (1965).—Proc. Int. Conf. on Weak Interactions, Argonne National Laboratory (Report nr. ANL-7130), Argonne, Illinois, p. 247.

Lee, T. D., and Wu, C. S. (1965).—*Ann. Rev. nucl. Sci.* **15**, 381.

Lee, T. D., and Yang, C. N. (1960*a*).—*Phys. Rev. Lett.* **4**, 307.

Lee, T. D., and Yang, C. N. (1960*b*).—*Phys. Rev.* **119**, 1410.

Loebenstein, H. M., Mingay, D. W., Winkler, H. C., and Zaidins, C. S. (1967).—*Nucl. Phys.* A **91**, 481.

Marshak, R. E. (1966).—"High-energy Physics." (Ed. G. Takeda.) p. 60. (W. A. Benjamin Inc. and Syokabō Publishing Co.: Tokyo.)

O'Dell, C. R. (1963).—*Astrophys. J.* **138**, 67.

Seaton, M. J. (1966).—*Mon. Not. R. astr. Soc.* **132**, 113.

Stephenson, G. J. (1966).—*Astrophys. J.* **146**, 950.

Vogt, E., Michaud, G., and Reeves, H. (1965).—*Phys. Lett.* **19**, 570.

Zaidi, M. H. (1965).—*Nuovo Cim.* A **40**, 502.

THE EXCITED ATOMIC HYDROGEN LINES 126α AND 127α IN HII REGIONS

By R. X. McGee* and F. F. Gardner*

[*Manuscript received October* 16, 1967]

Summary

Forty radio sources have been observed for the presence of the hydrogen recombination lines 126α at 3248·708 MHz and 127α at 3172·864 MHz with a 6′ arc aerial beam and a receiver with 48 channels of 37 kHz bandwidth each. Detections were made in 34 sources, all of which were either HII regions or optically unidentified thermal sources.

The mean ratio of line intensity to thermal continuum intensity was 3·4% (±1·3% s.d.); the mean halfwidth of the lines was 340 kHz (±50 kHz s.d.), which is equivalent to 31·5 km/sec in radial velocity.

It is suggested that many of the profiles are complex and contain two or more major components that represent large-scale motions in the HII regions. The Orion and Omega nebulae are shown to have this type of profile and are discussed in some detail.

I. Introduction

The detection of the lines of atomic hydrogen in interstellar space by observing transitions between energy levels of high principal quantum numbers had not been seriously considered (e.g. Wild 1952) until Kardashev (1959), using the theory developed by Menzel and Pekeris (1935), showed that in HII nebulae the expected intensities and line widths in the decimetre wavelength band made investigation worth while.

Dravskikh and Dravskikh (1964) reported that the excited H line $n = 105$ to 104 had been observed in the Orion and Omega nebulae, while Sorochenko and Borodzich (1964) reported similar observations for 90α. Since then the n α-lines (i.e. emission lines from principal quantum numbers $n+1$ to n) for $n = 94$, 109, 126, 156, 158, 166, and 253 have been investigated in a number of HII nebulae.

The physical quantities most conveniently measured are the ratio of the intensities of the emission line and the thermal continuum background and the line halfwidth. Several authors (Höglund and Mezger 1965; Lilley *et al.* 1966; Palmer and Zuckerman 1966; Penfield, Palmer, and Zuckerman 1967) have used the product of these two quantities to compute the electron temperature of HII nebulae. The values thus obtained have been less than 6000°K rather than near the 10000°K derived from many optical measurements. Comments on such results have been made by Goldberg (1966), Weedman (1966), and the present authors (Gardner and McGee 1967; McGee and Gardner 1967); further explanation is offered here in discussing the results of the present survey. It is suggested that in a number of cases the observed profiles contain more than one component of systematic motion and may not be suitably represented by single Gaussian curves.

---

* Division of Radiophysics, CSIRO, Box 76, P.O. Epping, N.S.W. 2121.

Aust. J. Phys., 1968, **21**, 149–66

The 126α and 127α recombination H lines at frequencies $3248\cdot708$ and $3172\cdot864$ MHz respectively have been sought in 40 objects. They have been detected in 34, all of which are either recognized as HII nebulae or are optically unidentified thermal radio sources.

II. Theoretical Relationships between the Quantities Measured

The total energy emitted per unit volume per second by an assembly containing N_n atoms per unit volume in quantum state n is (e.g. Menzel and Pekeris 1935)

$$\begin{aligned} P_{\nu,\mathrm{line}} &= N_n A_{nn'} h\nu \\ &= \int_0^\infty I(\nu)\,\mathrm{d}\nu = I_{\mathrm{peak}}\,\Delta w\,, \end{aligned} \tag{1}$$

where I_{peak} and Δw refer to the peak intensity and the equivalent width in terms of the peak intensity, and from Menzel (1937)

$$N_n = \frac{b_n N_{\mathrm{i}} N_{\mathrm{e}} h^3}{(2\pi m k T_{\mathrm{e}})^{3/2}} \frac{g_n}{2} \exp(hRZ^2/n^2kT)\,.$$

In the present case (for hydrogen atoms and $n = 126$) only the first term of the expansion of the exponential is significant (the second term is less by a factor of 10^{-14}), and we write

$$N_n = \frac{b_n N_{\mathrm{i}} N_{\mathrm{e}} h^3}{(2\pi m k T_{\mathrm{e}})^{3/2}} \frac{g_n}{2}\,.$$

$A_{nn'}$, the Einstein probability coefficient for spontaneous transition from state n to n', is given by

$$A_{nn'} = \frac{g_{n'}}{g_n} \frac{8\pi^2 e^2 \nu^2}{mc^3} f_{nn'}\,,$$

where g_n and $g_{n'}$ are the statistical weights for the n and n' levels and $f_{nn'}$ is the number of dispersion electrons per atom, or the oscillator strength; $f_{nn'} = un$. Kardashev (1959) gives $u = 0\cdot18$, but Sorochenko (1965) gives a value of $0\cdot15$.*

For a discrete state of hydrogen $g_n = 2n^2$. b_n is a numerical factor ($0 < b_n \leqslant 1$) that is used to include departures from thermodynamic equilibrium; at local thermodynamic equilibrium $b_n = 1$ (see, for example, Seaton 1964).

The continuum temperature of the HII nebula is measured simultaneously with the line temperature. Using the expression derived for the emission coefficient (e.g. Oster 1961), we can write for the power per unit volume

$$P_{\nu,\mathrm{continuum}} = \frac{32 N_{\mathrm{e}} N_{\mathrm{i}} Z^2 e^6 (2\pi m)^{\frac{1}{2}}}{3 m^2 c^3 (kT_{\mathrm{e}})^{\frac{1}{2}}} \ln\left(\frac{(2k)^{3/2}}{\pi e^2 m^{\frac{1}{2}} \gamma^{5/2}} \frac{T_{\mathrm{e}}^{3/2}}{\nu}\right), \tag{2}$$

where, in equations (1) and (2), N_{e} and N_{i} are the numbers of electrons and ions per unit volume, Z is the atomic number, e the electronic charge, m the electron mass,

---

* *Note added in proof.* After evaluating oscillator strengths on a computer Dr. P. Palmer (personal communication) finds $u = 0\cdot19$ is more accurate.

c the velocity of light, k Boltzmann's constant, h Planck's constant, T_e the kinetic temperature of the electrons, $\gamma = 1\cdot7807$ (derived from Euler's constant), and ν the line frequency. If T_1 is the observed peak value of the line temperature, which is measured above T_c, the thermal continuum temperature, equations (1) and (2) may now be combined to give $(T_1/T_c)\Delta\nu$ in terms of atomic hydrogen constants, kinetic temperature, and frequency as

$$\left(\frac{T_1}{T_c}\right)\Delta\nu = \left(\frac{4\ln 2}{\pi}\right)^{\frac{1}{2}} \frac{3h^4 b_n u n n'^2 \nu^3}{16mke^4 T_e \ln[\{(2k)^{3/2}/\pi m^{\frac{1}{2}} e^2 \gamma^{5/2}\}\{T_e^{3/2}/\nu\}]}\,. \tag{3}$$

The first term on the right-hand side of this equation is the correction from Δw to a half-power width for a Gaussian line shape ($\Delta\nu$). It is assumed in (3) that the line shape is a single Gaussian and that the optical depth for both radiations is low.

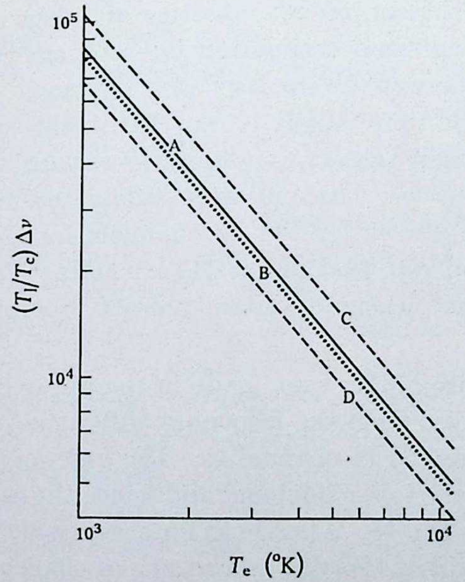

Fig. 1.—Relation between $(T_1/T_c)\Delta\nu$ and the kinetic temperature T_e of electrons in the nebulae for (A) $n = 126$ at local thermodynamic equilibrium, $b_n = 1$, $u = 0\cdot15$; and (B) $n = 127$, $b_n = 1$, $u = 0\cdot15$. The dashed lines C ($b_n = 1$, $u = 0\cdot19$) and D ($b_n = 0\cdot8$, $u = 0\cdot15$) show the effects of changes in u up to $0\cdot19$ and departure from local thermodynamic equilibrium to $b_n = 0\cdot8$.

In Figure 1 $(T_1/T_c)\Delta\nu$ is plotted against T_e between 1 000 and 11 000°K for $n = 126$, $b_n = 1$, and $u = 0\cdot15$ (line A). The dashed lines indicate limits by values $b_n = 0\cdot8$, $u = 0\cdot15$ (line D), and $b_n = 1$, $u = 0\cdot19$ (line C). The relation for $n = 127$, $b_n = 1$, $u = 0\cdot15$ is given by the dotted line (B). The values used in the calculations were taken from the report on fundamental constants by Cohen and Du Mond (1965).

Although not attempted here, the calculations combined with observational results may be carried further, if information on electron density is available and certain assumptions are made, to produce the r.m.s. velocity of internal turbulence in an HII region (see, for example, Mezger and Höglund 1967).

III. Methods and Observations

The observations were made with the 210 ft radio telescope of the Australian National Radio Astronomy Observatory at Goobang Valley near Parkes, N.S.W. The aerial beamwidth at 3250 MHz was measured as 6′ arc. The receiver had an overall system noise temperature of 300°K approximately on the cold sky. The crystal mixer input accepted both sidebands with the first intermediate frequency at 30·43 MHz. For observation of the line a second conversion was made to the main amplifier at 6·74 MHz, where the output was split into 48 channels of filters and detectors. The filter widths were 37 kHz spaced at intervals of 33 kHz. The continuum or total-power channel of width 3 MHz was detected at the 30 MHz amplifier to give T_{c}. A description of the back end of the receiver is given by McGee and Murray (1963). The local oscillators, derived from tunable oscillators near 6 MHz in frequency, were switched between the "signal" band and a "reference" band 2·16 MHz away, which was well outside the line frequency band. Intensity calibrations were made from time to time using a noise lamp modulated in synchronism with the switching frequency and introduced at the receiver input by means of a directional coupler. The frequencies were continually monitored.

In making an observation four profiles, each requiring a time of 2 min, were recorded at the position of the maximum of the continuum intensity and four at a neighbouring reference position, usually at the same declination but of such right ascension that the zenith angle of the telescope was the same at each position. The effects of changes in baseline with zenith angle were largely eliminated in this way. The procedure was repeated until a sufficiently good signal-to-noise ratio was achieved for the observation. The r.m.s. fluctuations per channel were calculated from several series of test observations. Average values for the 48 channels for single profiles were $\pm 0\cdot 63$ degK at 3248·7 MHz and $\pm 0\cdot 42$ degK at 3172·9 MHz. These values are in satisfactory agreement with the measured system noise temperature mentioned above.

The observations of the 126α line at 3248·7 MHz were made in the upper sideband and the equivalent radial velocity (derived from the frequency difference) was such that it was increasing in value from channel 1 to channel 48. The observations of the 127α line at 3172·9 MHz were made in the lower sideband and hence the radial velocity was decreasing in value from channels 1 to 48. When both lines were observed in a source the entirely different receiver conditions served as a means of confirming or rejecting features of doubtful nature. At the 126α line the conversion of frequency to radial velocity is such that 1 km/sec $= -10\cdot 8365$ kHz; at the 127α line, 1 km/sec $= -10\cdot 5835$ kHz.

The original data were corrected for gain and baseline differences in the various channels, averaged, and plotted in the CDC 3200 computer of the Division of Computer Research, CSIRO.

The HII nebulae (and other thermal sources) investigated in the survey include most of the more intense southern Milky Way radio sources, all of which have been previously observed for the presence of OH emission or absorption (McGee, Gardner, and Robinson 1967). Some nonthermal sources were used as controls. Several northern sources were observed so that comparisons of radial velocities and spectra of $T_{\mathrm{l}}/T_{\mathrm{c}}$ and $\Delta\nu$ against frequency could be studied.

IV. RESULTS

Forty sources were observed for at least one of the 126α or 127α lines; some were checked for angular extensions and possible changes in velocity in the line-emitting regions by making observations at half-beamwidth intervals around them.

The astronomical and physical data are listed in Table 1. Columns 1–5 contain the source name, the right ascension and declination (epoch 1950·0), and the galactic coordinates l^{II} and b^{II}. Column 6 shows which lines were observed.

The observational data begin with the continuum aerial temperature T_{c} in column 7 of Table 1. The maximum intensity of the continuum radiation was located for each source before line observations were made. This followed the same procedure as for the absorption lines in the OH survey (McGee, Gardner, and Robinson 1967). Owing to the improved angular resolution, the confusion effects of the blending of sources with background radiation or other sources were reduced. As a result, all the positions in column 7 differ by a few minutes of arc from the 1660 MHz (OH line) positions. Additional sources (marked "II" and "III" in column 1) were discovered near η Carinae, 1308−62, 1617−50, and NGC 6357.

Columns 8, 9, 12, and 13 of Table 1 contain the observed line data: the radial velocity (km/sec) at the profile peak intensity referred to the local standard of rest (l.s.r.); the aerial temperature of the line T_1 (°K); and the line halfwidth $\Delta\nu$ (kHz and km/sec) measured between points of half the maximum intensity. The equivalent r.m.s. noise (degK) is given in column 10. It varies according to the number of profiles included in each observation—the overall average is $\pm 0\cdot 26$ degK. An additional uncertainty not included here is caused by the slight alterations in baseline from one set of profiles to another taken at a different time but combined to complete the "observation". Two approaches have been made in deciding the shape of the observed profile. One author has fitted the best possible Gaussian curve to each set of points. The other has fitted a curve to the points as closely as possible, established a baseline from the trends on either side of the line, and made the above measurements. Good agreement was found for the radial velocities and line temperatures, but the Gaussian curves tended to be wider by an average of about 3·5 km/sec. The values given are compromises obtained by combination and suitable weighting of both sets of measurements. However, in some important cases the latter method revealed more than one profile peak. This aspect will be discussed in the next section.

The ratio of the temperature of the line to the thermal continuum and the product of this ratio with the halfwidth are given in columns 11 and 14 of Table 1.

It will be noticed that, although two lines (126α and 127α) have been observed, in many cases the results have been averaged. The effective signal-to-noise ratio is not good enough to give separate sets of information from the neighbouring lines.

The remaining columns 15 and 16 of Table 1 contain the OH-line radial velocities (rounded off) and references to remarks given as footnotes to the table.

(a) *Comments on Table 1*

(i) *Surrounding Points*

In the five sources Orion Nebula, RCW 38, η Carinae, NGC 6334, and Omega Nebula we have made observations at surrounding points (usually at approximately half-beamwidth spacing) to determine any marked spread or changes in the area of recombination line emission. At the present sensitivity and angular resolution only

TABLE 1

POSITIONS OF SOURCES AND PHYSICAL CHARACTERISTICS OF EXCITED HYDROGEN

(1)	(2)	(3)	(4)	(5)	(6)	(7)	(8)	(9)	(10)	(11)	(12)	(13)	(14)	(15)	(16)
Source	Position (1950·0)		Galactic Coordinates		α Line Obs.*	T_c (°K)	R.V. at Line Peak (km/sec)	T_1 (°K)	R.M.S. Noise (±degK)	$\frac{T_1}{T_c}$ (%)	Halfwidth $\Delta\nu$		$\frac{T_1}{T_c}\Delta\nu$ (kHz)	R.V. of OH Lines (km/sec)	Remarks†
	R.A. h m s	Dec. ° ′	l^{II} °	b^{II} °							(kHz)	(km/sec)			
Crab Nebula	05 31 30	+21 59·1	184·5	−5·8	6	364	—	—	0·4	—	—				
	05 31 46	+21 59·1	184·6	−5·7	6, 7	178	—	—	0·3	—	—				
Orion Nebula	05 32 50	−05 25·8	209·0	−19·4	6, 7	183	−7‡	4·4	0·1	2·4	406	38	9·74	+8, +3, +21	1
Orion Δα−3′	05 32 37	−05 25·7	209·0	−19·4	6, 7	100	−7‡	2·1	0·3	2·1	342	32	7·17		
Orion Δα+3′	05 33 02	−05 25·7	209·0	−19·3	6, 7	109	−5‡	2·8	0·3	2·6	332	31	8·63		
Orion Δδ−3′	05 32 50	−05 28·7	209·0	−19·4	6	110	−7‡	2·7	0·3	2·5	410	38	10·25		
Orion Δδ+3′	05 32 50	−05 22·3	209·0	−19·4	6	105	−1‡	2·5	0·3	2·4	410	38	9·85		
30 Doradus	05 39 05	−69 06·9	279·4	−31·7	6	13	—	—	0·2	—	—				
NGC 2024	05 39 10	−01 56·0	206·5	−16·4	6, 7	30	+4	1·0	0·2	3·3	225	21	7·43		
IC 443	06 14 48	+22 48·4	188·9	+3·2	6	3	—	—	0·3	—	—				
RCW 38	08 57 20	−47 19·5	267·9	−1·1	6, 7	97	+1	1·9	0·2	2·0	320	30	6·40	+1, +3	
RCW 38 Δα−3′	08 57 02	−47 19·5	267·9	−1·1	6	39	+11	0·6	0·4	1·6	380	35	6·08		
RCW 38 Δα+3′	08 57 38	−47 19·5	268·0	−1·0	6	75	+2	1·4	0·4	1·9	270	25	5·12		2
RCW 38 Δδ−3′	08 57 20	−47 22·5	268·0	−1·1	6	48	−3	1·0	0·4	2·1	270	25	5·66		
RCW 38 Δδ+3′	08 57 20	−47 16·5	267·9	−1·0	6	62	(−1)	(1·3)	0·4	(2·1)	(380)	(35)	(7·98)		
RCW 36	08 57 34	−43 34·3	265·1	+1·4	7	12	−3	0·8	0·2	6·7	380	36	25·5	+11, +27	
RCW 46	10 04 54	−56 58·5	282·0	−1·2	7	14	+19	0·7	0·2	5·0	233	22	11·65	−8, 0, +3, +7	
RCW 49	10 22 22	−57 31·7	284·3	−0·3	6, 7	62	−2	1·7	0·2	2·8	290	27	8·12	−20	
η Carinae I	10 41 47	−59 19·9	287·4	−0·6	6, 7	37	−20	1·3	0·1	3·4	396	37	13·47	−21	
η Car Δα−3′	10 41 23	−59 19·9	287·6	−0·7	6	31	−16	1·1	0·4	3·5	325	30	11·40		
η Car Δα+3′	10 42 11	−59 19·9	287·5	−0·6	6	28	—	—	0·4	—	—				
η Car Δδ−3′	10 41 48	−59 22·9	287·8	−0·7	6	30	—	—	0·4	—	—				
η Car Δδ+3′	10 41 47	−59 16·9	287·9	−0·6	6	30	−20	1·0	0·4	3·3	347	32	11·46		
η Carinae II	10 42 52	−59 22·6	287·9	−0·6	6	34	−40	1·1	0·2	3·2	(304)	(28)	9·72		
							−1	0·8	0·2	2·4	(270)	(25)	6·48		
1109−61	11 09 49	−61 02·7	291·3	−0·7	6	52	−23	1·0	0·3	2·0	433	40	8·66		
							+30	0·6	0·3	1·2	304	28	3·64		3
RCW 57	11 12 58	−60 59·2	291·6	−0·5	6	67	+10	1·5	0·2	2·2	422	39	9·30	−8	
1207−62	12 07 18	−62 33·6	298·2	−0·3	7	17	+11	0·5	0·2	3·2	264	25	8·45	−52, +4	
1308−62I	13 09 09	−62 18·9	305·3	+0·2	6, 7	22	−49	0·5	0·2	2·5	(278)	(26)	6·95	−44, −39	
							−30	0·8	0·2	3·6	(278)	(26)	10·00	−36	
1308−62II	13 08 09	−62 29·5	305·2	0·0	7	14	−50	1·0	0·2	7·1	(339)	(32)	24·10		
							−13	0·6	0·2	4·3	(318)	(30)	13·68		
13S6A	13 43 37	−60 08·1	309·8	+1·7	7	11			0·2	—	—				

1404−61	14	04	07	−61	13·6	311·9	+0·1	7	4·5	—	—	0·2	—	—			−8	
1441−59	14	41	26	−59	37·8	316·8	−0·1	7	17	—	—	0·2	—	—			−37, −26	4
1442−59	14	42	04	−59	11·7	317·0	+0·3	7	4·5	—	—	0·2	—	—			−19	
1540−53	15	40	55	−53	58·5	326·6	+0·6	7	16·5	(−45)	(0·5)	0·2	(3·0)	318	30	9·55	−31, −15	5
1549−54	15	49	07	−54	26·9	327·3	−0·5	7	26	−62	1·1	0·2	4·3	(318)	(30)	13·70	−94, −54	
										−19	0·9	0·2	3·5	(318)	(30)	11·14	−51, −43, −26	
1608−51	16	08	14	−51	19·5	331·5	−0·1	6, 7	18	−91	0·7	0·2	4·0	310	29	12·40	−101, −97, −90	
1617−50I	16	17	01	−50	31·8	333·1	−0·4	6, 7	20	−48	1·2	0·2	6·0	328	31	19·70	−59, −45	
1617−50II	16	17	40	−50	19·6	333·3	−0·4	7	20	−59	1·7	0·2	3·0	(381)	(36)	11·43		
										−11	1·5	0·2	2·5	(286)	(27)	7·15		5
1618−49	16	18	22	−49	59·3	333·6	−0·2	6, 7	38·5	−57	1·1	0·2	2·8	(354)	(33)	9·90	−115, −73	6
										−28	1·1	0·2	2·8	(440)	(41)	12·33	−55, −31, −22, +8	
1630−47	16	30	46	−47	29·7	336·8	+0·1	7	14·5	−71	0·5	0·2	3·6	275	26	9·88	−120, −53	
1637−46	16	37	03	−46	17·4	338·4	+0·1	7	13·5	−38	0·6	0·2	4·2	381	36	16·00	−92, −24	
1716−38	17	16	35	−38	55·2	348·7	−1·0	7	21	−6	0·4	0·2	2·1	423	40	8·88	+31	
										+69	0·7	0·2	3·3	413	39	13·64		
NGC 6334	17	17	09	−35	47·1	351·3	+0·7	6, 7	40	−4	2·2	0·2	5·4	374	35	20·25	−5, +6	
Source A	17	17	32	−35	43·8	351·4	+0·6	6	20	−4	1·0	0·3	5·0	390	36	19·51	−12, −8, −11	
Source B	17	16	34	−35	55·8	351·1	+0·7	6	11	—	—	—	—	—			−9, −6, −13	
NGC 6357I	17	21	24	−34	08·6	353·2	+0·9	6	45	−5	1·3	0·3	2·8	368	34	10·30		
NGC 6357II	17	22	17	−34	20·0	353·3	+0·6	6	38	−1	1·1	0·2	2·9	324	30	9·39	−11, −6, +1, +5	
NGC 6357III	17	22	42	−34	15·6	353·2	+0·6	6	23·5	−1	1·6	0·4	6·8	260	24	17·70		
SGR A	17	42	28	−28	59·5	359·9	−0·0	6, 7	129	—	—	0·3	—	—				
SGR B$_2$	17	44	09	−28	23·6	0·6	−0·0	6, 7	26	—	—	0·2	—	—				7
M 8	18	00	35	−24	23·7	005·9	−1·2	6	21·5	−4	0·6	0·3	2·8	347	32	9·71		
Omega Nebula (M 17)	18	17	34	−16	12·7	015·0	−0·7	6	183	+9	4·5	0·1	2·5					
										+19	6·0	0·1	3·3	390	36	10·40	+20	8
										+32	4·1	0·1	2·2					
M 17 Δα−4′	18	17	20	−16	12·1	015·0	−0·6	6	94	+18‡	2·9	0·4	3·1	347	32	10·77		
M 17 Δα+4′	18	17	52	−16	12·1	015·0	−0·7	6	90	+17‡	2·4	0·4	3·7	390	36	14·45		
M 17 Δδ−4′	18	17	37	−16	16·1	015·0	−0·7	6	107	+10‡	3·6	0·4	3·4	369	34	12·56		
M 17 Δδ+4′	18	17	38	−16	08·1	015·1	−0·7	6	100	+18‡	3·6	0·4	3·6	390	36	14·05		
W 48	18	44	59	−02	00·9	030·7	−0·0	7	38·5	+89	0·8	0·2	2·2	286	27	6·29		
W 49	19	07	52	+09	01·8	043·2	−0·4	6	30	+7	1·9	0·3	6·4	282	26	18·07	+6, +13, +16, +18, +22	
W 51	19	21	26	+14	25·0	049·5	−0·4	6	50	+55	2·1	0·3	4·2	400	37	16·80		

* 6 = 126α, 7 = 127α.

† Relevant remarks are: 1. Peaks occur at −10, +1, and +18 for the median value of −7 km/sec (column 8). 2. +6·5 mean. 3. There was a bad baseline for measurements. 4. There is a possible line at −36 km/sec. 5. Results are doubtful. 6. There is an intermediate peak at −46 km/sec, $T_l/T_c = 3{\cdot}2\%$. 7. See Section IV (*a*) (iii). 8. The median value is +17 km/sec.

‡ Median values.

the median radial velocities have been considered. Some remarks on the five sources follow.

Orion Nebula. The radial velocity is more positive at the northern point (−1 km/sec) with a similar tendency at the eastern point (−5 km/sec) than at the central position (−7 km/sec, median).

RCW 38. The observations have a rather poor signal-to-noise ratio. The profile at the western point has a median value of +11 km/sec but a peak occurs at +2 km/sec. The central-point median velocity is +1 km/sec.

η Carinae. Any line signal at the eastern and southern points is lost in noise. The northern and western observations indicate that the source of excited H line may be displaced in their directions.

NGC 6334. The additional observations were made at the positions of OH emission—sources A and B. The same velocity as at the continuum maximum was measured at A; no line was detected at B.

Omega Nebula. There is an indication that the radial velocity is less positive at the northern and eastern points (+16 km/sec) than at the southern and western points (+19 and +18 km/sec respectively). The central point is at +17 km/sec median velocity.

(ii) *Companion Sources*

Excited H lines were observed at more than one continuum peak in five of the thermal sources. They are designated: η Carinae I and II, RCW 57 and 1109−61, 1308−62 I and II, 1617−50 I and II, and NGC 6357 I, II, and III.

(iii) *Negative Results*

Ten cases were found where no line signal was detected above the noise. They include the nonthermal sources Crab Nebula, IC 443, and 13S6A. Another source is 30 Doradus, which is the very large HII nebula or group of nebulae in the Large Cloud of Magellan. Three sources have a comparatively weak continuum temperature: 1404−51, 4·5°K; 1442−59, 4·5°K; and source B (NGC 6334), 11°K. Source 1441−59 has a possible line at −36 km/sec. No line was observed in Sagittarius A. Preliminary observations of Sagittarius B2 gave indications of the 126α line at +74 km/sec, but two later series over different velocity ranges near this value gave a negative result. A similar effect was found with a feature indicated at −113 km/sec in source 1618−49 by the preliminary observations.

(iv) *Very Broad Profiles*

In some cases the observed profile widths were so broad that it was obvious that more than one component must be present. Broad profiles have been divided into separate line contributions in a somewhat arbitrary fashion using such indications as changes in the envelope shape and suggestions of peaks. The halfwidths of these lines are given in parentheses in Table 1. The sources were η Carinae II, 1308−62 I, 1308−62 II, 1549−54, 1617−50 II, and 1618−49.

(v) *Average Values from Table 1*

Average values may be calculated from 55 entries in Table 1 for the following quantities

$$(T_1/T_c)_{av} = 3\cdot4\% \pm 1\cdot3\% \text{ s.d.} \quad (\text{Max. } 7\cdot1\%, \text{ min. } 1\cdot2\%);$$

$$(\Delta\nu)_{av} = 340 \text{ kHz} = 31\cdot5 \text{ km/sec};$$

$$\{(T_1/T_c)\Delta\nu\}_{av} = 1\cdot1 \times 10^4 \text{ Hz}.$$

TABLE 2

COMPARISON OF RADIAL VELOCITIES AND HALFWIDTHS AT OTHER LINES

All values are in units of km/sec

Source	109α		104α		158α		166α		126, 127α	
	R.V.	Δν	R.V.	Δν	R.V.	Δν	R.V.	Δν	R.V.	Δν
Orion Nebula	−2·0	29·0	−2	39·1	−4·9	37·1	0	45·2	−7*	38
Orion Δα−3′	−9·5	47·7							−7*	32
Orion Δα+3′	−2·4	28·6							−5*	31
Orion Δδ−3′	−7·0	36·3							−7*	38
Orion Δδ+3′	−2·6	27·5							+1*	38
NGC 2024	+4·4	22·4			+5·9	26·7			+4	21
RCW 38							+8	32·8	+1	30
NGC 6334					−5·1	25·8			−4	35
NGC 6357I	−1·2	26·9							−5	34
NGC 6357III	−5·9	31·5			−3·2	31·2			−1	34
M 8	+3·5	24·1			+4·6	24·2			−4	32
M 17 Omega Nebula	+17·6	38·5	+28	37·5	+18·3	41·8	+20	42·7	+10 +19 +32 } +17*	36
					+25 +21	42·3	+20	38·5		
M 17 Δα−4′	+16·3	35·2							+18*	32
M 17 Δα+4′	+17·5	32·6							+16*	36
M 17 Δδ−4′	+16·8	30·3							+19*	34
M 17 Δδ+4′	+13·3	38·6							+16*	36
W 43	+88·6	41·7	+93	28·7	+97·0	32·1			+89	27
W 49	+7·4	26·6	+17	31·3	+5·2	32·4			+7	26
W 51	+40·9	41·5	+53	28·7	+57·6	25·0			+55	37
Mean Δν		32·8		33·1		30·6				32·5

* Median values.

V. DISCUSSION OF RESULTS

(a) *Comparison with Other Results*

A comparison of the values of radial velocities and halfwidths from five excited Hα lines over 19 positions is made in Table 2. The 109α line was observed by Mezger and Höglund (1967), the 104α by Gudnov and Sorochenko (1966), the 158α by Lilley *et al.* (1966) and Dieter (1967), and the 166α by Palmer and Zuckerman (1966) and McGee and Gardner (1967). In many cases the agreement in radial velocity is satisfactory but in M 8, W 49, and W 51 differences of 10 km/sec and more are noted.

The halfwidths, usually stated in kilohertz by the above authors, have been converted to kilometres per second. The mean halfwidths of the values in Table 2 for four of the lines are within 1 km/sec of 32·5 km/sec; large individual differences occur in some sources.

In considering values of T_l/T_c from the five α-lines, mean spectra of T_l/T_c with ν have been plotted in Figure 2 for 11 sources. Additional data were available for the Orion and Omega nebulae (Meeks, personal communication). Mean values of all measurements for four lines are shown as circles. The 109α mean value appears higher than would be expected from the trend of the others. Some of the spread could well be caused by different estimates of the relevant thermal continuum temperature.

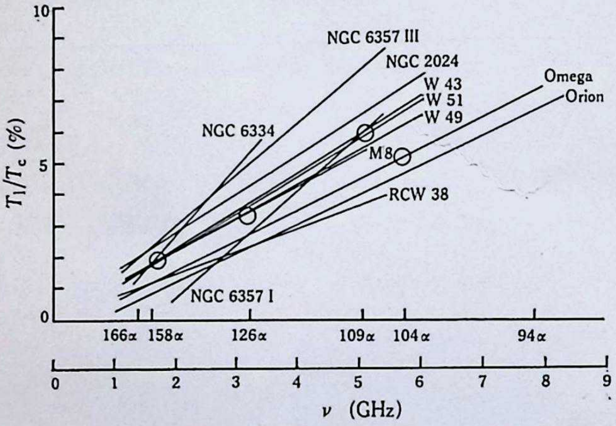

Fig. 2.—Line-to-continuum intensity ratio T_l/T_c as a function of frequency ν for 11 sources for lines between 94α and 166α. Mean values (○) were available at 158α, 126α, 109α, and 104α.

(b) *Location of HII Regions using the Excited H-line Radial Velocities*

The location of HII regions, on the assumption that the radial velocities of the nebulae and the excited H lines must be reasonably close, could be attempted in the same way as was outlined for OH clouds by McGee, Gardner, and Robinson (1967). Dieter (1967) and Mezger and Höglund (1967) have positioned about 30 of the northern sources by similar means. In the present survey the majority of the sources lie in the area of positional ambiguity and have no optical identifications. Thus we have decided not to attempt locations until more comprehensive data become available.

(c) *Comparison of Radial Velocities of Excited Hydrogen and Other Interstellar Constituents*

The interstellar constituents of interest in this comparison are the ionized gases of the nebulae and the neutral gases in their immediate vicinity. Unfortunately, optical radial velocities of ionized gas could be found for only 5 of the present sources. Hydroxyl radial velocities may be compared in 11, HI absorption in 9, and HI emission velocities have been listed for each of the 11. The comparisons are made in Table 3. Some agreements may be seen but the data are too scanty for useful conclusions.

TABLE 3

COMPARISON OF RADIAL VELOCITIES OF IONIZED AND NEUTRAL GASES

Nebula	Radial Velocity (km/sec) of:					
	Excited H		Ionized H*	OH Gas*	HI Absorption*	HI Emission*
Orion Nebula	−10 +1 +18	−7 med.	−6 to +8[a]†	+8 +3 +21	+4·5 +2·5[d]	+8[e]
NGC 2024	+4		+13·3[b]	+10		+6[e]
RCW 38	+1			+1 +3	+3·8 −4·2[d]	+3 +58[e]
η Carinae I+II	−20 −40 −1		−22·9[b] −36·6[a]	−21	−12	−15 +18 +36[e]
NGC 6334	−4			−5 +6	−5·7 +4·2[d]	−6[e]
NGC 6357II	−1			−11 −6 +1 +5	−12·7 −1·3 +4·9 +11·4[d]	−6[e]
M 8	−4 (+4)		+7·5[b] +8·7[a]	+10[c]	0 +6·3[d]	−8 +6[e]
M 17	+10 +19 +32	+17 med.	+25·1[b] +21[a]	+20	+6·9 +14·5 +20·7 +6·3[d] +26·4	−21 +21[e]
W 43	+89			+7·5 +12·5 +81·5 +89·5[c] +94	+12·7 +54·9 +83·6[d]	+18 +43 +97[e]
W 49	+7			+6 +13 +16 +18 +22		+12[e]
W 51	+55			+5·8 +51 +64[c]	+7·2 +12·7 +47·5 +54·9[d]	+12[e]

* References are: a, Wilson *et al.* (1959); b, Courtès, Cruvellier, and Georgelin (1967); c, Goss (1967); d, Clark (1965); e, McGee, Milton, and Wolfe (1966).

† For the lines [OIII], [OII], and Hγ.

Ionized gas. A further difficulty is that, whereas the excited hydrogen observations are centred on the positions of the radio continuum maxima and probably represent an average because of beamwidth limitations, the Hα velocities quoted in the table (Courtès, Cruvellier, and Georgelin 1967) have been measured in filaments of much smaller size comparatively and in general not in the central positions. Dieter (1967) found a velocity correlation in 6 of 12 cases.

Hydroxyl gas. Table 1 contains 22 cases of corresponding radial velocity measurements of the excited hydrogen and hydroxyl gas. In 9 cases values agreed within 2 km/sec. Differences between nearest values for all range between ± 18 km/sec (with one -37 km/sec). However, the sources of recombination H lines are intrinsically associated with HII regions but hydroxyl gas has been shown to exist frequently in neutral hydrogen regions away from the nebulae.

Neutral hydrogen absorption. At least one radial velocity value in each of the nine sets in Table 3 indicates that an HI cloud must lie in front of and fairly close to a corresponding HII region.

Neutral hydrogen emission. The HI emission velocities are taken from peaks of profiles observed in the directions of the 11 sources in Table 3. One of the values in each set is typical of the HI gas cloud surrounding the particular nebula.

(*d*) *Excited H-line Halfwidths*

We now discuss what is perhaps the most important result of this investigation. In all the published reports to date authors have been content to fit Gaussian curves to rather noisy sets of intensity readings spread across the expected frequency band. The halfwidth of the single Gaussian shape, corrected for instrumental bandwidth, has been used to calculate the kinetic temperature of the electrons in the HII nebulae in formulae similar to equation (3).

If the values for T_l/T_c of $0\cdot034$ and $\Delta\nu$ of 340 kHz stated in Section IV (*a*) (v) are substituted in equation (3), a mean kinetic temperature of 5500°K may be read from Figure 1 for $n = 126$, $u = 0\cdot15$ (line A) under conditions of local thermodynamic equilibrium ($b_n = 1$). This is in excellent agreement with the values of 5800°K found by Mezger and Höglund (1967) from 109α measurements and 5200°K by Dieter (1967) from 158α results.

On the other hand, optical determinations for T_e in HII nebulae have given a value of about 10000°K. Pottasch (1965) has shown that the average value over a number of nebulae may be lower and that T_e varies in the nebula itself, but no value comes as low as 5800°K.

Recently Peimbert (1967), using intensity ratios of auroral to nebular forbidden lines and of bound–free continuum to bound–bound emission lines of hydrogen for some HII regions, concluded that temperature fluctuations inside nebulae have a significant effect on values of electron temperatures determined from different physical processes. For example, temperatures derived from the Balmer jump and forbidden lines showed fluctuations of a few thousands of degrees (10500–13700°K) in the Orion Nebula.

A certain amount of controversy has appeared in recent literature with attempts to explain the differences in optical and radio results. Goldberg (1966) has pointed out that a departure from local thermodynamic equilibrium may be the cause (see Fig. 1) and that $\mathrm{d}b_n/\mathrm{d}n$ (Seaton 1964) is important in gaseous nebulae The present authors (Gardner and McGee 1967) have offered some experimental results supporting Goldberg's arguments.

It should be kept in mind that, if the profile departs from the Gaussian shape, $T_1\Delta\nu$ must be replaced by $\int T_1\,\mathrm{d}\nu$. The estimation of T_e depends on the area under the curve. The estimation of turbulence velocities depends on the halfwidths.

In general the sensitivity level leaves much to be desired and most of the sources have been observed for the minimum possible time that is consistent with producing the line "signal". However, the two most important sources Orion and Omega nebulae have received much more attention. In the first series of 126α observations in September 1966 it was noticed that the two profiles were not simple single-peaked curves. For Orion, peaks in the profile were discernible near -10, $+1$, and $+18$ km/sec and for Omega, peaks at $+9$, $+19$, and $+32$ km/sec. In earlier notes (McGee and Gardner 1967) we have quoted median radial velocity values (there was a possibility that the peaks were caused by instrumental effects). However, with further 126α and 127α line observations in March 1967 the three profile peaks were again recorded in each case. It will be remembered that the receiver conditions were completely different for the 127α line (Section III).

(i) *Orion Nebula*

In showing how the complex profile for the Great Nebula in Orion fits in with current ideas, the surrounding envelope and the radio and optical evidence for the motions in and near the nebula are briefly discussed.

One of us (R. X. McG.) has made a survey of neutral hydrogen in the region of $\sim 45'$ radius from θ^1 Ori using a $14'\cdot 5$ aerial beam. The HI intensity contours reveal the striking absorption dip ($T_\mathrm{a} \sim -150$ degK) coincident with the visible ionization region. Although the earlier low resolution observations did not indicate any significant change in the line emission in the vicinity, the present beam was able to distinguish a fairly well-defined cloud of HI surrounding the nebula. The velocity information substantiates this. The "expected" emission HI profile at the continuum maximum is given in Figure 3 (curve C). The peak radial velocity is $+8$ km/sec, which is approximately the kinematical model velocity at the distance of Orion. The asymmetry in the negative wing is repeated in all the surrounding emission profiles. It corresponds closely in velocity to the absorption indicated in Figure 3 by the halfwidth spacing -5 to $+6$ km/sec and the maximum absorption velocity $+2\cdot 5$ km/sec. Thus we can distinguish HI gas in front of and behind the nebula and in both cases it is probable that such gas is in its immediate neighbourhood. The halfwidth of the positive component $+2\cdot 5$ to $+13\cdot 5$ km/sec has the same value, 11 km/sec, as the absorption line profile.

The OH line observations in the direction of the Orion Nebula have been discussed by McGee, Gardner, and Robinson (1967). The results were unusual in that a very broad emission line profile was recorded at 1665 MHz over the total velocity range −16 to +36 km/sec—the same overall width as the HI profile. Narrow-band peaks similar to those at other HII regions were superimposed at +3, +7, and +21 km/sec. Goss (1967) has published profiles at the four OH lines, from which we note almost the same features at 1665 MHz after allowing for his improved frequency resolution. Absorption features at +6 and +8 km/sec are seen in the 1667 and 1720 MHz lines. We do not attempt to explain the wide-band emission, but we do know from other observations (McGee, Gardner, and Robinson 1967) that the narrow-band emission comes from areas at the edges of HII regions and that the absorbing hydroxyl gas may be spread through the HI cloud.

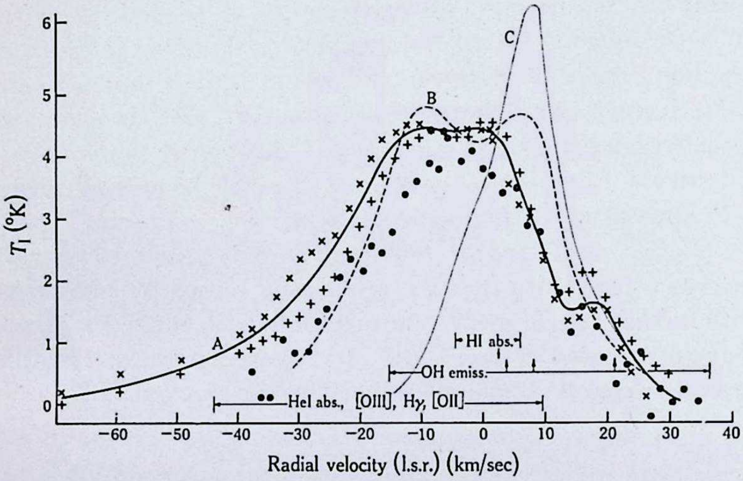

Fig. 3.—Line profiles for the Orion Nebula: curve A, composite recombination line from 126α (+) and 127α (×) measurements; ●, points from the 158α profile; curve B, double [OIII] line profile; curve C, expected HI profile. The HI line absorption is shown as a halfwidth range and the OH line emission as an overall range. The velocities at intensity maxima are marked. The velocity range of optical lines is taken from Wilson *et al.* (1959). The T_1 scale applies only to 126α and 127α lines.

The neutral hydrogen and hydroxyl gas then form the outer envelope of the nebula. The hydrogen gas in which the recombination lines form has always been found in the direction of maximum continuum emission. The composite 126α–127α line profile is given in Figure 3 (curve A). Dieter's (1967) observation points for 158α, suitably scaled, are superimposed. Peaks can be seen near −10, +1, and +18 km/sec radial velocity. The halfwidth extends from −26 to +11 km/sec (37 km/sec). Therefore the profile contains a component or components that are more negative in radial velocity than the HI and OH. It may be inferred that a large proportion of the excited hydrogen is expanding outwards in our direction. In the opposite direction expansion is not so obvious, except for the presence of the moderately intense component at +18 km/sec.

It should be noted that we are pointing to three main peaks in the profile as evidence of a number of large-scale motions. If the broadening was caused by turbulence then the observed profile would be truly Gaussian in shape.

However, Goss (personal communication) has pointed out that the observation of different radial velocities across the nebula by Mezger and Höglund (1967) and the present authors (see Section IV (*a*) (i)) clearly indicates that two or more large-scale motions are present and hence doubts must be cast on the derivation of large values of turbulent velocities (+17 km/sec by Mezger and Höglund, and +32 km/sec by Dieter for the Orion Nebula) from the single Gaussian. Two recent investigations seem to establish this view beyond doubt. Mills and Shaver (1967) have resolved the main body of the Orion Nebula, NGC 1976, and its northerly companion NGC 1982 as separate radio sources 7′·5 arc apart. Gordon and Meeks (1968) using the H 94α line report a radial velocity of −3 km/sec for NGC 1976 and +7 km/sec for NGC 1982.

The velocity range of the recombination line profile is paralleled by the radial velocities of the optical lines. Wilson *et al.* (1959) measured velocities at several thousand points over an area 4′ by 4′ centred on the Trapeziuun (θ^1 Ori). They found that the overall mean radial velocity of OIII is about −10 km/sec with respect to the Trapeziuun stars, which was interpreted as an expansion of the HII region into the surrounding cold gas. Different velocities for constituents [OIII], Hα, [OII] were found to be caused by the different ionization potentials. Absorption lines for HeI were also measured. The typical halfwidth for an Hγ line was measured as 29 km/sec. In many places the lines became considerably broader and even distinctly double with separations up to 25 km/sec. A double [OIII] line (curve B) has been included in Figure 3 from details given in Figure 7 of Wilson *et al.* (1959). Its halfwidth is almost identical with the recombination profile. The approximate range of the optical velocities is also marked in Figure 3.

Weedman (1966) has shown that if these optical data are considered as distributed over the area of the aerial beam (6′·4 arc) of Höglund and Mezger (1965) and are subject only to optical instrumental broadening effects a Gaussian profile similar to the radio case will result. The width measured by Höglund and Mezger was 29 km/sec, but other observers report widths near 38 km/sec for the Orion Nebula (Table 2).*

(ii) *Omega Nebula*

The recombination H line profile at 126α for the Omega Nebula (M 17) is shown in Figure 4. Again we have taken the 10 kHz points from the 158α profile (Dieter 1967) and scaled them to fit on our diagram. The agreement is good. The presence of at least two major components of motion is strongly supported by the observations of Zisk (1966) in the λ2 cm continuum. With a 2′·3 arc aerial beam M 17 is resolved into two distinct sources 3′·5 arc apart. Dieter (1967) refers to these in commenting on the large halfwidth of the 158α line. In the present work the 6′ beam centred on the apparent maximum at 3249 MHz intercepted major contributions from both sources. The change of 3 km/sec in the median radial velocities in the north-east and south-west of the nebula (Section IV (a) (i)) may be further evidence of components of differing velocities.

---

* *Note added in proof.* We are indebted to Dr. P. Palmer of the Harvard College Observatory for comments on Figure 3. He finds that, except for the flat top and the +18 km/sec feature, fair agreement with recent observations of the 94α line (Gordon and Meeks 1968) and the 109α line (Palmer, personal communication) is possible if a baseline of slope −1/110 degK km^{-1} sec^{-1} is assumed for curve A in Figure 3.

The observed profile was approximated fairly well by three computer-produced Gaussian curves with the following parameters:

Radial velocity (km/sec)	$+2\cdot7$	$+18\cdot4$	$+34\cdot5$
Maximum T_1 (°K)	$2\cdot7$	$5\cdot0$	$1\cdot8$
Halfwidth (km/sec)	$18\cdot5$	$20\cdot9$	$17\cdot5$

These values do not constitute a unique solution but they indicate the halfwidths that may be expected and how great the error in turbulence may be if a single Gaussian curve represents this profile.

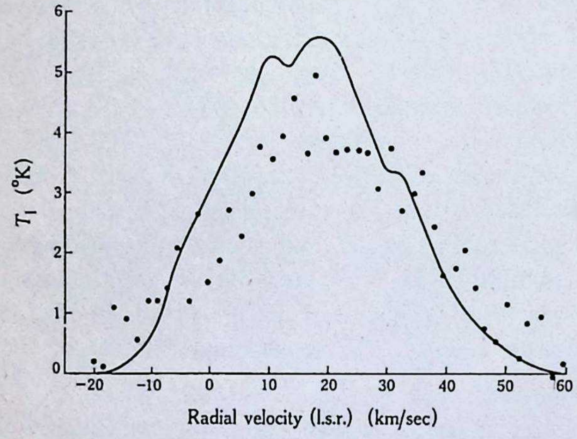

Fig. 4.—Line profiles for the Omega Nebula. The curve is the recombination line for 126α while the points are from the 158α profile. The T_1 scale applies only to the 126α line.

(iii) *Other Nebulae*

Wide profiles that were not quite resolved into separate components were observed in several sources. They are not the "very broad" cases mentioned in Section IV (*a*) (iv). The signal-to-noise ratio was much lower than for (i) and (ii) above so that, in general, median values of radial velocity had to be given in Table 1. Some notes on these sources follow.

RCW 38. The nebula consists of four concentrations of Hα in an area 40′ by 40′. Thus it is reasonable to expect differing velocity components.

RCW 36. Three bright S-shaped Hα regions in an area 12′ by 6′ imply differing motions.

η Carinae. The two continuum maxima of sources I and II are about 8′ arc apart at 3 249 MHz. The complex profile is in source I. The two components of source II given in Table 1 are clearly separate in the observed profile.

1109—61 and RCW 57. These are neighbouring sources.

NGC 6334. The Table 1 entry for the radial velocity is —4 km/sec but there is evidence of a secondary peak near +6 km/sec.

NGC 6357 II. The value in Table 1 of —1 km/sec is median. Components possibly exist at —6 and +4 km/sec.

We sum up this section by suggesting that the primary cause of the wider recombination H line profiles is the presence of two or more components representing differing radial velocities of filaments or other large-scale concentrations in motion in the HII regions. However, the problem is not yet solved. The recognition of such components has been achieved with the aid of frequency resolution in the line observations. The corresponding values of the continuum thermal emission T_c of these components are not obtained at the present angular resolution.

Two conclusions result: (1) the electron temperature T_e for any particular filament is unlikely to exceed the optically derived values ($\sim 10^4$ °K), and (2) the electron temperatures for all individual filaments or clouds are likely to be higher than the values derived by simply taking $(T_l/T_c)\Delta\nu$ for the whole line profile. In addition, the possibility of departures from low opacity in the continuum and from local thermodynamic equilibrium requires consideration.

VI. Conclusions

The survey of 40 sources for the presence of radiation from excited hydrogen in the two lines 126α and 127α near 3200 MHz has provided a useful "midpoint" in the overall preliminary investigation of this aspect of the interstellar medium.

Evidence has been presented to show that, as far as present equipment sensitivities will allow, the excited hydrogen occurs in association with all HII nebulae or thermal emitters. Thus with the improved receivers already coming into use and increased angular resolution much data will become available to greatly enhance the study of galactic structure.

The necessity for caution in making calculations of electron temperature and turbulence in HII regions from the observed quantities T_l/T_c and $\Delta\nu$ has been shown. In some outstanding cases the observed recombination line profiles are not, in fact, of a simple Gaussian shape but exhibit two or more peaks. Improved angular resolution, even to 2′ or 3′ arc, would contribute much towards accurate estimates of the properties of HII regions.

VII. Acknowledgments

The authors are grateful to Miss Mary Chapman and Miss Janice Milton for their assistance in data processing. Miss Peggy Beswick computed the curves in Figure 1. Dr. Miller Goss drew attention to several publications that had not yet become available here. The authors thank him for his helpful suggestions and discussions and for the Gaussian curve-fitting computer programme in Section V.

Dr. M. A. Gordon, Massachusetts Institute of Technology, has kindly made available information on the Orion Nebula prior to publication.

VIII. References

Clark, B. G. (1965).—*Astrophys. J.* **142**, 1398–422.
Cohen, E. R., and Du Mond, J. W. M. (1965).—*Rev. mod. Phys.* **37**, 537–94.
Courtès, G., Cruvellier, P., and Georgelin, Y. (1967).—*Publs Obs. Hte Provence* **8**, 34.
Dieter, Nannielou H. (1967).—*Astrophys. J.* **150**, 435–51.
Dravskikh, Z. V., and Dravskikh, A. F. (1964).—*Astr. Tsirk. Byuro astr. Soobshch.* No. 292.
Gardner, F. F., and McGee, R. X. (1967).—*Nature, Lond.* **213**, 480–1.
Goldberg, L. (1966).—*Astrophys. J.* **144**, 1225–9.

Gordon, M. A., and Meeks, M. L. (1968).—Observations of 8 GHz continuum and hydrogen recombination lines in the Orion Nebula. *Astrophys. J.* (in press).

Goss, W. M. (1967).—OH absorption in the Galaxy. *Astrophys. J. Suppl. Ser.* 15, No. 137 (in press).

Gudnov, V. M., and Sorochenko, R. L. (1966).—Emission of excited hydrogen line n_{105}–n_{104} in certain nebulae in the Northern Sky. Fizicheskii inst. imeni P.N. Lebedev Akad. nauk S.S.S.R. Lab. Rad. Astr. Moskva.

Höglund, B., and Mezger, P. G. (1965).—*Science, N.Y.* **150**, 339–48.

Kardashev, N. S. (1959).—*Astr. Zh.* **36**, 838–44. Translated (1960) in *Soviet Astr.* **3**, 813–19.

Lilley, A. E., Menzel, D. H., Penfield, H., and Zuckerman, B. (1966).—*Nature, Lond.* **209**, 468–70.

McGee, R. X., and Gardner, F. F. (1967).—*Nature, Lond.* **213**, 579.

McGee, R. X., Gardner, F. F., and Robinson, B. J. (1967).—*Aust. J. Phys.* **20**, 407–20.

McGee, R. X., Milton, Janice A., and Wolfe, Wendy (1966).—*Aust. J. Phys. Astrophys. Suppl.* No. 1.

McGee, R. X., and Murray, J. D. (1963).—*Proc. Instn Radio Engrs Aust.* **24**, 191–6.

Menzel, D. H. (1937).—*Astrophys. J.* **85**, 330–9.

Menzel, D. H., and Pekeris, C. L. (1935).—*Mon. Not. R. astr. Soc.* **96**, 77–111.

Mezger, P. G., and Höglund, B. (1967).—*Astrophys. J.* **147**, 490–518.

Mills, B. Y., and Shaver, P. (1967).—Cornell–Sydney University Astr. Centre Preprint No. 69.

Oster, L. (1961).—*Rev. mod. Phys.* **33**, 525–43.

Palmer, P., and Zuckerman, B. (1966).—*Nature, Lond.* **209**, 1118.

Peimbert, M. (1967).—*Astrophys. J.* **150**, 825–34.

Penfield, H., Palmer, P., and Zuckerman, B. (1967).—*Astrophys. J.* **148**, L25–8.

Pottasch, S. (1965).—*Vistas Astr.* **6**, 149–206.

Seaton, M. J. (1964).—*Mon. Not. R. astr. Soc.* **127**, 177–84.

Sorochenko, R. L. (1965).—Akad. nauk S.S.S.R. Fizicheskii inst. Trudy 28, 65–72. Translated by Consultants Bureau, New York (1966).

Sorochenko, R. L., and Borodzich, E. V. (1964).—Paper presented at 12th Gen. Ass. IAU, Hamburg (unpublished).

Weedman, D. W. (1966).—*Astrophys. J.* **145**, 965–7.

Wild, J. P. (1952).—*Astrophys. J.* **115**, 206–21.

Wilson, O. C., Münch, G., Flather, Edith M., and Coffeen, Mary F. (1959).—*Astrophys. J. Suppl. Ser.* **4**(40), 199–256.

Zisk, S. H. (1966).—*Science, N.Y.* **153**, 1107–9.

AN INTERPRETATION OF THE DISTRIBUTION OF METRE WAVELENGTH RADIO EMISSION

By K. W. Yates*

[*Manuscript received November* 1, 1967]

Summary

A recent 85 MHz survey of the southern sky had an absolute calibration accuracy and resolution comparable with a number of surveys made for the northern skies. By combining the results of these surveys in both hemispheres a complete sky map has been produced, and in this paper an analysis is made of the distribution of the medium and high latitude emission. A fundamental difficulty encountered is the identification and isolation of the spurs of emission projecting from the galactic plane. Two hypotheses are proposed. The first attributes the spurs to a large-scale feature associated with the galactic core and the remaining emission to a galactic halo. The second postulates the origin of the spurs within the local spiral arm, which is itself considered to contribute significantly to the high latitude background. An upper-limit estimate of the emissivity of the local arm is made from currently available independent data. Using this result a model local arm is proposed, which, together with an isotropic component from beyond the Galaxy and a small additional galactic component, explains the observed distribution.

I. INTRODUCTION

Study of the metre wavelength background brightness distribution is an important source of information on galactic structure. Analysis of the distribution is made by identifying components in the background related to known galactic features. Most of the observed radiation may be explained by superposition of four components, three with galactic symmetries and one that is isotropic. These components are the halo, distributed about the galactic centre; the disk, distributed about the galactic plane; the local arm radiation, distributed about the arm axis; and the isotropic component being the extragalactic emission. Complete synthesis of the observed distribution requires, in addition, components with no obvious symmetries to account for the apparently random features of the background, such as the spur features and the fine detail visible with high resolution instruments. If independent information is available concerning the magnetic field and the electron energy density spectrum of any one of the regions, then synchrotron emission theory may be used to compute the magnitude of its contribution to the background. In the absence of this information the estimation of the relative magnitudes of the components must be made from symmetry arguments alone.

Early metre wavelength surveys (Baldwin 1955*a*; Hill, Slee, and Mills 1958) were confined to sections of the sky that were visible from particular observatories and their interpretation (Baldwin 1955*b*; Mills 1959) was further hampered by the

---

* School of Electrical Engineering, University of Sydney, N.S.W. 2006.

Aust. J. Phys., 1968, **21**, 167–83

absence of reliable data giving independent values for the galactic magnetic field strength and relativistic electron energy distribution. In recent years the position has greatly improved. Polarization measurements, both of the radio background and of sources seen through the Galaxy (Faraday rotation studies), have contributed to knowledge of the order and direction of the local field. Observations of Zeeman splitting of 21 cm spectral lines and of the polarization of starlight, together with the radio polarization data, have set upper and lower limits to the magnetic field magnitude. Moreover, the cosmic ray electron energy spectrum has been measured directly a number of times, giving reasonably consistent results.

A further improvement has been brought about by the recent completion of an 85 MHz survey of the southern sky (Yates, Wielebinski, and Landecker 1967). This survey was made with a beam of $3\cdot5^{\circ}\times3\cdot8^{\circ}$ making it most suitable for studies of large-scale galactic structure. The survey was also comparable in resolution and absolute calibration accuracy with a number of northern surveys. In the present paper a complete sky map is produced by combination of the results from both hemispheres. An analysis is then made of emission distribution away from the galactic plane. Because of the present doubt that has been cast upon the existence of the halo (an account of which is given in Felton 1966), the analysis is based on two alternative prior assumptions about the nature of the halo. These are that the halo contributes either a maximum or a minimum proportion of the background intensity.

The discussion commences with a description of the technique used for the production of the complete sky map, after which the map is used for a study of the spur features. Certain conclusions are reached, leading to an identification and isolation of the spur component. The remaining analysis is then based upon the minimum-halo assumption. The approach taken is to determine the maximum emission contribution from the local arm that is consistent with independent data, and to then make a study of the remaining emission, which on the basis of the simple subdivision referred to earlier, must originate in the halo and beyond the Galaxy.

II. Preparation of Complete Sky Map

Unless an exactly corresponding survey is available, a number of difficulties are encountered in combining northern and southern sky survey results. Combination of surveys made at different frequencies involves an assumption of spectrum, while combination of different resolution involves an imprecise smoothing process. Furthermore, unless the results are corrected to true full beam temperatures in an identical manner, the results are not completely comparable.

Three northern surveys were considered suitable for combination with the southern results referred to above in order to produce a complete sky map of the 85 MHz emission. Although each survey had one of the limitations mentioned, it was possible to combine them in such a way so as to produce minimum error. The $81\cdot5$ MHz $15^{\circ}\times2^{\circ}$ survey of Baldwin (1955*a*) was used to set the minimum temperature in the northern skies without making any assumption about the spectrum. The discrepancy in beamwidth is not important in the slowly changing regions near the minima, although an error associated with beam-temperature correction does remain. After establishing the baselevel, detailed structure visible from the north was filled in by smoothing the 178 MHz contours obtained by Turtle and Baldwin (1962), who used a $4^\circ \times 13'$ instrument. The temperature scale was deduced from the direct overlap between the two surveys on the North spur and the ratio of the 178 and 81·5 MHz minimum temperatures. This technique minimized any error from spectrum change between high and low temperature regions. Finally, some modifications were made to the map to account for the different methods of reduction to beam temperatures by scaling the 404 MHz survey of Pauliny-Toth and Shakeshaft (1962) to 85 MHz. The results of this 404 MHz survey are presented as modified beam temperatures of the same form as the southern results.

The complete sky map produced by this procedure is shown in Figure 1. Maximum relative error between directions in opposite hemispheres is estimated to be 10%. Internal consistency of each hemisphere is no doubt much better than this. In some directions the error is increased by further uncertainties. Firstly, the usefulness of the contours in the vicinity of the disk is reduced by the inadequate resolution. Secondly, the area enclosed by the dashed lines represents that portion of the sky observed by neither the 178 nor the 85 MHz surveys. Finally, crosses on the map indicate directions in which an estimate of the galactic background has had to be made because of obscuration by strong sources.

III. Spur Features

The great amount of detailed structure revealed by high resolution surveys has led to a belief that much of the radiation from high galactic latitudes emanates from isolated discrete features rather than from a uniform halo. Many attempts have been made to identify the more obvious features in order to ascertain their contribution to the background radiation. In particular, through lack of suitable high resolution studies elsewhere, the great North spur has received a lot of attention. Theories have been proposed in turn explaining the existence of the spur in terms of a collision between our Galaxy and another system (Johnson 1957), an anisotropic population of electrons radiating in a local ordered field (Tunmer 1958), an interarm link, and emission from a supernova remnant (Hanbury-Brown, Davies, and Hazard 1960).

At present no one theory can claim universal acceptance. The steep outer edge of the spur near $l = 35^\circ$, $b = 30^\circ$ supports the theory that an incomplete shell of emission is responsible for the feature. In a detailed study, Davies (1964) showed that a supernova remnant of the same age and size as the Cygnus loop, positioned about 30 pc from the Sun would produce such an emitting shell. Previously, van der Laan (1962) had shown that an expanding shock wave associated with the supernova causes a local increase in the magnetic field which is responsible for the increased emission. It was explained that the limited angular extent of the spur could be the result of expansion into a nonuniform medium.

Two experimental results cast doubt on the supernova theory. The first was the absence of any optical evidence for the feature, indicating that it must have a much higher radio to optical brightness ratio than other supernovae such as the Cygnus loop

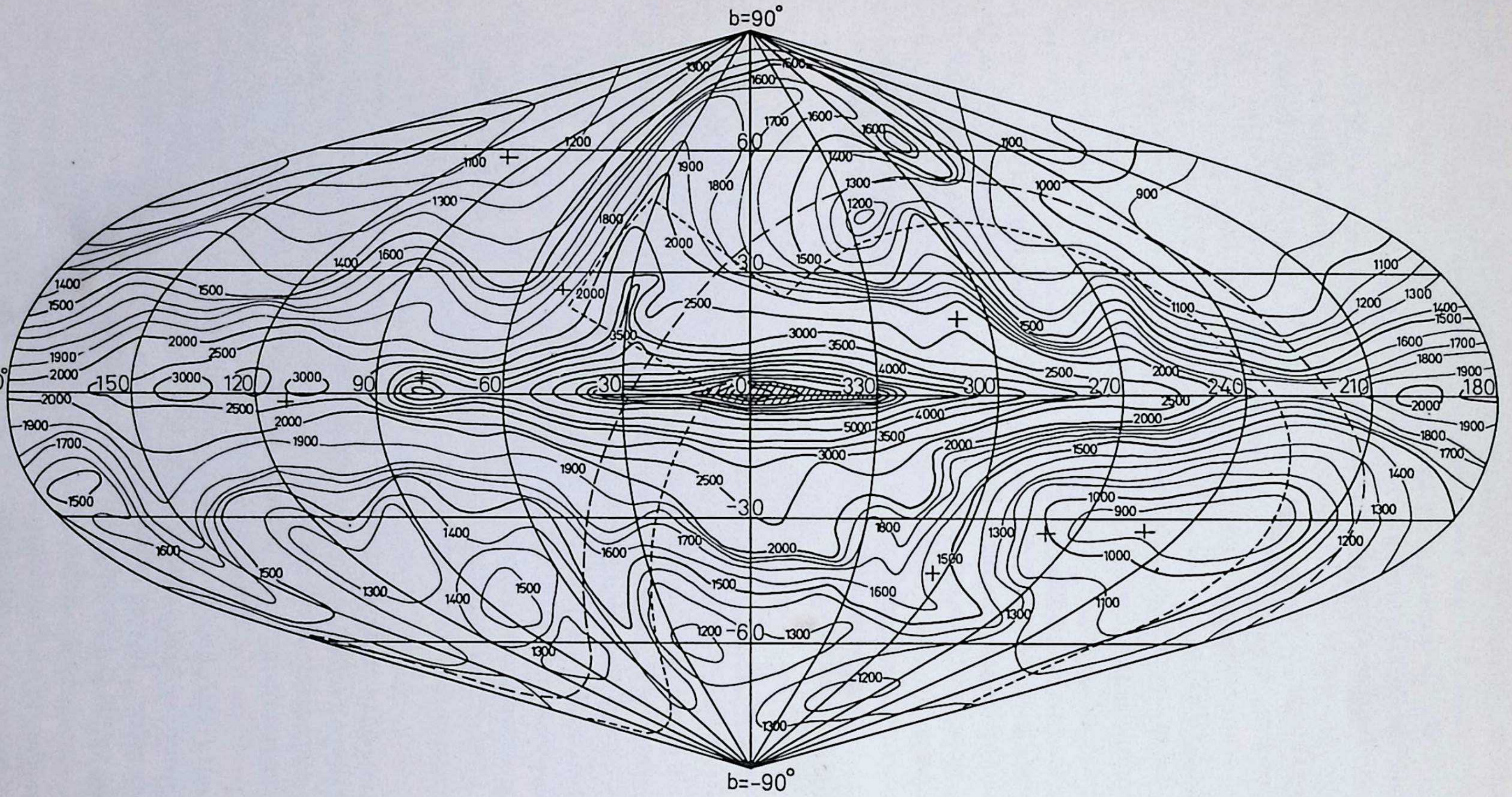
b=90°
60
30
=180°
150
120
90
60
30
0
330
300
270
240
210
180
-30
-60
b=-90°

Fig. 1.—Contours of brightness temperature at 85 MHz obtained from the combination of northern and southern surveys. The zone enclosed by the dashed lines and the directions indicated by the crosses have reduced accuracy (see text).

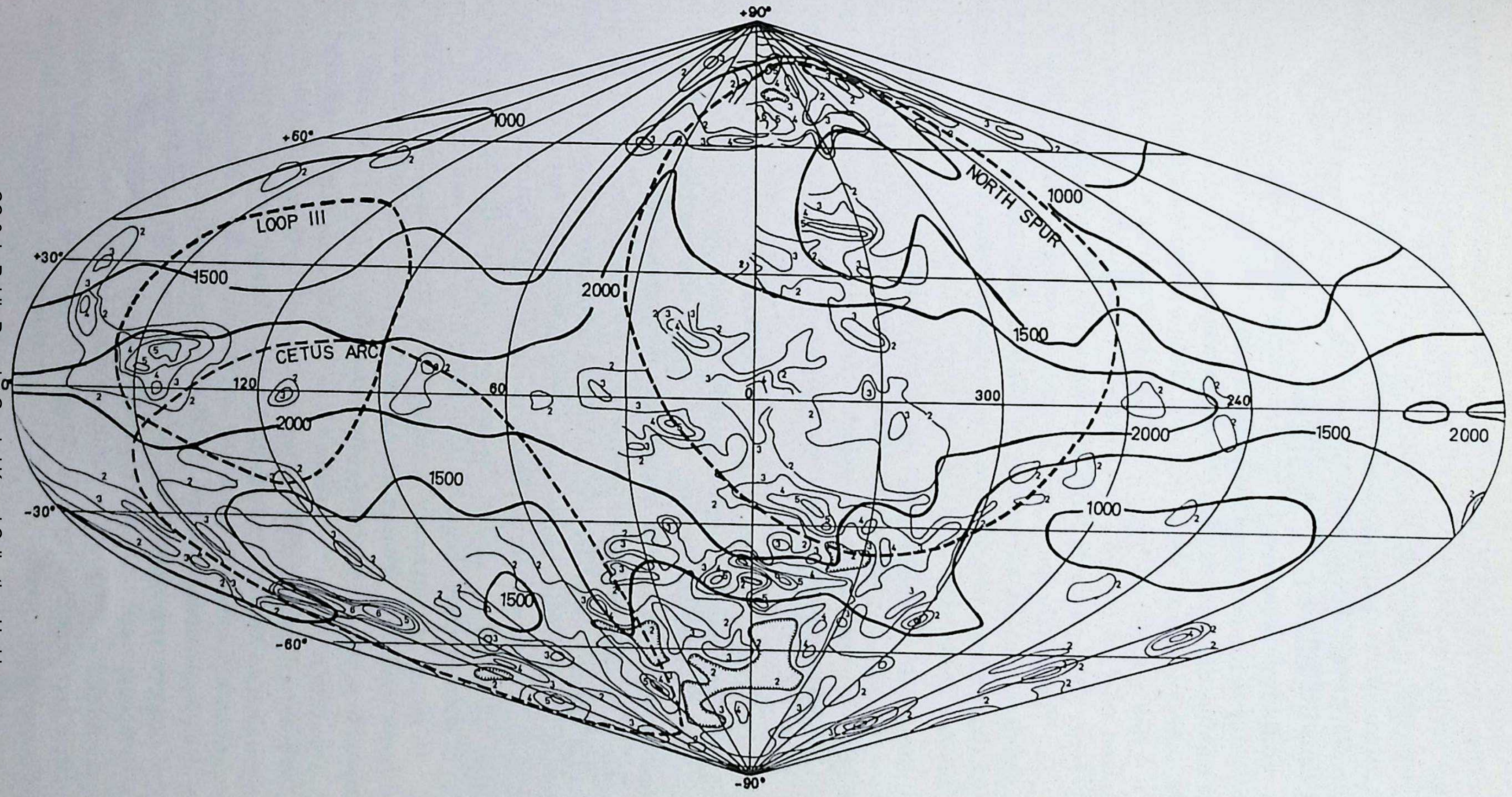
+90°
+60°
+30°
0
-30°
-60°
-90°
LOOP III
CETUS ARC
NORTH SPUR
120
60
0
300
240
1000
1500
2000

Fig. 2.—Contours of brightness temperature at 85 MHz for T = 1000, 1200, 1500, and 2000°K superimposed on the 408 MHz polarization results of Mathewson and Milne (1965). The dashed lines indicate the small circles associated with the spur features, as defined by Quigley and Haslam (1965).

(Davies, Hanbury-Brown, and Meaburn 1963). The second was the discovery of a feature of similar angular size south of the galactic plane, the so-called "Cetus arc" (Large, Quigley, and Haslam 1962).

The existence of two remnants in the close vicinity of the Sun implies a density in the distribution of such features through the Galaxy that would result in a higher background emission intensity than is observed.

Using results from a number of northern surveys, Quigley and Haslam (1965) were able to show, without suggesting a mechanism, that most of the large spurs of radiation leaving the galactic plane lie either along or within one of three small circles on the celestial sphere: the North spur along a circle with diameter 113°±3°, centred on $l = 330°\pm2°$, $b = 19\cdot5°\pm2°$; the Cetus arc along a circle with diameter 92°±3°, centred on $l = 100°\pm3°$, $b = -33°\pm3°$; and a third feature designated "Loop III" lying along a circle with diameter 71°±2° and centre $l = 124°\pm1°$, $b = 11\cdot5°\pm2°$. The North spur circle feature was closely examined by Haslam, Large, and Quigley (1964) at a frequency of 237 MHz with resolution of 1° and they demonstrated the existence of a number of concentric ridges and filaments of emission within the bounds of the circle.

Until the present it had not been possible to follow any of the features across the galactic plane with any certainty. Both the Cetus arc and the Loop III circles lie for part of their length along the galactic plane and are thus obscured by disk emission. The North spur circle has been inaccessible below the plane to northern observers.

Against the circle hypothesis of Quigley and Haslam, Rougoor (1966) proposed that the major ridges may be part of a single feature, such as a helix, with axis in the direction of $l = 110°$ and $b = 0°$. Once again, any southern extension of the proposed feature has been hidden from northern observatories.

The recent 85 MHz southern survey used for the production of the galactic map shown in Figure 1 provides the additional information required to obtain an overall picture of the spur phenomena. One large-scale feature having a size comparable with the spurs observed in the north, yet hitherto unrecorded, is visible in the south. This feature is first discernible from the disk emission at $l = 0°$, $b = -25°$. It then extends through $l = -335°$, $b = -37°$ and out to $l = -275°$, $b = -55°$. It is not so obviously a ridge and is much broader than equivalent brightness spurs visible in the north. Along the inner side of the feature further high temperature areas are apparent, particularly at $l = 320°$, $b = -30°$.

The orientation of this southern "arc" lends considerable support to the small-circle theory of Quigley and Haslam as against the theory that the spurs have origin in a single galactic feature such as a helix. This latter theory predicts a spur leaving the galactic plane southwards at $l = 270°$, but in fact this region is observed to be one of the coldest in the sky. In Figure 2, the paths of the three reference circles have been superimposed onto a galactic map showing the main 85 MHz brightness contours and the polarization temperatures observed at 408 MHz (Mathewson and Milne 1965). The strong orientation of the southern feature along the small circle associated with the North spur is apparent out to $l = 330°$, $b = 35°$. Beyond this point the centre line of the spur becomes tangential to the circle.

It has thus been established that features symmetrical about small circles may be followed across the galactic plane.

From a study of the complete sky maps in Figures 1 and 2, the following general remarks about the spur features may be made.

(1) High latitude ridge features broad enough to be detected by $3\cdot5°$ resolution are evident at the following galactic directions:

$l = 90°$, $b = 30°$; $l = 32°$, $b = 30°$; $l = 310°$, $b = 40°$;
$l = 268°$, $b = 25°$; $l = 160°$, $b = 30°$; $l = 160°$, $b = -40°$;
$l = 105°$, $b = -30°$; $l = 75°$, $b = -30°$; $l = 45°$, $b = -50°$;
and $l = 330°$, $b = -35°$.

Of these, all but three either lie along or are tangential to one of the three small circles on the celestial sphere.

(2) The remaining three features lie within one or other of these small circles. If north–south symmetry is assumed there is also considerable evidence for a general increase over the whole of the interior of the Cetus arc circle.

(3) In almost all cases the brightness decreases along the features as galactic latitude is increased. The exception is the bright region on the North spur circle at $l = 285°$, $b = 65°$.

(4) There is a strong concentration of the spur features towards the galactic centre. The strongest features lie within the zone $0 < l < 90°$ and $270° < l < 360°$.

(5) Examination of the polarization results of Mathewson and Milne (1965) reveals some evidence for an enhancement of polarization in the directions of the spurs, and the regions enclosed by the spur "circles". Mathewson and Milne drew attention to the fact that the directions in which polarization of the background has been detected are mainly confined to a 60° band containing the great circle through $l = 340°$ and 160°. The present results indicate that it is possible that at least some of the observed polarized emission has its origins within the spur features. It is also interesting to note that polarization has been detected in the direction $l = 285°$, $b = -22°$, a point on the small circle defined by the North spur at which no brightness ridge is discernible.

(6) For completeness in this study of the spur features it is noted that a difference in spectral index has been detected between the North spur and adjacent regions (Pugh 1964).

Items (1), (2), (5), and the exception referred to in (3) support the theory that the features have common origin and that they are local to the Sun. This is further supported by the fact that of the three discernible circle features, the brightest has the largest diameter. The theory that the features are due to local supernova remnants is attractive, particularly in view of the increased bright structure and polarization within the defined circles, although this explanation has the disadvantage of requiring the Sun to be in a very special location in the Galaxy.

Items (3) and (4), on the other hand, favour more the idea that the visible spurs are associated with features that are a part of the large-scale galactic structure, such as filaments associated with the galactic core, which extend up from the galactic plane. It is not possible to make a definite identification of the features from the data available, and reference must now be made to the basic assumptions referred to in the Introduction. If the minimum-halo assumption is accepted, some alternative to an extended emission distribution away from the galactic plane must be found to explain the observed medium and high latitude radiation intensity. The obvious alternative is emission of local origin. In this case it is reasonable to regard the spur features as being of common local origin, contributing to the background alongside emission from the local spiral arm. The maximum-halo assumption implies an insignificant contribution from local sources and consequently requires the spurs to be manifestations of large-scale features.

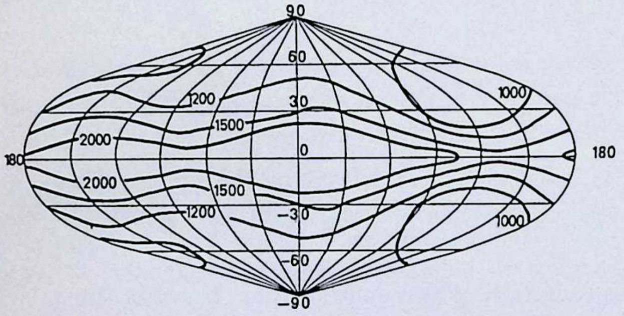

Fig. 3.—Contours of brightness temperature at 85 MHz below $T = 2000$°K after radiation associated with the spur features has been subtracted from the background in the manner indicated in the text.

The subsequent analysis is based on the assumption of a minimum-halo contribution. It is further assumed that the contribution of the spur features may be subtracted from the observed background in the following manner.

(1) Any components in the background with symmetry about, or associated with, the small circles previously defined are removed.

(2) The temperature of regions enclosed by the small circles is reduced in such a way as to produce symmetry in the background brightness about the galactic plane.

In following this procedure, directions in either galactic hemisphere outside the circular features are useful in setting maximum temperatures. The minimum temperature observed across a feature may be taken as the maximum temperature of the background beyond.

In Figure 3 a map is presented of the 85 MHz background radio emission after removal of the spur features in the manner indicated. Only contours below 2000°K are shown and subsequent analysis will be confined to corresponding latitudes. The magnitude of the radiation subtracted and its distribution about the small circles may be seen in Figure 4. This figure shows constant azimuth profiles of the features, in the range included by circles with diameters 20° either side of the diameter of the reference circle. For comparison, the observed background temperatures are plotted in the same way.

IV. Local Arm Radiation

Some contribution to the background radiation is to be expected from the local arm as a consequence of synchrotron emission by galactic electrons spiralling about the magnetic field aligned along the arm.

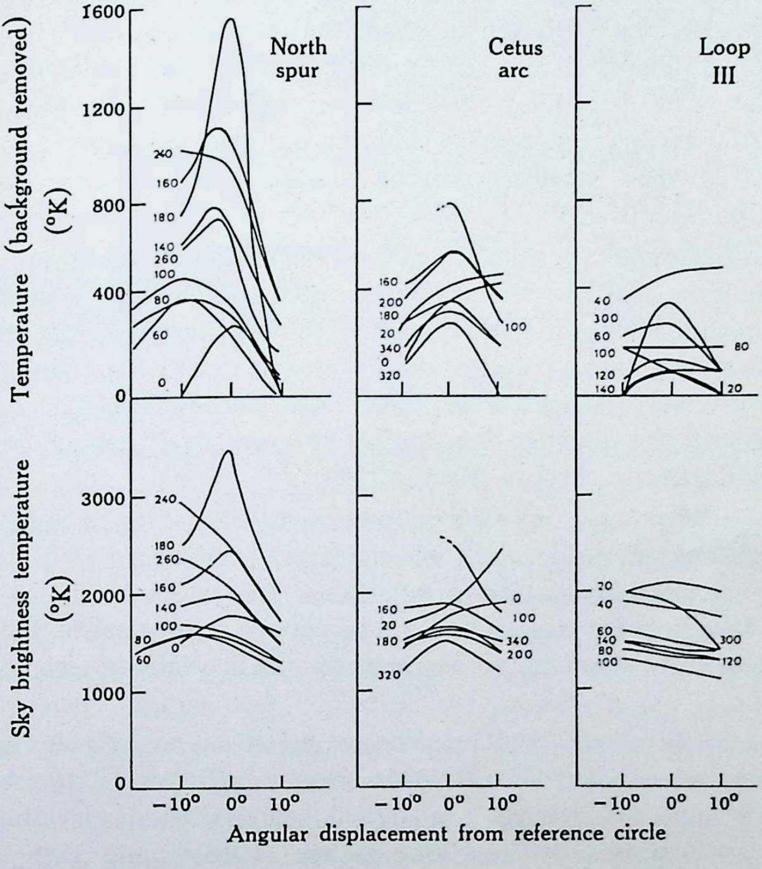

Fig. 4.—Constant azimuth profiles of the spur features showing the observed temperatures (*below*) and the temperatures after removal of the radiation distribution in Figure 3 (*above*).

A direct assessment of its magnitude, using synchrotron emission theory, would require a knowledge of field and electron conditions more detailed than present experimental techniques allow, since, although the existence of a magnetic field associated with the arm has been firmly established, its exact magnitude and form remain uncertain. Present experimental results are inadequate to permit a choice between the number of helical and aligned field models that have been proposed (Hoyle and Ireland 1961; Wentzel 1963; Hornby 1966). At best, the large number of independent investigations may be used to set upper and lower limits to the field and electron parameters required to compute the arm emissivity.

In the subsections that follow current independent results concerning the local field and electron conditions are reviewed as a prerequisite to setting up a model arm with a maximum contribution to the background radiation.

(a) *Local Magnetic Field*

The orderedness of the local arm field near the Sun has been established from the detection of polarized radio emission. Polarization results at 408 MHz from northern and southern hemispheres have been collected by Mathewson and Milne (1965), who found that the polarized emission is confined to a band 60° wide containing the great circle and crossing the plane at $l = 340°$ and 160°. Polarization is expected from nearby synchrotron radiation in directions at right angles to the axis of an ordered local field. The field direction implied by the band of polarization is thus $l = 250°$ and 70°. This direction for the field was supported by the Faraday rotation observations of polarized sources by Gardner and Davies (1966), which showed that for $b > 20°$ reverse rotations occurred in the zone $\sim 160° < l < \sim 340°$ to those in the zone $\sim 340° < l < \sim 160°$.

The radio polarization results give a good indication of conditions out to about 150 pc from the Sun (Mathewson and Milne), but there is evidence that the ordered field extends much further out. Field alignment in directions $l = 242°$, 235°, and 230° are indicated from the optical polarization of stars out to 250, less than 600, and more than 600 pc respectively (Schmidt 1956; Behr 1959; Serkowski 1962). The alignment compares well with the direction $l = 240°$ of the arm itself defined by O, B stars, HII regions, and galactic clusters (Becker 1964).

Hornby (1966) pointed out that radio brightness results also indicated a much more extended ordered field, since a brightness minimum occurs at $l = 240°$. This direction corresponds to a line of sight along the local field. If the order of the field were confined to solar regions and fields were tangled elsewhere (as would be expected from supernovae remnants), then a maximum in brightness would be expected in this direction.

The magnitude of the field may be estimated independently of brightness results by using stellar polarization and the Zeeman splitting of the 21 cm spectral line. The field value determined from optical polarization results depends on the nature of the polarizing particles. Visvanathon (1966) found that the observed wavelength dependence of polarization and extinction favoured dirty ice as the interstellar grains. The field magnitude required in this case has a minimum value of 3×10^{-5} gauss. Zeeman splitting of the 21 cm spectral line allows a completely independent measurement of field strength within neutral hydrogen clouds. Clouds studied so far indicate an upper limit of 10^{-5} gauss and in one case 5×10^{-6} gauss (Davies 1965). Although these results give conditions within clouds only, it seems unlikely that there is much variation in field conditions between cloud and intercloud regions, since the presence of a large-scale ordered field has been established.

The two independent methods of field determination therefore do not permit a choice between a high ($> 10^{-5}$ gauss) and a low ($< 5 \times 10^{-6}$ gauss) value for the magnitude of the aligned field. For the purpose of computing the upper limit of emissivity from the local arm, a value of $H = 10^{-5}$ gauss will be used here. This value is consistent with the conclusions of Okuda and Tanaka (personal communication) based on an analysis of the disk emission. Although a higher value of magnetic field is allowed by the optical evidence, the lower one was chosen to provide some compensation for simplicity of the model used. It is, for instance, most unlikely that the arm field is uniform to its extremities, dropping to zero outside the arm, as we will assume. Furthermore, it is possible that the arm emission originates in patches or filaments rather than uniformly. Both these situations would cause the radiation calculated from the simple model to be unrealistically high, and hence the choice of the lower value of H.

The direction taken for the model arm field will be that implied by the polarization results (that is, $l = 250°$ and $70°$). These results give the most accurate estimate of the alignment near the Sun, which is the region responsible for the medium and high latitude radiation to be studied.

(b) *Electrons within the Local Spiral Arm*

The population of electrons at any galactic location may be described by the function $n(\gamma,\phi,\theta)\,\mathrm{d}\gamma\,\mathrm{d}\Omega$, which specifies the number of electrons per unit volume with energies within the range defined by $\mathrm{d}\gamma$ and velocities directed within $\mathrm{d}\Omega$. For energies of interest here, this function may be approximated by a power law and thus

$$n(\gamma,\phi,\theta)\,\mathrm{d}\gamma\,\mathrm{d}\Omega = \bar{n}(\phi,\theta)\,\gamma^{-m}\,\mathrm{d}\gamma\,\mathrm{d}\Omega \qquad \mathrm{cm}^{-3}, \tag{1}$$

where ϕ and θ define the velocity direction and γ is the electron Lorentz factor ($\gamma = \dot{E}/m_0 c^2$). Some indication of the values of the unknowns, $\bar{n}(\phi,\theta)$ and m, applicable to the galactic electron population near the Sun is given by the results of high altitude electron flux measurements made from balloons. At low energies these measurements have limited value, since the flux of galactic electrons is distorted by solar modulation and contaminated both by secondaries generated in the overlying atmosphere and by electrons from the re-entrant albedo. These influences, however, become less dominant as electron energy increases and for $E > 2$ GeV the Earth flux, with the exception of its directional distribution, may be taken as being characteristic of a far more extended region.

Observations in the vicinity of the Earth indicate an isotropic distribution of velocity directions, but we are not immediately justified in assuming isotropy throughout the arm because of the possible influence of the Earth's magnetic field on the local flux. The likelihood of a genuine isotropy depends on the origin of the electrons. Although some generation mechanisms do establish an anisotropic flux, small field variations will act to re-establish randomness in the velocity directions and it is therefore unlikely that gross anisotropy exists. The absence of a narrow bright band of emission lying along a great circle in the celestial sphere (Tunmer 1958) further supports this contention, and it will therefore be assumed that the galactic population has an isotropic directional distribution. Equation (1) then becomes

$$n(\gamma)\,\mathrm{d}\gamma = n_0\,\gamma^{-m}\,\mathrm{d}\gamma \qquad \mathrm{cm}^{-3}. \tag{2}$$

Finally, before using the measured flux values to compute the local arm radiation, it is necessary to make the assumption that n_0 and m are constant along each line of sight through the arm. Since this study is confined to latitudes $> 10°$, corresponding to short lines of sight through the arm, this assumption is not unreasonable, even though a difference in m between arm and interarm regions has been reported (Bridle 1967).

We turn now to the flux measurements themselves. In Figure 5 results from a number of balloon experiments, which were made during the recent solar minimum, are presented (Bleeker *et al.* 1965; L'Heureux and Meyer 1965; Waddington and Freier 1965; Okuda and Tanaka, personal communication). The experiments chosen were those in which the differential energy spectrum was measured specifically. Other results of the integral spectrum were not included, since their representation in the differential form is strongly dependent on the value of m assumed (Felton 1966).

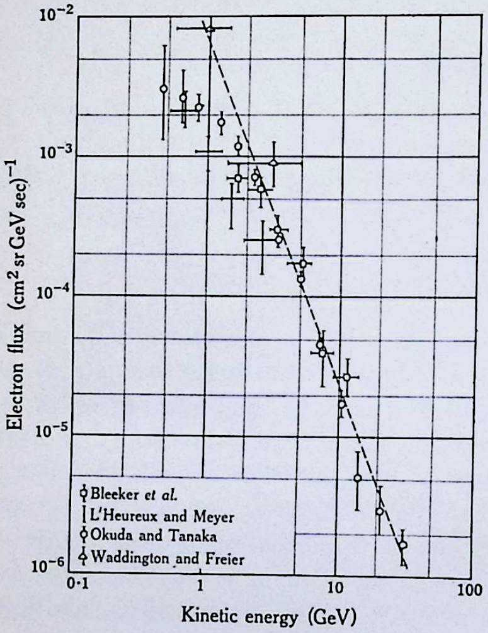

Fig. 5.—Results of balloon measurements of the differential energy spectrum of electrons for $0 \cdot 1 < E < 100$ GeV, made during the recent solar minimum.

Electrons contributing to the radiation at 85 MHz in a field of 10^{-5} gauss have energies centred on 0·7 GeV, which, unfortunately, lies within the zone where the measured flux depends on solar influence and secondary contamination. To overcome this we may extrapolate from the more accurate higher energy results, on the assumption that there is no change of slope in the spectrum for the range $0 \cdot 7 < E < 2$ GeV. The dashed line in Figure 5 shows the flux value to be adopted in this analysis, which corresponds to

$$N(E)\,\mathrm{d}E = 0 \cdot 7 \times 10^{-2} E^{-2 \cdot 4}\,\mathrm{d}E \qquad (\mathrm{cm}^2\,\mathrm{sr}\,\mathrm{GeV}\,\mathrm{sec})^{-1}.$$

(c) *Calculation of Radiation from the Local Arm*

The equivalent black body temperature T (°K) observed in the direction of an isotropic synchrotron emission region is given by the expression (Felton and Morrison 1966)

$$T = 5 \cdot 33 \times 10^{11} (4 \cdot 9 \times 10^{2})^{3-m}\, n_0(R)\, H^{(1+m)/2}\, \nu^{-(m+3)/2}, \qquad (3)$$

where H (μgauss) is the field, ν (MHz) is the frequency, R (kpc) is the dimension of the emission region, and n_0 is the coefficient of the electron energy density function (equation (2)) in CGS units. When the radiation is from an ordered field region, and $m \simeq 2{\cdot}4$, as in the present case, the term $H^{(1+m)/2}$ in equation (3) is replaced by $1{\cdot}25\, H^{(1+m)/2} \sin^{(1+m)/2} \theta$, where θ is the angle between the line of sight and the field.

In the previous subsections maximum values have been assigned to H and n_0 in accordance with the aim of finding the local arm with maximum emissivity that is consistent with available independent data. It remains to determine R, the dimension of the emitting region of the arm along the line of sight. The value assumed by R, for a particular observing direction, is a function of the profile of the arm, the location of its axis relative to the Sun, and, to a lesser extent, its radius of curvature from the galactic centre. Since this study is restricted to medium and high latitudes the assumption of infinite radius of curvature for the arm may be made without loss of accuracy.

The extent of the arm above the galactic plane may be deduced from the width of the band of radio emission along the galactic plane. A value of 250 pc to the half-power point was derived by Mills (1959), using the results of a high resolution 85 MHz survey. A similar conclusion was reached by McGee and Milton (1964), based on observations of neutral hydrogen. In the present study a simple model arm with uniform emissivity to its extremities is adopted, having a half-width of 400 pc perpendicular to the galactic plane. The axial ratio of the arm is taken to be $< 2{\cdot}5$ (Fujimoto 1961).

The position of the Sun relative to the arm axis may be deduced if the assumption is made that the radiation remaining after subtraction of both spur and local arm contributions from the background intensity is symmetrically distributed about the plane $l = 0°$. It will be recalled that the basic assumption behind this part of the analysis has been that the halo contribution is minimized. This new assumption simply defines the "halo" remaining to be symmetrically distributed about $l = 0°$.

Using equation (3) and the various parameters determined earlier, the radiation from a number of model arms was computed. To fulfil the requirement of symmetry of the remaining radiation two conditions had to be met. The first was that the Sun had to be immersed in the arm, and displaced slightly from its axis in the direction of the anticentre. This configuration was necessary to explain the greater high latitude intensity towards $l = 0°$ compared with that towards $l = 180°$. The second was that the field associated with the arm had to expand slightly about the axis $l = 250°$ instead of being strictly parallel to it. Although there is evidence for the latter situation from the asymmetry of the band of background polarization (Mathewson and Milne 1965), the former condition detracts from the feasibility of the model, since it contradicts neutral hydrogen evidence that the Sun is on the inside edge of the local arm.

The radiation from the model arm that is consistent with the field and electron values and the symmetry condition is shown in Figure 6. The arm profile is also shown in this figure. This has a minor axis of 400 pc and an axial ratio of 2, with the Sun displaced 100 pc from the axis in the direction of the anticentre. The magnetic field associated with the arm has a magnitude of $1{\cdot}2 \times 10^{-5}$ gauss and expands from an axis along $l = 250°$ with $7\cdot5°$ semi-axis angle. The electron energy density spectrum taken for the model was

$$N(E)\,\mathrm{d}E = 0\cdot7\times10^{-2}\,E^{-2\cdot4}\,\mathrm{d}E \qquad (\mathrm{cm^2\,sr\,GeV\,sec})^{-1}.$$

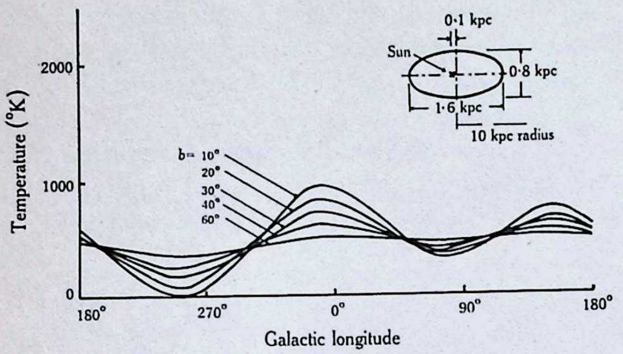

Fig. 6.—Contribution to the background radiation from the model arm adopted for latitudes $b = 10°$, $20°$, $30°$, $40°$, and $60°$.

In Figures 7(*a*) and 7(*b*) the background temperature variation before and after subtraction of the radiation associated with the model is shown. The model satisfies the symmetry conditions to within the accuracy justified by the arbitrariness of the method used to assess the contribution of the spur features. Truly symmetric profiles are indicated by the dashed lines in Figure 7(*b*).

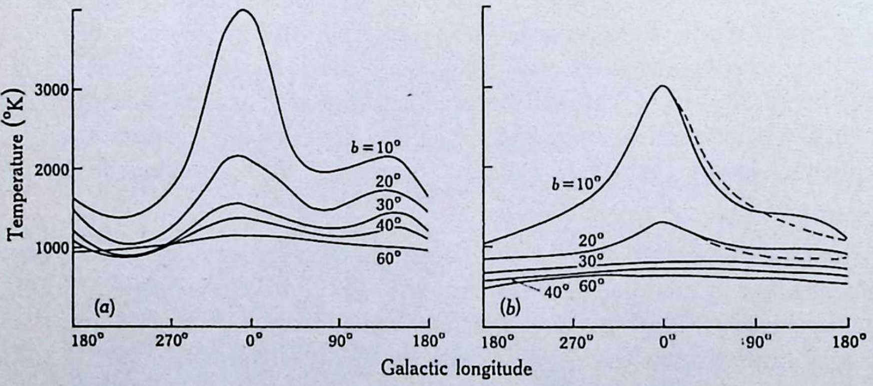

Fig. 7.—Constant latitude profiles of the background brightness temperature (*a*) after radiation from the spur features has been subtracted and (*b*) after radiation from both the spur and the local arm model has been subtracted.

Before proceeding it is worth examining the plausibility of the assumptions that have been made in developing the model. The location of the Sun and the nature of the field have already been referred to. The magnitude of the local arm contribution is very sensitive to the value assumed for the local arm field. A field of $1\cdot7\times10^{-5}$ gauss would result in an arm contribution double the size of the one adopted (derived from a field of $1\cdot2\times10^{-5}$ gauss). On the other hand, a model with a field of 8×10^{-6} gauss and circular cross section with 400 pc radius would have made only a minor contribution to the background. A similar conclusion would follow if synchrotron emission regions were confined to clouds instead of being uniformly spread through the arm. A check on the emissivity value adopted is the temperature of the outer arm and this may be observed as the disk temperature in the direction of the anticentre. The outer arm temperature of 1000°K compares reasonably well with the value of 1800°K, which is the temperature of the model arm observed along its cross section major axis, considering the latter is an upper-limit estimate. The process of elimination of the local arm radiation from the background is also fairly dependent on the orderedness of the field. Mills (1959) found step increases in the disk emission when looking along the spiral arms, indicating some departure of the field from strict alignment with the arms, but in the present study (confined to latitudes of $> 10°$) lines of sight are sufficiently limited for one to be confident of the assumption of orderedness. Some departure from this condition obviously occurs in the spur-feature sources. If any of the major assumptions adopted are in error, i.e. if the arm contributes only a minor proportion to the background or if some other kind of model is more appropriate, then another large-scale emission distribution must be found to explain the asymmetry of the background emission about $l = 0°$.

V. REMAINING RADIATION—HALO AND EXTRAGALACTIC COMPONENTS

The distribution shown in Figure 7(*a*) represents the portion of the background radiation that cannot reasonably be ascribed to either the spur features or the local arm. It consists of a galactic component exhibiting symmetry about the plane $l = 0°$ and an isotropic extragalactic component. The galactic component is not characteristic of a uniform spherical emitting halo since it shows an extended minimum in the direction of the pole.

It is beyond the scope of this discussion to consider a detailed halo model to fit the derived remainder distribution. Nevertheless, it is interesting to note that the remainder distribution that has been derived is consistent with a galactic model proposed by Sciama (1962). According to this theory, the galactic magnetic field is not closed and the halo is that part of the intergalactic gas distribution under gravitational control of the Galaxy. As a result of this gravitational control, electrons and field are concentrated according to the mass distribution of the Galaxy and the halo emissivity of this model thus decreases from the galactic plane and centre. Such a model would produce both the low latitude increase in temperature towards the galactic centre and the high latitude extended minima in the direction of the pole, which are apparent in the present results in Figure 7(*b*).

A test for the similarity of the derived "remainder" emission and the emission from a *uniform* disk is given by considering the latitude variation of their brightness. For a uniform disk T is proportional to $\operatorname{cosec} b$, where b is the latitude. In Figure 8 brightness temperatures for three longitudes (derived from Fig. 7(*b*)) are plotted against $\operatorname{cosec} b$. In directions towards the galactic centre, where nonuniformity in the emission is to be expected, there is considerable departure from linearity. However, at $l = 240°$ the linear region extends from 10° to 60°, consistent with a model in which extragalactic sources contribute E and the remainder originates in a disk-shaped "halo" contributing A to the pole temperature, where

$$A \operatorname{cosec} 10° + E = 1340°\mathrm{K}, \qquad A \operatorname{cosec} 60° + E = 580°\mathrm{K}.$$

These equations give $A = 165°\text{K}$ and $E = 390°\text{K}$. The value for E is well within the range of values for the extragalactic component given by independent measurements (results of which are summarized in Yates and Wielebinski 1966).

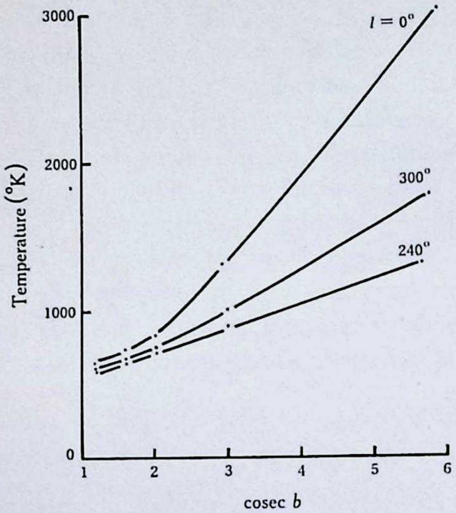

Fig. 8—Variation of cosec b with the brightness temperatures given in Figure 7(b) for $l = 0°$, 240°, and 300°.

VI. Conclusions

A study of the complete sky distribution of the metre wavelength continuum emission has led to the following general conclusions.

(1) Apart from the general concentration of emission towards the galactic plane and centre, the distribution is characterized by a number of ridges or spurs extending from the plane to high latitudes in each hemisphere.

(2) Most of the spurs can be traced along small circles in the celestial sphere, some of which cross the galactic plane. This configuration favours the theory that the spur radiation has local origin. On the other hand, there appears to be a concentration of the stronger features towards the galactic centre, supporting the theory that the spurs are a manifestation of a large-scale galactic phenomenon.

(3) If it is assumed that the spur features are of local origin, the apparent small circle orientation of the features may be used, together with the assumption of symmetry of the remaining emission about the galactic plane, as a basis for the subtraction of the spur contribution from the background.

(4) The remaining emission is not symmetrically distributed about latitude $l = 0°$. It may be explained as being the sum of emission from a model local arm whose emissivity is consistent with the upper limits indicated by independent data, and an additional component that does show symmetry about $l = 0°$.

(5) The additional component has broad minima in the direction of the galactic pole, in which direction it contributes about half the observed intensity. It is satisfactorily explained by the integrated extragalactic emission and a small galactic component, resembling more closely a uniform disk than a uniform spherical halo.

VII. Acknowledgments

This work was carried out as part of the research programme of the School of Electrical Engineering at the University of Sydney. The author wishes to thank Dr. R. Wielebinski of the School of Electrical Engineering and Professor B. Y. Mills of the School of Physics for useful discussions.

VIII. References

Baldwin, J. E. (1955*a*).—*Mon. Not. R. astr. Soc.* **115**, 684.
Baldwin, J. E. (1955*b*).—*Mon. Not. R. astr. Soc.* **115**, 690.
Becker, W. (1964).—*Z. Astrophys.* **58**, 202.
Behr, A. (1959).—Veroff. Univ. Sternwerte Gottingen. No. 126.
Bleeker, J. A. M., Burger, J. J., Scheepmaker, A., Swanenburg, B. N., and Tanaka, Y. (1965).—Proc. 9th Int. Conf. on Cosmic Rays. Vol. 1, p. 327.
Bridle, A. H. (1967).—*Mon. Not. R. astr. Soc.* **136**(2), 219.
Davies, R. D. (1964).—*Mon. Not. R. astr. Soc.* **128**, 173.
Davies, R. D. (1965).—Proc. 9th Int. Conf. on Cosmic Rays. Vol. 1, p. 35.
Davies, R. D., Hanbury-Brown, R., and Meaburn, J. E. (1963).—*Observatory* **83**, 179.
Felton, J. E. (1966).—*Astrophys. J.* **145**, 589.
Felton, J. E., and Morrison, P. (1966).—*Astrophys. J.* **146**, 686.
Fujimoto, M. (1961).—*Sci. Rep. Res. Insts Tôhoku Univ.* A **45**, 202.
Gardner, F. F., and Davies, R. D. (1966).—*Aust. J. Phys.* **19**, 129.
Hanbury-Brown, R., Davies, R. D., and Hazard, C. (1960).—*Observatory* **80**, 191.
Haslam, C. G. T., Large, M. I., and Quigley, M. J. S. (1964).—*Mon. Not. R. astr. Soc.* **127**, 273.
Hill, E. R., Slee, O. B., and Mills, B. Y. (1958).—*Aust. J. Phys.* **11**, 530.
Hornby, J. M. (1966).—*Mon. Not. R. astr. Soc.* **133**, 213.
Hoyle, F., and Ireland, J. G. (1961).—*Mon. Not. R. astr. Soc.* **122**, 461.
Johnson, H. M. (1957).—*Publs astr. Soc. Pacif.* **69**, 130.
van der Laan, H. (1962).—*Mon. Not. R. astr. Soc.* **124**, 179.
Large, M. I., Quigley, M. J. S., and Haslam, C. G. T. (1962).—*Mon. Not. R. astr. Soc.* **124**, 405.
L'Heureux, J., and Meyer, P. (1965).—Proc. 9th Int. Conf. on Cosmic Rays. Vol. 1, p. 321.
McGee, R. X., and Milton, J. A. (1964).—*Aust. J. Phys.* **17**, 128.
Mathewson, D. S., and Milne, D. K. (1965).—*Aust. J. Phys.* **18**, 635.
Mills, B. Y. (1959).—*Publs astr. Soc. Pacif.* **71**, 267.
Pauliny-Toth, I. I. K., and Shakeshaft, J. R. (1962).—*Mon. Not. R. astr. Soc.* **124**, 61.
Pugh, J. F. (1964).—Ph.D. Thesis, Cambridge University.
Quigley, M. J. S., and Haslam, C. G. T. (1965).—*Nature, Lond.* **208**, 741.
Rougoor, G. W. (1966).—*Astrophys. J.* **144**, 852.
Schmidt, M. (1956).—*Bull. astr. Insts Neth.* **13**, 15.
Sciama, D. W. (1962).—*Mon. Not. R. astr. Soc.* **123**, 317.
Serkowski, K. (1962).—*Adv. Astr. Astrophys.* **1**, 289.
Tunmer, H. (1958).—*Phil. Mag.* **3**, 370.
Turtle, A. J., and Baldwin, J. E. (1962).—*Mon. Not. R. astr. Soc.* **124**, 459.
Visvanathon, N. (1966).—Symp. on Radio and Optical Studies of the Galaxy (Mt. Stromlo, 1966), p. 31.
Waddington, C. J., and Freier, P. S. (1965).—Proc. 9th Int. Conf. on Cosmic Rays. Vol. 1, p. 339.
Wentzel, D. (1963).—*A. Rev. Astr. Astrophys.* **1**, 198.
Yates, K. W., and Wielebinski, R. (1966).—*Aust. J. Phys.* **19**, 389.
Yates, K. W., Wielebinski, R., and Landecker, T. L. (1967).—*Aust. J. Phys.* **20**, 595.

A SURVEY OF THE GALACTIC PLANE AT 85 AND 150 MHz

By R. Wielebinski,* D. H. Smith,* and X. Garzón Cárdenas*

[*Manuscript received December* 4, 1967]

Summary

A survey has been made of the intense emission regions along the galactic plane from $l = 60°$ to $290°$ at frequencies of 85 and 150 MHz with the 210 ft radio telescope at Parkes. Aerial temperatures were accurately measured, essentially in terms of thermal standards, with a known baselevel. The spectrum and "steps" of the observed emission have been investigated.

I. Introduction

The investigation of nonthermal emission from the Galaxy is best carried out at metre wavelengths. To achieve any degree of resolution, which is particularly necessary for observation of the galactic plane region, very large instruments are required. While unfilled aperture instruments achieve good resolution there is also a need for well-calibrated surveys made with instruments of medium resolution. The 210 ft radio telescope at Parkes, N.S.W., was made available for the present investigation, which was carried out at frequencies of 85 and 150 MHz. The measured beamwidths are $3\cdot6°$ by $3\cdot8°$ and $2\cdot2°$ by $2\cdot2°$ at 85 and 150 MHz respectively. The aerial temperatures have been accurately calibrated, in terms of absolute thermal standards, with a known baselevel.

Surveys of the galactic plane region have been made at metre wavelengths by a number of observers. The 85 MHz Cross survey with a resolution of 50′ (Hill, Slee, and Mills 1958; Mills, Hill, and Slee 1958) remains, at metre wavelengths, the only such high resolution investigation. Surveys made in Cambridge at 85 MHz by Baldwin (1955), at 178 MHz by Turtle and Baldwin (1962), and at 38 MHz by Kenderdine (1963) have been prevented by geographical position from reaching regions of the galactic plane near the galactic centre. A recent survey at 85 MHz, made at Parkes by Yates, Wielebinski, and Landecker (1967) with the same instrument as the present investigation, concentrated on regions of sky away from the intense galactic plane regions. Even a cursory inspection of this medium resolution survey reveals that the "step" observed by Mills (1959) in the direction $l = 325°$ can be discerned. This observation prompted the present investigation.

There are many high resolution surveys of the galactic plane in the decimetre wavelength range. Surveys by Large, Mathewson, and Haslam (1961) and Komesaroff (1966) at 408 MHz, Moran (1965) at 610 MHz, Wilson and Bolton (1960) and Nicholson (1965) at 960 MHz, Westerhout (1958) at 1390 MHz, and Mathewson, Healey, and Rome (1962) at 1440 MHz are available in this range of wavelengths. All these surveys have been made with instruments giving beamwidths smaller than 1°. These high resolution surveys at decimetre wavelengths reveal a wealth of detail, particularly of the thermal radiation observed close to the galactic plane. The separation of the thermal and nonthermal components was carried out by most of the observers making high frequency surveys (e.g. Westerhout 1958; Mathewson, Healey, and Rome 1962). The separation was always based on the use of the 85 MHz high resolution survey of Hill, Slee, and Mills (1958) and on various assumptions about spectra and baselevels.

---

* School of Electrical Engineering, University of Sydney, N.S.W. 2006.

The present survey was used to derive sky maps at 85 and 150 MHz of a region of the galactic plane that is symmetrical about the galactic centre within the limits $+10^\circ > b > -10^\circ$, $60^\circ > l > 290^\circ$. The absolutely calibrated aerial temperatures and the aerial polar patterns have been used to estimate spectral index. Profiles were drawn at constant galactic latitudes to reveal the structure of emission steps.

II. EQUIPMENT

The aerial used for the survey was the 210 ft fully steerable paraboloidal reflector at Parkes. At 85 MHz the primary feed was a $\lambda/2$ dipole mounted in the focus, $\lambda/4$ below the reflecting area of the aerial cabin. The dipole was matched to an impedance near 50 Ω by adjustment of the dipole length and of the position relative to the reflecting plate. Final matching at 85 MHz was done by means of a matching unit. The primary feed for 150 MHz consisted of two dipoles mounted orthogonally relative to the 85 MHz dipole. The 150 MHz two-dipole feed is a standard configuration used for the Parkes reflector (Minnett and Yabsley 1966). The isolation of the two feeds was measured to be better than 45 dB at both survey frequencies.

The receivers used at both frequencies were switched radiometers of the type described by Yates, Wielebinski, and Landecker (1967). The receiver configuration allowed remote switching to a matched load at ambient temperature and calibration with a monitored noise current. The standards of noise were calibrated in terms of absolute thermal standards. A noise source similar to that described by Harris (1961) was used at 150 MHz, and a well-matched noise diode type CV 2398 was used for the 85 MHz calibrations. The linearity of the receivers was checked for the complete range of deflections encountered in the survey of the galactic plane.

The bandwidth of the 30 MHz i.f. amplifiers in both receivers was 1 MHz, which could be reduced to 150 kHz by a filter in case of interference. During most of the observing period, conditions allowed the use of the full bandwidth of 1 MHz. The output deflections on a pen recorder gave readings of aerial temperature measured above the baselevel, which was obtained by replacing the aerial with a matched termination at ambient temperature (taken to be 285°K).

III. OBSERVATIONS

The observing procedure for most of the scans was to drive in declination through the galactic plane at constant right ascension using a telescope drive rate of 2·5 deg/min. Some of the northern portions of the galactic plane were observed at transit with a telescope zenith-angle drive rate of 5 deg/min. Additional right ascension scans at a number of declinations were made to provide a check on temperature values. The intervals of scanning were chosen to allow some beam overlap at 150 MHz. South celestial pole calibrations were performed occasionally to check overall system performance. The observations were made during two nights in August 1967.

The sky temperatures determined from the scans were plotted as maps in new galactic coordinates and are shown in Figures 1(*a*) and 1(*b*), which correspond to frequencies of 85 and 150 MHz respectively. The graphical method of reduction from paper chart records may introduce up to 0·5° error in placement of the isophotes.

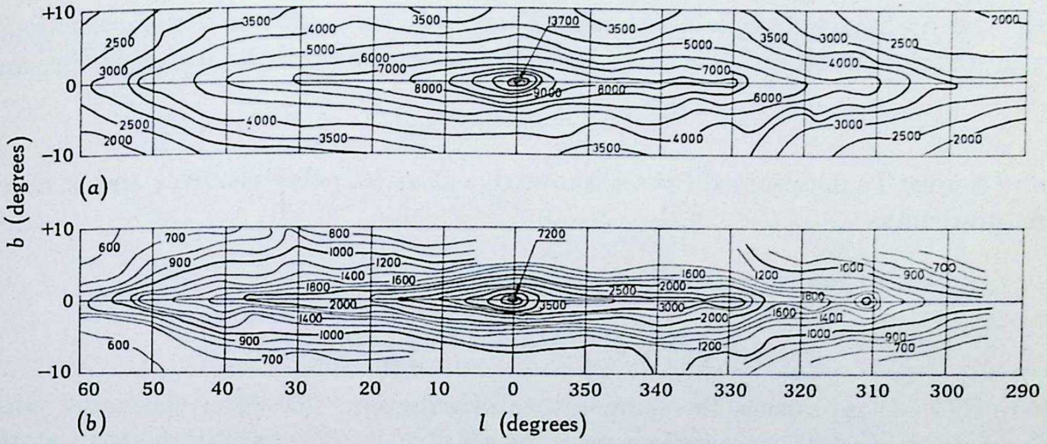
+10
0
−10
b (degrees)
(a)
2500
3000
2500
2000
3500
4000
5000
6000
7000
8000
4000
3500
3500
13700
9000
8000
3500
3500
5000
7000
6000
4000
3500
3000
4000
3000
2500
2500
2000
2000
(b)
600
700
900
600
800
1000
1200
1400
1600
1800
2000
1400
1000
900
700
7200
3500
2500
1600
2000
3000
2000
1200
1200
1000
900
700
1800
1600
1400
1000
900
700
60
50
40
30
20
10
0
350
340
330
320
310
300
290
l (degrees)

Fig. 1.—Maps of aerial temperatures (°K) along the galactic plane at (*a*) 85 MHz, 3·7° beam, and (*b*) 150 MHz, 2·2° beam.

The random errors in aerial temperatures are estimated as 3% r.m.s. at both frequencies. This value includes the mismatch error deduced from the scatter of observed south pole temperatures, and the error due to noise fluctuations on records. Systematic errors of 7% at 85 MHz and 4% at 150 MHz must be allowed in the survey temperatures. The systematic errors are the combination of absolute noise diode calibration error, ground effects, and error due to leakage of the reflector, particularly at the lower survey frequency. A leakage of electromagnetic radiation may arise due to the discontinuous nature of the surface of the Parkes reflector. The reflector panels are small in size compared with the wavelength of 3·5 m. The ground elevation dependence was investigated by tracking two areas of sky from zenith down to a zenith angle of 60°. A temperature reduction of 100 degK was observed at 85 MHz for zenith angles near 60°. No ground elevation effects were observed at 150 MHz, at which frequency a more directive primary feed was used. The possibility of a systematic reduction in the sky temperatures at 85 MHz was investigated by comparing the aerial temperatures measured in the survey by Yates, Wielebinski, and Landecker (1967) and the temperatures measured with a broad beam aerial at 85 MHz by Yates and Wielebinski (1966). A systematic reduction of 5% was found to be consistent with the measurements.

IV. TEMPERATURE SPECTRUM

The temperature scales of the galactic plane surveys at 85 and 150 MHz are determined in terms of thermal standards with a known baselevel. The data are therefore suitable for spectral investigations. The temperature spectral index β is given in terms of temperatures T_1 and T_2 measured at wavelengths λ_1 and λ_2 respectively by

$$T_1/T_2 = (\lambda_1/\lambda_2)^{\beta}\,. \tag{1}$$

The temperatures T_1 and T_2 in equation (1) should be either "full beam temperatures" or else aerial temperatures measured with aerials that are scaled with wavelength. In the case of the present surveys, the aerial beams are dissimilar and full beam temperatures have not been determined. Therefore a further beam factor k is required in the spectral equations. The spectral equation for the present frequencies becomes

$$(1\cdot 76)^{\beta} = k(T_{85}/T_{150})\,, \tag{2}$$

where k must be determined from a knowledge of aerial polar patterns and temperature gradients.

The aerial temperature T_{a} is given by

$$T_{\mathrm{a}} = \int_{4\pi} T(\theta,\ \phi)\ f(\theta,\ \phi)\ \mathrm{d}\omega \div \int_{4\pi} f(\theta,\ \phi)\ \mathrm{d}\omega\,, \tag{3}$$

where $T(\theta,\ \phi)$ represents the temperature distribution, $f(\theta,\ \phi)$ is the aerial power polar pattern, and $\mathrm{d}\omega$ is an increment of the solid angle. To simplify the computation the aerial beam can be divided into n areas. The aerial temperature T'_{a}, given by the expression

$$T'_{\mathrm{a}} = \sum_{r=1}^{n} T_r a_r p_r \div \sum_{r=1}^{n} a_r p_r\,, \tag{4}$$

is an approximation of the aerial temperature T_{a}. In (4) T_r is the mean temperature of the rth region, a_r is the area of this region, and p_r is the mean level of the polar pattern in the rth region. The beam factor k can be determined by convolution of either of the two surveys by the beams at both survey frequencies. This convolution process will yield two values of k:

$$k_1 = \frac{T_{85}(150\ \text{beam})}{T_{85}(85\ \text{beam})} \qquad \text{and} \qquad k_2 = \frac{T_{150}(150\ \text{beam})}{T_{150}(85\ \text{beam})}\,. \tag{5}$$

The two beam factors should be identical if temperature gradients are low. A mean value of k_1 and k_2 can be used.

The polar patterns of the survey aerials were obtained from a number of scans through the strong radio sources, Pictor, Fornax, Virgo, and Hydra. These polar patterns in the E and H planes are shown in Figure 2. The scans were made in right ascension and declination at various parallactic angles. The 150 MHz polar pattern was found to be circular with a half-power beamwidth of 2·2°. The corresponding 85 MHz beam was elliptical with half-power beamwidths of 3·6° by 3·8°. The polar patterns are taken to be zero, on a linear scale, at beamwidths of 9° at 85 MHz and 5·5° at 150 MHz. In the derivation of the beam correction factors k_1 and k_2, the beam area was divided into 41 squares, each 1° by 1°. Mean values of the power level were assigned to the squares at both frequencies from the knowledge of aerial polar patterns. At the frequency of 150 MHz, 16 of the outer squares were assigned the power level value of zero. The mean temperature values for each of the 41 points for both survey frequencies were derived from the maps in Figures 1(*a*) and 1(*b*) for a number of sky directions away from the galactic centre.

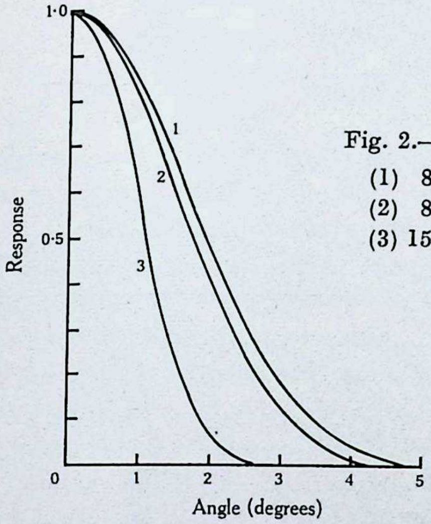

Fig. 2.—Aerial power polar patterns for:
(1) 85 MHz, *E* plane
(2) 85 MHz, *H* plane
(3) 150 MHz, *E* and *H* planes

Table 1

VALUES OF BEAM FACTOR k AND SPECTRAL INDEX β FOR 12 POINTS AWAY FROM GALACTIC CENTRE

Point	b (deg)	l (deg)	T_{85} (°K)	T_{150} (°K)	$\frac{T_{85}}{T_{150}}$	k	β
1	+5	45	3550	940	3·8	1·04	2·4
2	0	45	4900	1650	3·0	1·09	2·1
3	−5	45	3750	800	4·6	1·05	2·8
4	+5	35	4500	1050	4·3	1·06	2·7
5	0	35	6500	2050	3·2	1·11	2·2
6	−5	35	4200	980	4·3	1·07	2·7
7	+5	325	4000	1000	4·0	1·04	2·5
8	0	325	6500	2000	3·3	1·09	2·2
9	−5	325	4000	1050	3·8	1·04	2·5
10	+5	315	3250	1000	3·3	1·05	2·2
11	0	315	5500	1800	3·1	1·09	2·2
12	−5	315	3250	900	3·6	1·04	2·4

The detailed computations for the derivation of the beam factors k_1 and k_2 were made for 12 points away from the galactic centre. The galactic direction, the temperatures, and the mean value k of the beam factors k_1 and k_2 are given in Table 1. The mean value of k is 1·05 for directions away from the galactic plane, and 1·1 on the galactic plane. The mean value of the temperature spectral index is found to be $\beta = 2 \cdot 5 \pm 0 \cdot 15$ for directions away from the galactic plane, and $\beta = 2 \cdot 2 \pm 1$ on the plane. The lower value of the temperature spectral index on the plane is consistent with the fact that the thermal emission component that has $\beta < 2 \cdot 5$ is concentrated along the galactic plane. The temperature ratio T_{85}/T_{150} was computed for some 100 points in various directions. For most of these points the value of the temperature ratio was found to be

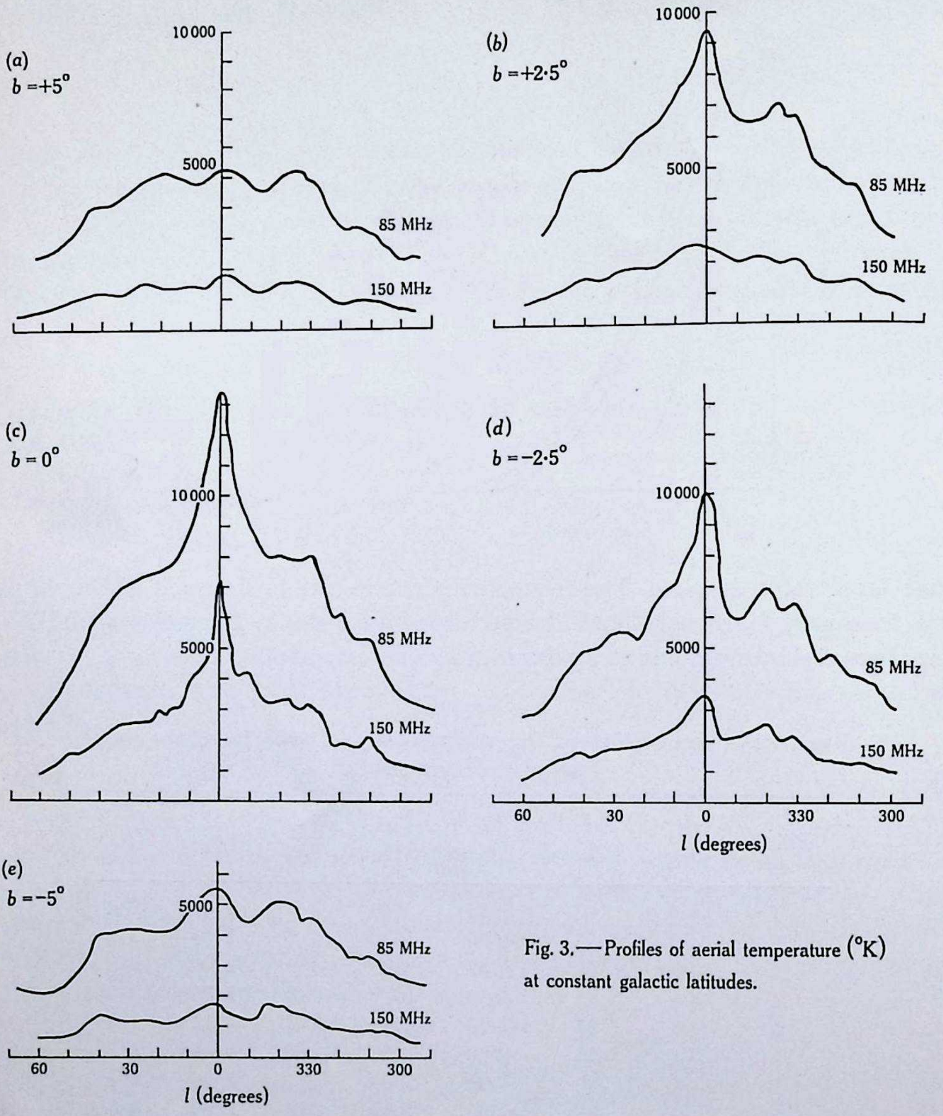

Fig. 3.—Profiles of aerial temperature (°K) at constant galactic latitudes.

$$T_{85}/T_{150} = 3 \cdot 7 \pm 0 \cdot 25 \,.$$

The ratio with the beam factor $k = 1 \cdot 05$ corresponds to the value of spectral index $\beta = 2 \cdot 4 \pm 0 \cdot 15$. Reduced values of the temperature ratio are found for some points in the directions $l = 340°$, $b = -5°$ and $l = 335°$, $b = +5°$. The temperature ratio values are as low as $3 \cdot 1 \pm 1$, which is significantly lower than for all other directions.

V. Steps of Emission

Features that are clearly discernible in the maps shown in Figure 1 are the sudden increases in measured aerial temperatures along the galactic plane. These sharp increases or "steps" can be seen towards $l = 305°$ and $325°$ from the sky maps. By producing diagrams of aerial temperatures at constant galactic latitude the steps can be investigated more effectively. Five diagrams have been drawn from the original records rather than from the maps, where some loss of detail is unavoidable. The profiles at $b = +5°$, $+2{\cdot}5°$, $0°$, $-2{\cdot}5°$, and $-5°$ are shown in Figures 3(*a*)–3(*e*) respectively.

Examination of the temperatures along the galactic plane shown in Figure 3(*c*) indicates the existence of steps in the directions $l = 305°$, $325°$, $345°$, $14°$, and $35°$. The step effects are more pronounced at 150 MHz, which may be due only to the higher resolution of the beam. The positions of the steps agree well with the positions of the original observations of these features by Mills (1959). The observations also confirm the fact that the features visible in the northern sky are not as well defined as those in the south. The diagrams for latitudes $b = \pm 2{\cdot}5°$ contain much the same information as the galactic plane section. However, in the direction $l = 335°$ both at $b = +2{\cdot}5°$ and $-2{\cdot}5°$, a step is replaced by a "bump". This effect is even more pronounced at $b = +5°$ and $-5°$. A further observation is that there is some evidence for a similar bump at $l = 25°$, $b = +5°$ but none is seen at $l = 25°$, $b = -5°$. One conclusion that must be drawn from the diagrams in Figure 3 is that the directions near $l = 330°$ and $30°$ correspond to some special galactic features.

VI. Discussion

The regions of the sky near the galactic plane have been mapped at 85 and 150 MHz. The maps extend over 120° of galactic longitude, symmetrically about the galactic centre. The aerial temperatures have been absolutely calibrated.

The temperature spectral index has been found for a number of points near the galactic plane. The mean value for the directions $b = \pm 5°$ (from Table 1) is $\beta = 2{\cdot}5 \pm 0{\cdot}15$. This value of spectral index is in agreement with that for the galactic spectrum derived from low resolution scaled aerial measurements (Yates and Wielebinski 1966), which was also $\beta = 2{\cdot}5 \pm 0{\cdot}15$ for a somewhat lower frequency range. These values of spectral index indicate a nonthermal emission mechanism. Along the galactic plane the values of spectral index are lower, indicating a mixing of emission from thermal and nonthermal mechanisms. Some reduction in spectral index occurs also in the directions $l = 340°$, $b = -5°$ and $l = 335°$, $b = +5°$. This significant reduction of spectral index away from the plane may be due to the extension of the thermal emission from the plane into higher galactic latitudes.

The steps of emission along the plane are very pronounced in the directions $l = 325°$ and $305°$. The temperature gradient in the direction $l = 35°$ is not very steep. The assertion of the existence of a ring of emission by Komesaroff (1966) requiring symmetrical temperature steps must be questioned. There is, however, evidence from surveys (Baldwin 1955; Yates, Wielebinski, and Landecker 1967) that the directions $l = 30°$ and $325°$ are associated with spurs rising into both hemispheres. The directions $l = 30°$, $b = +20°$ and $l = 330°$, $b = -20°$ are associated with the two most intense spur features in the sky. The possibility of the association of these spurs with the thermal emission in the plane should be further investigated.

The absolute calibration of the present aerial temperatures enables a comparison to be made with the temperatures observed in the high resolution survey of Hill, Slee, and Mills (1958). To achieve this, a convolution procedure similar to that used in the derivation of the spectral index must be used. This was done for eight points away from the galactic centre. The mean ratio of convolved high resolution temperatures to the present aerial temperatures gave a factor of $1\cdot 27 \pm 0\cdot 1$. If allowance is made for the possibility of a 5% systematic error that reduced the aerial temperatures of the present survey, then the brightness temperatures of Hill, Slee, and Mills (1958) are 22%±8% too high. It should be noted, however, that the conversion of the aerial temperatures to beam temperatures (discussed in Yates, Wielebinski, and Landecker 1967) will in fact bring the temperature values into good agreement.

The present survey, although limited by resolution, clearly shows the advantages of galactic observations at metre wavelengths. Observations of other galaxies like M 31 at metre wavelengths, if made with sufficient resolution, could add much to the understanding of our own Galaxy, which we must observe only from within.

VII. ACKNOWLEDGMENTS

The work described in this paper is a part of the research programme in radio astronomy of the School of Electrical Engineering, University of Sydney. We wish to thank Dr. E. G. Bowen and Mr. J. G. Bolton, CSIRO, for permission to use the Parkes radio telescope. Observations were made with the help of Mr. K. W. Yates and Mr. T. L. Landecker.

One of us (X.G.C.) was a recipient of a post-graduate scholarship from the Instituto Nacional de la Investigación Científica, México.

VIII. REFERENCES

BALDWIN, J. E. (1955).—*Mon. Not. R. astr. Soc.* **115**, 684.
HARRIS, I. A. (1961).—*Proc. Instn elect. Engrs* B **108**, 651.
HILL, E. R., SLEE, O. B., and MILLS, B. Y. (1958).—*Aust. J. Phys.* **11**, 530.
KENDERDINE, S. (1963).—*Mon. Not. R. astr. Soc.* **126**, 41.
KOMESAROFF, M. M. (1966).—*Aust. J. Phys.* **19**, 75.
LARGE, M. I., MATHEWSON, D. S., and HASLAM, C. G. T. (1961).—*Mon. Not. R. astr. Soc.* **123**, 113.
MATHEWSON, D. S., HEALEY, J. R., and ROME, J. M. (1962).—*Aust. J. Phys.* **15**, 354.
MILLS, B. Y. (1959).—Symp. IAU No. 9 (Paris 1958). pp. 431–46.
MILLS, B. Y., HILL, E. R., and SLEE, O. B. (1958).—*Observatory* **78**, 116.
MINNETT, H. C., and YABSLEY, D. E. V. (1966).—*Proc. Instn Radio Engrs Aust.* **27**, 304.
MORAN, M. (1965).—*Mon. Not. R. astr. Soc.* **129**, 447.
NICHOLSON, G. D. (1965).—*Publs astr. Soc. Pacif.* **77**, 260.
TURTLE, A. J., and BALDWIN, J. E. (1962).—*Mon. Not. R. astr. Soc.* **124**, 459.
WESTERHOUT, G. (1958).—*Bull. astr. Insts Neth.* **14**, 215.
WILSON, R. W., and BOLTON, J. G. (1960).—*Publs astr. Soc. Pacif.* **72**, 331.
YATES, K. W., and WIELEBINSKI, R. (1966).—*Aust. J. Phys.* **19**, 389.
YATES, K. W., WIELEBINSKI, R., and LANDECKER, T. L. (1967).—*Aust. J. Phys.* **20**, 595.

RADIO EMISSION OF 158 GALAXIES

By H. M. Tovmassian*

[*Manuscript received October* 30, 1967]

Summary

Radio observations of 158 mainly spiral galaxies have been made at 21 cm and additional observations have been made for some at 11 and 75 cm. The observations at 11 and 21 cm were made with the CSIRO 210 ft radio telescope at Parkes and those at 75 cm with the east–west arm of the Mills Cross at the Molonglo Observatory of the University of Sydney. Radio emission was detected from central regions of 20 of the galaxies.

I. Introduction

Optical investigation of the central parts of barred spiral galaxies (Kalloglian and Tovmassian 1964; Tovmassian 1965, 1966*a*) and their radio observations (Tovmassian 1966*b*) have shown that a definite correlation exists between the optical appearance of the nuclear region of a galaxy and its radio emission (Tovmassian 1966*c*). Enhanced radio emission, originating in the nuclear region of the galaxy, is observed only when there is optical evidence of activity at the nucleus. Such evidence may be that either (1) the galaxy possesses a starlike nucleus with Byurakan classification type 4 or 5, or (2) there is evidence of explosive phenomena at the nucleus (Byurakan type 2 or 2S).

The present paper contains the results of radio observations of 158 galaxies, most of which are spirals. The observations were undertaken to permit further investigation of the correlations between the likelihood of radio emission from galaxies and the structure of their central parts. In order to have sufficient overlap of the radio and optical studies (the latter being made at Byurakan by other observers), only galaxies north of declination —20° were chosen for observation. However, in the final list (Table 1) of the galaxies investigated a few elliptical and irregular galaxies and a few southern galaxies are included. The photographic magnitudes of galaxies given in the table are corrected Harvard magnitudes from the catalogue compiled by de Vaucouleurs and de Vaucouleurs (1964). Morphological types of galaxies are from de Vaucouleurs (1963).

The basic survey of galaxies was made in August 1965 at 21 cm using the 210 ft radio telescope of the Australian National Radio Astronomy Observatory, CSIRO, at Parkes. The observing procedure and equipment employed were the same as for the observations of barred spiral galaxies and galaxies with peculiar spectra and colour that are described in two previous papers (Tovmassian 1966*b*, 1966*d*).

---

* Visiting Scientist, Division of Radiophysics, CSIRO, Box 76, P.O. Epping, N.S.W. 2121; present address: Byurakan Astrophysical Observatory, Armenia, U.S.S.R.

Aust. J. Phys., 1968, **21**, 193–9

Table 1

LIST OF GALAXIES OBSERVED AT 21 CM

No.	Galaxy		Type	m_{pg}	No.	Galaxy		Type	m_{pg}
1	NGC	128	SOp	12·8	48	NGC	2217	SBO	12·0
2		134*†	SABbc	11·2	49		2613	SAb	11·2
3		157*†	SABbc	11·4	50		2716	SBO	13·6
4		210	SABb	11·9	51		2775*†	SAab	11·7
5		214	SABc	13·1	52		2784	SAO	11·8
6		428*†	SABm	11·8	53		2811	SBa	12·8
7	IC	1613	Im	9·8	54		2835	SBc	11·4
8	NGC	488	SAb	11·6	55		2855	SAOa	12·4
9		514	SABc	12·3	56		3109	Im	10·6
10		520*†	Pec	12·4	57		3145	SBbc	12·5
11		524	SAO	12·2	58		3162	SABbc	12·3
12		578	SABc	11·5	59		3169*	SAap	11·7
13		615	SAb	12·5	60		3190	SAap	12·6
14		681	SABab	13·0	61		3607	SAO	11·8
15		718	SABa	12·7	62		3611	SAap	13·0
16		772	SAb	11·5	63		3623	SABa	10·5
17		778	SAO/a	13·4	64		3626	SAO	12·1
18		864	SABc	11·9	65		3646	SAbcp	11·8
19		877*†	SABbc	12·3	66		3672	SAc	11·8
20		908*†	SAc	11·2	67		3887	SBbc	11·9
21		1084*	SAc	11·9	68		3955	IO	13·0
22		1087*†	SABc	11·7	69		4038/9*	IBmp	10·6
23		1140	Im	13·4	70		4123	SBc	12·3
24	HB	914	SBc	12·0	71		4162	SAbc	12·8
25	NGC	1156	IBm	12·6	72		4178	SBdm	12·2
26		1201	SAO	11·9	73		4212	SAbc	12·3
27		1297	SAc	13·0	74		4216	SABb	11·2
28		1302*†	SBO/a	11·8	75		4254*	SAc	10·6
29		1326	SBO	11·6	76		4273	SBc	12·5
30		1332	SAO	11·7	77		4281	SO	12·3
31		1359	SBmp	12·9	78		4324	SAO	12·6
32		1380*	SAO	11·6	79		4382	SAOp	10·5
33		1385*†	SBcd	12·1	80		4429	SAO	11·6
34		1415	SABO/a	12·7	81		4433*	SABab	13·1
35		1417*†	SABb	12·8	82		4438†	SAO/ap	11·2
36		1487	Pec	12·6	83		4450	SAab	11·4
37		1512	SBO	11·6	84		4459	SAO	12·1
38		1518	SBdm	12·4	85		4461	SBO	12·3
39		1533	SBO	11·9	86		4474	SAO	13·0
40		1543*	SBO	11·9	87		4517	SAcd	11·3
41	IC	2056	SBOp	12·7	88		4519	SBd	12·4
42	NGC	1637*†	SABc	11·5	89		4526*	SABO	10·8
43		1744*†	SBd	11·9	90		4527	SABbc	11·3
44		1832*†	SBbc	12·6	91		4535	SABc	10·8
45		1964	SABb	11·8	92		4565*	SAb	10·3
46		2139*†	SABcd	12·7	93		4567	SAbc	12·4
47		2207*†	SABbcp	12·0	94		4647	SABc	12·2

* Observed also at 11 cm.

† Observed also at 75 cm.

TABLE 1 (*Continued*)

No.	Galaxy	Type	m_{pg}	No.	Galaxy	Type	m_{pg}
95	NGC 4666*	SABc	11·7	127	NGC 6753*	SAb	12·1
96	4691	SBO/ap	12·0	128	6769	SABap	12·7
97	4699	SABb	11·1	129	6771	SBO	13·8
98	4713	SABd	12·6	130	IC 4797	E5–6	12·5
99	4725	SABabp	10·2	131	HA 85	SO	12·4
100	4753	IO	10·8	132	NGC 6810	SAa	12·6
101	4762	SBO	11·7	133	6861	SAO	12·6
102	4781	SBd	12·1	134	IC 4889	E5–6	12·7
103	4900	SBc	12·2	135	NGC 6868	E2	12·3
104	4995	SABb	12·2	136	6962	SABab	13·1
105	5087	SAO	12·8	137	7029	E6	12·6
106	5101	SBO/a	11·9	138	7070A*	IO	—
107	5248*	SABbc	10·8	139	7171	SBb	12·7
108	5360*†	IO	11·1	140	7177	SABb	12·3
109	5363*†	IO	11·5	141	7218	SAcd	12·9
110	5364*†	SAbcp	11·2	142	7252	SAO	13·1
111	5468	SABcd	12·4	143	7302	SAO	13·4
112	5493	SOp	12·8	144	7332*	SOp	12·5
113	5668*†	SAd	12·2	145	7377	SAO	12·8
114	5746	SABb	11·6	146	7392	SABc	12·9
115	5806	SABb	12·6	147	7448	SABc	12·3
116	5838	SAO	12·1	148	7541*†	SBbc	12·7
117	5859	SBbc	13·6	149	7585	SAOp	12·8
118	5878	SAb	12·6	150	7606	SAb	11·7
119	5962*†	SAc	12·6	151	7625	SAap	13·2
120	6070	SAcd	12·5	152	7678	SABc	12·9
121	6181	SABc	12·8	153	7679	SBOp	13·3
122	6384*	SABbc	11·8	154	7716	SABb	13·2
123	IC 4662	IBm	12·0	155	7727	SABap	11·8
124	NGC 6574*	SABbc	13·3	156	7742	SAb	13·0
125	6674*	SBm	13·2	157	7769*	SAb	13·0
126	6699	SABb	12·7	158	7814*†	SAab	11·9

* Observed also at 11 cm. † Observed also at 75 cm.

With the 210 ft telescope and the degenerate parametric amplifier at 21 cm it is possible to detect sources as faint as 0·2 f.u., provided repeated scans are made across the position of the galaxy. A total of 158 galaxies were investigated.

The galaxies in or near the positions from which radio emission was detected at 21 cm were observed in September 1965 at 11 cm with the 210 ft telescope. The aim of these observations was to increase the accuracy of positional measurements of the detected sources and thus the reliability of identifications. The beamwidth of the telescope at 11 cm is about 7′·5 arc and thus is about one-half of the width at 21 cm. A total of 42 galaxies were investigated. Those with flux densities in excess of 0·2 f.u. could be easily recognized on the records. Owing to the weakness of the detected sources, their positions could only be determined with an accuracy that is estimated as 1′·5 to 2′ arc at either wavelength. Finally, in October 1965, 23 galaxies that had been detected at the shorter wavelengths were observed at 75 cm with the east–west arm of the Mills Cross at the Molonglo Radio Astronomical Observatory of the University of Sydney. The beamwidth of the telescope is about 1′·5 arc in right ascension and about 4° in declination. Sources with flux densities of about 1 f.u. could be detected with certainty.

The accuracy of flux density measurements for weak sources is about 30% at all three wavelengths. The calibration of the receiver equipment was achieved by injection of the standard signals from discharge tubes to the inputs of the receivers, and by observations (a few times each day) of strong radio sources with well-known positions and flux densities.

II. Results

(a) *Accuracy of Identifications*

The detected sources were assumed to be identified with corresponding galaxies when the discrepancies between their coordinates were not larger than 1′·5 arc. For the sources observed at 75 cm the maximum acceptable discrepancy in right ascension was taken as 1′ arc. Under these conditions 20 of the detected sources were identified with the corresponding galaxies.

To avoid false conclusions the expected number of chance coincidences of radio sources with galaxies must be calculated, and to do this we need to know the number of radio sources per unit solid angle having flux densities greater than a given value. The number of sources per steradian can be estimated using the source counts given in the Parkes catalogue of radio sources (Bolton, Gardner, and Mackey 1964; Price and Milne 1965; Day *et al.* 1966; Shimmins *et al.* 1966), which are based on observations with the same telescope and receivers. The catalogue extends to sources with flux densities as low as 0·4 f.u. at 21 cm. In the present list of identifications there are sources as weak as 0·25 f.u. Source counts given in the Parkes catalogue show that the graph of (log N)/(log S) at 21 cm has a cutoff for sources with flux densities less than 1 f.u. Obviously this cutoff is due to the confusion of radio sources at 408 MHz, at which the finding surveys for the Parkes catalogue have been made. By linearly extrapolating the straight parts of the (log N)/(log S) curves to sources with flux densities equal to 0·25 f.u., we find that the expected number of sources per steradian with flux densities greater than 0·25 f.u. is about 1800.

If the distribution of sources is random, it would thus be anticipated that within 158 areas, each 1′·5 arc in radius, less than 1 source would be found. In fact, 20 sources were detected not further than 1′·5 arc from the centres of corresponding galaxies.

On the other hand, from the known density of sources (1800 per steradian) at a level of 0·25 f.u. at 1410 MHz we are far from the confusion limit, because at this level there is 1 source per 42 beamwidths. In addition, this level is well in excess of the sensitivity limit of the telescope. Thus we may conclude that almost all the sources detected are real and are physically associated with the corresponding galaxies.

The fact that 14 out of 20 sources were also detected at 11 cm with better resolution increases appreciably the certainty of most of the identifications. The remaining 6 sources were observed at 21 cm only and the flux densities of 4 of them exceed 0·3 f.u., which is three times more than the limit sensitivity of the receiver. The existence of 2 of these sources is less certain than the others because of nearby confusing sources. None of the identified sources were detected at 75 cm.

TABLE 2

GALAXIES WITH DETECTED RADIO EMISSION

(1)	(2)	(3)	(4)	(5)	(6)	(7)	(8)
NGC No.	R.A. (1950) h m	ΔR.A. m	Dec. (1950) ° ′	ΔDec. ′	Flux Density (f.u.)* at: 11 cm	21 cm	75 cm
134	00 27·9	0	−33 32	−1	0·25(4)	0·40(5)	<1·0(1)
520	01 22·0	0	+03 32	0	0·25(6)	0·25(6)	<1·0(2)
908	02 20·8	−1	−21 27	−1	0·25(4)	0·30(5)	<1·0(1)
1084	02 43·5	0	−07 47	−1	0·30(4)	0·40(4)	<1·0(1)
1385	03 35·2	+1·5	−24 40	−1	0·20(7)	0·30(5)	<1·0(1)
1832	05 10·0	+1	−15 47	+1·5	0·20(5)	0·30(15)	<1·0(1)
2207	06 14·3	0	−21 21	0	0·20(4)	0·40(6)	<1·0(1)
3109	10 00·8	+1·5	−25 55	+1·5	—	0·25(6)	—
4038/9	11 59·3	0	−18 35	0	0·40(4)	0·60(6)	—
4254	12 16·3	0	+14 42	0	0·40(4)	0·50(4)	—
4433	12 25·0	0	−08 01	+1	0·20(5)	0·25(4)	—
4438	12 25·3	+1	+13 17	0	—	0·30(7)	<1·0(1)
4527	12 31·6	−1·5	+02 56	0	—	0·30(6)	—
4567	12 34·0	+1·5	+11 32	+1	—	0·40(6)	—
4666	12 42·6	−1	−00 12	0	0·30(5)	0·60(4)	—
5248	13 35·1	−1	+09 08	+1	0·25(4)	0·35(7)	—
5363	13 53·6	0	+05 29	0	0·25(6)	0·25(4)	<1·0(2)
6384	17 29·9	+1·5	+07 06	+1·5	<0·20(8)	0·40(4)	—
6810	19 39·4	−1	−58 47	−1	0·25(6)	0·30(4)	—
7541	23 12·2	0	+04 15	+1	<0·20(6)	0·35(7)	<1·0(1)

* Number of scans is shown in parentheses after each value.

The list of the galaxies from which radio emission has been detected is given in Table 2. The first column of the table contains the NGC numbers of the galaxies. The right ascensions and declinations of the galaxies and the corresponding displacements of the sources are given in columns 2, 3, 4, and 5. Displacements of the sources to the east and to the north from the centres of the corresponding galaxies are given as positive. Columns 6, 7, and 8 contain the flux densities of the sources at 11, 21, and 75 cm respectively. The numbers of scans are given in parentheses.

(*b*) *Comparison with Other Radio Data*

Twenty-six of the galaxies on our list have been observed also by Heeschen and Wade (1964) at 1400 MHz; they found radio emission from six. The present observations confirmed the existence of radio emission from four of the galaxies: NGC 1084, 4254, 4753, and 5248. The radio sources in the regions of two other galaxies, NGC 157 and 1417, are displaced at about 6′ arc in declination from the centres of corresponding galaxies and are therefore omitted from our list of identifications. However, radio emission was detected from two other galaxies in their list: NGC 4038 and 6384.

NGC 157 and 1084 are in the list of 22 galaxies observed by Kurilchik and Sytsko (1965) at 32 cm. They detected radio emission from the latter galaxy only.

(c) *Angular Sizes*

None of the sources were resolved by the present observations. Thus their dimensions are not larger than about 4′ to 5′ arc.

TABLE 3

SPECTRAL INDICES, RADIO MAGNITUDES, RADIO INDICES, AND ABSOLUTE RADIO MAGNITUDES OF SOURCES OBSERVED AT TWO WAVELENGTHS

(1) NGC No.	(2) α	(3) m_{21}	(4) R_{21}	(5) $-M_{21}$	(1) NGC	(2) α	(3) m_{21}	(4) R_{21}	(5) $-M_{21}$
134	0·7	12·5	2·5	18·5	4433	0·3	13·1	0·7	17·2
520	0·0	13·0	1·7	18·0	4438	1·1	12·8	2·5	17·5
908	0·1	12·9	2·4	18·2	4527	—	12·9	2·9	17·4
1084	0·7	12·4	1·1	17·8	4567	—	12·5	0·6	17·8
1385	0·5	13·0	1·4	18·2	4666	1·1	12·1	2·5	18·8
1832	0·8	13·0	1·0	17·5	5248	0·4	12·7	2·3	17·1
2207	0·8	12·5	2·6	18·4	5363	0·0	13·1	2·1	17·1
3109	—	13·0	4·0	13·4	6384	—	12·5	1·6	18·7
4038/9	0·5	12·1	2·1	19·8	6810	0·3	12·9	2·0	18·3
4254	0·4	12·3	2·0	18·0	7541	—	12·6	0·7	19·4

(d) *Spectral and Radio Indices*

Spectral indices of the radio sources observed at two wavelengths are given in Table 3. The spectral index α is defined by the expression $S \propto f^{-\alpha}$.

To calculate the radio indices $R = m_{\mathrm{r}} - m_{\mathrm{pg}}$ the radio magnitudes m_{21} (which are given in column 3 of Table 3) were determined from the relationship

$$m_{\mathrm{r}} = 53 \cdot 45 - 2 \cdot 5 \log S,$$

as defined by Hanbury Brown and Hazard (1959).

(e) *Absolute Radio Magnitudes*

Values of the absolute radio magnitude are given in column 5 of Table 3. The distance moduli were taken from de Vaucouleurs (1968) for the galaxies in nearby groups of galaxies and from van den Berg (1960) for the others.

In calculating the radio indices (given in column 4 of Table 3) the photographic magnitudes of galaxies have been corrected for absorption in our Galaxy by $\Delta m = -0 \cdot 25 \operatorname{cosec} b$, and for absorption in the galaxies themselves according to Holmberg's (1957) results. For the irregular galaxy NGC 3109 the results for Sc galaxies were used.

III. ACKNOWLEDGMENTS

I wish to thank Dr. E. G. Bowen and Mr. J. G. Bolton for permission to use the facilities of the Australian National Radio Astronomy Observatory at Parkes, and Professor B. Y. Mills for the opportunity of making observations with the east–west arm of the Cross at the Molonglo Observatory of the University of Sydney. I am indebted to the staff at Parkes and Molonglo for help in carrying out the observations.

Thanks are due to Dr. J. A. Roberts and Mr. J. G. Bolton for reading the manuscript and for making many valuable comments.

The financial support of the Academy of Sciences of the U.S.S.R. is acknowledged.

IV. REFERENCES

VAN DEN BERG, S. (1960).—*Publs. David Dunlap Obs.* **2**(6), 159.

BOLTON, J. G., GARDNER, F. F., and MACKEY, M. B. (1964).—*Aust. J. Phys.* **17**, 340.

DAY, G. A., SHIMMINS, A. J., EKERS, R. D., and COLE, D. J. (1966).—*Aust. J. Phys.* **19**, 35.

HANBURY BROWN, R., and HAZARD, C. (1959).—*Mon. Not. R. astr. Soc.* **119**, 297.

HEESCHEN, D. S., and WADE, C. M. (1964).—*Astr. J., N.Y.* **69**, 277.

HOLMBERG, E. (1957).—*Meddn Lunds astr. Obs.* (2) No. 136.

KALLOGLIAN, A. T., and TOVMASSIAN, H. M. (1964).—*Soobshch. byurak. Obs.* **36**, 31.

KURILCHIK, Y. N., and SYTSKO, G. A. (1965).—*Soviet Astr.* **42**, 531.

PRICE, R. M., and MILNE, D. K. (1965).—*Aust. J. Phys.* **18**, 329.

SHIMMINS, A. J., DAY, G. A., EKERS, R. D., and COLE, D. J. (1966).—*Aust. J. Phys.* **19**, 837.

TOVMASSIAN, H. M. (1965).—*Astrophysika* **1**, 197.

TOVMASSIAN, H. M. (1966*a*).—*Astrophysika* **2**, 317.

TOVMASSIAN, H. M. (1966*b*).—*Aust. J. Phys.* **19**, 883.

TOVMASSIAN, H. M. (1966*c*).—*Astrophysika* **2**, 417.

TOVMASSIAN, H. M. (1966*d*).—*Aust. J. Phys.* **19**, 565.

DE VAUCOULEURS, G. (1963).—*Astrophys. J. Suppl. Ser.* **8**, 31.

DE VAUCOULEURS, G. (1968).—"Stars and Stellar Systems." (Eds. G. P. Kuiper and B. M. Middlehurst.) Vol. 9, Ch. 17. (Univ. Chicago Press.)

DE VAUCOULEURS, G., and DE VAUCOULEURS, A. (1964).—"Reference Catalogue of Bright Galaxies." (Univ. Texas Press.)

RADIO EMISSION FROM THE SUPERNOVA REMNANT VELA–X

By D. K. Milne*

[*Manuscript received December 4, 1967*]

Summary

Radio observations are presented of the fairly large galactic complex Vela-X, Y, and Z. These sources are believed to be the remnant of a supernova having an optical identification with the filamentary nebula Stromlo 16. The brightness distributions, obtained at four frequencies, indicate an open annular structure reminiscent of other supernova remnants. The variation of spectral index over the region is investigated and shows that the radiation is substantially nonthermal, the integrated fluxes yielding a spectral index of $-0 \cdot 3$. A high resolution distribution of magnetic field direction is deduced from polarization measurements made at three frequencies; a circumferential magnetic field is a possible interpretation of the field orientations.

I. Introduction

Up to the present time, radio emission has been detected from some 20 objects believed to be the remnants of galactic supernovae. Most of these objects are characterized at radio frequencies by a nonthermal spectral index and by a structure suggesting that the emission arises predominantly from the outer envelope of the expanding gas volume. Radio polarization has been detected from very few of these objects—many are of small angular dimensions or low surface brightness, making detailed observations difficult.

One of the largest and brightest objects believed to be of supernova origin is the complex of radio sources known as Vela-X, Y, and Z. Its area is about 8 square degrees and its flux density greater than 1000 f.u.† at decimetre wavelengths. It is believed that this complex is the remnant of a supernova having an optical identification with the filamentary nebulosity Stromlo 16 (Gum 1955).

Little attention has been given to this southern object. It appears as part of an isolated region (the Vela–Puppis complex) in the galactic surveys of Piddington and Trent (1956), Hill, Slee, and Mills (1958), Wilson and Bolton (1960), and Mathewson, Healey, and Rome (1962). The only detailed radio study of this region was made by Rishbeth (1958) with the Mills Cross instruments at 85 MHz ($0^\circ \cdot 8$ beamwidth) and $19 \cdot 6$ MHz ($1^\circ \cdot 2$ beamwidth). The three sources Vela-X, Y, and Z can be distinguished in his 85 MHz isotherms but are not resolved at $19 \cdot 6$ MHz. Rishbeth concluded that the three sources were all of a nonthermal character, with Vela-X possibly having a flatter spectral index than the other two. Rishbeth decided against the identification of Vela-X with Stromlo 16 on the grounds that the radio brightness distribution was of smaller extent than that outlined by Stromlo 16 and that the peak radio emission was in an area devoid of filaments. The first proposal of the supernova origin of these radio sources was by Wilson and Bolton (1960), who from their 960 MHz galactic survey concluded that Vela-X, Y, and Z were portions of the one source, a supernova associated with Stromlo 16. Harris (1962) included Vela-X, Y, and Z in his evolutionary studies of supernova remnants. He arrived at estimated distances of 460 pc by Shklovsky's radio method and 700 pc from the angular dimensions of individual filaments. Harris adopted a flat spectral index ($\alpha = 0 \cdot 00 \pm 0 \cdot 15$) from the 85 MHz results of Rishbeth and the 960 MHz results of Wilson and Bolton.

---

* Division of Radiophysics, CSIRO, Box 76, P.O. Epping, N.S.W. 2121.

† 1 flux unit = 10^{-26} W m^{-2} Hz^{-1}.

Mathewson, Healey, and Rome (1962), from their 1440 MHz survey, showed that Vela-X had a thermal spectrum and Vela-Y a nonthermal spectrum. Linear polarization in the brightest region of Vela-X has been reported at 1410 MHz by Gardner and Whiteoak (1962), showing that Vela-X is not entirely thermal. Optical spectra have been obtained for two of the filaments in Stromlo 16 (Milne 1968). Indications are of the presence of collisionally excited gas, probably associated with shock fronts.

The results reported here are of radio surveys of the Vela complex carried out by the author between March 1963 and April 1966. From these results it would appear that Vela-X, Y, and Z is a supernova remnant having a reasonably well-defined magnetic field and a positive identification with the filamentary nebula Stromlo 16.

II. RADIO OBSERVATIONS

The 210 ft radio telescope of the Australian National Radio Astronomy Observatory at Parkes, N.S.W., was used to map the intensity and polarization of the continuum radio emission from the Vela complex. The surveys were carried out using a 408 MHz double sideband crystal-mixer receiver (described by Mackey 1964), a 635 MHz nondegenerate parametric receiver (Ferranti model VCA/L10), a 1410 MHz degenerate parametric receiver (Gardner and Milne 1963), a 1660 MHz crystal-mixer receiver, and a 2650 MHz degenerate parametric receiver (Cooper, Cousins, and Gruner 1964). Details of the receiver–antenna performance at each frequency are given in Table 1. Nightly calibration of the receiver–antenna system was made

TABLE 1

DETAILS OF RECEIVING SYSTEM

Centre Frequency (MHz)	Bandwidth (MHz)	System Noise Temp. (°K)	Beamwidth (min arc)	Assumed Flux Densities of Calibrating Sources (f.u.)	
				Hydra A	04−71
408	8	350	48	135	40
635	8	180	31	91	Not used
1410	10	100	14·1	42	13·5
1660	10	400	12·6	36	Not used
2650	50	180	7·5	23·5	7·5

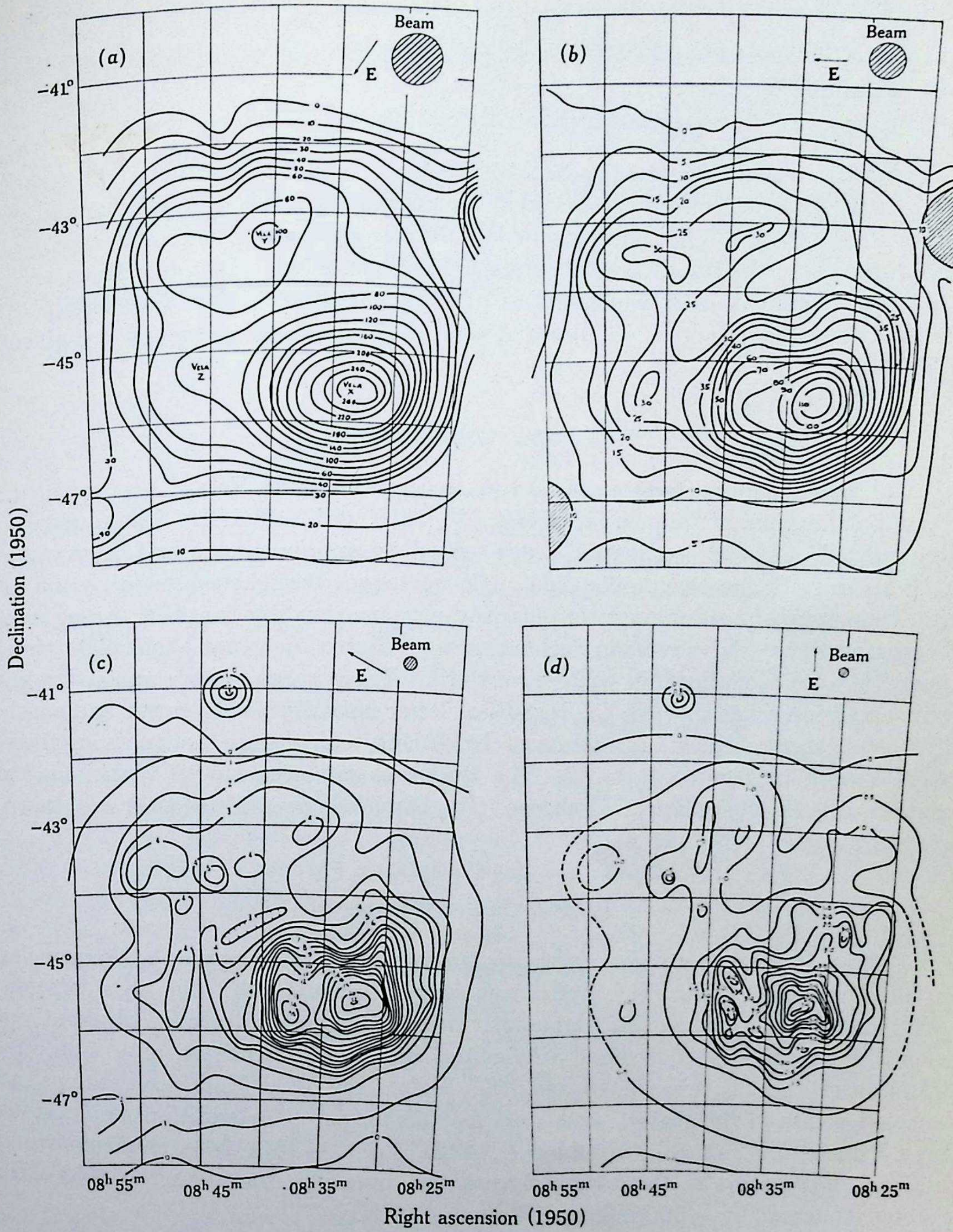
(a)
Beam
E
-41°
-43°
-45°
-47°
Vela Y
Vela Z
Vela X
(b)
Beam
E
(c)
Beam
E
-41°
-43°
-45°
-47°
(d)
Beam
E
Declination (1950)
08h 55m
08h 45m
08h 35m
08h 25m
08h 55m
08h 45m
08h 35m
08h 25m
Right ascension (1950)

Fig. 1.—Isotherms of brightness temperature at (*a*) 408, (*b*) 635, (*c*) 1410, and (*d*) 2650 MHz. The respective directions of the electric vector of the aerial feed are shown on each figure. For (*a*) at the frequency of 408 MHz the beamwidth of the 210 ft telescope is comparable with that used by certain earlier workers. This figure shows the three sources Vela-X, Y, and Z into which these observers resolved the region.

using the radio sources Hydra A or MSH 04−7*1*. An argon discharge noise generator was used to interpolate equipment performance between these observations.

The brightness temperatures T_b quoted here were derived at each frequency from the relationship

$$T_\mathrm{b} = \lambda^2 S/2k(1\cdot 13\,B^2),$$

where k is Boltzmann's constant ($1\cdot 38\times 10^{-23}$ J degK^{-1}), λ is the wavelength (metres), and B is the half-power width (radians) of the antenna response to a point source of known flux S (f.u.). This relationship is valid for a Gaussian antenna response, the solid angle of the beam being given by $1\cdot 13\,B^2$ under this condition. Scans were made over Hydra A from which values of B and peak deflection were obtained. The flux densities adopted for Hydra A and 04−7*1* at each frequency are given in Table 1.

(*a*) *Continuum Surveys*

A region amounting to some 40 square degrees around Vela-X was mapped, in one polarization, at frequencies of 408, 635, 1410, and 2650 MHz. These surveys were carried out using declination scans spaced by approximately half-beamwidth intervals in right ascension. The feed angle was changed slightly between scans to keep the average position angle of polarization approximately constant throughout the observations. Drive rates in declination were chosen such that about eight time constants were contained in each beamwidth. These scans were combined with right ascension scans through the regions of lower intensity to the north and south of the brighter complex. Isotherms of brightness temperature drawn from these scans appear in Figures 1(*a*)–1(*d*). The isotherms are accurate to within half a contour unit for the polarization chosen. The baselevels over which they are drawn are arbitrary.

(*b*) *Polarization Surveys*

These investigations were carried out over most of the complex at frequencies of 1410 and 2650 MHz. The region was sampled at 408 MHz but no significant polarization was found at this frequency. It was necessary to provide observations at a third frequency to remove ambiguities of integral multiples of π from the Faraday rotation between 1410 and 2650 MHz. The 1660 MHz observations, at selected points in the region, were used for this purpose. In addition, two regions near R.A. $08^\mathrm{h}\,36^\mathrm{m}$, Dec. −45° and R.A. $08^\mathrm{h}\,31^\mathrm{m}$, Dec. −46° (1965), showing strong uniform polarization at these three frequencies, were observed with the 1660 MHz receiver detuned by ±30 MHz to 1630 and 1690 MHz.

The basic procedure that was followed for the polarization measurements was to rotate the feed on the telescope at 180 deg/min at each of a series of grid points over the region. This, in principle, would contain a sinusoidal modulation of period 180° (in feed angle). The amplitude of this would be proportional to the linearly polarized component of the continuum emission. The feed angle of maximum emission gives, after correcting for parallactic angle, the position angle of the electric vector of the emission. In practice, however, there are two classes of spurious effects that must be removed from the observations. These are due to:

(1) Ground reflection and emission. This effect, being a function of telescope position relative to the ground, can be removed by comparing the modulation on the source with that off the source at the same altitude–azimuth position.

(2) Beam ellipticity and squint. These effects depend on the brightness gradient at the point of observation. They were assessed on a strong source each observing run and found to be negligible for the fairly shallow brightness gradients in the Vela-X region.

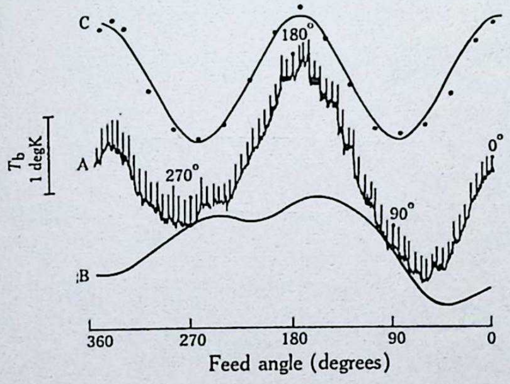

Fig. 2.—Tracing of a record used to determine the polarization at a point in the nebula showing (A) the receiver output when the aerial feed is rotated with the antenna pointed at a strongly polarized point in the region; (B) the receiver output when the feed is rotated on the unpolarized background, in this case the average of rotations on several unpolarized points; and (C) the difference between (A) and (B) showing the sinusoidal modulation from which the magnitude and feed angle of the polarized component is measured.

For a detailed discussion of these spurious effects, and their removal in the analysis, the reader is referred to Gardner and Davies (1966). A sample record of the receiver output during feed rotations on a strongly polarized region and on the background is shown in Figure 2. The resultant modulation obtained by subtracting the modulation on the background from that on the source is also shown.

In addition to the measurements described, scans were made over selected regions with polarization position angles spaced at intervals of 30°. These measurements provided an independent check on the main method used and gave additional information on the distribution of polarization over these regions.

The results of the polarization measurements are presented in Figure 3 and Table 2.

(i) *Figure 3*

The magnitudes and directions of the electric vectors, measured at all the sky positions investigated, are plotted in equatorial coordinates (1950 epoch) in Figures 3(*a*)–3(*c*) for 1410, 1660, and 2650 MHz respectively. The **E** vector position angle and magnitude are shown in the usual convention—the thicker the vector the more reliable the observation.

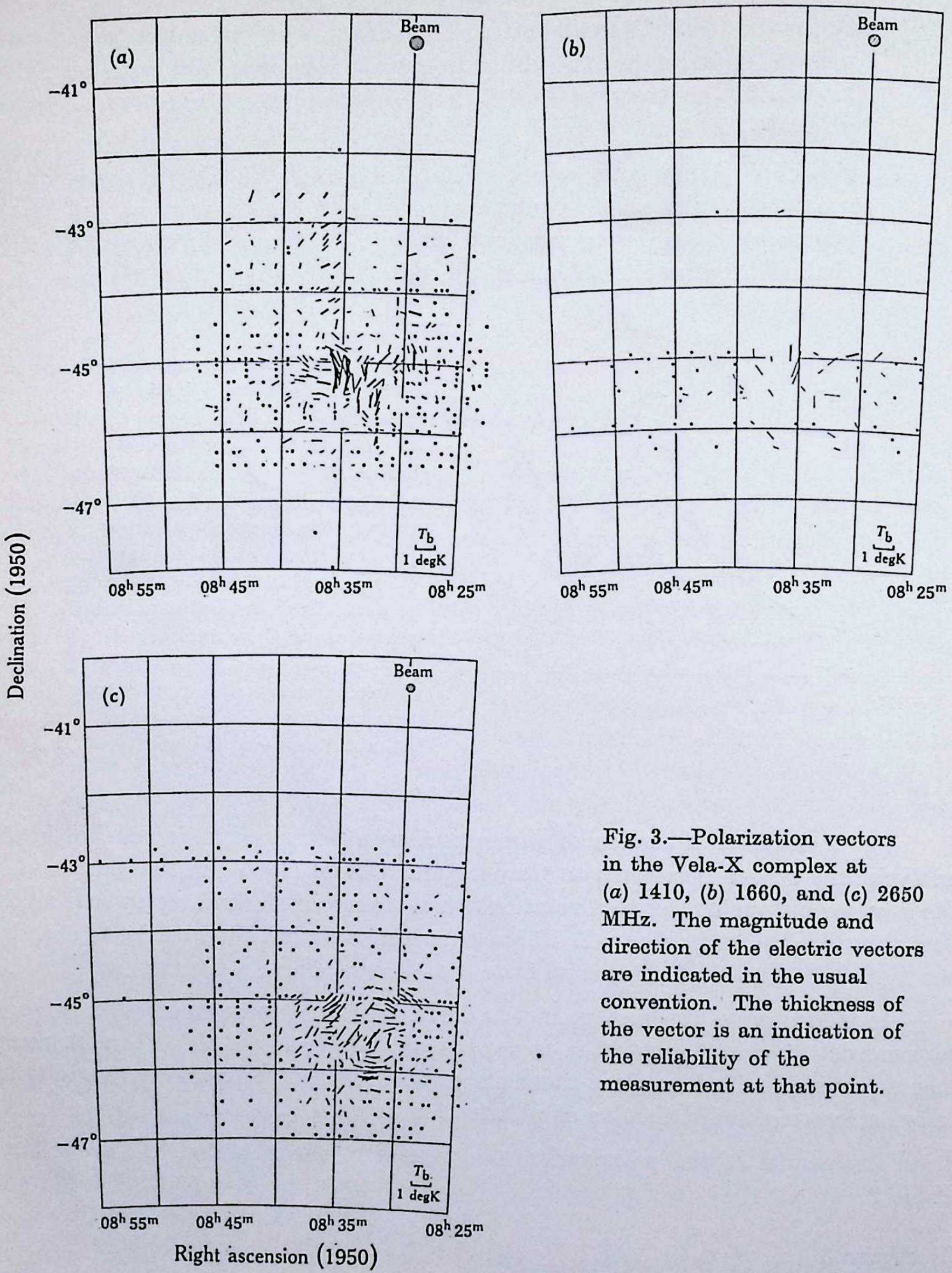

Fig. 3.—Polarization vectors in the Vela-X complex at (*a*) 1410, (*b*) 1660, and (*c*) 2650 MHz. The magnitude and direction of the electric vectors are indicated in the usual convention. The thickness of the vector is an indication of the reliability of the measurement at that point.

(ii) *Table 2*

Space does not permit the inclusion in tabular form of all the polarization results.* Table 2 is therefore limited to those sky positions where there are sufficient data to derive the directions of the intrinsic polarization, in accordance with Section IV. The notation used in Table 2 to specify the polarization is: the electric vector position angle (degrees); polarization brightness temperature, $\frac{1}{2}$(maximum — minimum) (degK). The number of independent observations made is given in parentheses (only one observation is implied when this is omitted). The equatorial positions quoted are those at which the observations were made (∼ 1965·0).

Table 2

POLARIZATION RESULTS

The number of independent observations (when more than one was made) is given in parentheses

Position (1965)					Posn. Angle (deg); Pol. Temp. (°K) for Frequency (MHz) of:			Intrinsic Position Angle °	Rotation Measure (rad/m²)	Polarization Ratio
R.A. h	m	s	Dec. °	′	1410	1660	2650			
08	27	30	−45	30	24; 0·2		17; 0·2(2)	12	+7	2·3
08	27	30	−45	45	144; 0·3		117; 0·2	106	+15	1·5
08	28	00	−44	40	138; 0·15		79; 0·35	54	+34	6·2
08	28	30	−44	30	144; 0·35		151; 0·15	85	+90	1·0
08	28	30	−45	00	0; 0·2		59; 0·3	10	+67	4·0
08	28	30	−45	05	178; 0·2		55; 0·4	10	+61	5·3
08	28	30	−45	15	17; 0·2	49; 0·2	164; 0·3	100	+64	3·4
08	29	00	−44	50	26; 0·4		69; 0·35(3)	16	+59	2·6
08	29	00	−45	00		136; 0·5	58; 0·4(2)	5	+72	
08	29	00	−45	10	59; 0·2		49; 0·2(2)	45	+5	2·4
08	29	30	−45	00	179; 1·0(3)		59; 0·4(4)	10	+67	1·3
08	30	00	−44	40	10; 0·2		75; 0·35(2)	30	+57	5·5
08	30	00	−44	50	19; 0·4		60; 0·3(2)	0	+82	2·8
08	30	30	−45	00	161; 0·2		57; 0·4	10	+64	6·6
08	30	30	−45	20		12; 0·3	90; 0·4	73	+17	
08	30	30	−46	00	65; 0·2	29; 0·3		115	+35	
08	31	00	−45	00	145; 0·45(2)	108; 0·6(2)	56; 0·45(3)	20	+49	3·5
08	31	00	−45	05	55; 0·2(2)		60; 0·65	30	+41	11·0
08	31	00	−45	15	33; 0·35		93; 0·5	45	+65	4·8
08	31	00	−45	20	29; 0·35		83; 0·35	36	+64	3·3
08	31	00	−46	00	61; 0·2		106; 0·3	55	+69	5·0
08	32	00	−45	00	139; 0·85		77; 0·5(2)	52	+34	2·0
08	32	00	−45	20	170; 0·35		85; 0·45	50	+48	3·7
08	32	00	−46	00	82; 0·3		92; 0·4(2)	30	+84	4·3
08	32	00	−46	20	134; 0·2	110; 0·3	80; 0·5(4)	60	+27	6·6
08	32	00	−46	30	Nil		78; 0·3	84	−8	
08	32	00	−46	40	61; 0·3		Nil			
08	32	24	−45	34	164; 0·8(15)	88; 0·8	150; 0·8	70	+109	3·1
08	32	30	−44	50	0; 0·4		116; 0·3	111	+7	
08	32	30	−45	05	159; 0·65	129; 0·6	98; 0·5(2)	74	+24	11·0
08	32	30	−45	40	173; 0·75(2)		162; 0·4	90	+98	1·6
08	32	30	−45	45	157; 0·7		114; 0·5	100	+19	2·2
08	32	30	−46	08	177; 0·4		112; 0·5	16	+130	4·4
08	32	30	−46	10	172; 0·45	61; 0·4	90; 0·8(6)	171	+135	7·0
08	33	00	−45	00	126; 0·2(2)		125; 0·2(2)	125	0	3·1
08	33	00	−45	34	158; 0·65		154; 0·3	80	+100	1·4
08	33	30	−45	05	161; 0·5		130; 0·15	120	+14	1·0
08	33	30	−45	10	166; 0·5		120; 0·35(2)	100	+27	2·4
08	33	30	−45	15		132; 0·3	91; 0·3	65	+35	

---

* Complete results of the polarization measurements are available in tabular form on request to the Chief, Division of Radiophysics, CSIRO, Box 76, P.O. Epping, N.S.W. 2121.

TABLE 2 (*Continued*)

Position (1965)					Posn. Angle (deg); Pol. Temp. (°K) for Frequency (MHz) of:			Intrinsic Position Angle	Rotation Measure (rad/m²)	Polarization Ratio
R.A.			Dec.							
h	m	s	°	′	1410	1660	2650	°		
08	33	30	−45	50	48; 0·35		8; 0·5(2)	173	+20	4·1
08	33	30	−45	55	31; 0·2			20	+74	9·0
08	33	30	−46	00			74; 0·5			
08	34	00	−44	50	133; 0·2		4; 0·15(2)	135	+67	2·5
08	34	00	−45	00	144; 0·35	61; 0·2	4; 0·3(4)	134	+68	2·7
08	34	00	−45	30	169; 0·8		145; 1·05	135	+13	4·2
08	34	00	−45	40	0; 0·65(3)	0; 0·6	148; 0·8	134	+19	4·0
08	35	00	−44	20	107; 0·15		95; 0·3	90	+7	4·5
08	35	00	−44	40	25; 0·2		151; 0·3	131	+27	5·0
08	35	00	−44	50	85; 0·35		140; 0·3	90	+67	3·0
08	35	00	−45	00	47; 0·5(2)		154; 0·35(3)	124	+41	2·6
08	35	00	−45	10	179; 1·4		145; 0·75(2)	132	+18	1·7
08	35	00	−45	30	100; 0·35	43; 0·35	147; 0·8	93	+74	7·7
08	35	00	−45	40	132; 0·35		137; 0·35	139	−3	3·3
08	35	00	−46	10	102; 0·2		169; 0·15	124	+60	2·4
08	35	30	−45	05	23; 1·4		128; 0·65(2)	95	+45	1·6
08	35	30	−45	10	177; 1·6	162; 1·4	128; 0·8(2)	108	+27	1·6
08	35	30	−45	20		159; 0·9	133; 0·75(2)	115	+24	
08	36	00	−42	55	132; 0·2		27; 0·15	170	+50	3·7
08	36	00	−43	00						
08	36	00	−43	05	125; 0·3					
08	36	00	−44	00	141; 0·35		170; 0·15	116	+74	1·2
08	36	00	−44	10						
08	36	00	−44	20	130; 0·35					
08	36	00	−44	30	169; 0·5		155; 0·3	149	+8	1·8
08	36	00	−45	00	32; 1·0(10)	178; 0·8(2)	136; 0·5(10)	108	+38	1·5
08	36	00	−45	05	30; 0·135		126; 0·85	91	+48	2·1
08	36	00	−45	10	15; 1·2(2)		120; 0·85(2)	91	+40	2·6
08	36	00	−45	15	7; 1·1(2)		124; 0·8	100	+33	2·8
08	36	00	−45	20	169; 1·25(2)		90; 0·85	73	+23	2·8
08	36	00	−45	40	5; 0·35		80; 0·5	40	+54	4·7
08	36	00	−45	50	5; 0·3		159; 0·3(2)	150	+12	3·3
08	37	00	−43	00		114; 0·3	70; 0·35(3)	48	+30	
08	37	00	−43	05	128; 0·3(4)		92; 0·2	75	+23	2·0
08	37	00	−43	10						
08	37	00	−43	15	141; 0·4					
08	37	00	−45	00	85; 0·4		23; 0·2(3)	112	+123	2·2
08	37	00	−45	10	92; 0·45		135; 0·35	80	+55	3·2
08	37	00	−45	20	78; 0·75(2)		90; 0·3	120	+48	1·7
08	37	00	−45	30	71; 0·65		155; 0·45	115	+40	2·6
08	37	00	−46	00	110; 0·4		160; 0·35	108	+71	3·1
08	37	00	−46	20	117; 0·2	69; 0·3	Nil	120	+68	
08	37	30	−45	05	90; 0·2	12; 0·25		85	+54	5·5
08	37	30	−45	10	69; 0·3		135; 0·5			
08	37	30	−45	30	87; 0·5		151; 0·75	110	+56	2·7
08	37	30	−45	34	93; 0·35	36; 0·35	168; 0·3	130	+52	3·6
08	37	30	−46	10	92; 0·5	42; 0·55	168; 0·5	130	+52	3·7
08	38	30	−45	00	39; 0·45		132; 0·3	100	+44	2·6
08	38	30	−45	05	45; 0·4		123; 0·35	85	+52	2·8
08	38	30	−45	10	76; 0·4		160; 0·4	125	+48	2·9
08	38	30	−45	15	90; 0·6	38; 0·6	150; 0·65	95	+75	3·2
08	38	30	−45	45	171; 0·2		143; 0·4	132	+15	5·9
08	39	00	−45	00	47; 0·35	6; 0·4	126; 0·3(2)	88	+52	2·8
08	40	00	−45	30	112; 0·2	49; 0·3	163; 0·35	115	+65	6·6
08	40	00	−46	10	118; 0·5		13; 0·15	155	+52	11·0
08	41	00	−44	30	132; 0·2		163; 0·2	103	+82	2·5
08	41	00	−45	15	Nil		128; 0·2	65	+82	1·4
08	41	00	−45	20	107; 0·5					
08	41	00	−45	25			121; 0·2			
08	42	30	−44	50	105; 0·2		157; 0·2	105	+71	3·1
08	42	30	−45	05	75; 0·4	14; 0·2		40	+54	
08	45	00	−44	50	157; 0·2		170; 0·15	110	+82	7·7

Coordinates of these points for the 1950 epoch are approximately given by the addition of $-0^{\mathrm{m}}\cdot 5$ and $+3'$ to the right ascension and declination respectively.

III. Radio Spectral Index

Basically two determinations for the relationship between brightness temperature (or flux) and frequency are available. The first of these, yielding "the spatial distribution of spectral index", compares brightness distributions at different frequencies but with the same resolution. This can be accomplished by convolving high resolution maps with a function designed to degrade the resolution to that of a lower resolution survey. This comparison can be made directly if brightness distributions are available at the same resolution. The second method, producing "the total integrated spectral index", is to integrate the brightness contours obtained for the source at each frequency and to fit a relationship of the form $S \propto f^{a}$ to these integrated fluxes.

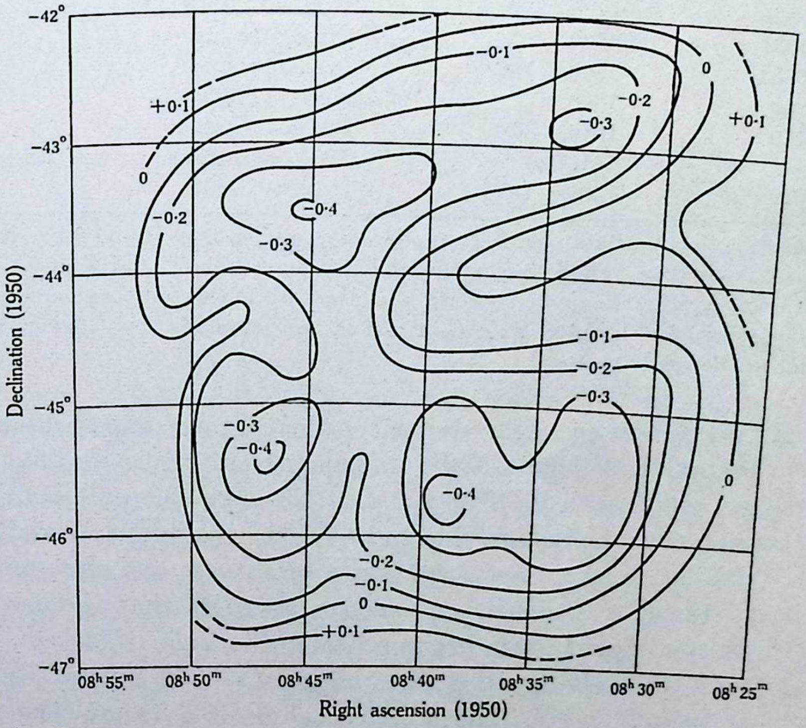

Fig. 4.—Contours of spectral index α in the Vela-X region. These contours were constructed from a comparison of the 635 MHz isotherms (Fig. 1(*b*)) with the 1410 and 2650 MHz isotherms (Figs. 1(*c*) and 1(*d*)) degraded in resolution to 31′ arc.

(*a*) *Spatial Distribution of Spectral Index*

Four brightness distributions, at a comparable resolution, are available for the Vela region: the surveys of Rishbeth (1958) at 85 MHz, Wilson and Bolton (1960) at 960 MHz, Mathewson, Healey, and Rome (1962) at 1440 MHz, and the present survey at 408 MHz—with beamwidths of $0^{\circ}\cdot 8$, $0^{\circ}\cdot 8$, $50'$, and $48'$ respectively. Three points in the region were compared for these four surveys, yielding values of α

in the relation $T_b \propto f^{a-2}$ of $-0\cdot3\pm0\cdot2$ for Vela-X and $-0\cdot6\pm0\cdot4$ for both Vela-Y and Z.

The distribution of spectral index was also investigated at two higher resolutions. Using the CDC 3600 computer of CSIRO the 2650 and 1410 MHz brightness distributions were convolved (Figs. 1(*d*) and 1(*c*)) with functions designed to degrade these 7′·5 and 14′·1 beamwidths to 3′·0, the beamwidth of the 635 MHz map. A comparison was then made between the degraded 2650 and 1410 MHz brightness isotherms and the observed isotherms at 635 MHz, resulting in the distribution of spectral index shown in Figure 4. There is good agreement in the contour shape between the three maps of equal resolution, with most of the differences resulting from what is apparently a thermal region centred at R.A. $08^h 35^m$, Dec. −44° and a steepening of the spectrum (more nonthermal) over the eastern side and a nonthermal region near R.A. $08^h 34^m$, Dec. −43°. This latter area is of low surface brightness and the steepness of its spectrum is questionable, although we see in Section IV that there is an isolated patch of polarization close to this position. Over the bulk of Vela-X the spectral index α was found to be about $-0\cdot3$ with values of $-0\cdot35$ on the peak of Vela-X and $-0\cdot4$ near Vela-Y and Z. The positive values of α around the periphery of the source are not significant; the errors are large here and the baselevels of the three surveys used are not absolutely determined.

TABLE 3

INTEGRATED FLUXES FOR VELA-X, Y, AND Z

Frequency (MHz)	Integrated Flux (f.u.)	Reference
19	960	Rishbeth (1958)
86	2900±1000*	Rishbeth (1958)
408	2300± 300	Present result
635	2360± 300	Present result
960	1560	Harris (1962)
1410	1640± 300	Present result
1440	1610*	Mathewson, Healey, and Rome (1962)
2650	1400± 250	Present result

* Rishbeth (1958) and Mathewson, Healey, and Rome (1962) give integrated fluxes for Vela-X only. The values given above include Vela-Y and Z and have been obtained by integrating the previous workers' isotherms. It was not considered necessary to estimate errors for the 1440 MHz point; it is very close to the value measured at 1410 MHz in the present paper.

(*b*) *Total Integrated Spectrum*

Integrated fluxes* have been obtained for the surveys described here and are shown in Table 3, together with estimates made by other workers. The variation of integrated flux with frequency is displayed in Figure 5. The power-law spectrum of best fit is indicated; the spectral index is in this case $-0\cdot3\pm0\cdot1$ and applies to the whole region Vela-X, Y, and Z.

---

* These fluxes are revised values of those given in Milne (1966); both sets lie within the estimated errors.

All these spectral indices confirm earlier suggestions that the region is nonthermal, with Vela-Y and Z having steeper radio spectra than Vela-X (Rishbeth 1958). There is the possibility of considerable free–free radio emission from this region; this is evident from the presence of Hα emission and the fairly flat spectral index. The magnitude of this thermal component could be estimated if observations were made at a frequency high enough to observe a flattening of the spectral index when the flux of the nonthermal component falls to well below that of the thermal part. This flattening is not evident in Figure 5.

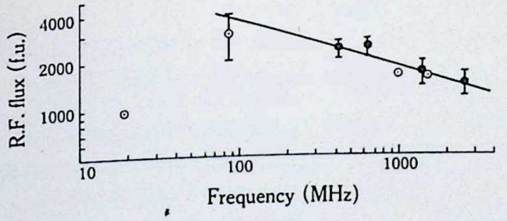

Fig. 5.—Integrated radiofrequency spectrum of Vela-X, Y, and Z. The data used in this figure are taken from Table 3. The full circles represent the present flux determinations. The line shown is for a spectral index of $-0\cdot3$.

Estimates of free–free radio emission made from the Hα flux are discussed in Section VII.

IV. Radio Polarization and Directions of Magnetic Field

An important feature of the radio emission from this complex is the considerable degree of linear polarization detected over much of the region. With polarization greater than 20%, this source is one of the most highly polarized galactic objects known. The distributions over the source of the magnitude and direction of the polarization at 1410, 1660, and 2650 MHz are shown in the vector presentations of Figures 3(*a*)–3(*c*). The percentage polarization, which is not given in the diagrams but can be gauged at 1410 and 2650 MHz by comparing Figures 3(*a*) and 1(*c*) or Figures 3(*c*) and 1(*d*), is greatest around the periphery of the principal source (Vela-X). At 2650 MHz the polarization is in excess of 20% in three substantial regions centred on R.A. $08^{\mathrm{h}}30^{\mathrm{m}}$, Dec. $-45°$; $08^{\mathrm{h}}35^{\mathrm{m}}$, $-45°10'$; and $08^{\mathrm{h}}32^{\mathrm{m}}\cdot5$, $-46°$. Weaker polarization extends over the region to the east occupied by Vela-Y and Z, whilst the peak of Vela-X is polarized at a lower percentage polarization than the surrounding region. Most of the outlying parts examined for polarization yielded magnitudes of T_{b} less than $0\cdot1$°K, the lower limit of the survey. The presence of polarization near R.A. $08^{\mathrm{h}}36^{\mathrm{m}}$, Dec. $-43°$ is, however, worth noting. There is a steepening of the spectral index close to this position (Fig. 4).

Intrinsic directions of polarization obtained over most of the source are given in Table 2, together with the rotation measures at these points. The derivation of these followed a simple graphical fit of the position angles at each frequency to a λ^2 law (i.e. Faraday rotation). The lowest values for the rotation measure consistent with the data were the ones accepted. No corrections for ionospheric Faraday rotation were made to the values of Table 2. For these observations, made at night near sunspot minima, the errors introduced by neglecting this can be no more than 2° at 1410 MHz, and less than 1° at 2650 MHz.

An expression for the error in the magnitude of the polarization, introduced by the finite bandwidth of the receiving system, is given by Gardner and Whiteoak

(1966). With the bandwidths used here and the rotation measures detected it is clear that no correction need be made for this effect. It is thought that the error in a single observation is ±10° in position angle and ±0·1 degK in magnitude. This conclusion was reached from an analysis of the sets of independent observations made on certain sky positions. This would lead to an error of ±20° in the position angle of the intrinsic vector.

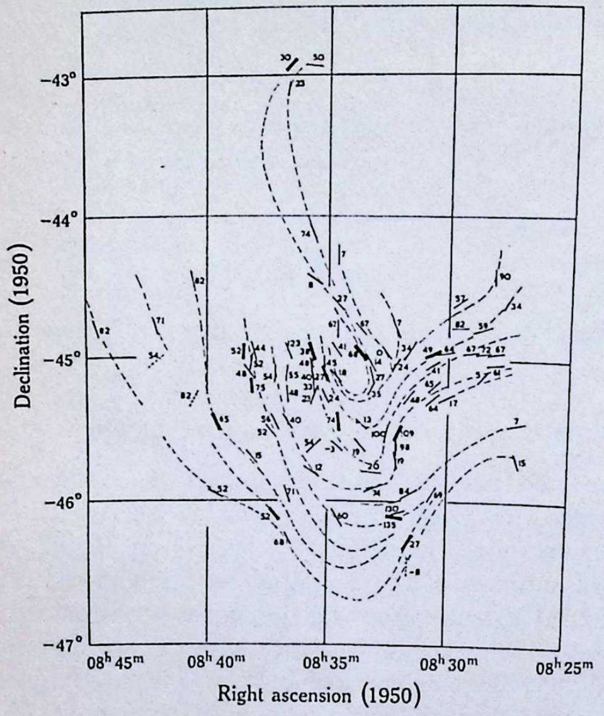

Fig. 6.—Direction of the transverse component of magnetic field in the Vela complex. The vectors shown have direction only; the magnitude of the field is not known at any point. The thickness of each vector is an indication of the reliability of the determination of direction at that point. The magnetic field suggested by these directions has been sketched in (the interpretation is discussed in the text). The number beside each vector is the rotation measure at that point (rad m^{-2}).

Magnetic field directions, orthogonal to the intrinsic polarization, are displayed in Figure 6. This figure also shows the rotation measure at each point where the magnetic field direction has been obtained. A magnetic field directed down the eastern side of the source, through Vela-X, and up the western side is a possible interpretation (sketched in Fig. 6). Certainly there is some evidence of a general circumferential field plus a more complicated field in the inner region. The low percentage polarization on the brighter parts of Vela-X may indicate that the field is directed along the line of sight at this point, lowering the intrinsic polarization and increasing the depolarization due to Faraday rotation effects. The picture is very complicated near the peak of Vela-X, with the rotation measure changing from its lowest value to almost its highest in the space of less than one-quarter of a degree.

It is possible to deduce something about the line-of-sight component of the magnetic field in the source. If it is assumed that Faraday rotation occurs in the source itself and that the field directions taken over the entire source are symmetrical in the line of sight, then the average rotation measure (+46 rad m^{-2}) would represent the rotation in the interstellar medium between the Sun and the source. Those parts of the source exhibiting a rotation measure greater than $+46$ rad m^{-2} would have a line-of-sight magnetic field component directed towards the observer. A magnetic field away from the observer is implied by rotation measures less than $+46$ rad m^{-2}. An interstellar rotation measure of $+46$ rad m^{-2} is acceptable in this direction, where we are looking almost directly along the galactic magnetic field (Gardner and Whiteoak 1966). With an assumed distance of 500 pc this rotation measure would require an electron density by magnetic field product of 10^{-7} G cm^{-3}, say an average electron density of $0\cdot02$ cm^{-3} with a magnetic field of 5×10^{-6} G, acceptable values for these parameters. It does seem that the regions of highest percentage polarization avoid those areas where the rotation measure has extreme values (both high and low). This is to be expected if these extreme values are located where the magnetic field in the source is directed along the line of sight.

The integrated polarization of the whole source is of interest for comparison with the polarization of other, unresolved sources. The 2650 MHz electric vectors distributed over the source were added vectorially and combined with the integrated brightness of the source. This gave 109° and less than 1% for the position angle and percentage polarization respectively. The integrated brightness temperature of the source is 90°K at 2650 MHz. The low percentage polarization of the source if seen unresolved is an indication of the complexity or random nature of the source compared with many of the extragalactic objects (Gardner and Davies 1966). It may explain why polarization has been detected only weakly in the other smaller and less intense supernova remnants.

Depolarization of the polarized emission follows the most commonly occurring trend, i.e. decreasing percentage polarization with decreasing frequency. The depolarization over the region expressed as a parameter, the polarization ratio, has been calculated where possible (and listed in Table 2). This ratio, which is the ratio of percentage polarization at 2650 MHz to that at 1410 MHz, varies from 1 to 11 over the region, with a mean value of about 3. There appears to be no correlation between the polarization ratio and any other parameter. In particular no correlation was found with rotation measure, which might be expected if the rotation or part of it occurred within the emitting region. There is evidence of considerable beamwidth effect in the distribution of depolarization. This is to be expected in a source of this nature, and it further complicates any deductions from the depolarization data.

V. Optical–Radio Comparison

Observationally there is a strong resemblance between the distribution of radio emission and optical features for most optically unobscured supernova remnants, e.g. the Cygnus loop (Harris 1962) and IC 443 (Hogg 1964). This agreement is contrary to what one would expect with two different emission mechanisms operating, if they are sufficiently independent. Optically the objects are bright only in line emission, whilst at radio frequencies the distribution often contains an intense nonthermal source or sources, which derive their emission from the motion of high energy electrons in relatively strong magnetic fields. One does, however, expect that the optical filaments and the more widely distributed but lower density ionized hydrogen would be seen as thermal emission at the shortest radio wavelengths. In the Vela complex the agreement between the general outline on Hα light and the weaker 2650 MHz contours (Fig. 7) is good. The strongest radio emission does, however, come from a region devoid of optical emission and where optical absorption does not seem excessively high. A minimum in the radio emission, at all frequencies, is centred on R.A. $08^{h}35^{m}$, Dec. $-43°30'$ and has its optical counterpart in the dark patch bounded rather abruptly by the northern arcs and the shells to the west. At 2650 MHz general agreement is evident in the boundary up the eastern face and the shells that form the western side of the nebula, but at lower frequencies (e.g. see Fig. 1(*b*)) the radio emission extends more eastward of this eastern face.

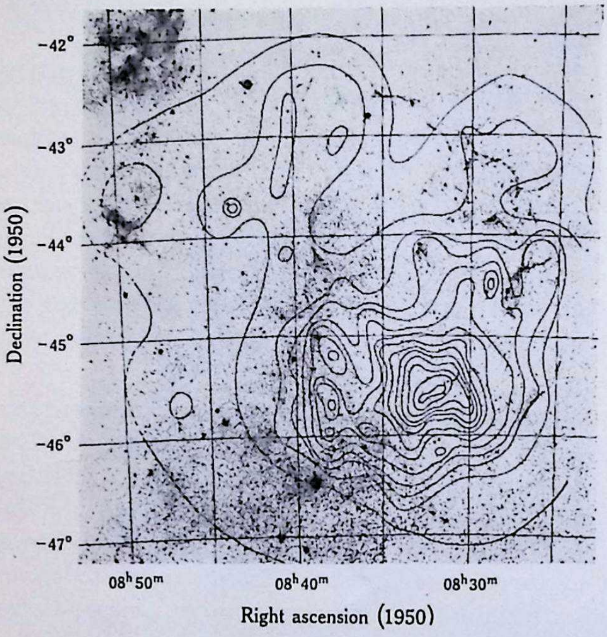

Fig. 7.—A mosaic, made from four 26 in. Schmidt plates, taken in Hα light showing the Stromlo 16 nebula overlaid with the 2650 MHz isotherms of Figure 1(*d*). The mosaic has been reproduced from Milne (1968).

In other words, there is an essentially nonthermal region beyond the boundary of the thermal radio emission and Hα emission. This has already been noted in the steepening of the radio spectrum near Vela-Y and Z (Section III). The faint Hα emission that forms the eastern face of Stromlo 16 is not easily discernible on published plates of the region and it has been assumed that the nebula had circular symmetry with obscuration over the eastern half. As has been pointed out above, the thermal radio emission does not in fact extend eastward of the optical features. We interpret this as a D-shaped nebula possibly formed by non-uniform radial expansion.

A lower expansion of the nebula in the easterly direction would suggest that interstellar density in this region is substantially higher than around other portions of the nebula. It can be established by inspection of Figure 7 that higher absorption does exist to the east of R.A. $08^{h}46^{m}$ and an estimate of its magnitude has been made from the colours and magnitude of OB stars in this direction (Velghe 1963). In Figure 8 is plotted the colour excess E_{B-V} against the distance modulus m_0-M_v for Velghe's stars west of R.A. $08^{h}45^{m}$ and those east of R.A. $08^{h}48^{m}$. An absorption of $0\cdot6$ mag/kpc is indicated in the former region with an additional $1\cdot5$ mag/kpc in the latter region. It is not completely clear where this additional absorption takes place, although a maximum distance of 500±100 pc ($m_0 - M_v = 8^m$ to 9^m) is suggested from Figure 8. It is possible that this absorption is the western extremity of the Vela dark cloud, which Greenstein (1937) estimates to be at a distance of between 500 and 750 pc.

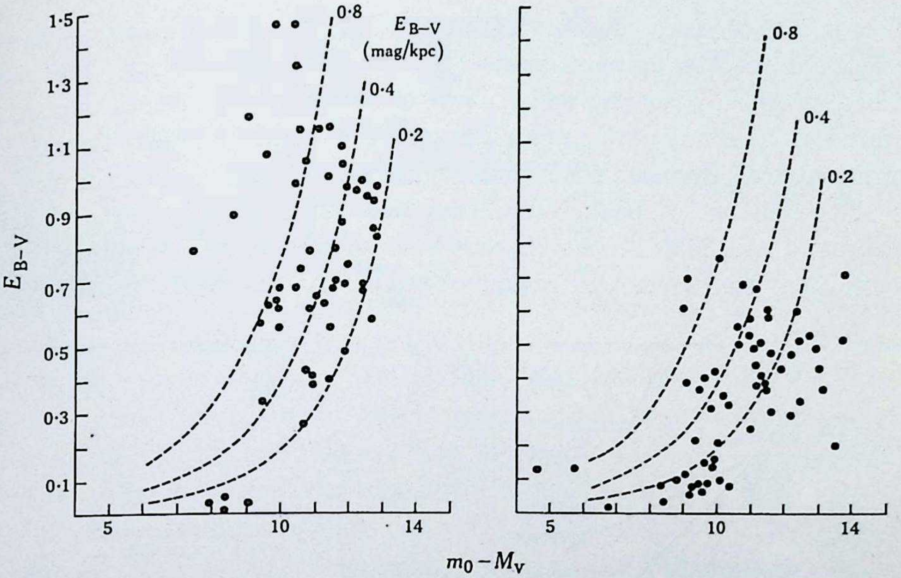

Fig. 8.—Diagram of colour excess E_{B-V} versus distance modulus $m_0 - M_v$ for the OB stars measured by Velghe (1963) in the region (*a*) east of R.A. 08^h 48^m and (*b*) west of R.A. 08^h 45^m (covering Stromlo 16). The increased absorption on the eastern side of Stromlo 16 is evident.

VI. Distance to the Nebula

Harris (1962) suggested two distances for Vela-X: 700 pc from the angular size of the filaments in the nebula and 460 pc from Shklovsky's relationship between the surface brightness and radius of an expanding synchrotron emitter. The validity of the first of these methods has not been adequately demonstrated. Observations confirming Harris's findings have not been made and our understanding of the physics of filament formation still does not provide a basis for a constancy of filament size, object to object. The second method (Shklovsky's) considers the source as a filled spherical synchrotron emitter, whilst it is indicated here that Vela-X may have a shell structure and that part of the radio emission is certainly thermal (see Section VII).

The similarities between Vela-X, IC 443, and the Cygnus loop have been noted. The Cygnus loop has a well-determined distance of 770 pc (Harris 1962) and IC 443 has a probable distance of 2000 pc, although hydrogen line absorption indicates that IC 443 could be as close as 800 pc (Hogg 1964). Taking the angular diameters of the Cygnus loop and IC 443 to be 170′ and 45′ (Harris 1962) then with a diameter of 4° for Vela-X we would, by analogy with the Cygnus loop, expect it to be at a distance of 540 pc. The analogy with IC 443 (at 2000 pc) would indicate a distance of 375 pc.

If Vela-X is associated with the Vela dark nebula, as has been suggested in Section V, the distance would lie between 500 and 750 pc, following Greenstein's (1937) estimate for the distance to the absorption. We will adopt a value of 500 pc giving a diameter of 35 pc.

VII. Thermal Radio Emission and Electron Temperature

Johnson (1960) gives contours of surface brightness for the Stromlo 16 region in Plate 7 of his absolute isophotometric survey of the Milky Way. The correlation between his λ6560 Å (passband 326 Å) and the author's Hα plates is good in form and brightness. The comparison isophotes in the band at λ6070 Å are, however, inconsistent, and so Johnson's method could not be used to obtain the emission measure of the region. A background brightness of $1\cdot5\times10^{-4}$ erg $\mathrm{sr^{-1}\ cm^{-2}\ sec^{-1}}$ in the passband at λ6560 Å was therefore adopted and the isophotes, above this level, were integrated over the region occupied by the radio source to give an approximation for the free–free radio emission expected from the region. A flux at λ6560 Å of $4\cdot7\times10^{-7}$ erg $\mathrm{cm^{-2}\ sec^{-1}}$ was obtained from this integration. A large fraction of this may be due to the [N11] λ6583 and 6548 Å contribution, which could be easily as high as the Hα intensity if much of the gas is collisionally excited (e.g. see Milne 1968, Fig. 3). Allowing for this, and for 0·3 magnitude of absorption (i.e. average of 0·6 mag/kpc (Section V) and a distance of 500 pc), a final estimated Hα flux of about 3×10^{-7} erg $\mathrm{cm^{-2}\ sec^{-1}}$ was obtained.

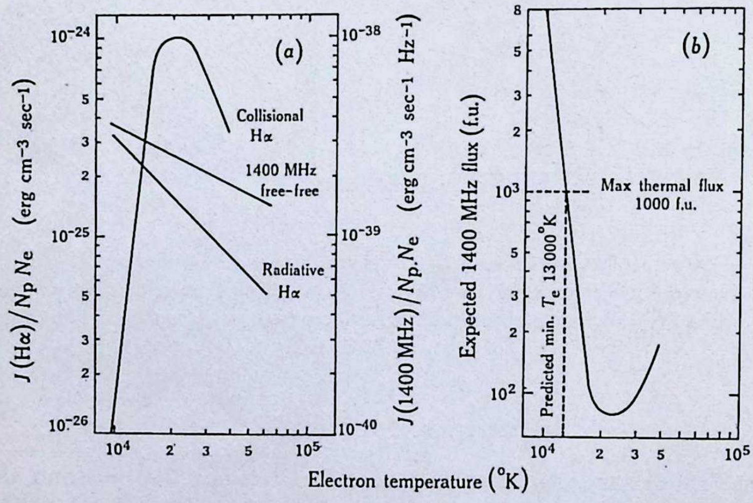

Fig. 9.—Plots as a function of electron temperature of (*a*) volume emissivities at 1400 MHz and in the Hα line for collisional and radiatively excited models, and (*b*) 1400 MHz flux expected from the measured Hα flux (3×10^{-7} erg $\mathrm{cm^{-2}\ sec^{-1}}$); (*b*) is based on a collisionally excited model optically thick in the Lyman lines and optically thin in the Hα line and at 1400 MHz. The total flux at the highest frequency indicates, as described in the text, a lower limit to the electron temperature.

We can relate this Hα flux to the radio frequency free–free emission if the excitation process populating the third quantum level of the hydrogen atom is known. Provided the nebula is optically thin in both the Hα line and at the radio frequency then the ratio of the fluxes $S_{\mathrm{r.f.}}/S_{\mathrm{H}\alpha}$ is simply the ratio of the volume emissivities $j_{\mathrm{r.f.}}/j_{\mathrm{H}\alpha}$ of the radio frequency and in the Hα line. Figure 9(*a*) gives the volume emissivities at 1400 MHz (Oster 1961) and in the Hα line, the latter for collisional excitation (Parker 1964*a*) and for radiative excitation (Burgess 1958) when the nebula is optically thick in the Lyman lines in both these cases.

Using the data of Figure 9(*a*) and the Hα flux (3×10^{-7} erg cm^{-2} sec^{-1}) estimates have been made of the 1400 MHz radio flux that would obtain from Stromlo 16 if it were a collisionally excited nebula. This is displayed as a function of electron temperature T_{e} in Figure 9(*b*). It is likely that Stromlo 16 is a collisionally excited region with an electron temperature of between 10^4 and 2×10^4 °K, the range suggested from optical measurements made on filaments in the region (Milne 1968) and near those obtained by Parker (1964*b*) for other supernova remnants. It is unfortunate that Hα volume emissivity, for a collisionally excited nebula, is a steep function of temperature below 20 000°K; we can therefore say very little about the magnitude of the expected free–free radio flux. However, from the radio spectrum of the source (Fig. 5) we expect that the optically thin thermal radio flux is less than 1000 f.u., which from Figure 9(*b*) would impose a lower electron temperature limit of about 13 000°K on the nebula. The minima in the collisional function near $T_{\mathrm{e}} = 20\,000$°K (Fig. 9(*b*)) requires that the free–free radio flux is at least 70 f.u., i.e. about 5% of the total 1410 MHz flux.

Dr. Whiteoak (personal communication) has suggested that the above allowance for absorption might be inadequate, particularly with recent determinations of the absorption-to-reddening ratio. An increase in the absorption, say by a factor of 2, to $0^{m}\cdot6$ would displace the curve of Figure 9(*b*) upward by a factor of $1\cdot3$. Because of the steepness of this curve the predicted minimum temperature would rise only by a small factor to a little less than 14 000°K.

VIII. MASS OF THE NEBULA

We can make estimates of the "visible" mass of Vela-X from either the Hα flux or the free–free radio flux. However, unless we know the electron temperature more accurately estimates made from the former measure will contain an uncertainty of the order of 100, as will estimates made from the limits of free–free radio flux discussed in Section VII. Until a more reliable temperature can be used or an estimate of the free–free flux is made (i.e. from higher frequency measurements) we can only place limits on the visible mass of the nebula.

Assuming a distance of 500 ± 100 pc to Vela-X and adopting an average electron density of 300 ± 100 cm^{-3} (Westerlund 1966), we arrive at limiting hydrogen masses of $0\cdot05$ and $4M_{\odot}$ from the limits on the free–free radio flux discussed in Section VII (i.e. 70 and 1000 f.u.). For this determination a free–free volume emissivity of $3\times10^{-39}\,N_{\mathrm{e}}N_{\mathrm{p}}$ erg cm^{-3} sec^{-1} Hz^{-1} was used. This assumes a temperature of about 15 000°K (the free–free emissivity is only dependent on the square root of the temperature).

A further estimate of the mass may be made by considering how much mass has been swept up by the nebula expanding into an ambient interstellar gas density of say $0\cdot1$ hydrogen atoms cm^{-3}. Once again assuming a distance of 500 ± 100 pc, and taking an average diameter between $3°\cdot5$ and $4°\cdot5$, we estimate this mass to be between 30 and $170M_{\odot}$. These mass estimates are similar to Parker's (1964*b*) values for the Cygnus loop, for which the complete mass is believed to be about $100M_{\odot}$. Parker has suggested that this higher mass could be responsible for the observed Hα flux if the temperature is lowered to 10 000°K. (This, however, would then not produce the observed forbidden spectra.) A similar argument applies to Vela-X, but in this case the excessively high radio emission produced would rule out the lower temperature—this, of course, is the basis of the upper limit imposed on the mass in this section.

IX. CONCLUSIONS

Summing up, it would appear from the brightness distributions shown here that Vela-X, Y, and Z comprise one source having a bright nonthermal component on the southern side (Vela-X) with substantial thermal emission, mainly to the north of Vela-X. The shape is reminiscent of certain other remnants having an annular brightness distribution (suggestive of shell structure) with one or two very bright regions on this distribution.

The radio polarization is stronger in the Vela complex than is usually found in supernova remnants. Some explanation for this may lie in the high effective resolution that we have as a consequence of the large angular size of this source. With this large angular size we have been able to obtain a fairly clear idea of the projected direction of the magnetic field over the object. However, without knowing with certainty the line-of-sight component of field it is difficult to establish a model for the magnetic field distribution. A circumferential field is a possible deduction from the data.

It has been proposed that the nebula is prevented from expanding on the eastern side by the presence of dense interstellar material, and it is suggested here that this would lead to a distance of about 500 pc. A comparison of the Hα flux and the radio flux leads to a possible minimum electron kinetic temperature of 13 000°K.

X. ACKNOWLEDGMENTS

The author is grateful to Miss Peggy Beswick for her assistance in the reduction of observations, and to Dr. F. F. Gardner and Dr. J. B. Whiteoak for discussion of the manuscript.

XI. REFERENCES

BURGESS, A. (1958).—*Mon. Not. R. astr. Soc.* **118**, 477.

COOPER, B. F. C., COUSINS, T. E., and GRUNER, L. (1964).—*Proc. Instn Radio Engrs Aust.* **25**, 221.

GARDNER, F. F., and DAVIES, R. D. (1966).—*Aust. J. Phys.* **19**, 441.

GARDNER, F. F., and MILNE, D. K. (1963).—*Proc. Instn Radio Engrs Aust.* **24**, 127.

GARDNER, F. F., and WHITEOAK, J. B. (1962).—*Phys. Rev.* **9**, 197.

GARDNER, F. F., and WHITEOAK, J. B. (1966).—*A. Rev. Astr. Astrophys.* **4**, 245.

GREENSTEIN, J. L. (1937).—*Ann. Harv. Coll. Obs.* **105**, 359.

GUM, C. S. (1955).—*Mem. R. astr. Soc.* **67**, 155.

HARRIS, D. E. (1962).—*Astrophys. J.* **135**, 661.

HILL, E. R., SLEE, O. B., and MILLS, B. Y. (1958).—*Aust. J. Phys.* **11**, 530.
HOGG, D. E. (1964).—*Astrophys. J.* **140**, 992.
JOHNSON, H. M. (1960).—Memoir No. 15, Mt. Stromlo Observatory.
MACKEY, M. B. (1964).—*Proc. Instn Radio Engrs Aust.* **25**, 515.
MATHEWSON, D. S., HEALEY, J. R., and ROME, J. M. (1962).—*Aust. J. Phys.* **15**, 354.
MILNE, D. K. (1966).—Symp. on Radio and Optical Studies of the Galaxy, Mt. Stromlo, p. 74.
MILNE, D. K. (1968).—The optical spectrum of Vela-X. *Aust. J. Phys.* **21** (in press).
OSTER, L. (1961).—*Astrophys. J.* **134**, 1010.
PARKER, R. A. R. (1964*a*).—*Astrophys. J.* **139**, 208.
PARKER, R. A. R. (1964*b*).—*Astrophys. J.* **139**, 493.
PIDDINGTON, J. H., and TRENT, G. H. (1956).—*Aust. J. Phys.* **9**, 481.
RISHBETH, H. (1958).—*Aust. J. Phys.* **11**, 550.
VELGHE, A. G. (1963).—Preprint, Royal Obs. of Belgium.
WESTERLUND, B. (1966).—*In* Discussion following Milne (1966), Symp. on Radio and Optical Studies of the Galaxy, Mt. Stromlo, p. 77.
WILSON, R. W., and BOLTON, J. G. (1960).—*Publs astr. Soc. Pacif.* **72**, 331.

ACCURATE RIGHT ASCENSIONS OF SELECTED SOUTHERN RADIO SOURCES

By J. M. Sutton*

[*Manuscript received November 27, 1967*]

Summary

Right ascensions of selected radio sources were measured using the east–west arm of the Molonglo radio telescope. A calibration curve was obtained by surveying the aerial structure and site, and by observing radio sources with accurately known positions. Right ascensions are given for 58 sources stronger than 5 f.u. at 408 MHz and in the declination range +19° to −90°. The standard errors are typically 2″.

I. Introduction

The Molonglo radio telescope (Mills *et al.* 1963) is a meridian transit instrument for which observations are restricted to declinations between +19° and −90°. This paper describes some measurements with the first section of the instrument to be completed, the east–west arm operating at the principal frequency of 408 MHz. Used as a total-power device it has a fan-shaped beam with half-power widths of approximately 1′·5 east–west and 4°·2 north–south corresponding in beam area to a circular beam of diameter 19′·5. The array is extremely stable both mechanically and electrically due to (1) its construction from many relatively small elements independently mounted close to the ground, (2) the use of a constant phase local oscillator system (Little, Hunstead, and Calhoun 1966), and (3) the use of components with identical temperature properties in parallel situations. A long-term pointing accuracy of several seconds of arc was expected and measurements and reductions were intended to include all effects of 1″ or greater.

At the time of the observations, the aperture distribution had been adjusted approximately for equal amplitude and equal phase; corresponding to a theoretical aerial pattern of the form $\{(\sin x)/x\}^2$ and a half-power beamwidth of 1′·43. The measured pattern had a symmetric main beam, a half-power beamwidth of 1′·46, and maximum side lobes of 8%. In order to overcome baseline drifts produced by instabilities in the total-power receiver, many sources were also observed by using the east arm and the west arm as the two elements of a phase-switched interferometer and using the receiver that had been built for the complete cross. A quarter wavelength cable was added to one arm, producing an aerial pattern of the form $\{(\sin \frac{1}{2}x)/\frac{1}{2}x\}^2 \sin x$, that is, sinusoidal oscillations of period 3′·24 within an envelope of half-power beamwidth 2′·88.

---

* Cornell–Sydney University Astronomy Centre, School of Physics, University of Sydney, N.S.W. 2006; present address: Arecibo Ionospheric Observatory, P.O. Box 995, Arecibo, Puerto Rico.

Aust. J. Phys., 1968, 21, 221–34

II. Observations

The primary objective of the observations was the pointing calibration of the instrument. Measurements were restricted to catalogued sources stronger than 5 f.u.* at 408 MHz, with diameters (if known) less than 1′ and galactic latitudes greater than 15°. North of −50° these included only a small number of sources, most of which had been observed by the method of lunar occultations (Hazard, Mackey, and Shimmins 1963) or had been reliably identified with quasi-stellar objects on the basis of positional coincidences and characteristically large redshifts (see Section V and Burbridge *et al.* 1966). South of declination −50° they included all sources for which identifications had been suggested (Bolton, Gardner, and Mackey 1964; Price and Milne 1965; Westerlund and Smith 1966) and which satisfied the conditions above. In a search for new identifications, many unidentified sources south of declination −50° (Bolton, Gardner, and Mackey 1964; Price and Milne 1965) were also observed.

Total-power transit measurements were made in May, June, and July 1965 and interferometer measurements were made in September 1965. Each observation extended at least 10 beamwidths on either side of transit. Transit observations were also made 2° north and 2° south of most sources in order to investigate confusion in the north–south direction.

Records were obtained on a chart recorder having a paper speed of 80 mm/min. Local sidereal time marks correct to $0^{\mathrm{s}}\cdot 03$ were superimposed on the records at intervals of 30^{s} and the paper speed was sufficiently uniform to enable times to be measured to the nearest $0^{\mathrm{s}}\cdot 1$. In order to calibrate the local sidereal clock relative to coordinated radio time signals with an accuracy of better than $0^{\mathrm{s}}\cdot 1$, it was necessary to include corrections for the travel times from the stations to the site, and for the differences between UT2 and UTC.

III. Analysis of Observations

(a) *Right Ascension*

On each chart record the transit time of the source through the beam was measured to the nearest $0^{\mathrm{s}}\cdot 1$ by averaging the midpoints of the observed distribution at approximately 30, 50, 70, and 90% of the peak amplitude. In the several cases where asymmetry was detected, the extrapolated position of the peak was used or, if confusion by a strong neighbouring source was evident, an attempt was made to remove its effects. For the observations with the phase-switched system, the transit time was measured by averaging the axes of symmetry of the two major lobes.

The apparent right ascension was obtained from the transit time by applying corrections for

(1) tilt of the aerial (see Section V),
(2) clock error,
(3) time constant of receiver and recorder, and
(4) pointing calibration, including change in collimation error.

---

* 1 flux unit = 10^{-26} W m^{-2} Hz^{-1}.

The effective RC time constant of the receiver–recorder system was measured as $0^{\mathrm{s}}{\cdot}80 \pm 0^{\mathrm{s}}{\cdot}05$ (standard error) by rapidly connecting the input from the aerial to the receiver and measuring the response on the chart recorder. It was assumed that transit times were delayed by this amount. By convolving time-constant responses with the aerial pattern, it can be shown that these corrections are slightly overestimated, by as much as $0^{\mathrm{s}}{\cdot}06$ near the equator.

Owing to the omission of inoperative sections of the array, and the inaccuracy of the quarter wavelength cable used for the interferometer measurements, the collimation error changed between observing periods. The calibration curve was derived relative to the aerial system used for the June and July observations. Systematic corrections of $9''{\cdot}0 \pm 1''{\cdot}5$ (standard error) and $19''{\cdot}5 \pm 0''{\cdot}4$ were derived for the May and September observations respectively by repeating measurements of the same sources.

The apparent right ascension was reduced to the mean equator and equinox of 1950·0 using the Besselian Day Numbers and the precessional constants M and N as described in the Astronomical Ephemeris. The reductions include errors of as much as 1″ due to the combined effects of

(1) the omission of diurnal aberration (maximum error $0''{\cdot}3$),

(2) reducing observations for periods as long as 48 hr without changing the Day Numbers ($0''{\cdot}4$), and

(3) the use of the precessional formulae involving M and N rather than the rigorous results given in the Explanatory Supplement to the Astronomical Ephemeris ($0''{\cdot}12 \tan\delta$, where δ is the declination of the source).

At the time of analysis it was anticipated that an accuracy of 1″ would be adequate. However, the measurements proved to be more accurate than expected, and the maximum errors in reduction are comparable with the random experimental errors.

(*b*) *Declination*

Declination could be derived from the deflections a source produced on drift scans at different elevations. The limiting accuracy, as determined by the uncertainty in setting the elevation and the day-to-day variations in the gains of the preamplifiers, was approximately 20 min of arc.

(*c*) *Equivalent Width*

Equivalent width θ, as defined by $\theta^2 = W_1^2 - W_2^2$, was calculated for each source; W_1 is the width of the observed record and W_2 is the effective width of the beam, both measured between half-power points. By combining measurements of narrow sources at different declinations, W_2 was found to be $1'{\cdot}46 + 0'{\cdot}07 \cos^2\delta$, where the term in $\cos^2\delta$ allows for the broadening caused by the RC time constant.

(*d*) *Flux Density*

Flux density was measured by the product of peak amplitude and equivalent width. Calibration was achieved by comparing flux densities recorded at Molonglo with those measured at Parkes at 408 MHz. Owing to differences in confusion errors for the two instruments, uncertainties in the Parkes flux densities, and possible temperature-dependent variations in the gain of the Molonglo system, the calibration is rather inaccurate.

IV. Errors in the Measurements of Right Ascension

The uncertainty in the right ascension derived for each source can be expressed as a standard error σ given by

$$\sigma^2 = \sigma_c^2 + n^{-1}(\sigma_n^2 + \sigma_t^2 + \sigma_r^2),$$

where n is the number of observations and the subscripted quantities are the component standard errors (for single measurements) due to confusion (σ_c), noise (σ_n), timing (σ_t), and refraction, reduction, and instrumental effects (σ_r). Systematic errors due to the uncertainties in the calibration curve and in the corrections for the time constant are not included. For convenience, all errors will be expressed as pointing errors in seconds of arc.

For the particular receiving and recording systems used, both total-power and phase-switched, the theoretical r.m.s. fluctuations due to random noise were 0·13 f.u. This level, which was attained only for the phase-switched measurements, corresponded to $\sigma_n = 3''\cdot 1/S$, where S is the source intensity in flux units. For the total-power records, baseline instabilities increased σ_n to $16''/S$.

By superimposing source distributions on random sections of low noise total-power records, σ_c was found to be less than $10''/S$. This maximum value of $10''/S$ has been assumed for all error calculations. For phase-switched observations it is assumed that the decrease in random noise compensates approximately for the increased confusion errors.

Referring to Section III, the r.m.s. errors due to timing and reduction were expected to be about $0''\cdot 75 \cos\delta$ and $0''\cdot 5$ respectively. Since all measurements are of right ascension and are made on the meridian, errors caused by refraction in the spherically symmetric components of the atmosphere and ionosphere are zero. However, some refraction is to be expected from large-scale fluctuations and east–west gradients in the electron distribution of the ionosphere, particularly at sunrise and sunset. For meridian measurements at 19·7 MHz, Komesaroff (1960) observed maximum east–west refraction of 1°. Assuming that refraction is proportional to the square of the wavelength, this value corresponds to $8''$ at 408 MHz.

Errors due to the combined effects of timing, reduction, refraction, and instrumental variations were found by comparing repeated measurements of the same sources. Confusion errors produced no variations and noise errors were reduced to a negligible level by confining attention to phase-switched measurements and to total-power measurements of strong sources. The errors were dependent on declination and were compatible with $\sigma_t = 1'' \cos\delta$ and $\sigma_r = 1''$. This low value for σ_r implies that the pointing of the instrument is remarkably stable over periods of weeks and that ionospheric refraction is considerably less than expected. A search for systematic refraction near sunset and sunrise showed that the effect was less than $1''$.

V. Pointing Calibration

It was intended to determine the pointing calibration of the instrument by two independent methods:

(a) *Absolute calibration*, which consists of measuring the position and orientation of the aerial structure on the surface of the Earth, and also determining the relationship of the aerial beam to the physical structure (by measuring the phase distribution along the aperture), and

(b) *Relative calibration*, which consists of measuring the times of transit of radio sources whose positions are already accurately known.

An accuracy of 1″ was aimed for.

The absolute calibration was completed except for the measurement of the phase distribution. The relative calibration was completed but, owing to the small number of suitable calibration sources in the southern skies, was not sufficiently reliable. The final calibration curve was obtained by using observations of northern radio sources to provide the missing parameter in the absolute calibration. It was then found that the relative calibration curve was in fact substantially correct.

(a) *Absolute Calibration*

An ideal meridian transit instrument can be considered as one in which the aerial beam is restricted to the local astronomical meridian, i.e. the plane defined by two lines through the electrical centre of the instrument, the direction of gravity, and the direction to the south celestial pole. Such is the case if the instrument is an array of identical elements situated along a horizontal east–west line and the electrical paths from the elements to the receiver are equal. If local apparent sidereal time is calculated with respect to the astronomical longitude of the electrical centre of the instrument, the right ascension of a source is then given by the local apparent sidereal time at which the source transits the beam.

The east–west arm of the Molonglo radio-telescope was erected so as to approximate to these conditions, except that, in order to reduce the cost of foundations, it was inclined so as to better follow the surface of the Earth. The nominal slope was 11′51″·1 to the west, causing sources to transit late. (It is noted that in construction it was necessary to allow for the curvature of the Earth over the dimensions of the instrument.) The corresponding error in transit time was computed by rigorously solving the appropriate spherical triangle—the usual small-angle approximations were inadequate for such a large error in level. Although only preliminary electrical adjustments had been made to the array at the time of the observations, it was estimated that the mean phase gradient was less than 0·1 wavelengths in 2130 wavelengths, corresponding to a maximum collimation error of 10″.

The east–west pointing error of the telescope, in the sense that the beam points west of its assumed direction thus causing sources to transit late, can be written as

$$l\cos\delta + a\sin(\phi-\delta) + t\cos(\phi-\delta) + c\,,$$

where l is the angle by which the assumed longitude is east of the true longitude, a is the error in the mean astronomical azimuth (which is measured positively from north to east), t is the error in the mean level (a downward slope to the west is positive), c is the collimation error (a deflection of the beam to the west is positive), ϕ is the latitude of the instrument, δ is the declination, and l, a, t, and c are all measured in seconds of arc.

The astronomical coordinates of the electrical centre of the instrument were measured relative to FK4 stars as

$$\text{E. } 149^\circ 25' 25''\cdot 6 \pm 0''\cdot 3, \qquad \text{S. } 35^\circ 22' 19''\cdot 0 \pm 0''\cdot 2$$

and the telescope errors were found to be

$$l = 1''\cdot 8 \pm 0''\cdot 3, \qquad a = 3''\cdot 9 \pm 1''\cdot 5 \qquad \text{and} \quad t = 0''\cdot 4 \pm 0''\cdot 3,$$

where all errors are standard errors. It is noted that an angle of 1″ corresponds to a displacement of 0·31 in. at a distance of 1 mile, the length of the east–west arm.

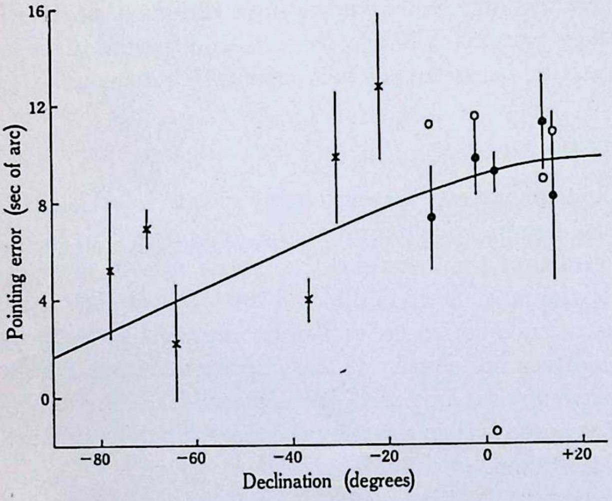

Fig. 1.—Adopted calibration curve and points of observed right ascension minus calibration right ascension expressed as pointing errors in seconds of arc and plotted as functions of declination. A positive error corresponds to the beam pointing west of its assumed position. The points are based on occultation positions (●) and optical positions (×). Also shown are the points obtained for the occultation sources by using the corresponding optical positions (○). Vertical bars indicate standard errors.

The error c was not measured directly. A value of 4″·6 was chosen so as to make the absolute calibration curve pass through that part of the relative calibration curve defined by the five occultation sources (see Section V (b)). The final calibration curve based on these values of l, a, t, and c is shown in Figure 1. It is estimated that the standard error of this curve is 0″·7 near the equator, increasing gradually to 1″·5 near the south celestial pole.

For transit instruments, relationships between the telescope errors can be obtained by observing the same sources at both upper and lower culmination. Such results could not be obtained with the present instrument as it could not be pointed more than 1° below the south celestial pole.

(*b*) *Relative Calibration*

Sources suitable for relative calibration were carefully selected so as to obtain a small number of accurate calibration points rather than a large number of less accurate ones. Since the intensity distribution across a radio source can vary with frequency, as in the case of 3C 273 (Hazard, Mackey, and Shimmins 1963), the sources of highest quality for relative calibration are those whose diameters are small and whose positions have been measured at 408 MHz. Some use can also be made of positions measured optically or at other radio frequencies, providing the overall dimensions of the source are sufficiently small. Observations were restricted to sources having radio diameters less than 30″ (as detected by nonbroadening of the Molonglo beam), galactic latitudes greater than 15°, and flux densities greater than 5 f.u. at 408 MHz (so that confusion errors were generally less than 3″) and whose positions had been measured with an accuracy of 1″. The diameter restriction ensured that the aerial response was symmetric and the measured position was that of the centroid of radio emission at 408 MHz.

TABLE 1

ADOPTED POSITIONS OF CALIBRATION SOURCES

Catalogue No.	Position (1950·0) R.A. h	m	s	Dec. °	′	″	S. Error ″	Ref.*	S_{408} (f.u.)	Nature of Position
Occultation Positions										
3C 15	00	34	30·63	−01	25	39·6	0·5	(1)	10	Centroid at 408 MHz
3C 212	08	55	55·8	+14	21	23	2·0	(2)	7	Centroid at 237 MHz
3C 245	10	40	5·95	+12	19	16·0	0·5	(1)	8	Centroid at 408 MHz
3C 273	12	26	32·61	+02	19	33·1	0·5	(1)	59	Centroid at 408 MHz
MSH 14−*121*	14	53	12·48	−10	56	51	1·0	(1)	9	Centroid at 408 MHz
Optical Positions										
MSH 05−*36*	05	21	13·03	−36	30	15·8	0·5	(3)	32	15^{m} N galaxy
P 1327−21	13	27	23·2	−21	36	34	1·0	(4)	5	16^{m}·5 QSO
P 1655−77	16	55	12·49	−77	37	33·0	0·5	(5)	5	16^{m}·5 E0 galaxy
P 1934−63	19	34	47·57	−63	49	37·7	0·5	(3)	6	18^{m} N galaxy?
MSH 21−*34*	21	15	11·1	−30	31	50	1·0	(4)	6	16^{m}·7 QSO
MSH 21−*64*A	21	52	57·80	−69	55	40·2	0·5	(5)	63	14^{m} E3 galaxy

* References to positions are from:

(1) Reanalysis of occultation records of Hazard, Mackey, and Shimmins (1963),

(2) Hazard (1962),

(3) Remeasurement of photographic plates,

(4) Ekers and Bolton (1965),

(5) Westerlund and Smith (1966).

The adopted calibration positions and their standard errors are given in Table 1. North of declination −20° they include only radio positions that have been measured by the method of lunar occultations. South of declination −20° optical positions are given for those objects that are considered most reliably identified with radio sources. Spectroscopic measurements by Burbridge and Kinman (1966) and Westerlund and Stokes (1966) confirm the identifications for P 1327−21 and MSH 05−*36*, while Ekers and Bolton (1965) find MSH 21−*34* to have UBV colours characteristic of a quasi-stellar object. The other three positions are for interesting objects located close to accurate Parkes radio positions (Shimmins, Clarke, and

TABLE 2

RADIO SOURCE DATA

(1) Catalogue Number MSH	(2) 3C	(3) Parkes	(4) R.A. (1950·0) h m s	(5) R.M.S. Error in R.A. s	(5) ″	(6) No. Obs.	(7) S_{408} (f.u.)	(8) EW Equiv. Width	(9) Remarks*
			(a) Declinations North of −20°						
	9	0017+15	00 17 49·9	0·14	2·1	2	8	<40″	
	15	0034−01	00 34 30·65	0·09	1·4	6	10	<30″	
	47	0133+20	01 33 40·05	0·17	2·4	2	—	35″	1°·5 beyond N. dec. limit
03+08	93	0340+04	03 40 51·6	0·14	2·1	2	8	<1′	
	208	0850+14	08 50 23·2	0·17	2·5	2	8	<40″	
	212	0855+14	08 55 55·7	0·19	2·8	2	7	<40″	
	228	0947+14	09 47 28·0	0·13	1·9	2	9	<40″	
	245	1040+12	10 40 06·1	0·12	1·8	6	8	<30″	
12+08	273	1226+02	12 26 32·60	0·04	0·6	10	59	<20″	
12−020	279	1253−05	12 53 35·75	0·08	1·2	6	12	<30″	Scint. 18° from Sun
13−011		1335−06	13 35 31·2	0·11	1·7	6	8	<30″	Conf.
14−121		1453−10	14 53 12·3	0·13	1·9	5	9	<40″	
19+010	403	1949+02	19 49 44·1	0·13	2·0	1	14	1′·9	
Cygnus A	405		19 57 44·8	0·24	2·7	4	—	2′·2	Obs. in side lobes, posn. of centroid given(a)
22−010	446	2223−05	22 23 10·85	0·10	1·4	4	11	<30″	
CTA 102		2230+11	22 30 08·0	0·12	1·8	4	8	<40″	Conf.
			(b) Declinations South of −20°						
00−51		0003−56	00 03 25·8	0·6	4·9	1	4	<1′	Conf. by 1·5 f.u. source 2′ to W.
		0349−88	03 52 08	10·2	4·5	2	4	1′	1·5 f.u. source 4′ to E.(b)
04−62		0408−65	04 07 57·7	0·17	1·0	2	45	<30″	MSH 15″ EW
04−71		0410−75	04 09 58·5	0·19	0·7	6	31	<20″	MSH 20″ EW
04−63		0420−62	04 20 18·3	0·21	1·5	4	9	<30″	MSH 20″ EW
04−64		0429−61	04 29 34·7	0·5	3·9	1	5	1′·4	
05−36		0521−36	05 21 12·8	0·06	0·7	9	32	25″	MSH 20″ EW
06−55		0625−53	06 25 19·0	0·12	1·1	2	20	50″	MSH 20″ EW(c)
			06 25 46·4	0·4	3·1	2	10	1′·2	Not catalogued
		0744−67	07 43 21·3	0·4	2·6	1	8	40″	
08−71		0842−75	08 42 10·4	0·4	1·5	2	12	<50″	MSH 20″ EW
		0905−68	09 06 14·7	0·6	3·3	1	6	<1′	
		0943−76	09 43 22·3	1·1	3·9	1	5	<1′	2 f.u. source 5′ to E.
11−64		1136−67	11 36 06·9	0·6	3·3	1	6	<1′	
11−66		1151−69	11 52 03·5	0·8	4·4	1	—	~1′	Source ⩾1 f.u. 4′ to W.
		1327−21	13 27 23·55	0·20	2·8	3	5	<30″	
		1547−79	15 47 38·7	0·5	1·4	5	11	<40″	Spectral index 0·7 sep. 27′
		1549−79	15 49 26·7	0·6	1·7	5	9	<40″	Spectral index 0·3
		1602−63	16 01 40	0·6	4·3	1	9	2′·3	EW sep. 5′·9, each comp. ext. towards centre
			16 02 33	0·5	3·5	2	8	1′·5	
		1610−77	16 10 51·3	0·9	2·9	4	5	<40″	
		1637−77	16 37 03·1	0·4	1·3	4	15	1′·5	
		1655−77	16 55 13·3	0·9	2·8	5	5	<1′	
		1716−80	17 16 36·0	0·9	2·4	5	6	<1′	
		1733−56	17 33 09·5	0·3	2·5	3	7	40″	EW sep. 2′·4
			17 33 27·8	0·19	1·6	3	13	<30″	
		1737−60	17 37 27·6	0·3	2·1	4	8	50″	
17−51		1754−59	17 54 37·95	0·17	1·3	6	12	<20″	
18−61		1814−63	18 14 46·0	0·11	0·7	6	32	<25″	Possibly 20″ EW MSH 20″ EW(d)
		—	18 17 26	—	—	1	~10	<40″	Not catalogued
19−61		1922−62	19 22 52·2	0·5	3·1	2	6	1′·2	
		1934−63	19 34 47·3	0·4	2·3	4	6	<30″	
19−57		1954−55	19 54 18·5	0·16	1·4	3	16	0′·9	
20−52		2006−56	—	—	—	4	—	>3′	Possibly 2 comps. sep. 10′ EW
20−54		2014−55	—	—	—	3	—	>3′	Not detected
20−55		2020−57	20 20 21·7	0·21	1·7	4	9	<40″	Conf., MSH 15″ EW

Table 2 (*Continued*)

(1)	(2)	(3)	(4)	(5)		(6)	(7)	(8)	(9)
Catalogue Number MSH	3C	Parkes	R.A. (1950·0) h m s	R.M.S. Error in R.A. s	″	No. Obs.	S_{408} (f.u.)	EW Equiv. Width	Remarks*
20−*71*		2028−73	20 28 21·8	0·7	3·0	3	5	1′·5	Ext. late
20−*61*		2041−60	20 41 17·7	0·21	1·6	4	12	<40″	Conf., MSH 15″ EW
20−*57*		2048−57	20 48 12·1	0·5	3·7	3	6	1′·1	Conf.(e)
21−*34*		2115−30	21 15 11·3	0·23	2·5	4	6	<30″	
		2141−81	21 40 34·0	0·7	1·6	4	9	<50″	
21−*64*		2152−69	21 52 58·5	0·11	0·6	6	63	35″	EW sep. 3′·42, MSH 24″ EW
			21 53 38·1	0·3	1·5	4	12	<1′	
		2227−66	22 27 39	0·7	4·4	1	—	1′·5	
23−*63*		2332−66	23 32 19·6	0·3	2·0	2	8	40″	
23−*64*		2356−61	23 56 12·3	0·4	3	2	32	1′·0	EW sep. 2′·7, MSH 40″ EW
			23 56 34·4	0·4	3	2	34	2′·0	

* Further remarks are:

(a) Cygnus A. This source is 21°·5 beyond the northern declination limit of the aerial but can be observed in side lobes of approximately 0·5%. The observed east–west distribution at 408 MHz is 0′·4 narrower than the corresponding distribution that would be seen with a 1′·5 beam at 1420 MHz (derived from the results obtained by Ryle, Elsmore, and Neville (1965) with a 20″ beam). The difference can be attributed to a larger proportion of radiation coming from the region between the two main components at low frequencies than at high frequencies.

(b) P 0349−88. Owing to the large variation in the level correction near the south celestial pole, a 1′ change in declination will change the east–west position by 4″. The assumed declination was −88° 25′ 57″ (1950·0).

(c) MSH 06−*55*. The weaker component, approximately 1° south of P 0625−53, was missed in the Parkes survey even though MSH 06−*55* was listed by Mills, Slee, and Hill (1961) as "extended; perhaps two sources, (20″)". The declination of the weaker component was measured as −54° 30′ at Parkes (F. Gardner, personal communication). It has a flux density of 3·4 f.u. at 21 cm, giving a spectral index of 0·9.

(d) MSH 18−*61*. The weaker component was missed in the Parkes survey. It is 18′ east of P 1814−63 and, although its declination has not yet been measured, its omission from the Parkes catalogue suggests that it is 0°·5 to 1° away, i.e. sufficiently close to be unresolved by the Parkes finding survey at 408 MHz, but sufficiently distant to be outside the search area about the peak deflection.

(e) MSH 20−*57*. There is a 2 f.u. source 4′ earlier and within 2° in declination. The difference of 50″ between the Molonglo and accurate Parkes right ascensions (Shimmins, Clarke, and Ekers 1966) suggests that the two sources are separated in declination by less than 5′.

Ekers 1966). As suggested by the remainder of the calibration data, it is assumed that only the stronger component of the double radio source MSH 21−*64* is associated with the listed galaxy.

Right ascensions of the calibration sources were measured as described in Section III (except of course for the application of pointing corrections) and the deviations from the calibration right ascensions were expressed as east–west pointing errors in seconds of arc. The individual differences were assigned standard errors according to the expressions given in Section IV, together with additional terms covering the uncertainties in the optical positions. The results are plotted in Figure 1.

Also shown are the calibration points that would result if the optical positions of the objects associated with occultation sources were used rather than the radio centroids (Jeffreys 1964; Sandage, Véron, and Wyndham 1965; Véron 1965*b*, 1966; Wills and Parker 1966).

VI. Radio Source Data

The basic programme of positional calibration has also led to accurate determinations of right ascension and east–west structure for a number of sources. These results are presented in Table 2, which gives, in detail:

Column 1. Number in the MSH catalogue (Mills, Slee, and Hill 1958, 1960, 1961).

Column 2. Number in the revised 3C catalogue (Bennett 1962).

Column 3. Number in the Parkes catalogue (Bolton, Gardner, and Mackey 1964; Price and Milne 1965; Day *et al.* 1966; Shimmins *et al.* 1966). In the text, Parkes sources are denoted by the prefix P.

Column 4. Measured right ascension (1950·0). Level corrections were computed using declinations given in the Parkes catalogue. In combining observations, weight 1/2 is given to scans 2° north or south of the source, and to all records obtained in May 1965 when the change in collimation error was not well determined. The positions of sources marked confused are unlikely to be affected by more than 5″.

Column 5. R.M.S. error in right ascension calculated according to Section IV and expressed in both seconds of time and seconds of arc. In assessing n, results of weight 1/2 count as quarter observations. No estimate of the error in the calibration curve is included.

Column 6. Number of observations.

Column 7. Measured flux density at 408 MHz expressed in flux units. Standard errors due to noise and confusion are approximately $2 \cdot 5/S$ f.u. and systematic errors due to calibration are not expected to exceed 20%.

Column 8. East–west equivalent width as defined in Section III.

Column 9. Remarks and references to further remarks given as footnotes to the table. Where available, east–west diameters (EW) measured by interferometry at 85 MHz (Mills, Slee, and Hill 1960, 1961) are included. Also recorded are any sources stronger than 1 f.u. and within 5′ in right ascension and 2° in declination. Abbreviations used in the column are: comp., component; conf., confused; ext., extended; scint., scintillating; sep., separation.

VII. Comparison of Radio and Optical Positions

In Tables 3(*a*) and 3(*b*), Molonglo right ascensions are compared with those of similar accuracy measured optically and at other radio frequencies (omitting occultation results). Standard errors are given for radio positions; for the optical positions they are 0″·5 to 1″·0.

TABLE 3(*a*)

COMPARISONS OF RIGHT ASCENSIONS FOR SOURCES NORTH OF DECLINATION −20°

Positions are for epoch 1950·0 and only the seconds of right ascension are tabulated. The radio positions are the centroids of radio emission

Source	Right Ascension Molonglo (408 MHz)	Malvern* (610 MHz)	N.R.A.O.† (2695 MHz)	Optical‡		Optical Object
	s s	s s	s s	s		
3C 9	49·9 ±0·14	49·95±0·18		49·83	(1)	QSO
3C 15	30·65±0·09			30·52	(2)	Galaxy
3C 47	40·05±0·17			40·3	(1)	QSO
3C 93	51·6 ±0·14	51·38±0·19		51·47	(3)	QSO
3C 208	23·2 ±0·17			22·79	(1)	QSO
3C 212	55·7 ±0·19	55·91±0·17		55·62	(4)	N galaxy
3C 228	28·0 ±0·13	27·73±0·14				QSO?
3C 245	06·1 ±0·12	06·07±0·13	06·00±0·10	06·11	(1)	QSO
3C 273	32·60±0·04		33·27±0·11	33·31	(5)	QSO
3C 279	35·75±0·08	35·85±0·11	35·87±0·14	35·94	(1)	QSO
13−0*11*	31·2 ±0·11			31·34	(1)	QSO
14−1*21*	12·3 ±0·13			12·22	(6)	QSO
3C 403	44·1 ±0·13		44·0	44·45	(7)	Galaxy§
Cyg. A	44·8 ±0·24			44·35 44·52	(8)	Galaxy
3C 446	10·85±0·10	10·94±0·12		11·05	(3)	QSO
CTA 102	08·0 ±0·12	07·71±0·14	07·76±0·09	07·71	(3)	QSO

* Adgie and Gent (1966).

† Clark and Hogg (1966).

‡ References to optical positions are: (1) Sandage, Véron, and Wyndham (1965); (2) Véron (1966); (3) Véron (1965*a*); (4) Wills and Parker (1966); (5) Jeffreys (1964); (6) Véron (1965*b*); (7) Sandage and Wyndham (1965); (8) Griffin (1963).

§ The Molonglo position for 3C 403 is consistent with that of the galaxy suggested by Sandage and Wyndham (1965) and 18″ east of the blue starlike object they first suggested as the identification. In addition, the Molonglo east–west width of 1′·9 is consistent with the double structure obtained by Maltby and Moffett (1962), and exceptionally large for a quasi-stellar radio source.

Table 3(*a*) includes all sources observed north of declination −20°. The right ascensions are in excellent agreement, and only in the cases of 3C 208, 3C 273, and 3C 403 do the differences between the Molonglo and optical values exceed twice their standard errors. The result for 3C 273 is due to the radio contribution from the jet, and the difference of 5″ for 3C 403 is quite reasonable considering its equivalent width of 1′·9. The difference of 6″ for 3C 208 may well be real and suggests two radio components separated by at least 10″ either having unequal intensities or being asymmetrically placed about the optical object. This would be consistent with the east–west diameter of about 20″ obtained by Allen *et al.* (1962). The relatively large difference for CTA 102 is attributed to confusion.

The new right ascension data presented in Table 3(*b*) can be used to support or reject the suggested southern identifications.

TABLE 3(*b*)

COMPARISONS OF RIGHT ASCENSIONS FOR SUGGESTED IDENTIFICATIONS SOUTH OF DECLINATION −20°

Positions are for the mean equinox of epoch 1950·0 and only the seconds of right ascension are tabulated. $M-O$ is the difference between the Molonglo and optical right ascensions expressed as an angular separation in seconds of arc

Source*	Right Ascension Molonglo (408 MHz) s s	Optical† s	Suggested Identification	$M-O$
MSH 00−*51*(a)	25·8 ±0·6	26·64 (1)	17^m E galaxy	−7″
MSH 04−*71*(b)	58·5 ±0·19	58·1 (1)	15^m S0 galaxy	1″
MSH 05−*36*	12·8 ±0·06	13·0 (5)	15^m N galaxy	−2″·5
P 1327−21	23·55±0·20	23·2 (2)	17^m QSO	5″
P 1655−77	13·3 ±0·9	12·4 (1)	$16^m{\cdot}5$ E0 galaxy	3″
P 1716−80(c)	36·0 ±0·9	−23 (3)	IC 4640	153″
P 1934−63(d)	47·3 ±0·4	47·6 (5)	18^m N galaxy?	−2″
MSH 19−57(e)	18·5 ±0·16	18·74 (1)	13^m G0 star	−2″
MSH 20−*71*	21·8 ±0·7	132 (3)	IC 5016	−480″
MSH 20−6*1*	17·7 ±0·21	12·7 (1)	17^m E galaxy	37″
MSH 20−57	12·1 ±0·5	$0^m{\cdot}2$ (4)	IC 5063 13^m S0 galaxy	<60″
MSH 21−3*4*	11·3 ±0·23	$11^s{\cdot}1$ (2)	$17^m{\cdot}5$ QSO	2″·5
MSH 21−6*4*A(f)	58·5 ±0·11	57·8 (1)	14^m E3 galaxy	3″·5
MSH 23−6*4*(g)	12·3 ±0·4 34·5 ±0·4	29·3 (1)	17^m E3 galaxy	−123″ 37″

* Remarks on individual sources are:

(a) MSH 00−*51*. The optical position of the listed galaxy is consistent with the Molonglo right ascension, but is 79″±14″ (standard error) north of the accurate Parkes declination (Shimmins, Clarke, and Ekers 1966). The discrepancy in declination could possibly be due to the nearby source mentioned in Table 2(*b*), column 9.

(b) MSH 04−*71*. The alternative galaxy suggested by Westerlund and Smith (1966) is 80″ further east and clearly not involved. However, the galaxy listed here is 74″±13″ (standard error) north of the accurate Parkes declination. Considering the strength of the source and the lack of beam broadening, it is unlikely that the declination discrepancy can be attributed to confusion or to a north–south elongation of the source. It is concluded that either the identification is incorrect, or else one of the declination measurements is in error.

(c) P 1716−80. The accurate location of the radio position on a photographic plate shows that the suggested identification is incorrect.

(d) P 1934−63. The peculiar radio spectrum of this source has been discussed in some detail by Kellermann (1966). It is similar to that of the quasi-stellar radio source CTA 102, being markedly curved and having a maximum flux density near 1000 MHz. The suggested identification, which has an apparent extension of 3″ at position angle 300°, is the only peculiarly shaped optical object in the vicinity of the radio position. Its position is consistent with the Molonglo right ascension. It has a diameter less than 2″ and could be either a compact N galaxy or a quasi-stellar radio source. UBV colours, which would help decide its optical classification, are not yet available.

[*Footnotes to Table 3(b) continued opposite*]

Three identifications (P 1716−80, MSH 20−*71*, and MSH 20−*61*) can be rejected on the basis of poor positional agreement. For MSH 20−*57* a more accurate optical position is required, and the declination of the nearby radio source needs to be measured.

For the remaining 10 sources, the agreement in right ascension is good. However, as indicated in the footnotes, there are some doubts concerning the identifications for MSH 00−*51*, MSH 04−*71*, P 1934−63, MSH 19−*57*, and MSH 23−*64*. The five remaining identifications (MSH 05−*36*, P 1327−21, P 1655−77, MSH 21−*34*, and MSH 21−*64*A) are considered reliable.

VIII. Acknowledgments

It is a pleasure to acknowledge the helpful advice of Professor B. Y. Mills throughout the course of this work. The author is also greatly indebted to Mr. P. B. Jones of the University of Sydney, and Mr. A. Bomford and Mr. B. P. Cook of the Department of National Development for their excellent work in surveying the radio telescope structure. Thanks are also due to Dr. C. Hazard for making available his occultation records, and to Mr. R. Ekers, Miss L. F. Smith, and Professor B. Bok of Mt. Stromlo Observatory for making available photographic plates and facilities for their reduction.

This work was supported by grants from the U.S. National Science Foundation and the Science Foundation for Physics within the University of Sydney.

IX. References

Adgie, R. L., and Gent, H. (1966).—*Nature, Lond.* **209**, 549.

Allen, L. R., Anderson, B., Conway, R. G., Palmer, H. P., Reddish, V. C., and Rowson, B. (1962).—*Mon. Not. R. astr. Soc.* **124**, 477.

Bennett, A. S. (1962).—*Mem. R. astr. Soc.* **68**, 163.

Bolton, J. G., Gardner, F. F., and Mackey, M. B. (1964).—*Aust. J. Phys.* **17**, 340.

[*Continuation of footnotes to Table 3(b)*]

(e) MSH 19−*57*. Westerlund and Smith (1966) have located a stellar object with a typical G0 spectrum close to the radio position, but do not consider it as the identification. The east–west radio diameter is 0′·9. The radio source may be related to two very faint nebulosities situated on opposite sides of the star at distances of 10″ and 20″.

(f) MSH 21−*64*. Scans north and south show that the two components of the radio source are separated in declination by less than 15′. The stronger and earlier component, of diameter 30″, is identified with a 14th magnitude D galaxy having a prominent nucleus and an extended envelope of diameter 30″ to 50″. The later component is most likely an unrelated object.

(g) MSH 23−*64*. This is probably a double radio source unsymmetrically placed about the galaxy listed here. There may also be some radiation from the adjacent galaxies 1 and 3 of Westerlund and Smith (1966).

† References to optical positions are: (1) Westerlund and Smith (1966), (2) Ekers and Bolton (1965), (3) Index catalogue, (4) Becvar catalogue, (5) Remeasurement of a photographic plate.

Burbridge, E. M., and Kinman, T. D. (1966).—*Astrophys. J.* **145**, 654.

Burbridge, G. R., Burbridge, M., Hoyle, F., and Lynds, G. R. (1966).—*Nature, Lond.* **210**, 774.

Clark, B. G., and Hogg, D. E. (1966).—*Astrophys. J.* **145**, 21.

Day, G. A., Shimmins, A. J., Ekers, R. D., and Cole, D. J. (1966).—*Aust. J. Phys.* **19**, 35.

Ekers, R. D., and Bolton, J. G. (1965).—*Aust. J. Phys.* **18**, 669.

Griffin, R. F. (1963).—*Astr. J.* **68**, 421.

Hazard, C. (1962).—*Mon. Not. R. astr. Soc.* **124**, 343.

Hazard, C., Mackey, M. B., and Shimmins, A. J. (1963).—*Nature, Lond.* **197**, 1037.

Jeffreys, W. H. (1964).—*Astr. J.* **69**, 255.

Kellermann, K. I. (1966).—*Aust. J. Phys.* **19**, 195.

Komesaroff, M. (1960).—*Aust. J. Phys.* **13**, 153.

Little, A. G., Hunstead, R. W., and Calhoun, G. C. (1966).—*IEEE Trans. Antennas Propag.* **AP-14**, 645.

Maltby, P., and Moffett, A. T. (1962).—*Astrophys. J. Suppl. Ser.* **7**, 141.

Mills, B. Y., Aitchison, R. E., Little, A. G., and McAdam, W. B. (1963).—*Proc. Instn Radio Engrs Aust.* **24**, 156.

Mills, B. Y., Slee, O. B., and Hill, E. R. (1958).—*Aust. J. Phys.* **11**, 360.

Mills, B. Y., Slee, O. B., and Hill, E. R. (1960).—*Aust. J. Phys.* **13**, 676.

Mills, B. Y., Slee, O. B., and Hill, E. R. (1961).—*Aust. J. Phys.* **14**, 497.

Price, R. M., and Milne, D. K. (1965).—*Aust. J. Phys.* **18**, 329.

Ryle, M., Elsmore, B., and Neville, A. C. (1965).—*Nature, Lond.* **205**, 1260.

Sandage, A., Véron, P., and Wyndham, J. D. (1965).—*Astrophys. J.* **142**, 1307.

Sandage, A., and Wyndham, J. D. (1965).—*Astrophys. J.* **141**, 328.

Shimmins, A. J., Clarke, Margaret E., and Ekers, R. D. (1966).—*Aust. J. Phys.* **19**, 649.

Shimmins, A. J., Day, G. A., Ekers, R. D., and Cole, D. J. (1966).—*Aust. J. Phys.* **19**, 837.

Véron, P. (1965*a*).—*Astrophys. J.* **141**, 332.

Véron, P. (1965*b*).—*Astrophys. J.* **141**, 1284.

Véron, P. (1966).—*Astrophys. J.* **144**, 861.

Westerlund, B. E., and Smith, Lindsey F. (1966).—*Aust. J. Phys.* **19**, 181.

Westerlund, B. E., and Stokes, N. B. (1966).—*Astrophys. J.* **145**, 355.

Wills, D., and Parker, E. A. (1966).—*Mon. Not. R. astr. Soc.* **131**, 503.

SHORT COMMUNICATIONS

INELASTIC SCATTERING OF DEUTERONS FROM ^{56}Fe†

By A. R. Majumder‡ and H. M. Sen Gupta‡

Inelastic scattering has been found to be an extremely useful tool in studying the collective states in nuclei. Following the early work of Cohen and Rubin (1958) there has been tremendous interest in the investigation of vibrational states, particularly in the first 2^+ and "anomalous" 3^- states, in even–even nuclei and in their possible interplay with the well-defined single-particle levels in stripping and pickup reactions and even in (p, n) reactions (Guglet 1960). These states in ^{56}Fe have recently been studied mostly through the inelastic scattering of α-particles (McDaniels *et al.* 1960) and protons (Matsuda 1962; Aspinall, Brown, and Warren 1963; Brown, Warren, and Middleton 1966). Except for a few measurements on some of these states (Jahr *et al.* 1961; Gofman and Nemets 1962) no systematic information is available on the inelastic scattering of deuterons from ^{56}Fe. The present work was undertaken with this in view, and in this communication we report on the properties of a few levels of ^{56}Fe, including the 2^+ state at 0·844 MeV and the 3^- state at 4·503 MeV, deduced from the inelastic scattering of 12 MeV deuterons.

The experiment was carried out with the Aldermaston multichannel magnetic spectrograph (Middleton and Hinds 1962). The target was self-supporting and isotopically enriched ($\sim 99\%$) ^{56}Fe of nominal thickness 100 μg cm^{-2}. A beam of 12 MeV deuterons, obtained from the Tandem generator, was scattered from it and detected simultaneously at 24 angles between 5° and 175° in Ilford K2 emulsion 50 μ thick, positioned in the spectrograph. The plates were scanned in Dacca for deuterons and all the levels up to an excitation of 4·5 MeV were identified and the corresponding angular distributions obtained.

Figure 1 shows the angular distributions of deuterons inelastically scattered from ^{56}Fe leading to the first two excited states at 0·844 and 2·077 MeV and the 4·450 and 4·503 MeV states. The spin and parity of the 4·450 MeV state have not been identified previously; the spins and parities of the remaining states are 2^+, 4^+, and 3^- respectively (Brown, Haigh, and MacGregor 1967). The angular distributions are characterized by a principal maximum the position of which can be seen to vary markedly from one state to another, thus helping in the determination of their spins and parities from theoretical analyses.

The distributions for the 2^+ and 3^- states were analysed in terms of the diffraction model of Blair (1960) and the surface deformation parameters were extracted from the normalized cross sections. The present work confirms the spin and parity assignments of the levels at 0·844, 2·077, and 4·503 MeV and suggests $J^\pi = 6^+$

---

† Manuscript received December 29, 1967.

‡ Department of Physics, University of Dacca, Dacca, East Pakistan.

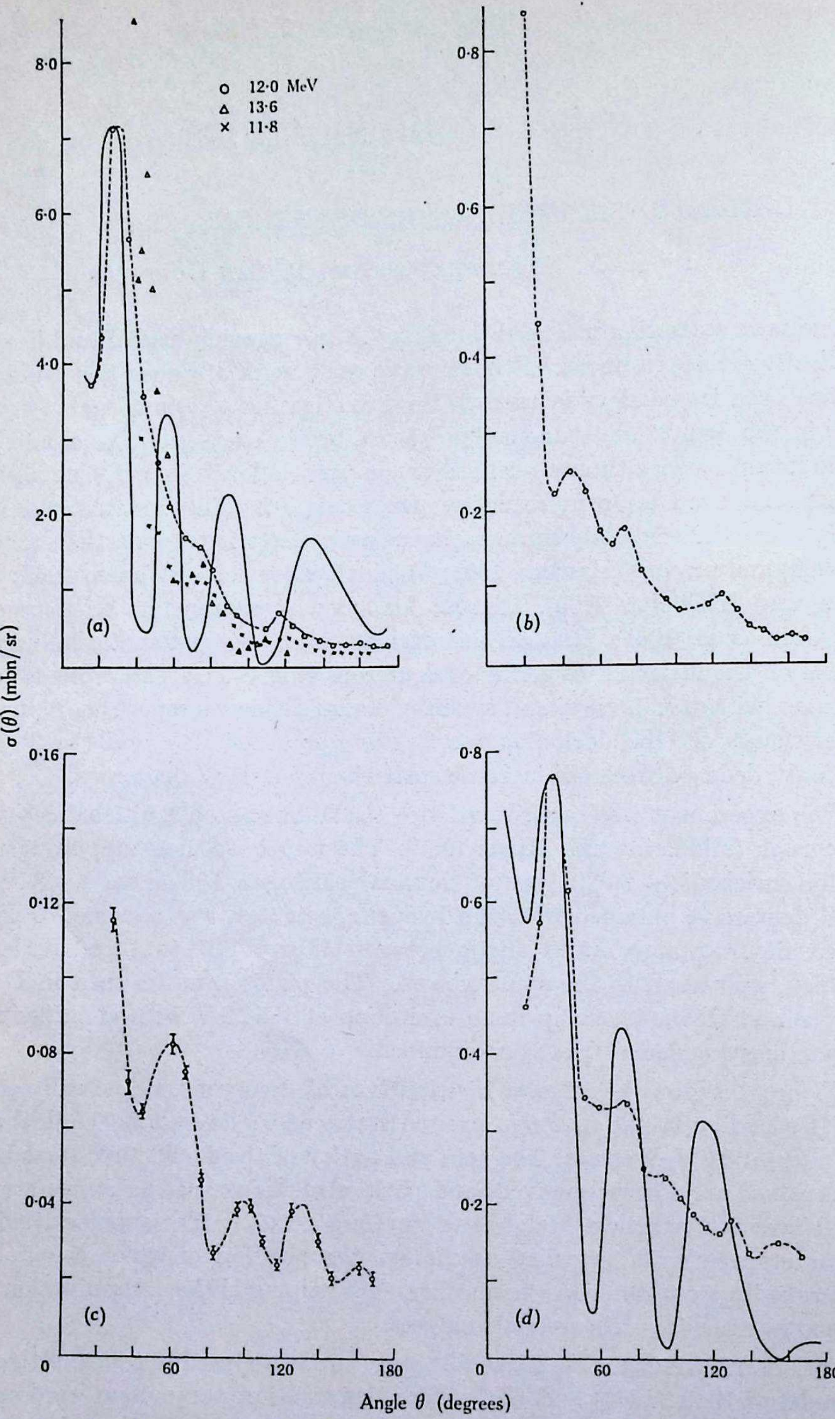

Fig. 1.—Angular distribution of 12 MeV deuterons inelastically scattered from ^{56}Fe with the excitation of the (*a*) 0·844, (*b*) 2·077, (*c*) 4·450, and (*d*) 4·503 MeV states. Also plotted in (*a*) are data from Gofman and Nemets (1962) for 13·6 MeV and from Jahr *et al.* (1961) for 11·8 MeV scattering. The dashed curves are the best eye-estimated ones representing the experimental results and the solid curves are from Blair model analyses.

for the 4·450 MeV level. The relative intensities of these groups at the principal maximum and at 42·5° (lab. angle) are given in Table 1 as a guide. The yield for the octupole vibrational state (4·503 MeV) is extremely large compared with those for the excited states in the range 0·85–4·5 MeV; it is, however, smaller than that for the quadrupole vibrational state (0·844 MeV). This result agrees with those from (p, p′) and (α, α') experiments. The 4·450 MeV state, on the other hand, is one of the weakest groups (this has possibly been caused by the centrifugal potential barrier) thus confirming its large angular momentum.

TABLE 1

LEVEL STRUCTURES STUDIED IN ^{56}Fe

Excitation (MeV)	$J\pi$	Relative Intensity at: Peak	42·5°	Deformation Parameter
0·844	2^+	100	100	0·41 (quadrupole deformation)
2·077	4^+	3·9	8·0	
4·450	6^+	1·6	2·5	
4·503	3^-	14·4	24·0	0·16 (octupole deformation)

The authors wish to thank Professor M. Innas Ali for his interest in the work, Dr. S. Hinds for making the plates available, and the computer personnel of the Atomic Energy Centre, Dacca, for the facilities for computational work. One of the authors (A.R.M.) acknowledges a financial grant from the Dacca University.

References

ASPINALL, A., BROWN, G., and WARREN, S. E. (1963).—*Nucl. Phys.* **46**, 33.
BLAIR, J. S. (1960).—Proc. Int. Conf. on Nuclear Structure, Kingston, Canada, p. 824.
BROWN, G., HAIGH, J. G. B., and MACGREGOR, A. E. (1967).—*Nucl. Phys.* A **97**, 353.
BROWN, G., WARREN, S. E., and MIDDLETON, R. (1966).—*Nucl. Phys.* **77**, 365.
COHEN, B. L., and RUBIN, A. G. (1958).—*Phys. Rev.* **111**, 1568.
GOFMAN, YU. V., and NEMETS, O. F. (1962).—*Zh. éksp. teor. Fiz.* **42**, 1013.
GUGLET, P. C. (1960).—Proc. Int. Conf. on Nuclear Structure, Kingston, Canada, p. 157.
JAHR, R., MÜLLER, J. K. D., OSWALD, W., and SCHMIDT-ROHR, U. (1961).—*Z. Phys.* **161**, 509.
MCDANIELS, D. K., BLAIR, J. S., CHEN, S. W., and FARWELL, G. W. (1960).—*Nucl. Phys.* **17**, 614.
MATSUDA, K. (1962).—*Nucl. Phys.* **33**, 536.
MIDDLETON, R., and HINDS, S. (1962).—*Nucl. Phys.* **34**, 404.

0^+ STATES OF ^{8}Be

By F. C. Barker,* H. J. Hay,* and P. B. Treacy*

[*Manuscript received December* 21, 1967]

Summary

The light even nuclei with $A \geqslant 10$ have 0^+ excited states near 6 MeV, probably with large α-particle reduced widths. A similar state in ^{8}Be would be very broad. Evidence for 0^+ excited states in ^{8}Be has been obtained here using many-level *R*-matrix fits to known α–α scattering data, but the excitation energies depend strongly on the assumed channel radius. For a simultaneous fit to the ^{9}Be(p, d)^{8}Be cross section, assuming these higher states are not strongly populated, the channel radius is restricted to (7^{+2}_{-1}) fm, implying a 0^+ excited state at (6 ∓ 3) MeV of width (9 ∓ 4) MeV.

I. Introduction

The nucleus ^{8}Be has been studied in considerable detail (Lauritsen and Ajzenberg-Selove 1966) and its level structure below 16 MeV appears to be very simple, consisting of a 0^+ ground state, a broad 2^+ state at 2·9 MeV, and a very broad 4^+ state at 11·4 MeV. Other light even nuclei from ^{10}Be to ^{16}O have 0^+ excited states at excitation energies of order 6 MeV, probably with large α-particle reduced widths and not belonging to the lowest shell model configuration. In this paper, we consider the possible existence of such a state in ^{8}Be; because of the large energy available for α-particle decay, one would expect such a state to be very broad and this would make its identification difficult. The properties of these 0^+ excited states in light nuclei are more fully discussed in Section II, where it is considered how a similar state in ^{8}Be could fit in with theories of nuclear structure that have been applied to ^{8}Be.

Evidence for such an excited 0^+ state in ^{8}Be could come from α–α elastic scattering and from reactions that proceed through states of ^{8}Be to give three final particles. The analysis of α–α scattering in this region is particularly simple as the channel spin is zero and there is only one open channel, so the phase shifts δ_l for relative orbital angular momentum l are fairly well known. The present procedure is to use a many-level one-channel *R*-matrix formalism, given in Section III, to fit the observed s-wave phase shift δ_0 for a range of values of channel radius a_0 and for a particular choice of the boundary condition parameter B_0. The same fit can be obtained for any other value of B_0 by adjusting the level parameters. This is described in Section IV.

---

* Research School of Physical Sciences, Australian National University, Canberra, A.C.T. 2600.

In order to limit the acceptable values of a_0 and the level parameters, the R-matrix formalism of Section III with parameters that fit δ_0 is also required to give a fit to the measured ^{9}Be(p, d)^{8}Be cross section in the region of the ground state main peak and its ghost (Section V). For this purpose certain reasonable "model" restrictions are imposed on the values of B_0 and the feeding factors for the higher 0^+ levels in this reaction.

The final acceptable values of the R-matrix parameters, and the derived properties of the ground and excited 0^+ states, are given in Section VI. Appendixes I, II, and III contain a justification of the use of the one-channel approximation, the relations between the level parameters and B_0 that are needed in order to make the fits independent of the choice of B_0, and a discussion of the best choice of B_0. Some of the formulae in Section III and the appendixes are given for general l values, so that they can also be used in a later paper in which 2^+, 4^+, . . . states of ^{8}Be will be discussed.

II. SYSTEMATICS AND MODELS FOR ^{8}Be

Table 1 gives the excitation energies of 0^+ excited states observed in the even nuclei from ^{10}Be to ^{16}O, as well as the energies of the corresponding $T = 1$ states in their odd–odd isobars (Ajzenberg-Selove and Lauritsen 1959; Lauritsen and Ajzenberg-Selove 1966). Also given are the Q values Q_α for α-particle decay. There is no obvious correlation of the level position with either the mass number A or Q_α. Over a wider range of A values, the excitation energies of low-lying 0^+ states in closed shell nuclei appear to vary as $A^{-2/3}$ (Sheline and Wildermuth 1960; Meyerhof 1966).

These states probably do not belong to the lowest shell model configuration $(1s)^4(1p)^{A-4}$. This is obviously the case for the ^{16}O state, which appears to contain an appreciable 4p–4h component (e.g. see Brown and Green 1966). Also 2p–2h configurations have been suggested for the ^{14}N state by Unna and Talmi (1958), for the ^{10}Be and ^{10}B states by True and Warburton (1961), and for the ^{12}C state by Cohen and Kurath (1965).

There is some evidence that these excited 0^+ states have large α-particle reduced widths. Only for the ^{12}C state is the α-channel the only open channel, and here the measured width leads to an α-particle reduced width near the "single-particle" value, even when a channel radius considerably larger than the conventional one is used (Barker and Treacy 1962). An appreciable reduced width has been obtained for the ^{16}O state from the ^{6}Li(^{12}C, d)^{16}O reaction (Loebenstein *et al.* 1967; see also Bethge *et al.* 1967).

There is no obvious reason why a similar 0^+ excited state belonging to a higher configuration should not exist in ^{8}Be in the region of 6 MeV excitation energy. Such a state with an α-particle reduced width near the single-particle value would be very broad* with a width of order 10 MeV.

---

* Early evidence from α–α scattering and from ^{7}Li(p, $\gamma\alpha$)^{4}He for a narrower 0^+ state near 7·6 MeV with width about 1 MeV has not been substantiated (see Ajzenberg-Selove and Lauritsen 1959; Lauritsen and Ajzenberg-Selove 1966).

It is frequently stated that models of ^{8}Be predict only the well-known 0^+, 2^+, and 4^+ states below 16 MeV. This is not true for all models. Thus, in the cluster model of Wildermuth and Kanellopoulos (1959), completely antisymmetric states are constructed from single-particle oscillator wave functions, the lowest eigenstates consisting of two α-particles in relative 3s, 2d, and 1g oscillations, i.e. 0^+, 2^+, and 4^+ states. The next higher α-particle states are the 0^+, 2^+, 4^+, 6^+ sequence coming from the 4s, 3d, 2g, and 1i oscillations, and it was estimated that these lay well above the 1g state (at the order of 20 MeV excitation energy); however, by changing the two-particle interaction it would be possible to reduce the energies of these states.

TABLE 1

EXCITATION ENERGIES OF 0^+ EXCITED STATES OF LIGHT EVEN NUCLEI AND OF CORRESPONDING $T = 1$ STATES IN THEIR ODD–ODD ISOBARS

Nucleus	E_x (MeV)	Q_α (MeV)	Nucleus	E_x (MeV)	Q_α (MeV)
^{8}Be		$0\cdot09$	^{14}C	$6\cdot59$	$-12\cdot02$
^{10}Be	$6\cdot18$	$-7\cdot42$	^{14}N ($T = 1$)	$6\cdot31$*	$-11\cdot04$*
^{10}B ($T = 1$)	$5\cdot82$*	$-6\cdot28$*	^{14}O	($5\cdot91$)†	$-10\cdot08$
^{12}C	$7\cdot66$	$-7\cdot38$	^{16}O	$6\cdot06$	$-7\cdot16$

* Measured from the lowest $T = 1$ state.

† Ball and Cerny (1967) suggest that the $5\cdot91$ MeV level is probably 0^+.

A shell model calculation including only the lowest $(1s)^4(1p)^4$ configuration does not predict a 0^+ excited state of ^{8}Be below about 16 MeV (see Cohen and Kurath 1965; Barker 1966). A shell model calculation with configuration mixing, including only a limited class of states, predicted in addition to the lowest 0^+, 2^+, 4^+ levels also a 0^+, 2^+, 4^+, 6^+ band starting with a 0^+ level at $9\cdot66$ MeV (Gupta, Khadkikar, and Parikh 1966).

It seems therefore that neither the cluster model nor the shell model excludes the existence of a 0^+ excited state of ^{8}Be below 10 MeV.

III. *R*-MATRIX FORMULAE IN THE ONE-CHANNEL APPROXIMATION

To describe processes involving the ^{8}Be nucleus, the formalism of R-matrix theory is employed. This provides a general and convenient representation for two-stage reactions. For practical applications it is necessary to assume that only a finite number of levels and channels are involved.

Lane and Thomas (1958) have given the R-matrix formulae for the cross section of a nuclear reaction in the general many-level many-channel case. For α–α scattering below the ^{7}Li+p threshold, i.e. for channel energies $E < 17\cdot35$ MeV, there is only one open channel for a given total angular momentum J, i.e. the $\alpha+\alpha$ channel with relative orbital angular momentum $l = J$, and use of the one-channel approximation seems appropriate. This is justified in Appendix I.

In the one-channel approximation there is a simple connection between the nuclear phase shift δ_l and the R_l function (Lane and Thomas 1958),

$$R_l = \{P_l \cot(\delta_l+\phi_l)+S_l-B_l\}^{-1}. \tag{1}$$

Here P_l, S_l, and $-\phi_l$ are respectively the penetration factor, shift factor, and hard-sphere phase shift, which are energy dependent and can be calculated for a given channel radius a_l; B_l is a real constant boundary condition parameter. Also R_l must be of the form (Lane and Thomas 1958)

$$R_l = \sum_\lambda \gamma^2_{\lambda l}/(E_{\lambda l}-E), \tag{2}$$

in terms of the eigenenergies $E_{\lambda l}$ and the reduced widths $\gamma^2_{\lambda l}$.

The present procedure is to make a q-level approximation and to choose the parameters $E_{\lambda l}$ and $\gamma^2_{\lambda l}$ for given a_l and B_l to give the best fit to the experimental values of δ_l by minimizing

$$X_l = \frac{1}{N}\sum_{i=1}^{N}\left|\frac{\delta_l^{\text{exp.}}(E_i)-\delta_l(E_i)}{\epsilon_l(E_i)}\right|^2. \tag{3}$$

Here $\delta_l^{\text{exp.}}(E_i)$ and $\epsilon_l(E_i)$ are the measured phase shift and error at the energy E_i $(i = 1 \ldots N)$ respectively, and $\delta_l(E_i)$ is the phase shift calculated from (1) and (2):

$$\delta_l(E) = -\phi_l+\arctan\left[P_l \div \left\{\left(\sum_{\lambda=1}^{q}\gamma^2_{\lambda l}/(E_{\lambda l}-E)\right)^{-1}-S_l+B_l\right\}\right]. \tag{4}$$

The IBM 360/50 computer of the Australian National University was used for the minimization. From equation (4), the dependence of $\delta_l(E)$ on E can be made independent of the choice of B_l by suitably adjusting the values of the level parameters $E_{\lambda l}$ and $\gamma^2_{\lambda l}$. The resulting relations between these parameters and B_l are given in equations (A12) and (A13) of Appendix II.

In this paper we are interested in the case $l = 0$, and for this we may use the fact that the ^{8}Be ground state energy E_g has been measured very accurately in α–α scattering, in order to obtain a relation between the parameter values a_0, B_0, $E_{\lambda 0}$, and $\gamma^2_{\lambda 0}$. Since $\delta_0 = 90°$ at $E = E_\text{g}$ and since ϕ_0 is negligible at this energy, one obtains from (4)

$$\left(\sum_{\lambda=1}^{q}\gamma^2_{\lambda 0}/(E_{\lambda 0}-E_\text{g})\right)^{-1} = S_0(E_\text{g})-B_0. \tag{5}$$

Thus it is convenient to do the initial fitting to δ_0 with the choice

$$B_0 = S_0(E_\text{g}), \tag{6}$$

so that (5) can be satisfied with

$$E_{10} = E_\text{g}. \tag{7}$$

Then the relations (A12) and (A13) can be used to obtain the parameter values that will give the same fit for any other value of B_0. The width Γ_g of the ^{8}Be ground state, defined as the difference of the energies at which δ_0 equals 45° and 135°, is similarly given by a simple formula if one makes the choice (6), (7):

$$\Gamma_g = 2\gamma_{10}^2 P_0(E_g)/\{1+\gamma_{10}^2 S_0'(E_g)\}\,, \tag{8}$$

where the prime denotes the energy derivative.

In various reactions, ^{8}Be is formed as a product nucleus which then decays into two α-particles. The dependence on the ^{8}Be excitation energy of the cross section for such reactions has been obtained, by a reasonable generalization of the R-matrix formula for the one-level approximation, for the case where many levels of ^{8}Be with the same spin and parity may contribute (Barker 1967). The form appropriate for discussing the low-lying levels of ^{8}Be with spin J, for which only the $\alpha+\alpha$ channel with $l = J$ is open, is

$$\sigma_\alpha \propto P_l \sum_x \left| \frac{\sum_{\lambda=1}^{q} \{G_{\lambda x}^{\frac{1}{2}} \gamma_{\lambda l}/(E_{\lambda l}-E)\}}{1-(S_l-B_l+\mathrm{i}P_l)\sum_{\lambda=1}^{q}\{\gamma_{\lambda l}^2/(E_{\lambda l}-E)\}} \right|^2 , \tag{9}$$

where $G_{\lambda x}$ is a real positive feeding factor (usually a slowly varying function of E) and x labels the quantum numbers for the formation process that give incoherent contributions to σ_α. For the case $l = 0$, normalization of (9) to the ^{8}Be ground state main peak leads to a simple relation for the G_{1x} when the choice (6), (7) is made. Simultaneously with the requirement that the $E_{\lambda l}$, $\gamma_{\lambda l}^2$ should be such as to make δ_l given by (4) independent of B_l, the $G_{\lambda x}$ can be required to make σ_α independent of B_l. The resulting relation is equation (A14) of Appendix II.

IV. R-MATRIX PARAMETERS FROM α–α SCATTERING DATA

(*a*) *Experimental Data*

Experimental values of the phase shifts $\delta_l^{\text{exp.}}$ and their errors ϵ_l have been obtained by several authors from analyses of the α–α elastic scattering cross sections measured at various α-particle beam energies up to 120 MeV, corresponding to channel energies E up to 60 MeV. The phase shifts must be real for $E < 17 \cdot 35$ MeV but may be complex at higher energies.

For the lower energies, we use the values of $\delta_0^{\text{exp.}}$ and ϵ_0 given for $E = 0 \cdot 2$–$1 \cdot 5$ MeV (Heydenberg and Temmer 1956), $E = 1 \cdot 92$–$5 \cdot 94$ MeV (Tombrello and Senhouse 1963), and $E = 6 \cdot 15$–$11 \cdot 45$ MeV (Nilson *et al.* 1958). Bredin *et al.* (1959) have extracted real phase shifts from their data for $E = 11 \cdot 55$–$19 \cdot 2$ MeV, but their values are given only graphically and no convenient values of ϵ_0 are given. The above data have all been reanalysed by Berztiss (1965) assuming real phase shifts; the $\delta_0^{\text{exp.}}$ values are similar to those previously obtained but the associated errors (obtained using a different criterion) are sometimes quite different. We use Berztiss's values of $\delta_0^{\text{exp.}}$ for $E = 11 \cdot 55$–$17 \cdot 1$ MeV, and for the accompanying errors round off his values to $\epsilon_0 = 5°$. Some values of $\delta_0^{\text{exp.}}$ appear to be relatively less precise, e.g. those at $6 \cdot 15$, $7 \cdot 6$, and $15 \cdot 15$ MeV, and we have doubled the corresponding ϵ_0 values.

Complex phase shifts are available at higher energies, e.g. $E = 26 \cdot 7$ to $59 \cdot 93$ MeV (Darriulat *et al.* 1965), but we have not tried to fit δ_0 above the ^{7}Li+p threshold.

From α–α scattering at very low energies Benn *et al.* (1966) have observed the ground state of ^{8}Be at a channel energy $E = E_g = (92 \cdot 12 \pm 0 \cdot 05)$ keV with a width $\Gamma_g = (6 \cdot 8 \pm 1 \cdot 7)$ eV.

(*b*) *Three-level* R-*matrix Fits to* δ_0

R-matrix fits to δ_0 in the low energy region have previously been made in the one-level one-channel approximation, e.g. Barker and Treacy (1962) obtained acceptable fits for $E \lesssim 3$ MeV for channel radii a_0 between $3 \cdot 2$ and $4 \cdot 2$ fm, but deviations increased at higher energies. These deviations may be attributed to the effects of higher 0^+ levels, so we try a many-level approximation in order to fit δ_0 over a larger energy range. As we wish to retain the one-channel approximation, fits are restricted to $E \lesssim 17$ MeV, as discussed in Appendix I.

Table 2

PARAMETER VALUES FOR BEST FITS TO $\delta_0^{\mathrm{exp.}}$ IN THE THREE-LEVEL APPROXIMATION FOR VARIOUS CHANNEL RADII

$B_0 = S_0(E_g)$ and $E_{10} = E_g = 92 \cdot 12$ keV

a_0 (fm)	$E_{\max}$ (MeV)	N	B_0	γ_{10}^2 (MeV)	E_{20} (MeV)	γ_{20}^2 (MeV)	E_{30} (MeV)	γ_{30}^2 (MeV)	X_0	Γ_g (eV)
5·5	17·1	36	−1·428	0·295	12·58	1·003	30·5	1·74	0·44	5·53
6·0	17·1	36	−1·491	0·193	9·80	0·835	34·7	2·27	0·44	5·46
6·5	17·1	36	−1·550	0·126	7·79	0·712	28·5	1·85	0·43	5·22
7·0	17·1	36	−1·605	0·081	6·28	0·609	22·4	1·38	0·47	4·78
7·5	14·9	33	−1·657	0·052	5·20	0·521	18·8	1·14	0·45	4·27
8·0	13·8 12·75	32 31	−1·707	0·036	4·39	0·454	16·1	1·00	0·47	4·01
8·5	10·9	26	−1·754	0·022	3·74	0·395	13·4	0·79	0·44	3·28
9·0	9·55	23	−1·799	0·016	3·25	0·338	11·9	0·77	0·48	3·13

In Section II it was suggested that the second 0^+ level might be expected near 6 MeV, so that a third or higher 0^+ level could also be contributing appreciably in $E \lesssim 17$ MeV. To allow for the higher 0^+ levels, we use a three-level approximation, where the third "level" is considered to include the effects of all levels above the second. Since from equation (4) the third level is expected to occur for $\delta_0 + \phi_0 \simeq 450°$, we restrict the energy range over which fits are made by requiring $\delta_0^{\mathrm{exp.}} + \phi_0 \lesssim 440°$. Since ϕ_0 increases with a_0, this restriction becomes effective for the larger channel radii $a_0 > 7 \cdot 0$ fm.

The parameter values that give best fits to $\delta_0^{\mathrm{exp.}}$ for various channel radii are given in Table 2. These values are obtained by taking $B_0 = S_0(E_g)$ so that $E_{10} = E_g$, and varying γ_{10}^2, E_{20}, γ_{20}^2, E_{30}, and γ_{30}^2 to minimize X_0 given by equation (3). The range of data fitted is specified by the maximum E_l value $E_{\max}$ and the number of data points N used in each fit. It is roughly within the range of channel radii given in Table 2 that acceptable fits to both scattering and reaction data can be found.

The minimum X_0 is about $0 \cdot 45$ for each a_0, the irregular fluctuations being due to the different ranges of data being fitted. In fact, to obtain a suitable minimum X_0 for $a_0 = 8 \cdot 0$ fm, we had to average the fits obtained for the two cases of $E_{\max} = 13 \cdot 8$ and $12 \cdot 75$ MeV, as experimental phase shifts are available only at widely spaced energies in this region and they do not vary smoothly with energy. Table 2 also includes calculated values of $\Gamma_{\rm g}$. These all tend to be lower than the experimental value of $(6 \cdot 8 \pm 1 \cdot 7)$ eV, the discrepancy increasing as a_0 increases.

TABLE 3

PARAMETER VALUES FOR FITS TO $\delta_0^{\rm exp.}$ IN THE THREE-LEVEL APPROXIMATION FOR $a_0 = 7 \cdot 0$ fm AND VARIOUS FIXED VALUES OF γ_{10}^2

$E_{\max} = 17 \cdot 1$ MeV, $B_0 = S_0(E_{\rm g}) = -1 \cdot 605$, $E_{10} = E_{\rm g} = 92 \cdot 12$ keV

γ_{10}^2 (MeV)	E_{20} (MeV)	γ_{20}^2 (MeV)	E_{30} (MeV)	γ_{30}^2 (MeV)	X_0	$\Gamma_{\rm g}$ (eV)
0·05	6·20	0·568	20·8	1·04	0·90	3·10
0·06	6·22	0·582	21·2	1·13	0·66	3·66
0·07	6·25	0·595	21·7	1·24	0·52	4·21
0·08	6·28	0·608	22·3	1·36	0·47	4·73
0·09	6·31	0·620	23·0	1·50	0·51	5·24
0·10	6·34	0·631	23·8	1·65	0·62	5·74
0·11	6·37	0·642	24·6	1·83	0·80	6·22
0·12	6·40	0·652	25·7	2·04	1·04	6·69

The parameter values in Table 2 correspond to the best fits for each a_0. Variations of the parameters about these values can still lead to acceptable fits. We impose the somewhat arbitrary condition $X_0 \lesssim 1$ for an acceptable fit. Then for the particular case $a_0 = 7 \cdot 0$ fm, Table 3 gives parameter values for fits with $X_0 \lesssim 1$ obtained by taking a set of fixed values of γ_{10}^2 and varying only E_{20}, γ_{20}^2, E_{30}, and γ_{30}^2. It is seen that acceptable fits can be obtained for a wide range of γ_{10}^2 values (and consequently of $\Gamma_{\rm g}$ values), but the corresponding values of E_{20} and γ_{20}^2 stay fairly constant, while we are not particularly interested in the parameter values for the third "level". In this way, even for the larger channel radii, acceptable fits can be obtained with the calculated $\Gamma_{\rm g}$ in the experimental range.

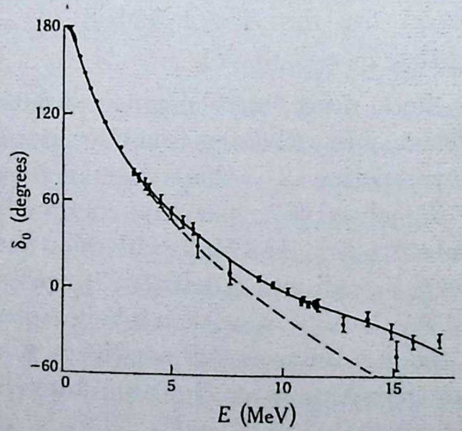

Fig. 1.—The α–α scattering s-wave phase shift δ_0 as a function of ^{8}Be channel energy E. The points are experimental values and the solid curve is the R-matrix three-level fit for the channel radius $a_0 = 7 \cdot 0$ fm and other parameters as in Table 6. The dashed curve is the best one-level fit for $E \lesssim 3$ MeV obtained with $a_0 = 3 \cdot 5$ fm (Barker and Treacy 1962).

These fits to $\delta_0^{\text{exp.}}$ are illustrated in Figure 1, where the calculated curve is for $a_0 = 7\cdot0$ fm, $\gamma_{10}^2 = 0\cdot087$ MeV, and other parameter values obtained by interpolation in Table 3, so that $X_0 = 0\cdot49$. These values give the best overall fit to the scattering and reaction data involving the 0^+ levels of ^{8}Be (see Table 6 below).

Thus acceptable three-level fits to the α–α scattering data, including δ_0, E_g, and Γ_g, can be obtained for a wide range of channel radii, including at least $5\cdot5$ to $9\cdot0$ fm, and the corresponding values of E_{20} are seen from Table 2 to vary widely.

(c) *Width of* ^{8}Be *Ground State*

Before making use of data from other reactions involving ^{8}Be to limit the range of acceptable a_0 values, we discuss more fully the value of Γ_g. The only directly measured experimental value is that of Benn *et al.* (1966) giving $\Gamma_g = (6\cdot8 \pm 1\cdot7)$ eV.

Values calculated from three-level R-matrix fits to δ_0 are given in Tables 2 and 3. Some values previously calculated (Barker and Treacy 1962) using the one-level approximation ($\Gamma_g \simeq 6\cdot8$ eV) or the effective range expansion ($\Gamma_g \simeq 6\cdot7$ eV) were considerably larger than the values of Tables 2 and 3, mainly because they were calculated using an older value of the ground state energy of 94 keV; if calculated at the newer value of $92\cdot12$ keV they should be reduced by 17% to give $\Gamma_g \simeq 5\cdot6$ eV. The values of Γ_g obtained from the effective range expansion can vary considerably, depending on the order of the polynomial expansion assumed for the function K and on the energy range over which the experimental data are fitted. Thus with K assumed to be a quadratic function of E, a good fit ($X = 0\cdot25$, where the definition of X is similar to that of X_l in equation (3)) is obtained to the data for $E \leqslant 1\cdot5$ MeV giving $\Gamma_g = 5\cdot1$ eV, but a much poorer fit is obtained for $E \leqslant 5\cdot0$ MeV ($X = 0\cdot82$, $\Gamma_g = 4\cdot4$ eV). The lower limit of the energy range is taken as $E = 0\cdot2$ MeV in all cases. A cubic function gives good fits for $E \leqslant 1\cdot5$ MeV ($X = 0\cdot19$, $\Gamma_g = 4\cdot1$ eV) and for $E \leqslant 5\cdot0$ MeV ($X = 0\cdot31$, $\Gamma_g = 5\cdot8$ eV).

Tombrello (1966) also considered the effect of varying the range of data fitted and concluded that the ground state width is extremely ill determined by this method; however, he did not impose the necessary restriction $K = h$ at resonance and this accounts for the wide spread of his values. Rasche (1967; personal communication) used the effective range expansion to fit data for $E \leqslant 1\cdot5$ MeV with K a quadratic function of E and obtained $\Gamma_g = (5\cdot1 \pm 0\cdot4)$ eV. Ali and Afzal (1967) used a cubic function and also fitted the data for $E \leqslant 1\cdot5$ MeV, but with a phenomenological α–α potential as an intermediary. They did not impose the condition $K = h$ at $E = E_g = 92\cdot12$ keV; instead they found that $K = h$ at $E_R \simeq 95\cdot1$ keV, giving $\Gamma_R \simeq 6\cdot4$ eV. This leads to $\Gamma_g \simeq 4\cdot8$ eV if calculated at $E = E_g$.

A hard-core effective range theory has been developed by Kermode (1965) to treat α–α scattering, and applied by him (Kermode 1967) to obtain $\Gamma_g = (6\cdot14 \pm 0\cdot04)$ eV. He assumed his function y_0 to be a quadratic function of E and fitted data for $E \leqslant 12$ MeV. The hard-core theory is capable of fitting δ_0 up to higher energies than the conventional theory, as the expansion of K in the latter certainly breaks down before δ_0 decreases to 0°, which happens at $E \simeq 10$ MeV. To obtain the best value of Γ_g, however, one requires to extrapolate δ_0 to low energies and it is not necessarily advantageous to use an expansion that gives a fit to high energies. Thus for a fit up to only $1\cdot5$ MeV, the quadratic hard-core theory with hard-core radius $\simeq 1\cdot5$ fm gives $X = 0\cdot28$ and $\Gamma_g = 5\cdot4$ eV, while cubic fits for $E \leqslant 1\cdot5$ MeV and $E \leqslant 5\cdot0$ MeV give respectively $X = 0\cdot16$, $\Gamma_g = 4\cdot3$ eV and $X = 0\cdot24$, $\Gamma_g = 5\cdot5$ eV. These values are similar to those obtained from the conventional theory. For Kermode's fit up to 12 MeV, X is considerably larger ($X = 0\cdot48$).

Thus from effective range expansions, the best fits to δ_0 values measured at energies $E \geqslant 0\cdot2$ MeV give Γ_g values in the range 4–6 eV. Acceptable fits to δ_0 would provide a wider range of Γ_g values, probably similar to that indicated in Tables 2 and 3, which are for R-matrix fits to δ_0. In the following section, the range of Γ_g values is considerably reduced by requiring the R-matrix parameters to fit reaction data as well.

V. *R*-MATRIX PARAMETERS FROM REACTION DATA

(*a*) *Choice of Reaction and Experimental Data*

From R-matrix fits to the α–α scattering data we have found a wide range of parameters that are acceptable for describing the low-lying 0^+ states of ^{8}Be. In order to limit the range of these parameters, we wish to use experimental data from reactions that appear to proceed through an intermediate stage involving states of ^{8}Be. To do this it is necessary to separate out the contribution from 0^+ states of ^{8}Be. One difficulty is that, in such reactions giving three final products, the order in which the particles are emitted is usually not certain so that contributions from broad levels cannot be disentangled from the background due to alternative modes of decay. Only for a few special reactions involving β- or γ-decay, such as $^8\mathrm{Li}(\beta^-)^8\mathrm{Be}(\alpha)^4\mathrm{He}$ and $^7\mathrm{Li}(\mathrm{p},\gamma)^8\mathrm{Be}(\alpha)^4\mathrm{He}$, can one be reasonably sure which "particle" is emitted first. The β-decay, however, does not populate 0^+ states; also any γ-decay populating 0^+ states would populate 2^+ states as well and these would interfere if γ–α coincidences were measured. It seems unlikely therefore that the contribution of 0^+ states of ^{8}Be to a reaction cross section can be obtained in the region of the broad excited 0^+ state, and one is restricted to using the cross section in the neighbourhood of the ground state. In spite of the extremely small value of Γ_g, the contribution from the ground state does show structure in addition to the ground state main peak. This is in the form of a subsidiary peak or ghost near 1 MeV (Beckner, Jones, and Phillips 1961; Barker and Treacy 1962), and analysis of the size and shape of the ghost can be useful in limiting the R-matrix parameters.

The most accurate information on the ghost peak appears to be that of Hay *et al.* (1967) obtained from the $^9\mathrm{Be}(\mathrm{p,d})^8\mathrm{Be}$ reaction at a beam energy of $5\cdot2$ MeV. From deuteron spectra measured at three angles, the contribution having an angular distribution similar to that of the ground state main peak was separated out for ^{8}Be channel energies $E \leqslant 2\cdot5$ MeV. The strong forward peak in the ground state angular distribution suggested that the reaction proceeds as a direct pickup of a p-wave neutron from ^{9}Be, so this contribution was divided by a neutron penetration factor in order to give a spectral density. This presumably excludes the contributions from the 2·9 MeV 2^+ state of ^{8}Be and from the competing mode of decay* (^{9}Be(p, α)^{6}Li(d)^{4}He), but may contain some or all of the contributions from higher 0^+ levels in addition to that of the ground state.

(b) *Three-level* R-*matrix Fits to Ghost*

We attempt to fit the spectral density obtained by Hay *et al.* (1967), using the form (9) for the cross section. The parameters a_0, B_0, $E_{\lambda 0}$, and $\gamma^2_{\lambda 0}$ are assumed to have values that give acceptable fits to $\delta_0^{\text{exp.}}$, leaving only the $G_{\lambda x}$ to be varied.

Since only one x value is expected to contribute (corresponding to pickup of a $p_{3/2}$ neutron), the calculated spectral density in the three-level approximation can be written

$$\rho_0(E) = cP_0 \left| \frac{\sum_{\lambda=1}^{3} \{g_\lambda \gamma_{\lambda 0}/(E_{\lambda 0}-E)\}}{1-(S_0-B_0+\mathrm{i}P_0)\sum_{\lambda=1}^{3}\{\gamma^2_{\lambda 0}/(E_{\lambda 0}-E)\}} \right|^2, \tag{10}$$

where we have put $G_\lambda = g_\lambda^2 P_{\mathrm{n}}$, with g_λ constant and P_{n} the neutron penetration factor, and c is a normalization constant. A fit obtained initially for one particular value of B_0 can be obtained for any other value of B_0 by using the relations of Appendix II.

At this point, however, it is useful to make an approximation based on a model for the levels of ^{8}Be and ^{9}Be involved in the ^{9}Be(p, d)^{8}Be reaction, and this has the effect of limiting the range of B_0 values over which a given fit can be obtained. In the shell model, the ground state of ^{9}Be belongs to the lowest configuration $(1s)^4(1p)^5$, so that direct pickup of a p-wave neutron is expected to populate the higher 0^+ states of ^{8}Be only through the admixtures of lowest configuration $(1s)^4(1p)^4$ that they contain. More admixture is expected in the second state than in the third, so we make the reasonable restrictions

$$|g_2/g_1| \lesssim 0\cdot 3, \qquad |g_3/g_1| \ll 0\cdot 3, \tag{11}$$

corresponding to 10% or less intensity of the lowest configuration in the second state and much less than 10% in the third. If the condition (11) is imposed for all B_0 then a given fit to the spectral density can be obtained for only a limited range of B_0 values. Since changing B_0 changes the composition of the states $\lambda = 1, 2, 3$, there will be some value of B_0 that makes the shell model argument above most accurate. The question of the best choice of B_0 is discussed in Appendix III, where it is concluded that it probably lies in the region $S_0(E_{10})$ to $S_0(E_{20})$, where $S_0(E_{20}) \simeq 0$. The initial fitting is done here with $B_0 = S_0(E_{10}) = S_0(E_{\mathrm{g}})$ and with $g_3 = 0$, then the relations of Appendix II are used to obtain parameters that give the same fit for $B_0 = 0$. It is found that these parameters satisfy (11), provided the initial parameters satisfy (11), so that within this range of B_0 values the dependence of the fit on B_0 is not significant.

---

* A reaction for which the ghost peak is obscured by a competing mode of decay is ^{6}Li(^{3}He, p)^{8}Be, as shown by the results of Lorenz (1966).

If (10) is normalized to make $\int \rho_0(E)\,\mathrm{d}E$ over the ground state main peak equal to unity then for $B_0 = S_0(E_g)$

$$cg_1^2 = \pi^{-1}\{1+\gamma_{10}^2 S_0'(E_g)\}. \qquad (12)$$

For other B_0, c is given by a complicated expression depending on all the $E_{\lambda 0}$, $\gamma_{\lambda 0}$, and g_λ.

As the criterion of best fit we minimize

$$Y_0 = \frac{1}{24}\sum_{i=1}^{24}\left|\frac{\rho_0^{\text{exp.}}(E_i)-\rho_0(E_i)}{\eta_0(E_i)}\right|^2, \qquad (13)$$

where the E_i are 24 equally spaced values of E from 0·2 to 2·5 MeV, and $\rho_0^{\text{exp.}}(E)\pm\eta_0(E)$ are the boundaries of the band given in Figure 5(ii) of Hay *et al.* (1967). Since the η_0 are therefore not probable errors there is no expectation for Y_0 to be near unity for good fits; indeed the best fits we get give $Y_0 \simeq 0\cdot25$ and fits with $Y_0 \lesssim 0\cdot5$ appear to be acceptable when judged by eye.

TABLE 4

PARAMETER VALUES FOR FITS TO $\rho_0^{\text{exp.}}$ IN THE THREE-LEVEL APPROXIMATION FOR $a_0 = 7\cdot0$ fm AND VARIOUS SETS OF PARAMETER VALUES GIVING ACCEPTABLE FITS TO $\delta_0^{\text{exp.}}$

γ_{10}^2 (MeV)	X_0	Y_0	$B_0 = S_0(E_g)$ g_2/g_1	$B_0 = S_0(E_g)$ g_3/g_1	$B_0 = 0$ g_2/g_1	$B_0 = 0$ g_3/g_1
0·0775	0·48	0·55	−0·16	0·0	−0·24	−0·01
0·08	0·47	0·42	−0·13	0·0	−0·21	−0·01
0·0825	0·47	0·33	−0·10	0·0	−0·18	−0·02
0·085	0·48	0·28	−0·07	0·0	−0·15	−0·02
0·0875	0·49	0·27	−0·04	0·0	−0·13	−0·02
0·09	0·51	0·29	−0·02	0·0	−0·10	−0·02
0·0925	0·53	0·34	0·01	0·0	−0·07	−0·03
0·095	0·55	0·43	0·04	0·0	−0·04	−0·03
0·0975	0·59	0·55	0·07	0·0	−0·02	−0·03

The fitting procedure is to use, for each value of a_0 and for $B_0 = S_0(E_g)$, sets of level parameters that give $X_0 \lesssim 1$ (such as those in Table 3 for $a_0 = 7\cdot0$ fm), and to vary g_2/g_1 (with $g_3 = 0$) so as to minimize Y_0 for each set. As an example, values so obtained for $a_0 = 7\cdot0$ fm are shown in Table 4, for those sets of level parameters that give $Y_0 \lesssim 0\cdot5$. The level parameters are specified by the values of γ_{10}^2 and the corresponding X_0. Table 4 also includes values of g_2/g_1 and g_3/g_1 for both cases $B_0 = S_0(E_g)$ and $B_0 = 0$; this change of B_0 does not produce large changes in either g_2/g_1 or g_3/g_1, and all the entries in the table satisfy the restrictions (11).

For $a_0 = 7\cdot0$ fm, the smallest value of Y_0 is obtained for approximately the same level parameters as those that give the smallest value of X_0. This is not the case for other channel radii, as may be seen from Table 5, where the smallest value of Y_0 for each of the different channel radii is given together with the corresponding values of γ_{10}^2 and of X_0. The values of g_2/g_1 and g_3/g_1, for both $B_0 = S_0(E_g)$ and $B_0 = 0$, satisfy (11) for channel radii between 6 and 9 fm, but this applies to the smallest Y_0 values and a wider range of channel radii could yield fits with acceptable values of Y_0. The Y_0 values in Table 5 show a shallow minimum at $a_0 \simeq 7 \cdot 5$ fm, but there is a more pronounced minimum in the corresponding X_0 values at $a_0 \simeq 6 \cdot 5$ fm. In order to obtain a best simultaneous fit to $\delta_0^{\text{exp.}}$ and $\rho_0^{\text{exp.}}$, and to allow a more pictorial if somewhat less accurate presentation of the results, we introduce the quantity $Z_0 = 0 \cdot 5 X_0 + Y_0$, and take the smallest Z_0 as giving the best fit, provided (11) is satisfied. The conditions $X_0 \lesssim 1$, $Y_0 \lesssim 0 \cdot 5$ for acceptable fits are replaced by $Z_0 \lesssim 0 \cdot 7$.

TABLE 5

PARAMETER VALUES FOR BEST FITS TO $\rho_0^{\text{exp.}}$ IN THE THREE-LEVEL APPROXIMATION FOR VARIOUS CHANNEL RADII AND FOR PARAMETER VALUES GIVING ACCEPTABLE FITS TO $\delta_0^{\text{exp.}}$

a_0 (fm)	γ_{10}^2 (MeV)	X_0	Y_0	$B_0 = S_0(E_g)$		$B_0 = 0$	
				g_2/g_1	g_3/g_1	g_2/g_1	g_3/g_1
5·5	0·250	0·63	0·36	0·58	0·0	0·48	−0·09
6·0	0·170	0·51	0·33	0·27	0·0	0·19	−0·05
6·5	0·120	0·44	0·29	0·07	0·0	−0·01	−0·03
7·0	0·087	0·50	0·27	−0·05	0·0	−0·13	−0·02
7·5	0·064	0·53	0·25	−0·13	0·0	−0·22	−0·01
8·0	0·048	0·59	0·26	−0·18	0·0	−0·27	0·00
8·5	0·036	0·71	0·29	−0·22	0·0	−0·31	0·00
9·0	0·027	0·69	0·30	−0·25	0·0	−0·34	0·01

TABLE 6

PARAMETER VALUES FOR BEST FITS TO $\delta_0^{\text{exp.}}$ AND $\rho_0^{\text{exp.}}$ IN THE THREE-LEVEL APPROXIMATION FOR VARIOUS CHANNEL RADII

$B_0 = S_0(E_g)$, $E_{10} = E_g = 92 \cdot 12$ keV, $g_3/g_1 = 0$

a_0 (fm)	γ_{10}^2 (MeV)	E_{20} (MeV)	γ_{20}^2 (MeV)	E_{30} (MeV)	γ_{30}^2 (MeV)	g_2/g_1	Γ_g (eV)	X_0	Y_0	Z_0
6·0	0·173	9·78	0·833	30·5	1·71	0·30	5·00	0·49	0·33	0·58
6·5	0·121	7·78	0·709	27·8	1·74	0·08	5·03	0·44	0·29	0·51
7·0	0·087	6·30	0·616	22·8	1·45	−0·05	5·07	0·49	0·27	0·51
7·5	0·064	5·23	0·536	19·5	1·28	−0·14	5·12	0·52	0·26	0·52
8·0	0·047	4·42	0·470	16·5	1·10	−0·19	5·15	0·58	0·26	0·55
8·5	0·036	3·77	0·411	13·8	0·90	−0·22	5·19	0·70	0·29	0·64
9·0	0·027	3·28	0·346	12·3	0·91	−0·26	5·18	0·68	0·30	0·64

In Table 6 is given the complete set of parameter values showing the best fits, in this sense, for each channel radius for which the condition (11) is satisfied. Complementary to Table 6 is Figure 2, where contours of constant Z_0 are shown as functions of g_2/g_1 and of Γ_g for various channel radii. Γ_g is used as abscissa rather than γ_{10}^2 in order to make the contours comparable for different a_0. Acceptable fits correspond to regions within the contours $Z_0 = 0 \cdot 7$ and the lines $g_2/g_1 = \pm 0 \cdot 3$.

From Table 6 and Figure 2 it is seen that the best overall fit, with smallest Z_0 and smallest $|g_2/g_1|$, is obtained for a_0 near $7\cdot0$ fm, and that acceptable fits can be obtained for a_0 between about $6\cdot0$ and $9\cdot0$ fm. Exclusion of smaller channel radii depends on the restrictions (11), e.g. for $a_0 = 5\cdot5$ fm, $Z_0 \lesssim 0\cdot7$ only for $g_2/g_1 \gtrsim 0\cdot5$. Larger channel radii are excluded because Z_0 does not become sufficiently small, e.g. for $a_0 = 11$ fm, the minimum Z_0 is $0\cdot95$. The best fits to $\delta_0^{\text{exp.}}$ and $\rho_0^{\text{exp.}}$, for the parameter values of Table 6 for $a_0 = 7\cdot0$ fm, are shown in Figures 1 and 3 respectively.

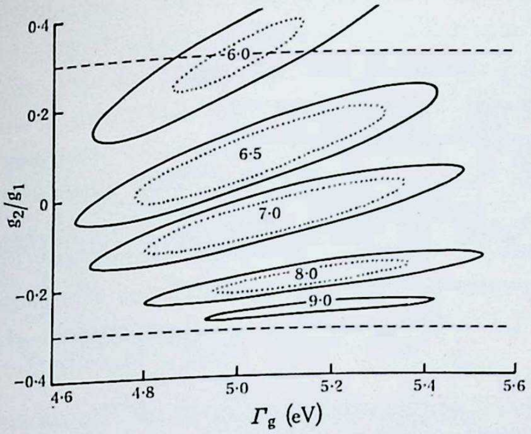

Fig. 2.—Acceptable regions for R-matrix three-level fits to $\delta_0^{\text{exp.}}$ and $\rho_0^{\text{exp.}}$ for various channel radii a_0. The values of a_0 (in fm) are indicated within the sets of contours, which are for $Z_0 = 0\cdot7$ (solid curves) and $Z_0 = 0\cdot6$ (dotted curves). The acceptable regions are within the contours $Z_0 = 0\cdot7$ and between the lines $g_2/g_1 = \pm0\cdot3$ (dashed lines).

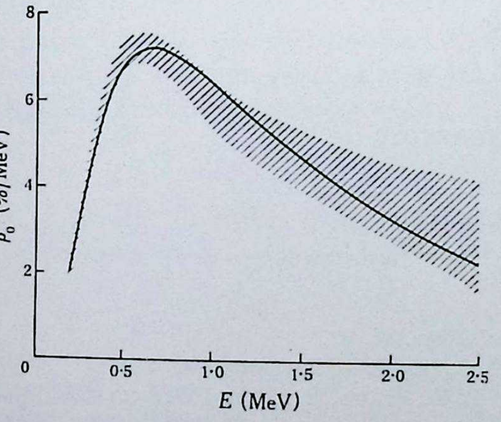

Fig. 3.—Spectral density ρ_0 associated with ^{8}Be ground state as a function of ^{8}Be channel energy E. The hatched region is as obtained from the reaction ^{9}Be(p, d)^{8}Be, and the curve is the fit for $a_0 = 7\cdot0$ fm and other parameters as in Table 6.

VI. Conclusions

Parameter values that give the best three-level R-matrix fits to the s-wave α–α scattering data and to the ^{9}Be(p, d)^{8}Be ghost data, subject to the restriction (11), are given in Table 6, and an indication of the variations of these values for which acceptable fits are possible may be obtained from Figure 2 in conjunction with Tables 2, 3, and 6. These values are all for $B_0 = S_0(E_g)$, but almost identical fits exist for any B_0 in the reasonable range between this value and zero. The best fit is obtained for channel radius $a_0 \simeq 7\cdot0$ fm, and acceptable fits are possible for a_0 between about 6 and 9 fm.

For the ^{8}Be ground state, the width Γ_g required to fit these data is found to be $(5\cdot1\pm0\cdot4)$ eV, with a considerably narrower range than is obtained from fitting $\delta_0^{\text{exp.}}$ alone.

The initial problem of this paper concerned the properties of the second 0^+ level of ^{8}Be, in particular to see if its position and width agreed with expectations based on properties of other light nuclei. From Table 6, the dimensionless reduced width of the second 0^+ state, defined by $\theta_{20}^2 = \gamma_{20}^2(\hbar^2/M_0 a_0^2)^{-1}$ (where M_0 is the reduced mass of the $\alpha+\alpha$ channel), is close to $1\cdot4$ for all the values of a_0. This is the same as the value of the dimensionless reduced width obtained for the second 0^+ state of ^{12}C for a channel radius of $6\cdot5$ fm (Barker and Treacy 1962). Also the ratio $\gamma_{10}^2/\gamma_{20}^2$ of the reduced widths of the first and second 0^+ states of ^{8}Be is seen from Table 6 to be about $0\cdot1$–$0\cdot2$. This is similar to the ratio of the reduced widths of the ground and first excited states of ^{16}O, found to be in the range 0–$0\cdot36$ (Loebenstein *et al.* 1967).

We define the energy E_e and width Γ_e of the second 0^+ level of ^{8}Be as being the peak energy and width at half maximum of the expression (10) when $g_1 = g_3 = 0$, $g_2 \neq 0$, i.e. when only the second level is fed. These values depend to some extent on the choice of B_0. For the three channel radii $a_0 = 6\cdot0$, $7\cdot0$, and $9\cdot0$ fm, the values of E_e are $9\cdot7$, $6\cdot0$, and $3\cdot1$ MeV for $B_0 = S_0(E_g)$ ($9\cdot1$, $5\cdot6$, and $2\cdot8$ MeV for $B = 0$), and the values of Γ_e are $13\cdot6$, $9\cdot5$, and $5\cdot0$ MeV for $B_0 = S_0(E_g)$ ($13\cdot1$, $9\cdot0$, and $4\cdot7$ MeV for $B = 0$). In particular the value $E_e \simeq 6$ MeV corresponding to the best fit to the scattering and reaction data is consistent with expectations based on the systematics of the light even nuclei.

VII. REFERENCES

AJZENBERG-SELOVE, F., and LAURITSEN, T. (1959).—*Nucl. Phys.* **11**, 1.

ALI, S., and AFZAL, S. A. (1967).—*Nuovo Cim.* **LB**, 355.

BALL, G. C., and CERNY, J. (1967).—*Phys. Rev.* **155**, 1170.

BARKER, F. C. (1966).—*Nucl. Phys.* **83**, 418.

BARKER, F. C. (1967).—*Aust. J. Phys.* **20**, 341.

BARKER, F. C., and TREACY, P. B. (1962).—*Nucl. Phys.* **38**, 33.

BECKNER, E. H., JONES, C. M., and PHILLIPS, G. C. (1961).—*Phys. Rev.* **123**, 255.

BENN, J., DALLY, E. B., MÜLLER, H. H., PIXLEY, R. E., STAUB, H. H., and WINKLER, H. (1966).—*Phys. Lett.* **20**, 43.

BERZTISS, A. T. (1965).—Ph.D. Thesis, University of Melbourne.

BETHGE, K., MEIER-EWERT, K., PFEIFFER, K., and BOCK, R. (1967).—*Phys. Lett.* B **24**, 663.

BREDIN, D. J., *et al.* (1959).—*Proc. R. Soc.* A **251**, 143.

BROWN, G. E., and GREEN, A. M. (1966).—*Nucl. Phys.* **75**, 401.

COHEN, S., and KURATH, D. (1965).—*Nucl. Phys.* **73**, 1.

DARRIULAT, P., IGO, G., PUGH, H. G., and HOLMGREN, H. D. (1965).—*Phys. Rev.* **137**, B315.

GUPTA, K. K., KHADKIKAR, S. B., and PARIKH, J. C. (1966).—*Nucl. Phys.* **86**, 449.

HAY, H. J., SCARR, E. F., SULLIVAN, D. J., and TREACY, P. B. (1967).—*Aust. J. Phys.* **20**, 59.

HEYDENBERG, N. P., and TEMMER, G. M. (1956).—*Phys. Rev.* **104**, 123.

KERMODE, M. W. (1965).—*Nucl. Phys.* **68**, 93.

KERMODE, M. W. (1967).—*Phys. Lett.* B **24**, 357.

LANE, A. M., and THOMAS, R. G. (1958).—*Rev. mod. Phys.* **30**, 257.

LAURITSEN, T., and AJZENBERG-SELOVE, F. (1966).—*Nucl. Phys.* **78**, 1.

LOEBENSTEIN, H. M., MINGAY, D. W., WINKLER, H., and ZAIDINS, C. S. (1967).—*Nucl. Phys.* A **91**, 481.
LORENZ, T. (1966).—*Z. Naturf.* **21a**, 1196.
MEYERHOF, W. E. (1966).—*Phys. Rev. Lett.* **16**, 1114.
NILSON, R., JENTSCHKE, W. K., BRIGGS, G. R., KERMAN, R. O., and SNYDER, J. N. (1958).—*Phys. Rev.* **109**, 850.
RASCHE, G. (1967).—*Nucl. Phys.* A **94**, 301.
SHELINE, R. K., and WILDERMUTH, K. (1960).—*Nucl. Phys.* **21**, 196.
TOMBRELLO, T. A. (1966).—*Phys. Lett.* **23**, 106.
TOMBRELLO, T. A., and SENHOUSE, L. S. (1963).—*Phys. Rev.* **129**, 2252.
TRUE, W. W., and WARBURTON, E. K. (1961).—*Nucl. Phys.* **22**, 426.
UNNA, I., and TALMI, I. (1958).—*Phys. Rev.* **112**, 452.
WILDERMUTH, K., and KANELLOPOULOS, T. (1959).—CERN No. 59–23.

APPENDIX I

Validity of One-channel Approximation

By one-channel approximation, we mean that the elastic scattering cross section can be expressed in terms of an R-function that has the usual form as a function of energy, although the constant level parameters may have modified meanings.

To justify the use of the R-matrix one-channel approximation for α–α scattering, we use the formulae given by Lane and Thomas (1958), especially in Section X of their paper. With only one retained channel (the $\alpha+\alpha$ channel with $l = J$, which is labelled by l), the reduced R-matrix $\boldsymbol{R}_{rr}$ contains only the one element $(\boldsymbol{R}_{rr})_{ll} \equiv R_{ll}$ and the collision matrix element for α–α scattering becomes

$$U_{ll} = \exp\{2i(\omega_l - \phi_l)\}\{1 + 2iP_l/(R_{ll}^{-1} - L_l^0)\}, \tag{A1}$$

where ω_l is the Coulomb phase shift and $L_l^0 = S_l^0 + iP_l$, with $S_l^0 = S_l - B_l$. The nuclear phase shift δ_l is defined by

$$U_{ll} = \exp\{2i(\omega_l + \delta_l)\}. \tag{A2}$$

One can therefore express δ_l in terms of R_{ll} or vice versa.

Lane and Thomas (1958) show that R_{ll} can be expressed in the form

$$R_{ll} = \sum_{\lambda\mu} \gamma_{\lambda l}\gamma_{\mu l} A_{\lambda\mu}, \tag{A3}$$

where the level matrix A is defined by

$$(A^{-1})_{\lambda\mu} = (E_\lambda - E)\delta_{\lambda\mu} - \xi_{\lambda\mu} \tag{A4}$$

with

$$\xi_{\lambda\mu} = \sum_c \gamma_{\lambda c}\gamma_{\mu c} L_c^0, \tag{A5}$$

the sum being over all channels c with total angular momentum $J = l$ except the retained channel l.

If all the channels c with nonzero $\gamma_{\lambda c}$ are closed then the $\xi_{\lambda\mu}$ are real, making R_{ll} and hence δ_l real. In this case (A1) and (A2) give

$$R_{ll} = \{P_l \cot(\delta_l + \phi_l) + S^0\}^{-1}, \tag{A6}$$

which is of the form assumed in Section III provided R_{ll} can be expressed in the form (2). This is possible if the $L_c^0 \equiv S_c^0$ are linear functions of E throughout the energy range considered. Then

$$R_{ll} = \sum_\lambda \bar{\gamma}_{\lambda l}^2 / (\bar{E}_\lambda - E), \tag{A7}$$

where the $\bar{E}_\lambda$ are the q roots (for the q-level approximation) of the qth-order equation

$$\det |\,(E_\lambda - E)\delta_{\lambda\mu} - \xi_{\lambda\mu}\,| = 0, \tag{A8}$$

and

$$\bar{\gamma}_{\lambda l}^2 = -\left[\left\{\frac{\mathrm{d}}{\mathrm{d}E}\left(\sum_{\mu\nu} \gamma_{\mu l}\gamma_{\nu l} A_{\mu\nu}\right)^{-1}\right\}_{E=\bar{E}_\lambda}\right]^{-1}. \tag{A9}$$

Thus the one-channel approximation for α–α scattering may be justified over a certain energy range provided that only the $\alpha+\alpha$ channel is open and that for all other channels the S_c are linear functions of E. The parameters that enter the formulae are then, however, the $\bar{E}_\lambda$ and $\bar{\gamma}_{\lambda l}^2$ rather than the original E_λ and $\gamma_{\lambda l}^2$, the relation between them being given by (A8), (A9).

Thus for $l = 0$ one should not try to fit δ_0 above the energy $E = 17 \cdot 35$ MeV at which the ^{7}Li(0)+p channel opens, as the ^{8}Be ground state at least probably has a large reduced width for this channel—the spectroscopic factor from a shell model calculation (Barker 1966) is $\mathscr{S} \simeq 1 \cdot 5$. Also for this channel S is sufficiently linear for E from 0 to 17 MeV (confirmed by a two-channel fit to δ_0 over this range), although its curvature increases rapidly near threshold. Other channels are not expected to restrict further the range of validity of the one-channel approximation.

We should also comment on the connection between $\bar{E}_\lambda$, $\bar{\gamma}_{\lambda l}^2$ and E_λ, $\gamma_{\lambda l}^2$. Lane and Thomas (1958) considered one case in which these are simply related; in this they made ξ diagonal by choosing B_c to make S_c^0 small throughout the energy region of interest. This is not applicable here as S for the ^{7}Li(0)+p channel varies from about $-4 \cdot 0$ to $-1 \cdot 5$ as E goes from 0 to 17 MeV. A different approximation can make ξ diagonal and this may have more relevance for the present case. This is to assume that, apart from the $\alpha+\alpha$ channel, there is no channel c that has nonvanishing $\gamma_{\lambda c}$ for more than one level λ. This would be the case for nucleon channels for instance if the lowest 0^+ state belongs to the lowest configuration, the second 0^+ state to a 2p–2h configuration, the third to a 4p–4h configuration, etc. In this approximation

$$\bar{E}_\lambda = E_\lambda - \frac{\sum_c \gamma_{\lambda c}^2 S_c^0(E_\lambda)}{1 + \sum_c \gamma_{\lambda c}^2 S_c'(E_\lambda)}, \qquad \bar{\gamma}_{\lambda l}^2 = \frac{\gamma_{\lambda l}^2}{1 + \sum_c \gamma_{\lambda c}^2 S_c'(E_\lambda)}. \tag{A10}$$

One may choose B_c to make $\gamma_{\lambda c}^2 S_c^0(E_\lambda) = 0$ for each c, giving $\bar{E}_\lambda = E_\lambda$. Then (A7), (A10) are just the formulae (X, 2.3), (X, 2.4) of Lane and Thomas (1958), and their following discussion regarding the modified normalization of the $\gamma^2_{\lambda c}$ applies. The present fits give values of $\bar{\gamma}^2_{\lambda l}$, and, to the extent that closed channels are not normally included explicitly in R-matrix fits to levels, this corresponds to the quantity usually quoted as the reduced width of a level.

Similar arguments justify the use of a similar one-channel approximation for interpreting reactions, such as that discussed in Section V, as long as the ^{8}Be energies remain below about 17 MeV.

Appendix II

Variation of Level Parameters with Change of B

In order that the dependence on E of $\delta(E)$ given by equation (4) should be independent of B, we require the level parameters E'_λ and γ'^2_λ corresponding to some other value B' of B to satisfy

$$\left(\sum_{\lambda=1}^{q} \gamma'^2_\lambda/(E'_\lambda - E)\right)^{-1} + B' = \left(\sum_{\lambda=1}^{q} \gamma^2_\lambda/(E_\lambda - E)\right)^{-1} + B \tag{A11}$$

(for convenience we drop the suffix l). This requires the E'_λ to be the roots of the qth-order equation

$$E'^q_\lambda + \sum_{n=1}^{q} E'^{q-n}_\lambda \frac{(-1)^n}{n!} \sum_{\lambda_1 \ldots \lambda_n} \{1 - n(B'-B)\gamma^2_{\lambda_1}/E_{\lambda_1}\} E_{\lambda_1} E_{\lambda_2} \ldots E_{\lambda_n} = 0, \tag{A12}$$

and the γ'^2_λ to be given by

$$\gamma'^2_\lambda = \left(\sum_{n=1}^{q} E'^{q-n}_\lambda \frac{(-1)^{n-1}}{(n-1)!} \sum_{\lambda_1 \ldots \lambda_n} (\gamma^2_{\lambda_1}/E_{\lambda_1}) E_{\lambda_1} E_{\lambda_2} \ldots E_{\lambda_n}\right) \div \left(\prod_{\mu \neq \lambda} (E'_\lambda - E'_\mu)\right), \tag{A13}$$

where the Greek indices run from 1 to q, except that in $\sum\limits_{\lambda_1 \ldots \lambda_n}$ terms for which any two of $\lambda_1 \ldots \lambda_n$ are the same are omitted.

In order that the dependence on E of σ_α given by equation (9) should be simultaneously independent of B, we similarly require

$$G'^{\frac{1}{2}}_{\lambda x} = \left(\prod_{\mu} (E'_\lambda - E_\mu) \sum_{\nu} G^{\frac{1}{2}}_{\nu x} \gamma_\nu/(E'_\lambda - E_\nu)\right) \div \left(\gamma'_\lambda \prod_{\mu \neq \lambda} (E'_\lambda - E'_\mu)\right). \tag{A14}$$

In the one-level case (A12), (A13) reduce to the well-known relations

$$E'_1 = E_1 - (B'-B)\gamma^2_1, \qquad \gamma'^2_1 = \gamma^2_1, \tag{A15}$$

while (A14) becomes

$$G'_{1x} = G_{1x}. \tag{A16}$$

APPENDIX III

Choice of B_0 *Value*

There are two criteria to consider in selecting the best value of B_0 to use in the present calculation. One lies within R-matrix theory and comes from the use of a three-level approximation. The other is dependent on the use of a nuclear model and is related to the physical assumption that the higher 0^+ levels are not fed appreciably in the ${}^9\mathrm{Be}(\mathrm{p,d}){}^8\mathrm{Be}$ reaction.

Within R-matrix theory, although the same fit to the data can be obtained with a q-level approximation for any value of B (we omit the suffix l), there may be some value of B that makes the parameters E_λ, γ_λ^2 giving this fit closest to their "correct" values, i.e. closest to those obtained with an ∞-level fit with the same B. Lane and Thomas (1958) point out that for the one-level approximation this is the case for $B \simeq S(E_1)$. As an illustration of how this should be generalized for more than one level, we consider an idealized case where the correct R-function is assumed to be a four-level R-function and one tries to fit this with a three-level approximation over a restricted energy range. For the correct R-function for arbitrary B we take

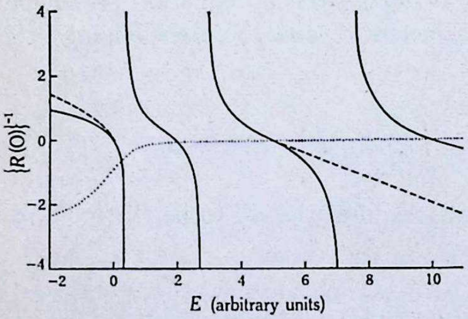

Fig. 4.—Illustrative example of three-level approximation (dashed curves) to "correct" R-function (solid curves). The ordinate is R^{-1} (for $B = 0$) and the abscissa is energy E. The shift factor S is shown as a dotted curve. Fitting is over the energy range $E = 0{\cdot}2$ to $4{\cdot}5$.

$$R(B) = \sum_{\lambda=1}^{4} \gamma_\lambda^2(B)/(E_\lambda(B)-E) \tag{A17}$$

with

$$\{R(B)\}^{-1}+B = \{R(0)\}^{-1}, \tag{A18}$$

in order that δ should be independent of B. The three-level approximation is taken as

$$\bar{R}(B) = \sum_{\lambda=1}^{3} \bar{\gamma}_\lambda^2(B)/(\bar{E}_\lambda(B)-E) \tag{A19}$$

with

$$\{\bar{R}(B)\}^{-1}+B = \{\bar{R}(0)\}^{-1}. \tag{A20}$$

In order to correspond to the type of fit to δ used in this paper we assume that the parameters of $\bar{R}(B)$ are chosen to make $\bar{R}(B)$ approximate $R(B)$ as closely as possible over an energy range from $E_\mathrm{g} = E_1(S(E_\mathrm{g}))$ to just below $E_3(0)$. This is illustrated schematically in Figure 4, where the solid curves give $\{R(0)\}^{-1}$ as a function of E. From (A17), (A18), these curves cut the line $\{R(0)\}^{-1} = B$ at the points

$E = E_\lambda(B)$ (Lane and Thomas 1958, equation (IV, 2.7)). Also $\gamma_\lambda^2(B)$ is given by the slope of the curves at $E = E_\lambda(B)$, since

$$\gamma_\lambda^2(B) = -([\mathrm{d}\{R(0)\}^{-1}/\mathrm{d}E]_{E=E_\lambda(B)})^{-1}$$

(Lane and Thomas 1958, equation (IV, 2.9)). The dashed curves in Figure 4 give $\{\bar{R}(0)\}^{-1}$, which closely approximates $\{R(0)\}^{-1}$ within the energy range used in the fit. The dotted curve gives S as a function of E.

Thus, provided $\bar{E}_\lambda(B)$ lies within the energy range used in the fit, both $\bar{E}_\lambda(B)$ and $\bar{\gamma}_\lambda^2(B)$ should be close to the correct values.* In the present example, $\bar{E}_2(B)$ and $\bar{\gamma}_2^2(B)$ should be accurate for all B, while $\bar{E}_1(B)$ and $\bar{\gamma}_1^2(B)$ should be accurate for any $B \leqslant S(E_g)$. Actually they will be accurate for more positive values of B than this, as the two curves do not diverge rapidly. From realistic numerical fits (in which the two curves are made to agree exactly at $E = E_g$) we have found that $\bar{E}_1(B)$ lies within 50 keV of $E_1(B)$ and $\bar{\gamma}_1^2(B)$ within 10% of $\gamma_1^2(B)$ for $B \leqslant 1\cdot 5$. Thus provided B is not too positive, we can assume that the parameters obtained for the first and second levels are close to their correct values.

A possible restriction on the choice of B also comes from the use of condition (11), which is based on the assumption that the ^{8}Be and ^{9}Be levels are well described by shell model wave functions with little configuration mixing. Then the eigenfunction X_λ of the R-matrix theory should best describe the internal part of the actual wave function if $B = S(E_\lambda)$, as then X_λ joins smoothly onto an outgoing external wave function. Thus to describe the first level we should want to take $B = S(E_1)$ and, for the second level, $B = S(E_2)$, so the best compromise value of B should be somewhere in the region $S(E_1)$ to $S(E_2)$. Any B value in this range is acceptable according to the first criterion discussed above.

---

* In the one-level approximation $\{\bar{R}(0)\}^{-1}$ is a linear function of E and it is obvious that only a limited range of B values can give accurate parameter values.

THE RAY THEORY OF DOPPLER FREQUENCY SHIFTS

By J. A. Bennett*

[*Manuscript received December* 28, 1967]

Summary

A general expression is obtained according to ray theory for the Doppler frequency shift observed when both receiver and transmitter are in motion in a time-varying anisotropic but lossless medium. The result is obtained using Hamilton's optical method. The range of application of the resulting expression and its relationship to a number of published results are considered. The method of analysis is also applied to the calculation of the group path of a radio wave.

I. Introduction

One method of probing the ionosphere involves transmitting a sinusoidal radio signal from a vehicle (satellite or rocket) moving through the ionosphere and measuring the Doppler frequency shift of the received signal at a ground-based station. The results of such experiments have been analysed using ray theory.

Expressions for the Doppler shift in terms of the vehicle motion and the ionospheric structure have been obtained using various approximations. These may be classified as:

(i) straight ray paths, i.e. neglecting refraction;
(ii) isotropic ray theory; and
(iii) quasi-isotropic ray theory.

By (ii) we mean the ray theory appropriate to propagation in an isotropic inhomogeneous medium. The meaning of (iii) is discussed in Section X.

The corresponding general expression for the Doppler shift observed when both transmitter and receiver are moving in a time-dependent inhomogeneous anisotropic lossless medium will be obtained here by a method based on Fermat's principle and Hamilton's optical method.†

While we are particularly concerned with radio propagation in the ionosphere, the results apply to any wave propagation obeying Fermat's principle.

---

* Physics Department (RAAF Academy), University of Melbourne, Parkville, Vic. 3052.

† Since the present paper was prepared, two other papers (Kimura, Nishina, and Maeda 1967; Maeda and Kimura 1967) have come to the author's attention. In these, the major result of the present paper, equation (13), is obtained by an extension of Kelso's method. The term due to time variation of the medium is, however, not explicitly evaluated.

Aust. J. Phys., 1968, **21**, 259–72

II. Doppler Shift

We assume that the Doppler frequency shift Δf is given by

$$\Delta f = -(f/c)\mathrm{d}P/\mathrm{d}t\,, \tag{1}$$

(e.g. Weekes 1958; Davies 1965). f is the operating frequency and P is regarded as a function of time t. The phase path P of a ray between points A and B is given by

$$P = \int_{\mathrm{A}}^{\mathrm{B}} \mu \cos \alpha \,\mathrm{d}s\,, \tag{2}$$

where μ is the refractive index at a point on the ray path, α is the angle between the wave normal and the ray direction, and the integration is carried out along the ray path. The minus sign on the right-hand side of (1) should be noted. It has been omitted by some authors. Increasing phase path corresponds to decreasing frequency.

III. Conditions

In this section we regard P as a function of both f and t and introduce a partial derivative notation. Equation (1) leads to useful results in connection with ionospheric radio propagation. However, it is not a simple matter to justify its use rigorously; the following assumptions are certainly necessary.

(i) The medium is slowly varying in space and lossless so that ray theory could be applied if the transmitter and receiver were fixed and the medium time stationary. Also we must have

$$fP/c > 1\,, \tag{3}$$

i.e. the phase path must be greater than several wavelengths.

(ii) The velocities of transmitter and receiver relative to the medium must be small in comparison with c.

(iii) The phase path does not change greatly during one cycle of the transmitted frequency, i.e.

$$\left|\frac{1}{fP}\frac{\partial P}{\partial t}\right| \ll 1\,. \tag{4}$$

This is necessary if the changes taking place at the signal frequency are to be treated separately from the much slower changes in the phase path.

(iv) In order that the undisplaced frequency may be used as an argument of P we must have

$$\left|\frac{f}{cP}\frac{\partial P}{\partial t}\frac{\partial P}{\partial f}\right| \ll 1\,. \tag{5}$$

Conditions (4) and (5) are related to the "pointwise" conditions (30.27) and (30.28) of Ginzburg (1964).

It is found in Section V that $\partial P/\partial t$ can be divided into two parts. Conditions (4) and (5) must be interpreted as applying separately to both.

Combining (3), (4), and (5) leads to

$$\left|\frac{1}{cP}\frac{\partial P}{\partial t}P'\right| \ll 1\,, \tag{6}$$

where $P' = \partial(Pf)/\partial f$ is the group path and the time of flight of a pulse of centre frequency f over the path is P'/c. The physical meaning of (6) is that the phase path must not change much during the time of flight of a pulse or element of the wave. Thus this important condition is implied by the preceding conditions. Also combining (1) with (3) and (4) leads to

$$|\Delta f/f| \ll 1\,,$$

i.e. the Doppler shift must be small.

Despite this fairly extensive list of conditions it is likely that they are not *sufficient* for two distinct reasons:

(i) because integral conditions have been given that are less restrictive than pointwise conditions to be satisfied at each point on the ray, and

(ii) because they are what might be called first-order conditions involving only first derivatives.

Higher order conditions will be necessary, for instance, the group path must not change greatly during the time of flight of a pulse, a condition involving $\partial^2 P/(\partial f\,\partial t)$.

Difficulties of type (i) occur at ionospheric reflection points in the vicinity of which the W.K.B. solutions of the wave equation (upon which ray theory may be regarded as being based) break down. However, such points do not lead to serious error in the calculated phase and direction of energy flow, provided that the points A and B are sufficiently remote from reflection points. For points at which $\mu = 0$ (these are reflection points for rays propagating with wave normals perpendicular to surfaces of constant refractive index in stratified media), the pointwise conditions corresponding to (4), (5), and (6) will be violated because of the occurrence of a μ^{-1} factor on the left-hand side.

Finally, we note that an observer in a laboratory frame, with respect to which the medium is in motion with a velocity v, will observe a refractive index μ given by

$$\mu_1 = \mu - (\mu^2 - 1)(v/c)\cos\Theta + O(v^2/c^2)$$

for $v/c \ll 1$. μ_1 is the refractive index in a frame at rest with respect to the medium and Θ is the angle between the wave normal and the velocity (Papas 1965).

We have neglected effects of this order. If μ_1 is small when the correction is large, we have another example where the assumptions apparently break down at an isolated point. As is found in the application of ray theory, it seems likely that isolated points of this type will not lead to serious error provided that they are not too near the transmitter or receiver.

IV. FERMAT'S PRINCIPLE AND HAMILTON'S OPTICAL METHOD

It is convenient for our purposes to write P in the form

$$P = \int_{A}^{B} p_i \, \mathrm{d}q^i ,$$

where $\mathbf{p} = (p_1, p_2, p_3)$ is a vector in the direction of the wave normal of magnitude μ, space coordinates are written $\mathbf{q} = (q_1, q_2, q_3)$, and a repeated index implies a summation over all possible values of the index. For the sake of generality in the choice of reference axes, tensor notation has been used. Note that the p_i are covariant components and $\mathrm{d}q^i$ contravariant components so that $p_i \, \mathrm{d}q^i$ is invariant (e.g. McConnell 1957). If u is an arbitrary parameter increasing monotonically along the ray from transmitter to receiver then

$$P = \int_{u_1}^{u_2} p_i(u) \, q'^i(u) \, \mathrm{d}u ,$$

where $u = u_1$ at A and u_2 at B, and

$$q'^i = \mathrm{d}q^i / \mathrm{d}u .$$

We introduce the notation

$$P = \int_{u_1}^{u_2} F \, \mathrm{d}u ,$$

where

$$F = p_i q'^i .$$

Fermat's principle may be stated, in the notation of the calculus of variations,

$$\delta \int_{u_1}^{u_2} F(q, q', \chi) \, \mathrm{d}u = 0 , \tag{7}$$

i.e. the first variation of the phase path with respect to variations of the path is zero. The end points are regarded as fixed and the parameter χ, introduced by Hamilton to represent the colour, is regarded as fixed since each ray must be characterized by a single colour.

It should be noted that in this form Fermat's principle may yield a true minimum or a type of saddle point (minimum for one class of variations and maximum for another class) but never a true maximum in the sense of the calculus of variations (e.g. Born and Wolf 1965).

What will be called Hamilton's optical method here may be stated as

$$\delta \int_{u_1}^{u_2} p_i q'^i \, \mathrm{d}u = 0 , \tag{8a}$$

$$\Omega(\mathbf{p}, \mathbf{q}, \chi) = 0 , \tag{8b}$$

where $\mathbf{p}$ is arbitrary except that $\Omega = 0$ is satisfied, and again the end points of the ray and χ are regarded as fixed (Hamilton 1837, 1931; Synge 1954). Ω is written in the form

$$\Omega = (p_i p^i)^{\frac{1}{2}} \mu^{-1} - 1$$

and μ is regarded as a function of the variables indicated as

$$\mu = \mu(\mathbf{p}(p_i p^i)^{-\frac{1}{2}}, \mathbf{q}, \chi).$$

This form of Ω corresponds to that used by Hamilton, and not the more general form of Synge. While the equation $\Omega = 0$ can be regarded as the Hamilton–Jacobi equation for P, it is also recognizable as the equation to the refractive index surface. We take (8) as our starting point since the equation $\Omega = 0$ is given by magnetoionic theory, and since, following the work of Haselgrove (1955), ionospheric ray tracing is usually based on this approach. Equations (8) lead to the equations to the ray in the form (see Appendix)

$$q'^i = F\,\partial\Omega/\partial p_i, \tag{9a}$$

$$p'_i = -F\,\partial\Omega/\partial q^i, \tag{9b}$$

where

$$p'_i = \mathrm{d}p_i/\mathrm{d}u.$$

The seven equations (8b), (9a), and (9b) may be solved for the seven unknowns, F and the components of $\mathbf{p}$ and $\mathbf{q}$.

V. Differentiation

Consider the dependence of P on t. If the end points of the ray are changing with time then the path in space of the ray must change with time. Also, if the properties of the medium change with time, this can give rise to a change in the ray path. If we consider a particular point on the ray path at one instant then not only may the refractive index calculated in a given wave-normal direction change, but the direction of the wave normal may change with time. All these factors may contribute to the way P changes with time. Although the possible contributions to the time dependence of P are very complicated, a careful consideration of the various terms will show that most of them make no contribution to the time derivative of P.

Since each ray we are considering may be characterized by a single value of the variable t, the parameter χ that was introduced first in (7) as a colour index is now identified with t. Along a ray

$$P = \int_{u_1}^{u_2} p_i q'^i \,\mathrm{d}u.$$

Since $\Omega = 0$ at all points on a ray

$$P = \int_{u_1}^{u_2} \{p_i q'^i + \theta\Omega(\mathbf{p}, \mathbf{q}, t)\}\,\mathrm{d}u, \tag{10}$$

where θ is a function of u that is undetermined at this stage. Now in (10) $\mathbf{p}$, $\mathbf{q}$, $\mathbf{q}'$, as well as Ω are functions of t, and we allow θ also to depend on t. For clarity this dependence, and the dependence of $\mathbf{p}$, $\mathbf{q}$, $\mathbf{q}'$, and θ on u, is not shown explicitly.

The parameter u is now specialized so that it is independent of t and

$$\mathrm{d}u_1/\mathrm{d}t = \mathrm{d}u_2/\mathrm{d}t = 0.$$

If the trajectories of the end points of the ray lie in surfaces of constant u this condition will be satisfied for all t (see Fig. 1). With this choice of u we can differentiate (10) regarding $\mathbf{p}$, $\mathbf{q}$, and $\mathbf{q}'$ as independent functions of t. Then

$$\frac{\mathrm{d}P}{\mathrm{d}t} = \int_{u_1}^{u_2} \frac{\mathrm{d}}{\mathrm{d}t}\Big(p_i q'^i + \theta\Omega(\mathbf{p},\mathbf{q},t)\Big)\,\mathrm{d}u\,,$$

since u is independent of t. Using the chain rule of partial differentiation leads to

$$\frac{\mathrm{d}P}{\mathrm{d}t} = \int_{u_1}^{u_2}\Big\{q'^i\frac{\partial p_i}{\partial t} + p_i\frac{\partial q'^i}{\partial t} + \theta\Big(\frac{\partial\Omega}{\partial p_i}\frac{\partial p_i}{\partial t} + \frac{\partial\Omega}{\partial q^i}\frac{\partial q^i}{\partial t} + \frac{\partial\Omega}{\partial t}\Big)\Big\}\,\mathrm{d}u\,,$$

since it follows from the fact that $\Omega = 0$ along a ray that

$$\int_{u_1}^{u_2} (\partial\theta/\partial t)\Omega\,\mathrm{d}u = 0\,.$$

Integrating $\int p_i(\partial q'^i/\partial t)\,\mathrm{d}u$ by parts and rearranging, yields

$$\frac{\mathrm{d}P}{\mathrm{d}t} = \int_{u_1}^{u_2}\Big\{\Big(q'^i + \theta\frac{\partial\Omega}{\partial p_i}\Big)\frac{\partial p_i}{\partial t} + \Big(\theta\frac{\partial\Omega}{\partial q^i} - p'_i\Big)\frac{\partial q^i}{\partial t} + \theta\frac{\partial\Omega}{\partial t}\Big\}\,\mathrm{d}u + \Big[p_i\frac{\partial q^i}{\partial t}\Big]_{u_1}^{u_2}.$$

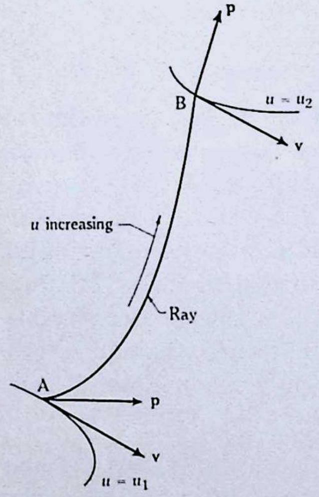

Fig. 1.—Parametric representation of ray path for calculation of Doppler shift.

Now, as can be seen from the Appendix, by taking as the variations of $\mathbf{p}$ and $\mathbf{q}$ the particular variations $\partial\mathbf{p}/\partial t$ and $\partial\mathbf{q}/\partial t$, θ can be chosen so that the first two terms of the integrand (which actually expand to the sum of 12 factors when written in full) make zero contributions to the integral along a ray. We therefore choose θ to satisfy equation (A6), that is, $\theta = -F$. Note that for this choice of θ the contribution from the first two terms is obviously zero because of (9) or (A7). Evaluating $\partial\Omega/\partial t$ leads to the result

$$\frac{\mathrm{d}P}{\mathrm{d}t} = \int_{u_1}^{u_2}\frac{F}{\mu}\frac{\partial\mu}{\partial t}\,\mathrm{d}u + \Big[p_i\frac{\partial q^i}{\partial t}\Big]_{u_1}^{u_2}, \tag{11}$$

This may be rewritten in what may be more familiar notation

$$\frac{\mathrm{d}P}{\mathrm{d}t} = \int_{\mathrm{A}}^{\mathrm{B}}\frac{\partial\mu}{\partial t}\cos\alpha\,\mathrm{d}s + \Big[\mathbf{p}\,.\,\mathbf{v}\Big]_{\mathrm{A}}^{\mathrm{B}}, \tag{12}$$

where $\mathbf{v}$ represents the velocity of transmitter and receiver in turn.

VI. Importance of Introducing the Parameter u

A certain amount of confusion has arisen in the past through attempting to handle calculations related to that of Section V by using an integration variable that is a function of t (or whatever the corresponding variable may be). This confusion is avoided here and the calculation simplified since (i) the time dependence of the end points of the ray need not be separately considered, (ii) the dependence of $\mathbf{q}$, $\mathbf{q}'$, and $\mathbf{p}$ on u need not be explicitly considered, and (iii) all space variables are afforded equal treatment. This simplification should not be unexpected since it is well known that the treatment of geometrical problems in the calculus of variations, especially problems involving end points that are partly variable, is much simplified by the parametric approach, a method that is due to Weierstrass (see, for example, Forsyth 1927).

VII. Expressions for the Doppler Shift

Substitution from (12) into (1) yields

$$\Delta f = -\frac{f}{c}\left(\int_{\mathrm{A}}^{\mathrm{B}} \frac{\partial \mu}{\partial t} \cos \alpha \, \mathrm{d}s + \Big[\mathbf{p}.\mathbf{v}\Big]_{\mathrm{A}}^{\mathrm{B}}\right), \tag{13}$$

the major result of this paper. For a time-stationary medium, with moving transmitter and receiver,

$$\Delta f = -\frac{f}{c}\Big[\mathbf{p}.\mathbf{v}\Big]_{\mathrm{A}}^{\mathrm{B}}, \tag{14}$$

while, if the medium is isotropic, (13) reduces to

$$\Delta f = -\frac{f}{c}\left(\int_{\mathrm{A}}^{\mathrm{B}} \frac{\partial \mu}{\partial t} \mathrm{d}s + \Big[\mathbf{p}.\mathbf{v}\Big]_{\mathrm{A}}^{\mathrm{B}}\right), \tag{15}$$

where the vector $\mathbf{p}$ now lies in the ray direction since the wave-normal and ray directions correspond at all points in an isotropic medium. If transmitter and receiver are fixed, (13) gives

$$\Delta f = -\frac{f}{c}\int_{\mathrm{A}}^{\mathrm{B}} \frac{\partial \mu}{\partial t} \cos \alpha \, \mathrm{d}s. \tag{16}$$

VIII. Physical Significance of the Result (13)

From (13) it can be seen that, in this approximation, the Doppler shift can be split into two components. The first is due to time changes in refractive index of the medium along the ray, which is regarded as fixed in space. The change in refractive index at each point of the ray is calculated for a constant wave-normal direction. This is the Doppler shift that would be observed if transmitter and receiver were stationary.

The second contribution is due to movements of the end points of the ray. We notice that the Doppler shift is completely specified by the velocities of the end points of the ray and the value of $\mathbf{p}$ at the ends of the ray. This is the Doppler shift that would be observed in a time-stationary medium.

The fact that it is the wave-normal direction, and not the ray direction, that is important in determining the Doppler shift means that in an anisotropic time-stationary medium a Doppler shift may be observed if the ray and velocity vectors are orthogonal. This should be contrasted with the case of an isotropic medium when a transverse Doppler shift is only possible in the relativistic case.

IX. COMPARISON WITH OTHER RESULTS

The $-(\mathbf{p}.\mathbf{v})f/c$ terms occurring in (13), (14), and (15) are the ray-theory equivalent of the general form $-\nabla\Phi.\mathbf{v}$, where Φ is the phase of the wave variable (Tisher 1959; Lee and Papas 1963), since according to ray theory $\nabla\Phi = \mathbf{p}f/c$.

For a transmitter moving with velocity $\mathbf{v}$ in a homogeneous anisotropic medium the Doppler shifted frequency f, for an observer stationary with respect to the time-invariant medium, satisfies

$$(f/c)\mathbf{p}.\mathbf{v} = f - f_0, \tag{17}$$

where $\mathbf{p} = \mathbf{p}(f)$, $f_0 = f_0^*(1-|v/c|^2)^{\frac{1}{2}}$, and f_0^* is the proper frequency of the transmitter (e.g. Barsukov 1959, 1962). Under the assumptions of Section III it can be seen that (17) reduces to the result given by (13) or (14) with the point B regarded as fixed. It should be noted that the assumptions of Section III preclude the occurrence of Čerenkov radiation or the complex Doppler effect (Frank 1960; Barsukov 1962), which are results that arise from (17).

Returning to the consideration of an inhomogeneous medium, expression (15) for the isotropic case has been obtained by Kelso (1960, 1964) by making use of Fermat's principle. Equation (16) has been obtained by a technique based on Hamilton's principle (Bennett 1967*a*). However, the handling of the function Ω in that paper is not very satisfactory.

X. QUASI-ISOTROPIC EXPRESSION FOR THE DOPPLER SHIFT

Kelso (1960) obtained (15) as a special case of a result obtained using a quasi-isotropic ray theory. His result, stated for a moving transmitter only, is

$$\Delta f = -\frac{f}{c}\left[\mu_v v_{11} + \int \frac{\partial\mu}{\partial t}\,\mathrm{d}s + \left\{\left(\frac{\partial\mu}{\partial x'}\frac{\partial x}{\partial t} + \frac{\partial\mu}{\partial y'}\frac{\partial y}{\partial t}\right)\left(1+(x')^2+(y')^2\right)^{\frac{1}{2}}\right\}_{z=\zeta}\right], \tag{18}$$

where v_{11} is the component of the transmitter velocity in the (negative) ray direction, $x' = \partial x/\partial z$ and $y' = \partial y/\partial z$ refer to the ray, and μ_v is the refractive index at the transmitter, calculated in the ray direction. The term in braces is to be evaluated at the transmitter end of the ray, subject to the condition $z = \zeta$, so that $\partial x/\partial t$ and $\partial y/\partial t$ are the components of the velocity of the point on the ray having a z component ζ.

In general they are not components of the transmitter velocity. A minus sign has been inserted for consistency with (1). Also Kelso has regarded the ray as being traversed from the receiver to the transmitter. Thus his ray direction is, in the present notation, the negative ray direction.

It is interesting to compare the complicated analytical form of (18), derived using the calculus of variations in its nonparametric form, with the much simpler equation (13).

The assumptions underlying the derivation of (18) are the following. The refractive index is calculated as if the wave-normal and ray directions coincided and the expression for the phase path appropriate to isotropic propagation is used, but the refractive index is allowed to depend upon direction. The path of the ray is determined by applying Fermat's principle.

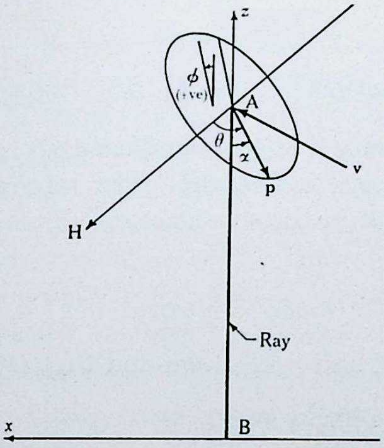

Fig. 2.—An example used in the comparison of the anisotropic and quasi-isotropic expressions. The refractive index surface is shown superimposed at one end of the ray.

It is of considerable interest to determine if, and under what circumstances, (18) is an approximation to (13). The assumptions would be expected to be most nearly valid when the refractive index calculated for a wave normal in the supposed ray direction is approximately equal to the refractive index in the corresponding true wave-normal direction. In this case the angle α will be small and the integral terms of (13) and (18) will be approximately equal. It is difficult to compare the terms quantitatively since slightly different ray paths will be calculated in the two cases unless the medium should be homogeneous.

In order to focus attention on the remaining terms of (13) and (18) consider the simple example illustrated in Figure 2. A sinusoidal signal of frequency f is transmitted from a transmitter moving with velocity $\mathbf{v}$ through a homogeneous anisotropic plasma, the properties of which do not change with time. Axes are chosen so that the observer is at the origin and the ray lies along the $(0,z)$ axis. Since a magnetoionic medium is assumed if the intensity vector of the applied magnetic field $\mathbf{H}$ (or in the general case an axis of rotational symmetry of the refractive index surface) is chosen to lie in the (x,z) plane, $\mathbf{p}$ also lies in that plane (e.g. Budden 1961).

Consider first Kelso's expression (18). At the transmitter

$$x' = \partial x/\partial z = 0\,, \qquad y' = \partial y/\partial z = 0\,,$$

$$(\partial x/\partial t)_z = v_x\,, \qquad (\partial y/\partial t)_z = v_y\,, \qquad v_{11} = v_z\,.$$

If the medium is approximately isotropic

$$\partial\mu/\partial x' \simeq \partial\mu/\partial\phi\,, \qquad \partial\mu/\partial y' = 0\,,$$

where ϕ is defined by $\partial x/\partial z = \tan\phi$ and increases in the sense indicated in Figure 2. Therefore we have approximately

$$\Delta f = -(f/c)\{\mu v_z + (\partial\mu/\partial\phi)v_x + 0v_y\}\,.$$

The v_y term is included to emphasize that a y component of velocity makes no contribution to the Doppler shift.

Now from (13) we obtain

$$\Delta f = -(f/c)\{(p\cos\alpha)v_z + (p\sin\alpha)v_x + 0v_y\}\,, \qquad \tan\alpha = p^{-1}\partial p/\partial\psi\,,$$

where ψ is the angle between the wave normal and **H** (e.g. Budden 1961) and angles are positive when measured in a clockwise sense from **H**. The refractive index is written p to emphasize that it is calculated in the wave-normal direction. Since **H** remains constant in direction we have

$$\partial p/\partial\phi = \partial p/\partial\psi \qquad \text{and} \qquad \partial p/\partial\phi = p\tan\alpha\,.$$

Now, making use of the facts that α is small and $p \simeq \mu$, we find that (13) leads to

$$\Delta f = -(f/c)\{\mu v_z + (\partial\mu/\partial\phi)v_x + 0v_y\}\,,$$

showing that in this case at least (18) is an approximation to (13). In a more general case either (18) could be rewritten in terms of the arc length s as parameter, or the z axis could be chosen to lie in the calculated direction of the ray at its end point. Thus it can be seen that, in general, (18) is an approximation to (13) which is valid when the anisotropy is small, provided the quasi-isotropic ray theory leads to a sufficiently accurate estimate of the final ray direction.

XI. APPLICATION TO CALCULATION OF GROUP PATH

The main step in the preceding derivation was essentially a differentiation of P with respect to χ. The expression for the derivative therefore applies to the differentiation of P with respect to any parameter that can be formally identified with χ. For instance χ may be identified with the frequency f, which is perhaps more natural than the identification with t made in Section V.

The expression

$$P' = \mathrm{d}(Pf)/\mathrm{d}f \tag{19}$$

arises naturally if the group path of a pulse is defined in terms of the time of flight of a pulse along the ray. Equation (19) leads to

$$P' = \int_A^B \mu' \cos\alpha \, ds \tag{20}$$

for a slowly varying lossless medium (Gautier 1966; Bennett 1967*b*). The pulse travels between points A and B, which are regarded as fixed.

Titheridge (1965) has pointed out that if a ray is regarded as being divided into a number of segments by intersecting surfaces then the group path for each section is not obtained by applying (19) to the expression for $P(f)$ obtained for each segment since the end point of the segments are, in general, functions of frequency. To investigate under what circumstances (19) can be used in this case we make use of (11) and find

$$\frac{d(Pf)}{df} = \int_{u_1}^{u_2} \mu' \cos\alpha \, ds + \left[p_i \frac{\partial q^i}{\partial f} f\right]_{u_1}^{u_2}, \tag{21}$$

where P is the phase path of the section of the path lying between surfaces defined by $u = u_1$ and $u = u_2$. $\mu' = \partial(\mu f)/\partial f$ is known as the group refractive index. However, it should be noted that the group velocity is of magnitude $c/(\mu' \cos\alpha)$ and lies in the ray and not the wave-normal direction. The integral term on the right-hand side of (21) arises when the end points of the segment are held constant during the differentiation and can be recognized as the group path of the segment of the ray (see equation (20)). Thus, formally (19) can be applied to the calculation of the group path if $\mathbf{p}$ and $\partial\mathbf{q}/\partial f$ are orthogonal at both ends of the segment, i.e. if the terminating surfaces are tangential to surfaces of *constant phase*, a condition making excellent sense physically.

An example where this condition applies is the case of vertical incidence on a spherically stratified ionosphere when the ray is divided by a number of concentric spheres, a procedure often adopted in analysing ionograms. The phase path of a section of the ray lying between two consecutive spheres is frequency dependent. Although the points of intersection are also frequency dependent, because the wave normal remains vertical and orthogonal to the intersecting surfaces, (19) may be applied directly to the calculation of the group path of each segment of the ray.

XII. CONCLUSIONS

An expression (13) has been found according to ray theory for the Doppler shift which is present when both source and transmitter are moving in a time-varying medium. This expression should help to remove the confusion that arises in considering the various contributions to the Doppler shift. The Doppler shift can be split into two parts, one due to movement of transmitter and receiver and the other due to changes in the refractive index taking place along the ray, the ray being regarded as fixed in space, with the change in refractive index at each point being calculated for a wave-normal direction that is regarded as unchanging.

The result may be of practical application since Kelso (1960) has suggested that the isotropic formula (15) be used for analysis of satellite Doppler experiments, while (16) has been successfully used in computing theoretical Doppler shifts for a path with fixed transmitter and receiver (Jones 1968).

The method can also be applied to the calculation of the group path.

Note added in proof. Because all derivatives have been implicitly assumed to exist and be continuous the argument of this paper cannot be applied directly to a ray having corners (where $\mathbf{q}'$ in particular is discontinuous). For a ray with corners it is natural to apply (13) to the segments lying between corners and sum the several results to obtain the total Doppler shift.

At a corner lying in a continuous medium $\mathbf{p}$ is continuous (Weierstrass–Erdmann corner condition, e.g. Forsyth 1927) and there is no contribution associated with the corner. On the other hand, at a corner lying on a surface of discontinuity of refractive index $\mathbf{p}$ is discontinuous ($\mathbf{p}$ satisfies the law of reflection or refraction). There is thus, in general, a contribution to the Doppler shift associated with such a corner.

XIII. Acknowledgments

The author wishes to thank Dr. J. A. Thomas for his help and encouragement. Financial support has been received from the Radio Research Board, the Royal Australian Air Force, and the University of Melbourne. The author is the grateful holder of an Australian Commonwealth Post-graduate Award.

XIV. References

Barsukov, K. A. (1959).—On the Doppler effect in an anisotropic and gyrotropic medium. *Soviet Phys. JETP* **36**, 1052–6.

Barsukov, K. A. (1962).—Certain features of the Doppler effect in anisotropic media. *Soviet Phys. tech. Phys.* **7**, 112–16.

Bennett, J. A. (1967*a*).—The calculation of Doppler shifts due to a changing ionosphere. *J. atmos. terr. Phys.* **29**, 887–91.

Bennett, J. A. (1967*b*).—The relation between group and phase path. *J. atmos. terr. Phys.* **29**, 893–6.

Born, M., and Wolf, E. (1965).—"Principles of Optics." 3rd Ed. (Pergamon Press: Oxford.)

Budden, K. G. (1961).—"Radio Waves in the Ionosphere." (Cambridge Univ. Press.)

Davies, K. (1965).—Ionospheric radio propagation. *Natn. Bur. Stand. Monogr.* No. 80.

Forsyth, A. R. (1927).—"Calculus of Variations." (Cambridge Univ. Press.)

Frank, I. M. (1960).—Critical velocity for radiation of light in optically anisotropic media. *Soviet Phys. JETP* **11**, 1263–7.

Gautier, T. N. (1966).—Generality of the relation between the group and the phase path. *J. atmos. terr. Phys.* **28**, 1125–8.

Ginzburg, V. L. (1964).—"The Propagation of Electromagnetic Waves in Plasmas." (Pergamon Press: Oxford.)

Hamilton, W. R. (1837).—Third supplement to an essay on the theory of systems of rays. *Trans. R. Ir. Acad.* **17**, 1–144.

Hamilton, W. R. (1931).—"The Mathematical Papers of Sir William Rowan Hamilton." Vol. 1. (Cambridge Univ. Press.)

Haselgrove, J. (1955).—Ray theory and a new method of ray tracing. *In* "Physics of the Ionosphere". pp. 355–64. (Physical Society: London.)

Jones, R. M. (1968.)—A three dimensional ray tracing computer program. *Radio Sci.* **3**, 93–4.

Kelso, J. M. (1960).—Doppler shifts and Faraday rotation of radio-signals in a time-varying, inhomogeneous ionosphere. I. Single signal case. *J. geophys. Res.* **65**, 3909–14.

KELSO, J. M. (1964).—"Radio Ray Propagation in the Ionosphere." (McGraw-Hill: New York.)

KIMURA, I., NISHINA, R., and MAEDA, K. (1968).—Rocket observation of the night-time ionosphere using the VLF Doppler technique. *Space Research* **8**, (in press).

LEE, K. S. H., and PAPAS, C. H. (1963).—Doppler effects in inhomogeneous anisotropic ionized gases. *J. Math. Phys.* **42**, 189–99.

McCONNELL, A. J. (1957).—"Applications of Tensor Calculus." (Dover: New York.)

MAEDA, K., and KIMURA, I. (1967).—Rocket observation of the night-time ionosphere by using the VLF Doppler technique. Proc. 7th Int. Symp. on Space Technology and Science, Tokyo 1967 (in press).

PAPAS, C. H. (1965).—"Theory of Electromagnetic Wave Propagation." (McGraw-Hill: New York.)

SYNGE, J. L. (1954).—"Geometrical Mechanics and De Broglic Waves." (Cambridge Univ. Press.)

TISHER, F. J. (1959).—Doppler phenomena in space communications. *I.R.E. Trans. Commun. Syst.* **CS-7**, 25–30.

TITHERIDGE, J. E. (1965).—The relation between the group and phase paths in a non-homogeneous ionosphere. *J. atmos. terr. Phys.* **27**, 1115–16.

WEEKES, K. (1958).—On the interpretation of the Doppler effect from senders in an artificial satellite. *J. atmos. terr. Phys.* **12**, 335–8.

APPENDIX

A Derivation of the Hamiltonian Equation to the Ray by a Lagrangean Method

The following method is an interesting way of obtaining the Hamiltonian equations to the ray. However, it is presented here because it parallels the differentiation of P in Section V, and because it is convenient in considering ionospheric radio propagation to start from equation (8) rather than (7), since the equation $\Omega = 0$ is given by magnetoionic theory. We wish to solve

$$\delta \int_{u_1}^{u_2} p_i q'^i \, \mathrm{d}u = 0, \qquad \Omega(\mathbf{p}, \mathbf{q}, \chi) = 0, \tag{A1}$$

where

$$\Omega = (p_i p^i)^{\frac{1}{2}} \mu^{-1} - 1 \qquad \text{and} \qquad \mu = \mu\big(\mathbf{p}(p_i p^i)^{-\frac{1}{2}}, \mathbf{q}, \chi\big).$$

The end points and χ are regarded as fixed. By the method of Lagrange, we seek a solution of

$$\delta \int_{u_1}^{u_2} \{p_i q'^i + \theta \Omega(\mathbf{p}, \mathbf{q}, \chi)\} \, \mathrm{d}u = 0, \tag{A2}$$

i.e.

$$\delta J = 0,$$

where θ is a function of u to be determined, $\mathbf{p}$ and $\mathbf{q}$ may now be chosen freely, and J is written for the integral. If $\mathbf{p}$ is varied by $\delta\mathbf{p}$, $\mathbf{q}$ by $\delta\mathbf{q}$, and $\mathbf{q}'$ by $\delta\mathbf{q}'$ then

$$\delta J = \int_{u_1}^{u_2} \{q'^i \delta p_i + p_i \delta q'^i + \theta(\partial\Omega/\partial p_i)\delta p_i + \theta(\partial\Omega/\partial q^i)\delta q^i\} \, \mathrm{d}u = 0. \tag{A3}$$

Integrating $\int p_i \delta q'^i \, \mathrm{d}u$ by parts and rearranging yields

$$\delta J = \int_{u_1}^{u_2} [\{q'^i + \theta(\partial\Omega/\partial p_i)\}\delta p_i + \{\theta(\partial\Omega/\partial q_i) - p'^i\}\delta q^i] \, \mathrm{d}u. \tag{A4}$$

Now $\delta\mathbf{p}$ and $\delta\mathbf{q}$ are arbitrary except for mild restrictions on their smoothness. Therefore we must have

$$q'^{i} = -\theta\,\partial\Omega/\partial p_i, \tag{A5a}$$

$$p'_i = \theta\,\partial\Omega/\partial q^i \tag{A5b}$$

(see Synge 1954).

The six equations (A5), together with $\Omega = 0$, determine the seven unknowns, the components of $\mathbf{p}$ and $\mathbf{q}$ and the function θ. θ can be determined as follows. From (A5a) we find

$$p_i\,q'^{i} = -\theta p_i\,\partial\Omega/\partial p_i.$$

However, $\Omega+1$ is homogeneous of degree one in $\mathbf{p}$. Therefore

$$p_i\,\partial\Omega/\partial p_i = p_i\,\mathrm{d}(\Omega+1)/\mathrm{d}p_i = \Omega+1 = 1$$

and

$$-\theta = p_i\,q'^{i} = F. \tag{A6}$$

Thus (A5) becomes

$$q'^{i} = F\,\partial\Omega/\partial p_i, \qquad p'^{i} = -F\,\partial\Omega/\partial q^i. \tag{A7}$$

If we choose $u = u^*$ say, so that $F = 1$, then

$$p_i\,\mathrm{d}q^i/\mathrm{d}u^* = 1 \qquad \text{or} \qquad p_i\,\mathrm{d}q^i = \mathrm{d}u^*.$$

For this particular parameter we find

$$q'^{i} = \partial\Omega/\partial p_i, \qquad p'_i = -\partial\Omega/\partial q^i, \tag{A8}$$

which may be identified with the canonical form of the equations of dynamics.

FINITE SAMPLE CORRELATIONS OF QUANTIZED GAUSSIANS

By T. Cole*

[*Manuscript received February 27, 1968*]

Summary

A theory is developed for the treatment of quantized signals and for the estimate of correlation from quantized signals of only finite length. Different quantization systems can be compared on the accuracy of estimation of correlation for the same record length. For Gaussian statistics it is shown that with low values of correlation the efficiencies of one, two, and three bit quantizations are respectively 64, 89, and 95% with respect to continuous multiplication. For highly correlated signals the one bit system becomes the most efficient.

I. Introduction

In practical systems of correlation measurement one has only a finite record length of the random variables $X(t)$ and $Y(t)$. The normalized correlation ρ^T will hence be only an approximation to the true correlation ρ obtained from an infinite record length. If ergodicity is assumed, different records of the same length T will give ρ^T, which will fluctuate about ρ with some standard deviation σ_T. It is convenient then, to consider ρ as the "signal" and σ_T as the "noise" in a definition of output signal to noise ratio.

The signals $X(t)$ and $Y(t)$ would have to be sampled in time and quantized in amplitude if a computer were to be used to determine the correlation. We define $\{\hat{X}(i)\}$ and $\{\hat{Y}(i)\}$ as the quantized and sampled forms of $X(t)$ and $Y(t)$. The normalized and averaged product of $\hat{X}(i)$ and $\hat{Y}(i)$ over N samples is denoted by $\hat{\rho}^N$. However, ρ is not, in general, a linear function in $\hat{\rho}$. For the quantized signals the estimate of correlation is given in terms of the function A relating ρ to $\hat{\rho}$ as

$$\bar{\rho}^N = A(\hat{\rho}^N). \tag{1}$$

By a knowledge of the statistics of $\hat{X}(t)$ and $\hat{Y}(t)$ and hence those of $\hat{\rho}^N$, the output signal to noise for the record length N and quantization system chosen is given by $\rho/\bar{\sigma}_N$ where $\bar{\sigma}_N$ is the standard deviation of the value of $\bar{\rho}^N$ about ρ. The signals $X(t)$ and $Y(t)$ could be quantized in an infinite number of ways and each system would produce its own estimate of correlation and output signal to noise ratio. By defining efficiency as the decrease in output signal to noise of the estimate of ρ in one quantization system with respect to continuous multiplication for the same signals and record length, one can compare the various quantization systems.

It is well known that the output noise is inversely proportional to the square root of the record length, so a knowledge of the statistics, and hence efficiency, for only one sample length is sufficient for all record lengths.

---

* Observatoire de Meudon, Meudon 92, France; present address: Cavendish Laboratories, University of Cambridge, Cambridge, England.

Aust. J. Phys., 1968, **21**, 273–82

Systems to which such a theory is applicable include the square-law detector ($X(t) = Y(t)$), the polarity coincidence correlator (one bit correlation), and the more complex forms of correlation detection. The problem of correlation of quantized signals but with infinite records has been treated before, and after a review of the quantization process the later sections develop an approach to the less elegant problem of finite record length. The results are from an application of this to four types of quantizations of Gaussian signals.

II. Quantization Process

Bonnet (1962) considers a general quantization function, but it is only necessary here to consider the one which is shown by him to maintain a zero mean and which gives a finite correlation output for very weak signals. The quantizing system consists of bands of width q such that, if $X(t)$ lies within this band, it takes on the value of the midpoint of the band. In general we consider the origin at a transition between bands and an equal number $(K-1)$ of bands on either side of the origin. That is, for integers K, k, and q,

$$\hat{X}(i) = \left.\begin{array}{ll} (-K+\frac{1}{2})q & \text{if} \quad X(t) < (-K+1)q\,, \\ (k-\frac{1}{2})q & \text{if} \quad (k-1)q \leqslant X(t) < kq\,, \\ (K-\frac{1}{2})q & \text{if} \quad X(t) \geqslant (K-1)q\,, \end{array}\right\} \tag{2}$$

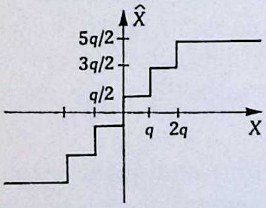

Fig. 1.—Finite quantization system with $K = 3$ and bands of width q in which X is transformed to $\hat{X}$.

Figure 1 illustrates the case where $K = 3$. The above definition is general in that it includes infinite clipping ($K = 1$), infinite quantization ($K \to \infty$, q finite), the linear limiter ($q \to 0$, $K \to \infty$, Kq constant), and the identity ($Kq \to \infty$).

III. Finite Quantization

Given the statistical properties of the signals $X(t)$ and $Y(t)$, it is possible to give formulae for the estimate $\hat{\rho}^N$, the standard deviation $\hat{\sigma}^N$ of $\hat{\rho}^N$ about $\hat{\rho}$, and the function A relating $\hat{\rho}$ to ρ.

If $p(X)$ is the probability distribution (pdf) of X, we define a quantity P_j by

$$\left.\begin{array}{ll} P_K = \displaystyle\int_{(K-1)q}^{\infty} p(X)\,\mathrm{d}X\,, & \\ & (-K+2) \leqslant j \leqslant (K-1)\,, \\ P_j = \displaystyle\int_{(j-1)q}^{jq} p(X)\,\mathrm{d}X\,, & \\ & j \text{ integer.} \\ P_{(-K+1)} = \displaystyle\int_{-\infty}^{(-K+1)q} p(X)\,\mathrm{d}X\,, & \end{array}\right\} \tag{3}$$

Then $p(\hat{X})$, the probability density distribution of $\hat{X}$, is

$$p(\hat{X}) = \sum_{-K+1}^{K} P_j\, \delta(\hat{X}-(j-\tfrac{1}{2})q), \tag{4}$$

where $\delta(x)$ is the Dirac delta function.

In two dimensions consider functions X and Y with correlation coefficient ρ and joint pdf of $p(X, Y; \rho)$. If both X and Y undergo the same quantization to $\hat{X}$ and $\hat{Y}$ we can express the joint distribution of $\hat{X}$ and $\hat{Y}$ in terms of ${}^2P_{jk}$, where

$$\left.\begin{aligned} {}^2P_{jk} = \int_{a_j}^{b_j}\int_{c_k}^{d_k} p(X, Y; \rho)\, \mathrm{d}Y\, \mathrm{d}X, \qquad & (-K+1) \leqslant j, k \leqslant K, \\ & j, k \text{ integers.} \end{aligned}\right\} \tag{5}$$

The limits of integration are defined as:

$$a_j = \begin{matrix} (j-1)q & \text{if } (-K+2) \leqslant j \leqslant K, \\ -\infty & \text{if } j = (-K+1), \end{matrix}$$

$$b_j = \begin{matrix} \infty & \text{if } j = K, \\ jq & \text{if } (-K+1) \leqslant j \leqslant K-1, \end{matrix}$$

$$c_k = \begin{matrix} (k-1)q & \text{if } (-K+2) \leqslant k \leqslant K, \\ -\infty & \text{if } j = (-K+1), \end{matrix}$$

$$d_k = \begin{matrix} \infty & \text{if } k = K, \\ kq & \text{if } (-K+1) \leqslant k \leqslant K-1. \end{matrix}$$

The joint pdf is then $p(\hat{X}, \hat{Y}; \hat{\rho})$ and is given by

$$p(\hat{X}, \hat{Y}; \hat{\rho}) = \sum_{-K+1}^{K} \sum_{-K+1}^{K} {}^2P_{jk}\, {}^2\delta(\hat{X}-(j-\tfrac{1}{2})q, \hat{Y}-(k-\tfrac{1}{2})q), \tag{6}$$

where ${}^2\delta(x, y)$ is the two-dimensional Dirac delta function. For the case of interest here, we desire an expression for the pdf of the random variable z equal to the product $\hat{X}\hat{Y}$. Evidently $p(z)$ is a discrete distribution given by

$$p(z) = \sum_{-K+1}^{K} \sum_{-K+1}^{K} {}^2P_{jk}\, \delta(z-(k-\tfrac{1}{2})(j-\tfrac{1}{2})q^2) \qquad j, k \text{ integers.} \tag{7}$$

The mean of z is

$$\bar{z} = \int_{-\infty}^{\infty} z\, p(z)\, \mathrm{d}z = \sum_j \sum_k {}^2P_{jk}\, (k-\tfrac{1}{2})(j-\tfrac{1}{2})q^2 \tag{8}$$

and the mean square is

$$\overline{z^2} = \int_{-\infty}^{\infty} z^2 p(z)\, \mathrm{d}z. \tag{9}$$

When $\bar{z}$ is normalized to the value at $\rho = 1$, it is identical with $\hat{\rho}$ while $\hat{\sigma}^1$ is the standard deviation of $p(z)$ normalized in the same way, i.e.

$$\hat{\sigma}^1 = \left(\overline{z^2}-(\bar{z})^2\right)^{\frac{1}{2}}/(\bar{z})_{\rho=1}. \tag{10}$$

IV. CALCULATION

Another way of considering the transformation is via a plot of $p(X, Y; \rho)$ on the two-dimensional X, Y plane cut into squares of side Q. The distribution $p(\hat{X}, \hat{Y}; \hat{\rho})$ is a two-dimensional distribution of delta functions on the centres of the squares and with values ${}^2P_{ij}$, where ${}^2P_{ij}$ is the integral of $p(X, Y; \rho)$ over that particular square (see Fig. 2). That is, $p(\hat{X}, \hat{Y}; \hat{\rho})$ can be represented as the two-dimensional array of numbers $A(I,J) = {}^2P_{ij}$ in which an increment of unity in the index represents a shift of q on the $\hat{X}$ or $\hat{Y}$ axis. When the product $\hat{X}\hat{Y}$ is formed, a one-dimensional array of numbers $B(M)$ is obtained in which M represents multiples of $\frac{1}{4}Q^2$. The multiplication can thus be considered as a transformation on the indices rather than an operation on the actual values of P_{ij}.

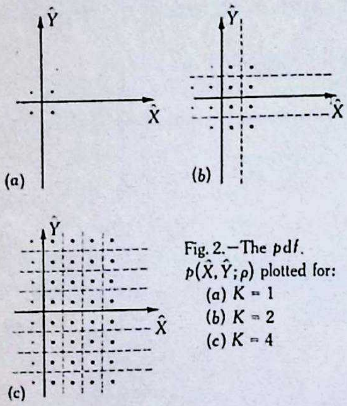

Fig. 2.—The pdf. $p(\hat{X}, \hat{Y}; \rho)$ plotted for:
(a) $K = 1$
(b) $K = 2$
(c) $K = 4$

Henceforth consider a symmetrical pdf so that we need treat only the first and fourth quadrants, say. In the first quadrant let the array $A(I,J) = {}^2P_{ij}$ be the representation of $p(\hat{X}, \hat{Y}; \hat{\rho})$, where I and J are positive integers by definition. A symmetrical pdf implies that $p(\hat{X}, \hat{Y}; \hat{\rho})$ is symmetrical about the 45° axis and so, for the case $I \neq J$, XY takes the value $(I-\frac{1}{2})(J-\frac{1}{2})$ in four positions on the X, Y plane:

$$(I-\tfrac{1}{2})(J-\tfrac{1}{2}) = (J-\tfrac{1}{2})(I-\tfrac{1}{2}) = (-I+\tfrac{1}{2})(-J+\tfrac{1}{2}) = (-J+\tfrac{1}{2})(-I+\tfrac{1}{2}).$$

Therefore if $I \neq J$ and $I > J$, $B(M) = 4A(I,J)$, where $M = (2I-1)(2J-1)$ is a multiple of $\frac{1}{4}Q^2$.

On the 45° axis $I = J$ and there are only two positions where $\hat{X}\hat{Y}$ takes the value $(I-\frac{1}{2})^2$. Hence $B(M) = 2A(I,I)$ in the first quadrant. Thus the positive axis of $B(M)$ can be found:

$$B(M) = \sum_{I=1}^{K}\left(\sum_{J=1}^{I-1} 4A(I,J)\,\delta\big(M-(2I-1)(2J-1)\big)\right) + \sum_{I=1}^{K} 2A(I,I)\,\delta\big(M-(2I-1)^2\big). \tag{11}$$

In the fourth quadrant the same arguments apply and $p(\hat{X}, \hat{Y}; \hat{\rho})$ is represented by the array $C(N,L) = P_{n,-l+1}$ and N and L are integers $1 \ldots +K$. Taking the product $\hat{X}\hat{Y}$ gives the negative axis of $B(M)$, represented by $B(W)$,

$$B(W) = \sum_{N=1}^{K}\left(\sum_{L=1}^{N-1} 4C(N,L)\,\delta\big(W-(2N-1)(2L-1)\big)\right) + \sum_{N=1}^{K} 2C(N,N)\,\delta\big(W-(2N-1)^2\big). \tag{12}$$

Evidently the mean value of $\hat{X}\hat{Y}$ is

$$\bar{z} = \left(\sum_{M=1}^{\infty} M\,B(M)\right)\frac{Q^2}{4} - \left(\sum_{W=1}^{\infty} W\,B(W)\right)\frac{Q^2}{4} \tag{13}$$

and the mean square is

$$\overline{z^2} = \left(\sum_{M=1}^{\infty} M^2\,B(M)\right)\frac{Q^4}{16} + \left(\sum_{W=1}^{\infty} W^2\,B(W)\right)\frac{Q^4}{16}. \tag{14}$$

In general it is very difficult to determine the values of P_{ij}. Numerical integration seems the only solution. For example, if X and Y are Gaussian variables, the case $\rho = 1$ is the only one expressible in closed form (and then in terms of the error function). A computer programme can perform the operations specified by the above equations. It would give results enabling the function $\rho = A(\hat{\rho})$ and the value of $\hat{\sigma}^1$ to be plotted for various values of ρ and quantization systems.

V. Product of Two Gaussians

The primary purpose of the calculations is to compare the various quantization systems with the signal to noise ratio of continuous multiplication of two Gaussian signals of finite length. The pdf $p(z)$ has to be found where $z = XY$, the product of the two Gaussians X and Y, and where $p(z)\,\mathrm{d}z$ is the probability that z is between z and $z+\mathrm{d}z$. On a plot of the two-dimensional pdf, $p(x, y; \rho)$, $p(z)\,\mathrm{d}z$ is thus the integral of the areas between the curves $z = xy$ and $z+\mathrm{d}z = xy$, that is, the area C,

$$p(z)\,\mathrm{d}z = \iint_C p(x, y; \rho)\,\mathrm{d}x\,\mathrm{d}y. \tag{15}$$

The result is one that is well known in statistics and is given, for example, in more general form by Wishart and Bartlett (1932). In an information-theory context it is derived by Lampard (1956), and in the present notation it is the less general expression

$$p(z) = \frac{1}{\pi(1-\rho)^{\frac{1}{2}}}\exp\left(\frac{\rho z}{1-\rho^2}\right) K_0\left(\frac{z}{1-\rho^2}\right), \tag{16}$$

where $K_0(x)$ is the modified Bessel function of the first kind of zero order.

As $p(z)$ is a proper probability density, it normalizes and so, integrating (16) from $-\infty$ to $+\infty$,

$$1 = \int_{-\infty}^{\infty} p(z)\,\mathrm{d}z = \frac{1}{\pi(1-\rho)^{\frac{1}{2}}}\int_{-\infty}^{\infty} \exp\left(\frac{\rho z}{1-\rho^2}\right) K_0\left(\frac{z}{1-\rho^2}\right)\mathrm{d}z. \tag{17}$$

With the new variable $u = z/(1-\rho^2)$,

$$1 = \pi^{-1}(1-\rho^2)^{\frac{1}{2}}\int_{-\infty}^{\infty} \exp(\rho u)\,K_0(u)\,\mathrm{d}u, \tag{18}$$

and so

$$(1-\rho^2)^{-\frac{1}{2}} = \pi^{-1}\int_{-\infty}^{\infty} \exp(\rho u)\,K_0(u)\,\mathrm{d}u. \tag{19}$$

This can be differentiated on both sides with respect to ρ to give

$$-\tfrac{1}{2}(1-\rho^2)^{-3/2}(-2\rho) = \pi^{-1}\int_{-\infty}^{\infty} u\exp(\rho u)\,K_0(u)\,\mathrm{d}u\,, \tag{20}$$

which is just

$$\rho = \pi^{-1}(1-\rho^2)^{3/2}\int_{-\infty}^{\infty} u\exp(\rho u)\,K_0(u)\,\mathrm{d}u \tag{21}$$

$$= \int_{-\infty}^{\infty} z\,p(z)\,\mathrm{d}z\,. \tag{22}$$

Hence the mean of z is

$$\bar{z} = \rho\,. \tag{23}$$

This is also clear from first principles.

Equation (20) may be differentiated again to give

$$3\rho^2(1-\rho^2)^{-5/2}+(1-\rho^2)^{-3/2} = \pi^{-1}\int_{-\infty}^{\infty} u^2\exp(\rho u)\,K_0(u)\,\mathrm{d}u\,, \tag{24}$$

and so

$$1+2\rho^2 = \pi^{-1}(1-\rho^2)^{5/2}\int_{-\infty}^{\infty} u^2\exp(\rho u)\,K_0(u)\,\mathrm{d}u \tag{25}$$

$$= \int_{-\infty}^{\infty} z^2\,p(z)\,\mathrm{d}z\,. \tag{26}$$

Hence

$$\overline{z^2} = 1+2\rho^2 \tag{27}$$

and the variance is

$$\overline{z^2}-(\bar{z})^2 = (1+2\rho^2)-\rho^2 = 1+\rho^2\,. \tag{28}$$

The output noise to signal ratio for continuous multiplication is hence

$$\sigma/\rho = (1+\rho^2)^{\frac{1}{2}}/\rho\,. \tag{29}$$

Obviously the higher moments could be found by continuation of the differentiation process.

VI. Results

By using the formulae of Section IV, the output noise to signal ratio could be calculated for Gaussian statistics and for values of K from 1 to 4 with correlation coefficient ρ and quantization level Q (fraction of standard deviation) as parameters. The mean of $\hat{X}\hat{Y}$ represents $\hat{\rho}$ when it is normalized to the value for the case $\rho = 1$. Hence it is possible to trace curves of $\rho = A(\hat{\rho})$ for various K and Q as shown in Figure 3. As expected, for K increasing, the system behaves more closely in character to the continuous multiplication, while for a given value of K there is a value of Q at which the quantization best approximates the continuous case. $K = 1$ represents the infinite clipping or one bit case and the curve is the $(2/\pi)\sin^{-1}\rho$ curve given by Van Vleck (1943).

It is also possible to plot the ratio of $\hat{\sigma}^1/\hat{\rho}$ against ρ, K, and Q. Denoting this ratio by N/S, Figure 4 also shows that, for a given K and ρ, an optimum Q exists for least noise.

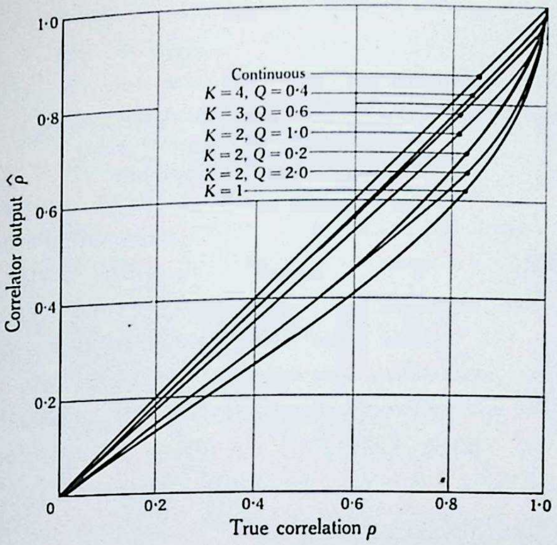

Fig. 3.—Plots of output correlation coefficient $\hat{\rho}$ against input ρ for various quantization systems and operating conditions.

To obtain the relative efficiencies of the quantization systems, the values of $\bar{\sigma}^1$ must be found through the use of the curves of $\hat{\rho}$ versus ρ. A quantized correlation measure on one sample would give an estimate $\bar{\rho}^1 = A(\hat{\rho}^1)$, and $\bar{\sigma}^1$ is the standard deviation of $\bar{\rho}^1$ about ρ. The σ's are related since errors in the measurement of $\hat{\rho}$ and ρ are related; $\bar{\sigma}^1$ is merely the value $\hat{\sigma}^1$ divided by the slope of the appropriate curve in Figure 3 at the relevant value of ρ. The ratio $\bar{\sigma}^1/\rho$ is hence the noise to signal ratio of the estimate of correlation with that particular quantization system and record length. This ratio is plotted in Figure 5 as a function of ρ for various

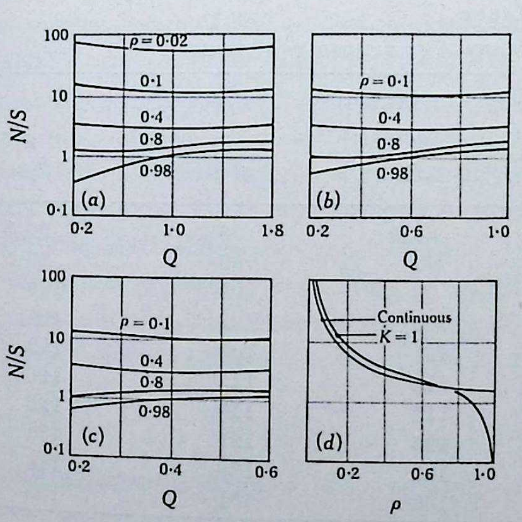

Fig. 4.—Plots of output noise to signal ratio N/S against step width Q (fraction of standard deviation) for various values of ρ and
(a) $K = 2$,
(b) $K = 3$,
(c) $K = 4$,
and against ρ for
(d) $K = 1$ and continuous.

quantization types. The following section interprets these curves in terms of the two practical uses: correlation and power measurement.

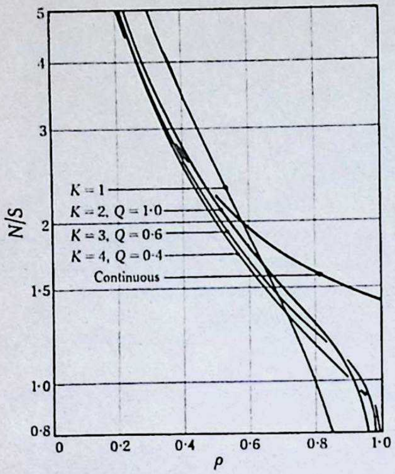

Fig. 5.—Output noise to signal ratio N/S plotted against ρ for various systems to indicate relative efficiencies.

VII. Practical Measurement

The determination of correlation between two slightly correlated signals is important in radio astronomy for the study of polarization and also spectral lines. In these cases the correlation is usually small and, as Figures 3, 4, and 5 indicate, linearity is approached. By normalizing the output signal to noise ratio of the various systems to that of continuous multiplication at each value of ρ, Figure 5 is re-represented in Table 1 as a list of relative efficiencies. This table confirms the relative efficiencies of 0·64 for one bit and 0·88 for two bit as given by Weinreb (1963) and Clark (1967) (for his $n = 9$ and $m = 3$), in the limiting case where ρ tends to zero.

Table 1

Efficiencies relative to a continuous system

ρ	Continuous	System $K = 1$	 2 $Q = 1·0$	 3 0·6	 4 0·4
0·1	100	64·2	88·5	93·6	94·6
0·2	100	67	90	95	96·5
0·3	100	71	93·5	99	100
0·4	100	77·5	98	103	106
0·5	100	87	103	109	112
0·6	100	102	110	115	120
0·7	100	121	113	119	125
0·8	100	168	125	131	138
0·9	100	282	142	138	148
0·95	100	480	160	151	155

However, against these curves and efficiencies must be placed the practical complexities of implementing a quantization system. For a rapid many-point determination of a correlation function, many multipliers are needed and in this case the one bit system is simplest. The operations for a one bit system would be binary arithmetic so that the only source of error could be in determination of the point where the signals change sign. The electronics are simple and work rapidly (5 MHz), as has been shown, for example, by Weinreb (1963).

Calibration is simply a count of N, the record length. This gives the value which would be obtained in the case $\rho = 1$ and which enables an immediate determination of $\bar{\rho}^N$ as $\sin(\frac{1}{2}\pi\hat{\rho}^N)$. Systems of two, three, or higher bits involve several levels apart from zero that divide the amplitude of the signal into bands of width Q. It is evidently important to consider the effect of absolute level and stability of level on the system performance. Determination at the zero level of amplitude is extremely accurate by the use of amplifiers and limiters. The levels above and below zero must be generated in the quantizer and held stable. The theory in this paper uses levels as a fraction of the standard deviation of the signal, which is generally an unknown. In other words, the absolute level as a fraction of the standard deviation would not be known extremely accurately. The theory would indicate the region of maximum efficiency and only calibration could determine the actual function $\rho = A(\hat{\rho})$. Fortunately Figure 4 indicates that efficiency is a slowly varying function of the level Q.

Consequently, the important point with multiple bit systems is the stability of the quantizer. The quantizer as well as the level of the signal would need to be stable between calibrations to a level commensurate with the level of correlation coefficient being measured. Calibration would be more complicated as it not only requires a knowledge of the output for two completely correlated signals but another test signal is required to determine the level Q and hence the relation $\rho = A(\hat{\rho})$.

In other applications (particularly in radio astronomy for correlation receivers, for compound arrays, and for polarization measurements) the actual correlation coefficient between two signals is not required. In these cases the actual output of the correlator is used as an indication of power of the correlated component. Calibration is then achieved by insertion of a signal of known power.

The two applications are related in that, if σ_s^2 is the power of the correlated part and σ_n^2 the power in the uncorrelated part of each of the assumed equal channels, the value σ_s^2 can be expressed in terms of the correlation coefficient of the two signals as

$$\sigma_s^2 = \{\rho/(1-\rho)\}\sigma_n^2. \tag{30}$$

For small excursions around the operating point, the relative efficiencies will be the same as before. Again the result emerges that for operating points at high values of ρ the one bit system is the most efficient.

VIII. Conclusions

This paper has presented an approach to the general problem of correlation measurements on quantized Gaussians of only finite length. The results for Gaussian statistics and one, two, and three bit quantizers indicate that for ρ greater than $0 \cdot 3$, three bit is more efficient than continuous, while for ρ greater than $0 \cdot 6$ or so, one bit is the most efficient. For the other extreme of low values of ρ, one bit is only 65% efficient and a large increase in efficiency to 89% can be obtained by the small increase in complexity of two bit representation. The rewards of three bit representation are only another 6% greater than two bit.

In general the efficiencies and optimum operating positions are very much a function of the system parameters and one would need to know the approximate system parameters before any ideal operating conditions could be chosen.

IX. ACKNOWLEDGMENTS

This work was performed while the author was under a Gledden Research Fellowship from the University of Western Australia. The author would like to thank Dr. E. J. Blum of the Observatory at Meudon for suggesting the topic, and the referee, who suggested the derivation in Section V and provided the author with references to the product of continuous Gaussians.

X. REFERENCES

BONNET, G. (1962).—*C. r. hebd. Séanc. Acad. Sci., Paris* **255**, 825–7.

CLARK, B. G. (1967).—Two bit correlator. Rep. Natn. Radioastron. Obs., Greenbank, U.S.A. (unpublished).

LAMPARD, D. G. (1956).—*I.R.E. Trans. Inf. Theory* **IT2**, No. 1, 4–11.

VAN VLECK, J. H. (1943).—Radio Res. Lab. Harvard Univ. Rep. No. 51.

WEINREB, S. (1963).—M.I.T. Res. Lab. of Electronics Tech. Rep. No. 412.

WISHART, J., and BARTLETT, M. F. (1932).—*Proc. Camb. phil. Soc. math. phys. Sci.* **28**, 455.

STRUCTURE OF POLYTROPES WITH PURELY TOROIDAL MAGNETIC FIELDS

By Narendra K. Sinha*

[*Manuscript received November* 10, 1967]

Summary

In this paper the influence of a purely toroidal magnetic field upon the structure of a polytrope is investigated and the first-order perturbations in the density distribution, the geometry of the boundary, and the mass–radius relation are obtained.

I. Introduction

In a recent paper, Van der Borght (1967) has investigated the structure of a polytrope in the presence of a magnetic field having both poloidal and toroidal components. The structure of a polytrope in the case of only a toroidal field does not, however, follow from his investigations. Roxburgh (1966) investigated the structure of a toroidal magnetic field in a polytrope, and in a following paper (Roxburgh 1967) indicated the form of the radial perturbation of the polytrope $n = 3$ in the presence of a toroidal magnetic field but did not give any detailed calculations.

The existence of a toroidal magnetic field in a polytrope is not unrealistic. In the present work, we study the effect of a toroidal field on the structure of polytropes employing a method previously used by Chandrasekhar (1933) to study rotating polytropes. The geometry of the boundary, the oblateness, and the mass variation are obtained for polytropes $n = 1\cdot5(0\cdot5)3\cdot5$.

II. General Equations

The general Lundquist equations for a self-gravitating fluid are

$$\frac{\mathrm{D}\mathbf{V}}{\mathrm{D}t} = -\frac{\nabla p}{\rho} - \nabla\Phi + \frac{1}{\bar{\mu}\rho}(\nabla\times\mathbf{B})\times\mathbf{B}\,, \tag{1}$$

$$\partial\rho/\partial t = -\nabla.(\rho\mathbf{V})\,, \tag{2}$$

$$\partial\mathbf{B}/\partial t = \nabla\times(\mathbf{V}\times\mathbf{B})\,, \tag{3}$$

$$\nabla.\mathbf{B} = 0\,, \qquad \nabla\times\mathbf{B} = \bar{\mu}\mathbf{J}\,, \tag{4}$$

and

$$\mathrm{D}S/\mathrm{D}t = 0\,, \tag{5}$$

where **V** is the velocity of the fluid, **B** is the magnetic field, p is the pressure, ρ is the density, S is the entropy, $\mathbf{J}$ is the current density, $\bar{\mu}$ is the permeability of the medium, and $\mathrm{D}/\mathrm{D}t \equiv \partial/\partial t + \mathbf{V}.\nabla$. Further, the gravitational potential Φ satisfies the Poisson equation

---

* Department of Mathematics, Monash University, Clayton, Vic. 3168.

$$\nabla^2\Phi = 4\pi G\rho\,. \tag{6}$$

In spherical coordinates (r, ϑ, ϕ), the field may be expressed as

$$\mathbf{B} \equiv (0,0,B)\,.$$

In the absence of any azimuthal velocity component, equations (2)–(5) may be solved to obtain

$$B/r \sin\vartheta\,\rho = f(S)\,,$$

giving a general expression for B.

III. EQUILIBRIUM CONFIGURATION

In the steady state, which we take as the equilibrium configuration, the energy equation (5) can be replaced by the polytropic equation

$$p = K\rho^{1+n^{-1}}\,, \tag{7}$$

where K is a constant and n is the polytropic index. B now may be given by

$$B = Lr\sin\vartheta\,\rho\,, \tag{8}$$

where L is a constant. The equation (8) gives the same expression for B as that obtained by Roxburgh (1966) in a different way for a polytrope in equilibrium.

In the equilibrium state, equation (1) gives rise to the equations

$$\frac{\partial p}{\partial r} + \rho\frac{\partial\Phi}{\partial r} + \frac{B}{\bar{\mu}}\frac{\partial B}{\partial r} + \frac{B^2}{\bar{\mu}r} = 0\,,$$

$$\frac{\partial p}{\partial\vartheta} + \rho\frac{\partial\Phi}{\partial\vartheta} + \frac{B}{\bar{\mu}}\frac{\partial B}{\partial\vartheta} + \frac{B^2}{\bar{\mu}}\cot\vartheta = 0\,.$$

Using equations (7) and (8), the above equations can be solved to give the integral

$$(n+1)K\rho^{n^{-1}} + (L^2/\bar{\mu})r^2\sin^2\vartheta\,\rho + \Phi = \text{constant}\,. \tag{9}$$

On substituting equation (9) into equation (6) we obtain

$$\nabla^2\{(n+1)K\rho^{n^{-1}} + (L^2/\bar{\mu})r^2\sin^2\vartheta\,\rho\} + 4\pi G\rho = 0\,. \tag{9a}$$

We write

$$\rho = \lambda\Theta^n, \qquad \mu = \cos\vartheta, \qquad \alpha^2 = \{(n+1)/4\pi G\}K\lambda^{n^{-1}-1}\,,$$

$$r = \alpha\xi, \qquad \beta^2 = L^2/4\pi G\bar{\mu}\,,$$

where λ is the central density, ξ is a dimensionless distance, and β^2, the square of a characteristic Alfvén Mach number of the medium, is a measure of the strength of the magnetic field. The equation (9a) becomes

$$\frac{1}{\xi^2}\left[\frac{\partial}{\partial\xi}\left(\xi^2\frac{\partial}{\partial\xi}\right)+\frac{\partial}{\partial\mu}\left\{\left(1-\mu^2\right)\frac{\partial}{\partial\mu}\right\}\right]\left(\Theta+\beta^2\xi^2(1-\mu^2)\Theta^n\right)=-\Theta^n, \qquad (10)$$

and it is this equation that has to be solved to find the density distribution in a polytrope in equilibrium with a toroidal magnetic field.

In the absence of a magnetic field ($\beta = 0$) the above equation reduces to Emden's equation

$$\frac{1}{\xi^2}\frac{\mathrm{d}}{\mathrm{d}\xi}\left(\xi^2\frac{\mathrm{d}\theta}{\mathrm{d}\xi}\right)+\theta^n=0, \qquad (11)$$

of index n, where the spherically symmetric function θ is introduced by $\rho_{\mathrm{u}} = \lambda\theta^n$, the subscript u denoting the solution for the unperturbed polytrope.

Assuming the magnetic field to be small ($\beta^2 \ll 1$), a solution of equation (7) will be sought in terms of θ, up to first order in β^2, by considering a solution of the type (cf. Chandrasekhar 1933)

$$\Theta = \theta+\beta^2\Psi(\xi,\mu). \qquad (12)$$

Substituting equation (12) into equation (10) and using equation (11), it is found that Ψ satisfies the equation

$$\frac{1}{\xi^2}\frac{\partial}{\partial\xi}\left(\xi^2\frac{\partial\Psi}{\partial\xi}\right)+\frac{1}{\xi^2}\frac{\partial}{\partial\mu}\left\{\left(1-\mu^2\right)\frac{\partial\Psi}{\partial\mu}\right\}+n\theta^{n-1}\Psi$$

$$=\left(\mu^2-1\right)\frac{1}{\xi^2}\frac{\mathrm{d}}{\mathrm{d}\xi}\left\{\xi^2\frac{\mathrm{d}}{\mathrm{d}\xi}\left(\xi^2\theta^n\right)\right\}-(6\mu^2-2)\theta^n. \qquad (13)$$

From equation (12), it follows that

$$\Psi = \partial\Psi/\partial\xi = 0, \qquad \text{at} \qquad \xi = 0.$$

Ψ is expanded as

$$\Psi = \psi_0(\xi)+\sum_{j=1}^{\infty}\psi_j(\xi)\,P_j(\mu), \qquad (14)$$

and we find that

$$\psi_j(0) = \psi_j'(0) = 0.$$

Substituting the expansion (14) into equation (13) and equating coefficients of $P_j(\mu)$, we get the equations

$$\frac{1}{\xi^2}\frac{\mathrm{d}}{\mathrm{d}\xi}\left(\xi^2\frac{\mathrm{d}\psi_j}{\mathrm{d}\xi}\right)=\left(\frac{j(j+1)}{\xi^2}-n\theta^{n-1}\right)\psi_j, \qquad j\neq 0,2, \qquad (15)$$

$$\frac{1}{\xi^2}\frac{\mathrm{d}}{\mathrm{d}\xi}\left(\xi^2\frac{\mathrm{d}\psi_2}{\mathrm{d}\xi}\right) = \left(\frac{6}{\xi^2}-n\theta^{n-1}\right)\psi_2+\frac{2}{3}\frac{1}{\xi^2}\frac{\mathrm{d}}{\mathrm{d}\xi}\left\{\xi^2\frac{\mathrm{d}}{\mathrm{d}\xi}\left(\xi^2\theta^n\right)\right\}-4\theta^n \tag{16}$$

and

$$\frac{1}{\xi^2}\frac{\mathrm{d}}{\mathrm{d}\xi}\left(\xi^2\frac{\mathrm{d}\psi_0}{\mathrm{d}\xi}\right) = -n\theta^{n-1}\psi_0-\frac{2}{3}\frac{1}{\xi^2}\frac{\mathrm{d}}{\mathrm{d}\xi}\left\{\xi^2\frac{\mathrm{d}}{\mathrm{d}\xi}\left(\xi^2\theta^n\right)\right\} \tag{17}$$

to determine the ψ_j.

The equation (15) is different in form from equations (16) and (17), in as much as if ψ_j is a solution of (15) so is $A_j\psi_j$, where A_j is an arbitrary constant. A proper expansion of Ψ would then be

$$\Psi = \psi_0(\xi)+\psi_2(\xi)P_2(\mu)+\sum_{j=1}^{\infty}{}' A_j\psi_j(\xi)P_j(\mu), \tag{18}$$

where the prime denotes exclusion of the term with $j = 2$ from the summation. Equation (10) does not contain Φ explicitly and remains the same whatever be the external gravitational field. This indeterminacy may be resolved by calculating the potential from the solutions found and then making it satisfy the basic equation (9). This will also lead to the determination of the A_j.

Poisson's equation (6) may be rewritten as

$$\frac{1}{\xi^2}\frac{\partial}{\partial\xi}\left(\xi^2\frac{\partial\Phi}{\partial\xi}\right)+\frac{1}{\xi^2}\frac{\partial}{\partial\mu}\left((1-\mu^2)\frac{\partial\Phi}{\partial\mu}\right)$$
$$= -D[\theta^n+n\theta^{n-1}\beta^2\{\psi_0+\psi_2P_2(\mu)+\Sigma' A_j\psi_jP_j(\mu)\}], \tag{19}$$

where $D = -(n+1)K\lambda^{n^{-1}}$. To the first order in β^2, Φ may be developed as

$$\Phi = \overline{\Phi}+\beta^2\left(\Phi_0(\xi)+\sum_{j=1}^{\infty}\Phi_j(\xi)P_j(\mu)\right),$$

where $\overline{\Phi}$ is the potential of the polytrope without a magnetic field. Substituting in equation (19) and equating the coefficients of $P_j(\mu)$, we get the equations

$$\frac{1}{\xi^2}\frac{\mathrm{d}}{\mathrm{d}\xi}\left(\xi^2\frac{\mathrm{d}\Phi_j}{\mathrm{d}\xi}\right) = \frac{j(j+1)}{\xi^2}\Phi_j-Dn\theta^{n-1}A_j\psi_j, \qquad j\neq 0,2, \tag{20}$$

$$\frac{1}{\xi^2}\frac{\mathrm{d}}{\mathrm{d}\xi}\left(\xi^2\frac{\mathrm{d}\Phi_2}{\mathrm{d}\xi}\right) = \frac{6}{\xi^2}\Phi_2-Dn\theta^{n-1}\psi_2, \tag{21}$$

$$\frac{1}{\xi^2}\frac{\mathrm{d}}{\mathrm{d}\xi}\left(\xi^2\frac{\mathrm{d}\Phi_0}{\mathrm{d}\xi}\right) = -Dn\theta^{n-1}\psi_0, \tag{22}$$

$$\frac{1}{\xi^2}\frac{\mathrm{d}}{\mathrm{d}\xi}\left(\xi^2\frac{\mathrm{d}\overline{\Phi}}{\mathrm{d}\xi}\right) = -D\theta^n. \tag{23}$$

Equation (20) becomes, using equation (15),

$$\frac{1}{\xi^2}\frac{\mathrm{d}}{\mathrm{d}\xi}\left(\xi^2\frac{\mathrm{d}\Phi_j}{\mathrm{d}\xi}\right)-\frac{j(j+1)}{\xi^2}\Phi_j = DA_j\left\{\frac{1}{\xi^2}\frac{\mathrm{d}}{\mathrm{d}\xi}\left(\xi^2\frac{\mathrm{d}\psi_j}{\mathrm{d}\xi}\right)-\frac{j(j+1)}{\xi^2}\psi_j\right\}.$$

Since there is no singularity at the centre, the admissible complementary function is $DB_j\xi^j$, where B_j is any constant. A particular solution is given by $\Phi_j = DA_j\psi_j$. Hence the general solution is

$$\Phi_j = D(A_j\psi_j+B_j\xi^j), \qquad j\neq 0,2.$$

Equation (21) treated with equation (16) yields

$$\frac{1}{\xi^2}\frac{\mathrm{d}}{\mathrm{d}\xi}\left(\xi^2\frac{\mathrm{d}\Phi_2}{\mathrm{d}\xi}\right)-\frac{6}{\xi^2}\Phi_2$$

$$= D\left[\frac{1}{\xi^2}\frac{\mathrm{d}}{\mathrm{d}\xi}\left\{\xi^2\frac{\mathrm{d}}{\mathrm{d}\xi}\left(\psi_2-\tfrac{2}{3}\xi^2\theta^n\right)\right\}-\frac{6}{\xi^2}\left(\psi_2-\tfrac{2}{3}\xi^2\theta^n\right)\right],$$

and, as above, its solution is

$$\Phi_2 = D(\psi_2-\tfrac{2}{3}\xi^2\theta^n+B_2\xi^2),$$

where B_2 is constant. Substituting for ψ_0 from equation (17) into equation (22), we get

$$\frac{1}{\xi^2}\frac{\mathrm{d}}{\mathrm{d}\xi}\left(\xi^2\frac{\mathrm{d}\Phi_0}{\mathrm{d}\xi}\right) = D\frac{1}{\xi^2}\frac{\mathrm{d}}{\mathrm{d}\xi}\left\{\xi^2\frac{\mathrm{d}}{\mathrm{d}\xi}\left(\psi_0+\tfrac{2}{3}\xi^2\theta^n\right)\right\},$$

which has the solution

$$\Phi_0 = D(\psi_0+\tfrac{2}{3}\xi^2\theta^n)+\text{constant}.$$

Finally, comparing equation (23) with Emden's equation (11), we get

$$\overline{\Phi} = D\theta+\text{constant}.$$

Substituting these values of $\overline{\Phi}$ and Φ_j in equation (14), the expression for Φ becomes after a readjustment of terms

$$\Phi = D\left\{\Theta+\beta^2\left(\sum_{j=1}^{\infty}B_j\xi^jP_j(\mu)+\tfrac{2}{3}\xi^2\theta^n\{1-P_2(\mu)\}\right)\right\}+\text{constant}.$$

Φ so obtained must satisfy equation (9) identically, and this gives

$$\Theta+\tfrac{2}{3}\beta^2\xi^2\{1-P_2(\mu)\}\theta^n = \Theta+\beta^2\left(\sum_{j=1}^{\infty}B_j\xi^jP_j(\mu)+\tfrac{2}{3}\xi^2\theta^n\{1-P_2(\mu)\}\right).$$

It follows that $B_j = 0$ for all j. Hence

$$\Phi = D[\Theta+\tfrac{2}{3}\beta^2\xi^2\theta^n\{1-P_2(\mu)\}]+\text{constant}. \qquad (24)$$

Furthermore, the potential arising from the mass must be continuous with the potential in the free space outside on the boundary. The density, being of higher order than the first, in the space between $\xi = \xi_1$, the first zero of Emden's function with index n, and the new boundary $\xi = \xi_0$, is negligible here. Thus on $\xi = \xi_1$, Φ and its normal derivative should be continuous to the first order with those of Φ_{ext}, which may be expressed as

$$\Phi_{\text{ext}} = D\left(\frac{c_0}{\xi} + \beta^2 \sum_{j=1}^{\infty} \frac{c_j}{\xi^{j+1}} P_j(\mu)\right) + \text{constant.}$$

Bearing in mind the requirement $n > 1$, arising from the fact that ρ and $\nabla \times \mathbf{B}$ vanish at the boundary, we find that the above conditions imply that

$$\text{(i)}\ A_j = 0\,, \qquad j \neq 2, \qquad \text{and}$$

$$\text{(ii)}\ \xi_1 \psi_2'(\xi_1) + 3\psi_2(\xi_1) = 0\,. \tag{25}$$

Hence the solution is given as

$$\Theta = \theta(\xi) + \beta^2\{\psi_0(\xi) + \psi_2(\xi) P_2(\mu)\}\,,$$

where ψ_2 and ψ_0 are the solutions of equations (16) and (17) respectively. This specifies the structure of a polytrope in equilibrium with a toroidal magnetic field.

IV. NUMERICAL INTEGRATION

It is not possible to solve equations (16) and (17) exactly. Assuming the expansions

$$\psi_0 = -\tfrac{2}{3}\xi^2 + \ldots,$$

$$\psi_2 = \bar{\psi}_2 \xi^2 + \ldots,$$

and

$$\theta = 1 - \tfrac{1}{6}\xi^2 + \ldots$$

at the centre, these equations were integrated numerically using a Runge–Kutta method together with Emden's equation (11) for the cases $n = 1{\cdot}5(0{\cdot}5)3{\cdot}5$. A suitable value for $\bar{\psi}_2$ was determined so that the boundary condition (25) is satisfied. Values of ψ_0 and ψ_2 obtained for polytropes of different indices are given in Table 1. The value of $\bar{\psi}_2$ in each case is also given there.

V. NEW BOUNDARY

On the surface $\Theta(\xi_0) = 0$ and this gives the expression

$$\xi_0 = \xi_1 - \frac{\beta^2}{(\mathrm{d}\theta/\mathrm{d}\xi)_{\xi=\xi_1}}\Big(\psi_0(\xi_1) + \psi_2(\xi_1) P_2(\mu)\Big)\,,$$

for the new boundary. The second term gives the mean expansion of the polytrope,

TABLE 1

PERTURBATIONS IN DENSITY FOR $n = 1{\cdot}5(0{\cdot}5)3{\cdot}5$

Parameter	Perturbations										$\overline{\psi}_2$
$n = 1{\cdot}5$											
ξ/ξ_1	0·1	0·2	0·3	0·4	0·5	0·6	0·7	0·8	0·9	1·0	1·149
$10\psi_0$	−0·852	−2·984	−5·339	−6·732	−6·382	−4·182	−0·654	3·323	6·812	8·824	
$10\psi_2$	1·489	5·384	10·230	14·321	16·379	15·942	13·380	9·609	5·751	3·087	
$n = 2{\cdot}0$											
ξ/ξ_1	0·1	0·2	0·3	0·4	0·5	0·6	0·7	0·8	0·9	1·0	1·153
$10\psi_0$	−1·163	−3·627	−5·311	−4·884	−2·495	0·792	3·891	6·161	7·417	7·746	
$10\psi_2$	2·049	6·797	11·290	13·325	12·553	9·962	6·841	4·125	2·266	1·376	
$n = 2{\cdot}5$											
ξ/ξ_1	0·1	0·2	0·3	0·4	0·5	0·6	0·7	0·8	0·9	1·0	1·157
$10\psi_0$	−1·637	−4·113	−4·108	−1·589	1·618	4·179	5·728	6·429	6·582	6·458	
$10\psi_2$	2·944	8·390	11·246	10·450	7·796	5·034	2·944	1·633	0·937	0·635	
$n = 3{\cdot}0$											
ξ/ξ_1	0·1	0·2	0·3	0·4	0·5	0·6	0·7	0·8	0·9	1·0	1·160
$10\psi_0$	−2·335	−3·764	−1·216	2·118	4·301	5·303	5·585	5·521	5·526	5·114	
$10\psi_2$	4·374	9·433	9·078	6·232	3·653	1·991	1·066	0·596	0·374	0·268	
$n = 3{\cdot}5$											
ξ/ξ_1	0·1	0·2	0·3	0·4	0·5	0·6	0·7	0·8	0·9	1·0	1·162
$10\psi_0$	−3·106	−1·382	2·434	4·301	4·790	4·719	4·476	4·212	3·975	3·778	
$10\psi_2$	6·461	8·287	5·036	2·516	1·216	0·606	0·327	0·200	0·141	0·109	

whereas the third term gives rise to an ellipticity. Since the value of $P_2(\mu)$ is $+1$ at the poles and $-\frac{1}{2}$ at the equator, the oblateness of the configuration is given by

$$\delta = \frac{3}{2}\,\frac{\psi_2(\xi_1)}{\xi_1(\mathrm{d}\theta/\mathrm{d}\xi)_{\xi=\xi_1}}\,\beta^2 ,$$

and depends upon the strength of the magnetic field. The values of the relevant quantities are given in Table 2, for different values of n.

TABLE 2

VALUES OF PARAMETERS DEFINING NEW CONFIGURATION

n	ξ_1	$-\psi_0(\xi_1)/\theta'(\xi_1)$	$-\psi_2(\xi_1)/\theta'(\xi_1)$	δ/β^2	$-\psi_0'(\xi_1)/\theta'(\xi_1)$
1·5	3·65375	4·340	1·389	0·570	−0·181
2·0	4·35287	6·087	1·081	0·373	0·142
2·5	5·35528	8·464	0·832	0·233	0·434
3·0	6·89685	12·045	0·631	0·137	0·681
3·5	9·53581	18·166	0·526	0·083	0·899

VI. MASS OF NEW CONFIGURATION

To the first order in β^2, the mass of the polytrope may be given by

$$M = 4\pi \int r^2 \rho \,\mathrm{d}r .$$

The ellipticity term does not contribute anything on the average. The mass is, therefore,

$$M = 4\pi\left(\frac{n+1}{4\pi G}K\,\lambda^{\frac{1}{2}(3-n)n^{-1}}\right)^{3/2}\int_0^{\xi_1}(\theta^n+\beta^2 n\theta^{n-1}\psi_0)\xi^2\,\mathrm{d}\xi$$

$$= -4\pi\left(\frac{n+1}{4\pi G}K\,\lambda^{\frac{1}{2}(3-n)n^{-1}}\right)^{3/2}\xi_1^2\left(\frac{\mathrm{d}\theta}{\mathrm{d}\xi}\right)_{\xi_1}\left\{1+\beta^2\left(\frac{\mathrm{d}\psi_0}{\mathrm{d}\xi}\div\frac{\mathrm{d}\theta}{\mathrm{d}\xi}\right)_{\xi_1}\right\},$$

obtained on using equations (11) and (17) and remembering that $n > 1$.

If M_{u} is the mass of the polytrope with the same central density when there is no magnetic field, we get

$$M = M_{\mathrm{u}}\left\{1+\beta^2\left(\frac{\mathrm{d}\psi_0}{\mathrm{d}\xi}\div\frac{\mathrm{d}\theta}{\mathrm{d}\xi}\right)_{\xi_1}\right\},$$

which shows that a magnetic polytrope with a toroidal field has a greater mass only if $\mathrm{d}\psi_0/\mathrm{d}\xi < 0$ at the boundary. Values of $(\psi_0'/\theta')_{\xi_1}$ are given in Table 2.

VII. DISCUSSION

It is found that ψ_0 is negative from the centre up to a fraction ϵ of the radius, when it becomes positive and remains so to the surface, which shows that the inner core of the perturbed polytrope is less dense and the outer layers are more dense than the unperturbed one. The value of ϵ decreases with increasing value of n.

The structure of the polytrope depends largely upon the strength of the magnetic field, but the polytropic index n has also a remarkable influence on it. The relative mean expansion, $-\psi_0(\xi_1)/\{\xi_1\,\theta'(\xi_1)\}$, of the polytrope increases and its ellipticity decreases with increasing values of n. Thus perturbed polytropes with larger n are relatively larger in size and less elliptical in shape.

The mass M has been shown to be greater than, equal to, or less than M_{u} according as

$$\left(\frac{\mathrm{d}\psi_0}{\mathrm{d}\xi}\right)_{\xi=\xi_1} \overset{<}{\underset{>}{=}} 0\,.$$

It is found that $(\psi_0')_{\xi_1}$ is positive for small values and negative for large values of n. Equation (17) was integrated with n as an eigenvalue and the above critical value was found to correspond to $n = 1\cdot 80$. It follows that a magnetic polytrope with the toroidal field (8) has a greater or smaller mass according as its polytropic index is greater than or less than $1\cdot 80$, and further, that this ratio increases with n.

VIII. ACKNOWLEDGMENTS

The author wishes to thank Dr. E. D. Fackerell and Professor R. Van der Borght for their helpful comments and interest in this work.

IX. REFERENCES

CHANDRASEKHAR, S. (1933).—*Mon. Not. R. astr. Soc.* **93**, 390.
ROXBURGH, I. W. (1966).—*Mon. Not. R. astr. Soc.* **132**, 347.
ROXBURGH, I. W. (1967).—*Mon. Not. R. astr. Soc.* **135**, 329.
VAN DER BORGHT, R. (1967).—*Aust. J. Phys.* **20**, 643.

EQUILIBRIUM POLOIDAL MAGNETIC FIELDS IN ROTATING STARS

By G. F. Davies*

[*Manuscript received February* 1, 1968]

Summary

Solutions are presented for equilibrium poloidal dipole magnetic fields in a uniformly rotating upper main-sequence star with no meridional circulation currents. An upper limit is found for the ratio of kinetic energy of rotation to the magnetic field energy. The perturbations to the structure of the star are also given.

I. Introduction

Ferraro (1937) has established that, if a star has no internal mass motions, the presence of a poloidal magnetic field tends strongly to keep the star in a state of "isorotation" in which the angular velocity is constant around any given field line. Such a rotation law implies that meridional circulation currents will be generated, but these will tend to destroy the state of isorotation by convecting angular momentum. Since the high conductivity of the stellar material means that the magnetic field is "frozen" into the material, the circulation will also convect magnetic flux and so distort the field, which will eventually react on the circulation and tend to suppress it.

In the absence of rotation, an arbitrary field will, in general, itself cause meridional circulation. An equilibrium poloidal field has been calculated approximately by Monaghan (1966*a*) for which the meridional circulation ceases in a nonrotating star, assuming infinite conductivity. The existence of this solution suggests that an equilibrium state may exist in a rotating star in which the poloidal field stops the circulation that would be induced by the rotation alone and maintains a state of isorotation.

In the present paper we consider an upper main-sequence star in uniform (solid body) rotation. Assuming that the conductivity is infinite, equilibrium solutions for a poloidal dipole magnetic field with no meridional circulation have been found. It has been found that, as the ratio of kinetic energy of rotation to magnetic energy is increased from zero, the equilibrium field is progressively distorted and "submerged", the surface field strength being reduced to zero when the rotational energy is comparable with the magnetic energy.

---

* Department of Mathematics, Monash University, Clayton, Vic. 3168.

Aust. J. Phys., 1968, **21**, 293–305

II. BASIC EQUATIONS

A star having infinite electrical conductivity and rotating with uniform angular velocity $\mathbf{\Omega}$ with a poloidal magnetic field $\mathbf{H}_\mathrm{p}$ and in which no circulation of matter occurs is described by the following set of equilibrium equations:
hydrostatic equilibrium

$$\frac{\nabla P}{\rho}+\nabla\phi=\frac{(\nabla\times\mathbf{H}_\mathrm{p})\times\mathbf{H}_\mathrm{p}}{4\pi\rho}+\Omega^2\boldsymbol{\tilde\omega}\,, \tag{1}$$

Poisson's equation

$$\nabla^2\phi=4\pi G\rho\,, \tag{2}$$

divergence of field

$$\nabla.\mathbf{H}_\mathrm{p}=0\,, \tag{3}$$

conservation of energy

$$\nabla.\mathbf{F}=\epsilon\rho\,, \tag{4}$$

radiative thermal equilibrium

$$\mathbf{F}=-(4ac/3\kappa\rho)T^3\,\nabla T\,, \tag{5}$$

convective thermal equilibrium

$$\frac{T}{P}\frac{\mathrm{d}P}{\mathrm{d}T}=4-\frac{1\cdot5\,\beta^2}{4-3\beta}=(n+1)_\mathrm{ad}\,. \tag{6}$$

Here P, ρ, T, and κ represent respectively the gas pressure, density, temperature, and opacity; ϕ is the gravitational potential, $\mathbf{F}$ the radiative energy flux, β the ratio of radiation pressure to total pressure, ϵ the rate of energy generation per unit mass, $\boldsymbol{\tilde\omega}$ the vector displacement from the axis of rotation, and the other symbols have their usual meaning.

It will be assumed that the star is perturbed only slightly from a spherically symmetric model that has been obtained previously. The model chosen is of an initial main-sequence star (with uniform composition) of 15 solar masses as described by Stothers (1963). In Stothers's notation, the composition is

$$X=0\cdot70\,,\qquad Y=0\cdot27\,,\qquad Z=0\cdot03\,,\qquad X_\mathrm{CNO}=\tfrac{1}{2}Z\,.$$

The opacity is due to electron scattering and is given by $\kappa=0\cdot19(1+X)$. The energy generation law is taken as

$$\epsilon=\epsilon_0\,XX_\mathrm{CNO}\,\rho T^\nu, \tag{7}$$

where $\nu=15$ and $\log\epsilon_0=-106\cdot6$.

Radiation pressure is important in stars of this mass. Consequently, the equation of state is

$$P=(\mathscr{R}/w)\rho T+\tfrac{1}{3}aT^4=(\mathscr{R}/w)\rho T/\beta\,, \tag{8}$$

where $\mathscr{R}$ is the gas constant and w is the mean molecular weight of the gas.

We will assume that the field is symmetric about the axis of rotation and use spherical polar coordinates (r, θ, φ), where θ is measured from the positive axis of rotation. Equation (3) can be satisfied by writing

$$H_r = r^{-2}\,\partial\psi/\partial\mu\,, \qquad H_\theta = r^{-1}(1-\mu^2)^{-\frac{1}{2}}\,\partial\psi/\partial r\,, \tag{9}$$

where $\mu = \cos\theta$, ψ is a scalar function of r and θ, and H_r and H_θ are the r and θ components of $\mathbf{H}_\mathrm{p}$.

According to the assumption that the star is only slightly perturbed from the spherical, we will use a first-order perturbation method with $\lambda = \mathscr{B}^2/GM^2$ as expansion parameter, where M is the mass of the star and $\mathscr{B}$ is a constant of the dimensions of ψ defined by

$$\psi = \mathscr{B}b\,. \tag{10}$$

The set of dimensionless variables (similar to those of Schwarzschild 1947) defined as follows will be used:

$$\left.\begin{aligned} r &= Rx\,, & \phi &= (GM/R)(\pi_0+\lambda\pi_1)\,, \\ P &= \frac{GM^2}{4\pi R^4}\left(p_0+\lambda\frac{\beta_0 p_0}{t_0}p_1\right), & T &= \frac{w}{\mathscr{R}}\frac{GM}{R}\left(t_0+\lambda\beta_0 t_1\right), \\ & & 4\pi r^2 F_r &= L\{f_0+\lambda(xt_0^4/Cp_0)f_1\}\,, \end{aligned}\right\} \tag{11}$$

where the subscript 0 denotes unperturbed variables, 1 denotes first-order perturbations, F_r is the radial component of $\mathbf{F}$, R and L are the radius and luminosity of the star respectively, and

$$C = \frac{3\kappa}{64\pi^2 ac}\left(\frac{\mathscr{R}}{wG}\right)^4\frac{L}{M^3}.$$

It is also convenient to define the parameter ω^2 by

$$\omega^2\lambda = R^3\Omega^2/GM\,.$$

$\omega^2\lambda$ is thus a measure of the ratio of the kinetic energy of rotation to the gravitational energy, while λ is a measure of the ratio of total magnetic energy to gravitational energy. Both must be assumed small.

With the variables thus defined, the following set of first-order perturbation equations can be derived.

$$\frac{\partial\pi_1}{\partial x}+\frac{\partial p_1}{\partial x} = \left(\frac{4}{\beta_0}-3\right)\frac{V}{x}\left(t_1-\frac{p_1}{n+1}\right)+D_r\,, \tag{12a}$$

$$\frac{\partial\pi_1}{\partial\mu}+\frac{\partial p_1}{\partial\mu} = -(1-\mu^2)^{-\frac{1}{2}}xD_\mu\,, \tag{12b}$$

$$\frac{\partial^2\pi_1}{\partial x^2}+\frac{2}{x}\frac{\partial\pi_1}{\partial x}+\frac{1}{x^2}\frac{\partial}{\partial\mu}\left((1-\mu^2)\frac{\partial\pi_1}{\partial\mu}\right) = \frac{\beta_0 p_0}{t_0^2}\left(p_1-(4-3\beta_0)t_1\right), \tag{12c}$$

$$\frac{\partial f_1}{\partial x} = \left(\frac{4V}{n+1} - V - 1\right)\frac{f_1}{x} + \frac{1}{x}\frac{\partial}{\partial \mu}\left((1-\mu^2)\frac{\partial t_1}{\partial \mu}\right), \tag{12d}$$

the radiative equation

$$\frac{\partial t_1}{\partial x} = -\frac{f_1}{x} - \frac{V}{\beta_0(n+1)x}\Big(p_1 - \{4\beta_0 + (n+1)(1-\beta_0)\}t_1\Big), \tag{12e}$$

and the convective equation

$$\{(n+1)-4\}\,\mathrm{d}[(\beta_0/t_0)\{p_1-(n+1)t_1\}] = (\beta_0/t_0)\{p_1-(n+1)t_1\}\,\mathrm{d}[(n+1)-4], \tag{12f}$$

where

$$D_r = -\frac{1}{x^2(1-\mu^2)}\frac{\partial b}{\partial x}\left(\frac{\partial^2 b}{\partial x^2} + \frac{1-\mu^2}{x^2}\frac{\partial^2 b}{\partial \mu^2}\right)\frac{t_0}{\beta_0 p_0} + (1-\mu^2)\omega^2 x,$$

$$D_\mu = -\frac{1}{x^3(1-\mu^2)^{\frac{1}{2}}}\frac{\partial b}{\partial \mu}\left[\frac{\partial^2 b}{\partial x^2} + \frac{1-\mu^2}{x^2}\,\frac{\partial^2 b}{\partial \mu^2}\right]\frac{t_0}{\beta_0 p_0} - \mu(1-\mu^2)^{\frac{1}{2}}\,\omega^2 x,$$

and

$$V = -(x/p_0)\,\mathrm{d}p_0/\mathrm{d}x, \qquad (n+1) = (t_0/p_0)\,\mathrm{d}p_0/\mathrm{d}t_0.$$

The perturbation to the adiabatic relation, equation (12f), can be integrated to give

$$p_1 - (n+1)t_1 = \alpha(t_0/\beta_0)\{(n+1)-4\}, \tag{13}$$

where α is a constant of integration.

Separation of the independent variables is achieved by writing

$$b(x,\mu) = (1-\mu^2)\,B(x), \tag{14}$$

and expanding the other variables in the form

$$Q_1(x,\mu) = Q_{10}(x) + Q_{12}(x)\,\mathrm{P}_2(\mu), \tag{15}$$

where $\mathrm{P}_2(\mu) = (\frac{3}{2}\mu^2 - \frac{1}{2})$ is the second Legendre polynomial.

The equations (12) can be reduced to first order by putting

$$\eta = \mathrm{d}B/\mathrm{d}x, \qquad q_1 = x^2\,\partial\pi_1/\partial x. \tag{16}$$

Then q_1 corresponds to the perturbation in mass fraction. It is also convenient to define

$$\Gamma_1 = \pi_1 + p_1 - \tfrac{1}{2}\omega^2 x^2(1-\mu^2). \tag{17}$$

Substituting in (12) according to equations (14)–(17) and separating the coefficients of $\mathrm{P}_2(\mu)$, we obtain the following set of equations.

$$\frac{\mathrm{d}\Gamma_{12}}{\mathrm{d}x} = \left(\frac{4}{\beta_0} - 3\right)\frac{V}{x}\left(t_{12} - \frac{p_{12}}{n+1}\right) + \frac{\eta\Gamma_{12}}{B}, \tag{18a}$$

$$\frac{\mathrm{d}\eta}{\mathrm{d}x} = \frac{2B}{x^2} + \frac{3}{2}\frac{\beta_0 p_0}{t_0}\frac{x^2\Gamma_{12}}{B}, \tag{18b}$$

$$\frac{\mathrm{d}B}{\mathrm{d}x} = \eta, \tag{18c}$$

$$\frac{\mathrm{d}\pi_{12}}{\mathrm{d}x} = \frac{q_{12}}{x^2}, \tag{18d}$$

$$\frac{\mathrm{d}q_{12}}{\mathrm{d}x} = 6\pi_{12} + \frac{\beta_0 p_0 x^2}{t_0}\Big(p_{12} - (4-3\beta_0)t_{12}\Big), \tag{18e}$$

$$\frac{\mathrm{d}f_{12}}{\mathrm{d}x} = \left(\frac{4V}{n+1} - V - 1\right)\frac{f_{12}}{x} - \frac{6t_{12}}{x}, \tag{18f}$$

the radiative equation

$$\frac{\mathrm{d}t_{12}}{\mathrm{d}x} = \frac{V}{\beta_0(n+1)x}\Big(t_{12}\{4\beta_0 + (n+1)(1-\beta_0)\} - p_{12}\Big) - \frac{f_{12}}{x}, \tag{18g}$$

and the convective equation

$$p_{12} = (n+1)t_{12}, \tag{18h}$$

where

$$p_{12} = \Gamma_{12} - \pi_{12} - \tfrac{1}{3}\omega^2 x^2.$$

The terms independent of μ remaining in (12) give the set

$$\frac{\mathrm{d}\Gamma_{10}}{\mathrm{d}x} = \left(\frac{4}{\beta_0} - 3\right)\frac{V}{x}\left(t_{10} - \frac{p_{10}}{n+1}\right) - \frac{\eta\Gamma_{12}}{B}, \tag{19a}$$

$$\frac{\mathrm{d}\pi_{10}}{\mathrm{d}x} = \frac{q_{10}}{x^2}, \tag{19b}$$

$$\frac{\mathrm{d}q_{10}}{\mathrm{d}x} = \frac{\beta_0 p_0 x^2}{t_0}\Big(p_{10} - (4-3\beta_0)t_{10}\Big), \tag{19c}$$

$$\frac{\mathrm{d}f_{10}}{\mathrm{d}x} = \left(\frac{4V}{n+1} - V - 1\right)\frac{f_{10}}{x}, \tag{19d}$$

the radiative equation

$$\frac{\mathrm{d}t_{10}}{\mathrm{d}x} = \frac{V}{\beta_0(n+1)x}\Big(t_{10}\{4\beta_0 + (n+1)(1-\beta_0)\} - p_{10}\Big) - \frac{f_{10}}{x}, \tag{19e}$$

and the convective equation

$$p_{10} = (n+1)t_{10} + \alpha\{(n+1) - 4\}t_0/\beta_0, \tag{19f}$$

where

$$p_{10} = \Gamma_{10} - \pi_{10} + \tfrac{1}{3}\omega^2 x^2.$$

III. BOUNDARY CONDITIONS

The boundary conditions are exactly as stated by Monaghan (1966*a*) and are restated here in the final form appropriate to equations (18) and (19).

(1) *At* $x = 0$

(i) $\mathrm{d}p_{12}/\mathrm{d}x = p_{12}/x = 0$ and similarly for t_{12} and π_{12}.

(ii) $\mathrm{d}p_{10}/\mathrm{d}x = \mathrm{d}t_{10}/\mathrm{d}x = \mathrm{d}\pi_{10}/\mathrm{d}x = 0.$

(2) *At* $x = 0$

$B'' - 2B/x^2 = 0$ and B/x^2, B'/x are finite.

(3) *At* $x = 1$

(i) $3\pi_{12} + \mathrm{d}\pi_{12}/\mathrm{d}x = 0,$

(ii) $\pi_{10} = \mathrm{d}\pi_{10}/\mathrm{d}x = 0.$

(4) *At* $x = 1$

(i) $p_{12} - 4t_{12} = 0,$

(ii) $p_{10} - 4t_{10} = 0.$

(5) *At* $x = 1$

$B + \mathrm{d}B/\mathrm{d}x = 0.$

(6) *At* $x = x_c$, *the boundary of the convective core*

(i) B, $\mathrm{d}B/\mathrm{d}x$, p_{12}, t_{12}, π_{12}, $\mathrm{d}\pi_{12}/\mathrm{d}x$, $\mathrm{d}p_{12}/\mathrm{d}x$, $\mathrm{d}^2B/\mathrm{d}x^2$, and $\mathrm{d}^2\pi_{12}/\mathrm{d}x^2$ are continuous;

(ii) p_{10}, t_{10}, π_{10}, $\mathrm{d}p_{10}/\mathrm{d}x$, $\mathrm{d}\pi_{10}/\mathrm{d}x$, and $\mathrm{d}^2\pi_{10}/\mathrm{d}x^2$ are continuous.

IV. SOLUTION OF EQUATIONS

The nonlinear equations (18) initially had to be solved with zero rotation by an approximation method described by Monaghan (1966*a*). Thereafter solutions could be found directly.

In the convective core, where the adiabatic relation holds, the equations in Γ_{12}, η, and B decouple from those in π_{12} and q_{12}, and equation (18*a*) can be integrated to give

$$\Gamma_{12} = kB,$$

where k is a constant. A transformation of the form

$$\left.\begin{aligned}(B,\eta,\omega) &= a(B^*,\eta^*,\omega^*),\\ (\Gamma_1,\pi_1,q_1,t_1,p_1,f_1) &= a^2(\Gamma_1^*,\pi_1^*,q_1^*,t_1^*,p_1^*,f_1^*),\end{aligned}\right\} \qquad (20)$$

where a is a constant, can be used to normalize the solution such that

$$\Gamma_{12} = B.$$

Singularities at $x = 0$ are avoided, and boundary conditions (1) (i) and (2) in Section III are satisfied by starting the solutions with the expansions

$$B = a_1 x^2, \qquad \pi_{12} = a_2 x^2.$$

The constants a_1 and a_2 determine the solution in the core. f_{12} is not determined in the core and its value at the core boundary is treated as a free parameter, since no condition is placed on this value by the energy equation (see below). This value and the boundary conditions (6) (i) then determine the envelope solution in terms of the core solution. The three outer boundary conditions (3) (i), (4) (i), and (5) then determine the three parameters a_1, a_2, and $(f_{12})_{\text{core}}$. The singularities at $x = 1$ mean that the solutions are divergent near $x = 1$, but it was found to be sufficiently accurate to apply the boundary conditions at $x = 0{\cdot}98$, rather than use series expansions from $x = 1$.

With η, B, and Γ_{12} determined from (18), equations (19) are linear and there is no difficulty in determining the correct values of the parameters involved. Solutions at $x = 0$ are started, according to the boundary conditions (1) (ii), with

$$\pi_{10} = a_3, \qquad \Gamma_{10} = a_4.$$

There is also the constant α in the adiabatic relation to be determined. However, the value of f_{10} at the core boundary is determined in terms of the core solution, as discussed below, and so the boundary conditions (6) (ii) completely determine the envelope solution in terms of the core solution. Once again the three outer boundary conditions (3) (ii) and (4) (ii) are applied at $x = 0{\cdot}98$ and determine the correct values of a_3, a_4, and α.

The value of f_{10} at the surface of the core is determined by the condition that the total change of flux through the core surface is due to the first-order change in energy generation. The energy generation in the unperturbed model is confined to the core. Integration of equation (4) gives

$$\int F_r \, \mathrm{d}S = \int \rho\epsilon \, \mathrm{d}V, \tag{21}$$

where the first integral is over the core surface and the second is over the core volume. Using formula (7) for ϵ we get, in the variables of (11)

$$\int \rho\epsilon \, \mathrm{d}V = \epsilon_0 X X_{\text{CNO}} \left(\frac{w}{\mathscr{R}}\right)^{\nu} \frac{G^{\nu} M^{\nu+2}}{4\pi R^{\nu+3}} (I_0 + \lambda I_1), \tag{22}$$

where

$$I_0 = \int_0^{x_c} \beta_0^2 p_0^2 t_0^{\nu-2} x^2 \, \mathrm{d}x,$$

$$I_1 = \int_0^{x_c} \beta_0^2 p_0^2 t_0^{\nu-3} [2p_{10} + \{(\nu+6)\beta_0 - 8\} t_{10}] x^2 \, \mathrm{d}x,$$

and $x = x_c$ is the core boundary. The terms dependent on angle make no contribution when the integration over θ is carried out. Similarly the left-hand side of (21) becomes

$$\int F_r \, \mathrm{d}S = L_0\left\{1+\lambda\left(\frac{xt_0^4}{Cp_0}f_{10}\right)_{x=x_c}\right\}. \tag{23}$$

Again there is no contribution by the angular-dependent terms. There will thus be no condition on f_{12}. Substituting (22) and (23) in (21), we get

$$(f_{10})_{x=x_c} = \left(\frac{Cp_0}{xt_0^4}\right)_{x=x_c}\frac{I_1}{I_0}. \tag{24}$$

The correct values of the parameters specifying the solution of the nonlinear equations were obtained as follows. The equations were integrated for four linearly independent trial sets of (a_1, a_2, f_{12}) and the outer values of these solutions compared with the boundary conditions. If the trial values are "sufficiently" accurate then a simultaneous linear extrapolation will give values of (a_1, a_2, f_{12}) for which the boundary conditions are more accurately satisfied. The boundary conditions can be satisfied to the desired accuracy by successive extrapolation.

The same procedure was used for the linear equations, except that only one extrapolation was necessary to satisfy the boundary conditions exactly. Since the whole process was done automatically on a computer, there was no advantage in superposing solutions of the homogeneous equations with particular solutions.

V. RESULTS

The solution with zero rotation was first found using the "pseudopolytropic" approximation, followed by successive corrections (Monaghan 1966*a*). The accuracy of this solution was sufficient to provide values of the parameters (a_1, a_2, f_{12}) for which the method described in the previous section would converge to the solution of the nonlinear equations (18). The results provide a check on the accuracy of the approximation. The solutions for B are compared in Table 1: in column 2, the pseudopolytropic approximation; in column 3, the approximate solution after one cycle of corrections has been added; in column 4, the direct solution of the nonlinear equations. The comparison shows that the field structure can be obtained quite accurately by the approximation method. Of the other variables, π_{12} and q_{12} were obtained with similar accuracy, but two cycles of correction were needed to achieve 10% accuracy of p_{12}, t_{12}, and f_{12} in the outer layers of the star. Successive corrections did not improve this accuracy significantly.

For small amounts of rotation the approximation method can be used, but for rotation fast enough to distort the field significantly the method breaks down. This is because, in the first approximation, the field is unaffected by rotation, since the equations in B are decoupled from the other equations. Direct solutions of the nonlinear equations can still be obtained by extrapolating from the values of (a_1, a_2, f_{12}) obtained for solutions with slower rotation.

TABLE 1

COMPARISON OF APPROXIMATE SOLUTIONS WITH DIRECT SOLUTION

For the case $\omega^2 = 0$

(1) x	(2) B 1st Approx.	(3) B After 1st Correction	(4) B Direct Solution	(1) x	(2) B 1st Approx.	(3) B After 1st Correction	(4) B Direct Solution
0·0	0·0	0·0	0·0	0·6	−0·124	−0·108	−0·106
0·1	−0·016	−0·016	−0·015	0·7	−0·112	−0·095	−0·094
0·2	−0·055	−0·053	−0·053	0·8	−0·100	−0·084	−0·083
0·3	−0·097	−0·092	−0·091	0·9	−0·089	−0·075	−0·074
0·4	−0·124	−0·115	−0·113	0·98	−0·082	−0·069	−0·068
0·5	−0·131	−0·117	−0·115				

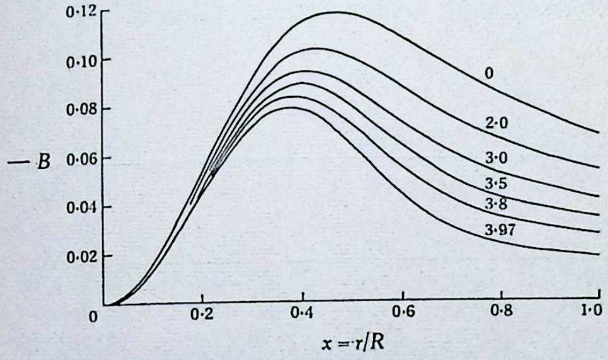

Fig. 1.—Solutions for B for different amounts of rotation, specified by ω^2 (see text). The curves are labelled with the respective values of ω^2.

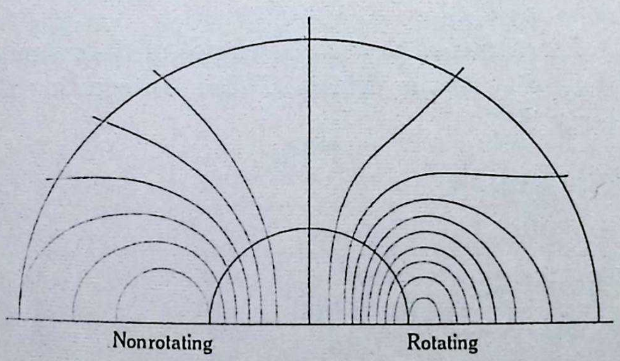

Fig. 2.—Equilibrium magnetic field lines in the uniformly rotating star. The left-hand quadrant shows the field in the absence of rotation. The right-hand quadrant shows the field for the case $\omega^2 = 3\cdot97$.

Solutions have been obtained for a series of values of ω^2 ranging from 0 up to about 4. The variation of B with x for different values of ω^2 is given in Figure 1. The corresponding field lines are given by

$$\psi = \mathscr{B} B \sin^2\theta = \text{constant},$$

and are illustrated in Figure 2 for the cases $\omega^2 = 0$ and $3\cdot97$. As ω^2 approaches its largest value, it can be seen that the surface field strength becomes progressively smaller relative to the field inside the star.

From equation (9), the surface polar field strength is

$$H_{\mathrm{s}} = 2\mathscr{B}B(1)/R^2, \tag{25}$$

and the field strength H_{c} at the centre of the star, where $|B| = -a_1 x^2$, is

$$H_{\mathrm{c}} = 2\mathscr{B}a_1/R^2. \tag{26}$$

We can use either of these expressions to eliminate $\mathscr{B}$ from the definition of λ. H_{c} will be the more useful parameter here, so we obtain

$$\lambda = R^4 H_{\mathrm{c}}^2/4GM^2 a_1^2. \tag{27}$$

Now the angular velocity is obtained from the definition of ω^2:

$$\Omega^2 = R\omega^2 H_{\mathrm{c}}^2/4Ma_1^2. \tag{28}$$

In Table 2 are listed values of a_1 and $B(x=1)$ for different values of ω^2. We see that the angular velocity increases steadily with ω^2 for a given value of H_{c}.

TABLE 2

APPROACH TO LIMITING ROTATION

(1)	(2)	(3)	(4)	(1)	(2)	(3)	(4)
ω^2	a_1	$B(1)$	I_B	ω^2	a_1	$B(1)$	I_B
0	1·62	$6{\cdot}66\times10^{-2}$	$12{\cdot}42\times10^{-2}$	3·8	1·43	$2{\cdot}64\times10^{-2}$	$7{\cdot}17\times10^{-2}$
2·0	1·55	$5{\cdot}13\times10^{-2}$	$9{\cdot}90\times10^{-2}$	3·9	1·42	$2{\cdot}27\times10^{-2}$	$6{\cdot}88\times10^{-2}$
3·0	1·50	$4{\cdot}09\times10^{-2}$	$8{\cdot}60\times10^{-2}$	3·97	1·40	$1{\cdot}75\times10^{-2}$	$6{\cdot}55\times10^{-2}$
3·5	1·46	$3{\cdot}32\times10^{-2}$	$7{\cdot}74\times10^{-2}$				

These results are best presented in terms of the total energies of the magnetic field and the rotation. The energy density of the field is $H^2/8\pi$. Integrating this through all space, the total field energy is

$$E_{\mathrm{M}} = R^3 H_{\mathrm{s}}^2 I_B/12B^2(1), \tag{29}$$

where

$$I_B = \int_0^1 \left\{\frac{2B^2}{x^2} + \left(\frac{\mathrm{d}B}{\mathrm{d}x}\right)^2\right\} \mathrm{d}x + B(1)$$

and the integral outside the star was evaluated using the exterior solution $B = B(1)/x$. I_B is tabulated in column 4 of Table 2. The kinetic energy of rotation is

$$E_\Omega = \tfrac{1}{2}\int \rho\Omega^2\varpi^2\,\mathrm{d}V = \tfrac{1}{3}MR^2\Omega^2 I_\Omega, \tag{30}$$

where

$$I_\Omega = \int_0^1 t^{-1}\beta p x^4\,\mathrm{d}x = 0{\cdot}159.$$

From (29) and (30) the ratio of rotational energy to magnetic energy is

$$E_{\Omega}/E_{\mathrm{M}} = I_{\Omega}\,\omega^2/I_B\,. \tag{31}$$

In Figure 3, the dependence of the surface field strength on the energy of rotation for a given magnetic energy has been displayed by plotting $B^2(1)/I_B$ against ω^2/I_B. Also plotted is ω^2. From this we see that the surface field is reduced to zero at $\omega^2/I_B \simeq 65$, corresponding to $\omega^2 \simeq 4\cdot 0$ and $E_{\Omega}/E_{\mathrm{M}} \simeq 10$. From (28) we get the limiting relation

$$\Omega \simeq 4\cdot 2 \times 10^{-12} H_{\mathrm{c}}(\bar{R}/\bar{M})^{\frac{1}{2}}\,. \tag{32}$$

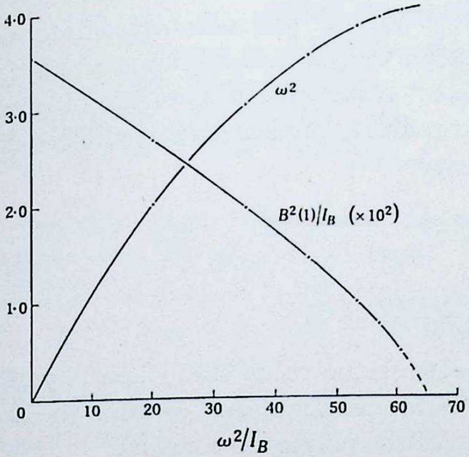

Fig. 3.—Showing the dependence of the surface field strength,
$H_{\mathrm{s}}^2 = (12E_{\mathrm{M}}/R^3)\,B^2(1)/I_B$,
and ω^2 on the ratio of rotational to magnetic energy,
$E_{\Omega}/E_{\mathrm{M}} = I_{\Omega}\,\omega^2/I_B$.

The perturbations to the structure of the star can be obtained from the solutions for the remaining variables of equations (18) and (19). Observable changes in the star will depend on the values of the perturbations at the surface, and in Table 3 are listed the values at $x = 1$ of p_{10}, p_{12}, f_{10}, and f_{12} for five values of ω^2.

TABLE 3

PERTURBATIONS AT THE SURFACE

For the case $x = 1$

ω^2	0	2·0	3·0	3·5	3·97
p_{10}	−0·1034	0·319	0·549	0·666	0·772
p_{12}	−0·0304	−0·684	−1·016	−1·179	−1·332
f_{10}	−0·0178	−0·180	−0·263	−0·301	−0·340
f_{12}	0·0437	0·387	0·564	0·647	0·729

The radial energy flux at the surface is (using the surface series solutions for the zero-order model)

$$F_{\mathrm{R}} = F_{\mathrm{R}0}\{1+\lambda(4f_{10}+4f_{12}\mathrm{P}_2)\}\,, \tag{33}$$

$F_{\mathrm{R}0}$ being the surface energy flux of the unperturbed model. The total luminosity is

$$L = L_0(1+4f_{10}\,\lambda)\,. \tag{34}$$

The position of the distorted surface is defined by the boundary condition $P = T = 0$.

To the first order in λ this condition gives, at $x = 1$,

$$p_1 + x_1(\mathrm{d}p_0/\mathrm{d}x)_{x=1} = 0\,, \tag{35}$$

where the new surface is given by

$$x = 1 + \lambda x_1 = 1 + \lambda(x_{10} + x_{12}\,\mathrm{P}_2)\,.$$

From the zero-order model and (35) we get

$$x_1 = p_1/\beta_0 = 1\cdot 04\,p_1\,. \tag{36}$$

In all cases the total luminosity of the star is decreased, the surface is brighter near the poles than near the equator, and the surface is distorted into an oblate spheroid. The nonrotating model shows an overall contraction, as was found by Monaghan (1966*b*) for the polytrope $n = 3$. Rotation increases the oblateness and causes an overall expansion, but the polar radius is further decreased. The distortion of the surface corresponds to an eccentricity

$$e^2 = -3x_{12}\,\lambda\,. \tag{37}$$

For zero rotation

$$e^2 = 5\cdot 3(R^4 H_s^2/GM^2)\,,$$

the coefficient in this expression falling between the value $15\cdot 1$, found by Monaghan (1966*b*) for the nonrotating polytrope $n = 3$, and the value ~ 2 for the same case corrected to keep the central temperature of the polytrope constant.

It is interesting to note the mechanical effect of the combined field and rotation as revealed by the density perturbation. In the nonrotating model the star is compressed simultaneously towards the centre and the equatorial plane, so that the core density increases, but the maximum density perturbation occurs at $x \simeq 0\cdot 25$ on the equatorial plane. The effect of rotation is to increase the compression of the core, so that the density perturbation maximum shifts rapidly to $x = 0$. The increase in density is accompanied by a decrease in the central temperature and an increase in the central pressure.

VI. Discussion

The distortion produced in the equilibrium magnetic field by rotation reflects the pattern of meridional circulation that was found by Sweet (1950) in a uniformly rotating star of uniform composition in the absence of a magnetic field. However, the results must have been affected by the angular dependence of the field assumed in equation (14), which selects the dipole component of the field. As the effects produced by rotation become more important the field structure should become more complicated. These complications cannot easily be treated, because the field cannot be expanded as a multipole series of the form

$$b = \sum B_{2n}(x)\,\mathrm{P}_{2n}(\mu)\,,$$

say, since b enters the hydrostatic equation nonlinearly.

The assumption of infinite electrical conductivity overestimates the coupling between the circulation currents and the field, but this overestimate will be least for a large-scale field of the form considered here, since this would have the slowest diffusion rate if the conductivity were finite. The limiting case with zero surface field that was found should therefore be an indication of the stage at which a more realistic field would be dragged below the surface. From the limiting relation (32), a slowly rotating star with $\Omega \simeq 10^{-6}$ would require an internal field strength of about 5×10^{5} gauss to halt circulation, while for a star with $\Omega \simeq 5\times10^{-4}$, near the maximum allowable angular velocity, a field of about 2×10^{8} gauss would be required.

The validity of the equilibrium solutions obtained here depends on the time scale of approach to equilibrium. Large-scale changes of the field structure due to the circulation currents require the circulation to transport matter a distance of the order of the stellar radius or more within the lifetime of the star. This requires (Roxburgh 1964)

$$\Omega^2 \gtrsim 10^{-13}\overline{R}\overline{L}/\overline{M}\,,$$

where the bars denote solar units. For very massive stars this implies an angular velocity close to the dynamical limit. For, say, an A5 star with $\log\overline{M} = 0\cdot34$, $\log\overline{R} = 0\cdot25$, and $\log\overline{L} = 1\cdot3$ (Allen 1963) it implies $\Omega \gtrsim 10^{-6}$. It is unlikely that the star would be so near its limiting state that the field would be highly concentrated towards the centre, so, with the minimum interior field strength found for $\Omega = 10^{-6}$, the surface field strength might be of the order of 10^{4} gauss. A-stars characteristically have angular velocities much greater than this, of the order of 10^{-4}. The corresponding surface field is 10^{6} gauss.

In conclusion, if a star has sufficient angular velocity for a magnetic field to approach the equilibrium state within the star's lifetime, these results indicate that an observable field much stronger than those that have been observed would be required to halt the induced meridional circulation. Otherwise, the results give an indication of the mechanical effects on the star of a large-scale poloidal field.

VII. ACKNOWLEDGMENT

The author would like to thank Professor R. Van der Borght for suggesting the problem and for many useful discussions.

VIII. REFERENCES

ALLEN, C. W. (1963).—"Astrophysical Quantities." (Athlone Press, Univ. London.)

FERRARO, V. A. C. (1937).—*Mon. Not. R. astr. Soc.* **97**, 458.

MONAGHAN, J. J. (1966*a*).—*Mon. Not. R. astr. Soc.* **132**, 1.

MONAGHAN, J. J. (1966*b*).—*Mon. Not. R. astr. Soc.* **134**, 275.

ROXBURGH, I. W. (1964).—*Mon. Not. R. astr. Soc.* **128**, 157.

SCHWARZSCHILD, M. (1947).—*Astrophys. J.* **106**, 427.

STOTHERS, R. (1963).—*Astrophys. J.* **138**, 1074.

SWEET, P. A. (1950).—*Mon. Not. R. astr. Soc.* **110**, 548.

GAMMA RADIATION FROM THE REACTIONS ^{20}Ne$(\alpha, \alpha'\gamma_{1\cdot63})^{20}$Ne AND ^{20}Ne$(\alpha, p\gamma_{0\cdot44})^{23}$Na

By R. H. Spear* and I. F. Wright†

[*Manuscript received January 5, 1968*]

Summary

Excitation functions for γ-radiation from the reactions ^{20}Ne$(\alpha, \alpha'\gamma_{1\cdot63})^{20}$Ne and ^{20}Ne$(\alpha, p\gamma_{0\cdot44})^{23}$Na have been studied for bombarding energies from 3·96 to 6·08 MeV. Angular distribution measurements provide spin and parity assignments of 2^+ for ^{24}Mg levels at excitation energies of 12·74 and 12·81 MeV, and 4^+ or 5^- (possibly 6^+) for a level at 12·98 MeV.

I. Introduction

This paper reports a survey of the excitation functions for 1·63 and 0·44 MeV γ-rays from the reactions ^{20}Ne$(\alpha, \alpha'\gamma_{1\cdot63})^{20}$Ne and ^{20}Ne$(\alpha, p\gamma_{0\cdot44})^{23}$Na; the work was undertaken to obtain new information on the level structure of ^{24}Mg at excitation energies of about 13 MeV. Data were taken at 55° for α-particle energies E_α from 5·21 to 6·08 MeV, and at 0°, 90°, and 125° for E_α from 3·96 to 5·25 MeV. The α-particle energies from 3·96 to 6·08 MeV correspond to excitation energies E_x in ^{24}Mg from 12·61 to 14·37 MeV. This region of ^{24}Mg has been previously studied from several reactions. Extensive investigations of states populated in the proton bombardment of ^{23}Na have been made by a number of authors (see Endt and Van der Leun 1962); collectively these extend up to $E_x = 14\cdot0$ MeV. The reaction ^{20}Ne$(\alpha, \gamma)^{24}$Mg has recently been studied by Highland and Thwaites (1967) for α-particle energies from 3 to 6 MeV. Ollerhead and Kuehner (1965) and McGough and Wright (personal communication) have studied some states in the region using the reaction ^{12}C$(^{16}$O$, \alpha)^{24}$Mg.

Both ^{4}He and ^{20}Ne have zero spin and even parity; therefore α-particle bombardment of ^{20}Ne can populate only natural parity states of ^{24}Mg, i.e. $J^\pi = 0^+$, 1^-, 2^+, 3^-, 4^+, etc. For the reaction ^{20}Ne$(\alpha, \alpha'\gamma_{1\cdot63})^{20}$Ne, the angular momentum situation is relatively simple; since barrier-penetrability considerations are expected to limit the orbital angular momentum of the outgoing α-particle to the two lowest possible values, straightforward γ-ray angular distribution measurements may provide unambiguous J^π values for ^{24}Mg states.

II. Experimental Procedure

Beams of singly and doubly ionized helium were obtained from the Australian National University tandem accelerator. The ^{20}Ne target‡ was prepared in an

---

* Research School of Physical Sciences, Australian National University, Canberra, A.C.T. 2600.

† University of Manchester, Manchester, England.

‡ Supplied by the Electromagnetic Separation Group, A.E.R.E., Harwell, England.

Aust. J. Phys., 1968, **21**, 307–16

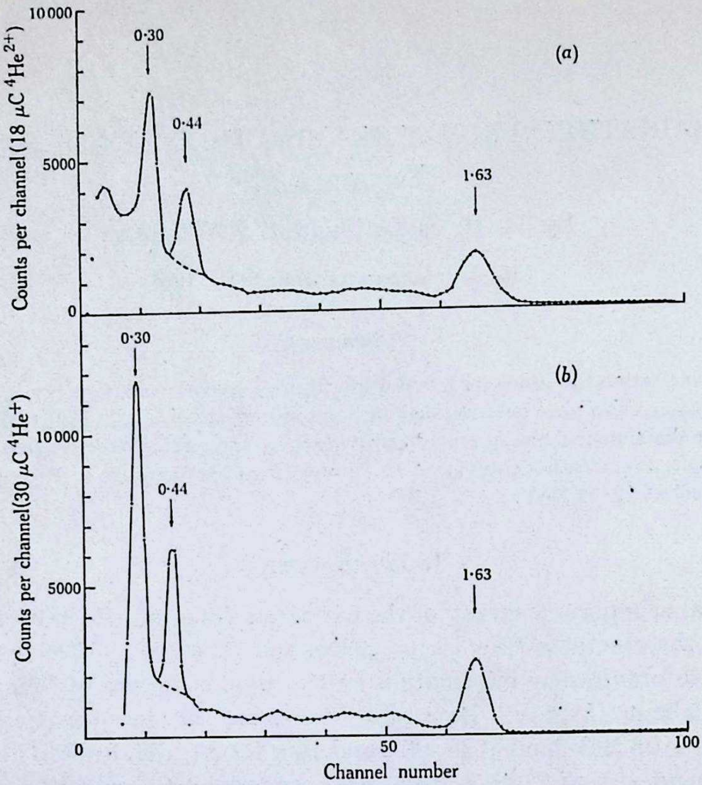

Fig. 1.—Typical γ-ray spectra from α-particle bombardment of ^{20}Ne for (*a*) $E_\alpha = 5\cdot80$ MeV, $12\cdot7$ cm diameter by $10\cdot2$ cm long crystal, and 55°; (*b*) $E_\alpha = 5\cdot25$ MeV, $7\cdot6$ cm diameter by $7\cdot6$ cm long crystal, and 0°.

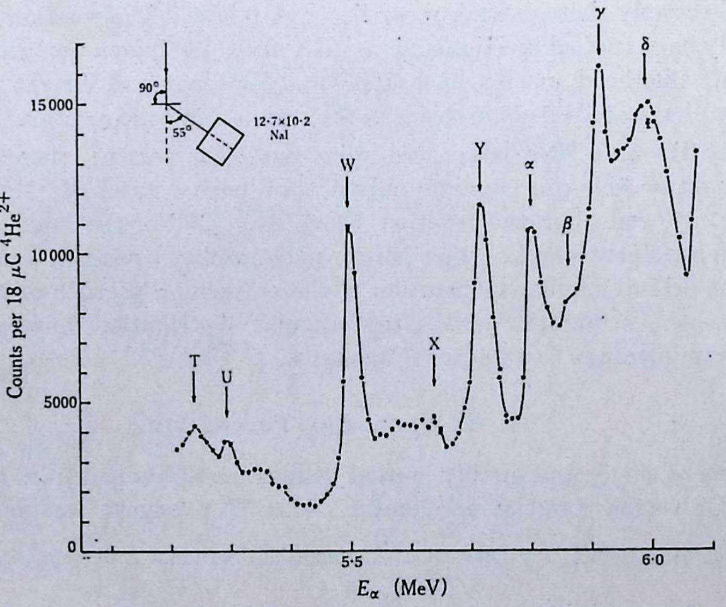

Fig. 2.—Excitation function for $1\cdot63$ MeV γ-radiation from $^{20}\mathrm{Ne}(\alpha, \alpha'\gamma_{1\cdot63})^{20}\mathrm{Ne}$ at 55° for $5\cdot21 < E_\alpha < 6\cdot08$ MeV.

electromagnetic isotope separator by ion bombardment at 30 kV onto a 0·025 mm tantalum foil. It had a nominal loading of 5 μg/cm^2. The target was supported by a backing of 0·56 mm tantalum on the vertical axis of a cylindrical glass target chamber. In order to minimize beam deposition of carbon, the target was surrounded by a cylindrical copper sleeve maintained at liquid nitrogen temperature (Bashkin and Ophel 1962). Tantalum collimators were used to produce a beam spot of approximately 3 mm diameter on the target. Beam currents ranged from about 0·1 to 0·3 μA. Precautions were taken to suppress secondary electrons, and current integration was accurate to about 1%.

Gamma rays were detected using NaI(Tl) crystals. For α-particle energies E_α from 5·21 to 6·08 MeV, a single 12·7 cm diameter by 10·2 cm long crystal was set at 55° to the beam axis with h, the distance of the front face of the crystal from the target spot, equal to 9·51 cm. For E_α from 3·96 to 5·25 MeV, 7·6 cm diameter by 7·6 cm long crystals were set at 0° and 125° ($h = 7\cdot43$ and $7\cdot38$ cm respectively) and a 12·7 cm diameter by 10·2 cm long crystal was set at 90° ($h = 12\cdot03$ cm). Pulses were analysed using standard electronics and displayed on 400-channel pulse height analysers.

III. EXCITATION FUNCTIONS

Two typical γ-ray spectra are shown in Figure 1 for (a) $E_\alpha = 5\cdot80$ MeV, 12·7 cm by 10·2 cm crystal, and 55°; and (b) $E_\alpha = 5\cdot25$ MeV, 7·6 cm by 7·6 cm crystal, and 0°. Gamma rays of energies 1·63, 0·44, and 0·30 MeV are clearly evident in both spectra.

The 0·44 MeV radiation is attributed to the reaction $^{20}\mathrm{Ne}(\alpha, \mathrm{p}\gamma_{0\cdot44})^{23}\mathrm{Na}$ proceeding via the $\frac{5}{2}^+$ first excited state of ^{23}Na. Sodium contamination of the target or beam collimators could produce 0·44 MeV radiation through the reaction $^{23}\mathrm{Na}(\alpha, \alpha'\gamma_{0\cdot44})^{23}\mathrm{Na}$. The complete absence of any 1·81 MeV radiation (from the reaction $^{23}\mathrm{Na}(\alpha, \mathrm{p}\gamma_{1\cdot81})^{26}\mathrm{Mg}$) shows that such contamination was negligible.

The 1·63 MeV radiation is attributed to the reaction $^{20}\mathrm{Ne}(\alpha, \alpha'\gamma_{1\cdot63})^{20}\mathrm{Ne}$ proceeding via the 2^+ first excited state of ^{20}Ne. For E_α greater than 5·35 MeV the reaction $^{20}\mathrm{Ne}(\alpha, \mathrm{p})^{23}\mathrm{Na}^*$ (2·08 MeV) is energetically possible and would produce γ-radiation of energies 1·64, 0·44, and 2·08 MeV. The absence of any observable 2·08 MeV radiation shows that this reaction did not contribute any significant background to the yields of the two reactions studied.

The 0·30 MeV radiation comes from Coulomb excitation of ^{181}Ta (Vivargent 1959).

Excitation functions for 1·63 MeV radiation are shown in Figures 2 and 3. For $5\cdot21 < E_\alpha < 6\cdot08$ MeV (Fig. 2), the target surface was perpendicular to the beam direction, and the ordinate represents the number of pulses within a window from 1·50 to 1·76 MeV for a bombardment equivalent to 18 μC $^4\mathrm{He}^{2+}$. For $3\cdot96 < E_\alpha < 5\cdot25$ MeV (Fig. 3), the target surface was at 45° to the beam direction, and the ordinate represents the number of pulses within a window from 1·50 to 1·79 MeV for a bombardment equivalent to 30 μC $^4\mathrm{He}^+$. In each case small corrections have been made for dead-time losses (< 3%), room background, and pulses within the window arising from higher energy radiation produced by the beam. Statistical error bars are indicated at 100 keV intervals, except in cases where they are smaller than the size of the data points.

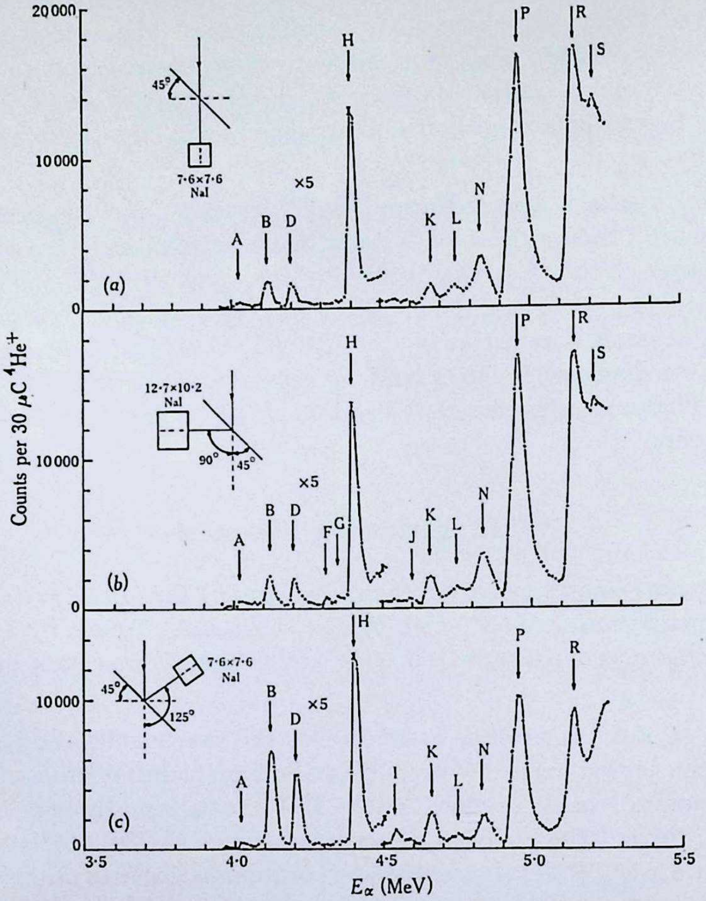

Fig. 3.—Excitation functions for 1·63 MeV γ-radiation from ^{20}Ne($\alpha, \alpha'\gamma_{1\cdot63}$)^{20}Ne at (*a*) 0°, (*b*) 90°, and (*c*) 125° for $3\cdot96 < E_\alpha < 5\cdot25$ MeV.

In the case of the 0·44 MeV radiation, underlying contributions from other γ-rays provided a much more severe problem. Excitation functions were derived using a window from 0·39 to 0·49 MeV. Approximate corrections for effects of underlying pulses from higher energy radiations and room background were made graphically by drawing a smooth curve joining the valley below the 0·44 MeV peak to the spectrum extending above the 0·44 MeV peak; examples are shown by the dashed lines in Figure 1. This procedure is admittedly rather subjective, and the fraction of the total 0·44 MeV spectrum accepted depends on the intensity and slope of the underlying spectrum. Nevertheless, it gives a reasonably good representation of the gross features of the excitation function; peak positions are certainly significant, but the yields in the valleys between peaks may be somewhat unreliable. Dead-time corrections have been applied. Results are shown in Figure 4 ($5\cdot21 < E_\alpha < 6\cdot08$ MeV, 18 μC ^{4}He^{2+}) and Figure 5 ($3\cdot96 < E_\alpha < 5\cdot25$ MeV, 30 μC ^{4}He$^+$).

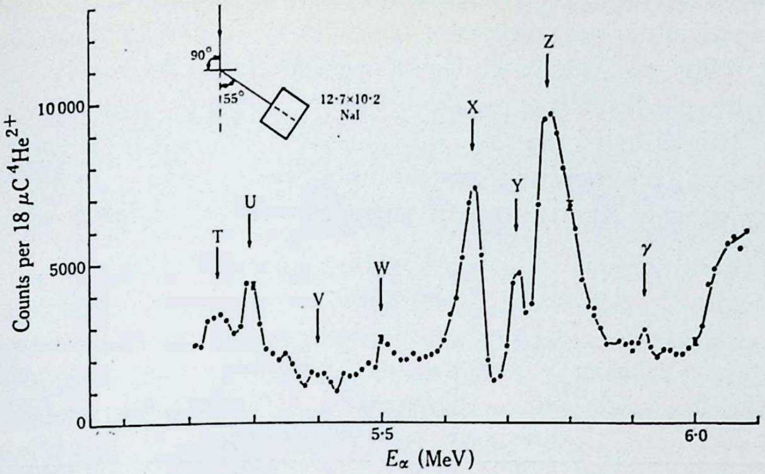

Fig. 4.—Excitation function for 0·44 MeV γ-radiation from ^{20}Ne(α, p$\gamma_{0\cdot44}$)^{23}Na at 55° for $5\cdot21 < E_\alpha < 6\cdot08$ MeV.

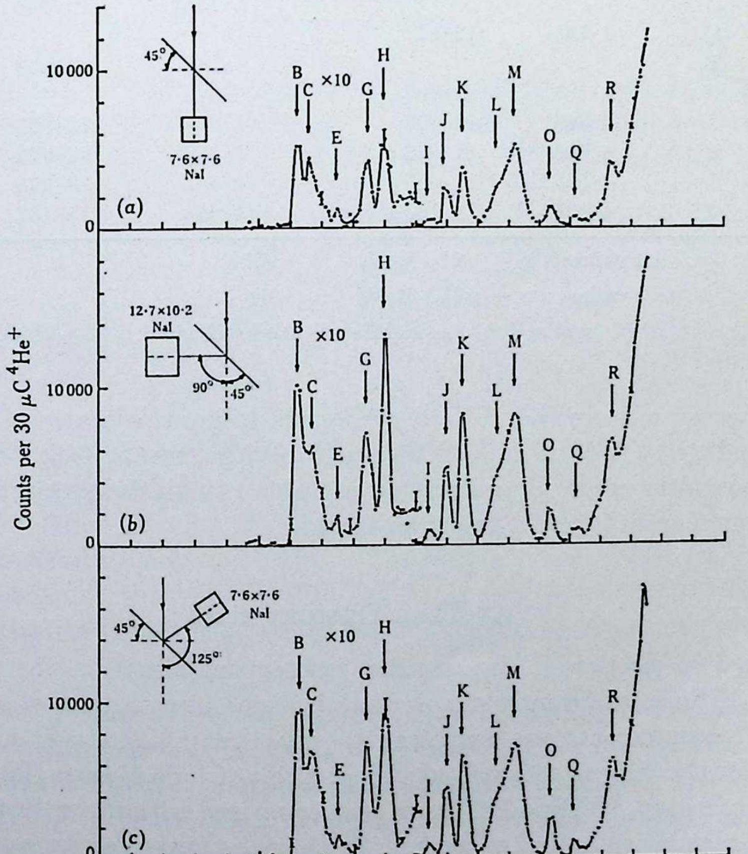

Fig. 5.—Excitation functions for 0·44 MeV γ-radiation from ^{20}Ne(α, p$\gamma_{0\cdot44}$)^{23}Na at (a) 0°, (b) 90°, and (c) 125° for $3\cdot96 < E_\alpha < 5\cdot25$ MeV.

For ease of reference, peaks in the excitation functions in Figures 2–5 are labelled alphabetically. The energies of peaks for $E_\alpha < 4\cdot6$ MeV are listed with the corresponding ^{24}Mg excitation energies in Table 1. Individual peaks for E_α greater than 4·6 MeV are not listed because most of them are probably due to more than one level in ^{24}Mg. It is assumed that $E_x = (9\cdot317 + 0\cdot833\,E_\alpha)$ MeV. Uncertainties in the values of E_x and E_α are conservatively estimated at ±13 and ±15 keV respectively. The resonance energies listed represent averages from all angles at which the peaks were observed.

TABLE 1

RESONANCE ENERGIES (E_α) AND EXCITATION ENERGIES (E_x) OF ^{24}Mg STATES OBSERVED IN ^{20}Ne($\alpha, \alpha'\gamma_{1\cdot63}$)^{20}Ne AND ^{20}Ne($\alpha, p\gamma_{0\cdot44}$)^{23}Na

Assuming that each peak observed in the excitation function corresponds to a state in ^{24}Mg

Peak	1·63 MeV Radiation E_α* (MeV)	E_x† (MeV)	0·44 MeV Radiation E_α* (MeV)	E_x† (MeV)
A	4·022	12·667		
B	4·115	12·745	4·115	12·745
C			4·158‡	12·781
D	4·195	12·811		
E			4·245	12·853
F	4·305	12·903		
G	4·345	12·936	4·338	12·931
H	4·395	12·978	4·395	12·978
I	4·535	13·095	4·535	13·095
J	4·590	13·140	4·593	13·143

* All values are ±0·015 MeV.

† All values are ±0·013 MeV.

‡ If this peak is due to a single level, the level width is 28±9 keV.

Using narrow resonances in ^{20}Ne(α, γ)^{24}Mg, the target thickness was measured as 24±5 keV and 21±5 keV at $E_\alpha = 3\cdot05$ and $6\cdot08$ MeV respectively. These values show that the widths of all the peaks listed in Table 1 (with the exception of peak C) can be attributed entirely to the target thickness.

IV. ANGULAR DISTRIBUTIONS

As noted in Section I, the angular momentum situation for the reaction ^{20}Ne($\alpha, \alpha'\gamma_{1\cdot63}$)^{20}Ne is sufficiently simple that in some circumstances γ-ray angular distribution measurements are sufficient to give unambiguous spin and parity assignments for the ^{24}Mg state involved. Yield ratios of 1·63 MeV radiation obtained from the crystals at 0°, 90°, and 125° have been compared with theoretical ratios in an attempt to determine spins and parities for some of the lower energy resonances. No angular distribution analysis has been attempted for the 0·44 MeV radiation because of (1) the non-unique channel spin and (2) the difficulty of assessing background reliably.

The angular distribution of 1·63 MeV radiation will have the form

$$W(\theta) = 1 + Q_2 A_2 \mathrm{P}_2(\cos\theta) + Q_4 A_4 \mathrm{P}_4(\cos\theta),$$

where the A's are the theoretical coefficients for perfect geometry and the Q's are the attenuation coefficients that correct for finite geometry. For the case in which the compound ^{24}Mg state has well-defined spin and parity, the theoretical coefficients can be readily calculated for particular values of l', the orbital angular momentum of the outgoing α-particle; if there are contributions from more than one value of l', these contributions add incoherently (Kraus *et al.* 1956). In the energy range considered here the energies of the emitted α-particles are low compared with the Coulomb and centrifugal barriers, so that only the two lowest possible values of l' will contribute appreciably. Theoretical angular distribution coefficients were calculated for all possible values of J^π and l' up to $J^\pi = 6^+$. Corrections for finite geometry were made using angular attenuation coefficients deduced from the values calculated by Yates (1965). The consequent ratios of yields for the three angles used are given in Table 2.

TABLE 2

THEORETICAL YIELD RATIOS OF 1·63 MeV GAMMA RADIATION CORRECTED FOR FINITE GEOMETRY

(1) J^π, l'	(2) $W(90°)/W(0°)$	(3) $W(90°)/W(125°)$	(1) J^π, l'	(2) $W(90°)/W(0°)$	(3) $W(90°)/W(125°)$
$0^+, 2$	1·00	1·00	$4^+, 2$	0·56	0·61
$1^-, 1$	0·53	0·77	$4^+, 4$	3·25	0·84
$1^-, 3$	0·83	0·94	$4^+, 6$	0·72	0·86
$2^+, 0$	0·53	0·15	$5^-, 3$	0·58	0·66
$2^+, 2$	1·83	0·83	$5^-, 5$	3·61	0·84
$2^+, 4$	0·77	0·90	$5^-, 7$	0·71	0·85
$3^-, 1$	0·53	0·51	$6^+, 4$	0·59	0·68
$3^-, 3$	2·70	0·84	$6^+, 6$	3·81	0·84
$3^-, 5$	0·74	0·88	$6^+, 8$	0·70	0·85

The relative efficiencies of the three crystals for the geometry used were determined from the yields observed for the isotropic 1·77 MeV γ-rays emitted in the decay of ^{28}Al (half-life 2·28 min). The ^{28}Al was produced via the reaction ^{25}Mg(α, p)^{28}Al using a thick target of natural magnesium. The results obtained were adjusted to give the relative efficiencies for 1·63 MeV radiation by taking account of the variation with energy of the intrinsic crystal efficiencies and of absorption in materials surrounding the target.

From these efficiencies relative yields of 1·63 MeV γ-radiation have been calculated for all data points in peaks B, D, H, K, N, and P. For peaks B, D, H, and N the angular distributions remained constant across the peak and the mean values are given in Table 3. The errors quoted are a combination of statistical errors and an allowance for geometrical errors due to variations in beam spot position and uncertainty about the relative positions of the ^{20}Ne and magnesium targets. For peaks K and P the angular distributions varied across the peak, indicating that they are not due to single levels.

Comparison of Tables 2 and 3 shows that the results for peaks B and D are in very good agreement with $J^{\pi} = 2^{+}$, $l' = 0$, with a small admixture of $l' = 2$. For both peaks no other value of J^{π} is consistent with the data. The data for peak H fit equally well to $(J^{\pi}, l') = (4^{+}, 2)$, $(5^{-}, 3)$, or $(6^{+}, 4)$; they exclude values of J less than 4.

Table 3

EXPERIMENTAL YIELD RATIOS FOR 1·63 MeV GAMMA RADIATION

(1) Peak	(2) $W(90°)/W(0°)$	(3) $W(90°)/W(125°)$	(1) Peak	(2) $W(90°)/W(0°)$	(3) $W(90°)/W(125°)$
B	$0\cdot58 \pm 0\cdot04$	$0\cdot20 \pm 0\cdot01$	H	$0\cdot56 \pm 0\cdot03$	$0\cdot66 \pm 0\cdot02$
D	$0\cdot66 \pm 0\cdot05$	$0\cdot25 \pm 0\cdot02$	N	$0\cdot60 \pm 0\cdot03$	$1\cdot04 \pm 0\cdot04$

Although the angular distribution for peak N remained fairly constant across the peak, the results cannot be fitted to any of the theoretical distributions for $J \leqslant 6$. The peak is quite broad and not well resolved; it seems likely that this peak also is complex.

V. Partial Widths

Estimates of $(2J+1)\Gamma_{\alpha_0}\Gamma_{\alpha_1}/\Gamma$ and $(2J+1)\Gamma_{\alpha_0}\Gamma_{p_1}/\Gamma$ for some of the lower energy resonances are listed in Table 4; here Γ_{α_0} is the partial width of the state for emission of ground state α-particles, Γ_{α_1} is the partial width for emission of α-particles to the 1·63 MeV state of ^{20}Ne, and Γ_{p_1} is the partial width for emission of protons to the 0·44 MeV state of ^{23}Na. The results are derived from the 125° data, assuming in each case that the peak height represents the thick target yield. Absolute values were obtained by comparing observed yields with the yield of ground state γ-rays obtained from the reaction $^{20}\mathrm{Ne}(\alpha, \gamma)^{24}\mathrm{Mg}$ at the 3·05 MeV resonance; measurements by Smulders (1965) indicate that for this resonance $J^{\pi} = 1^{-}$ and $\Gamma_{\gamma_0} = 0\cdot5$ eV. Values for B, D, and H in column 2 of Table 4 have been corrected for angular distribution effects; it is estimated that they are accurate to ±40%. Other values are probably accurate to within a factor of two. The results of Table 4 do not give Γ_{α_1} and Γ_{p_1} explicitly; however, since $\Gamma > \Gamma_{\alpha_0}$, they may be used to set a lower limit on $(2J+1)\Gamma_{\alpha_1}$ and $(2J+1)\Gamma_{p_1}$.

Table 4

SUMMARY OF PARTIAL WIDTH INFORMATION FOR SOME RESONANCES OBSERVED IN $^{20}\mathrm{Ne}(\alpha, \alpha'\gamma_{1\cdot63})^{20}\mathrm{Ne}$ AND $^{20}\mathrm{Ne}(\alpha, p\gamma_{0\cdot44})^{23}\mathrm{Na}$

(1) Peak	(2) $(2J+1)\Gamma_{\alpha_0}\Gamma_{\alpha_1}/\Gamma$ (eV)	(3) $(2J+1)\Gamma_{\alpha_0}\Gamma_{p_1}/\Gamma$ (eV)	(1) Peak	(2) $(2J+1)\Gamma_{\alpha_0}\Gamma_{\alpha_1}/\Gamma$ (eV)	(3) $(2J+1)\Gamma_{\alpha_0}\Gamma_{p_1}/\Gamma$ (eV)
A	60	$\lesssim 10$	E	$\lesssim 40$	30
B	800*	270	G	50	205
C	$\lesssim 45$	185	H	2050*	270
D	600*	$\lesssim 100$	I	600	230

* Corrected for angular distribution effects.

VI. Discussion

In discussing these results it is convenient to divide the energy range covered at an α-particle energy of 4·6 MeV. Above this energy many of the peaks appear to include contributions from more than one level. This is apparent from inspection of the yield curves; the peaks are generally wider than the target thickness and show an increasing degree of overlapping. In addition, the angular distribution data show that peaks K, N, and P ($E_\alpha = 4\cdot658$, $4\cdot827$, and $4\cdot950$ MeV respectively) are definitely complex. For this reason no detailed analysis of the data for E_α greater than 4·6 MeV has been attempted.

The present results can be compared with those of Highland and Thwaites (1967) on the ^{20}Ne$(\alpha,\gamma)^{24}$Mg reaction. The appearance of the (α,γ) yield curve is quite distinct since it consists of a series of sharp peaks whose separation increases perceptibly above 4·6 MeV bombarding energy. With the exception of the peaks at $E_\alpha = 3\cdot997$ and $4\cdot483$ MeV, all the (α,γ) resonances are close in energy to prominent peaks in one or both of the ^{20}Ne$(\alpha,\alpha'\gamma_{1.63})^{20}$Ne and ^{20}Ne$(\alpha,\mathrm{p}\gamma_{0.44})^{23}$Na yield curves, although a number of these latter peaks appear to be complex. The levels seen in the ^{20}Ne$(\alpha,\gamma)^{24}$Mg reaction are presumably those with large values of Γ_α/Γ and Γ_γ. It appears that these levels contribute a significant, but not dominant, fraction of the ^{20}Ne$(\alpha,\alpha'\gamma_{1.63})^{20}$Ne and ^{20}Ne$(\alpha,\mathrm{p}\gamma_{0.44})^{23}$Na cross sections.

Below 4·6 MeV the peaks in the present data are generally well separated, and an attempt has been made to correlate these with levels observed in the ^{20}Ne$(\alpha,\gamma)^{24}$Mg and ^{23}Na+p reactions.

Peak B ($E_x = 12\cdot745$ MeV) appears clearly in both the 1·63 and 0·44 MeV data, and the angular distribution measurements give an unambiguous 2^+ assignment. It corresponds well to the 12·740 MeV 2^+ state observed by Highland and Thwaites (1967) in the ^{20}Ne$(\alpha,\gamma)^{24}$Mg reaction, and is probably the same level as that reported at $E_x = 12\cdot737$ MeV from ^{23}Na+p studies (Endt and Van der Leun 1962).

Peak D ($E_x = 12\cdot811$ MeV) appears clearly in the 1·63 MeV data and the angular distribution measurements give a definite 2^+ assignment. No corresponding peak is evident in the 0·44 MeV data; however, the close proximity of peaks C and E would make it difficult to resolve such a peak, and consequently the upper limit set on the appropriate partial width is relatively high (Table 4). It probably corresponds to the state observed at $E_x = 12\cdot805$ MeV in ^{23}Na+p (given a tentative 2^+ assignment by Stelson 1954; Baumann *et al.* 1956) and at $E_x = 12\cdot810$ MeV in ^{20}Ne$(\alpha,\gamma)^{24}$Mg (assigned 2^+ by Highland and Thwaites 1967).

Peak H ($E_x = 12\cdot978$ MeV) appears strongly in both sets of data. The angular distribution measurements indicate $J^\pi = 4^+$, 5^-, or 6^+. There is no obvious matching level in either the ^{23}Na+p or ^{20}Ne$(\alpha,\gamma)^{24}$Mg data. The results of Table 4 indicate that $(2J+1)\Gamma_{\alpha_1} \gtrsim 2050$ eV. Comparison with Wigner single-particle limits for $l' = 2$, 3, and 4 suggests that $J^\pi = 6^+$ is considerably less likely than $J^\pi = 4^+$ or 5^-. If the peaks H observed in the 0·44 and 1·63 MeV data do correspond to the same level then $(2J+1)\Gamma_{\mathrm{p}_1} \gtrsim 270$ eV; in this case $J^\pi = 6^+$ would be impossible, since the observed value of Γ_{p_1} would be many times larger than the Wigner limit. Thus the overall conclusion from the angular distribution and partial width data is that for the

$12 \cdot 978$ MeV level J^π is almost certainly 4^+ or 5^-, although a 6^+ assignment cannot be completely excluded.

Peaks A, G, and J correspond in energy to levels observed in ^{23}Na+p reactions at $E_x = 12 \cdot 659$ MeV (3^-), $12 \cdot 920$ MeV (1^-), and $13 \cdot 142$ MeV respectively and do not have any properties that would exclude identification with these levels.

The excitation energy and apparent width of peak C suggest that it may correspond to the $12 \cdot 779$ MeV level observed in the ^{23}Na(p, α_0)^{24}Mg reaction with $\Gamma = 30$ keV. However, this level is reported to have a negligible ^{23}Na(p, p$'\gamma_{0.44}$)^{23}Na yield and an observable ^{23}Na(p, γ)^{24}Mg yield (Prosser *et al.* 1956). If this is so, the suggested correspondence seems unlikely since peak C has an appreciable ^{20}Ne(α, p$\gamma_{0.44}$)^{23}Na yield and no yield was observed from ^{20}Ne(α, γ)^{24}Mg at the appropriate bombarding energy.

Peak I probably corresponds to the 2^+ level observed in ^{20}Ne(α, γ)^{24}Mg at $E_x = 13 \cdot 089$ MeV. The smallness of the yields of $1 \cdot 63$ MeV radiation at 0° and 90° is consistent with this spin and parity. The relative values of Γ_{α_1} and Γ_{p_1} show that it does not correspond to the $13 \cdot 088$ MeV (3^-) level observed in ^{23}Na+p reactions.

Thus, while many of the peaks observed for $4 \cdot 0 < E_\alpha < 4 \cdot 6$ MeV correspond to levels already observed in ^{23}Na+p reactions, a significant fraction are due to previously unobserved levels.

VII. ACKNOWLEDGMENTS

The authors are grateful to Mr. R. V. Elliott, Dr. B. M. Sowerby, and Dr. B. V. Rao for assistance with some of the experimental work, to Dr. H. J. Hay for assistance with penetrability calculations, and to Dr. G. J. Highland and Dr. T. T. Thwaites for sending us their results prior to publication. One of us (I.F.W.) would like to thank Professor E. W. Titterton for his hospitality, and the Australian National University for the award of a Visiting Fellowship.

VIII. REFERENCES

BASHKIN, S., and OPHEL, T. R. (1962).—*Nucl. Instrum.* **15**, 112.

BAUMANN, N. P., PROSSER, F. W., READ, W. G., and KRONE, R. W. (1956).—*Phys. Rev.* **104**, 377.

ENDT, P. M., and VAN DER LEUN, C. (1962).—*Nucl. Phys.* **34**, 1.

HIGHLAND, G., and THWAITES, T. T. (1967).—Pennsylvania State University preprint.

KRAUS, A. A., SCHIFFER, J. P., PROSSER, F. W., and BIEDENHARN, L. C. (1956).—*Phys. Rev.* **104**, 1667.

OLLERHEAD, R. W., and KUEHNER, J. A. (1965).—Atomic Energy of Canada Ltd Rep. No. 2612, p. 13.

PROSSER, F. W., BAUMANN, N. P., BRICE, D. K., READ, W. G., and KRONE, R. W. (1956).—*Phys. Rev.* **104**, 369.

SMULDERS, P. J. M. (1965).—*Physica* **31**, 973.

STELSON, P. H. (1954).—*Phys. Rev.* **96**, 1584.

VIVARGENT, M. (1959).—*Annls Phys.* **4**, 1047.

YATES, M. J. L. (1965).—"Alpha-, Beta-, and Gamma-ray Spectroscopy." (Ed. K. Siegbahn.) p. 1691. (North-Holland: Amsterdam.)

DIRECTIONAL CORRELATION OF GAMMA RAYS IN THE DECAY OF 2·3 d ^{115}Cd

By M. M. Bajaj,* S. L. Gupta,* and N. K. Saha*

[*Manuscript received January* 3, 1968]

Summary

The gamma–gamma directional correlation of the 35–493 keV cascade in the decay of 2·3 d ^{115}Cd has been studied by the coincidence method. The results seem to favour the spin and parity assignments $^1/_2{}^+$, $^3/_2{}^+$, and $^1/_2{}^-$ for the levels at 864, 829, and 336 keV respectively, and indicate that the 35 keV transition is $(96\cdot5\pm0\cdot5)\%$ M1 and $(3\cdot5\pm0\cdot5)\%$ E2, with a mixing parameter $\delta = -0\cdot191\pm0\cdot014$. These results agree with the recent I.C.C. measurements of Bäcklin, Fogelberg, and Malmskog but differ from those of earlier work. Computation of the partial lifetimes of the 35 keV radiation on this basis indicates that the M1 transition is retarded by a factor of $\simeq 23$ and the E2 transition is enhanced by a factor of $\simeq 958$. The E1 component of 493 keV radiation is estimated to be hindered by a factor of $\simeq 4\times10^{-7}$, while the M2 component is retarded by a factor of $\simeq 3$. The possible collective nature of the 829 keV level is discussed.

I. Introduction

The low lying excited states of the odd-mass isotopes of indium have been of considerable interest in recent years. Of particular interest are the energy levels of ^{115}In at 336, 597, 829, 864, and 934 keV above the ground state. Beta transitions of the 2·3 d ground state and the 43 d isomeric state of ^{115}Cd populating the ^{115}In levels and the resulting de-excitation γ-rays have been studied by a number of authors (Cork *et al*. 1950; Hayward 1952; Langer, Moffat, and Graves 1952; Wahl and Bonner 1952; Estulin and Moiseeva 1955; Varma and Mandeville 1955; Gorodetzky *et al*. 1960; Gorodetzky, Manquenonille, and Knipper 1961; Hans and Rao 1963; Bornemeier *et al*. 1964; Tandon and Devare 1964; Graeffe and Tang 1966; Graeffe *et al*. 1966; Pandharipande *et al*. 1966; Bäcklin, Fogelberg, and Malmskog 1967; McDonald, Porter, and Stewart 1967; Ranakumar and Lakshminarayana 1967). The spins and parities of these levels, assigned from the above studies, are shown in Figure 1; uncertain values are given in parentheses.

The ground state of ^{115}In has the well-established spin and parity of $\frac{9}{2}+$ and the isomeric state at 336 keV is $\frac{1}{2}-$. From the shell model, they are expected to be single-proton hole states $g_{9/2}$ and $p_{1/2}$ respectively. The spin and parity of the 597 keV level are also more or less well established as $\frac{3}{2}-$, and those of the 934 keV level as $\frac{7}{2}+$. However, considerable uncertainty seems to exist for the spin and parity of the two excited levels at 829 and 864 keV. The 864 keV level de-excites to the 336 keV level via the 35–493 keV gamma–gamma cascade. Directional correlation measurements on this cascade seem to have been performed only by Hans and Rao (1963), who also determined the K-conversion coefficient α_K for the 35 keV radiation. On the basis of these data, they assigned spins and parities $\frac{3}{2}-$ or $\frac{1}{2}-$ to the 864 keV level, $\frac{3}{2}-$ to the 829 keV level, and an M1 multipolarity for the 35 keV transition. Bornemeier *et al.* (1964) remeasured the K-shell conversion coefficient of the 35 keV γ-ray and assigned E1 multipolarity to it. Consequently, the 864 keV level would have positive parity (assuming negative parity for the 829 keV level) and this contradicts the earlier conclusions. Recently Graeffe *et al.* (1966) have performed accurate α_K measurements for the 35 keV γ-ray using a Ge(Li) detector and a NaI(Tl) scintillation counter. They have obtained the spin and parity $\frac{3}{2}-$ for the 864 keV level and find a predominantly M1 multipolarity for the 35 keV transition (with some mixing of E2). Further, the possible spins and parities of the 829 keV level according to these authors are either $\frac{3}{2}+$ or $\frac{5}{2}-$. One way of deciding between the two alternatives would be to ascertain the multipolarity of the observed 105 keV γ-transition (between the 934 and 829 keV excited states), which has not been previously attempted. Quite recently Bäcklin, Fogelberg, and Malmskog (1967) measured the conversion coefficients of the various transitions in ^{115}In. They favour $\frac{3}{2}+$ for the 829 keV level, $\frac{1}{2}+$ (or $\frac{3}{2}+$) for the 864 keV level, and predominantly E1 multipolarity for the 493 keV radiation. The overall data for these two levels are therefore fairly conflicting.

---

* Department of Physics and Astrophysics, University of Delhi, Delhi–7, India.

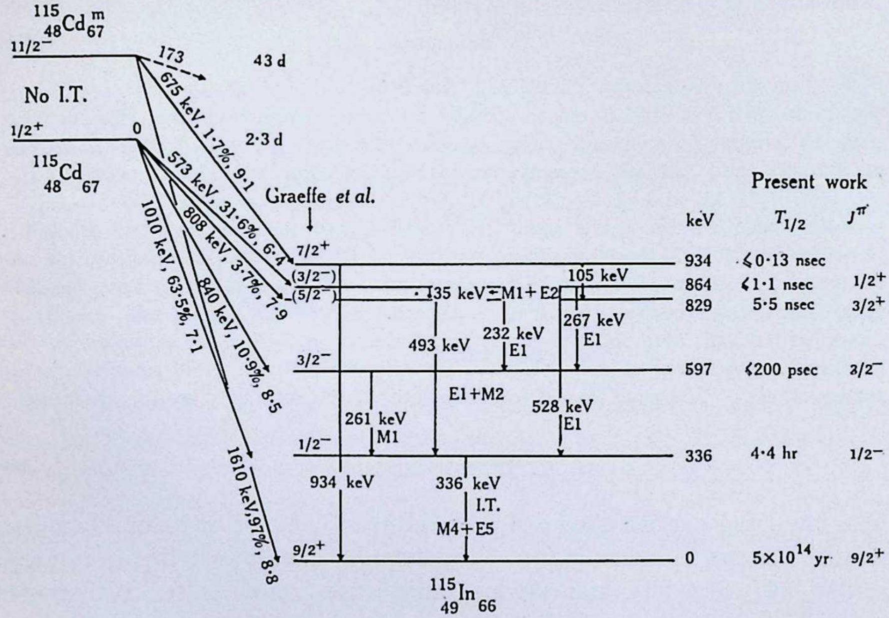
$^{115}_{48}$Cd$^{m}_{67}$
11/2−
173
43 d
No I.T.
1/2+
0
2·3 d
$^{115}_{48}$Cd$_{67}$
675 keV, 1·7%, 9·1
573 keV, 31·6%, 6·4
808 keV, 3·7%, 7·9
1010 keV, 63·5%, 7·1
840 keV, 10·9%, 8·5
1610 keV, 97%, 8·8
Graeffe et al.
7/2+
(3/2−)
(5/2−)
3/2−
1/2−
9/2+
35 keV M1+E2
105 keV
493 keV
232 keV
E1
267 keV
E1
E1+M2
528 keV
E1
261 keV
M1
934 keV
336 keV
I.T.
M4+E5
$^{115}_{49}$In$_{66}$
Present work
keV
$T_{1/2}$
J^{π}
934
≤0·13 nsec
864
≤1·1 nsec
1/2+
829
5·5 nsec
3/2+
597
≤200 psec
3/2−
336
4·4 hr
1/2−
0
5×10^{14} yr
9/2+

Fig. 1.—Decay scheme of 2·3 d ^{115}Cd (and part of 43 d ^{115}Cd^{m}) based on some of the earlier results and on results obtained in the present work.

The importance of the low lying levels of ^{115}In stems from the fact that, while the ground state and the first isomeric state at 336 keV are considered to be the two single-proton hole states, the higher excited states might arise from a coupling of the 2^+ vibrational phonon of the doubly even core to the lowest two levels. This picture would be consistent with the observed behaviour (McGowan and Stelson 1958) of the 45- and 47-proton nuclides in their collective core excitations and their possible couplings with single quasi-particles to produce the low lying excited states. In view of the observed half-life of 5·5 nsec for the 829 keV level in ^{115}In, the study of multipolarities of the 35 and 493 keV γ-transitions would be of great importance. This is the more so because Graeffe *et al.* (1966) have concluded from their recent work that the collective effect of the 49-proton nucleus ^{115}In is rather weak, and this nucleus may stand out from the general pattern of behaviour of the neighbouring odd-proton nuclei.

In view of the position stated above, we considered it necessary to remeasure the directional correlation of the 35–493 keV gamma–gamma cascade and to examine the spin values of the excited levels involved as well as the multipole character of the γ-transitions.

II. Coincidence Measurements

The source used in the present work was in the form of cadmium nitrate dissolved in nitric acid solution. It was produced by irradiating spectrographically standardized pure cadmium metal with neutrons in the Apsara Reactor, Trombay.

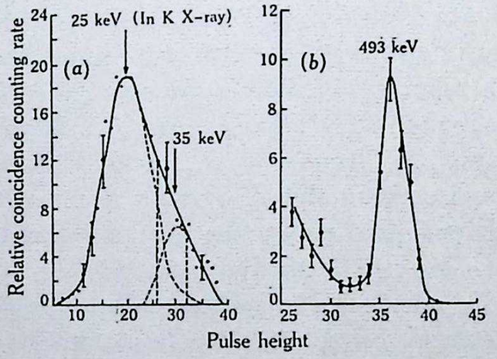

Fig. 2.—Gamma spectrum in coincidence with:
(*a*) 493 keV γ-ray
(*b*) 35 keV γ-ray

All the coincidence and directional correlation measurements were carried out with a fast–slow scintillation coincidence spectrometer with an effective resolving time of $\simeq$ 30 nsec. The counting time for directional correlation measurements was over 30 hr at each angular position.

Figures 2(*a*) and 2(*b*) show the γ-spectra recorded in coincidence with the 493 and 35 keV γ-rays respectively. These spectra clearly establish the coincidence relationship between the 493 and the 35 keV γ-rays.

III. Results

(*a*) *Directional Correlation of 35–493 keV Cascade*

Evaluation of the experimental data yielded the solid-angle corrected directional correlation function

$$W(\theta) = 1+(0\cdot0695\pm0\cdot0175)P_2(\cos\theta)-(0\cdot0036\pm0\cdot0431)P_4(\cos\theta). \qquad (1)$$

The only contribution in this cascade comes from the interference produced by the coincidence of the 493 keV γ-ray with the 25 keV K-conversion quanta of the 35 keV γ-ray. A careful analysis of the coincidence spectrum (Fig. 2(*a*)) shows that this interference is $(37\cdot6\pm5\cdot0)\%$ of the observed number of total coincidences. Since this interference is isotropic in nature, the directional correlation function after correction is

$$W(\theta) = 1+(0\cdot111\pm0\cdot029)\mathrm{P}_2(\cos\theta)-(0\cdot006\pm0\cdot069)\mathrm{P}_4(\cos\theta)\,. \qquad (2)$$

As the half-life of the 829 keV intermediate state is $5\cdot5\pm0\cdot2$ nsec (Tandon and Devare 1964), an attenuation of the expansion coefficients may possibly occur. By using solid and liquid sources, however, we observed that there is no appreciable change in the anisotropy within the statistical error. We, therefore, conclude that the measured directional correlation is unperturbed, and equation (2) does not require further correction. A discussion of the directional correlation data in terms of equation (2) is set out below.

(*b*) *Spin and Parity of 829 and 864 keV Levels*

This cascade involves the excited states at 336, 829, and 864 keV (Fig. 1). For the 336 keV isomeric state, the $\frac{1}{2}^-$ spin and parity assignment has been made on the basis of the log *ft* value of the beta group feeding this level and the I.C.C.* measurement of the 336 keV ground state transition in ^{115}In (Estulin and Moiseeva 1955; Hans and Rao 1963). The results of beta spectra and some theoretical considerations (Walters, Bemis, and Gordon 1965) allow a wide range of spin and parity values for the 829 keV level, namely, $\frac{1}{2}^+$, $\frac{1}{2}^-$, $\frac{3}{2}^+$, $\frac{3}{2}^-$, and $\frac{5}{2}^-$. Nevertheless, the situation has been carefully analysed by Graeffe *et al.* (1966). The 934 keV level has been shown to have a spin and parity value of $\frac{7}{2}^+$ as a result of the beta transition feeding it from ^{115}Cd$^{\mathrm{m}}$ and its formation by the Coulomb excitation of the $\frac{9}{2}^+$ ground state of ^{115}In. Further, because of the observed 105 keV transition from this level to the 829 keV level, we can limit the assignments to $\frac{3}{2}^+$, $\frac{3}{2}^-$, or $\frac{5}{2}^-$ for the latter. Recent I.C.C. measurements carried out with Ge(Li) detectors and a double-focusing beta spectrometer by Bäcklin, Fogelberg, and Malmskog (1967) show that the 493 keV transition from the 829 to the 336 keV level ($\frac{1}{2}^-$) is predominantly E1 with an M2 content of 4%. The spin values $\frac{3}{2}^-$ and $\frac{5}{2}^-$ are then not compatible with the E1 multipolarity of the 493 keV transition. Therefore, the only possible assignment for this state is $\frac{3}{2}^+$. In conclusion, we may say that the experimental result of Bäcklin, Fogelberg, and Malmskog has been a decisive factor in uniquely determining the spin and parity of the 829 keV level.

For the 864 keV level, the probable spin values are $\frac{1}{2}^+$, $\frac{3}{2}^+$, or $\frac{5}{2}^+$ because the 35 keV transition between the 864 and 829 keV levels has been shown to be predominantly M1 on the basis of I.C.C. measurements (Hans and Rao 1963; Graeffe *et al.* 1966; Bäcklin, Fogelberg, and Malmskog 1967). Of these, $\frac{5}{2}^+$ is unlikely because of the E1 character of the 528 keV transition between the 864 and 336 keV levels found on the basis of conversion coefficient measurements (Bäcklin, Fogelberg, and Malmskog 1967). The probable values are thus limited to $\frac{1}{2}^+$ and $\frac{3}{2}^+$.

---

* I.C.C. = internal conversion coefficient.

As a result of the above discussion, two alternative spin sequences, namely (i) $\frac{1}{2}(\mathrm{D, Q})\frac{3}{2}(\mathrm{D, Q})\frac{1}{2}$ and (ii) $\frac{3}{2}(\mathrm{D, Q})\frac{3}{2}(\mathrm{D, Q})\frac{1}{2}$, follow for the 35–493 keV cascade. Taking approximately 4% M2 admixture (Bäcklin, Fogelberg, and Malmskog 1967) in γ_{493}, the mixing ratio analysis of equation (2) carried out in terms of the spin sequence (i) (Fig. 3) shows that the 35 keV transition is predominantly M1 with an E2 content of $(3\cdot5\pm0\cdot5)\%$. This is in close agreement with Bäcklin, Fogelberg, and Malmskog's recent result of $\simeq 97\%$ M1 and $\simeq 3\%$ E2 admixture for this transition. The analysis also gives the mixing parameter δ $(=\{I(\mathrm{E2})/I(\mathrm{M1})\}^{\frac{1}{2}})$ of the 35 keV transition as $-0\cdot191\pm0\cdot014$. The spin sequence (ii), on the other hand, leads to an E2 admixture of $(11\cdot15\pm1\cdot85)\%$ $(\delta_{35}<0)$ for the same transition and is therefore not acceptable. As a result of the present directional correlation measurements and the other known data, the spin and parity of the 864 keV level are assigned as $\frac{1}{2}^{+}$ and those of the 829 keV level as $\frac{3}{2}^{+}$.

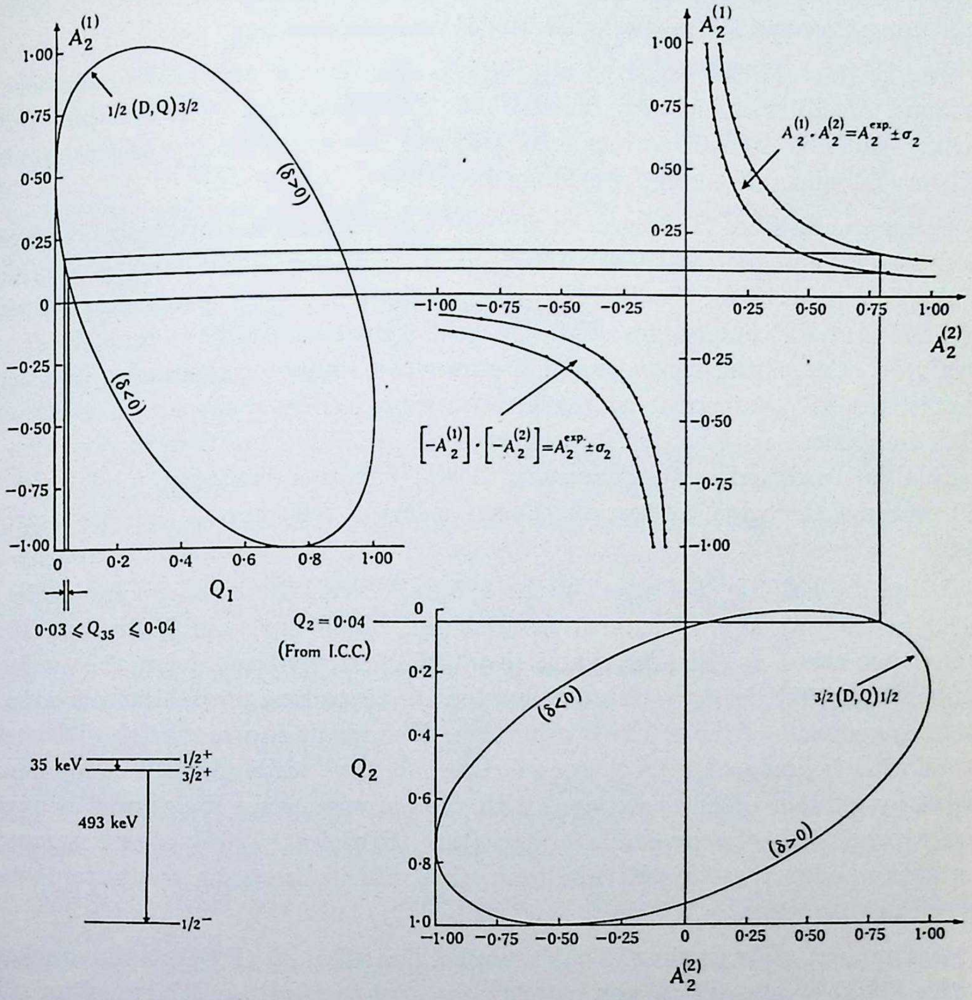

Fig. 3.—Mixing ratio analysis of the 35–493 keV cascade in terms of a $^1/_2(\mathrm{D, Q})^3/_2(\mathrm{D, Q})^1/_2$ spin sequence.

IV. DISCUSSION

It will be noticed that the expansion coefficients obtained here differ markedly from those reported by Hans and Rao (1963), namely, $A_2 = -0\cdot10 \pm 0\cdot03$, $A_4 = +0\cdot03 \pm 0\cdot03$. These authors assigned spin and parity values of $\frac{1}{2}^-$, $\frac{3}{2}^-$, and $\frac{1}{2}^-$ to the levels at 864, 829, and 336 keV respectively. As the multipolarity of γ_{493} was not known earlier, their conclusions could not be unambiguous. From the present directional correlation data and other recent results, we arrive at definite assignments of $\frac{1}{2}^+$ and $\frac{3}{2}^+$ to the levels at 864 and 829 keV.

Graeffe *et al.* (1966) favoured a $\frac{5}{2}^-$ spin value for the 829 keV level, because they found an E1 multipolarity for the 105 keV transition. The assignment $\frac{5}{2}^-$, however, would be difficult to reconcile with the E1 multipolarity of the 493 keV transition (Bäcklin, Fogelberg, and Malmskog 1967).

Using the half-life (1·1 nsec) of the 864 keV level, the conversion coefficient $\alpha_K = 9\cdot6 \pm 1\cdot2$, and the measured value $(-0\cdot191 \pm 0\cdot014)$ of the mixing parameter from the present work for the 35 keV γ-ray, we find that the experimental lifetimes for the M1 and E2 components of the 35 keV transition are 17·4 and 479·7 nsec respectively. Comparing these partial lifetimes with the corresponding Weisskopf estimates, the M1 component is found to be retarded by a factor of $\simeq 23$ while the E2 component is enhanced by a factor of $\simeq 958$. This fast rate of the E2 transition is consistent with Sorensen's (1964) superconductivity model for the 28–50 proton-shell region, as here the Fermi energy λ falls above the single-proton levels.

Using the half-life (5·5 nsec) of the 829 keV level, the quadrupole admixture ($\simeq 4\%$) in the 493 keV E1 transition (Bäcklin, Fogelberg, and Malmskog 1967), and the theoretical α_K (E1+M2) value (0·002373) extrapolated from the tables of Sliv and Band (1957, 1958), we have computed the transition probabilities for the E1 and M2 components of the 493 keV transition. The result shows that the E1 part of this radiation is hindered by a factor of $\simeq 4\cdot14 \times 10^{-7}$ while the M2 component is retarded by a factor of $\simeq 3$ compared with the corresponding Weisskopf estimates. A comparison with the available systematics (Perdrisat 1966) of E1 transition probabilities shows that this E1 hindrance factor is in line with the general trend observed in this region.

Assignment of $\frac{5}{2}^-$ to the 829 keV state led Graeffe *et al.* (1966) to the conclusion that the 493 keV γ-transition was too slow for a phonon-mixed E2 transition. The dominant collective effects generally observed in the nuclei having $Z = 45$ or 47 were therefore supposed to have markedly changed in ^{115}In. This difficulty clearly vanishes when we assign $\frac{3}{2}^+$ to the 829 keV level, the resulting predominantly E1 493 keV γ-transition having the right order of the hindrance factor consistent with nuclear systematics.

Attempts have been made to construct theoretically (Vogt 1963) the levels of ^{115}In by a first-order perturbation treatment of the interaction of the 2^+ vibrational phonon of the core to the lowest two single-proton hole levels (Kisslinger and Sorensen 1960). The collective levels have been extrapolated further by Silverberg (1961). However, these theoretical treatments appear to be far from satisfactory in describing the experimentally observed levels of ^{115}In. The present spin and parity assignments to the observed levels do not bring us any nearer to agreement, but a qualitative picture of the collective nature of the levels seems to be generally supported.

V. Acknowledgments

The authors wish to express their sincere thanks to Professor R. C. Majumdar, Head of the Department of Physics and Astrophysics, University of Delhi, for providing facilities for carrying out this work. Thanks are also due to Dr. S. C. Pancholi (now at Oak Ridge National Laboratory, U.S.A.) for his active help during the initial stages of this work. The work was supported by Research Fellowships granted to one of the authors (M.M.B.) by the Council of Scientific and Industrial Research, New Delhi, in the early stages and by the University Grants Commission, New Delhi, later.

VI. References

Bäcklin, A., Fogelberg, B., and Malmskog, S. G. (1967).—*Nucl. Phys.* A **96**, 539.

Bornemeier, D. D., Ellsworth, L. D., Mandeville, C. E., and Potnis, V. R. (1964).—*Phys. Rev.* **134**, B740.

Cork, J. M., Rutledge, W. C., Stoddard, A. E., Branyan, C. E., and LeBlanc, J. M. (1950).—*Phys. Rev.* **79**, 938.

Estulin, I. V., and Moiseeva, E. M. (1955).—*Soviet Phys. JETP* **1**, 463.

Gorodetzky, S., Manquenonille, R. R., and Knipper, A. (1961).—Electromagnetic lifetimes and properties of nuclear states. p. 79. Nat. Acad. Sci. Publ. No. 974.

Gorodetzky, S., Manquenonille, R., Richert, R., and Knipper, A. (1960).—*J. Phys. Radium, Paris* **21**, 439.

Graeffe, G., and Tang, C. W. (1966).—*Bull. Am. phys. Soc.* **11**, 394.

Graeffe, G., Tang, C. W., Coryell, C. D., and Gordon, G. E. (1966).—*Phys. Rev.* **149**, 884.

Hans, H. S., and Rao, G. N. (1963).—*Nucl. Phys.* **44**, 320.

Hayward, R. W. (1952).—*Phys. Rev.* **87**, 202A.

Kisslinger, L. S., and Sorensen, R. A. (1960).—*Math.-fys. Meddr* **32**(9), 1.

Langer, L. M., Moffat, R. D., and Graves, G. A. (1952).—*Phys. Rev.* **86**, 632A.

McDonald, J., Porter, D., and Stewart, D. T. (1967).—*Nucl. Phys.* A **104**, 177.

McGowan, F. K., and Stelson, P. H. (1958).—*Phys. Rev.* **109**, 901.

Pandharipande, V. R., Prasad, K. G., Singru, R. M., and Sharma, R. P. (1966).—*Phys. Rev.* **143**, 740.

Perdrisat, C. F. (1966).—*Rev. mod. Phys.* **38**, 41.

Ranakumar, N., and Lakshminarayana, V. (1967).—Proc. Low Energy Nucl. Phys. Symp., Kanpur, Dep. Atomic Energy, Government of India.

Silverberg, L. (1961).—*Ark. Fys.* **20**, 341.

Sliv, L. A., and Band, I. M. (1957).—Rep. No. 57 ICC K1 Phys. Dept, Univ. Illinois, Urbana, Illinois.

Sliv, L. A., and Band, I. M. (1958).—Rep. No. 58 ICC L1, Phys. Dept, Univ. Illinois, Urbana, Illinois.

Sorensen, R. A. (1964).—*Phys. Rev.* **133**, B281.

Tandon, P. N., and Devare, H. G. (1964).—*Phys. Lett.* **10**, 113.

Varma, J., and Mandeville, C. E. (1955).—*Phys. Rev.* **97**, 977.

Vogt, E. W. (1963).—*Phys. Lett.* **7**, 61.

Wahl, A. C., and Bonner, N. A. (1952).—*Phys. Rev.* **85**, 570.

Walters, W. B., Bemis, C. E., Jr, and Gordon, G. E. (1965).—*Phys. Rev.* **140**, B268.

COMPUTED ELECTRON MICROGRAPHS FOR TILTED FOILS CONTAINING DISLOCATIONS AND STACKING FAULTS

By P. Humble*

[*Manuscript received December* 18, 1967]

Summary

The method of computation of electron microscope images developed by Head (1967) produces micrographs of single dislocations in about 1 min of numerical integration. In Head's original programme, the electron beam direction and the normal to the foil surface are coincident. Since this condition is not often realized in practical electron microscopy, the programme has been extended to compute the images of dislocations in tilted foils. It has been further modified to compute the images from a configuration containing up to two dislocations and up to three stacking faults. These programmes are thus applicable to a wide range of defect configurations in tilted thin foils. The derivation of these programmes is described and several examples of their use in experimental situations are given. These include the "skewing" of dislocation images due to the noncoincidence of the beam direction and the foil normal, and images due to interactions between dislocations and stacking faults.

I. Introduction

Until recently, computations of the intensity of electron microscope images of dislocations and other defects in thin foils have been limited to graphs (or profiles) of the way in which the intensity of the image varies along a line crossing the defect. These profiles are not continuous curves but consist of discrete points, each of which has been computed by a separate numerical integration. Thus, the computation of several profiles takes a considerable amount of computer time. In addition, it is often difficult to interpret the profiles in terms of an actual experimental micrograph of the defect, since the experimental counterpart of a profile, namely a microphotometer trace across the defect, is seldom used. Indeed, the profiles are usually translated into the form of a picture mentally by the observer. Hence, the computation of complete theoretical pictures of a defect which can be compared directly with experimental micrographs would be extremely helpful in reducing the subjectiveness of the comparison.

In a recent paper, Head (1967) has described a way of producing computer-simulated images of dislocations in which all the information required can be obtained in about 1 min of numerical integration of the Howie–Whelan (1961) differential equations for two-beam electron diffraction. This information is presented, not in the form of profiles, but in the form of a half-tone picture using the computer line

---

* Division of Tribophysics, CSIRO, University of Melbourne, Parkville, Vic. 3052.

Aust. J. Phys., 1968, **21**, 325–36

printer. Head has shown that when the important information is contained in the topology of the image, as is generally the case, such theoretical "micrographs" are extremely valuable.

In the programme developed by Head, the normal to the foil surface and the electron beam direction are coincident. However, tilting devices in electron microscopes may commonly tilt the specimen up to ±30° and such noncoincidence of the foil normal and electron beam direction must be taken into account in direct comparisons between experimental and computed images. Section II(*a*) deals with the derivation of a computer programme of the type described by Head which takes into account any given foil normal. Section II(*b*) outlines the extension of this programme to the case of two parallel dislocations connecting three stacking faults. Simpler configurations than are allowed for in Section II(*b*) can be obtained by putting the appropriate Burgers vectors and/or the shears on the planes to zero.

Section III describes some of the uses of these programmes and compares the computed and experimental images of several defects.

II. COMPUTATIONS

Following Head, we consider only straight dislocations sloping through a foil of constant thickness t. Since we consider only configurations consisting of single dislocations or dislocations that are parallel, and since no surface relaxations are allowed, the elastic displacement field of the dislocations is constant along any line parallel to them. This is true even when the displacement fields are computed in full elastic anisotropy, as is the case here. With the foregoing restrictions, it is possible to define a "generalized cross section" (Head 1967) that, for a given dislocation, has a fixed displacement field. On this cross section a pair of lines of constant separation, but variable position, can represent the foil surfaces and delineate the parts of the displacement field through which the electron beam passes for the various profiles.

The equations of Howie and Whelan (1961, equations (5)), based on a two-beam column approximation (including absorption), describe the dynamical interaction of the electron beam with the displacement field. These equations are a pair of first-order linear differential equations in T' and S', the transmitted and scattered amplitudes respectively, and thus have only two independent solutions. If these are known, all other solutions may be obtained by taking linear combinations of them.

The speed of Head's method of producing theoretical micrographs comes from combination of the facts that a generalized cross section, in which the displacement fields are fixed, *can* be established and that only *two* numerical integrations per column of this cross section, followed by linear combinations of solutions, provides the information for corresponding points on many profiles. Previous methods have used a separate integration for each point on each profile. The problem, therefore, in applying this method to other configurations is to establish the generalized cross section for the configuration being considered and to define the way in which the integrations are to be done so that the appropriate linear combinations may be chosen.

(*a*) *Generalized Cross Section for Tilted Foil*

Figure 1(*a*) shows a dislocation sloping through an untilted foil in the manner considered by Head. The dislocation enters the bottom surface of the foil on the line HG and leaves the top surface on the line LM. The vertical lines in Figure 1(*a*) are parallel to the beam direction. The generalized cross section for this configuration is obtained by projection in a direction parallel to the dislocation onto the plane LMNO. This generalized cross section is shown in Figure 1(*b*). The dislocation is coming out of the paper but is not normal to it. The dashed letters in Figure 1(*b*) correspond to the undashed letters in Figure 1(*a*). Note that the line HG projects into H′G′, which is coincident with L′M′, the projection of LM. Lines E′F′ and H′G′ represent the top and bottom surfaces of the foil respectively for the profile in which the dislocation is just entering the bottom of the foil; L′M′ and O′N′ represent the top and bottom surface of the foil for the profile in which the dislocation is just leaving the top of the foil. Intermediate profiles on, for example, the shaded plane shown in Figure 1(*a*), are obtained by taking the portion of the displacement field between the two dashed lines on the generalized cross section in Figure 1(*b*).

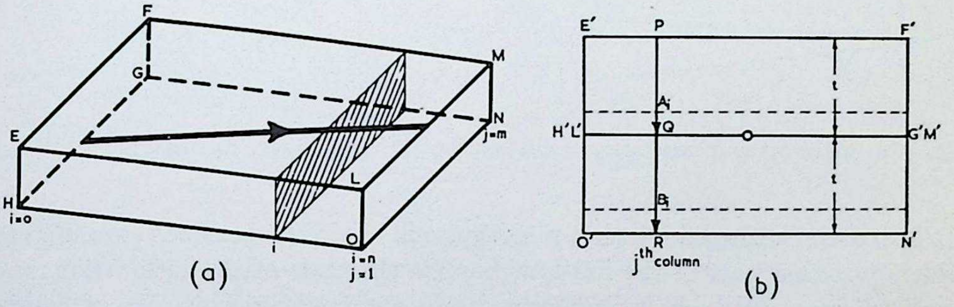

Fig. 1.—Geometry (*a*) and generalized cross section (*b*) for a single dislocation in an untilted foil.

The amplitudes T' and S' are integrated down columns in the cross section parallel to the beam direction. An equal number of columns on either side of the dislocation is considered, care being taken not to integrate down a column that is within one-quarter of the normal column spacing of the dislocation core. If columns closer to the dislocation core are considered, the programme takes an excessive amount of time to integrate through the rapidly changing strain field.

Consider the *j*th column from the dislocation as shown in Figure 1(*b*). The integration down this column is done in two main parts, the first part (A) from P to Q and the second part (B) from Q to R. Each part is divided into *n* steps of equal size. Two beams, with independent initial amplitudes at the top of the cross section are integrated down the column simultaneously, and the amplitudes at the end of each step stored in the computer memory. The intensity of the image for the surfaces of the foil in the positions shown by the dashed lines in Figure 1(*b*) is obtained by combining the two solutions for the position A_i with the two for the position B_i linearly and in such a manner as to give the correct boundary conditions for the top surface of the foil; that is, $T' = 1$ and $S' = 0$ at A_i.

By allowing i to run from 0 to n, we obtain $n+1$ values of the intensity for the jth column in successive profiles running from the plane EFGH to the plane LMNO in Figure 1(a). Thus we have $n+1$ intensity values to establish the points on one row of the theoretical micrograph parallel to the dislocation line. By repeating the procedure for $j = 1$ to m, we obtain the m rows of the picture. In the present case, $n = 128$ and $m = 60$. The spacing of the columns and the rows is related to the intercharacter spacing on the line printer so that the magnification across the picture is the same in all directions and all angles are true.

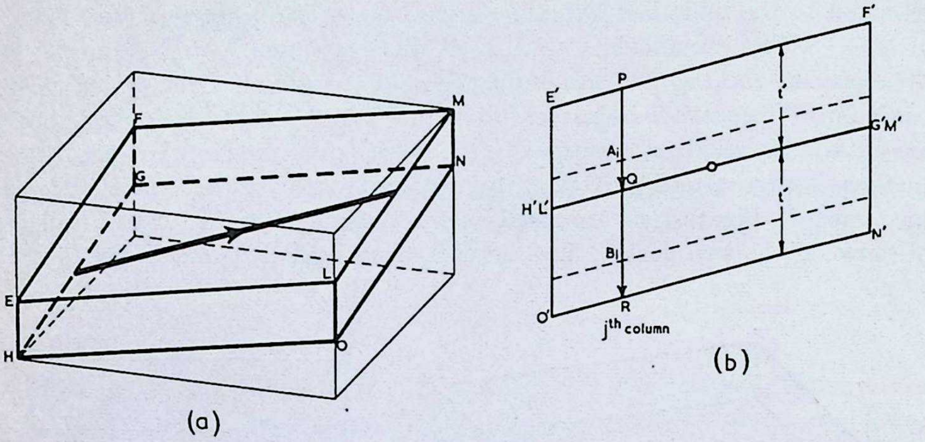

Fig. 2.—Geometry (a) and generalized cross section (b) for a single dislocation in a tilted foil.

The case of a tilted foil is shown in Figure 2. As in the previous case, Figure 2(a) considers just that part of the foil that bounds the ends of the dislocation, and the generalized cross section shown in Figure 2(b) is obtained by projection of Figure 2(a) along the dislocation direction onto the plane LMNO. Thus, the projections of HG and LM are coincident.

As in the case of untilted foils, the integration is carried out in two parts PQ and QR, and the rows of the picture obtained in a similar way. However, there are two modifications that have to be made. Firstly, PQ and QR are now each equal to t', rather than t, where t' is the thickness of the foil in the direction of the beam. Secondly, the integration in each column of the generalized cross section is started on the line E′F′, but this line is now at an angle to the beam that is determined by the component of tilt of the foil in the generalized cross section plane. The other component of tilt of the foil is automatically taken into account by this method of forming the picture.

(b) *Generalized Cross Section for Tilted Foil involving Dislocations and Stacking Faults*

It was mentioned at the beginning of this section that, provided cases involving more than one dislocation are restricted to configurations of parallel dislocations, a generalized cross section can still be defined. The corresponding restriction on the geometry of stacking faults is that the faulted planes must contain the dislocation direction. Thus the generalized cross section for one possible configuration involving two dislocations and three stacking faults is shown in Figure 3(*b*). The faulted planes are shown as dotted lines, dislocation *X* being at the intersection of planes *a* and *b*, and dislocation *Y* at the intersection of planes *b* and *c*. The corresponding view of the tilted foil is shown in Figure 3(*a*), but here, for the sake of clarity, only one faulted plane (*b*) has been shaded.

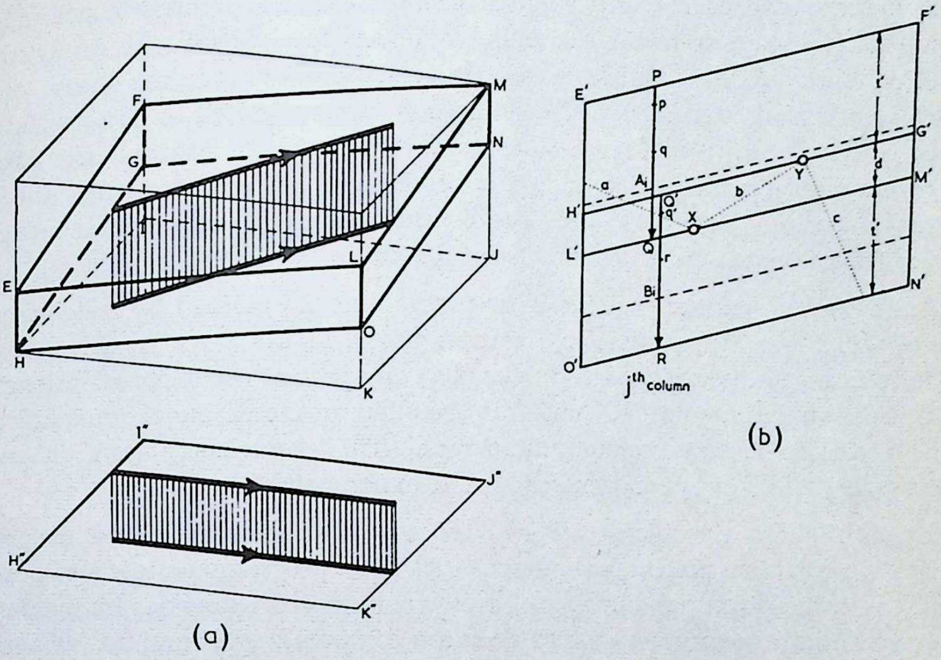

Fig. 3.—Geometry (*a*) and generalized cross section (*b*) for two dislocations and three stacking faults in a tilted foil. In (*a*) only the central fault has been shown, and the projection H″I″J″K″ illustrates the arrangement of the dislocations and the central stacking fault in the computed micrograph.

The portion of the foil shown in Figure 3(*a*) is bounded in a similar way to that shown in Figures 1(*a*) and 2(*a*), being that portion which just contains the dislocations. The layout of the computed picture is obtained by projection onto the plane HIJK, and this is shown in the lower part of Figure 3(*a*). With this geometry, the generalized cross section is obtained, as before, by projection in the dislocation direction onto the plane LMNO. Note, however, that now the projections of HG and LM are no longer coincident, but are separated by an amount *d* measured in the direction of the electron beam. The corresponding two ranges of integration for parts A and B are now PQ and Q′R, where $PQ = Q'R = t'+d$. For clarity, PQ and Q′R are shown as separate arrows in Figure 3(*b*); in fact, they both refer to integrations carried out down the same (*j*th) column.

As before, PQ and Q′R are each divided into *n* equal steps and the amplitudes integrated down the column of the cross section. However, before integrating through each step note is taken whether a stacking fault occurs in this step, or perhaps the position Q′ at which the B part of the integration starts. If a stacking fault does occur in the particular step, the integration is stopped at the fault, the scattered waves are changed in phase (determined by the shear on the plane), and the integration then continued to the end of the step. If the point Q′ occurs in a step, the amplitudes of the transmitted and scattered waves at this point are stored in the computer memory and, after the completion of the A part of the integration, are put into the integration programme as the starting conditions for the B part of the integration.

As mentioned earlier, many different geometrical arrangements containing up to two dislocations and up to three stacking faults are possible with the configuration depicted in Figure 3, since either of the Burgers vectors and/or the shears on the faulted planes may be zero. Also, the programme is not limited to non-overlapping stacking faults, as shown in Figure 3(*b*), but can compute the contrast from two or three overlapping faults. Of course this programme, in common with the ones described in Section II(*a*), computes the contrast from the dislocations using the full anisotropic elastic strain fields of these defects.

An important variation of the basic programme is obtained by restricting the ranges of integration, to pq and q′r, for example, in Figure 3(*b*). In this way, it is possible to frame the computed picture so that any part of the dislocation length in the foil is shown in the picture. This has the effect of increasing the magnification and the resolution of the computed micrograph. This is extremely useful in making detailed comparisons between computed and experimental images.

In addition to the micrographs of the many stacking-fault and dislocation configurations that it is possible to compute with these programmes, it is also possible, in some cases, to compute the images of more complex configurations by making the total image from a composite of two or more computed micrographs. This is an allowed procedure only when there are no dislocations present, or when the dislocation strain fields are negligible at the place where the micrographs are joined.

III. DISCUSSION AND EXAMPLES OF USE OF THE PROGRAMMES

Figure 4(*a*) shows the computed image of a pure screw dislocation in β-brass. The Burgers vector **b** is $[\bar{1}11]$, the reflecting vector **g** is $[\bar{1}\bar{1}0]$, and the beam direction **B** and the foil normal **F** are both [001]. It can be seen that the image is symmetrical either side of the dislocation line. It consists of oppositely positioned black dots along the line of the dislocation, with a region shaped like an arrow head where the dislocation leaves the top surface of the foil and a marked white region just before the dislocation leaves the bottom surface.

Figures 4(*b*) and 4(*c*) are images of the same dislocation under the same diffracting conditions, except that the foil normal has been moved away from [001] in a direction that is normal to the dislocation line in the image. For Figure 4(*b*) **F** = [115] and for Figure 4(*c*) **F** = [113]. It is apparent that the effect of varying the foil normal in this way is to "skew" the image. The dots in the image no longer correspond exactly across the dislocation line, but have been displaced in directions parallel to this line in opposite senses on either side of the line. This effect was predicted by Head, Loretto, and Humble (1967), but is extremely difficult to detect with the profile method of image computation.

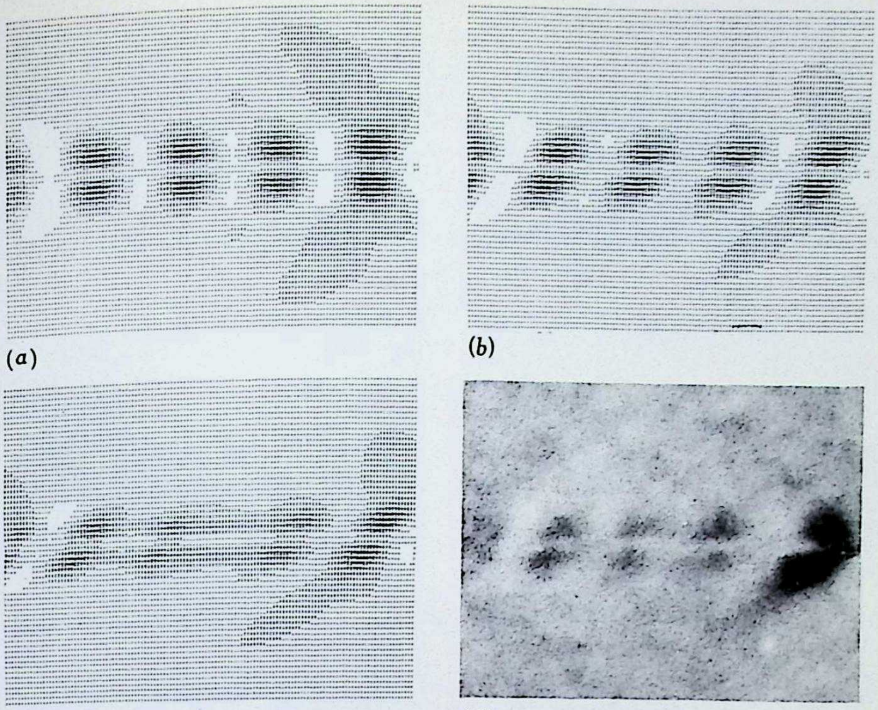

(a) (b)

(c) (d)

Fig. 4.—Micrographs of a screw dislocation of Burgers vector [$\bar{1}$11] in β-brass using the [$\bar{1}\bar{1}$0] reflecting vector in the [001] beam. The computed micrographs have foil normals of [001] in (a), [115] in (b), and [113] in (c). The foil normal for the experimental micrograph in (d) is [115].

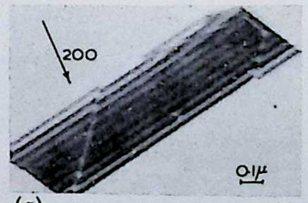

(a)

Fig. 5.—Theoretical micrographs (b) and (c) computed using two different contrast scales. The geometry and diffracting conditions are the same as for the central portion of the complex Frank loop shown in the experimental micrograph in (a).

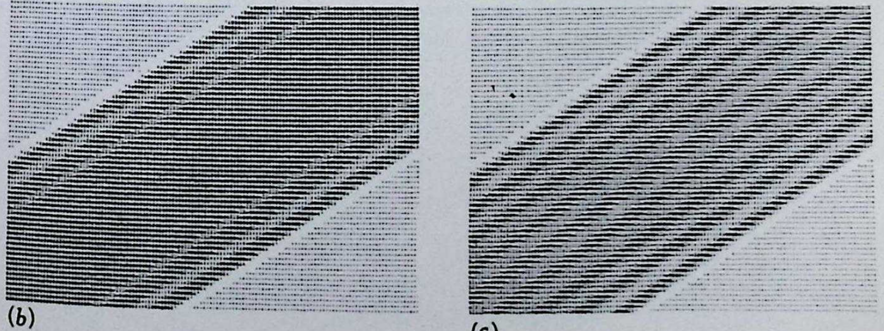

(b) (c)

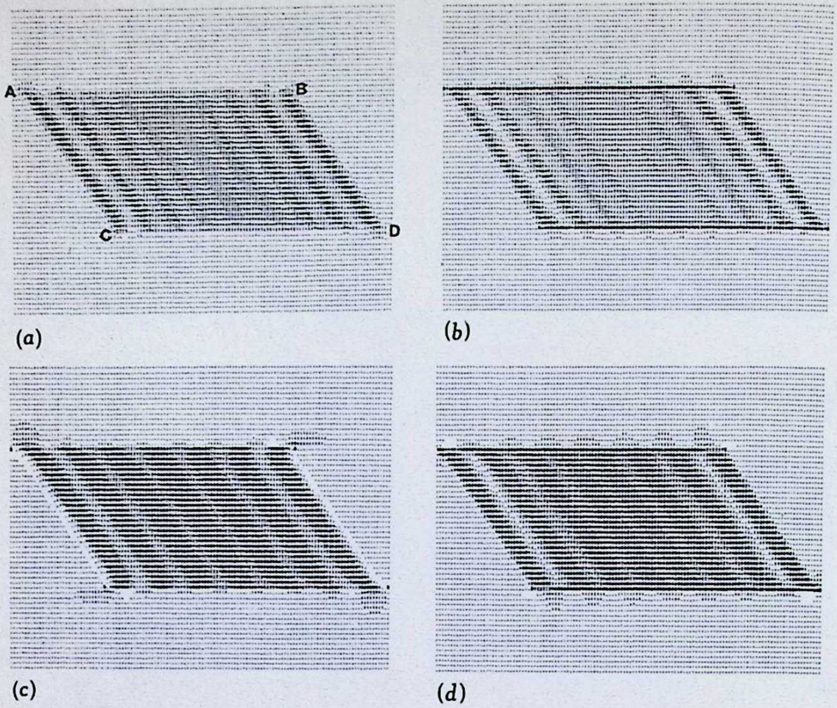

(a) (b)

(c) (d)

Fig. 6.—Computed micrographs illustrating the effect on the dislocations AB and CD bounding a faulted Frank loop of reversing the reflecting vector from $[0\bar{2}0]$ in (*a*) and (*c*) to [020] in (*b*) and (*d*). For (*a*) and (*b*) w is $0 \cdot 9$ and for (*c*) and (*d*) w is $0 \cdot 3$. Note the variations in the intensity and spacing of the fault fringes and the change in contrast of the fringes close to the surfaces of the foil AC and BD.

Fig. 7(*opposite*).—A Frank dislocation loop ABHG and a glide dislocation CDEF taken on four different reflecting vectors. Note that in (*d*) the portions CD and EF of the glide dislocation are virtually out of contrast whereas the segment DE, which passes close to the fault, shows a strong image.

Fig. 8(*opposite*).—Computed micrographs corresponding to the areas of the experimental micrographs outlined by dashed lines in Figure 7.

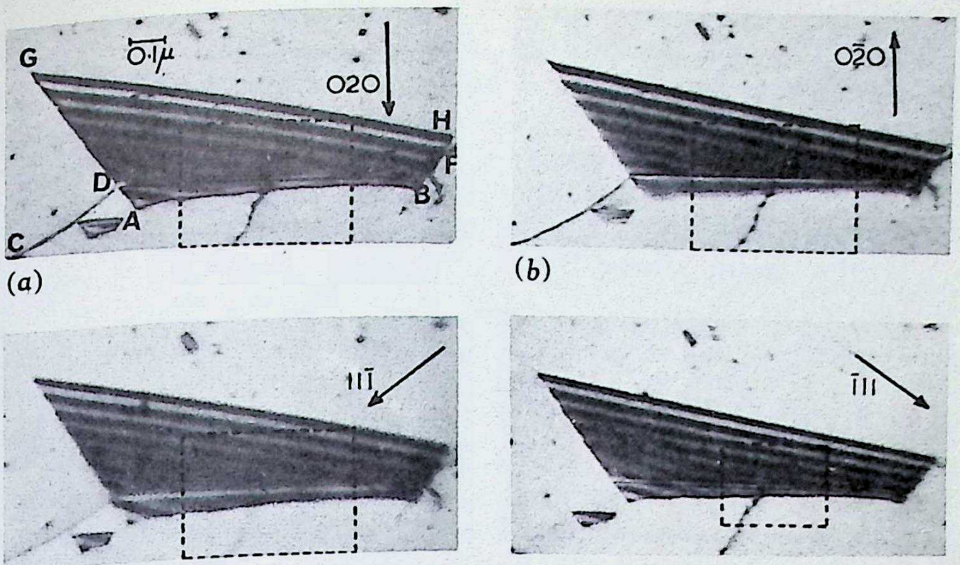
G
0·1μ
020
H
F
D
B
A
C
0$\bar{2}$0
11$\bar{1}$
$\bar{1}$11

(a) (b)

(c) (d)

Fig. 7

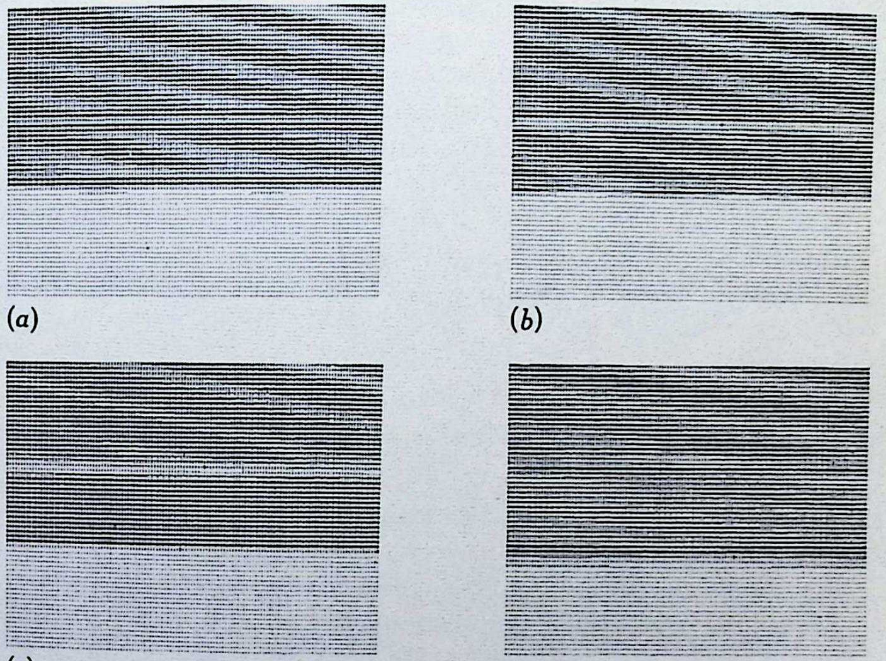

(a) (b)

(c) (d)

Fig. 8

Figure 4(*d*) shows the experimental image of such a screw dislocation of $\mathbf{b} = [\bar{1}11]$ in β-brass. The diffraction conditions are the same as those used for the computed micrographs in Figures 4(*a*)–4(*c*). The foil normal for this specimen is very close to [115]. Hence, this experimental micrograph may be compared directly with the computed micrograph in Figure 4(*b*), and in fact the angles through which the images are skewed are almost exactly the same.

The choice of the scale of grey to be used for images of different types of defects has been discussed by Head (1967), who suggested, for example, that the visibility of stacking-fault fringes might require a different scale from that used for dislocation images. Figure 5(*a*) shows a complicated faulted loop in a quenched copper–aluminium (9%) alloy and Figure 5(*b*) shows the computed image corresponding to the central portion of this defect. The fringes in the middle of the computed image become indistinct in Figure 5(*b*), whereas they are clearly visible in the experimental micrograph. In fact, it is possible to vary both the contrast (the apportioning of the grey scale symbols to the intensity values) and the exposure (the symbol in the grey scale which represents background intensity) of the computed pictures. Figure 5(*c*) shows a computed micrograph of the central portion of the loop in Figure 5(*a*) with a grey scale of less contrast, and now the fringes are plainly visible in the middle of the image. The contrast of the grey scale used in Figure 5(*b*) is the one generally used for images involving only dislocations and is such that the symbol representing background intensity (a full stop) changes to its neighbouring symbols (a blank and a colon) at 15% above and 7% below background intensity. The contrast used for the image shown in Figure 5(*c*) has visibility limits 26% above and 14% below background intensity. Although the visibility limits for the first scale are close to the estimated experimental visibility limits for electron images, those of the second scale are not. However, it must be remembered that since the exposure, development, and printing of experimental micrographs are often chosen to enhance the detail in the particular defect under observation, there is often a large variation in the photographic parameters from one experimental image to another. It is considered, therefore, that the grey scale for computed micrographs may be chosen on a similar basis, variations in the grey scale being selected to enhance the visibility of a particular defect.

The programmes may, of course, be used to form pictures for many of the contrast effects described in the literature, and previously only illustrated by intensity profiles. For example, Silcock and Tunstall (1964) have shown that, for 020 reflecting vectors, a Frank dislocation will be out of contrast when $\mathbf{g}.\mathbf{b} = -\frac{2}{3}$ but in contrast when $\mathbf{g}.\mathbf{b} = +\frac{2}{3}$, provided that the deviation from the Bragg condition w is large ($w \sim 0{\cdot}9$).

Figures 6(*a*) and 6(*b*) show the computed images for a faulted Frank loop, in which only the opposite parallel edges are included. The direction of these dislocations $\mathbf{u}$ is $[0\bar{1}1]$. Comparing this configuration with that shown in Figure 3(*a*), the shears on planes *a* and *c* are zero, plane *b* is (111), and the dislocations X and Y have Burgers vectors $\frac{1}{3}[111]$ and $\frac{1}{3}[\bar{1}\bar{1}\bar{1}]$ respectively. The Burgers vectors refer to the same loop and yet have opposite signs because the programme is arranged so that the dislocation directions are constrained to have the same positive sense. The electron beam direction and the foil normal are both [101] and the reflecting vectors are [0$\bar{2}$0] ($\mathbf{g}.\mathbf{b} = -\frac{2}{3}$) in Figure 6(*a*) and [020] ($\mathbf{g}.\mathbf{b} = +\frac{2}{3}$) in Figure 6(*b*). The value of w is 0·9. The dislocations run from A to B and from C to D, and the fringe direction is parallel to the intersection of the fault plane with the surface, AC or BD. Figures 6(*c*) and 6(*d*) show the same portion of the Frank loop under the same reflecting conditions, except that the value of w is now 0.3. It is immediately apparent that the difference in contrast of the dislocations observed between Figures 6(*c*) and 6(*d*) (the small w case) is not nearly so marked as in Figures 6(*a*) and 6(*b*) (the large w case). Closer inspection shows, however, that this effect is so marked in Figures 6(*a*) and 6(*b*) not because the dislocation images themselves are markedly blacker, but mainly because the higher value of w has decreased the contrast in the fringes in these pictures, allowing the dislocation images to be clearly seen. The case computed here corresponds to the case for which $\mathbf{g}.\mathbf{b}\times\mathbf{u} \neq 0$ in Silcock and Tunstall (1964).

It should be noted that these pictures also illustrate that reversing the reflecting vector produces a change in the shade of the outermost fringe (Hashimoto, Howie, and Whelan 1962). For Figures 6(*c*) and 6(*d*), where w is small, this effect is most marked; the outermost fringe is white in Figure 6(*c*), $\mathbf{g} = [0\bar{2}0]$, and black in Figure 6(*d*), $\mathbf{g} = [020]$. For $w = 0{\cdot}9$ the outermost fringe in the image for $\mathbf{g} = [0\bar{2}0]$ (Fig. 6(*a*)) is not visibly lighter than background intensity, although measurement of the relative widths of the images in Figures 6(*a*) and 6(*b*) shows that a similar reversal occurs here also. The larger number of fringes for the larger value of w is also a characteristic effect in the imaging of stacking faults.

Figures 7(*a*)–7(*d*) are electron micrographs of a Frank dislocation loop with a glide dislocation running very close to it. The different reflecting vectors are indicated on the micrographs. For Figures 7(*a*), 7(*b*), and 7(*d*) the beam direction is [101] and for Figure 7(*c*) [213]. The foil normal is close to [407]. One edge of the loop lies along AB, which is the [$\bar{1}$01] direction, and the glide dislocation runs along CDEF, AB and DE being almost parallel. The loop intersects one surface of the foil along GH. Figures 8(*a*)–8(*d*) show theoretical micrographs computed for the corresponding diffraction conditions and for the same geometry as in Figure 7, except that AB and DE have been made exactly parallel. The dislocation DE is 12 Å above the plane of the loop in the computed micrographs. The Burgers vector of the Frank dislocation is $\frac{1}{3}[111]$ and that of the glide dislocation $\frac{1}{2}[\bar{1}\bar{1}0]$. The range of integration used to produce these pictures has been restricted (c.f. Section II(*b*)) thus giving theoretical micrographs that cover a thickness of just one or two extinction distances within the foil, which is eight extinction distances thick for Figures 8(*a*) and 8(*b*) and nine extinction distances thick for Figures 8(*c*) and 8(*d*). Thus the computed micrographs correspond to areas about equal to those shown by the dashed lines in Figures 7(*a*)–7(*d*). This restriction is necessary to obtain the resolution in the fine detail of the image of the dislocation passing over the fault. For example, the image of this dislocation in Figure 7(*b*) consists of a black line and a white line each about 100 Å wide. These lines are reproduced in Figure 8(*b*), where 100 Å corresponds to the height of two rows of print. Using this technique of restricted ranges of integration to vary the magnification of the computed micrograph, it has been possible to match detail in experimental micrographs that is of the order of 20 Å wide.

In Figures 7(*d*) and 8(*d*) the value of $\mathbf{g}.\mathbf{b}$ is zero for the glide dislocation. Although this is not a pure screw dislocation and, therefore, cannot be completely out of contrast, the residual intensity in the portions of the dislocation CD and EF that are outside the loop is very small. However, it is interesting that, where this dislocation passes close to the loop and the stacking fault fringe contrast is present, there is a very definite image consisting of two thin black lines separated by a thin white line.

The foregoing examples illustrate some of the uses of computer programmes that produce theoretical electron micrographs. The programmes are capable of handling all the conditions of two-beam electron diffraction, the full geometry and anisotropic strain fields of many dislocation and stacking-fault configurations, and variations in photographic parameters. For images in which the information is contained in the topology of the image rather than its intensity, these programmes enable experimental images to be accurately matched. The examples of the use of the programme given here have been confined solely to the accurate reproduction of simple, and in some cases, well known, dislocation and fault configurations. However, the main usefulness of the programmes lies in the matching of computed and experimental images of less well understood defect configurations with the consequent determination of their geometry, their Burgers vectors, and their fault shears.

IV. ACKNOWLEDGMENTS

The author wishes to thank Dr. M. H. Loretto for allowing him to use the electron micrograph shown in Figure 4(*c*), and Dr. L. M. Clarebrough for the use of the electron micrographs in Figures 5(*a*) and 7. He also wishes to acknowledge many helpful discussions with Dr. A. K. Head, and to thank Dr. L. M. Clarebrough and Dr. A. J. Morton for their comments on the manuscript.

V. REFERENCES

HASHIMOTO, H., HOWIE, A., and WHELAN, M. J. (1962).—*Proc. R. Soc.* A **269**, 80.
HEAD, A. K. (1967).—*Aust. J. Phys.* **20**, 557.
HEAD, A. K., LORETTO, M. H., and HUMBLE, P. (1967).—*Phys. Status Solidi* **20**, 505.
HOWIE, A., and WHELAN, M. J. (1961).—*Proc. R. Soc.* A **263**, 217.
SILCOCK, J. M., and TUNSTALL, W. J. (1964).—*Phil. Mag.* **10**, 361.

THE LINEAR POLARIZATION OF RADIATION FROM JUPITER AT 6 CM WAVELENGTH

By D. Morris,* J. B. Whiteoak,* and F. Tonking*

[*Manuscript received January* 30, 1968]

Summary

At a wavelength of 6 cm the degree of linear polarization of the radiation from Jupiter is 0·076±0·002. The variation of the direction of polarization with longitude of the central meridian is consistent with the increased period of rotation determined by Komesaroff and McCulloch (1967). There is evidence of an asymmetrical beaming of the nonthermal radiation with longitude in addition to the latitude asymmetry that was detected previously by Roberts and Komesaroff (1965). The mean flux density normalized to a distance of 4·04 a.u. is 10·7±0·2 f.u. The small nonthermal contribution (3·7 f.u.) is further evidence for a high frequency cutoff in the synchrotron radiation; the thermal component corresponds to a brightness temperature of about 250°K.

I. Introduction

Observations of the linear polarization of the 6 cm radiation from Jupiter were obtained with the 210 ft radio telescope at Parkes during the period December 10–13, 1966. The receiver utilized polarization switching. Its initial stages were attached to the feed platform of the telescope and therefore rotated with the feed during polarization observations. The dual-mode feed consisted of a circular waveguide with an expanded entrance designed to provide a circular beam. This was followed by a ferrite waveguide switch which, operating at a frequency of 40 Hz, varied the direction of polarization of the incident radiation by ±45° before analysis by a linearly polarized probe. With a tunnel diode preamplifier the resulting system noise temperature was 900°K. The r.f. bandwidth was 200 MHz, centred at 4995 MHz. The amplitude of the 40 Hz signal at the detector output provided a measure of the linearly polarized flux, while the d.c. component contained a contribution corresponding to the total flux density. The relative gains of the a.c. and d.c. channels were established by the use of an argon discharge tube which provided linearly polarized radiation in the waveguide ahead of the ferrite switch. Both the switched and total power outputs were recorded on paper tape, and subsequent analyses were effected with a CDC 3200 computer.

II. Observations

A single polarization measurement consisted of a set of observations made with the orientation of the feed at a succession of angles at 30° intervals. A complete observation at each angle consisted of 50 sec integrations with the telescope directed near the source, at the source, and near the source, terminating with a measurement of a calibration signal from the discharge tube.

---

* Division of Radiophysics, CSIRO, Box 76, P.O. Epping, N.S.W. 2121.

Aust. J. Phys., 1968, 21, 337–40

The instrumental polarization, a function of feed orientation and zenith angle of the telescope, was obtained by observation of several bright HII regions. For the observations of Jupiter, the zenith angle ranged between 53° and 60° and the instrumental polarization was essentially constant at 0·6%. The approximate zero of the position-angle scale for the feed was established from observations of a linearly polarized c.w. signal radiated from the apex of the paraboloid. The scale of flux density is based on a value of 13·0 f.u. for Hydra A, as adopted by Kellermann (1964). The errors quoted do not contain any allowance for a systematic error in the flux density scale.

III. RESULTS

Figure 1 shows the variation of flux density, percentage polarization, and position angle of the electric vector as a function of the system III (1957·0) longitude of the central meridian of Jupiter (Morrison 1964). For comparison purposes, all flux densities refer to the standard distance of 4·04 a.u. The continuous curves represent sinusoids fitted to the observations by the method of least squares. For the analyses of percentage polarization and position angle, a second harmonic term has been fitted, although the limited number of observations barely justifies its inclusion. For the analysis of flux density it was felt that the accuracy of the observations did not warrant the addition of the higher harmonic, despite its observation at longer wavelengths. The computer programme for the fitting was kindly provided by Mr. M. M. Komesaroff.

The solutions to the observations are:

Normalized flux density $S = S_0+S_1\sin(l-\alpha_1)$;

Percentage polarization $M = M_0+M_1\sin(l-\beta_1)+M_2\sin 2(l-\beta_2)$;

Direction of polarization $P.A. = A_0+A_1\sin(l-\theta_1)+A_2\sin 2(l-\theta_2)$;

where

$$S_0 = 10\cdot 68\pm 0\cdot 04,\qquad S_1 = 0\cdot 07\pm 0\cdot 06,\qquad \alpha_1 = 140°\pm 40° ;$$

$$M_0 = 7\cdot 63\pm 0\cdot 14,\qquad M_1 = 0\cdot 52\pm 0\cdot 28,\qquad M_2 = 0\cdot 21\pm 0\cdot 28,$$

$$\beta_1 = 165°\pm 28°,\qquad \beta_2 = 65°\pm 53° ;$$

$$A_0 = 110\cdot 5\pm 0\cdot 6,\qquad A_1 = 8\cdot 8\pm 1\cdot 0,\qquad A_2 = 1\cdot 2\pm 1\cdot 0,$$

$$\theta_1 = 22°\pm 6°,\qquad \theta_2 = 113°\pm 40°.$$

Each calculated value is accompanied by its corresponding standard deviation.

(a) *Variation of Direction of Polarization with Longitude*

The mean direction of the maximum electric vector, 110°·5, differs from the orientation of the Jovian equator during the period of observations (105°·2), but the difference probably indicates a zero error in the calibration of position angle.

The amplitudes and phases of the harmonics determined from 11 cm observations by Komesaroff and McCulloch (1967) are:

$$\text{1st harmonic} \qquad A_1 = 9\cdot6\,(8\cdot8 \pm 1\cdot0), \qquad \theta_1 = 21\cdot8\,(22 \pm 6);$$
$$\text{2nd harmonic} \qquad A_2 = 1\cdot0\,(1\cdot2 \pm 1\cdot0), \qquad \theta_2 = 81\cdot9\,(113 \pm 40)\,.$$

The values in parentheses are the corresponding values from the present observations.

The agreement of the phases of the first harmonic is excellent. The present results therefore support the conclusion of Komesaroff and McCulloch that the period of rotation of Jupiter exceeds that adopted in the I.A.U. system III (1957·0) definition by $0^{\mathrm{s}}\cdot5$ (Morrison 1964). In contrast, Dickel (1967) obtained a lower first harmonic phase at 6 cm (14±10) and concluded that the period is within $0^{\mathrm{s}}\cdot2$ of the I.A.U. value. However, the uncertainties in his results do not preclude the existence of the larger period.

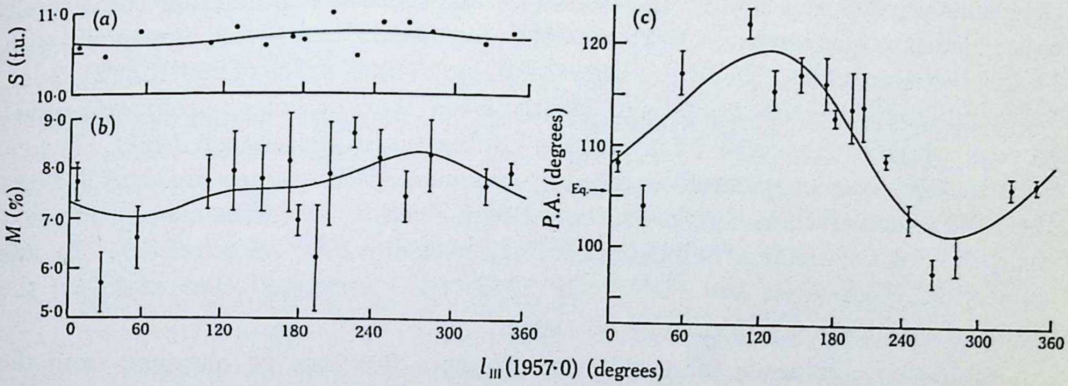

Fig. 1.—The 6 cm variation of (*a*) normalized flux density S, (*b*) percentage polarization M, and (*c*) direction of polarization $P.A.$ with longitude of the central meridian of Jupiter (l_{III}). Error bars represent standard deviations.

The first harmonic amplitude (8°·8±1°·0), assumed to correspond to the angle between the rotational and magnetic axes of Jupiter, agrees well with those determined by Komesaroff and McCulloch at 11 cm (9°·6) and Dickel at 6 cm (8°·3).

(*b*) *Variations of Intensity and Percentage Polarization with Longitude*

The present observations yield only an upper limit of about 3% for the peak-to-peak variation in the total flux from the planet. Previous observations at longer decimetric wavelengths (Roberts 1965; Roberts and Komesaroff 1965; Barber 1966) have shown a large second harmonic term due to a beaming of the radiation into the magnetic equator of Jupiter. A smaller first harmonic variation was also present, due in part to the tilt of the rotational axis of the planet to the plane of the sky and in part to a north–south asymmetry in the beaming. In the present case the tilt is small (0°·8), and any first harmonic is due to asymmetries in the beaming pattern.

The variation of percentage polarization with longitude shows evidence of first and second harmonic terms. As was the case in the observation of total flux, the presence of the first harmonic reflects an asymmetry in the beaming pattern. The similarity of the phases for the variations of flux and percentage polarization suggests that both types of observations are affected by the same asymmetry. Since the phase of the first harmonic (165°±28°) is not that expected of a north–south asymmetry alone (112°), the radiation pattern appears to be asymmetrical in longitude as well as latitude.

(c) *Thermal and Nonthermal Contributions to the Radiation*

The mean flux density corrected to 4·04 a.u. is 10·7±0·2 f.u., in good agreement with Dickel's (1967) value of 10·8±0·6 f.u. (Dickel also used the flux density scale established by Kellermann 1964.) The radiation is composed of nonthermal emission from the radiation belts and a thermal component from the planetary disk. Assuming that the degree of polarization of the nonthermal component is 0·22 at 6 cm, as applies at longer wavelengths, the nonthermal and thermal contributions are 3·7 and 7·0 f.u. respectively. The thermal contribution corresponds to a brightness temperature of about 250°K, a value in reasonable agreement with Dickel's estimate of 224°K at 6 cm, and with Berge's (1966) value of 260°K at 21·2 cm. The nonthermal flux density is significantly lower than at longer decimetric wavelengths, where a value of 6·7 f.u. prevails (Roberts and Komesaroff 1965). It confirms the high frequency cutoff reported by previous observers (see Fig. 1 of Roberts 1965). The actual value should be treated with caution, since the assumption that the degree of polarization is independent of frequency may be erroneous. In this connection, Komesaroff and McCulloch (1967) have suggested that at 11 cm the degree of polarization is decreasing secularly.

Additional evidence for the low nonthermal flux can be obtained from the observations of the beaming of the total flux at 6 cm. An upper limit of 3% variation has been set for the present measurements. At longer wavelengths, the variation is about 10%. Hence, if the nonthermal emission has a similar radiation pattern to that observed at 11 and 21 cm, then no greater than three-tenths of the total flux at 6 cm can be of nonthermal origin.

IV. ACKNOWLEDGMENTS

The authors wish to acknowledge the assistance in observation given by Miss J. K. Merkelijn, and useful discussions held with Mr. M. M. Komesaroff.

V. REFERENCES

BARBER, D. (1966).—*Mon. Not. R. astr. Soc.* **133**, 285.
BERGE, G. L. (1966).—*Astrophys. J.* **146**, 767.
DICKEL, J. R. (1967).—*Astrophys. J.* **148**, 535.
KELLERMANN, K. I. (1964).—*Astrophys. J.* **140**, 969.
KOMESAROFF, M. M., and MCCULLOCH, P. M. (1967).—*Astrophys. Lett.* **1**, 39.
MORRISON, B. L. (1964).—U.S. Naval Obs. Circ. No. 94.
ROBERTS, J. A. (1965).—*Radio Sci.* **69D**, 1543.
ROBERTS, J. A., and KOMESAROFF, M. M. (1965).—*Icarus* **4**, 127.

THE SOLAR WIND AND JOVIAN DECAMETRIC RADIO EMISSION

By O. B. Slee* and C. S. Higgins*

[*Manuscript received February* 9, 1968]

Summary

Spaced-receiver observations of the 19·7 MHz radio emission from Jupiter during 1963 and 1964 demonstrate that many of the so-called bursts with quasi-periods of 1–10 sec are caused by the sweeping of an interplanetary diffraction pattern across the receiver by the motion of scattering irregularities in the solar wind. Measurements made on these scintillations include arrival time differences at spaced receivers, scintillation rate, angular position scintillation, and the width of the scattered angular power spectrum.

The derived properties of the scattering irregularities are as follows. (1) The solar wind is radially directed with respect to the Sun and possesses an average velocity $V_S \sim 600$ km sec^{-1}. (2) R.M.S. deviations in the magnitude and direction of V_S, averaged over considerable path lengths through interplanetary space, are less than 20% and 5° respectively. (3) The scale size of the irregularities in electron density is approximately 150 km. (4) The scattering is strong at 19·7 MHz for all directions in the ecliptic plane; the r.m.s. phase modulation varies from about 1 rad near opposition to about 11 rad at an elongation of 20°. (5) The conclusions in (3) and (4) are consistent with an r.m.s. electron density that varies with heliocentric distance R (a.u.) according to the relation $\{\overline{(\Delta N)^2}\}^{\frac{1}{2}} \sim 0\cdot 2\,R^{-2}$ electrons cm^{-3}. (6) The irregularities in electron density with dimensions of hundreds of kilometres are relatively weak ($\sim 10\%$) in comparison with the average electron density.

Theoretical restrictions on source size are used to derive an upper limit of $\sim 0\cdot 6$ sec of arc to the angular diameter of the decametric source on Jupiter. It is shown that the intensity scintillations are significantly reduced when the line of sight passes within 60° of the Sun; if this is due to the finite source size, a lower limit of $\sim 0\cdot 1$ sec of arc can be assigned to the source diameter.

I. Introduction

Shortly after the discovery of the Jovian decametric radio emission by Burke and Franklin (1955) it was realized that some, if not all, of the intensity variations may be imposed on an essentially steady intrinsic emission by propagation effects between the planet and observer. Such considerations led Gardner and Shain (1958) to record bursts simultaneously at sites separated by 25 km, observations that showed the presence of considerable differences between the time variations at the two receivers. Subsequent spaced-receiver experiments by Smith *et al.* (1960) and Douglas and Smith (1961) over baselines varying in length from 15 to 7000 km showed that all degrees of burst correlation could be experienced; the differences were usually ascribed to the effects of ionospheric scintillations which, from discrete radio source observations, were known to be poorly correlated over distances greater than about 5 km.

---

* Division of Radiophysics, CSIRO, Box 76, P.O. Epping, N.S.W. 2121.

Aust. J. Phys., 1968, **21**, 341–68

The valuable work of Douglas (1964) has been instrumental in changing our basic notions on the origins of the Jupiter bursts. Using receivers spaced at distances up to 100 km he was able to detect a systematic difference between the burst arrival times; this led to the conclusion that much of the burst structure is not an intrinsic property of Jupiter but is due to the movement of an interplanetary diffraction pattern across the Earth's surface.

Slee and Higgins (1963) began spaced-aerial observations over a 32 km baseline in 1962 with the primary object of performing angular size measurements of the burst sources using a radio-linked phase-sensitive interferometer. An essential part of the measurement was the recording of the total power signals received at the spaced aerials using receiving systems with almost identical characteristics. The experiment was continued on a more comprehensive scale during 1963 and 1964 with baselines extending from 17 to 200 km.

Some of the results of this experiment with emphasis on the angular size observations have been published by Slee and Higgins (1965, 1966). The present paper considers more aspects of the Jupiter burst phenomenon, including burst arrival times, burst rate, angular position scintillations, and apparent angular size, and uses the results to derive some useful information about the interplanetary diffraction patterns and the electron irregularities in the solar wind.

One important advantage of the Jupiter burst method of observing the interplanetary medium lies in its ability to detect the scattering effects with relatively unsophisticated receivers and physically small aerial systems over a large range of heliocentric distances close to the ecliptic plane; this is brought about by the fortunate circumstance that Jupiter happens to be a very powerful low frequency radio source of very small angular dimensions. There are, however, a few disadvantages of this technique when compared with corresponding observations made with the extragalactic radio sources of very small angular size, generally at much higher frequencies. Firstly, the Jupiter decametric transmission appears to be inherently intermittent, with the result that one is limited to relatively short samples of the diffracting properties of the solar wind; typically, with a fixed receiving aerial at 20 MHz one could expect to see the Jupiter bursts for 1 hr every 3 days. Secondly, investigations of the interplanetary medium are limited to those regions close to the ecliptic plane. Finally, another element of uncertainty is introduced into the interpretation of the diffraction patterns in terms of the physical parameters of the solar wind by the fact that the source is located at a finite distance behind the diffracting irregularities; this results in the application of a generally unknown magnification factor to the diffraction scale size and pattern velocity. However, this may not be as disadvantageous as it first appears, since a comparison of these measurements from both Jupiter and extragalactic source observations should result in a determination of the magnification factor and hence of the location of the effective diffracting region along the line of sight.

The scheme of the present paper is as follows. In Section II the long baseline equipment and observational techniques are described, while Section III discusses the general appearance of the present Jupiter records and in particular the burst correlation at separated sites. Section IV introduces some relevant aspects of the diffraction theory, the results of which will be used to derive approximate physical characteristics for the scattering irregularities using their observed effects on the radiation reaching the ground. In Section V we demonstrate the validity of our measurements of the relative burst arrival time differences, which we then use to deduce the drift velocities of the diffraction patterns. Section VI introduces the topic of burst rate, which is shown to change systematically with Jupiter's elongation and to provide additional information on the pattern velocities. Section VII discusses the methods available for measuring the diffraction scale and deduces numerical values for a number of events. The question of the phase deviations associated with the amplitude scintillations is treated in Section VIII and measurements of the interferometer fringe phases are used to show that the r.m.s. phase deviations are also dependent on Jupiter's elongation. Finally, in Section IX, we attempt to use this information and that from other related experiments to deduce the physical state and dynamics of the solar wind.

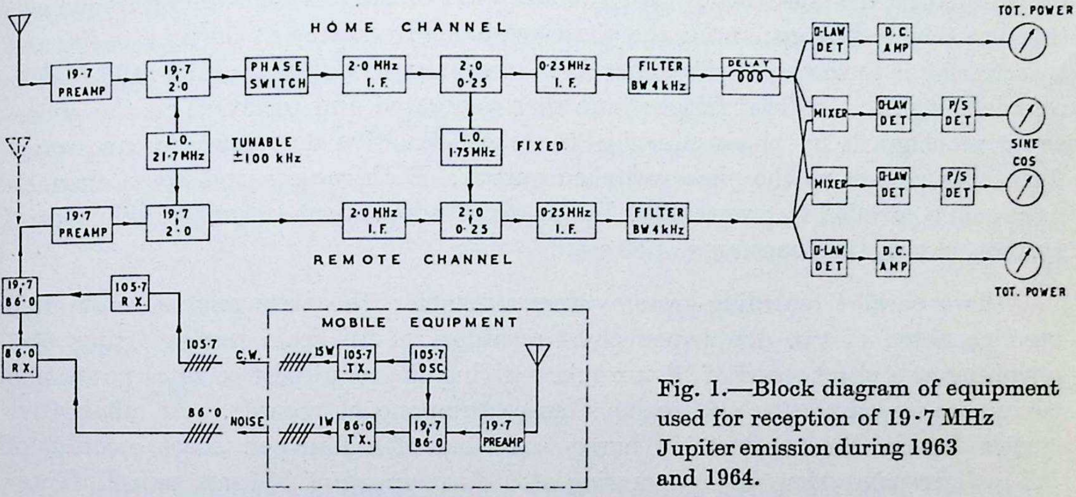
HOME CHANNEL
19·7 PREAMP
19·7 2·0
PHASE SWITCH
2·0 MHz I.F.
2·0 0·25
0·25 MHz I.F.
FILTER BW 4 kHz
DELAY
L.O. 21·7 MHz
TUNABLE ±100 kHz
L.O. 1·75 MHz
FIXED
Q-LAW DET
D.C. AMP
TOT. POWER
MIXER
P/S DET
SINE
COS
REMOTE CHANNEL
19·7 86·0
86·0 RX.
105·7 R X.
105·7
C.W.
86·0
NOISE
MOBILE EQUIPMENT
15W
1W
105·7 TX.
105·7 OSC
86·0 TX.
19·7 86·0
19·7 PREAMP

Fig. 1.—Block diagram of equipment used for reception of 19·7 MHz Jupiter emission during 1963 and 1964.

II. Equipment and Observational Techniques

Figure 1 is a block diagram of the equipment at both the remote and home site ends of the baseline; it excludes the power supplies, noise-diode calibrators, and pulse generation circuits. It consists basically of two double conversion superheterodyne receivers that use common local oscillators, the first being tunable over a band of ±100 kHz. Considerable attention was directed to the tuning of the two 4 kHz bandwidth filters which ultimately determine the centre frequencies and bandpasses of the receivers. The square-law detectors, phase-sensitive detectors, d.c. amplifiers, and chart recorders had identical gain and response time characteristics, so that for all practical purposes the responses of the two receivers were closely the same. The equipment at the remote site was mobile and included a 19·7 MHz preamplifier of 150 kHz bandwidth. Its output was upconverted to 86·0 MHz and transmitted, together with the 105·7 MHz c.w. upconversion signal, to the home site, where the noise signal was reconverted coherently to 19·7 MHz. Using transmitting and receiving Yagi aerials, with power gains of about 10, it was found that transmitted powers of 1·5 W r.m.s. noise and 15 W c.w. were sufficient to ensure signal to noise ratios in excess of 100/1 at the final detector output. At the shorter spacings these power levels were high enough to saturate the receivers, so that it was found necessary to insert attenuators in the radio-link receiving system; these were adjusted to ensure that approximately the same powers were delivered to the radio-link receivers on all spacings.

The overall noise figures of the two channels were about three in power, but of course in operation the effective noise figures were determined by the high cosmic background temperature of about 50 000°K. Identical high power noise diodes were located at each end of the baseline and were used to perform total power calibrations by injecting random noise up to twice the cosmic background level. The calibration from the remote site was recorded at the home site and hence calibrated the complete remote channel. In addition to calibrating the total power channels, we were able to check the gains of the interferometer mixing and phase-sensitive detector circuits by modulating the noise diodes with a square wave of the phase-switching frequency; this was achieved by generating the phase-switching frequency at the remote site and transferring it to the home site in the form of a pulse modulation on the 105·7 MHz reference signal. Artificial fringes were then generated and recorded on the phase-sensitive channels by phase sweeping the phase-sensitive detector reference waveform with respect to the phase-switched output. Both remote and home channels were gain controlled to preset levels by means of independent automatic gain control systems having time constants of 60 sec.

Two parallel recording systems were available; the arrangement most often used consisted of two double-pen chart recorders of full-scale response time $0^{s}\cdot 5$ operating at a chart speed of 76 mm min^{-1} giving the required two total power and two phase-sensitive (sine and cosine Fourier component) records. An alternative system for the shorter duration bursts consisted of a four-pen chart recorder of full-scale response time $0^{s}\cdot 02$ operating at a chart speed of 254 mm min^{-1}. These chart speeds were found adequate to resolve the majority of the burst structure and to provide a reasonable spacing for the interference fringes, even on the longest baseline.

A number of aerial configurations were used over the 2 yr recording interval; the usual arrangement was two pairs of $\lambda/2$ horizontally polarized dipoles at each site with one pair orientated with axes north-west–south-east and the other pair rotated by 90°, a configuration that allowed observation of Jupiter for up to 8 hr near upper transit. The dipoles in each pair were parallel and spaced $\lambda/4$ to $\lambda/2$ above ground and so phased as to achieve maximum response at the midpoint of the hour-angle coverage of each dipole. At the home site the aerial arrays were duplicated so that the radio link could be disconnected and the outputs of two aerial arrays spaced only a few metres apart could be applied to the home equipment in order to obtain a zero baseline reference point for the angular size measurements.

During the observing interval we used the three baselines shown in Figure 2, which is a map of that part of eastern Australia within a few hundred kilometres of

Sydney. The baselines were of lengths 17·4, 85·5, and 200·0 km respectively and were orientated generally in a north-northeast–south-southwest direction; this coincided with the direction of the relatively flat coastal plain bordered on one side by a mountain range with peaks up to 1600 m above sea level and on the other by the Pacific Ocean. By placing our extreme southern and northern sites on relatively high (750 m) outcrops of this mountain range, we achieved line-of-sight transmission across the coastal plain for the radio links.

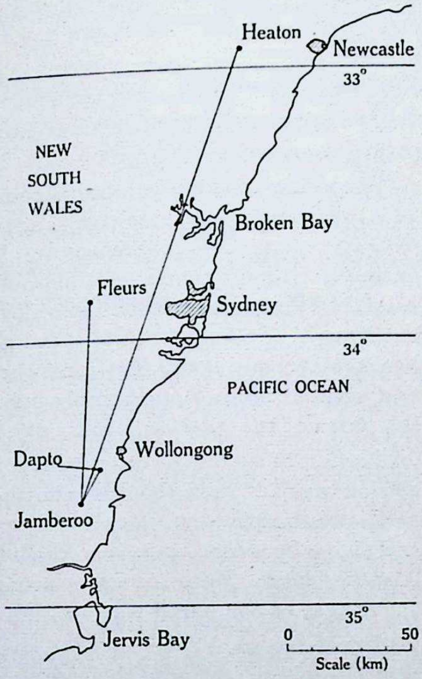

Fig. 2.—Sketch map of the eastern Australian coast near Sydney showing the locations of the receiving sites used during the Jupiter long baseline experiment. The home site was situated at Jamberoo.

Both the home and remote stations were manned during a Jupiter observation, since it was necessary to perform noise-diode calibrations at both sites before and after each recording session, which typically lasted about 8 hr. Our observations were confined to the interval 2300 to 0700 hr local time. The former limit was imposed on us by the fact that our radio link operated within the television bands, so that we could neither transmit nor receive during the normal television service hours. Observations usually ceased at dawn because of the rapidly increasing level of interference. This asymmetry in the observations with respect to local midnight resulted, unfortunately, in an almost complete lack of data after opposition during the apparitions of both 1963 and 1964.

Because of the difficulties of manning simultaneously two stations, often in rather remote mountain areas, we confined our observations to those nights on which there was a reasonable probability of Jupiter decametric emission during the observing period; these nights, usually two or three weekly, could be predicted from the published statistical data on the probability of burst occurrence as a function of Jupiter's system III longitude.

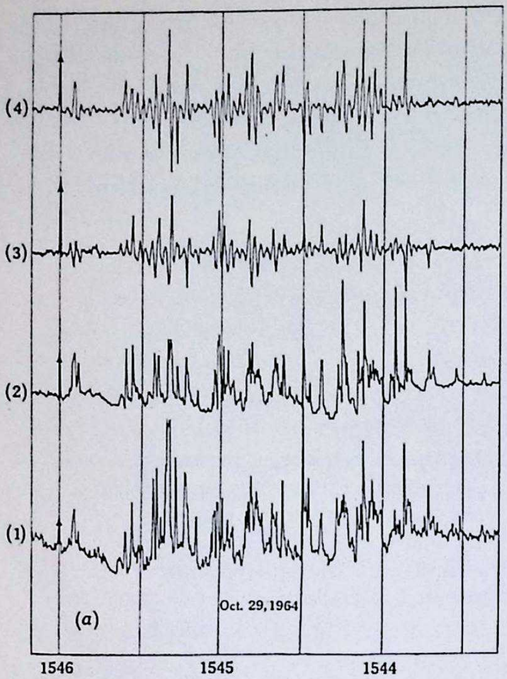

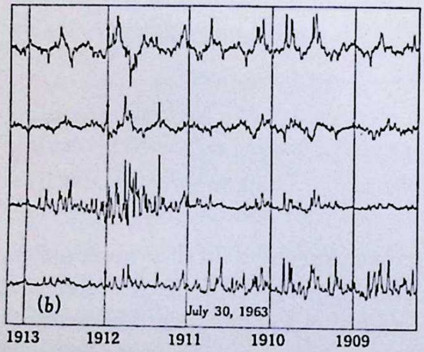

Fig. 3.—Examples of 19·7 MHz chart recordings obtained during the long baseline observations. The four traces in each figure refer respectively to (from the bottom): (1) total power from the outstation; (2) total power from the home station; (3) and (4) sine and cosine components of the interference pattern. At times of strong Jovian emission the automatic gain control produces a depression of the baselevel which is noticeable on some of the total power traces.

(*a*) Section of noise storm showing good correlation between burst amplitudes at sites 200 km apart. Regular fringes of correct period are also present.

(*b*) Recording showing poor amplitude correlation between bursts received at sites 85·5 km apart. The differences are due to uncorrelated ionospheric scintillations that vary the relative amplitudes at a slow rate but leave the individual Jovian bursts with similar relative shapes. The ionospheric scintillations are not appreciably perturbing the phase of the interferometer pattern.

(*c*) Portion of a noise storm recorded when Jupiter was 26° from the Sun, showing the characteristic poor correlation in amplitude and shape between bursts recorded at sites 85·5 km apart. Note the irregular nature of the fringes as compared with (*a*), (*b*), and (*d*).

(*d*) Bursts recorded over the 85·5 km baseline near opposition, showing the characteristic longer durations. The bursts at the separated sites possess similar shapes and give rise to fringes with a high degree of regularity.

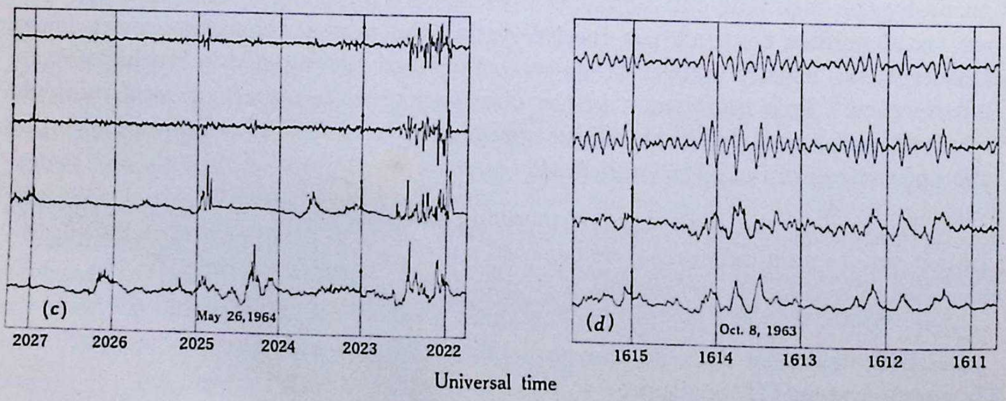

III. APPEARANCE OF RECORDINGS

Figure 3(*a*) shows a short section of a Jupiter noise storm recorded over the 200 km baseline. The four chart recordings normally taken at the home site have been carefully traced and aligned in time as accurately as possible. Beginning at the bottom of the figure, the fourth trace is a total power record of the bursts received at the remote station and transmitted to the home site over the radio link; the third trace shows the corresponding total power recording of the bursts arriving at the home site. The upper two traces show the sine and cosine Fourier components of the interferometer pattern formed by multiplying the signals in a phase-switched system.

The degree of correlation between the total power channels of Figure 3(*a*) is probably close to the highest observed over our long baselines, although there were probably some slightly better examples on the shorter 85·5 km spacing. This high degree of correspondence between burst shapes and amplitudes was, however, not usually maintained for long intervals of time; after perhaps 10 min of such recording the correlation would sometimes deteriorate to the situation shown in Figure 3(*b*). Here close inspection shows that although the individual bursts are present at both sites, their relative amplitudes can be markedly different. It would appear that the Jovian burst amplitude is here being deeply modulated at a relatively low frequency by completely uncorrelated ionospheric scintillations at the two sites. The short sections of record shown in Figures 3(*a*) and 3(*b*) are extreme cases and more often a degree of correlation intermediate between the two would be present.

In addition to burst amplitude decorrelation we have obtained some recordings in which there are relative changes on a time scale much shorter than the normal ionospheric scintillation periods of 30–60 sec. These changes take place within periods of a second or so and hence destroy the correspondence between individual burst shapes. Such a condition exists on the recordings shown in Figure 3(*c*), which applies to observations made when Jupiter was only 26° from the Sun; similar recordings were obtained on all six occasions in 1964 when bursts were observed while Jupiter was less than 50° from the Sun. Attention is also directed to the high degree of irregularity in the interferometer fringes, characteristic of this type of record.

In contrast to the high burst rate and general irregularity of fringes depicted in Figure 3(*c*), the much slower burst rate and high regularity of fringes characteristic of our recordings near opposition are shown in Figure 3(*d*); the typical appearance of bursts in groups, each of about 60 sec duration, is evident on these traces.

Measurements of burst arrival time differences at separated sites were necessarily restricted to those relatively infrequent occasions on which the total power recordings were well correlated in amplitude and shape; however, we were not necessarily restricted to the use of such highly correlated records as shown in Figure 3(*a*), since the presence of moderately intense ionospheric scintillations resulted only in rather slow relative intensity changes which did not affect our ability to identify the same bursts on the two total power traces. As Figure 3(*c*) shows, interferometer fringes could be recorded even at times of poor burst shape and amplitude correlation so that measurements of angular size and angular position are practicable for most portions of a Jupiter noise storm.

IV. Some Relevant Aspects of the Diffraction Theory

In this discussion it is assumed that the irregularities in refractive index that are responsible for the scattering are isotropic, so that the one-dimensional forms of the functions describing the complex amplitude of the radio wave and its autocorrelation coefficient across any plane transverse to the direction of propagation will be satisfactory.

The existing theory assumes that the irregularities are confined to a short section of the path between the source and observer. This ensures that, while the wave is in the scattering region, the variations in complex amplitude are composed only of phase fluctuations. The one-dimensional complex amplitude of the wave is defined by the equation

$$\mathbf{f}(x) = A(x)\exp\{\mathrm{i}\phi(x)\}, \tag{1}$$

where $A(x)$ and $\phi(x)$ are respectively the real amplitude and phase distributions across a plane transverse to the direction of propagation.

In the diffraction process of interest here, $\mathbf{f}(x)$ is a random function and its spatial variations across any transverse plane are conveniently described by its autocorrelation function

$$\rho_f(\xi) = \frac{[\mathbf{f}(x)\,\mathbf{f}^*(x+\xi)]_{\mathrm{av}} - \{[\mathbf{f}(x)]_{\mathrm{av}}\}^2}{[\mathbf{f}(x)\,\mathbf{f}^*(x)]_{\mathrm{av}} - \{[\mathbf{f}(x)]_{\mathrm{av}}\}^2}, \tag{2}$$

where the averages are taken over all values of x. The correlation functions for the real amplitude, intensity, and phase fluctuations are defined in a similar way.

(a) *Mean Square Phase Modulation* ϕ_0^2

Bramley (1954) has investigated the theory of scattering in an extended medium in which the scale sizes and electron contents of the irregularities are statistically similar for all samples of the region. It is assumed that the values of electron density are normally distributed and that their spatial distribution is described by an isotropic Gaussian autocorrelation function, $\rho_{\Delta N}(r) = \exp(-r^2/L^2)$, where L is the scale size. The resulting complex amplitude across a plane immediately below the diffracting region consists of a real amplitude that is independent of x and a phase $\phi(x)$ with a normal distribution of phase deviations having the mean square value

$$\phi_0^2 = (\pi^{\frac{1}{2}}e^4\lambda^2/m^2c^4)\,LZ\,\overline{(\Delta N)^2}, \tag{3}$$

where $\overline{(\Delta N)^2}$ is the mean square deviation of electron density, e and m are the electronic charge and mass, λ is the wavelength of the radio wave, and c is the velocity of light.

If the properties of the scattering medium vary as the wave propagates through it, that is, L and $\overline{(\Delta N)^2}$ are functions of Z, it appears legitimate to subdivide the region into a series of thin slabs, each of which contributes a mean square phase deviation given by equation (3). The total mean square phase deviation is then computed by summing the separate contributions so that

$$\phi_0^2 = \frac{\pi^{\frac{1}{2}} e^4 \lambda^2}{m^2 c^4} \int_Z L(Z)\ \overline{[\Delta N(Z)]^2}\, \mathrm{d}Z\,. \tag{4}$$

(b) *Angular Spectrum of Scattered Radiation*

A bundle of parallel rays from a distant point source is scattered into a cone with axis corresponding to the original direction of propagation and semi-opening angle dependent upon the scale and strength of the irregularities in electron density. The angular power spectrum $| \mathbf{F}(S) |^2$ and autocorrelation function $\rho_f(\xi)$ are Fourier transforms of each other and are independent of the distance from the diffracting region. Hence, although the complex amplitude changes with distance, a measurement of its autocorrelation function or angular power spectrum on the ground plane is sufficient to define the spatial distribution of $\mathbf{f}(x)$ over a plane directly below the scattering region.

The relationship of $\rho_f(\xi)$ and $| \mathbf{F}(S) |^2$ to the scale size of the electron irregularities in the diffracting region has been presented rather clearly by Ratcliffe (1956). If the irregularities possess a Gaussian autocorrelation function

$$\rho_{\Delta N}(r) = \exp(-r^2/L^2)\,,$$

then the autocorrelation function for the complex amplitude is of the form

$$\rho_f(\xi) = \exp(-\xi^2/\xi_0^2)$$

and the angular power spectrum is described by

$$| \mathbf{F}(S) |^2 = \exp(-S^2/S_0^2)\,.$$

The relationships between the scale sizes L, ξ_f, and S_0 depend upon the strength of the scattering:

(i) *Weak Scattering*, $\phi_0^2 \ll 1\ rad^2$

$$S_0 = \lambda/\pi L\,, \qquad \xi_f = L\,. \tag{5}$$

(ii) *Strong Scattering*, $\phi_0^2 \geqslant 1\ rad^2$

$$S_0 = \phi_0(\lambda/\pi L)\,, \qquad \xi_f = L/\phi_0\,. \tag{6}$$

It is of interest to note that the width of the angular power spectrum increases in proportion to λ for weak scattering, but as λ^2 for strong scattering. In addition, S_0 in equations (5) describes the half-width to $\exp(-1)$ of a relatively weak halo surrounding a bright undeviated component; for strong scattering most of the incident power is scattered into a spectrum whose half-width is measured by S_0 in equations (6).

The determination of ξ_f or S_0 involves measurements of both the real amplitude and phase distributions across the ground plane. This is most conveniently performed by means of a phase-sensitive interferometer with variable spacing between the aerials. Ratcliffe (1956) has demonstrated that the fringe visibility function $V(\xi)$ is identical with $\rho_f(\xi)$. Hence the spacing of the interferometer aerials for which the fringe visibility has been reduced to exp(−1) is a measure of ξ_f.

(c) *Interferometer Measurements of* ϕ_0^2

It is important to develop an experimental method of estimating the mean square phase modulation. Not only does a knowledge of ϕ_0^2 allow a determination to be made of the so-called scattering function,

$$\int_Z L(Z)\ \overline{[\Delta N(Z)]^2}\,\mathrm{d}Z\,,$$

given by equation (4) but also, for strong scattering, its value is needed before the scale size of the electron irregularities can be deduced from the interferometer measurements of the angular power spectrum.

The phase of the interferometer fringes undergoes random changes that are related to the value of ϕ_0^2. For a distant source, the mean square phase difference $\overline{(\Delta\phi)^2}$ between the signals at the spaced receiving sites (the quantity measured from the displacements of the fringes from their unperturbed positions) is given by

$$\overline{(\Delta\phi)^2} = 2\{1-\rho_\phi(\xi)\}\phi_0^2\,, \tag{7}$$

where $\rho_\phi(\xi)$ is the autocorrelation function for the phase deviations across the ground.

It may be thought that a lack of knowledge of $\rho_\phi(\xi)$ would prevent a determination of ϕ_0^2 from the measured value of $\overline{(\Delta\phi)^2}$. However, the approximate scale length of the phase fluctuations is known from the measurements of the complex amplitude scale; in addition, provided the interferometer spacing is long enough to ensure that the phase fluctuations are not highly correlated then the exact value of $\rho_\phi(\xi)$ is not important, since under these conditions $\overline{(\Delta\phi)^2} \to 2\phi_0^2$.

(d) *Intensity Fluctuations across the Ground Plane*

Interference between the components of the angular spectrum at the ground plane gives rise to a distribution of real amplitude $A(x)$. Previous experiments with interplanetary scintillations have been limited to obtaining a measure of the distribution of intensity $A^2(x)$, which is assumed to be adequately specified by its mean square fluctuation and a Gaussian autocorrelation function

$$\rho_{A^2}(\xi) = \exp(-\xi^2/\xi_0^2)\,.$$

The distance along the ground ξ_0 for which the correlation is reduced to exp(−1) is known as the scale length of the intensity fluctuations.

Bramley and Young (1967) have derived some general results for the diffraction of a plane wave by a phase-changing screen containing irregularities with a Gaussian autocorrelation function. For strong scattering ($\phi_0^2 \geqslant 1$), the case that is of greatest interest in these observations, the intensity fluctuations across the ground plane at distance Z from the diffracting region are fully developed when

$$2\lambda Z/\pi L^2 \geqslant 1\,. \tag{8}$$

The scale length of the intensity fluctuations varies considerably, but with $\phi_0^2 \geqslant 1$ and equation (8) satisfied so that the observer is in the Fraunhofer region

$$\xi_0 = L/\sqrt{2}\,\phi_0\,. \tag{9}$$

(*e*) *Effect of Spherical Wave Front*

Ratcliffe (1956) and Pisareva (1958) have discussed the case of an observer and point source distant Z_1 and Z_2 respectively from the diffracting screen. They show that the actual distance should be replaced by an equivalent distance $Z = Z_1 Z_2/(Z_1+Z_2)$ and the problem treated in the same manner as that of a point source at infinity.

One of the more important consequences of this modification to the theory is the increase in the scale of the diffraction patterns relative to those for an incident plane wave. The scale lengths for both the complex amplitude and intensity variations across the ground are increased by the factor $(Z_1+Z_2)/Z_2$.

(*f*) *Finite Angular Size of Source*

Little and Hewish (1966) have shown that the mean square intensity fluctuation due to a source of finite angular size is less than that from a point source. Provided the observer is in the Fraunhofer region so that equation (8) is satisfied, the r.m.s. intensity fluctuation has been reduced to half that of a point source when

$$\xi_0/Z\psi_0 \approx 1\,, \tag{10}$$

where ξ_0 is the scale length for the intensity fluctuations, Z is the distance to the scattering region, and ψ_0 is the angular radius of the source to $\exp(-1)$.

(*g*) *Measurements of ξ_0 by the Method of the Drifting Pattern*

This method relies on a knowledge of the drift velocity V of the intensity diffraction pattern across the ground; the velocity may be computed from measurements of the differences between the arrival times of diffraction peaks at two or more points on the ground within the scale length ξ_0.

If the diffraction pattern remains relatively unchanged as it drifts, the observations of the temporal autocorrelation function $\rho(\tau)$ at one of the receivers can be converted into a spatial autocorrelation function $\rho_A{}^2(\xi)$ by writing $\xi = V\tau$. Often, to avoid the difficulties of performing the autocorrelation analysis on analogue recordings, it is more convenient to measure the average time interval $\bar{\tau}$ between the arrival of successive diffraction peaks. This yields the average distance $V\bar{\tau}$ between diffraction peaks, which is shown by Ratcliffe (1956) to be related to ξ_0 by the expression

$$\xi_0 = (2\cdot 6)^{-1}\, V\bar{\tau}\,. \tag{11}$$

(*h*) *Limitations of Thin Screen Theory*

For Jovian decametric observations it appears that the requirements of the existing diffraction theory may not be satisfied. Both the source and observer are embedded in the solar wind, whose scattering properties will, no doubt, vary considerably along the line of sight.

The application of equation (8), with $\lambda = 15$ m and $L = 150$ km, to a thin slab of the diffracting medium shows that amplitude fluctuations are well developed within a distance of 0·1 a.u. Under these conditions, successive slabs of the solar wind are illuminated by waves possessing spatial variations of amplitude as well as phase; there is, as yet, no theoretical solution of such a problem. Nevertheless, there are good reasons for believing that the electron content of the irregularities in the solar wind changes rapidly with heliocentric distance, with the result that a relatively short section of the path contributes most of the scattering. Consequently, it appears probable that deductions about the scale length, electron density, and velocity of the irregularities based on the thin screen theory are at least qualitatively correct.

V. TIME SHIFTS BETWEEN BURSTS AT SEPARATED SITES

We have examined our recordings closely for periods of good total power correlation, with the result that we have selected 12 storms from a total of 39 for burst arrival time measurements.

The measurements were made by identifying a common fine structural feature for each burst event on the two total power records; the displacements of this feature from the nearest convenient time marks were then measured with an accurately graduated ruler to $\pm 0 \cdot 1$ mm. This procedure was repeated for every well-correlated burst recorded in the noise storm. In practice, after the measurement of the selected structural detail on one trace, the same feature was measured on the other, thus ensuring that the ruler zero was set independently for each burst.

The differences between the pairs of measurements were then subjected to a statistical test aimed at determining whether bursts for the storm as a whole showed a systematic tendency to arrive first at one site or the other. To do this the statistic chi-squared (χ^2), associated in this case with one degree of freedom, was calculated on the hypothesis that equal numbers of time shifts of both signs could be expected by chance. Table 1 summarizes the conclusions as to the validity of the measured time displacements. It can be seen that for 10 of the 12 storms, the value of χ^2 is significantly higher than would be expected for a random distribution of burst arrival time differences. Figure 4 shows several delay histograms that depict more clearly the distribution of measured time shifts on four of these occasions; it is apparent that the distributions are approximately Gaussian, so that their average values and r.m.s. dispersions provide meaningful information. The average time displacements $\overline{\Delta t}$ and their r.m.s. errors are listed in column 4 of Table 2. On all occasions except August 31, 1964 the bursts were received first at the north-east end of the baseline.

TABLE 1

VALIDITY OF TIME DIFFERENCES

Date of Observation	Number of Bursts				
	Total Measurable	Time Shift of S. Station relative to N. Station*			χ^2 †
		+	−	0	
1963 Sept. 7	35	7	20	8	8·08
9	55	4	41	10	37·20
Oct. 8	47	13	31	3	7·85
1964 July 13	43	20	15	8	0·90
23	33	7	19	7	7·00
28	47	10	30	7	5·88
Aug. 4	70	19	32	19	4·53
11	23	4	19	0	9·80
31	61	39	16	6	10·65
Sept. 24	96	42	37	17	1·50
Oct. 18	60	7	51	2	34·40
29	121	23	78	20	35·80

* +, Burst arrival earlier at southern station; −, burst arrival later at southern station; 0, no difference.

† Calculated by apportioning the "0" shift number to the other two categories so as to preserve the existing ratios. χ^2 would exceed 3·84 by chance in 5% of similar trials and 6·63 in 1% of similar trials.

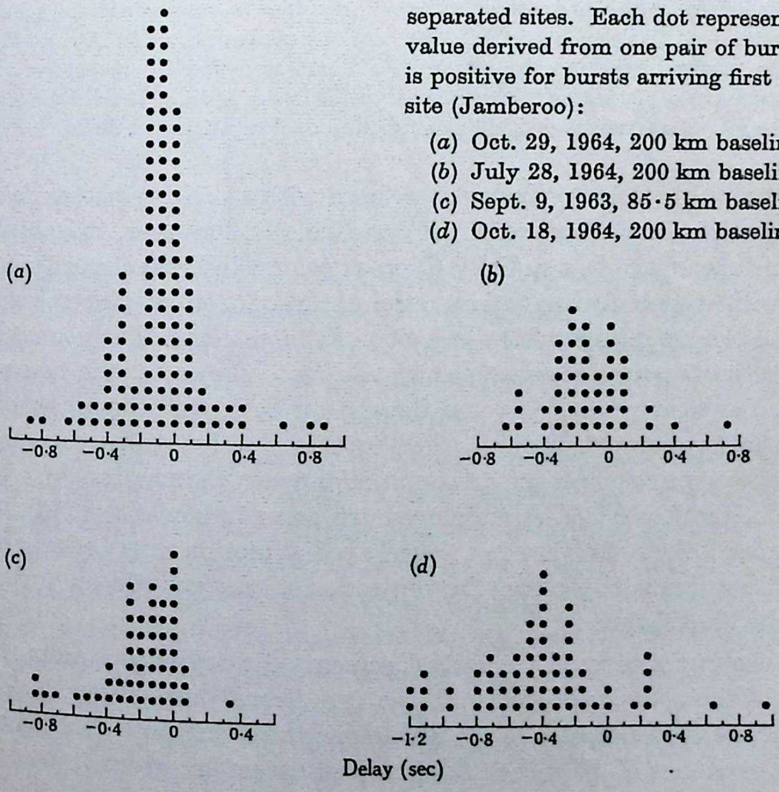

Fig. 4.—Histograms of the measured values of delay between the arrival times of bursts at separated sites. Each dot represents the delay value derived from one pair of bursts. The delay is positive for bursts arriving first at the home site (Jamberoo):

(*a*) Oct. 29, 1964, 200 km baseline
(*b*) July 28, 1964, 200 km baseline
(*c*) Sept. 9, 1963, 85·5 km baseline
(*d*) Oct. 18, 1964, 200 km baseline

The existence of systematic differences in burst arrival times at separated receivers suggests that much of the fine structure in Jovian bursts is not due to the emission mechanism but rather is imposed on the radiation during propagation. Such effects can be produced by a nonuniform distribution of radio brightness that drifts across the Earth's surface with a well-defined velocity. There is good evidence from the analysis of spaced-receiver observations of Jupiter by Douglas and Smith (1967) that the source of such brightness fluctuations lies in the diffracting properties of electron irregularities in the solar wind; the velocity of the latter is responsible for the transport of the resultant diffraction patterns across the Earth's surface.

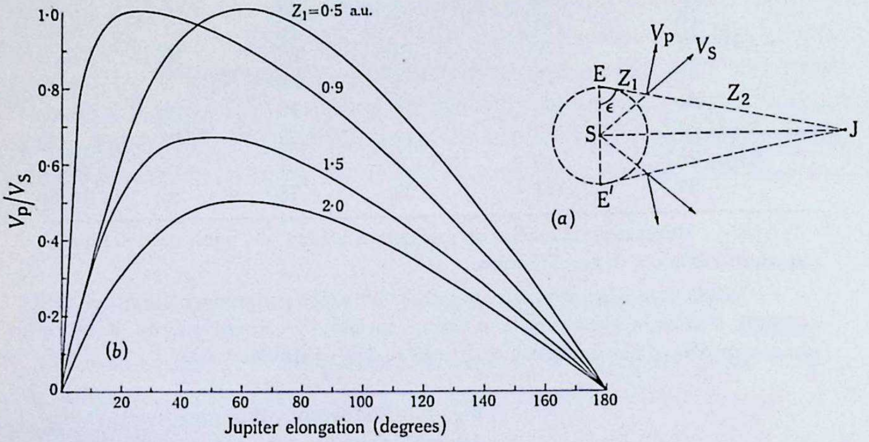

Fig. 5.—Geometry of the scattering problem in the ecliptic plane, assuming a radial solar wind V_S, is shown in (*a*). The Sun is at S, the Earth at E, and Jupiter at J; Z_1 and Z_2 are the distances to the diffracting layer from the Earth and Jupiter respectively, and V_p is the component of the solar wind transverse to the line of sight at the diffracting layer. The curves in (*b*) show the ratio V_p/V_S as a function of elongation and distance Z_1.

It is apparent that the velocity vector associated with a drifting pattern cannot be determined from observations over a single baseline. If, however, it is assumed that the diffraction takes place in a radially directed solar wind, thus specifying the direction of drift with respect to the baseline, the observed time displacements can be used to compute the magnitude of the velocity of the pattern. The geometry of the proposed model is shown in Figure 5, which illustrates how V_p, the transverse component of a radial solar wind V_S, would depend on both the elongation of the planet and the distance along the line of sight to the effective diffracting region. Except for the few days near opposition and conjunction when the small angle between the orbital planes of the Earth and Jupiter produces some important modifications and minor departures of the solar wind from purely radial motion may be important, V_p will be aligned approximately along the projection of the ecliptic on the plane perpendicular to the line of sight.

In order to use our measured time displacements for velocity computations, we have for each of the occasions listed in Table 2 projected both the ecliptic and baseline onto the plane perpendicular to the line of sight and computed the included angle θ; the average values of θ for each Jovian noise storm are given in column 3 of Table 2. The average velocity of the diffraction pattern across the plane perpendicular to the line of sight at the Earth, $\overline{V}'_{\mathrm{p}}$, was then obtained from the expression

$$\overline{V}'_{\mathrm{p}} = (S\cos\theta)/\overline{\Delta t},$$

where S is the spacing between receivers, $\overline{\Delta t}$ is the average arrival time difference, and it is assumed that the drifting brightness distributions are approximately circular. Values of $\overline{V}'_{\mathrm{p}}$ were deduced by this method on 10 occasions and are listed in column 5 of Table 2.

TABLE 2

MEASURED PARAMETERS OF DIFFRACTION PATTERNS

Elongation of Jupiter ϵ, average angle between baseline and ecliptic θ, average relative time shift $\overline{\Delta t}$, corrected average drift velocity of diffraction pattern $\overline{V}'_{\mathrm{p}}$, average burst spacing $\bar{\tau}$, average intensity of diffraction scale ξ_0

(1) Observation Date	(2) ϵ (deg)	(3) θ (deg)	(4) $\overline{\Delta t}$ (sec)	(5) $\overline{V}'_{\mathrm{p}}$ (km sec^{-1})	(6) $\bar{\tau}$ (sec)	(7) ξ_0 (km)
1963* Sept. 7	146	101·4	0·08±0·04	204	4·43±0·02	348
9	148	109·0	0·19±0·03	148‡	3·80±0·02	216‡
Oct. 8	179	116·5	0·34±0·10	111‡	7·66±0·06	327‡
1964† July 23	69	111·8	0·11±0·04	675‡	1·86±0·01	483‡
28	73	86·0	0·13±0·04	109	1·69±0·01	71
Aug. 4	79	97·2	0·09±0·02	288	1·60±0·01	177
11	85	112·5	0·22±0·06	344‡	2·03±0·01	269‡
31	103	87·0	0·20±0·04	54	2·09±0·01	44
Oct. 18	151	136·4	0·41±0·05	356‡	4·36±0·02	597‡
29	163	141·0	0·11±0·02	1410‡	1·45±0·01	785‡

* Baseline length 85·5 km, azimuth 5° east of north.

† Baseline length 200·0 km, azimuth 21° east of north.

‡ R.M.S. error unlikely to exceed 30%.

The errors involved in these determinations of $\overline{V}'_{\mathrm{p}}$ are comparatively large and come from two sources: (1) errors in $\overline{\Delta t}$, and (2) errors in θ due to departures of the solar wind from the radial direction. The random component of (1) due to the effects of noise and reading errors has been estimated from the dispersion displayed by individual values of Δt about the mean value for the storm; the r.m.s. errors in the values of $\overline{\Delta t}$ ranged from 12 to 50% with an average of 26%. In addition to the random component, there may at times be significant systematic errors, which are largely unknown. For example, the extremely high value of $\overline{V}'_{\mathrm{p}}$ for October 29, 1964 is probably due to a systematic underestimation of Δt because of the disturbing effects of s-pulses, which have been shown by Slee and Gent (1967) to be unconnected with the interplanetary medium. Errors due to (2) cannot be calculated with precision, but a consideration of the dispersion in burst rate described in Section VI suggests that the solar wind direction does not vary by more than ±5° from the radial direction, so that θ is not likely to be in error by more than 5°. Unfortunately, the use of approximately north–south baselines in this experiment has resulted in generally large values of θ so that $\cos\theta$ is a rapidly varying function. However, the values of

$\overline{V}'_{\mathrm{p}}$ indicated by a double dagger in Table 2 were obtained at hour angles for which an error in θ of 5° would give rise to an error in $\cos\theta$ of less than 23%. Consequently, combining the random components of (1) and (2), the r.m.s. errors in the more accurate values of $\overline{V}'_{\mathrm{p}}$ in Table 2 should be less than 35%.

In order to derive the magnitude of the solar wind velocity from these measurements, the values of $\overline{V}'_{\mathrm{p}}$ are first transformed to values of $\overline{V}_{\mathrm{p}}$, the transverse velocity in the diffracting region, by multiplying by the reciprocal of the magnification factor (see Section IV). Then by the use of the curves in Figure 5 the solar wind velocity V_{S} may be estimated. It turns out that this computation is relatively insensitive to the distance to the equivalent diffracting screen because the magnification factor changes with Z_1 in such a way as to largely cancel the change in the ratio $V_{\mathrm{p}}/V_{\mathrm{S}}$.

The more reliable measurements of $\overline{V}'_{\mathrm{p}}$ in Table 2, neglecting those obtained near opposition and the extremely high value of October 29, 1964, have been used to derive an average value for the solar wind. This is found to be $V_{\mathrm{S}} = 630$ km sec^{-1} for a diffracting layer at $Z_1 = 1$ a.u. or $V_{\mathrm{S}} = 560$ km sec^{-1} for a layer at $0{\cdot}5$ a.u.

VI. Burst Rates

The average time interval $\bar{\tau}$ between the reception of successive diffraction peaks at a fixed location on the Earth's surface can provide supplementary information about the average drift velocity of the diffraction pattern. The burst rates were measured by counting the diffraction peaks within time intervals that were kept short enough to embrace only those times of obvious burst activity with characteristic durations of between 30 and 60 sec. Typically, some 15–20 samples of burst rate were measured for each active night for which were calculated a sample average with an r.m.s. uncertainty of about 4%.

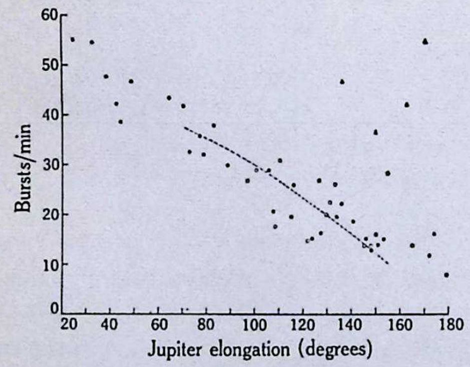

Fig. 6.—Nightly average values of burst rate plotted as a function of Jovian elongation. The open and full symbols refer respectively to measurements in 1963 and 1964. The triangular symbols represent the burst rates on nights during which a pronounced millisecond component (s-pulses) was detected. The dashed curve is described in the text.

Figure 6 shows the nightly average values of burst rate plotted as a function of Jupiter's elongation; it includes data from 1963 (open symbols) and 1964 (full symbols). The four values represented by triangles were obtained during Jovian emission that contained considerable numbers of the relatively uncommon millisecond pulses (s-pulses) recognized from their characteristic "spitting" sounds in the loudspeaker. If the results from the s-pulses are ignored, the average burst rate increases systematically from about 10 min^{-1} near opposition to 55 min^{-1} at an elongation of 25°. This trend is illustrated in the chart recordings of Figure 3, in which Figure 3(*d*) shows the slow burst structure typical of our records near opposition, while Figure 3(*c*) shows the much faster modulation recorded nearer the Sun.

The curves in Figure 5 show how the velocity component, which is responsible for sweeping the diffraction pattern across the Earth, changes as a function of Jupiter's elongation and the distance to the diffracting layer. In general, V_{p} increases as the line of sight to Jupiter approaches the Sun, with the result that the burst rate should also increase. At elongations in the range $20° < \epsilon < 60°$, depending on the distance to the diffracting screen, the transverse component of velocity will reach a maximum value and then decrease rather rapidly. However, the r.m.s. phase deviation introduced at decametric wavelengths may be increasing so rapidly that the diffraction scale length on the ground is becoming significantly smaller, according to equation (9) of Section IV; this effect would largely compensate for the decrease in V_{p}, with the result that the burst rate would probably continue to increase until the angular separation was only a few degrees.

The results plotted in Figure 6 agree qualitatively with the predictions of the simple radial model of the solar wind. Unfortunately, the relatively long response time of the recorder pen probably results in an underestimation of the burst rates at elongations less than $\sim 50°$. In addition, a legitimate comparison cannot be made with the curves of Figure 5 close to opposition or conjunction because of the known small defects in the geometry that was assumed in drawing these curves. In the range of elongations $70° < \epsilon < 160°$, in which the measurements are reliable and the geometrical defects play only an insignificant role, the results of Figure 6 could be fitted almost equally well by scaled versions of all of the curves in Figure 5; one such curve for a layer at 1 a.u. has been superimposed on Figure 6, and in what follows it will be assumed that it adequately represents the average burst rate over this restricted range of elongations.

The dispersion in the measured burst rates may be due to one or more of the following causes: (1) errors in counting bursts, (2) bursts on different nights may originate in thin diffraction screens situated at different distances along the line of sight, and (3) temporal changes in the velocity of the solar wind. The scatter of points in Figure 6 about the dashed curve possesses an r.m.s. value of $\sim 20\%$, which is much higher than the r.m.s. uncertainty of $\sim 4\%$ assigned to each estimate on the basis of measurement error. Consequently, the major source of dispersion is probably to be found in (2) or (3).

The effect of (2) is considerably reduced by the magnification factor $(Z_1+Z_2)/Z_2$, which acts to oppose the influence of the changing transverse component of velocity V_{p} as the distance to the diffracting screen Z_1 is varied. This process is so effective that an r.m.s. dispersion of $\sim 20\%$ from (2) could result only if the diffraction peaks originate in relatively thin screens that assume different positions from night to night over almost the complete path between Jupiter and the Earth. The focusing conditions specified by equation (8) in Section IV suggest that phase-changing screens with $\phi_0 \geqslant 1$ rad situated as close as $0{\cdot}05$ a.u. to the Earth or Jupiter would produce the observed high degree of intensity modulation. However, it seems more likely that interplanetary space is filled with a continuous distribution of scattering irregularities; as a result, the velocity dispersion due to (2) would be considerably lower than 20%.

A more likely origin for the dispersion in burst rate seems to be (3). Fluctuations in the magnitude of the solar wind with r.m.s. value of 20% averaged over the significant diffracting path would account for the results. Alternatively, r.m.s. angular deviations of a few degrees in the direction of the solar wind would also be effective.

Measurements by spacecraft of plasma velocities in the interplanetary medium near the Earth have shown a marked dependence on the degree of solar activity, the correlation with the K_p magnetic index being especially well developed. For the Jovian burst rate observations, many of the results relate to those parts of the interplanetary medium at appreciable distances from the Sun–Earth line; in these circumstances the K_p index may not be a suitable quantity with which to correlate our measurements of burst rate. Indeed, there appears to be no general correlation with either the K_p index or sunspot number in the comparatively few measurements of burst rate available to us. However, the most extreme deviation of +175% from the average burst rate was measured at a time of high geomagnetic and solar activity; this occurred on September 14, 1963 during strong Jovian emission in the interval $15^h 17^m$ to $15^h 47^m$ U.T. The rather high Jovian elongation of 155° probably ensured that the K_p index gave a reasonable indication of the magnetic disturbance in the diffracting region; accordingly, we suggest that the coincidence was not accidental, because both the Jovian burst rate and geomagnetic activity were exceptional events.

VII. Scale of Diffraction Patterns

In Section IV the spatial autocorrelation function has been defined by the Gaussian function

$$\rho(\xi) = \exp(-\xi^2/\xi_0^2),$$

where $\xi = \xi_0$, the distance along the ground for which the correlation has been reduced to exp(−1), is defined as the scale length. There are, in fact, various scale lengths corresponding respectively to the variations in complex amplitude, amplitude, intensity (amplitude squared), and phase. Cross-correlation of the post-detector outputs of spaced receivers yields estimates of the scale length of the amplitude or intensity variations. The method of the drifting pattern provides similar information. Phase-sensitive interferometers, on the other hand, measure the scale length of the complex amplitude variations, which include the effects of both amplitude and phase. There is no *a priori* reason for assuming that the various scale lengths are identical, especially in the case of a thick diffracting region that produces relatively strong phase deviations.

(a) *Cross-correlation of Post-detector Recordings*

This type of analysis results in a measure of the drift velocity of the diffraction pattern as well as providing information on the spatial autocorrelation of intensity.

Unfortunately, the method is not easy to apply to the analysis of pen recordings; in addition, it is of doubtful value in the presence of ionospheric scintillations, which often appeared to be affecting our observations. With these disadvantages in mind, it was not considered fruitful to compute the cross-correlation coefficients between total power recordings. However, many recordings taken over the 85·5 and 200 km baselines in the three months near opposition showed a reasonable degree of similarity between the bursts at the spaced sites. Thus it appears likely that the scale lengths associated with the intensity variations are of the order of hundreds of kilometres.

(b) *Method of the Drifting Pattern*

It was shown in Section IV that the average scale length of the intensity variations across the plane perpendicular to the line of sight is given by

$$\xi_0 = (2\cdot6)^{-1}\,\overline{V}'_{\mathrm{p}}\,\bar{\tau},$$

where ξ_0 is the scale length of a Gaussian autocorrelation function, $\overline{V}'_{\mathrm{p}}$ is the average velocity of the diffraction pattern, and $\bar{\tau}$ is the average interval between the arrival of diffraction peaks. Using this method the scale lengths have been calculated on the 10 occasions for which the pattern velocities were computed from the differences in burst arrival time. The more accurate values of $\bar{\xi}_0$ listed in column 7 of Table 2 possess random errors with an r.m.s. value of about 30%, although there may well be some additional systematic error (e.g. the very high value for ξ_0 on October 29, 1964 is believed to be influenced by the systematic error in $\overline{V}'_{\mathrm{p}}$ discussed in Section V). The average of the five most reliable estimates in Table 2 is $[\bar{\xi}_0]_{\mathrm{av}} = 380$ km, a value that is consistent with the high degree of correlation seen on our total power recordings over the 200 km baseline on a few occasions.

(c) *Measurements of Angular Power Spectrum*

Equations (5) and (6) of Section IV show that measurements of the angular power spectrum of the scattered radiation by a phase-sensitive interferometer provide estimates of the scale length of the complex amplitude variations across the plane perpendicular to the line of sight. In interpreting our measurements of fringe visibility, we have assumed that the scattering is strong enough to ensure that practically all of the radiation incident on the layer has been scattered into an angular power spectrum whose half-width to exp(−1) is given by equations (6). It will be shown in Section VIII that the phase modulation at 19·7 MHz is strong enough to ensure that this assumption is valid.

The angular size measurements have already been described by Slee and Higgins (1966), but in Figure 7 the information is presented in the form of a histogram in which the abscissae can be interpreted as either an angular size or a scale length. All the results in Figure 7 come from noise storms recorded when Jupiter's elongation exceeded 79°; interferometer fringes observed at lower values of elongation in 1964 were not adequately calibrated. An inspection of Figure 7 reveals that the majority of the measurements of scale length fell in the range $130 < \xi_f < 190$ km, values that are significantly lower than the intensity scale length derived from the method of the drifting pattern. This interesting difference in the scale lengths of the intensity and complex amplitude patterns may well be a consequence of the long diffracting path through the interplanetary medium. The implications of such an interpretation are left to the discussion in Section IX.

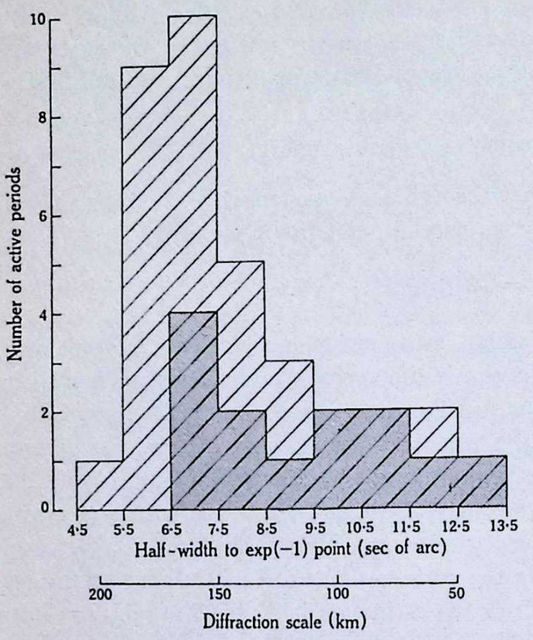

Fig. 7.—Histograms showing the distributions of half-widths in the angular power spectra of the scattered radiation at 19·7 MHz, deduced from measurements of interferometer fringe visibility. The shaded and hatched areas refer respectively to the results from 1963 and 1964. A second set of abscissae transforms the half-widths to the equivalent scale lengths in the complex amplitude variations across the ground.

VIII. Phase Deviations

Despite the limitations imposed upon 20 MHz interferometer observations by the phase stability of the Earth's ionosphere, recordings such as that shown in Figure 3(*a*) demonstrate that meaningful angular position measurements can be made for periods up to several minutes in duration. For these measurements, we are primarily interested in the relative positions of the fringe crossover points on the phase-sensitive recordings, since these are the only times at which the phase differences between the Jupiter signals at the spaced receiving sites are sampled.

Our method of measuring the phase deviations was determined by the fact that measurable fringes were normally recorded in groups with durations ranging from about 10 to 60 sec; each group or sample contained between 3 and 12 fringes. We computed the average fringe period for each sample and compared it with the expected period based on the hour angle and declination of Jupiter and the baseline parameters. This comparison resulted in obtaining: firstly, the fractional deviation of each sample mean from the theoretical period $\Delta T/T$; and secondly, the average fractional deviation of the individual crossover positions within each sample from their unperturbed positions, $n^{\frac{1}{2}}(\Delta T/T)$, in which n is the number of fringes in the sample. The latter calculation assumes that the diffraction peaks were frequent enough to ensure randomization from fringe to fringe, a condition almost certainly fulfilled by these observations. Lastly, it was then an easy matter to compute the r.m.s. phase deviations between the ends of the baseline from the relation

$$\left\{\overline{(\Delta\phi)^2}\right\}^{\frac{1}{2}} = 1\cdot25\, n^{\frac{1}{2}}\,(\Delta T/T)\,2\pi\,,$$

where 1·25 is the factor by which the r.m.s. deviation of a Gaussian distribution exceeds the mean deviation.

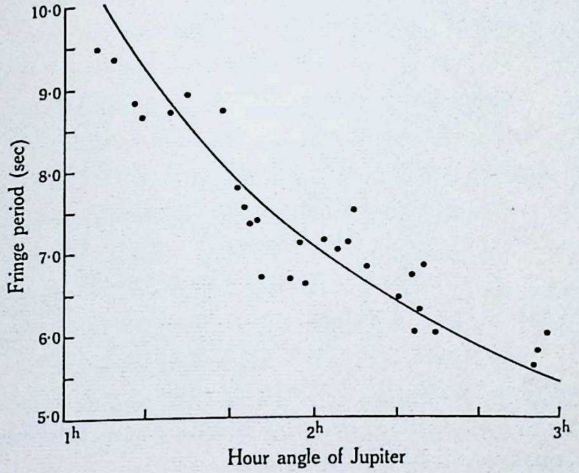

Fig. 8.—The interferometer fringe periods plotted against Jovian hour angle. Each point represents the average period in a sample of several fringes. The curve shows the expected fringe period calculated from the baseline parameters.

Some of the observational material from which the phase deviations were obtained is shown in Figure 8, where the fringe sample periods are plotted as a function of hour angle for a noise storm recorded on the 85·5 km baseline; the theoretical fringe period curve is superimposed on the figure. It is apparent that the points are distributed about the curve in a manner to be expected of sample periods that are being affected by random phase deviations.

Ionospheric scintillations are unlikely to have invalidated these measurements of phase for the reasons: (1) Except for low values of Jovian elongation, most fringes were recorded when the bursts at the separated sites showed a reasonable degree of correlation, indicating that scintillations at either site were not severe. (2) Many of the fringe samples were of durations less than 20 sec, which is considerably shorter than the time scale of most scintillations; consequently, the full effect of their associated phase deviations should not be felt. (3) The results in Figure 10 show that near opposition, when the Jovian radiation was recorded in the interval of maximum ionospheric scintillation activity, 2300 to 0200 hr local time, the measured phase deviations were comparatively low; on the other hand, the high r.m.s. phase deviations observed at Jovian elongations less than 40° were recorded just before local dawn when severe ionospheric scintillations are virtually absent.

The influence of the interplanetary medium on the phase deviations is shown in Figure 9, which contains histograms of the distribution of the quantity $\Delta T/T$ for all fringe samples recorded in 1963 and 1964. In order to construct these diagrams, the observations have been subdivided into three approximately equal numbers of fringe samples corresponding to the ranges of Jupiter's elongation $26° < \epsilon < 120°$,

$120° < \epsilon < 150°$, and $150° < \epsilon < 180°$. It is obvious that the fringe periods show a much larger dispersion about the theoretical values at the lower elongations.

A more detailed impression of the pronounced variation in the strength of the phase fluctuations on the ground is obtained from Figure 10. The data for this figure were obtained by averaging the r.m.s. phase differences over intervals of 10° to 20° in Jovian elongation. Open and full circles refer respectively to the 200 and 85·5 km baselines.

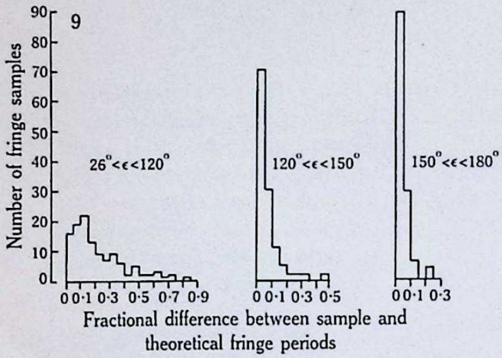

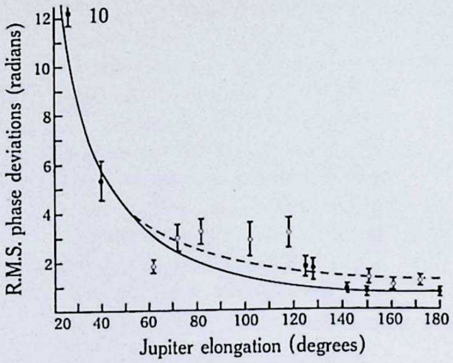

Fig. 9 (*left*).—Histograms of the deviations of the observed sample fringe periods from their unperturbed values for three ranges of Jovian elongation. Each deviation has been expressed as a fraction of the unperturbed fringe period.

Fig. 10 (*right*).—Estimates of the r.m.s. phase deviations between the ends of the baselines. Each point is an average of phase measurements made during several successive active nights. Full circles refer to 1963 measurements, 85·5 km baseline; full squares to 1964 measurements, 85·5 km baseline; open circles to 1964 measurements, 200 km baseline. The solid and dashed curves are respectively the r.m.s. phase differences over the 85·5 km and 200 km baselines predicted by a simple model for the scattering irregularities described in the text.

The curves superimposed on Figure 10 show the r.m.s. phase differences that would be measured over each baseline if the electron irregularities in the solar wind satisfied a model with the following characteristics: (1) The r.m.s. fluctuation in electron density near the ecliptic varies with heliocentric distance as R^{-2} and the irregularities possess a scale size that is substantially constant throughout the interplanetary medium. This assumption allows the form of the integral expression for the r.m.s. phase modulation $\phi_0(\epsilon)$ given by equation (4) in Section IV to be determined. (2) The phase fluctuations across the ground possess a Gaussian autocorrelation function and, at opposition, the scale length ξ_ϕ equals the irregularity scale in the scattering medium, L, which is assumed to be 150 km; at other elongations $\xi_\phi = L/\phi_0$. The latter condition is equivalent to specifying that $\phi_0 = 1$ rad at opposition. With ϕ_0 and ξ_ϕ determined at all elongations, equation (7) in Section IV has been used to derive $\{\overline{(\Delta\phi)^2}\}^{\frac{1}{2}}$ as a function of Jovian elongation for each of the baselines used in the experiment.

It is apparent from Figure 10 that the measured values of $\{\overline{(\Delta\phi)^2}\}^{\frac{1}{2}}$ are in reasonable agreement with the proposed model, particularly at the low and high values of elongation. In a sense, the curves have been forced to fit the observations at opposition by assuming a value for ϕ_0 that would produce the observed phase differences. However, the consistent difference between the results for the two baselines over the range of elongations $140° < \epsilon < 180°$ may be used to independently assess the agreement between the observations and the proposed model. The measurements in the range of elongations $80° < \epsilon < 130°$ suggest that either the model is not a particularly accurate one or the observations in this region are affected by some systematic source of error. The individual fringe samples contributing to these particular points yielded values of $\{\overline{(\Delta\phi)^2}\}^{\frac{1}{2}}$ showing a relatively large dispersion about the mean. Such behaviour would probably result from the influence of ionospheric scintillations, which would also systematically increase the observed r.m.s. phase differences.

Quite apart from the disturbing effects of ionospheric scintillations, it would be remarkable if observations taken over an interval of 16 months showed better agreement with the predictions of any simple model. Temporal changes in the properties of the solar wind would make it unlikely that a unique model for the scattering irregularities could be derived from these measurements. However, it is clear that these observations are at least consistent with the presence of scattering irregularities with an average scale size of ~ 150 km (similar to the scale derived from fringe visibility measurements) and with r.m.s. electron density varying approximately as the inverse square of the heliocentric distance. The r.m.s. phase modulation at $\epsilon = 180°$ is ~ 1 rad.

IX. Discussion of Results

The preceding sections have demonstrated that a slowly varying radio emission from Jupiter is often deeply modulated by interplanetary scintillations with quasi-periods of the order of seconds. In this section the observational results are used to deduce the physical properties of the solar wind and a comparison is made with the results of other experiments.

(a) *Velocity of Solar Wind*

The measurements of burst rate shown in Figure 6 demonstrate the presence of a radially directed outflow of scattering irregularities near the plane of the ecliptic. The comparatively few measurements of the time delay $\overline{\Delta t}$ between the arrival of bursts at spaced receivers suggest that the average velocity of the solar wind is ~ 600 km sec^{-1}. This result agrees well with the measurements of plasma velocity reported from the Mariner II experiments by Neugebauer and Snyder (1962). Information about the variability of the velocity has been deduced from the dispersion in burst rate; the results, which represent averages over considerable path lengths through the interplanetary medium, allow upper limits to be deduced for the variability in magnitude and direction of 20% and ±5° respectively. In localized regions the variations may be much higher.

(b) *Scale of Irregularities in Solar Wind*

The results of Section VII show that the diffraction scale length of the intensity fluctuations across the ground is approximately 400 km; this may be compared with the results of Douglas and Smith (1967), who derive a similar average scale size from their spaced-receiver observations. The scale length of the complex amplitude fluctuations is, however, significantly lower with a value of approximately 150 km; additional information from the angular position scintillations suggests that the scale length of the phase fluctuations across the ground is also of the order of 150 km. It therefore appears that the complex amplitude variations are largely in the form of phase fluctuations.

A plausible explanation of these results involves the presence of an extended diffracting medium in which the amplitude fluctuations are impressed on the radiation by phase irregularities at considerably greater distances than those that produce most of the phase fluctuations. Under these circumstances the scale length of the intensity fluctuations would be subjected to a larger magnification factor $(Z_1+Z_2)/Z_2$ than is applied to the phase scale.

An investigation of the integral equation (4) for the phase deviations, assuming that $\{\overline{(\Delta N)^2}\}^{\frac{1}{2}}$ varies as the inverse square of the heliocentric distance and L is constant, shows that near opposition $\sim 87\%$ of the total mean square phase deviation would be impressed on the radiation within a distance of 1 a.u. of the Earth. Nevertheless, the much weaker contributions to ϕ_0^2 from more distant irregularities could still give rise to appreciable intensity fluctuations if the total value of ϕ_0^2 is high enough. Without an adequate theory for the thick diffracting medium it is difficult to specify how the suggested spatial separation between regions producing intensity and phase deviations would be achieved. One plausible suggestion is that the intensity fluctuations that build up within the medium at some distance in front of the initial scattering irregularities are accompanied by apparent angular size increases, which eventually restrict the further growth of intensity modulation.

In any case, it is evident that the measurement of diffraction scale which takes account of the total phase modulation should be used to specify the scale length in the diffracting screen. Therefore, on the reasonable assumption that most of the phase modulation takes place within a distance of $Z_1 = 1$ a.u., the measurements of complex amplitude scale suggest that the irregularity scale in the solar wind is $L \sim 150$ km. This value agrees with the result of 143 km deduced by Hewish, Dennison, and Pilkington (1966) from studies of interplanetary scintillations from quasars at heliocentric distances of $\sim 0\cdot5$ a.u. There is therefore reasonable evidence that the scale of irregularities in the interplanetary medium remains approximately constant out to heliocentric distances of at least 1 to 2 a.u.

(c) *Electron Density in the Scattering Irregularities*

The measurements of angular scintillations have suggested that near opposition the value of ϕ_0 is approximately 1 rad; the rate of increase of ϕ_0 as the elongation decreases is consistent with a variation in r.m.s. electron density of the form

$$\{\overline{(\Delta N(R))^2}\}^{\frac{1}{2}} \sim \Delta N_0 R^{-2},$$

where R is the heliocentric distance and ΔN_0 is the r.m.s. electron density at $R = 1$ a.u. The irregularity scale in the solar wind is approximately constant with $L \sim 150$ km.

If this information is inserted in equation (4) and the integration performed with the limits appropriate to observations near opposition, the resulting equation can be solved for ΔN_0. The resulting expression for r.m.s. electron density is

$$\{\overline{(\Delta N(R))^2}\}^{\frac{1}{2}} \sim 0\cdot 2\,R^{-2}.$$

The deduced value of $\Delta N_0 \sim 0\cdot 2$ electrons cm^{-3} is an order of magnitude lower than the plasma densities measured by the spacecraft Mariner II in late 1962. Since the values obtained by the spacecraft were averages over volumes containing many scattering irregularities, it appears that the latter are rather weak fluctuations in the interplanetary plasma containing only about 10% of the total plasma density.

This computation of electron density agrees reasonably well with a result presented by Cohen *et al.* (1967), who used the variation in scintillation index of quasar 3C 273B at 430 MHz to derive the r.m.s. phase deviation ϕ_0 as a function of heliocentric distance. These authors also demonstrate that the r.m.s. electron density varies as the inverse square of the heliocentric distance, in agreement with the present conclusion.

(*d*) *Intrinsic Angular Dimensions of Jovian Decametric Sources*

The requirements to be satisfied by the angular size of a radio source if appreciable intensity fluctuations are observed on the ground plane are described by equation (10) in Section IV. The distance to the equivalent thin phase screen is not known with certainty, but it appears likely that near opposition $Z_1 \sim 2$ a.u. (based on the size of the intensity diffraction scale in relation to the phase scale on the ground). Hence, using $Z_1 = 2$ a.u. and $\xi_0 = 400$ km in equation (10), the angular radius of the Jovian decametric source is $< 0\cdot 3$ sec of arc.

As the line of sight to Jupiter approaches closer to the Sun the r.m.s. phase modulation associated with the intensity fluctuations is likely to exceed 1 rad, so that the intensity scale length is reduced according to equation (9). This may eventually result in a reduction of the r.m.s. intensity fluctuation across the ground due to the failure of the source to satisfy the angular size criterion. Such effects on the scintillating radio sources have already been noted by Little and Hewish (1966), who have used the information to estimate angular size.

In order to ascertain whether the finite angular sizes of the Jovian sources are producing similar effects, an examination has been made of the extensive observations made with the Boulder decametric spectrograph covering the Jovian apparitions 1960 to 1966; these are reported by Warwick and Kreiss (1964) and Warwick and Dulk (1965, 1966). The analysis has been restricted to frequencies above 17·5 MHz, where ionospheric absorption and station interference are unlikely to be important factors.

Figure 11 shows the probability of reception of Jovian radio emission as a function of elongation; the figure also shows the fraction of noise storms classified as "smooth" or "weak", where these terms refer to the degree of fine structure in the intensity modulation with periods of a few seconds. The probability of detecting noise storms falls steadily from a maximum value of $\sim 0\cdot 5$ near opposition to

$\sim 0{\cdot}15$ near the Sun, with a sudden marked reduction at elongations less than 60°. Figure 11 also shows clearly that the fine structure in the Jovian radiation virtually disappears at elongations less than 30°, although a marked reduction sets in well before at an elongation of about 60°.

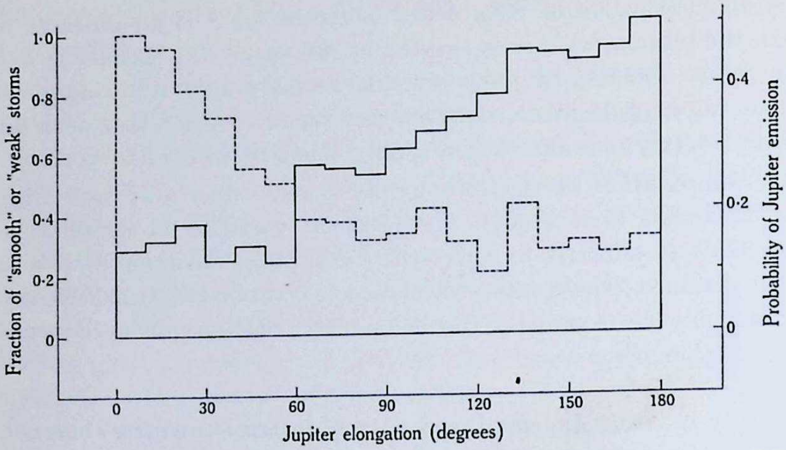

Fig. 11.—The full-line histogram (ordinate scale on right) is a plot of the probability of detection of Jovian emission $\geqslant 17{\cdot}5$ MHz as a function of Jovian elongation. The dashed-line histogram shows the "smoothness" (degree of very coarse time structure) present in the Jovian decametric emission plotted against elongation. (See text for further details.)

We suggest that the comparatively smooth intensity changes with periods of about 60 sec, which are recorded so often near the Sun, are the intrinsic changes in Jovian emission;* these can only be clearly distinguished when the short period modulation due to interplanetary scintillations has been removed by the failure of the source to satisfy the angular size criterion. The marked reduction in probability of reception of Jovian emission at the lower values of elongation is probably caused by difficulties in identifying the smooth emission, especially as it is usually of low peak intensity and partially obscured by interference and solar radio emission. The extension of the smooth emission into the antisolar region of elongations suggests that the angular dimensions of the Jovian sources may at times be large enough to ensure that the diffraction pattern is smoothed out, even with the comparatively weak scattering occurring near opposition.

If our explanation is correct, the finite angular sizes of the decametric sources are exerting a marked influence on the scintillation intensity at elongations $\leqslant 60°$. At $\epsilon = 60°$ the scale length of the intensity pattern is not known, but the poor correlation between total power recordings over our 85·5 km baseline at these low values of angular separation (see Fig. 3(*c*)) suggests that a value of $\xi_0 \sim 50$ km would be reasonable. The distance to the equivalent diffracting screen is assumed to be $Z_1 \sim 1$ a.u. because, for these comparatively low elongations, the scattering will be strongest in this section of the ray path. Substitution of these values in equation (10) shows that the angular radius of the source is greater than $0 \cdot 07$ sec of arc. Hence the results shown in Figure 11 are consistent with a range of intrinsic angular radii given by $0 \cdot 07 < \psi_0 < 0 \cdot 3$ sec of arc; these values should be regarded as qualitatively correct, but they may need revision if the thin screen theory is shown to be inapplicable to decametric observations of Jupiter.

---

* These slow intensity changes should not be confused with the modulation introduced by ionospheric scintillations. It can be demonstrated (see, for example, the grouping of Jovian bursts in Fig. 3(*d*)) that the radiation reaching the receiver almost always shows variability with a quasi-period of about 60 sec, even on those occasions when ionospheric scintillations are virtually absent.

It appears reasonable to suppose that the effects caused by the finite angular size of the source at frequencies near 20 MHz would be even more developed at lower frequencies. Indeed, at frequencies of ~ 5 MHz it appears possible that intensity scintillation would not be severe at any Jovian elongation. In support of this suggestion, it should be noted that Ellis (1962) and Carr *et al.* (1965), both operating near 5 MHz, have pointed out the much smoother appearance of the Jupiter emissions at this frequency.

The well-known inverse correlation between general solar activity and frequency of reception of Jovian decametric radiation, first pointed out by Carr *et al.* (1961), may be yet another consequence of the finite source size. It is known from the measurements of the scattered angular power spectra from discrete radio sources near the Sun (Slee 1966) that the r.m.s. phase modulation introduced by the outer corona increases by a factor of about three from sunspot minimum to maximum. This increase would be sufficient to significantly reduce the degree of intensity scintillation over a large range of Jovian elongations, especially at the lower frequencies. It would be instructive to reassess the data on the "smoothness" of the Jovian emission as functions of wavelength, elongation, and sunspot cycle.

X. ACKNOWLEDGMENTS

We wish to acknowledge the assistance of all those people who have contributed to the experiment in various ways. In particular, we thank Mr. C. F. Fryar and Mr. C. Tillack for help with the equipment and observations. We are indebted to the Postmaster-General's Department for allowing us to use the site and facilities at its radio-repeater station, Heaton. Our thanks are also due to the Electrical Engineering Department, University of Sydney, for permission to operate from the field station at Fleurs during 1964.

XI. REFERENCES

BRAMLEY, E. N. (1954).—*Proc. R. Soc.* A **225**, 515–18.

BRAMLEY, E. N., and YOUNG, M. (1967).—*Proc. Instn elect. Engrs* **114**, 553–6.

BURKE, B. F., and FRANKLIN, K. L. (1955).—*Nature, Lond.* **175**, 1074.

CARR, T. D., GULKIS, S., SMITH, A. G., MAY, J., LEBO, G. R., KENNEDY, D. J., and BOLLHAGEN, H. (1965).—*Radio Sci.* **69D**, 1530–6.

CARR, T. D., SMITH, A. G., BOLLHAGEN, H., SIX, N. F., and CHATTERTON, N. E. (1961).—*Astrophys. J.* **134**, 105–25.

COHEN, M. H., GUNDERMANN, E. J., HARDEBECK, H. E., and SHARP, L. E. (1967).—*Astrophys. J.* **147**, 449–66.

DOUGLAS, J. N. (1964).—*IEEE Trans. Antennas Propag.* **AP-12**, 839–53.

Douglas, J. N., and Smith, H. J. (1961).—*Nature, Lond.* **192**, 741.

Douglas, J. N., and Smith, H. J. (1967).—*Astrophys. J.* **148**, 885–903.

Ellis, G. R. A. (1962).—*Nature, Lond.* **194**, 667–8.

Gardner, F. F., and Shain, C. A. (1958).—*Aust. J. Phys.* **11**, 55–69.

Hewish, A., Dennison, P. A., and Pilkington, J. D. H. (1966).—*Nature, Lond.* **209**, 1188–9.

Little, L. T., and Hewish, A. (1966).—*Mon. Not. R. astr. Soc.* **134**, 221–37.

Neugebauer, M., and Snyder, C. W. (1962).—*Science* **138**, 1095–6.

Pisareva, V. V. (1958).—*Astr. Zh.* **35**, 112. (Translated in *Soviet Astr.* **2**, 97–111.)

Ratcliffe, J. A. (1956).—*Rep. Prog. Phys.* **19**, 188–267.

Slee, O. B. (1966).—*Planet. Space Sci.* **14**, 255–67.

Slee, O. B., and Gent, H. (1967).—*Nature, Lond.* **216**, 235–8.

Slee, O. B., and Higgins, C. S. (1963).—*Nature, Lond.* **197**, 781–3.

Slee, O. B., and Higgins, C. S. (1965).—*Radio Sci.* **69D**, 1536–7.

Slee, O. B., and Higgins, C. S. (1966).—*Aust. J. Phys.* **19**, 167–80.

Smith, A. G., Carr, T. D., Bollhagen, H., Chatterton, N., and Six, F. (1960).—*Nature, Lond.* **187**, 568–70.

Warwick, J. W., and Dulk, G. A. (1965).—High Altitude Observatory, Boulder, IGY Solar Activity Report, Series No. 32.

Warwick, J. W., and Dulk, G. A. (1966).—High Altitude Observatory, Boulder, IGY Solar Activity Report, Series No. 34.

Warwick, J. W., and Kreiss, W. T. (1964).—High Altitude Observatory, Boulder, IGY Solar Activity Report, Series No. 28.

A CATALOGUE OF GALACTIC RADIO SOURCES

By M. J. L. Kesteven*

[*Manuscript received December* 11, 1967]

Summary

The results of a survey of radio sources in the galactic plane in the longitude range 180° to 40° with the 1 mile Molonglo Cross telescope at 408 MHz are presented. The methods of observation and reduction are described briefly. The catalogue lists the position, flux density, size, and spectral index for 80 sources.

I. Introduction

In 1966 a survey of the southern galactic plane was made with the east–west arm of the Molonglo cross-type radio telescope (Mills *et al.* 1963). This was the first stage of an experiment designed to investigate the nature of galactic supernova remnants. The survey covered the longitude range 180° to 40°. From the results of the survey a catalogue of 80 radio sources has been compiled. The catalogue is believed to be complete to defined limits of flux density and angular size. Sources with an angular diameter of less than 1′ have been excluded from the catalogue since a variety of statistical tests indicate that this class of sources is not of galactic origin.

The catalogue sources have since been observed with the pencil beam imaging system of the radio telescope. This has permitted a more accurate determination of declination and has removed several uncertainties due to confusion. Contour maps have also been prepared of the brightness distribution across the larger sources, but a presentation of these and an examination of the results in the light of various theories of supernova remnants will be deferred to a later article.

II. Observations

The initial finding survey was made during the early part of 1966 with the then recently completed east–west arm of the Molonglo radio telescope. For this survey the arm (a cylindrical paraboloid 1 mile by 38 ft) had an approximately uniform east–west illumination. The operating frequency was 408 MHz and the bandwidth 2·5 MHz. The aerial radiation pattern was a fan beam 1′·43 (right ascension) by 4°·2 (declination). The system noise was about 600°K.

Drift scans were taken at 2° intervals in declination. A source should appear on at least three scans. Each scan was analysed independently by hand and the results were then collated to determine the declination of each source. The background in the neighbourhood of the source was estimated and a baseline interpolated beneath the source trace. For sources with a north–south extent of less than 1° the area between the baseline and the trace is a direct measure of the integrated flux density of the source. The flux density scale was related to the C.K.L. scale by

---

* Cornell–Sydney University Astronomy Centre, School of Physics, University of Sydney, N.S.W. 2006.

Aust. J. Phys., 1968, **21**, 369–76

adopting 3C 273 and 3C 444 as calibrating sources. The flux densities assumed were 56·8 and 27·1 f.u.* respectively (Kellerman 1964).

The extended sources of the survey have all been observed with the recently completed cross telescope. This instrument has an approximately circular response pattern, 2′·8 diameter at half-power at the zenith; the resolution in declination varies with zenith distance. Contour maps have been produced for the larger sources in the survey. The sensitivity of the telescope varies with declination in a way that has not yet been determined; the source flux densities have therefore been obtained from the fan beam observations. For several sources, inspection of the contour maps revealed that a few sources were present simultaneously in the fan beam. In these cases the flux densities have been estimated from the pencil beam records; the flux densities obtained by integrating the pencil beam contours were related to the fan beam flux densities.

Estimates have been made of the angular dimensions of each source. The measurements have been made at the half-power level; however, localized peaks in a complex source were averaged over the surface of the source so as to make the angular dimensions representative of the whole source. This procedure is clearly an approximation but it has the advantage of describing a complex source by two parameters.

For the small diameter sources ($\theta < 3'$) the diameters were estimated from the fan beam observations. The pencil beam records were used for the remainder.

Since the radio telescope operates, at present, on one frequency only (408 MHz), the spectral indices have been estimated from comparisons with surveys made at different frequencies with different instruments. Spectral indices have been determined principally from Hill's (1968) survey at 1410 MHz with a 13′ resolution, since this is the highest resolution survey available for comparison. Outside the region covered by Hill's survey, comparison was made with various published surveys: Mills, Slee, and Hill (1958, 1960, 1961); Westerhout (1958); Mathewson, Healey, and Rome (1962). All these surveys have a resolution of about 1°; the spectral information is therefore uncertain, but probably adequate to distinguish between a thermal and a nonthermal spectral index. Approximately 50% of the sources are listed in other catalogues. For the sources not listed, the sign of the spectral index has been estimated from an inspection of the contour maps.

Errors

No attempt has been made to achieve the high positional accuracy that is attainable with this instrument. Since the majority of the sources are resolved by the telescope, the accuracy is determined by the precision with which one can define the centroid of a source. The standard error is estimated as 9% of the source diameter.

The standard error in flux density is estimated as 15%. The error is due partly to the uncertainty in the aerial calibration but mainly to the difficulty in defining the zero level of an extended source. The error in the spectral index is estimated as 0·3 in the region common to Hill's survey. Outside this region only the sign is significant.

---

* 1 f.u. = 10^{-26} W m^{-2} Hz^{-1}.

III. Survey Limits

The survey covered the galactic plane between the limits $|b^{\mathrm{II}}| < 6^\circ \cdot 5$, $180^\circ < l^{\mathrm{II}} < 40^\circ$. As Hill's survey is restricted to the longitude range $280^\circ < l^{\mathrm{II}} < 355^\circ$, only in this region is the spectral information complete.

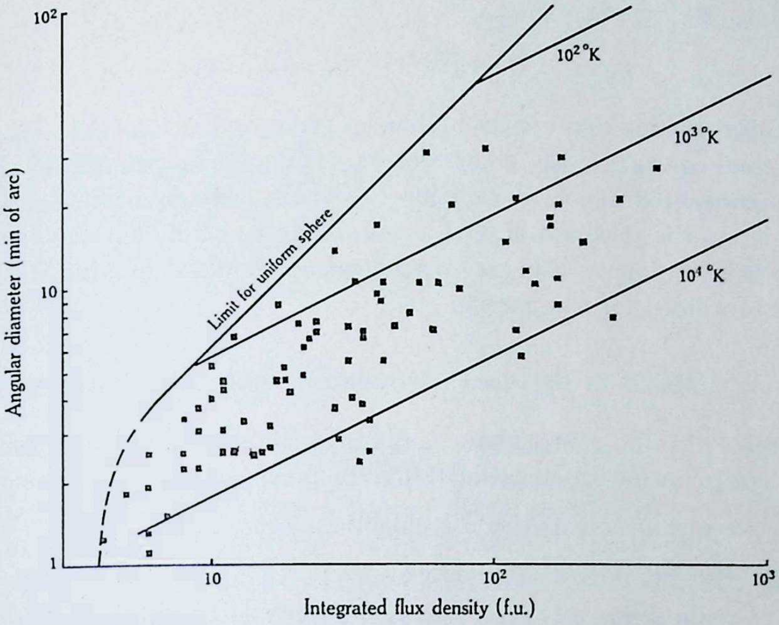

Fig. 1.—Angular diameter versus integrated flux density plotted for each source in the catalogue. The theoretical sensitivity limit (corresponding to a simple supernova model) is also shown. Curves corresponding to disks of uniform brightness 10^2, 10^3, and 10^4 °K are included for comparison.

For the purpose of the experiment it was important that the list of nonthermal sources constitute a statistically uniform sample. This requires that the selection criteria (which govern the inclusion of sources in the catalogue) be known and maintained during the data analysis.

Because source confusion is a major problem in surveys with a fan beam, sources were included in the fan beam catalogue only if they satisfied two conditions:

(1) the peak intensity S_{p} of the source should exceed 4 f.u., and

(2) the east–west half-power angular diameter should be less than 30′.

It was felt that with these restrictions the survey would be complete and the possibility of fluctuations in the galactic background being included in the catalogue might be minimized. The pencil beam records have been examined to ensure that no sources have been included which depended on the particular orientation of the fan beam.

It will be noted that the cutoff does not occur at a limiting brightness, but is some function of size and flux density. The precise relation depends on the particular distribution of energy over the surface of the source.

For a sphere of uniform emissivity (corresponding to a simple supernova remnant model), the limiting criterion takes the form

$$S_{\mathrm{p}} = 4\ \mathrm{f.u.} = \tfrac{3}{4}\sqrt{\pi}\, S_{\mathrm{int}}\, \theta_0/\theta_{\mathrm{r}}, \tag{1}$$

where S_{int} is the integrated flux density of the source, θ_{r} the angular radius of the source ($\theta_{\mathrm{r}} > 2'$), and θ_0 is related to the half-power beamwidth of the east–west radiation pattern (θ_{A}) by the relation

$$\theta_0 = \theta_{\mathrm{A}}/0\cdot 94\sqrt{\pi}, \qquad \theta_{\mathrm{A}} = 1'\cdot 43.$$

The limiting relation between $2\theta_{\mathrm{r}}$ and S_{int} given by equation (1) has been plotted in Figure 1. Also shown are the points corresponding to the sources in the survey. The sources show no marked concentration to the theoretical curve, suggesting that small variations in the selection criteria are unlikely to alter markedly the number of sources in the catalogue. Curves corresponding to disks of uniform brightness have also been included for comparison.

IV. Exclusion of Class II Sources from the Survey

Two classes of radio sources can be distinguished on the basis of their spatial distribution; the following classification (Mills 1952) has been adopted for convenience:

Class I. Sources concentrated to the galactic plane.

Class II. Sources distributed isotropically over the celestial sphere.

Since the main objective of the present survey is to obtain a list of galactic sources, it is clearly desirable to identify the class II sources observed in the survey, as the great majority of these sources are presumably extragalactic. A galactic component may exist but cannot yet be differentiated. Analyses of the 4C survey (Holden 1966; Hughes and Longair 1967) have shown no concentration of sources to the galactic plane, suggesting that the two classes might be distinguishable on the basis of their angular diameter, since the 4C interferometer has a reduced response for extended sources.

In Figure 2, the angular diameter of each source is plotted against its galactic latitude. It appears that the sources with angular diameters of less than 1′ are isotropic in b^{II} while those with larger diameters are concentrated to the plane. A χ^2 test on the distribution of the small diameter sources ($\theta < 1'$) in galactic coordinates showed a 60% probability that the sources were drawn from a population randomly distributed over the survey region. To test further the possibility that the small diameter sources are not class I, a survey was made at high latitudes to estimate the gross features of the class II population: areal density and number–flux distribution.

The number of small diameter sources observed in the galactic survey is 47 and the number predicted from an extrapolation of the high latitude survey is 53; the agreement is reasonable. Number–flux distributions were also constructed for both surveys. The distributions are similar, although the number of sources in each case is too small for much significance to be attached to the result.

From these tests it would appear that the sources with angular diameters of less than 1′ are predominantly class II. These sources have therefore been excluded from the catalogue.

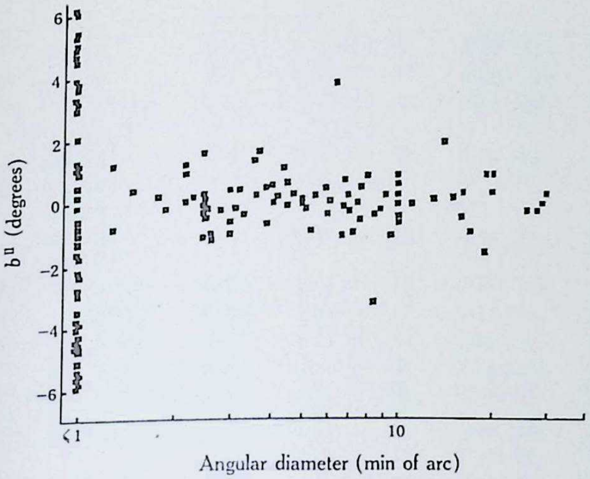

Fig. 2.—Angular diameter versus galactic latitude distribution for all sources in the survey.

The high latitude survey indicated that a small number of sources (five) with angular diameters in the range $1' < \theta < 2'$ should be found by chance in the galactic survey. The six such sources observed have been included in the catalogue as they are all close to the plane, $|b^{\text{II}}| < 2°$. In addition, three of the sources occur in regions of high source concentration. It is probable, however, that some of these sources are class II. An extrapolation of the high latitude survey results also suggests that the catalogue will contain approximately three class II sources with diameters exceeding 2′. These estimates are based on a high latitude survey to which were applied the same selection criteria as in the main survey. For this reason the proportion of sources with diameters exceeding 1′ is rather less than might be expected from the work of other observatories on the angular structure of extragalactic sources.

V. Survey Reliability

The good agreement between the number of small diameter sources of the survey and the extrapolated numbers from the high latitude survey suggests that the limiting peak flux density criterion is realistic. The probability of a source satisfying the selection criteria and not being included in the catalogue is felt to be low.

There are two further aspects of reliability that one would wish to estimate:

(1) the possibility of a large complex source being analysed as a set of small sources, and

(2) the converse problem, confusion.

The preliminary results from the Mills Cross revealed several cases of confusion and one possible case of component separation. After correcting these cases, it is believed that the survey is complete to the specified limits.

TABLE 1

SOURCE CATALOGUE

(1)	(2)	(3)	(4)			(5)		(6)	(7)	(8)	(9)
Source No.	Galactic Coordinates l^{II} °	b^{II} °	Position R.A. h	m	s	(1950·0) Dec. °	′	S_{int} (f.u.)	Spectral Index a	Angular Diam. ′	Other Catalogue Nos.
1	197·0	−0·9	06	16	09	+13	37·5	6	−0·2	1·3	4C 13·32
2	207·3	+1·1	06	42	38	+5	33·0	4	−1·0	1·3	4C 05·29
3	264·1	−3·3	08	33	18	−45	36·0	17	(−)	8·4	
4	265·16	+1·46	08	57	44	−43	33·6	34	+0·2	3·7	MHR4 RCW36 MSH08−48
5	267·95	−1·06	08	57	25	−47	19·2	159	+0·4	17	MSH08−47 RCW38 MHR5
6	268·9	−1·1	09	00	38	−48	6·0	20	(+)	7·2	
7	269·13	−1·12	09	01	47	−48	14·7	9	(+)	3·0	
8	274·01	−1·15	09	22	45	−51	46·7	16	(+)	2·6	
9	282·01	−1·15	10	04	55	−56	55·6	14	+0·6	2·3	
10	284·29	−0·29	10	22	28	−57	29·3	120	+0·3	6·8×12	
11	285·27	−0·04	10	29	42	−57	46·3	9	+0·5	2·2	
12	286·16	−0·06	10	35	27	−58	14·0	27	+0·5	13	
13	290·12	−0·76	11	00	52	−60	37·9	170	−0·7	10·4	MSH11−61
14	291·29	−0·71	11	09	55	−61	04·4	16	+0·8	2·1×4·5	RCW57(a) MSH11−62 MHR14 RCW57(b)
15	291·62	−0·53	11	12	56	−60	59·5	170	+0·8	8·4	
16	295·18	−0·60	11	41	12	−62	09·9	40	−0·2	10	
17	304·58	+0·11	13	02	40	−62	26·6	21	−0·7	4·7	
18	305·19	+0·14	13	07	54	−62	22·8	120	+0·6	20	RCW74 MHR25
19	309·73	+1·74	13	43	28	−60	10·0	210	−0·5	18×8	MHR29 MSH13−62
20	310·90	−0·49	13	57	03	−62	02·4	22	−0·5	3·5×9	
21	319·14	−0·38	14	59	06	−58	51·0	23	−0·1	7·1	
22	320·16	+0·80	15	01	33	−57	19·6	8	+0·3	2·2	
23	320·33	−1·03	15	09	33	−58	49·7	30	−0·2	5·3	
24	322·32	−1·21	15	23	03	−57	55·6	8	−0·8	2·5	
25	326·20	−1·75	15	48	28	−56	04·0	170	−0·2	19	MSH15−56 MHR44
26	326·66	+0·56	15	41	03	−53	58·0	60	−0·3	6·8	
27	327·35	+0·40	15	45	24	−53	39·9	54	−0·9	10	
28	327·7	−0·3	15	50	49	−53	39·6	6	−0·1	1·9	
29	328·45	+0·25	15	51	45	−53	05·7	13	−0·3	3·2	
30	331·1	+0·1	16	06	27	−51	58·4	5	+0·2	1·8	1606−51·9(B)
31	332·1	−0·4	16	12	49	−51	09·3	6	+0·4	2·5	1612−51(B)
32	332·41	+0·14	16	11	30	−50	33·3	28	−0·3	16	MSH16−51 1611−50(B)
33	332·43	−0·41	16	13	54	−50	55·8	30	−0·5	7	RCW103 1613−50(B)
34	333·0	−0·6	16	16	10	−50	54·0	36	Thermal*	9·3	1616−50(B)
35	333·1	−0·5	16	17	00	−50	33·0	200	Thermal*		1617−50·5(B)
36	333·3	−0·4	16	17	43	−50	20·0				1617−50·3(B)
37	333·6	−0·2	16	18	23	−50	0				1618−49(B)

* The fan beam observations were badly confused in this region. The quoted values are therefore approximations only, but the sources have been included in the catalogue for completeness. Beard (1966) indicated that these sources are all thermal.

TABLE 1 (*Continued*)

(1) Source No.	(2) Galactic Coordinates l^{II} °	(3) b^{II} °	(4) Position R.A. h	m	s	(5) (1950·0) Dec. °	′	(6) S_{int} (f.u.)	(7) Spectral Index α	(8) Angular Diam. ′	(9) Other Catalogue Nos.
38	335·6	−0·3	16	27	20	−48	24·0	10	−0·6	5·1	
39	337·0	0·0	16	31	30	−47	30·0	110	−0·5	21×6	MHR55
40	337·35	+0·95	16	29	06	−46	29·5	18	−0·2	11	
41	337·80	−0·21	16	35	22	−46	51·9	17	(−)	5×4	
42	337·92	−0·50	16	37	32	−47	02·0	8	+0	3·3	
43	338·39	+0·24	16	36	32	−46	16·5	11	+0·8	3·2×2·9	
44	338·43	+0·03	16	37	15	−46	18·5	12		5×8	
45	342·05	+0·13	16	50	11	−43	30·3	93	−0·3	30	MHR58 MSH16−4*8*
46	345·34	+1·43	16	55	52	−40	07·7	12	0·0	2·5	
47	348·62	+0·03	17	11	19	−38	27·2	124	−0·4	8×3	MSH17−3*3*
48	348·70	+0·36	17	10	47	−38	06·4	36	−0·4	1·5×5	MHR63
49	351·12	+0·65	17	16	29	−36	02·8	44	+0·2	7	NGC6334 MHR64
50	351·21	+0·47	17	17	38	−36	01·0	18		4·5	
51	351·29	+0·67	17	17	03	−35	49·6	140		15×5	
52	351·7	−1·2	17	25	47	−37	0	23	0·0	6·7	
53	353·10	+0·73	17	21	54	−34	15·0	280	+0·2	20	W22 MHR65
54	359·8	+1·2	17	37	07	−28	42·0	9		3·6	
55	0·84	+0·08	17	44	09	−28	10·3	33	(−)	2·3	
56	1·05	−0·15	17	45	33	−28	04·5	50	(−)	6·3×10	
57	4·5	+6·9	17	27	40	−21	25·0	36	−0·6	2·5	Kepler's supernova MSH17−2*11*
58	5·98	−1·18	18	00	38	−24	22·9	75	0·0	9·5	W29
59	6·6	−0·2	17	58	35	−23	19·0	57	(−)	29	W28
60	6·7	−5·9	18	20	17	−26	0	6		1·1	
61	9·3	−1·3	18	08	22	−21	24·0	31	(+)	3·9	
62	10·15	−0·33	18	06	18	−20	19·8	28	+0·2	2·8	W31
63	10·5	+0·7	18	02	45	−21	26·0	70	(+)	19	
64	12·78	−0·19	18	11	14	−17	57·7	63	(−0·2)	10	W33A MSH18−1*4*
65	14·65	+0·02	18	14	12	−16	13·1	38	+0·1	9·1	W33B
66	15·04	−0·70	18	17	37	−16	13·2	270	(+)	7·6	Omega
67	18·86	+0·32	18	21	24	−12	22·6	34	−0·9	6·6	MSH18−1*9*
68	21·2	+0·3	18	26	32	−10	54·5	21	(+)	5·9	
69	21·81	−0·59	18	30	18	−10	12·0	160	(+)	16	MSH18−1*3*
70	23·5	−0·2	18	31	35	−8	44·0	130	−0·2	11	W41 MSH18−0*8*
71	25·1	−0·1	18	33	36	−6	51·0	19	(+)	4·1	
72	25·37	−0·20	18	35	35	−6	51·7	18	(+)	5	
73	27·38	+0·01	18	38	41	−4	59·4	11	−0·4	4·2	4C−04·71 MSH18−0*9*
74	28·79	+3·46	18	28	57	−2	08·0	34	(+)	6·4	
75	29·70	−0·26	18	43	51	−3	02·7	11	−1·1	2·5	4C−03·70
76	30·77	−0·05	18	45	04	−1	59·9	40	+0·3	5·3	W43
77	31·90	+0·05	18	46	47	−0	56·9	27	+0·0	3·6	4C−00·72 MSH18−0*12*
78	33·07	+0·05	18	48	57	+0	05·0	32	(+)	10	
79	33·2	−0·4	18	50	14	−0·2		39	(+)	8·7	
80	34·64	−0·40	18	53	27	+01	18·0	390	−0·4	22×30	W44 MSH18+0*11*

VI. CATALOGUE

Table 1 gives details of the 80 sources. The sources are listed in order of increasing galactic longitude (l^{II}).

Column 1. Source number.

Columns 2 and 3. Mean position in galactic coordinates.

Columns 4 and 5. Mean position in equatorial coordinates (epoch 1950·0).

Column 6. Integrated flux density in flux units.

Column 7. Spectral index α; this is defined by the expression $S = f^{\alpha}$, so that a thermal source has a positive spectral index.

Column 8. Angular diameter in min of arc, measured at the half-power level.

Column 9. Other catalogue numbers. Abbreviations used are:
MSH, Mills, Slee, and Hill (1958, 1960, 1961); W, Westerhout (1958); RCW, Rodgers, Campbell, and Whiteoak (1960); MHR, Mathewson, Healey, and Rome (1962); (B), Beard (1966); 4C, Gower, Scott, and Wills (1967). No catalogue number has been quoted when there is a gross inconsistency between the low resolution flux densities and the present values. This situation would arise, for example, if a small source were embedded in a broad region of emission.

VII. ACKNOWLEDGMENTS

This work was supported by grants from the U.S. National Science Foundation and the Australian Research Grants Committee. I should like to thank Professor B. Y. Mills for his helpful suggestions. I am indebted to Mr. E. R. Hill for the use of his 1410 MHz survey results. I gratefully acknowledge a CSIRO Studentship and a General Motors–Holden Scholarship.

VIII. REFERENCES

BEARD, M. (1966).—*Aust. J. Phys.* **19**, 141.

GOWER, J. F. R., SCOTT, P. F., and WILLS, D. (1967).—*Mon. Not. R. astr. Soc.* **71**, 49.

HILL, E. R. (1968).—A continuum survey of the southern Milky Way at 1410 MHz. *Aust. J. Phys.* **21** (in press).

HOLDEN, D. J. (1966).—*Mon. Not. R. astr. Soc.* **133**, 229.

HUGHES, R. G., and LONGAIR, M. S. (1967).—*Mon. Not. R. astr. Soc.* **135**, 131.

KELLERMAN, K. I. (1964).—*Astrophys. J.* **140**, 969.

MATHEWSON, D. S., HEALEY, J. R., and ROME, J. M. (1962).—*Aust. J. Phys.* **15**, 354.

MILLS, B. Y. (1952).—*Aust. J. scient. Res.* A **5**, 266.

MILLS, B. Y., AITCHISON, R. E., LITTLE, A. G., and MCADAM, W. B. (1963).—*Proc. Instn Radio Engrs Aust.* **24**, 156.

MILLS, B. Y., SLEE, O. B., and HILL, E. R. (1958).—*Aust. J. Phys.* **11**, 360.

MILLS, B. Y., SLEE, O. B., and HILL, E. R. (1960).—*Aust. J. Phys.* **13**, 676.

MILLS, B. Y., SLEE, O. B., and HILL, E. R. (1961).—*Aust. J. Phys.* **14**, 497.

RODGERS, A. W., CAMPBELL, C. T., and WHITEOAK, J. B. (1960).—*Mon. Not. R. astr. Soc.* **121**, 103.

WESTERHOUT, G. (1958).—*Bull. astr. Insts Neth.* **14**, 215.

THE PARKES CATALOGUE OF RADIO SOURCES

DECLINATION ZONE +20° TO +27°

By A. J. Shimmins* and G. A. Day*

[*Manuscript received December* 4, 1967]

Summary

This paper gives details of 397 radio sources between declinations +20° and +27° which were compiled from a finding survey made at 635 MHz with the 210 ft reflector at the Australian National Radio Astronomy Observatory, Parkes, N.S.W.

The survey covers an area of 0·703 steradian but is incomplete in two regions within ±10° of the galactic equator. Additional measurements of flux densities and positions were made at 1410 and 2650 MHz. Some discussions on spectra, source counts, and source identifications are included, and a comparison is made between this survey and other published catalogues covering the same region.

I. Introduction

This paper is the fifth section of a survey for radio sources being made with the 210 ft radio telescope at the Australian National Radio Astronomy Observatory, Parkes, N.S.W. The earlier parts of the survey have already been published and cover the declination zones 0° to +20° (Day *et al.* 1966), 0° to −20° (Shimmins *et al.* 1966), −20° to −60° (Bolton, Gardner, and Mackey 1964), and −60° to −90° (Price and Milne 1965). The present paper covers the remaining declination zone that is visible with the Parkes telescope, +20° to +27°, and is complete except for two areas within ±10° of the galactic equator. The catalogue contains 397 sources within 0·703 steradian, 341 of these sources being outside the region ±10° of the galactic equator (effective area 0·606 steradian). The catalogue is thought to be substantially complete down to a flux density of 1·5 f.u.† at 635 MHz outside the galactic plane region but contains some weaker sources down to 0·8 f.u.

The observations differ from those of the earlier sections of the catalogue in that the finding survey was done at a frequency of 635 MHz. Positions and flux densities were subsequently measured at 1410 and 2650 MHz.

The estimated r.m.s. errors in position and the date of measurement are given for each source in the catalogue. For most of the sources the positions stated have an r.m.s. error of less than 1′·0 arc in each coordinate. A few of the weaker sources have errors of up to 2′·0 in each coordinate. Spectra and source counts at the three frequencies are discussed and a comparison is made between the results of this survey and the Cambridge 4C catalogue (Pilkington and Scott 1965) and the California Institute of Technology CTD list (Kellerman and Read 1965) for the regions of overlap. The results of an examination by J. G. Bolton of the source positions on the Palomar Sky Survey prints have been included.

---

* Division of Radiophysics, CSIRO, Box 76, P.O. Epping, N.S.W. 2121.

† 1 flux unit = 10^{-26} W m^{-2} Hz^{-1}.

II. Observations and Equipment

The observational procedures for this survey were similar to those for the previous surveys; they are given in detail in the first part of the catalogue (Bolton, Gardner, and Mackey 1964). The major difference is that the finding survey was carried out at 635 MHz rather than at 408 MHz. A degenerate parametric receiver with a 10 MHz bandwidth and a system temperature of 215°K was used. With a 2 sec time constant the peak-to-peak noise fluctuation was 0·33 degK, which corresponds to 0·50 f.u. At 635 MHz the telescope has a beamwidth of 30′·6 arc, and the flux limit was set by confusion between adjacent sources and by background irregularities rather than by the system noise.

The observations at 635 MHz consisted of a series of scans at 2·5 deg/min between declinations +20° and +27°. Adjacent scans were made at intervals of 2^{m} of right ascension. From these records 738 objects were selected down to a flux density of 0·7 f.u. at 635 MHz. Of these, approximately 400 of the strongest objects were subsequently selected for position and flux density measurement at 1410 and 2650 MHz. Most of the sources in this catalogue are stronger than 1 f.u. at 635 MHz.

All strong sources, with flux density greater than 3 f.u. at 635 MHz (or 0·8 f.u. at 2650 MHz), have been accurately positioned at 2650 MHz as part of a separate programme of accurate position measurement (Shimmins 1968). For the weaker sources some were positioned at 2650 MHz and some at 1410 MHz, the particular frequency being indicated in the catalogue (Table 2, column 13).

Table 1

DATES OF OBSERVATIONS AND POSITIONAL ERRORS

Reference	Observation Period	Frequency (MHz)	Estimated R.M.S. Error	Remarks
T6	July 29–30, 1965	2650	15″	Near transit
T10	Oct. 8–11, 1966	2650	16″	Near transit
T11A	Feb. 1–2, 1967	2650	16″	Near transit
T11B	Feb. 3–4, 1967	2650	30″	
T12A	June 22–27, 1967	2650	30″	
T20	Feb. 24–26, 1967	1410	1′–2′	
T21	May 15, 1967	1410	1′–2′	
T22	Sept. 14–15, 1967	1410	1′–2′	

III. Source Position Errors

The position errors depend on the flux density of the source and the frequency at which its position was measured. All the strong sources were measured at 2650 MHz either near transit across the northern meridian, with an average r.m.s. positional error of 16″ arc in each coordinate, or off the meridian, in which case the r.m.s. error is 30″ arc. The positions of the weakest sources were measured at 1410 MHz and have an r.m.s. error of 1′·0 arc in each coordinate for sources stronger than 0·5 f.u. at 1410 MHz and 2′·0 arc for those few sources weaker than 0·5 f.u. Table 1 shows the various observing sessions during which positions were measured, and the estimated r.m.s. error for each. For each source in the catalogue, the period of observation is indicated (Table 2, column 13).

IV. Notes on the Catalogue

Table 2 contains details of the 397 sources in the declination zone +20° to +27°:

Column 1. Parkes catalogue number derived from hours and minutes of right ascension and sign and degrees of declination.

Columns 2 and 3. Mean position for epoch 1950·0. For a discussion of position errors see Section III.

Columns 4 and 5. Annual precession in right ascension (seconds of time) and declination (seconds of arc).

Columns 6, 7, 8, and 9. Flux densities in flux units at frequencies of 178, 635, 1410, and 2650 MHz. The values at 178 MHz are from the 4C catalogue (Pilkington and Scott 1965). Where the flux density errors are thought to be significantly greater than those quoted in Table 3, Section V (*b*), the flux density has been placed in parentheses. For a discussion on the determination of flux densities, see Section V.

Columns 10 and 11. Values of the mean spectral index, flux density at 400 MHz, and estimated r.m.s. errors. C indicates a departure from a power law spectrum (see Section VI).

Column 12. Identification and remarks. The numerals I–IV refer to the classification of the optical field, on the Palomar Sky Survey prints, within a rectangle ±1′·0 from the position of the source (see Section VII). Where an optical identification has been made the following abbreviations apply: QSO, quasi-stellar object; QSO?, possible quasi-stellar object; E, elliptical galaxy; D, spherical galaxy with diffuse envelope; N, compact blue galaxy; S, spiral galaxy; DB, dumb-bell galaxy; M, estimated photographic magnitude; GAL, galaxy for which the type has not been determined. Other abbreviations used are: EXT, source appears extended, as indicated by beam broadening at 2650 MHz; CONF, confused, either with the background or with the source stated.

Column 13. Reference to period of observation during which position and flux density were measured (see Table 1).

Columns 14 and 15. New galactic coordinates.

Columns 16 and 17. Catalogue numbers as given by Pilkington and Scott (1965, 4C catalogue), Kellerman and Read (1965, CTD list), and Pauliny-Toth, Wade, and Heeschen (1966, NRAO); NPC = not previously catalogued. Parentheses around a catalogue number indicate that the source has been resolved at higher frequencies or that there is some doubt that the source and the Parkes catalogue source are identical.

TABLE 2

PARKES CATALOGUE OF RADIO SOURCES, DECLINATION ZONE +20° TO +27°

(1)	(2)	(3)	(4)	(5)	(6)	(7)	(8)	(9)	(10)	(11)	(12)	(13)	(14)	(15)	(16)	(17)
SOURCE NUMBER	POSITION (1950)		ANNUAL PRECESSION		FLUX DENSITY				SPECTRUM		REMARKS	DATE	GALACTIC COORDS		OTHER CATALOGUE NUMBERS	
	R.A.	DEC.	+	+	S178	S635	S1410	S2650	INDEX	S400			L2	B2	4C	OTHER
0004+21	00 04 55	+21 47.9	3.08	20.0	4.1	1.6	0.6	0.4	0.9±0.2	2.0±0.6	III	T11B	110	-40	4C21.1	
0010+26	00 10 06	+26 45.5	3.10	20.0		2.0	0.5	0.4	1.0±0.4	2.3±0.8	II	T21	112	-35		CTD 1
0010+20	00 10 42	+20 30.5	3.10	20.0	(5.3)	(3.1)	(0.9)	0.5	-		III CONF WITH 0011+20	T10	111	-41		
0011+20	00 11 19	+20 28.4	3.10	20.0	(5.3)	(3.1)	(0.7)	0.3	-		III CONF WITH 0010+20 QSO? 18M	T10	111	-41	4C20.1	
0015+21	00 15 42	+21 25.2	3.11	20.0	3.6	1.1	0.7	0.5	0.7±0.2	1.8±0.5	III	T11B	113	-41	4C21.2	
0017+25	00 17 00	+25 46.0	3.12	20.0	2.6	1.3	0.7		0.7±0.5	1.7±0.8		T22	114	-36	4C25.1	
0018+24	00 18 44	+24 11.1	3.12	20.0	3.8	1.2	0.9	0.6	0.6±0.2	2.1±0.5	III	T11B	114	-38	4C24.1	CTD 2
0025+21	00 25 48	+21 00.9	3.13	19.9	4.8	2.5	0.9	0.6	0.8±0.2	2.8±0.7	III	T11B	116	-41	4C20.2	
0029+21	00 29 09	+21 36.5	3.14	19.9	3.9	1.8	0.8	0.4	0.9±0.2	2.4±0.7	II	T11B	117	-41	4C21.3	
0033+26	00 33 25	+26 04.4	3.17	19.8	2.8	1.4	(0.4)	0.4	0.8±0.4	1.8±0.8	III	T20	119	-36	4C26.1	
0035+23	00 35 18	+23 50.6	3.16	19.8		1.7	0.9	0.7	0.5±0.4	1.8±0.5	III	T20	119	-39		CTD 5
0038+25	00 38 37	+25 33.2	3.18	19.8	5.0	1.5	0.4	0.2	1.2±0.2	2.1±0.9	III	T11B	120	-37	4C25.2	
0039+21	00 39 00	+21 07.8	3.16	19.8	2.0	(1.6)	0.5	0.3	0.7±0.5	1.3±0.5	II	T21	120	-41	4C21.5	
0043+20	00 43 49	+20 12.0	3.17	19.7	2.4	1.6	0.8	0.3	1.0±0.3	2.5±0.8	II	T21	121	-42	4C20.4	3C21 NRAO 39
0044+23	00 44 06	+23 54.7	3.19	19.7	2.1	1.2	0.4	0.2	1.0±0.4	1.4±0.7		T12B	122	-39	4C23.3	
0053+26	00 53 11	+26 08.5	3.22	19.5	16.3	5.0	1.8	0.6	1.2±0.1	7.6±1.3	II E 17.5M	T10	124	-36	4C26.2	3C28 CTD 6 NRAO 48
0055+26	00 55 43	+26 35.8	3.23	19.5	5.1	(4.8)	1.3	1.0	0.6±0.2	2.8±0.6		T12A	125	-36	4C26.3	CTD 7
0100+25	01 00 07	+25 35.9	3.24	19.4	4.8	2.8	0.9	0.6	0.9±0.2	3.0±0.7	II	T11B	126	-37	4C25.3	CTD 8

0108+25	01 08 35	+25 49.5	3.26	19.2	2.7	0.8	0.4	0.3	0.8±0.3	1.2±0.5	III			T20	128 -37	4C25.4	
0117+22	01 17 48	+22 40.1	3.26	18.9		1.5	0.7	0.5	0.7±0.4	1.8±0.5				T12B	132 -39		NPC
0121+23	01 21 05	+23 50.4	3.28	18.8	(3.7)	(2.0)	(1.1)	0.4	-		III	CONF WITH 0121+24		T11B	132 -38		NPC
0121+24	01 21 09	+24 03.0	3.28	18.8	(3.7)	(2.0)	(1.1)	0.2	-		III	CONF WITH 0121+23		T11B	132 -38	4C23.4	
0123+25	01 23 54	+25 41.5	3.30	18.7	2.5	1.1	0.5		0.8±0.6	1.4±0.9				T22	133 -36	4C25.5	
0124+22	01 24 23	+22 59.0	3.28	18.7	3.2	(1.4)	(0.3)	0.1	1.3±0.4	1.1±0.8	II	CONF		T11B	133 -39	4C23.5	
0127+23	01 27 15	+23 22.3	3.29	18.6	11.6	6.2	3.0	1.9	0.7±0.1	7.6±1.0	III	QSO	19M	T10	134 -38	4C23.6	3C43 NRAO 74
0127+25	01 27 38	+25 52.7	3.32	18.6	3.8	2.8	1.6	1.0	0.6±0.2	3.5±0.6	III			T11B	134 -36	4C25.6	CTD 11
0128+25	01 28 33	+25 05.0	3.31	18.6	8.6	3.5	1.3	1.0	0.8±0.1	4.2±0.8	III			T10	134 -37	4C25.7	CTD 12
0130+24	01 30 43	+24 13.4	3.30	18.5	2.8	1.4	0.4	0.3	0.9±0.3	1.5±0.6				T12B	135 -37	4C24.2	
0133+20	01 33 40	+20 42.0	3.27	18.4	26.4	8.2	3.5	2.0	1.0±0.1	12.2±1.5	III	QSO	18M	T 6	137 -41	4C20.7	3C47 NRAO 78
0135+22	01 35 26	+22 46.3	3.30	18.3	6.0	2.1	0.6	0.4	1.0±0.2	2.7±0.8	III			T10	137 -39	4C22.2	
0147+26	01 47 15	+26 43.7	3.38	17.9	3.3	1.7		0.2	1.2±0.4	2.0±1.2	III	CONF		T11B	139 -34	4C26.5	CTD 14
0148+20	01 48 01	+20 01.7	3.29	17.9	4.7	1.5	0.8	0.4	0.9±0.2	2.5±0.7	II			T11B	141 -40	4C20.8	
0149+21	01 49 28	+21 52.2	3.32	17.8		1.9	1.6	1.0	0.6±0.3	3.5±0.7				T12B	141 -39		NPC
0152+24	01 52 12	+24 12.1	3.36	17.7	2.6	1.3	0.4		1.0±0.6	1.5±1.0				T22	141 -36	4C24.3	
0153+20	01 53 47	+20 49.0	3.32	17.6	3.0	0.9	0.4	0.4	0.6±0.3	1.3±0.5	III			T11B	143 -39	4C20.9	
0208+21	02 08 23	+21 05.2	3.35	17.0	6.2	3.1	1.4	0.9	0.8±0.2	3.8±0.7	III			T10	147 -38	4C21.9	NRAO 94
0222+26	02 22 25	+26 39.5	3.46	16.3	4.5	1.0	0.6		1.0±0.4	2.0±1.0				T22	148 -31	4C26.8	
0232+22	02 32 33	+22 56.7	3.42	15.8	2.9	1.2	0.8	0.4	0.8±0.3	2.1±0.6	III			T11B	152 -34	4C22.4	
0248+21	02 48 06	+21 09.5	3.42	14.9	2.0	1.6	0.7	0.5	0.6±0.3	1.7±0.5				T12A	157 -34	4C21.10	
0251+20	02 51 07	+20 02.3	3.40	14.7	5.0	(1.2)	1.0	0.5	0.9±0.3	2.9±0.8	III-IV			T11B	158 -34	4C20.11	3C 74 NRAO 117
0302+25	03 02 01	+25 41.0	3.53	14.0	2.9	(2.2)	0.4	0.3	0.8±0.4	1.3±0.6	III			T11B	157 -28	4C25.10	
0308+25	03 08 39	+25 18.9	3.54	13.6	2.4	1.7	0.6	0.5	0.6±0.3	1.6±0.5	III			T20	159 -27	4C25.11	CTD22

TABLE 2 (*Continued*)

(1)	(2)	(3)	(4)	(5)	(6)	(7)	(8)	(9)	(10)	(11)	(12)	(13)	(14)	(15)	(16)	(17)
SOURCE NUMBER	POSITION (1950)		ANNUAL PRECESSION		FLUX DENSITY				SPECTRUM		REMARKS	DATE	GALACTIC COORDS		OTHER CATALOGUE NUMBERS	
	R.A.	DEC.	+	+	S178	S635	S1410	S2650	INDEX	S400			L2	B2	4C	OTHER
0309+24	03 09 41	+24 12.9	3.52	13,6	5,8	2,9	0,8	0,5	1,0±0,2	3,2±0.8	III	T11B	160	-28	4C24,5	CTD 23 3C83 NRAO 127
0310+26	03 10 26	+26 13.6	3.56	13.5	2.8	1.3	0,3		1.1±0.6	1.5±1.2	III	T20	158	-26	4C26.11	NRAO129
0310+22	03 10 58	+22 08.6	3.48	13.5	3.1	1.2	0,4	0.2	1.1±0.3	1.6±0.7	III	T20	161	-30	4C22.5	
0322+24	03 22 06	+24 33.7	3.54	12.7	3,2	1.4	0,6	0.4	0.8±0,3	1,8±0.6	III	T20	162	-26	4C24.6	
0322+21	03 22 32	+21 17.7	3.48	12.7	2.7	1.6	0,3		1.2±0,6	1,7±1.3	III	T20	164	-29	4C21.11	
0326+24	03 26 58	+24 07.2	3.54	12.4	3.1	1.0	0,4		1.0±0.5	1,5±1.0		T22	163	-26	4C24.7	
0328+24	03 28 07	+24 48.0	3.56	12.3	3.8	1.9	0.3	0.1	1.4±0.3	2,1±1.2	III	T20	163	-25	4C24.8	
0340+20	03 40 03	+20 51.2	3.49	11.5	2.2	1,7	0.5	0.3	0.9±0.3	1.8±0.7		T12A	168	-26	4C20.12	
0349+26	03 49 02	+26 15,3	3.63	10.8	6.5	3.1	1.1	0.7	0.9±0.2	3.6±0.8	III-IV	T10	166	-21	4C26.12	CTD 25
0349+22	03 49 35	+22 11.7	3.53	10.8	3.1	1.6	0,7	0.3	1.0±0.3	2.2±0.7	III-IV	T11B	169	-24	4C22,6	
0349+21	03 49 44	+21 16.0	3.51	10.8	2.5	1.1	0,6	0.4	0.7±0.3	1.5±0.5	II	T20	170	-25	4C21,13	
0350+23	03 50 02	+23 06.9	3.55	10.8	2.3	1.2	0.3	0.3	0.8±0.3	1.2±0.5		T12A	168	-23	4C23,7	
0352+21	03 52 56	+21 04,5	3.51	10.6	2.9	1.9	0,7	0.4	0.9±0.3	2.2±0.7	III	T11B	170	-24	4C21,14	
0403+20	04 03 24	+20 47,4	3.52	9.8	2.6	2.2	0,7	0.4	0.9±0.3	2.4±0,7	III	T20	172	-23	4C20,13	
0409+22	04 09 44	+22 57,5	3.58	9.3	5,1	3.1	1,3	1.0	0.6±0.2	3.3±0.6	III-IV	T11B	172	-20	4C22,8	3C 108 NRAO167
0410+26	04 10 19	+26 40.8	3.67	9.2	3,8	1.5	0,5	0.2	1.1±0.3	2.0±0,8	III-IV	T11B	169	-17	4C26,15	
0417+25	04 17 46	+25 19.1	3.64	8.6	5.5	1.5	1,1	0.5	0.9±0.2	3.1±0.8	III-IV	T10	171	-17	4C25,14	
0418+23	04 18 21	+23 41.2	3.60	8.6	2.9	1.0	0,5		0.9±0.5	1.5±0.9		T22	173	-18	4C23,8	
0421+21	04 21 22	+21 19.5	3.55	8.4	3.7	2.7		0.7	0.8±0.3	3.1±0.9		T12A	175	-19	4C21,16	
0424+26	04 24 44	+26 32.2	3.68	8.1	3.1	2.2		0.3	1.1±0.3	2.5±1.2	IV	T11B	172	-15	4C26,16	

0425+21	04 25 52	+21 27.5	3.55	8.0	3.2	1.3	1.1		0.5±0.5	2.0±0.7		T22	176	-18	4C21.17	
0425+23	04 25 55	+23 27.4	3.61	8.0	3.8	1.2	0.4		1.1±0.5	1.7±1.1	IV	T20	174	-17	4C23.9	
0427+24	04 27 25	+24 14.5	3.63	7.9	4.6	1.6	0.6		1.0±0.4	2.2±1.1	IV	T20	174	-16	4C24.9	CTD 28
0428+20	04 28 03	+20 31.2	3.53	7.8		4.5	2.8	3.4	C			T12A	177	-19		NPC
0430+23	04 30 47	+23 31.2	3.61	7.6	2.6	1.1	0.4		0.9±0.6	1.4±1.0	IV	T20	175	-16	4C23.10	
0436+23	04 36 29	+23 05.2	3.61	7.1	4.5	0.8	0.8	0.3	1.0±0.2	2.5±0.8	III-IV	T11B	176	-15	4C23.11	
0436+20	04 36 52	+20 19.0	3.54	7.1	3.5	1.7	0.4	0.2	1.2±0.3	1.9±0.9	III-IV	T20	178	-17	4C20.14	
0446+20	04 46 25	+20 38.1	3.55	6.3	2.9	2.2	0.3		1.3±0.6	2.3±1.5	III	T20	180	-15	4C20.15	
0447+22	04 47 43	+22 51.7	3.61	6.2	2.5	(2.6)	0.6	0.2	1.1±0.5	1.9±0.9	III EXT DEC	T20	178	-14	4C22.10	NRA0195
0452+23	04 52 17	+23 05.1	3.62	5.8	3.7	(1.0)	0.5	0.4	0.8±0.3	1.6±0.6		T22	178	-13	4C23.12	
0453+20	04 53 31	+20 34.4	3.55	5.7	4.1	1.8	0.5	0.3	1.0±0.2	2.1±0.8	III	T11B	181	-14	4C20.16	
0453+22	04 53 42	+22 44.7	3.61	5.7	12.4	7.8	3.4	2.1	0.8±0.1	9.0±1.1	II GAL 19M	T10	179	-13	4C22.11	3C132 NRA0198
0459+25	04 59 55	+25 12.0	3.68	5.2	21.0	11.4	5.8	3.7	0.7±0.1	14.0±1.4	III-IV	T11A	178	-10	4C25.16	3C133 CTD 31 NRA0199
0504+23	05 04 04	+23 47.3	3.64	4.8	(3.3)	1.6	0.6	0.5	0.6±0.4	1.6±0.5	III-IV	T11B	179	-10	(4C23.13)	
0507+21	05 07 22	+21 04.7	3.57	4.6		1.9	0.6	0.3	1.2±0.5	3.1±1.2	III	T21	182	-11		NPC
0512+24	05 12 58	+24 55.2	3.68	4.1	4.7	6.1	3.4	1.6	C		II D 17M	T10	180	-8	4C24.10	3C136,1 CTD 34 NRA0203
0514+23	05 14 38	+23 47.8	3.65	3.9	3.2	1.0	0.8	0.5	0.7±0.3	1.9±0.5	IV	T11B	181	-8	4C23.14	
0515+25	05 15 21	+25 08.1	3.69	3.9	(2.5)	1.0	0.3	0.1	1.6±0.9	2.3±1.7	III	T21	180	-7	(4C25.17)	
0520+24	05 20 16	+24 23.4	3.67	3.5		1.3	0.5	0.2	1.3±0.6	2.7±1.3	II	T21	181	-7		NPC
0520+23	05 20 53	+23 53.6	3.66	3.4		0.7	0.6		0.2±1.6	0.8±0.3	III-IV	T21	182	-7		NPC
0531+21	05 31 32	+21 58.9	3.61	2.5	(1530)				-		CRAB NEB		185	-6	4C21.19	3C144 NRA0214
0538+23	05 38 15	+23 43.9	3.66	1.9	3.7	(1.2)	1.1	0.5	0.9±0.3	3.0±0.8	IV COMPLEX AREA	T11B	184	-4	4C23.15	
0545+26	05 45 36	+26 35.1	3.74	1.3	4.5	2.0	1.2	0.6	0.8±0.2	3.1±0.7	III-IV	T10	182	-1	4C26.18	

TABLE 2 (*Continued*)

(1) SOURCE NUMBER	(2) POSITION (1950) R.A.	(3) DEC.	(4) ANNUAL PRECESSION +	(5) +	(6) FLUX DENSITY S178	(7) S635	(8) S1410	(9) S2650	(10) SPECTRUM INDEX	(11) S400	(12) REMARKS	(13) DATE	(14) GALACTIC COORDS L2	(15) B2	(16) OTHER CATALOGUE NUMBERS 4C	(17) OTHER
0600+219	06 00 51	+21 59.7	3.61	-0.1	8.4	3.7	2.9	1.9	0.6±0.1	5.6±0.8	III-IV	T11B	188	0	4C22.12	
0600+217	06 00 53	+21 42.4	3.61	-0.1				2.2	-		EXT SIZE 8'	T12A	188	-0		NPC
0601+20	06 01 30	+20 21.3	3.57	-0.1	12.4	5.3	2.1	0.8	1.1±0.1	7.4±1.2	III	T11A	190	-1	4C20.17	3C152 NRA0226
0601+24	06 01 51	+24 29.5	3.68	-0.2	3.8	2.0	0.9	0.7	0.6±0.2	2.2±0.5	III-IV	T10	186	1	4C24.11	CTD 40
0604+26	06 04 38	+26 37.3	3.74	-0.4	5.7		1.0	0.5	0.9±0.2	3.1±0.8	III-IV	T21	184	3	4C26.19	CTD 41
0605+21	06 05 34	+21 36.8	3.60	-0.5		2.0	1.1		0.7±0.6	2.8±0.6		T21	189	1		NRA0227
0606+20	06 06 37	+20 29.9	3.57	-0.6		23.0	11.3		0.9±0.2	34.7±2.6	HII EXT	T21	190	0		NRA0229 3C153,1
0609+22	06 09 46	+22 54.5	3.64	-0.9	3.4	1.4	0.6		0.9±0.5	1.9±0.9	III-IV	T21	188	2	4C22.13	
0610+26	06 10 43	+26 05.4	3.73	-0.9	23.1	9.2	5.0	3.4	0.7±0.1	12.5±1.3	III-IV EXT	T10	186	4	4C26.20	3C154 CTD 42 NRA0230
0615+22	06 15 01	+22 40.8	3.63	-1.3	6.3		(14.7)	(8.0)	-		IC443 EXT SIZE 24 MIN	T11A	189	3	4C22.15	3C157
0618+23	06 18 09	+23 23.6	3.65	-1.6	4.3	(3.8)	(1.0)		-		EXT SIZE 25 MIN III-IV	T21	189	4	4C23.16	
0619+26	06 19 33	+26 36.7	3.74	-1.7	2.6		0.4	0.1	1.1±0.5	1.4±0.9	II	T20	186	6	4C26.21	
0619+22	06 19 50	+22 01.8	3.61	-1.7	4.8		1.2	0.8	0.7±0.2	2.8±0.6	III-IV	T11B	190	4	4C22.16	
0623+26	06 23 58	+26 25.4	3.73	-2.1	4.1		1.4	1.0	0.5±0.3	2.8±0.6	II	T20	187	7	4C26.22	CTD 44 3C160 NRA0235
0628+25	06 28 20	+25 02.7	3.69	-2.5	5.6		1.2	0.6	0.9±0.2	3.4±0.8	II	T11A	188	7	4C25.18	CTD45 3C162 NRA0237
0632+26	06 32 30	+26 19.4	3.73	-2.8	3.8		0.7	0.6	0.6±0.3	1.8±0.5	II EXT SIZE 9'	T20	188	8	4C26.23	CTD 46
0635+20	06 35 37	+20 36.7	3.57	-3.1	3.1		0.3	0.2	1.0±0.4	1.3±0.8	III	T11B	193	7	4C20.19	

0640+23	06 40 05	+23 22.0	3.64	-3.5	13.5	5.3	2.5	1.4	0.9±0.1	7.4±1.0	III		T10	191	9	4C23.17	3C165 NRAO240
0642+21	06 42 25	+21 25.0	3.59	-3.7	14.7	5.1	2.5	1.8	0.8±0.1	7.1±1.0	II	GAL 19M	T10	193	8	4C21.21	3C166 NRAO242
0648+22	06 48 15	+22 53.4	3.63	-4.2	3.0	(2.3)	(0.2)	0.1	1.3±0.4	1.1±0.8	III	EXT LOWER DEC	T20	192	10	4C22.17	NRAO247
0648+26	06 48 35	+26 20.0	3.72	-4.2	2.9	1.3	0.6	0.4	0.7±0.3	1.6±0.5	III		T20	189	12	4C26.25	
0649+22	06 49 45	+22 36.1	3.62	-4.3	6.6	2.9	1.0	0.5	1.0±0.2	3.7±0.9	II	GAL 19M	T10	193	10	4C22.18	3C170 NRAO249
0655+22	06 55 42	+22 29.9	3.61	-4.8		1.5	0.3		2.0±1.0	3.8±2.1	III		T21	193	12		NPC
0656+21	06 56 39	+21 22.4	3.58	-4.9	3.1	1.0	0.7	0.3	0.9±0.3	2.0±0.7	II		T11B	195	11	4C21.22	
0658+23	06 58 29	+23 17.5	3.63	-5.1	3.6	1.9	1.1	0.7	0.7±0.2	2.5±0.6	II		T11B	193	12	4C23.18	
0659+25	06 59 04	+25 18.1	3.68	-5.1	13.7	5.8	3.0	1.7	0.8±0.1	8.1±1.1	III		T10	191	13	4C25.19	CTD48 3C172 NRAO254
0706+26	07 06 02	+26 09.3	3.70	-5.7	3.2	2.1	1.0	0.7	0.6±0.2	2.3±0.5	III		T11B	191	15	4C26.26	
0715+20	07 15 14	+20 14.0	3.54	-6.5		1.5	0.7		1.0±0.8	2.3±0.7	III		T21	198	15		NPC
0719+25	07 19 45	+25 34.7	3.67	-6.8		0.9	0.4	0.1	1.7±1.0	2.9±1.9	II		T20	193	18		CTD 50
0725+24	07 25 33	+24 25.2	3.64	-7.3		1.2	0.8	0.6	0.5±0.4	1.5±0.4	II	CONF WITH 0726+24	T21	195	19		3C182 NRAO267
0726+24	07 26 03	+24 48.2	3.65	-7.3	4.3	0.9	(0.2)	0.1	1.4±0.4	1.5±1.3	III	CONF WITH 0725+24	T11B	194	19	4C24.15	
0729+25	07 29 54	+25 54.7	3.67	-7.7	(3.3)	(2.2)	0.9	0.7	0.4±0.4	1.5±0.3	III	CONF WITH 0730+25	T11B	193	20	(4C25.21)	
0730+25	07 30 10	+25 43.8	3.67	-7.7	(3.3)	(2.2)	0.7	0.3	1.3±0.6	3.8±1.0	III	CONF WITH 0729+25	T11B	194	20	4C25.21	
0736+21	07 36 49	+21 01.5	3.54	-8.2	4.4	2.2	0.6	0.4	1.0±0.2	2.4±0.8	III		T10	199	20	4C21.23	
0740+23	07 40 54	+23 42.1	3.60	-8.5		1.5	0.4		1.7±0.9	3.2±1.5	III		T21	197	22		NPC
0754+22	07 54 11	+22 01.7	3.55	-9.6		1.6	0.3	0.2	1.4±0.6	2.5±1.4	III		T21	200	24		NPC
0802+24	08 02 37	+24 18.4	3.59	-10.2	15.0	8.3	5.0	3.3	0.6±0.1	10.5±1.1	I	D 15M	T10	198	26	4C24.16	CTD 52 3C192 NRAO280
0802+21	08 02 41	+21 15.1	3.52	-10.2		(2.0)	0.8	1.0	-0.4±0.4	0.5±0.1	II		T21	201	25		NPC

TABLE 2 (*Continued*)

(1)	(2)	(3)	(4)	(5)	(6)	(7)	(8)	(9)	(10)	(11)	(12)	(13)	(14)	(15)	(16)	(17)
SOURCE NUMBER	POSITION (1950)		ANNUAL PRECESSION		FLUX DENSITY				SPECTRUM		REMARKS	DATE	GALACTIC COORDS		OTHER CATALOGUE NUMBERS	
	R.A.	DEC.	+	+	S178	S635	S1410	S2650	INDEX	S400			L2	B2	4C	OTHER
0806+22	08 06 03	+22 32.3	3.55	-10.5	2.9	1.2	0.5	0.3	0.9±0.3	1.6±0.6	III	T11B	200	27	4C22.19	
0814+22	08 14 39	+22 46.5	3.54	-11.1	4.1	2.6	1.2	0.8	0.7±0.2	3.0±0.6	III	T11B	201	28	4C22.20	3C197 NRAO287
0815+23	08 15 09	+23 48.4	3.56	-11.1	2.0	1.2	0.5	0.2	1.0±0.4	1.7±0.7	III	T21	200	29	4C23.19	
0820+22	08 20 29	+22 32.6	3.53	-11.5	4.5	2.7	2.3	1.0	C		III	T11B	201	30	4C22.21	
0825+24	08 25 46	+24 46.3	3.57	-11.9	2.7	1.2	0.7	0.4	0.8±0.3	1.8±0.6	II	T20	199	32	4C24.17	
0825+23	08 25 53	+23 28.3	3.54	-11.9		(2.1)	0.3		-		III CONF WITH 0827+23	T21	201	31		NPC
0827+23	08 27 23	+23 32.7	3.54	-12.0		(2.1)	1.0	0.7	0.6±0.4	2.0±0.3	III CONF WITH 0825+23	T21	201	32		NPC
0832+26	08 32 07	+26 45.3	3.60	-12.3		2.0	0.4		2.0±0.8	5.1±2.2	III	T20	198	34		CTD 56
0835+25	08 35 53	+25 37.4	3.57	-12.6	4.2	2.0	0.7	0.5	0.8±0.2	2.3±0.6	III	T10	199	34	4C25.22	
0848+22	08 48 49	+22 53.4	3.49	-13.5	(2.0)	1.0	0.3		1.5±1.3	2.0±1.2	III	T21	203	36	(4C23.20)	
0901+22	09 01 57	+22 31.7	3.46	-14.3	5.1	2.1	0.9	0.5	0.9±0.2	2.8±0.7	III	T11B	205	39	4C22.22	
0903+25	09 03 22	+25 49.5	3.52	-14.4	3.0	1.0	0.6	0.4	0.7±0.3	1.6±0.5	III	T11B	201	40	4C25.23	
0905+23	09 05 08	+23 07.1	3.47	-14.5		1.3	0.4	0.2	1.3±0.6	2.1±1.1	III	T21	205	40		NPC
0907+24	09 07 30	+24 31.7	3.49	-14.6	3.2	1.6	0.7	0.5	0.7±0.2	1.9±0.5	III	T11B	203	41	4C24.19	CTD 60
0910+23	09 10 43	+23 49.5	3.47	-14.8	3.1	1.9	0.8	0.6	0.6±0.2	2.0±0.5	III	T11B	204	41	4C23.21	
0912+25	09 12 48	+25 22.0	3.50	-14.9	2.1	1.1	0.4	0.2	1.0±0.4	1.4±0.7	III	T21	202	42	4C25.24	
0914+23	09 14 50	+23 18.9	3.45	-15.1	2.9	1.3	0.4	0.2	1.1±0.3	1.6±0.8	III	T20	205	42	4C23.22	
0915+22	09 15 38	+22 45.0	3.44	-15.1	6.1	2.5	0.8	0.4	1.1±0.2	3.2±0.9	III	T10	206	42	4C22.23	
0919+21	09 19 54	+21 47.9	3.42	-15.3	2.6	1.5	0.4		1.0±0.6	1.7±1.1	III	T20	208	42	4C21.25	
0926+25	09 26 09	+25 25.7	3.47	-15.7	2.4	1.7	0.3	0.1	1.4±0.4	1.9±1.2	III EXT IN RA	T21	203	45	4C25.25	
0932+25	09 32 42	+25 23.2	3.45	-16.0	3.0	1.6	0.7	0.4	0.8±0.3	2.0±0.6	III	T11B	204	46	4C25.26	

0934+25	09 34 16	+25 34.4	3.45	-16.1	2.5	1.1	0.4	0.2	1.0±0.3	1.4±0.7	II		T20	204	47	4C25.27	
0935+26	09 35 58	+26 12.9	3.46	-16.2	3.5	2.6	0.7	0.4	1.0±0.2	2.8±0.8	III		T11B	203	47	4C26.28	
0939+26	09 39 33	+26 39.9	3.46	-16.4	4.1	1.4	0.6	0.4	0.8±0.2	2.0±0.6	III		T11B	203	48	4C26.29	
0943+25	09 43 23	+25 45.5	3.44	-16.6	2.2	1.1	0.5	0.3	0.8±0.3	1.4±0.5	III		T21	204	49	4C25.28	
0949+24	09 49 11	+24 36.5	3.40	-16.9	6.5	3.3	1.9	1.2	0.7±0.1	4.3±0.7	II	DR 18M	T10	206	50	4C24.22	CTD 62 3C 229 NRAO338
0950+25	09 50 48	+25 30.5	3.41	-16.9	5.7	2.1	0.9	0.5	0.9±0.2	2.9±0.7	II		T11B	205	50	4C25.29	
0951+21	09 51 20	+21 36.8	3.36	-17.0	3.3	2.0	0.8	0.6	0.7±0.2	2.1±0.5	III		T20	211	49	4C21.26	
0957+22	09 57 36	+22 47.5	3.36	-17.3	3.7	2.1	1.1	0.7	0.7±0.2	2.6±0.6	III		T11B	210	51	4C22.25	
0958+25	09 58 40	+25 40.0	3.40	-17.3	3.8	1.2	0.4	0.3	0.9±0.3	1.7±0.7	III		T11B	206	52	4C25.30	
1000+20	10 00 13	+20 06.2	3.32	-17.4	5.1	1.9	0.9	0.7	0.7±0.2	2.5±0.6	III		T20	214	51	4C20.20	
1000+26	10 00 59	+26 20.4	3.40	-17.4		(1.0)	0.5	0.3	0.8±0.7	1.4±0.4	III	CONF AT635	T21	205	53		NPC
1001+20	10 01 39	+20 42.1	3.32	-17.4	3.6	1.3	0.3	0.2	1.1±0.3	1.6±0.8	III		T20	214	51	4C20.21	
1002+22	10 02 00	+22 39.9	3.35	-17.4	3.8	1.2	0.6	0.3	1.0±0.3	1.9±0.7	III		T20	211	52	4C22.26	
1008+21	10 08 26	+21 26.9	3.32	-17.7	5.1	1.4	0.5	0.3	1.1±0.2	2.1±0.8	III		T11B	213	53	4C21.27	
1011+23	10 11 59	+23 16.7	3.33	-17.9	3.5	1.9	1.1	0.7	0.7±0.2	2.5±0.6	III		T11B	211	54	4C23.24	
1019+22	10 19 09	+22 14.3	3.31	-18.1	11.1	4.8	1.7	0.8	1.0±0.1	6.2±1.1	III		T10	213	56	4C22.28	3C241 NRAO352
1019+25	10 19 21	+25 38.0	3.35	-18.1	3.1	1.4	0.8	0.4	0.8±0.3	2.2±0.6	III		T11B	207	57	4C25.32	
1022+20	10 22 36	+20 25.5	3.28	-18.3	6.8	2.1	0.9	0.7	0.8±0.2	3.0±0.7	III	QSO? 18.5M	T10.	217	56	4C20.22	3C242 NRAO354
1028+23	10 28 05	+23 20.3	3.30	-18.5	3.7	1.0	0.4	0.2	1.1±0.3	1.6±0.8	III		T11B	212	58	4C23.25	
1030+25	10 30 02	+25 18.6	3.31	-18.5	4.3	1.2	0.8	0.5	0.8±0.2	2.2±0.6	III		T11B	209	59	4C25.33	
1044+22	10 44 10	+22 33.2	3.25	-19.0	3.6	1.3	0.5	0.3	0.9±0.3	1.8±0.7	III		T11B	216	61	4C22.29	
1048+24	10 48 49	+24 04.0	3.26	-19.1	2.9	1.6	0.5	0.2	1.1±0.3	2.0±0.8	III		T20	213	63	4C24.23	CTD 68
1049+21	10 49 07	+21 35.6	3.23	-19.1	2.4	(1.6)	1.4	1.3	0.2±0.3	1.8±0.3		CONF WITH 1049+20	T21	218	62	4C21.28	
1049+20	10 49 47	+20 45.5	3.23	-19.1	2.3	(2.2)	1.5	1.1	0.4±0.3	2.5±0.5	III	CONF WITH 1049+21	T21	220	62	4C20.23	

TABLE 2 (*Continued*)

(1) SOURCE NUMBER	(2) POSITION (1950) R.A.	(3) DEC.	(4) ANNUAL PRECESSION +	(5) +	(6) FLUX DENSITY S178	(7) S635	(8) S1410	(9) S2650	(10) SPECTRUM INDEX	(11) S400	(12) REMARKS	(13) DATE	(14) GALACTIC COORDS L2	(15) B2	(16) OTHER CATALOGUE NUMBERS 4C	(17) OTHER
1053+24	10 53 29	+24 12.0	3.24	-19.2		1.1	0.2	0.2	1.0±0.7	1.3±0.8	II	T21	213	64		NPC
1055+20	10 55 36	+20 08.2	3.21	-19.3	9.5	4.7	2.2	1.9	0.6±0.1	5.2±0.7	III QSO? 18.5M	T10	222	63	4C20.24	
1102+21	11 02 48	+21 08.2	3.20	-19.4		1.9	0.9	0.5	0.9±0.4	3.0±0.8	III	T20	222	65		NPC
1106+25	11 06 11	+25 17.4	3.22	-19.5	7.9	4.0	1.1	0.6	1.1±0.1	4.6±1.0	III	T10	212	67	4C25.34	CTD 70 3C250 NRAO365
1112+21	11 12 54	+21 50.6	3.18	-19.6	2.8	1.3	0.4	0.2	1.1±0.3	1.6±0.8	III	T20	222	68	4C21.30	
1114+26	11 14 06	+26 04.2	3.20	-19.6	3.7	1.9	0.5	0.3	1.0±0.2	2.1±0.8	III	T11B	211	69	4C26.31	
1118+23	11 18 05	+23 44.4	3.18	-19.7	9.2	3.0	1.2	0.7	1.0±0.1	4.3±0.9	II D 17,5M	T10	218	69	4C23.27	3C256 NRAO371
1119+21	11 19 50	+21 40.9	3.17	-19.7		2.2	0.6	0.3	1.3±0.4	3.7±1.4	III	T20	224	69		NPC
1123+26	11 23 14	+26 26.6	3.18	-19.8		0.6	0.7	0.7	-0.0±0.5	0.7±0.2	III	T11B	211	71		CTD 74
1123+201	11 23 20	+20 08.7	3.15	-19.8	(3.5)	(2.3)	(0.6)	0.3	-		II CONF WITH 1123+20.3	T11B	229	69	4C20.25	
1123+203	11 23 22	+20 22.1	3.15	-19.8	(3.5)	(2.0)	(0.8)	0.6	-		II CONF WITH 1123+20.1	T11B	228	69	(4C20,25)	
1125+26	11 25 30	+26 03.1	3.17	-19.8	2.8	1.2	0.4	0.2	1.0±0.3	1.5±0.7	III	T20	212	71	4C25.35	
1128+20	11 28 40	+20 12.2	3.14	-19.9	(2.7)	(0.8)	0.3	0.2	0.6±1.0	0.7±0.3	III	T21	230	70	(4C20,26)	
1128+21	11 28 48	+21 47.6	3.15	-19.9	3.0	1.0	0.3	0.1	1.3±0.4	1.4±0.9	II	T11B	226	71	4C21.31	
1129+19	11 29 01	+19 43.9	3.14	-19.9		(1.0)	0.4	0.3	0.5±0.7	0.7±0.2	III	T21	231	70		NPC
1131+21	11 31 23	+21 21.6	3.14	-19.9	(2.3)	(1.2)	0.7	0.4	0.9±0.5	2.1±0.5	II CONF WITH 1132+21	T21	228	71	4C21.32	
1132+21	11 32 37	+21 21.9	3.14	-19.9	(2.3)	(1.2)	0.2		-		II CONF WITH 1131+21	T21	228	72	(4C21,32)	
1133+26	11 33 13	+26 14.6	3.15	-19.9	4.3	1.5	0.6	0.2	1.2±0.3	2.3±0.9	III	T11B	213	73	4C26.32	NRAO379
1134+26	11 34 53	+26 35.9	3.15	-19.9	3.1	0.5	0.4	0.2	1.0±0.3	1.4±0.7	III	T20	211	73	4C26.33	

1139+234	11 39 00	+23 24.8	3.13	-20.0	(5.4)	(1.6)	0.5	0.2	1.5±0.8	3.1±1.0	II	CONF WITH 1139+23.0	T20	223	74	4C23.28	
1139+230	11 39 00	+23 04.0	3.13	-20.0	(5.4)	(1.6)	0.3		-		III	CONF WITH 1139+23.4	T20	224	74	(4C23.28)	
1140+20	11 40 00	+20 13.2	3.12	-20.0		(1.3)	0.3		-		III	CONF	T21	234	73		NPC
1140+21	11 40 25	+21 45.8	3.12	-20.0	(5.7)	1.6	1.0	0.4	1.2±0.4	4.2±1.2	III		T11B	229	73	(4C21.33)	
1140+22	11 40 48	+22 23.6	3.12	-20.0	18.3	7.0	2.9	1.6	0.9±0.1	9.6±1.2	III		T10	227	74	4C22.30	3C263.1 NRAO383
1144+25	11 44 40	+25 40.0	3.12	-20.0	3.7	1.6	0.9	0.4	0.9±0.2	2.6±0.7	III		T20	216	76	4C25.36	CTD 75
1148+22	11 48 24	+22 42.0	3.10	-20.0	2.4	(1.2)	0.3	0.1	1.2±0.5	1.2±0.9	III	CONF WITH 1150+22	T21	229	76	4C22.31	
1150+26	11 50 14	+26 31.4	3.10	-20.0	2.7	1.3	0.4	0.2	1.1±0.3	1.6±0.7	III		T20	213	77	4C26.34	
1150+22	11 50 40	+22 44.4	3.10	-20.0	2.4	(1.2)	0.3	0.1	1.2±0.5	1.2±0.9	II	CONF WITH 1148+22	T21	229	76	4C22.32	
1151+22	11 51 37	+22 44.7	3.09	-20.0		(1.2)	0.4	0.2	1.1±0.8	1.6±0.6	II	CONF WITH 1150+22	T21	229	76		NPC
1155+26	11 55 47	+26 38.2	3.09	-20.0	2.9	3.0	0.9	0.4	1.1±0.2	3.7±1.0	II		T20	214	78	4C26.35	
1158+252	11 58 16	+25 15.0	3.08	-20.0	4.2	2.3	0.7	0.3	1.1±0.2	2.8±0.9	III		T11B	221	78	4C25.37	
1158+256	11 58 51	+25 37.6	3.08	-20.0	3.6	2.2	0.6	0.4	0.9±0.2	2.3±0.7	III		T11B	219	79	4C25.38	
1201+24	12 01 03	+24 00.3	3.07	-20.0		1.4		0.2	1.4±0.5	2.6±1.2			T12B	228	79		NPC
1202+26	12 02 50	+26 50.7	3.06	-20.0	2.4	1.2	0.5	0.2	1.0±0.3	1.7±0.7			T21	213	80	4C26.36	
1204+22	12 04 01	+22 32.1	3.06	-20.0	3.4	(3.2)	1.1	0.6	0.8±0.3	2.7±0.7	I		T11B	236	79	4C22.33	
1206+23	12 06 30	+23 26.5	3.06	-20.0	3.7	1.7	0.6	0.3	1.0±0.3	2.1±0.7	III		T11B	233	80	4C23.29	
1210+20	12 10 23	+20 49.5	3.05	-20.0	6.5	2.7	1.4	0.8	0.8±0.2	3.8±0.7	III		T10	248	79	4C20.27	
1210+24	12 10 13	+24 15.5	3.05	-20.0	2.5	0.8	0.2		1.2±0.7	1.1±1.2	II		T20	231	81	4C24.25	
1215+25	12 15 25	+25 45.7	3.03	-20.0	4.2	1.6	0.8	0.4	0.9±0.2	2.4±0.7	III		T11B	223	82	4C25.39	3C269 NRAO394
1216+20	12 16 29	+20 12.4	3.04	-20.0	3.3	2.2	1.1	0.6	0.8±0.2	2.9±0.7	II		T11B	255	80	4C20.28	
1218+22	12 18 11	+22 49.8	3.03	-20.0	4.0	2.0	0.7	0.4	0.9±0.2	2.4±0.7	III		T20	244	82	4C22.35	
1222+26	12 22 03	+26 30.0	3.01	-20.0	4.0	1.5	0.6	0.4	0.9±0.2	2.0±0.6	III		T12A	220	84	4C26.37	

TABLE 2 (*Continued*)

(1)	(2)	(3)	(4)	(5)	(6)	(7)	(8)	(9)	(10)	(11)	(12)	(13)	(14)	(15)	(16)	(17)
SOURCE NUMBER	POSITION (1950)		ANNUAL PRECESSION		FLUX DENSITY				SPECTRUM		REMARKS	DATE	GALACTIC COORDS		OTHER CATALOGUE NUMBERS	
	R.A.	DEC.	+	+	S178	S635	S1410	S2650	INDEX	S400			L2	B2	4C	OTHER
1222+21	12 22 24	+21 39.5	3.02	-19.9	6.6	2.6	1.5	1.1	0.6±0.2	3.5±0.6	III QSO 18M	T10	255	82	4C21.35	
1225+20	12 25 41	+20 40.2	3.02	-19.9	4.3	2.5	1.3	0.8	0.7±0.2	3,1±0.6	III	T21	263	81	4C20.29	
1229+26	12 29 57	+26 23.3	2.99	-19.9	3.3	1.4	0,4	0.2	1.1±0.3	1.7±0.8	III	T11B	225	86	4C26.38	
1232+21	12 32 58	+21 37.2	3.00	-19.8	14.3	5.5	3,0	1.6	0.8±0.1	8.2±1.1	III	T10	270	83	4C21.36	3C274.1 NRA0402
1233+26	12 33 59	+26 51.4	2.97	-19.8	4.2	2.8	0,4	0.2	1.4±0.2	3.0±1.2	III	T11B	221	87	4C26.39	
1237+22	12 37 25	+22 29.3	2.98	-19.8	2.1	1.3	0,3	0.3	0.8±0.3	1.3±0.5	III	T21	274	84	4C22.36	
1241+23	12 41 22	+23 02.0	2.97	-19.7	2.5	1.7	0,3	0.2	1.2±0.3	1.8±0.9	III	T20	281	85	4C23.32	
1246+23	12 46 39	+23 51.2	2.95	-19.6	2.5	1.3	0,5	0.3	0.9±0.3	1.6±0.6	III	T20	294	86	4C23.33	
1251+26	12 51 44	+26 46.6	2.92	-19.5	3.3	1.0	0.4	0.2	1.1±0.3	1.5±0.7	II CONF	T21	348	89	4C26.40	
1256+21	12 56 10	+21 34.9	2.94	-19.4	3.0	1.1	0.4	0.2	1.0±0.3	1.5±0.7	III	T11B	319	84	4C21.37	
1257+23	12 57 51	+23 43.6	2.93	-19.4	2.5	1.0	0.3		1.1±0.6	1.3±1.1	III	T20	332	86	4C23.34	
1309+21	13 09 32	+21 03.7	2.92	-19.1	(2.2)	1.0	(0,4)	0.3	0.8±0.7	1.5±0.5	II	T21	341	82	(4C21.39)	
1312+21	13 12 36	+21 00.4	2.91	-19.0	3.5	1.5	1.0	0.6	0.7±0.2	2.3±0.6	III	T11B	344	82	4C20.31	
1317+25	13 17 30	+25 49.5	2.86	-18.9	2.5	1.6	0.7	0.2	1.1±0.3	2.5±0.9	III	T20	21	83	4C25.42	
1319+27	13 19 55	+27 00.7	2.84	-18.8	3.9	1.6	1,1	0.6	0.7±0.2	2.7±0.6	III	T11B	32	83	4C27.25	
1319+23	13 19 59	+23 01.9	2.88	-18.8	3.1	1.0	0,6	0.4	0.7±0.3	1.6±0.5	III	T11B	3	82	4C23.35	
1323+24	13 23 30	+24 47.9	2.85	-18.7		0.7	0,2	0.1	1.3±1.1	1.2±1.1	III	T21	16	82		NPC
1324+23	13 24 33	+23 01.2	2.87	-18.7	5.2	(1.0)	0.6	0.4	0.9±0.3	2.2±0.8	III	T11B	6	81	4C22.38	
1328+254	13 28 17	+25 24.5	2.83	-18.6	16.0	12.0	7.0	4.6	0.6±0.1	13.9±1.4	III QSO 17.7M	T11B	23	81	4C25.43	3C287 CTD81 NRA0424

1328+251	13 28 58	+25 06.2	2.84	-18.6	6.0	2.2	0.7	0.3	1.2±0.2	2.9±0.9	II		T20	21	81	4C25.44
1341+22	13 41 41	+22 33.2	2.83	-18.1	2.3	0.9	0.5	0.3	0.8±0.3	1.3±0.5	III		T11B	14	77	4C22.40
1345+26	13 45 46	+26 49.9	2.77	-17.9	(4.9)	1.8	1.0	0.5	1.0±0.4	3.4±0.9	III		T11B	34	77	(4C26.42)
1345+24	13 45 52	+24 30.9	2.80	-17.9	4.8	3.2	0.5	0.3	1.3±0.2	3.4±1.1	III		T11B	24	77	4C24.28
1347+21	13 47 15	+21 22.4	2.84	-17.9	7.6	5.0	1.1	0.5	C		III	QSO? 16M	T10	12	75	4C21.40 3C291 NRAO431
1354+25	13 54 44	+25 53.2	2.76	-17.6		1.5	0.3	0.2	1.3±0.6	2.2±1.3	III		T21	31	75	NPC
1357+26	13 57 00	+26 42.2	2.74	-17.5	2.4	1.1	0.3		1.1±0.7	1.3±1.1	III		T21	34	75	4C26.43
1358+24	13 58 43	+24 28.5	2.77	-17.4	2.3	1.3	0.6	0.4	0.7±0.3	1.5±0.5	III		T20	26	74	4C24.29 CTD 83
1402+20	14 02 42	+20 40.3	2.82	-17.2	2.2	(0.8)	0.2		1.2±0.6	0.9±0.7	III	ON RIDGE	T21	15	72	4C20.32
1405+23	14 05 42	+23 46.9	2.77	-17.1	3.5	(3.8)	0.7	0.5	0.7±0.3	1.8±0.6	III	CONF WITH 1406+24	T11B	26	72	4C23.36
1406+25	14 06 02	+25 48.3	2.74	-17.1		1.0	0.9	0.5	0.8±0.5	2.4±0.7	III		T21	32	73	NPC
1406+24	14 06 02	+24 01.3	2.76	-17.1	5.2	(3.8)	1.0	0.6	0.8±0.2	2.8±0.7	III	CONF WITH 1405+23	T11B	26	72	4C24.30 CTD 84
409+21	14 09 58	+21 06.4	2.80	-16.9		1.8	0.4	0.2	1.5±0.5	3.2±1.6	III		T20	19	71	NPC
1413+25	14 13 42	+25 23.5	2.72	-16.7	2.5	0.8	0.4	0.3	0.7±0.3	1.2±0.5	III		T20	32	71	4C25.45
1422+21	14 22 07	+21 15.2	2.77	-16.3	2.9	1.1	0.4	0.3	0.8±0.3	1.4±0.6	III		T20	22	68	4C21.41
1422+26	14 22 29	+26 49.9	2.68	-16.3		1.8	0.6	0.4	0.9±0.4	2.3±0.8			T20	37	69	CTD 86
1422+20	14 22 37	+20 13.8	2.79	-16.3	7.4	1.7	1.6	1.2	0.6±0.1	3.6±0.6	III		T11B	20	67	4C20.33
1423+24	14 23 35	+24 17.2	2.72	-16.2	7.7	4.4	1.5	1.0	0.8±0.1	4.8±0.8	III	QSO? 18M	T10	30	69	4C24.31 CTD 87
1427+22	14 27 07	+22 01.5	2.75	-16.1	3.2	1.4	1.0	0.4	0.9±0.3	2.7±0.7	III		T11B	25	67	4C22.41
1430+25	14 30 27	+25 08.8	2.69	-15.9	3.0	0.8	0.4	0.3	0.8±0.3	1.3±0.6	II		T11B	33	67	4C25.46
1433+23	14 33 24	+23 58.1	2.70	-15.7	4.7	1.3	0.7	0.2	1.1±0.2	2.5±0.9	III		T11B	31	66	4C23.38
1437+22	14 37 37	+22 03.7	2.73	-15.5	2.0	1.3	0.5	0.3	0.8±0.3	1.5±0.6	II		T20	27	65	4C22.42
1441+25	14 41 41	+25 14.8	2.66	-15.3		1.5	0.6	0.4	0.8±0.5	1.9±0.6	III		T20	35	65	NPC
1443+23	14 43 43	+23 15.7	2.70	-15.1	2.0	1.1	0.3	0.1	1.2±0.5	1.3±0.9	III		T20	30	64	4C23.40
1444+21	14 44 33	+21 43.9	2.72	-15.1	2.5	1.6	0.4	0.3	0.9±0.3	1.6±0.7	III		T20	27	63	4C21.42

TABLE 2 (*Continued*)

(1)	(2)	(3)	(4)	(5)	(6)	(7)	(8)	(9)	(10)	(11)	(12)	(13)	(14)	(15)	(16)	(17)
SOURCE NUMBER	POSITION (1950)		ANNUAL PRECESSION		FLUX DENSITY				SPECTRUM		REMARKS	DATE	GALACTIC COORDS		OTHER CATALOGUE NUMBERS	
	R.A.	DEC.	+	+	S178	S635	S1410	S2650	INDEX	S400			L2	B2	4C	OTHER
1446+20	14 46 37	+20 36.5	2.74	-15.0	5.4	1.7	1.0	0.5	0.9±0.2	2.9±0.7	III EXT RA	T21	25	62	4C20.34	3C304 NRAO454
1455+24	14 55 30	+24 47.9	2.64	-14.4	(2.6)	(1.5)	0.6	0.5	0.3±0.5	0.9±0.2	II CONF WITH 1455+25	T20	35	62	(4C25.47)	
1455+25	14 55 40	+25 17.4	2.63	-14.4	(2.6)	(1.5)	0.6	0.4	0.6±0.6	1.3±0.3	III CONF WITH 1455+24	T20	36	62	4C25.47	
1459+217	14 59 00	+21 47.5	2.70	-14.2	(2.8)	(1.4)	0.3		-		III CONF WITH 1459+21.2	T20	29	60	(4C21.44)	
1459+212	14 59 28	+21 12.5	2.71	-14.2	(2.8)	(1.4)	(0.5)	0.1	-		III CONF WITH 1459+21.7	T20	28	60	(4C21.44)	
1502+26	15 02 49	+26 08.5	2.60	-14.0	46.0	17.1	7.1	3.1	1.0±0.1	25.0±2.4	I DB 16M	T6	38	60	4C26.46	3C310 CTD 89 NRAO465
1511+23	15 11 30	+23 49.4	2.64	-13.4	2.1	2.7	1.5	1.2	0.4±0.2	2.7±0.5	III	T11B	35	58	4C23.41	CTD 90
1511+26	15 11 31	+26 18.4	2.58	-13.4	18.2	6.2	4.0	2.1	0.8±0.1	10.2±1.2	II DB 15M	T6	39	58	4C26.47	3C315 CTD 91 NRAO472
1516+24	15 16 32	+24 37.3	2.61	-13.1	2.8	1.3	(0.2)	0.1	1.3±0.5	1.5±1.3	III	T11B	37	57	4C24.33	
1517+20	15 17 51	+20 26.7	2.69	-13.0	13.2	4.6	2.3	1.5	0.8±0.1	6.6±0.9	II GAL 19M	T6	30	55	4C20.35	3C318 NRAO476
1529+24	15 29 39	+24 13.3	2.60	-12.2	11.2	7.3	3.6	2.2	0.7±0.1	8.7±1.1	III	T10	37	54	4C24.34	3C321 CTD 92 NRAO480
1530+20	15 30 23	+20 16.3	2.68	-12.2	2.7	1.4	0.4	0.3	0.9±0.3	1.5±0.6	III	T11B	31	53	4C20.36	
1545+21	15 45 31	+21 01.5	2.64	-11.1	10.0	4.5	2.3	1.6	0.7±0.1	5.7±0.8	III QSO 16M	T10	34	49	4C21.45	3C323.1 NRAO483
1547+21	15 47 36	+21 34.5	2.63	-10.9	13.6	5.0	2.8	1.5	0.8±0.1	7.6±1.0	III	T10	35	49	4C21.46	3C324 NRAO484

1549+26	15 49 06	+26 15.4	2.52	-10.8		1.5	0.6	0.3	1.1±0.5	2.5±1.0	III		T21	42	50		NPC
1550+20	15 50 12	+20 14.8	2.66	-10.8	7.8	7.6	2.2	1.0	C		II	EXT	T6	33	48	4C20.37	3C326 NRAO487
1551+23	15 51 36	+23 56.5	2.57	-10.7	2.1	0.8	0.8	0.5	0.6±0.3	1.6±0.5	III		T11B	39	49	4C23.42	
1553+24	15 53 46	+24 15.5	2.56	-10.5	3.0	1.0	0.2	0.2	1.0±0.3	1.3±0.7	II		T11B	39	49	4C24.35	
1553+20	15 53 57	+20 12.9	2.65	-10.5	9.0	4.1	2.4	1.4	0.7±0.1	5.8±0.8	III		T10	34	47	4C20.38	3C326.1 NRAO488
1601+21	16 01 23	+21 35.9	2.61	-9.9		1.3	0.5	0.2	1.3±0.6	2.7±1.3	II	EXT RA	T21	36	46		NPC
1602+24	16 02 50	+24 04.3	2.55	-9.8	2.6	1.0	0.6	0.3	0.9±0.3	1.7±0.6	I		T20	40	46	4C24.36	
1603+20	16 03 29	+20 36.4	2.63	-9.8		1.3	0.3		1.8±1.1	3.0±1.7	III		T21	35	45		NPC
1604+22	16 04 40	+22 47.6	2.58	-9.7		1.9	0.3		2.3±0.9	5.5±2.8	III		T21	38	46		NPC
1607+26	16 07 11	+26 49.0	2.48	-9.5		4.1	4.8	3.2	0.4±0.2	7.7±0.9	III		T11B	44	46		CTD 93
1610+22	16 10 09	+22 29.5	2.58	-9.2	7.1	3.9	1.2	0.7	1.0±0.1	4.4±0.9	III		T10	38	44	4C22.43	3C331 NRAO495
1614+26	16 14 36	+26 54.2	2.46	-8.9		1.0	1.2	0.9	0.4±0.4	1.9±0.4	III		T11B	45	45		CTD 95
1614+20	16 14 47	+20 34.0	2.62	-8.9	2.1	1.0	0.3		1.0±0.7	1.2±1.0	III		T21	36	43	4C20.39	
1615+21	16 15 04	+21 14.8	2.61	-8.9	6.9	4.1	1.8	1.0	0.8±0.1	5.0±0.8	III		T10	37	43	4C21.47	3C333 NRAO497
1619+24	16 19 47	+24 43.5	2.52	-8.5	2.8	2.1	0.7	0.3	1.1±0.3	2.6±0.9	III		T20	42	43	4C24.37	
1622+23	16 22 33	+23 52.1	2.53	-8.3	12.6	5.7	2.7	1.5	0.8±0.1	7.6±1.0	III	QSO 17.5M	T10	41	42	4C23.43	3C336 NRAO501
1623+25	16 23 03	+25 12.1	2.50	-8.2	3.9	1.3	0.6	0.4	0.8±0.2	1.9±0.6	III		T11B	43	42	4C25.48	
1623+26	16 23 17	+26 57.5	2.45	-8.2	3.5	2.3	1.2	0.5	0.9±0.2	3.5±0.8	III	QSO 18M	T11B	46	43	4C26.48	
1625+21	16 25 21	+21 19.3	2.59	-8.0	8.6	4.7	1.1	0.6	1.1±0.1	5.2±1.1	III		T10	38	41	4C21.48	
1627+23	16 27 30	+23 26.4	2.54	-7.9	10.3	6.3	2.3	1.3	0.9±0.1	7.3±1.1	III		T11B	41	41	4C23.44	3C340 NRAO506
1634+26	16 34 34	+26 54.1	2.44	-7.3	6.9	2.4	1.3	0.8	0.8±0.2	3.6±0.7	III	QSO 18M	T10	46	40	4C26.49	3C342 NRAO510
1638+20	16 38 37	+20 58.7	2.59	-7.0	2.6	(3.3)'	0.2	0.1	1.2±0.5	1.0±0.9	III	EXT HIGHER RA	T20	39	38	4C20.40	

TABLE 2 (*Continued*)

(1) SOURCE NUMBER	(2) POSITION (1950) R.A.	(3) DEC.	(4) ANNUAL PRECESSION +	(5) +	(6) FLUX DENSITY S178	(7) S635	(8) S1410	(9) S2650	(10) SPECTRUM INDEX	(11) S400	(12) REMARKS	(13) DATE	(14) GALACTIC COORDS L2	(15) B2	(16) OTHER CATALOGUE NUMBERS 4C	(17) OTHER
1642+25	16 42 56	+25 41.8	2.47	-6.6		1.1	0.5	0.4	0.5±0.6	1.1±0.4	III	T21	45	38		NPC
1700+24	17 00 53	+24 01.9	2.50	-5.1	2.3	1.0	0.4	0.3	0.7±0.3	1.2±0.5	III	T21	45	34	4C24.38	
1706+24	17 06 50	+24 37.5	2.48	-4.6	2.7	0.7	0.4	0.2	1.0±0.3	1.3±0.7	III	T20	46	33	4C24.39	
1708+24	17 08 32	+24 09.0	2.49	-4.5	2.6	(0.5)	0.4	0.2	1.0±0.5	1.3±0.7	II	T20	46	32	4C24.40	
1717+22	17 17 03	+22 48.1	2.52	-3.7	3.5	2.8	1.7	1.1	0.6±0.2	3.5±0.6	III	T11B	45	30	4C22.45	
1717+23	17 17 46	+23 33.4	2.50	-3.7		1.7		0.2	1.5±0.5	3.4±1.5		T12B	46	30		NPC
1719+24	17 19 58	+24 17.8	2.48	-3.5	(3.2)	(2.1)	0.8	0.5	0.7±0.5	2.0±0.4	II CONF WITH 1720+24	T11B	47	30	4C24.41	CTD 100
1720+24	17 20 08	+24 24.3	2.48	-3.5	(3.2)	(2.1)	(0.3)	0.2	-		III CONF WITH 1719+24	T11B	47	30	(4C24.41)	
1729+21	17 29 13	+21 07.4	2.56	-2.7	3.6	1.0	0.5	0.4	0.7±0.3	1.6±0.5	II	T11B	44	27	4C21.50	
1729+26	17 29 29	+26 01.5	2.43	-2.7	2.7	1.0	0.3	0.1	1.2±0.4	1.3±0.9	II	T20	49	28	4C26.52	
1729+22	17 29 45	+22 25.6	2.53	-2.6	2.7	0.6	0.4		0.9±0.6	1.3±0.9	III	T20	46	27	4C22.46	
1730+20	17 30 40	+20 39.9	2.57	-2.6	5.8	1.0	0.8	0.5	0.9±0.2	2.5±0.7	III	T10	44	26	4C20.42	3C359 NRAO531
1735+24	17 35 34	+24 02.5	2.48	-2.1	5.0	3.0	1.8	0.9	0.8±0.2	4.4±0.8	III	T11B	48	26	4C24.42	CTD 101
1737+20	17 37 36	+20 29.7	2.58	-2.0		(2.2)	0.4		-		II	T20	44	25		NPC
1740+23	17 40 40	+23 34.0	2.49	-1.7		(1.1)	0.2	0.1	1.1±1.5	0.8±0.5	III	T21	48	25		NPC
1744+20	17 44 19	+20 09.9	2.58	-1.4	3.8	0.7	0.8	0.6	0.6±0.2	1.9±0.5	III	T11B	45	23	4C20.43	
1744+23	17 44 25	+23 43.8	2.49	-1.4	4.4	2.4	1.6	0.8	0.8±0.2	3.8±0.7	III	T10	48	24	4C23.45	
1749+25	17 49 43	+25 53.9	2.42	-0.9	3.2	2.1	0.5	0.3	1.1±0.3	2.2±0.8	III	T11B	51	24	4C25.52	
1751+27	17 51 15	+27 00.4	2.39	-0.8	4.8	1.3	0.8	0.5	0.8±0.2	2.3±0.6	III	T20	52	24	4C27.40	CTD 104
1753+24	17 53 36	+24 28.4	2.46	-0.6	2.6	1.0	0.4	0.2	1.0±0.3	1.4±0.7	III	T20	50	23	4C24.43	

1759+21	17 59 38	+21 09.4	2.56	-0.0	3.7	2.2	0.9	0.4	1.0±0.2	2.9±0.8	II		T11B	47	20	4C21.51
1803+20	18 03 37	+20 27.7	2.57	0.3	3.0	1.1	1.0	0.5	0.8±0.3	2.4±0.6	III		T11B	47	19	4C20.44
1804+26	18 04 49	+26 04.7	2.42	0.4	3.4	1.8	0.8	0.4	0.9±0.2	2.4±0.7	III		T21	52	21	4C26.54 NRAO545
1804+23	18 04 50	+23 31.3	2.49	0.4	3.8	2.1	0.8	0.4	1.0±0.2	2.6±0.7	III-IV		T20	50	20	4C23.47 NRAO544
1805+20	18 05 45	+20 44.2	2.57	0.5	3.2	(0.5)	0.3	0.2	1.0±0.4	1.3±0.8	III		T11B	47	19	4C20.45
1809+21	18 09 57	+21 25.7	2.55	0.9		(1.8)	0.4	0.2	1.1±0.8	1.6±0.6	II	EXT RA	T21	48	18	
1810+26	18 10 29	+26 28.4	2.41	0.9	7.0	1.4	1.1	0.5	1.0±0.2	3.4±0.8	II	GAL 19.5M	T10	53	20	4C26.55
1818+26	18 18 57	+26 36.1	2.41	1.7		(1.9)	0.4		-		III		T21	54	18	(3C374) CTD106
1819+22	18 19 08	+22 49.6	2.51	1.7	6.0	2.2	1.1	0.6	0.9±0.2	3.3±0.7	III		T10	51	17	4C22.47
1819+24	18 19 35	+24 31.8	2.46	1.7	2.3	1.5	0.2	0.1	1.4±0.4	1.6±1.2	III	CONF	T21	52	17	4C24.45
1821+23	18 21 29	+23 03.0	2.51	1.9	3.3	(0.5)	0.2	0.2	1.0±0.4	1.3±0.8	III		T11B	51	16	4C22.48
1825+23	18 25 02	+23 05.0	2.51	2.2	2.3	0.9	0.4	0.2	0.9±0.4	1.3±0.6	III		T11B	51	15	4C23.49
1834+20	18 34 26	+20 42.0	2.57	3.0	2.7	1.0	0.8	0.3	1.0±0.3	2.3±0.7	III		T20	50	12	4C20.46
1836+21	18 36 41	+21 21.5	2.56	3.2		(1.8)	0.3	0.1	1.7±1.3	2.7±1.5	III	EXT RA	T21	51	12	NPC
1837+23	18 37 57	+23 59.1	2.49	3.3	7.0	(2.5)	1.2	0.7	0.9±0.2	3.6±0.8	III		T10	53	13	4C24.46 CTD 109
1840+23	18 40 47	+23 58.0	2.49	3.5	2.6	1.2	0.8	0.3	1.0±0.3	2.3±0.7	III-IV		T12A	54	12	4C23.50
1906+20	19 06 31	+20 22.9	2.60	5.7	3.3	(1.0)	0.6	0.4	0.8±0.3	1.7±0.6	III	CONF AT 635	T11B	53	6	4C20.47
1906+22	19 06 31	+22 06.9	2.55	5.7	2.5	(0.6)	0.4	0.2	1.0±0.5	1.3±0.7	III-IV	CONF 635	T20	55	6	4C22.51
1911+23	19 11 07	+23 27.7	2.52	6.1	3.5	1.4	0.8	0.4	0.9±0.2	2.2±0.6	IV		T11B	56	6	4C23.51
1911+22	19 11 09	+22 07.3	2.56	6.1	3.1	(1.6)	0.6	0.2	1.1±0.4	2.0±0.9	IV	CONF AT 635	T11B	55	5	4C22.53
1921+22	19 21 21	+22 30.8	2.55	7.0	4.5	1.2	0.6	0.4	0.9±0.2	2.0±0.6	IV		T11B	57	3	4C22.54
1922+206	19 22 21	+20 41.9	2.60	7.0	(3.1)	(1.6)	(0.8)	0.9	-		HII	CONF WITH 1922+20.4	T11B	55	2	(4C20.48)
1922+204	19 22 28	+20 29.0	2.61	7.1	(3.1)	(1.6)	0.8	0.5	0.7±0.5	2.0±0.4	IV	CONF WITH 1922+20.6	T11B	55	2	4C20.48
1930+25	19 30 47	+25 52.5	2.47	7.7	2.9	2.3	0.9	0.6	0.7±0.2	2.4±0.6	IV		T11B	61	3	4C25.53
1936+26	19 36 56	+26 39.5	2.46	8.2	4.8	1.9	0.7	0.4	1.0±0.2	2.5±0.7	IV		T11B	62	2	4C26.57

TABLE 2 (*Continued*)

(1) SOURCE NUMBER	(2) POSITION (1950) R.A.	(3) DEC.	(4) ANNUAL PRECESSION +	(5) +	(6) FLUX DENSITY S178	(7) S635	(8) S1410	(9) S2650	(10) SPECTRUM INDEX	(11) S400	(12) REMARKS	(13) DATE	(14) GALACTIC COORDS L2	(15) B2	(16) OTHER CATALOGUE NUMBERS 4C	(17) OTHER
1937+25	19 37 04	+25 57.5	2.48	8.2		2.6	0.9		1.3±0.5	4.8±1.2	IV	T21	61	2		NPC
1937+21	19 37 31	+21 30.7	2.59	8.3	2.9	2.5	1.5	0.9	0.6±0.2	3.3±0.6	IV	T11B	58	-0	4C21.53	
1938+22	19 38 40	+22 57.0	2.56	8.4	2.7	1.0	0.7	0.2	1.1±0.3	2.2±0.8	IV	T20	59	0	4C23.52	
1942+256	19 42 15	+25 41.2	2.49	8.6		2.0	1.5	0.9	0.7±0.3	3.5±0.7	IV COMPLEX AREA	T21	62	1		NPC
1942+252	19 42 16	+25 13.5	2.50	8.6		2.0	0.6	0.9	C		IV COMPLEX AREA	T21	61	1		NPC
1944+258	19 44 16	+25 50.3	2.49	8.8	2.7	0.8	0.4		0.9±0.6	1.3±0.9	IV COMPLEX AREA	T21	62	1	4C25.54	
1944+250	19 44 41	+25 04.9	2.51	8.8		8.5	5.6		0.5±0.2	10.8±1.0	HII COMPLEX AREA	T21	61	0		CTD 114
1947+266	19 47 07	+26 40.7	2.47	9.0			5.4		-		HII COMPLEX AREA	T21	63	0		CTD 116
1947+24	19 47 23	+24 15.7	2.54	9.1		2.4	0.7	0.4	1.2±0.4	3.5±1.1	IV	T21	61	-1		
1950+25	19 50 43	+25 19.4	2.51	9.3	6.4	3.0	(1.6)	1.0	0.7±0.2	3.9±1.0	IV	T11B	62	-1	4C25.55	CTD 117
1953+22	19 53 37	+22 53.4	2.58	9.5	3.2	1.2	(0.8)	0.2	1.1±0.4	1.6±1.0	IV	T12A	61	-3	4C22.55	
1958+25	19 58 59	+25 42.7	2.51	9.9		3.3	1.6	1.1	0.7±0.3	4.1±0.8	IV	T11B	64	-2		CTD 120
2000+20	20 00 04	+20 57.9	2.63	10.0	4.5	(1.4)	(0.6)	0.2	1.2±0.3	1.8±0.8	III-IV CONF WITH 2000+21	T21	60	-5	4C20.49	
2000+21	20 00 59	+21 02.2	2.63	10.1		(1.4)	(0.6)	0.3	-		III-IV CONF WITH 2000+20	T21	60	-5	(4C20.49)	
2007+24	20 07 16	+24 57.0	2.54	10.6	4.6	1.6	0.8	0.4	0.9±0.2	2.5±0.7	III-IV	T21	64	-4	4C24.48	CTD 121
2008+20	20 08 19	+20 33.7	2.65	10.6	2.8	1.4	0.7	0.4	0.8±0.3	1.9±0.6	III-IV	T21	60	-7	4C20.50	
2009+25	20 09 41	+25 29.2	2.53	10.7	2.6	1.3	0.8	0.3	1.0±0.3	2.4±0.8	III-IV EXT	T21	65	-4	4C25.56	
2012+23	20 12 18	+23 25.6	2.59	10.9	79.0	34.5	13.0	7.1	C		IV	T10	63	-6	4C23.53	3C409 NRAO625
2018+23	20 18 55	+23 09.3	2.60	11.4	5.7	2.3	1.5	1.3	0.5±0.2	3.0±0.5	IV	T11B	64	-8	4C23.54	
2029+20	20 29 34	+20 15.7	2.68	12.2	(2.5)	1.0	0.4	0.1	1.7±0.9	3.0±2.0	III-IV	T12A	63	-11	(4C20.51)	

2030+25	20 30 42	+25 41.9	2.56	12,2	5,6	3,6	2.0	1,1	0,8±0,1	5.2±0.8	IV		T11B	68	-8	4C25,56.1	3C414 CTD124 NRAO632
2031+21	20 31 19	+21 36.0	2.65	12.3	6.2	3.2	2,2	1.4	0.6±0.1	4.5±0.7	II	D 19.5M	T10	64	-11	4C21.55	
2039+24	20 39 26	+24 38,3	2.60	12.8	2.8	1.9	1,2	0.7	0.7±0.2	2.7±0.6	III-IV		T11B	68	-10	4C24.50	
2045+23	20 45 38	+23 14,4	2,64	13.3	3,2	1.1	0,8	0.5	0.7±0.3	1.9±0.5	III		T11B	68	-12	4C23.55	
2051+26	20 51 08	+26 01.6	2,59	13.6	4.5	2,4	1,2	0.6	0.9±0.2	3.3±0.7	III		T10	71	-12	4C26,58	
2053+22	20 53 41	+22 44.2	2,67	13,8	3.0	1.3	0.4		1.0±0,5	1.6±1.1	III		T20	69	-14	4C22.57	
2102+20	21 02 14	+20 19,0	2,73	14.3	2.3	(2.3)	0.3	0.2	0.9±0.5	1.1±0.6	II		T12A	68	-17	4C20.52	
2104+23	21 04 57	+23 20,5	2.67	14.5	4.2	1.0	0.4	0.2	1.1±0.3	1.7±0,8	III		T11B	71	-16	4C23.56	
2105+21	21 05 52	+21 27,5	2.71	14.5	4.3	1.1	0.4	0.3	1.0±0.2	1.8±0.7	III		T21	69	-17	4C21.58	NRAO646
2107+23	21 07 47	+23 51.0	2.67	14.6	3.3	1.7	0,7	0.3	1.0±0.3	2.3±0,8	III-IV		T11B	72	-16	4C23.57	CTD 127
2114+24	21 14 49	+24 46,9	2.67	15.1	4.9	2.5	1.5	0.7	0.8±0.2	3.9±0.8	III		T11B	73	-17	4C24.52	CTD 129
2121+24	21 21 31	+24 51.3	2.68	15.4	54.4	25.0	12,4	7.0	0.8±0.1	33.4±2.9	I	D 17M EXT	T10	74	-18	4C24,54	3C433 CTD 130 NRAO658
2137+20	21 37 30	+20 57,4	2.77	16,3		(1.6)	1.2	0.8	0.6±0.3	2.7±0.4	II		T21	74	-23		NPC
2142+22	21 42 31	+22 35,9	2.76	16.5	2.5	(1.4)	0,5	0.3	0.8±0.4	1.4±0.6	III		T21	76	-23	4C22,59	
2147+24	21 47 12	+24 53.0	2.73	16,8	5.5	1.9	0,6	0.4	1,0±0.2	2.5±0.8	III		T11B	79	-22	4C24,56	
2149+20	21 49 01	+20 42.5	2.80	16,9		1.0	0,4	0.2	1,1±0.7	1.7±0.9	II		T21	76	-25		NPC
2149+21	21 49 30	+21 15,5	2.79	16.9	5.3	2.1	0,8	0.5	0,9±0.2	2.7±0.7	III		T21	77	-25	4C21.59	
2156+26	21 56 10	+26 38,8	2,73	17.2	2,8	1.1	0,5	0.2	1,0±0.3	1.7±0.7	III		T21	82	-22	4C26,59	
2159+22	21 59 06	+22 31.7	2.79	17,3	2.1	1.5	0,7	0.3	1,0±0.3	2.2±0.7	II		T21	79	-25	4C22.61	
2203+24	22 03 01	+24 00.8	2.78	17.5	2.7	1.0	0.4		0,9±0.6	1.4±1.0			T22	81	-25	4C24,57	
2203+26	22 03 41	+26 30.5	2.75	17,5	2.5	1,1	0.3		1,1±0.6	1.3±1.1	III		T20	83	-23	4C26.60	
2222+21	22 22 47	+21 31,5	2.86	18.3	4.5	(1.5)	1.3	0.1	C		III		T11B	83	-30	4C21,60	
2223+21	22 23 15	+21 02.6	2.86	18.3		(2.0)	(2,7)	1.4	-		III		T20	83	-30		NPC
2227+26	22 27 15	+26 05.0	2.82	18.4	5.0	1.4	0.8	0,5	0.8±0.2	2.4±0.6	II		T11B	87	-27	4C26,62	

TABLE 2 (*Continued*)

(1)	(2)	(3)	(4)	(5)	(6)	(7)	(8)	(9)	(10)	(11)	(12)	(13)	(14)	(15)	(16)	(17)
SOURCE NUMBER	POSITION (1950)		ANNUAL PRECESSION		FLUX DENSITY				SPECTRUM		REMARKS	DATE	GALACTIC COORDS		OTHER CATALOGUE NUMBERS	
	R.A.	DEC.	+	+	S178	S635	S1410	S2650	INDEX	S400			L2	B2	4C	OTHER
2227+24	22 27 47	+24 56.3	2.83	18.4	(2.1)	(1.9)	0.4		-		III	T21	87	-28	(4C24.58)	
2232+24	22 32 35	+24 17.1	2.85	18.6	2.9	1.2	0.7	0.5	0.6±0.3	1.6±0.5	III	T11B	87	-29	4C24.59	
2234+20	22 34 09	+20 17.4	2.89	18.7	3.3	1.6	0.7	0.5	0.7±0.2	1.9±0.5	III	T11B	85	-32	4C20.54	
2240+24	22 40 24	+24 43.8	2.86	18.8	2.6	0.9	0.5	0.4	0.6±0.3	1.3±0.4	III	T20	89	-29	4C24.60	
2245+23	22 45 09	+23 12.3	2.89	19.0		1.4	0.5	0.3	1.0±0.5	1.9±0.8	III	T21	89	-31		NPC
2246+205	22 46 52	+20 31.7	2.92	19.0	3.2	(1.7)	0.4		1.0±0.4	1.4±0.7	III CONF WITH 2246+20.8	T21	88	-34	4C20.55	
2246+208	22 46 52	+20 50.9	2.91	19.0		(1.7)	0.5		-		III CONF WITH 2246+20.5	T21	88	-33		NPC
2251+24	22 51 45	+24 29.2	2.89	19.2	2.7	2.4	1.9	1.4	0.4±0.2	3.0±0.5	III	T11B	92	-31	4C24.61	CTD 136
2308+25	23 08 55	+25 31.5	2.93	19.5	4.0	2.6	1.1	0.7	0.7±0.2	2.9±0.6	III	T11B	96	-32	4C25.59	CTD 137
2318+20	23 18 26	+20 33.4	2.98	19.7	2.4	1.5	0.2	0.1	1.4±0.4	1.6±1.2	III	T21	96	-37	4C20.56	
2318+23	23 18 59	+23 30.5	2.97	19.7	8.1	3.1	2.0	0.9	0.9±0.1	5.3±0.9	III	T10	98	-35	4C23.58	3C460 NRAO710
2325+26	23 25 33	+26 56.4	2.97	19.8	6.0	2.9	1.3	0.6	0.9±0.2	4.0±0.8	III	T11B	101	-32	4C27.52	3C463 CTD 140 NRAO713
2335+26	23 35 57	+26 44.3	3.00	19.9	13.6	17.1	7.0	4.0	C		I D 12M	T10	103	-33	4C26.64	CTD 143 3C 465 NRAO715
2337+22	23 37 53	+22 04.3	3.02	19.9	6.1	3.5	2.2	1.4	0.6±0.1	4.6±0.7	III	T10	102	-38	4C22.63	3C 466 NRAO717
2339+23	23 39 09	+23 36.0	3.02	20.0	3.0	1.1	0.4	0.2	1.0±0.3	1.5±0.7	III	T11B	103	-36	4C23.59	
2339+25	23 39 28	+25 59.6	3.01	20.0	4.4	1.5	0.4	0.2	1.2±0.3	2.0±0.9	III	T11B	104 0	-34 0	4C25.60	

V. Determination of Flux Densities

(a) *Measurement of Flux Densities*

Flux densities at 635 MHz were obtained by measurement of the amplitude of the source on the finding survey. A correction was applied to allow for the difference between the measured right ascension of the source and that of the nearest survey scan. In a number of cases where the flux density was in doubt, several additional scans at 635 MHz were taken through the source. Source amplitude was expressed in terms of a noise calibration, which was injected at frequent intervals during the survey. The value of the calibration signal was obtained from measurements of Hydra A, which was taken as 90·0 f.u. at 635 MHz.

Where the sources were positioned at 2650 MHz as part of the accurate position programme (Shimmins 1968) the mean flux density measured at position angles 0° and 90° was used, thus eliminating errors due to polarization. These values were calibrated by assuming a flux density of 23·5 f.u. for Hydra A. Where the source was positioned at 2650 MHz, the flux density at 1410 MHz was obtained by on–off source measurements, using the 2650 MHz positions. Amplitudes were measured against a noise calibration, the value of which was obtained by measurements of Hydra A, for which a flux density of 42·0 f.u. at 1410 MHz was adopted.

Where the sources were positioned at 1410 MHz the 1410 MHz flux densities were obtained from the amplitudes of the positioning scans and the 2650 MHz flux densities from subsequent on–off source measurements. Flux densities at 178 MHz are from the 4C catalogue.

Table 3

ESTIMATED ERRORS IN FLUX DENSITY MEASUREMENTS

Source of Error	R.M.S. Error at a Frequency of: 2650 MHz	1410 MHz	635 MHz
Variation in calibration signal	8%	8%	8%
Angular extent of source	2%	1%	—
Noise fluctuation	0·05 f.u.	0·1 f.u.	0·2 f.u.
Confusion effects	0·03 f.u.	0·1 f.u.	0·4 f.u.
Estimated total r.m.s. error	8% ±0·06 f.u.	8% ±0·14 f.u.	8% ±0·5 f.u.

(b) *Errors in Flux Densities*

Table 3 gives estimates of the average errors that apply to flux density measurements. These estimates allow for variations in the calibration signal, possible source extension, noise fluctuation, and confusion effects. Where the error in a flux density is thought to be significantly greater than average, the flux density given in Table 2 is in parentheses.

VI. Spectra of Sources

The spectral index α is defined by the expression $S = kf^{-\alpha}$, where S is the flux density measured at frequency f and k is a constant. Excluding values outside the average error range, where a source had flux density measurements at two or more frequencies (including 178 MHz) the values were used to determine the straight line

$$\log S = -\alpha \log f + \text{constant}.$$

Each flux density was weighted by the inverse square of its r.m.s. error as given in Table 3. The values with more than average errors were considered as if they had double these errors.

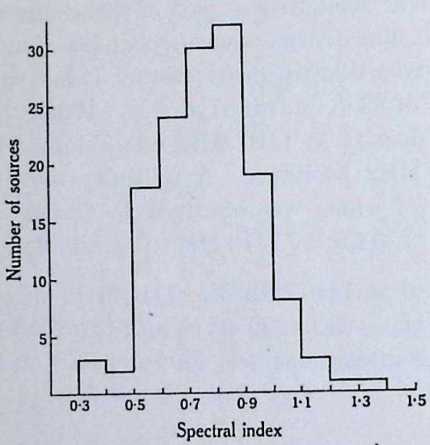

Fig. 1.—Histogram of spectral indices of 141 sources with well-defined spectra. The mean spectral index is 0·83 with a standard deviation of 0·19.

The spectral index and estimated flux density at 400 MHz are given in columns 10 and 11 of Table 2 with the r.m.s. errors determined from those quoted for flux densities. The r.m.s. error corresponding to the goodness of fit was calculated for each source, and where this was significantly greater than the expected error, indicating a departure from a power law spectrum, a C is given in column 10. As can be seen from Table 2, the errors in flux densities, particularly for the weaker sources, are high and this results in large probable errors in the determination of spectral indices.

For a sample of 141 sources for which the spectral indices are well defined with an error of $\pm 0\cdot 2$ or less, a histogram of the distribution of spectral indices is shown in Figure 1. The mean spectral index is $0\cdot 83$ with a standard deviation of $0\cdot 19$.

Of the 323 sources outside $\pm 10°$ from the galactic equator for which a spectral index is available, approximately 38 (i.e. 12%) have spectral indices of $0\cdot 6$ or less and only 5% have spectral indices of $0\cdot 5$ or less.

VII. Identifications

The optical classifications given in column 12 of Table 2 refer to the field within a rectangle $\pm 1'\cdot 0$ from the position of the source. The fields are defined:

class I, the error rectangle includes one galaxy or more brighter than $m_{\mathrm{pg}} = 17$; class II, the error rectangle includes one galaxy or more brighter than $m_{\mathrm{pg}} = 19\cdot5$ but fainter than $m_{\mathrm{pg}} = 17$; class III, the error rectangle includes no galaxies above the plate limit; class IV, the field is heavily obscured; class HII, the field contains an emission nebula.

J. G. Bolton and Jeannette Merkelijn have examined the fields of all sources, using the 48 in. Palomar Sky Survey prints, and the results are being published in separate papers. Only the results for the strong sources have been included in column 12; these have been taken from Merkelijn, Shimmins, and Bolton (1968).

VIII. Source Counts

The present survey gives the flux densities of 341 sources in an area of 0·606 steradian, i.e. excluding the region within 10° of the galactic equator. Figure 2 shows a plot of N, the number of sources per steradian of flux density equal to or greater than S, versus the flux density S, using logarithmic scales.

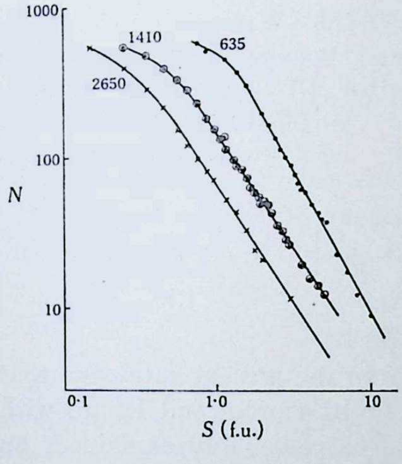

Fig. 2.—Relationship between flux density S and the number N of sources per steradian above a given level of flux density for frequencies of 2650, 1410, and 635 MHz.

The slopes of the lines for the three frequencies are $1\cdot86\pm0\cdot10$ at 635 MHz, $1\cdot65\pm0\cdot10$ at 1410 MHz, and $1\cdot55\pm0\cdot10$ at 2650 MHz. These slopes are very similar to those obtained for the 0° to +20° section of the Parkes catalogue. Of particular interest is the low slope of the $\log N - \log S$ curve at 2650 MHz. This is consistent with the sources having a small systematic increase in spectral index as they get weaker. It is not certain whether this increase is real or due to some systematic underestimation of the 2650 MHz flux densities with decreasing flux density.

As determined from the $\log N - \log S$ curves, it appears that the catalogue is substantially complete down to a flux density of 1·5 f.u. at 635 MHz (300 sources per steradian).

The density of sources at 1410 MHz is 139 sources per steradian with a flux density of 1·0 f.u. or stronger.

IX. Comparison with Other Catalogues

Two other catalogues that cover the same area of sky are: "A survey of radio sources between declinations +20° and +40°" by Pilkington and Scott (1965), which is part of the Cambridge 4C catalogue, and "A continuum survey for discrete radio sources at 1421 Mc/s" by Kellerman and Read (1965) (known as the CTD list).

(a) *Comparison with 4C Catalogue*

The 4C survey was carried out at 178 MHz and is complete to 2 f.u. at 178 MHz, with a positional accuracy of 0′·5 in right ascension and 3′ in declination. The 4C catalogue contains 436 sources in the area, of which 313 are in the present catalogue. Most of the 123 4C sources not presented here have been found on the 635 MHz finding survey but have not been positioned, 94 of them being weaker than 0·9 f.u. at 635 MHz (or 2·5 f.u. at 178 MHz).

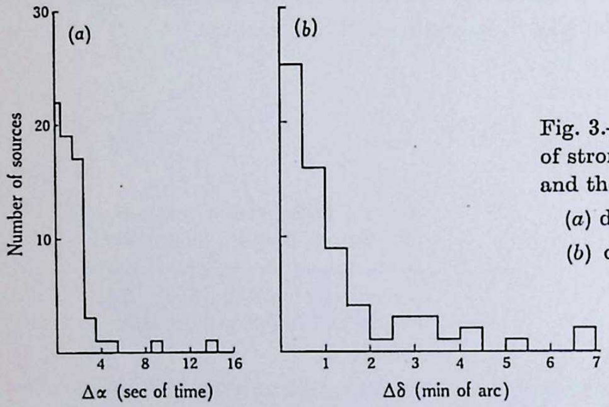

Fig. 3.—A comparison of the positions of strong sources in the present catalogue and those in the 4C catalogue:

(a) differences in right ascensions Δα

(b) differences in declinations Δδ

Of particular interest are the 82 sources in the present catalogue that are not in the 4C catalogue. Of these, 20 are close to 4C sources and 12 are within ±10° of the galactic plane. These 32 sources can be reasonably explained, but of the remaining 50 sources only 11 have spectra and flux densities at centimetre frequencies such that the expected flux density at 178 MHz would be below the 4C limit. A comparison of the positions given here with those in the 4C catalogue has been made for the stronger sources where the positional accuracy of the present catalogue is better than 30″ arc in each coordinate. The differences in right ascension and declination are shown in histogram form in Figures 3(*a*) and 3(*b*). The agreement in right ascension is less than 3 sec of time, and the declination shows a difference of approximately 1′ arc.

(b) *Comparison with CTD List*

The CTD survey was carried out at 1421 MHz and covers the declination range +23° 50′ to +30° 10′, thus providing a 3° 10′ overlap zone. The survey is stated to be complete to 1·15 f.u. at 1421 MHz and contains sources of flux density down to 0·5 f.u. at 1421 MHz. A comparison has been made between the CTD list and the present catalogue in the overlap zone, in which there are 63 CTD sources. Five of these sources are not given here; CTD 26, 29, and 138 were not present on the records of the finding survey, and CTD 110 and 113 are within ±10° of the galactic plane where the present survey is incomplete. There are 58 sources in the overlap region that are not in the CTD list. Of these, 10 are stronger than 1·0 f.u. at 1410 MHz and might reasonably have been expected in the CTD list, and the others are weaker than 1·0 f.u., where it is known that the CTD list is incomplete. The CTD list gives a source density of 145 ± 18 sources per steradian, at a flux level of 1 f.u., with a $\log N - \log S$ slope of $-1 \cdot 57 \pm 0 \cdot 20$ for sources more than 10° from the galactic equator. This compares with the value of 139 ± 15 sources per steradian, with slope $-1 \cdot 60$, obtained in the present survey.

The agreement in position is not inconsistent with the $\pm 12^{s}$ in right ascension and $\pm 5'$ in declination quoted in the CTD list.

X. Acknowledgments

Thanks are due to the maintenance staff at the Australian National Radio Astronomy Observatory, Parkes, N.S.W., who operated and maintained the 210 ft radio telescope and receiver during the observations.

Table 2 was produced on the CDC computer at the CSIRO Computing Research Section, Sydney. The programme for the computer was compiled by Mrs. Jennifer Ekers.

Thanks are also due to Miss Mary Chapman of the Division of Radiophysics, CSIRO, who carried out the precessions of the measured source positions and also assisted in the preparation of data for source identifications.

XI. References

Bolton, J. G., Gardner, F. F., and Mackey, M. B. (1964).—*Aust. J. Phys.* **17**, 340.

Day, G. A., Shimmins, A. J., Ekers, R. D., and Cole, D. J. (1966).—*Aust. J. Phys.* **19**, 35.

Kellerman, K. I., and Read, R. B. (1965).—*Publs Owens Valley Radio Observ.* No. 2.

Merkelijn, Jeannette K., Shimmins, A. J., and Bolton, J. G. (1968).—Accurate positions and some optical identifications for 67 radio sources between declinations +20° and +27°. *Aust. J. Phys.* **21** (in press).

Pauliny-Toth, I. I. K., Wade, C. M., and Heeschen, D. S. (1966).—*Astrophys. J. Suppl. Ser.* **13**, 116.

Pilkington, J. D. H., and Scott, P. F. (1965).—*Mem. R. astr. Soc.* **69**(5), 183.

Price, R. M., and Milne, D. K. (1965).—*Aust. J. Phys.* **18**, 329.

Shimmins, A. J. (1968).—*Aust. J. Phys.* **21**, 65.

Shimmins, A. J., Day, G. A., Ekers, R. D., and Cole, D. J. (1966).—*Aust. J. Phys.* **19**, 837.

SHORT COMMUNICATIONS

A STUDY OF THE 3·00 MeV LEVEL OF ^{27}Al VIA ^{24}Mg(α, pγ)^{27}Al†

By D. C. Kean,‡ R. V. Elliott,‡ and R. H. Spear‡

It is at present considered (Thankappan 1966) that the weak-coupling model is more appropriate to the ^{27}Al nucleus than the strong-coupling (Nilsson) model, which has been applied with some success to ^{25}Mg, ^{25}Al, and other lighter nuclei in the 2s–1d shell (Gove 1960). Thankappan (1966) has interpreted the low-lying $J = \frac{1}{2}, \frac{3}{2}, \frac{5}{2}, \frac{7}{2}$, and $\frac{9}{2}$ levels as a multiplet formed by the coupling of a $1d_{5/2}$ proton hole to the first excited (2^+) state of ^{28}Si. This model is able to fit simultaneously the level positions and many of the γ-ray transition rates. The proton inelastic scattering cross sections (Crawley and Garvey 1965) are also in better agreement with this model than with the strong-coupling model. The 3·00 MeV level has for some time been regarded as the low-lying $J^\pi = \frac{9}{2}^+$ state predicted by Thankappan's excited-core model, but the experimental evidence is somewhat contradictory. Towle and Gilboy (1962) claimed an unambiguous assignment of $J = \frac{9}{2}$ from inelastic neutron scattering; the γ-ray correlation results of Lawergren (1964) are consistent with this assignment. Wakatsuki and Kern (1966) used γ-ray correlation methods to make a firm assignment of $J = \frac{7}{2}$, but it is not obvious that the data used to exclude a $J = \frac{9}{2}$ assignment were free of contributions from the 2·98 MeV level. In addition, those authors made the dubious assumption that the reaction proceeds through an isolated level of the compound nucleus, and the mixing ratio obtained for the 3·00 to 0 transition is inconsistent with a recent lifetime measurement (Broude, Smulders, and Sharpey-Schafer 1967). Sheppard and van der Leun (1967), using a Ge(Li) γ-ray spectrometer, have measured gamma–gamma correlations in the ^{26}Mg(p, $\gamma\gamma$)^{27}Al reaction and claim a definite assignment of $J = \frac{9}{2}$. Gove *et al.* (1967*a*, 1967*b*) have performed a D.W.B.A. analysis of the angular distributions in the ^{28}Si(d, ^{3}He)^{27}Al reaction using a magnetic spectrograph to resolve the 2·98 and 3·00 MeV levels; they conclude that the 3·00 MeV level has $J = \frac{3}{2}$ or $\frac{5}{2}$. This raises the possibility that the 3·00 MeV "level" is, in fact, a doublet, one member of which has $J = \frac{9}{2}$ and the other, populated in the (d, ^{3}He) reaction, $J = \frac{3}{2}$ or $\frac{5}{2}$.

Since the presence of a low-lying $J = \frac{9}{2}$ level is essential to the excited-core model of the ^{27}Al nucleus (and not readily explicable with the simple Nilsson model), we have used the ^{24}Mg(α, pγ)^{27}Al reaction to investigate the spin of the 3·00 MeV level and the possibility that it is a doublet.

A thin, enriched ^{24}Mg target was bombarded with 9·025 MeV α-particles. The angular correlation of γ-rays in coincidence with protons populating the 3·00 MeV

---

† Manuscript received February 15, 1968.

‡ Research School of Physical Sciences, Australian National University, Canberra, A.C.T. 2600.

Aust. J. Phys., 1968, 21, 405–7

level was measured using a 12·7 cm by 10·2 cm NaI(Tl) crystal 20 cm from the target in conjunction with a double-focusing magnetic spectrometer (Elliott, Carter, and Spear 1968) set at 0° to the beam direction. Particle groups to the 2·98 and 3·00 MeV levels were adequately resolved. The collinear geometry ensures that only the $m = \pm\frac{1}{2}$ magnetic substates of the final nucleus are populated, so simplifying the correlation function (Litherland and Ferguson 1961).

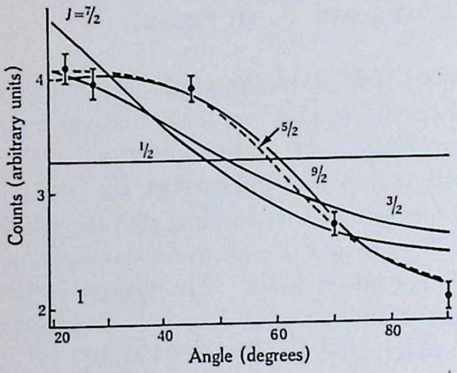

Fig. 1.—Experimental angular correlation for the 3·00 to 0 transition with best fits for various possible spins of the 3·00 MeV level.

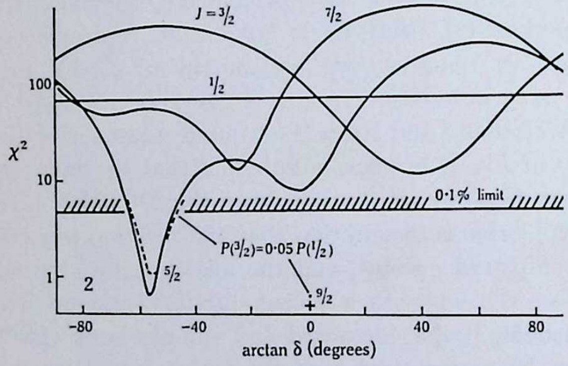

Fig. 2.—Plots of χ^2 versus the amplitude mixing ratio for the 3·00 to 0 angular correlation. Also shown is the effect on the fits for $J = {}^5/_2$ and ${}^9/_2$ of a 5% population of the $m = \pm{}^3/_2$ substates.

The measured correlations of the 3·00 to 0 and 3·00 to 2·21 γ-ray transitions were analysed assuming $J = \frac{5}{2}$ for the ground state (Endt and van der Leun 1962) and $\frac{7}{2}$ for the 2·21 MeV level (Ophel and Lawergren 1964; Sheppard and van der Leun 1967). The 3·00 to 0 correlation could only be fitted within the 0·1% confidence limit (see Figs. 1 and 2) for $J(3\cdot00) = \frac{9}{2}$ with δ (= M3/E2) = 0 and for $J(3\cdot00) = \frac{5}{2}$ with $-2\cdot00 < \delta$ (= E2/M1) $< -1\cdot07$. The 3·00 to 2·21 correlation could be fitted for $J = \frac{9}{2}$ with $|\delta| < 0\cdot1$ and for $J = \frac{5}{2}$ with $-0\cdot29 < \delta < 0\cdot03$ or $\delta < -8\cdot1$ or $\delta > 6\cdot3$. The last two possibilities can be eliminated since such large mixing ratios, when coupled with a recent lifetime measurement (Broude, Smulders, and Sharpey-Schafer 1967) of $(8\cdot3\pm0\cdot7)\times10^{-13}$ sec, imply an enhancement of the E2 width by a factor of about 1000 over the single-particle estimate.

For both transitions the mixing ratios obtained for $J = \frac{9}{2}$ are in agreement with the results of Lawergren (1964) and Sheppard and van der Leun (1967). It is noteworthy that for the 3·00 to 0 transition, the mixing ratio obtained from the present data if $J(3\cdot00) = \frac{5}{2}$ (i.e. $-2\cdot00 < \delta < -1\cdot07$) agrees with the value that Sheppard and van der Leun found to give a satisfactory fit at two of the resonances studied; their $J = \frac{9}{2}$ assignment was based on the fact that at a third resonance $J = \frac{5}{2}$ gave a solution that, although next best to $J = \frac{9}{2}$, fell outside the 0·1% limit.

The branching ratios extracted from the ^{24}Mg(α, pγ)^{27}Al correlation data are compared in Table 1 with those obtained using (p, p′) and (p, γ) reactions. The close agreement implies that, if we are in fact dealing with a doublet, either the two members are populated in the same ratio in all three reactions or they have almost identical decay schemes. It is therefore very improbable that the 3·00 MeV level is a doublet.

Table 1

BRANCHING RATIOS OF 3·00 MeV LEVEL OF ^{27}Al

Reaction	Branching (%)		Reference
	3·00 → 0	3·00 → 2·21	
^{27}Al(p, p′)	84±6	16±6	Lawergren (1964)
^{27}Al(p, p′)	93±4	7±4	Elliott, Ophel, and Spear (to be published)
^{26}Mg(p, γ)	91±3	9±3	Sheppard and van der Leun (1967)
^{24}Mg(α, p)	90±3	10±3	Present work

The authors are grateful to Mr. K. W. Carter for assistance in taking the data.

References

Broude, C., Smulders, P. J. M., and Sharpey-Schafer, J. F. (1967).—Atomic Energy of Canada Ltd Rep. No. 2752.

Crawley, G. M., and Garvey, G. T. (1965).—*Phys. Lett.* **19**, 228.

Elliott, R. V., Carter, K. W., and Spear, R. H. (1968).—*Nucl. Instrum. Meth.* **59**, 29.

Endt, P. M., and van der Leun, C. (1962).—*Nucl. Phys.* **34**, 1.

Gove, H. E. (1960).—Proc. Kingston Conference on Nuclear Structure, p. 438. (North-Holland: Amsterdam.)

Gove, H. E., Purser, K. H., Schwartz, J. J., Alford, W. P., and Cline, D. (1967*a*).—Contribs to Int. Conf. on Nuclear Structure, Tokyo, p. 113.

Gove, H. E., Purser, K. H., Skorka, S. J., Alford, W. P., and Cline, D. (1967*b*).—*Bull. Am. phys. Soc.* **12**, 1191.

Lawergren, B. T. (1964).—*Nucl. Phys.* **53**, 417.

Litherland, A. E., and Ferguson, A. J. (1961).—*Can. J. Phys.* **39**, 788.

Ophel, T. R., and Lawergren, B. T. (1964).—*Nucl. Phys.* **52**, 417.

Sheppard, D. M., and van der Leun, C. (1967).—*Nucl. Phys.* A **100**, 333.

Thankappan, V. K. (1966).—*Phys. Rev.* **141**, 957.

Towle, J. H., and Gilboy, W. B. (1962).—*Nucl. Phys.* **39**, 300.

Wakatsuki, T., and Kern, B. D. (1966).—*Bull. Am. phys. Soc.* **11**, 509.

INTERPRETATION OF THE RADIO ROTATION PERIOD OF JUPITER IN TERMS OF THE CYCLOTRON THEORY*

By P. M. McCulloch†

Since 1961 the most intense source of Jovian decametric emission has drifted with respect to system III longitude by about +10° per year (Douglas and Smith 1963; Smith *et al.* 1965). Interpreted as a change in the rotation rate, this would imply that the period increased by approximately 1·1 sec around 1960. Runcorn (1967) and Hide (1967) have interpreted this as a change in the rotation rate of the solid body of Jupiter, in which angular momentum is exchanged between Jupiter's core and the Great Red Spot.

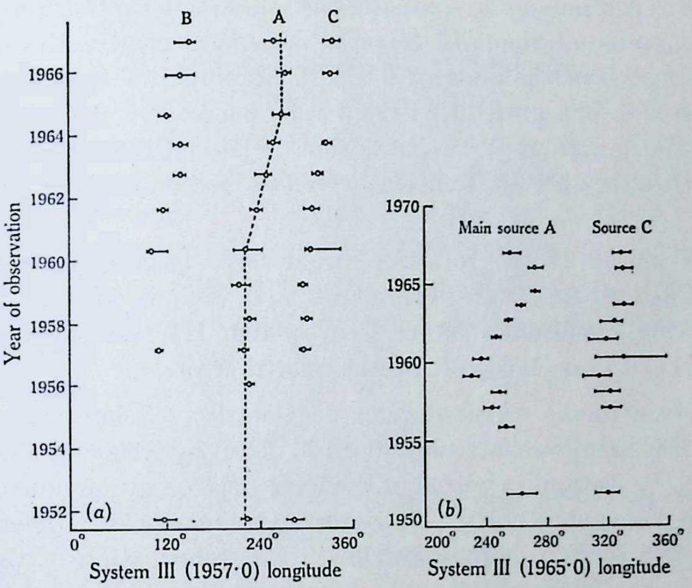

Fig. 1(*a*).—Estimated I.A.U. system III (1957·0) longitude positions of the three main sources in the longitude profiles at 18 MHz are plotted for each year of observation since 1951. The data are taken from Gulkis and Carr (1966) and Williams *et al.* (1967).

Fig. 1(*b*).—Data of Figure 1(*a*) for sources A and C are replotted on a revised system III (1965·0) longitude, which coincides with system III (1957·0) at 0^{h} U.T. on January 1, 1965 and has a rotation period of $9^{h}\,55^{m}\,29^{s}\cdot 67$.

A more plausible interpretation has recently been advanced by Gulkis and Carr (1966). They show that the results are consistent with a constant rotation period about 0·3 sec longer than the system III period, together with a cyclic drift in the longitude of source A.

---

* Manuscript received March 26, 1968.

† Physics Department, University of Tasmania, P.O. Box 252C, Hobart, Tas. 7001.

Aust. J. Phys., 1968, **21**, 409–13

Douglas (1960) and Carr *et al.* (1961) both analysed data obtained prior to 1961 and found that the rotation period was constant at about $9^h 55^m 29^s \cdot 37$ (system III). However, observations made since 1961 indicate that the rotation period has fluctuated. Between 1961 and 1965 the mean period was approximately $1 \cdot 0$ sec longer than the system III period quoted above, and since 1965 the period appears to have returned to near its former value. Figure 1(*a*) shows the estimated positions of the three main sources in the longitude profiles at 18 MHz since 1951. The drift in the main source A is quite distinct, while the points for sources B and C are not as consistent.

Gulkis and Carr (1966) have suggested that the apparent rotation period of Jupiter drifts cyclically about a constant mean value which is about $0 \cdot 3$ sec longer than system III. Figure 1(*b*) shows the data of Figure 1(*a*) for sources A and C replotted on a system III ($1965 \cdot 0$) longitude scale, which is defined to coincide with system III ($1957 \cdot 0$) at 0^h U.T. on January 1, 1965 and has a rotation period of $9^h 55^m 29^s \cdot 67$. The points for source A define a sine wave with an amplitude of about 18° and a period of about 12 years, in close agreement with Jupiter's orbital period and the length of the sunspot cycle. The points of source C also define a sine wave which is in phase with that defined by source A but has an amplitude of only about 8°. The data from the two early sources B1 and B2 have not been analysed in this way because they are not sufficiently well defined on the majority of longitude profiles.

Several estimates of the rotation period have been made from decimetric observations (Bash *et al.* 1964; Komesaroff and McCulloch 1967). These estimates give periods significantly larger than system III and agree with the mean period of Gulkis and Carr (1966) within the quoted errors.

The cyclotron theory of the Jupiter decametric emissions was first proposed by Ellis (1962, 1963) and was later developed in detail by Ellis and McCulloch (1963) and Ellis (1965). Radiation is emitted at the local electron gyrofrequency by electron streams in Jupiter's magnetic field. The observed frequency is Doppler shifted owing to the longitudinal motion of the electrons. The propagation of the radiation is controlled by the medium so that only radiation in the extraordinary mode in the forward direction escapes. In this case the observed frequency is slightly above the local gyrofrequency. The emission is concentrated onto the surface of a cone about the magnetic field direction, where the cone angle depends on the ratio of the gyrofrequency to plasma frequency at the emission point and the pitch angle of the electrons.

The electron streams are assumed to be confined to field lines that intersect the surface of Jupiter at latitudes greater than 75°, with the probability of finding an electron stream at 75° being zero but increasing linearly with magnetic latitude. All magnetic longitudes are assumed to be equally probable. The characteristics of the model are such that the probability of occurrence and power of the emissions depend on the angle between the observer's line of sight and the axis of the emission cone. As the cone angle is fixed for a given distribution of electron streams, the probability of occurrence as a function of longitude can only be varied by changing the inclination of the magnetic field (Fig. 2).

The main peak in the longitude profiles for frequencies above 15 MHz was explained by a local dip anomaly in Jupiter's magnetic field. The maximum tilt of the field lines from those of a dipole necessary to account for the observations was found to be about 15°.

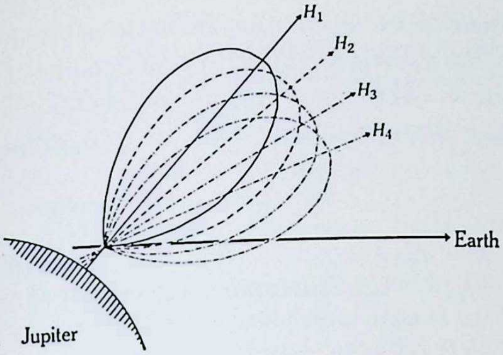

Fig. 2.—Probability-of-occurrence emission cones are illustrated for four different inclinations of Jupiter's magnetic field. The relative probability of occurrence at any time is given by the intersection of the cones with the Earth–Jupiter line.

As Jupiter revolves about the Sun the tilt D_E of its rotation axis to the Earth–Jupiter line changes cyclically. This results in a cyclic variation in the range of magnetic latitudes from which emission can be seen at any time. Hence, if the longitude of the maximum dip deviation changes with magnetic latitude, we would expect to see a cyclic change in the longitude of the corresponding emission region. The change in main source position can then be interpreted as a change in longitude of the maximum dip angle deviation with magnetic latitude. The dip anomalies needed at different latitudes to explain the observed main source positions are shown in Figure 3.

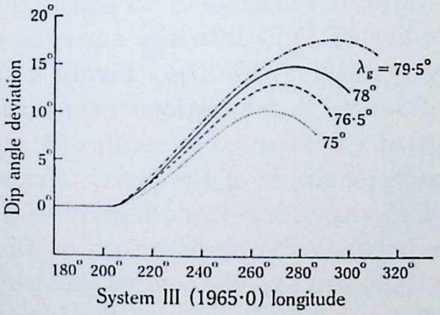

Fig. 3.—The proposed dip angle deviations at 18 MHz in the vicinity of source A are plotted for various values of λ_g, the magnetic latitude at which the undistorted field line intersects the surface of Jupiter.

The consequence of this explanation of the main source position drift is that each of the four individual sources in the longitude profiles could change positions in different ways, depending on the local dip anomalies. The sources associated with the magnetic poles would not be expected to change their positions appreciably. The small in-phase variation of source C can be explained on the basis of overlapping by source A, which is much larger and has a larger position variation. The earlier of the two B sources could change in position with appropriate dip angle deviations similar to those for source A. However, the present observations are not sufficiently accurate to demonstrate any such variation.

The different rotational periods determined by Dulk (1965) by analysing spectral data in different ways may be explained on the basis of the above discussion. The correlation or comparison of longitude profiles gives periods that are dominated by the period of the strongest source A in the longitude profiles. Comparison of individual features on dynamic spectra on the other hand are biased in favour of the early B source, as this is the region where the majority of repeatable dynamic spectra are obtained. We have seen that, according to the cyclotron theory, there is no need for the periods of sources A and B to be the same. These two types of observation give information about the configuration of Jupiter's magnetic field in two different longitude ranges.

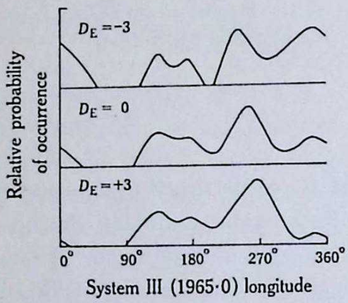

Fig. 4.—Theoretical profiles showing the relative probability of occurrence at 18 MHz are plotted for various values of D_E, the inclination of Jupiter's rotation axis to the Earth–Jupiter line.

Duncan (1967) has recently made a statistical analysis of Jupiter data at frequencies above 20 MHz (where possible) for the period 1957–66. He has found that the commencement of main source storms has recurred with a period that has been constant from 1951 to 1966, being $9^h 55^m 29^s{\cdot}70 \pm 0^s{\cdot}05$, in good agreement with that obtained by Gulkis and Carr.

The cyclotron theory predicts that the width in longitude of an emission peak depends on the penetration of the observer's line of sight into the emission cone. The width of the emission regions then vary cyclically with D_E. Figure 4 shows probability-of-occurrence longitude profiles of source A for various values of D_E. A most interesting feature of these profiles is that the increase in width of the peak is just sufficient to compensate for the change in longitude of the peak. Hence the leading section of the source always occurs at the same longitude regardless of the value of D_E. There is then no contradiction between the observations of Duncan and those of Gulkis and Carr, as the starting times are exactly compensated by the change in source width. Hence the centre of the emission region is the important feature and not the storm commencement. This is further emphasized by the observation of Duncan (1966) that Io's influence is sharpest for the peak in the emission region and is not as well correlated with the commencement time.

This research is supported financially by the Radio Research Board.

References

Bash, F. N., *et al.* (1964).—*Astrophys. J.* **139**, 975.
Carr, T. D., *et al.* (1961).—*Astrophys. J.* **134**, 105.
Douglas, J. N. (1960).—Ph.D. Dissertation, Yale University.
Douglas, J. N., and Smith, H. J. (1963).—*Astr. J.* **68**, 163.

DULK, G. A. (1965).—Ph.D. Dissertation, University of Colorado.

DUNCAN, R. A. (1966).—*Planet. Space Sci.* **14**, 1291.

DUNCAN, R. A. (1967).—*Planet. Space Sci.* **15**, 1687.

ELLIS, G. R. A. (1962).—*Aust. J. Phys.* **15**, 344.

ELLIS, G. R. A. (1963).—*Aust. J. Phys.* **16**, 74.

ELLIS, G. R. A. (1965).—*J. Res. natn. Bur. Stand.* **69D**, 1513.

ELLIS, G. R. A., and MCCULLOCH, P. M. (1963).—*Aust. J. Phys.* **16**, 380.

GULKIS, S., and CARR, T. D. (1966).—*Science* **154**, 257.

HIDE, R. (1967).—"Magnetism and the Cosmos." (Eds. W. R. Hindmarsh *et al.*) p. 378. (Oliver & Boyd: Edinburgh.)

KOMESAROFF, M. M., and MCCULLOCH, P. M. (1967).—*Astrophys. Lett.* **1**, 39.

RUNCORN, S. K. (1967).—"Magnetism and the Cosmos." (Eds. W. R. Hindmarsh *et al.*) p. 365. (Oliver & Boyd: Edinburgh.)

SMITH, A. G. *et al.* (1965).—*Astrophys. J.* **141**, 457.

WILLIAMS, J. *et al.* (1967).—"A Catalogue of Radio Observations of Jupiter 1965–67." (Radio Astronomy Observatory, Florida State University.)

R-MATRIX FIT TO ^{9}Be(γ, n)^{8}Be CROSS SECTION NEAR THRESHOLD

By F. C. BARKER* and B. M. FITZPATRICK*

[*Manuscript received March* 12, 1968]

Summary

Satisfactory fits to the ^{9}Be(γ, n)^{8}Be cross section just above the neutron threshold are obtained with the one-level approximation of R-matrix theory but not with that of complex eigenvalue theory. Restrictions on the R-matrix parameters from other sources are discussed.

I. INTRODUCTION

The ^{9}Be(γ, n)^{8}Be cross section is observed to have a peak just above the neutron threshold (Lauritsen and Ajzenberg-Selove 1966). Mahaux (1965) has suggested that analysis of the cross section in this region should show significant differences between the R-matrix and complex eigenvalue theories of nuclear reactions.

It is not obvious that these differences exist, as the cross section formulae of the two theories, in the one-level approximation and for s-wave neutron emission, have the same forms of energy dependence in both numerators and denominators. The expressions appear to be equivalent; however, differences can arise due to the restrictions on the parameters of the two theories.

II. R-MATRIX AND COMPLEX EIGENVALUE EXPRESSIONS FOR CROSS SECTION

In the one-level approximation of R-matrix theory (Lane and Thomas 1958), the contribution to the cross section from a level of spin J is

$$\sigma_R(\gamma, \mathrm{n}) = \frac{(2J+1)\pi\hbar^2c^2}{8}\frac{\Gamma_\gamma \Gamma_\mathrm{n}}{E_\gamma^2\,(E_R+\Delta-E)^2+\frac{1}{4}\Gamma^2}. \qquad (1)$$

As is usual, we retain in the denominator the contributions to Δ and Γ from the neutron channel only. Then for a $\frac{1}{2}^+$ level formed by E1 γ-radiation and decaying by s-wave neutrons, and for $E > 0$ (with E measured from the neutron threshold, so that $E_\gamma = E+E_\mathrm{T}$ with $E_\mathrm{T} = 1\cdot665$ MeV), we have

$$\Gamma_\gamma = \frac{16\pi}{9}\frac{e^2}{\hbar^3c^3}E_\gamma^3 B, \qquad \Gamma_\mathrm{n} = 2(\epsilon_R E)^{\frac{1}{2}}, \qquad \Delta_\mathrm{n} = 0. \qquad (2)$$

Here $B \equiv B(\mathrm{E1}, \frac{1}{2}^+ \to \frac{3}{2}^-)$ and $\epsilon_R = 2M_\mathrm{n} a_\mathrm{n}^2 \gamma_\mathrm{n}^4/\hbar^2 > 0$, where M_n, a_n, and γ_n^2 are

---

* Research School of Physical Sciences, Australian National University, Canberra, A.C.T. 2600.

Aust. J. Phys., 1968, 21, 415–21

the reduced mass, channel radius, and reduced width for the ^{8}Be+n channel, and the boundary condition parameter B_n is taken as zero. Thus (1) becomes

$$\sigma_R(\gamma, \mathrm{n}) = \alpha_R E_\gamma E^{\frac{1}{2}}/(E^2+\beta_R E+\gamma_R)\,, \tag{3}$$

with

$$\alpha_R = \frac{8\pi^2}{9}\frac{e^2}{\hbar c}\epsilon_R^{\frac{1}{2}}B\,, \qquad \beta_R = \epsilon_R - 2E_R\,, \qquad \gamma_R = E_R^2\,. \tag{4}$$

Similarly in the complex eigenvalue theory (Mahaux 1965), the one-level approximation can be written

$$\sigma_S(\gamma, \mathrm{n}) = \alpha_S E_\gamma E^{\frac{1}{2}}/(E^2+\beta_S E+\gamma_S)\,, \tag{5}$$

with

$$\alpha_S = \frac{\pi}{4}\frac{\hbar^2 c^2 \bar{G}_{\gamma\mathrm{n}}\bar{G}_{\mathrm{nn}}}{(E_S+E_T)^3\,|\,E_S\,|^{\frac{1}{2}}}\,, \qquad \beta_S = -2E_S\,, \qquad \gamma_S = E_S^2+\tfrac{1}{4}\Gamma_S^2\,, \tag{6}$$

using the notation of Mahaux except that E_S and Γ_S replace E_{nn} and Γ_{n}. Thus the cross sections (3) and (5) are identical provided $\alpha_R = \alpha_S$, $\beta_R = \beta_S$, and $\gamma_R = \gamma_S$, which makes it appear that the two theories can give identical fits to any experimental $\sigma(\gamma, \mathrm{n})$.

There are, however, restrictions on the values of the parameters (4) and (6), i.e. $\gamma_R \geqslant 0$ and $\gamma_S \geqslant \frac{1}{4}\beta_S^2$. These imply that any cross section that is an admissible form of σ_S is also an admissible form of σ_R, with $E_R = +(E_S^2+\frac{1}{4}\Gamma_S^2)^{\frac{1}{2}}$ and $\epsilon_R = 2(E_R-E_S)$, giving $\epsilon_R \leqslant 4E_R$. On the other hand, there are some cross sections that are admissible forms of σ_R with $\epsilon_R > 4E_R$ and these are inadmissible forms of σ_S. In this latter case the same values of α_R, β_R, and γ_R correspond to two sets of values of E_R, ϵ_R, and B, related by

$$E_{R2} = -E_{R1}\,, \qquad \epsilon_{R2} = \epsilon_{R1}-4E_{R1}\,, \qquad B_2 = B_1(\epsilon_{R1}/\epsilon_{R2})^{\frac{1}{2}}\,. \tag{7}$$

The solution with $E_R < 0$ can be rejected on the following grounds. For reactions of the type ^{9}Be(p, p′)^{9}Be*, the cross section in the one-level R-matrix approximation is (Lane and Thomas 1958; Barker and Treacy 1962)

$$\sigma_R(\mathrm{p}, \mathrm{p}') \propto \tfrac{1}{2}(\Gamma_\gamma+\Gamma_{\mathrm{n}})/\{(E_R+\Delta-E)^2+\tfrac{1}{4}\Gamma^2\}\,. \tag{8}$$

Whereas $\sigma_R(\gamma, \mathrm{n})$ given by (1) vanishes for $E < 0$ because of the factor Γ_{n} in the numerator, $\sigma_R(\mathrm{p}, \mathrm{p}')$ in the case $E_R < 0$ has a sharp peak at $E = E_{\mathrm{r}} < 0$, where $E_{\mathrm{r}} = E_R+\Delta_{\mathrm{n}}(E_{\mathrm{r}})$ (as was discussed by Barker and Treacy (1962) for a similar case in ^{17}F). If $E_R \geqslant 0$ the cross section $\sigma_R(\mathrm{p}, \mathrm{p}')$ is zero for $E < 0$. Experimentally Spencer, Phillips, and Young (1960) found no peak below the neutron threshold, so fits with $E_R < 0$ (bound states) can be excluded, contrary to the previous conclusion of Corman, Sherwood, and John (1963).

III. Fits to ^{9}Be(γ, n)^{8}Be Cross Section near Neutron Threshold

Mahaux (1965) used the complex eigenvalue formulae (5) and (6) to fit experimental values (Gibbons *et al.* 1959; John and Prosser 1962) of $\sigma(\gamma, \mathrm{n})$ at four energies E between 26 and 185 keV, obtaining $E_S = -85$ keV, $\Gamma_S = 0$, and $\alpha_S = 1\cdot 87$ mbn keV$^{\frac{1}{2}}$. These give a peak of $\sigma_S(\gamma, \mathrm{n})$ at $E = 29$ keV. Exactly the same fit is obtained with the R-matrix formulae (3) and (4) with $E_R = 85$ keV, $\epsilon_R = 340$ keV, and $B = 1\cdot 58$ mbn. An earlier R-matrix fit (Barker and Treacy 1962) to the data of Gibbons *et al.* (1959) used a calculated value $\epsilon_R = 820$ keV and obtained $E_R = 110$ keV and $B = 2\cdot 22$ mbn, giving the peak at $E = 19$ keV.

Recently Berman, Van Hemert, and Bowman (1967) measured $\sigma(\gamma, \mathrm{n})$ from < 1 to about 40 keV above the neutron threshold and found that the peak occurs at $E \simeq 6$ keV, in marked disagreement with the previous fits to $\sigma(\gamma, \mathrm{n})$. Berman, Van Hemert, and Bowman attempted to fit their own and the earlier data using the R-matrix formulae (3) and (4) but did not obtain a satisfactory fit. This appears to be due to the use of unrealistic weights for the data points. Berman, Van Hemert, and Bowman used a linear least squares fit to a quantity Y, which is an energy-dependent function of σ, and gave all the data points equal weights in Y. This corresponds to very unequal weights in σ, e.g. the highest energy point of Berman, Van Hemert, and Bowman had a weight 100 times greater than the lowest energy point, and the highest energy point of the earlier data had a weight 6000 times greater. Consequently the low energy points contributed little to the fit and the peak was obtained at too high an energy.

We measure the goodness of fit by

$$X_R = N^{-1} \sum_{i=1}^{N} \mid \{\sigma_R(E_i) - \sigma(E_i)\}/\eta(E_i) \mid^2, \tag{9}$$

where $\sigma(E_i)$ and $\eta(E_i)$ are the measured cross section and error at the energy E_i, $\sigma_R(E_i)$ is calculated from (3) and (4), and $N = 86$ (two points from Gibbons *et al.* 1959, three from John and Prosser 1962, and 81 from Berman, Van Hemert, and Bowman 1967). The assigned experimental errors are used for the earlier data and we take equal errors of $0\cdot 1$ mbn for all the cross sections of Berman, Van Hemert, and Bowman, on the basis of the scatter of their points. Our results are insensitive to changes in this value of $0\cdot 1$ mbn.

Berman, Van Hemert, and Bowman normalized their experimental cross sections to the earlier measurements at 26 keV. A somewhat better overall fit may be obtained by increasing their cross sections by about 15%; this seems to be justifiable as their absolute cross sections were subject to an overall uncertainty of about 40%. With this increase of 15%, the minimum values of X_R obtained by varying E_R and ϵ_R for fixed values of B are shown in Figure 1. The minimum X_R stays essentially constant at about $1\cdot 1$ for $B \gtrsim 3$ mbn. The corresponding values of E_R and ϵ_R are given within about 10% by

$$E_R \simeq 31\, B \quad \mathrm{mbn}^{-1}\,\mathrm{keV}, \qquad \epsilon_R \simeq 200\, B^2 \quad \mathrm{mbn}^{-2}\,\mathrm{keV}. \tag{10}$$

As examples the fits to the experimental $\sigma(\gamma, \mathrm{n})$ are shown in Figure 2 for the two cases

$$B = 2\cdot 0\ \mathrm{mbn}, \qquad E_R = \ 63\ \mathrm{keV}, \qquad \epsilon_R = 0\cdot 82\ \mathrm{MeV}, \tag{11}$$

and

$$B = 5\cdot 0\ \mathrm{mbn}, \qquad E_R = 151\ \mathrm{keV}, \qquad \epsilon_R = 4\cdot 59\ \mathrm{MeV}. \tag{12}$$

As B increases, the high energy tail of $\sigma_R(\gamma, \mathrm{n})$ increases, since (for $E_R \geqslant 0$)

$$\int_0^\infty E_\gamma^{-1}\, \sigma_R(\gamma, \mathrm{n})\, \mathrm{d}E = (8\pi^3/9)(e^2/\hbar c)B. \tag{13}$$

The increase of X_R as B decreases below 3 mbn is due mainly to poorer fits to the earlier data, and the fits for B much less than 2 mbn are regarded as unacceptable.

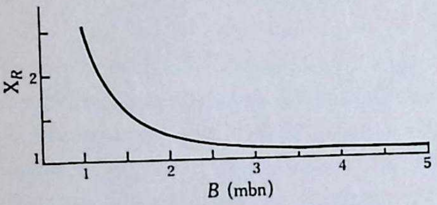

Fig. 1.—Quantity X_R, which measures the goodness of fit of the R-matrix one-level approximation to $\sigma(\gamma, \mathrm{n})$, shown as a function of the transition matrix element B.

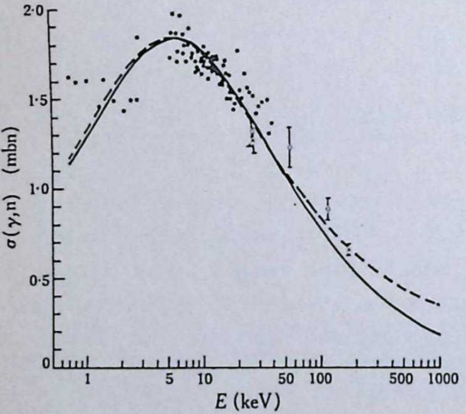

Fig. 2.—Cross section of ${}^9\mathrm{Be}(\gamma, \mathrm{n})^8\mathrm{Be}$ shown as a function of energy E above neutron threshold. The curves are calculated fits in the R-matrix one-level approximation with the parameter values of (11) (solid curve) and of (12) (dashed curve). The experimental points are from:
×, Gibbons *et al.* (1959)
o, John and Prosser (1962)
●, Berman, Van Hemert, and Bowman (1967)

The fits for $B \gtrsim 5$ mbn appear to be significantly better than those obtained by Berman, Van Hemert, and Bowman (1967).

From the relations (10), it follows that the acceptable R-matrix fits have $\epsilon_R > 4E_R$ and therefore these same fits are not obtainable from the complex eigenvalue formulae (5) and (6). In fact the smallest value of the quantity X_S, corresponding to (9) with σ_S replacing σ_R, is about $5\cdot 0$, and in this case the fit to the earlier data is much poorer than in the best R-matrix fits, the contribution of these points to X_S being about 20 times that to X_R. This is due to the fact that, for a given peak energy, σ_R can have a larger high energy tail than σ_S.

Thus the measured ^{9}Be(γ, n)^{8}Be cross section just above the neutron threshold can be fitted satisfactorily by the R-matrix one-level approximation, but the one-level approximation of the complex eigenvalue theory cannot give a satisfactory fit.

IV. FURTHER RESTRICTIONS ON R-MATRIX PARAMETERS

In the previous section, satisfactory R-matrix fits to $\sigma(\gamma, \mathrm{n})$ for $E \lesssim 200$ keV are obtained for a range of values of B, E_R, and ϵ_R. Further experimental information may be used to restrict the values of these parameters.

Jakobson (1961) measured $\sigma(\gamma, \mathrm{n})$ at higher energies using bremsstrahlung, and obtained a minimum in σ of about $(0\cdot27\pm0\cdot07)$mbn at $E_\gamma \simeq 2\cdot2$ MeV. A radioactive source measurement at $E_\gamma = 2\cdot185$ MeV gave $\sigma = (0\cdot39\pm0\cdot06)$mbn (Hamermesh and Kimball 1953). Contributions to σ from other levels of ^{9}Be, such as the $\frac{1}{2}^-$ level expected at about $2\cdot4$ MeV excitation energy (Barker 1966), may start to be appreciable at about these energies. Thus we require $\sigma_R(\gamma, \mathrm{n}) \lesssim 0\cdot3$ mbn at $E \simeq 500$ keV, and this implies $B \lesssim 2\cdot0$ mbn (cf. Fig. 2). Acceptable fits to all the $\sigma(\gamma, \mathrm{n})$ data therefore need $B \simeq 2\cdot0$ mbn, and parameter values near those given in (11). These correspond to $\Gamma_\gamma = 0\cdot98$ eV at $E_\gamma = 1\cdot67$ MeV.

From the inelastic scattering of high energy electrons on ^{9}Be, Nguyen Ngoc, Hors, and Perez y Jorba (1963) have given a value $B = (10\cdot4\pm1\cdot2)$mbn. The reliability of this value is doubtful, however, as a more recent similar measurement at Darmstadt has led to a form factor which is 15 times smaller than that of Nguyen Ngoc, Hors, and Perez y Jorba and is compatible with the $\sigma(\gamma, \mathrm{n})$ measurements (Clerc, personal communication). There is the same difficulty in extracting a unique value of B from ^{9}Be(e, e$'$)^{9}Be* as from ^{9}Be(γ, n)^{8}Be, due to possible variation in the high energy tail of the peak.

A calculated value of B, based on a weak coupling model for the $\frac{1}{2}^+$ state of ^{9}Be (Barker 1961), is $B = 3\cdot3$ mbn, but this number depends on some approximations of unknown accuracy.

A given value of ϵ_R implies a relation between a_n and γ_n^2, or alternatively between a_n and the dimensionless reduced width $\theta_\mathrm{n}^2 = \gamma_\mathrm{n}^2(\hbar^2/M_\mathrm{n} a_\mathrm{n}^2)^{-1}$. From the definition of ϵ_R and the relations (10), one has

$$a_\mathrm{n}/\theta_\mathrm{n}^2 \simeq 22\,B^{-1}\,\mathrm{mbn\,fm}\,. \tag{14}$$

The conventional value of the channel radius $1\cdot45(A_1^{\frac{1}{3}}+A_2^{\frac{1}{3}})$fm is in this case $a_\mathrm{n} = 4\cdot35$ fm, and one might reasonably expect $a_\mathrm{n} \gtrsim 3$ fm. Also one expects $\theta_\mathrm{n}^2 \lesssim 1$ (a value estimated from the weak coupling model (Barker 1961) is $0\cdot41$), and these with (14) lead to $B \lesssim 7$ mbn.

Alternatively, another relation between a_n and θ_n^2 may be obtained by fitting the width of the analogous $\frac{1}{2}^+$ level of the mirror nucleus ^{9}B (assuming the same channel radius and reduced width for the ^{8}Be+p channel as for the ^{8}Be+n channel). This first excited state of ^{9}B has apparently been seen at an excitation energy E_x of about $1\cdot5$ MeV and with an observed width Γ^o of order 1 MeV (Islam and Treacy

1965; Treacy, personal communication; Slobodrian *et al.* 1967). For a given value of Γ^{o} and from (14), values of a_{n} and θ_{n}^2 may be obtained for each value of B. These are shown in Figure 3 for $\Gamma^{\mathrm{o}} = 1\cdot 0$, $1\cdot 5$, and $2\cdot 0$ MeV (at $E_x = 1\cdot 5$ MeV). For $B \simeq 2$ mbn, the values of a_{n} and θ_{n}^2 are reasonable ($3\text{ fm} \lesssim a_{\mathrm{n}} \lesssim 5\text{ fm}$, $0\cdot 3 \lesssim \theta_{\mathrm{n}}^2 \lesssim 0\cdot 5$) for $1\cdot 2\text{ MeV} \lesssim \Gamma^{\mathrm{o}} \lesssim 1\cdot 5$ MeV. If B were much larger than 2 mbn, the $\frac{1}{2}^+$ level of ^{9}B would probably be too broad to be identified in reactions.

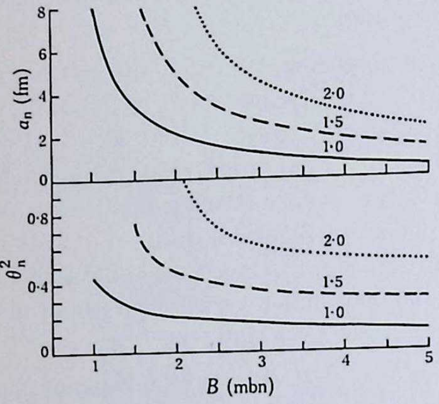

Fig. 3.—Channel radius a_{n} and dimensionless reduced width θ_{n}^2 shown as functions of the transition matrix element B for simultaneous fits to ^{9}Be(γ, n)^{8}Be cross section and to width Γ^{o} (values on curves in MeV) of ^{9}B first excited state.

V. Discussion

The R-matrix one-level approximation with parameters for the $\frac{1}{2}^+$ level of ^{9}Be given in (11) appears to fit satisfactorily the experimental data from ^{9}Be(γ, n)^{8}Be and ^{9}Be(e, e′)^{9}Be* in the region of ^{9}Be excitation energies just above the neutron threshold, and gives an observed width Γ^{o} of about $1\cdot 4$ MeV for the corresponding $\frac{1}{2}^+$ level of ^{9}B.

With these parameter values, $\sigma_R(\gamma, \mathrm{n})$ peaks at $E \simeq 6$ keV, in agreement with the data of Berman, Van Hemert, and Bowman (1967). These were obtained with ^{9}Be targets of thickness $0\cdot 5$ and $1\cdot 0$ in., and it seems likely that neutron energy loss in the targets could be appreciable† as the mean free path is of order $0\cdot 5$ in. and the mean energy loss per collision about 20%. Some evidence to support this comes from fits to the data from the $0\cdot 5$ in. target and from the $1\cdot 0$ in. target separately; the former gives the peak energy as $8\cdot 3$ keV, the latter as $4\cdot 7$ keV. A rough method of overcoming this discrepancy, assumed to be due to neutron energy loss in the targets, is to increase all the values of E_i obtained with the $0\cdot 5$ in. target by a factor $8\cdot 3/4\cdot 7 = 1\cdot 77$, and all those obtained with the $1\cdot 0$ in. target by $(1\cdot 77)^2 = 3\cdot 12$. Acceptable R-matrix fits to these and the earlier data for $E \lesssim 200$ keV are obtained for $B \gtrsim 1\cdot 5$ mbn and $X_R \simeq 1$, with the fit to the earlier data much better than before (by a factor of six for $B = 2$ mbn). The best complex eigenvalue fits have $X_S \simeq 2$, with the early data points contributing six times as much to X_S as to X_R. Thus the R-matrix one-level approximation still allows a much better fit to the data than the complex eigenvalue one-level approximation. Consistency of the R-matrix fit with $\sigma(\gamma, \mathrm{n})$ at higher energies requires $B \lesssim 1\cdot9$ mbn. For $B \simeq 1\cdot7$ mbn, reasonable values of a_{n} and θ_{n}^2 are obtained for $\Gamma^{\mathrm{o}} \simeq 1\cdot2$ MeV. The main difference from the results of Sections III and IV is that $\sigma_R(\gamma, \mathrm{n})$ now peaks at $E \simeq 15$ keV.

---

† We are indebted to Dr. P. B. Treacy for suggesting this possibility.

Further investigation of the problem of neutron energy loss in ^{9}Be(γ, n)^{8}Be experiments of the type performed by Berman, Van Hemert, and Bowman (1967) seems necessary, and an independent measurement of the peak position in a particle reaction such as ^{9}Be(p, p$'$)^{9}Be* is desirable; a previous measurement with this reaction (Bronson, Beckner, and Phillips 1962) indicated that the peak occurs within 14 keV of the neutron threshold.

VI. References

Barker, F. C. (1961).—*Nucl. Phys.* **28**, 96.

Barker, F. C. (1966).—*Nucl. Phys.* **83**, 418.

Barker, F. C., and Treacy, P. B. (1962).—*Nucl. Phys.* **38**, 33.

Berman, B. L., Van Hemert, R. L., and Bowman, C. D. (1967).—*Phys. Rev.* **163**, 958.

Bronson, J. D., Beckner, E. H., and Phillips, G. C. (1962).—*Bull. Am. phys. Soc.* **7**, 119.

Corman, E. G., Sherwood, J. E., and John, W. (1963).—*Phys. Lett.* **4**, 146.

Gibbons, J. H., Macklin, R. L., Marion, J. B., and Schmitt, H. W. (1959).—*Phys. Rev.* **114**, 1319.

Hamermesh, B., and Kimball, C. (1953).—*Phys. Rev.* **90**, 1063.

Islam, M. M., and Treacy, P. B. (1965).—*Nucl. Phys.* **70**, 236.

Jakobson, M. J. (1961).—*Phys. Rev.* **123**, 229.

John, W., and Prosser, J. M. (1962).—*Phys. Rev.* **127**, 231.

Lane, A. M., and Thomas, R. G. (1958).—*Rev. mod. Phys.* **30**, 257.

Lauritsen, T., and Ajzenberg-Selove, F. (1966).—*Nucl. Phys.* **78**, 1.

Mahaux, C. (1965).—*Nucl. Phys.* **71**, 241.

Nguyen Ngoc, H., Hors, M., and Perez y Jorba, J. (1963).—*Nucl. Phys.* **42**, 62.

Slobodrian, R. J., Bischel, H., McKee, J. S. C., and Tivol, W. F. (1967).—*Phys. Rev. Lett.* **19**, 595.

Spencer, R. R., Phillips, G. C., and Young, T. E. (1960).—*Nucl. Phys.* **21**, 310.

THE BEHAVIOUR OF DWBA STRIPPING AMPLITUDES NEAR THE BUTLER POLE

By M. Andrews,* W. K. Bertram,* and L. J. Tassie*

[*Manuscript received November 24, 1967*]

Summary

Using integral representations of the bound state wave functions it is shown that, near the so-called Butler pole, DWBA amplitudes of (d, p) and certain (d, n) reactions depend only on the asymptotic parts of these wave functions. Furthermore, the zero-range approximation for the n–p interaction in the deuteron is exact at the pole. As well it is found that for (d, n) stripping to loosely bound levels of heavy nuclei the Butler pole disappears in the sense that the amplitude is no longer infinite there.

I. Introduction

The amplitude M of a (d, p) or (d, n) reaction, at fixed incident deuteron energy, may be regarded as a function of the variable Q^2,

$$Q^2 = |\,Q\,|^2,$$

where

$$\boldsymbol{Q} = \boldsymbol{k}_1 - \boldsymbol{k}_2, \qquad \boldsymbol{k}_2 = m_A/m_B\,\boldsymbol{k}_y.$$

$\boldsymbol{k}_1$ and $\boldsymbol{k}_y$ are the momenta, in the centre of mass frame, of the incident deuteron and the outgoing nucleon y, while m_A and m_B are the masses of the target nucleus A and the residual nucleus B, which consists of A plus a captured nucleon x.

For (d, p) and (d, n) reactions the amplitude $M(Q^2)$ has a singularity at the point $Q^2 = -\kappa_x^2$, where

$$\kappa_x^2 = -2m_{xA}B_x/\hbar^2, \qquad m_{xA} = m_x m_A/(m_x+m_A),$$

and B_x is the binding energy of the captured nucleon. If Coulomb interactions are neglected, this singularity is a pole, the Butler pole (Schnitzer 1962), but when Coulomb interactions are included this singularity is a branch point. In the case of (d, p) reactions the cut is in the phase of the amplitude only and there is a simple pole in the modulus. The (d, n) case is somewhat more complicated.

In both cases the amplitude in a neighbourhood of the singularity, the so-called pole term, is of considerable interest. It represents the high partial waves in the partial wave expansion of the amplitude. It can therefore be used to aid the computation of these amplitudes (Bertram and Tassie 1968).

Another reason for current interest in the pole term is that the residue at the pole is proportional to the reduced width of the captured nucleon so that, at least

---

* Department of Theoretical Physics, Faculty of Science, Australian National University, Canberra, A.C.T. 2600.

in principle, model independent reduced widths may be obtained from the angular distribution of the differential cross section either by extrapolation (Amado 1959) or, in the case of sub-Coulomb stripping, by employing the method of Morinigo (1967).

In the distorted wave Born approximation (DWBA) the amplitude for deuteron stripping reactions is (see, for example, Glendenning 1963)

$$M = \int \psi_{\mathrm{f}}^{(-)*}\{(m_A/m_B)\boldsymbol{r}+\boldsymbol{R}\}\,\phi_x^*(\boldsymbol{r})\,\phi_{\mathrm{d}}(\boldsymbol{R})\,V_{\mathrm{d}}(\boldsymbol{R})\,\psi_{\mathrm{i}}^{(+)}\{\boldsymbol{r}+(m_y/m_{\mathrm{d}})\boldsymbol{R}\}\,\mathrm{d}\boldsymbol{r}\,\mathrm{d}\boldsymbol{R}\,, \qquad (1)$$

where $\psi_{\mathrm{i}}^{(+)}$ and $\psi_{\mathrm{f}}^{(-)}$ are elastic scattering optical model wave functions of the incoming deuteron and the outgoing nucleon respectively, ϕ_{d} is the internal wave function of the deuteron, ϕ_x the bound state wave function of the captured nucleon, and V_{d} represents the neutron–proton interaction in the deuteron. The aim of this paper is to show that near the pole the amplitude $M(Q^2)$ depends only on the asymptotic parts of the wave functions and that the zero-range approximation is exact at the pole. We shall neglect the spins of the particles involved and choose our units such that $\hbar = 1$.

II. (d, p) AND (d, n) REACTIONS

If we introduce the Fourier transforms $F_1(\boldsymbol{p}_1)$ and $F_2(\boldsymbol{p}_2)$ of the scattered wave functions by the relations

$$\psi_{\mathrm{i}}^{(+)}(\boldsymbol{r}) = \int F_1(\boldsymbol{p}_1)\exp(\mathrm{i}\boldsymbol{p}_1.\boldsymbol{r})\,\mathrm{d}\boldsymbol{p}_1\,, \qquad (2)$$

$$\psi_{\mathrm{f}}^{(-)*}(\boldsymbol{r}) = \int F_2(\boldsymbol{p}_2)\exp(-\mathrm{i}\boldsymbol{p}_2.\boldsymbol{r})\,\mathrm{d}\boldsymbol{p}_2\,, \qquad (3)$$

then the amplitude (1) can be written as (Clement 1965)

$$M = -\tfrac{1}{2}m_{\mathrm{np}}^{-1}\int F_1(\boldsymbol{p}_1)\,F_2(\boldsymbol{p}_2)\,(\kappa_{\mathrm{d}}^2+q_2^2)\,G_1(\boldsymbol{q}_1)\,G_2(\boldsymbol{q}_2)\,\mathrm{d}\boldsymbol{p}_1\,\mathrm{d}\boldsymbol{p}_2\,, \qquad (4)$$

where

$$\boldsymbol{q}_1 = \boldsymbol{p}_1-(m_A/m_B)\boldsymbol{p}_2\,, \qquad \boldsymbol{q}_2 = (m_y/m_{\mathrm{d}})\boldsymbol{p}_1-\boldsymbol{p}_2\,,$$

$$(m_B/m_A)(q_1^2+\kappa_x^2) = (m_{\mathrm{d}}/m_y)(q_2^2+\kappa_{\mathrm{d}}^2)\,, \qquad (5)$$

$$G_1(\boldsymbol{q}_1) = \int \phi_x^*(\boldsymbol{r})\exp(\mathrm{i}\boldsymbol{q}_1.\boldsymbol{r})\,\mathrm{d}\boldsymbol{r}\,, \qquad (6)$$

$$G_2(\boldsymbol{q}_2) = \int \phi_{\mathrm{d}}(\boldsymbol{R})\exp(\mathrm{i}\boldsymbol{q}_2.\boldsymbol{R})\,\mathrm{d}\boldsymbol{R}\,. \qquad (7)$$

Suppose that the potential V_{d} and the potential V_{xA}, acting between A and the captured nucleon, can be expressed as superpositions of exponential or Yukawa potentials

$$V_{\mathrm{d}}(r) = -\int_{\gamma}^{\infty} C(\alpha)\exp(-\alpha r)\,\mathrm{d}\alpha\,, \qquad (8)$$

$$V_{xA} = (2\eta\kappa_x)r^{-1} - \int_{\mu}^{\infty} B(\alpha)\, r^{-1} \exp(-\alpha r)\, \mathrm{d}\alpha . \tag{9}$$

The use of exponential potentials in one case and Yukawa potentials in the other is of no great significance as they can be related by partial integration. The first term of V_{xA} represents the Coulomb interaction between x and A with

$$\eta = \begin{array}{ll} Z_A e^2 m_{xA}/\kappa_x & \text{if } x \text{ is a proton} \\ 0 & \text{if } x \text{ is a neutron.} \end{array}$$

The wave function for the internal motion of the deuteron, which is assumed to be in a pure s-state, can be expressed as (Martin 1959)

$$\phi_{\mathrm{d}}(R) = (4\pi)^{-\frac{1}{2}} N_{\mathrm{d}} R^{-1} \exp(-\kappa_{\mathrm{d}} R) \left(1 + \int_{\gamma}^{\infty} \rho(\alpha) \exp(-\alpha R)\, \mathrm{d}\alpha\right), \tag{10}$$

where $\rho(\alpha)$ satisfies the equation

$$\alpha(\alpha + 2\kappa_{\mathrm{d}})\rho(\alpha) = C(\alpha) + \int_{0}^{\alpha-\gamma} C(\alpha-\beta)\, \rho(\beta)\, \mathrm{d}\beta$$

and N_{d} is a normalization constant.

The bound state wave function of the captured particle, which is assumed to be captured into a state of definite angular momentum, may be written as (Andrews, to be published)

$$\phi_x(r) = N_L\, Y_{LM}(\boldsymbol{r})\, r^L \exp(-\kappa_x r) \int_0^{\infty} \sigma(\alpha) \exp(-\alpha r)\, \mathrm{d}\alpha . \tag{11}$$

The constant N_L is related to the reduced width (see, for example, Dullemond and Schnitzer 1963) and $\sigma(\alpha)$ satisfies the equation

$$\alpha(\alpha+2\kappa_x)\sigma'(\alpha) - 2\{L(\alpha+\kappa_x) + \kappa_x \eta\}\sigma(\alpha) = \int_0^{\alpha-\mu} B(\alpha-\beta)\, \sigma(\beta)\, \mathrm{d}\beta . \tag{12}$$

The right-hand side does not contribute for $0 \leqslant \alpha \leqslant \mu$, and the solution can easily be seen to be

$$\sigma(\alpha) = \sigma_0(\alpha) \qquad 0 \leqslant \alpha \leqslant \mu , \tag{13}$$

where

$$\sigma_0(\alpha) \equiv \alpha^{L+\eta}(\alpha+2\kappa_x)^{L-\eta} .$$

For all greater values of α equation (12) can then be solved recursively.

If we define

$$\sigma_1(\alpha) = \sigma(\alpha) - \sigma_0(\alpha) ,$$

equation (11) becomes

$$\phi_x(\boldsymbol{r}) = N_L\, Y_{LM}(\boldsymbol{r})\, r^L \exp(-\kappa_x r) \left(\int_0^{\infty} \sigma_0(\alpha) \exp(-\alpha r)\, \mathrm{d}\alpha + \int_{\mu}^{\infty} \sigma_1(\alpha) \exp(-\alpha r)\, \mathrm{d}\alpha \right) . \tag{14}$$

Substituting (14) in (6) and (10) in (7), we find

$$G_1(q_1) = 8\pi(2\mathrm{i})^L(L+1)!\,q_1^L\,Y_{LM}^*(q_1)\,N_L\Biggl(\int_0^\infty \sigma_0(\alpha)\frac{\alpha+\kappa_x}{\{q_1^2+(\alpha+\kappa_x)^2\}^{L+2}}\,\mathrm{d}\alpha + \int_\mu^\infty \sigma_1(\alpha)\frac{\alpha+\kappa_x}{\{q_1^2+(\alpha+\kappa_x)^2\}^{L+2}}\,\mathrm{d}\alpha\Biggr), \tag{15}$$

$$G_2(q^2) = (4\pi)^{\frac{1}{2}}N_\mathrm{d}\biggl(\frac{1}{q_2^2+\kappa_\mathrm{d}^2}+\int_\mu^\infty \frac{\rho(\alpha)}{q_2^2+(\alpha+\kappa_\mathrm{d})^2}\,\mathrm{d}\alpha\biggr). \tag{16}$$

Using (15) and (16) in equation (4), the amplitude M becomes

$$-2m_{\mathrm{np}}M = M_1+M_2+(m_\mathrm{d}m_A/m_y m_B)(M_3+M_4).$$

Writing

$$R(p_1,p_2) = (4\pi)^{3/2}(2\mathrm{i})^L(L+1)!\,2N_\mathrm{d}N_L q_1^L\,Y_{LM}^*(q_1)F_1(p_1)F_2(p_2),$$

we have

$$M_1 = \int_0^\infty \sigma_0(\alpha)\,\mathrm{d}\alpha\int R(p_1,p_2)\frac{\alpha+\kappa_x}{\{q_1^2+(\alpha+\kappa_x)^2\}^{L+2}}\,\mathrm{d}p_1\,\mathrm{d}p_2, \tag{17a}$$

$$M_2 = \int_\mu^\infty \sigma_1(\alpha)\,\mathrm{d}\alpha\int R(p_1,p_2)\frac{\alpha+\kappa_x}{\{q_1^2+(\alpha+\kappa_x)^2\}^{L+2}}\,\mathrm{d}p_1\,\mathrm{d}p_2, \tag{17b}$$

$$M_3 = \int_0^\infty \sigma_0(\alpha)\,\mathrm{d}\alpha\int_\gamma^\infty \rho(\beta)\,\mathrm{d}\beta\int R(p_1,p_2)\frac{(\alpha+\kappa_x)(q_1^2+\kappa_x^2)}{\{q_1^2+(\alpha+\kappa_x)^2\}^{L+2}\{q_2^2+(\beta+\kappa_\mathrm{d})^2\}}\,\mathrm{d}p_1\,\mathrm{d}p_2, \tag{17c}$$

$$M_4 = \int_\mu^\infty \sigma_1(\alpha)\,\mathrm{d}\alpha\int_\gamma^\infty \rho(\beta)\,\mathrm{d}\beta\int R(p_1,p_2)\frac{(\alpha+\kappa_x)(q_1^2+\kappa_x^2)}{\{q_1^2+(\alpha+\kappa_x)^2\}^{L+2}\{q_2^2+(\beta+\kappa_\mathrm{d})^2\}}\,\mathrm{d}p_1\,\mathrm{d}p_2. \tag{17d}$$

In Section III it is shown that the term M_1 is infinite at the point $Q^2 = -\kappa_x^2$ for $\eta \leqslant 1$ and that this singularity is an end-point singularity from the lower limit of the integration with respect to α. Since $R(p_1,p_2)$ does not explicitly depend on α, κ_d, and κ_x, and since $\sigma_0(\alpha) = 0$ at $\alpha = 0$, the singularity of M_1 can only come from the vanishing of the term $q_1^2+(\alpha+\kappa_x)^2$ at $\alpha = 0$ in the integrand, i.e. the singularity arises from $q_1^2+\kappa_x^2 = 0$ or equivalently from $q_2^2+\kappa_\mathrm{d}^2 = 0$.

Comparing equations (17b) and (17d) with (17a) it follows immediately that M_2 and M_4 in general have no singularities at $Q^2 = -\kappa_x^2$.

The term M_3 may be rewritten as

$$M_3 = \int_\gamma^\infty \rho(\beta)\,\mathrm{d}\beta\int\frac{R(p_1,p_2)}{q_2^2+(\beta+\kappa_\mathrm{d})^2}\,\mathrm{d}p_1\,\mathrm{d}p_2\int_0^\infty \alpha^{L+\eta}(\alpha+2\kappa_x)^{L-\eta}\frac{\alpha+\kappa_x}{\{q_1^2+(\alpha+\kappa_x)^2\}^{L+1}}\,\mathrm{d}\alpha$$
$$-\int_\gamma^\infty \rho(\beta)\,\mathrm{d}\beta\int\frac{R(p_1,p_2)}{q_2^2+(\beta+\kappa_\mathrm{d})^2}\,\mathrm{d}p_1\,\mathrm{d}p_2\int_0^\infty \alpha^{L+\eta+1}(\alpha+2\kappa_x)^{L-\eta+1}\frac{\alpha+\kappa_x}{\{q_1^2+(\alpha+\kappa_x)^2\}^{L+2}}\,\mathrm{d}\alpha. \tag{18}$$

When $q_1^2 = -\kappa_x^2$ the integrands of both terms on the right of (18) behave like $\alpha^{\eta-1}$ as $\alpha \to 0$. Therefore, for $\eta > 0$, the lower limit of the integration with respect to α does not cause any singularities in M_3 at $Q^2 = -\kappa_x^2$.

In the case of $\eta = 0$, the integration with respect to α in (17c) can be carried out explicitly to yield

$$M_3 = \int_\gamma^\infty \rho(\beta)\,\mathrm{d}\beta \int R(\boldsymbol{p}_1,\boldsymbol{p}_2)\{q_2^2+(\beta+\kappa_\mathrm{d})^2\}^{-1}\,\mathrm{d}\boldsymbol{p}_1\,\mathrm{d}\boldsymbol{p}_2\,.$$

The integrand is finite at the point $q_2^2 = -\kappa_\mathrm{d}^2$, and M_3 cannot have a singularity at $Q^2 = -\kappa_x^2$. Therefore, as $Q^2 \to \kappa_x^2$, $M(Q^2) \to M_1(Q^2)$, except when the Coulomb parameter η of the captured particle is greater than unity.

The amplitude M_1 when expressed in terms of wave functions is

$$M_1 = \int \psi_\mathrm{f}^{(-)*}\{(m_A/m_B)\boldsymbol{r}\}\,\phi_0^*(\boldsymbol{r})\,\psi_\mathrm{i}^{(+)}(\boldsymbol{r})\,\mathrm{d}\boldsymbol{r}\,, \tag{19}$$

with

$$\phi_0(\boldsymbol{r}) = N_L\,Y_{LM}(\boldsymbol{r})\exp(-\kappa_x r)\,r^L \int_0^\infty \alpha^{L+\eta}(\alpha+2\kappa_x)^{L-\eta}\exp(-\alpha r)\,\mathrm{d}\alpha\,. \tag{20}$$

Thus M_1 is the DWBA amplitude for the stripping reaction when the zero-range approximation for the deuteron is made and with the bound state wave function of the captured nucleon replaced by its asymptotic part.

After carrying out the integration in (20) we find that for (d, p) reactions ($\eta = 0$) the correct asymptotic form of the bound state wave function is

$$\phi_0(\boldsymbol{r}) = N_L \mathrm{h}_L^{(1)}\,(\mathrm{i}\kappa_x r)\,Y_{LM}(\boldsymbol{r})\,,$$

where $\mathrm{h}_L^{(1)}(z)$ is the spherical Hankel function of the first kind, and for (d, n) reactions ($\eta > 0$)

$$\phi_0(\boldsymbol{r}) = N_L r^{-1}\,\mathrm{W}_{L,\eta}(\kappa_x r)\,Y_{LM}(\boldsymbol{r})\,,$$

where $\mathrm{W}_{L,\eta}(z)$ is the Whittaker function.

III. THE TERM M_1

In this section we shall show that the term M_1 in the amplitude is infinite at $Q^2 = -\kappa_x^2$, the singularity arising from the lower limit of the integration with respect to α in equation (17a).

The scattering wave functions $\psi_\mathrm{i}^{(+)}$ and $\psi_\mathrm{f}^{(-)}$ in (19) can be expanded as Born series; the leading terms in these expansions are given as (Mott and Massey 1965)

$$\psi_\mathrm{i}^{(+)}(\boldsymbol{r}) = \exp(-\tfrac{1}{2}\pi\eta_1)\,\Gamma(1+\mathrm{i}\eta_1)\exp(\mathrm{i}\boldsymbol{k}_1.\boldsymbol{r})F\{-\mathrm{i}\eta_1;1;\mathrm{i}(k_1 r-\boldsymbol{k}_1.\boldsymbol{r})\}\,, \tag{21}$$

$$\psi_\mathrm{f}^{(-)*}(\boldsymbol{r}) = \exp(-\tfrac{1}{2}\pi\eta_2)\,\Gamma(1+\eta_2)\exp(-\mathrm{i}\boldsymbol{k}_2.\boldsymbol{r})F\{-\mathrm{i}\eta_2;1;\mathrm{i}(k_2 r+\boldsymbol{k}_2.\boldsymbol{r})\}\,, \tag{22}$$

where

$$\eta_1 = (Z_A e^2 m_{A\mathrm{d}})/k_1$$

and

$$\eta_2 = \begin{array}{ll} Z_B e^2 m_{By}/k_y & \text{for (d, p) reactions} \\ 0 & \text{for (d, n) reactions}\,. \end{array}$$

The amplitude M_1 is then

$$M_1 = K \int_0^\infty \sigma_0(\alpha)\,\mathrm{d}\alpha \int \exp(\mathrm{i}\boldsymbol{Q}\,.\,\boldsymbol{r})\, r^L\, Y_{LM}^*(\boldsymbol{r}) \exp\{-(\alpha+\kappa_x)r\}\, F\{-\mathrm{i}\eta_1; 1; \mathrm{i}(k_1 r - \boldsymbol{k}_1\,.\,\boldsymbol{r})\}$$
$$\times F\{-\mathrm{i}\eta_2; 1; \mathrm{i}(k_2 r + \boldsymbol{k}_2\,.\,\boldsymbol{r})\}\,\mathrm{d}\boldsymbol{r}\,. \tag{23}$$

All the constant factors that occur in M_1 have been absorbed in the quantity K. In order to keep the expressions in the remainder of this section as concise as possible, any other constant factors that may appear as the result of our manipulations shall be automatically included in K.

If we assume that η_1 and η_2 contain a small imaginary part $\mathrm{i}\epsilon$ ($\epsilon > 0$), which we can put equal to zero after the calculations, we may use the integral representation of the hypergeometric functions (Erdélyi 1953) and write

$$M_1 = K \int_0^1 \int_0^1 s^{-1-\eta_1}(1-s)^{\mathrm{i}\eta_1} t^{-1-\mathrm{i}\eta_2}(1-t)^{\mathrm{i}\eta_2}\,\mathrm{d}s\,\mathrm{d}t \int_0^\infty \sigma_0(\alpha)\,\mathrm{d}\alpha$$
$$\times \int r^L \exp\{-(\alpha+a)r\}\, Y_{LM}^*(r) \exp(\mathrm{i}\boldsymbol{q}\,.\,\boldsymbol{r})\,\mathrm{d}r\,, \tag{24}$$

where

$$a = k_x - \mathrm{i}(k_1 s + k_2 t)\,, \tag{25}$$

$$\boldsymbol{q} = \boldsymbol{Q} - \boldsymbol{k}_1 s + \boldsymbol{k}_2 t\,. \tag{26}$$

Integration with respect to $\boldsymbol{r}$ yields

$$M_1 = K \int_0^1 \int_0^1 s^{-1-\mathrm{i}\eta_1}(1-s)^{\mathrm{i}\eta_1} t^{-1-\mathrm{i}\eta_2}(1-t)^{\mathrm{i}\eta_2}\,\mathrm{d}s\,\mathrm{d}t$$
$$\times q^L\, Y_{LM}(q) \int_0^\infty \sigma_0(\alpha)\,(\alpha+a)\{q^2+(\alpha+a)^2\}^{-(L+2)}\,\mathrm{d}\alpha\,. \tag{27}$$

For large α the integrand goes as α^{-4} and thus the integral converges at the upper limit of the α-integration. Hence, if M_1 is to have a singularity at $Q^2 = -\kappa_x^2$, the only way this can happen is when the term $\{q^2+(\alpha+a)^2\}$ in the integrand vanishes at $Q^2 = -\kappa_x^2$. From equations (25) and (26) we find that this occurs only when $\alpha = s = t = 0$. Hence we have shown that if M_1 has a singularity at $Q^2 = -\kappa_x^2$ it must arise from the lower limit of the integration with respect to α.

In order to show that M_1 is in fact infinite at $Q^2 = -\kappa_x^2$ we make use of a result due to Cejpek (1966)

$$A(Q^2,\beta) \equiv \int_0^1 s^{-1-\mathrm{i}\eta_1}(1-s)^{\mathrm{i}\eta_1}\,\mathrm{d}s \int_0^1 t^{-1-\mathrm{i}\eta_2}(1-t)^{\mathrm{i}\eta_2}\,\mathrm{d}t$$
$$\times \int r^{L-1}\, Y_{LM}^*(\boldsymbol{r}) \exp\{\mathrm{i}(\boldsymbol{Q}-\boldsymbol{k}_1 s+\boldsymbol{k}_2 t)\,.\,\boldsymbol{r}\} \exp[-\{\beta-\mathrm{i}(k_1 s+k_2 t)\}r]\,\mathrm{d}\boldsymbol{r}$$
$$= K\frac{(1+C)^{\mathrm{i}\eta_1}(1+B)^{\mathrm{i}\eta_2}}{(Q^2+\beta^2)^{L+1}} \sum_{l=0}^{L} \sum_{m=-l}^{l} \left(\frac{4\pi}{2l+1}\right)^{\frac{1}{2}} \binom{2L+1}{2l}^{\frac{1}{2}} \Big(L-l, M-m, l, m \mid LM\Big) \times$$

$$\times k_1^{L-l}(-k_2)^l\, Y^*_{L-l,M-m}(\boldsymbol{k}_1)\, Y^*_{lm}(\boldsymbol{k}_2)\, \Gamma(L-l+1+\mathrm{i}\eta_1)\, \Gamma(l+1)$$

$$\times \sum_{s=0}^{l} \frac{\Gamma(-\mathrm{i}\eta_1+s)}{\Gamma(-\mathrm{i}\eta_1)} \frac{1}{(L-l+s+1)\,\Gamma(l-s+1)\,\Gamma(s+1)} \frac{(-1)^s C^s}{(1+C)^s}$$

$$\times \sum_{j=0}^{L-l} (1+B)^{-j} \frac{\Gamma(-\mathrm{i}\eta_2+j)\,\Gamma(L-j+1+\mathrm{i}\eta_2)}{\Gamma(-\mathrm{i}\eta_2)\,\Gamma(L-l-j+1)\,\Gamma(j+1)}$$

$$\times {}_2F_1(-\mathrm{i}\eta_2+j;\, -\mathrm{i}\eta_1+s;\, L-l+s+1;\, H)\,, \tag{28}$$

with

$$B = \frac{-2\mathrm{i}k_2\,\beta + k_1^2 - k_2^2 - Q^2}{Q^2+\beta^2}, \quad C = \frac{-2\mathrm{i}k_1\,\beta - k_1^2 + k_2^2 - Q^2}{Q^2+\beta^2}, \quad H = 1 - \frac{Q^2+\beta^2}{\beta^2+(k_1-k_2)^2}.$$

Comparing this formula with equation (24) it follows immediately that, with $\beta = \alpha + \kappa_x$,

$$M_1 = K \int_0^\infty \sigma_0(\alpha)\, \frac{\mathrm{d}}{\mathrm{d}\beta}\Big(A(Q^2,\beta)\Big)\, \mathrm{d}\alpha\,. \tag{29}$$

When $Q^2 = -\kappa_x^2$, a typical term in the integrand of (29) behaves like $\alpha^{\eta+j-2}$ as $\alpha \to 0$. Therefore, due to the terms with $j = 0$ in (28), M_1 is infinite at $Q^2 = -\kappa_x^2$ only if $\eta \leqslant 1$.

IV. Conclusions

We have shown that the DWBA amplitude $M(Q^2)$ for stripping reactions can be expressed as a sum of four terms, the first of which $M_1(Q^2)$ corresponds to DWBA when the zero-range approximation is used for the deuteron, and with the bound state wave function of the captured nucleon replaced by its asymptotic part. The term M_1 is infinite at $Q^2 = -\kappa_x^2$, this singularity being known as the Butler pole. Since the other terms are finite at the Butler pole, $M(Q^2) \to M_1(Q^2)$ as $Q^2 \to -\kappa_x^2$.

There is, however, one exception. In the case of (d, n) reactions with $\eta > 1$, that is, when the proton is captured into a loosely bound level of a highly charged nucleus, M_1 is no longer infinite at the point $Q^2 = -\kappa_x^2$ and therefore in this case $M(Q^2)$ does not approach $M_1(Q^2)$ as $Q^2 \to -\kappa_x^2$.

V. References

Amado, R. D. (1959).—*Phys. Rev. Lett.* **2**, 399.

Bertram, W. K., and Tassie, L. J. (1968).—*Phys. Rev.* **166**, 1029.

Cejpek, J. (1966).—Preprint, J. E. Purkyne Univ., Brno, Czechoslovakia.

Clement, C. F. (1965).—*Nucl. Phys.* **66**, 241.

Dullemond, C., and Schnitzer, H. J. (1963).—*Phys. Rev.* **129**, 821.

Erdélyi, A. (1953).—"Higher Transcendental Functions." Vol. 1. (Bateman manuscript project.) (McGraw-Hill: New York.)

Glendenning, N. K. (1963).—*A. Rev. nucl. Sci.* **13**, 191.

Martin, A. (1959).—*Nuovo Cim.* **14**, 403.

Morinigo, F. B. (1967).—*Nucl. Phys.* **90**, 113.

Mott, N. F., and Massey, M. S. W. (1965).—"The Theory of Atomic Collisions." 3rd Ed. p. 56. (Clarendon Press: Oxford.)

Schnitzer, H. J. (1962).—*Nucl. Phys.* **36**, 505.

VARIATIONAL CALCULATIONS FOR THREE-BODY S-STATES WITH COULOMB INTERACTIONS

By L. M. Delves* and T. Kalotas*

[*Manuscript received February* 26, 1968]

Summary

A general purpose programme designed to deal economically with the S-states of arbitrary systems interacting only via the static Coulomb interactions is described. Its aim is to simplify the calculation of the matrices of arbitrary operators with respect to the basis chosen; these matrices are then available for use in a variety of variational calculations. A number of illustrative calculations are presented which yield both upper and lower bounds for the energy of some typical systems and expectation values for a number of operators.

I. Introduction

There have been a number of previous attempts (Kolos, Roothaan, and Sack 1960; Frost, Inokuti, and Lowe 1964) to produce a general purpose programme for treating the S-states of three-body systems interacting through Coulomb forces. These programmes have been based on the use of the Rayleigh–Ritz variation principle for the energy and, for a given choice of basis, have provided a convenient means of calculating the Hamiltonian and normalization matrices with respect to this basis set which are needed for an energy calculation.

The present programme has a similar aim. However, it differs in emphasis in two ways. Firstly, we are not primarily interested in calculations of the binding energy but in using the matrices produced by the programme to test a number of new variation principles and approximation schemes for bound and scattering states, and especially for investigating methods of calculating the expected values of operators in atomic systems. This aim requires that we produce the matrices of a large number of different operators W, including the Hamiltonian H, H^2, and compound (though not necessarily Hermitian) operators such as $W_1 W_2$ and HW. We have made it especially easy to add new operators to the system; provided that these fall within the class of operators considered, the user has only to specify them in a formal way and is not concerned with the integrations involved.

The second difference in emphasis follows from the first. The major time in any variational calculation of the types considered is spent in performing the integrals needed to set up the Hamiltonian and other relevant matrices. We therefore gain considerable economy by computing and storing these matrices once and for all. Since we wish to vary the wave-function scale and the system parameters (the particle masses and charges), the operators H, H^2, and HW are split into parts each of which has a simple behaviour under a scale change, and which are independent of the masses and charges.

---

* School of Mathematical and Physical Sciences, University of Sussex, Falmer, Brighton, Sussex, England.

II. BASIS USED

We use the following unsymmetrized set of basis functions

$$\psi_{lmn}(123) = \exp[-S^{-1}\{Z^*(lr_1+mr_2)+nr_{12}\}] \tag{1}$$

and store all matrices with respect to the symmetrized set

$$\psi^{\pm}_{lmn}(123) = \psi_{lmn}(123) \pm \psi_{lmn}(213)\,. \tag{2}$$

Here r_1, r_2, and r_{12} are the three interparticle distances (with particle 3 at the origin of the centre of mass frame). S is an overall scale factor that is set equal to 1 when the matrices of all operators are produced and stored. Matrices of interest to us for which the scale is not 1 are simply related to these by some power of S. Thus if $\langle T\rangle_S$, $\langle V\rangle_S$, and $\langle 1\rangle_S$ are the matrices for the kinetic energy, potential energy, and normalization for arbitary scale S then

$$\langle T\rangle_S = S^4\langle T\rangle_{S=1}, \qquad \langle V\rangle_S = S^5\langle V\rangle_{S=1}, \qquad \langle 1\rangle_S = S^6\langle 1\rangle_{S=1}\,.$$

TABLE 1

NUMBER OF COMPONENTS OF $\psi^{\pm}_{lmn}$ AS GIVEN BY (3) FOR $N_{\min} = -1$

$Q_{\max}$	1	2	3	4	5	6	7	8	9	10	11	12
$Z^* > 1$												
ψ^+	1	3	7	13	22	34	50	70	95	125	161	203
ψ^-	0	1	3	7	13	22	34	50	70	95	125	161
$Z^* = 1$												
ψ^+	0	1	4	9	17	28	43	62	86	115	150	191
ψ^-	0	0	1	4	9	17	28	43	62	86	115	150

This makes it obvious how the scale can be varied during a calculation.

Z^* is a nonlinear parameter that is fixed within a given set of calculations. It is included to make some direct discrimination between the pair of particles (1, 2) and the third particle 3.

The triplets l, m, n are allowed to run through the integers subject to the restrictions

$$\left.\begin{array}{c} n \geqslant N_{\min}, \qquad l \geqslant m, \qquad l+m+n = Q, \\ Q = N_{\min}+1, N_{\min}+2, \ldots, Q_{\max}. \end{array}\right\} \tag{3}$$

$N_{\min}$ in (3) is not restricted to be positive, but is considered as a nonlinear parameter. The parameter Q is conveniently used to order the triplets, all triplets of given Q being run through together. The total number of terms in the trial wave function that includes all components up to a given $Q_{\max}$ is listed in Table 1 for the choice $N_{\min} = -1$.

The basis (1), (3) was chosen firstly to give a good representation of the wave functions of the helium sequence while minimizing the time required to construct the Hamiltonian and other matrices with the integration scheme used (see Section IV). For the ground state of the helium sequence the dominant term is expected to be $(l, m, n) = (1, 1, 0)$. However, the terms (j, j, o), $j > 1$, also appear in the sequence as defined by condition (3), and these terms dominate for appropriate choice of the scale S. The result is that for the ground state of the helium-like ions, although not necessarily for other systems, the energy shows a marked structure as a function of the scale S, with peaks at these preferred scales. For large numbers of terms, these peaks are not well resolved and the energy is almost independent of the scale factor over a wide region. This property of the basis is illustrated in Figure 1, which plots the energy versus scale for the system He ($1\,^1$S).

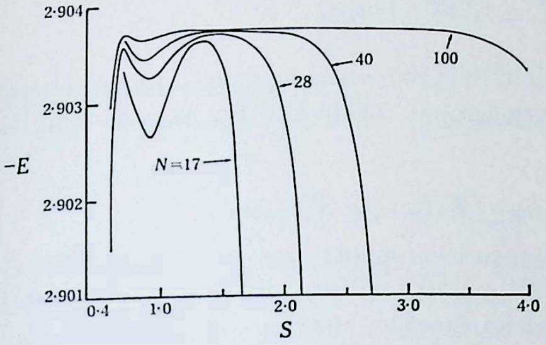

Fig. 1.—Helium ground state (He(1^1S)) energies calculated with the wave function (1) for various numbers of terms N. Note the structure in the dependence on the scale parameter S.

For systems other than helium and the helium-like ions we do not expect any one term to give a good approximation. The extent to which the basis (1) proves suitable for other systems is discussed in Section VI.

III. Hamiltonian and Other Operators

The S-state Coulomb Hamiltonian for three particles of mass m_1, m_2, and m_3 has the form (in atomic units)

$$H = -\tfrac{1}{2}(\mu_1^{-1}+\mu_2^{-1})T_0+m_3^{-1}\,T_1+\tfrac{1}{4}(\mu_1^{-1}-\mu_2^{-1})T_2-ZV_0+V_1\,,$$

where the reduced masses μ_1 and μ_2 are given by

$$\mu_1 = m_1\,m_3/(m_1+m_3)\,, \qquad \mu_2 = m_2\,m_3/(m_2+m_3)\,.$$

The S-state operators T_0, T_1, T_2, V_0, and V_1 are given by

$$T_0 \equiv -\tfrac{1}{2}(\nabla_1^2+\nabla_2^2)_{\mathrm{S}} = -\tfrac{1}{2}\Big(1+P_{12}\Big)\left\{\frac{1}{r_1^2}\frac{\partial}{\partial r_1}\left(r_1^2\frac{\partial}{\partial r_1}\right)+\frac{1}{r_{12}^2}\frac{\partial}{\partial r_2}\left(r_{12}^2\frac{\partial}{\partial r_{12}}\right)+2\cos\theta_1\frac{\partial^2}{\partial r_1\,\partial r_{12}}\right\},$$

$$T_1 \equiv -(\nabla_1\,.\,\nabla_2)_{\mathrm{S}} = -\Big(1+P_{12}\Big)\left\{\tfrac{1}{2}\cos\theta_{12}\frac{\partial^2}{\partial r_1\,\partial r_2}-\cos\theta_1\frac{\partial^2}{\partial r_1\,\partial r_{12}}-\frac{1}{2r_{12}^2}\frac{\partial}{\partial r_{12}}\left(r_{12}^2\frac{\partial}{\partial r_{12}}\right)\right\},$$

$$T_2 \equiv -(\nabla_1^2-\nabla_2^2)_{\mathrm{S}} = -\Big(1-P_{12}\Big)\left\{\frac{1}{r_1^2}\frac{\partial}{\partial r_1}\left(r_1^2\frac{\partial}{\partial r_1}\right)+2\cos\theta_1\frac{\partial^2}{\partial r_1\,\partial r_{12}}\right\},$$

$$V_0 \equiv r_1^{-1}+r_2^{-1}, \qquad V_1 \equiv r_{12}^{-1}.$$

Here

$$\cos\theta_1 = (r_1^2+r_{12}^2-r_2^2)/2r_1\,r_{12}\,, \qquad \cos\theta_{12} = (r_1^2+r_2^2-r_{12}^2)/2r_1\,r_2\,.$$

The above operators are separately Hermitian and are independent of the masses and charges of the system considered. Their matrices are stored separately in the computer programme. The operator H^2 is also split into separately Hermitian parts such as T_0^2, $(T_1 V_0 + V_0 T_1)$, etc., which again do not depend on physical parameters such as mass and charge.

The operators W that we shall consider have the following effect when operating on the unsymmetrized basis (1)

$$W\psi_{lmn} = \left(\sum_i a_i r_1^{\alpha_i} r_2^{\beta_i} r_{12}^{\gamma_i}\right)\psi_{lmn}. \tag{4}$$

The parameters a_i, α_i, β_i, and γ_i are used in the programme to define any one operator. Product operators such as $W_1 W_2$ are generated within the programme from their separate expansions,

$$(\psi_{l'm'n'}, W_1 W_2 \psi_{lmn}) = (W_1^{+} \psi_{l'm'n'}, W_2 \psi_{lmn}). \tag{5}$$

This approach makes it straightforward to include extra operators in the code, provided that they have expansions of type (4), and at present some 60 operators have been included. In addition the delta function operators $\delta(r_{12})$, $\delta(r_1)$, and $\delta(r_2)$ have been coded.

IV. Integrations

In general, it is required to evaluate integrals of the form

$$(\psi_{l'm'n'}, W_1 W_2 \psi_{lmn}).$$

For the simpler integrals one or both of the operators W_1, W_2 may be the unit operator 1. For the other cases we use the result (5) and the defining expansions (4) for W_1, W_2 in order to arrive at a typical integral

$$(\alpha\beta\gamma) = \int \psi_{l'm'n'} r_1^{\alpha} r_2^{\beta} r_{12}^{\gamma} \psi_{lmn}\, d\tau. \tag{6}$$

Those integrals with $\alpha, \beta, \gamma \geqslant -1$ can be expanded in terms of perimetric coordinates (see Pekeris 1962) into a sum of analytic integrals. Working with single precision (48 bit word) the accuracy attained in evaluating such integrals is better than 1 part in 10^{10} on the machine used.

For some operators, for instance in parts of H^2, one or at the most two of the exponents α, β, γ can take the values -2. Integrals with one such exponent can also be evaluated term by term in perimetric coordinates. Those with two exponents with value -2 are reduced by a change of variables to a one-dimensional numerical integration for which the computed accuracy achieved is better than 1 part in 10^6.

V. Applications

Some of the calculations carried out using matrices provided by the programme have already been published (Delves 1967, 1968; Delves and Kalotas 1968). We give here some examples of their use in standard variational calculations, which demonstrate the application of the basis used to a variety of different systems.

Table 2 gives upper and lower bounds for the energy of the lowest triplet and singlet states of helium, and for the heavy mu-mesonic molecule d–μ–d, the hydrogen molecule ion H_2^+, and the positronium ion $e^+e^-e^-$. These bounds explicitly include contributions coming from the finite-accuracy arithmetic used (see Delves 1968). The table also gives the expected values of a number of operators for these systems, calculated from the variational wave functions giving the upper bounds. In this table, the following parameters in (1) and (3) were used

$$N_{\min} = -1,$$

$$Z^* = \begin{array}{ll} 2 & \text{lower bounds,} \\ 1 & \text{upper bounds and expected values.} \end{array}$$

VI. Discussion

The results of Table 2 show firstly that the basis (1) does provide a good representation of the lowest singlet and triplet states of helium. In addition, it provides at least a reasonably good representation of other Coulombic three-body S-states for a wide range of the relative particle masses. Indeed, the upper bound for the positronium ion $e^+e^-e^-$ appears to be the lowest yet published. The basis is least successful in describing systems, such as H_2^+, containing two heavy and one light particle; this is a defect it shares with other general purpose bases that have been proposed (Kolos, Roothaan, and Sack 1960; Frost, Inokuti, and Lowe 1964), which also fail to reflect adequately the extremely sharp peaking of the H_2^+ wave function around the equilibrium position of the protons.

The lower bounds shown are interesting in that they demonstrate the flexibility of the programme. Lower-bound calculations have not been popular in the past, firstly because the bounds obtained are in general much worse than the upper bounds, and secondly because of the labour involved in deriving the necessary integrals. At least this second factor is alleviated by the method used here, the specification of the integrals of H^2 being a trivial exercise. We hope to use the programme to test a number of other variation principles that also involve the matrices of H^2. For this purpose the lower bounds given here are very encouraging; the upper and lower bounds for helium have merged to five significant figures.

Also of interest is the technique used to deal with round-off errors in Table 2. It is well known that the errors due to the finite-accuracy arithmetic used can build up disastrously in a variational calculation. These errors can, however, be *bounded* and the bound added to the raw upper or lower bounds generated to give a rigorous bound including the round-off error (Delves 1968). This has been done in Table 2. The round-off contribution to the bounds are significant only for the lower bounds, since our matrices of H^2 are less accurate than those of H. Figure 2 illustrates the size of the round-off errors for the lower bound to the state He ($2\,^3S$). In this figure both the uncorrected and the corrected lower bounds are plotted against the scale parameter S, together with the corrected upper bound. We see that the round-off errors may be large for some values of S, but are satisfactorily small near the optimum

TABLE 2

ENERGIES AND EXPECTATION VALUES FOR SOME ATOMIC SYSTEMS

Values are expressed in electron atomic units a_0, but for the d–μ–d system muon atomic units a_μ are used except for the energy, which is given in eV. For the upper and lower bounds the number of terms used in the expansion is shown in parentheses, and the scale factor S in equation (1) is given. Previous upper and lower bound calculations are shown for comparison

Energy or			System		
Operator	He ($1\,^1S$)	He ($2\,^3S$)	d–μ–d	H_2^+	$e^+e^-e^-$
m_1	1	1	17·7511244	1836·08	1
m_2	1	1	17·7511244	1836·08	1
m_3	∞	∞	1	1	1
Z	2	2	1	1	1
E (upper bound)	−2·903724313 (100)	−2·1752267 (71)	−2988·5373 eV (100)	−0·592947 (100)	−0·2620035 (100)
S (upper bound)	1·4	3·4	2·9	3·0	9·0
E (lower bound)	−2·9037945 (50)	−2·1753306 (34)	—	—	−0·2662 (50)
S (lower bound)	2·0	4·25	—	—	10·5
Upper bound from previous calculations*	−2·903724375 (1078)[b]	−2·175229378237 (715)[b]	−2981 eV (32)[a]	−0·58305 (32)[a]	−0·2620011 (50)[c]
Lower bound from previous calculations*	−2·903726615 (1078)[b]	−2·175229379 (715)[b]	—	−0·60263†	—
$\langle T_0 \rangle$	2·903724313	2·1752267	0·75397	—	0·1332387
$\langle T_1 \rangle$	0·1590695	0·0074447	−0·2665	—	−0·004472412
$\langle r_1^{-1}+r_2^{-1} \rangle$	3·376634	2·3093	1·4551	—	0·6796438
$\langle r_{12}^{-1} \rangle$	0·9458191	0·26822	0·39403	—	0·155634
$\langle r_1+r_2 \rangle$	1·858940	5·1002	4·2478	—	10·979
$\langle r_1^2+r_2^2 \rangle$	2·386941	22·921	11·9428	—	96·89
$\langle r_{12} \rangle$	1·422066	4·4468	2·8416	—	8·549
$\langle \delta(r_1)+\delta(r_2) \rangle$	3·620719	2·6406	0·3169	—	0·041458
$\langle \delta(r_{12}) \rangle$	0·1063434	0·0	$5·5 \times 10^{-6}$	—	1·71045
$\langle \cos\theta_1 + \cos\theta_2 \rangle$	1·296036	1·1256	1·0685	—	1·183968

* References are: a, Kolos, Roothaan, and Sack (1960); b, Pekeris (1962); c, Frost, Inokuti, and Lowe (1964).

† Fixed nuclei approximation (Bates, Ledsham, and Stewart 1953).

value of S. The round-off corrections depend on the computed eigenvector, and this dependence accounts for the structure observed in curve C.

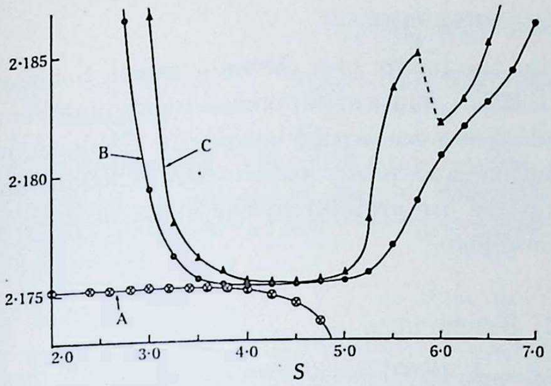

Fig. 2.—Upper and lower bounds on the energy of the He($2\,^3$S) state:
A, upper bound (71-term wave function).
B, uncorrected lower bound (34-term wave function).
C, lower bound corrected for the contribution from round-off errors in the computed matrix elements. The corrections depend on the computed eigenvector and hence are not necessarily smoothly varying with the scale factor S.

Also given in Tables 2 and 3 are the expected values of some representative operators, calculated from the 100-term wave function yielding the best energy upper bound. The accuracy of these values has been estimated by comparison with the accurate results of Pekeris (1962), where available, and by observing the convergence with increasing numbers of terms (Delves and Kalotas 1968). For the expectation values the last digit quoted may be in error.

Table 3

EXPECTATION VALUES OF POWERS OF THE INTERPARTICLE DISTANCES

Results are for operators of the form $(l,m,n) = r_1^l r_2^m r_{12}^n (2-\delta_{lm})$. All values are expressed in electron atomic units a_0 except for the d–μ–d system, where muon units a_μ are used

l	m	n	He (1^1S)	He (2^3S)	d–μ–d	$e^+e^-e^-$	l	m	n	He (1^1S)	He (2^3S)	d–μ–d	$e^+e^-e^-$
−1	−1	−1	4·167157	0·18661	0·20821	0·0220342	−1	−1	1	2·631789	2·0644	1·0985	0·5476255
−1	0	−1	3·841888	0·64545	0·60864	0·121397	−1	0	1	4·136490	9·9298	3·9288	5·2768
−1	1	−1	2·849227	2·0932	1·2735	0·585452	−1	1	1	4·980830	45·698	10·113	46·23
−1	2	−1	2·993350	8·8639	3·3443	4·293	−1	2	1	8·009495	261·74	32·206	587·8
−1	3	−1	4·133502	44·646	10·363	43·82	−1	3	1	16·01758	1722·3	118·96	9760
0	1	−1	1·448933	1·18539	1·5526	1·384483	0	1	1	3·104986	25·829	12·937	113·97
0	2	−1	1·540627	4·5322	4·0329	9·5265	0	2	1	4·668667	134·15	39·209	1275
0	3	−1	2·129992	22·362	12·779	93·48	1	1	1	1·548576	16·893	13·304	269·78
1	1	−1	0·5653453	0·72318	1·4719	2·77406	−1	−1	2	3·406223	9·0513	3·0316	4·4497
1	2	−1	1·210745	3·9037	7·5777	34·536	−1	0	2	6·466397	50·070	11·808	53·88
1	3	−1	1·672415	17·286	24·427	314·8	−1	1	2	9·333429	266·86	33·336	613·2
2	2	−1	0·648927	3·1342	9·7665	95·045	−1	2	2	17·66658	1737·0	115·85	9860
−1	−1	0	2·708656	0·56078	0·44712	0·090935	0	0	2	2·516414	23·038	8·9262	93·23
−1	1	0	3·277818	9·0196	3·3926	4·4893	0	1	2	6·310569	150·749	43·368	1496
−1	2	0	4·354313	44·825	9·8463	44·04	−1	−1	3	5·514115	46·289	9·2794	46·93
−1	3	0	7·364284	259·91	33·409	581·7	−1	0	3	12·28134	290·728	39·103	702·77
0	3	0	3·935817	130·40	40·872	1218	−1	1	3	20·74915	1769·8	120·46	10200
1	1	0	0·8271069	3·2301	4·2030	24·174	0	0	3	5·307917	136·71	30·713	1269
1	2	0	2·043074	19·704	22·842	356·2							

We see that except for the system H_2^+ we obtain an accuracy of from five to seven significant digits in these expected values, a very satisfactory result. For the hydrogen molecule ion the expected values we obtained behave extremely erratically and they have not been quoted here.

VII. ACKNOWLEDGMENTS

This work was carried out during the tenure of a Commonwealth Scholarship (T.K.) and an S.R.C. research grant (L.M.D.), and was supported by a grant from the Shell Petroleum Company. The calculations were carried out on the Atlas computer of the Science Research Council, Chilton, and partly on the ICT 1905 computer of the University of Sussex. The authors are grateful to the staffs of both these computing centres for their facilities and help.

VIII. REFERENCES

BATES, D. R., LEDSHAM, K., and STEWART, A. L. (1953).—*Phil. Trans. R. Soc.* A **246**, 215.
DELVES, L. M. (1967).—*Proc. phys. Soc.* **92**, 55.
DELVES, L. M. (1968).—*J. computl Phys.* **3**, 444.
DELVES, L. M., and KALOTAS, T. (1968).—*Aust. J. Phys.* **21**, 1.
FROST, A. A., INOKUTI, M., and LOWE, J. P. (1964).—*J. chem. Phys.* **41**, 482.
KOLOS, W., ROOTHAAN, C. C. J., and SACK, R. A. (1960).—*Rev. mod. Phys.* **32**, 178.
PEKERIS, C. L. (1962).—*Phys. Rev.* **126**, 1470.

DIELECTRIC SATURATION IN IONIC CRYSTALS

II.* DEFORMABLE IONS

By J. Oitmaa†

[*Manuscript received January 26, 1968*]

Summary

The lowest order field-dependent term in the static dielectric constant is calculated for an ionic crystal with deformable ions, and is evaluated numerically for NaI using a simple shell model. Some terms of higher order are also calculated.

I. Introduction

In general the static dielectric constant of a crystal would be expected to be a function of the external electric field E, since the change in dipole moment caused by a given change in the field strength would be less at high fields, when the crystal already has a large dipole moment, than at low fields. For a centro-symmetrical crystal the field-dependent static dielectric constant ϵ_S can be written as a Taylor expansion in powers of the field strength as

$$\epsilon_S = \epsilon_0 + \epsilon_2 E^2 + \epsilon_4 E^4 + \ldots . \tag{1.1}$$

In most situations the field-independent term ϵ_0 dominates.

In a previous paper (Oitmaa 1967*a*; hereafter referred to as Part I), in which references to earlier experimental and theoretical work are given, the lowest order contribution to the coefficient ϵ_2 was calculated for the alkali halides using a rigid ion model. It was found that the field dependence of the dielectric constant is directly attributable to the anharmonic terms in the crystal potential energy. The lowest order contribution evaluated in Part I was due to a particular quartic anharmonic term.

We consider a thin rod of dielectric (e.g. Szigeti 1959; this was also implicit in Part I) for which the macroscopic and external fields are identical. The static dielectric constant is then given by

$$\epsilon_S - \epsilon_\infty = -\frac{4\pi}{EV}\left(\frac{\partial F}{\partial E}\right)_{V,T}, \tag{1.2}$$

where F is the Helmholtz free energy of the crystal of volume V. To obtain the dielectric constant it is thus necessary to calculate the free energy of an anharmonic crystal in the presence of an external electric field.

In Part I the free energy was calculated by a straightforward application of perturbation theory. In the present paper we use a slightly different formulation of perturbation theory, in which the various terms are represented by diagrams (e.g.

---

[*] Part I, *Aust. J. Phys.*, 1967, **20**, 11–27.

[†] School of Physics, University of New South Wales, P.O. Box 1, Kensington, N.S.W. 2033; present address: Department of Physics, University of California, Irvine, California 92664, U.S.A.

Aust. J. Phys., 1968, **21**, 439–54

Cowley 1963; Parry and Turner 1964; Wilcox 1965). Some of the advantages of using diagrams are

1. they often lead to greater clarity and insight into the structure of the perturbation series,
2. they provide a systematic way of obtaining all of the terms of a given order, and
3. it is sometimes possible to sum certain classes of terms to all orders, and in this way to obtain physical approximations that cannot be readily obtained from a conventional perturbation theory.

In Section II the Hamiltonian of the model is obtained. This Hamiltonian contains higher order dipole moments that do not occur in a rigid ion model but do occur when the ions are deformable. In Section III the formalism of the diagrammatic perturbation theory to be used is summarized. In Section IV the free energy and dielectric constant are obtained, and in Section V the result is evaluated numerically for NaI using a simple shell model. Finally, in Section VI some higher order correction terms are calculated.

II. Hamiltonian

In the theory of an anharmonic crystal, and in many-body problems in general, it is usually most convenient to express the Hamiltonian and other operators in terms of creation and annihilation operators for the elementary excitations. In terms of these operators the Hamiltonian of an anharmonic crystal, in the absence of an external field, can be written (e.g. Born and Huang 1954; Cowley 1963)

$$H = H_0 + \gamma H_3 + \gamma^2 H_4 + \ldots, \tag{2.1}$$

where

$$H_0 = \sum_{\lambda} \hbar\omega_{\lambda}(a_{\lambda}^{*} a_{\lambda} + \tfrac{1}{2}), \tag{2.2}$$

$$H_3 = \sum_{\lambda_1 \lambda_2 \lambda_3} V(\lambda_1 \lambda_2 \lambda_3) A_{\lambda_1} A_{\lambda_2} A_{\lambda_3}, \tag{2.3}$$

$$H_4 = \sum_{\lambda_1 \lambda_2 \lambda_3 \lambda_4} V(\lambda_1 \lambda_2 \lambda_3 \lambda_4) A_{\lambda_1} A_{\lambda_2} A_{\lambda_3} A_{\lambda_4}. \tag{2.4}$$

In these expressions H_0 is the harmonic Hamiltonian and H_3 and H_4 are respectively the cubic and quartic anharmonic terms. The parameter γ is the usual order parameter that indicates the number of factors of $\bar{u}/r_0$ by which a particular term is smaller than the harmonic term, $\bar{u}$ being some sort of mean displacement and r_0 the nearest neighbour distance. For convenience the double suffix qj for each phonon mode has been replaced by a single suffix λ. The operators a_{λ}^{*} and a_{λ} are respectively the creation and annihilation operators for the phonons of mode λ, and have the usual properties. The operator A_{λ} is defined by

$$A(qj) = a(qj) + a(-qj)^{*} \tag{2.5}$$

and is related to the normal coordinate $Q(qj)$ of Part I by

$$A(qj) = (2\omega(qj)/\hbar)^{\frac{1}{2}} Q(qj). \tag{2.6}$$

The anharmonic coefficients $V(\lambda_1\lambda_2\lambda_3)$ and $V(\lambda_1\lambda_2\lambda_3\lambda_4)$ are related to those of Part I by

$$V(q_1 j_1;\, q_2 j_2;\, q_3 j_3) = \frac{1}{6N^{\frac{1}{2}}}\Delta(q_1+q_2+q_3)\left(\frac{\hbar^3}{8\omega(q_1 j_1)\,\omega(q_2 j_2)\,\omega(q_3 j_3)}\right)^{\frac{1}{2}} \times \Phi(q_1 j_1;\, q_2 j_2;\, q_3 j_3) \tag{2.7}$$

and

$$V(q_1 j_1;\, q_2 j_2;\, q_3 j_3;\, q_4 j_4) = \frac{1}{24N}\Delta(q_1+q_2+q_3+q_4) \times\left(\frac{\hbar^4}{16\omega(q_1 j_1)\,\omega(q_2 j_2)\,\omega(q_3 j_3)\,\omega(q_4 j_4)}\right)^{\frac{1}{2}} \times \Phi(q_1 j_1;\, q_2 j_2;\, q_3 j_3;\, q_4 j_4)\,. \tag{2.8}$$

In the presence of an external electric field E, in the x direction, the Hamiltonian of the crystal becomes

$$H(E) = H - EM\,, \tag{2.9}$$

where M is the x component of the dipole moment of the crystal. M can be expanded as a series in the phonon coordinates A_λ (Born and Huang 1954) to give

$$M = \mathscr{M}_0 A_0 + \gamma \sum_{\lambda_1\lambda_2} \mathscr{M}(\lambda_1\lambda_2) A_{\lambda_1} A_{\lambda_2} + \gamma^2 \sum_{\lambda_1\lambda_2\lambda_3} \mathscr{M}(\lambda_1\lambda_2\lambda_3) A_{\lambda_1} A_{\lambda_2} A_{\lambda_3} + \ldots\,. \tag{2.10}$$

The suffix 0 refers to that $q = 0$ optic mode which has displacements in the x direction, i.e. the mode (04). The first term in (2.10) contains both the effect of the displacements of the ions as a whole and the first-order effect of the electronic deformations, while the second and third terms are due entirely to electronic deformation.

III. Perturbation Formalism

We consider a general system having a Hamiltonian

$$H = H_0 + V\,, \tag{3.1}$$

where H_0 is the unperturbed Hamiltonian, which will hereafter be taken to be the harmonic Hamiltonian (2.2), and V is the sum of all perturbation terms.

The free energy can then be obtained from the partition function Z according to

$$F = -\beta^{-1}\ln Z\,, \tag{3.2}$$

where

$$Z = \mathrm{Tr}\{\exp(-\beta H)\} \tag{3.3}$$

and $\beta = 1/kT$.

The exponential operator in (3.3) can be expanded in powers of the perturbation V (e.g. Parry and Turner 1964) as

$$\exp(-\beta H) = \exp(-\beta H_0) \sum_{n=0}^{\infty} \frac{(-1)^n}{n!} \int_0^\beta \mathrm{d}u_1 \ldots \int_0^\beta \mathrm{d}u_n\, \mathrm{T}\{\tilde{V}(u_1)\ldots\tilde{V}(u_n)\}\,. \tag{3.4}$$

In this expansion the $\tilde{V}(u)$ operators are defined by

$$\tilde{V}(u) = \exp(uH_0)\, V \exp(-uH_0)\,, \tag{3.5}$$

which is a type of interaction representation, and T is the Dyson ordering operator, which orders the $\tilde{V}(u_i)$ operators so that the u_i's are in descending order with the largest on the left, and so on. For example

$$\mathrm{T}\, \tilde{V}(u_1)\, \tilde{V}(u_2) = \left.\begin{array}{ll} \tilde{V}(u_1)\, \tilde{V}(u_2)\,, & u_1 > u_2\,; \\ \tilde{V}(u_2)\, \tilde{V}(u_1)\,, & u_1 < u_2\,. \end{array}\right\} \tag{3.6}$$

Using the expansion (3.4) the partition function (3.3) becomes

$$Z = Z_0\left(1+\sum_{n=1}^{\infty} \frac{(-1)^n}{n!} \int_0^\beta \mathrm{d}u_1 \ldots \int_0^\beta \mathrm{d}u_n\, \langle \mathrm{T}\, \tilde{V}(u_1) \ldots \tilde{V}(u_n)\rangle_0\right), \tag{3.7}$$

where Z_0 is the partition function of the unperturbed system and $\langle\ \ \rangle_0$ denotes the unperturbed canonical ensemble average, i.e.

$$\langle 0\rangle_0 = Z_0^{-1}\, \mathrm{Tr}\{\exp(-\beta H_0)\, 0\}\,. \tag{3.8}$$

In evaluating the thermodynamic average in (3.5) the $\tilde{V}(u)$ operators are first written explicitly in terms of the phonon coordinates A_λ. It is then necessary to find the unperturbed average of an ordered product of A_λ operators. This can be done by using Wick's theorem (e.g. Gaudin 1960), which states that the average of an ordered product is equal to the sum of the products of all possible "contractions". A contraction is the unperturbed expectation value of the ordered product of two operators. In the present case the only nonvanishing contractions are of the form

$$\begin{aligned} g(\lambda, u) &= \langle \mathrm{T}\, \tilde{A}_\lambda(u)^*\, \tilde{A}_\lambda(0)\rangle_0 \\ &= \bar{n}_\lambda \exp(+\mid u \mid \hbar\omega_\lambda) + (\bar{n}_\lambda+1)\exp(-\mid u \mid \hbar\omega_\lambda)\,, \end{aligned} \tag{3.9}$$

where $\bar{n}_\lambda$ is the mean occupation number of the mode λ, given by

$$\bar{n}_\lambda = \{\exp(\beta\hbar\omega_\lambda - 1)\}^{-1}\,. \tag{3.10}$$

In addition to being an even function of u, $g(\lambda, u)$ also satisfies the periodicity condition

$$g(\lambda, u+\beta) = g(\lambda, u)\,, \qquad -\beta < u < 0\,, \tag{3.11}$$

and so can be expanded in a Fourier series

$$g(\lambda, u) = \sum_{l=-\infty}^{\infty} g_l(\lambda) \exp(2\pi \mathrm{i} l u/\beta)\,. \tag{3.12}$$

The Fourier coefficients are given by

$$\begin{aligned} g_l(\lambda) &= \frac{1}{2\beta} \int_{-\beta}^{\beta} g(\lambda, u) \exp(-2\pi \mathrm{i} l u/\beta)\, \mathrm{d}u \\ &= \frac{2\omega_\lambda}{\beta\hbar} \frac{1}{\omega_l^2+\omega_\lambda^2}\,, \end{aligned} \tag{3.13}$$

where

$$\omega_l = 2\pi l/\beta\hbar . \tag{3.14}$$

The Fourier coefficient $g_l(\lambda)$ is called the "free phonon propagator".

Returning to the partition function (3.7), the procedure then is to substitute for $\tilde{V}(u)$ in terms of the A_λ's from (2.3), (2.4), (2.9), and (2.10) and then to take all possible contractions of the A_λ's. If the Fourier expansion (3.12) is then substituted for each contraction, the u-integrations in (3.7) can be carried out directly, using the result

$$\int_0^\beta \mathrm{d}u \, \exp\{2\pi \mathrm{i}(l_1 - l_2)u/\beta\} = \beta\, \delta_{l_1 l_2} . \tag{3.15}$$

The above procedure can be most conveniently carried out in terms of diagrams. We consider the nth term in (3.7). Since each of the $\tilde{V}$ factors contains a number of separate perturbation terms, there are many combinations that all contribute to the nth term. For each perturbation term we draw a vertex with a number of lines, representing the A_λ operators, joined to it. The process of contraction is then represented by joining up the lines, pairwise, in all possible ways.

The nth-order contribution to Z is then obtainable from the following rules.

(1) Draw all topologically distinct diagrams with n vertices.

(2) With each phonon line labelled λ associate a factor

$$g_l(\lambda) = \frac{2\omega_\lambda}{\beta\hbar} \frac{1}{\omega_l^2 + \omega_\lambda^2} .$$

(3) At each vertex conserve $\boldsymbol{q}$ vectors, since each of the perturbation terms contains a delta function in the $\boldsymbol{q}$'s.

(4) At each vertex insert the appropriate coefficient.

(5) At each vertex conserve the ω_l's because of the u-integrations (3.15).

(6) Insert a factor $\{(-1)^n/n!\}\beta^n$, where β^n comes from the n u-integrations.

(7) Multiply by a combinational factor, representing the number of equivalent ways of pairing the operators, and also the number of permutations in (3.7) if there are several perturbation terms.

(8) Sum over the independent λ's and l's.

This type of perturbation formalism was first developed by Matsubara (1955) and has been further developed by Bloch and de Dominicis (1958), Luttinger and Ward (1960), and others. Specific application of this formalism to a system of interacting phonons has been made by Maradudin and Fein (1962) and Cowley (1963).

In the present work it is convenient to distinguish between those perturbation vertices that arise from the anharmonic terms (2.3) and (2.4), and those that are due to the perturbation of the external field, given by $-EM$, with M given by (2.10). Following Wilcox (1965) we will call the former "internal vertices", represented by ●, and the latter "external vertices", represented by ○.

The possible first-order diagrams, i.e. those with one perturbation vertex, are shown in Figure 1.

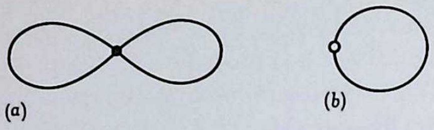

Fig. 1.—First-order contributions to Z.

The diagram in Figure 1(a) gives the contribution

$$-\gamma^{2}3\beta \sum_{\lambda_1\lambda_2 l_1 l_2} V(\lambda_1-\lambda_1\,\lambda_2-\lambda_2)\,g_{l_1}(\lambda_1)\,g_{l_2}(\lambda_2)$$

$$= -\gamma^{2}3\beta \sum_{\lambda_1\lambda_2} V(\lambda_1-\lambda_1\,\lambda_2-\lambda_2)\,(2\bar{n}_{\lambda_1}+1)(2\bar{n}_{\lambda_2}+1)\,. \qquad (3.16)$$

The diagram in Figure 1(b) has the value

$$-\gamma E \sum_{\lambda l} \mathscr{M}(\lambda-\lambda)\,g_l(\lambda) = -\gamma E \sum_{\lambda} \mathscr{M}(\lambda-\lambda)\,(2\bar{n}_\lambda+1)\,,$$

which vanishes for a centro-symmetrical crystal.

Some of the second-order diagrams that contribute to the partition function are shown in Figure 2.

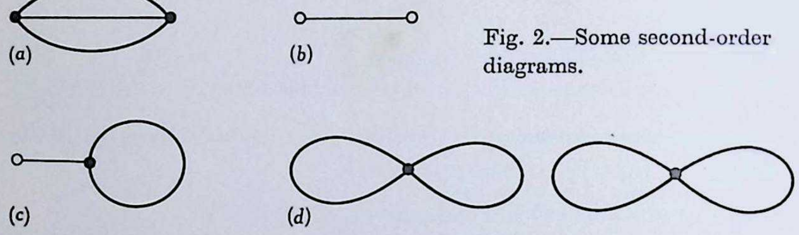

Fig. 2.—Some second-order diagrams.

It is important to distinguish between "connected" and "disconnected" diagrams. A disconnected diagram is one, such as Figure 2(d), which consists of several parts that are not connected by a phonon line.

If we denote the contribution of the connected diagrams to the partition function by L, then the contribution from all disconnected diagrams with n components is $L^n/n!$. Hence

$$Z = Z_0\left(1+\sum_{n=1}^{\infty} L^n/n!\right) = Z_0\,\mathrm{e}^{L}. \qquad (3.17)$$

The free energy is from (3.2) and (3.17) given by

$$F = F_0-\beta^{-1}L. \qquad (3.18)$$

Thus only the connected diagrams contribute to the free energy. This is a well-known result (Cowley 1963) and results in the automatic elimination from F of those diagrams with the wrong volume dependence (Goldstone 1957; Hugenholtz 1957).

IV. Free Energy and Dielectric Constant

As mentioned in Section III, to obtain the free energy it is necessary to consider only the connected diagrams. Furthermore, since we have included in the Hamiltonian (2.1) terms up to order γ^2 we can consistently only consider those diagrams that give contributions to F up to order γ^2.

From (2.4) and (2.10) it follows that each external vertex gives a factor of $-E$ to a diagram. This shows one advantage of the diagrammatic formulation, namely, that the field dependence of the contribution of any diagram to the free energy is given immediately by the number of external vertices in the diagram in question.

The diagrams that give contributions to the free energy of a centro-symmetrical crystal, up to order γ^2, are shown in Figure 3. The γ and E dependence is shown for each diagram.

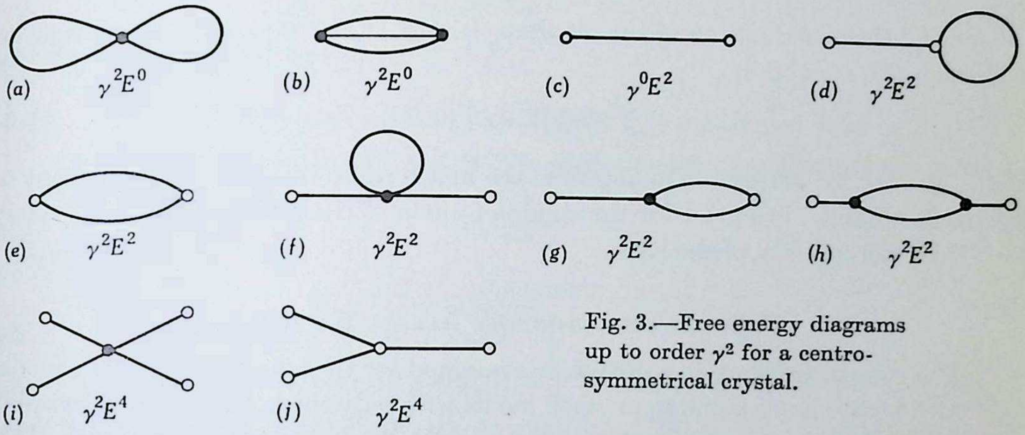

Fig. 3.—Free energy diagrams up to order γ^2 for a centro-symmetrical crystal.

There are nine additional diagrams that give contributions to F up to this order, but these vanish for a centro-symmetrical crystal because of the selection rules

$$V(0\lambda-\lambda)=0\,,\qquad \mathscr{M}(\lambda-\lambda)=0\,. \tag{4.1}$$

For a centro-symmetrical crystal the free energy can then be written, using (3.18) and the diagrams in Figure 3, as

$$\begin{aligned} F = F_0 &- \gamma^2\beta^{-1}[(a)+(b)] - E^2\beta^{-1}(c) - \gamma^2E^2\beta^{-1}[(d)+(e)+(f)+(g)+(h)] \\ &- \gamma^2E^4\beta^{-1}[(i)+(j)] + O(>\gamma^2)\,. \end{aligned} \tag{4.2}$$

The first term F_0 is the free energy of a harmonic crystal in the absence of an external field. The second term (diagrams (a) and (b)) is the usual correction due to the anharmonic terms, but still in the absence of the electric field. The third term (diagram (c)) is the correction to the free energy of a harmonic crystal due to the external field, and gives rise to the field-independent dielectric constant of the harmonic crystal. The fourth term (diagrams (d), (e), (f), (g), and (h)) depends both on the anharmonicity and the field, and gives anharmonic contributions to the field-independent dielectric constant. This term has been evaluated by Szigeti (1959) for the quantum mechanical case and by Wilcox (1965) for the classical case, and gives rise to the observed temperature dependence of the field-independent dielectric constant. The last term (diagrams (*i*) and (*j*)) gives a contribution to the dielectric constant that is proportional to E^2, i.e. the lowest order contribution to the field-dependent part of the dielectric constant.

From (1.2) and (4.2) the static dielectric constant is given by

$$\begin{aligned}\epsilon_s = \epsilon_\infty &+ (8\pi/\beta V)(c) + \gamma^2(8\pi/\beta V)[(d)+(e)+(f)+(g)+(h)] \\ &+ \gamma^2(16\pi/\beta V)[(i)+(j)]E^2 + \ldots . \end{aligned} \tag{4.3}$$

Comparing this with the phenomenological expansion (1.1), the lowest order contribution to the coefficient ϵ_2 is given by

$$\epsilon_2 = \gamma^2(16\pi/\beta V)[(i)+(j)]. \tag{4.4}$$

Evaluating the contributions of the diagrams (*i*) and (*j*) by means of the rules given in Section III, we obtain

$$\epsilon_2 = -\gamma^2(128\pi\mathscr{M}_0^3/V\hbar^4\omega_0^4)\{2\mathscr{M}_0\, V(0000) - \hbar\omega_0\,\mathscr{M}(000)\}. \tag{4.5}$$

Allowing for differences in notation, the first term in this result is equivalent to the result obtained in Part I for the rigid ion model. The second term arises solely from the deformability of the ions.

V. EVALUATION FOR THE ALKALI HALIDES

The general result (4.5) will now be evaluated for the alkali halides. The model to be used is the simple anharmonic shell model with only the negative ion polarizable and with short range repulsive forces between shells of nearest neighbours. This model has been discussed in a previous paper (Oitmaa 1967*b*).

The coefficients in (4.5) can be expressed in terms of the coefficients used in Oitmaa (1967*b*) as

$$\left.\begin{aligned} V(0000) &= \tfrac{1}{24}N^{-1}(\hbar/2\omega_0)^2\,\Psi(04;04;04;04), \\ \mathscr{M}_0 &= N^{\frac{1}{2}}(\hbar/2\omega_0)^{\frac{1}{2}}\,M(04), \\ \mathscr{M}(000) &= \tfrac{1}{6}N^{-\frac{1}{2}}(\hbar/2\omega_0)^{3/2}\,M(04;04;04). \end{aligned}\right\} \tag{5.1}$$

Using these results (4.5) can be written as

$$\epsilon_2 = -\gamma^2(2\pi M(04)^4/3v\omega_0^8)\{\Psi(04;04;04;04) - (4\omega_0^2/M(04))\,M(04;04;04)\}. \tag{5.2}$$

From Appendix I it follows that

$$\Psi(04;04;04;04) = \Phi(04;04;04;04) + \eta\Phi^{\mathrm{R}}(04;04;04;04), \tag{5.3}$$

where $\Phi(04;04;04;04)$ and $\Phi^{\mathrm{R}}(04;04;04;04)$ are respectively the total and repulsive anharmonic coefficients for rigid ions. The parameter η is given by

$$\eta = -4(R-YC)/(R+k+Y^2C), \tag{5.4}$$

where R is defined in terms of the derivatives of the short range repulsive potential $\phi_R(r)$ by

$$R = 2\phi_R''(r_0)+(4/r_0)\phi_R'(r_0) \tag{5.5}$$

and where

$$C = -4\pi e^2/3v\,. \tag{5.6}$$

In this work we consider both the repulsive and Coulomb contributions to the coefficient $\Phi(04;04;04;04)$. The Coulomb contribution is considerably less than the repulsive part, and to simplify the calculation we consider the Coulomb contribution only for nearest neighbours. The coefficient $\Phi(04;04;04;04)$ is then given by

$$\Phi(04;04;04;04) = \frac{1}{\bar{m}^2}\left(2\phi^{(4)}(r_0)+\frac{12}{r_0^2}\phi''(r_0)-\frac{12}{r_0^3}\phi'(r_0)\right), \tag{5.7}$$

where $\phi(r)$ is the total nearest neighbour potential given by

$$\phi(r) = \phi_R(r)-e^2/r \tag{5.8}$$

and $\bar{m}$ is the reduced mass given by

$$\bar{m}^{-1} = m_1^{-1}+m_2^{-1}\,. \tag{5.9}$$

From Appendix II it follows that the dipole moment coefficients are given by

$$M(04) = (e/\bar{m}^{\frac{1}{2}})(1+\chi)\,, \tag{5.10}$$

where

$$\chi = Y(R-YC)/(R+k+Y^2C) \tag{5.11}$$

and

$$M(04;04;04) = \{eY\bar{m}^{\frac{1}{2}}/(R+k+Y^2C)\}\,\Phi^{R}(04;04;04;04)\,. \tag{5.12}$$

For a thin rod of dielectric the frequency ω_0 of the $\boldsymbol{q} = 0$ optic mode, with displacements parallel to the long direction, can be obtained from the theory in Oitmaa (1967*b*) as

$$\bar{m}\omega_0^2 = R+C-(R-YC)^2/(R+k+Y^2C)\,. \tag{5.13}$$

This result is equivalent to the expression obtained by Woods, Cochran, and Brockhouse (1960) for the infrared absorption frequency of this model.

The adjustable parameters Y and k can be obtained by using the results (Havinga 1960)

$$\frac{Y^2e^2}{R+k} = \alpha_\infty\,, \qquad \frac{(1+Y)^2e^2}{k}+\frac{e^2}{R} = \alpha_0\,, \tag{5.14}$$

where the polarizabilities α_∞ and α_0 are given by

$$\frac{4\pi}{3v}\alpha_0 = \frac{\epsilon_0-1}{\epsilon_0+2} \qquad \text{and} \qquad \frac{4\pi}{3v}\alpha_\infty = \frac{\epsilon_\infty-1}{\epsilon_\infty+2}. \tag{5.15}$$

The result (5.2) can then be evaluated numerically. We do this for NaI, using the following room-temperature data (Born and Huang 1954): $r_0 = 3{\cdot}231\times10^{-8}$ cm, $\epsilon_0 = 6{\cdot}60$, $\epsilon_\infty = 2{\cdot}91$, $e = 4{\cdot}803\times10^{-10}$ e.s.u., $m_1 = 3{\cdot}809\times10^{-23}$ g, $m_2 = 21{\cdot}027\times10^{-23}$ g.

For the short range repulsive potential we use a Born–Mayer potential of the form

$$\phi_R(r) = D\exp(-r/\rho)\,, \tag{5.16}$$

with

$$\rho = 0\cdot 363\times 10^{-8}\ \text{cm}, \qquad D\exp(-r_0/\rho) = 2\cdot 33\times 10^{-13}\ \text{erg}.$$

These data then give the results:

$$R = 2\cdot 742\times 10^4\ \text{erg cm}^{-2},\quad v = 6\cdot 746\times 10^{-23}\ \text{cm}^3,\qquad C = -1\cdot 432\times 10^4\ \text{erg cm}^{-2},$$

$$Y = -2\cdot 106,\qquad k = 13\cdot 58\times 10^4\ \text{erg cm}^{-2},\quad \bar{m} = 3\cdot 225\times 10^{-23}\ \text{g},$$

$$\omega_0 = 2\cdot 01\times 10^{13}\ \text{sec}^{-1},\qquad \eta = 0\cdot 110,\qquad \chi = 0\cdot 058,$$

$$\Phi(04;04;04;04) = 2\cdot 269\times 10^{66},\qquad \Phi^{R}(04;04;04;04) = 2\cdot 798\times 10^{66}.$$

From these results it follows that

$$\Psi(04;04;04;04) = 2\cdot 576\times 10^{66},\quad M(04) = 89\cdot 46,\quad M(04;04;04) = -1\cdot 611\times 10^{41}.$$

Substituting these results in (5.2) gives for NaI

$$\epsilon_2 = -4\cdot 11\times 10^{-10}\quad (\text{CGS}).$$

This compares with $-1\cdot 32\times 10^{-10}$ that was obtained in Part I for NaI on the basis of a rigid ion model. Thus for the shell model the predicted value of the coefficient ϵ_2 is increased by a factor of approximately three over the rigid ion result. Some of this increase is due to the fact that the linear dipole moment coefficient and the quartic anharmonic coefficient are increased in the shell model, but most of the increase in ϵ_2 is due to the contribution of an additional term (depending on the third-order dipole moment coefficient) which does not appear for the rigid ion model. This term arises solely from the deformability of the ions.

VI. SOME HIGHER ORDER TERMS

In Section IV the lowest order contributions to the field-dependent terms in the dielectric constant expansion (1.1) were obtained. These contributions arose from terms in the free energy proportional to γ^2E^4. These terms did not depend explicitly on the temperature but only implicitly through the weak temperature dependence of r_0 and hence of ω_0 and of the anharmonic coefficients.

Further contributions to the field-dependent terms in (1.1) can be obtained by expanding the free energy to higher order than γ^2. For consistency, higher order terms must then also be included in the Hamiltonian (2.1). By evaluating such higher order contributions to the dielectric constant we obtain a check on the convergence of the perturbation expansion.

In this section we include terms up to order γ^4 in the Hamiltonian, i.e. terms up to sixth order in the particle displacements in the potential energy expansion. The free energy is then also expanded up to order γ^4. Since we are only interested in terms that give contributions to the dielectric constant proportional to E^2, or higher powers of E, it is only necessary to consider the free energy diagrams that are proportional to E^4 or higher powers of E.

For a centro-symmetrical crystal there are 5 free energy diagrams proportional to γ^4E^6, shown in Figure 4. For a crystal without a centre of symmetry there are 28 additional diagrams of this type. These diagrams give the lowest order contribution to the E^4 term in the expansion (1.1). This contribution is again independent of the temperature.

Several of these terms were evaluated for NaI. For a large field of 1000 e.s.u. cm^{-1} (3×10^5 V cm^{-1}) the change in dielectric constant due to these terms was smaller by a factor of at least 10^4 than the change calculated in Section V. Thus these terms are completely negligible. From this we can conclude that any decrease that might occur in the dielectric constant of such simple ionic crystals at large fields would be proportional to the square of the field strength.

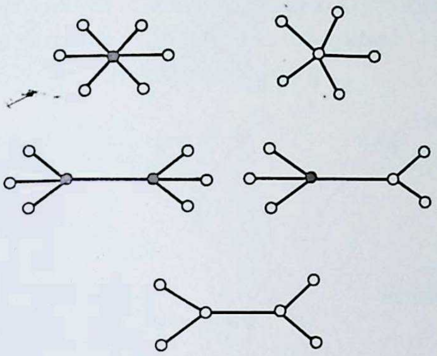

Fig. 4.—Free energy diagrams proportional to γ^4E^6 for a centro-symmetrical crystal.

There also occur a total of 89 free energy diagrams proportional to γ^4E^4, of which 29 are nonvanishing for a centro-symmetrical crystal. The 29 diagrams are shown in Figure 5.

These 29 diagrams give additional contributions to the E^2 term in the expansion (1.1). These contributions all involve a single or multiple summation over the normal modes of the crystal and are explicitly dependent on the temperature, in contrast to the lowest order contributions evaluated in Section IV. The summations were evaluated numerically by taking a sample of $\boldsymbol{q}$ vectors evenly distributed throughout the first Brillouin zone. The sample used was the same as that used by Hardy (1962), which is a slight modification of that used originally by Kellermann (1940). This sample consists of 48 distinct $\boldsymbol{q}$'s, which by symmetry corresponds to exactly 1000 points in the zone. In this work it was necessary to distinguish between $\boldsymbol{q}$'s that merely involved an interchange of x and y, or x and z, components, since the anharmonic coefficients involved were not symmetric in x, y, z. This made it necessary to consider 106 distinct $\boldsymbol{q}$'s corresponding to the 1000 points. The 29 terms were then evaluated numerically for various temperatures between 0°K and 500°K using the IBM 360/50 computer of the University of New South Wales Computing Centre. One approximation that was made in evaluating these higher order terms was to replace the modified shell model anharmonic coefficients Ψ by the rigid ion ones Φ. This should not introduce an error of more than about 10% and greatly decreases the amount of work involved in calculating the various anharmonic coefficients.

The variation with temperature of the total contribution of these diagrams to the coefficient ϵ_2 in (1.1) is shown in Figure 6. At high temperatures the variation with temperature is almost linear. Using this result and the result of Section V, the high temperature dielectric constant of NaI can be expressed in the form

$$\epsilon_S = \epsilon_0 - (4\cdot 0 - 1\cdot 6 \times 10^{-3} T)E^2. \tag{6.1}$$

At low temperatures the variation with T is more complicated.

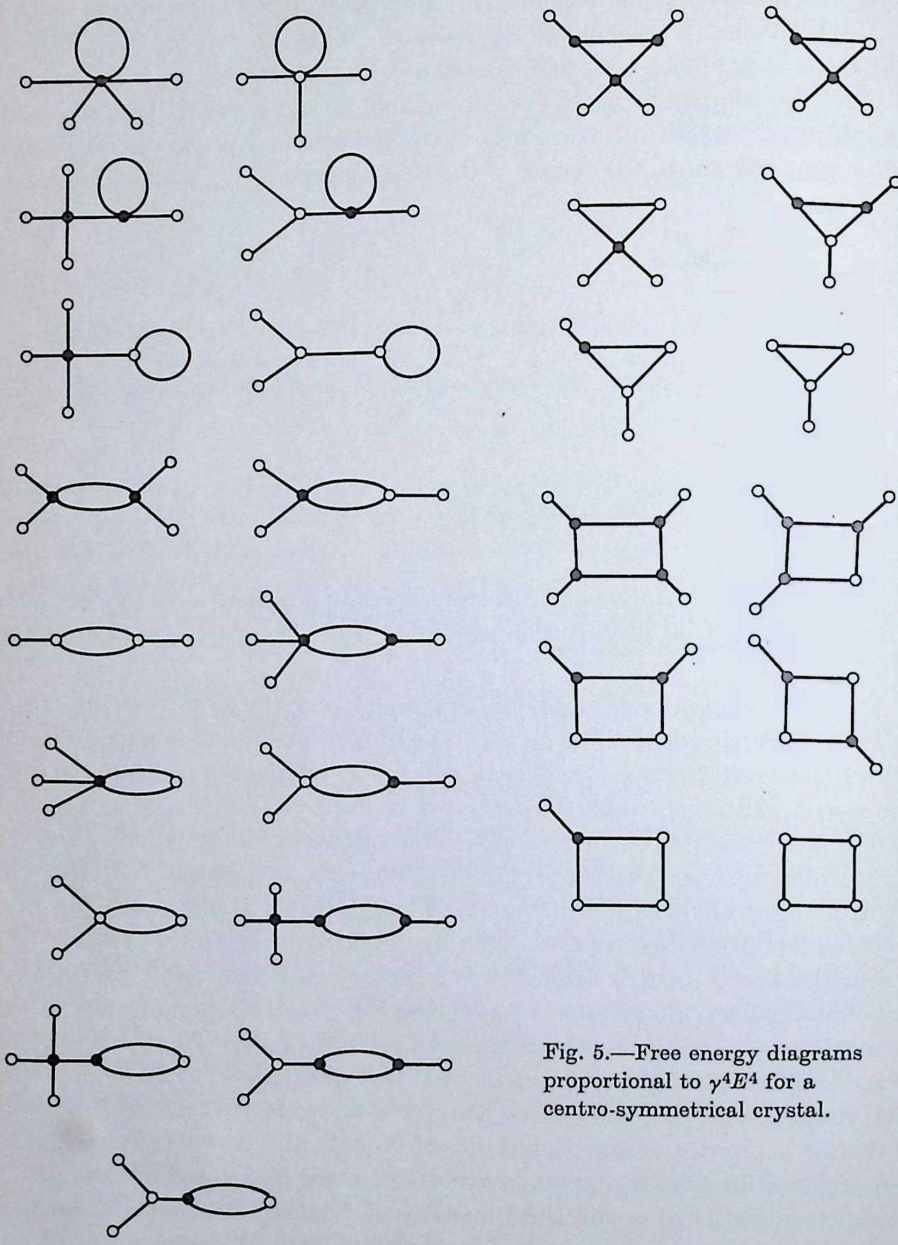

Fig. 5.—Free energy diagrams proportional to $\gamma^4 E^4$ for a centro-symmetrical crystal.

At all temperatures the contribution of these terms to the coefficient ϵ_2 is of the order of 10–20% of the lowest order term, and so the perturbation expansion appears to be quite good.

VII. Discussion

The lowest order contribution to the coefficient of the E^2 term in the phenomenological expansion (1.1) of the static dielectric constant of a crystalline solid with deformable ions has been calculated. This contribution is independent of the temperature, and the same result can in fact be obtained for a classical static lattice model. For NaI this results in a small decrease in the static dielectric constant of 4×10^{-4} in a field of 1000 e.s.u. cm^{-1}.

The next order terms give a temperature-dependent contribution to this coefficient which is of the order of 10% of the lowest order contribution. This situation is completely analogous to that which occurs with the ordinary field-independent static dielectric constant ϵ_0. To a first approximation ϵ_0 is independent of the temperature and can be obtained for a static lattice model. Higher order terms, which at low temperatures must be calculated quantum mechanically, give a small temperature-dependent correction to ϵ_0.

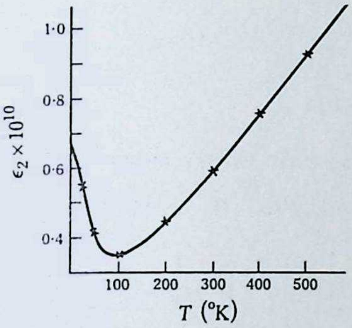

Fig. 6.—Contribution to ϵ_2 of the diagrams of order γ^4.

The lowest order contribution to the coefficient of the E^4 term in the expansion (1.1) is also independent of the temperature. The change in dielectric constant due to this term is negligible compared with the change due to the E^2 term. Thus any decrease that might be observed in the static dielectric constant of simple ionic crystals, such as the alkali halides, would be proportional to the square of the field strength.

VIII. Acknowledgments

The author wishes to thank Professor J. J. O'Dwyer for suggesting this problem to him and for many helpful discussions. He also wishes to thank Mr. P. L. Sanger for supplying the data used in Section VI, and for assistance with the computing. The data were obtained from a programme written originally by Dr. A. W. Pryor.

IX. References

Bloch, C., and de Dominicis, C. (1958).—*Nucl. Phys.* **7**, 449.

Born, M., and Huang, K. (1954).—"Dynamical Theory of Crystal Lattices." (Clarendon Press: Oxford.)

Cowley, R. A. (1963).—*Adv. Phys.* **12**, 421.

Gaudin, N. (1960).—*Nucl. Phys.* **15**, 89.

Goldstone, J. (1957).—*Proc. R. Soc.* A **239**, 267.

HARDY, J. R. (1962).—*Phil. Mag.* (8) **7**, 315.
HAVINGA, E. E. (1960).—*Phys. Rev.* **119**, 1193.
HUGENHOLTZ, N. M. (1957).—*Physica* **23**, 481.
KELLERMANN, E. W. (1940).—*Phil. Trans. R. Soc.* **238**, 513.
LUTTINGER, J. M., and WARD, J. C. (1960).—*Phys. Rev.* **118**, 1417.
MARADUDIN, A. A., and FEIN, A. E. (1962).—*Phys. Rev.* **128**, 2589.
MATSUBARA, T. (1955).—*Prog. theor. Phys., Kyoto* **14**, 351.
OITMAA, J. (1967*a*).—*Aust. J. Phys.* **20**, 11.
OITMAA, J. (1967*b*).—*Aust. J. Phys.* **20**, 495.
PARRY, W. E., and TURNER, R. E. (1964).—*Rep. Prog. Phys.* **27**, 23.
SZIGETI, B. (1959).—*Proc. R. Soc.* A **252**, 217.
WILCOX, R. M. (1965).—*Phys. Rev.* **139**, A1281.
WOODS, A. D. B., COCHRAN, W., and BROCKHOUSE, B. N. (1960).—*Phys. Rev.* **119**, 980.

APPENDIX I

Shell Model Anharmonic Coefficient

The shell model anharmonic coefficient $\Psi(04;04;04;04)$ is given from Oitmaa (1967*b*) by

$$\Psi(04;04;04;04) = \sum_{\substack{l'l''l'''\\ \kappa\kappa'\kappa''\kappa'''}} \frac{e_x(\kappa\mid 04)\,e_x(\kappa'\mid 04)\,e_x(\kappa''\mid 04)\,e_x(\kappa'''\mid 04)}{(m_\kappa m_{\kappa'} m_{\kappa''} m_{\kappa'''})^{\frac{1}{2}}} \times\psi_{xxxx}(0\kappa,l'\kappa',l''\kappa'',l'''\kappa''') . \tag{A1}$$

This expression can be simplified considerably by using the invariance relations

$$\psi_{xxxx}(l\kappa,l'\kappa',l''\kappa'',l'''\kappa''') = \psi_{xxxx}(0\kappa,(l'-l)\kappa',(l''-l)\kappa'',(l'''-l)\kappa''')$$

and

$$\sum_{l\kappa}\psi_{xxxx}(l\kappa,l'\kappa',l''\kappa'',l'''\kappa''') = 0\,,$$

the latter of which implies that

$$\sum_{l}\psi_{xxxx}(l1,l'\kappa',l''\kappa'',l'''\kappa''') = -\sum_{l}\psi_{xxxx}(l2,l'\kappa',l''\kappa'',l'''\kappa''')\,.$$

Using these invariance relations and the result

$$\frac{e_x(1\mid 04)}{m_1^{\frac{1}{2}}} - \frac{e_x(2\mid 04)}{m_2^{\frac{1}{2}}} = \left(\frac{1}{m_1}+\frac{1}{m_2}\right)^{\frac{1}{2}},$$

the expression (A1) simplifies to

$$\Psi(04;04;04;04) = \left(\frac{1}{m_1}+\frac{1}{m_2}\right)^{2} \sum_{l'l''l'''}\psi_{xxxx}(01,l'1,l''1,l'''1)\,. \tag{A2}$$

The anharmonic force constant $\psi_{xxxx}(01, l'1, l''1, l'''1)$ is given by the result (3.15) of Oitmaa (1967*b*). Using this result, the expression (A2) can be simplified to give

$$\Psi(04;04;04;04) = \frac{1}{m^2}\left(\Phi_{xxxx}(01,01,01,01) - 4\sum_{l\kappa}(BD)_{xx}(1\kappa,0)\,\Phi^{\mathrm{R}}_{xxxx}(0\kappa,l1,l1,l1)\right), \tag{A3}$$

where $\Phi_{xxxx}(01,01,01,01)$ and $\Phi^{\mathrm{R}}_{xxxx}(0\kappa,l1,l1,l1)$ are rigid ion force constants and **B** and **D** are $3n\times 3n$ matrices, defined in Oitmaa (1967*b*).

Using the result of Part I for the rigid ion coefficients $\Phi(04;04;04;04)$ and $\Phi^{\mathrm{R}}(04;04;04;04)$, and using the explicit forms, for the NaCl structure, of the 6×6 matrices **B** and **D** for $\boldsymbol{q}=0$, gives for (A3)

$$\Psi(04;04;04;04) = \Phi(04;04;04;04) + \eta\Phi^{\mathrm{R}}(04;04;04;04), \tag{A4}$$

where

$$\begin{aligned}\eta &= -4(BD)_{xx}(11,0) + 4(BD)_{xx}(12,0)\\ &= -4\frac{k_1(R-Y_2C)+k_2(R+Y_1C)+RC(Y_1+Y_2)^2}{k_1k_2+k_1(R+Y_2^2C)+k_2(R+Y_1^2C)+RC(Y_1+Y_2)^2},\end{aligned} \tag{A5}$$

where k_1, k_2, and Y_1, Y_2 are respectively the core–shell force constants and the shell charges for the positive and negative ions.

For the simpler case, if only the negative ion is polarizable, putting $k_1\to\infty$, $k_2=k$, $Y_1=0$, and $Y_2=Y$ we obtain

$$\eta = -4(R-YC)/(R+k+Y^2C). \tag{A6}$$

For $k\to\infty$, $\eta\to 0$ so that (A4) reduces to the rigid ion result.

APPENDIX II

Dipole Moment Coefficients

From the result (4.4) of Oitmaa (1967*b*) the first-order dipole moment coefficient $M(04)$ is given by

$$M(04) = e\sum_{\kappa} m_\kappa^{-\frac{1}{2}} Z_\kappa e_x(\kappa\mid 04) - e\sum_{\kappa\kappa'} m_{\kappa'}^{-\frac{1}{2}} Y_\kappa e_x(\kappa'\mid 04)\,(BD)_{xx}(\kappa'\kappa,0). \tag{A7}$$

Writing out the summations and using the results of Appendix I for the case when only the negative ion is polarizable gives

$$M(04) = e\bar{m}^{-\frac{1}{2}}(1+\chi), \tag{A8}$$

where

$$\chi = Y(R-YC)/(R+k+Y^2C). \tag{A9}$$

For $k\to\infty$, $\chi\to 0$ so that (A8) reduces to the rigid ion result.

From the result (4.6) of Oitmaa (1967*b*) the third-order dipole moment coefficient $M(04;04;04)$ is given by

$$M(04;04;04) = -e \sum_{\substack{l_3 l_4 l_5 \\ \kappa_1\kappa_2\kappa_3\kappa_4\kappa_5}} \frac{Y_{\kappa_1} e_x(\kappa_3 \mid 04)\, e_x(\kappa_4 \mid 04)\, e_x(\kappa_5 \mid 04)}{(m_{\kappa_3} m_{\kappa_4} m_{\kappa_5})^{\frac{1}{2}}} \times D_{xx}(\kappa_1 \kappa_2, 0)\, \Phi^{\mathrm{R}}_{xxxx}(0\kappa_2, l_3\kappa_3, l_4\kappa_4, l_5\kappa_5)\,. \qquad \text{(A10)}$$

For two-body forces only, the force constants in this expression are nonzero only if they refer to at most two distinct ions. For this case (A10) can be simplified to give

$$\begin{aligned} M(04;04;04) &= e(m_1^{-1}+m_2^{-1})^{3/2} \sum_{\kappa} Y_\kappa \{D_{xx}(\kappa 1,0)-D_{xx}(\kappa 2,0)\} \sum_{l} \Phi^{\mathrm{R}}_{xxxx}(01,01,01,l2) \\ &= \zeta\, \Phi^{\mathrm{R}}(04;04;04;04)\,, \end{aligned} \qquad \text{(A11)}$$

where

$$\zeta = e\bar{m}^{\frac{1}{2}} \frac{Y_1 k_2 - Y_2 k_1}{k_1 k_2 + k_1(R+Y_2^2 C) + k_2(R+Y_1^2 C) + RC(Y_1+Y_2)^2}\,. \qquad \text{(A12)}$$

For the case when only the negative ion is polarizable (A12) simplifies to

$$\zeta = eY\bar{m}^{\frac{1}{2}}/(R+k+Y^2 C)\,. \qquad \text{(A13)}$$

For $k \to \infty$ this gives $\zeta \to 0$, so that (A11) reduces to the rigid ion result, namely, that the higher order dipole moments vanish.

MULTIPOLE ANALYSIS

I. THEORY, AND GEOMAGNETIC MULTIPOLES 1965·0

By R. W. JAMES*

[*Manuscript received March* 18, 1968]

Summary

A reduction of order procedure is outlined which allows virtually any order multipole analysis for a general spherical surface harmonic to be rapidly carried out. The geomagnetic multipoles, to order eight, are found for the epoch 1965·0 and the theory is used to obtain the spherical harmonic coefficients when the dipole axis is chosen as polar axis.

I. INTRODUCTION

The idea of using a multipole representation in potential theory appears to have been initially suggested by Gauss (1877) but the first attempt at a fuller development is due to Maxwell (1892) and the basic theory has become known as Maxwell's theory of poles. The subject has undergone further discussion and development in the works of Sylvester (1909), Courant and Hilbert (1953), and Hobson (1955). Geomagnetic multipoles have been considered by Umov (1904), Chargoy (1950, 1955), Chargoy and Alvarez (1957), Zolotov (1966), Winch and Slaucitajs (1966*a*, 1966*b*), and Winch (1967*a*, 1967*b*). Whilst multipole representations are frequently mentioned in electromagnetic theory, they are generally regarded as redundant to the normal expansions in terms of orthogonal functions. However, knowledge of the multipole axes does allow a geometrical visualization of the field and it is of interest to enquire into the behaviour and relative importance of the multipoles representing the geomagnetic field. Moreover, since the multipole strengths and axes are invariant under rotation of the coordinate frame, it is a definite advantage to have a procedure that can rapidly transfer back and forth between the multipole representation and the more usual spherical harmonic representation. For, once this can be done, we have a very practical method for carrying out the transformation of the Gaussian coefficients of the field, under a rotation of polar axis. The outline of such a method is included in this paper and it is shown how this allows evaluation of the field at any point without requiring knowledge of the explicit forms of the spherical harmonics.

---

* Department of Applied Mathematics, University of Sydney, N.S.W. 2006.

Aust. J. Phys., 1968, **21**, 455–64

II. BASIC THEORY

We start from the definitions for the spherical harmonics $\mathrm{P}_n^m(\cos\theta)\cos m\phi$ and $\mathrm{P}_n^m(\cos\theta)\sin m\phi$, which can be written as

$$\mathrm{P}_n^m(\cos\theta)\cos m\phi = A_{nm}\, r^{n+1}\left\{\left(\frac{\partial}{\partial z}\right)^{n-m}\prod_i \frac{\partial}{\partial t_m^i}\right\}\frac{1}{r}, \tag{1a}$$

$$\mathrm{P}_n^m(\cos\theta)\sin m\phi = A_{nm}\, r^{n+1}\left\{\left(\frac{\partial}{\partial z}\right)^{n-m}\prod_i \frac{\partial}{\partial s_m^i}\right\}\frac{1}{r}, \tag{1b}$$

where θ is the geographic north colatitude and ϕ the Greenwich east longitude as usual. Here, the products $\prod_i$ are over all integral values of i satisfying $0 < |i| \leqslant \frac{1}{2}m$ and zero is included when m is odd. The derivatives $\partial/\partial t_m^i$ are derivatives in the directions of the vectors $\boldsymbol{t}_m^i$, which are just unit vectors in the x–y plane displaced symmetrically at intervals of π/m about the positive x axis ($\phi = 0$), so that $\boldsymbol{t}_m^{-i}$ is the reflection of $\boldsymbol{t}_m^i$ (in the x axis) and $\boldsymbol{t}_m^0$, when it exists (i.e. for odd values of m), coincides with the x direction. The derivatives $\partial/\partial s_m^i$ are in the directions of the unit vectors $\boldsymbol{s}_m^i$, which can be obtained from the $\boldsymbol{t}_m^i$ by an eastward rotation of $\pi/2m$ (this follows from $\sin m\phi = \cos m(\phi-\pi/2m)$).

Whilst these definitions are different from the usual ones, the equivalence can be easily shown (Hobson 1955). For Schmidt quasi-normalization we must take

$$A_{nm} = (-)^n\, 2^m\{(2-\delta_{m0})\,(n-m)!\,(n+m)!\}^{-\frac{1}{2}}.$$

The points where the vectors $\hat{z} = (0,0,1)$ and $\boldsymbol{t}_m^i$ (or $\boldsymbol{s}_m^i$) meet a sphere, centred at $r = 0$, are called the poles of the surface harmonic $\mathrm{P}_n^m(\cos\theta)\cos m\phi$ (or $\mathrm{P}_n^m(\cos\theta)\sin m\phi$) on the sphere. If $m = 0$, $\hat{z}$ is the only pole, and if $m = n$ then $\hat{z}$ is not a pole.

This idea may be generalized to give an analogous representation for a general surface harmonic of the nth degree given by

$$Y_n = \sum_{m=0}^{n}(g_n^m\cos m\phi + h_n^m\sin m\phi)\,\mathrm{P}_n^m(\cos\theta), \tag{2}$$

for, using equations (1), we may write

$$\begin{aligned} Y_n &= r^{n+1}\sum_{m=0}^{n}\left(\frac{\partial}{\partial z}\right)^{n-m}\left(g_n^m\prod_i\frac{\partial}{\partial t_m^i} + h_n^m\prod_i\frac{\partial}{\partial s_m^i}\right)\frac{1}{r} \\ &= r^{n+1}\sum_{m=0}^{n}\sum_{l=0}^{m} c_{ml}\left(\frac{\partial}{\partial z}\right)^{n-m}\left(\frac{\partial}{\partial x}\right)^{l}\left(\frac{\partial}{\partial y}\right)^{m-l}\frac{1}{r}, \end{aligned} \tag{3}$$

where the coefficients c_{ml} are obtained by expanding the above products. When it is taken into account that for harmonic functions

$$(\partial/\partial x)^2+(\partial/\partial y)^2+(\partial/\partial z)^2 = 0,$$

it can be shown (Sylvester 1909) that the ternary quantic of differential operators in (3) can be written as the product of n real linear factors (canonical form), i.e.

$$Y_n = (-)^n\, r^{n+1} M_n\left\{\prod_{i=1}^{n}\left(u_i\frac{\partial}{\partial x} + v_i\frac{\partial}{\partial y} + w_i\frac{\partial}{\partial z}\right)\right\}\frac{1}{r}, \tag{4}$$

and that this representation is unique except that the n unit vectors $\boldsymbol{u}_i = (u_i, v_i, w_i)$ may be reversed in pairs. Equation (4) is called the multipole representation of Y_n; M_n is called the multipole strength and the vectors $\boldsymbol{u}_i$ the multipole axes, which meet the sphere at the poles (θ_i, ϕ_i). A potential of the form

$$V_n = r^{-(n+1)} Y_n$$

will be called a multipole potential and can be thought of as due to a singular point of degree n at $r = 0$. It is easy to see that such a potential is formed when two singular points of degree $n-1$, having the same $n-1$ axes but opposite strengths, are brought together at $r = 0$ along an nth axis in such a manner that the product of their strength and distance apart is kept constant. This procedure is an obvious generalization of the technique employed in forming the familiar dipole potential (multipole of order one) by bringing together two equal but opposite poles (order zero).

In practice, for the geomagnetic field, the coefficients g_n^m and h_n^m in equation (2) are known from the harmonic analysis of the field at the surface of the Earth, being just the usual Gaussian coefficients. We thus have to combine (2) and (4) and solve for the axes $\boldsymbol{u}_i$ and the strength M_n.

III. Recurrence Relations

The highest order geomagnetic multipole analysis that has been carried out is the fifth (Winch 1967*b*), but the solution by any of the methods so far put forward of any higher order multipole problem is virtually, although not theoretically, impossible due to algebraic complexity and difficulties in solving the final nonlinear equations. However, using recently derived recurrence relations for P_n^m a technique has been perfected which quickly gives the solution to multipole problems of much higher orders. It has been shown (James 1967) that the equations to be solved for the $\boldsymbol{u}_i$ and M_n are of the form

$$M_n \begin{vmatrix} a_n^m \\ b_n^m \end{vmatrix} = \begin{vmatrix} g_n^m \\ h_n^m \end{vmatrix}, \qquad m = 0, 1, \ldots, n, \tag{5}$$

where the a_n^m and b_n^m are generated as functions of the $\boldsymbol{u}_i$ through the relations (starting from $a_0^0 = 1$)

$$2a_{k+1}^m = u_{k+1}\{(1+\delta_{m1})\,\alpha_{k+1}^m\,a_k^{m-1} - \beta_{k+1}^m\,a_k^{m+1}\} - v_{k+1}\{\alpha_{k+1}^m\,b_k^{m-1} + \beta_{k+1}^m\,b_k^{m+1}\} + 2w_{k+1}\,\gamma_{k+1}^m\,a_k^m, \tag{6a}$$

$$2b_{k+1}^m = u_{k+1}\{\alpha_{k+1}^m\,b_k^{m-1} - \beta_{k+1}^m\,b_k^{m+1}\} + v_{k+1}\{(1+\delta_{m1})\,\alpha_{k+1}^m\,a_k^{m-1} + \beta_{k+1}^m\,a_k^{m+1}\} + 2w_{k+1}\,\gamma_{k+1}^m\,b_k^m. \tag{6b}$$

Here

$$\alpha_{k+1}^m = \{\tfrac{1}{2}(2-\delta_{m1})(k+m)(k+m+1)\}^{\frac{1}{2}}, \qquad \beta_{k+1}^m = \{(1+\delta_{m0})(k-m)(k-m+1)\}^{\frac{1}{2}},$$

$$\gamma_{k+1}^m = \{(k-m+1)(k+m+1)\}^{\frac{1}{2}}.$$

In all this work the conventions

$$a_n^m = g_n^m = 0 \qquad \text{when either} \qquad m < 0 \quad \text{or} \quad m > n$$

and

$$b_n^m = h_n^m = 0 \qquad \text{when either} \qquad m \leqslant 0 \quad \text{or} \quad m > n$$

are to be understood and δ_{mp} is the Kronecker delta

$$\delta_{mp} = \begin{matrix} 1, & m = p, \\ 0, & m \neq p. \end{matrix}$$

IV. Transformed Coefficients

Using the relations (6) it is a simple matter to transform back and forth between the multipole and spherical harmonic representations. This is particularly advantageous when it is required to find the harmonic expansion of a potential in a new polar and meridional reference frame. For, suppose we have a potential

$$V = \sum_{n=1}^{\infty} V_n = \sum_{n=1}^{\infty} (-)^n r^{-n-1} M_n \left(\prod_{i=1}^{n} (\boldsymbol{u}_{ni} \cdot \nabla) \right) \frac{1}{r},$$

where $\boldsymbol{u}_{ni}$ represents the ith axis of the nth order multipole V_n, or equivalently,

$$V = \sum_{n=1}^{\infty} r^{-n-1} \sum_{m=0}^{n} (g_n^m \cos m\phi + h_n^m \sin m\phi) \, \mathrm{P}_n^m(\cos\theta),$$

and we transfer to a new system of coordinates (θ^*, ϕ^*). We wish to determine the new coefficients $(g_n^m)^*$ and $(h_n^m)^*$ such that

$$V = \sum_{n=1}^{\infty} r^{-n-1} \sum_{m=0}^{n} \{(g_n^m)^* \cos m\phi^* + (h_n^m)^* \sin m\phi^*\} \, \mathrm{P}_n^m(\cos\theta^*).$$

If the new polar axis has direction cosines given by $\boldsymbol{U} = (U, V, W)$ and if we suppose for the moment that longitude is measured anticlockwise around the new pole, looking from above the pole, from the great semicircle containing the north geographic pole and the two extremities of the new polar axis, then, from the sine and cosine formulae of spherical trigonometry, the components of $\boldsymbol{u}_{ni}$ in the new coordinate system are easily seen to be

$$u_{ni}^* = \{w_{ni} - (\boldsymbol{u}_{ni} \cdot \boldsymbol{U}) W\}(1 - W^2)^{-\frac{1}{2}}, \qquad v_{ni}^* = \{u_{ni} V - v_{ni} U\}(1 - W^2)^{-\frac{1}{2}}, \qquad w_{ni}^* = \boldsymbol{u}_{ni} \cdot \boldsymbol{U},$$

so the new multipole representation of V, namely

$$V = \sum_{n=1}^{\infty} (-)^n r^{-n-1} M_n \left(\prod_{i=1}^{n} (\boldsymbol{u}_{ni}^* \cdot \nabla^*) \right) \frac{1}{r},$$

is immediately obtainable. Substitution of the "transformed" axes $\boldsymbol{u}_{ni}^*$ into equations (6) then quickly generates $(g_n^m)^*$ and $(h_n^m)^*$. Note that in (6) the subscript n on $\boldsymbol{u}_{ni}$ has been omitted for conciseness and i is represented by $k+1$. We see, in particular, from the canonical form (4) that if we choose our new polar axis to coincide with one of the multipole axes, say $\boldsymbol{u}_{ni}$, then the corresponding factor $(\boldsymbol{u}_{ni} \cdot \nabla)$ transforms merely to $\partial/\partial z^*$, and thus in this new system the number of coefficients required to represent the field is reduced by two. Indeed, it is easily seen from relations (6) that the coefficients $(g_n^n)^*$ and $(h_n^n)^*$ will be zero so that terms containing $P_n^n(\cos\theta^*)$ will be missing from the expansion of V. If for some reason it were desired to use the point G (with direction cosines $\boldsymbol{U}_G$) as reference for longitude, instead of the geographic north pole, it is merely necessary to replace $(g_n^m)^*$ and $(h_n^m)^*$ by

$$(g_n^m)^*\cos m\alpha + (h_n^m)^*\sin m\alpha \qquad \text{and} \qquad -(g_n^m)^*\sin m\alpha + (h_n^m)^*\cos m\alpha$$

respectively, where α is the angle between the vectors $\boldsymbol{U}\times\boldsymbol{z}$ and $\boldsymbol{U}\times\boldsymbol{U}_G$ and can be obtained from

$$R\cos\alpha = (\boldsymbol{U}\times\hat{\boldsymbol{z}}).(\boldsymbol{U}\times\boldsymbol{U}_G) = W_G(U^2+V^2)-W(UU_G+VV_G),$$

$$R\sin\alpha = (\boldsymbol{U}\times\hat{\boldsymbol{z}})\times(\boldsymbol{U}\times\boldsymbol{U}_G).\boldsymbol{U} = VU_G-UV_G.$$

For many purposes in geomagnetism it is desirable to use geomagnetic coordinates (Θ, Λ). In this case the reversed dipole axis $-\boldsymbol{u}_{11}$ is taken as polar axis and the longitude is referred to the south geographic pole. For comparison the geomagnetic coefficients are given in Table 1 together with the data of Hurwitz *et al.* (1966) which were used for the computations of the present paper.

If the transformation has to be made on a more general field that has parts due to internal, external, and non-potential sources then a separation of the field should be made first and the above procedure applied to each part separately. Whilst in the present paper external and non-potential sources are neglected, it is interesting to note a very recent method of field separation that has been put forward by Winch (1968). Winch's method involves the use of Cartesian force components of the field and, interestingly, is based on the recurrence relations (6) together with the corresponding relations for the other sources of the field.

V. Field Evaluation

Normally in order to evaluate the function V at any point P on the Earth it is necessary to find the explicit forms of the functions $P_n^m(\cos\theta)$ and evaluate these at the colatitude of P. However, if we bear in mind that $P_n^m(1) = \delta_{m0}$, we see that the value of V at the geographic pole is just $\sum_{n=1}^{\infty} g_n^0$. Similarly, if we make use of the transformation technique of the previous section and rotate our polar axis so that it passes through P, then the value of V at P can be obtained as $\sum_{n=1}^{\infty} (g_n^0)^*$.

VI. Relative Magnitudes

Useful magnitudes in comparing the overall importance of each of the multipoles are the r.m.s. values of the parameters X_n, Y_n, Z_n, and T_n on the surface of the Earth ($r = 1$). Here, as usual,

$$(X_n, Y_n, Z_n) = \left(-\frac{1}{r}\frac{\partial V_n}{\partial\theta}, \frac{1}{r\sin\theta}\frac{\partial V_n}{\partial\phi}, -\frac{\partial V_n}{\partial r}\right), \qquad T_n = (X_n^2+Y_n^2+Z_n^2)^{\frac{1}{2}}.$$

TABLE 1

SCHMIDT SPHERICAL HARMONIC COEFFICIENTS IN γ(EARTH RADII)$^{n+2}$

Coefficients are geographic (g, h) and geomagnetic (g^*, h^*)

n		$m = 0$	1	2	3	4	5	6	7	8
1	g	−30450	−2135							
	g^*	−31066	0							
	h		5772							
	h^*		0							
2	g	−1616	2967	1585						
	g^*	−588	2969	−1883						
	h		−1999	132						
	h^*		2232	499						
3	g	1159	−1976	1300	864					
	g^*	796	−1154	−1080	−552					
	h		−411	245	−156					
	h^*		−1706	1154	−508					
4	g	923	782	494	−366	252				
	g^*	808	−476	5	294	−291				
	h		142	−285	4	−243				
	h^*		941	187	−50	−301				
5	g	−184	345	244	−37	−158	−62			
	g^*	−113	66	−305	63	−149	−4			
	h		14	124	−108	−109	65			
	h^*		332	−47	161	101	37			
6	g	34	65	5	−228	−14	13	−111		
	g^*	45	−7	46	188	−137	33	−47		
	h		−22	112	51	−24	−19	−22		
	h^*		10	−49	97	−54	−47	−93		
7	g	89	−45	6	4	−25	−22	22	10	
	g^*	66	−61	17	−18	6	4	40	−1	
	h		−40	−25	−18	3	31	−27	−25	
	h^*		−24	61	2	35	17	−1	23	
8	g	0	11	3	−13	−2	10	−14	11	6
	g^*	11	2	−4	2	−19	6	33	2	−10
	h		−10	1	5	−19	7	21	4	−19
	h^*		6	−3	3	1	5	1	12	13

Making use of the orthogonality of the harmonics we know that, when $r = 1$ Earth radius,

$$\overline{V_n^2} = \frac{1}{4\pi}\int_{4\pi} V_n^2 \sin\theta \, \mathrm{d}\theta \, \mathrm{d}\phi = \frac{1}{2n+1}\sum_{m=0}^{n} \{(g_n^m)^2 + (h_n^m)^2\}$$

and

$$\overline{Z_n^2} = (n+1)^2 \overline{V_n^2}.$$

Using the perhaps less familiar relation (see, for example, Copson 1962)

$$\int_0^\pi (\sin\theta)^{-1}\,\mathrm{P}_n^m(\cos\theta)\,\mathrm{P}_n^l(\cos\theta)\,\mathrm{d}\theta = \delta_{ml}/2m\,,$$

we find

$$\overline{Y_n^2} = \tfrac{1}{2}\sum_{m=0}^{n} m\{(g_n^m)^2+(h_n^m)^2\}$$

and

$$\overline{X_n^2} = \sum_{m=0}^{n} \{(g_n^m)^2+(h_n^m)^2\}\int_0^\pi (\mathrm{dP}_n^m/\mathrm{d}\theta)^2\sin\theta\,\mathrm{d}\theta$$

$$= \sum_{m=0}^{n} \{n(n+1)/(2n+1)-\tfrac{1}{2}m\}\{(g_n^m)^2+(h_n^m)^2\}\,.$$

In evaluating this last integral we have also made use of the differential equation satisfied by P_n^m. A simple addition gives us

$$\overline{T_n^2} = (n+1)\sum_{m=0}^{n} \{(g_n^m)^2+(h_n^m)^2\}\,.$$

Similar equations to the above have been listed by Lowes (1966).

TABLE 2

$\bar{X}_n$, $\bar{Y}_n$, AND $\bar{T}_n$ IN γ UNITS AND $n!M_n$ IN γ(EARTH RADII)$^{n+2}$

	$n = 1$	2	3	4	5	6	7	8
$\bar{X}_n$	24989	3550	2944	1872	729	379	219	59
$\bar{Y}_n$	4352	2988	2223	1043	498	371	118	74
$\bar{T}_n$	43934	7336	5635	3214	1310	781	364	138
$n!M_n$	31066	4888	4122	2553	976	900	482	214

Some interesting relationships between the r.m.s. values can be drawn from these equations. For instance, the r.m.s. vertical intensity $\bar{Z}_n = (\overline{Z_n^2})^{\frac{1}{2}}$, the r.m.s. horizontal intensity $\bar{H}_n = (\overline{X_n^2}+\overline{Y_n^2})^{\frac{1}{2}}$, and the r.m.s. total intensity $\bar{T}_n = (\overline{T_n^2})^{\frac{1}{2}}$ bear constant ratios to each other, independent of the field anomalies and depending only on the order of the multipole. Specifically

$$\bar{Z}_n : \bar{H}_n : \bar{T}_n = \sqrt{(n+1)} : \sqrt{n} : \sqrt{(2n+1)}\,.$$

Thus the r.m.s. vertical field is always at least slightly greater than the r.m.s. horizontal field and knowledge of any one of $\bar{V}_n = (\overline{V_n^2})^{\frac{1}{2}}$, $\bar{Z}_n$, $\bar{H}_n$, or $\bar{T}_n$ is sufficient to determine the others.

The values of $\bar{X}_n = (\overline{X_n^2})^{\frac{1}{2}}$, $\bar{Y}_n = (\overline{Y_n^2})^{\frac{1}{2}}$, $\bar{T}_n$, and $n!M_n$, are given in Table 2. The dipole is seen to be by far the most important multipole. Indeed, the total magnetostatic energy, exterior to the Earth, associated with all the other multipoles, namely $\frac{1}{2}\sum_{n=2}^{\infty}\overline{T_n^2}/(2n+1)$, amounts to less than 3% of the dipole's energy $\frac{1}{6}\overline{T_1^2}$.

VII. Solution of Equations

In previous attempts to solve the multipole problem of order n the authors generally have been forced in the end to find the solutions to a set of $2n+1$ nonlinear equations of degree $n+1$, the nonlinearity being due to products of M_n and one component taken from each of the unit vectors $\mathbf{u}_{ni}$ $(i = 1, \ldots, n)$, supplemented by the n equations $\mathbf{u}_{ni} \cdot \mathbf{u}_{ni} = 1$.

Zolotov (1966) has made use of Sylvester's (1909) theory and has reduced the problem to that of solving two polynomial equations of degree $2n$. Like the other techniques this is also very awkward to apply for n greater than about five. In the method of the present paper none of the difficulties associated with the nonlinearity arise since equations (6) are essentially of degree two only. Another advantage is that nowhere are the explicit forms for the spherical harmonics required to be known. The method of solving equations (5) and (6) is briefly as follows.

It is easily seen that each term on the left-hand side of equation (5), if written out in full by making use of the recurrence relations (6), contains as a factor either u_{n1}, v_{n1}, or w_{n1}. Hence, by removing the restriction that $\mathbf{u}_{n1}$ be a unit vector and letting it have length M_n, equations (5) can be rewritten

$$\begin{vmatrix} a_n^m \\ \\ b_n^m \end{vmatrix} = \begin{vmatrix} g_n^m \\ \\ h_n^m \end{vmatrix}, \qquad m = 0, 1, \ldots, n.$$

Then equations (6), with $k = n-1$, namely

$$2g_n^m = u_{nn}\{(1+\delta_{m1})\, a_n^m\, a_{n-1}^{m-1} - \beta_n^m\, a_{n-1}^{m+1}\} - v_{nn}\{a_n^m\, b_{n-1}^{m-1} + \beta_n^m\, b_{n-1}^{m+1}\} + 2w_{nn}\, \gamma_n^m\, a_{n-1}^m\,,$$

$$2h_n^m = u_{nn}\{a_n^m\, b_{n-1}^{m-1} - \beta_n^m\, b_{n-1}^{m+1}\} + v_{nn}\{(1+\delta_{m1})\, a_n^m\, a_{n-1}^{m-1} + \beta_n^m\, a_{n-1}^{m+1}\} + 2w_{nn}\, \gamma_n^m\, b_{n-1}^m\,,$$

can be regarded as a set of $2n+1$ equations of degree two in the $2n+2$ unknowns a_{n-1}^m, b_{n-1}^m, u_{nn}, v_{nn}, and w_{nn}, and the last one can be eliminated through $\mathbf{u}_{nn} \cdot \mathbf{u}_{nn} = 1$.

If any guess is made for the axis $\mathbf{u}_{nn}$ the above equations, with $m \neq n$, become $2n-1$ linear equations in the $2n-1$ unknowns a_{n-1}^m, b_{n-1}^m and this system is easily inverted by any of the standard methods to yield a self-consistent set of initial values. By using this technique it is only necessary to make guesses for two of the $2n+1$ unknowns and one then obtains $2n+1$ values that satisfy all but two of the $2n+1$ equations. These values can be used to start a Newton–Raphson iteration on the full set of $2n+1$ equations. This type of iteration scheme was found to converge extremely quickly with apparently any initial guess for the axis. The "reduced Gaussian coefficients" a_{n-1}^m and b_{n-1}^m are then used in the left-hand sides of (6), with $k = n-2$, and the preceding method is repeated with a guess for $\mathbf{u}_{n,n-1}$. This process is continued until the final set of equations "to be solved" (equations (6) with $k = 0$) are $u_{n1} = a_1^1$, $v_{n1} = b_1^1$, and $w_{n1} = a_1^0$. In practice, the geographic polar axis was used for all initial guesses and this generated the multipoles in order of increasing distance from the geographic pole.

Using

$$M_n = \{(a_1^0)^2 + (a_1^1)^2 + (b_1^1)^2\}^{\frac{1}{2}} \tag{7}$$

we can easily reconvert $\mathbf{u}_{n1}$ to a unit vector to complete the analysis. The resulting poles (θ_{ni}, ϕ_{ni}) are given in Table 3. Equation (7) is interesting since it describes M_n as if it were the strength of an ordinary dipole whose axis coincided with one of the multipole axes.

A fifth-order test deck was run consisting of arbitrarily chosen numbers as data and initial guesses that reproduced these data with errors as large as 100 000%. In seven iterations the first axis was obtained and all errors were less than 0·01%, which illustrates the speed at which multipole analysis can now be carried out. Thus we have at our disposal a very rapid and interesting means of transforming a series of spherical harmonics under change of polar axis.

TABLE 3

POLES (θ_{ni}, ϕ_{ni}) TO NEAREST TENTH OF A DEGREE

n		$i = 1$	2	3	4	5	6	7	8
1	θ	168·6							
	ϕ	110·3							
2	θ	22·9	105·0						
	ϕ	32·8	332·0						
3	θ	20·7	58·5	63·5					
	ϕ	344·7	140·8	224·3					
4	θ	24·1	36·0	56·5	67·8				
	ϕ	108·1	218·3	307·1	42·5				
5	θ	16·5	43·0	49·4	63·2	90·6			
	ϕ	270·4	348·5	189·5	51·3	354·0			
6	θ	29·4	40·1	38·8	73·0	80·7	93·2		
	ϕ	248·2	131·0	2·1	51·0	120·4	357·9		
7	θ	17·6	39·6	51·5	54·8	58·6	64·7	65·4	
	ϕ	348·4	158·8	311·7	17·3	201·1	95·8	238·6	
8	θ	25·5	31·5	60·8	61·7	69·1	70·4	79·0	96·3
	ϕ	326·7	197·9	182·8	34·5	93·7	227·3	358·1	306·5

In a following paper (Multipole analysis. II) the secular variation of the geomagnetic multipoles will be discussed.

VIII. REFERENCES

CHARGOY, A. (1950).—*J. geophys. Res.* **55**, 47.
CHARGOY, A. (1955).—*An. Inst. Geofis. Univ. Méx.* **1**, 24.
CHARGOY, A., and ALVAREZ, M. G. (1957).—*An. Inst. Geofis. Univ. Méx.* **3**, 137.
COPSON, E. T. (1962).—"Functions of a Complex Variable." p. 299. (Cambridge Univ. Press.)
COURANT, R., and HILBERT, D. (1953).—"Methods of Mathematical Physics." Vol. 1, p. 514. (Interscience: New York.)

Gauss, C. F. (1877).—"Werke." 2nd Ed. Vol. 5, p. 631. (Roy. Soc. Sciences: Gőttingen.)
Hobson, E. W. (1955).—"Spherical and Ellipsoidal Harmonics." p. 129. (Chelsea: New York.)
Hurwitz, L., Knapp, D. G., Nelson, J. H., and Watson, D. E. (1966).—*J. geophys. Res.* **71**, 2373.
James, R. W. (1967).—*Geofis. pura appl.* **68**, 103.
Lowes, F. J. (1966).—*J. geophys. Res.* **71**, 2179.
Maxwell, J. C. (1892).—"Treatise on Electricity and Magnetism." 3rd Ed. Vol. 1, Ch. 9. (Oxford Univ. Press.)
Sylvester, J. J. (1909).—"Mathematical Papers." Vol. 3, p. 37. (Cambridge Univ. Press.)
Umov, N. (1904).—*Terr. Magn. atmos. Elect.* **9**, 105.
Winch, D. E. (1967*a*).—*Geofis. pura appl.* **67**, 112.
Winch, D. E. (1967*b*).—*Geofis. pura appl.* **68**, 90.
Winch, D. E., and Slaucitajs, L. (1966*a*).—*Geofis. pura appl.* **63**, 121.
Winch, D. E., and Slaucitajs, L. (1966*b*).—*Geofis. pura appl.* **65**, 95.
Zolotov, I. G. (1966).—*Geomag. Aeron.* **6**, 413.

NONLINEAR ADIABATIC PULSATIONS OF MASSIVE STARS

By J. O. Murphy*

[*Manuscript received March* 25, 1968]

Summary

The pulsational properties of a sequence of massive stars have been investigated in this paper. The second-order approximation to the equation of motion governing the adiabatic radial oscillations of these stars has been determined allowing for the variation of the radiation pressure throughout the star. In each case the form of the radial velocity curve at the surface of the star has been established taking into account the influence of higher modes of oscillation.

I. Introduction

This investigation into the pulsational properties of massive stars, with any uniform composition, has been based on a sequence of four stellar models $\mathscr{M} = 10$, 15, 20, and 30, where

$$\mathscr{M} = \mu^2 M/M_\odot,$$

μ being the mean molecular weight of the stellar material. These models were initially constructed by Van der Borght (1964*a*) to study the evolution of massive stars. Radiation pressure has been taken into account fully with electron scattering as the main source of opacity:

$$\kappa = 0\cdot2004(1+X),$$

where X is the abundance of hydrogen. Furthermore, if β defines the ratio of the gas pressure to the total pressure we have

$$\Gamma_1 = \beta+\tfrac{2}{3}(4-3\beta)^2/\{\beta+8(1-\beta)\}$$

for the adiabatic exponent in the presence of radiation. Table 1 gives the range of β throughout the star in each case (Van der Borght 1964*a*). These stellar models have provided the equilibrium values of the pressure p, the density ρ, the mass $M(r)$ contained within a sphere of radius r, as well as the values of g and β throughout the star.

In this paper we consider the anharmonic radial pulsations of these models and determine the radial velocity curve at the surface of the star when the variation of the radiation pressure throughout the star is taken into account. In addition, having taken a sequence of models with different mass, yet of similar chemical composition, we have been able to form comparative conclusions about the effect of increasing mass, as well as observing the effect of including higher modes of oscillation, on the form of the radial velocity curve. The pulsational stability of these models

---

* Department of Mathematics, Monash University, Clayton, Vic. 3168.

has also been investigated and will be the subject of a later study concerned with the effect of including the nonadiabatic terms in the equation of motion.

An unexpected facet of stellar pulsations was encountered with the massive star of $\mathscr{M} = 20$ when resonance was established between the first and second modes of oscillation.

Table 1

variation of β

$$\beta = \frac{\text{gas pressure}}{\text{total pressure}}$$

$\mathscr{M}$	β Surface	β Centre	$\mathscr{M}$	β Surface	β Centre
10	0·904	0·794	20	0·790	0·654
15	0·843	0·714	30	0·706	0·571

II. Linear Equation

To establish the exact form of the radial velocity curve of a pulsating star it is first necessary to determine the solution of the equation of motion governing the pulsations. However, for the stellar models under consideration in this paper, no general solution of this partial differential equation can be established, and accordingly we have introduced an expansion involving the eigenfunctions of the linear problem as a method of solution for this equation. Hence as a first step we consider the linear problem and derive the eigenfunctions for the respective stellar models.

The linear differential equations governing small radial adiabatic pulsations may be written in the form (Schwarzschild and Härm 1959)

$$x\frac{\mathrm{d}}{\mathrm{d}x}\left(\frac{\delta r}{r}\right) = -\frac{1}{\Gamma_1}\frac{\delta p}{p} - 3\frac{\delta r}{r}, \tag{1}$$

$$x\frac{\mathrm{d}}{\mathrm{d}x}\left(\frac{\delta p}{p}\right) = \left\{\frac{\delta p}{p} + \left(4+\omega^2\frac{x^3}{q}\right)\frac{\delta r}{r}\right\}\frac{\rho}{p}\frac{GM(r)}{Rx}, \tag{2}$$

where δr and δp are the amplitudes of the pulsations in position and pressure with $\delta r/r$ and $\delta p/p$ defining the relative amplitudes respectively. In these equations p, ρ, and r refer to the equilibrium values of pressure, density, and radius respectively, R is the radius of the star, and the nondimensional variables x and q, together with ω^2, have been introduced such that

$$x = \frac{r}{R}, \qquad q = \frac{M(r)}{M}, \qquad \text{and} \qquad \omega^2 = \frac{R^3}{GM}\left(\frac{2\pi}{\text{period}}\right).$$

The boundary conditions associated with equations (1) and (2) require $\delta r = 0$ at the centre for $r = 0$, and $\delta p = 0$ at the surface for $r = R$. These conditions arise from the physical requirements that the Lagrangian displacement and the Lagrangian variation in pressure should be zero at the centre and surface respectively.

The solution of the eigenvalue problem, represented by equations (1) and (2) subject to the above boundary conditions, was undertaken using the method given by Van der Borght (1964*b*). Table 2 gives for each stellar model the first six eigenvalues ω_k, with ω_1 corresponding to the fundamental mode of oscillation. Furthermore, the associated eigenfunctions $\eta_k = \delta r/r$ together with their first derivatives $\eta_k' = \mathrm{d}\eta_k/\mathrm{d}x$ were derived and tabulated in normalized form for the later calculation of the coefficients $C_{ij,k}$ as detailed in the next section.

TABLE 2

EIGENVALUES FOR FIRST SIX MODES OF OSCILLATION

Model	Mode					
$\mathscr{M}$	ω_1	ω_2	ω_3	ω_4	ω_5	ω_6
10	2·0507	3·6487	4·9764	6·2587	7·5160	8·7563
15	1·8657	3·5699	4·8924	6·1628	7·4069	8·6355
20	1·7457	3·5187	4·8358	6·0976	7·3343	8·5572
30	1·5971	3·4525	4·7602	6·0125	7·2430	8·4604

III. NONLINEAR RADIAL OSCILLATIONS

From the basic Lagrangian equations, as given by Ledoux and Walraven (1958), the equation of motion for radial adiabatic oscillations can be written in the form

$$\frac{\partial^2 r}{\partial t^2} = -\frac{r^2}{\rho_0 r_0^2}\frac{\partial}{\partial r_0}\left\{p_0\left(\frac{3r_0^2}{\partial(r^3)/\partial r_0}\right)^{\Gamma_1}\right\} - G\frac{M(r_0)}{r^2}, \tag{3}$$

where the zero subscript indicates the equilibrium value.

Substituting

$$r = r_0(1+\xi), \qquad \xi(r_0,t) \tag{4}$$

into equation (3) and using primes to denote differentiation with respect to r_0, it follows that

$$\rho_0 r_0 \frac{\partial^2 \xi}{\partial t^2} = -(1+\xi)^2 \frac{\partial}{\partial r_0}\left(p_0(1+\xi)^{-2\Gamma_1}(1+\xi+r_0\xi')^{-\Gamma_1}\right) - g_0\rho_0(1+\xi)^{-2}.$$

Neglecting third and higher order terms of ξ on expansion, and recalling that Γ_1 varies with r_0, we obtain

$$\begin{aligned}\rho_0 r_0 \frac{\partial^2 \xi}{\partial t^2} = {} & r_0 p_0 \Gamma_1 \xi'' + (p_0\Gamma_1' r_0 + 4p_0\Gamma_1 - g_0\rho_0\Gamma_1 r_0)\xi' + (4g_0\rho_0 + 3p_0\Gamma_1' - 3g_0\rho_0\Gamma_1)\xi \\ & -(9p_0\Gamma_1\Gamma_1' + \tfrac{15}{2}p_0\Gamma_1' - \tfrac{9}{2}g_0\rho_0\Gamma_1^2 + \tfrac{9}{2}g_0\rho_0\Gamma_1 + 2g_0\rho_0)\xi^2 \\ & -(6p_0\Gamma_1'\Gamma_1 r_0 - p_0\Gamma_1' r_0 + 12p_0\Gamma_1^2 - 4p_0\Gamma_1 - 3g_0\rho_0\Gamma_1^2 r_0 + g_0\rho_0 r_0\Gamma_1)\xi\xi' \\ & -(3p_0 r_0\Gamma_1^2 - p_0 r_0\Gamma_1)\xi\xi'' \\ & -(p_0\Gamma_1'\Gamma_1 r_0^2 + \tfrac{1}{2}p_0\Gamma_1' r_0^2 + 4p_0\Gamma_1^2 r_0 + 2p_0\Gamma_1 r_0 - \tfrac{1}{2}g_0\rho_0\Gamma_1^2 r_0^2 - \tfrac{1}{2}g_0\rho_0\Gamma_1 r_0^2)\xi'^2 \\ & -(p_0 r_0^2\Gamma_1 + p_0 r_0^2\Gamma_1^2)\xi'\xi''.\end{aligned} \tag{5}$$

The eigenfunctions $\eta_i(r_0)$ of the linear problem have been introduced by adopting a solution of the form

$$\xi = \sum_{i=1}^{n} \eta_i(r_0)\, q_i(t)\,. \tag{6}$$

Noting that the $\eta_i(r_0)$ determined in Section II satisfy the orthogonality conditions

$$\int_0^R \rho_0 r_0^4 \eta_i \eta_j \,\mathrm{d}r_0 = 0 \qquad \text{if} \qquad i \neq j\,, \tag{7}$$

and taking $n = 6$, that is, considering the first six modes of oscillation, we now proceed to establish the differential equations that will give the q's as functions of time.

On substitution of (6) into (5) the linear terms in ξ on the right-hand side of (5) reduce to

$$-\sum_{i=1}^{6} \sigma_i^2 \rho_0 r_0 \eta_i q_i$$

when an alternative form of the linear problem

$$\eta_i'' + \left(\frac{4}{r_0} + \frac{\Gamma_1'}{\Gamma_1} - \frac{g_0\rho_0}{p_0}\right)\eta_i' + \left(\frac{\sigma_1^2\rho_0}{\Gamma_1 p_0} + \frac{3\Gamma_1'}{r_0\Gamma_1} - \frac{3g_0\rho_0}{r_0 p_0} + \frac{4g_0\rho_0}{r_0 p_0 \Gamma_1}\right)\eta_i = 0\,, \tag{8}$$

where $\sigma_i^2 = \omega_i^2 GM/R^3$, is taken into account.

Following this substitution we multiply the resulting equation successively by

$$r_0^3 \eta_k(r_0)\,\mathrm{d}r_0\,, \qquad k = 1, 2, \ldots, 6$$

and then integrate over the volume of the star, observing that this procedure enables us to apply the orthogonality conditions (7). Finally, by writing $\tau = \sigma_1 t$ for the time variable, and with $x = r/R$, the resulting differential equations take the form

$$\frac{\mathrm{d}^2 q_k}{\mathrm{d}\tau^2} = -(\sigma_k^2/\sigma_1^2) q_k - \sum_{i,j} C_{ij,k}\, q_i q_j\,, \qquad k = 1, 2, \ldots, 6\,, \tag{9}$$

where

$$\sigma_k^2 = (GM/R^3)\omega_k^2\,, \qquad I_k = \frac{\omega_1^2 G}{\mathscr{R}} \int_0^1 \frac{\beta\bar{p}}{\bar{t}} x^4 \eta_k^2 \,\mathrm{d}x\,,$$

and

$$\begin{aligned} C_{ij,k} = \mathscr{M}^{-1}\Bigg[&\int_0^1 \left\{ 2\Gamma_1'(9\Gamma_1 + \tfrac{15}{2})x^2 - (9\Gamma_1^2 - 9\Gamma_1 - 4)\frac{\beta G\bar{m}}{\mathscr{R}\bar{t}} \right\} \bar{p} x \eta_i \eta_j \eta_k \,\mathrm{d}x \\ &+ \int_0^1 \left\{ \Gamma_1' x^2 (6\Gamma_1 - 1) - \Gamma_1(1 - 3\Gamma_1)\left(4x - \frac{\beta G\bar{m}}{\mathscr{R}\bar{t}}\right) \right\} \bar{p} x^2 (\eta_i \eta_j' + \eta_i' \eta_j)\eta_k \,\mathrm{d}x \\ &+ \int_0^1 \Gamma_1(3\Gamma_1 - 1)\bar{p} x^4 (\eta_i \eta_j'' + \eta_i'' \eta_j)\eta_k \,\mathrm{d}x \\ &+ \int_0^1 \left\{ 2\Gamma_1' x^2 (\Gamma_1 + \tfrac{1}{2}) - \Gamma_1\left(\frac{G\bar{m}(\Gamma_1 + 1)}{\mathscr{R}\bar{t}} - 4x(2\Gamma_1 + 1)\right) \right\} \bar{p} x^3 \eta_i' \eta_j' \eta_k \,\mathrm{d}x \\ &+ \int_0^1 \Gamma_1(\Gamma_1 + 1)\bar{p} x^5 (\eta_i \eta_j'' + \eta_i'' \eta_j)\eta_k \,\mathrm{d}x \Bigg] \Big((1 + \delta_j^i) I_k\Big)^{-1}\,, \end{aligned}$$

δ_j^i being the Kronecker delta.

Moreover, we have introduced the new variables $\bar{p}$, $\bar{t}$, and $\bar{m}$ as tabulated in Van der Borght (1964*a*), which enables us to evaluate the coefficients of the six differential equations (9) directly from the data provided by the stellar models.

TABLE 3

VALUES OF COEFFICIENTS σ_k^2/σ_1^2 AND $C_{ij,k}$ OCCURRING IN EQUATIONS (9) FOR SIX MODES OF OSCILLATION

For the model $\mathscr{M} = 20$

i, j	$k = 1$	2	3	4	5	6
			σ_k^2/σ_1^2			
	1·0000					
		4·0629				
			7·6736			
				12·2005		
					17·6513	
						24·0284
			$C_{ij,k}$			
1, 1	3·3194	−14·6495	31·7457	−49·9432	57·1571	−47·4572
1, 2	−0·2103	−0·5776	−5·6690	4·4219	−6·1191	2·4007
1, 3	0·0215	−1·2276	−2·9899	−6·4225	0·7110	−5·9993
1, 4	−0·0065	−0·0940	−2·8324	−6·1965	−8·8701	−5·1163
1, 5	−0·0012	−0·0880	−0·6617	−5·5409	−11·3863	−14·4451
1, 6	0·0010	−0·0670	−0·5849	−2·7893	−11·2610	−19·9250
2, 2	−0·0087	−2·2999	−8·4981	−7·8841	−3·3469	−8·2862
2, 3	−0·0108	−1·0348	−7·9207	−16·3942	−14·5574	−14·9762
2, 4	−0·0014	−0·3322	−4·0605	−17·1232	−28·9952	−30·5427
2, 5	−0·0015	−0·1522	−1·9184	−11·6683	−34·4221	−51·4463
2, 6	−0·0015	−0·1616	−1·6132	−8·8369	−31·4068	−64·8958
3, 3	−0·0035	−0·8571	−7·0089	−21·5485	−32·2827	−34·6511
3, 4	−0·0034	−0·4662	−4·9857	−20·6151	−45·5674	−62·5901
3, 5	−0·0021	−0·2798	−3·3428	−17·7354	−50·9637	−88·7908
3, 6	−0·0026	−0·2836	−2·9855	−16·2186	−53·3670	−108·0211
4, 4	−0·0028	−0·4907	−4·9584	−22·1682	−57·6872	−96·4446
4, 5	−0·0034	−0·4340	−4·6840	−23·0341	−67·6441	−127·7014
4, 6	−0·0039	−0·4527	−4·7801	−24·6854	−77·5751	−157·4310
5, 5	−0·0043	−0·5588	−5·7257	−28·1125	−85·0959	−168·9295
5, 6	−0·0057	−0·6591	−6·7403	−33·5582	−104·1346	−213·0241
6, 6	−0·0076	−0·8699	−8·6996	−42·8874	−133·1334	−274·7825

Indeed one can readily verify the following relationships between the two sets of variables

$$\rho = \frac{M_\odot \beta \bar{p}}{R^3 \mathscr{R} \bar{t} \mu^2}, \qquad p = \frac{M_\odot^2 \bar{p}}{R^4 \mu^4}, \qquad g = \frac{G}{R^2 x^2} \bar{m} \frac{M_\odot}{\mu^2},$$

$$M(r) = \bar{m}(M_\odot/\mu^2), \qquad \text{and} \qquad \mathscr{M} = \mu^2(M/M_\odot),$$

where the mean molecular weight $\mu = (2X + 0{\cdot}75\,Y + 0{\cdot}5\,Z)^{-1}$. After making

allowance for the separate formulation of $\mathrm{d}\beta/\mathrm{d}x$ in the core and envelope (Van der Borght 1964*a*), that is,
in the convective core

$$\frac{\mathrm{d}\beta}{\mathrm{d}x}=\frac{G\beta(1-\beta)}{\mathscr{R}x^2}\frac{\bar{m}}{\bar{t}}\frac{3\beta^2}{32-24\beta-3\beta^2}$$

and in the radiative envelope

$$\frac{\mathrm{d}\beta}{\mathrm{d}x}=\frac{1}{\mathscr{R}}\frac{\beta(1-\beta)}{\bar{t}}\frac{1}{x^2}\left(\frac{\kappa\mu^2L}{4\pi c(1-\beta)M_\odot}-\bar{m}G\right),$$

we computed values of Γ_1' throughout the star using

$$\frac{\mathrm{d}\Gamma_1}{\mathrm{d}x}=\frac{(21\beta^2-48\beta+32)}{3(8-7\beta)^2}\frac{\mathrm{d}\beta}{\mathrm{d}x}.$$

To calculate η_i'' we expressed (8) in terms of the new variables and then used the values of η_i and η_i' as determined previously from (1) and (2).

The coefficients $C_{ij,k}$ of the differential equations (9) have been tabulated in Table 3 for the star $\mathscr{M}=20$ only, as the coefficients determined in the case of the other three stars under consideration follow a similar pattern. We should remark at this stage that the radius R of the star has been eliminated from these calculations and that whereas the quantities X, Y, and Z, determining the uniform composition of the star, are not directly involved in the calculations they do enter implicitly through the quantity $\mathscr{M}$.

IV. Numerical Solutions and Radial Velocity Curves

The system of simultaneous second-order differential equations (9) has been solved by numerical integration for each stellar model. The following initial values were adopted

$$q_1(0)=0\cdot 03\,,\qquad \frac{\mathrm{d}q_k(0)}{\mathrm{d}\tau}=0\,,\qquad \text{for}\quad k=1,2,\ldots,6\,,$$

and an iterative procedure was used to determine the values of

$$q_k(0)\,,\qquad k=2,3,\ldots,6\,,$$

under the requirement that the solutions for the second and higher modes of oscillation should be periodic and have the same period as the first mode $q_1(\tau)$.

As evidenced in Table 4, which lists the values of $q_k(0)$ as determined above, a factor that no doubt assisted in the simultaneous solution of the differential equations is the relative independence of the $q_k(0)$ values when additional higher modes are taken into account.

As mentioned in Section I, a resonance interaction was encountered between the first and second modes of oscillation for the star $\mathscr{M}=20$. From Table 3 it is seen that

$$\sigma_2^2/\sigma_1^2=\omega_2^2/\omega_1^2=4\cdot 0629$$

and some significance can apparently be placed on the value of this ratio.

The radial velocity curve at the surface of the star is determined, for one period of τ, by

$$\frac{\mathrm{d}q(\tau)}{\mathrm{d}\tau} = \sum_{k=1}^{6} \frac{\mathrm{d}q_k(\tau)}{\mathrm{d}\tau}\eta_k(1) = \sum_{k=1}^{6} \frac{\mathrm{d}q_k(\tau)}{\mathrm{d}\tau}$$

as the $\eta_k(x)$ have been normalized at the surface $x = 1$.

The skewness of the radial velocity curve is established by the factor K, the ratio of the rise of the radial velocity from minimum to maximum to the total period, and can be considered to some extent as a measure of the effect of including the nonlinear terms in the equation of motion. We would expect the value of K from the linear theory to be one-half. Values of K, taking into account the first four, five, and six modes of oscillation, are tabulated in Table 4.

TABLE 4

RESULTS OF NUMERICAL COMPUTATIONS

Values are given of $q_k(0)$ adopted to ensure periodicity, skewness of the radial velocity curve K, and period of oscillation τ

No. of Modes	$q_1(0)$	$q_2(0)$	$q_3(0)$	$q_4(0)$	$q_5(0)$	$q_6(0)$	K	τ
				$\mathscr{M} = 10$				
First 4	0·0300	−0·0036	−0·0048	0·0044			0·302	6·290
5	0·0300	−0·0036	−0·0048	0·0040	−0·0030		0·302	6·290
6	0·0300	−0·0036	−0·0048	0·0040	−0·0030	0·0025	0·310	6·290
				$\mathscr{M} = 15$				
4	0·0300	−0·0158	−0·0048	0·0046			0·254	6·300
5	0·0300	−0·0159	−0·0046	0·0043	−0·0121		0·159	6·300
6	0·0300	−0·0158	−0·0047	0·0044	−0·0083	0·0025	0·159	6·300
				$\mathscr{M} = 20$				
4	0·0300	0·0632	−0·0078	0·0009			0·671	6·335
5	0·0300	0·0632	−0·0079	0·0010	0·0011		0·679	6·335
6	0·0300	0·0641	−0·0077	0·0012	0·0074	0·0077	0·758	6·335
				$\mathscr{M} = 30$				
4	0·0300	0·0146	−0·0036	0·0046			0·717	6·350
5	0·0300	0·0146	−0·0043	0·0046	−0·0036		0·701	6·350
6	0·0300	0·0146	−0·0051	0·0047	−0·0034	0·0027	0·693	6·350

The main significance of these results is that, overall, the inclusion of higher modes of oscillation has relatively little effect on the value of K and the general shape of the radial velocity curve, whereas an increase in mass (and radiation pressure) produces an appreciable change in both the skewness and the form of the radial velocity curve. This trend is illustrated in Figure 1. There is also an increase in the period of oscillation corresponding to an increase in mass; for the star $\mathscr{M} = 10$ we have the value of $\tau = 6{\cdot}29$ for one period, and for the star $\mathscr{M} = 30$,

$\tau = 6 \cdot 35$, as compared with the linear case where $\tau = 6 \cdot 28$ for one period. Values of the period τ are also given in Table 4.

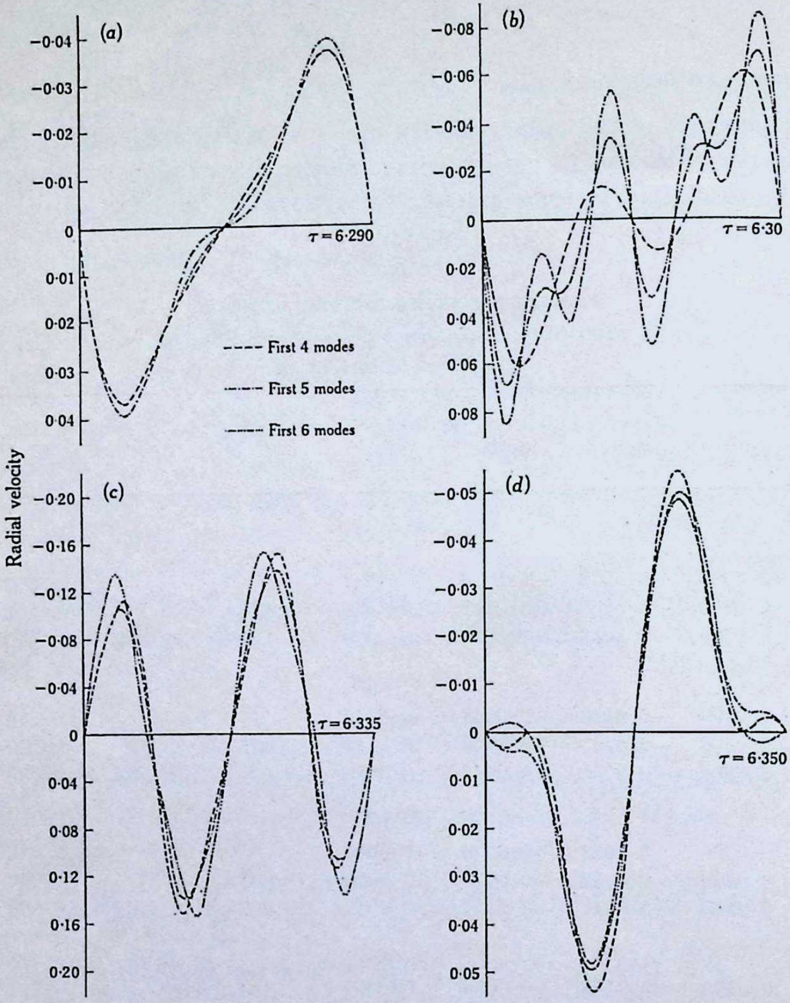

Fig. 1.—Radial velocity curves determined at the surface of the star taking into account the influence of the first four, five, and six modes of oscillation for (a) $\mathscr{M} = 10$, (b) $\mathscr{M} = 15$, (c) $\mathscr{M} = 20$, and (d) $\mathscr{M} = 30$.

Finally, it should be stressed that these results apply to stars having any uniform composition. However, if we were to consider a "normal" composition, say $X = 0 \cdot 70$, $Y = 0 \cdot 27$, $Z = 0 \cdot 03$, then these results would equally apply to stars in the mass range $26 \cdot 2\, M_\odot$ to $78 \cdot 5\, M_\odot$.

V. ACKNOWLEDGMENT

I thank Professor R. Van der Borght for suggesting the problem and for his assistance and encouragement throughout this investigation.

VI. REFERENCES

LEDOUX, P., and WALRAVEN, T. (1958).—*In* "Handbuch der Physik". Vol. 51, p. 353. (Springer-Verlag: Berlin.)

SCHWARZSCHILD, M., and HÄRM, R. (1959).—*Astrophys. J.* **129**, 637.

VAN DER BORGHT, R. (1964*a*).—*Aust. J. Phys.* **17**, 165.

VAN DER BORGHT, R. (1946*b*).—*Bull. Acad. r. Belg. Cl. Sci.* (5^e) **50**, 959.

THE DISTRIBUTION OF LINEAR POLARIZATION OVER 13 EXTENDED SOURCES AT 21·2 CM WAVELENGTH

By D. Morris* and J. B. Whiteoak*

[*Manuscript received February* 8, 1968]

Summary

The distribution of linear polarization over 13 bright radio sources has been determined at 21 cm wavelength with an east–west interferometer. The results are presented in the form of strip brightness distributions of polarized flux and direction of polarization, with a resolution of 1′ by 20′. It is suggested that axial rotation during evolution contributes to the observed polarization features of extended radio sources.

I. Introduction

Observations of the distribution of linear polarization over radio sources, particularly if obtained at more than one wavelength, help to trace their evolution by providing information about the magnetic field configurations and associated internal mass motions and depolarization mechanisms. At present, data are available for only those sources that can be resolved by single antennas and for a few additional bright sources observed by interferometer techniques. With regard to the latter group, the work of Seielstad (1967) at 10·6 cm is the most comprehensive and also contains a summary of previous investigations. The observations to be described here form the initial observations taken to provide comparable data at 21 cm, and to extend the programme to sources at southern declinations.

Thirteen radio sources identified with galaxies and containing multiple components were studied using the east–west baseline of the interferometer at Parkes. The measured Fourier transforms of the Stokes parameters Q and U were inverted by an approximate method to yield strip scans across each source with an effective resolution of approximately 1′ by 20′. The choice of sources was confined to those that are appreciably resolved by a beam of half-power width 1′ and have an integrated polarized flux density of at least 0·5 f.u.† at 21 cm wavelength.

II. Equipment

The interferometer has been described by Cole (1967) and Batchelor, Cole, and Shimmins (1968). The collecting elements consist of the 210 ft radio telescope and a 60 ft parabola mounted on railway tracks which run from separations of 400 ft to 1400 ft in north–south and east–west directions. Both telescopes have altazimuth mountings, the pointing of the 60 ft telescope being slaved to the 210 ft one. As a consequence of this type of mounting, position angle (i.e. orientation with respect to celestial coordinates) is related to feed orientation through the parallactic angle.

---

* Division of Radiophysics, CSIRO, P.O. Box 76, Epping, N.S.W. 2121.

† 1 flux unit = $10^{-26}\,\mathrm{W\,m^{-2}\,Hz^{-1}}$.

Aust. J. Phys., 1968, **21**, 475–92

Two servo systems driven from the "master equatorial" system of the 210 ft telescope constrained the orientation of the feeds to a selected position angle. Although the absolute accuracy of the servo control was about 1°, the relative orientation of the two feeds could be maintained to a higher accuracy. The zero point of the position angle scale was ascertained by radiating a linearly polarized signal from the apex of the 210 ft paraboloid. The receivers used identical crystal mixers without image rejection and were operated with a 1412 MHz local oscillator. The i.f. bandwidth was 10 MHz.

The factors contributing to the instrumental polarization and their removal have been described by Seielstad (1967). At Parkes, in preliminary observations using double-dipole primary feeds, the instrumental circular polarization was 2% on-axis, increasing to as much as 15% off-axis. However, an acceptable performance was obtained by using a hybrid-mode horn (Minnett and Thomas 1966) to illuminate the 210 ft antenna, and a cylindrical horn with surrounding chokes (von Geyer 1966) for the smaller telescope. The desirable characteristics of the hybrid-mode horn are a circularly symmetric beam and a polarization that is linear and constant in direction over the entire aperture of the telescope. In principle there are no cross-polarized side lobes. In contrast to conventional feeds, for which the overall linear polarization of the telescope depends on the cancellation of contributions with different polarizations from different sectors of the antenna surface, the overall polarization is less sensitive to surface irregularities and their variation with zenith angle. The design of the particular feeds used was effected by Dr. B. McA. Thomas of the Division of Radiophysics, CSIRO. The residual instrumental circular polarization was further reduced by appropriate adjustment of the feed ellipticity. For this purpose, the hybrid-mode feed contained orthogonal probes. One of these supplied the receiver directly; the other fed the receiver through a line-stretcher, variable attenuator, and directional coupler. By adjustment of these components during observations of the Orion Nebula, the residual instrumental circular polarization was reduced to 0·74%.

The resulting characteristics of the interference polarimeter are shown in Figure 1; (*a*) shows the variation in offset (F.A.(60)—F.A.(210)) required for oppositely polarized telescopes as a function of feed orientation of the 210 ft telescope, while (*b*) similarly shows the variation in instrumental circular polarization (the residual fringe for the appropriate offset). The deviation from orthogonality in the scale readings and the variation of the offset reflect instrumental linear polarization together with any dial errors (Morris, Radhakrishnan, and Seielstad 1964). The variation is sufficiently slow with feed angle for corrections to be applied during the observations. The primary beam patterns with parallel and orthogonal feeds are shown in Figure 2. Figure 2(*b*) shows the changes in the instrumental circular polarization during two scans in right ascension across M87 taken with the feeds set orthogonal at position angles of 0° and 90° approximately. One scan (solid curve) was taken through the position of the source, the other (dashed curve) at the declination where the maximum responses in the cross-polarized side lobes are located. It can be seen that at no position does the response exceed 2% of the response with parallel feeds on-axis. No detectable variation in these characteristics occurred with zenith angle.

III. Observations

The theory and assumptions underlying the techniques used have been described in detail by Seielstad (1967). The linear polarization distribution was initially derived in terms of the brightness distributions for the Stokes parameters I (the total flux density), Q ($= I_p \cos 2\theta$, where I_p is the polarized flux density and θ the position angle of polarization), and U ($= I_p \sin 2\theta$). The fourth parameter V (representing circular polarization) was assumed to be zero. The interferometer observations yielded the Fourier transforms of these parameters. Complete restoration of the observations to brightness distributions requires absolute phase as well as amplitude information for I, Q, and U at each antenna spacing. Since the Parkes interferometer was neither phase-stable nor accurately surveyed, only measurements of the phases of Q and U relative to $I+Q$ could be made.

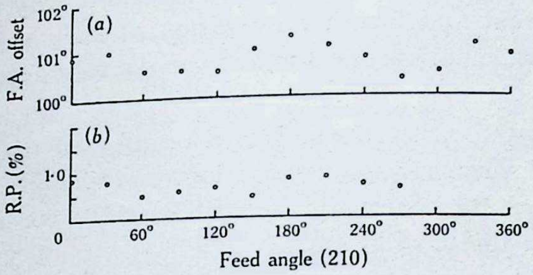

Fig. 1.—Variation with feed angle of the 210 ft telescope for (a) the offset of the feed orientation of the 60 ft telescope to produce feed orthogonality, and (b) the residual polarization (R.P.) with orthogonal feeds.

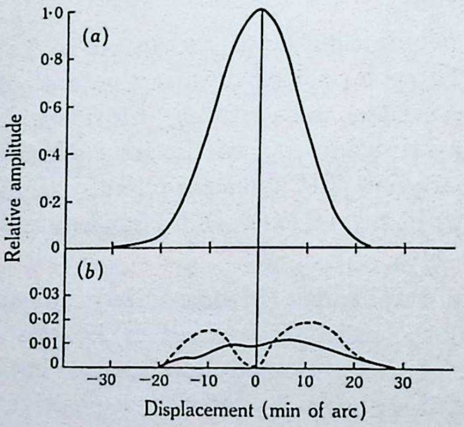

Fig. 2.—Primary beam shapes of the interferometer with (a) parallel feeds and (b) orthogonal feeds. The dashed curve in (b) represents a scan taken off-source showing the maximum contributions from cross-polarized side lobes.

Each source was observed at a series of antenna spacings separated by 100 or 200 ft. If possible, the time of observation was usually chosen so that the projected baseline of the interferometer was parallel to either the major or minor axis of the source. At each separation four measurements were made. Firstly, $\frac{1}{2}(I+Q)$ was observed, with the position angles of both feeds equal to the direction of integrated polarization (as given by single-dish observations and listed in Table 1). The quantity $\frac{1}{2}U$ was then observed by rotating the feed of the 60 ft telescope in a positive sense to its orthogonal position. Further rotation of both feeds through +45° in the same direction yielded observations of the quantity $\frac{1}{2}Q$. The fourth and final observation consisted of a repetition of the first. In theory, the chosen frame of reference for the Stokes vectors is such that the zero-spacing value of U is zero, while that of Q is the integrated polarized flux (Morris, Radhakrishnan, and Seielstad 1964). In practice, however, ionospheric Faraday rotation caused a small rotation of this frame of reference. With a receiver time constant of 1 sec, the natural fringes were recorded on paper tape at half-second intervals. The observations of U and Q generally extended over 3 or 4 min; somewhat smaller times were used for $I+Q$. All subsequent reductions were effected with a CDC 3200 computer. For each observation, values of fringe amplitude and phase were calculated by the method of least squares. The relative phases of U and Q were determined by interpolation between the phases of the first and fourth observation at each spacing. At this stage, corrections for signal attenuation due to the receiver time constant were applied.

The observation of PKS 1226+02 with parallel feeds confirmed that the variation of the interferometer gain with antenna separation was negligible. A flux density calibration was provided by observation of PKS 0521−36, which was assumed to have a flux density of 16 f.u. at 21 cm.

IV. Results

The sources observed and relevant polarization data are listed in Table 1. Most of the columns are self-explanatory. The polarization data in the first columns were obtained with a single dish and were used as zero-spacing information. The last column contains the calculated Faraday rotation due to the ionosphere at the time of observation. The calculations are based on $f_0 F_2$ data supplied by the Ionospheric Prediction Service and assume a thin uniform slab as a model for the ionosphere (Roberts and Komesaroff 1965, p. 138).

Table 2 contains the measured fringe amplitudes (in flux units) and relative phases (in degrees). For each measurement the baseline parameters, i.e. the length S in wavelengths and position angle P.A. of the projected baseline at the source position are shown. The sign convention of the phases is such that a positive value corresponds to an apparent displacement to greater right ascensions (in accordance with the conventions of Fomalont (1976*a*) and Seielstad (1967)). The errors quoted are standard deviations derived from the least squares programme that was used to derive the amplitudes and phases. Additional errors in phase due to inaccuracy in interpolation may amount to ±20°. The values adopted for zero antenna spacing contained an allowance for ionospheric Faraday rotation. As an illustration, Figure 3 shows the result for the source PKS 0043−42.

Only for PKS 1648+05, where the percentage polarization is low, have corrections for a constant instrumental circular polarization (0·74%) been included. The correction was regarded as unnecessary in all other cases.

(*a*) *Approximate Inversion of Visibility Functions*

Rather than fit models to the observations, with the disadvantage of requiring certain assumptions regarding basic model shapes, approximate one-dimensional brightness distributions of $I+Q$, U, and Q were calculated by Fourier inversion, following the method of Fomalont (1967*b*). These enabled the distribution of polarized flux density and polarization direction to be derived. For such a technique, absolute phases for the observations are necessary. It was assumed that the phase of $I+Q$ was not significantly dependent on the Q contribution, so that the results of other observers, which in general are for some combination of both U and Q, could be used. It was possible to interpolate between the observations of Fomalont (1967*a*) when the present results were obtained with a projected baseline directed near position angle 90°. For sources not observed by Fomalont, absolute phases of $I+Q$ were calculated from the models of Ekers (1967), or in the case of PKS 0106+13 from a simple model composed of Gaussian components. For Ekers's models, the sign of the calculated phase is not known, and both senses were tried in the inversions. Only one sense is shown in the figures, since the changes produced by sign reversal were small. In the case of PKS 2356−61, the assumed model is symmetrical and the resultant phase is either ±180° or 0°. Naturally, the uncertainties in the derived brightness distributions are larger when models are used to calculate the phases. For each inversion it was assumed that all the observations were made at a constant direction of projected baseline. In reality, observations were taken over a period of time during which this direction varied continuously. The effect of this variation is not too important when the position angle is aligned along the major axis of the

Table 1

ASSUMED SOURCE PARAMETERS

PKS Source No.	Brightness Temp.* $(10^3\ ^\circ\mathrm{K})$	Polarization (%)	Position Angle (°)	Major Axis‡ (°)	Intrinsic Angle§ (°)	Flux Density‖ (f.u.)	Faraday Rotation¶ (°)
		at 21·5 cm†					
0043−42	2·5	9·8±0·6	137±2	136±2	136±2	8·1	6·3
0106+13	12	8·2±0·3	58±3	20±8	91±2	15·5	7·3
0356+10	1·0	6·0±0·6	74±5	25±10	50±6	11·7	6·8
0518−45	0·9	3·1±0·4	50±5	105±2	104±4	71·8	4·0
0618−37	1·0	14·0±4·3	71±6	84±4	69±3	3·0	3·1
0945+07	1·6	5·5±0·4	136±2	90±10	160±6	8·5	6·5
1216+06	0·6	7·7±0·3	118±3	85±7	94±2	18	3·0
1322−42	4·5	7·0±0·5	175±3	46·5±2	147±3	288	2·0
1559+02	1·4	6·0±0·9	2±5	90	156±5	7·4	3·3
1648+05	19	0·9±0·2	41±2	100±2	28±3	46	4·1
1717−00	6·1	2·9±0·3	167±2	90	82±8	50	7·2
2152−69	5·0	2·7±0·2	116±4	96±10	32±3	32	3·3
2356−61	2·5	4·9±0·3	66±2	132±2	7±5	23	6·6
0521−36		Flux calibration				16·0	

* Morris and Berge (1964) and Ekers (1967).

† Gardner and Davies (1966*b*).

‡ Maltby and Moffet (1962) and Ekers (1967).

§ Gardner and Davies (1966*a*).

‖ At 21 cm from the Parkes catalogue of radio sources.

¶ Calculated from data from the Ionospheric Prediction Service.

TABLE 2

OBSERVED VALUES OF FRINGE AMPLITUDE AND RELATIVE PHASE

(1)	(2)	(3)	(4)	(5)	(6)	(7)	(8)	(9)	(10)	(11)
Parallel Feeds			Orthogonal Feeds							
S (λ)	P.A. (°)	$I+Q$ (f.u.)	S (λ)	P.A. (°)	U (f.u.)	$\Delta\phi(U)$ (°)	S (λ)	P.A. (°)	Q (f.u.)	$\Delta\phi(Q)$ (°)
PKS 0043−42										
0	—	9·1±0·5	0	—	0·21±0·06	—	0	—	0·96±0·1	—
403	153	6·2±0·4	400	155	0·34±0·05	50±8	397	157	0·83±0·08	346±6
511	146	4·9±0·12	508	147	0·21±0·04	22±10	503	149	0·95±0·06	1±3
636	140	4·1±0·13	631	141	0·18±0·06	345±21	624	143	0·81±0·04	3±4
783	134	2·7±0·14	777	135	0·18±0·12	275±40	768	136	0·44±0·06	24±9
953	125	1·6±0·14	947	126	0·05±0·05	299±62	937	128	0·28±0·04	41±11
1116	121	1·2±0·13	1108	122	0·15±0·07	238±28	1099	123	0·17±0·04	108±18
1278	116	1·8±0·12	1271	117	0·14±0·05	287±23	1261	118	0·23±0·05	137±13
1440	113	2·5±0·13	1434	113	0·15±0·15	37±58	1425	114	0·11±0·06	93±28
1578	109	2·8±0·1	1572	110	0·10±0·20	—	1563	111	0·12±0·13	—
1732	106	3·1±0·6	1727	106	0·21±0·07	7±26	1718	107	0·07±0·07	212±58
1877	102	2·7±0·1	1873	103	0·07±0·21	—	1865	104	0·16±0·16	—
PKS 0106+13 (3C 33)										
0	—	14·2±0·09	0	—	0·24±0·08	180	0	—	0·95±0·09	360
472	77	9·8±0·2	466	77	0·29±0·06	195±10	457	76	0·77±0·05	342±10
601	79	8·2±0·1	596	79	0·22±0·05	150±12	588	79	0·77±0·05	338±11
761	81	6·8±0·1	750	80	—	—	739	80	—	—
921	83	5·3±0·1	914	82	0·29±0·04	206±10	906	82	0·65±0·05	6±12
1104	85	4·4±0·1	1093	84	—	—	1081	84	0·57±0·06	5±15
1275	86	4·8±0·1	1270	86	0·42±0·05	199±8	1263	86	0·73±0·09	25±10
1424	87	3·9±0·1	1420	87	0·44±0·11	148±16	1416	87	0·66±0·05	354±16
1574	89	5·4±0·4	1573	88	0·40±0·08	175±15	1571	88	0·77±0·05	2±8
1895	91	5·9±0·1	1899	91	0·31±0·08	—	1904	91	0·87±0·06	—
PKS 0356+10 (3C 98)										
0	—	11·7±0·7	0	—	0·16±0·06	180	0	—	0·65±0·06	360
432	77	7·1±0·2	428	77	0·20±0·05	152±14	421	77	0·30±0·06	10±12
621	80	5·1±0·1	615	80	0·48±0·09	176±10	603	79	0·11±0·07	—
832	82	2·5±0·1	825	82	0·51±0·05	147±6	811	81	0·16±0·05	11±18
1041	83	1·2±0·1	1032	83	0·47±0·05	95±10	1018	83	0·10±0·05	20±20
1248	85	2·0±0·2	1241	85	0·52±0·05	—	1228	85	0·23±0·05	—
1465	86	3·2±0·1	1460	86	0·49±0·05	30±7	1447	85	0·16±0·06	309±20
1686	87	3·9±0·1	1678	87	0·43±0·06	24±8	1666	87	0·16±0·08	354±25
1919	88	4·2±0·1	1916	88	0·47±0·09	60±12	1908	88	0·13±0·06	10±27
PKS 0518–45 (Pictor A): Scan 1										
0	—	71·8±4·0	0	—	0·42±0·2	360	0	—	2·2±0·3	360
458	26	41·0±1·0	459	27	1·3±0·07	0±5	462	28	3·2±0·1	330±5
673	30	23·2±0·3	676	31	1·4±0·06	12±6	679	32	2·5±0·08	272±8
921	35	2·7±0·5	925	36	1·0±0·07	189±11	930	37	1·5±0·08	67±12
1161	39	15·5±0·3	1166	40	0·66±0·06	150±6	1172	41	2·3±0·07	4±6
1419	43	4·9±0·1	1423	44	0·88±0·07	195±12	1429	45	0·71±0·17	57±5
1610	47	14·6±0·3	1615	47	1·27±0·06	196±5	1622	48	0·72±0·08	292±5
PKS 0518–45 (Pictor A): Scan 2										
0	—	71·8±4	0	—	0·28±0·2	360	0	—	2·2±0·3	360
463	138	11·4±0·2	461	138	0·44±0·05	25±6	457	140	2·6±0·1	343±6
571	133	25·0±0·2	568	134	0·27±0·05	337±8	564	135	2·8±0·1	358±10
721	128	24·5±0·2	717	129	0·56±0·12	270±12	712	130	2·4±0·05	317±11
892	120	7·5±0·2	888	121	0·15±0·05	89±22	883	122	2·8±0·05	305±20
1038	117	15·7±0·2	1034	117	0·27±0·06	206±14	1028	118	3·5±0·05	331±13
1199	113	8·8±0·2	1194	114	0·25±0·06	180±15	1187	115	2·9±0·06	316±14
1350	109	10·4±0·2	1346	110	0·22±0·05	141±13	1339	111	2·3±0·05	19±12
1511	106	15·7±0·2	1507	107	0·07±0·07	195±20	1500	108	2·8±0·25	355±20

TABLE 2 (*Continued*)

(1)	(2)	(3)	(4)	(5)	(6)	(7)	(8)	(9)	(10)	(11)
Parallel Feeds			Orthogonal Feeds							
S (λ)	P.A. (°)	*I*+*Q* (f.u.)	*S* (λ)	P.A. (°)	*U* (f.u.)	*Δφ*(*U*) (°)	*S* (λ)	P.A. (°)	*Q* (f.u.)	*Δφ*(*Q*) (°)
PKS 0618–37										
0	—	3·0±0·2	0	—	0·05±0·03	180	0	—	0·42±0·05	360
504	115	2·5±0·08	500	116	0·12±0·06	115±30	495	117	0·17±0·05	4±25
753	111	2·0±0·11	748	112	0·20±0·05	103±13	742	113	0·28±0·05	19±12
1056	107	1·4±0·11	1050	108	0·12±0·07	40±32	1042	109	0·19±0·05	357±30
1292	103	0·61±0·10	1286	104	0·14±0·06	285±25	1279	105	0·07±0·05	220±40
1452	100	0·31±0·12	1445	101	0·16±0·06	300±40	1438	102	0·09±0·04	283±45
1619	97	0·54±0·09	1615	98	0·07±0·07	289±50	1609	98	0·04±0·05	229±54
1776	94	0·77±0·1	1773	94	0·10±1·0	—	1769	95	0·05±0·10	—
1929	91	1·13±0·1	1928	91	0·10±0·20	—	1926	92	0·04±0·12	—
PKS 0945+07 (3C 227)										
0	—	8·5±0·5	0	—	0·11±0·05	180	0	—	0·47±0·06	360
534	92	2·9±0·10	538	92	0·11±0·04	142±30	548	92	0·20±0·06	71±25
628	84	1·7±0·11	622	84	—	—	607	93	0·22±0·04	—
768	92	1·26±0·13	773	92	0·23±0·04	55±15	783	92	0·31±0·04	66±10
903	85	1·64±0·09	928	85	—	—	916	85	—	—
1071	92	2·92±0·12	1077	92	0·19±0·05	32±14	1087	92	0·42±0·10	26±16
1259	87	2·9±0·12	1254	87	0·16±0·10	342±35	1242	87	—	—
1379	91	1·94±0·13	1385	91	0·04±0·08	—	1398	87	0·35±0·05	—
1583	89	0·72±0·12	1581	89	0·12±0·05	344±20	1576	88	0·35±0·05	328±18
1695	91	0·46±0·10	1701	91	0·24±0·05	294±25	1710	90	0·35±0·06	260±20
1944	90	1·85±0·13	1946	90	0·17±0·04	268±18	1949	90	0·18±0·05	282±14
PKS 1226+06 (3C 270): Scan 1										
0	—	18·1±0·9	0	—	0·16±0·06	180	0	—	1·39±0·06	360
423	81	2·0±0·1	418	81	0·22±0·06	158±20	409	81	0·35±0·05	137±11
637	83	6·7±0·1	630	83	0·54±0·06	306±7	619	83	0·42±0·05	—
838	84	4·1±0·1	830	84	0·41±0·06	317±9	818	84	0·35±0·05	313±8
1011	85	1·4±0·11	1002	85	0·24±0·05	50±15	987	85	0·56±0·06	40±10
1189	86	0·93±0·09	1179	86	0·16±0·04	127±20	1167	86	0·38±0·05	142±14
1366	87	0·18±0·11	1358	87	0·04±0·05	—	1345	87	0·14±0·07	—
1544	88	0·64±0·10	1536	88	0·29±0·05	342±17	1524	88	0·23±0·04	186±14
1713	89	0·10±0·13	1709	88	0·27±0·08	83±40	1702	88	0·14±0·08	258±50
1917	89	0·78±0·14	1917	89	0·23±0·06	20±22	1915	89	0·08±0·05	180±22
PKS 1226+06 (3C 270): Scan 2										
0	—	18·1±0·9	0	—	0·13±0·06	180	0	—	1·39±0·06	360
420	81	1·67±0·24	414	81	0·46±0·07	—	406	80	0·26±0·06	—
592	83	6·24±0·15	592	83	—	—	574	82	0·42±0·12	316±16
804	84	4·78±0·12	797	84	0·26±0·05	—	786	84	0·55±0·06	303±6
1110	85	0·84±0·12	1102	85	0·44±0·08	—	1087	85	0·24±0·04	115±15
1282	86	0·23±0·10	1271	86	0·09±0·05	—	1256	86	0·30±0·05	—
1472	87	0·72±0·12	1462	87	0·34±0·09	15±20	1449	86	0·17±0·06	—
1703	87	0·17±0·11	1694	87	0·18±0·10	330±25	1682	87	0·10±0·06	—
1900	88	0·89±0·11	1895	88	0·21±0·04	40±18	1883	88	0·12±0·05	296±50
PKS 1322–42 (Centaurus A): Scan 1										
0	—	288±18	0	—	0·8±0·4	—	0	—	20·1±2·0	360
442	138	195±2	441	139	10·9±0·3	84±3	439	139	19·2±0·3	6±3
581	135	161±3	578	135	9·5±0·3	72±3	576	136	12·7±0·5	2±3
730	132	152±4	727	133	11·6±0·2	72±3	725	133	14·3±0·4	11±3
905	129	118±3	900	130	9·9±0·3	98±3	897	130	13·2±0·2	6±4
1144	127	47±1	1140	127	6·8±0·2	94±3	1136	128	9·4±0·2	32±4
1327	124	9·9±1	1322	125	5·0±0·2	79±7	1318	125	9·3±0·3	2±6
1640	122	21·5±1·3	1644	123·	4·9±0·2	14±5	1638	123	5·3±0·2	236±5
1509	120	36·4±	1502	121	6·1±0·2	—	1497	121	6·7±0·1	—

TABLE 2 (*Continued*)

(1)	(2)	(3)	(4)	(5)	(6)	(7)	(8)	(9)	(10)	(11)
Parallel Feeds			Orthogonal Feeds							
S (λ)	P.A. (°)	I+Q (f.u.)	S (λ)	P.A. (°)	U (f.u.)	Δφ(U) (°)	S (λ)	P.A. (°)	Q (f.u.)	Δφ(Q) (°)
PKS 1322−42 (Centaurus A): Scan 2										
0	—	288±18	0	—	0·8±0·4	180	0	—	20·1±2·0	360
556	106	53·4±1	555	106	8·5±0·2	140±4	554	106	14·2±0·2	16±4
752	104	102±1	750	104	6·6±0·2	75±3	749	104	12·7±0·2	347±3
977	102	79±1	976	102	1·0±1·0	90±10	974	103	10·3±0·1	2±10
1238	100	24±1	1236	100	2·5±0·1	97±3	1234	101	8·7±0·2	327±4
1482	98	41·7±1	1480	99	1·7±0·1	119±4	1479	99	5·8±0·1	114±4
1715	97	22·7±0·08	1713	97	3·6±0·2	205±5	1712	97	6·1±0·2	339±5
1905	95	18·8±0·2	1904	95	1·0±0·1	167±7	1902	96	2·8±0·1	309±8
PKS 1322−42 (Centaurus A): Scan 3										
0	—	288±18	0	—	1·3±0·4	180	0	—	20·1±2·0	360
399	157	96±3	398	158	10·8±0·4	92±4	396	159	12·3±0·4	345±3
495	153	86±1	494	154	11·7±0·1	58±3	492	155	11·3±0·1	334±3
606	150	82±2	604	150	10·5±0·3	83±4	602	151	10·5±0·2	330±4
730	147	76±1·5	727	147	12·3±0·3	55±3	725	148	10·0±0·4	307±3
845	144	82·2±0·9	842	144	11·9±0·3	56±4	839	145	11·3±0·3	321±4
977	141	75·5±0·6	974	141	12·8±0·2	35±3	970	142	10·3±0·1	325±3
1101	138	67·0±1·5	1097	139	12·5±0·2	43±3	1093	139	9·6±0·1	328±4
1233	135	61·9±1·5	1228	140	11·6±0·3	48±5	1224	137	8·3±0·2	320±4
1343	133	46·2±0·4	1338	133	10·8±0·1	50±4	1334	134	7·4±0·2	333±3
1464	131	21·8±0·4	1459	131	7·4±0·1	45±3	1453	132	6·3±0·2	11±3
1580	128	3·6±0·2	1574	129	4·0±0·1	25±4	1569	129	6·3±0·4	321±5
PKS 1559+02 (3C 327a)										
0	—	7·4±0·4	0	—	0·05±0·03	180	0	—	0·44±0·07	348±6
434	89	4·1±0·1	439	89	0·13±0·04	124±16	450	89	0·46±0·05	351±8
552	89	4·0±0·1	558	89	0·24±0·05	103±13	570	89	0·39±0·05	351±8
701	90	5·4±0·2	710	90	0·22±0·05	41±15	722	90	0·43±0·05	340±8
868	90	5·7±0·1	877	90	0·28±0·04	28±9	889	90	0·43±0·04	341±6
1038	90	4·8±0·1	1046	90	0·37±0·05	13±9	1058	90	0·47±0·08	357±7
1220	90	3·6±0·1	1227	90	0·13±0·05	49±20	1238	90	0·38±0·06	15±10
1383	90	2·5±	1389	90	0·25±0·08	14±16	1397	90	0·35±0·06	352±10
1551	90	2·5±0·1	1555	90	0·19±0·07	356±20	1561	90	0·38±0·05	332±8
1715	90	2·5±0·1	1717	90	0·18±0·08	321±21	1719	90	0·35±0·07	320±20
1860	89	2·3±0·13	1859	89	0·37±0·1	330±16	1857	89	0·15±0·17	345±25
PKS 1648+05 (Hercules A)										
0	—	46±3	0	—	0·07±0·05	360	0	—	0·46±0·1	360
497	91	31±1	501	91	0·57±0·05	22±6	508	90	0·75±0·05	41±7
769	91	14±0·5	775	91	0·40±0·06	15±10	784	91	0·72±0·05	33±10
1063	91	14±0·6	1069	91	0·23±0·05	135±15	1081	91	0·43±0·06	89±8
1375	91	25±0·7	1381	91	0·16±0·05	166±22	1392	91	0·44±0·05	11±20
1712	91	28±0·9	1719	90	0·22±0·07	151±40	1727	90	0·26±0·16	28±40
1895	90	26±0·5	1899	90	—	—	1904	90	—	—
PKS 1717−00 (3C 353)										
0	—	50±3	0	—	0·4±0·1	180	0	—	1·6±0·16	360
368	88	30±0·5	362	88	—	—	351	88	—	—
488	88	20±0·5	481	88	—	—	470	88	—	—
640	89	11·5±0·15	633	89	0·69±0·16	279±13	620	89	2·3±0·1	301±12
872	89	13·7±0·2	863	89	1·00±0·08	60±4	836	89	1·60±0·06	109±5
1039	89	18·9±0·2	1033	89	0·97±0·07	129±5	1022	89	1·50±0·05	115±5
1215	89	18·5±0·6	1209	89	1·21±0·08	150±6	1199	89	1·63±0·06	94±5
1360	89	—	1356	89	1·03±0·1	135±6	1347	89	1·52±0·11	—
1556	89	16·3±0·2	1553	89	1·4±0·12	170±5	1545	89	1·29±0·05	89±5
1686	89	15·1±0·2	1684	89	1·2±0·16	102±8	1680	89	1·32±0·08	2±8
1808	89	12·5±0·2	1808	89	0·94±0·16	115±10	1807	89	1·10±0·05	282±10

TABLE 2 (*Continued*)

(1)	(2)	(3)	(4)	(5)	(6)	(7)	(8)	(9)	(10)	(11)
Parallel Feeds						Orthogonal Feeds				
S (λ)	P.A. (°)	$I+Q$ (f.u.)	S (λ)	P.A. (°)	U (f.u.)	$\Delta\phi(U)$ (°)	S (λ)	P.A. (°)	Q (f.u.)	$\Delta\phi(Q)$ (°)
PKS 2152−69 (21–64)										
0	—	2·7 ± 0·2	0	—	0·11 ± 0·05	—	0	—	0·94 ± 0·09	360
582	62	1·81 ± 0·03	582	63	0·77 ± 0·05	305 ± 5	583	64	0·91 ± 0·05	334 ± 4
705	67	1·90 ± 0·2	705	68	0·83 ± 0·05	356 ± 4	705	69	1·46 ± 0·13	30 ± 8
844	71	2·1 ± 0·06	845	72	0·87 ± 0·05	—	845	73	1·29 ± 0·06	—
1000	77	2·2 ± 0·05	1000	78	1·29 ± 0·07	358 ± 5	1001	79	1·45 ± 0·07	1 ± 4
1147	81	2·0 ± 0·05	1147	82	0·97 ± 0·05	10 ± 4	1147	83	1·5 ± 0·06	340 ± 6
1292	85	1·61 ± 0·02	1292	86	0·67 ± 0·06	—	1292	87	—	—
1433	89	1·46 ± 0·03	1433	90	0·76 ± 0·05	12 ± 10	1433	91	1·13 ± 0·09	28 ± 10
1577	93	1·57 ± 0·19	1577	94	1·08 ± 0·08	320 ± 10	1576	95	1·40 ± 0·09	60 ± 12
1717	98	1·85 ± 0·03	1716	98	1·03 ± 0·08	0 ± 15	1716	99	1·53 ± 0·13	46 ± 10
1890	103	1·87 ± 0·04	1890	103	1·02 ± 0·06	0 ± 15	1888	104	1·18 ± 0·07	48 ± 12
PKS 2356−61 (23–64)										
0	—	23·0 ± 1·6	0	—	0·26 ± 0·1	—	0	—	1·13 ± 0·1	360
525	146	2·8 ± 0·1	524	147	1·02 ± 0·08	278 ± 6	523	148	0·59 ± 0·09	100 ± 10
641	140	5·7 ± 0·1	640	141	0·84 ± 0·05	16 ± 4	638	142	0·05 ± 0·04	63 ± 4
797	132	5·8 ± 0·14	795	133	0·26 ± 0·15	351 ± 35	792	134	0·33 ± 0·15	128 ± 25
945	128	5·3 ± 0·2	943	129	0·22 ± 0·04	12 ± 12	941	130	0·24 ± 0·04	118 ± 10
1100	124	4·5 ± 0·1	1098	124	0·20 ± 0·06	10 ± 16	1095	126	0·27 ± 0·04	199 ± 11
1251	119	2·94 ± 0·1	1249	120	0·06 ± 0·06	345 ± 20	1245	121	0·46 ± 0·14	300 ± 20
1394	115	2·01 ± 0·11	1392	116	0·17 ± 0·04	138 ± 12	1389	117	0·45 ± 0·04	310 ± 8
1543	111	4·3 ± 0·11	1540	112	0·37 ± 0·04	204 ± 8	1537	113	0·38 ± 0·04	354 ± 8
1659	107	5·9 ± 0·1	1657	108	0·34 ± 0·18	180 ± 30	1654	109	0·27 ± 0·07	348 ± 28
1777	103	6·3 ± 0·1	1775	103	0·21 ± 0·12	158 ± 16	1772	105	0·53 ± 0·04	301 ± 12
1897	99	6·4 ± 0·1	1896	99	0·20 ± 0·04	61 ± 13	1893	101	0·27 ± 0·04	287 ± 15

source but can be significant elsewhere, e.g. if the projected baseline crosses the minor axis during observation. In the present case it has been assumed that the inversion yields the strip brightness distribution in a direction parallel to the mean position angle of the projected baseline. In the figures this has been designated the scan position angle. For PKS 2356−61 the rotation of the source in relation to the projected baseline was significant. Ekers (1967) has suggested that the source

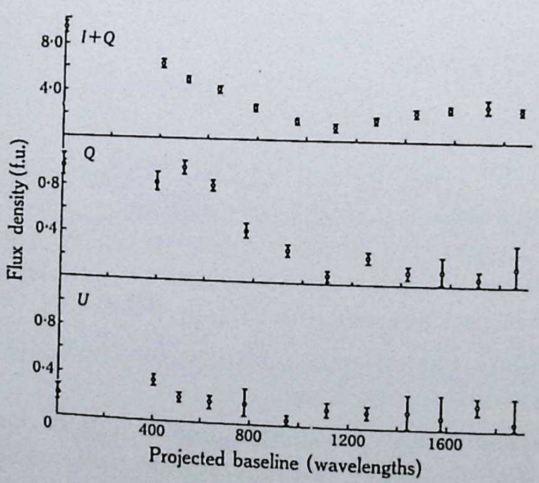

Fig. 3.—Visibility functions for $I+Q$, Q, and U for the source PKS 0043−42. The values for zero spacing correspond to the single-dish observations of Table 1.

consists of a number of small-diameter components distributed along the major axis. Hence, in the inversion it was assumed that rotation merely caused a variation of projected baseline without affecting the shape of the effective strip brightness distributions.

Values for amplitude and phase at projected baseline intervals of 200 wavelengths were interpolated from the measurements, and the one-dimensional brightness distributions were derived for $I+Q$, U, and Q for a 17′ arc scan. No correction for the tapering of these distributions by the primary beam shape (Fig. 2(*a*)) has been made. To reduce the side lobe responses produced by the cutoff of the Fourier transform at the maximum spacing, further smoothing was generally carried out with a 1′ Gaussian beam. Apart from any additional loss of resolution produced by source rotation, the overall beamwidth then corresponds to 1′·2 arc. Figure 4 illustrates the resulting distributions of $I+Q$, Q, and U for PKS 0356+10. The corresponding distributions of the polarized flux $(U^2+Q^2)^{\frac{1}{2}}$ and the position angle of polarization $0\cdot 5\tan^{-1}(U/Q)+\theta$ (integrated polarization) are given in Figure 7. The observations with parallel feeds were also inverted as a check on the plausibility of the assumed phases and on any systematic errors due to source rotation.

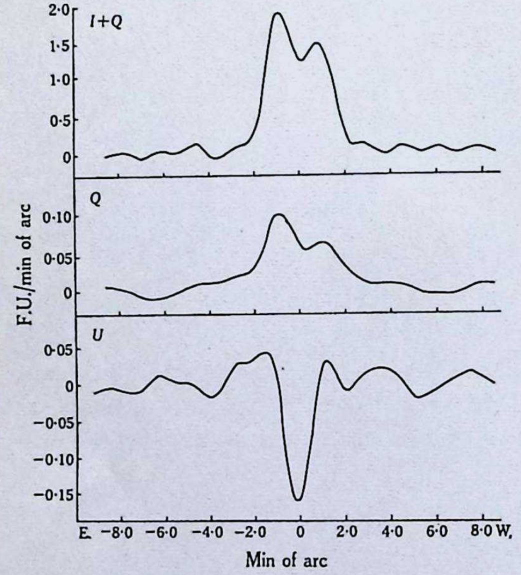

Fig. 4.—Restored strip brightness distributions of $I+Q$, Q, and U for the source PKS 0356+10. The results have been smoothed with a Gaussian function of 1′ arc width to half-intensity points.

Table 3 indicates how the absolute phases were obtained for each source. It also presents a summary of the results of the inversions.

Figures 5–18 illustrate the derived brightness distributions. For each source the one-dimensional strip brightness distribution of the polarized radiation $(U^2+Q^2)^{\frac{1}{2}}$ is plotted together with that of $I+Q$. Accompanying each brightness distribution is the variation of the position angle of polarization. The appended position angle scale has been corrected for ionospheric Faraday rotation. The "modified axis" corresponds to the position angle of the major axis after allowance for the Faraday rotation from zero wavelength to 21·2 cm, as determined from measurements of the integrated radiation (Gardner and Davies 1966*a*). If the changes in Faraday rotation and spectral index over a source are insignificant, the modified axis is of help in visualizing the orientation of the magnetic field in the source relative to its major axis.

Table 3

SUMMARY OF CONCLUSIONS AT 21·2 CM

PKS Source No.	Derivation of Phase*	Distribution of Polarization	Angle between Polarization Components† (°)	Intrinsic Angle Minus P.A. Major Axis‡ (°)	Peak Polarization (%)
0043−42	E	Single	0±10	0±3	20
0106+13	S	Double	6	71±9	7 (E.) 11 (W.)
0356+10	S	Triple ?	50±20	25±12	∼10
0518−45	F	Double+ Bridge	0±2 ∼40	−1±5	8 (E.) 11 (W.) ∼4
0618−37	E	Single	20±20	−15±5	13
0945+07	F	Triple ?	V	70±12	12 (E.) 7 (W.)
1216+06	F	Double	0±20	9±8	15 (E.) 13 (W.)
1322−42	F^{b} S^{c}	Double	20 (V)	100±4	10 (E.) 7 (W.)
1559+02	F	Double	V	66	9 (E.) 3 (W.)
1648+05	F	Single ?§	70 ?	−72±4	1·5 (E.) 0·5 ? (W.)
1717−00	F	Double	V	−8±8	2·5 (E.) 11 (W.)
2152−69	E^{a}	Double	∼40 (V)	−64±12	9 10
2356−61	E^{a}	Double‖	50±10	−125±6	5 8

* E, from Ekers (1967) model; F, Fomalont (1967*a*, 1967*b*) observations; S, Seielstad (1967) model. E^{a}, Ekers model, sign of calculated phases unknown; F^{b}, Fomalont observations for scans close to east–west line; S^{c}, Seielstad model for scans close to the minor axis.

† V, varies over source.

‡ See Table 1.

§ There is some evidence for polarization of the western component.

‖ With additional components (Ekers 1967).

Calculated estimates of the errors introduced into the distribution of polarized radiation $(U^2+Q^2)^{\frac{1}{2}}$ by receiver noise are indicated by the error bars situated to the left of each scan. A better indication of the uncertainties involved is provided by the baseline variations in directions adjacent to the source. They reflect errors due to noise, errors in interpolation, and errors in the assumed phases. Systematic effects due to the rotation of the source during the observations are more difficult to assess since they depend on the two-dimensional brightness distributions.

(*b*) *Individual Sources*

PKS 0043−42: Figure 5

The polarization is distributed over the whole source and shows no structure when scanned with the 1′·2 beam. The direction of polarization is constant to within ±10° over the source. The constancy of this direction and the lack of depolarization shown by the single-dish observations (Gardner and Davies 1966*b*) both imply simple polarization structure. The intrinsic angle of polarization is similar to the position angle of the major axis (136°) and suggests that the projected magnetic field over a major portion of the source is aligned almost perpendicular to its major axis. In this respect the source is similar to 3C452 (Seielstad 1967).

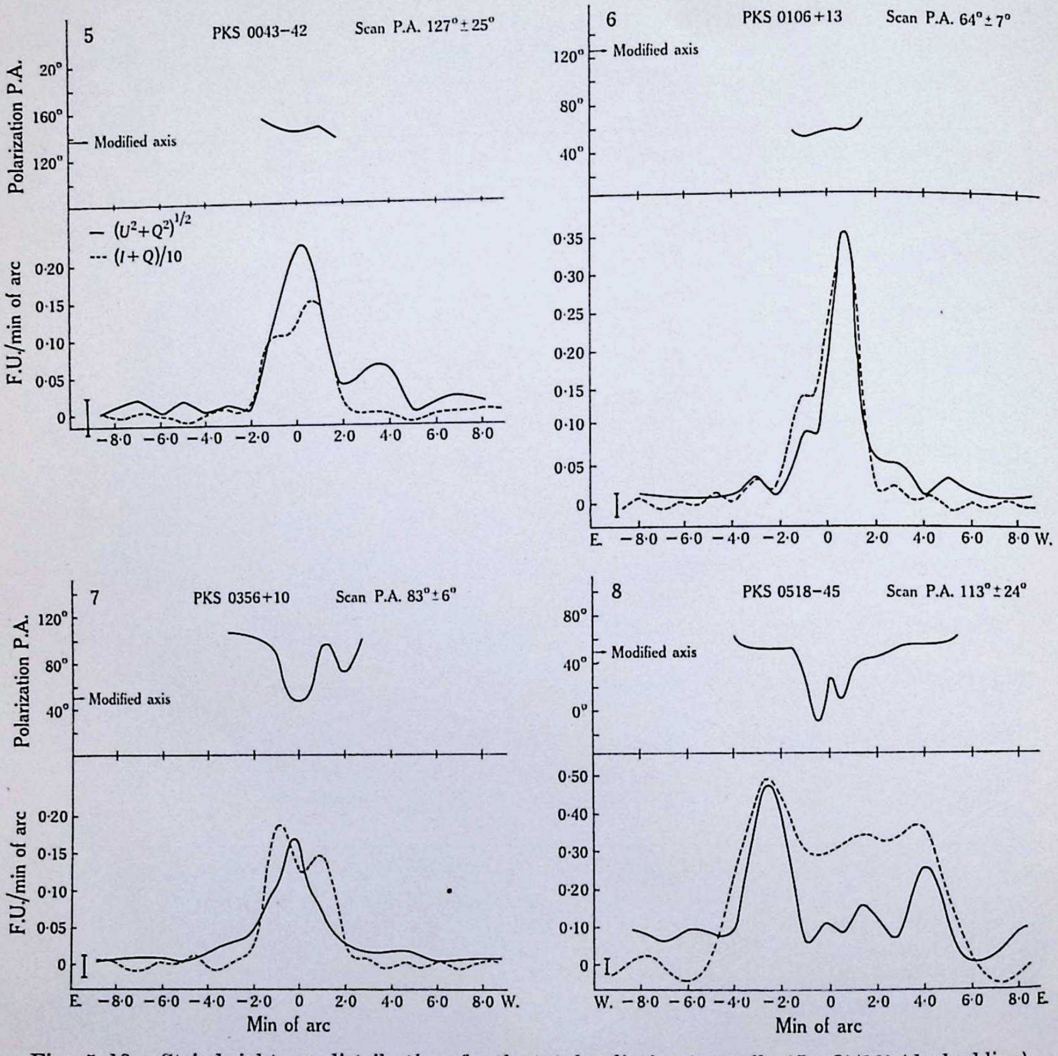

Figs. 5–18.—Strip brightness distributions for the total radiation (actually $(I+Q)/10$) (dashed line), the polarized flux density $(U^2+Q^2)^{\frac{1}{2}}$ (full line), and the direction of polarization. The effective resolution is 1′·2 by 20′. The flux densities have not been corrected for the shape of the primary beam.

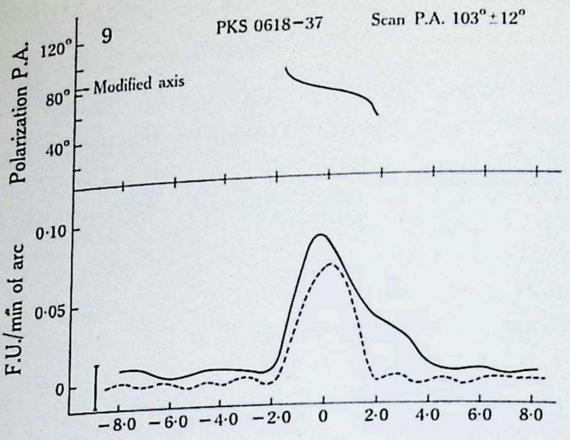

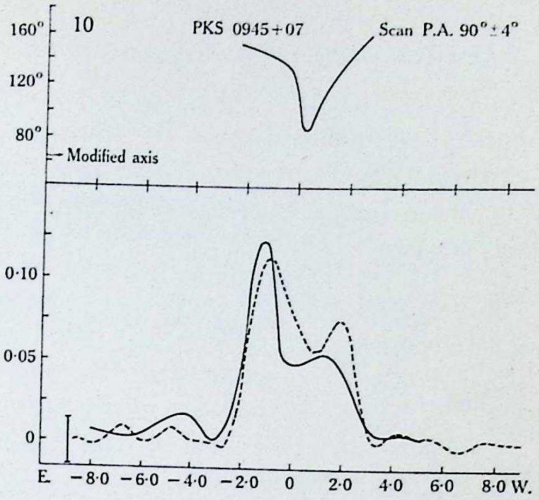

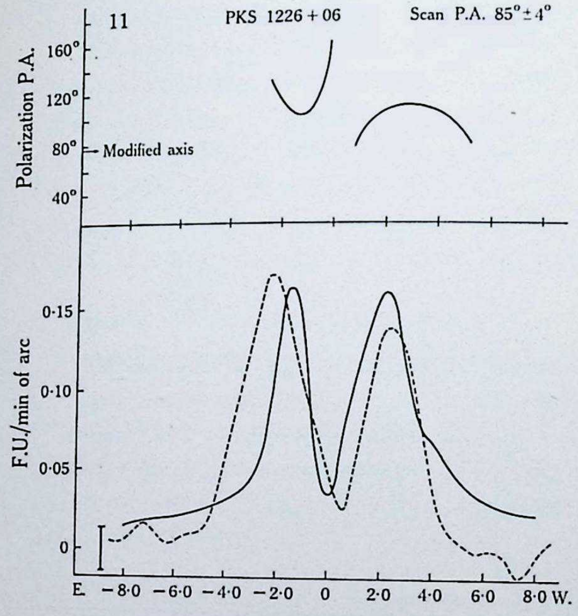

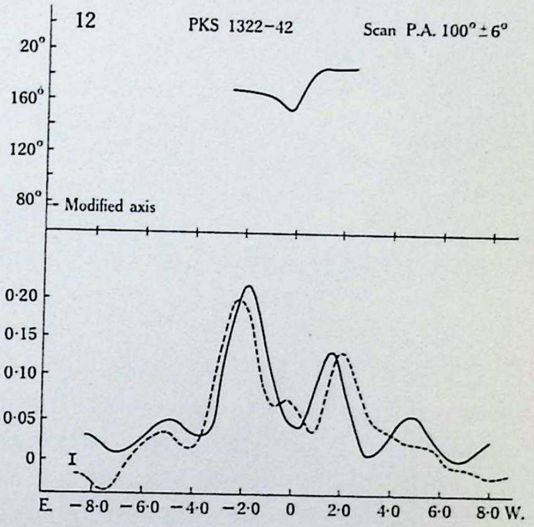

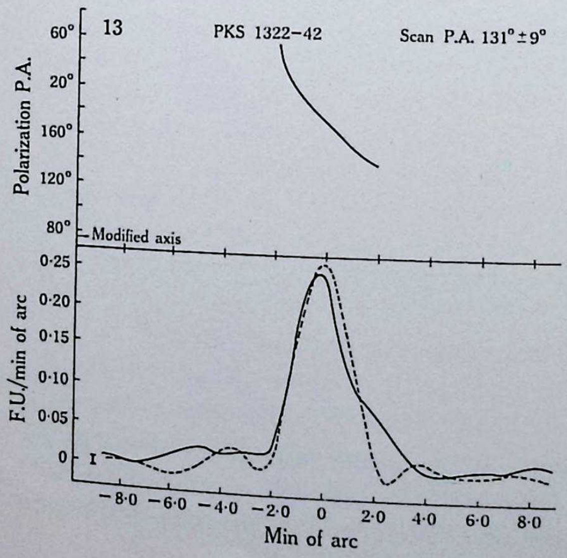

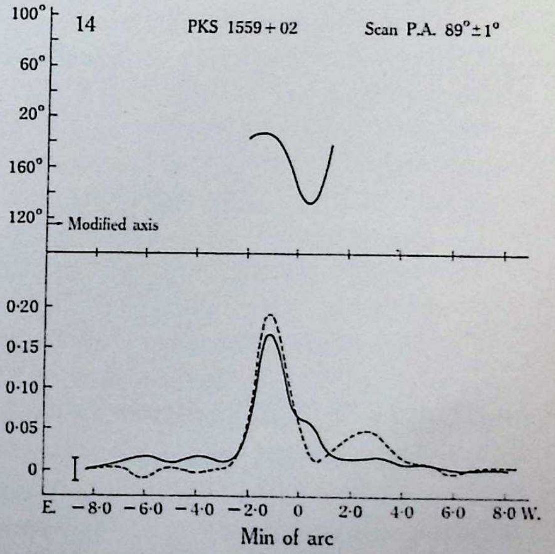

Figs. 5–18 (*continued*)

PKS 0106+13 (3C 33): Figure 6

Both components of the source show polarization; the more intense one has a peak polarization of about 9%, the other about 6%. The position angle of polarization is similar for both cases. These results simulate those of Seielstad (1967) at 10·6 cm. It would appear that the projected magnetic field is almost parallel (±25°) to the major axis.

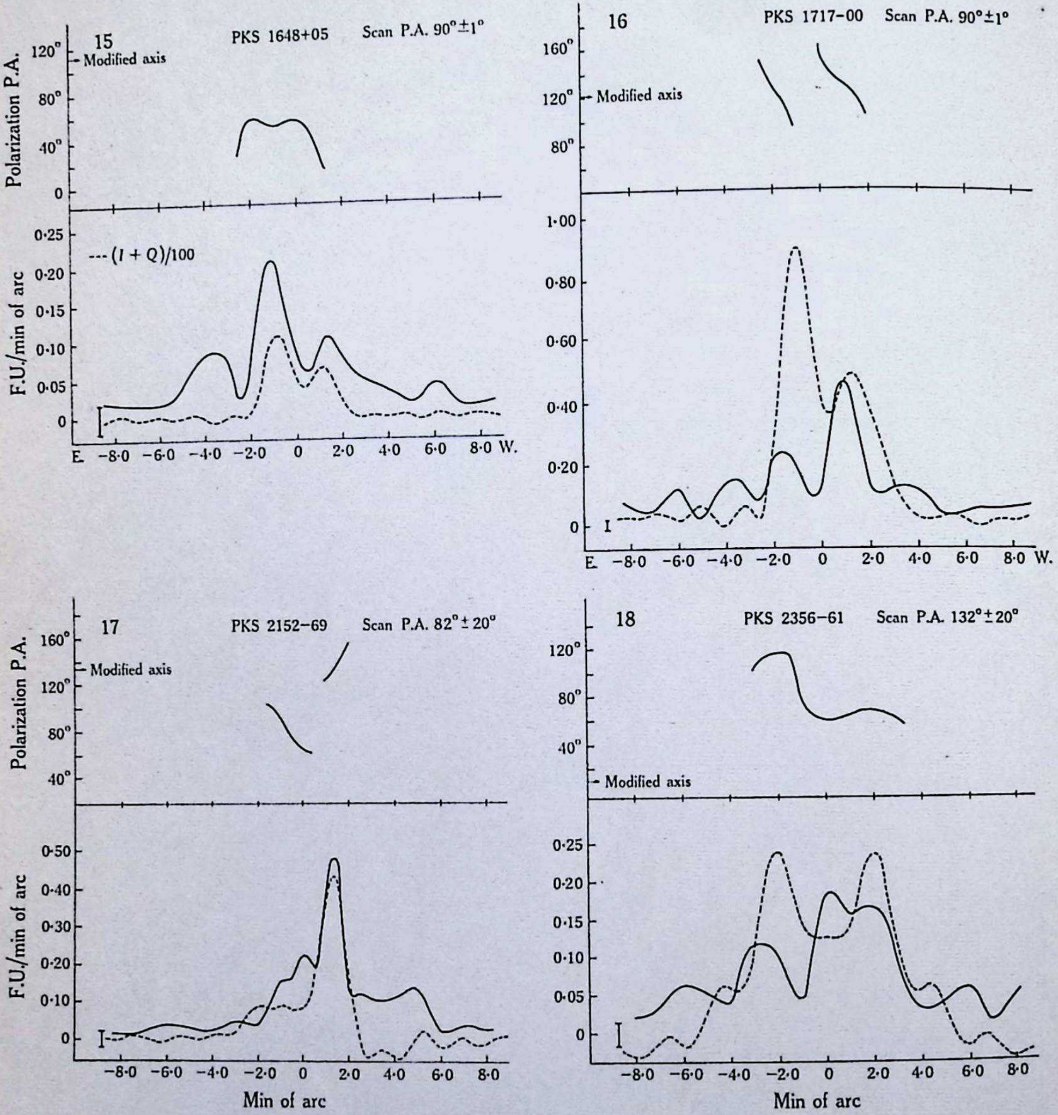

Figs. 5–18 (*continued*). (Note the change of scale for $I+Q$ in Fig. 15.)

PKS 0356+10 (3C 98): Figures 4 and 7

Although both components are polarized in similar directions there is an unresolved core between them which is polarized at an angle differing by about 45°. This is most clearly shown by the variation of U in Figure 4. This result conflicts with the conclusions of Seielstad (1967). However, the apparent difference is probably due to the limited number of antenna spacings available to Seielstad.

PKS 0518−45 (Pictor A): Figure 8

The source was not observed at maximum spacing, so the results have been smoothed with a 2′ Gaussian beam. In accordance with Seielstad (1967) at 10·6 cm, most of the polarized radiation originates in two compact regions at opposite extremities of the source. The peak polarizations are about 5% and 8% for the western and eastern components respectively. The intervening "bridge", on the other hand, shows some polarization of probably 2% and certainly less than 5%. There is some indication of quite complex structure in the distribution of degree and direction of polarization within the bridge. This is not evident in Seielstad's model, since he confines the polarization to the extremities. His conclusion appears to be a consequence of the limited number of antenna separations used. Perhaps for the same reason the 10·6 cm results indicate that the directions of polarization of the two components differ by 72°. The present 21·2 cm results suggest that the two components are polarized approximately parallel to one another. However, the directions of polarization at 6 cm (Broten *et al.* 1965; Morris and Whiteoak 1968) show differences of 50° and 43°±6° respectively, and it appears that the rotation measures of the two components differ by about 16 rad/m². The projected magnetic field in the two extreme components is approximately perpendicular to the major axis.

PKS 0618−37: Figure 9

This source has polarization characteristics similar to PKS 0043—42. The polarization is distributed over a large fraction of the source and has a peak value of about 10%; approximately the single-dish value. Therefore, the characteristics of the polarization are adequately described by the integrated values (Table 1), which imply that the projected magnetic field is almost orthogonal to the major axis (within 15°).

PKS 0945+07 (3C 227): Figure 10

Fomalont (1967*b*) has suggested that the source consists of three components. All components are polarized but the position angle of polarization of the central component differs from that of the outer components by about 50°. In this respect the source is similar to PKS 0356+10 (3C 98). There is apparently a change in direction of polarization over the face of the western component. The integrated values (Gardner and Davies 1966*b*) show depolarization, and the magnetic field structure must be complex.

PKS 1226+06 (3C 270): Figure 11

Both components show quite high (7–10%) peak polarizations and similar directions of polarization. It appears that the angular sizes of the two polarized regions differ significantly at 21·2 cm. At 10·6 cm, on the other hand, the models of Seielstad (1967) indicate identical angular diameters; the difference may be due to depolarization at the outer edge of the eastern component at the longer wavelength. Any associated changes in polarization direction must be too small to be shown. The projected magnetic field is approximately perpendicular to the major axis (within 25°).

PKS 1322−42 (Central Component of Centaurus A): Figures 12 and 13

The scan at P.A. 100° (Fig. 12) shows the polarization of the two main components of the source. The baseline variations indicate quite large errors but the integrated polarization of the components amounts to $6\cdot5\%\pm1\cdot5\%$ and $3\cdot7\%\pm1\cdot5\%$ for the eastern and western components respectively. Their directions of polarization differ by 20° in the sense ΔP.A.(W.–E.) = 20°. This is similar to the 10·6 cm results of Seielstad (1967), but at 6 cm the sense is reversed, since ΔP.A.(W.–E.) = −43° (Morris and Whiteoak 1968) or ΔP.A.(W.–E.) = −28° (Cooper, Price, and Cole 1965). These variations with wavelength are mirrored in the changing ratio of the integrated percentage polarization of the two components. At 21·2 cm a ratio of almost two is indicated; at 10·6 cm the ratio is about four, and at 6 cm wavelength the ratio is between six and eight.

The scan in the direction of the minor axis (Fig. 13) shows the rapid variation in direction of polarization previously pointed out by Seielstad (1967). In view of this variation, some of the difference in Faraday rotation between the two components of the source may be due to variations in spectrum over the eastern source.

The intrinsic polarization angle (Table 1), if physically significant for a source with such polarization complexities, indicates that on the average the projected magnetic field direction is within 10° of the orientation of the major axis. The details are clearly very complicated, and more data are needed.

PKS 1559+02 (3C 327a): Figure 14

The present observations indicate that most of the polarized radiation arises in the more intense eastern component. The peak polarization in the 1′·2 by 20′ beam is about 8%.

PKS 1648+05 (Hercules A): Figure 15

At 21·2 cm the integrated polarization of this source is only 0·9% and the observations are consequently subject to large errors. In agreement with Seielstad (1967) at 10·6 cm, most of the polarized radiation is from the more intense eastern component. The present resolution is not sufficient to estimate the angular extent of this region. This source is of high brightness temperature (Maltby and Moffet 1962). The extensive variation of integrated polarization with wavelength (Gardner and Davies 1966*b*) suggests the presence of internal depolarization.

PKS 1717−00 (3C 353): Figure 16

This source is unusual amongst those studied in that the more intense component shows less polarization. Moreover, both components exhibit a large variation in direction of polarization over their diameters. This unusual behaviour is probably related to the substantial depolarization and to the nonlinear relationship between Faraday rotation and wavelength squared that is so evident in the single-dish observations of Gardner and Davies (1966*a*) and Gardner, Morris, and Whiteoak (1968).

The distribution of polarization agrees with that suggested by Seielstad (1967) in his discussion of the work of Gol'nev and Soboleva (1965).

PKS 2152−69: Figure 17

The observations are not of high quality, since considerable uncertainty exists in the assumed absolute phases. Both components are evidently polarized but at angles differing by about 60°. The structure is complex, since the two components have different spectral indices. In addition, this is the only bright double source associated with a D galaxy for which the integrated polarization decreases between 11 cm and 6 cm (Morris and Whiteoak 1968).

PKS 2356−61: Figure 18

This inversion must be treated as strictly a qualitative result. Polarization is associated with one of the principal components and possibly both.

V. Discussion

Of the 13 sources observed, the results for 10 are sufficiently extensive to provide some evidence of their magnetic field structure. In general the distribution of polarization is complex, since several sources have polarization characteristics that vary from one component to the other. Differences of the intrinsic properties of individual components of a source may represent features of a common mode of evolution which are viewed at different epochs in the manner suggested by Ryle and Longair (1967). In the case of the sources PKS 0356+10, PKS 0945+07, and PKS 1322−42, a series of ejecta may have occurred over a substantial period of time to add to the complexity. However, insufficient data are available to determine whether the variation in direction of polarization is due to changes in magnetic field orientation or merely reflects a variation in Faraday rotation.

From observations of the polarization of integrated radiation, it has been pointed out that sources consisting of multiple components fall into two loosely defined classes (Gardner and Whiteoak 1963). In one class the intrinsic angle of polarization is coincident with the major axis; in the other it is orthogonal. Various explanations have been advanced in terms of the evolution of the sources from one class to the other (Gardner and Davies 1964; Morris and Berge 1964; Gardner and Whiteoak 1966). They suggest that the sources with low brightness temperatures and magnetic fields aligned orthogonal to the direction of component separation are the most evolved. In the present investigation this group contains the cources with particularly simple structure, namely, PKS 0043−42, PKS 0518−45, PKS 0618−37, PKS 1226+06, Fornax A, 13–33, and 3C 452 (see Gardner and Whiteoak 1966; Seielstad 1967). The southernmost of the outer components of Centaurus A (Cooper, Price, and Cole 1965) may also fall in this group. We suggest that the highly ordered magnetic fields in these sources may be a consequence of rotation about their major axes. In the last stages of evolution, when the connection of the ejected plasma with the parent galaxy is broken and the internal motions of the plasma in the axial direction have been damped, the rotation that existed in the embryonic stages of the explosion must still persist to conserve angular momentum.

In this way the magnetic lines may be drawn into closely wound helices, and in projection will appear to be aligned perpendicular to the major axis. This idea follows naturally from the theory of Piddington (1966). Any compression of the intergalactic medium will assist in the alignment of the magnetic lines (Gardner and Whiteoak 1966). When viewed along its major axis a single or core–halo source may be visible in which the magnetic lines form tightly wound spirals. The electric vectors of the radiation will be directed radially in projection and the net polarization will be small. On the other hand, the young sources of high brightness temperature, e.g. PKS 0106+13, PKS 1648+05, Centaurus A (central component), and possibly the quasi-stellar sources (Sastry, Pauliny-Toth, and Kellermann 1967), will have axially directed magnetic fields, since the axial motions of the explosion will presumably be dominant. Viewed along the major axis, a single or core–halo source will be visible with a projected magnetic field that appears radial and gives rise to circumferentially directed polarization.

VI. ACKNOWLEDGMENTS

We are indebted to Mr. V. Radhakrishnan for assistance with the reductions. Dr. B. McA. Thomas and Mr. P. W. Butler of the aerial development group were responsible for the design, construction, and installation of the feeds used. Miss J. Merkelijn rendered invaluable help with the observations and their reduction, and Dr. R. W. Clarke advised on computer programming.

VII. REFERENCES

BATCHELOR, R. A., COLE, D., and SHIMMINS, A. J. (1968).—The Parks interferometer. *Instn Radio Engrs Aust.* (in press).

BROTEN, N. W., *et al.* (1965).—*Aust. J. Phys.* **18**, 85.

COLE, D. J. (1967).—*Proc. astr. Soc. Aust.* **1**, 30.

COOPER, B. F. C., PRICE, R. M., and COLE, D. J. (1965).—*Aust. J. Phys.* **18**, 589.

EKERS, R. (1967).—Ph.D. Thesis, Australian National University.

FOMALONT, E. B. (1967*a*).—*Publs Owens Valley Radio Observatory* **1**, No. 3.

FOMALONT, E. B. (1967*b*).—*Obs. Owens Valley Radio Observatory* No. 7/1967.

GARDNER, F. F., and DAVIES, R. D. (1964).—*Nature, Lond.* **201**, 144.

GARDNER, F. F., and DAVIES, R. D. (1966*a*).—*Aust. J. Phys.* **19**, 129.

GARDNER, F. F., and DAVIES, R. D. (1966*b*).—*Aust. J. Phys.* **19**, 442.

GARDNER, F. F., MORRIS, D., and WHITEOAK, J. B. (1968).—Measurements of the linear polarization of radio sources between 11 and 20 cm. *Aust. J. Phys.* (in press).

GARDNER, F. F., and WHITEOAK, J. B. (1963).—*Nature, Lond.* **197**, 1162.

GARDNER, F. F., and WHITEOAK, J. B. (1966).—*A. Rev. Astr. Astrophys.* **4**, 245.

VON GEYER, H. (1966).—*Frequenz* **20**, 28.

GOL'NEV, V. YA, and SOBOLEVA, N. S. (1965).—*Astr. Zh.* **42**, 694.

MALTBY, P., and MOFFET, A. T. (1962).—*Astrophys. J. Suppl. Ser.* **7**, 93.

MINNETT, H. C., and THOMAS, B. MCA. (1966).—*IEEE Trans. Antennas Propag.* **AP14**, 654.

MORRIS, D., and BERGE, G. L. (1964).—*Astr. J.* **69**, 641.

MORRIS, D., RADHAKRISHNAN, V., and SEIELSTAD, G. A. (1964).—*Astrophys. J.* **139**, 551.

MORRIS, D., and WHITEOAK, J. B. (1968).—*Aust. J. Phys.* **21**, 493.

PIDDINGTON, J. H. (1966).—*Mon. Not. R. astr. Soc.* **133**, 163.

ROBERTS, J. A., and KOMESAROFF, M. (1965).—*Icarus* **4**, 127.

RYLE, M., and LONGAIR, M. S. (1967).—*Mon. Not. R. astr. Soc.* **136**, 123.

SASTRY, Ch. V., PAULINY-TOTH, I. I. K., and KELLERMANN, K. I. (1967).—*Astr. J.* **72**, 234.

SEIELSTAD, G. A. (1967).—*Astrophys. J.* **147**, 24.

OBSERVATIONS OF THE LINEAR POLARIZATION OF RADIO SOURCES AT 6 CM WAVELENGTH

By D. Morris* and J. B. Whiteoak*

[*Manuscript received March* 4, 1968]

Summary

The polarizations of 45 sources have been measured at 6 cm wavelength and have been compared with values obtained at longer wavelengths. The resulting wavelength dependence has been studied in relation to the spectra of the sources. For the quasi-stellar objects in particular, polarization features at short wavelengths are associated with the young components of the source which radiate at high frequency. However, it is not possible to distinguish between radio galaxies and quasi-stellar objects solely on the basis of polarization data.

I. Introduction

Extensive observations of the linear polarization of radio sources have been carried out at wavelengths between 11 and 74 cm (Berge and Seielstad 1967; Gardner, Morris, and Whiteoak 1968; see also references to earlier papers in the review by Gardner and Whiteoak 1966). However, at wavelengths shorter than 11 cm the only extensive observations are those of Sastry, Pauliny-Toth, and Kellermann (1967) at 6 cm and Dent and Haddock (1966) at 3·75 cm.

The observations to be discussed here are the initial results of a programme to investigate the polarization of a larger sample of radio sources at short wavelengths and at southern declinations.

II. Observations

The observations were obtained with the Parkes 210 ft radio telescope in June and December 1966 and in March 1967. A few earlier observations had been made by Broten *et al.* (1965) and by F. F. Gardner (unpublished). The receiving equipment and methods of observation and reduction have been described previously (Morris, Whiteoak, and Tonking 1968). Summarizing, the receiver had an r.f. bandwidth of 200 MHz centred at 4995 MHz and a system noise temperature of about 900°K. For a time constant of 2 sec, the observed r.m.s. noise of the switched output was $0^\circ{\cdot}1$. The 210 ft telescope was illuminated by a dual-mode primary feed and provided a beamwidth of $4'{\cdot}1$ to half-power points. Observations were made using the "on–off" technique at a series of feed orientations. The sequence at each feed angle generally consisted of a 50 sec observation 10′ west of the source, a 100 sec observation with the telescope tracking the source, and another observation of duration 50 sec at a position 10′ east of it. In this way changes of zenith angle during each sequence were minimized. The switched (i.e. polarized) and total power outputs were recorded on paper tape for subsequent reduction on a CDC 3200 computer. Their relative gains were

---

* Division of Radiophysics, CSIRO, P.O. Box 76, Epping, N.S.W. 2121.

Aust. J. Phys., 1968, **21**, 493–500

established at each feed angle by the use of a calibration signal from a discharge tube. The observations were affected by instrumental polarization, which varied with feed orientation and zenith angle of the telescope. It was determined by the observation of several thermal radio sources over a range of zenith angle. The variation of the instrumental effect was almost sinusoidal with feed angle, and was approximated by a sinusoid of period 360° at each zenith angle. The amplitude of the correction varied from 1·4% at a zenith angle of 15° to 0·6% at 60°, attaining a minimum of 0·5% at 30°. The phase was reasonably constant at zenith angles less than 30° and at angles greater than 35°. However, between these limits the phase increased from 175° to 290°. It is believed that the variation is due to distortion of the dish at zenith angles greater than or less than 35°, at which position the surface has been adjusted to a parabolic figure. In view of the characteristics of the instrumental polarization, sources were generally observed at large zenith angles. Errors in telescope pointing were not significant since for each source the telescope was directed at the position where the total power was maximum. Thus for most sources the setting errors were less than $\pm 0'\cdot 5$. The basic calibration of the zero of the position angle scale was determined by radiating a linearly polarized signal from the apex of the telescope. Observations of the polarization of Jupiter during the December period (Morris, Whiteoak, and Tonking 1968) indicated an error of $5^\circ \pm 1^\circ$ in the calibration, and the results were adjusted accordingly.

The sources were selected from a list observed at longer wavelengths by Gardner, Morris, and Whiteoak (1968). Selection was confined to the brighter sources, or to fainter sources with appreciable polarization at 11 cm. Apart from the observation of several HII regions for the determination of instrumental polarization, a total of 45 objects was investigated. With a beamwidth of $4'\cdot 1$ it was possible to measure the polarization in the individual components of two of the sources (PKS 0518−45 and PKS 1322−42).

III. Results

The sources, their peak flux densities, percentage polarization, and directions of polarization are listed in Table 1. In addition to the Parkes nomenclature, alternative catalogue numbers are included. All errors quoted are standard deviations. The peak flux densities were obtained from the total power output of the receiver and have not been corrected for the effects of resolution. The intensity scale is based on a value of 13·0 f.u.* for PKS 0915−11 (Hydra A), as adopted by Kellermann (1966). As a result of instabilities in the total power output the accuracy of the flux densities is not high.

Twenty of the sources have also been observed by Sastry, Pauliny-Toth, and Kellermann (1967) with the NRAO 140 ft radio telescope. Excluding the source PKS 0430+05 (see later), the average differences in polarization ($\overline{\Delta p}$) and position angle ($\overline{\Delta \text{P.A.}}$) are

$$\overline{\Delta p}(210-140) = -0\cdot 2\% \pm 1\cdot 2\% \text{ (r.m.s.)}, \qquad \overline{\Delta \text{P.A.}}(210-140) = 3^\circ\cdot 7 \pm 5^\circ\cdot 5 \text{ (r.m.s.)}.$$

The scatter about the mean values has probably been enhanced by the partial resolution of some of the sources by the 210 ft telescope, since most extended sources

---

[*] 1 flux unit = 10^{-26} W m^{-2} Hz^{-1}.

TABLE 1

LINEAR POLARIZATION AT 6 CM

Parkes Catalogue Number	Alternative Catalogue Number	Peak Flux Density (f.u.)	Linear Polarization (%)	Position Angle °
PKS 0106+13	3C 33	2·9	8·2±0·8	94±7
0356+10	3C 98	3·3	6·5±1·5	80±3
0410−75	MSH 04−7*1*	4·5	1·7±0·4	40±4
0430+05	3C 120	7·0	1·3±0·3	13±12
0438−43	MSH 04−*49*	6·1	2·0±1·0	45±15
0440−00		3·5	2·5±1·5	30±10
0518+16	3C 138	4·2	8·9±1·0	169±4
0518−45(NW.)	Pictor A	11·2	8·8±0·7	124±3
0518−45(SE.)		10·0	6·5±1·2	81±5
0521−36	MSH 05−*36*	8·6	3·0±0·5	69±6
0531+22	3C 144	>450	5·6±0·1	141±1
0539−01	3C 147	38	0·2±0·2	165±12
0624−05	3C 161	7·0	4·1±0·6	122±3
0637−75	MSH 06−7*1*	5·3	1·4±1·0	179±15
0915−11	3C 218	13·0	<0·5	
1055+01	MSH 10+0*10*	3·2	4·3±1·0	94±7
1127−14		6·7	3·1±1·0	132±6
1216+06	3C 270	4·1	10·8±0·9	94±2
1226+02	3C 273	43	2·0±0·3	150±3
1228+12	3C 274	64	2·0±0·1	26±1
1252−12	3C 278	2·4	8·0±3·0	13±15
1253−05	3C 279	14·6	4·3±0·4	110±3
1302−49	MSH 13−4*1*	2·4	4·5±2·5	165±15
1322−42(W.)	Centaurus A (central component)	43	1·9±0·2	96±2
1322−42(E.)		54	16·3±0·3	139±2
1323−61		3·5	4·7±1·0	45±5
1328+25	3C 287	2·9	6·4±1·8	154±10
1343−60	13S6A	9·1	8·9±0·3	41±1
1549−79		3·3	3·5±1·0	114±5
1610−60	MSH 16−6*1*	4·7	5·0±1·0	4±6
1610−77		3·3	7·1±2·2	104±6
1648+05	3C 348	11·3	7·0±0·9	25±3
1717−00	3C 353	17·3	6·2±0·5	85±3
1727−21	3C 358	5·7	1·6±1·0	103±20
1737−30	MSH 17−*39*	8·7	2·5±0·6	27±7
1742−28	Sagittarius A	>126	0·8±0·5	164±20
1814−46	HII region		1·6±1·0	170±15
1814−63	MSH 18−6*1*	4·4	2·4±0·8	37±12
1932−46	MSH 19−*46*		<1·5	
1934−63		6·0	<0·5	
2121+24	3C 433	3·9	3·9±1·0	144±5
2145+06		4·2	2·0±2·0	42±20
2152−69	MSH 21−*64*	10·8	1·3±0·6	30±10
2223−05	3C 446	3·9	4·4±1·0	3±10
2230+11	CTA 102	4·0	5·5±0·6	47±6
2251+15	3C 454·3	17·5	1·8±0·3	3±7
2356−61	MSH 23−*64*	4·1	3·4±0·9	177±10

are characterized by variations of polarized flux and position angle across their diameters. In addition, for quasi-stellar objects there may have been variations in the parameters in the period between the two sets of observations. However, on the basis of the present results, there appears to be a systematic difference in the position angle scales of 4°.

The data for sources with significant polarization are shown in Figures 1–3, together with observations at longer wavelengths (Gardner, Morris, and Whiteoak 1968). The sources have been grouped into radio galaxies, quasi-stellar objects, and galactic and unidentified objects, according to the identifications compiled in Gardner, Morris, and Whiteoak. On the left-hand side of each figure is shown the relationship between percentage polarization and the square of the wavelength. The continuous lines represent the approximate trends in the observations. The right-hand side of each figure contains the variation of log(flux density) with log(frequency). The variations of direction of polarization with the square of the wavelength are not shown as they are linear for most sources and more likely to be associated with our Galaxy than to be indigenous to the sources (Gardner and Whiteoak 1966). Sources showing departures from linearity will be discussed individually. The characteristics of the intrinsic angles of polarization are discussed in Gardner, Morris, and Whiteoak.

(a) *Radio Galaxies*

The radio sources identified with galaxies are shown in Figure 1. For each, the identification, its magnitude, and radio dimensions are given in the accompanying table. The component separation is designated Sep. for double sources, and the halo and core estimates for sources with more complex structure are followed by H and C respectively. The data are from the compilation of Gardner, Morris, and Whiteoak (1968). Because of the lack of corresponding data at longer wavelengths, the resolved sources PKS 0518−45 and PKS 1322−42 have been excluded.

The sources associated with D and E galaxies and with simple single or double radio structure have linear spectra except in the cases where obvious resolution effects are present at 6 cm (PKS 1216+06, PKS 1302−49, PKS 1610−60, PKS 1717−00, and PKS 2356−61). Their spectral indices are quite similar at wavelengths longer than 11 cm. The percentage polarization is relatively constant except for PKS 2152−69 and for the objects of greater brightness temperature, namely, PKS 1648+05 and PKS 1717−00, where the substantial decrease of polarization with increasing wavelength suggests the presence of internal Faraday depolarization. The interpretation of the structure of PKS 2152−69, and possibly its optical identification, are open to doubt, as Ekers (1967) has pointed out. One of the components is seven times fainter than the other at 1400 MHz and has a significantly steeper spectral index, and the source cannot be considered a typical double source. Moreover, it is difficult to interpret the polarization relationship merely by the association of the polarization with the source having the steeper spectral index, or by the presence of internal Faraday depolarization.

For the two halo–core objects PKS 1228+12 and PKS 1302−49, the rapid increase of percentage polarization at 6 cm could occur if the polarization were associated with the core of the objects, since in each case the halo is extensively resolved at this wavelength.

The source PKS 0430+05 is identified with a Seyfert-type galaxy. At least some of the radio emission emanates from a region of $\leqslant 0''\cdot1$ as the radiation scintillates at a sufficiently small elongation from the Sun. At high frequencies the radiation is variable (Pauliny-Toth and Kellermann 1966). The shape of the spectrum shown may not be that existing at the time at which the 6 cm observations were obtained, since the data for longer wavelengths were determined at different epochs. However, the general shape conforms to the two-component model proposed for the radiation of quasi-stellar objects (Pauliny-Toth and Kellermann 1966; Harris 1967). In this model

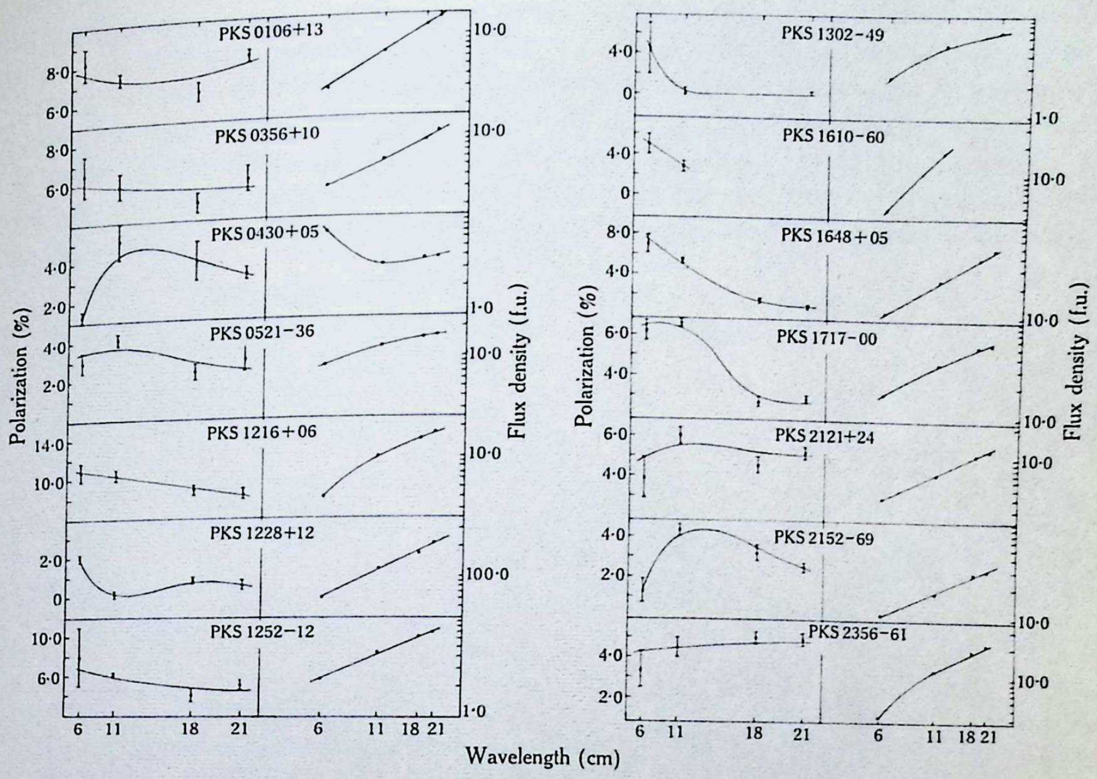

Source	Optical Identification	Radio Dimen. (min of arc)	Source	Optical Identification	Radio Dimen. (min of arc)
PKS 0106+13	$15\cdot6^{m}$D	Sep. 3·8	PKS 1302−49	9^{m} Sc	$9\cdot0\times4\cdot5$H $<0\cdot5$C
PKS 0356+10	$15\cdot0^{m}$E	Sep. 3·4	PKS 1610−60	$12\cdot8^{m}$E	6·0
PKS 0430+05	$15\cdot0^{m}$Sey.	$<10^{-3}$	PKS 1648+05	$18\cdot3^{m}$D	Sep. 2·0
PKS 0521−36	$16\cdot8^{m}$N	$<0\cdot3$	PKS 1717−00	$16\cdot8^{m}$D	Sep. 2·5
PKS 1216+06	$12\cdot0^{m}$E	Sep. 4·7	PKS 2121+24	17^{m} D	Sep. 0·2 (at P.A. 67°)
PKS 1228+12	$9\cdot9^{m}$E	6·6H, $<10^{-3}$C	PKS 2152−69	$13\cdot8^{m}$D	Sep. 3·8
PKS 1252−12	$13\cdot5^{m}+13\cdot2^{m}$	1·5 (at P.A. 90°)	PKS 2356−61	16^{m} D	Sep. 4·0, 8·1

Fig. 1.—Variation of percentage polarization with (wavelength)² together with corresponding spectral information (log–log scale) for radio sources identified with galaxies.

the high frequency component originates in a young compact region. For PKS 0430+05 most of the polarization at 6 cm is probably associated with the low frequency component, the small percentage being due to the addition of unpolarized radiation from the variable high frequency component. Also, the polarized flux density is independent of the intensity variations of this second component. In this respect, Sastry, Pauliny-Toth, and Kellermann (1967) list a total flux density only half the value measured in the present observations, and a percentage polarization that is approximately double that shown in Figure 1. However, it appears that the high frequency component must be polarized to a certain extent, but with a different direction of polarization, to account for a 30° difference between the observed angle at 6 cm and the value extrapolated from observations at longer wavelengths.

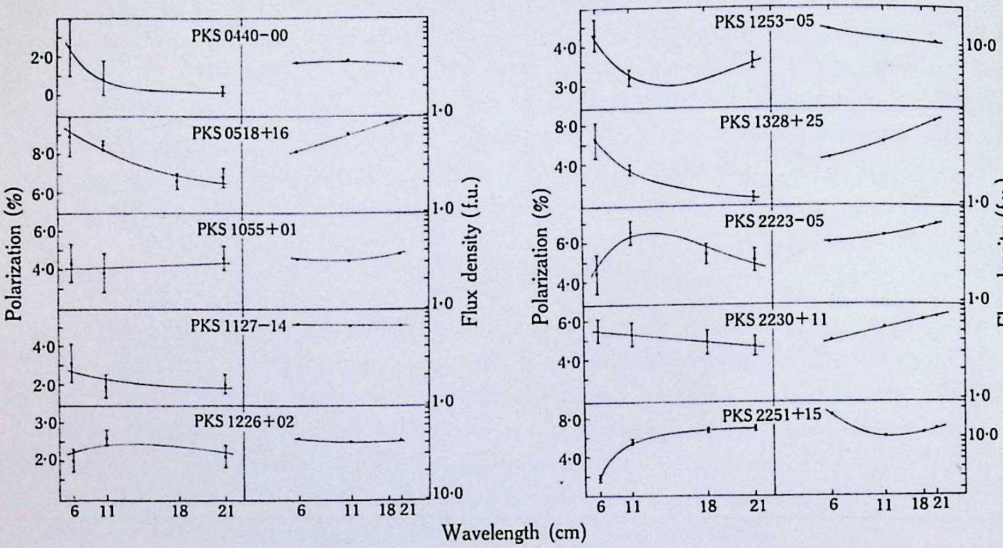

Fig. 2.—Variation of percentage polarization with (wavelength)^2 together with corresponding spectral information (log–log scale) for quasi-stellar sources.

The source PKS 0521−36, associated with an N-type galaxy, is characterized by a flatter spectrum than average. It may represent an object of a type between the normal radio galaxy and PKS 0430+05.

(*b*) *Quasi-stellar Objects*

The quasi-stellar objects (Fig. 2) show a variety of features. Most of the spectra differ considerably from those observed for radio galaxies. The differences are due in many cases to the presence of a high frequency component of radiation that vanishes at decimetre wavelengths because of synchrotron self-absorption. For the sources PKS 2223−05 and PKS 2251+15 the polarization appears to be associated predominantly with the low frequency component, showing a decrease at 6 cm. For such cases, the high frequency component may be essentially unpolarized at 6 cm. This could occur if it were optically thick, or in the presence of sufficiently large values of internal Faraday rotation. The sources PKS 0518+16 and PKS 1328+25 have the characteristics of highly luminous radio galaxies such as PKS 1648+05 and may lack a significant high frequency component. The extensive depolarization suggests the presence of differential Faraday rotation. Although it is not evident in the present results, observations of PKS 1226+02 by Aller and Haddock (1967) at 3·75 cm imply an association of the polarization with the varying (i.e. high frequency) component.

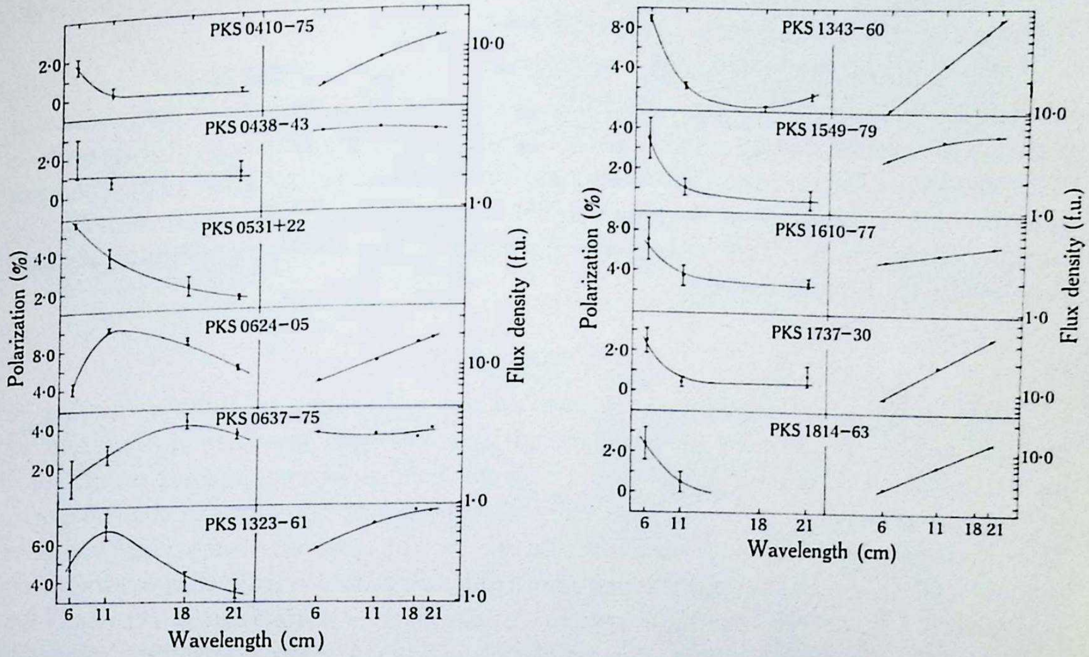

Fig. 3.—Variation of percentage polarization with (wavelength)^2 together with corresponding spectral information (log–log scale) for galactic and unidentified sources:

PKS 0410−75, <0·4′;	PKS 1343−60, galactic;
PKS 0438−43, <0·3′ (at P.A. 90°);	PKS 1549−79, <0·4′;
PKS 0531+22, Crab Nebula;	PKS 1737−30, galactic;
PKS 0624−05, <0·03′ (at P.A. 67°);	PKS 1814−63 <0·4′.
PKS 0637−75, <0·3′.	

Of the remainder, PKS 1127−14 and PKS 1253−05 are outstanding owing to a nonlinear relationship between Faraday rotation and (wavelength)^2. A simple interpretation is that both the components of radiation are polarized but in different directions. In particular, PKS 1253−05 has a position angle of polarization at 6 cm that differs by 20° from the value to be expected by extrapolation from longer wavelengths. The shift is towards the value determined by Kinman (1967) for the optical radiation. The polarization of this source at 3·75 cm has been observed over a considerable period of time by Aller and Haddock (1967) and shows short-period fluctuations.

(c) *Unidentified and Galactic Objects*

The results for the unidentified and galactic sources are shown in Figure 3. The galactic sources consist of PKS 0531+22 (Crab Nebula), PKS 1343−60, and possibly PKS 1737−30. A fourth source listed in Table 1, PKS 1727−21 (Kepler's Nova), is virtually unpolarized at all frequencies employed. The source PKS 1343−60 is an extended object ($> 10'$), the resolution of which probably accounts for the apparently steep spectrum. It is of particular interest, as it lies within a few degrees of the recently determined position of the variable X-ray source Cen XR-2 (Francey *et al.* 1967), and an association between the two objects is not currently out of the question. The apparent depolarization for these galactic sources may be due to differential internal Faraday rotation or, in the case of PKS 1343−60, to the concentration of polarization into a region of small angular size.

The sources PKS 0624−05, PKS 0637−75, and PKS 1323−61 have the polarization features characteristic of objects with a high frequency component of radiation, as exemplified by some quasi-stellar objects or intermediate objects such as PKS 0430+05. In contrast, PKS 0438−43, PKS 1549−79, and PKS 1610−77 have characteristics similar to quasi-stellar objects such as PKS 2230+11 or the N-type galaxy PKS 0521−36. The remaining sources are probably of high luminosity and associated with faint D galaxies.

IV. Conclusions

The polarization measurements at 6 cm have brought to light a number of features in the variation of polarization with wavelength that are not present at longer wavelengths. For the quasi-stellar objects the short-wave dependence of polarization on wavelength can in many cases be associated with features in the spectrum. These features have usually been attributed to the presence of young compact components. In some cases, there is evidence that the radiation from these components is polarized. In others, the high optical depths of the radiation at 6 cm may be responsible for the observed low polarization. However, it is not possible to distinguish all quasi-stellar objects from radio galaxies on the basis of their short-wave polarization properties alone.

V. Acknowledgments

We thank Miss J. K. Merkelijn, for assistance with the observations, and Mr. F. Tonking, who was responsible for the receiving equipment.

VI. References

Aller, H. D., and Haddock, F. T. (1967).—*Astrophys. J.* **147**, 833.

Berge, G. L., and Seielstad, G. A. S. (1967).—*Astrophys. J.* **148**, 367.

Broten, N. W., *et al.* (1965).—*Aust. J. Phys.* **18**, 85.

Dent., W. A, and Haddock, F. T. (1966).—*Astrophys. J.* **144**, 568.

Ekers, R. D. (1967).—Ph.D. Thesis, Australian National University.

Francey, R. J., Fenton, A. G., Harries, J. R., and McCracken, K. G. (1967).—*Nature, Lond.* **216**, 773.

Gardner, F. F., Morris, D., and Whiteoak, J. B. (1968).—Measurements of the linear polarization of radio sources between 11 and 20 cm. *Aust. J. Phys.* (in press).

Gardner, F. F., and Whiteoak, J. B. (1966).—*A. Rev. Astr. Astrophys.* **4**, 245.

Harris, B. J. (1967).—*Publs astr. Soc. Aust.* **1**, 26.

Kellermann, K. I. (1966).—*Aust. J. Phys.* **19**, 577.

Kinman, T. D. (1967).—*Astrophys. J. Lett.* **148**, L53.

Morris, D., Whiteoak, J. B., and Tonking, F. G. (1968).—*Aust. J. Phys.* **21**, 337.

Pauliny-Toth, I. I. K., and Kellermann, K. I. (1966).—*Astrophys. J.* **146**, 634.

Sastry, Ch. V., Pauliny-Toth, I. I. K., and Kellermann, K. I. (1967).—*Astr. J.* **72**, 234.

THE OPTICAL SPECTRUM OF VELA X

By D. K. MILNE*

[*Manuscript received February* 26, 1968]

Summary

The optical spectra of two filaments in the nebula Stromlo 16 (the radio source Vela X) were obtained with the photoelectric spectrum scanner. Electron temperature stratification over the filaments has been deduced from the intensity ratios between certain lines in these spectra. Indications are of a small-sized high temperature region with an electron temperature $T_e \simeq 10^5$ °K together with a much greater volume of cooler gas with $T_e \simeq 10^4$ °K. The former region is bright in the lines of OIII whilst the latter region is bright in the lower excitation lines of OII, NII, and H. The collisionally excited nature of these spectra confirms previous conclusions that this object is the remnant of a supernova.

I. INTRODUCTION

In a previous paper (Milne 1966) evidence was given for accepting Vela X (Stromlo 16) as a supernova remnant. One of the points raised but not fully discussed was the stratification of the electron temperature in the filaments. It is the purpose of this paper to present the observations and deductions leading to this conclusion.

The filamentary nebula Stromlo 16 covers an area about 4° by 2° centred on right ascension $08^h 32^m$ and declination $-45°$. It is composed of a faint background emission over most of this area with many bright sharp filaments around its northern and western boundaries and more diffuse nebulosities on the eastern face. This is illustrated in Figure 1, which is a mosaic composed of four plates taken with the Uppsala 26 in. Schmidt camera at Mount Stromlo. The exposures were each 120 min and were made on 103aE plates through an RG-2 filter.

II. OBSERVATIONS

The two bright sharp filaments indicated in Figure 1 were examined for line emission with the photoelectric spectrum scanner on the Mt. Stromlo 50 in. reflector. Most of the observations were made by integrating the signal received when the grating angle was set for the wavelength of expected lines and comparing this with the integrated signal each side of the line. Integrating times were 50 sec each, usually carried out in sets of three for each wavelength. The estimated total integration time for each line was of the order of 1 hr in filament "A" and somewhat less in the other filament "B". The entrance and exit slits were set at 2 mm, giving a triangular response of half-intensity width 18 Å; the projected angular resolution on the sky was then 18 sec of arc. A decker 15 mm long was used; the entrance slit was not rotatable and was fixed in the north–south direction in the positions shown in Figure 1.

---

* Mount Stromlo and Siding Spring Observatories, Research School of Physical Sciences, Australian National University, Canberra, A.C.T. 2600; present address: Division of Radiophysics, CSIRO, P.O. Box 76, Epping, N.S.W. 2121.

Aust. J. Phys., 1968, **21**, 501–9

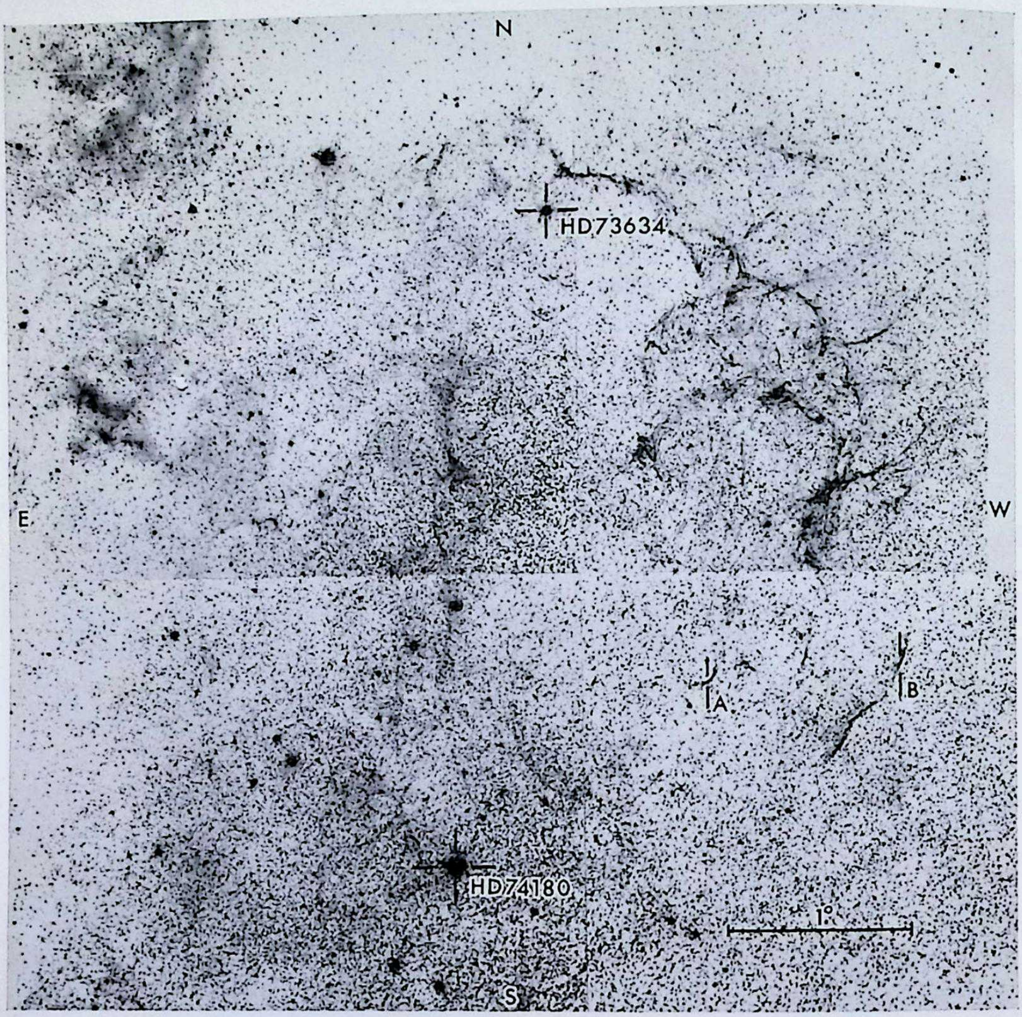
N
S
E
W
HD73634
HD74180
A
B
1°

Fig. 1.—The filamentary nebula Stromlo 16 taken in Hα light. The positions of the entrance slit of the spectrum scanner on filaments "A" and "B" are indicated.

The scanner was equipped with a monitor cell (2P21), and either a 2P21 cell working in the second-order blue or a 7102 cell in the first-order red was used for the spectral measurements. The scanner response was determined from scans on ϵ Ori, whose monochromatic magnitudes are given by Oke (1964). Appropriate filters were used to cut out overlapping orders when making the stellar scans but were not used for the emission line measurements. Scans and integrations were made on the Orion nebula to calibrate the wavelength scale. Very little work was done in the red—the scanner sensitivity is severely limited and the nights chosen to use the red cell were not favourable.

TABLE 1

LINE INTENSITIES

(1) Line	(2) Multiplier Current (10 ^{13} A)	(3) Corrected for Scanner Response	(4) Corrected for Reddening
Filament A (R.A. $08^h 31^m$, Dec. −45° 25′, 1950·0)			
[OII] 3727 Å	518±40	285±22	322±22
? 4040*	35±10	19·1±5·5	22±7
[SII] 4070*	22±10	12·2±5·5	14±6
Hδ 4108	9±5	4·8±2·7	5·2±3
Hγ 4340	44±3	27·8±2	31±2
[OIII] 4303	21±5	13·7±3·3	51±4
Hβ 4861	60±7	100(±12)	100(±12)
[OIII] 4959	22±4	40·6±17	40±7
[OIII] 5007	49±8	100±16	97±16
[NI] 5200	7±5	18±13	17±13
[NII] 6548*	5±3	3000±1500	2600±1300
Hα 6563	5±2	3000±1000	2600±1300
[NII] 6588*	3±2	1800±1000	1600±900
Filament B (R.A. $08^h 25^m$, Dec. −45° 15′, 1950·0)			
[OII] 3727	960±60	590±37	670±50
Hδ 4102	< 15±15 (not seen)	< 9±9	< 10±10
Hγ 4340	54±15	38±11	42±12
[OIII] 4363	42±15	30±11	32±12
Hβ 4861	54±15	100(±28)	100(±28)
[OIII] 4959	72±15	115±30	114±40
[OIII] 5007	174±20	390±45	385±45

* These lines were only measured from scans. Other lines, except 5200 Å, were scanned and integrated; 5200 Å was not scanned.

Two spectral scans were made on filament A. These were used to confirm (roughly) the integrations and were the means by which the SII doublet at 4070 Å and the unidentified line at 4040 Å were found. These two features were present in both scans. The results of this investigation are given in Table 1. The errors shown in column 2 were arrived at for each line individually and depend on the observational method employed; they are generally standard deviations (where sufficient readings were taken). The errors were found to originate from two basic sources: a ±8% error in the reading due to instability of the sky transparency, and an absolute error in each reading of $\pm 10^{-12}$ A for the blue cell ($\lambda < 5500$ Å) and about $\pm 2\times 10^{-13}$ A for the red cell. Columns 3 and 4 of Table 1 are normalized to $I(\mathrm{H}\beta) = 100$; a reddening correction was applied proportional to $1/\lambda$ and normalized to $A_v = 0\cdot 3 \pm 0\cdot 1$ mag. This absorption was estimated from Velghe's (1963) colours and magnitudes of OB stars in this direction (see Milne 1968).

III. ELECTRON TEMPERATURE IN THE FILAMENTS

Estimates of the electron temperature of the two filaments observed depend on the following three basic approaches.

(1) Measurement of intensity ratios of lines of the same ion; these ratios do not depend on ionic abundances. This is applied to the Balmer lines and to the [OIII] lines.

(2) Determination of ratios of line intensities from different ions of the same atomic species, e.g. the [OIII] and [OII] lines. The relative gas masses and electron densities in the regions occupied by each ionic state must, however, be known.

(3) Lastly, relative intensities of lines originating from ions of similar ionization potential but different atomic species can be related to give the electron temperature of the nebula region where these ions mutually exist. The relative abundances must be known. This treatment is used for H, [OII], and [NIII] lines.

(a) [OIII] Lines

Following Seaton (1960) the relative population of the ^{1}D and ^{1}S levels of the O^{2+} ion is given by

$$\frac{N(^1\mathrm{D})}{N(^1\mathrm{S})} = \frac{5\cdot 4\times 10^{-3}\,\mathrm{e}^{-2\cdot 89/t}\,K\{1+0\cdot 12\,E+4\cdot 1\times 10^{-4}K(1+0\cdot 11\,E)\}}{1\cdot 16\times 10^{-5}\,\mathrm{e}^{-6\cdot 19/t}\,K\{1+3\cdot 8\times 10^{-2}K(1+0\cdot 10\,E)\}}, \tag{1}$$

where $E(\mathrm{O}^{2+}) = \mathrm{e}^{-3\cdot 30/t}$, $t = 10^{-4}T_e$, and $K = 10^{-4}n_e/t^{\frac{1}{2}}$, T_e being the electron temperature (°K) and n_e the electron density (cm^{-3}).

Equation (1) reduces to

$$\frac{N(^1\mathrm{D})}{N(^1\mathrm{S})} = \frac{4\cdot 65\times 10^{2}\{1+0\cdot 12\,E+4\cdot 1\times 10^{-4}K(1+0\cdot 11\,E)\}}{E\{1+3\cdot 8\times 10^{-2}K(1+0\cdot 10\,E)\}}. \tag{2}$$

Multiplying by the relative photon energies and transition probabilities, we arrive at an expression for the relative intensities in the nebular and auroral lines; namely,

$$\frac{I(\lambda 4959+5007\ \text{Å})}{I(\lambda 4363\ \text{Å})} = \frac{7\cdot 1\{1+0\cdot 12\,E+4\cdot 1\times 10^{-4}K(1+0\cdot 11E)\}}{E\{1+3\cdot 8\times 10^{-2}K(1+0\cdot 10\,E)\}}. \tag{3}$$

Equation (3) is displayed graphically in Figure 2. The shaded regions are outside the limit that the line ratio can assume as T_e approaches infinity and at an electron density too high for radiative [OIII] transitions (i.e. for n_e such that the spontaneous downward transitions are much fewer than the collisional depopulation of the upper level). The ratio of the fluxes in the nebular [OIII] lines $F(\lambda 5007\ \text{Å})/F(\lambda 4959\ \text{Å})$ is a well-determined value both theoretically (Garstang 1951) and observationally (Liller and Aller 1954). This ratio should be 3·0 and is independent of the exciting conditions. The value obtained for filament A was 2·4 and, for filament B, 3·4. The value 3·0 is included in the error limits, so no attempt has been made to adjust them to the theoretical value.

Proceeding with the assessment of electron temperature from the [OIII] lines, we have for filament A

$$\log\left\{\frac{I(\lambda 5007+4959\ \text{Å})}{I(\lambda 4363\ \text{Å})}\right\} = 1\cdot 00 \pm 0\cdot 1\,. \tag{4}$$

It may be seen from Figure 2 that this would yield an electron temperature in excess of 8×10^4 °K, provided the electron density is less than about 10^4 cm^{-3}. Temperatures lower than this are permissible only if the electron density is in excess of 10^4 cm^{-3}.

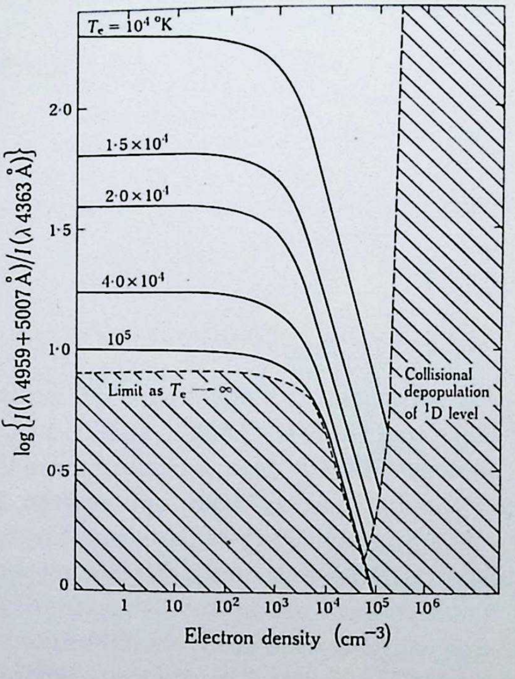

Fig. 2.—Dependence on electron temperature and density of the nebula and auroral line intensity ratio for OIII. The curves have been plotted from equation (3).

(b) *Hydrogen Lines*

The Balmer decrement obtained for filament A,

$$\text{H}\alpha:\text{H}\beta:\text{H}\gamma:\text{H}\delta = 26\pm13:1\cdot0:0\cdot32\pm0\cdot02:0\cdot06\pm0\cdot3\,,$$

cannot be satisfied by the radiative models investigated under various conditions by Baker and Menzel (1938), Capriotti (1964), and Pengelly (1964); the observed decrement is far too steep. A steep decrement is a feature of a collisionally excited nebula at a fairly low kinetic temperature, where the lower levels of the hydrogen atom are populated by electron collisions. As the electron temperature increases, ionization will result from the same mechanism and at about $T_e = 10^5$ °K, when the bulk of the gas is fully ionized, recombination and subsequent cascade will be responsible for most of the line emission. The Balmer decrement will then approximate the radiative excitation decrement.

Parker (1964*a*) has published calculations for collisionally excited nebulae, both for hydrogen lines and certain forbidden transitions. From a comparison of the observed decrement and Parker's data it would appear that an electron kinetic temperature of less than 10^4 °K is indicated. This estimate seems a reasonable one, although it depends critically on the Hα/Hβ ratio, which contains a very large degree of uncertainty. If the filament is optically thin in the Lyman lines, then the electron temperature could be a little lower.

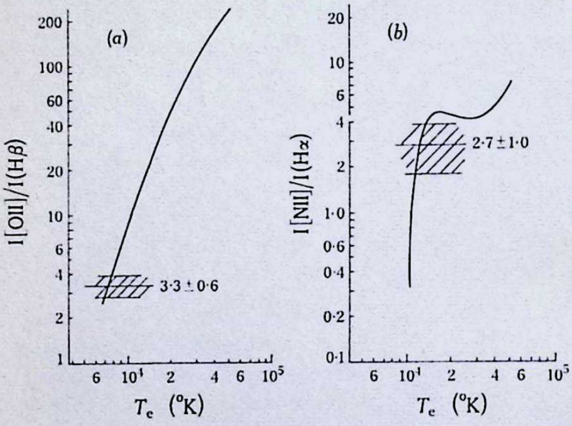

Fig. 3.—Temperature variation of the intensity ratios of the nebula lines of (*a*) OII to Hβ and (*b*) NII to Hα. The shaded strips enclose the values of these intensity ratios determined for filament A.

(*c*) [*OII*] *and* [*NII*] *Lines*

Figures 3(*a*) and 3(*b*) illustrate the temperature dependence of the intensity ratios $I(\lambda 3727 \text{ Å})/I(\text{H}\beta)$ $(= I[\text{OII}]/I(\text{H}\beta))$ and $I(\lambda 6548 + 6583 \text{ Å})/I(\text{H}\alpha)$ $(= I[\text{NII}]/I(\text{H}\alpha))$. The curves were drawn from Parker's (1964*a*) data assuming normal cosmic abundances (O/H $= 6 \times 10^{-4}$ and N/H $= 3 \times 10^{-4}$; Allen 1962) and electron densities in the range $200 \leqslant n_e \leqslant 1000$ cm^{-3}. The cross-hatched regions are the observed [OII]/Hβ and [NII]/Hα ratios for filament A ($3 \cdot 3 \pm 0 \cdot 6$ and $2 \cdot 7 \pm 1 \cdot 0$ respectively). The electron temperatures suggested by these data are about 7–8 $\times 10^3$ °K in [OII] and $1 \cdot 1$–$1 \cdot 3 \times 10^4$ °K in [NII]. The temperature derived from the OII lines could be raised if the estimate of absorption at $\lambda 3727$ Å relative to that at $\lambda 4681$ Å were increased, either by an increase in the dependence of the reddening-wavelength law or by increasing the value of A_v. As an example of this, if a $1/\lambda$ reddening law were retained then a temperature of 10^4 °K would be indicated from the observed [OII]/Hβ ratio providing $A_v = 1^m \cdot 12$, an absorption much higher than we estimate from Velghe's stars. The [NII]/Hα ratio is not affected by changes in the absorption, and even with the wide errors we have imposed on the intensities of these lines, a temperature above 10^4 °K is still indicated in the NII region. We deduce a slightly lower temperature from the observed [NII]/Hα ratio if a hydrogen temperature colder than that of the NII region is adopted—which is consistent with the slightly lower ionization potential of hydrogen compared with nitrogen.

These differences in electron temperature derived from the lower excitation lines of H, [NII], and [OII] and the higher excitation lines of [OIII] could be a real feature of this nebula if the shock fronts believed to exist in supernova remnants are responsible for the ionization and excitation of the filamentary gas.

(*d*) *Oxygen Doublets*

Estimation of the electron temperature from the oxygen doublets [OII], $\lambda 3726+3729$ Å, and [OIII], $\lambda 4959+5007$ Å, is straightforward enough if one assumes mixing of the ionic species. The electron temperature obtained for our observed ratio of $2\cdot 5\pm 0\cdot 5$ would be about 4×10^4 °K, using Parker's data. This well-mixed model is not, however, a very realistic interpretation of our previous deductions. If we assume that the [OII] and [OIII] lines originate in regions of electron temperature 10^4 and 10^5 °K and have hydrogen densities n_{H1} and n_{H2} and volumes V_1 and V_2 respectively, we can write for the ratio of the [OII]/[OIII] intensity

$$\frac{I(\lambda 3726+\lambda 3729)}{I(\lambda 5007+\lambda 4959)} = \frac{(f_4\, j_1^{+}\, n_{\mathrm{H1}}^2\, V_1)+(f_5\, j_2^{+}\, n_{\mathrm{H2}}^2\, V_2)}{(f_4\, j_1^{2+}\, n_{\mathrm{H1}}^2\, V_1)+(f_5\, j_2^{2+}\, n_{\mathrm{H2}}^2\, V_2)}, \qquad (5)$$

where it has been assumed that all the electrons are derived from the ionized hydrogen, and f_4 and f_5 are the ionization fractions at temperatures 10^4 and 10^5 °K respectively and j_1^{+}, j_2^{+}, j_1^{2+}, and j_2^{2+} are the volume emissivities of the lines from each ionic species and at each temperature. Using Parker's values for these and the ionization fractions at each temperature, we have

$$\frac{I(\lambda 3726+\lambda 3729)}{I(\lambda 5007+\lambda 4959)} \simeq 3\cdot 65\times 10^{-5}\frac{n_{\mathrm{H1}}^2\, V_1}{n_{\mathrm{H2}}^2\, V_2}+5\cdot 9\times 10^{-3}.$$

Equating this to the observed intensity ratio for filament A, namely, $2\cdot 5\pm 0\cdot 5$, we arrive at a density times mass ratio for the two regions of

$$\frac{n_{\mathrm{H1}}^2\, V_1}{n_{\mathrm{H2}}^2\, V_2} \simeq 7\times 10^4.$$

Dr. B. E. Westerlund (see Milne 1966) has estimated the electron density in filaments of this object to be 300 cm^{-3}. This estimate was made from the ratio of the line intensities in the [OII] doublet and is therefore applicable to the lower temperature region. This density compares well with densities obtained by Parker (1964*b*) for other supernova remnant filaments, and together with Parker's value for f_4 would yield a hydrogen density of 10^5 cm^{-3} for the low temperature region.

If we then consider that the [OIII] emission is generated in a region where $n_e < 10^4$ cm^{-3} (see Fig. 2), we will obtain a hydrogen density of $< 10^4$ cm^{-3} for this fully-ionized high temperature region, implying that the volume of this region is perhaps only 10^{-3} of the volume of the low temperature region, in order to satisfy the density times mass ratio of 7×10^4 above.

It is possible that the temperature stratification deduced here does not in fact exist. It would then be feasible to allow that an electron temperature of about 10^4 °K could obtain. However, this would require an electron density of near 10^5 cm^{-3} to give the observed ratio for the [OIII] nebula and auroral lines, which would conflict with the densities estimated from the [OII] doublet now required to originate in the same electron temperature and density field.

The above discussion was applied only to filament A; the observations were not so complete or accurate for filament B. The data obtained do, however, suggest similar stratification but with a lower temperature for the [OIII] region than that deduced from [OIII] in filament A—more like 5×10^4 °K with the lower excitation lines originating in a region of about $T_e = 10^4$ °K as before.

IV. MASS OF THE FILAMENTS

Estimates have been made of the mass in the filaments A and B. These estimates were made from the Hβ intensities after calibrating the scanner response on the star ϵ Ori for which Oke (1964) gives a monochromatic magnitude of $1^m\cdot555$ at $\lambda4861$ Å. Using Code's (1960) value of $3\cdot8\times10^{-9}$ erg cm^{-2} sec^{-1} Å^{-1} for the flux corresponding to zero visual magnitude, together with a measured multiplier current of $1\cdot515\times10^{-7}$ A in an 18 Å band near $\lambda4861$ Å on ϵ Ori, an Hβ sensitivity for the scanner of $0\cdot108$ erg cm^{-2} sec^{-1} per ampere was derived. From Table 1 the multiplier current for the Hβ line in filament A is 6×10^{-12} A, which, allowing for $0^m\cdot3$ of interstellar absorption and $0^m\cdot3$ of atmospheric absorption would give a total radiated energy at 500 pc (the assumed distance of Vela X; see Milne 1968) of 3×10^{31} erg sec^{-1} in the Hβ line.

From Parker (1964*a*) the collisionally excited Hβ volume emissivity at $T_e = 10^4$ °K is $1\cdot5\times10^{-27}\, n_e n_H$ erg cm^{-3} sec^{-1} and $1\cdot88\times10^{-25}\, n_e n_H$ erg cm^{-3} sec^{-1} at $T_e = 2\times10^4$ °K, which when equated to the observed Hβ energy would yield values for $n_e n_H V$ of 2×10^{58} cm^{-3} and $1\cdot6\times10^{56}$ cm^{-3}, where V is the emitting volume. If m_H is the mass of the hydrogen atom, then $m_H n_H V$ is the mass of the emitting region. Therefore we can say that the emitting mass lies between $3\cdot4\times10^{34}/n_e$ and $2\cdot7\times10^{32}/n_e$ grams for an electron temperature between 10^4 and 2×10^4 °K respectively. Furthermore, we estimate that only 1/20 of the filament was in the entrance slit of the scanner. Allowing for this and for an electron density of 300 cm^{-3} (as in Section III), we find that the total visible mass of filament A lies between 1 and 10^{-2} solar mass.

Returning to the values for $n_e n_H V$ (2×10^{58} cm^{-3} at $T_e = 10^4$ °K, and $1\cdot6\times10^{56}$ cm^{-3} at $T_e = 2\times10^4$ °K), if all the electrons are from the ionization of the hydrogen, we can substitute n_e/f for n_H, where f is the ionization fraction ($= 2\cdot4\times10^{-3}$ at $T_e = 10^4$ °K, and $0\cdot928$ at $T_e = 2\times10^4$ °K; Parker 1964*a*), and using $n_e = 300$ cm^{-3}, as before, we arrive at emitting volumes of 5×10^{50} and 20×10^{50} cm^3 for $T_e = 10^4$ and 2×10^4 °K respectively. Estimating the length of filament A to be 1 pc we would have cross sectional areas of $1\cdot5\times10^{32}$ and 5×10^{32} cm^2. There are two feasible models for the filaments in these objects: (1) the circular filament model and (2) the "sheet-seen-edge-on" model. The radius arrived at if model (1) is assumed is $0\cdot7$–$1\cdot26\times10^{16}$ cm, whilst if model (2) is adopted and a depth is taken equal to its length then the width would be $4\cdot4$–15×10^{13} cm. It has been found that the narrowest filaments in supernova remnants have a width of about 2×10^{16} cm (Harris 1962), and in fact for filament A the thickness appears to be more like 10^{17} cm—a thickness that would support a circular model for filament A. The mass and volume were obtained for filament B in a similar manner, and they are almost identical with those of filament A.

V. Conclusions

We have shown that electron temperature stratification exists for two filaments of Vela X. This is not a newly discovered feature for objects of this type. Parker (1964*b*) used such a stratification to explain physical conditions in other supernova remnants, concluding that the temperature for the Cygnus Loop was $1 \cdot 7 \times 10^4$ °K from the lower excitation lines and near 10^5 °K from the [OIII] lines with similar behaviour evident in other remnants. It was Parker's conclusion that physical conditions do not change greatly from filament to filament and that the greatest gains could be obtained by making very intensive measurements of one or two filaments in an object and extending the conclusions to other filaments in the object.

We have suggested that the mass of an individual filament could be as high as a solar mass (which means that the total mass could be as high as 30 $M_{\odot}$) provided the temperature is, as we have measured it from the H, OII, and NII lines, near 10^4 °K. These "visible" masses are higher than have previously been obtained for objects of this type and are a direct outcome of the lower electron temperature found in these filaments. The upper limit obtained for the mass does in fact approach the mass that one would expect to be swept up by the expansion of this object to its present size. Whilst an argument is presented in favour of the circular filament model, which seems to be physically less likely than the "sheet-seen-edge-on" model, it is not easy to explain the stratification in the electron temperature in filaments of circular section. The detection of stratification may be an argument in favour of the sheet model.

V. Acknowledgments

The author would like to thank Dr. A. Rodgers and Dr. L. Searle for helpful discussion during the course of this work and the preparation of the manuscript. The receipt of an Australian National University research scholarship is gratefully acknowledged.

VI. References

Allen, C. W. (1962).—"Astrophysical Quantities." (Univ. London Press.)

Baker, J. C., and Menzel, D. H. (1938).—*Astrophys. J.* **88**, 52.

Capriotti, E. R. (1964).—*Astrophys. J.* **139**, 225.

Code, A. D. (1960).—*In* "Stellar Atmosphere". (Ed. J. L. Greenstein.) p. 50. (Chicago Univ. Press.)

Garstang, R. H. (1951).—*Mon. Not. R. astr. Soc.* **111**, 115.

Harris, D. E. (1962).—*Astrophys. J.* **135**, 661.

Liller, W., and Aller, L. H. (1954).—*Astrophys. J.* **120**, 48.

Milne, D. K. (1966).—Proc. Symp. Radio and Optical Studies of the Galaxy, Mt. Stromlo, p. 74.

Milne, D. K. (1968).—*Aust. J. Phys.* **21**, 201.

Oke, J. B. (1964).—*Astrophys. J.* **140**, 689.

Parker, R. A. (1964*a*).—*Astrophys J.* **139**, 208.

Parker, R. A. (1964*b*).—*Astrophys. J.* **139**, 493.

Pengelly, R. M. (1964).—*Mon. Not. R. astr. Soc.* **127**, 145.

Seaton, M. J. (1960).—*Rep. Prog. Phys.* **22**, 313.

Velghe, A. G. (1963).—Preprint, Royal Observatory of Belgium.

RADIO SOURCES IN CLUSTERS OF GALAXIES

By B. Y. Mills,* R. R. Shobbrook,* and D. Stewart-Richardson*

[*Manuscript received December* 28, 1967]

Summary

Fifty-eight clusters from Abell's catalogue have been examined for radio emission using the Arecibo 1000 ft reflector and the Molonglo 1 mile Cross. The positions, sizes, and flux densities at 408 MHz of 30 radio sources close to these clusters have been measured. Nineteen of these offer reasonable identifications with galaxies or blue stellar objects. Thirteen appear to be identifiable with individual cluster galaxies. No evidence for integrated cluster emission has been obtained. It has been concluded that either the centroid of radio sources may sometimes be well displaced from the parent galaxies or, in a significant number of cases, the only detectable radio source in a cluster is associated with a faint cluster galaxy, not a giant.

I. Introduction

There have been many investigations of the statistical association between radio sources and clusters of galaxies. The present aim is rather different, namely, to identify the sources of emission where there is an apparent association between a radio source and a cluster. This may lead to a better understanding of the types of galaxies that may become radio galaxies and, providing there is a statistically significant association of clusters and radio sources, may provide some positive evidence about the nature of unidentified sources and the radio luminosity function. Also, it allows a direct check on the existence of intergalactic emission unassociated with any particular galaxy.

The investigation has, in the first instance, been limited to an examination of a relatively small number of clusters, 58 in all. However, the results are promising and a full-scale programme has now been undertaken with the 1 mile Cross at the Molonglo Radio Observatory. The results from the preliminary investigation are described here.

A selection of clusters was made from Abell's (1958) catalogue and the Arecibo 1000 ft reflector was used as a finding instrument to detect nearby radio sources and roughly measure their position and flux densities. More accurate positions and also the angular sizes and flux densities of these sources were then measured again with the 1 mile Cross. From the 58 clusters observed, a selection of 30 radio sources stronger than about 1 f.u.† at 408 MHz was made for detailed examination using the Palomar Sky Atlas together with some direct photographs made at Mt. Stromlo Observatory. Not all the chosen sources are physically associated with the clusters, so that we have also obtained information about a random selection of comparatively weak sources.

---

* Cornell–Sydney University Astronomy Centre, School of Physics, University of Sydney, N.S.W. 2006.

† 1 flux unit = $10^{-26}\,\mathrm{W\,m^{-2}\,Hz^{-1}}$.

Aust. J. Phys., 1968, **21**, 511–21

II. OBSERVATIONS

Selections were made from Abell's catalogue of clusters in the declination range common to the Arecibo and Molonglo radio telescopes, i.e. between about +18° and −1°. Clusters in this range were selected according to three criteria.

(1) All clusters of distance 3 or closer on the Abell scale.

(2) More distant clusters for which an association with a radio source had been found earlier by Mills (1960); this category extended only to a declination of +10°, which was the limit of an earlier survey (Mills, Slee, and Hill 1958).

(3) Rich clusters (richness 3 or greater on Abell's scale) not included in either of the above categories.

TABLE 1

CLUSTERS OBSERVED

Listed according to their numbers in Abell's catalogue

Category 1			Category 2			Category 3		
Cluster	Distance	Richness	Cluster	Distance	Richness	Cluster	Distance	Richness
76	3	0	16	5	2	41	6	3
102	3	0	55	5	0	750	5	3
119	3	1	520	6	3	1437	5	3
147	3	0	526	4	1	1525	6	3
168	3	2	623	5	1	1530	6	3
240	3	0	732	6	1	1882	5	3
397	3	0	862	6	1	1942	6	3
399	3	1	869	6	0	2204	5	3
400	1	1	1148	6	1	2224	6	3
401	3	2	1346	5	1	2397	6	3
539	2	1	1620	5	0	2610	6	3
592	3	1	1850	6	1	2623	5	3
999	3	0	2029	4	2	2631	6	3
1139	3	0	2050	5	1			
1142	3	0	2512	5	1			
1773	3	1	2551	6	1			
1890	3	0	2644	5	1			
1983	3	1						
2052	3	0						
2063	3	1						
2147	1	1						
2151	1	2						
2152	1	1						
2572	3	0						
2589	3	0						
2593	3	0						
2630	3	0						
2657	3	1						

There are 28 clusters in the first category, 17 in the second, and 13 in the third; they are listed in Table 1. The first category was chosen to give a homogeneous sample of clusters to a fixed limiting distance. The second was included to check on the physical reality of the associations noted earlier. The third was added in the thought that rich clusters might be likely to exhibit a weak integrated emission which may have been overlooked in the earlier investigation.

Initially, constant declination scans were made at the nominal cluster positions with the Arecibo 1000 ft reflector using the 430 and 195 MHz radio astronomy feeds plus, occasionally, the 610 MHz feed. If a radio source was observed within about 1 min in right ascension from the cluster position on any of these frequencies, a scan in declination at the indicated right ascension was made to locate the source more accurately and to measure its flux density. In a few cases, several such scans were necessary to isolate confused sources.

As a result of this programme some 37 sources were listed with flux densities greater than about 0·5 f.u. at 430 MHz. A search was then made for these sources at the Molonglo Radio Observatory using both the fan beam of the east–west antenna and the multiple pencil beams of the full Cross. The former beam measures 1′·5 east–west by 4° north–south, the latter 2′·8 east–west by about 4′ north–south at the mean declination of the observations. After excluding some of the more remote sources which had been listed in the analysis of confused regions and two in which the Arecibo observations had been confused by solar interference, it was decided to restrict the analysis to sources equal to or stronger than 1 f.u. at 408 MHz, which should form a homogeneous sample.

There are 30 such sources and these are listed in Table 2. The associated cluster is indicated, although it is not suggested that the association is physical in all cases. The positions given are those measured at Molonglo. Because the completed Cross had been in use for only a short time and was relatively untested, it was used only where necessary, i.e. for declination measurements and for obtaining the structure of the larger extended sources. Right ascensions and flux densities were obtained from the fan beam measurements, for which the calibration had been well established over nearly two years of observation. Flux densities are based on the absolute scale derived by Wyllie (1968), which is about 10% higher than the commonly used CKL scale (Kellermann 1964) when averaged over the southern sources common to both. For many of the stronger sources, however, flux densities given in the Parkes catalogue (Day *et al.* 1966) have been used in order to avoid a separate determination, particularly where the source is resolved and an integration is necessary. Such flux densities are given in parentheses in the table. Angular sizes or structural details quoted are based usually on the east–west extension (EW) measured on the fan beam but, if the source is large or appears confused, pencil beam contours have been used. The observational class divides the measurements into good (a), average (b), or poor (c); the overall standard errors in the measured positions in each of these classes is believed to be approximately as follows: for right ascensions, (a) 3″, (b) 5″, (c) 10″; for declinations, (a) 6″, (b) 9″, (c) 12″. The right ascension estimates are based on considerable accumulated experience and should be reliable; the largest values are due principally to confusion effects. The declination accuracy has been checked against a few source positions determined from lunar occultations and is believed to be conservative; with the higher resolution of the pencil beams, confusion is not a problem. Most of the sources have been listed in one or more of the principal radio catalogues, and the appropriate catalogue numbers are quoted in Table 2 for easy reference.

TABLE 2

LIST OF RADIO SOURCES SELECTED FOR EXAMINATION

Although the appropriate Abell cluster number is quoted the association is not always physical

Source No.	Abell No.	Position (1950·0) R.A.			Dec.		Flux Density (f.u.)	Class	Size and Structure	Catalogue References
		h	m	s	°	′				
1	55	00	30	39·9	+06	11·9	3·0	b	<1′	MSH00+0*7*, PKS0030+06, 4C06/1
2	119	00	53	39·1	−01	34·6	(10)	b	Double sp–nf sep. 7′	MSH00−0*17*, PKS0053−01, 4C−01/4
3	119	00	55	01·5	−01	39·6	(12)	b	<0′·5	MSH00−0*17*, PKS0055−01, 4C−01/5
4	240	01	37	59·6	+07	21·5	1·2	b	∼2′EW	
5	400	02	55	04·3	+05	50·6	(16)	b	Ext. np–sf ∼4′	MSH02+0*10*, PKS0255+05, 4C06/15
6	400	02	54	32·5	+06	25·9	4·3	b	∼1′EW	MSH02+0*9*
7	539	05	15	34·6	+06	21·8	1·5	b	∼1′·5EW	4C06/22
8	623	08	03	03·3	−00	49·4	(5·8)	b	<0′·5	MSH08−0*2*, PKS0803−00, 4C−00/32
9	862	09	41	37·0	+10	00·0	(8·7)	c	<0′·5	MSH09+0*5*, PKS0941+10, 4C10/27
10	1139	10	55	55·6	+01	50·3	3·8	a	<0′·5	MSH10+0*10*, PKS1055+01, 4C01/28
11	1142	10	59	40·3	+10	45·4	2·5	b	<1′	4C10/31
12	1148	10	59	30·7	−01	00·1	(8·1)	a	<0′·5	MSH10−0*21*, PKS1059−01, 4C−00/42
13	1346	11	38	36·4	+06	00·6	(1·8)	b	<1′	MSH11+0*9*, PKS1138+05, 4C06/42
14	1850	14	01	04·4	+09	14·2	1·1	b	<1′	MSH14+0*1*
15	1890	14	15	02·0	+08	26·8	1·8	c	3′EW	
16	1942	14	35	03·2	+03	53·2	4·3	c	∼4′EW	MSH14+0*10*
17	2029	15	08	28·2	+05	56·0	(3·4)	c	<1′	MSH15+0*3*, PKS1508+05, 4C06/53
18	2050	15	14	06·0	+00	25·9	(4·4)	b	Ext. np–sf ∼5′	MSH15+0*6*, PKS1514+00, 4C00/56
19	2052	15	14	17·2	+07	12·3	(26)	a	<0′·5	MSH15+0*5*, PKS1514+07, 4C07/40
20	2147	15	59	06·2	+15	45·8	4·6	b	∼1′EW	4C15/52
21	2147	16	00	20·9	+15	52·3	2·9	b	∼2′EW	4C15/53
22	2151	16	02	54·2	+17	52·2	2·3	b	∼2′EW	4C17/66
23	2224	16	43	09·9	+13	28·0	2·6	a	<1′	PKS1643+13

TABLE 2 (*Continued*)

Source No.	Abell No.	Position (1950·0) R.A. h	m	s	Dec. °	′	Flux Density (f.u.)	Class	Size and Structure	Catalogue References
24	2551	23	08	08·9	+07	19·1	(5·8)	a	2′EW	MSH23+0*2*, PKS2308+07, 4C07/40
25	2593	23	21	55·0	+14	22·0	1·0	c	~2′EW	
26	2610	23	26	04·8	+16	58·3	1·9	b	<1′	4C16/83
27	2610	23	29	28·5	+17	12·2	3·7	b	~1′EW	PKS2329+17, 4C17/94
28	2644	23	38	27·3	−00	11·8	2·7	c	~3′EW	MSH23−0*15*, 4C−00/83
29	2657	23	43	49·0	+08	36·4	1·4	c	~1′EW	
30	2657	23	44	03·9	+09	14·1	2·4	b	<1′	PKS2344+09, 4C09/74

As a rough indication of the completeness of the earlier catalogues it is interesting to see what proportion of the present sources are listed. For example the 4C (Gower, Scott, and Wills 1967) and Parkes (Day *et al.* 1966) catalogues contain 70% and 53% of the sources respectively, while the MSH catalogue (Mills, Slee, and Hill 1958), which extends only to a declination of +10°, contains 77% of the sources within this area.

Finally, no evidence could be found for integrated emission either from the intergalactic gas or from more than one galaxy in a cluster. When a source is detectable the radio emitting area occupies only a small fraction of the total area of the cluster; an extended region would be easily recognizable by comparing the low resolution Arecibo and high resolution Molonglo responses.

III. IDENTIFICATIONS

In searching for optical identifications, the usual criteria have been employed, namely, that only galaxies or blue stellar objects close to the centroid of a radio source have been considered. In general we have accepted an identification when the radio centroid lies within two standard errors of the optical image, but when the radio source is resolved and extended we have considered the overlap of optical and radio images to be an alternative criterion. As shown below it has proved necessary to consider also the position of giant members of a cluster with respect to the radio source. For the 30 sources listed, reasonable identifications can be suggested for 19.

It has been found convenient to examine the first category of 28 close clusters separately as it is believed to form a homogeneous sample. The beamwidths given by the Arecibo 430 and 195 MHz radio astronomy feeds are approximately 17′ and 30′ arc respectively, and the sensitivity is such that it is believed all sources stronger than 1 f.u. at 408 MHz within 10′ arc of the nominal cluster centre have been detected in the finding programme. However, half of the total number of sources listed fall outside this angular distance. For a statistical analysis we have taken 10′ arc as a convenient limiting separation to define a possible physical association with the cluster; it is found that only a small proportion of the remaining sources are likely to be so associated.

The probability of a chance location of one of these radio sources within a 20′ arc circle is quite small. From some rough counts we would expect about 1 source stronger than 1 f.u. per 4 square degrees. This corresponds to a probability of 0·022 or, in the 28 clusters of category 1, the expectation of chance coincidences is 0·6. Actually there are 8 sources within 10′ arc, one of which is listed as a double; it is reasonable to assume that practically all of these are physically associated with the clusters. For example, from the first three terms of the Poisson series, we find the probability that more than two chance associations are involved is

$$p = 1-e^{-0\cdot 6}(1+0\cdot 6+0\cdot 18) = 0\cdot 02\,.$$

The eight sources concerned are numbers 2, 5, 10, 15, 19, 21, 22, and 25 in Table 2. In four cases (5, 19, 21, and 22) there is a clear identification with a giant cluster member, in which the radio source overlaps the optical image of the galaxy. In the remaining four there is some degree of ambiguity: if the identification is made with the brightest or second brightest member of the cluster one must accept a radio source well displaced from the parent galaxy; on the other hand three of the four sources may be identified with much fainter galaxies, presumably cluster members, within the positional uncertainty. The remaining source, number 10, coincides in position with a blue stellar object that is displaced by nearly 5′ arc from the brightest cluster member, and it seems likely that this represents the chance coincidence expected. Source number 2 is a well-separated double in which one of the components is some 2′ arc from a giant elliptical cluster member (14^m). It would not be impossible to identify this component with the galaxy and to assume that the other component is a chance interloper; there is, however, a faint cluster member (approximately 17^m) close to the centroid of the two components.

It seems one must accept either that the centroid of radio sources may be well separated from their parent galaxies or that, in a significant number of cases, the strongest radio source in a cluster is associated with a faint cluster galaxy, not a giant. Because the radio sources do not always overlap the images of the giant galaxies it is clear that acceptance of these identifications, and consequent displacements, implies the probability that galaxies can sometimes eject single as well as double "plasmoids".

The other groups of clusters may also be investigated to help resolve this uncertainty. The distant rich clusters of category 3 may be eliminated immediately as there are no radio sources within the limit of 10′ arc. However, of the 17 sources in category 2, there are 6 within the selection limit, numbers 1, 8, 13, 14, 17, and 28. Four of these (8, 13, 17, and 28) meet the earlier identification criteria and can be identified with a giant cluster galaxy. The remaining two sources are quite distant from the brightest cluster member and, in fact, cannot reasonably be identified with any of the cluster galaxies. No reasonable identification can be suggested for number 14, but number 1 is 0′·4 arc distant from a faint blue stellar object which may prove to be a quasar. Because of the strong selection imposed on the group of clusters in category 2 we cannot come to any reliable statistical conclusion, but the results are certainly consistent with an assumption that only the giant galaxies in clusters are the source of radio emission.

Table 3

PROJECTED SEPARATIONS OF PROBABLE CLUSTER SOURCES

Separations from (1) brightest or second brightest galaxy of cluster and (2) closest galaxy

Source No.	Abell No.	Distance (Mpc)	Angular Separation (′) Giant Galaxy (1)	Angular Separation (′) Closest Galaxy (2)	Spatial Separation (kpc) Giant Galaxy (1)	Spatial Separation (kpc) Closest Galaxy (2)
Close Clusters						
2	119	200	5·1	0·6	300	35
5	400	80	1·4		32	
10	1139	200	5·1		300	
15	1890	200	3·0	0·7	180	40
19	2052	200	0·05		3	
21	2147	80	1·2		28	
22	2151	80	0·6		14	
25	2593	200	1·6	0·1	90	3
Distant Clusters						
1	55	420	14·9		1800	
8	623	420	0·6		72	
13	1346	420	0·3		36	
14	1850	540	7·8		1200	
17	2029	270	0·35		38	
28	2644	420	1·8	0·2	220	24

To investigate this assumption statistically we have derived the actual projected separation in kiloparsecs, between the centroid of the radio source and the first or second brightest galaxy in a cluster, whichever is closest. For this, we have taken Abell's own calibration of his distance scale in terms of redshift and have assumed a Hubble constant of 100 km sec^{-1} Mpc^{-1}. Distances for the 14 sources already discussed are tabulated in Table 3 and the results are displayed as a histogram in Figure 1(*a*). It seems obvious that the two large separations in the case of numbers 1 and 14 represent chance coincidences; the probability of a chance association increases with the square of the separation. The others could all be cluster sources, but number 10, with a separation of 300 kpc, seems most probably also a chance coincidence because of the likely quasar identification. Also, identifications with fainter galaxies

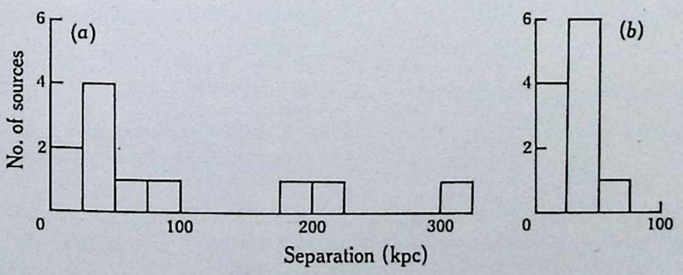

Fig. 1.—Histograms of the projected linear separations between radio sources within 10′ arc from the nominal cluster position and
(*a*) the brightest or second brightest galaxy in the cluster, and
(*b*) the closest galaxy.

much closer to the radio centroid may be suggested for four of the other sources of large separations, namely, numbers 2, 15, 25, and 28; the corresponding histogram when these identifications are assumed is shown in Figure 1(*b*). In view of the

TABLE 4

RADIO SOURCES THAT MAY BE IDENTIFIED WITH GALAXIES OR BLUE STELLAR OBJECTS

Source No.	Abell No.	Size and Structure	Possible Ident.*	Position of Source w.r.t. Object		Refs.†	Remarks
1	55	<1′	20^mB.S.O.	0′·1W.	0′·4S.		Only on Palomar O print
2	119	Double sp–nf sep. 7′	14^mE	1′·0W.	4′·5S.		Position of centroid of double source w.r.t. brightest galaxy in cluster
		Early source ~1′EW Late source <½′EW	17^mG	0′·2W.	0′·2S.		Position of centroid w.r.t. nearest galaxy The earlier source is close to some very faint objects on the E Palomar print, but there is a plate fault on the O print in this region. The later source is close to a star, which, however, is not blue
3	119	<0′·5	15^mE	<0′·1	<0′·1	1,6	Galaxy 20′ from A119
5	400	~4′nf–sp	15^mdb E	0′·4E.	1′·3N.	1,2, 3,5	Brightest in cluster
6	400	~1′EW	17^mE	<0′·1	0′·4N.		Probably the giant in a very faint dense cluster. 25′N. of A400
8	623	<0′·5	15^mE	0′·6W.	<0′·1		Brightest in cluster
10	1139	<0′·5	18^mB.S.O.	<0′·1	0′·1N.	5	Source is 4′·6E. and 2′·2S. of brightest galaxy
13	1346	<1′	15^mE	0′·2E.	0′·2N.		Brightest in cluster
15	1890	3′EW	15^mE	1′·7W.	2′·3N.		Brightest in cluster
			16^mE	0′·4W.	0′·6N.		Second brightest in cluster
17	2029	<1′	14^mE	0′·4E.	0′·1N.		Brightest in cluster
18	2050	~5′ np–sf	15^mE	0′·4E.	<0′·1	5	11′ from cluster and brighter than cluster giant. Therefore probably a field galaxy
19	2052	<0′·5	14^mE	<0′·1	<0′·1	1,4, 5	Brightest in cluster
21	2147	~2′EW	15^mE	0′·2W.	1′·2S.		Many 14^m–16^m galaxies in this region, including several clusters
22	2151	~2′EW	14^mE	0′·6E.	<0′·1		Second brightest in cluster
24	2551	2′EW	14^mE	0′·4W.	1′·3N.	5	One of 3 bright gals. in a loose cluster 19′S of 2551 (not listed by Abell)
			16^mdb G	0′·6E.	0′·5S.		Possibly a faint member of this cluster
25	2593	~2′	14^mE	1′·5E.	0′·5S.		Brightest in cluster
			17^mG	0′·2W.	<0′·1		Faint member
28	2644	~3′	15^mE	1′·5W.	1′·0N.		Brightest in cluster
			16^mTriple	0′·2E.	0′·1S.		Triple galaxy extended to SE. (on O print). Third brightest in cluster
29	2657	~1′EW	16^mG	0′·2E.	0′·1S.		28′SE. of A2657
30	2657	<1′	16^mB.S.O.	0′·1E.	<0′·1		30′NE. of A2657

* Many of the E galaxies may be SO types, or even spirals. For galaxies 16^m or fainter, it is generally not possible to be certain of whether the outer extensions have spiral structure or not.

† References to previously published identifications and optical data are: 1, Mills (1960); 2, Minkowski (1960); 3, Maltby, Matthews, and Moffet (1963); 4, Schmidt (1965); 5, Clarke, Bolton, and Shimmins (1966); 6, Shimmins *et al.* (1966).

statistics of chance association quoted earlier, it would be expected that, if these identifications are correct, the galaxies in question would all be cluster members.

With the present small number of cases it is not possible to decide between the two possibilities (giant galaxies with a wide radio–optical separation or faint galaxies with a small separation) on a purely statistical basis. None of the separations exceed displacements already observed for the components of double sources. It would be helpful to measure redshifts of all the suspected identifications, particularly in the case of the fainter galaxies, in order to check for cluster membership of the galaxy. Even if the closest galaxies are taken as identifications, projected separations of the order of 30 kpc between the radio and optical centroids appear to be common.

Let us now turn to the 16 sources located more than 10′ arc from the nominal centres of their associated clusters. Only 6 of these, or 37% offer reasonable identifications, namely, numbers 3, 6, 18, 24, 29, and 30. Two of these, 6 and 24, may be identified with galaxies in clusters not listed in Abell's catalogue. Number 6 is approximately 0′·4 arc from what appears to be a giant galaxy (17^m) in a very faint but rich cluster, while number 24 may be identified either with a giant member (14^m) of a loose cluster or a faint member (16^m) of the same cluster. Number 18 is identified with a galaxy only 11′ arc from the cluster centre. It is, however, brighter than the giant near the cluster centre and is therefore probably a field galaxy. Numbers 3 and 29 may be identified with field galaxies. Number 30 coincides well with a blue stellar object, quite possibly a quasar. Thus in this effectively random sample of six identified sources we have probably two cluster members, three field galaxies, and one quasar.

Approximate data for all possible identified objects are given in Table 4.

IV. Unidentified Sources

One of the interesting questions arising out of the above results concerns the unidentified sources; there are 11 sources which are definitely in this category. It has been possible rather easily to eliminate radio–optical displacements of the magnitude discussed above as a cause. For example, if it is assumed, that radio galaxies have an optical magnitude of −21·0 and that a linear displacement between radio and optical positions of 100 kpc is common, we would expect that a 17th magnitude radio galaxy would be commonly displaced by about 1′ arc from the associated radio source. Brighter galaxies might be found at correspondingly greater angles. However, a search of the fields surrounding the unidentified sources has yielded no such displaced identifications.

To compare the average properties of identified and unidentified sources we have calculated the geometric mean flux densities of each class. These are shown below, along with corresponding angular size data.

	Geometric Mean Flux Density (f.u.)	Number Resolved	Number Unresolved
Identified sources	3·7	12	7
Unidentified sources	3·2	4	7

The mean flux densities are comparable but there is a clear suggestion that the unidentified sources have a smaller angular size because a smaller proportion can be resolved. There still remain four unidentified sources with sizes between 1′ and 4′ arc, namely, 7, 16, 20, and 27. However, these again are smaller than the maximum sizes of identified sources.

The usual assumption is that such unidentified sources represent known categories of objects at distances too great for the corresponding optical image to be registered on a photographic plate. In the present instance this would require that the unidentified sources have a very much greater ratio of radio to optical emission than those we have been able to identify. It is, however, well known that in a random collection of strong radio sources the most numerous identifications are made with the most distant powerful radio emitters; in a given volume of space, however, the most numerous radio sources are the weakest radio emitters. This exemplifies the difference between the apparent and true luminosity functions. The random collection of weak sources unassociated with clusters will thus be dominated by the distant very strong radio emitters; the selection of cluster sources in a limited volume of space is likely to be weighted towards the lower radio luminosities.

Some general considerations show that this interpretation is possible. For example, if we consider the sources associated with distance 3 clusters, the geometric mean flux density is 4 f.u. and the mean distance 200 Mpc. The geometric mean luminosity of the radio sources is therefore $1 \cdot 5 \times 10^{24}$ W Hz^{-1} sr^{-1}. The median luminosity of identified radio galaxies in the 3C catalogue was obtained by Longair and Scott (1965) at a frequency of 178 MHz. Assuming a spectral index of $0 \cdot 8$, their result at 408 MHz is 4×10^{25} W Hz^{-1} sr^{-1}. That is, the restriction to a fixed volume has weighted the apparent luminosity function towards the weaker and more numerous radio emitters.

This analysis may be extended a little further to predict the identifications expected from the collection of 16 sources unassociated with clusters. We will assume that their median luminosity is 4×10^{25} W Hz^{-1} sr^{-1}, as above, and that the mean absolute magnitude of the associated radio galaxies has the commonly accepted value of $-21 \cdot 0$. It is easily shown that the mean flux density of these sources, $3 \cdot 2$ f.u., corresponds to a median photographic magnitude of the associated galaxies of about $19 \cdot 5$. The identification limit is about magnitude 20, so that one might reasonably expect that rather more than half of the 16 sources would be identifiable with galaxies. In fact only 5 could be identified but, in view of the low numbers involved, this is probably not a significant discrepancy. Note, however, that the lack of quasar identifications is more significant, for their mean ratio of radio to optical emission appears to be rather less than for radio galaxies; consequently a greater proportion of quasar identifications might have been expected. However, the small number of sources involved at this stage does not permit an adequate statistical investigation either of quasars or radio galaxies.

V. CONCLUSIONS

The numbers of clusters in the preliminary investigation have proved to be too small for definite conclusions to be made about some of the questions raised. However, it can be seen that the procedure of seeking statistically valid identifications between radio sources and clusters of galaxies has considerable promise, both for studying individual sources and for obtaining information about the radio luminosity function.

It has been possible to show that quite substantial displacements can occur between the optical and radio centroids of emission of a radio galaxy. In several cases the overall size of the radio source is less than the displacement from the presumed parent galaxy and there is no evidence of a corresponding source on the opposite side. However, in the most striking of these cases an identification with a faint but closer galaxy is not unlikely, so that it is not possible to state with confidence that ejection of a single plasmoid from a galaxy has been observed. The alternative explanation is that faint cluster members are often radio sources.

In future programmes it will be necessary to measure the redshifts of all possible galaxy identifications. Also, it is clear that many more clusters must be observed for better statistical checks. In fact all clusters in distance category 4 are included in our current programmes.

The 11 unidentified sources can probably be explained as distant radio galaxies or quasars beyond the limit of the Palomar Sky Atlas prints. No cases were found of a likely spatial displacement from a bright galaxy. However, there are some indications that this may not be the complete explanation and a special investigation of strong unidentified sources is desirable.

Finally, none of the clusters investigated show evidence of general intergalactic emission. When it occurred, the radio emitting area occupied only a very small fraction of the total area of the cluster.

VI. ACKNOWLEDGMENTS

We are indebted to Mrs. L. D. Emerson and Dr. D. E. Harris for assistance with the observations at Arecibo. We also wish to thank Professor Eggen of Mount Stromlo for the use of the 74 in. telescope. The work forms part of the programme of the Cornell–Sydney University Astronomy Centre operated with support from the Advanced Projects Agency under a research contract with the Air Force Office of Scientific Research, the National Science Foundation, and the Australian Research Grants Committee.

VII. REFERENCES

Abell, G. O. (1958).—*Astrophys. J. Suppl. Ser.* **3**, No. 31.
Clarke, Margaret E., Bolton, J. G., and Shimmins, A. J. (1966).—*Aust. J. Phys.* **19**, 375.
Day, G. A., Shimmins, A. J., Ekers, R. D., and Cole, D. J. (1966).—*Aust. J. Phys.* **19**, 35.
Gower, J. F. R., Scott, P. F., and Wills, D. (1967).—*Mem. R. astr. Soc.* **71**, 49.
Kellermann, K. I. (1964).—*Astrophys. J.* **140**, 969.
Longair, M. S., and Scott, P. F. (1965).—*Mon. Not. R. astr. Soc.* **130**, 379.
Maltby, P., Matthews, T. A., and Moffet, A. T. (1963).—*Astrophys. J.* **137**, 153.
Mills, B. Y. (1960).—*Aust. J. Phys.* **13**, 550.
Mills, B. Y., Slee, O. B., and Hill, E. R. (1958).—*Aust. J. Phys.* **11**, 360.
Minkowski, R. L. (1960).—*Proc. natn. Acad. Sci. U.S.A.* **46**, 13.
Schmidt, M. (1965).—*Astrophys. J.* **141**, 1.
Shimmins, A. J., Day, G. A., Ekers, R. D., and Cole, D. J. (1966).—*Aust. J. Phys.* **19**, 837.
Wyllie, D. V. (1968).—An absolute flux density scale at 408 MHz. *Mon. Not. R. astr. Soc.* (in press).

पुस्तकालय

ACCURATE POSITIONS AND SOME OPTICAL IDENTIFICATIONS FOR 67 RADIO SOURCES BETWEEN DECLINATIONS +20° AND +27°

By Jeannette K. Merkelijn,* A. J. Shimmins,* and J. G. Bolton*

[*Manuscript received February 7, 1968*]

Summary

Thirty-four identifications have been made from a total of 67 radio sources for which accurate positions have been measured with the 210 ft telescope. Nineteen of these are galaxies and 15 possible quasi-stellar objects. Only one of the identifications has been previously suggested.

I. Introduction

A survey has been made of discrete radio sources between declinations +20° and +27° using the 210 ft radio telescope of the Australian National Radio Astronomy Observatory at Parkes, N.S.W. (Shimmins and Day 1968). This survey provides a list of radio source positions with an accuracy varying from 30″ arc to 2′ arc for the weaker sources in both right ascension and declination. The survey positions were used to obtain tentative identifications, following the method described by Clarke, Bolton, and Shimmins (1966). Because of the magnitude of the errors in the survey positions the suggested identifications were not considered sufficiently reliable to publish. Transit observations as described by Shimmins, Clarke, and Ekers (1966) have now been made for 67 of the sources for which a tentative identification was obtained and the results were used to confirm, reject, or occasionally change the earlier identifications. The estimated r.m.s. errors in the positions are less than 12″ arc in both coordinates.

II. Equipment

The 210 ft telescope was used for the observations in combination with a new 2700 MHz receiver of four times the sensitivity of that used by Shimmins, Clarke, and Ekers (1966) and Shimmins (1968). Thus, although the sources observed in the present work were considerably weaker than those measured previously, the errors due to noise fluctuations are somewhat smaller.

Two feed horns were used in the receiving system, one of which was offset 18′·6 arc from the geometrical axis. The signals from the two horns pass through a hybrid network that forms the sum and difference of the signals at the inputs of two independent receivers. Each receiver consists of two degenerate parametric amplifiers in series followed by conventional superheterodyne crystal mixers and i.f. amplifiers. The output voltages of these receivers are multiplied to give the difference in power received between the two feed horns. The receiver has been described in detail

---

* Division of Radiophysics, CSIRO, P.O. Box 76, Epping, N.S.W. 2121.

Aust. J. Phys., 1968, **21**, 523–37

by Batchelor, Brooks, and Cooper (1968). It has a system temperature of 80°K and an i.f. bandwidth of 200 MHz. With an output time constant of 2 sec, peak-to-peak noise fluctuations are approximately 0·04 degK, which is equivalent to 0·07 f.u.* for the 210 ft telescope.

The beam shape for the on-axis feed was approximately Gaussian with a half-power beamwidth of 7′·6 arc. In order to avoid the effects of the offset feed horn, the position angle of the feed system was set to 0° for the right ascension measurements and 90° for the declination measurements. In the occasional cases where confusion occurred from the effects of a nearby source in the offset beam, the observations were repeated with the feed system in a more favourable position angle. A typical record of a source with a flux density of 0·66 f.u. is shown in Figure 1.

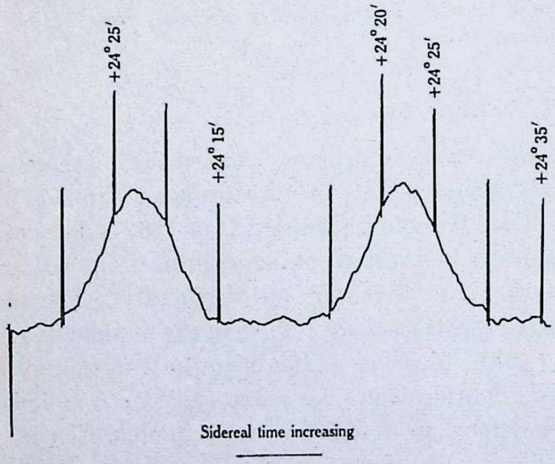

Fig. 1.—Typical record of two declination scans (R.A. set at $07^h 26^m 36^s$). The flux density of the source is 0·66 f.u.

III. Observations and Reductions

A more extensive description of the method of observations and reductions has been given by Shimmins, Clarke, and Ekers (1966). Briefly the procedure was as follows.

(a) *Right Ascension Measurements*

The observations in right ascension were obtained by setting the telescope under master equatorial control to the declination of the source and to a series of accurately set hour angles within 2½° of the meridian and letting the source drift through for each hour angle.

The receiver output was recorded on a paper chart run at 3 in/min. Sidereal time markers were recorded at 10 sec intervals on the same trace as the recorder output.

The records were analysed by hand. After the apparent right ascension had been determined from the centres of symmetry of the drift scans, the results were averaged and by means of the calibration sources were corrected for time constant, clock error, an error dependent on zenith angle, and a diurnal pointing error. The calibration sources were taken from a list of sources for which reliable identifications and accurate radio or optical positions exist. A list of the calibration sources used is given in Table 1.

---

* 1 flux unit = $10^{-26}\,\mathrm{W\,m^{-2}\,Hz^{-1}}$.

(*b*) *Declination Measurements*

The declinations were also measured with the telescope under master equatorial control and within $2\frac{1}{2}°$ of the meridian. The telescope was set to the right ascension of the source and a number of scans in declination were made at a rate of 0·25 deg/min through the source position. The receiver output was recorded on paper chart run at 3 in/min. Markers were recorded on the same trace every 5′ in declination. Again the apparent declination was determined from the centre of symmetry of each scan and the results were corrected for time constant and averaged. The average declination found was then corrected for an error dependent on zenith angle and a diurnal pointing error.

TABLE 1

POSITION CALIBRATORS, DECLINATIONS +20° TO +27°

PKS Catalogue No.	Position (1950·0) R.A. h m s	Dec. ° ′ ″	S_{1410}	S_{2700}	Optical Identification	References*	Other Catalogue Nos.
0017+15	00 17 49·83	15 24 16·5	2·1	1·1	18^m QSO	1	3C 9
0127+23	01 27 15·18	23 22 52·0	3·0	1·9	19^m QSO	1	3C 43
0202−17	02 02 34·4	−17 15 37·0	1·4	1·4	$18^m·5$ QSO	2	
0316+16	03 16 09·11(±0·2)	16 17 41·2(±10)	8·2	5·1	Occultation†	3	CTA 21
0518+16	05 18 16·51	16 35 26·2	9·3	6·3	$18^m·5$ QSO†	1	3C 138
0736+01	07 36 42·40(±0·14)	01 43 57·0(±1·9)	2·9	1·7	$17^m·5$ QSO	4	
0915−11	09 15 41·18(±0·03)	−11 53 04·4(±0·4)	42·0	23·5	16^m E galaxy†	5	Hydra A
1040+12	10 40 06·03(±0·02)	12 19 15·0(±0·4)	3·0	2·2	17^m QSO	6	3C 245
1328+25	13 28 16·12	25 24 37·1	7·0	5·5	$17^m·5$ QSO	7	3C 287
1510−08	15 10 08·97(±0·06)	−08 54 48·3(±0·6)	3·4	3·2	$16^m·5$ QSO	6	
1622+23	16 22 32·45	23 52 00·7	2·7	1·5	$17^m·5$ QSO	1	3C 336
2120+16	21 20 25·64	16 51 46·0	1·7	0·7	18^m QSO	8	3C 432
2230+11	22 30 07·71	11 28 22·8	6·7	5·2	$17^m·5$ QSO†	7	CTA 102

* References to positions used are: 1, Sandage, Véron, and Wyndham (1965); 2, Kinman *et al.* (1967); 3, Clarke and Batchelor (1965); 4, Bolton and Kinman (1966); 5, Griffin (1963); 6, Bolton (1968); 7, Véron (1965); 8, Véron (1966).

† Flux calibrator.

The calibration sources used were the same as those used for the right ascension calibration. The calibration curves for both coordinates are given in Figure 2.

After the corrections were applied the source positions were precessed to epoch 1950·0. For those sources that were included in both the Parkes catalogue and the Owens Valley list of accurate positions of 4C sources (Olsen 1967) the transit positions were compared with the positions from the Owens Valley list. For all but two sources the differences were well within the estimated errors of both lists.

For PKS 1155+26 the difference in right ascension was 8^s and for PKS 1708+24 the difference in declination was 11′ arc. However, for these sources the difference between the Parkes catalogue position and the Parkes transit position was very small ($0^s·5$ and 0′·1 arc respectively). As the possibility of confusion with nearby sources is lower for the Parkes telescope than for the Owens Valley interferometer, the present observations are believed to be correct.

(*c*) *Errors in Position Measurements*

For a sample of sources, covering the range of flux densities, the r.m.s. error per scan was computed from the scatter in positions between individual scans. The r.m.s. error as a function of flux density is shown in Figure 3. This curve was used together with the number of scans on each source to estimate the probable error in position due to noise fluctuation. It was combined with the estimated error of 6″ arc in the pointing calibration to give a final estimated error in the source position. Of the sources investigated, 85% have estimated errors of less than 10″ arc.

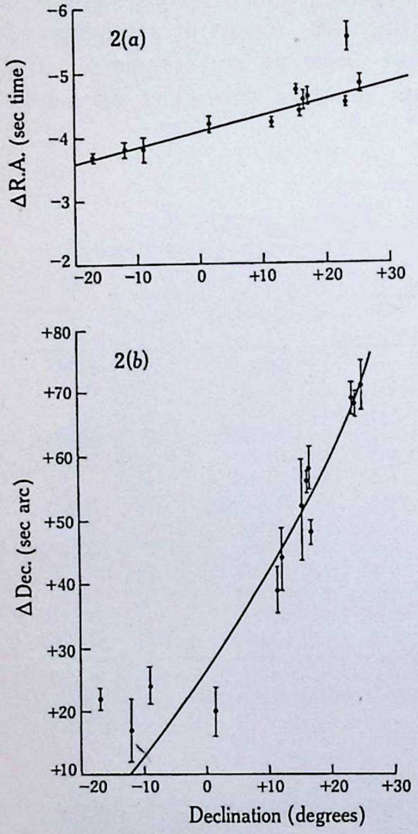

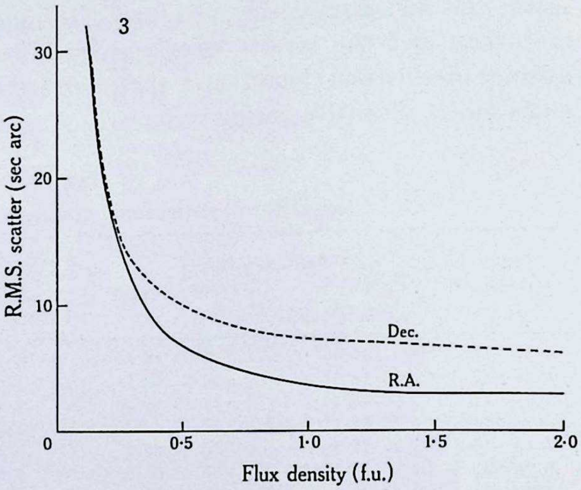

Fig. 3 (*above*).—The r.m.s. error per scan plotted against flux density at 2700 MHz.

Fig. 2 (*left*).—Differences between (*a*) true and apparent right ascensions and (*b*) true and apparent declinations for calibrator sources plotted as a function of declination. The errors shown are due to receiver noise.

(*d*) *Flux Densities*

The 2700 MHz flux density of each source was obtained by measuring the peak amplitude of the smoothed scan relative to the baseline, which was averaged out to ±15′ arc from the centre of the source. After averaging the scans in one coordinate a correction was applied for the difference between the set and measured values for the other coordinates. Finally the values from both coordinates were averaged. The radio sources PKS 2230+11 (CTA 102), PKS 0316+16 (CTA 21), PKS 0518+16 (3C 138), and PKS 0915−11 (Hydra A) were used to calibrate the flux density scale (Table 1).

TABLE 2

POSITIONS OF RADIO SOURCES, DECLINATIONS +20° TO +27°

(1)	(2)	(3)	(4)	(5)	(6)	(7)	(8)	(9)	(10)	(11)	(12)	(13)	(14)	(15)	(16)
PKS Catalogue Number	Position (1950·0) R.A. h m s	Dec. ° ′ ″	No. of Scans R.A.	Dec.	R.M.S. Error R.A. ″	Dec. ″	Optical Posn. relative to Radio Source R.A. s	Dec. ′	Ident.	Mag.	S_{2650}	S.I.	Remarks	Gal. Coords. l^{II} b^{II}	Other Catalogue Nos.
0004+21	00 04 53·7	+21 47 13	5	4	7	8	0·8 f	0·2 N.	QSO?	19·5	0·48	0·9±0·2	Two other blue objects nearby	110 −40	4C21·1
0010+26	00 10 03·5	+26 45 48	3	4	8	8			III		0·40	C	19^m gal. 2^s·5 foll.	112 −35	CTD1
0029+21	00 29 10·3	+21 37 18	5	6	7	8			III		0·42	0·9±0·2	19^m blue object 0′·6 N.	117 −41	4C21·3
0043+20	00 43 52·2	+20 11 42	6	6	7	8	1·3 p	0	E2	16·5	0·36	1·0±0·3	Brightest member of cluster. Conf. source 6′ N.	121 −42	4C20·4, 3C21
0100+25	01 00 08·0	+25 36 09	6	7	6	7			III		0·59	0·9±0·2	18^m E3 gal. 0′·6 S.	126 −37	4C25·3, CTD8
0121+23	01 21 08·7	+23 50 27		4		8			III		0·59		Conf. with 0121+24	132 −38	
0121+24	01 21 11·6	+24 02 36	5	4	9	10			III		0·26		Conf. with 0121+23	132 −38	4C23·4
0148+20	01 48 00·1	+20 02 10	7	8	6	6			III		0·41	0·6±0·3	Faint object 0′·2 n.p. might be gal.	141 −39	
0232+22	02 32 33·2	+22 57 00	11	11	7	7	0·8 p	0·3 S.	QSO?	20	0·33	0·8±0·3		152 −34	4C22·4
0328+24	03 28 07·5	+24 48 02	6	2	11	19			III		0·16	1·4±0·3		163 −25	4C24·8
0436+20	04 36 49·5	+20 18 20	6	6	8	9			III		0·26	1·2±0·3	19^m·5 gal. 0′·5 n.f.	178 −17	4C20·14
0453+20	04 53 32·9	+20 34 07	9	6	7	8			III		0·27	1·0±0·2		181 −14	4C20·16
0520+24	05 20 18·2	+24 24 18	5	6	9	9			III		0·26	1·3±0·6	Ext. in R.A.	181 −7	
0619+26	06 19 34·3	+26 37 42	5	6	14	13			III		0·14	1·1±0·5	16^m Sp gal. 0′·7 S.	186 6	4C26·21
0632+26	06 32 30·8	+26 19 11	4	6	7	7	1·8 p	0·2 S.	E0	15·5	0·53	0·6±0·3	Ext. in R.A. size 9′	188 8	4C26·23
0656+21	06 56 39·0	+21 22 10	4	6	8	8	0	0·2 S.	g	19	0·31	0·9±0·3		195 11	4C21·22
0658+23	06 58 29·0	+23 17 46	4	6	7	7	1·4 p	0·2 S.	D	17	0·57	0·7±0·2		193 12	4C23·18
0719+25	07 19 46·5	+25 34 37	4	4	8	9	1·4 p	0·2 S.	E2	16·5	0·30	1·7±1·0		193 18	CTD50
0725+24	07 25 29·2	+24 25 22	3	3	7	8	0·2 p	0·1 S.	E1	16·5	0·66	0·5±0·4		195 19	3C182, NRAO267,
0729+25	07 29 52·4	+25 55 19	3	4	7	8	0·7 p	0·3 S.	QSO?	19	0·62	0·4±0·4		193 20	(4C25·21)
0754+22	07 54 14·5	+22 01 33	4	4	10	11			III		0·22	1·4±0·6	Gal. 1′ s.f.	200 24	
0802+21	08 02 42·4	+21 15 38	4	4	6	7			III		1·03	−0·4±0·4	Blue object 0′·5 s.f.	201 25	
0814+22	08 14 38·4	+22 46 40	4	4	6	7	1·2 p	0·1 S.	QSO?	18·5	0·76	0·7±0·2		201 28	4C22·20, 3C197, NRAO287

TABLE 2 (*Continued*)

(1) PKS Catalogue Number	(2) Position (1950·0) R.A. h m s	(3) Dec. ° ′ ″	(4) No. of Scans R.A.	(5) Dec.	(6) R.M.S. Error R.A. ″	(7) Dec. ″	(8) Optical Posn. relative to Radio Source R.A. s	(9) Dec. ′	(10) Ident.	(11) Mag.	(12) S_{2650}	(13) S.I.	(14) Remarks	(15) Gal. Coords. l^{II}	b^{II}	(16) Other Catalogue Nos.
0820+22	08 20 28·5	+22 33 02	4	4	6	7	0·3 f	0·3 S.	QSO?	19·5	0·97	C		201	30	4C22·21
0825+24	08 25 46·0	+24 46 04	4	3	8	9			III		0·38	0·8±0·3	db 1′ n.p.	199	32	4C24·17
0901+22	09 01 56·0	+22 32 24	5	10	7	7			III		0·44	0·9±0·2		205	39	4C22·22
0926+25	09 26 10·3	+25 25 33	4	3	12	15			III		0·17	1·4+0·4		203	45	4C25·25
0935+26	09 36 01·5	+26 12 28	4	4	7	8	1·1 p	0·1 N.	g	19·5	0·40	1·0±0·2		203	47	4C26·28
0950+25	09 50 49·7	+25 30 41	4	3	7	6	1·3 f	0·3 S.	g	19	0·52	0·9±0·2		205	50	4C25·29
0957+22	09 57 34·6	+22 47 55	4	3	7	8	1·0 p	0·1 S.	QSO?	18	0·74	0·7±0·2		210	51	4C22·25
1012+23	10 12 00·1	+23 16 18	4	5	6	7	0·1 p	0·1 N.	QSO?	18	0·74	0·7±0·2		211	54	4C23·24
1019+25	10 19 22·5	+25 38 42	3	5	12	10	0·2 p	0·3 S.	QSO?	18	0·21	0·8±0·3		201	57	4C25·32
1048+24	10 48 47·1	+24 04 05	4	1	8	15	0·4 p	0	QSO?	19	0·28	1·1±0·3		213	63	4C24·23, CTD68
1053+24	10 53 31·3	+24 11 48	5	4	11	12			III		0·18	1·0±0·7	Blue object 0′·6 n.p.	213	64	
1112+21	11 12 58·0	+21 50 13	6	6	8	9			III		0·25	1·1±0·3	Faint blue object 0′·6 n.p.	222	68	4C21·20
1123+26	11 23 15·6	+26 26 56	4	4	6	7			III		0·78	−0·0±0·5	Faint blue object 0′·5 p.	211	71	CTD74
1131+21	11 31 20·8	+21 22 12	4	6	7	8	0	0·1 S.	E1	16	0·43	0·9±0·5		228	71	4C21·32
1155+26	11 55 46·5	+26 38 20	5	6	7	7	1·0 p	0·5 S.	E	19	0·55	1·1±0·2	0′·5 S. but poss. jet at P.A. 330°	214	78	4C26·35
1204+22	12 04 00·7	+22 32 32	6	6	6	7	0·8 p	0·1 S.	E0	15·5	0·62	0·8±0·3		236	79	4C22·33
1225+20	12 25 41·1	+20 40 03	6	6	6	7	0·1 p	0·4 N.	QSO?	18	0·83	0·7±0·2		263	81	4C20·29
1237+22	12 37 21·0	+22 29 20	6	6	8	8			III		0·28	0·8±0·3	E4 gal. 0′·7 foll.	274	84	4C22·36
1251+26	12 51 43·4	+26 46 41	4	9	12	9			III		0·18	1·1±0·3	Conf. source $1^{m}04^{s}$ prec.	348	89	4C26·40
1309+21	13 09 32·7	+21 03 45	6	4	7	8	0·5 f	0·2 N.	E5	15	0·36	0·8±0·7	Ext. to lower R.A.	341	82	4C21·39
1354+25	13 54 46·7	+25 52 12	5	6	10	10	1·8 f	0·2 S.	QSO?	18	0·20	1·3±0·6	Conf. source approx. 18′ away	31	75	
1405+25	14 05 59·8	+25 47 57	7	6	6	7	0·8 p	0·1 N.	E2	19	0·53	0·7±0·3		32	73	
1422+20	14 22 37·4	+20 14 04	4	6	6	7	0·3 f	0	QSO?	17·5	1·14	0·6±0·1		20	67	4C20·33
1430+25	14 30 28·8	+25 08 36	6	4	8	8	2·1 p	0·1 S.	E3	17	0·31	0·8±0·3		33	67	4C25·46
1441+25	14 41 44·5	+25 14 58	5	5	7	8	0·8 p	0·4 S.	QSO?	19·5	0·42	0·8±0·5		35	65	
1455+24	14 55 31·5	+24 47 38	6	5	6	7			III		0·58	0·3±0·5	Several members of cluster within 0′·7	35	62	4C25·47

1549+26	15 49 06·1	+26 15 27	6	7	8	8			III		0·27	1·1±0·5		42	50	
1551+23	15 51 34·8	+23 57 27	5	6	7	7	0·1 p	0·3 S.	E2	17	0·53	0·6±0·3	Blue object 0′·2 s.f.	39	49	4C23·42
1602+24	16 02 50·0	+24 04 12	5	6	7	8	1·5 p	0·1 S.	E3	14·9	0·37	0·9±0·3	Caswell and Wills (1967)	40	46	4C24·36
1614+26	16 14 35·9	+26 54 24	4	4	6	7			III		0·96	0·4±0·4	Blue object 0′·6 S.	45	45	CTD95
1642+25	16 42 56·6	+25 41 48	7	3	7	8			III		0·50	0·5±0·6	Faint blue object 0′·6 n.p.	45	38	
1700+24	17 00 54·0	+24 02 49	6	5	9	10			III		0·23	0·7±0·3		45	34	4C24·38
1708+24	17 08 29·4	+24 08 54	6	5	8	8			III		0·30	1·0±0·5		46	32	4C24·40
1719+24	17 19 57·4	+24 17 49	4	5	7	8			III		0·52	0·7±0·5		47	30	4C24·41, CTD100
1729+26	17 29 26·0	+26 01 18	5	5	11	12			III		0·17	1·2±0·4		49	28	4C26·52
1759+21	17 59 40·6	+21 09 48	3	5	7	8	0·1 p	0·3 S.	D	17·5	0·52	1·0±0·2		47	20	4C21·51
1809+21*	18 09 57·0	+21 25 38	5	4	8	9			III		0·28	1·1±0·8	14^m E gal. 1′ n.p. Ext. in R.A.	48	18	
1819+24	18 19 35·5	+24 31 45	5	6	17	17			III		0·10	1·4±0·4		52	17	4C24·45
2102+20	21 02 12·3	+20 19 09	8	6	8	9			III		0·26	1·1±0·6		68	−17	4C20·52
2149+20	21 49 04·6	+20 43 43	5	6	9	9	0·4 p	0	E0	17	0·26	1·1±0·7		76	−25	
2159+22	21 59 06·9	+22 32 34	6	6	7	8			III		0·34	1·0±0·3	Small source 37^s foll.	79	−25	4C22·61
2223+21	22 23 14·8	+21 02 52	5	2	6	8	0·6 p	0·1 S.	QSO?	18	0·86	1·7±0·3	Small source 28′ N.	83	−30	
2240+24	22 40 23·2	+24 43 41	5	4	7	8	1·8 p	0·1 S.	E2	18	0·40	0·6±0·3		89	−29	4C24·60
2251+24	22 51 44·6	+24 20 27	4	4	6	7	0·4 f	0	QSO?	19	1·40	0·4±0·2		92	−31	4C24·61, CTD136
2339+23	23 39 09·9	+23 35 03	8	9	8	8			III		0·26	1·0±0·3		103	−36	4C23·59

---

* Both this source and PKS 1810+21 may be associated with the brightest member of the cluster between the two sources.

As the position angle of the feed was changed by 90° between the right ascension and declination measurements, the flux densities represent the average of two orthogonal polarizations.

IV. IDENTIFICATIONS

The identifications were obtained by searching the Palomar Sky Survey prints near the positions of the sources. The search for identifications was carried out with the aid of transparent overlays, each containing a 2′ arc square centred on the radio position with the positions of 10 nearby stars from the Yale catalogue. A more extensive description of the method is given by Clarke, Bolton, and Shimmins (1966). By examining the fields within approximately 1′ arc from the positions of the 67 sources the following results were obtained:

19 fields contained galaxies and one a possible galaxy,

15 fields contained stars that were noticeably blue and thus could be quasi-stellar objects,

9 fields contained galaxies outside the error limits but within 1′ arc of the source position,

7 fields contained blue stellar objects outside the error limits but within 1′ arc of the source position,

15 fields contained stars of normal colours only,

1 field was blank.

One identification has been proposed previously; this is the identification of PKS 1602+24 (4C 24·36) with a 15^m E galaxy (Caswell and Wills 1967).

V. SOURCE TABLE AND FINDING CHARTS

All sources observed are listed in Table 2.

Column 1. Parkes catalogue number.

Columns 2 and 3. Transit positions.

Columns 4 and 5. Number of scans used in deriving the final value of right ascension and declination respectively.

Columns 6 and 7. Probable error in seconds of arc for right ascension and declination respectively.

Columns 8 and 9. Difference between the position of the suggested identification and the radio position. These differences were estimated from the Sky Survey prints with the aid of the transparent overlay and are given to $0^s·1$ in right ascension and 0′·1 in declination. The uncertainty is probably of the order of 0′·1 arc.

Column 10. Type of object: E, elliptical galaxy; D, elliptical galaxy with diffuse outer envelope; Sp, spiral galaxy; db, dumb-bell or double galaxy; QSO?, possible quasi-stellar object; III, stars only, normal colours; g, galaxies that could not be classified owing to poor print quality.

Figs. 4–8.—Finding charts for the identified sources. The scale is approximately 5 mm = 1′ arc. North-east is at the top left-hand corner of each chart.

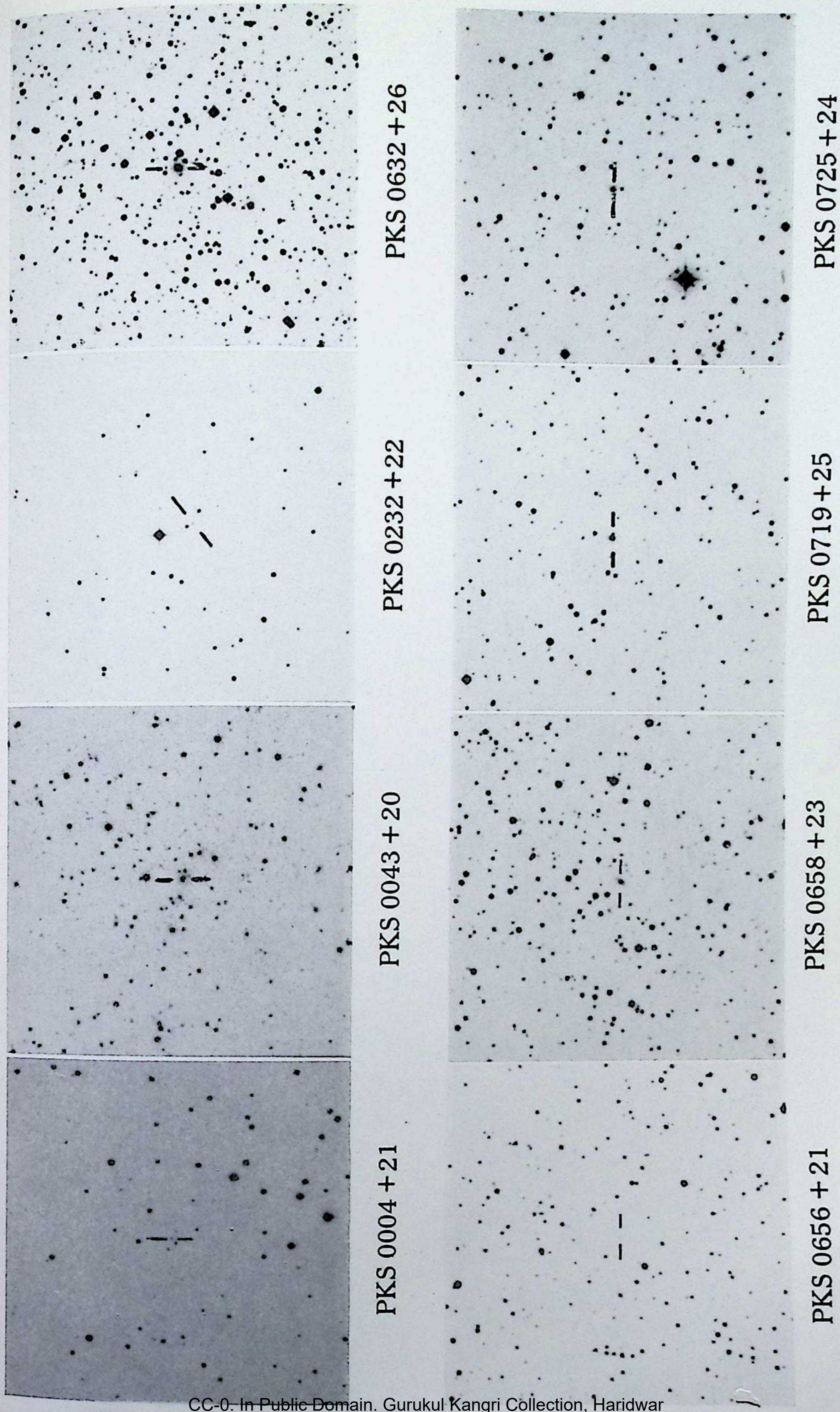

PKS 0004+21

PKS 0043+20

PKS 0232+22

PKS 0632+26

PKS 0656+21

PKS 0658+23

PKS 0719+25

PKS 0725+24

Fig. 4

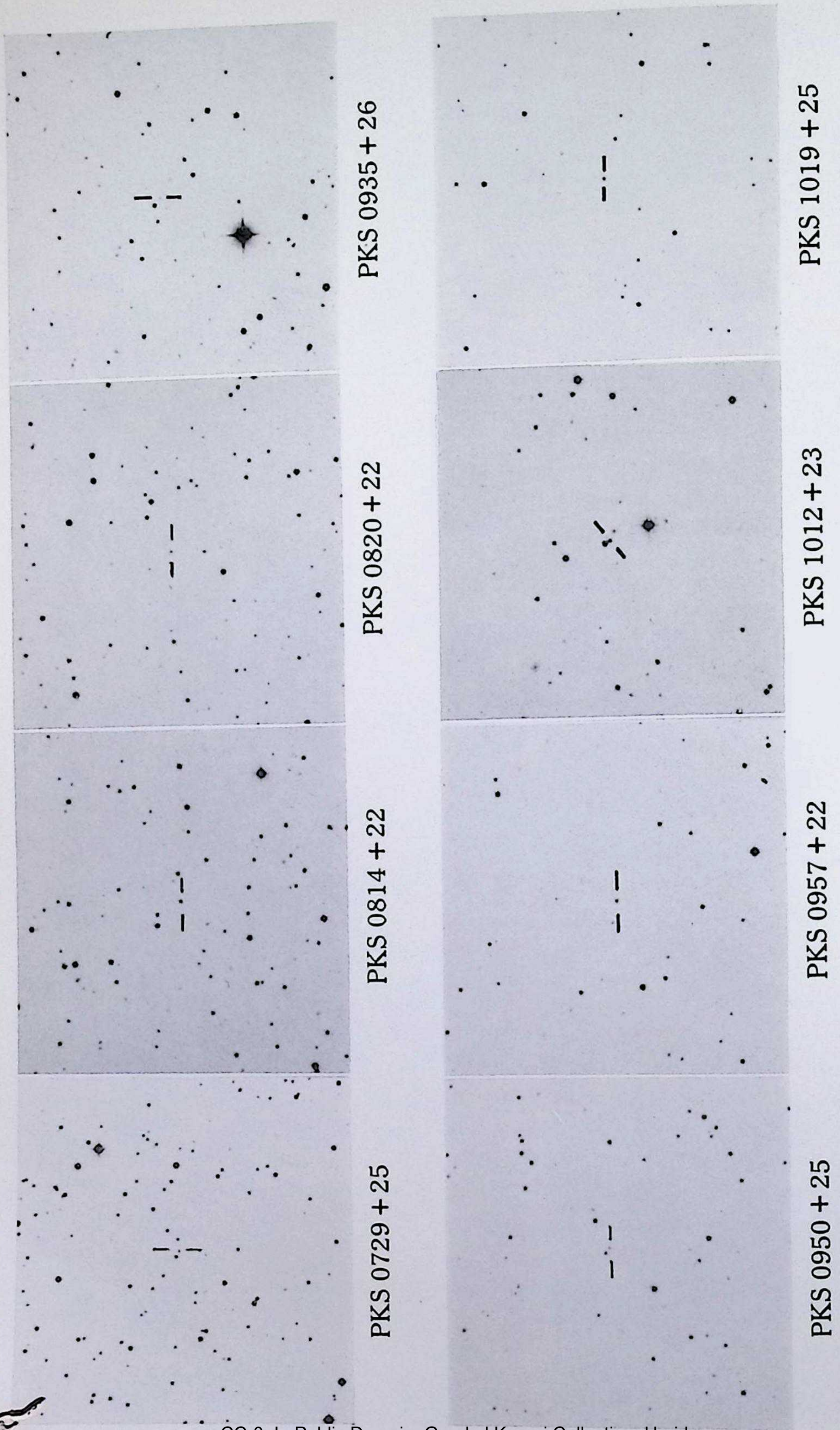
PKS 1019+25
PKS 1012+23
PKS 0957+22
PKS 0950+25
PKS 0935+26
PKS 0820+22
PKS 0814+22
PKS 0729+25

Fig. 5

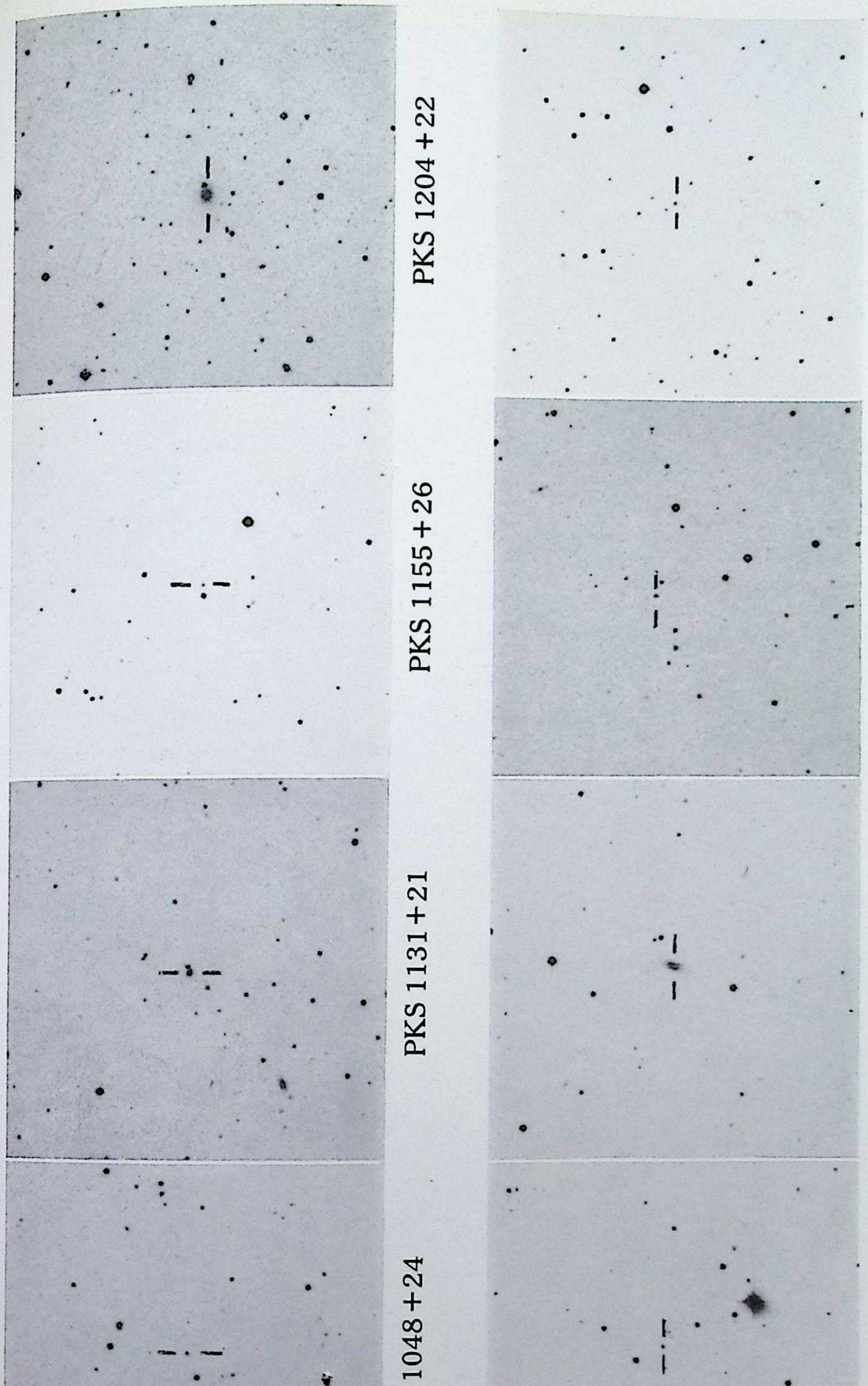
PKS 1204+22
PKS 1155+26
PKS 1131+21
PKS 1048+24
PKS 1405+25
PKS 1354+25
PKS 1309+21
PKS 1225+20

Fig. 6

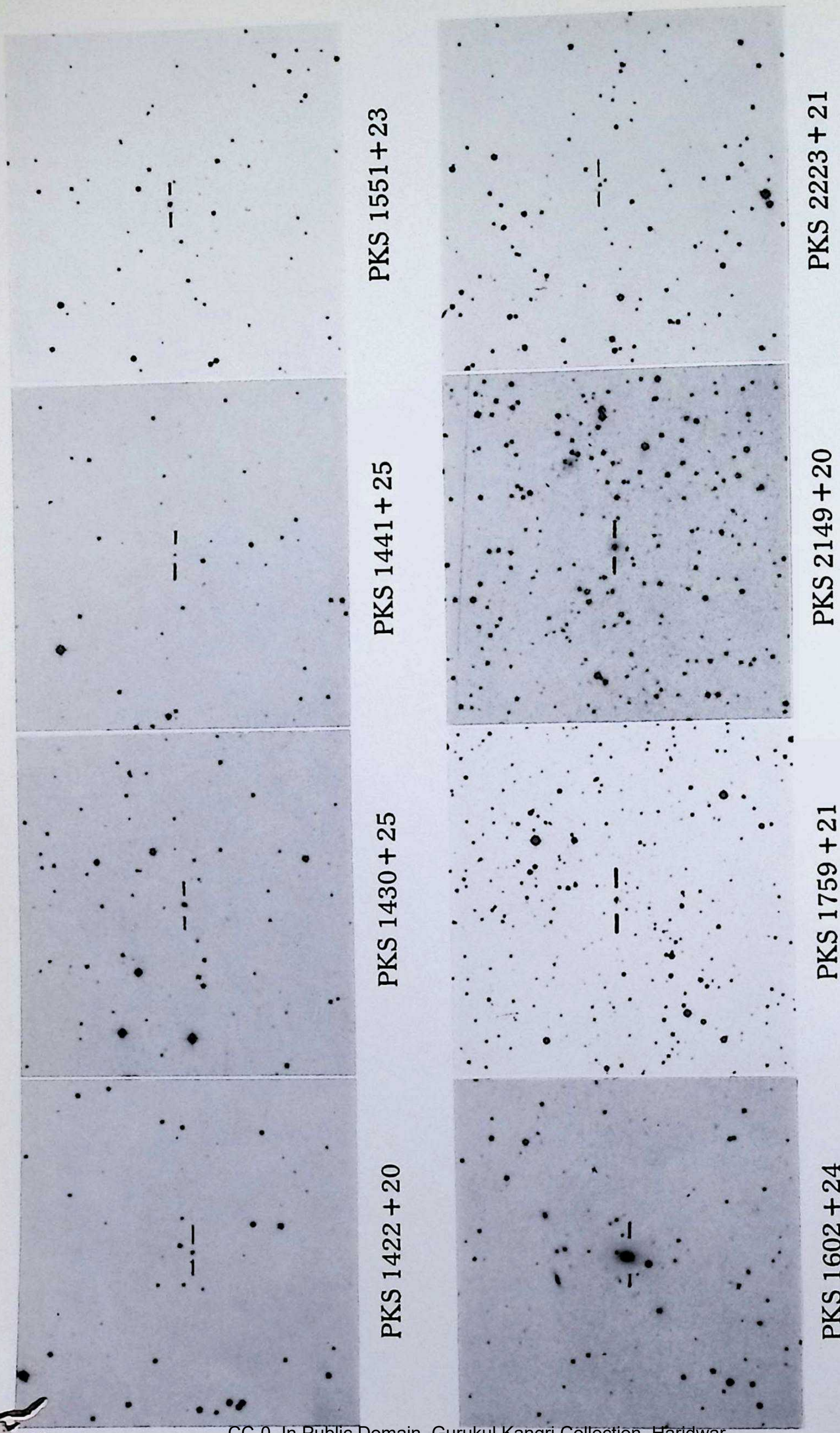
PKS 1551+23
PKS 1441+25
PKS 1430+25
PKS 1422+20
PKS 2223+21
PKS 2149+20
PKS 1759+21
PKS 1602+24

Fig. 7

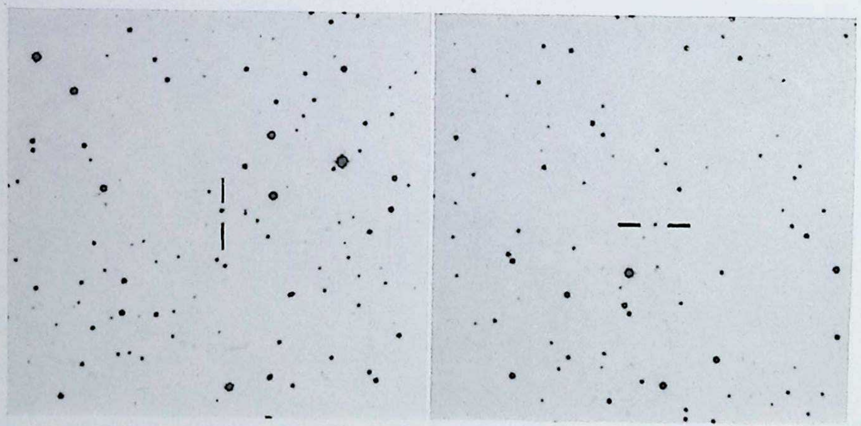

PKS 2240+24 PKS 2251+24

Fig. 8

Column 11. Estimates of the photographic magnitude for galaxies and of the visual magnitude for quasi-stellar objects. The estimates may be as much as 1^m in error.

Columns 12 and 13. Flux density at 2700 MHz and spectral index respectively. The value of the spectral index is taken from the Parkes catalogue.

Column 14. Remarks on individual objects, including other possible identifications within the search area.

Column 15. New galactic coordinates of the source.

Column 16. Other catalogue numbers where the source has been previously listed in the 3C (Edge *et al.* 1959), revised 3C (Bennett 1962), 4C (Pilkington and Scott 1965), or CTD (Kellermann and Read 1965) catalogues.

Finding charts for the suggested identifications are given in Figures 4–8. These were prepared from the Sky Survey prints and contrast has been increased slightly over that of the original prints. Finding charts for the galaxies were made from the "E" or red print and for the quasi-stellar objects from the "O" or blue print. The scale is approximately 5 mm = 1′ arc and north-east is at the top left-hand corner.

VI. Probability of Chance Coincidences

The present observations have also provided a useful opportunity to assess the probability of the chance coincidence in making suggested identifications from radio positions of different accuracies. Apart from seven sources that were observed in order to fill in gaps in the programme, the sources were selected for observation because tentative identifications were made from the catalogue positions.

For 26 of the sources the estimated errors in the catalogue positions were ±30″ arc. In 3 cases the more accurate position made it possible to decide between two alternative identifications. Of the remaining 23, 14 (60%) of the identifications were retained. However, of those rejected the new positions of 5 are within 0′·6 arc of the tentative identification (as noted in Table 2) and could be cases where the optical and radio centroids are not coincident.

For 33 of the sources the estimated errors in the catalogue positions were ±2′ arc. In 3 cases the more accurate position made it possible to decide between two alternative identifications. Of the remaining 30, 8 (27%) of the tentative identifications were retained. In 5 cases where the tentative identifications were rejected new identifications resulted from the transit positions.

The estimated errors in the present positions are ±10″ arc and the reliability of the identifications should be of the order of 90%, a value that is supported by optical confirmation of suggested quasi-stellar objects whose identifications have been based on positions of similar accuracy.

VII. Acknowledgment

We wish to thank Mr. J. V. Wall for taking part in the position observations.

VIII. References

Batchelor, R. A., Brooks, J. W., and Cooper, B. F. C. (1968).—*IEEE Trans. Antennas Propag.* **AP-16**, 228.

Bennett, A. S. (1962).—*Mem. R. astr. Soc.* **68**, 163.

Bolton, J. G. (1968).—Accurate positions of identified radio sources. *Publs astr. Soc. Pacif.* **80** (in press).

Bolton, J. G., and Kinman, T. D. (1966).—*Astrophys. J.* **145**, 951.

Caswell, J. L., and Wills, D. (1967).—*Mon. Not. R. astr. Soc.* **135**, 231.

Clarke, Margaret E., Bolton, J. G., and Shimmins, A. J. (1966).—*Aust. J. Phys.* **19**, 375.

Clarke, R. W., and Batchelor, R. A. (1965).—*Nature, Lond.* **207**, 511.

Edge, D. O., Shakeshaft, J. R., McAdam, W. B., Baldwin, J. E., and Archer, S. (1959).—*Mem. R. astr. Soc.* **68**, 37.

Griffin, R. F. (1963).—*Astr. J.* **68**, 421.

Kellermann, K. I., and Read, R. B. (1965).—*Publs Owens Valley Radio Observ.* No. 2.

Kinman, T. D., Bolton, J. G., Clarke, R. W., and Sandage, A. R. (1967).—*Astrophys. J.* **147**, 849.

Olsen, E. T. (1967).—*Astr. J.* **72**, 738.

Pilkington, J. D., and Scott, P. F. (1965).—*Mem. R. astr. Soc.* **69**, 183.

Sandage, A. R., Véron, P., and Wyndham, J. D. (1965).—*Astrophys. J.* **142**, 1307.

Shimmins A. J. (1968).—*Aust. J. Phys.* **21**, 65.

Shimmins A. J., Clarke, Margaret E., and Ekers, R. D. (1966).—*Aust. J. Phys.* **19**, 649.

Shimmins, A. J., and Day, G. A. (1968).—*Aust. J. Phys.* **21**, 377.

Véron, P. (1965).—*Astrophys. J.* **141**, 332.

Véron, P. (1966).—*Astrophys. J.* **144**, 861.

SHORT COMMUNICATIONS

OBSERVATIONS OF 11 RADIO SOURCES NEAR 55 MHz*

By R. F. HAYNES,† P. A. HAMILTON,† and P. M. MCCULLOCH†

A recent investigation of radio sources in the northern hemisphere was made by Kellermann (1966). He attempted to explain some of the characteristics of the sources that were observed to have curved spectra. In order to make a similar investigation possible for sources in the southern hemisphere, more observations especially at low frequencies are needed. Recently surveys have been published at 153 MHz (Hamilton and Haynes 1967) and between 40 and 120 MHz (Haynes and Hamilton 1968). Continuing these observations, we report here on measurements of 11 radio sources made at the Australian National Radio Astronomy Observatory, Parkes, N.S.W., in January 1968.

A total power receiver tuned from 50 to 70 MHz was used. The bandwidth was 1 MHz and the receiver noise temperature was 630°K. The feed was a broad band helix mounted at the focus of the 210 ft telescope. The helix, with diameter 20 in. and length 8 ft, consisted of two coaxial windings in the same sense with pitch angles of 35°. The two windings were fed 180° out of phase and matching from 300 Ω to a 70 Ω cable was achieved with a broad band transformer. The feed was sensitive to waves with right-hand circular polarization.

The spectrum of the source Hydra A (PKS 0915−11) as given by Conway, Kellermann, and Long (1963) was used as the reference spectrum for all the observations. This source was used to calibrate a temperature saturated noise diode which was used as a secondary standard. The noise diode was coupled to the receiver with a directional coupler. Repeated scans of Hydra A showed that the beamwidth of the telescope near 55 MHz is close to 6°.

The sources to be observed were selected with the following criteria.

(1) The source is sufficiently strong to permit reliable measurements.

(2) No nearby strong sources exist to produce confusion.

(3) The galactic background radiation in the vicinity of the source is low.

Of the sources measured, five were known to have curved spectra.

Below 100 MHz observations of sources are hindered by the presence of man-made interference, and during the present observations only three channels were found to be sufficiently clear to permit reliable measurements. These were centred at 54·2, 59·2, and 67·4 MHz and were generally clear between 0000 and 1000 hr local time.

---

* Manuscript received April 22, 1968.

† Department of Physics, University of Tasmania, P.O. Box 252C, Hobart, Tasmania 7001.

Aust. J. Phys., 1968, 21, 539–42

TABLE 1

SOURCE MEASUREMENTS

(1)	(2)	(3)	(4)	(5)	(6)	(7)	(8)	(9)	(10)	(11)	(12)	(13)
PKS Catalogue Number	Position (1950·0) R.A. h m s	Dec. ° ′	Present Results (f.u.) $S_{54\cdot2}$	$S_{59\cdot2}$	$S_{67\cdot4}$	Previous Observations (f.u.) $S_{85\cdot5}$	S_{153}	S_{408}	S_{1410}	Freq.	S	Remarks
0320−37	03 20 42	−37 25·0	1022	—	985	950	474	249	—	42·7 46·3 58·0	1255 1532 1309	NGC1316, Fornax A
0859−25	08 59 37	−25 44·2	—	44·2	—	54	51	16·4	5·8	—	—	
1226+02	12 26 34	+02 19·1	338·6	377·8	—	167	(150)	55·1	41·2	99·2	134	3C273
1302−49	13 02 32	−49 12·1	—	19·2	—	20	—	14·0	7·4	—	—	NGC4945
1355−41	13 55 56	−41 38·0	—	64·2	—	35·0	22·0	13·2	4·6	—	—	
1459−41	14 59 11	−41 54·3	—	76·0	—	55·0	32·9	17·4	4·7	87·0 105·2	60·9 40·7	Extended
1648+05	16 48 42	+05 04·5	—	—	1050	890	424	161	46·0	98·0 113·0	695·6 627·0	3C348
1814−63	18 14 49	−63 46·9	—	76·0	—	71·0	—	34	14·2	94·0 108 113·2	74·6 80·0 86·4	
1932−46	19 32 20	−46 28·2	284·7	—	—	141	(157)	39	13·4	89 116 97	136 112 124	Polarized Extended E–W
2152−69	21 52 58	−69 55·8	—	355·0	—	253	—	80	32	89·0 99 112·5	218·7 198 160·7	
2356−61	23 56 24	−61 11·7	364·0	—	—	296·0	—	66	23·7	84·0 99 115	254·8 208 165·0	

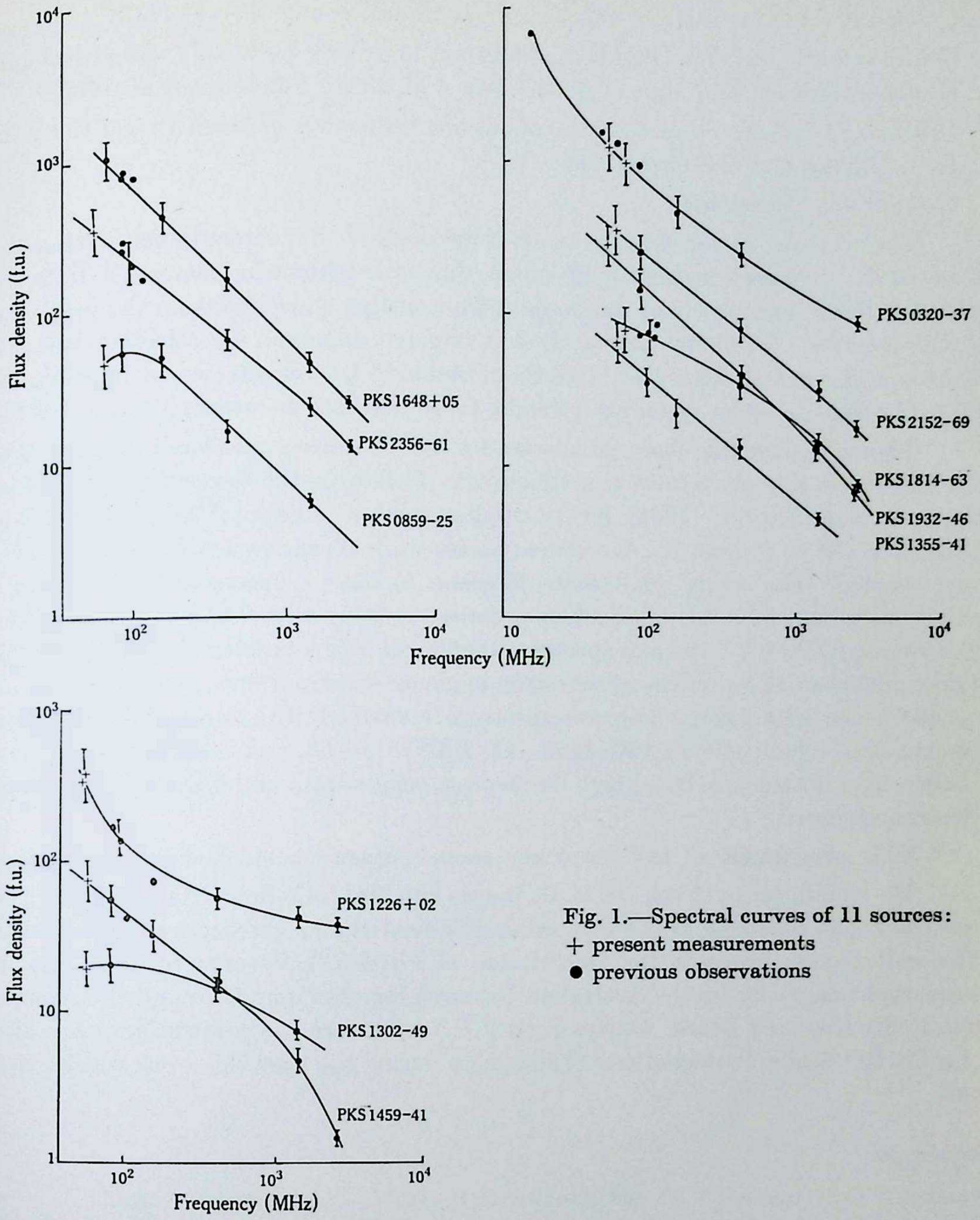

Fig. 1.—Spectral curves of 11 sources:
+ present measurements
● previous observations

The results of the source measurements are given in Table 1, together with observations of other workers. Notes on the table are as follows.

Column 1. Parkes catalogue number.

Columns 2 and 3. Right ascension and declination (1950·0).

Columns 4, 5, and 6. Present observations of flux density at 54·2, 59·2, and 67·4 MHz.

Column 7. Flux density at 85·5 MHz from Mills, Slee, and Hill (1958).

Column 8. Flux density at 153 MHz from Hamilton and Haynes (1967).

Columns 9 and 10. Flux densities at 408 and 1410 MHz from the Parkes catalogue (Bolton, Gardner, and Mackey 1964; Day *et al.* 1966; Shimmins *et al.* 1966).

Columns 11 and 12. Flux densities at various frequencies between 40 and 120 MHz from Haynes and Hamilton (1968).

Column 13. Remarks.

The accuracy of the measurements is affected by: (1) errors in calibrating the noise diode secondary standard, (2) errors due to neighbouring sources within the telescope beam, and (3) errors due to faint transmitting stations within the passband of the receiver. Of these factors (2) was largely eliminated by selecting suitable sources, and repeated scans permitted the rejection of records affected by interference (3). The flux densities given are thought to be accurate to within 12% ±3·8 f.u.

Figure 1 gives the observed spectra for the 11 sources measured. In all, 8 of the 11 sources appear to have curved spectra. Following the convention of Bolton, Gardner, and Mackey (1964) for classifying spectra, sources PKS 1226+02 and PKS 0320−37 have negative curvature spectra while 6 sources show positive curvature spectra. The source PKS 0859−25 seems to have a spectrum that implies a single source in which the synchrotron radiation is being affected by self absorption. The source PKS 1302−49 has a spectrum that is not characteristic of a single absorption mechanism affecting the synchrotron emission spectrum but may result from a cutoff in the high energy electron spectrum combined with absorption at lower frequencies. Three sources PKS 1459−41, PKS 1814−63, and PKS 1932−46 show a steepening of their spectra at high frequencies, suggesting a cutoff in the high energy electron spectrum.

This programme of low frequency source measurements is being continued.

We would like to thank Dr. E. G. Bowen and Mr. J. G. Bolton for permission to use the 210 ft telescope of the Australian National Radio Astronomy Observatory. The radiophysics group in the Department of Physics, University of Tasmania, is supported financially by the Australian Research Grants Committee and the Australian Radio Research Board. One of us (R.F.H.) would like to acknowledge the receipt of a CSIRO Senior Post-graduate Studentship during the time this work was carried out.

References

Bolton, J. G., Gardner, F. F., and Mackey, M. B. (1964).—*Aust. J. Phys.* **17**, 340.

Conway, R. G., Kellermann, K. I., and Long, R. G. (1963).—*Mon. Not. R. astr. Soc.* **125**, 261.

Day, G. A., Shimmins, A. J., Ekers, R. D., and Cole, D. L. (1966).—*Aust. J. Phys.* **19**, 35.

Hamilton, P. A., and Haynes, R. F. (1967).—*Aust. J. Phys.* **20**, 697.

Haynes, R. F., and Hamilton, P. A. (1968).—*Aust. J. Phys.* **21**, 87.

Kellermann, K. I. (1966).—*Astrophys. J.* **146**, 621.

Mills, B. Y., Slee, O. B., and Hill, E. R. (1958).—*Aust. J. Phys.* **11**, 360.

Shimmins, A. J., Day, G. A., Ekers, R. D., and Cole, D. J. (1966).—*Aust. J. Phys.* **19**, 837.

AN EXACT SOLUTION OF BOLTZMANN'S EQUATION FOR A RIGID SPHERE GAS

By P. I. Brooker* and H. S. Green*

[*Manuscript received January* 30, 1968]

Summary

The second approximation to Boltzmann's equation, in Chapman and Cowling's form, is solved exactly for a rigid sphere gas by using appropriate transformations to reduce the integral equation to a differential equation, which is solved numerically. The values of the transport coefficients, calculated directly from this solution for the velocity distribution function, are in good agreement with those obtained from the usual approximation techniques. A solution for part of the third approximation, with a term of zero order in V, the velocity of a molecule relative to the stream velocity, is also obtained analytically.

I. Introduction

The fact that an exact solution of Boltzmann's equation for a simple gas of hard, perfectly smooth, and elastic spheres should be possible was first noted by Cotter (1952) and later by Pekeris (1955) and Pekeris and Alterman (1957). Cotter obtained the coefficient of thermal conduction of a gas of rigid spheres after a very long and tedious calculation. The present paper presents a considerable simplification of Cotter's analysis, and its generalization to the calculation of other transport coefficients. Essentially the method of solution consists of a reduction of the integro-differential equation to a linear differential equation by appropriate transformation. The differential equation is then solved numerically and in some cases analytically.

An important feature of this method is that it enables the actual velocity distribution function, and not only its moments, to be determined. It is widely recognized that, although the method of Chapman and Enskog yields rapidly summable series for the transport coefficients, the expansion in polynomials probably diverges at least in some region of velocity space. The present calculations allow the only exact determination of the velocity distribution function, for other than the Maxwellian force law.

Further extensions of this method are possible. For instance, the third approximation (in Chapman's sense) to the solution of Boltzmann's equation can be readily obtained (Section IV(a)). It is also possible that a similar method could be devised for any potential that is constant, except at a number of discontinuities; and, as most potentials could be approximated in this way, the range of application of the method would then be very wide indeed.

---

* Department of Mathematical Physics, University of Adelaide, Adelaide, S.A. 5000.

Aust. J. Phys., 1968, **21**, 543–61

II. Boltzmann's Equation for Rigid Sphere Gas

The Boltzmann equation for a simple gas subject to an external force $\boldsymbol{F}$, which is independent of velocity, has the form

$$\frac{\partial f}{\partial t}+\boldsymbol{v}.\frac{\partial f}{\partial \boldsymbol{r}}+\frac{\boldsymbol{F}}{m}.\frac{\partial f}{\partial \boldsymbol{v}}=I_0(f)\,, \tag{1}$$

where the velocity distribution function f is a function of time t, position $\boldsymbol{r}$, and molecular velocity $\boldsymbol{v}$ of a molecule; the collision integral $I_0(f)$ is a function of f, and involves knowledge of the dynamics of a binary collision between molecules of the gas; and m is the mass of a molecule.

This equation is solved by writing

$$f=f_0+f_0\,\Phi^{(1)}+f_0\,\Phi^{(2)}+\ldots\,, \tag{2}$$

where the first approximation f_0 is of Maxwellian form

$$f_0=n(m/2\pi kT)^{3/2}\exp\{-m(\boldsymbol{v}-\boldsymbol{c}_0)^2/2kT\}\,, \tag{3}$$

with $n=n(\boldsymbol{r},t)$ the molecular number density at $(\boldsymbol{r},t)$, $\boldsymbol{c}_0=\boldsymbol{c}_0(\boldsymbol{r},t)$ the stream velocity at $(\boldsymbol{r},t)$, $T=T(\boldsymbol{r},t)$ the temperature at $(\boldsymbol{r},t)$, and k Boltzmann's constant.

The difference between this and an equilibrium solution is that the parameters n, $\boldsymbol{c}_0$, and T describing the system are now functions of time and position.

The nth approximation to f is obtained by taking n terms of (2), substituting in (1), and solving the resulting equation. The functions $\Phi^{(N)}$ are of order N in the spatial gradients of n, $\boldsymbol{c}_0$, and T.

III. Second Approximation to Velocity Distribution Function

Since the transport coefficients are linear in the gradients they are obtained from the second approximation to f. Thus

$$f=f_0+f_0\,\Phi^{(1)}$$

is substituted in (1) and only terms linear in the gradients are retained. The resulting equation, to be solved for $\Phi^{(1)}$, can be written as

$$\begin{aligned}-n^2I(\Phi^{(1)})&=\sigma^2\iint_{\boldsymbol{\rho}.\boldsymbol{a}>0}\boldsymbol{\rho}.\boldsymbol{a}\,f_0(\boldsymbol{u})\,f_0(\boldsymbol{v})\\&\qquad\times\{\Phi^{(1)}(\boldsymbol{u}_0)+\Phi^{(1)}(\boldsymbol{v}_0)-\Phi^{(1)}(\boldsymbol{u})-\Phi^{(1)}(\boldsymbol{v})\}\,\mathrm{d}\boldsymbol{a}\,\mathrm{d}\boldsymbol{u} &(4)\\&=f_0(\boldsymbol{v})\left\{\left(\alpha V^2-\frac{5}{2}\right)\boldsymbol{V}.\frac{\partial\log T}{\partial\boldsymbol{r}}+2\alpha\boldsymbol{V}^0\boldsymbol{V}:\frac{\partial\boldsymbol{c}_0}{\partial\boldsymbol{r}}\right\}, &(5)\end{aligned}$$

where

$$\boldsymbol{V}=\boldsymbol{v}-\boldsymbol{c}_0\,,\qquad \boldsymbol{\rho}=\boldsymbol{v}-\boldsymbol{u}\,,\qquad \alpha=m/2kT\,,$$

$\boldsymbol{V}^0\boldsymbol{V}=\boldsymbol{V}\boldsymbol{V}-\frac{1}{3}V^2\boldsymbol{\delta}$ is a symmetric nondivergent tensor, σ is the diameter of a molecule, $\boldsymbol{u}$ and $\boldsymbol{v}$ are the velocities of two molecules that have collided, their velocities before collision being $\boldsymbol{u}_0$ and $\boldsymbol{v}_0$ respectively, and $\boldsymbol{a}$ is a unit vector in the direction of the line of centres at the instant of collision.

Equation (4) follows upon substituting rigid sphere collision dynamics into the general expression for the collision integral; and the left-hand side of the Boltzmann equation is reduced to (5) by use of the equations of continuity, motion, and energy balance.

Following Chapman and Cowling (1960) the function $\Phi^{(1)}$ can be written

$$\Phi^{(1)} = -\frac{1}{n\sigma^2}\phi^{(1)}(V)\,\tilde{V}.\frac{\partial \log T}{\partial r} - \frac{\alpha^{\frac{1}{2}}}{n\sigma^2}\phi^{(2)}(V)\,\tfrac{3}{2}\tilde{V}^0\tilde{V}:\frac{\partial c_0}{\partial r}, \tag{6}$$

where $\phi^{(1)}$ and $\phi^{(2)}$ are dimensionless scalar functions of αV^2 only,

$$\tilde{V} = V/\,|\,V\,|, \qquad \text{and} \qquad \tilde{V}^0\tilde{V} = V^0V/V^2.$$

Substituting (6) in (4) and equating coefficients in the components of ∇T and ∇c_0, two separate equations are obtained:

$$(\alpha V^2 - \tfrac{5}{2})V = \left(\frac{\alpha}{\pi}\right)^{3/2} \iint_{\boldsymbol{\rho}.\boldsymbol{a}>0} \boldsymbol{\rho}.\boldsymbol{a}\exp(-\alpha U^2)\{\phi^{(1)}(U)\,\tilde{U}.\tilde{V} + \phi^{(1)}(V)\,\tilde{V}.\tilde{V} - \phi^{(1)}(U_0)\,\tilde{U}_0.\tilde{V}$$
$$-\phi^{(1)}(V_0)\,\tilde{V}_0.\tilde{V}\}\,\mathrm{d}\boldsymbol{a}\,\mathrm{d}\boldsymbol{u}, \tag{7}$$

$$\tfrac{4}{3}\alpha V^2 = \frac{\alpha^2}{\pi^{3/2}} \iint_{\boldsymbol{\rho}.\boldsymbol{a}>0} \boldsymbol{\rho}.\boldsymbol{a}\exp(-\alpha U^2)\{\phi^{(2)}(U)\,\tfrac{3}{2}\tilde{U}^0\tilde{U}:\tilde{V}^0\tilde{V} + \phi^{(2)}(V)\,\tfrac{3}{2}\tilde{V}^0\tilde{V}:\tilde{V}^0\tilde{V}$$
$$-\phi^{(2)}(U_0)\,\tfrac{3}{2}\tilde{U}_0^0\tilde{U}_0:\tilde{V}^0\tilde{V} - \phi^{(2)}(V_0)\,\tfrac{3}{2}\tilde{V}_0^0\tilde{V}_0:\tilde{V}^0\tilde{V}\}\,\mathrm{d}\boldsymbol{a}\,\mathrm{d}\boldsymbol{u}. \tag{8}$$

These are of the general form

$$F(V) = \iint_{\boldsymbol{\rho}.\boldsymbol{a}>0} \boldsymbol{\rho}.\boldsymbol{a}\exp(-\alpha U^2)\{\phi^{(n)}(U)\,\mathrm{P}_n(\tilde{U}.\tilde{V}) + \phi^{(n)}(V)\,\mathrm{P}_n(\tilde{V}.\tilde{V})$$
$$-\phi^{(n)}(U_0)\,\mathrm{P}_n(\tilde{U}_0.\tilde{V}) - \phi^{(n)}(V_0)\,\mathrm{P}_n(V_0.\tilde{V})\}\,\mathrm{d}\boldsymbol{a}\,\mathrm{d}\boldsymbol{u}, \tag{9}$$

where $F(V)$ is some known function of V and P_n is the Legendre polynomial of order n.

Now (9) can be written

$$F(V) = J^{(n)} + K^{(n)} - J_0^{(n)} - K_0^{(n)}, \tag{10}$$

where

$$J^{(n)} = \iint_{\boldsymbol{\rho}.\boldsymbol{a}>0} \boldsymbol{\rho}.\boldsymbol{a}\exp(-\alpha U^2)\,\phi^{(n)}(U)\,\mathrm{P}_n(\tilde{U}.\tilde{V})\,\mathrm{d}\boldsymbol{a}\,\mathrm{d}\boldsymbol{u}, \tag{11}$$

$$K^{(n)} = \iint_{\boldsymbol{\rho}.\boldsymbol{a}>0} \boldsymbol{\rho}.\boldsymbol{a}\exp(-\alpha U^2)\,\phi^{(n)}(V)\,\mathrm{d}\boldsymbol{a}\,\mathrm{d}\boldsymbol{u}, \tag{12}$$

$$J_0^{(n)} = \iint_{\boldsymbol{\rho}.\boldsymbol{a}>0} \boldsymbol{\rho}.\boldsymbol{a}\exp(-\alpha U^2)\,\phi^{(n)}(U_0)\,\mathrm{P}_n(\tilde{U}_0.\tilde{V})\,\mathrm{d}\boldsymbol{a}\,\mathrm{d}\boldsymbol{u}, \tag{13}$$

$$K_0^{(n)} = \iint_{\boldsymbol{\rho}.\boldsymbol{a}>0} \boldsymbol{\rho}.\boldsymbol{a}\exp(-\alpha U^2)\,\phi^{(n)}(V_0)\,\mathrm{P}_n(\tilde{V}_0.\tilde{V})\,\mathrm{d}\boldsymbol{a}\,\mathrm{d}\boldsymbol{u}. \tag{14}$$

In simplifying (11)–(14) we note firstly that

$$\int_{\boldsymbol{\rho}.\boldsymbol{a}} \boldsymbol{\rho}.\boldsymbol{a}\,\mathrm{d}\boldsymbol{a} = \pi\rho;$$

then

$$\begin{aligned}
J^{(n)}(V) &= \int \exp(-\alpha U^2)\,\phi^{(n)}(U)\,\mathrm{P}_n(\tilde{U}.\tilde{V})\,\pi\rho\,\mathrm{d}\boldsymbol{u} \\
&= 4\pi^2 \int_0^\infty U^2 \exp(-\alpha U^2)\,\phi^{(n)}(U)\,\tfrac{1}{2}\int_{-1}^{1} \mathrm{P}_n(x)\,(U^2+V^2-2UVx)^{\frac{1}{2}}\,\mathrm{d}x\,\mathrm{d}U \\
&= 4\pi^2 \Bigg[\int_0^V U^2 \exp(-\alpha U^2)\,\phi^{(n)}(U)\,\frac{V}{2n+1}\left\{\frac{1}{2n+3}\left(\frac{U}{V}\right)^{n+2} - \frac{1}{2n-1}\left(\frac{U}{V}\right)^{n}\right\}\mathrm{d}U \\
&\qquad + \int_V^\infty U^2 \exp(-\alpha U^2)\,\phi^{(n)}(U)\,\frac{U}{2n+1}\left\{\frac{1}{2n+3}\left(\frac{V}{U}\right)^{n+2} - \frac{1}{2n-1}\left(\frac{V}{U}\right)^{n}\right\}\mathrm{d}U\Bigg].
\end{aligned} \tag{15}$$

To obtain (15) use has been made of the identity

$$\left(1+\frac{U^2}{V^2}-\frac{2U}{V}x\right)^{\frac{1}{2}} = \frac{1}{2n+1}\sum_{n=0}^{\infty}\left\{\mathrm{P}_{2n}(x)-\frac{U}{V}\mathrm{P}_{2n+1}(x)\right\} \qquad \text{for} \qquad U<V,$$

$x = \tilde{U}.\tilde{V}$, and the orthogonality of the Legendre polynomials.

$$\begin{aligned}
K^{(n)}(V) &= \phi^{(n)}(V)\int \exp(-\alpha U^2)\,\pi\rho\,\mathrm{d}\boldsymbol{u} \\
&= 4\pi^2\phi^{(n)}(V)\int_0^\infty U^2\exp(-\alpha U^2)\,\tfrac{1}{2}\int_{-1}^{1}(U^2+V^2-2UVx)^{\frac{1}{2}}\,\mathrm{d}x\,\mathrm{d}U \\
&= 4\pi^2\phi^{(n)}(V)\Bigg(\int_0^V U^2\exp(-\alpha U^2)\,\frac{\frac{1}{3}U^3+UV^2}{UV}\,\mathrm{d}U \\
&\qquad + \int_V^\infty U^2\exp(-\alpha U^2)\,\frac{\frac{1}{3}V^3+VU^2}{UV}\,\mathrm{d}U\Bigg).
\end{aligned} \tag{16}$$

$$J_0^{(n)}(V) = \iint \tfrac{1}{2}\delta(\rho_0^2-\rho^2)\exp(-\alpha U^2)\,\phi^{(n)}(U_0)\,\mathrm{P}_n(\tilde{U}_0.\tilde{V})\,\mathrm{d}\boldsymbol{\rho}_0\,\mathrm{d}\boldsymbol{u},$$

using the fact that in a rigid sphere collision the relative velocity before and after collision is unchanged and $|\boldsymbol{\rho}_0.\boldsymbol{a}| = |\boldsymbol{\rho}.\boldsymbol{a}|$,

$$= \iint 4\delta(\rho_0^2-\rho^2)\exp(-\alpha U^2)\,\phi^{(n)}(U_0)\,\mathrm{P}_n(\tilde{U}_0.\tilde{V})\,\mathrm{d}\boldsymbol{u}_0\,\mathrm{d}\boldsymbol{u} \qquad (\rho_0 = 2\boldsymbol{u}_0-\boldsymbol{u}-\boldsymbol{v})$$

$$= \iint \delta\{\boldsymbol{U}.(\boldsymbol{V}-\boldsymbol{U}_0)-\boldsymbol{U}_0(\boldsymbol{V}-\boldsymbol{U}_0)\}\,\phi^{n}(U_0)\,\mathrm{P}_n(\tilde{U}_0.\tilde{V})\exp(-\alpha U^2)\,\mathrm{d}\boldsymbol{u}\,\mathrm{d}\boldsymbol{u}_0.$$

Let $\boldsymbol{W} = \boldsymbol{U} - \boldsymbol{U}_0$, then

$$J_0^{(n)} = \iint \delta\{\boldsymbol{W}.(\boldsymbol{V}-\boldsymbol{U}_0)\} \exp\{-\alpha(U_0+W)^2\} \phi^{(n)}(U_0) \,\mathrm{P}_n(\tilde{U}_0 . \tilde{V}) \,\mathrm{d}\boldsymbol{W} \,\mathrm{d}\boldsymbol{u}_0$$

$$= \int \frac{\phi^{(n)}(U_0)}{|\boldsymbol{V}-\boldsymbol{U}_0|} \mathrm{P}_n(\tilde{U}_0 . \tilde{V}) \exp[-\alpha\{\boldsymbol{U}_0.(\boldsymbol{V}-\boldsymbol{U}_0)\}^2 (\boldsymbol{V}-\boldsymbol{U}_0)^{-2}] \,\mathrm{d}\boldsymbol{u}_0 . \tag{17}$$

It can be shown that

$$K_0^{(n)} = J_0^{(n)} . \tag{18}$$

Define

$$\exp(-\alpha U^2) \, L^n(U, V) = \tfrac{1}{2} \int_{-1}^{1} \frac{\exp[-\alpha\{\boldsymbol{U}.(\boldsymbol{U} \simeq \boldsymbol{V})\}^2]}{|\boldsymbol{U}-\boldsymbol{V}|} \mathrm{P}_n(x) \,\mathrm{d}x , \tag{19}$$

with $x = \boldsymbol{U}.\boldsymbol{V}$. Then

$$J_0^{(n)}(V) = (4\pi^2/\alpha) \int_0^V U^2 \phi^{(n)}(U) \exp(-\alpha U^2) \, L^n(U, V) \,\mathrm{d}U$$

$$+ \int_V^\infty U^2 \phi^{(n)}(U) \exp(-\alpha U^2) \, L^n(V, U) \,\mathrm{d}U . \tag{20}$$

It can be shown in particular that

$$L^0(U, V) = (UV)^{-1} \exp(\alpha U^2) \int_0^U \exp(-\alpha K^2) \,\mathrm{d}K , \tag{21}$$

$$L^{(1)}(U, V) = (U^2 V^2)^{-1} \exp(\alpha U^2) \int_0^U \exp(-\alpha K^2) (U^2 - 2K^2) \,\mathrm{d}K , \tag{22}$$

$$L^{(2)}(U, V) = (U^3 V^3)^{-1} \exp(\alpha U^2) \int_0^U \exp(-\alpha K^2) \, \tfrac{1}{2} [3\{(U^2 - 2K^2)^2 + (V^2 - U^2) K^2\} - U^2 V^2] \,\mathrm{d}K . \tag{23}$$

Further functions are now defined to facilitate operations with some of these expressions. Define

$$k(V) = \int_0^V U \exp(-\alpha U^2) (\tfrac{1}{3} U^3 + U V^2) \,\mathrm{d}U + \int_V^\infty U \exp(-\alpha U^2) (\tfrac{1}{3} V^3 + V U^2) \,\mathrm{d}U , \tag{24}$$

$$\psi(V) = \int_0^V \exp(-\alpha K^2) \,\mathrm{d}K , \tag{25}$$

$$\epsilon(V) = \exp(-\alpha V^2) . \tag{26}$$

Then

$$\left.\begin{aligned} k(V) &= \{(2\alpha V^2+1)\psi + V\epsilon\}/4\alpha^2, \\ k'(V) &= (2\alpha V\psi+\epsilon)/2\alpha^2, \\ k''(V) &= \psi/\alpha, \\ k'''(V) &= \epsilon/\alpha, \qquad \text{and} \qquad k''+2\alpha k'V-4\alpha k = 0. \end{aligned}\right\} \tag{27}$$

Equation (10) has $\phi^{(n)}$ under an integral. The procedure now is to define new variables and carry out integration by parts. This reduces the integral equation in $\phi^{(n)}$ to a differential equation in some new variable. The differential equation is solved and $\phi^{(n)}$ found from its relations with the new variables.

(a) *Solution for* $n = 1$

Define

$$\beta(V) = \int_V^\infty \exp(-\alpha U^2)\,\phi^{(1)}(U)\,\mathrm{d}U \tag{28}$$

and

$$\gamma(V) = \int_V^\infty U\,\beta(U)\,\mathrm{d}U. \tag{29}$$

Then, using (15), (16), (20), (22), and (24),

$$\begin{aligned} \frac{V^2J^{(1)}}{4\pi^2} &= \int_0^V \exp(-\alpha U^2)\,\phi^{(1)}(U)\,\tfrac{1}{3}U^3(\tfrac{1}{5}U^2-V^2)\,\mathrm{d}U \\ &\qquad + \int_V^\infty \exp(-\alpha U^2)\,\phi^{(1)}(U)\,\tfrac{1}{3}V^3(\tfrac{1}{5}V^2-U^2)\,\mathrm{d}U \\ &= \int_0^V \beta(U)\,U^2(\tfrac{1}{3}U^2-V^2)\,\mathrm{d}U + \int_V^\infty \beta(U)\,(-\tfrac{2}{3}UV^3)\,\mathrm{d}U \\ &= \int_0^V \gamma(U)\,(U^2-V^2)\,\mathrm{d}U, \end{aligned} \tag{30}$$

$$\frac{V^2K^{(1)}}{4\pi^2} = V\phi^{(1)}\,k(V), \tag{31}$$

$$\begin{aligned} \frac{V^2J_0^{(1)}}{4\pi^2} &= \frac{1}{\alpha}\left(\int_0^V \exp(-\alpha U^2)\,\phi^{(1)}(U)\exp(\alpha U^2)\int_0^U \exp(-\alpha K^2)\,(U^2-2K^2)\,\mathrm{d}K\,\mathrm{d}U\right. \\ &\qquad \left. + \int_V^\infty \exp(-\alpha U^2)\,\phi^{(1)}(U)\exp(\alpha V^2)\int_0^V \exp(-\alpha K^2)\,(V^2-2K^2)\,\mathrm{d}K\,\mathrm{d}U\right) \\ &= \frac{1}{\alpha}\int_0^V \beta(U)\,\frac{\mathrm{d}}{\mathrm{d}U}\left(\exp(\alpha U^2)\int_0^U \exp(-\alpha K^2)\,(U^2-2K^2)\,\mathrm{d}K\right)\mathrm{d}U \\ &= \frac{1}{\alpha}\int_0^V \beta(U)\left(U^2+2\alpha U^3\exp(\alpha U^2)\int_0^U \exp(-\alpha K^2)\,\mathrm{d}K\right)\mathrm{d}U. \end{aligned} \tag{32}$$

Using (7) and (10)

$$\epsilon\frac{\mathrm{d}}{\mathrm{d}V}\left\{\frac{V^2}{4\pi^2}\left(J^{(1)}+K^{(1)}-2J_0^{(1)}\right)\right\} = \epsilon\frac{\mathrm{d}}{\mathrm{d}V}\left\{\frac{V^2}{4\pi^2}\left(\frac{\pi}{\alpha}\right)^{3/2}\left(\alpha V^2-\tfrac{5}{2}\right)V\right\}$$

$$= -\frac{5}{8(\pi\alpha^3)^{\frac{1}{2}}}\frac{\mathrm{d}}{\mathrm{d}V}\left(V^3\epsilon\right). \tag{33}$$

From (30), (31), and (32)

$$\epsilon\frac{\mathrm{d}}{\mathrm{d}V}\left\{\frac{V^2}{4\pi^2}\left(J^{(1)}+K^{(1)}-2J_0^{(1)}\right)\right\} = -2\epsilon V\int_0^V \gamma(U)\,\mathrm{d}U+\epsilon\frac{\mathrm{d}}{\mathrm{d}V}\left(Vk\phi^{(1)}\right)$$

$$-\beta\left(\frac{2V^2\epsilon}{\alpha}+4V^3\int_0^V \exp(-\alpha K^2)\,\mathrm{d}K\right)$$

$$= \frac{\mathrm{d}}{\mathrm{d}V}\left(\frac{\epsilon}{\alpha}\int_0^V \gamma(U)\,\mathrm{d}U-\frac{\psi\gamma}{\alpha}-2\alpha V^2k\beta+Vk\epsilon\phi^{(1)}\right). \tag{34}$$

Define

$$\left.\begin{aligned} X(V) &= \int_0^V \gamma(U)\,\mathrm{d}U \\ \text{so that}\qquad X'(V) &= \gamma(V), \qquad X''(V) = -V\beta(V), \\ X'''(V) &= -\beta(V)+V\exp(-\alpha V^2)\,\phi^{(1)}(V). \end{aligned}\right\} \tag{35}$$

Substituting (35) into (34) gives, after integration of (33) and (34),

$$kX'''+\left(2\alpha V-\frac{1}{V}\right)kX''-\frac{\psi}{\alpha}X'+\frac{\epsilon}{\alpha}X = -\frac{5}{8(\pi\alpha^3)^{\frac{1}{2}}}V^3\epsilon. \tag{36}$$

The constant of integration is zero. Writing $c^2 = \alpha V^2$ and $\alpha^2X(V) = \tilde{X}(c)$ gives a dimensionless equation

$$k\tilde{X}'''+(2c-c^{-1})k\tilde{X}''-\psi\tilde{X}'+\epsilon\tilde{X} = -(5/8\pi^{\frac{1}{2}})c^3\epsilon. \tag{37}$$

In this and the following, k, now a function of the dimensionless variable, and its derivatives, now taken with respect to this variable, are defined by (27) with $\alpha = 1$.

Thus (7) has been reduced to a third-order linear differential equation which is solved numerically by a Runge–Kutta technique.

From the definition of X, the boundary conditions for X and its derivatives are

$$\left.\begin{aligned} X(0) &= 0 &\quad \text{and as } V\to\infty \quad X' &\to 0 \text{ exponentially,} \\ X'(0) &= a_1 & X'' &\to 0 \text{ exponentially,} \\ X''(0) &= 0 & X''' &\to 0 \text{ exponentially,} \\ X'''(0) &= a_2. & & \end{aligned}\right\} \tag{38}$$

Also

$$X(V) = VX' - \tfrac{1}{3}V^2X'' + \tfrac{1}{3}\int_0^V \exp(-\alpha U^2)\,\phi^{(1)}\,U^3\,\mathrm{d}U\,.$$

Thus

$$\lim_{V\to\infty} X(V) = \tfrac{1}{3}\int_0^\infty \exp(-\alpha U^2)\,\phi^{(1)}\,U^3\,\mathrm{d}U\,.$$

Now there are auxiliary conditions that must be placed upon $\Phi^{(K)}$ to ensure correct definitions of n, c_0, and T; namely, for all K

$$\int \epsilon\,\Phi^{(K)}\,\mathrm{d}\boldsymbol{u} = 0\,, \tag{39}$$

$$\int \epsilon\,\Phi^{(K)}\,\boldsymbol{U}\,\mathrm{d}\boldsymbol{u} = 0\,, \tag{40}$$

$$\int \epsilon\,\Phi^{(K)}\,U^2\,\mathrm{d}\boldsymbol{u} = 0\,. \tag{41}$$

The definition of $\Phi^{(1)}$ in (6) satisfies (39) and (41); and (40) requires that

$$\int_0^\infty \epsilon\,\phi^{(1)}\,U^3\,\mathrm{d}U = 0\,.$$

Thus as $V \to \infty$, X, X', X'', and X''' all tend to zero exponentially. This condition is sufficient to fix the constants a_1 and a_2 of (38) and so enables a numerical solution to be found.

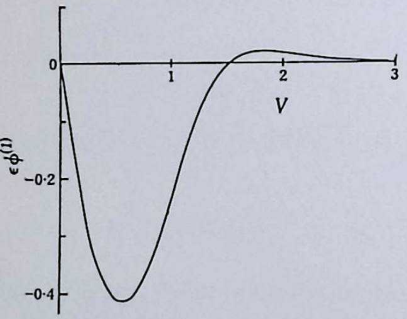

Fig. 1.—Velocity distribution function for thermal conduction.

$\phi^{(1)}$ is then simply related to $\widetilde{X}$ via

$$\phi^{(1)}(c) = (c\epsilon)^{-1}(\widetilde{X}''' - c^{-1}\widetilde{X}'')\,. \tag{42}$$

Figure 1 gives the solution $\phi^{(1)}$.

It is worth noting that one analytic solution of the homogeneous equation obtained by neglecting the right-hand side of (37) can be found. The solution is

$$\widetilde{X} = \psi\,.$$

This means that (37) can be reduced to a second-order equation. Writing $\tilde{X} = \psi\lambda$ and substituting in (37),

$$k\psi\lambda''' + k\{3\epsilon + (2c - c^{-1})\psi\}\lambda'' - \{2\epsilon k(c + c^{-1}) + \psi^2\}\lambda' = -(5/8\pi^{\frac{1}{2}})c^3\epsilon. \tag{43}$$

This equation could be solved for λ' numerically, and then $\tilde{X}$ obtained by integration and hence $\phi^{(1)}$. However, since a solution of the homogeneous equation obtained by neglecting the right-hand side of (43) cannot be found, it is impossible to reduce (43) further, to a first-order equation, which could be solved analytically. In his paper Cotter (1952) reduced the Boltzmann equation to a similar second-order linear differential equation by more involved transformations.

(*b*) *Solution for* $n = 2$

Define

$$m(V) = \int_V^\infty \exp(-\alpha U^2)\, U^{-1} \phi^{(2)}(U)\, \mathrm{d}U \tag{44}$$

and

$$n(V) = \int_V^\infty m(U)\, U\, \mathrm{d}U. \tag{45}$$

Using (15), (16), (20), (23), and (24),

$$\begin{aligned} \frac{V^3 J^{(2)}}{4\pi^2} &= \int_0^V \exp(-\alpha U^2)\, U^{-1} \phi^{(2)}(U)\, \tfrac{1}{5} U^5 (\tfrac{1}{7} U^2 - \tfrac{1}{3} V^2)\, \mathrm{d}U \\ &\quad + \int_V^\infty \exp(-\alpha U^2)\, U^{-1} \phi(U)\, \tfrac{1}{5} V^5 (\tfrac{1}{7} V^2 - \tfrac{1}{3} U^2)\, \mathrm{d}U \\ &= \int_0^V m(U)\, (\tfrac{1}{5} U^6 - \tfrac{1}{3} U^4 V^2)\, \mathrm{d}U + \int_V^\infty m(U)\, (-\tfrac{2}{15} U V^5)\, \mathrm{d}U \\ &= \int_0^V n(U)\, (U^2 - V^2) U^2\, \mathrm{d}U, \end{aligned} \tag{46}$$

$$\frac{V^3 K^{(2)}}{4\pi^2} = V^2 k(V)\, \phi^{(2)}(V) = -V^3 k \exp(\alpha V^2)\, m'(V) = V^3 k \exp(\alpha V^2) \frac{\mathrm{d}}{\mathrm{d}V}\left(\frac{n'}{V}\right), \tag{47}$$

$$\begin{aligned} \frac{\alpha V^3 J_0^{(2)}}{4\pi^2} &= \int_0^V \exp(-\alpha U^2)\, U^{-1} \phi^{(2)} \exp(\alpha U^2) \\ &\quad \times \int_0^U \exp(-\alpha K^2)\, \tfrac{1}{2}[3\{(U^2 - 2K^2)^2 + (V^2 - U^2) K^2\} - U^2 V^2]\, \mathrm{d}K\, \mathrm{d}U \\ &\quad + \int_V^\infty \exp(-\alpha U^2)\, U^{-1} \phi^{(2)} \exp(\alpha V^2) \\ &\quad \times \int_0^V \exp(-\alpha K^2)\, \tfrac{1}{2}[3\{(V^2 - 2K^2)^2 + (U^2 - V^2) K^2\} - U^2 V^2]\, \mathrm{d}K\, \mathrm{d}U \end{aligned}$$

$$
\begin{aligned}
&= \int_0^V m(U)\frac{\mathrm{d}}{\mathrm{d}U}\Big(\exp(\alpha U^2)\int_0^U \exp(-\alpha K^2) \\
&\qquad\qquad \times \tfrac{1}{2}[3\{(U^2-2K^2)^2+(V^2-U^2)K^2\}-U^2V^2\Big)\,\mathrm{d}K\,\mathrm{d}U \\
&\quad + \int_V^\infty m(U)\,U\exp(\alpha V^2)\int_0^V \exp(-\alpha K^2)\,(3K^2-V^2)\,\mathrm{d}K\,\mathrm{d}U \\
&= -n(V)\Big\{\frac{1}{V}\frac{\mathrm{d}}{\mathrm{d}V}\Big(\exp(\alpha V^2)\int_0^V \exp(-\alpha K^2)\,\tfrac{3}{2}\{(V^2-2K^2)^2-V^2K^2\}\,\mathrm{d}K\Big) \\
&\qquad + V^2\frac{1}{V}\frac{\mathrm{d}}{\mathrm{d}V}\Big(\exp(\alpha V^2)\int_0^V \exp(-\alpha K^2)\,\tfrac{1}{2}(3K^2-V^2)\,\mathrm{d}K\Big)\Big\} \\
&\quad + \int_0^V n(U)\Big[\frac{\mathrm{d}}{\mathrm{d}U}\Big\{\frac{1}{U}\frac{\mathrm{d}}{\mathrm{d}U}\Big(\exp(\alpha U^2)\int_0^U \exp(-\alpha K^2)\,\tfrac{3}{2}\{(U^2-2K^2)^2-U^2K^2\}\,\mathrm{d}K\Big)\Big\} \\
&\qquad + V^2\frac{\mathrm{d}}{\mathrm{d}U}\Big\{\frac{1}{U}\frac{\mathrm{d}}{\mathrm{d}U}\Big(\exp(\alpha U^2)\int_0^U \exp(-\alpha K^2)\,\tfrac{1}{2}(3K^2-U^2)\,\mathrm{d}K\Big)\Big\}\Big]\mathrm{d}U \\
&\quad + n(V)\exp(\alpha V^2)\int_0^V \exp(-\alpha K^2)\,(3K^2-V^2)\,\mathrm{d}K. \qquad (48)
\end{aligned}
$$

Using (8) and (10),

$$
\epsilon\frac{\mathrm{d}}{\mathrm{d}V}\Big\{\frac{1}{V}\frac{\mathrm{d}}{\mathrm{d}V}\Big(\frac{V^3}{4\pi^2}(J^{(2)}+K^{(2)}-2J_0^{(2)})\Big)\Big\} = \epsilon\frac{\mathrm{d}}{\mathrm{d}V}\Big[\frac{1}{V}\frac{\mathrm{d}}{\mathrm{d}V}\Big\{\frac{V^3}{4\pi^2}\Big(\frac{\pi^3}{\alpha^4}\Big)^{\frac{1}{2}}\frac{4\alpha V^2}{3}\Big\}\Big] = 5V^2\epsilon/\pi^{\frac{1}{2}}\alpha. \qquad (49)
$$

Using (46), (47), and (48) and calculating this same expression gives a differential equation of fourth order in $n(V)$. Straightforward but lengthy algebra shows this equation to be

$$
\begin{aligned}
&Vkn^{(4)}+2\{k(2\alpha V^2+1)+Vk'\}n''' \\
&+\{kV^{-1}(4\alpha^2V^4+4\alpha V^2-1)+k'(4\alpha V^2+1)+Vk''+4V^3\psi+2V^2\epsilon/\alpha\}n'' \\
&-\{kV^{-2}(4\alpha^2V^4+4\alpha V^2-1)+k'V^{-1}(4\alpha V^2+1)+k''-4V^2(2\alpha V^2+3)\psi-4V(\alpha V^2+1)\epsilon/\alpha\}n' \\
&+\{4V(2\alpha V^2+1)\psi+2V^2\epsilon\}n = 5\epsilon V^2/\pi^{\frac{1}{2}}\alpha. \qquad (50)
\end{aligned}
$$

From a study of the indicial equation of the homogeneous equation, obtained by omitting the right-hand side of (50), the solutions near zero are proportional to V^{-1}, constant, V, and V^2. The first is not amenable to numerical solution from a starting value of $V = 0$, so instead the equation satisfied by $g = nV$ is solved numerically.

This equation is

$$\begin{aligned}
&g^{(4)}\left\{\left(\frac{V^2}{2\alpha}+\frac{1}{4\alpha^2}\right)\psi+\frac{V\epsilon}{4\alpha^2}\right\}\\
&+g'''\left\{\left(2V^3+\frac{2V}{\alpha}-\frac{1}{2\alpha^2V}\right)\psi+\left(\frac{V^2}{\alpha}+\frac{1}{2\alpha^2}\right)\epsilon\right\}\\
&+g''\left\{\left(2\alpha V^4+5V^2-\frac{7}{2\alpha}+\frac{5}{4\alpha^2V^2}\right)\psi+\left(V^3+\frac{2V}{\alpha}-\frac{5}{4\alpha^2V}\right)\epsilon\right\}\\
&+g'\left\{\left(2\alpha V^3-5V+\frac{9}{2\alpha V}-\frac{9}{4\alpha^2V^3}\right)\psi+\left(V^2-\frac{3}{\alpha}+\frac{9}{4\alpha^2V^2}\right)\epsilon\right\}\\
&+g\left\{\left(6\alpha V^2+9-\frac{9}{2\alpha V^2}+\frac{9}{4\alpha^2V^4}\right)\psi+\left(V+\frac{3}{\alpha V}-\frac{9}{4\alpha^2V^3}\right)\epsilon\right\}\\
&=5\epsilon V^2/\pi^{\frac{1}{2}}\alpha\,. \qquad (51)
\end{aligned}$$

Writing $c^2=\alpha V^2$ and $\tilde{g}(c)=\alpha^{3/2}g(V)$ makes the above equation dimensionless and has the effect of putting $\alpha=1$ in (51).

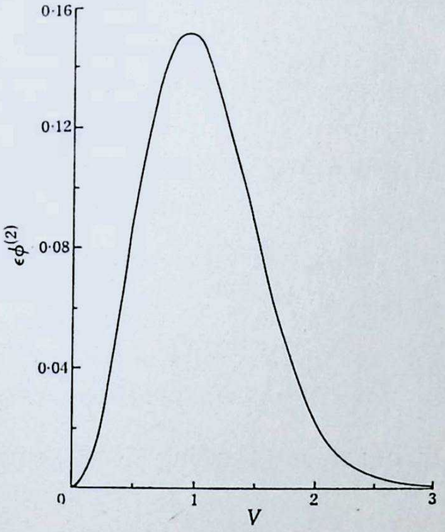

Fig. 2.—Velocity distribution function for viscosity.

Thus (8) has been reduced to the fourth-order linear differential equation (51), which is solved numerically by a Runge–Kutta technique, as before.

The definition of g requires the boundary conditions

$$g(0)=0\,,\quad g'(0)=a_3\,,\quad g''(0)=0\,,\quad g'''(0)=a_4\,,\quad g^{(4)}(0)=0\,, \qquad (52)$$

and, as $V\rightarrow\infty$, g and all its derivatives tend to zero exponentially. This latter condition fixes a_3 and a_4.

$\phi^{(2)}$ is then related to $\tilde{g}$ via the equation

$$\phi^{(2)}(c)=(c\epsilon)^{-1}(\tilde{g}''-3c^{-1}g'+3c^{-2}\tilde{g})\,. \qquad (53)$$

Figure 2 gives the solution $\phi^{(2)}$.

(c) *Transport Coefficients*

Since the second approximation, $f_0+f_0\,\Phi^{(1)}$, is now known, it is possible to calculate the heat flux vector and pressure tensor and so obtain the coefficient of thermal conduction and the coefficient of shear viscosity.

(i) *Heat Flux Vector*

The heat flux vector $\boldsymbol{q}$ is given by

$$\boldsymbol{q} = \tfrac{1}{2}m\int f^{(0)}\,\Phi^{(1)}\,V^2\boldsymbol{V}\,\mathrm{d}\boldsymbol{v}\,. \tag{54}$$

Substituting from (6) and neglecting integrals of odd functions of the components of $\boldsymbol{V}$, this becomes

$$\begin{aligned}\boldsymbol{q} &= -\frac{m}{2n\sigma^2}\int f^{(0)}\phi^{(1)}(U)\,\tilde{\boldsymbol{U}}.\frac{\nabla T}{T}\,U^2\boldsymbol{U}\,\mathrm{d}\boldsymbol{u}\\ &= -\frac{2\pi m}{3\sigma^2}\left(\frac{\alpha}{\pi}\right)^{3/2}\int_0^\infty \exp(-c^2)\,\frac{\phi^{(1)}(c)}{\alpha^3}\,c^5\,\mathrm{d}c\,\frac{\nabla T}{T}\\ &= -\lambda\nabla T\,, \end{aligned} \tag{55}$$

where λ is the coefficient of thermal conduction

$$\lambda = \frac{4\sqrt{2}}{3\sigma^2}\left(\frac{k^3T}{\pi m}\right)^{\frac{1}{2}}\int_0^\infty \exp(-c^2)\,\phi^{(1)}(c)\,c^5\,\mathrm{d}c\,. \tag{56}$$

The integral can be calculated by numerically integrating the solution for $\phi^{(1)}$, equation (42). The result is

$$\lambda = \frac{4\sqrt{2}}{3\sigma^2}\left(\frac{k^3T}{\pi m}\right)^{\frac{1}{2}}\times 0\cdot 637153\,,$$

which, when put in a form comparable with Chapman and Cowling (10.21, equation (1)) is

$$\lambda = \frac{75}{64\sigma^2}\left(\frac{k^3T}{\pi m}\right)^{\frac{1}{2}}\times 1\cdot 02522\,. \tag{57}$$

(ii) *Pressure Tensor*

The pressure tensor is given by

$$\mathbf{P} = m\int (f_0+f_0\,\Phi^{(1)})\boldsymbol{V}\boldsymbol{V}\,\mathrm{d}\boldsymbol{v}\,. \tag{58}$$

Substituting from (6) and neglecting integrals of odd functions of the components of $\boldsymbol{V}$ this becomes

$$\mathbf{P} = nkT\boldsymbol{\delta}+\mathbf{P}^{(1)}\,, \tag{59}$$

with $\mathbf{P}^{(1)}$, the correction to the pressure tensor, given by

$$\mathbf{P}^{(1)} = -\frac{3m\alpha^{\frac{1}{2}}}{2n\sigma^2}\int f^{(0)}\,\phi^{(2)}(U)\,\tilde{\boldsymbol{U}}^0\tilde{\boldsymbol{U}} : \nabla \boldsymbol{c}_0 \boldsymbol{U}\boldsymbol{U}\,\mathrm{d}\boldsymbol{u}$$

$$= -\frac{4\pi m}{5\sigma^2}\left(\frac{\alpha^4}{\pi^3}\right)^{\frac{1}{2}}\int_0^\infty \exp(-c^2)\frac{\phi^{(2)}(c)}{\alpha^{5/2}}c^4\,\mathrm{d}c\;\nabla^{\mathrm{s}}\boldsymbol{c}_0\,,$$

where $\nabla^{\mathrm{s}}\boldsymbol{c}_0$, the shear viscosity tensor is a symmetric nondivergent tensor formed from the components of $\nabla\boldsymbol{c}_0$. Now

$$\mathbf{P}^{(1)} = -2\eta_{\mathrm{s}}\,\nabla^{\mathrm{s}}\boldsymbol{c}_0 \qquad (60)$$

defines the coefficient of shear viscosity η_{s}. Thus

$$\eta_{\mathrm{s}} = \frac{2}{5\sigma^2}\left(\frac{2mkT}{\pi}\right)^{\frac{1}{2}}\int_0^\infty \exp(-c^2)\,\phi^{(2)}(c)\,c^4\,\mathrm{d}c\,. \qquad (61)$$

The integral is calculated from the solution for $\phi^{(2)}$, equation (53). The result is

$$\eta_{\mathrm{s}} = \frac{2}{5\sigma^2}\left(\frac{2mkT}{\pi}\right)^{\frac{1}{2}}\times 0{\cdot}561285\,,$$

which, when put in a form comparable with Chapman and Cowling (10.21, equation (1)), is

$$\eta_{\mathrm{s}} = \frac{5}{16}\frac{\sqrt{(kTm)}}{\pi^{\frac{1}{2}}\sigma^2}\times 1{\cdot}01603\,. \qquad (62)$$

The second approximation to the Boltzmann equation is usually obtained by expressing $\phi^{(1)}\boldsymbol{U}$ and $\phi^{(2)}\boldsymbol{U}^0\boldsymbol{U}$, each as a series of Sonine polynomials, e.g.

$$\phi^{(1)}\,\alpha\boldsymbol{U} = \sum_r d_r\,\mathrm{S}_{3/2}^r(\alpha U^2)\alpha\boldsymbol{U}$$

and solving for d_r.

The transport coefficients are then obtained as an infinite series as explained in Chapman and Cowling, Section 7.5. For many models of a gas only the first few terms of the series are significant. For a rigid sphere gas the first approximation for the transport coefficients, obtained by taking only the first term of the appropriate series, is

$$\lambda_1 = \frac{75}{64\sigma^2}\left(\frac{k^3T}{\pi m}\right)^{\frac{1}{2}}, \qquad (63)$$

$$\eta_1 = \frac{5}{16}\frac{\sqrt{(kTm)}}{\pi^{\frac{1}{2}}\sigma^2}. \qquad (64)$$

Taking five terms gives

$$\lambda_5 = 1\cdot 02520\,\lambda_1\,, \tag{65}$$

$$\eta_5 = 1\cdot 01603\,\eta_1\,, \tag{66}$$

and for a gas of rigid spheres the series is so rapidly convergent that higher terms contribute nothing to this accuracy.

These results agree well with the values obtained from the direct solution of the Boltzmann equation given in Sections III(*a*) and III(*b*).

IV. Third Approximation to the Velocity Distribution Function

The second approximation to the Boltzmann equation (5) has terms on the left-hand side that are of either first or second degree in V. The third approximation has terms involving the scalar $|\,V\,|$ as well as terms of odd and even degree in V (see Chapman and Cowling, Section 15.2, equations (11), (12), (14)). These terms are of course multiplied by squares and products of the gradients of n, c_0, and T.

In Section III it was demonstrated how to solve the approximation to the Boltzmann equation with terms of first and second degree in V. The present section indicates the method when there is a term in the scalar V.

From Chapman and Cowling (15.2, equation (11))

$$-\eta^2 I(\Phi^{(2)}) = -\frac{1}{P}f^{(0)}\left(\tfrac{2}{3}\alpha V^2-1\right)\left(\mathbf{P}^{(1)}:\frac{\partial}{\partial r}c_0+\frac{\partial}{\partial r}\cdot q^{(1)}\right)-\frac{1}{\rho n\sigma^2}\frac{\phi^{(1)}}{V}\frac{\partial P}{\partial r}\cdot\frac{\partial T}{\partial r}\,, \tag{67}$$

where $P \doteq nkT$, ρ is the mass density,

$$\mathbf{P}^{(1)} = -2\eta_s\,\nabla^s c_0\,, \qquad \text{and} \qquad q^{(1)} = -\lambda\,\partial T/\partial r\,.$$

There are other terms of even and odd degree in V but these are ignored. In fact to illustrate the method only the first term will be considered, this being permissible as separate terms are independent.

The equation then is

$$-\frac{1}{P}f^{(0)}\left(\tfrac{2}{3}\alpha V^2-1\right)\mathbf{P}^{(1)}:\frac{\partial c_0}{\partial r}$$
$$=\sigma^2\iint_{\boldsymbol{\rho}.\boldsymbol{a}>0}\boldsymbol{\rho}.\boldsymbol{a}\,f^{(0)}(U)\,f^{(0)}(V)\{\Phi^{(2)}(U_0)+\Phi^{(2)}(V_0)-\Phi^{(2)}(U)-\Phi^{(2)}(V)\}\,\mathrm{d}\boldsymbol{a}\,\mathrm{d}\boldsymbol{u}\,. \tag{68}$$

A solution $\Phi^{(2)}$ is sought, of the form

$$\Phi^{(2)} = -\frac{\alpha^{\frac{1}{2}}}{n\sigma^2 P}\phi^{(0)}(V)\,\mathbf{P}^{(1)}:\frac{\partial c_0}{\partial r}. \tag{69}$$

Substituting (69) into (68) gives

$$-\left(\tfrac{2}{3}\alpha V^2-1\right) = \alpha^2\pi^{-3/2}\iint_{\boldsymbol{\rho}.\boldsymbol{a}>0}\boldsymbol{\rho}.\boldsymbol{a}\exp(-\alpha U^2)$$
$$\times\{\phi^{(0)}(U)+\phi^{(0)}(V)-\phi^{(0)}(U_0)-\phi^{(0)}(V_0)\}\,\mathrm{d}\boldsymbol{a}\,\mathrm{d}\boldsymbol{u}\,. \tag{70}$$

This is an equation of the form (10) with $n = 0$. The method of solution is the same as before (equation (15); equations (16) and (20) are specialized for $n = 0$). The integral equation in $\phi^{(0)}$ is then reduced to a linear differential equation by defining new variables and integrating by parts.

(a) *Solution for* $n = 0$

Define

$$\theta(V) = \int_V^\infty \exp(-\alpha U^2)\, U\, \phi^{(0)}(U)\, \mathrm{d}U. \tag{71}$$

Then

$$\begin{aligned}\frac{VJ^{(0)}}{4\pi^2} &= \int_0^V \exp(-\alpha U^2)\, \phi^{(0)}(U)\, U(\tfrac{1}{3}U^3 + UV^2)\, \mathrm{d}U \\ &\quad + \int_V^\infty \exp(-\alpha U^2)\, \phi^{(0)}(U)\, U(\tfrac{1}{3}V^3 + VU^2)\, \mathrm{d}U \\ &= -\int_V^\infty \theta(U)\,(U-V)^2\, \mathrm{d}U + \int_0^\infty \exp(-\alpha U^2)\, \phi^{(0)}(U)\, U(\tfrac{1}{3}U^3 + UV^2)\, \mathrm{d}U.\end{aligned}$$

The second term is zero as a consequence of the auxiliary relations (39) and (41). Thus

$$\frac{VJ^{(0)}}{4\pi^2} = -\int_V^\infty \theta(U)\,(U-V)^2\, \mathrm{d}U, \tag{72}$$

$$\frac{VK^{(0)}}{4\pi^2} = \phi^{(0)}(V)\, k(V), \tag{73}$$

$$\begin{aligned}\frac{VJ_0^{(0)}}{4\pi^2} &= 2\int_0^V \exp(-\alpha U^2)\, \phi^{(0)}(U)\, \frac{U \exp(\alpha U^2)}{2\alpha} \int_0^U \exp(-\alpha K^2)\, \mathrm{d}K\, \mathrm{d}U \\ &\quad + 2\int_V^\infty \exp(-\alpha U^2)\, \phi^{(0)}(U)\, \frac{U \exp(-\alpha V^2)}{2\alpha} \int_0^V \exp(-\alpha K^2)\, \mathrm{d}K\, \mathrm{d}U \\ &= 2\int_0^V \theta(U) \left(\frac{1}{2\alpha} + U \exp(\alpha U^2) \int_0^U \exp(-\alpha K^2)\, \mathrm{d}K\right) \mathrm{d}U \\ &= 2\int_0^V \exp(\alpha U^2)\, \theta(U)\, \alpha k'(U)\, \mathrm{d}U.\end{aligned} \tag{74}$$

Then from (10) and (70)

$$\begin{aligned}\epsilon \frac{\mathrm{d}}{\mathrm{d}V}\left\{\frac{V}{4\pi^2}\left(J^{(0)} + K^{(0)} - 2J_0^{(0)}\right)\right\} &= \epsilon \frac{\mathrm{d}}{\mathrm{d}V}\left\{\frac{V}{4\pi^2} \frac{\pi^{3/2}}{\alpha^2}\left(1 - \tfrac{2}{3}\alpha V^2\right)\right\} \\ &= (\epsilon/4\pi^{\frac{1}{2}}\alpha^2)(1 - 2\alpha V^2) \\ &= (4\pi^{\frac{1}{2}}\alpha^2)^{-1}\, \mathrm{d}(V\epsilon)/\mathrm{d}V.\end{aligned} \tag{75}$$

From (72), (73), and (74)

$$\epsilon\frac{\mathrm{d}}{\mathrm{d}V}\left\{\frac{V}{4\pi^2}\left(J^{(0)}+K^{(0)}-2J_0^{(0)}\right)\right\} = 2\epsilon\int_V^\infty \theta(U)\,(U-V)\,\mathrm{d}U + \epsilon\frac{\mathrm{d}}{\mathrm{d}V}\left(\phi^{(0)}k\right) - 4\alpha\theta k'. \tag{76}$$

Define

$$\left.\begin{aligned} X(V) &= V\int_0^V \theta(U)\,\mathrm{d}U + \int_V^\infty U\,\theta(U)\,\mathrm{d}U \\ \text{so that}\qquad X'(V) &= \int_0^V \theta(U)\,\mathrm{d}U, \\ X''(V) &= \theta(V), \\ X'''(V) &= -V\exp(-\alpha V^2)\,\phi^{(0)}(V). \end{aligned}\right\} \tag{77}$$

Substituting (77) into (76) gives

$$\begin{aligned}\epsilon\frac{\mathrm{d}}{\mathrm{d}V}\left\{\frac{V}{4\pi^2}\left(J^{(0)}+K^{(0)}-2J_0^{(0)}\right)\right\} &= -\epsilon\frac{\mathrm{d}}{\mathrm{d}V}\left(\frac{X'''\exp(\alpha V^2)\,k}{V}\right) - 4\alpha k'X'' + 2\epsilon X \\ &= -\frac{\mathrm{d}}{\mathrm{d}V}\left(\frac{kX'''}{V} + 2\alpha(kX''+k'X'-k''X)\right). \end{aligned} \tag{78}$$

Once again the auxiliary relation (39) has been used. On integration (75) and (78) give

$$kX'''/V + 2\alpha(kX''+k'X'-k''X) = -V\epsilon/4\pi^{\frac{1}{2}}\alpha^2, \tag{79}$$

the constant of integration being zero. Writing $\alpha V^2 = c^2$ and $X(c) = \alpha^2 X(V)$ gives the dimensionless equation

$$k\tilde{X}'''/c + 2(k\tilde{X}''+k'\tilde{X}'-k''\tilde{X}) = -c\epsilon/4\pi^{\frac{1}{2}}. \tag{80}$$

Thus (70) has been reduced to (80), a third-order linear differential equation in $\tilde{X}$. This is now solved analytically.

The homogeneous equation

$$k\tilde{X}'''/V + 2(k\tilde{X}''+k'\tilde{X}'-k''X) = 0, \tag{81}$$

obtained by neglecting the right-hand side of (80), has the solutions

$$\tilde{X} = k', \tag{82}$$

$$\tilde{X} = \epsilon. \tag{83}$$

Since (80) is a third-order linear differential equation and two solutions of the homogeneous equation (81) are known, it is possible to find the solution of (80) analytically.

The auxiliary relationships (39) and (41) require that

$$\int_0^\infty U^2 \epsilon \phi^{(0)}\,\mathrm{d}U = -\int_0^\infty U\,X'''(U)\,\mathrm{d}U = 0 \tag{84}$$

and

$$\int_0^\infty U^4 \epsilon \phi^{(0)}\,\mathrm{d}U = -\int_0^\infty U^3 X'''(U)\,\mathrm{d}U = 0\,. \tag{85}$$

However,

$$\int_0^V U\,X'''(U)\,\mathrm{d}U = V\,X''(V) - X'(V) + X'(0) \tag{86}$$

and

$$\int_0^V U^3 X'''(U)\,\mathrm{d}U = V^3 X''(V) - 3V^2 X'(V) + 6V\,X(V) - 6\int_0^V X(U)\,\mathrm{d}U\,. \tag{87}$$

Using the definition (77) of X and its derivatives together with (86) and (87), the boundary conditions on X are seen to be

$$\left.\begin{aligned} X'(0) &= 0\,, \\ X'''(0) &= 0\,, \end{aligned}\right\} \tag{88}$$

$$\left.\begin{matrix} X,\ X', \\ X'', X''' \end{matrix}\right\} \to 0 \quad \text{exponentially} \quad \text{as} \quad V \to \infty\,, \tag{89}$$

and

$$\int_0^\infty X(U)\,\mathrm{d}U = 0\,. \tag{90}$$

The solution of (80) will now be obtained, making use of the solutions (82) and (83) of the homogeneous equation, and the above boundary conditions. Write

$$\tilde{X} = \lambda\epsilon \tag{91}$$

and substitute in (80). This gives

$$(k/c)\lambda''' - 4k\lambda'' + 2\{(2c - 3/c)k + k'\}\lambda' = -c/4\pi^{\frac{1}{2}}\,. \tag{92}$$

The homogeneous equation obtained by neglecting the right-hand side of (92) has a solution $\lambda' = k/\epsilon$ (a consequence of the fact that $\tilde{X} = k'$ is a solution of (81)).

Write

$$\lambda' = (k/\epsilon)\mu\,. \tag{93}$$

Substitution of (93) into (92) gives

$$k\mu'' + 2k'\mu' = -(4\pi^{\frac{1}{2}})^{-1} c^2 \epsilon / k\,, \tag{94}$$

a first-order linear differential equation in μ', which has the solution

$$\mu'(c) = (4\pi^{\frac{1}{2}}k^2)^{-1}\int_c^\infty x^2\epsilon\,\mathrm{d}x\,. \tag{95}$$

This solution approaches zero exponentially as $c \to \infty$, a consequence of the behaviour of X as $V \to \infty$.

Define

$$\omega(c) = \int_c^\infty \exp(-x^2)\,\mathrm{d}x\,. \tag{96}$$

The right-hand side of (95) can be integrated to give

$$\mu' = (\omega + c\epsilon)/8\pi^{\frac{1}{2}}k^2\,. \tag{97}$$

Thus

$$\mu = -\int_c^\infty (x\epsilon+\omega)/8\pi^{\frac{1}{2}}k^2\,\mathrm{d}x\,, \tag{98}$$

a solution that approaches zero exponentially as $c \to \infty$. Then

$$\lambda(c) = -\int_0^c \frac{k(y)}{\epsilon(y)}\int_y^\infty \frac{x\epsilon(x)+\omega(x)}{8\pi^{\frac{1}{2}}k^2(x)}\,\mathrm{d}x\,\mathrm{d}y + \lambda(0)\,. \tag{99}$$

From (90) and (91)

$$\int_0^\infty \lambda(x)\,\epsilon(x)\,\mathrm{d}x = \tfrac{1}{2}\pi^{\frac{1}{2}}\lambda(0) + \int_0^\infty \omega(x)\,\lambda'(x)\,\mathrm{d}x = 0\,.$$

Thus

$$\lambda(0) = -\frac{2}{\pi^{\frac{1}{2}}}\int_0^\infty \frac{\omega(x)\,k(x)}{\epsilon(x)}\mu(x)\,\mathrm{d}x\,; \tag{100}$$

$$\lambda(c) = -\frac{1}{8\pi^{\frac{1}{2}}}\int_0^c \frac{k(y)}{\epsilon(y)}\int_y^\infty \frac{x\,\epsilon(x)+\omega(x)}{k^2(x)}\,\mathrm{d}x\,\mathrm{d}y$$

$$-\frac{1}{4\pi}\int_0^\infty \frac{\omega(y)\,k(y)}{\epsilon(y)}\int_y^\infty \frac{x\,\epsilon(x)+\omega(x)}{k^2(x)}\,\mathrm{d}x\,\mathrm{d}y\,. \tag{101}$$

Equation (101) is an analytic expression for $\lambda(c)$ from which $\tilde{X} = \lambda\epsilon$ can be obtained. $\phi^{(0)}$ can then be obtained from the relation

$$\phi^{(0)}(c) = -(c\epsilon)^{-1}\tilde{X}'''\,.$$

V. CONCLUSIONS

The equations for the second and third approximations to the Boltzmann equation have been solved for a gas of rigid spheres, when the left-hand side has terms of zero, first, and second order in V, the velocity of a molecule relative to the stream velocity. The solutions obtained for the second and third approximations to the velocity distribution function are analytic when the left-hand side has terms involving the scalar V, and numerical in the other two cases.

The second approximation to the Boltzmann equation has terms linear in the gradients of c_0 and T multiplying terms of second and first order in V on the left-hand side. Thus the solution for the velocity distribution function is useful in calculating exact values of the transport coefficients, instead of employing approximation techniques to obtain them. The values obtained are in good agreement with the other theoretical calculations.

The equation involving scalar V on the left-hand side that was solved was part of the third approximation to the Boltzmann equation. The solution gives no contribution to the pressure tensor or heat flux vector but is of importance in Grad's many-moment scheme. The latter is at present being considered.

Of course it is possible to use forms of the Boltzmann equation that describe more exactly dense gases. Such equations give rise to terms scalar in V in the second approximation (Snider and Curtiss 1958). The calculation of the transport coefficients for a billiard ball gas, from the exact solution of the second approximation to this corrected Boltzmann equation, is also being carried out.

VI. ACKNOWLEDGMENT

P. I. Brooker wishes to acknowledge the support of a CSIRO Post-graduate Studentship.

VII. REFERENCES

CHAPMAN, S., and COWLING, T. G. (1960).—"The Mathematical Theory of Non Uniform Gases." (Cambridge Univ. Press.)

COTTER, J. R. (1952).—*Proc. R. Ir. Acad.* A **55**, 1.

PEKERIS, C. L. (1955).—*Proc. natn. Acad. Sci. U.S.A.* **41**, 661.

PEKERIS, C. L., and ALTERMAN, Z. (1957).—*Proc. natn. Acad. Sci. U.S.A.* **43**, 998.

SNIDER, R. F., and CURTISS, C. F. (1958).—*Physics Fluids* **1**, 122.

ORNSTEIN–ZERNIKE RELATION FOR A DISORDERED FLUID

By R. J. Baxter*

[*Manuscript received April* 4, 1968]

Summary

The Ornstein–Zernike equation for a homogeneous fluid relates the direct correlation function $c(r)$ and the indirect correlation function $h(r)$. In this paper it is shown that if $c(r)$ vanishes beyond a range R then a third function $Q(r)$ can be introduced which is related to $c(r)$ and $h(r)$ by equations that involve the functions only over the range $(0,R)$. The analytic solution of the Percus–Yevick approximation for hard spheres can then be obtained very simply and, as $c(r)$ normally tends rapidly to zero with increasing r, it is expected that the results should be of use in numerical calculations based on the Percus–Yevick, convolution-hypernetted chain, or similar approximations.

I. Introduction

The Ornstein–Zernike (OZ) relation (Ornstein and Zernike 1914) for a classical homogeneous fluid with central forces can be written as

$$h(r) = c(r) + \rho \int \mathrm{d}\boldsymbol{r}'\, c(r')\, h(\,|\,\boldsymbol{r}-\boldsymbol{r}'\,|\,)\,, \tag{1}$$

where r and r' are the magnitudes of the vectors $\boldsymbol{r}$ and $\boldsymbol{r}'$, ρ is the particle density, $c(r)$ is the direct correlation function, and $h(r)$ is the indirect correlation function. If $g(r)$ is the radial distribution function then

$$h(r) = g(r) - 1\,. \tag{2}$$

Interest in the OZ relation has been stimulated by certain approximate relations between $c(r)$ and $g(r)$ that have been proposed. In particular, if $\phi(r)$ is the interparticle potential, k is Boltzmann's constant, and T is the temperature, the Percus–Yevick (PY) approximation (Percus and Yevick 1958; Percus 1962) supplements equations (1) and (2) with the relation

$$c(r) = \{1 - \exp(\phi(r)/kT)\} g(r)\,. \tag{3a}$$

Similarly, the convolution-hypernetted chain (CHNC) approximation (Van Leeuwen, Groenveld, and de Boer 1959; Meeron 1960; Morita and Hiroike 1960) supplements them with

$$c(r) = h(r) - \log g(r) - \phi(r)/kT\,. \tag{3b}$$

It is found that the function $c(r)$ tends to zero with increasing r much more rapidly than the function $h(r)$ (Goldstein 1955). In particular, the PY approximation (3a) predicts that $c(r)$ should vanish beyond the range of the potential, while the CHNC approximation (3b) predicts that $c(r)$ should be of order $\frac{1}{2}h^2(r)$

---

* Research School of Physical Sciences, Australian National University, P.O. Box 4, Canberra, A.C.T. 2600.

Aust. J. Phys., 1968, **21**, 563–9

when $h(r)$ is small. In the present paper it will be shown that when $c(r)$ vanishes beyond a range R equation (1) can be transformed so as to involve the function $h(r)$ only over the range $(0, R)$. As an example of the utility of this result it will be shown that the analytic solution of the PY approximation for hard spheres can be obtained very simply from the transformed equations. Further, the result should be of use in numerical calculations.

As far as the author is aware the equations obtained are new, but are related to the work of Wertheim (1964) and to a previous paper by the author (Baxter 1967). It is believed that the results and their derivation represent a considerable simplification of this previous work.

II. Derivation of Required Equations

Multiplying both sides of equation (1) by $\exp(\mathrm{i}\,\boldsymbol{k}.\boldsymbol{r})$ and integrating with respect to $\boldsymbol{r}$ over all space, it is found that

$$\tilde{h}(k) = \tilde{c}(k) + \rho\tilde{c}(k)\tilde{h}(k)\,, \tag{4}$$

where $\tilde{h}(k)$ and $\tilde{c}(k)$ are the three-dimensional Fourier transforms of $h(r)$ and $c(r)$ and depend only on the magnitude k of the vector $\boldsymbol{k}$. Using spherical polar coordinates about an axis along the vector $\boldsymbol{k}$, the angle integrations can be performed to give

$$\tilde{h}(k) = 4\pi k^{-1}\int_0^\infty \mathrm{d}r\,\sin kr\,r\,h(r)\,, \tag{5}$$

$$\tilde{c}(k) = 4\pi k^{-1}\int_0^\infty \mathrm{d}r\,\sin kr\,r\,c(r)\,. \tag{6}$$

From equation (4) it can be seen that

$$1+\rho\tilde{h}(k) = \{\tilde{A}(k)\}^{-1}\,, \tag{7}$$

where

$$\tilde{A}(k) = 1-\rho\tilde{c}(k)\,. \tag{8}$$

If the direct correlation function $c(r)$ vanishes beyond a range R, then the integration in equation (6) can be truncated at R. Integrating by parts and substituting the result in equation (8) gives

$$\tilde{A}(k) = 1-4\pi\rho\int_0^R \mathrm{d}r\,\cos kr\,S(r)\,, \tag{9}$$

where

$$S(r) = \int_r^R \mathrm{d}t\,t\,c(t)\,. \tag{10}$$

For a disordered fluid the integral on the right-hand side of equation (5) must be convergent for real k. Thus $\tilde{h}(k)$ is finite and from equation (7) it follows that $\tilde{A}(k)$ can have no zeros on the real k axis. When this is so it is shown in the Appendix that $\tilde{A}(k)$ can be factorized according to the equation

$$\tilde{A}(k) = \tilde{Q}(k)\tilde{Q}(-k)\,, \tag{11}$$

where the function $\tilde{Q}(k)$ is regular, has zeros only in the lower half-plane, and can be written in the form

$$\tilde{Q}(k) = 1 - 2\pi\rho \int_0^R \mathrm{d}r\, \mathrm{e}^{\mathrm{i}kr} Q(r)\,, \tag{12}$$

$Q(r)$ being a real function.

Substituting the forms (9) and (12) of $\tilde{A}(k)$ and $\tilde{Q}(k)$ into equation (11), multiplying by $\exp(-ikr)$, and integrating with respect to k from $-\infty$ to ∞ gives

$$S(r) = Q(r) - 2\pi\rho \int_r^R \mathrm{d}t\, Q(t)\, Q(t-r)\,, \qquad 0 < r < R\,. \tag{13}$$

From equations (7) and (11) it follows that

$$\tilde{Q}(k)\,\{1+\rho\tilde{h}(k)\} = \{\tilde{Q}(-k)\}^{-1}\,, \tag{14}$$

and from equation (5) the function $\tilde{h}(k)$ can be written as

$$\tilde{h}(k) = 2\pi \int_{-\infty}^{\infty} \mathrm{d}r\, \mathrm{e}^{\mathrm{i}kr} J(|r|)\,, \tag{15}$$

where

$$J(r) = \int_r^{\infty} \mathrm{d}t\, t\, h(t)\,. \tag{16}$$

Consider the effect of multiplying both sides of equation (14) by $\exp(-ikr)$ and integrating with respect to k from $-\infty$ to ∞. The contribution from the right-hand side vanishes when $r > 0$ as the integration can then be closed round the lower half k plane, where $\tilde{Q}(-k)$ is regular, has no zeros, and tends to unity at infinity. Substituting the forms (15) and (12) of $\tilde{h}(k)$ and $\tilde{Q}(k)$ into the left-hand side of equation (14) and performing the integration, it follows that

$$-Q(r) + J(r) - 2\pi\rho \int_0^R \mathrm{d}t\, Q(t)\, J(|r-t|) = 0 \tag{17}$$

for $r > 0$, where the range of $Q(r)$ is extended by defining

$$Q(r) = 0 \qquad \text{for} \qquad r > R\,. \tag{18}$$

From equations (10) and (13) it can be seen that $Q(r) \to 0$ as $r \to R$ from below, so the definition (18) ensures that $Q(r)$ is continuous at $r = R$.

Equations (13) and (17) may be expressed in terms of $c(r)$ and $h(r)$, rather than $S(r)$ and $J(r)$, by differentiating them with respect to r. Using equations (10) and (16) and the fact that $Q(R) = 0$, it is found that

$$r\,c(r) = -Q'(r) + 2\pi\rho \int_r^R \mathrm{d}t\, Q'(t)\, Q(t-r) \tag{19}$$

for $0 < r < R$, and

$$r\,h(r) = -Q'(r) + 2\pi\rho \int_0^R \mathrm{d}t\, (r-t)\, h(|r-t|)\, Q(t) \tag{20}$$

for $r > 0$, where $Q'(r)$ is the derivative of $Q(r)$.

Although equation (20) is valid for all positive r, it is of particular interest when r is restricted to lie in the range $(0, R)$ for then it involves the function $h(r)$ only over this range. With this restriction, equations (19) and (20), together with the PY or CHNC approximations (3), form a closed set of equations for the functions $c(r)$, $Q(r)$, and $h(r)$ in the range $(0, R)$ within which $c(r)$ is nonzero. The PY approximation can be reduced to a form suitable for computation by Newton–Raphson techniques by using equations (2) and (3a) to express $h(r)$ explicitly in terms of $c(r)$. Using equation (19) it is then possible to express $h(r)$ in terms of $Q(r)$, and substituting this form for $h(r)$ into equation (20) gives a single equation for $Q(r)$.

The inverse compressibility equation of state is known to be given by

$$(kT)^{-1}\frac{\partial P}{\partial \rho}\bigg|_{T} = 1-\rho\int \mathrm{d}\boldsymbol{r}\; c(r) = 1-\rho\,\tilde{c}(0)\,, \tag{21}$$

where P is the pressure. From equation (8) the right-hand side of equation (21) is simply $\tilde{A}(0)$, which must be positive since $\tilde{A}(k)$ is required to have no zeros on the real axis and can be seen from equation (9) to tend to unity as k tends to infinity. Further, from the factorization (11) of $\tilde{A}(k)$, equation (21) can be written as

$$(kT)^{-1}\frac{\partial P}{\partial \rho}\bigg|_{T} = \{\tilde{Q}(0)\}^{2}\,, \tag{22}$$

so, if $Q(r)$ is known, $\tilde{Q}(0)$ can be evaluated from equation (12), giving the inverse compressibility as proportional to the square of a real parameter.

III. PY Approximation for Hard Spheres

The PY approximation for hard spheres of diameter R, which was first solved by Thiele (1963) and Wertheim (1963), can be expressed as

$$g(r) = 0\,, \qquad 0 < r < R; \qquad\qquad c(r) = 0\,, \qquad r > R\,. \tag{23}$$

Thus $h(r)$ has the value -1 throughout the range $(0, R)$ within which $c(r)$ is nonzero. Substituting this value in equation (20) for $0 < r < R$, it follows that

$$Q'(r) = ar+b\,, \qquad 0 < r < R\,, \tag{24}$$

where a and b are constants determined by $Q(r)$.

Using the condition $Q(R) = 0$, $Q(r)$ can be obtained by integrating equation (24). Substituting the result into the expressions for a and b gives two linear equations that can be solved to give

$$a = (1+2\eta)/(1-\eta)^{2}\,, \qquad b = -\tfrac{3}{2}R\eta/(1-\eta)^{2}\,, \tag{25}$$

where

$$\eta = \tfrac{1}{6}\pi\rho R^{3}\,. \tag{26}$$

Thus $Q(r)$ is now a known function and $c(r)$ can be calculated from equation (19).

It is also possible to use equations (19) and (20) to obtain the analytic solution of the PY approximation for the adhesive hard spheres model (Baxter 1968). Indeed, some of the properties of this model, such as the fact that the inverse compressibility was found to be a perfect square, prompted the present work.

IV. Discussion

It has been shown that equations (19) and (20) can be of use in analytic calculations based on the Ornstein–Zernike relation. The same may be expected to be true of numerical calculations, for in these it is always necessary to truncate $h(r)$ and $c(r)$ at some range R. If the OZ relation is used directly then R must be large enough for $h(r)$ to be small, whereas if equations (19) and (20) are used it should be sufficient for $c(r)$ to be small. The equations are particularly applicable to the PY approximation for a potential of finite range, for then truncation errors can be completely avoided.

In Section II it was indicated that in the PY approximation the equations can be reduced to a single equation for $Q(r)$. The more natural function to calculate is not $Q(r)$ but rather its derivative $Q'(r)$. The fact that $Q'(r)$ is a linear function in the PY approximation for hard spheres, while $c(r)$ is a cubic, suggests that in general $Q'(r)$ may be an even smoother and better-behaved function than $c(r)$.

Once $Q(r)$, $h(r)$, and $c(r)$ are known in the range $(0, R)$, the values of $h(r)$ for $r > R$ can be obtained. One way to do this is to multiply both sides of equation (20) by $\exp(ikr)$ and integrate with respect to r from 0 to ∞, giving

$$\tilde{h}_+(k) = -\frac{1}{\tilde{Q}(k)}\int_0^R \mathrm{d}r\, \mathrm{e}^{ikr}\left(Q'(r) + 2\pi\rho\int_0^{R-r}\mathrm{d}t\, t\, h(t)\, Q(t+r)\right), \tag{27}$$

where $\tilde{h}_+(k)$ is the one-sided Fourier transform of $r\,h(r)$, that is,

$$\tilde{h}_+(k) = \int_0^\infty \mathrm{d}r\, \mathrm{e}^{ikr}\, r\, h(r)\,. \tag{28}$$

The right-hand side of equation (27) can be evaluated to give $\tilde{h}_+(k)$, and $h(r)$ can then be evaluated by inverting the Fourier transform (28).

Another way to obtain $h(r)$ is to invert the two-sided Fourier transform $\tilde{h}(k)$ given by equation (4). From an analytic viewpoint this method is more complicated, since both $\tilde{Q}(k)$ and $\tilde{Q}(-k)$ occur in the denominator of the expression for $h(k)$, while only $\tilde{Q}(k)$ occurs in the expression (27) for $\tilde{h}_+(k)$.

From equations (27) and (28), the condition that $Q(k)$ has zeros only in the lower half-plane implies that the integral on the right-hand side of equation (28) is convergent for all k with non-negative imaginary parts. It is possible that equations (19) and (20) may have solutions which violate this condition; such solutions must be discarded. In particular $\tilde{Q}(0)$ must be positive, for as $Q(k)$ is real and continuous on the positive imaginary axis and tends to unity at infinity, a negative value of $\tilde{Q}(0)$ implies that there is a zero on this axis.

The function $Q(r)$ can be eliminated from equations (19) and (20) to give the relation between $c(r)$ and $h(r)$ previously derived (Baxter 1967) and used in numerical calculations by Watts (1968). The complexity of this relation, together with the usefulness of $Q(r)$ in determining the long-range behaviour of $h(r)$, makes it more convenient to work with equations (19) and (20) directly.

V. Acknowledgments

The author is grateful to Professor K. J. Le Couteur for comments that led the author to seek the theorem given in the Appendix, and to Mr. W. A. Coppel for supplying pertinent references.

VI. References

Baxter, R. J. (1967).—*Phys. Rev.* **154**, 170.

Baxter, R. J. (1968).—Percus–Yevick equation for hard spheres with surface adhesion. *J. chem. Phys.* (in press).

Goldstein, L. (1955).—*Phys. Rev.* **100**, 981.

Krein, M. G. (1962).—*Am. math. Soc. Transl.* (2) **22**, 194.

Levin, B. Ja. (1964).—*In* "Distribution of Zeros of Entire Functions". Appendix V. (American Mathematical Society: Providence, Rhode Island.)

Meeron, E. (1960).—*J. math. Phys.* **1**, 192.

Morita, T., and Hiroike, K. (1960).—*Prog. theor. Phys., Kyoto* **23**, 1003.

Noble, B. (1958).—"Methods based on the Wiener–Hopf Technique." (Pergamon Press: London.)

Ornstein, L. S., and Zernike, F. (1914).—*Proc. Sect. Sci. K. ned. Akad. Wet.* **17**, 793.

Paley, R. E. A., and Wiener, N. (1934).—"Fourier Transforms in the Complex Domain." (American Mathematical Society: New York.)

Percus, J. K. (1962).—*Phys. Rev. Lett.* **8**, 462.

Percus, J. K., and Yevick, G. J. (1958).—*Phys. Rev.* **110**, 1.

Thiele, E. (1963).—*J. chem. Phys.* **39**, 474.

Van Leeuwen, J. M. J., Groenveld, J., and de Boer, J. (1959).—*Physica* **25**, 792.

Watts, R. O. (1968).—The Percus–Yevick equation applied to a Lennard–Jones fluid. *J. chem. Phys.* **48**, 50.

Wertheim, M. S. (1963).—*Phys. Rev. Lett.* **10**, 321.

Wertheim, M. S. (1964).—*J. math. Phys.* **5**, 643.

Appendix

The factorization theorem represented by equations (9), (11), and (12) can be found in the literature on Fourier transforms (Krein 1962, and associated references; Levin 1964). The derivation presented here is based on the Wiener–Hopf technique (Paley and Wiener 1934; Noble 1958).

Consider the behaviour of $\tilde{A}(k)$ in the complex k plane and set $k = x+\mathrm{i}y$. $\tilde{A}(k)$ is required to have no zeros on the real axis and from equation (9) it tends uniformly to unity as $|x| \to \infty$ in any strip $y_0 \leqslant y \leqslant y_1$. There thus exists a strip $|y| \leqslant \epsilon$ about the real axis within which $\tilde{A}(k)$ has no zeros.

As $\tilde{A}(k)$ is a Fourier transform over a finite interval it is regular throughout the complex plane. The function $\log \tilde{A}(k)$ is therefore regular within the strip $|y| \leqslant \epsilon$ and tends uniformly to zero as $|x| \to \infty$. Integrating round the strip and applying Cauchy's theorem it follows that when $|y| < \epsilon$

$$\log \tilde{A}(k) = \log \tilde{Q}(k) + \log \tilde{P}(k)\,, \tag{A1}$$

where

$$\log \tilde{Q}(k) = \frac{1}{2\pi\mathrm{i}}\int_{-\mathrm{i}\epsilon-\infty}^{-\mathrm{i}\epsilon+\infty} \mathrm{d}k'\,\frac{\log \tilde{A}(k')}{k'-k}\,, \tag{A2}$$

$$\log \tilde{P}(k) = -\frac{1}{2\pi \mathrm{i}}\int_{\mathrm{i}\epsilon-\infty}^{\mathrm{i}\epsilon+\infty} \mathrm{d}k' \, \frac{\log \tilde{A}(k')}{k'-k}. \tag{A3}$$

Negating k' in equation (A3) and using the fact that $\tilde{A}(k)$ is an even function, it can be seen that

$$\log \tilde{P}(k) = \log \tilde{Q}(-k). \tag{A4}$$

The function $\log \tilde{Q}(k)$ is regular in the domain $y > -\epsilon$, so it follows from equations (A1) and (A4) that when $|\, y \,| < \epsilon$

$$\tilde{A}(k) = \tilde{Q}(k)\tilde{Q}(-k), \tag{A5}$$

where $\tilde{Q}(k)$ is regular and has no zeros in the domain $y > -\epsilon$. This proves equation (11).

When $|\, x \,| \to \infty$ within the strip $|\, y \,| < \epsilon$ it follows from equation (A2) that $\log \tilde{Q}(k) \sim O(x^{-1})$, so that $\tilde{Q}(k) \sim 1+O(x^{-1})$. The function $1-\tilde{Q}(k)$ is therefore Fourier integrable along the real axis, and a function $Q(r)$ can be defined by

$$2\pi\rho\, Q(r) = \frac{1}{2\pi}\int_{-\infty}^{\infty} \mathrm{d}k \; \mathrm{e}^{-\mathrm{i}kr}\{1-\tilde{Q}(k)\}. \tag{A6}$$

From equation (A2) it can be seen that when k is real the complex conjugate of $\tilde{Q}(k)$ is $\tilde{Q}(-k)$, from which it follows that $Q(r)$ is a real function.

When $y \leqslant 0$, $\tilde{Q}(k)$ tends to unity as k tends to infinity. If $r < 0$, the integration in equation (A6) can therefore be closed round the upper half-plane, where $\tilde{Q}(k)$ is regular, giving

$$Q(r) = 0 \qquad \text{for} \qquad r < 0. \tag{A7}$$

The right-hand side of equation (A2) is a different analytic function of k according as y is greater than or less than $-\epsilon$. The analytic continuation of the function $\tilde{Q}(k)$ into the lower half-plane is therefore *not* given by equation (A2) but by equation (A5), that is,

$$\tilde{Q}(k) = \tilde{A}(k)/\tilde{Q}(-k), \tag{A8}$$

where equation (A2) can be used to evaluate $\tilde{Q}(-k)$ on the right-hand side of (A8).

As $\tilde{A}(k)$ is regular everywhere and $\tilde{Q}(-k)$ is regular and has no zeros for $y < \epsilon$, from equation (A8) the function $\tilde{Q}(k)$ is regular in this domain. Further, as $\tilde{Q}(-k) \to 1$ when $y \to -\infty$, it follows from equations (9) and (A8) that both $\tilde{A}(k)$ and $\tilde{Q}(k)$ grow exponentially as $\exp(\mathrm{i}kR)$ when y becomes large and negative. When $r > R$ the integration in equation (A6) can therefore be closed round the lower half-plane, giving

$$Q(r) = 0 \qquad \text{for} \qquad r > R. \tag{A9}$$

Inverting the Fourier transform in equation (A6), equations (A7) and (A9) give

$$\tilde{Q}(k) = 1-2\pi\rho\int_{0}^{R} \mathrm{d}r \; \mathrm{e}^{\mathrm{i}kr}Q(r), \tag{A10}$$

which is the desired equation (12).

THE INTERACTION ENERGY OF AN ION PAIR WITH OVERLAPPING HYDRATION SHELLS

I. A TRUNCATED SPHERES MODEL

By D. K. Ross* and S. Levine†

[*Manuscript received February 22, 1968*]

Summary

The energy of interaction of two univalent ions of opposite charge with overlapping hydration shells and in an aqueous medium is discussed in terms of a truncated spherical cavity model. The general trend of the effective dielectric constant considered as a function of the separation between the ion centres is found to be in agreement with some earlier results on a spheroidal cavity model. The present investigation has the advantage that the boundary of the ion pair varies continuously with separation and hence that no matching of a two-sphere model onto a spherical cavity model is required. It is found that the effective dielectric constant has a maximum value at very small ion overlap.

I. Introduction

A monovalent ion in an aqueous medium consists of a central charge surrounded by layers of water molecules in thermal motion. In the first hydration or coordination shell these molecules are strongly bound to the ion centre, while in subsequent layers the water molecules are more or less free to move about. Frank and Wen (1957) have discussed this idea in more detail. For a single ion many authors have introduced a spherical hydration shell of oriented water molecules and have treated the water outside this shell as a continuous dielectric medium. In one such model (Bernal and Fowler 1933; Eley and Evans 1938; Everett and Coulson 1940; Verwey 1941, 1942; Rowlinson 1951; Buckingham 1957; Vaslow 1963) the molecular configuration of the water inside the hydration shell is considered and the electrical and short-range interactions between the ions and these molecules are examined in detail. In a simplified variant of this model (Born 1920; Webb 1926; Latimer, Pitzer, and Slansky 1939; Noyes 1962, see also 1964) the inner shell is treated as a spherical cavity of low dielectric constant to account for the dielectric saturation that is due to a very intense electric field. For a pair of ions the situation is much more complicated; nevertheless, Levine and Wrigley (1957), Levine and Bell (1962), and Levine and Rosenthal (1966) have developed several two-sphere models for non-overlapping hydration shells. (These papers will henceforth be referred to as L.W., L.B., and L.R. respectively.) At small separations, where the coordination shell overlaps, Levine and Rosenthal used a spheroidal cavity model but they found considerable difficulty in treating the transition between the non-overlapping and overlapping stages.

---

* Department of Mathematics, University of Melbourne, Parkville, Vic. 3052.

† Health Sciences Center, State University of New York at Buffalo, 4248 Ridge Lea Road, Amherst, New York 14226, U.S.A.; present address: Department of Mathematics, University of Manchester, Manchester 13, England.

Aust. J. Phys., 1968, **21**, 571–85

It is the purpose of the present paper to extend the work of Levine and co-authors to the case of overlapping hydration shells by using a truncated spheres model in which the radius of the spheres increases with decrease in the separation between the ion centres in such a way that the volume of the two cavities remains constant. With this model there is no difficulty associated with the abrupt change in the shape of the cavity. Several variations are considered but calculations are only carried out for the K^+ and F^- ions in water at 25°C.

In problems of electrostatics and hydrodynamics relating to two truncated spheres, so-called peripolar coordinates were found useful by a number of authors, including Snow (1949), Morse and Feshbach (1953), Payne and Pell (1960), Pell and Payne (1960*a*, 1960*b*), Lebedev (1965), and Ranger (1965). However, in the present paper these coordinates are not used because of the different nature of the conditions at the boundary of the cavity. We therefore use spherical harmonic expansions and, by adopting a least-squares technique, find that a finite number of terms (< 8) in such an expansion satisfies the appropriate boundary conditions to a high degree of accuracy provided that the separation between the ions is not less than about 90% of the diameter of a single ion complex. (For brevity an ion with its attached water molecules will be referred to as an ion complex.) Actually the method used here leads to an infinite set of equations for which it is important to prove the existence of a unique solution. The validity of the expansions can be proved as in Mitra (1944).

Now one purpose of the present investigation is to confirm the general trend of the effective dielectric constant ϵ_{eff} defined by the relation

$$V(R) = e^2/\epsilon_{\text{eff}} R, \tag{1}$$

where $V(R)$ is the interaction energy corresponding to the separation R between the ion centres. In particular, we show that ϵ_{eff} has a maximum at very small overlap. An explanation is also given for the large discontinuity in the electric field at the ion centres, as found in the L.R. spheroidal cavity model at the transition stage from one model to the other. In view of the complexity of the problem, we shall begin with the simplified model of two point charges at the centre of the truncated spheres, which are treated as a continuous medium of low dielectric constant. This is an extension to overlapping spheres of the model considered in L.B. The next step is to place the two ions in a cavity of dielectric constant 1, containing the appropriate distribution of water molecules (see L.W. for this approach). We find that the determination of the interaction energy with such a distribution is very difficult and, since this will be considered in a following paper, only some preliminary results are given here.

II. Potential Problems for Two Intersecting Spheres

In order to estimate the interaction energy of two ion complexes in close proximity we can use as a model two intersecting spheres, S_1 containing the positive charge $+e$ and S_2 containing the negative charge $-e$, of equal radius a and dielectric constant ϵ' (which may or may not be unity). Each sphere represents an ion and its attached water dipoles and encloses the charge distribution which, for the sake of simplicity, is taken to be symmetrical about the line of centres and which lies at the centre of the sphere to which it belongs. The whole system is embedded in a continuous medium of dielectric constant ϵ.

The potential inside the dielectric spheres is harmonic except at those points where there is an electric charge. We shall assume that the charge distribution is confined to two spherical neighbourhoods each of radius b ($b < \min(a, \frac{1}{2}R)$) centred at O_1 and O_2, for then the potential outside these neighbourhoods can be represented by a set of multipoles lying at the centres of the spheres so that the potential inside the overlapping spheres can be written in the form

$$\Psi_1 = \Psi_R + \frac{e}{\epsilon'}\left(\frac{1}{r_1} - \frac{1}{r_2}\right) + \sum_{n=1}^{\infty}\left(\frac{a_n \mathrm{P}_n(\cos\theta_1)}{r_1^{n+1}} + \frac{b_n \mathrm{P}_n(\cos\theta_2)}{r_2^{n+1}}\right), \tag{2}$$

where Ψ_R is harmonic inside the whole region bounded by the overlapping spheres and the second term on the right-hand side represents the potential due to an equivalent multipole distribution situated at O_1 and O_2, with (r_1, θ_1, ϕ_1) and (r_2, θ_2, ϕ_2) as the spherical polar coordinates referred to the ion centres and P_n denoting the Legendre polynomials of order n. These coordinates are so defined that $(r_1, \theta_1, \phi_1) = (r_2, \theta_2, \phi_2)$ for any point P on the median plane. This geometry is illustrated in Figure 1.

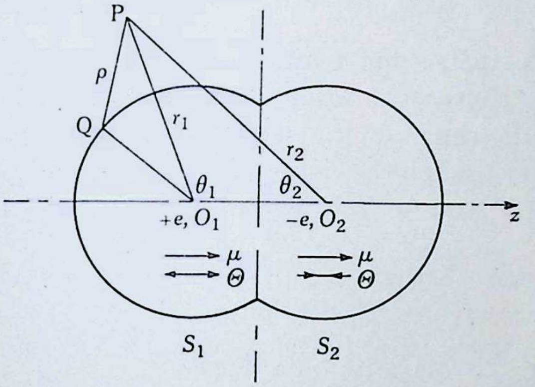

Fig. 1.—Model of two truncated spherical cavities containing point charges $+e$ and $-e$, induced dipoles μ, and induced quadrupoles Θ at the centres. This model is taken to represent overlapping hydration ions.

Since the charge distribution is antisymmetric with respect to the median plane perpendicular to the line joining the ion centres, it is sufficient to determine the potential Ψ_R inside one sphere S_1. Let Q be any point on the boundary of the two spheres with spherical polar coordinates $(a, \theta_1^*, \phi_1^*)$ when on S_1 and $(a, \theta_2^*, \phi_2^*)$ when on S_2. Then, using Green's theorem at any point P interior to the spheres, we get

$$\Psi_R(\mathrm{P}) = \frac{1}{4\pi}\int_{S_1+S_2}\left\{\Psi_R\frac{\partial}{\partial n}\left(\frac{1}{\rho}\right) - \frac{1}{\rho}\frac{\partial \Psi_R}{\partial n}\right\}\mathrm{d}S, \tag{3}$$

where $\rho = \mathrm{PQ}$ and $\partial/\partial n$ denotes differentiation along the outward normal $\boldsymbol{n}$. When Q is a point on the surface S_1 and $r_1 < a$, we introduce the expansion

$$\frac{1}{\rho} = \frac{1}{(r_1^2+a^2-2ar_1\cos\gamma_1)^{\frac{1}{2}}} = \frac{1}{a}\sum_{n=0}^{\infty}\left(\frac{r_1}{a}\right)^n \mathrm{P}_n(\cos\gamma_1), \tag{4}$$

with

$$\cos\gamma_1 = \cos\theta_1\cos\theta_1^* + \sin\theta_1\sin\theta_1^*\cos(\phi_1-\phi_1^*),$$

and, when Q is on the surface S_2 and $r_2 > a$, the expansion

$$\frac{1}{\rho} = \frac{1}{(r_2^2+a^2-2ar_2\cos\gamma_2)^{\frac{1}{2}}} = \frac{1}{a}\sum_{n=0}^{\infty}\left(\frac{a}{r_2}\right)^{n+1} \mathrm{P}_n(\cos\gamma_2)\,, \tag{5}$$

with

$$\cos\gamma_2 = \cos\theta_2\cos\theta_2^* + \sin\theta_2\sin\theta_2^*\cos(\phi_2-\phi_2^*)\,.$$

By a well-known addition formula for the Legendre polynomials (see Hobson 1931) we may write the function $\mathrm{P}_n(\cos\gamma_i)$ as a sum of terms of the type

$$\mathrm{P}_n^m(\cos\theta)\,\mathrm{P}_n^m(\cos\theta^*)\cos m(\phi-\phi^*)\,. \tag{6}$$

On each surface S_1 and S_2, $\partial/\partial n$ becomes $\partial/\partial r_1$ and $\partial/\partial r_2$ respectively, so that the final result should be axially symmetric, and, in the region $r_1 < a < r_2$, $\Psi_R(\mathrm{P})$ takes on the form

$$\sum_{n=0}^{\infty}\left(c_n r_1^n \mathrm{P}_n(\cos\theta_1) + d_n r_2^{-n-1}\mathrm{P}_n(\cos\theta_2)\right). \tag{7}$$

On expanding each term in (r_2, θ_2) in terms of (r_1, θ_1) the expression (7) becomes

$$\sum_{n=0}^{\infty}\left(c_n r_1^n \mathrm{P}_n(\cos\theta_1) + (d_n/R^{n+1})\sum_{m=0}^{\infty}\binom{m+n}{n}(r_1/R)^m \mathrm{P}_m(\cos\theta_1)\right), \tag{8}$$

valid in the region $r_1 < a < R$. Here the second term is a double power series in (r_1/R) and (a/R) and so is absolutely convergent inside the radius of convergence. It follows that we can interchange the order of the summation and so, with the aid of (2) and (8), we obtain an expression for the potential Ψ_1 inside the sphere S_1 as a sum of a reaction field potential Ψ_R and a "self-potential" Ψ_s. Thus

$$\Psi_1 = \Psi_R + \Psi_s\,, \tag{9}$$

where

$$\Psi_R = (e/a)\left(B_0 + \sum_{n=1}^{\infty} B_n (r_1/a)^n \mathrm{P}_n(\cos\theta_1)\right), \tag{10}$$

valid in the whole interior of the sphere S_1 and

$$\Psi_s = (e/a)\left(a/\epsilon' r_1 + \sum_{n=1}^{\infty} W_n (a/r_1)^{n+1}\mathrm{P}_n(\cos\theta_1)\right), \tag{11}$$

valid for $b < r_1 < a$. Here the reaction field Ψ_R is precisely the Taylor series expansion of the potential inside S_1 with a set of coefficients B_n which are related to the sequence of numbers c_j and d_j of (8) and which are determined by the appropriate boundary conditions. On the other hand, the self-potential Ψ_s is expressed in terms of the dimensionless quantities $W_n = p_n/ea^n$, where p_n is the moment of the point multipole of order n situated at the centre of each sphere.

The potential outside the two spheres may be written in the form

$$\Psi_0 = \frac{e}{\epsilon a}\left(\frac{a}{r_1} - \frac{a}{r_2}\right) + \psi_0(\mathrm{P})\,, \tag{12}$$

where $\psi_0(\mathrm{P})$ is harmonic outside the two spheres. An expression for $\Psi_0(\mathrm{P})$ can then be found by using Green's theorem once again and setting

$$\frac{1}{\rho} = \frac{1}{a}\sum_{n=0}^{\infty}\left(\frac{a}{r_i}\right)^{n+1} \mathrm{P}_n(\cos\gamma_i)\,, \tag{13}$$

with $i = 1$ when Q is on S_1 and $i = 2$ when on S_2. On each surface S_1 and S_2, n is the unit inward normal and $\partial/\partial n$ becomes $-\partial/\partial r_1$ and $-\partial/\partial r_2$ respectively. It follows that, since the potential is antisymmetric with respective to the median plane (S_{m}),

$$\Psi_0 = \frac{e}{\epsilon a}\left(\frac{a}{r_1} - \frac{a}{r_2}\right) + \frac{e}{a}\sum_{n=0}^{\infty} A_n\left(\frac{\mathrm{P}_n(\cos\theta_1)\,a^{n+1}}{r_1^{n+1}} - \frac{\mathrm{P}_n(\cos\theta_2)\,a^{n+1}}{r_2^{n+1}}\right), \tag{14}$$

where the constants A_n depend on the potential on the surface of the two spheres and are determined from the boundary conditions appropriate to this problem; namely

$$\left.\begin{array}{lll} \Psi_0 = \Psi_{\mathrm{i}}, \quad \epsilon\,\partial\Psi_0/\partial r_1 = \epsilon'\,\partial\Psi_{\mathrm{i}}/\partial r_1 & \text{on} & S_1\,, \\ \text{with} \qquad\qquad \Psi_{\mathrm{i}} = 0 & \text{on} & S_{\mathrm{m}}\,. \end{array}\right\} \tag{15}$$

Since the boundary conditions at the surface of the sphere S_1 and on the median plane S_{m} will be used to obtain formulae involving the coefficients A_n, it is necessary to express the potential Ψ_0 in terms of (r_1, θ_1). In that case equation (14) becomes

$$\begin{aligned} \Psi_0 = {} & \frac{e}{\epsilon a}\left(\frac{a}{r_1} - \frac{a}{r_2}\right) - \frac{e}{a}\sum_{m=0}^{\infty}\frac{A_m\,a^{m+1}}{R^{m+1}} \\ & + \frac{e}{a}\sum_{n=0}^{\infty}\left[\frac{A_n\,a^{n+1}}{r_1^{n+1}} - \left\{\frac{a^{n+1}}{\epsilon R^{n+1}} + \sum_{m=0}^{\infty}\binom{m+n}{n}\frac{A_m\,a^{m+n+1}}{R^{m+n+1}}\right\}\right]\left(\frac{r_1}{a}\right)^n \mathrm{P}_n(\cos\theta_1)\,, \end{aligned} \tag{16}$$

valid for $\frac{1}{2}R < r_1 < R$.

We now assume that the potential inside the sphere S_1 may be represented sufficiently accurately by the first N coefficients B_n of the series in equations (9)–(12) and that the potential outside S_1, but near the boundary, may be represented by the first N coefficients A_n of the series in (16). This assumption seems reasonable since the potential must be continuous on the whole of the boundary. Now equation (10) shows that the contribution to the potential inside one of the spheres from the reaction field Ψ_R can be written as a Taylor series in r_1 with coefficients that depend on θ_1. Thus, once the multipole moments of the charge distribution inside the spheres are known, the set of constants B_n is uniquely determined by the values of the potential Ψ_{i} on the boundary. However, the same argument does not apply to the potential on the outside for there exists an expansion of the form

$$\sum_{n=0}^{\infty} A_n^{*}\left(\frac{\mathrm{P}_n(\cos\theta_1)}{r_1^{n+1}} - \frac{\mathrm{P}_n(\cos\theta_2)}{r_2^{n+1}}\right) \tag{17}$$

which is identically zero everywhere outside the two spheres. One such identity can be obtained by expressing the function r^{-1}, where r is the radial distance measured from the origin O, in terms of Legendre series in (r_1, θ_1) and subtracting from it a similar series in (r_2, θ_2). In that case $A_n^{*} = (\frac{1}{2}R)^n$. At first sight it seems as if the non-uniqueness of the coefficients A_n would lead to further complications but, as it happens, the equations that determine the B_n (equations (20) and (21);

see below) do not depend on the individual values of these constants but rather on the potential Ψ_0 and on its derivative $\partial\Psi_0/\partial r_1$. Hence, it is clear that the inclusion of terms like (17) cannot affect the determination of the set of constants B_n. This state of affairs is verified by checking that the final result is unaltered when the number of terms in the series is increased from $N = 8$ to 40.

For spheres that do not overlap we may equate the coefficients of the Legendre polynomials that arise when substituting equations (9)–(11) and (16) in the boundary conditions (15), because these polynomials are orthogonal in the range $-\pi < \theta_1 < \pi$; however, when there is overlap the orthogonality condition does not hold and we are not justified in merely equating coefficients because this would take no account of the last condition in (15).

If we look at the case of small overlap then we might expect a least-squares procedure to give reasonable answers. Such an approach has the advantage that it is continuously connected with the non-overlap case. Suppose that the potential is known in the region exterior to the two spheres. We can then determine the B_n's which minimize the integrals

$$\Delta_1 = \int_{S_1} (\Psi_1 - \Psi_0)^2 \,\mathrm{d}S_1 + \int_{S_\mathrm{m}} \Psi_1^2 \,\mathrm{d}S_\mathrm{m} \tag{18}$$

and

$$\Delta_2 = \int_{S_1} (\epsilon\,\partial\Psi_0/\partial r_1 - \epsilon'\,\partial\Psi_1/\partial r_1) \,\mathrm{d}S_1 . \tag{19}$$

This leads to the set of simultaneous equations

$$\int_{S_1} (\Psi_1 - \Psi_0) r_1^n \mathrm{P}_n(\cos\theta_1) \,\mathrm{d}S_1 + \int_{S_\mathrm{m}} \Psi_1 r_1^n \mathrm{P}_n(\cos\theta_1) \,\mathrm{d}S_\mathrm{m} = 0 \tag{20}$$

and

$$\int_{S_1} (\epsilon\,\partial\Psi_0/\partial r_1 - \epsilon'\,\partial\Psi_1/\partial r_1) r_1^n \mathrm{P}_{n+1}(\cos\theta_1) \,\mathrm{d}S_1 = 0 \tag{21}$$

for $n = 0, 1, 2, \ldots$.

For convenience we shall now define a new set of constants E_n and F_n by the relations

$$\Psi_1 - \Psi_0 = (e/a) \sum_{n=0}^{\infty} E_n \mathrm{P}_n(\cos\theta_1) \qquad \text{on} \quad S_1 \tag{22}$$

and

$$\partial\Psi_1/\partial r_1 - (\epsilon/\epsilon')\,\partial\Psi_0/\partial r_1 = (e/a^2) \sum_{n=1}^{\infty} F_n \mathrm{P}_n(\cos\theta_1) \qquad \text{on} \quad S_1 . \tag{23}$$

By comparison with equations (9)–(11) and (16) we see that

$$E_n = B_n + W_n + (\tfrac{1}{2}x)^{n+1}/\epsilon - A_n + \sum_{m=0}^{\infty} \binom{m+n}{n} A_m (\tfrac{1}{2}x)^{m+n+1} \tag{24}$$

for $n = 0, 1, 2, \ldots$ and that

$$F_n = nB_n - (n+1) W_n + n(\tfrac{1}{2}x)^{n+1}/\epsilon' + (n+1) A_n\, \epsilon/\epsilon' + \sum_{m=0}^{\infty} \binom{m+n}{n} n\, A_m (\tfrac{1}{2}x)^{m+n+1} \epsilon/\epsilon' \tag{25}$$

for $n = 1, 2, 3, \ldots$, where we define $W_0 = 1/\epsilon' - 1/\epsilon$, $A_0 = 0$, and $x = 2a/R$. If we substitute these expressions into (20) and (21) we obtain

$$F_n = 0 \text{ for } n = 1, 2, 3, \ldots \quad \text{and} \quad G_n = 0 \text{ for } n = 0, 1, 2, \ldots, \tag{26}$$

where

$$G_n = \sum_{m=0}^{\infty} \{E_m I_{m,n} + B_m J_{m,n} x^{-m-n-2} + W_m K_{m,n} x^{m-n-1}\}, \tag{27}$$

with

$$I_{m,n} = \int_{-1}^{\cos\alpha^*} \mathrm{P}_m(t)\,\mathrm{P}_n(t)\,\mathrm{d}t, \tag{28}$$

$$J_{m,n} = \int_{-1}^{\cos\alpha^*} \mathrm{P}_m(t)\,\mathrm{P}_n(t)\,t^{-m-n-3}\,\mathrm{d}t, \tag{29}$$

$$K_{m,n} = \int_{-1}^{\cos\alpha^*} \mathrm{P}_m(t)\,\mathrm{P}_n(t)\,t^{m-n-2}\,\mathrm{d}t, \tag{30}$$

and

$$\cos\alpha^* = \left.\begin{array}{ll} 1/x, & \text{if } x > 1, \\ 1, & \text{if } x \leqslant 1. \end{array}\right\} \tag{31}$$

In order to complete the discussion we must consider the charge distribution in each ion complex. We shall use the model of L.W., where it was supposed that there are four water molecules in each hydration shell forming a tetrahedral configuration. (A detailed discussion of this model is given in Section IV.) At infinite separation of the ion complexes the water dipoles point directly towards a negative ion and away from a positive ion and hence the equivalent dipole and quadrupole moments of the ion complexes at their centres vanish, that is, $p_1 = 0 = p_2$. However, at finite separations, the reaction field that one ion complex and the surrounding dielectric medium produce inside the other ion complex will induce dipole and quadrupole moments. These induced dipole and quadrupole moments situated at O_1 are taken as

$$\mu = p_1 = -\alpha\,\mathrm{d}\Psi_R/\mathrm{d}z, \qquad \Theta = p_2 = -\gamma\,\mathrm{d}^2\Psi_R/\mathrm{d}z^2, \tag{32}$$

where α and γ are the dipole and quadrupole polarizabilities respectively and depend on the arrangement of the water molecules in the first hydration shell (see L.W. with a correction in L.R.). In nondimensional forms the induced multipole moments can be expressed as

$$\mu' = W_1 = -\alpha' B_1, \qquad \Theta' = W_2 = -\gamma' B_2, \tag{33}$$

where

$$\alpha' = \alpha/a^3, \qquad \gamma' = \gamma/a^5. \tag{34}$$

In L.R. higher order terms in μ' and Θ' were introduced to describe field gradient polarizabilities and hyperpolarizabilities. However, it was found that even at contact of the two spheres their contributions to the interaction energy was less than 0·01%. Furthermore, the inclusion of such terms raises new problems, such as the loss of axial symmetry, and at this stage of the theory there is little point in considering such refinements. So if we now neglect the higher order multipole moments we have a complete set of nonlinear equations in terms of the parameter x representing the ion separation. Once these equations have been solved for A_n and B_n we can substitute these values into the integrals (18) and (19) and so obtain an estimate of the accuracy of this least-squares method. In fact the second integral vanishes identically and the first integral is given by

$$\begin{aligned}\Delta_1 = 2\pi e^2 \sum_{m=0}^{\infty} \sum_{n=0}^{\infty} (E_m E_n I_{m,n} + B_m B_n J_{m,n} x^{-m-n-2} + 2B_m W_n K_{n,m} x^{n-m-1} \\ + W_m W_n L_{m,n} x^{m+n}),\end{aligned} \tag{35}$$

where

$$L_{m,n} = \int_{\cos\alpha^*}^{1} \mathrm{P}_m(t)\,\mathrm{P}_n(t)\,t^{m+n-1}\,\mathrm{d}t. \tag{36}$$

To solve these simultaneous equations we can use the following procedure. First assume that the dipole and quadrupole moments are known and then rewrite (27) in terms of the column matrix $x_i = (B_0, A_1, A_2, A_3, \ldots)'$ by eliminating the other unknown B_n's from (24) and (25). This leaves the set of linear equations

$$a_{i,j} x_i = y_j, \qquad a_{i,1} = -I_{0,i-1} - J_{0,i-1} x^{-i-1}, \tag{37}$$

where

$$\begin{aligned}a_{i,j+1} = I_{j,i-1}\{1+(1+j^{-1})\epsilon/\epsilon'\} + J_{j,i-1}(1+j^{-1})x^{-i-j-1}\epsilon/\epsilon' \\ + \sum_{m=0}^{\infty} \tbinom{m+j}{j} (\tfrac{1}{2}x)^{m+j+1} \{I_{m,i-1}(\epsilon/\epsilon'-1) + J_{m,i-1} x^{-m-i-1}\epsilon/\epsilon'\}\end{aligned} \tag{38}$$

and the y_j's are determined by setting the column matrix x_i equal to zero in (24) and (25) and then substituting into (27) once again. Hence

$$y_{j+1} = \sum_{r=0}^{\infty} (E_r^* I_{r,j} + B_r^* J_{r,j} x^{-r-j-2} + W_r K_{r,j} x^{r-j-1}), \tag{39}$$

where

$$B_0^* = 0, \qquad B_n^* = (1+n^{-1})W_n - (\tfrac{1}{2}x)^{n+1}/\epsilon' \tag{40}$$

and

$$E_0^* = 1/\epsilon' - 1/\epsilon - \tfrac{1}{2}x/\epsilon, \qquad E_n^* = B_n + W_n + (\tfrac{1}{2}x)^{n+1}/\epsilon. \tag{41}$$

We now solve (37) by using a matrix inversion and then make use of (25) to determine the B_n's. This in turn enables us to calculate the induced dipole and quadrupole moments from equations (33). This process is repeated in order to evaluate μ' and Θ' by successive approximations.

III. INTERACTION ENERGY FOR INTERSECTING SPHERE MODEL

To determine the interaction energy $V(R)$ for the ion complexes we can use a Güntelberg–Müller-type charging process (Kirkwood 1934), i.e. we calculate the work that has to be done to bring the point charges from infinity in infinitesimal increments to separation R, the energy needed to produce the dipole and quadrupole moments, and the change in the internal energy associated with their formation.

Now the potential at the positive charge due to the presence of the negative ion is given by

$$\Psi_R^* = \lim_{r_1 \to 0} \left\{ \Psi_1 - \Psi_s - \lim_{R \to \infty} \left(\Psi_1 - \frac{e}{\epsilon' r_1} \right) \right\} = \frac{e}{a} \left\{ B_0 + \frac{a}{a_0} \left(\frac{1}{\epsilon'} - \frac{1}{\epsilon} \right) \right\}, \tag{42}$$

because the induced multipole moments must vanish at infinity. Here a_0 is the radius of the ion complex at infinite separation. If we imagine that the two ion complexes are charged simultaneously (i.e. that each ion centre and each multipole moment is charged at the same rate) and denote by the fraction λ the stage in the charging process, then at any stage $\lambda < 1$ the potential against which the ion complexes are being formed is $\lambda \Psi_R^*$ and hence the difference between the work done in charging the ion centres at separation R and that at infinite separation is

$$V_e(R) = 2 \int_0^1 \lambda \Psi_R^* \, \mathrm{d}(\lambda e) = \frac{e^2}{a} \left\{ B_0 + \frac{a}{a_0} \left(\frac{1}{\epsilon'} - \frac{1}{\epsilon} \right) \right\}. \tag{43}$$

To calculate the contribution to the interaction energy from the induced dipole moments we may consider each dipole as a doublet of length L' and moment $\mu = e'L'$ situated at the ion centre and pointing in the appropriate sense along the z axis. At any stage λ the corresponding potential is again $\lambda \Psi_R^*$ and hence the energy of charging the dipole is obtained by contracting these charges in such a way that $\mu = e'L'$. Thus

$$\begin{aligned} V_\mu(R) &= \lim_{L' \to 0} \; 2 \int_0^1 \lambda \{ (\Psi_R^*)_{L'} - (\Psi_R^*)_0 \} \, \mathrm{d}(\lambda e') \qquad (44) \\ &= e^2 B_1 \mu' / a . \end{aligned}$$

In a similar manner we can find the energy of charging the quadrupoles. This time we imagine three point charges e'', $-2e''$, and e'' situated at distances of 0, L'', and $2L''$ from the ion centres and along the z axis. Then, by contracting these charges in such a way that $\Theta = 2e''L''^2$, we obtain an expression for the energy of charging the quadrupole, namely

$$V_\Theta(R) = e^2 B_2 \Theta' / a . \tag{45}$$

Finally, we have to include in the interaction energy the change in the internal energy associated with the formation of the dipole and quadrupole. If the reaction field is regarded as an external field then, according to Böttcher (1952), the work done by this external field when μ changes by an amount $\delta\mu$ and Θ changes by an amount $\delta\Theta$ is

$$-(\partial \Psi_R^* / \partial z) \delta\mu - \tfrac{1}{2} (\partial^2 \Psi_R^* / \partial z^2) \delta\Theta \tag{46}$$

and, since this is equal to the work done on the internal field, it follows that the change in the internal energy associated with the formation of the dipole and quadrupole is

$$-2(e^2/a) \int_0^{\mu'} B_1 \, \mathrm{d}\mu' - 2(e^2/a) \int_0^{\Theta'} B_2 \, \mathrm{d}\Theta' , \tag{47}$$

which, in view of equations (33), becomes $-(e^2/a)(B_1 \mu' + B_2 \Theta')$. The interaction energy is now obtained by adding the above-mentioned contributions. It is given by

$$V(R) = (e^2/a)\{B_0+(a/a_0)(1/\epsilon'-1/\epsilon)\}\,. \tag{48}$$

We note that the interaction energy does not contain terms linear in the field or field gradient. A similar result, but involving only the dipole moment, was obtained by Mandel and Mazur (1958).

In the model of the ion complexes to be considered here we shall assume that the ion complexes have radius a_0 as long as their coordination shells do not overlap; however, in order that the radius of the complexes may change with separation in the case of overlap (e.g. so as to keep the volume of the two cavities constant), we shall define a volume factor f by the relation

$$4\pi a_0^3\,f/3 = \pi\int_{-a}^{\frac{1}{2}R}(a^2-t^2)\,\mathrm{d}t\,. \tag{49}$$

It will be found convenient to make $R/2a$ the subject of this equation, in which case

$$R/2a = \{c+c(1-c)^{\frac{1}{2}}\}^{\frac{1}{3}}+\{c-c(1-c)^{\frac{1}{2}}\}^{\frac{1}{3}}\,, \tag{50}$$

with

$$c = \{1+4f(R/2a_0)^3\}^{-1}\,. \tag{51}$$

IV. INDUCED MULTIPOLE MOMENTS FOR A TETRAHEDRAL CONFIGURATION

In this work we are primarily interested in potassium fluoride solution where the K+ and F− ions have equal radius $r_1 = 1\cdot33$ Å and where, for the sake of simplicity, we choose them to have the same polarizability $\alpha_1 = 0\cdot93\times10^{-24}$ cm³ (the mean of their actual polarizabilities). For the water molecule we take $r_\mathrm{w} = 1\cdot38$ Å, $\alpha_\mathrm{w} = 1\cdot68\times10^{-24}$ cm³, and the permanent dipole moment $\mu_\mathrm{w} = 1\cdot84$ debye. An upper estimate for the radius of the ion complex a_0 is $r_1+2r_\mathrm{w} = 4\cdot09$ Å while, for the case of a tetrahedral water structure, a lower estimate is $3\cdot09$ Å, which is the radius of the sphere touching the nearest molecules that are not in contact with the ion. We shall use the mean value $a_0 = 3\cdot59$ Å to be consistent with the papers of Levine and co-authors.

To begin we can follow the method of L.W. and imagine that the ion complexes lie in a cavity (or two cavities if $R > 7\cdot18$ Å) that contains four water molecules per ion. Each arrangement of four water molecules is assumed to be situated at the alternate vertices of a cube of sides $2(r_1+r_\mathrm{w})/\sqrt{3} = 3\cdot13$ Å with the ion at the centre. For this model the distance of nearest approach of the ion centres is $2\cdot86$ Å. At ion separations less than $2(r_1+r_\mathrm{w}) = 5\cdot42$ Å the Taylor series expansions (9)–(11) for the potential inside the cavity are no longer valid and so there is no point in pushing this model to smaller separations. In any case water molecules cannot be treated as point dipoles when the potential at intermolecular distances is calculated.

The polarizabilities of the ion complexes are now estimated by neglecting the interaction of adjacent water molecules inside the same hydration shell and determining the orientation of the water dipoles so as to make the potential energy of the water dipoles in the field of the other ion and of the reaction field a minimum.

The dipole moment of the ion complex is then given by

$$\alpha = \alpha_0 + 4\alpha_w + \alpha_1, \tag{52}$$

with

$$\alpha_0 = \mu_w\{(r_1+r_w)^2/e\} \sum (1-\cos^2\theta_1), \tag{53}$$

where α_w and α_1 are the polarizabilities of the water molecule and the ion respectively, θ_1 is the angle between a typical water dipole of the ion complex O_1 and the z axis at infinite separation, and the summation is carried out over the positions of the attached water molecules. This is only the leading approximation since higher order terms in the reaction field are neglected and the rotation of the water dipoles from the line joining the centre of the water molecule to the centre of the ion to which it belongs is assumed to be small. Thus, if θ_1 becomes $(\theta_1-\beta)$ due to the reaction field at finite separation R, we need $|\beta| \ll 1$. Of course, this assumption is not valid for small ion separations R, in which case the dipole–dipole interactions become more significant and the region between the ions has a coordination rather like that for a divalent ion.

Now a feature of this model is that $\sum (1-\cos^2\theta_1) = 8/3$ is independent of the positions of the water molecules. Similarly, L.R. showed that for an arrangement of six water molecules placed in an octahedral structure the same result holds except that the 4 in equation (52) is replaced by a 6 and that $\sum (1-\cos^2\theta_1) = 4$. No calculations on this model are included here since their general characteristics are the same as that of the four-coordinated ions.

The quadrupole moments of the tetrahedral and octahedral structures were calculated by L.R. They obtained an expression for the quadrupole polarizability; namely

$$\gamma = \tfrac{1}{2}m\alpha_w(r_1+r_w)^2 + 2\cdot25\{\mu_w(r_1+r_w)^4/e\} \sum (\cos^2\theta_1 - \cos^4\theta_1), \tag{54}$$

with $\sum (\cos^2\theta_1 - \cos^4\theta_1) = 2m/9$ when the coordination number m is 4 or 6. The first term in (54) is the contribution to the quadrupole moment from the induced dipoles in the attached water molecules while the second term is due to the change in the orientation of the water dipoles of fixed moment μ_w, caused by the reaction field. The results of the calculations on the tetrahedral structure are shown in Table 1.

These data show that ϵ_{eff} has a maximum at very small overlap and that it is there greater than the dielectric constant of the aqueous medium. This is no cause for concern since ϵ_{eff} is only a dielectric constant by convention. At large separations it is clear that the value of ϵ_{eff} approaches that of the aqueous medium ϵ while at very small separations it tends to the internal molecular dielectric constant ϵ'.

The calculations also show that the induced dipole and quadrupole moments are very small when the coordination shells do not overlap and that these moments increase rapidly as the separation between the ions decreases from the contact value $R = 2a_0$. The smallness of the induced multipole moments at larger separations is related to the shielding effect of one ion complex from the other by the aqueous medium. Thus, as $\epsilon'/\epsilon \to \infty$ the ions behave like conducting spheres and so cannot influence each other or be affected by the surrounding aqueous medium. On the other hand, once overlap occurs the amount of shielding is much reduced and the ions interact with each other much more strongly. This illustrates the importance of choosing a realistic model to describe the ion complexes, particularly in the case where overlap of the coordination shells begins. A further point to note is that the positions of the attached water molecules will have to be known even at moderate overlap because there will be a significant contribution to the potential energy from the dipole–dipole interactions of water molecules that belong to the same ion complex. Furthermore, the thermal motions of the water molecules will be increasingly important because there will now be certain geometrical constraints to consider.

TABLE 1

EFFECTIVE DIELECTRIC CONSTANT (ϵ_{eff}), INDUCED DIPOLE (μ) AND QUADRUPOLE (Θ) MOMENTS, AND FIELD INTENSITY (E) FOR THE TWO SPHERES CAVITY MODEL ($\epsilon' = 1$) WITH EIGHT ATTACHED WATER MOLECULES PLACED IN TWO TETRAHEDRAL CONFIGURATIONS

$a_0 = 3\cdot 59$ Å, $\alpha = 15\cdot 15\times 10^{-24}$ cm^3, $\gamma = 66\cdot 01\times 10^{-40}$ cm^5. For $N = 8, 20$ the ratio Δ_1/e^2B_0 has the maximum value 10^{-22} when $R/2a_0 \geqslant 1$ and ranges from 10^{-5} at $R/2a_0 = 1$ to 10^{-4} at $R/2a_0 = 0\cdot 9$

$R/2a_0$	ϵ_{eff}	μ (debye)	$\Theta\times 10^{26}$ (e.s.u.)	$E\times 10^{-6}$ (e.s.u.)
1·60	79·61	0·0149	0·0106	0·0010
1·40	80·34	0·0191	0·0153	0·0013
1·20	81·61	0·0250	0·0226	0·0017
1·00	84·23	0·0332	0·0332	0·0022
0·99	83·16	0·0363	0·0427	0·0024
0·98	80·18	0·0449	0·0713	0·0030
0·96	69·35	0·0819	0·1948	0·0054
0·94	55·47	0·1486	0·4166	0·0098
0·92	42·24	0·2457	0·7390	0·0162
0·90	31·42	0·3773	1·1763	0·0249

These will have the effect of introducing into the cavity permanent dipole, quadrupole, and other moments associated with these molecules. Moreover, at small separations the water molecules can no longer be treated as point dipoles and a much more detailed knowledge of the charge distribution of these molecules is needed than is at present available. The above results show that the field intensity E at each ion centre increases very quickly with increase in the amount of overlap.

There are certainly quite a number of problems associated with choosing a detailed molecular structure for the ion complexes. Thus, as an alternative, we can follow Marcus (1963*a*, 1963*b*) and separate the "electronic" polarizability of an ion complex from its "orientation" polarizability, which is due to the permanent charge distribution of the two ions and their attached water molecules. We imagine that the point charges and multipoles are placed at the ion centres in a dielectric medium for which $\epsilon' = n^2$, where n is its optical refractive index. However, since no data are available for this problem we follow Kirkwood and Westheimer (1938) and Hill (1944), who chose a small value for this dielectric constant to account for the dielectric saturation associated with the strong field between the ions. We shall use $\epsilon' = 2\cdot5$ and halve the polarizabilities α and γ. Table 2 shows the results of this calculation.

In order to make a comparison of the above two sets of calculations it is found useful to assign the value 5 to the dielectric constant ϵ' and thereby replace the induced multipole moments altogether. These results are also shown in Table 2.

We see from the calculations that, when the ion complexes are treated as a cavity ($\epsilon' = 1$) containing the charge distribution associated with the coordination water molecules, the effective dielectric constant is found to change rather abruptly near contact separation. On the other hand, if we use the dielectric spheres model ($\epsilon' = 5$) then this change is much more gradual. Of course, it is unlikely that such a crude macroscopic theory of dielectric saturation is applicable to the water molecules in the first coordination shell, but, by a comparison of these results with the third model ($\epsilon' = 2\cdot5$), the trends become clearer. It appears that the effective dielectric constant reaches a maximum at very small overlap and then begins to decrease fairly rapidly with decrease in ion separation.

Table 2

VARIATION IN EFFECTIVE DIELECTRIC CONSTANT (ϵ_{eff}) AND FIELD INTENSITY (E), AT THE ION CENTRES, WITH IONIC SEPARATION FOR THE CASES $\epsilon' = 5$ WITH $\mu = \Theta = 0$ AND $\epsilon' = 2\cdot5$ WITH POLARIZABILITIES HALF THE PREVIOUS VALUES

For $N = 8, 20$ and $\epsilon' = 2\cdot5$ or 5 the ratio Δ_1/e^2B_0 has the maximum value 10^{-23} when $R/2a_0 \geqslant 1$ and ranges from 10^{-7} at $R/2a_0 = 1$ to 10^{-5} at $R/2a_0 = 0\cdot9$

	$\epsilon' = 5$		$\epsilon' = 2\cdot5$			
$R/2a_0$	ϵ_{eff}	$E\times10^{-6}$ (e.s.u.)	ϵ_{eff}	$E\times10^{-6}$ (e.s.u.)	μ (debye)	$\Theta\times10^{26}$ (e.s.u.)
1·60	79·52	0·0007	79·56	0·0008	0·0060	0·0046
1·40	80·17	0·0008	80·23	0·0010	0·0076	0·0066
1·20	81·38	0·0011	81·48	0·0013	0·0100	0·0098
1·00	83·78	0·0015	83·95	0·0018	0·0133	0·0145
0·99	83·73	0·0016	83·64	0·0018	0·0139	0·0163
0·98	83·22	0·0016	82·48	0·0020	0·0153	0·0211
0·96	80·76	0·0019	77·60	0·0028	0·0209	0·0401
0·94	76·46	0·0025	69·88	0·0041	0·0307	0·0733
0·92	70·61	0·0033	60·50	0·0060	0·0455	0·1228
0·90	63·71	0·0045	50·79	0·0088	0·0664	0·1914

A comparison of the field intensities at the ion centres reveals that E is small and hence that $|\beta| \ll 1$; it follows that the approximations regarding the tetrahedral structure that are used here and in L.W. and L.R. are acceptable. On examination of the cases where $\epsilon' = 1$ and 5 we see that the field intensity is smaller when the dielectric constant of the cavity is larger, in other words, the induced multipole moments are not completely accounted for by the introduction of a dielectric cavity model with $\epsilon' = 5$, although the trends in the two cases are clearly the same. For the case where $\epsilon' = 2\cdot5$ the field intensities lie between those for the other two models considered above, but the induced dipole moment is much smaller (approximately 40% at contact) and it increases with decrease in separation at only about half the rate observed in the cavity model ($\epsilon' = 1$). This is a satisfactory result for it shows a measure of success in replacing an induced dipole moment by a dielectric medium.

To represent the cavity as two truncated spheres is by no means the only possibility. Thus, Kirkwood and Westheimer (1938) estimated the dissociation constants of two similarly constituted acids by using a spheroidal cavity model to calculate the electrostatic work necessary to transfer a proton from the first acid to the ion of the second. They showed the importance not only of the charges present and the distance between them, but also of the shape of the molecule and the positions of the charges. Later Tanford (1957) proved that the interaction energy is critically dependent on the depth of the charges below the surface of the cavity and that this depth is a much more important variable than is the size or shape of the molecule. He suggested that this depth can be interpreted as a measure of the distance of nearest approach of the solvent to the charge or dipolar site and that it increases with increase in temperature.

The success of Kirkwood's model with organic ions suggests that we might try the same model here at small ion separations. Preliminary calculations made in L.R. show the extreme difficulty of matching the interaction energy and, at the same time, the force between the ions for the two spheres at contact separation onto the spheroidal cavity model. However, it may be possible to choose a spheroidal cavity so that there is continuity in the interaction energy and field intensity at each ion centre at some smaller ion separation. Of course, it is not clear which is the better cavity shape to use once the hydration shells overlap or even when they are nearly in contact, since then there is considerable distortion associated with the strong electrical field between the ions. A comparison of the two models is given in the following paper (Part II, pp. 587–95 of the present issue).

V. ACKNOWLEDGMENTS

The authors wish to thank Mr. F. Forti for preparing the diagram.

The calculations were carried out with the kind permission of the Manchester University Computing Service on their Atlas electronic computer.

VI. REFERENCES

BERNAL, J. D., and FOWLER, R. H. (1933).—*J. chem. Phys.* **1**, 515.
BORN, M. (1920).—*Z. Phys.* **1**, 45.
BÖTTCHER, G. J. F. (1952).—"Theory of Electric Polarisation." (Elsevier: Amsterdam.)
BUCKINGHAM, A. D. (1957).—*Discuss. Faraday Soc.* **24**, 151.
ELEY, D. D., and EVANS, M. G. (1938).—*Trans. Faraday Soc.* **34**, 1093.
EVERETT, D. H., and COULSON, C. A. (1940).—*Trans. Faraday Soc.* **36**, 633.
FRANK, H. S., and WEN, WEN-YANG (1957).—*Discuss. Faraday Soc.* **24**, 133.
HILL, T. L. (1944).—*J. chem. Phys.* **12**, 147.
HOBSON, E. W. (1931).—"Spherical and Ellipsoidal Harmonics." (Cambridge Univ. Press.)
KIRKWOOD, J. G. (1934).—*J. chem. Phys.* **2**, 351.
KIRKWOOD, J. G., and WESTHEIMER, F. H. (1938).—*J. chem. Phys.* **6**, 506, 513.
LATIMER, W. M., PITZER, K. S., and SLANSKY, C. M. (1939).—*J. chem. Phys.* **7**, 108.

LEBEDEV, N. N. (1965).—"Special Functions and their Applications." (Prentice Hall: New Jersey.)

LEVINE, S., and BELL, G. M. (1962).—*In* "Trieste Symposium on Electrolytes". (Ed. G. Pesce.) (Pergamon Press: London.)

LEVINE, S., and ROSENTHAL, D. K. (1966).—*In* "Chemical Physics of Ionic Solutions". (Eds. B. E. Conway and R. G. Barradas.) (Wiley: New York.)

LEVINE, S., and WRIGLEY, H. E. (1957).—*Discuss. Faraday Soc.* **24**, 43, 73.

MANDEL, M., and MAZUR, P. (1958).—*Physica* **24**, 116.

MARCUS, R. A. (1963*a*).—*J. chem. Phys.* **38**, 1335.

MARCUS, R. A. (1963*b*).—*J. chem. Phys.* **39**, 460.

MITRA, S. K. (1944).—*Bull. Calcutta math. Soc.* **36**, 31.

MORSE, P. M., and FESHBACH, H. (1953).—"Methods of Theoretical Physics." (McGraw–Hill: New York.)

NOYES, R. M. (1962).—*J. Am. chem. Soc.* **84**, 513.

NOYES, R. M. (1964).—*J. Am. chem. Soc.* **86**, 971.

PAYNE, L. E., and PELL, W. H. (1960).—*J. Fluid Mech.* **7**, 529.

PELL, W. H., and PAYNE, L. E. (1960*a*).—*Mathematika* **7**, 78.

PELL, W. H., and PAYNE, L. E. (1960*b*).—*Q. appl. Math.* **18**, 257.

RANGER, K. B. (1965).—*Proc. Camb. phil. Soc.* **61**, 271.

ROWLINSON, J. S. (1951).—*Trans. Faraday Soc.* **47**, 120.

SNOW, C. (1949).—*J. Res. natn. Bur. Stand.* **43**, 377.

TANFORD, C. (1957).—*J. Am. chem. Soc.* **79**, 5348.

VASLOW, F. (1963).—*J. phys. Chem.* **67**, 2773.

VERWEY, E. J. W. (1941).—*Recl Trav. chim. Pays-Bas Belg.* **60**, 127.

VERWEY, E. J. W. (1942).—*Recl Trav. chim. Pays-Bas Belg.* **61**, 127.

WEBB, T. (1926).—*J. Am. chem. Soc.* **48**, 2589.

THE INTERACTION ENERGY OF AN ION PAIR WITH OVERLAPPING HYDRATION SHELLS

II.* A SPHEROIDAL CAVITY MODEL

By D. K. Ross†

[*Manuscript received March* 1, 1968]

Summary

The energy of interaction of two monovalent ions of opposite charge with overlapping hydration shells and in an aqueous medium is discussed in terms of a spheroidal cavity model. Some of the calculations carried out in an earlier paper by Levine and Rosenthal (1966) are shown to be inadequate and an improved model is tested for consistency with the "truncated spheres model" proposed in Part I. The calculations suggest that this new model can be adapted to an examination of the water molecules in the first hydration shells of an ion pair. Only calculations for the K^+ and F^- ions are included.

I. Introduction

In Part I (pp. 571–85 of the present issue) the interaction energy of an ion pair in an aqueous medium is discussed in terms of a "truncated spheres model" embedded in a dielectric continuum that represents the aqueous medium. However, although this model may be mathematically satisfactory it is unlikely to represent the "true" physical situation because the hydration shells of the ions tend to repel, particularly at small separations. There is, therefore, a considerable distortion of the cavity shape, which should be accounted for with an improved model. Now it appears (Levine and Rosenthal 1966) that it is difficult to choose a spheroidal cavity in such a way that both the interaction energy and the force between the ions is continuous at an ion separation equal to the diameter of an isolated ion complex. Levine and Rosenthal were unable to effect such a matching when the cavity is empty because the interaction energy of the two ions, which is defined as the difference between the free energy associated with the two ions at the given separation and that at infinite separation, is a very small difference and is extremely sensitive to changes in cavity shape and cavity volume. On the other hand, when the cavity contains both point charges and a system of poles and multipoles situated in empty cavities (or the multipoles replaced by a dielectric medium) continuity in the energy and force is obtained for various geometries in either of two ways: (1) by setting the volume of the cavity equal to a linear function of the separation and keeping the position of the ionic charges fixed relative to the ends of the major axis of the spheroid, or (2) by varying the position of the two charges relative to the ends of the major axis and keeping the volume fixed. Clearly, some combination of these two possibilities

---

* Part I, *Aust. J. Phys.*, 1968, **21**, 571–85.

† Department of Mathematics, University of Melbourne, Parkville, Vic. 3052.

Aust. J. Phys., 1968, **21**, 587–95

is better but any future work on such lines requires the use of a discrete model representing the ions and their attached water molecules. Before attempting such a complicated analysis it is important to see if a refined model based on the spheroidal cavity can meet with more success.

A failing of the spheroidal cavity model of Levine and Rosenthal (1966) that is not pointed out by them stems from the fact that the field intensity at the ion centres (and hence the induced multipole moments) exhibits a discontinuity at contact separation of at least two orders of magnitude. The reason for such an abrupt change is made clear in Part I. It is with this fact in mind that a variation of the spheroidal model is suggested, namely, that matching of the interaction energy and the force between the ions should be carried out at a smaller separation, say 90% of the diameter of a single ion complex. In that case the discontinuity in the field intensity at the ion centres is very much reduced and the redistribution of the water molecules, originally in a tetrahedral configuration (at infinite separation), is kept to a minimum. The possible success of this model suggests that a spheroidal cavity may be useful in studying the behaviour of the attached water molecules and, in particular, it may be possible to determine the ionic separation at which, on average, the coordination number per ion changes. Such a change is suggested in the work of Eigen and Tamm (1962).

Some characteristics of the spheroidal model have already been investigated by Westheimer and Kirkwood (1938, 1939), Hill (1944, 1956), Buckingham (1953), Linderstrøm-Lang (1953), Buckley and Maryott (1954), and Tanford (1957), to mention but a few. None of these authors were concerned with the same type of problem but each found the model sufficiently accurate for their purposes. The numerical work in the present paper is based on the data in Part I.

II. Potential Problem for Spheroidal Cavity

To begin we shall consider a cavity model whose boundary is an ellipsoid of revolution. Some of the characteristics of this spheroidal model have already been investigated by Levine and Rosenthal (1966; subsequently referred to as L.R.) in which the water molecules in the coordination shells are represented by induced dipoles and quadrupoles placed at the centre of each ion. In the present discussion it is found convenient to use confocal elliptical coordinates (ξ, η, ϕ); thus, if ρ_1 and ρ_2 are the distances of a typical point P from the two foci, whose distance apart is $2a$, then $\xi = (\rho_1+\rho_2)/2a$, $\eta = (\rho_1-\rho_2)/2a$, and ϕ is the angle by which the typical point has been rotated past a fixed plane through the major axis. Since we have chosen an ellipsoid of revolution to represent the boundary and we confine all the charges to lie on the major axis between the two foci, the model is axially symmetrical and the angle ϕ does not enter the formulation explicitly. In this coordinate system the boundary of the ellipsoidal cavity will be defined by $\xi = \xi_0 = 1/E$, where E is the eccentricity of the spheroid and the ion centres are symmetrically placed between the foci f_1 and f_2 at a distance R apart, as shown in Figure 1. If the spheroid is treated as a uniform medium of dielectric constant ϵ' embedded in an aqueous medium of dielectric constant ϵ then the potential at a point $r(\xi, \eta)$ outside the spheroid has the form

$$\psi_0 = \frac{1}{\epsilon} \sum_k \frac{e_k}{|\boldsymbol{r}-\boldsymbol{r}_k|} + \sum_{n=0}^{\infty} A_n \,\mathrm{Q}_n(\xi)\,\mathrm{P}_n(\eta)\,, \tag{1}$$

where e_k is the set of charges placed on the major axis, P_n and Q_n represent the Legendre functions of order n of the first and second kind respectively, and the A_n are constants to be determined from the boundary conditions. Similarly, the potential inside the spheroid may be written in the form

$$\psi_1 = \frac{1}{\epsilon'} \sum_k \frac{e_k}{|\boldsymbol{r}-\boldsymbol{r}_k|} + \sum_{n=0}^{\infty} B_n \,\mathrm{P}_n(\xi)\,\mathrm{P}_n(\eta)\,. \tag{2}$$

At this stage we shall replace the actual charge distribution inside the cavity by point charges $+e$ and $-e$ at positions O_1 and O_2, and the molecules inside the ion complex by dipoles μ and quadrupoles Θ also situated at these points and having directions in the appropriate sense along $O_1\,O_2$. In order to take account of the changes with ion separation in the induced dipole and quadrupole moments at each ion centre under the influence of the reaction field, it seems sufficient for the present to assume that these moments are proportional to the reaction field and the reaction field gradient respectively. Thus, at the ion centre O_1 we have the relations

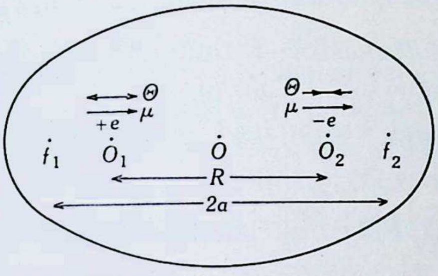

Fig. 1.—Model of a spheroidal cavity with foci at f_1 and f_2 which is taken to represent overlapping hydration shells; μ and Θ are the induced dipole and quadrupole moments respectively.

$$\mu = -\alpha\,\partial\psi_R/\partial z\,, \qquad \Theta = -\gamma\,\partial^2\psi_R/\partial z^2\,, \tag{3}$$

where the reaction field ψ_R is that part of the potential ψ_1, given in (2), which excludes the poles of various orders situated at $z = -\tfrac{1}{2}R$ and α and γ are the dipole and quadrupole polarizabilities respectively. Making use of this and the boundary conditions appropriate to the problem; namely

$$\psi_0 = \psi_1, \qquad \epsilon\,\partial\psi_0/\partial\xi = \epsilon'\,\partial\psi_1/\partial\xi \qquad \text{at} \quad \xi = 1/E\,, \quad -1 \leqslant \eta \leqslant 1\,, \tag{4}$$

we find that

$$B_n = (\beta_n/a)(1/\epsilon - 1/\epsilon')C_n\,, \tag{5}$$

where

$$C_n = (2n+1)\mathrm{Q}_n(E^{-1})/\mathrm{P}_n(E^{-1})(1-D_n)\,, \tag{6}$$

$$D_n = \frac{\epsilon'}{\epsilon}\,\frac{E^{-1} - \mathrm{P}_{n-1}(E^{-1})/\mathrm{P}_n(E^{-1})}{E^{-1} - \mathrm{Q}_{n-1}(E^{-1})/\mathrm{Q}_n(E^{-1})}, \tag{7}$$

and

$$\beta_n = \sum_k e_k \,\mathrm{P}_n(\eta_k)\,, \tag{8}$$

because the point charges e_k are assumed to lie on the line joining the foci ($\xi = 1$) at the positions given by $\eta = \eta_k$. It follows that

$$\mu'\left\{-1+\frac{\alpha'}{4\epsilon' z^3}-2\alpha'\left(\frac{a_0}{a}\right)^3\left(\frac{1}{\epsilon'}-\frac{1}{\epsilon}\right)\Sigma' C_n \mathrm{P}'^2_n\right\}+\Theta'\left\{\frac{3\alpha'}{16\epsilon' z^4}+2\alpha'\left(\frac{a_0}{a}\right)^4\left(\frac{1}{\epsilon'}-\frac{1}{\epsilon}\right)\Sigma' C_n \mathrm{P}'_n \mathrm{P}''_n\right\}$$

$$= -\alpha'\left\{\frac{1}{4\epsilon' z^2}+2\left(\frac{a_0}{a}\right)^2\left(\frac{1}{\epsilon'}-\frac{1}{\epsilon}\right)\Sigma' C_n \mathrm{P}_n \mathrm{P}'_n\right\}, \tag{9}$$

$$2\gamma'\mu'\left\{-\frac{3}{16\epsilon' z^4}-\left(\frac{a_0}{a}\right)^4\left(\frac{1}{\epsilon'}-\frac{1}{\epsilon}\right)\Sigma' C_n \mathrm{P}'_n \mathrm{P}''_n\right\}+\Theta'\left\{1-\frac{3\gamma'}{8\epsilon' z^5}+2\gamma'\left(\frac{a_0}{a}\right)^5\left(\frac{1}{\epsilon'}-\frac{1}{\epsilon}\right)\Sigma' C_n \mathrm{P}''^2_n\right\}$$

$$= \gamma'\left\{\frac{1}{4\epsilon' z^3}-2\left(\frac{a_0}{a}\right)^3\left(\frac{1}{\epsilon'}-\frac{1}{\epsilon}\right)\Sigma' C_n \mathrm{P}_n \mathrm{P}''_n\right\}, \tag{10}$$

where $\mathrm{P}_n = \mathrm{P}_n(R/2a)$, $\mathrm{P}'_n = \mathrm{P}'_n(R/2a)$, $\mathrm{P}''_n = \mathrm{P}''_n(R/2a)$, and we have introduced the dimensionless quantities

$$\mu' = \mu/ea_0, \quad \Theta' = \Theta/ea_0^2, \quad \alpha' = \alpha/a_0^3, \quad \gamma' = \gamma/a_0^5, \quad z = R/2a_0\,; \tag{11}$$

a_0 is the radius of the spherical ions corresponding to infinite separation and Σ' means that the summation is taken over the odd values of n.

As in Part I the interaction energy can be obtained by using the Güntelberg–Muller charging process. Thus

$$V(R) = \tfrac{1}{2}e\{\psi_1(1, -R/2a)-\psi_1(1, R/2a)\}+(e^2/a_0)(1/\epsilon'-1/\epsilon), \tag{12}$$

where the last term on the right-hand side is minus the Born energy of the ion complexes, i.e. the interaction energy corresponding to infinite separation. From L.R. it follows that

$$V(R) = V_e(R)+V_\mu(R)+V_\Theta(R), \tag{13}$$

with

$$V_e(R) = -\frac{e^2}{\epsilon R}\left\{\frac{\epsilon}{\epsilon'}+\frac{2R}{a}\left(\frac{\epsilon}{\epsilon'}-1\right)\Sigma' C_n \mathrm{P}_n^2-\frac{R}{a_0}\left(\frac{\epsilon}{\epsilon'}-1\right)\right\}, \tag{14}$$

$$V_\mu(R) = -\frac{e^2}{\epsilon R}\left\{\frac{\epsilon}{\epsilon'}\left(\frac{\mu'}{z}+\frac{\mu'^2}{2z^2}\right)-4\left(\frac{a_0}{a}\right)^2\left(\frac{\epsilon}{\epsilon'}-1\right)\mu' z\,\Sigma' C_n \mathrm{P}_n \mathrm{P}'_n\right\}, \tag{15}$$

and

$$V_\Theta(R) = -\frac{e^2}{\epsilon R}\left\{\frac{\epsilon}{\epsilon'}\left(\frac{\Theta'}{2z^2}+\frac{3\Theta'^2}{4z^4}\right)+4\left(\frac{a_0}{a}\right)^3\left(\frac{\epsilon}{\epsilon'}-1\right)\Theta' z\,\Sigma' C_n \mathrm{P}_n \mathrm{P}''_n\right\}. \tag{16}$$

It is now important to choose a suitable geometry for the spheroid. Let $2a_1$ and $2b_1$ be the lengths of the major and minor axes of the spheroid respectively and ga_0 denote the distance from the centre of each ion to the nearer end of the major axis. Then, if the volume of the spheroid is f times the sum of the volumes of the two hydration shells at infinite separation

$$2fa_0^3 = a_1^3(1+E^2), \qquad \text{with} \qquad a = a_1 E\,. \tag{17}$$

A knowledge of f and g then leads to a complete specification of the spheroid at the given separation.

Already it is shown in L.R. the difficulty of matching both the interaction energy and the force between the ions with the two-sphere model at contact separation. Thus, continuity in the energy could be obtained by choosing a large volume for the spheroid and by keeping the positions of the ion centres fixed relative to the ends of the major axis. Continuity in the force was obtained in two ways: (1) by allowing the positions of the ion charges to remain fixed relative to the ends of the major axis and varying the volume linearly with the separation, and (2) by keeping the volume fixed and varying the positions of the ion charges linearly with the separation. In the first case we set

$$f = f(R/2a_0) = f(1) - \lambda_f(1 - R/2a_0), \tag{18}$$

while in the second case

$$g = g(R/2a_0) = g(1) + \lambda_g(1 - R/2a_0), \tag{19}$$

where λ_f and λ_g are constants. It is interesting to note that continuity in the force could be obtained for $\epsilon' > 1$ either by decreasing the volume or increasing the distance from the ends of the major axis with decrease in separation; however, for $\epsilon' = 1$ the volume has to be increased or the distance of the ion charges from the ends of the major axis has to be increased with decreasing separation. It is clear that the induced multipole moments of the charge distribution in the cavity are very important and may account for this curious behaviour. To show their effect we have matched the spheroid with the two spheres at contact separation.

Here we fix g, allow the volume to vary with separation, and neglect the quadrupole moment, since this will be sufficient to show the essential characteristics of the matching procedure. Thus, Figure 2(a) shows the variation in effective dielectric constant ϵ_{eff} with separation when $\epsilon' = 1$ and the induced dipole moment is taken into account. It is seen that matching is effected with $g = 0\cdot936$, $f(1) = 1\cdot35$, and $\lambda_f = -0\cdot8$. In Figure 2(b), the induced multipole moments are replaced by a dielectric medium with $\epsilon' = 5$ and this time $g = 1\cdot007$, $f(1) = 1\cdot25$, and $\lambda_f = +0\cdot6$. Finally, if we separate the "electronic" from the "orientation" polarizability, introduce a dielectric medium with $\epsilon' = 2\cdot5$, and use half the dipole polarizability, as was done in Part I, then matching is obtained for $g = 0\cdot942$, $f = 1\cdot20$, and $\lambda_f = 0\cdot4$, as shown in Figure 2(c). These results are to be compared with the truncated spheres model discussed in Part I. By way of example such a comparison is shown in Figure 3. It becomes clear that the effective dielectric constant decreases more quickly with decreasing separation for the truncated spheres model (curve C) than for the spheroidal model (curves A and B).

A fact that emerges is that the induced dipole moment at contact separation is very much larger than the value one would have expected from the two-spheres model, being about 100-fold for the case $\epsilon' = 1$ and 30-fold for the case $\epsilon' = 2\cdot5$. Actually, Tanford (1957) pointed out the difficulty of positioning the ion charges, for in his calculations he shows that a movement of the charges by as little as 1 Å can alter the interaction energy threefold. It is not surprising therefore that it is so difficult to match the induced dipole moment as well as the energy and force at contact separation, for there is an abrupt change in cavity shape in going from the

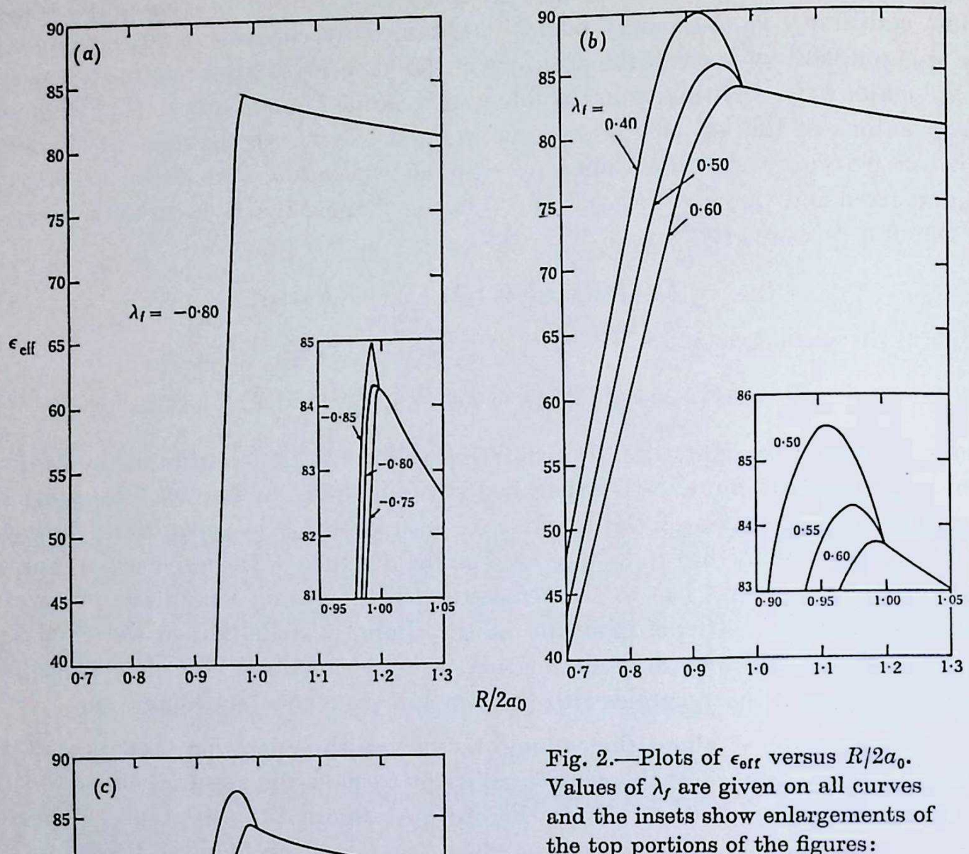

Fig. 2.—Plots of ϵ_{eff} versus $R/2a_0$. Values of λ_f are given on all curves and the insets show enlargements of the top portions of the figures:

(*a*) Two spheres in contact ($R/2a_0 = 1$) matched onto a spheroidal model ($\epsilon' = 1$) with the induced dipole moment taken into account. The volume of the spheroid changes linearly with R according to the relation

$$f(R/2a_0) = f(1) - \lambda_f(1 - R/2a_0)\,,$$

with $f(1) = 1{\cdot}35$ and $g = 0{\cdot}936$.

(*b*) Two spheres in contact matched onto a dielectric spheroid ($\epsilon' = 5$) with $g = 1{\cdot}007$ and $f(1) = 1{\cdot}25$.

(*c*) Two spheres in contact matched onto a spheroidal cavity ($\epsilon' = 2{\cdot}5$, half the dipole and quadrupole polarizabilities) with $g = 0{\cdot}942$ and $f = 1{\cdot}20$.

one model to the other. This difficulty does not arise in the truncated spheres model. Nevertheless, it is not known which is the better model to represent the physical situation. A further point worth examining is whether or not the assumption that $|\beta|$ is small (that is, $|(r_1+r_w)^2E/e| \ll 1$) remains valid at small separation where there is a strong field, and hence whether the water dipoles point away from the line joining the centre of the water molecule to its ion.

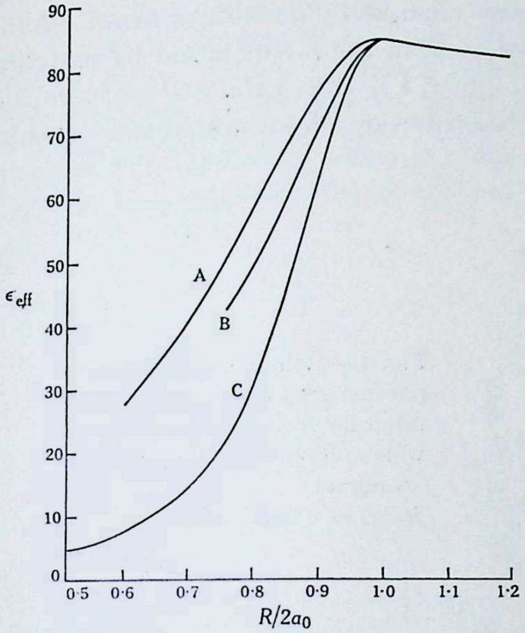

Fig. 3.—Comparison of two dielectric spheroid models ($\epsilon' = 5$) with truncated spheres model matched at contact:

A, spheroidal model, $g = 1\cdot007$, $f(R/2a_0) = 1\cdot25-0\cdot6(1-R/2a_0)$;

B, spheroidal model, $f = 1\cdot25$, $g(R/2a_0) = 1\cdot007+1\cdot3(1-R/2a_0)$;

C, truncated spheres model, $f = 1$.

TABLE 1

COMPARISON OF INDUCED DIPOLE MOMENTS (μ) AND FIELD INTENSITY (E) AT THE ION CENTRES FOR TWO-SPHERES AND SPHEROIDAL CAVITY MODELS AT CONTACT SEPARATION

	Two-spheres Model			Spheroidal Model				
ϵ'	ϵ_{eff}	μ (debye)	$E\times10^{-6}$ (e.s.u.)	$f(1)$	$g(1)$	λ_f	μ (debye)	$E\times10^{-6}$ (e.s.u.)
1	84·23	0·0332	0·0022	1·35	0·936	−0·8	3·5633	0·2352
5	83·78	—	0·0015	1·25	1·007	0·6	—	0·0913
2·5	83·95	0·0133	0·0018	1·20	0·942	0·4	0·7751	0·0498

Now an inspection of Table 1 shows that this criterion is not satisfied at contact separation and so we expect the transition from the two-spheres to the spheroidal cavity model to be unsatisfactory in taking account of the water molecules in the first hydration shell. A possible alternative is to match the spheroid onto the truncated spheres model at some smaller separation $R/2a_0 = 0\cdot9$, say, for then the change in cavity shape is not so pronounced. Some preliminary calculations are now carried out on the dielectric cavity model $\epsilon' = 5$ in order to ascertain whether such a matching could meet with more success.

We know from L.R. that the force between the ions can be made continuous by varying the factors f and/or g in accordance with (18) and (19). It is therefore sufficient, in the first stage of the matching procedure, to make the interaction energy continuous and to find a spheroidal shape for which the electric field intensity at the ion centres is also continuous, at least, if this is possible. Figure 4 shows the f versus g relation, which allows matching in the energy at $R/2a_0 = 0 \cdot 9$.

It is seen that the smallest possible volume factor $f = 1 \cdot 13$ gives the best result, for then the field intensity at the ion centres changes by a factor of about 8/5 during the transition. This is certainly much better than the factor found by matching at contact separation. The assumption that $|\beta| \ll 1$ is then valid and so there is some hope of using this model to study the redistribution of the water molecules in the first hydration shells associated with their overlap. However, the field intensity between the two ions increases with decreasing separation and a stage is reached where the water molecules begin to interlock and where it is no longer possible to represent the charge distribution of the two ion complexes by a set of multipoles placed at the two ion centres. Perhaps a better approach is to examine an arrangement of water molecules *in vacuo* at close proximity and to find out what is the effect of surrounding these molecules with an aqueous medium. Such an approach has been used by Eley and Evans (1938) and Buckingham (1957) with a more recent development by Coulson and Eisenberg (1966). A discussion of this model has been developed by the author and will be presented in a subsequent paper.

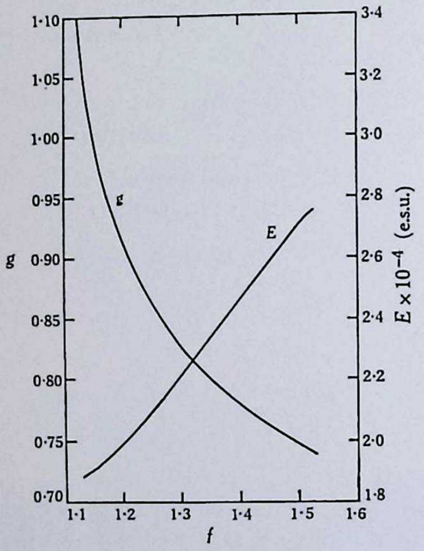

Fig. 4.—Relation between the parameters f and g and the field intensity E at the ion centres, which allows matching in the energy at $R/2a_0 = 0 \cdot 9$ ($\epsilon' = 5$).

III. ACKNOWLEDGMENTS

The author wishes to thank Dr. S. Levine for suggesting this problem and for his criticism of the original manuscript, and Mr. F. Forti for preparing the diagrams.

The calculations were carried out with the kind permission of the Manchester University Computing Service on their Atlas electronic computer.

IV. REFERENCES

BUCKINGHAM, A. D. (1953).—*Trans. Faraday Soc.* **49**, 881.

BUCKINGHAM, A. D. (1957).—*Discuss. Faraday Soc.* **24**, 151.

BUCKLEY, F., and MARYOTT, A. A. (1954).—*J. Res. natn. Bur. Stand.* **53**, 229.

COULSON, C. A., and EISENBERG, D. (1966).—*Proc. R. Soc.* A **291**, 445, 454.

EIGEN, M., and TAMM, K. (1962).—*Z. Elektrochem.* **66**, 93, 107.

ELEY, D. D., and EVANS, M. G. (1938).—*Trans. Faraday Soc.* **34**, 1093.

HILL, T. L. (1944).—*J. chem. Phys.* **12**, 147.

HILL, T. L. (1956).—*J. phys. Chem.* **60**, 253.

LEVINE, S., and ROSENTHAL, D. K. (1966).—*In* "Chemical Physics of Ionic Solutions". (Eds. B. E. Conway and R. G. Barradas.) (Wiley: New York.)

LINDERSTRØM-LANG, K. (1953).—*C. r. Trav. Lab. Carlsberg* **28**, 281.

TANFORD, C. (1957).—*J. Am. chem. Soc.* **79**, 5348.

WESTHEIMER, F. H., and KIRKWOOD, J. G. (1938).—*J. chem. Phys.* **6**, 506, 513.

WESTHEIMER, F. H., and KIRKWOOD, J. G. (1939).—*J. chem. Phys.* **7**, 437.

THE INTERACTION ENERGY OF AN ISOLATED MONOVALENT ION

By D. K. Ross*

[*Manuscript received April* 1, 1968]

Summary

The interaction energy of a monovalent ion in an aqueous medium at 25°C is determined. It is also found that the water molecules in the first hydration shell of the ion have a mean dipole moment far in excess of their permanent dipole moments. Thus, for example, the increase in the dipole moment of the attached water molecules due to the presence of an ion is about 60% for the small four-coordinated Li^+ ion and about 30% for the larger four-coordinated I^- ion. Calculations are also carried out on the assumption that the ions are six coordinated.

I. INTRODUCTION

A formula for the Gibb's free energy of hydration of an isolated ion in an aqueous solution was first obtained by Born (1920). He assumed that the ion could be replaced by an empty spherical cavity containing a point charge at its centre with the surrounding medium having the macroscopic dielectric constant of water. This model has been used by many authors, including Webb (1926), Latimer, Pitzer, and Slansky (1939), and Noyes (1962), to mention but a few. Nevertheless the continuum model has met with much criticism since, for example, according to Powell and Latimer (1951), Cobble (1953), and Connick and Powell (1953), it cannot be used to calculate the hydration energies of other than monovalent ions. Laidler (1956) does not agree with their argument. In any case it is clear that this mathematical model is fairly crude and that a refinement should take some account of the discrete nature of the water molecules. It is with this fact in mind that we shall develop a discrete model here.

As a guide we can refer to the papers of Bernal and Fowler (1933), Verwey (1941, 1942), Rowlinson (1951), Buckingham (1957), Vaslow (1963), Ross (1968*a*), and Ross and Levine (1968). All but the last two papers omitted the polarizability of the water molecules, and in each case the water molecule was replaced by a point dipole (and sometimes a point quadrupole as well). In fact Ross (1968*a*) showed that, at 25°C, a good approximation can be obtained by replacing the polarizable water dipoles of the first hydration shell in the position of minimum electrostatic energy with the water outside this shell replaced by a dielectric continuum.

Now Bernal and Fowler (1933) indicated that the most likely coordination number of a monovalent ion is four, whereas Verwey (1941, 1942), who took into consideration the geometrical constraints in the second hydration shell, suggested that it is six or even eight. In the present paper we shall deal only with coordination number four or six, the former being the most probable. Similar calculations were

---

* Department of Mathematics, University of Melbourne, Parkville, Vic. 3052.

Aust. J. Phys., 1968, **21**, 597–608

carried out by Buckingham (1957) but he did not take full account of the polarizability of the water molecules near the strong field of the ion. Instead he found a formula for the electrostatic energy of formation of four solvent molecules tetrahedrally disposed and of six solvent molecules octahedrally disposed about a spherical ion *in vacuo*. These formulae are used here and the effects of polarization and the surrounding dielectric are included.

It is not the purpose of this paper to calculate the free energy of hydration of an ion because this has been done successfully by Randles (1956), Noyes (1962, 1964), and others. Rather, this discrete model is used to determine the zero energy level of a 10-coordinated ion pair with the hope that it will be possible to include it with the calculations of Ross and Levine (1968) in a later paper. In that case the interaction energy is taken as the difference between the energies at finite and infinite separations. This definition of interaction energy was used by Levine and Wrigley (1957), Levine and Bell (1962), Levine and Rosenthal (1966), and Ross (1968*b*). It is thought to be a satisfactory one in determining the Gibb's free energy of hydration, although it differs from the hypothetical five stage cycle of change proposed by Eley and Evans (1938). Those authors had great success in determining the hydration energy and the heat of solvation of ions in water. However, the aim of the present work is to find a discrete model that predicts these quantities as well as the mean coordination number and the induced dipole moment of the attached water molecules.

II. Further Discussions of the Physical Model

In order to study the energy of hydration of an ion in water it is necessary to know the spatial locations of each of the sets of electrical charges within the molecules themselves. Models for the charge distribution inside the water molecule have been obtained by theoretical and empirical means. Thus, Duncan and Pople (1953) were able to calculate the contribution to the dipole and quadrupole moments of the water molecule from the lone pair electrons and from the binding electrons and the protons; while Rowlinson (1951) determined the dipole and quadrupole moments of the water molecule by comparing the experimental values of the second virial coefficient of water vapour with values calculated on the basis of an assumed intermolecular potential. Unfortunately there is a large difference between the quadrupole moments of the water molecule obtained by these two methods (see McWeeny and Ohno 1960; Stogryn and Stogryn 1966, 1967). Campbell (1952) examined various point-charge models of the water molecule and showed that in ice the higher order multipole moments through the fifth are important. Furthermore the energy of interaction depends upon the assumed relative orientations not only of neighbouring molecules but also of more distant ones. The problems that this involves are extremely complicated and so we shall begin by replacing each water molecule by a point dipole $\mu_W = 1 \cdot 84$ debye at the centre of a sphere of radius $r_W = 1 \cdot 38$ Å. This seems the best that we can do at this stage for there is still considerable doubt about the values of the quadrupole and higher multipole moments of the charge distribution inside the water molecule. A tentative calculation involving the quadrupole moments will, however, be included.

With the exception of Verwey (1942) and Vaslow (1963), it has generally been supposed that in an aqueous solution of electrolytes the dipole of a water molecule adjacent to a small or highly charged ion points directly at the centre of the ion. In such a model the attached water molecules form a symmetrical tetrahedron or octahedron as the primary hydration shell and, moreover, there is then no induced dipole or quadrupole moment of the ion itself. The evidence for this type of structure is not experimental but present theories are not inconsistent with this possibility (cf. Vaslow 1963). We shall follow the model proposed by Buckingham (1957) and others and suppose that, for both positive and negative ions, the water dipoles point directly away from or towards the ion centre (see Outhwaite 1967). As regards the quadrupole moment, it is supposed that the charge distribution of each water molecule is axially symmetric about its dipole axis. Then on changing the sign of the ionic charge, while keeping the radius fixed, the ion–quadrupole energy term must change sign. It is positive for a cation and negative for an anion.

Now the most important contributions to the interaction energy of a single ion complex *in vacuo* as given by Muirhead-Gould and Laidler (1966) are associated with (1) ion–dipole forces, (2) ion-induced dipole forces, (3) ion–quadrupole forces, (4) ion-induced quadrupole forces (nothing whatever is known about the magnitude of these and so they will be neglected here), (5) dipole–dipole forces, (6) dipole-induced dipole forces, (7) dipole–quadrupole forces, (8) dispersion forces (these, according to Buckingham (1957), are relatively small, for if they were not the inert gases would be soluble in liquids like water and this is in disagreement with the results of Slater and Kirkwood (1931), Eley (1939), and Frank and Evans (1945)), and (9) charge-transfer forces (see Mulliken 1952*a*, 1952*b*; Eusuf and Laidler 1963; Kortüm 1965). In the following calculations only the forces (1), (2), (3), (5), (6), and (7) are considered; in any case, if we calculate the difference between the energy of an ion pair at separation R and that at infinite separation the dispersive and charge-transfer forces are small and tend to cancel out.

III. The Ion and its Attached Water Molecules *in Vacuo*

As a first step we shall calculate the interaction energy for a single monovalent ion complex *in vacuo* for both four- and six-coordinated ions. In each case the water molecules are in contact with the ion to which they belong and the effect of polarization is neglected in the first instance. Thus, for an ion of radius r_{i} and coordination number m the ion–water molecule interaction energy is

$$U_m = -\frac{me\mu_{\mathrm{w}}}{(r_{\mathrm{i}}+r_{\mathrm{w}})^2}+\frac{zem\Theta}{(r_{\mathrm{i}}+r_{\mathrm{w}})^3}, \tag{1}$$

where $z = 1$ for a cation and -1 for an anion. Here μ_{w} and Θ ($=\frac{1}{2}(\Theta_{\mathrm{a}}+\Theta_{\mathrm{b}})$ in the notation of Buckingham 1957) are the permanent dipole and quadrupole moments of the water molecules respectively.

To determine the interaction energy between the m coordination water molecules it is necessary to calculate the field at the centre of the typical water molecule and therefore to choose a model to describe the relative positions of the water molecules.

Thus, in the tetrahedral structure ($m = 4$) the water molecules are placed at alternate vertices of a cube of sides $2(r_1+r_\mathrm{w})/\sqrt{3}$ and a z axis is so chosen that it contains one water dipole and passes through the ion centre. For the octahedral structure ($m = 6$) the water molecules are placed on either side of the ion centre on three mutually perpendicular lines (one of which is taken as the z axis) that intersect at the ion centre.

The field at the centre of the water molecules is radial and given by

$$F_\mathrm{w} = \frac{e}{(r_1+r_\mathrm{w})^2} - \frac{15\sqrt{6}\,\mu_\mathrm{w}}{32(r_1+r_\mathrm{w})^3} + \frac{45\sqrt{6}\,z\Theta}{128(r_1+r_\mathrm{w})^4} \tag{2}$$

when $m = 4$, and by

$$F_\mathrm{w} = \frac{e}{(r_1+r_\mathrm{w})^2} - \frac{(1+6\sqrt{2})\mu_\mathrm{w}}{4(r_1+r_\mathrm{w})^3} + \frac{3(1+6\sqrt{2})z\Theta}{16(r_1+r_\mathrm{w})^4} \tag{3}$$

when $m = 6$.

Now the electrostatic energy V_m of the ion complex *in vacuo* can be determined by using the Güntelberg–Müller-type charging process (see Kirkwood 1934). In that case

$$V_m = \tfrac{1}{2}e\phi_0 - \tfrac{1}{2}\sum F_\mathrm{w}\mu_\mathrm{w} - \tfrac{1}{2}\sum\left(\tfrac{1}{2}\,\partial F_\mathrm{w}/\partial r\,\Theta\right), \tag{4}$$

where the summations are carried out over the m water molecules, and the potential at the ion centre is given by

$$\phi_0 = -\frac{m\mu_\mathrm{w}}{(r_1+r_\mathrm{w})^2} + \frac{mz\Theta}{(r_1+r_\mathrm{w})^3}. \tag{5}$$

On combining equations (2)–(5) we see that

$$V_m = U_m + U_m^*, \tag{6}$$

where

$$U_4^* = \frac{15\sqrt{6}\,\mu_\mathrm{w}^2}{16(r_1+r_\mathrm{w})^2} - \frac{45\sqrt{6}\,z\mu_\mathrm{w}\Theta}{32(r_1+r_\mathrm{w})^4} + \frac{45\sqrt{6}\,\Theta^2}{64(r_1+r_\mathrm{w})^5} \tag{7}$$

and

$$U_6^* = \frac{3(1+6\sqrt{2})\mu_\mathrm{w}^2}{4(r_1+r_\mathrm{w})^3} - \frac{9(1+6\sqrt{2})z\mu_\mathrm{w}\Theta}{8(r_1+r_\mathrm{w})^4} + \frac{9(1+6\sqrt{2})\Theta^2}{16(r_1+r_\mathrm{w})^5}. \tag{8}$$

Thus the electrostatic energy can be written as the sum of two terms U_m, the interaction of the ion with the attached water molecules, and U_m^*, the interaction energy between them.

The above equations are the same as those obtained by Buckingham (1957) but he omitted the quadrupole–quadrupole term, which turns out to be extremely small. Table 1 shows the relative magnitudes of the energy terms for some monatomic ions for both the tetrahedral and octahedral configurations. The ionic radii r_1 are those given by Pauling (1927).

We are now in a position to calculate the induced dipole moment μ_{wi} by making use of the relation

$$\mu_{\mathrm{wi}} = \alpha_{\mathrm{w}} F_{\mathrm{w}}, \tag{9}$$

where F_{w} is obtained from (2) or (3), as the case may be, by replacing the dipole moment μ_{w} by $\mu_{\mathrm{w}}+\mu_{\mathrm{wi}}$ and substituting it in equation (9). This enables us to calculate the energy terms given in Table 1 and to take into account the induced dipole moment.

TABLE 1

FIELD AT CENTRE OF TYPICAL WATER MOLECULE AND VARIOUS ENERGY TERMS FOR MONOVALENT IONS *in vacuo* AT 298°K

E_{id}, E_{iq}, E_{dd}, E_{dq}, and E_{qq} are the ion–dipole, ion–quadrupole, dipole–dipole, dipole–quadrupole, and quadrupole–quadrupole interactions respectively and F_{w} is the field at the centre of the water molecule. The contribution to the field and to the energy terms from the induced dipole moment is neglected. The odd rows correspond to $m = 4$ and the even rows to $m = 6$

Ion	r_{i} (Å)	Energy Terms (10^{-12} erg/ion)					$F_{\mathrm{w}}\times 10^{-6}$ (e.s.u.)
		E_{id}	E_{iq}	E_{dd}	E_{dq}	E_{qq}	
Li^+	0·78	−7·575	0·572	0·771	0·087	0·003	0·831
		−11·363	0·858	2·390	0·271	0·010	0·621
Na^+	0·98	−6·346	0·438	0·591	0·061	0·002	0·710
		−9·518	0·658	1·832	0·190	0·007	0·547
K^+	1·33	−4·812	0·290	0·391	0·035	0·001	0·552
		−7·219	0·434	1·210	0·109	0·003	0·445
Rb^+	1·49	−4·291	0·244	0·329	0·028	0·001	0·497
		−6·436	0·366	1·019	0·087	0·002	0·406
Cs^+	1·65	−3·850	0·207	0·279	0·023	0·001	0·450
		−5·774	0·311	0·866	0·070	0·002	0·373
F^-	1·33	−4·812	−0·290	0·391	−0·035	0·001	0·543
		−7·219	−0·434	1·210	−0·109	0·003	0·425
Cl^-	1·81	−3·473	−0·178	0·240	−0·018	0·000	0·404
		−5·210	−0·266	0·742	−0·057	0·001	0·332
Br^-	1·96	−3·168	−0·155	0·209	−0·015	0·000	0·371
		−4·752	−0·232	0·646	−0·047	0·001	0·309
I^-	2·19	−2·773	−0·127	0·171	−0·012	0·000	0·329
		−4·160	−0·190	0·529	0·036	0·001	0·278

Thus, the ion–(dipole + induced dipole) energy is

$$E_{\mathrm{id}} = -me(\mu_{\mathrm{w}}+\mu_{\mathrm{wi}})/(r_{\mathrm{i}}+r_{\mathrm{w}})^2 + \tfrac{1}{2}me\mu_{\mathrm{wi}}(r_{\mathrm{i}}+r_{\mathrm{w}})^2, \tag{10}$$

where the first term is the electrostatic interaction energy and the second term is the change in the internal energy of the induced dipoles due to the proton charge $+e$. Similarly, $E_{\mathrm{dd}}+E_{\mathrm{dq}}$ can be deduced from equation (7) (and (8)) by replacing the factor μ_{w} by $\mu_{\mathrm{w}}+\frac{1}{2}\mu_{\mathrm{wi}}$ and the factor μ_{w}^2 by $\mu_{\mathrm{w}}(\mu_{\mathrm{w}}+\mu_{\mathrm{wi}})$ and neglecting the quadrupole–quadrupole contribution. Table 2 shows the amended values of E_{id}, E_{dd}, E_{dq}, and F_{w} and gives the value of the induced dipole moment μ_{wi}.

As expected, a comparison of Tables 1 and 2 shows that the field intensity F_w is smaller when (1) the coordination number is larger, and (2) the induced dipole moment is taken into account. Also, it is seen that the dipole–dipole interaction energy is a little larger than the ion–quadrupole term and can be as much as 20% of the ion–dipole interaction. This alone does not invalidate the assumption made by Levine and Wrigley (1957) that "as a first approximation the interaction between adjacent water molecules inside a hydration shell may be neglected compared with that between the ion and a hydration molecule" since, in their calculations, it is only the change in the dipole–dipole energy associated with the reaction field that matters.

TABLE 2

FIELD F_w AND ENERGY TERMS E_{id}, E_{dd}, AND E_{dq} *in vacuo* AT 298°K FOR CASE WHERE INDUCED DIPOLE MOMENT μ_{wi} IS INCLUDED IN CALCULATIONS

Ion	Energy Terms (10^{-12} erg/ion)			μ_{wi} (debye)	$F_w \times 10^{-6}$ (e.s.u.)
	E_{id}	E_{dd}	E_{dq}		
Li^+	−9·989	1·263	0·115	1·172	0·699
	−13·671	3·361	0·326	0·747	0·445
Na^+	−8·139	0·926	0·079	1·040	0·619
	−11·344	2·535	0·226	0·706	0·420
K^+	−5·919	0·570	0·043	0·846	0·504
	−8·439	1·619	0·128	0·622	0·370
Rb^+	−5·192	0·467	0·034	0·773	0·460
	−7·458	1·342	0·101	0·584	0·348
Cs^+	−4·589	0·386	0·027	0·707	0·421
	−6·633	1·123	0·080	0·547	0·326
F^-	−5·890	0·567	−0·043	0·832	0·495
	−8·385	1·601	−0·127	0·595	0·354
Cl^-	−4·078	0·323	−0·022	0·641	0·382
	−5·914	0·942	−0·065	0·497	0·296
Br^-	−3·679	0·275	−0·018	0·594	0·354
	−5·358	0·811	−0·053	0·469	0·279
I^-	−3·172	0·220	−0·013	0·530	0·315
	−4·644	0·653	−0·040	0·425	0·255

In what follows the quadrupole moment of the water molecules will be neglected, since to include it in the calculation of the reaction field due to the aqueous medium would raise a number of new problems regarding the orientation of the water molecules about their dipole axes. This is a very complicated analysis (something along the lines followed by Vaslow 1963) and requires an *accurate* knowledge of the quadrupole tensor. In any case, it is felt that its contribution is small.

IV. THE ION AND ITS ATTACHED WATER MOLECULES EMBEDDED IN A DIELECTRIC MEDIUM

Since the ion complex is actually surrounded by an aqueous medium, other terms have to be considered. So far we have determined the interaction energy V_m *in vacuo*. We shall now calculate the work that has to be done to bring up the aqueous medium. According to Böttcher (1952) this is given by

$$W_m = -\frac{\epsilon-1}{8\pi}\int_V \boldsymbol{E}_0 . \boldsymbol{E}\,\mathrm{d}V\,, \tag{11}$$

where V is the volume of the dielectric, $\boldsymbol{E}_0$ the electric field at any point in the volume V before it is filled with the dielectric, and $\boldsymbol{E}$ the corresponding field in the dielectric medium $\epsilon = 78 \cdot 30$ after this operation. Following Levine and Rosenthal (1966) this work done can be written

$$W_m = -\frac{\epsilon-1}{8\pi}\int_S \psi_0 \frac{\partial \Psi_0}{\partial n}\,\mathrm{d}S\,, \tag{12}$$

where S is the surface bounding the volume V of the dielectric, $\partial/\partial n$ denotes differentiation along the normal to S drawn outwards from V, and the potentials ψ_0 and Ψ_0 are such that $\boldsymbol{E}_0 = -\nabla\psi_0$ and $\boldsymbol{E} = -\nabla\Psi_0$. If we apply the usual boundary conditions to this problem then, since the integral (12) vanishes on the outer boundary V, we see that

$$W_m = -\frac{1-\epsilon^{-1}}{8\pi}\int_{S*} \psi_1 \frac{\partial \Psi_1}{\partial n}\,\mathrm{d}S\,, \tag{13}$$

where S^* is the surface of the spherical cavity and ψ_{i} and Ψ_{i} are the potentials inside corresponding to ψ_0 and Ψ_0 outside.

Now the potential in the cavity of radius $a_0 = r_{\mathrm{i}} + 2r_{\mathrm{w}}$ may be written in the form

$$\Psi_{\mathrm{i}} = \sum_k \frac{e_k}{|\boldsymbol{r}-\boldsymbol{r}_k|} + \frac{1}{a_0}\sum_{n=0}^{\infty}\sum_{l=-n}^{n} B_{n,l}\left(\frac{r}{a_0}\right)^l \mathrm{P}_n^l(\cos\theta)\exp(il\phi)\,, \tag{14}$$

where the first term is the potential due to the set of charges e_k placed at $\boldsymbol{r} = \boldsymbol{r}_k$ and the second term is the reaction field ψ_{R} due to the presence of the outside medium. Hence the $\mathrm{P}_n^l(\cos\theta)$ represent the associated Legendre functions of the first kind and $B_{n,l}$ are a set of constants determined by the boundary conditions.

Using some of the results of Kirkwood (1934), Linderstrøm-Lang (1953), and Tanford and Kirkwood (1957) we find that, for $\max|\boldsymbol{r}_k| < r < a_0$,

$$\sum_k \frac{e_k}{|\boldsymbol{r}-\boldsymbol{r}_k|} = \frac{1}{a_0}\sum_{n=0}^{\infty}\sum_{l=-n}^{n} E_{n,l}\left(\frac{a_0}{r}\right)^{n+1}\mathrm{P}_n^l(\cos\theta)\exp(il\phi)\,, \tag{15}$$

where

$$E_{n,l} = \sum_k e_k(r_k/a_0)^n\,(-1)^l\,\mathrm{P}_n^{-l}(\cos\theta_k)\exp(-il\phi_k)\,, \tag{16}$$

and also that

$$B_{0,0} = -e(1-\epsilon^{-1}) \tag{17}$$

and

$$B_{n,l} = -\frac{(n+1)\epsilon}{(n+1)\epsilon+n}(1-\epsilon^{-1})E_{n,l}\,. \tag{18}$$

The contribution to the interaction energy from the aqueous medium must be a real quantity and so it is sufficient to consider only the values of $E_{n,l}$ for which $l \geqslant 0$. To begin with we have

$$E_{0,0} = B_{0,0} \tag{19}$$

and, for the tetrahedral structure, the numbers $E_{n,l}$ (with $n \geqslant 1$) are given by

$$E_{n,l} = \begin{cases} n\dfrac{\overset{*}{\mu}_{\mathrm{W}}}{a_0}\left(\dfrac{r_1+r_{\mathrm{W}}}{a_0}\right)^{n-1}(-1)^l\{\mathrm{P}_n^{-l}(1)+3\mathrm{P}_n^{-l}(-\tfrac{1}{3})\} & \text{if } \; l = 3, 6, 9, \ldots \\ 0 & \text{otherwise}, \end{cases} \tag{20}$$

where

$$\overset{*}{\mu}_{\mathrm{W}} = \mu_{\mathrm{W}}+\mu_{\mathrm{Wi}},$$

while, for the octahedral structure, the numbers $E_{n,l}$ (with $n \geqslant 1$) are given by

$$E_{n,l} = \begin{cases} n\dfrac{\overset{*}{\mu}_{\mathrm{W}}}{a_0}\left(\dfrac{r_1+r_{\mathrm{W}}}{a_0}\right)^{n-1}(-1)^l\{2\mathrm{P}_n^{-l}(1)+4\mathrm{P}_n^{-l}(0)\} & \text{if } \; n \text{ even and } l = 4, 8, 12, \ldots \\ 0 & \text{otherwise}. \end{cases} \tag{21}$$

Now the potential ψ_1 before the volume V is filled with dielectric is given by

$$\psi_1 = \sum_k e_k/|\boldsymbol{r}-\boldsymbol{r}_k| \tag{22}$$

and so, on substitution of equations (14)–(22) into (13) and making use of the usual addition formula for the Legendre polynomials, we find that

$$W_4 = -\tfrac{1}{2}e^2(1-\epsilon^{-1})/a_0$$
$$-\tfrac{1}{2}(1-\epsilon^{-1})\sum_{n=1}^{\infty}\frac{n^2(n+1)\,\epsilon(\overset{*}{\mu}{}_{\mathrm{W}}^2/a_0^3)}{(n+1)\epsilon+n}\left(\frac{r_1+r_{\mathrm{W}}}{a_0}\right)^{2n-2}\left(4+12\mathrm{P}_n(-\tfrac{1}{3})\right), \tag{23}$$

where the first term is the Born energy of the ion of radius a_0 and the second term represents the interaction of the water dipoles with their "images" in the aqueous medium. Similarly,

$$W_6 = -\tfrac{1}{2}e^2(1-\epsilon^{-1})/a_0$$
$$-\tfrac{1}{2}(1-\epsilon^{-1})\sum_{n=1}^{\infty}\frac{n^2(n+1)\,\epsilon(\overset{*}{\mu}{}_{\mathrm{W}}^2/a_0^3)}{(n+1)\epsilon+n}\left(\frac{r_1+r_{\mathrm{W}}}{a_0}\right)^{2n-2}\left(6\{1+(-1)^n\}+24\mathrm{P}_n(0)\right). \tag{24}$$

Now it turns out that

$$W_m = \tfrac{1}{2}e\phi_{\mathrm{r}}-\tfrac{1}{2}\sum \boldsymbol{\mu}_{\mathrm{W}}.\boldsymbol{F}_{\mathrm{r}}, \tag{25}$$

where ϕ_{r} and $\boldsymbol{F}_{\mathrm{r}}$ are respectively the contributions to the potential at the ion centre and to the field at the typical water molecule from the aqueous medium. It follows that W_m is the energy of charging up the ion and the dipoles against their respective reaction fields. Now the change in internal energy of the induced dipole is given by

$\frac{1}{2}\sum \boldsymbol{\mu}_{\mathrm{wi}}.\boldsymbol{F}_{\mathrm{r}}$ and so the total electrostatic energy is obtained from V_m+W_m by replacing the factor μ_{w} by $\mu_{\mathrm{w}}+\frac{1}{2}\mu_{\mathrm{wi}}$ and the factor μ_{w}^2 (and $\overset{*}{\mu}{}_{\mathrm{w}}^2$ in W_m) by $\mu_{\mathrm{w}}(\mu_{\mathrm{w}}+\mu_{\mathrm{wi}})$.

The data in Table 3 show that the reaction field F_{r} of the ion complex plays a significant part in the determination of the free energy of hydration of an ion complex. (Some further calculations were carried out and it was found that, for $m = 4$, $\Theta = 0$ and (1) $a_0 = 3{\cdot}09$ Å, $\frac{1}{2}\sum \boldsymbol{\mu}_{\mathrm{w}}.\boldsymbol{F}_{\mathrm{r}} = 31{\cdot}98$, (2) $a_0 = 3{\cdot}59$ Å, $\frac{1}{2}\sum \boldsymbol{\mu}_{\mathrm{w}}.\boldsymbol{F}_{\mathrm{r}} = 2{\cdot}69$, and (3) $a_0 = 4{\cdot}09$ Å, $\frac{1}{2}\sum \boldsymbol{\mu}_{\mathrm{w}}.\boldsymbol{F}_{\mathrm{r}} = 0{\cdot}68$ in units of 10^{-12} erg/ion.) All of the

TABLE 3

FIELD INTENSITY $F_{\mathrm{w}}+F_{\mathrm{r}}$ AT CENTRE OF TYPICAL WATER MOLECULE, INDUCED DIPOLE MOMENT μ_{wi}, AND ENERGY TERMS E_{id}, E_{dd}, E_{dq}, AND W_{mi}

W_{mi} is the energy of charging the dipoles and quadrupoles against their reaction field

Ion	Born Energy	Energy Terms (10^{-12} erg/ion) E_{id}	E_{dd}	E_{dq}	W_{mi}	μ_{wi} (debye)	$(F_{\mathrm{w}}+F_{\mathrm{r}})$ $\times 10^{-6}$ (e.s.u.)
Li⁺	−3·215	−10·961	1·461	0·126	−2·334	1·645	0·979
		−14·448	3·688	0·344	−1·782	0·999	0·595
Na⁺	−3·043	−8·978	1·082	0·087	−2·236	1·526	0·909
		−12·088	2·822	0·241	−1·898	0·994	0·591
K⁺	−2·783	−6·566	0·675	0·048	−2·056	1·341	0·798
		−9·097	1·840	0·138	−2·011	0·958	0·570
Rb⁺	−2·678	−5·768	0·555	0·038	−1·978	1·267	0·754
		−8·072	1·537	0·109	−2·035	0·936	0·557
Cs⁺	−2·581	−5·105	0·462	0·030	−1·906	1·200	0·714
		−7·205	1·295	0·087	−2·047	0·912	0·543
F⁻	−2·783	−6·544	0·672	−0·048	−2·034	1·324	0·788
		−9·035	1·819	−0·137	−1·966	0·926	0·551
Cl⁻	−2·491	−4·539	0·386	−0·024	−1·827	1·129	0·672
		−6·441	1·093	−0·070	−2·023	0·870	0·518
Br⁻	−2·412	−4·096	0·331	−0·020	−1·771	1·078	0·642
		−5·850	0·945	−0·058	−2·024	0·850	0·506
I⁻	−2·299	−3·533	0·265	−0·015	−1·693	1·009	0·600
		−5·085	0·765	−0·044	−2·015	0·819	0·488

authors mentioned previously have omitted this term, have taken as the radius of the ion complex $a_0 = r_{\mathrm{i}}+2r_{\mathrm{w}}$, and have compensated for the difference between the theoretical and experimental results in a number of rather arbitrary ways. Thus, for example, Bernal and Fowler (1933) used a large energy of making a hole in the water, Latimer, Pitzer, and Slansky (1939) added an arbitrary length to the ionic radii, and Buckingham (1957) accounted for the difference by introducing a rather large quadrupole moment for the attached water molecules. However, Coulson and Eisenberg (1966) took into account a large number of water molecules and, for an ice structure, estimated the contribution to the electric field and to the induced dipole moment at the centre of an ice molecule from 85 nearest neighbours. These contributions are of the same order of magnitude as those given here in the presence of an ion in solution and show the importance of taking into account the induced dipole moment.

The total electrostatic energy V_{el} of the four-(or six-)coordinated ion complexes is given by

$$V_{\mathrm{el}} = E_{\mathrm{id}} + E_{\mathrm{iq}} + E_{\mathrm{dd}} + E_{\mathrm{dq}} + E_{\mathrm{qq}} + W_{m\mathrm{i}}\,\mu_{\mathrm{w}}/\overset{*}{\mu}_{\mathrm{w}} - \tfrac{1}{2}e^2(1-\epsilon^{-1})/a_0 \tag{26}$$

and is listed in Table 4.

The energy of hydration of an ion depends on the choice of a zero energy level. Thus, for example, Eley and Evans (1938) considered a hypothetical series of steps leading to the transfer of an ion from a dilute gas to a dilute aqueous solution, while Noyes (1962, 1964) discharged the gaseous ion, hydrated the resulting neutral species (i.e. monatomic inert species of the same radius as the ion of interest), and then recharged it. In an alternative treatment, Stokes (1964) used a simple electrostatic model in which he made use of the crystal radii of the ions when in water and the van der Waals radii calculated from those of the iso-electronic noble gases by the quantum mechanical scaling principle when in the gas phase. He used these to compare the experimental free energies of hydration of ions of noble gas structure with the values calculated from the electrostatic model. In this model Stokes used a technique developed by Hasted, Ritson, and Collie (1948) in which he assumed that the effective dielectric constant ranged from 5 at the ion to > 78 over one or two layers (each 2·8 Å thick) depending on the charge. His results (as are those of Noyes 1962, 1964) are in good agreement with the known data.

TABLE 4

ELECTROSTATIC ENERGY V_{el} OF FOUR-COORDINATED ION COMPLEXES WHEN $a_0 = r_{\mathrm{i}} + 2r_{\mathrm{w}}$

Ion	$W_{m\mathrm{i}}\,\mu_{\mathrm{w}}/\overset{*}{\mu}_{\mathrm{w}}$	μ_{wi} (debye)	V_{el} (kcal/mole)	Experimental Energy of Hydration†
$\mathrm{Li^+}$	−17·71	1·65	−190	−122 (−122)
$\mathrm{Na^+}$	−17·57	1·53	−167	−98 (−98)
$\mathrm{K^+}$	−17·09	1·34	−137	−81 (−80)
$\mathrm{Rb^+}$	−16·83	1·27	−126	−76 (−76)
$\mathrm{Cs^+}$	−16·57	1·20	−117	−68 (−68)
$\mathrm{F^-}$	−17·01	1·32	−146	−99 (−90)
$\mathrm{Cl^-}$	−16·27	1·13	−114	−71 (−76)
$\mathrm{Br^-}$	−16·04	1·08	−107	−65 (−69)
$\mathrm{I^-}$	−15·71	1·01	−98	−57 (−60)

† From Randles (1956), with more recent values from Noyes (1964) in parentheses.

Now, according to Eley and Evans (1938), the energy of reorientation of the water molecules near a positive ion is 8 kcal/mole and near a negative ion is 20 kcal/mole. If we accept these values here and add them to the electrostatic energy V_{el} listed in Table 4 then we can obtain a good estimate of the free energy of hydration of both cations and anions by adding on 64 kcal/mole.

One of the main differences between the calculations on the discrete model and those of most other authors is the appearance of the term $W_{m\mathrm{i}}\,\mu_{\mathrm{w}}/\overset{*}{\mu}_{\mathrm{w}}$, which is the work done in bringing up the aqueous medium plus the corresponding change in the internal energy of the attached water dipoles. The importance of this term was pointed out by Böttcher (1952), Levine and Wrigley (1957), and Levine and Rosenthal (1966). It follows that both the radius of the ion, here taken to be the Pauling (1927) radius, and the size of the cavity are critical. Thus, for example, in the hypothetical cycle discussed by Eley and Evans (1938) this energy is omitted and, as it happens, it would tend to cancel out round the cycle. In essence, they say that the difference between the energy of bringing up the dielectric to the tetrahedral group of five water dipoles and to the ion with its four attached water dipoles is small since the change in the size of the hole into which the groups fit is negligible. This is only an approximation and in a more refined treatment this energy and the effects of the induced dipole moment should be taken into account.

Recently, Fumi and Tosi (1964) suggested that the actual radii of the monovalent ions are different from those proposed by Pauling (1927); however, since there is no known method of calculating the cavity size (see Linder and Hoernschemeyer 1967), there is little point in using these values at such an early stage in the theory.

V. ACKNOWLEDGMENT

The author wishes to thank the referee for pointing out the papers by Fumi and Tosi (1964) and Stokes (1964).

VI. REFERENCES

BERNAL, J. D., and FOWLER, R. H. (1933).—*J. chem. Phys.* **1**, 515.

BORN, M. (1920).—*Z. Phys.* **1**, 45.

BÖTTCHER, C. F. (1952).—"Theory of Electric Polarisation." (Elsevier: Amsterdam.)

BUCKINGHAM, A. D. (1957).—*Discuss. Faraday Soc.* **24**, 151.

CAMPBELL, E. S. (1952).—*J. chem. Phys.* **20**, 1411.

COBBLE, J. W. (1953).—*J. chem. Phys.* **21**, 1443, 1446, 1451.

CONNICK, R. E., and POWELL, R. E. (1953).—*J. chem. Phys.* **21**, 2206.

COULSON, C. A., and EISENBERG, D. (1966).—*Proc. R. Soc.* A. **291**, 445, 454.

DUNCAN, A., and POPLE, J. (1953).—*Trans. Faraday Soc.* **49**, 217.

ELEY, D. D. (1939).—*Trans. Faraday Soc.* **35**, 1281.

ELEY, D. D., and EVANS, M. G. (1938).—*Trans. Faraday Soc.* **34**, 1093.

EUSUF, M., and LAIDLER, K. J. (1963).—*Trans. Faraday Soc.* **59**, 2750.

FRANK, H. S., and EVANS, M. W. (1945).—*J. chem. Phys.* **13**, 507.

FUMI, F. G., and TOSI, M. P. (1964).—*J. Phys. Chem. Solids* **25**, 31.

HASTED, J. B., RITSON, D. M., and COLLIE, C. H. (1948).—*J. chem. Phys.* **16**, 1.

KIRKWOOD, J. G. (1934).—*J. chem. Phys.* **2**, 351.

KORTÜM, G. (1965).—"Treatise on Electrochemistry." (Elsevier: Amsterdam.)

LAIDLER, K. J. (1956).—*Can. J. Chem.* **34**, 1107.

LATIMER, W. M., PITZER, K. S., and SLANSKY, C. M. (1939).—*J. chem. Phys.* **7**, 108.

LEVINE, S., and BELL, G. M. (1962).—*In* "Trieste Symposium on Electrolytes". (Ed. G. Pesce.) (Pergamon Press: London.)

LEVINE, S., and ROSENTHAL, D. K. (1966).—*In* "Chemical Physics of Ionic Solutions". (Eds. B. E. Conway and R. G. Barradas.) (Wiley: New York.)

LEVINE, S., and WRIGLEY, H. E. (1957).—*Discuss. Faraday Soc.* **24**, 43, 73.

LINDER, B., and HOERNSCHEMEYER, D. (1967).—*J. chem. Phys.* **46**, 784.

LINDERSTRØM-LANG, K. (1953).—*C.r. Trav. Lab. Carlsberg* **28**, 281.

McWEENY, R., and OHNO, K. A. (1960).—*Proc. R. Soc.* A **255**, 367.

MUIRHEAD-GOULD, J. S., and LAIDLER, K. J. (1966).—*In* "Chemical Physics of Ionic Solutions". (Eds. B. E. Conway and R. G. Barradas.) (Wiley: New York.)

MULLIKEN, R. S. (1952*a*).—*J. Am. chem. Soc.* **74**, 811.

MULLIKEN, R. S. (1952*b*).—*J. phys. Chem.* **56**, 801.

NOYES, R. M. (1962).—*J. Am. chem. Soc.* **84**, 513.

NOYES, R. M. (1964).—*J. Am. chem. Soc.* **86**, 971.

OUTHWAITE, C. (1967).—Ph.D. Thesis, Manchester University.

PAULING, L. (1927).—*J. Am. chem. Soc.* **49**, 765.

POWELL, R. E., and LATIMER, W. M. (1951).—*J. chem. Phys.* **19**, 1139.

RANDLES, J. E. B. (1956).—*Trans. Faraday Soc.* **52**, 1573.

ROSS, D. K. (1968*a*).—The dipole moment of water in the first hydration shell of a monovalent ion. *Can. J. Phys.* (in press).

ROSS, D. K. (1968*b*).—*Aust. J. Phys.* **21**, 587.

ROSS, D. K., and LEVINE, S. (1968).—*Aust. J. Phys.* **21**, 571.

ROWLINSON, J. S. (1951).—*Trans. Faraday Soc.* **47**, 120.

SLATER, J. C., and KIRKWOOD, J. G. (1931).—*Phys. Rev.* **37**, 682.

STOGRYN, D. E., and STOGRYN, A. P. (1966).—*Molec. Phys.* **11**, 371.

STOGRYN, D. E., and STOGRYN, A. P. (1967).—Douglas Research Rep. No. G-50401.

STOKES, R. H. (1964).—*J. Am. chem. Soc.* **86**, 979.

TANFORD, C., and KIRKWOOD, J. G. (1957).—*J. Am. chem. Soc.* **79**, 5333.

VASLOW, F. (1963).—*J. phys. Chem.* **67**, 2773.

VERWEY, E. J. W. (1941).—*Recl Trav. chim. Pays-Bas Belg.* **60**, 887.

VERWEY, E. J. W. (1942).—*Recl Trav. chim. Pays-Bas Belg.* **61**, 127.

WEBB, J. T. (1926).—*J. Am. chem. Soc.* **48**, 2589.

THE FORMAL NONEQUILIBRIUM THEORY OF PARTIALLY IONIZED AND/OR NONUNIFORM GAS MIXTURES

By E. L. Bydder* and B. S. Liley*

[*Manuscript received March* 12, 1968]

Summary

Starting from Boltzmann-like equations, moment equations for a general gas mixture are developed. The equations are closed, and the collision integrals evaluated, by using Grad's 13-moment approximations for the velocity distribution functions. The collision integrals are determined for all possible types of binary encounters, which include recombination and attachment, spontaneous fission and natural decay, charge exchange and elastic collisions, and excitation and fission- and fusion-like processes. The derivation of transport relationships is considered, while the extension of the results to include such direct radiative phenomena as absorption, photo-ionization, stimulated emission, and Compton scattering is also briefly discussed.

CONTENTS

I. Introduction .. 610

II. General equations .. 611
  (*a*) Basic equations and definitions .. 611
  (*b*) Fundamental equations of change .. 613
  (*c*) Collision integrals .. 614
  (*d*) Closure of equations of change .. 615

III. Collision integrals .. 616
  (*a*) Collision dynamics .. 616
  (*b*) Transformations .. 617
  (*c*) Integration over the azimuth .. 618
  (*d*) Integration over x velocity space .. 619
  (*e*) The coefficients c_{js} .. 622

IV. Special cases .. 623
  (*a*) Natural decay and spontaneous fission .. 625
  (*b*) Recombination and attachment .. 626
  (*c*) Charge exchange and elastic collisions .. 627
  (*d*) General inelastic collision .. 628

V. Reduction of equations to practical forms .. 631

VI. Discussion .. 634

VII. References .. 636

---

* Department of Engineering Physics, Research School of Physical Sciences, Australian National University, P.O. Box 4, Canberra, A.C.T. 2600.

Aust. J. Phys., 1968, 21, 609–36

I. Introduction

In deriving equations for a partially ionized or nonuniform gas a multitude of collision phenomena must be taken into account. Of these the most important are elastic and inelastic collisions, including collisions of the second kind and fission- and fusion-like processes, recombination and attachment, and charge exchange. Furthermore, in any exact treatment the natural decay and spontaneous fission of excited states, the absorption of radiation, and a multitude of other radiative phenomena must also be included. Add to this the nonequilibrium properties of such a mixture and the interaction with electric and magnetic fields and the problem becomes extremely complex.

Fortunately, in a relatively dilute mixture all collision phenomena are essentially of a binary nature, so-called three-body processes being simply a single two-body collision followed by another such collision in competition with a spontaneous fission. Because of this all the processes mentioned in the first paragraph are mathematically similar and may be dealt with in an identical manner. Furthermore, in developing equations of change for the system each excited state of an atom, molecule, or ion may be treated as a particular particle type, the equations for each particle type being formally the same. Therefore, at least mathematically, the development of equations for a relatively dilute gas is a well-defined and logical problem. Ignoring the direct interaction of radiation with particles, the object of this paper is to develop such equations. However, primarily due to notational complications and the multitude of physical phenomena possible, the reduction of these equations to useful practical forms is extremely difficult. Nevertheless, conservation-type equations and transport relationships may be formally obtained and these aspects are also discussed.

General equations for monatomic gas mixtures have been developed by various authors (Kolodner 1950; Herdan and Liley 1960; Liley 1963). However, in such treatments elastic collisions only were considered. On the other hand, certain authors have studied the effects of inelastic processes on transport phenomena for a variety of special cases. For instance, Engelhardt and Phelps (1963) have studied the effects in a Townsend-type discharge, while Wang-Chang and Uhlenbeck (1951) have investigated the effects in a polyatomic nonionized simple gas. However, in addition to being more general, the approach in the present paper to inelastic collision phenomena is entirely different to that of other authors. In essence the method is to extend the analysis of Herdan and Liley (and Kolodner) for monatomic gas mixtures to the case in which inelastic processes are of importance. In particular, equations of change for various moments of the particle velocity distribution functions are generated. In principle, the associated collision integrals are evaluated by expanding the distribution functions in terms of multidimensional Hermite polynomials, although in practice only the first few terms of these integrals, corresponding to Grad's (1949) 13-moment approximations are determined. These equations are then closed by using Grad's 13-moment approximation to express otherwise physically indeterminate moments in terms of significant physical quantities. In carrying this analysis through, the effects of electric and magnetic fields, spatial gradients, and differences in particle temperatures are taken into account.

Since the general form of the equations is essentially identical with that developed by Herdan and Liley for a simple monatomic mixture, as is the form of the elastic collision integrals, the prime object of this paper is to determine general expressions for the inelastic integrals. Unfortunately, the derivation of these is somewhat tedious and therefore only an outline of the method and the final results are presented here, the details being given elsewhere (Bydder and Liley 1967). In Section II the derivation of the relevant equations of change is briefly summarized and the notation employed adequately defined. In Section III the collision integrals are evaluated, while in Section IV special and limiting cases of these are derived. Practical forms of the results, including conservation equations, transport relationships, Ohm's law, and equilibrium solutions are briefly discussed in Section V.

II. General Equations

(a) *Basic Equations and Definitions*

Each particle present in a general gas mixture is typed according to its mass, charge, and internal energy (assumed quantized). For each such particle type j a velocity distribution function $f_j(\boldsymbol{x},\boldsymbol{c},t)$, may be defined. Ignoring subscripts, these distribution functions satisfy the "Maxwell–Boltzmann" equations

$$\frac{\partial f}{\partial t}+\boldsymbol{c}.\frac{\partial f}{\partial \boldsymbol{x}}+(\boldsymbol{a}+\boldsymbol{c}\times\boldsymbol{b}).\frac{\partial f}{\partial \boldsymbol{c}}=\frac{\delta f}{\delta t}, \tag{1}$$

where

$$\boldsymbol{a}=(e/m)\boldsymbol{E}+\boldsymbol{g}, \qquad \boldsymbol{b}=(e/m)\boldsymbol{B},$$

$\boldsymbol{c}$ is the velocity vector, $\boldsymbol{x}$ the position vector, t the time, e the particle charge, m the particle mass, $\boldsymbol{g}$ any non-electromagnetic body force, $\boldsymbol{E}$ the electric field vector, $\boldsymbol{B}$ the magnetic induction vector, $\delta f/\delta t$ the "collision" term, $\partial/\partial \boldsymbol{z}\equiv \boldsymbol{e}^{\lambda}\,\partial/\partial z^{\lambda}$ the gradient operator, and $\boldsymbol{e}^{\lambda}$ an appropriate set of base vectors.

There is one such equation for each particle type present. In developing equations of change it is convenient to define a "peculiar" velocity $\boldsymbol{w}_j$ by the equation

$$\boldsymbol{w}_j=\boldsymbol{c}-\boldsymbol{v}_j,$$

where $\boldsymbol{v}_j$ is a function of $\boldsymbol{x}$ and t but may be otherwise unspecified. In practice, however, it is usual to take $\boldsymbol{v}_j$ equal to $\boldsymbol{v}_0$, the mean mass velocity of the system as a whole. Multiplying equation (1), applicable to particles type j, by any tensor (absolute) function $\psi_j(\boldsymbol{w}_j)$ and integrating over velocity space, a general equation of change is obtained. Ignoring subscripts, this equation may be written in the form (cf. Chapman and Cowling 1952, Ch. 18 and p. 49)

$$\frac{\partial n\langle\psi\rangle}{\partial t}+\frac{\partial}{\partial \boldsymbol{x}}.n\langle\boldsymbol{c}\psi\rangle-n\Big\langle\Big(\boldsymbol{f}+\boldsymbol{w}\times\boldsymbol{b}-\boldsymbol{w}.\frac{\partial\boldsymbol{v}}{\partial\boldsymbol{x}}\Big).\frac{\partial\psi}{\partial\boldsymbol{w}}\Big\rangle=I(\psi), \tag{2}$$

where

$$n\langle\psi\rangle=\int f(\boldsymbol{x},\boldsymbol{c},t)\,\psi(\boldsymbol{w})\,\mathrm{d}\boldsymbol{c}, \tag{3}$$

$$\boldsymbol{f}=\boldsymbol{a}+\boldsymbol{v}\times\boldsymbol{b}-\frac{\mathrm{d}\boldsymbol{v}}{\mathrm{d}t}, \qquad \frac{\mathrm{d}}{\mathrm{d}t}\equiv\frac{\partial}{\partial t}+\boldsymbol{v}.\frac{\partial}{\partial\boldsymbol{x}},$$

$$\frac{\partial}{\partial \boldsymbol{x}}\cdot \equiv \boldsymbol{e}^{\lambda}\cdot\frac{\partial}{\partial x^{\lambda}}, \qquad\qquad I(\psi) \equiv \int \psi \frac{\delta f}{\delta t}\,\mathrm{d}\boldsymbol{c},$$

n is the particle number density, and $\frac{\partial}{\partial \boldsymbol{x}}\cdot$ the divergence operator.

The velocity space averaged functions $n\langle\psi\rangle$ are referred to as moments of f. Those moments of interest in the subsequent analysis are

$\rho \equiv n\langle m\rangle$	particle mass density;
$U \equiv n\langle \mathscr{E}\rangle$	internal energy density, $\mathscr{E}$ being the internal energy per particle;
$\boldsymbol{u} \equiv \langle \boldsymbol{w}\rangle$	"mean" particle velocity;
$\boldsymbol{p} \equiv n\langle m\boldsymbol{w}\boldsymbol{w}\rangle$	"stress" tensor;
$p \equiv n\langle \frac{1}{3}mw^2\rangle$	"hydrostatic" pressure;
$\{\boldsymbol{p}\} \equiv n\langle m\{\boldsymbol{w}\boldsymbol{w}\}\rangle$	"nonhydrostatic" component of the "stress" tensor;
$\boldsymbol{q} \equiv n\langle \frac{1}{2}m\boldsymbol{w}w^2\rangle$	"thermal energy" flux vector;
$\boldsymbol{H} \equiv n\langle m\boldsymbol{w}\boldsymbol{w}\boldsymbol{w}\rangle$	un-named;
$\boldsymbol{h} \equiv n\langle m\boldsymbol{w}\{\boldsymbol{w}\boldsymbol{w}\}\rangle$	un-named;
$\boldsymbol{l} \equiv n\langle \frac{1}{2}mw^2\boldsymbol{w}\boldsymbol{w}\rangle$	un-named.

Inverted commas are used in naming these moments since they are defined with respect to a frame moving with an arbitrary velocity $\boldsymbol{v}_j$, and do not, therefore, necessarily correspond to the true physical quantities.

The bracket symbol $\{\ \}$ used in the definition of the "nonhydrostatic" component of the "stress" tensor is of general significance. If $\boldsymbol{T}$ is any second rank tensor then

$$\{\boldsymbol{T}\} \equiv \tfrac{1}{2}(\boldsymbol{T}+\overline{\boldsymbol{T}})-\tfrac{1}{3}\boldsymbol{I}\boldsymbol{I}:\boldsymbol{T},$$

where $\boldsymbol{I} \equiv \boldsymbol{e}^{\lambda}\boldsymbol{e}_{\lambda}$ is a unit tensor (or idemfactor), $\boldsymbol{e}^{\lambda}$ and $\boldsymbol{e}_{\lambda}$ being an appropriate set of reciprocal base vectors,

$$\boldsymbol{T} = T^{\lambda\mu}\boldsymbol{e}_{\mu}\boldsymbol{e}_{\lambda}, \qquad \text{and} \qquad \overline{\boldsymbol{T}} = T^{\mu\lambda}\boldsymbol{e}_{\mu}\boldsymbol{e}_{\lambda}.$$

In particular,

$$\{\boldsymbol{w}\boldsymbol{w}\} \equiv \boldsymbol{w}\boldsymbol{w}-\tfrac{1}{3}\boldsymbol{I}w^2.$$

Other general definitions of interest are

$$\boldsymbol{v}_0 = \rho^{-1}\sum_j \rho_j\langle \boldsymbol{c}_j\rangle \qquad \text{mean mass velocity,}$$

$$\rho = \sum_j \rho_j \qquad \text{mass density,}$$

$$\boldsymbol{r} = \boldsymbol{q}-\tfrac{5}{2}p\boldsymbol{u} \qquad \text{heat flux vector.}$$

We have also

$$p = nkT,$$

where k is Boltzmann's constant and T is the kinetic "temperature" as defined by this relationship,

$$\boldsymbol{p} = \{\boldsymbol{p}\} + p\boldsymbol{I}, \qquad \text{and} \qquad \boldsymbol{H} = \boldsymbol{h} + \tfrac{2}{3}q\boldsymbol{I}.$$

Concerning other aspects of the tensor notation employed, the dot product between two tensors $\boldsymbol{A}$ and $\boldsymbol{T}$ is

$$\boldsymbol{A}.\boldsymbol{T} = A^{\alpha\ldots\beta\gamma\delta}T^{\zeta\rho\nu\ldots\epsilon}\boldsymbol{e}_\alpha\ldots\boldsymbol{e}_\gamma(\boldsymbol{e}_\delta.\boldsymbol{e}_\zeta)\boldsymbol{e}_\rho\ldots\boldsymbol{e}_\epsilon$$

and the double dot product is

$$\boldsymbol{A}:\boldsymbol{T} = A^{\alpha\ldots\beta\gamma\delta}T^{\zeta\rho\nu\ldots\epsilon}\boldsymbol{e}_\alpha\ldots{}_\beta(\boldsymbol{e}_\gamma.\boldsymbol{e}_\rho)(\boldsymbol{e}_\delta.\boldsymbol{e}_\zeta)\boldsymbol{e}_\nu\ldots\boldsymbol{e}_\epsilon.$$

The cross product between a vector $\boldsymbol{V}$ and a tensor $\boldsymbol{T}$ is determined as

$$\begin{aligned}\boldsymbol{V}\times\boldsymbol{T} &= T^{\alpha\beta\gamma\ldots}(\boldsymbol{V}\times\boldsymbol{e}_\alpha)\boldsymbol{e}_\beta\boldsymbol{e}_\gamma\ldots\\ &\neq \boldsymbol{T}\times\boldsymbol{V} = T^{\ldots\alpha\beta\gamma}\ldots\boldsymbol{e}_\alpha\boldsymbol{e}_\beta(\boldsymbol{e}_\gamma\times\boldsymbol{V}).\end{aligned}$$

It should also be noted that Greek suffixes are used to denote tensor components, a double suffix summation convention applying. On the other hand, Roman suffixes are used to denote particle type, any associated summation being explicity indicated.

(b) *Fundamental Equations of Change*

Taking ψ equal to m, $m\boldsymbol{w}$, $\frac{1}{2}mw^2$, and $\mathscr{E}$ respectively, equation (2) becomes alternatively the continuity, momentum, translational thermal energy, and internal heat energy equation. Ignoring subscripts, the equations are

$$\frac{\partial\rho}{\partial t} + \frac{\partial}{\partial\boldsymbol{x}}.(\rho\boldsymbol{u}+\rho\boldsymbol{v}) = I(m), \tag{4}$$

$$\frac{\partial\rho\boldsymbol{u}}{\partial t} + \frac{\partial}{\partial\boldsymbol{x}}.(\rho\boldsymbol{v}\boldsymbol{u}+\boldsymbol{p}) - \rho\boldsymbol{f} - \rho\boldsymbol{u}\times\boldsymbol{b} + \rho\boldsymbol{u}.\frac{\partial\boldsymbol{v}}{\partial\boldsymbol{x}} = I(m\boldsymbol{w}), \tag{5}$$

$$\frac{\partial\frac{3}{2}p}{\partial t} + \frac{\partial}{\partial\boldsymbol{x}}.(\tfrac{3}{2}p\boldsymbol{v}+\boldsymbol{q}) - \rho\boldsymbol{f}.\boldsymbol{u} + \boldsymbol{p}:\frac{\partial\boldsymbol{v}}{\partial\boldsymbol{x}} = I(\tfrac{1}{2}mw^2), \tag{6}$$

$$\frac{\partial U}{\partial t} + \frac{\partial}{\partial\boldsymbol{x}}.(U\boldsymbol{u}+U\boldsymbol{v}) = I(\mathscr{E}). \tag{7}$$

The derivation of these equations is straightforward and needs no comment. Again, taking ψ equal to $m\{\boldsymbol{w}\boldsymbol{w}\}$ and $\frac{1}{2}m\boldsymbol{w}w^2$, equations for the "nonhydrostatic" component of the "stress" tensor and the "thermal" energy flux vector may be obtained. These are

$$\frac{\partial\{\boldsymbol{p}\}}{\partial t} + \frac{\partial}{\partial\boldsymbol{x}}.(\boldsymbol{v}\{\boldsymbol{p}\}+\boldsymbol{h}) - 2\rho\{\boldsymbol{f}\boldsymbol{u}\} - 2\{\{\boldsymbol{p}\}\times\boldsymbol{b}\} + 2\left\{\boldsymbol{p}.\frac{\partial\boldsymbol{v}}{\partial\boldsymbol{x}}\right\} = I(m\{\boldsymbol{w}\boldsymbol{w}\}), \tag{8}$$

$$\frac{\partial\boldsymbol{q}}{\partial t} + \frac{\partial}{\partial\boldsymbol{x}}.(\boldsymbol{v}\boldsymbol{q}+\boldsymbol{l}) - \boldsymbol{f}.\boldsymbol{p} - \tfrac{3}{2}p\boldsymbol{f} - \boldsymbol{q}\times\boldsymbol{b} + \boldsymbol{q}.\frac{\partial\boldsymbol{v}}{\partial\boldsymbol{x}} + \boldsymbol{H}:\frac{\partial\boldsymbol{v}}{\partial\boldsymbol{x}} = I(\tfrac{1}{2}m\boldsymbol{w}w^2). \tag{9}$$

In terms of physically significant variables, equations (4)–(9) are the basic equations governing the behaviour of the gas mixture, there being an identical set for each particle type present. However, in certain instances various combinations of these equations may be of more use. In particular, an equation for r, derived by subtracting $\frac{5}{2}kT/m$ times equation (5) from equation (9), is of more direct value than (9) in the derivation of transport relationships.

(c) *Collision Integrals*

For the equations of the preceding subsection to be of value the "collision" terms must be determined explicitly. As implied in the Introduction, and as discussed further in the next two sections, only binary collisions need be considered. Consider a collision between two particles of types k and l such that

$$k+l \rightarrow k'+l'\,.$$

Let the differential cross section for such a collision be $\mathrm{d}\sigma_{kl}^{k'l'}$. Then the number of such collisions per unit volume per unit time involving those particles with velocities in the ranges $(\boldsymbol{c}_k, \boldsymbol{c}_k+\mathrm{d}\boldsymbol{c}_k)$, $(\boldsymbol{c}_l, \boldsymbol{c}_l+\mathrm{d}\boldsymbol{c}_l)$ is

$$f_k(\boldsymbol{c}_k)\,f_l(\boldsymbol{c}_l)\,g_{kl}\,\mathrm{d}\sigma_{kl}^{k'l'}\,\mathrm{d}\boldsymbol{c}_k\,\mathrm{d}\boldsymbol{c}_l \qquad \text{where} \qquad g_{kl} = |\boldsymbol{c}_k-\boldsymbol{c}_l|\,.$$

If $\Delta_{kl}^{k'l'}(\psi_j)$ denotes the change in ψ_j due to such a collision then the total rate of change, per unit volume, of ψ_j due to collisions between particles of types k and l is

$$I_{kl}(\psi_j) = \sum_{(k'l')} I_{kl}^{k'l'}(\psi_j)\,, \tag{10}$$

where

$$I_{kl}^{k'l'}(\psi_j) = \int f_k\,f_l\,\Phi_{kl}^{k'l'}(\psi_j)\,\mathrm{d}\boldsymbol{c}_k\,\mathrm{d}\boldsymbol{c}_l\,, \tag{11}$$

with

$$\Phi_{kl}^{k'l'}(\psi_j) = \int \Delta_{kl}^{k'l'}(\psi_j)\,g_{kl}\,\mathrm{d}\sigma_{kl}^{k'l'}\,. \tag{12}$$

The integrations are over all parameters of the differential cross section and over all velocity space $\boldsymbol{c}_k$, $\boldsymbol{c}_l$. The summation over $(k'l')$ applies to all possible combinations of k' and l', ensuring, however, that no such combination is counted twice.

Finally, the total rate change of ψ_j due to collisions between all particle types is

$$I(\psi_j) = \tfrac{1}{2}\sum_k \sum_l I_{kl}(\psi_j)\,, \tag{13}$$

where for symmetry the I_{kl} are summed over both k and l.

To evaluate the integrals (11), the distribution functions must be given explicitly in terms of the $\boldsymbol{c}$ or the $\boldsymbol{w}_k$, etc. If the latter are chosen, then to have uniformity and consistency in presentation it is advisable to make all $\boldsymbol{\nu}_j$ the same. In particular, it is convenient to take $\boldsymbol{\nu}_j$ equal to $\boldsymbol{\nu}_0$, where $\boldsymbol{\nu}_0$ is the mean mass velocity as defined in Section II(a). In general, to express f explicitly in terms of, say, $\boldsymbol{w}$ it is necessary to expand f in terms of known functions of $\boldsymbol{w}$. For a gas mixture in which the various components may have different temperatures, the most suitable of all such possible expansions is that originally proposed by Grad (1949), namely, an expansion in terms of multidimensional Hermite polynomials. However, in order to make the problem tractable it is necessary to approximate to this expansion by a finite number of terms. The resulting expression for f is known as Grad's 13-moment approximation. Ignoring subscripts, in terms of $\boldsymbol{w}$ (with $\nu_j = \nu_0$) this is

$$f = f^0[\boldsymbol{a}^0 + \boldsymbol{a}^1 . \boldsymbol{w} + \boldsymbol{a}^2 : \boldsymbol{w}\boldsymbol{w} + \boldsymbol{a}^3 . \boldsymbol{w}(\alpha w^2 - \tfrac{5}{2})], \tag{14}$$

where

$$f^0 = n(\alpha/\pi)^{3/2} \exp(-\alpha w^2) .$$

Using this expression for f in the defining equation (3) to determine $\langle 1 \rangle$, $\langle \boldsymbol{w} \rangle$, $\langle \frac{1}{2} m w^2 \rangle$, $\langle m\{\boldsymbol{w}\boldsymbol{w}\} \rangle$, and $\langle \frac{1}{2} m \boldsymbol{w} w^2 \rangle$, it is found that

$$\alpha = m/2kT , \qquad \begin{array}{ll} \boldsymbol{a}^0 = 1 , & \boldsymbol{a}^1 = 2\alpha \boldsymbol{u} , \\ \boldsymbol{a}^2 = (\alpha/p)\{\boldsymbol{p}\} , & \boldsymbol{a}^3 = \frac{4}{5}(\alpha/p)\boldsymbol{r} . \end{array}$$

Using the approximations (14) for the distribution functions in (11), knowing the differential cross sections and the dynamics of a collision, the collision integrals may be determined. These integrations are carried out in Section III and in the associated references. It is, however, important to note at this stage that the product $f_k f_l$ contains both linear and quadratic terms in the $\boldsymbol{a}_k$ and $\boldsymbol{a}_l$. In evaluating the integrals the quadratic terms are ignored. It follows therefore, from considerations of tensorial rank alone, that

$$I_j(m_j \boldsymbol{w}) = \sum_s (c_{js}^{uu} \rho_s \boldsymbol{u}_s + c_{js}^{ur} \boldsymbol{r}_s) , \tag{15}$$

$$I_j(m_j\{\boldsymbol{w}\boldsymbol{w}\}) = \sum_s c_{js}^{pp} \{\boldsymbol{p}_s\} , \tag{16}$$

$$I_j(\tfrac{1}{2} m_j \boldsymbol{w} w^2) = \sum_s (c_{js}^{qu} \rho_s \boldsymbol{u}_s + c_{js}^{qr} \boldsymbol{r}_s) . \tag{17}$$

In principle, the object of the following Sections III and IV is to explicitly determine the coefficients c and corresponding scalar terms for the continuity and energy equations.

(*d*) *Closure of Equations of Change*

Even with the collision integrals evaluated, equations (4)–(9) do not form a closed set of equations. The moments $\boldsymbol{h}$ and $\boldsymbol{l}$ are still undetermined. In general it is necessary to express these higher moments in terms of the lower moments before a closed set is obtained. Since the collision integrals are to be evaluated subject to (14), an obviously consistent method of closing these equations is to use the same expression for f to determine $\boldsymbol{h}$ and $\boldsymbol{l}$. Doing this, it is found (cf. Grad 1949; Liley 1963) that

$$\boldsymbol{l} = \tfrac{7}{2}(kT/m)\{\boldsymbol{p}\} + \tfrac{5}{2}(kT/m)p\boldsymbol{I}$$

and, referred to a rectangular system of unit base vectors $\boldsymbol{i}_\lambda$,

$$\boldsymbol{H} = \tfrac{2}{5}(q_\lambda \delta_{\sigma\mu} + q_\sigma \delta_{\lambda\mu} + q_\mu \delta_{\sigma\lambda}) \boldsymbol{i}_\lambda \boldsymbol{i}_\sigma \boldsymbol{i}_\mu ,$$

where the δ's are the usual Kronecker delta functions. In particular, it follows from this expression for H that

$$\frac{\partial}{\partial \boldsymbol{x}}.\boldsymbol{h} = \frac{4}{5}\left\{\frac{\partial \boldsymbol{q}}{\partial \boldsymbol{x}}\right\},$$

$$\boldsymbol{H}:\frac{\partial \boldsymbol{v}}{\partial \boldsymbol{x}} = \frac{2}{5}\left(\boldsymbol{q}.\frac{\partial \boldsymbol{v}}{\partial \boldsymbol{x}} + \boldsymbol{q}\frac{\partial}{\partial \boldsymbol{x}}.\boldsymbol{v} + \frac{\partial \boldsymbol{v}}{\partial \boldsymbol{x}}.\boldsymbol{q}\right).$$

III. COLLISION INTEGRALS

(a) *Collision Dynamics*

Before the collision integrals can be evaluated the parameters of the differential cross section must be specified and the $\Delta(\psi_j)$'s expressed in terms of the integration variables. To do this the relevant parameters of a collision must be first determined. As in Section II(*c*), consider a collision between two particles k and l such that

$$k+l \rightarrow k'+l'.$$

With respect to the mean mass velocity $\boldsymbol{v}_0$, the centre of mass velocity is

$$\boldsymbol{G} = M_k\,\boldsymbol{w}_k + M_l\,\boldsymbol{w}_l, \tag{18}$$

where $\boldsymbol{w}_k$ and $\boldsymbol{w}_l$ are the peculiar velocities prior to a collision and

$$M_k = m_k/m_0, \qquad M_l = m_l/m_0, \qquad m_0 = m_k+m_l.$$

Again, define a relative velocity

$$\boldsymbol{g} \equiv \boldsymbol{g}_{kl} = \boldsymbol{w}_k - \boldsymbol{w}_l = -\boldsymbol{g}_{lk}. \tag{19}$$

Then it follows that

$$\boldsymbol{w}_k = \boldsymbol{G}+M_l\,\boldsymbol{g}, \tag{20}$$

$$\boldsymbol{w}_l = \boldsymbol{G}-M_k\,\boldsymbol{g}. \tag{21}$$

Similarly, subsequent to the collision,

$$\boldsymbol{w}_{k'} = \boldsymbol{G}'+M_{l'}\,\boldsymbol{g}', \tag{22}$$

$$\boldsymbol{w}_{l'} = \boldsymbol{G}'-M_{k'}\,\boldsymbol{g}', \tag{23}$$

the primes, in general, denoting variables after a collision. However, from the conservation of mass and momentum

$$m_0' = m_0, \qquad \boldsymbol{G}' = \boldsymbol{G}, \tag{24}$$

while from the conservation of energy

$$\tfrac{1}{2}m_0'\,G'^2 + \tfrac{1}{2}m_{k'l'}\,g'^2 = \tfrac{1}{2}m_0\,G^2 + \tfrac{1}{2}m_{kl}\,g^2 - \Delta E_{kl,k'l'}, \tag{25}$$

where

$$m_{kl} = m_k\,m_l/m_0, \qquad m_{k'l'} = m_{k'}\,m_{l'}/m_0,$$

and

$$\Delta E_{kl,k'l'} \equiv \mathscr{E}_{k'}+\mathscr{E}_{l'}-\mathscr{E}_k-\mathscr{E}_l+\delta E_{kl,k'l'}.$$

$\mathscr{E}_{k'}$, $\mathscr{E}_k$, . . . are the internal energies and $\delta E_{kl,k'l'}$ is the loss in kinetic energy due to immediate radiation or any other such cause.

Defining

$$\lambda^2_{kl,k'l'} = (m_{kl}/m_{k'l'})(1-2\Delta E_{kl,k'l'}/m_{kl}\, g^2)\,, \tag{26}$$

it follows from (24) and (25) that

$$g' = \lambda g\,,$$

subscripts being ignored. Therefore, in particular,

$$\boldsymbol{g}' = \lambda \boldsymbol{g} \cos\chi + \lambda g \sin\chi \cos\epsilon\, \boldsymbol{i}_1 + \lambda g \sin\chi \sin\epsilon\, \boldsymbol{i}_2\,, \tag{27}$$

where $\boldsymbol{i}_1$ and $\boldsymbol{i}_2$ are two mutually orthogonal unit vectors both being perpendicular to $\boldsymbol{g}$, and χ and ϵ are the polar and azimuthal "scattering" angles. (It is important to note that as defined $\chi \equiv \chi_{k'l'} \neq \chi_{l'k'} = \pi - \chi_{k'l'}$.)

It follows that the parameters of the collision are $\boldsymbol{G}$, $\boldsymbol{g}$, λ, χ, and ϵ, or to be more exact $\boldsymbol{G}$, $\boldsymbol{g}$, χ, ϵ, the particle types k, l, k', l', and the energy loss δE. This means that the differential cross section, referred to a centre of mass system, must be expressed in the form

$$\mathrm{d}\sigma^{k'l'}_{kl} = \sigma^{k'l'}_{kl}(g, \chi, \epsilon, \delta E) \sin\chi\, \mathrm{d}\chi\, \mathrm{d}\epsilon\, \mathrm{d}(\delta E)\,, \tag{28}$$

the dependence on particle type being implicit in the sub- and super-script notation.

The $\Delta(\psi_j)$ must now be determined in terms of these same parameters. Obviously, collisions between particles of types k and l only contribute to particles of type j if one or more of the k, l, k', l' are of type j. That is, in particular, the $\Delta(\psi_j)$ are given by

$$\Delta^{k'l'}_{kl}(\psi_j) = \psi_{k'}\, \delta_{k'j} + \psi_{l'}\, \delta_{l'j} - \psi_k\, \delta_{kj} - \psi_l\, \delta_{lj}\,, \tag{29}$$

where the δ's are the usual Kronecker delta functions and the $\psi_{k'}, \ldots$ are given in terms of the $\boldsymbol{G}$, $\boldsymbol{g}$, λ, χ, and ϵ.

For example, take $\psi_j = m_j\, \boldsymbol{w}_j$. Then from (20)

$$m_k\, \boldsymbol{w}_k\, \delta_{kj} = m_k(\boldsymbol{G} + M_l\, \boldsymbol{g})\delta_{kj} \equiv m_j\, \delta_{kj}\, \boldsymbol{G} + m_{jr}\, \delta_{jk}\, \boldsymbol{g}\,,$$

where

$$m_{jr} = m_j(m_0 - m_j)/m_0\,,$$

with similar terms for $m_{k'}\, \boldsymbol{w}_{k'}\, \delta_{k'j}, \ldots$. Using (28) and (29) it follows that

$$\begin{aligned}\Delta^{k'l'}_{kl}(m_j\, \boldsymbol{w}_j) = {}& m_j(\delta_{k'j} + \delta_{l'j} - \delta_{kj} - \delta_{lj})\boldsymbol{G} + m_{jr}(\delta_{k'j} - \delta_{l'j})\boldsymbol{g}(1 - \lambda\cos\chi) \\ & + m_{jr}(\delta_{k'j} - \delta_{l'j})\lambda g \sin\chi\, (\cos\epsilon\, \boldsymbol{i}_1 + \sin\epsilon\, \boldsymbol{i}_2) + m_{jr}(\delta_{k'j} - \delta_{l'j} - \delta_{kj} + \delta_{lj})\boldsymbol{g}\,,\end{aligned} \tag{30}$$

there being corresponding, but in general more complicated, expressions for other values of ψ_j (see, in particular, Bydder and Liley 1967).

(b) *Transformations*

Since the Φ's of equations (11) and (12) are to be expressed in terms of $\boldsymbol{G}$ and $\boldsymbol{g}$, it is necessary to transform the integrals (11) from integrations over velocity space $\boldsymbol{c}_k$, $\boldsymbol{c}_l$ to integrations over velocity space $\boldsymbol{G}$, $\boldsymbol{g}$. Noting that $\boldsymbol{w}_k = \boldsymbol{c}_k - \boldsymbol{v}_0$, $\boldsymbol{w}_l = \boldsymbol{c}_l - \boldsymbol{v}_0$, with equations (20) and (21) giving w_k and w_l in terms of G and g, the Jacobian of the transformation is unity and

$$I_{kl}^{k'l'}(\psi_j) = \int f_k f_l \Phi_{kl}^{k'l'}(\psi_j)\,\mathrm{d}G\,\mathrm{d}g\,. \tag{31}$$

On expressing the $f_k f_l$ in terms of G and g and noting that σ is independent of G, that is, G only occurs in simple algebraic sums in the Φ's (i.e. in the $\Delta(\psi)$'s), integration over G should be immediately possible. Unfortunately, this is not the case. Due primarily to the fact that the different particle types concerned may have different kinetic temperatures, the exponential term in the product $f_k f_l$ inhibits direct integration. Therefore, a further transformation is necessary. This involves the definition of two dimensionless velocities:

$$x = \beta(G+\zeta g)\,, \tag{32}$$

$$y = \gamma g\,, \tag{33}$$

where

$$\beta^2 \equiv \alpha_k+\alpha_l\,, \qquad \gamma^2 \equiv \alpha_k \alpha_l/\beta^2\,, \qquad \zeta \equiv \zeta_{kl} = (\alpha_k M_l - \alpha_l M_k)/\beta^2 = -\zeta_{lk}\,. \tag{34}$$

In terms of these velocities, (20) and (21) become

$$w_k = \beta^{-1}x+\gamma^{-1}(M_l-\zeta)y\,, \tag{35}$$

$$w_l = \beta^{-1}x-\gamma^{-1}(M_k+\zeta)y\,. \tag{36}$$

From (32) and (33) the Jacobian of the transformation from G, g to x, y is such that

$$\mathrm{d}G\,\mathrm{d}g = (\alpha_k \alpha_l)^{-3/2}\,\mathrm{d}x\,\mathrm{d}y\,,$$

and on using (35) and (36) in the expressions for the distribution functions the collision integral (31) becomes

$$I_{kl}^{k'l'}(\psi_j) = n_k n_l \pi^{-3} \int d(x,y)\exp(-x^2-y^2)\,\Phi_{kl}^{k'l'}(\psi_j)\,\mathrm{d}x\,\mathrm{d}y\,. \tag{37}$$

$d(x,y)$ has a leading term equal to unity and, besides being a function of x and y, is also a function of terms that are both linear and quadratic in the moments of f_k and f_l. The integral form (37) is of course generally true. Not only is it obtained when the distribution functions are given by the approximations (14), but it is also obtained when the complete expansions in terms of multidimensional Hermite polynomials are used. (Using (14) and ignoring the quadratic terms, the exact expression for $d(x,y)$ in terms of the u, $\{p\}$, and r is given by Bydder and Liley (1967).)

(c) *Integration over the Azimuth*

Using (32) and (33) to express the $\Delta(\psi)$'s in terms of the x and y, and noting that σ is independent of x, integration over x is immediately possible. However, in performing such integrations many terms containing the azimuthal angle ϵ are involved. In most cases of practical interest σ is independent of ϵ and such terms are superfluous. (Of course, in the case of various asymmetric molecules it is to be expected that for given orientations individual cross sections will be functions of ϵ. However, in the absence of an external polarizing agent it is also to be expected that suitably averaged values over all possible orientations will be independent of ϵ.) Therefore, on the assumption that σ is independent of ϵ, it is logical to integrate over this parameter first. In fact it is convenient to carry out such integrations at a level characterized by equation (30), i.e. prior to the transformation from $\boldsymbol{G}, \boldsymbol{g}$ to $\boldsymbol{x}, \boldsymbol{y}$. The results are such that the Φ's of equation (12) may be expressed in terms of a general integral function ϕ defined by

$$\phi_{kl}^{k'l'}(\mu,\nu) = \int (1-\lambda_{kl,k'l'}^{\mu} \cos^{\nu}\chi) g_{kl}\, \sigma_{kl}^{k'l'} \sin\chi \,\mathrm{d}\chi\, \mathrm{d}(\delta E)\,, \tag{38}$$

where the μ and ν are power indices. The integration limits are from 0 to π for χ and embrace all possible values of δE. In order to maintain a uniform notation, this equation is also used to define a function $\phi(-\infty, 0)$. The associated term involving λ and χ is $\lambda^{-\infty} \cos^0 \chi$ and this term is always taken to be zero no matter what the magnitude of λ, that is, $\lambda^{-\infty} \equiv 0$.

As an example, on inserting (30) in (12) and integrating over ϵ from 0 to 2π,

$$\begin{aligned} \Phi_{kl}^{k'l'}(m_j \boldsymbol{w}_j) = {} & 2\pi m_j(\delta_{k'j}+\delta_{l'j}-\delta_{kj}-\delta_{lj})\, \phi_{kl}^{k'l'}(-\infty,0)\, \boldsymbol{G} \\ & +2\pi m_{jr}(\delta_{k'j}-\delta_{l'j}-\delta_{kj}+\delta_{lj})\, \phi_{kl}^{k'l'}(1,1)\, \boldsymbol{g} \\ & -2\pi m_{jr}(\delta_{k'j}-\delta_{l'j})\, \phi_{kl}^{k'l'}(-\infty,0)\, \boldsymbol{g}\,, \end{aligned} \tag{39}$$

there being corresponding expressions for other values of ψ_j (Bydder and Liley 1967).

(d) *Integration over* $\boldsymbol{x}$ *Velocity Space*

Having determined the Φ's in terms of the ϕ's, $\boldsymbol{G}$, and $\boldsymbol{g}$, these may be rewritten in terms of the ϕ's, $\boldsymbol{x}$, and $\boldsymbol{y}$. The ϕ's become functions of the scalar y and not of $\boldsymbol{x}$ or $\boldsymbol{y}$. Limiting the subsequent integrations to the case for which $d(\boldsymbol{x}, \boldsymbol{y})$ is given by only the linear terms in the product $f_k f_l$, the f's being given by (14), integration over $\boldsymbol{x}$ is therefore straightforward. However, the associated algebra is extremely tedious and only the results are quoted, the details being contained in the previously mentioned report by Bydder and Liley (1967). In carrying out these integrations it is also possible to reduce the integrals over velocity space $\boldsymbol{y}$ to integrals over the scalar y, the latter integrals being expressible in the common form

$$\Omega_{kl,k'l'}^{\mu,\nu}(r) \equiv \pi^{\frac{1}{2}} \int_0^{\infty} \exp(-y^2)\, y^{2r+2} \phi_{kl}^{k'l'}(\mu,\nu)\, \mathrm{d}y\,. \tag{40}$$

The Ω's and ϕ's as used here are in fact generalizations of similar functions defined by Chapman and Cowling (1952). They are, apart from a particle number density factor, essentially collision frequencies.

In order to avoid subsequent confusion, certain definitions will be restated before the final results are presented. The reduced mass m_{jr} is defined by

$$m_{jr} = m_j(m_0 - m_j)/m_0\,,$$

where m_j is the mass of particle type j. With respect to particle types k and l the parameter α is given by

$$\alpha_k = m_k/2kT_k, \qquad \alpha_l = m_l/2kT_l.$$

k is Boltzmann's constant and T the kinetic temperature. β, γ, and ζ are as defined by equation (34), it being important to remember that ζ is equivalent to $\zeta_{kl} = -\zeta_{lk}$. ρ is the particle mass density and n, $\boldsymbol{u}$, $\{\boldsymbol{p}\}$, and $\boldsymbol{r}$ are as defined in Section II(a).

Since certain combinations of the δ functions repeatedly occur it is notationally convenient to replace these by single functions. In particular, it is convenient to define

$$\left.\begin{aligned} \delta_{kl}(1) &\equiv \delta_{k'j}+\delta_{l'j}-\delta_{lj}-\delta_{kj}, & \delta_{kl}(2) &\equiv \delta_{k'j}-\delta_{l'j}-\delta_{kj}+\delta_{lj}, \\ \delta_{kl}(3) &\equiv \delta_{k'j}-\delta_{l'j}, & \delta_{kl}(4) &\equiv \delta_{k'j}+\delta_{l'j}. \end{aligned}\right\} \qquad (41)$$

Again, for notational convenience, the subscripts $kl, k'l'$ associated with the Ω's will be ignored, as will the superscripts associated with the I's and the subscripts associated with the $\delta_{kl}(1)$, $\delta_{kl}(2)$, ...

(i) *The Scalar $I_{kl}(\psi_j)$*

The integrals associated with the mass continuity, internal energy, and translational kinetic energy are all scalar functions and are given by

$$I_{kl}(m_j) = n_k n_l m_j \,\delta(1)\, 8\Omega^{-\infty,0}(0),$$

$$I_{kl}(\mathscr{E}_j) = n_k n_l \mathscr{E}_j \,\delta(1)\, 8\Omega^{-\infty,0}(0),$$

$$I_{kl}(\tfrac{1}{2}m_j w_j^2) = \frac{4n_k n_l}{\gamma^2}\left[m_j\,\delta(1)\left(\left[\left(\frac{m_{jr}}{m_j}\right)^2+\zeta^2\right]\Omega^{-\infty,0}(1)+\frac{3\gamma^2}{2\beta^2}\,\Omega^{-\infty,0}(0)\right)\right.$$
$$\left.-m_{jr}\,\delta(2)\,2\zeta\Omega^{-\infty,0}(1)+m_{jr}\,\delta(3)\,2\zeta\Omega^{1,1}(1)-\frac{(m_{jr})^2}{m_j}\,\delta(4)\,\Omega^{2,0}(1)\right].$$

(ii) *The Momentum Integral*

This integral may be written in the form

$$I_{kl}(m_j\,\boldsymbol{w}_j) = n_k n_l[c_1^{uu}(\alpha_k)+c_2^{uu}(\alpha_k)]\boldsymbol{u}_k+n_k n_l[c_1^{uu}(\alpha_l)-c_2^{uu}(\alpha_l)]\boldsymbol{u}_l$$
$$+n_k n_l[c_1^{ur}(\alpha_k)+c_2^{ur}(\alpha_k)]\boldsymbol{r}_k/\rho_k+n_k n_l[c_1^{ur}(\alpha_l)-c_2^{ur}(\alpha_l)]\boldsymbol{r}_l/\rho_l,$$

where

$$c_1^{uu}(\alpha) = 8(\alpha/\beta^2)m_j\,\delta(1)\,\Omega^{-\infty,0}(0),$$

$$c_2^{uu}(\alpha) = \tfrac{16}{3}[-m_j\,\delta(1)\,\zeta\Omega^{-\infty,0}(1)+m_{jr}\,\delta(2)\,\Omega^{-\infty,0}(1)-m_{jr}\,\delta(3)\,\Omega^{1,1}(1)],$$

$$c_1^{ur}(\alpha) = \tfrac{32}{3}(\gamma^2\alpha/\beta^2)m_j\,\delta(1)(\Omega^{-\infty,0}(1)-\tfrac{3}{2}\Omega^{-\infty,0}(0)),$$

$$c_2^{ur}(\alpha) = \tfrac{32}{3}\gamma^2[m_j\,\delta(1)\,\zeta(\Omega^{-\infty,0}(1)-\tfrac{2}{5}\Omega^{-\infty,0}(2))+m_{jr}\,\delta(2)\,(\tfrac{2}{5}\Omega^{-\infty,0}(2)-\Omega^{-\infty,0}(1))$$
$$+m_{jr}\,\delta(3)\,(\Omega^{1,1}(1)-\tfrac{2}{5}\Omega^{1,1}(2))].$$

It is to be appreciated that the subscripts j and $kl, k'l'$ should also be associated with these coefficients; that is, for example

$$c_1^{uu}(\alpha) \equiv c_{1,j,kl,k'l'}^{uu}(\alpha).$$

(iii) *The Stress Equation Integral*

This integral is given by

$$I_{kl}(m_j\{\mathbf{w}_j \cdot \mathbf{w}_j\}) = n_k n_l[c_1^{pp}(\alpha_k) + c_2^{pp}(\alpha_k)]\{\mathbf{p}_k\}/\rho_k + n_k n_l[c_1^{pp}(\alpha_l) - c_2^{pp}(\alpha_l)]\{\mathbf{p}_l\}/\rho_l\,,$$

where

$$\begin{aligned} c_1^{pp}(\alpha) = \frac{16}{3}\bigg[& m_j\,\delta(1)\left(\frac{3\alpha^2}{2\beta^4}\,\Omega^{-\infty,0}(0) + \frac{2}{5}\left[\zeta^2 + \left(\frac{m_{jr}}{m_j}\right)^2\right]\Omega^{-\infty,0}(2)\right) \\ & - m_{jr}\,\delta(2)\tfrac{4}{5}\zeta\Omega^{-\infty,0}(2) + m_{jr}\,\delta(3)\tfrac{4}{5}\zeta\Omega^{1,1}(2) \\ & + \frac{(m_{jr})^2}{m_j}\,\delta(4)\left(\tfrac{1}{5}\Omega^{2,0}(2) - \tfrac{3}{5}\Omega^{2,2}(2)\right)\bigg], \end{aligned}$$

$$c_2^{pp}(\alpha) = \frac{16}{3}\left[-m_j\,\delta(1)\frac{2\zeta\alpha}{\beta^2}\,\Omega^{-\infty,0}(1) + m_{jr}\,\delta(2)\frac{2\alpha}{\beta^2}\,\Omega^{-\infty,0}(1) - m_{jr}\,\delta(3)\frac{2\alpha}{\beta^2}\,\Omega^{1,1}(1)\right].$$

(iv) *The Thermal Energy Flux Integral*

Like the momentum integral this integral may be presented in the form

$$\begin{aligned} I_{kl}(\tfrac{1}{2}m_j\,\mathbf{w}w^2) = {} & n_k n_l[c_1^{qu}(\alpha_k) + c_2^{qu}(\alpha_k)]\mathbf{u}_k + n_k n_l[c_1^{qu}(\alpha_l) - c_2^{qu}(\alpha_l)]\mathbf{u}_l \\ & + n_k n_l[c_1^{qr}(\alpha_k) + c_2^{qr}(\alpha_k)]\mathbf{r}_k/\rho_k + n_k n_l[c_1^{qr}(\alpha_l) - c_2^{qr}(\alpha_l)]\mathbf{r}_l/\rho_l\,, \end{aligned}$$

where

$$\begin{aligned} c_1^{qu}(\alpha) = {} & m_j\,\delta(1)\left[\frac{10\alpha}{\beta^4}\,\Omega^{-\infty,0}(0) + \frac{20\alpha}{3\beta^2\gamma^2}\left(\zeta^2 + \left(\frac{m_{jr}}{m_j}\right)^2\right)\Omega^{-\infty,0}(1)\right] \\ & - m_{jr}\,\delta(2)\frac{40\alpha\zeta}{3\beta^2\gamma^2}\,\Omega^{-\infty,0}(1) \\ & + m_{jr}\,\delta(3)\frac{40\alpha\zeta}{3\beta^2\gamma^2}\,\Omega^{1,1}(1) \\ & - \frac{(m_{jr})^2}{m_j}\,\delta(4)\frac{20\alpha}{3\beta^2\gamma^2}\,\Omega^{2,0}(1)\,, \end{aligned}$$

$$\begin{aligned} c_2^{qu}(\alpha) = {} & -m_j\,\delta(1)\left[\frac{20\zeta}{3\beta^2}\,\Omega^{-\infty,0}(1) + \frac{8\zeta}{3\gamma^2}\left(\zeta^2 + 3\left(\frac{m_{jr}}{m_j}\right)^2\right)\Omega^{-\infty,0}(2)\right] \\ & + m_{jr}\,\delta(2)\left[\frac{20}{3\beta^2}\,\Omega^{-\infty,0}(1) + \frac{8}{\gamma^2}\left(\zeta^2 + \frac{1}{3}\left(\frac{m_{jr}}{m_j}\right)^2\right)\Omega^{-\infty,0}(2)\right] \\ & - m_{jr}\,\delta(3)\left[\frac{20}{3\beta^2}\,\Omega^{1,1}(1) + \frac{8\zeta^2}{\gamma^2}\,\Omega^{1,1}(2) + \frac{8}{3\gamma^2}\left(\frac{m_{jr}}{m_j}\right)^2\Omega^{3,1}(2)\right] \\ & + \frac{(m_{jr})^2}{m_j}\,\delta(4)\left[\frac{8\zeta}{3\gamma^2}\left(\Omega^{2,0}(2) + 2\Omega^{2,2}(2)\right)\right], \end{aligned}$$

$$
\begin{aligned}
c_1^{qr}(\alpha) = m_j\,\delta(1)\Big[&-\frac{20\alpha^2}{\beta^4}\Big(1-\frac{7\alpha}{5\beta^2}\Big)\Omega^{-\infty,0}(0)+\frac{40\alpha}{3\beta^2}\Big(\frac{\gamma^2}{\beta^2}-\zeta^2-\Big(\frac{m_{jr}}{m_j}\Big)^2\Big)\Omega^{-\infty,0}(1)\\
&+\frac{176\alpha}{15\beta^2}\Big(\Big(\frac{m_{jr}}{m_j}\Big)^2+\zeta^2\Big)\Omega^{-\infty,0}(2)\Big]\\
&+m_{jr}\,\delta(2)\Big[\frac{80\alpha}{3\beta^2}\,\zeta\Big(\Omega^{-\infty,0}(1)-\frac{22}{25}\,\Omega^{-\infty,0}(2)\Big)\Big]\\
&-m_{jr}\,\delta(3)\Big[\frac{80\alpha}{3\beta^2}\,\zeta\Big(\Omega^{1,1}(1)-\frac{22}{25}\,\Omega^{1,1}(2)\Big)\Big]\\
&-\frac{(m_{jr})^2}{m_j}\,\delta(4)\Big[-\frac{40\alpha}{3\beta^2}\,\Omega^{2,0}(1)+\frac{16\alpha}{15\beta^2}\Big(7\Omega^{2,0}(2)+4\Omega^{2,2}(2)\Big)\Big],
\end{aligned}
$$

$$
\begin{aligned}
c_2^{qr}(\alpha) = m_j\,\delta(1)\,\zeta\Big[&\frac{8\alpha}{3\beta^2}\Big(5-\frac{11\alpha}{\beta^2}\Big)\Omega^{-\infty,0}(1)+\frac{16}{3}\Big(\zeta^2-\frac{\gamma^2}{\beta^2}+3\Big(\frac{m_{jr}}{m_j}\Big)^2\Big)\Omega^{-\infty,0}(2)\\
&-\frac{32}{15}\Big(\zeta^2+3\Big(\frac{m_{jr}}{m_j}\Big)^2\Big)\Omega^{-\infty,0}(3)\Big]\\
&+m_{jr}\,\delta(2)\Big[-\frac{8\alpha}{3\beta^2}\Big(5-\frac{11\alpha}{\beta^2}\Big)\Omega^{-\infty,0}(1)+\frac{16}{3}\Big(\frac{\gamma^2}{\beta^2}-3\zeta^2-\Big(\frac{m_{jr}}{m_j}\Big)^2\Big)\Omega^{-\infty,0}(2)\\
&\qquad+\frac{32}{15}\Big(3\zeta^2+\Big(\frac{m_{jr}}{m_j}\Big)^2\Big)\Omega^{-\infty,0}(3)\Big]\\
&+m_{jr}\,\delta(3)\Big[\frac{8\alpha}{3\beta^2}\Big(5-\frac{11\alpha}{\beta^2}\Big)\Omega^{1,1}(1)-\frac{16}{3}\Big(\frac{\gamma^2}{\beta^2}-3\zeta^2\Big)\Omega^{1,1}(2)\\
&\qquad-\frac{32}{5}\,\zeta^2\Omega^{1,1}(3)+\frac{16}{3}\Big(\frac{m_{jr}}{m_j}\Big)^2\Omega^{3,1}(2)-\frac{32}{15}\Big(\frac{m_{jr}}{m_j}\Big)^2\Omega^{3,1}(3)\Big]\\
&-\frac{(m_{jr})^2}{m_j}\,\delta(4)\Big[\frac{16}{3}\,\zeta\Big(\Omega^{2,0}(2)+2\Omega^{2,2}(2)\Big)-\frac{32}{15}\,\zeta\Big(\Omega^{2,0}(3)+2\Omega^{2,2}(3)\Big)\Big].
\end{aligned}
$$

(e) *The Coefficients* c_{js}

To obtain the $I_j(\psi_j)$'s the integrals of the preceding subsection must be summed over all $(k'l')$ and over all k and l. For a real physical situation this is likely to be a complex process. However, in the case of the momentum, the stress, and the thermal flux equations formal simplifications are possible. On summing over $(k'l')$, and ignoring superscripts, define

$$c_{1,j,kl}(\alpha) = \sum_{(k'l')} c_{1,j,kl,k'l'}(\alpha)\,, \tag{42}$$

with a corresponding definition for $c_{2,j,kl}$. Furthermore, by identifying the order of the subscripts kl with the argument of these coefficients, a further notational simplification is possible. In particular, define

$$c_{j,kl}(\alpha_k) \equiv c_{1,j,kl}(\alpha_k)+c_{2,j,kl}(\alpha_k)\,, \qquad c_{j,kl}(\alpha_l) \equiv c_{1,j,kl}(\alpha_l)-c_{2,j,kl}(\alpha_l)\,; \tag{43}$$

then it follows, as inspection of the results of the preceding subsection confirms, that formally

$$I_{kl}(\psi_j) = \sum_d n_k n_l \left(c^{\alpha d}_{j,kl}(\alpha_k) \frac{\boldsymbol{d}_k}{\rho_k} + c^{\alpha d}_{j,kl}(\alpha_l) \frac{\boldsymbol{d}_l}{\rho_l} \right), \tag{44}$$

where $\boldsymbol{d}$ represents any one of the moments $\rho \boldsymbol{u}$, $\{\boldsymbol{p}\}$, or $\boldsymbol{r}$, and $\alpha \equiv n\langle\psi\rangle$.

Since I_{kl} must equal I_{lk}, on interchanging k and l in (44) and comparing the coefficients of the $\boldsymbol{d}$'s in these two different forms of the integral, it is immediately apparent that

$$c_{j,kl}(\alpha_k) = c_{j,lk}(\alpha_k), \qquad c_{j,kl}(\alpha_l) = c_{j,lk}(\alpha_l). \tag{45}$$

(Noting that

$$\zeta_{kl} = -\zeta_{lk}, \qquad \begin{matrix} \delta_{kl}(1) = \delta_{lk}(1), & \delta_{kl}(2) = -\delta_{lk}(2), \\ \delta_{kl}(3) = -\delta_{lk}(3), & \delta_{kl}(4) = \delta_{lk}(4), \end{matrix}$$

inspection of the results of the preceding subsection confirms that

$$c_{1,j,kl} = c_{1,j,lk}, \qquad c_{2,j,kl} = -c_{2,j,lk}.$$

Hence, on interchanging k and l in (43), equation (45) immediately follows, thus giving a direct confirmation of this result.)

On summing the I_{kl}, as given by (44), over both k and l,

$$I_j(\psi_j) = \sum_d \left[\sum_k \frac{n_k}{2\rho_k} \left(\sum_l n_l c^{\alpha d}_{j,kl}(\alpha_k) \right) \boldsymbol{d}_k + \sum_l \frac{n_l}{2\rho_l} \left(\sum_k n_k c^{\alpha d}_{j,kl}(\alpha_l) \right) \boldsymbol{d}_l \right]. \tag{46}$$

However, the summations over k and l are independent. Hence on changing subscripts, in particular putting $k = s$ and $l = k$ in the first summation and $l = s$ in the second,

$$I_j(\psi_j) = \sum_d \sum_s c^{\alpha d}_{js} \boldsymbol{d}_s,$$

where

$$c_{js} = \frac{1}{2m_s} \sum_k n_k \big(c_{j,sk}(\alpha_s) + c_{j,ks}(\alpha_s) \big).$$

Or, on using (43) and (45),

$$c_{js} = \frac{1}{m_s} \sum_k n_k c_{j,ks}(\alpha_s) \tag{47}$$

with

$$c_{j,ks}(\alpha_s) = c_{1,j,ks}(\alpha_s) - c_{2,j,ks}(\alpha_s).$$

Therefore, on using the subscripts k and s rather than k and l in the coefficients of the preceding subsection and summing over all k, the c_{js}'s of equations (15), (16), and (17) are explicitly determined.

IV. Special Cases

To complete the integrals the Ω's must be determined. In general this is not a simple task. An explicit knowledge of the differential cross sections is required, while each particular process, such as elastic, fission, recombination, etc., must be considered separately. Numerous calculations have been carried out, for different laws of interaction, for the elementary case of elastic collisions (e.g. Chapman and Cowling 1952; Hirschfelder, Curtiss, and Bird 1954). On the other hand, since the generalized Ω's as defined in Section III(d) are peculiar to this paper (and the associated references) few calculations have been performed for the general inelastic case. Bydder has considered those cases of importance involved in the formation of a hydrogenic-like plasma. However, the practical usefulness of his results is questionable since in order to obtain analytically tractable expressions certain approximations were made, the nature of which are only truly applicable to a very high temperature gas. Nevertheless, the results are extremely interesting in that they show (and generally imply) that, for a specific process, only one or two of the total number of Ω's (20 for the general case) have to be determined explicitly, the others being related to these in a relatively simple manner. Bydder's (1967a) results have been published elsewhere and will not be reproduced here. Instead, various cases of more general interest will be discussed. The Ω's are not determined, but in certain instances the results of Section III are considerably simplified. This is possible since much of the physics of a particular process is already explicitly contained within the δ's.

In the following subsections the more important of the possible physical processes are briefly considered. These were mentioned in the Introduction, being natural decay and spontaneous fission, recombination and attachment, elastic collisions and charge exchange processes, and the general inelastic collision, including excitation and fission- and fusion-like processes. As already implied, the integrals of Section III have been evaluated for the most general case possible, namely, the complete destruction of particles k and l and the creation of two entirely new particles k' and l'. Clearly, there are many possible combinations of k, l, k', and l', as well as various interpretations of ΔE (or to be more exact δE) that can lead to marked simplifications. Again, there are certain approximations and even certain limiting cases that also reduce the general results to simpler forms. For instance, if $T_k \simeq T_l$ then $\zeta \simeq 0$ and many terms may be ignored, while if $m_k \ll m_l$ or $m_{k'} \ll m_{l'}$ other approximations are possible. It is, however, beyond the scope of this paper to consider such cases in detail and only general aspects of those physical processes already mentioned will be discussed.

Before considering these various cases explicitly several points of a general nature should be noted. The collision integrals involve both "loss" (δ_{kj}, δ_{lj}) and "gain" ($\delta_{k'j}$, $\delta_{l'j}$) terms. The loss terms are only associated with the $\delta(1)$ and $\delta(2)$ terms and as such only involve the $\Omega^{-\infty,0}(r)$. Defining a "partial" cross section

$$Q_{kl}^{k'l'}(g) \equiv \int \sigma_{kl}^{k'l'} \sin\chi \, \mathrm{d}\chi \, \mathrm{d}(\delta E) \, \mathrm{d}\epsilon ,$$

it follows from the definition (38) that

$$\phi_{kl}^{k'l'}(-\infty, 0) = g\, Q_{kl}^{k'l'}(g)/2\pi , \tag{48}$$

or, on summing over all $(k'l')$, the loss terms only involve total cross sections.

Furthermore, if for any particular process $\lambda = 0$ then by definition

$$\phi(\mu, \nu) = \phi(-\infty, 0) , \tag{49}$$

and again only the $\Omega^{-\infty,0}(r)$ are involved. However, in this latter case summation over $(k'l')$ will not necessarily lead to explicit expressions in terms of a total cross section.

(a) *Natural Decay and Spontaneous Fission*

In spontaneous fission a particle type k changes into particle types k' and l', l being a hypothetical particle of mass zero. Such a process only occurs if k is in an excited state, the excitation energy appearing as kinetic energy. In the limit $m_l \to 0$ it follows from (26) and (33) that

$$\lambda^2 = -2\Delta E\, \gamma^2 / m_{k'l'}\, y^2 ,$$

ΔE being a negative (i.e. a gain) term.

Assuming that the hypothetical particles of type l have a Maxwellian distribution,

$$\boldsymbol{u}_l = \{\boldsymbol{p}_l\} = \boldsymbol{r}_l = 0 ;$$

while, since $\zeta \sim m_{kl}$, $\gamma^2 \sim m_{kl}$, on taking the limit as $m_l \to 0$ the integrals of Section III reduce to basically trivial forms. The loss terms are

$$I_{kl}(m_k) = -n_k m_k/\tau , \qquad I_{kl}(\mathscr{E}_k) = -n_k \mathscr{E}_k/\tau ,$$
$$I_{kl}(\tfrac{1}{2}m_k w_k^2) = -\tfrac{3}{2}n_k kT_k/\tau , \qquad I_{kl}(m_k \boldsymbol{w}_k) = -n_k m_k \boldsymbol{u}_k/\tau ,$$
$$I_{kl}(m_k\{\boldsymbol{w}_k \boldsymbol{w}_k\}) = -\{\boldsymbol{p}_k\}/\tau , \qquad I_{kl}(\tfrac{1}{2}m_k \boldsymbol{w}_k w_k^2) = -\boldsymbol{q}_k/\tau ,$$

where τ is the decay time, being given by

$$\tau^{-1} \equiv n_l\, 8\Omega^{-\infty,0}(0) = 8n_l \pi^{\frac{1}{2}} \int_0^\infty \exp(-y^2) y^2 \phi_{kl}(-\infty, 0)\, \mathrm{d}y , \tag{50}$$

with

$$\phi(-\infty, 0) = g\, Q_{kl}(g)/2\pi , \tag{51}$$

the summation over $(k'l')$ having been implicitly carried out. Subject to this approach, however, τ^{-1} must also equal $n_l g Q_{kl}$ since the lifetime of an excited state is independent of particle speed. On substituting (51) in (50) and integrating, such an identity is obtained, thus confirming the adequacy of the limiting process adopted.

Similarly, on letting $m_l \to 0$ the gain terms are

$$I_{kl}(m_j) = n_k m_j\, \delta(4)/\tau , \qquad I_{kl}(\mathscr{E}_j) = n_k \mathscr{E}_j\, \delta(4)/\tau ,$$
$$I_{kl}(\tfrac{1}{2}m_j w_j^2) = \left(\tfrac{3}{2}(m_j/m_k) n_k kT_k - (m_{jr}/m_j) n_k \Delta E\right)\delta(4)/\tau ,$$
$$I_{kl}(m_j \boldsymbol{w}_j) = n_k m_j \boldsymbol{u}_k\, \delta(4)/\tau , \qquad I_{kl}(m_j\{\boldsymbol{w}_j \boldsymbol{w}_j\}) = (m_j/m_k)\{\boldsymbol{p}_k\}\delta(4)/\tau ,$$
$$I_{kl}(\tfrac{1}{2}m_j \boldsymbol{w}_j w_j^2) = \left((m_j/m_k)\boldsymbol{q}_k - \tfrac{5}{3}(m_{jr}/m_j) n_k \boldsymbol{u}_k \Delta E\right)\delta(4)/\tau ,$$

where subscripts associated with ΔE have been ignored, while in this case τ is an abbreviation for $\tau_{k,k'l'}$, the summation over $(k'l')$ being necessarily explicit.

As a limiting case of these results let $m_{l'} \to 0$; then $m_j \to m_k$ and $m_{jr} \to 0$. To within the approximation of ignoring the momentum associated with photons, the results are those appropriate to natural decay.

(b) *Recombination and Attachment*

In this case two particles k and l combine to form a single particle j. This process may or may not be accompanied by the emission of radiation, while the particle j will usually be left in an excited state. The surplus energy will be either radiated, converted into kinetic energy in a subsequent collision (a collision of the second kind), or the excited particle will subsequently undergo a spontaneous fission or natural decay.

The correct physical approach to this problem is to put g', and hence λ, equal to zero, summing together the separate gain integrals for k' and l' to obtain the integrals for j. The loss terms may be obtained directly from the results of the preceding section, involving only the $\delta(1)$ and $\delta(2)$ terms and the $\Omega^{-\infty,0}(r)$. There is no real simplification. In the case of the gain terms, since $\lambda = 0$, only the $\Omega^{-\infty,0}(r)$ are again involved but all the δ terms must be considered. In particular, for $j = k'$,

$$\delta(1) = \quad \delta(2) = \quad \delta(3) = \delta(4) = 1\,,$$

while, for $j = l'$,

$$\delta(1) = -\delta(2) = -\delta(3) = \delta(4) = 1\,.$$

Using these relationships and the fact that

$$m_{k'} + m_{l'} = m_j = m_k + m_l\,,$$

on adding the separate integrals for k' and l', the gain integrals are

$$I_{kl}(m_j) = n_k n_l m_j 8\Omega^{-\infty,0}(0)\,, \qquad I_{kl}(\mathscr{E}_j) = n_k n_l \mathscr{E}_j 8\Omega^{-\infty,0}(0)\,,$$

$$I_{kl}(\tfrac{1}{2} m_j w_j^2) = \frac{4 n_k n_l}{\gamma^2}\left(m_j \zeta^2 \Omega^{-\infty,0}(1) + \frac{3 m_j \gamma^2}{2\beta^2} \Omega^{-\infty,0}(0) \right),$$

with

$$c_1^{uu}(\alpha) = \frac{8\alpha}{\beta^2} m_j\, \Omega^{-\infty,0}(0)\,,$$

$$c_2^{uu}(\alpha) = -\frac{16}{3} m_j\, \zeta \Omega^{-\infty,0}(0)\,,$$

$$c_1^{ur}(\alpha) = \frac{32}{3} \frac{\gamma^2 \alpha}{\beta^2} m_j [\Omega^{-\infty,0}(1) - \tfrac{3}{2} \Omega^{-\infty,0}(0)]\,,$$

$$c_2^{ur}(\alpha) = \frac{32}{3} \gamma^2 m_j\, \zeta [\Omega^{-\infty,0}(1) - \tfrac{2}{5} \Omega^{-\infty,0}(2)]\,,$$

$$c_1^{pp}(\alpha) = 8 m_j \frac{\alpha^2}{\beta^4} \Omega^{-\infty,0}(0) + \frac{32}{15} m_j\, \zeta^2 \Omega^{-\infty,0}(2)\,,$$

$$c_2^{pp}(\alpha) = -\frac{16 m_j}{3} \frac{2\zeta\alpha}{\beta^2} \Omega^{-\infty,0}(1)\,,$$

$$c_1^{qu}(\alpha) = m_j \frac{10\alpha}{\beta^4} \Omega^{-\infty,0}(0) + \frac{20\alpha}{3\beta^2\gamma^2} m_j\, \zeta^2 \Omega^{-\infty,0}(1)\,,$$

$$c_2^{qu}(\alpha) = -\frac{20m_j}{3}\frac{\zeta}{\beta^2}\,\Omega^{-\infty,0}(1) + \frac{8\zeta^3}{3\gamma^2}m_j\,\Omega^{-\infty,0}(2)\,,$$

$$c_1^{qr}(\alpha) = -20m_j\frac{\alpha^2}{\beta^4}\left(1-\frac{7\alpha}{5\beta^2}\right)\Omega^{-\infty,0}(0)$$

$$+\frac{40m_j}{3}\frac{\alpha}{\beta^2}\left(\frac{\gamma^2}{\beta^2}-\zeta^2\right)\Omega^{-\infty,0}(1)+\frac{176m_j}{15}\frac{\alpha\zeta^2}{\beta^2}\,\Omega^{-\infty,0}(2)\,,$$

$$c_2^{qr}(\alpha) = m_j\,\zeta\left[\frac{8\alpha}{3\beta^2}\left(5-\frac{11\alpha}{\beta^2}\right)\Omega^{-\infty,0}(1)+\frac{16}{3}\left(\zeta^2-\frac{\gamma^2}{\beta^2}\right)\Omega^{-\infty,0}(2)-\frac{32}{15}\zeta^2\Omega^{-\infty,0}(3)\right].$$

In these expressions,

$$\Omega_{kl,j}^{-\infty,0}(r) = \pi^{\frac{1}{2}}\int_0^\infty \exp(-y^2)\,y^{2r+2}\,\frac{g\,Q_{kl}^j(g)}{2\pi}\,\mathrm{d}y\,,$$

with

$$Q_{kl}^j(g) = \int \sigma_{kl}^j \sin\chi\,\mathrm{d}\chi\,\mathrm{d}\epsilon\,\mathrm{d}(\delta E)\,.$$

For $\lambda = 0$, $\frac{1}{2}m_{kl}\,g^2 = \Delta E$ and this means, in particular, that g (or y) and (δE) are not, for given k, l, and j, independent variables. However, this fact is implicit within the σ and need not be considered further.

Although the coefficients are still somewhat complex it is immediately obvious that they simplify markedly for $\zeta = 0$.

An alternative approach to the one just adopted is to take $m_{l'} \to 0$. This leads to λ being an infinite quantity but automatically ensures that all terms involving m_{jr} are zero. The fact that this approach leads to exactly the same results as those just obtained is of prime importance. Since in the first approach many terms in m_{jr} (that is, $m_{k'r}$ and $m_{l'r}$) have to be considered, the fact that such terms cancel gives an extremely precise confirmation of the algebraic accuracy of the general results.

(c) *Charge Exchange and Elastic Collisions*

In an elastic collision the identities of the particles are unchanged. Here $\Delta E = 0$, hence $\lambda = 1$, while $\delta(1) = \delta(2) = 0$. The relevant integrals may be obtained quite simply by inspection of the general case and will not, therefore, be recorded here. However, it is worth while noting the extreme simplicity of the self-collision terms. For this particular case, besides $\delta(1) = \delta(2) = 0$, $\delta(3)$ is also zero, as is ζ, while $\delta(4) = 2$. The relevant integrals are

$$I_{jj}(m_j) = I_{jj}(\mathscr{E}_j) = I_{jj}(\tfrac{1}{2}m_j\,w_j^2) = I_{jj}(m_j\,\boldsymbol{w}_j) = 0\,,$$

$$I_{jj}(m_j\{\boldsymbol{w}_j\,\boldsymbol{w}_j\}) = -\tfrac{16}{5}n_j\,\Omega^{2,2}(2)\,\{\boldsymbol{p}_j\}\,,\qquad I_{jj}(\tfrac{1}{2}m_j\,\boldsymbol{w}_j\,w_j^2) = -\tfrac{32}{15}n_j\,\Omega^{2,2}(2)\,\boldsymbol{r}_j\,.$$

It must of course be remembered that in obtaining the $I_j(\psi_j)$ these integrals are divided by two.

In the simplest and most common of the exchange processes (resonance charge exchange) particle k becomes particle l and particle l becomes particle k. However, in general it is possible that particles k' and l' are excited states of particles l and k and within the approach adopted here these are quite different particle types from l and k; that is, no simplification of the general results is possible. Nevertheless, returning to the case of resonant charge exchange, this is somewhat similar to the pure elastic case and a reduction of the various coefficients is possible. Since for the subscript order kl the scattering cross section refers to k' rather than l', consider l and k' as the identical particles. Then for

$$j = l = k' \neq k = l', \qquad \delta(1) = 0, \quad \delta(2) = 2, \quad \delta(3) = \delta(4) = 1.$$

(The case of $k = l$ is exactly the same as that for elastic collisions.) Unlike elastic collisions, however, δE need not be zero and hence λ may be different from unity. Therefore, for resonant charge exchange the integrals become

$$I_{kl}(m_l) = I_{kl}(\mathscr{E}_l) = 0,$$

$$I_{kl}(\tfrac{1}{2}m_l w_l^2) = \frac{4n_k n_l}{\gamma^2}\left[-2m_{kl}\,\zeta\left(2\Omega^{-\infty,0}(1) - \Omega^{1,1}(1)\right) - \frac{(m_{kl})^2}{m_l}\,\Omega^{2,0}(1)\right],$$

while

$$c_1^{uu}(\alpha) = 0,$$

$$c_2^{uu}(\alpha) = \tfrac{16}{3}m_{kl}(2\Omega^{-\infty,0}(1) - \Omega^{1,1}(1)),$$

$$c_1^{ur}(\alpha) = 0,$$

$$c_2^{ur}(\alpha) = \tfrac{32}{3}m_{kl}\gamma^2[(\tfrac{4}{5}\Omega^{-\infty,0}(2) - 2\Omega^{-\infty,0}(1)) + (\Omega^{1,1}(1) - \tfrac{2}{5}\Omega^{1,1}(2))],$$

$$c_1^{pp}(\alpha) = \frac{16}{3}\left[-\tfrac{4}{5}m_{kl}\,\zeta\left(2\Omega^{-\infty,0}(2) - \Omega^{1,1}(2)\right) + \frac{(m_{kl})^2}{m_l}\left(\tfrac{1}{5}\Omega^{2,0}(2) - \tfrac{3}{5}\Omega^{2,2}(2)\right)\right],$$

$$c_2^{pp}(\alpha) = \frac{16}{3}m_{kl}\frac{2\alpha}{\beta^2}\left(2\Omega^{-\infty,0}(1) - \Omega^{1,1}(1)\right),$$

with corresponding but appreciably more complicated expressions for the $c^{qu}(\alpha)$ and $c^{qr}(\alpha)$.

(*d*) *General Inelastic Collision*

In a general inelastic collision particles k' and l' are distinctly different particles from k and l and no precise simplification of the results of Section III is possible. Both loss and gain terms must be considered separately. On the other hand, if the identity of particle k remains unchanged throughout the collision, such as in the inelastic scattering of an electron, then considerable simplification is possible. However, before discussing this particular case several other aspects of the general inelastic collision will be briefly considered.

Besides simple excitation or de-excitation (a collision of the second kind), in an inelastic collision, fission-like or fusion-like processes are also possible. That is, instead of there being just two product particles k' and l' there may be more or only one. In the latter case the problem is similar to recombination and need not be reconsidered. If, however, there are more than two particles then the problem is different but as will be seen no new difficulties are introduced. If k' is the particle of interest then the other products of the collision may be regarded as a simple composite particle l', having an internal energy equal to the sum of the internal energies of the individual components plus their kinetic energies referred to the centre of mass of l'. The fact that the "internal" energy ceases to be a discrete quantity is of no consequence, since this has already been allowed for by the inclusion of a continuum energy δE in the definition of the cross sections. Thus a fission- or fusion-like process may be essentially regarded as excitation to the continuum. In particular, on writing $l' \equiv \sum_s l'_s$,

$$m_{l'} = \sum_s m_{l'_s}, \qquad \mathscr{E}_{l'} = \sum_s \mathscr{E}_{l'_s},$$

while

$$\delta E_{kl,k'l'} \equiv \delta E_{l'} = \sum_s \tfrac{1}{2} m_{l'_s} g^2_{l'l'_s},$$

where

$$g_{l'l'_s} = \boldsymbol{w}_{l'} - \boldsymbol{w}_{l'_s}.$$

In the case of simple ionization $\delta E_{l'}$ is readily identified with the energy of the ejected electron. In a more general case the problem need be no more difficult. It should always be possible to specify a cross section $\sigma(\ldots, \delta E_{k'})$ appropriate to the production of a particle k' with given energy $\delta E_{k'}$, the latter being referred (say) to the centre of mass velocity $\boldsymbol{G}$. Then since

$$\tfrac{1}{2} m_{k'l'} g^2_{k'l'} + \mathscr{E}_{k'} + \mathscr{E}_{l'} + \delta E_{kl,k'l'} = \tfrac{1}{2} m_{kl} g^2_{kl} + \mathscr{E}_k + \mathscr{E}_l,$$

while from (19) and (22)

$$\delta E_{k'} \equiv \tfrac{1}{2} m_{k'} g^2_{Gk'} = \tfrac{1}{2} m_{k'l'} M_{l'} g^2_{k'l'},$$

it follows that

$$\delta E_{k'} = M_{l'}\big[(\mathscr{E}_k + \mathscr{E}_l - \mathscr{E}_{k'} - \mathscr{E}_{l'}) + \tfrac{1}{2} m_{kl} g^2_{kl} - \delta E_{l'}\big].$$

Therefore the differential cross section

$$2\pi\sigma^{k'l'}_{kl}(g, \chi, \delta E_{k'}) \sin\chi \, \mathrm{d}\chi \, \mathrm{d}(\delta E_{k'})$$

may be readily transformed to the form adopted in the preceding sections, namely,

$$2\pi\sigma^{k'l'}_{kl}(g, \chi, \delta E) \sin\chi \, \mathrm{d}\chi \, \mathrm{d}(\delta E),$$

δE being equivalent to $\delta E_{l'}$. Again since

$$M_{l'} = (m_0 - m_{k'})/m_0 \equiv (m_0 - m_j)/m_0,$$

while λ, which only occurs in the gain terms, is "operated" on by $\delta_{k'j}$ leading to

$$\lambda^2_{kl,k'l'} = \frac{m_{kl}}{m_{k'l'}}\left(1 - \frac{2\Delta E_{kl,k'l'}}{m_{kl} g^2}\right) \equiv \frac{m_{kl}}{m_{jr}}\left(1 - \frac{2\Delta E_{kl,jl'}}{m_{kl} g^2}\right),$$

it follows that m_j ($\equiv m_{k'}$) and m_{jr} ($\equiv m_{k'r}$) are the only masses involved, and the determination of the ϕ's and the Ω's proceeds as in the case of simple excitation.

The final expression given above for λ^2 introduces a further point of general interest. This is that, provided $k' \neq l'$, the summations of the integrals over $(k'l')$ may be reduced to simple summations over l'. In fact such summations may be more succinctly included within the Ω's, the ϕ's being the only functions involved. In order to emphasize this conclusion consider the previously mentioned case of inelastic scattering of particle k. This corresponds to, with $k \neq l$, $k' \neq l'$:

$$k = j = k', \qquad \delta(1) = \delta(2) = 0, \quad \delta(3) = \delta(4) = 1.$$

Hence, from the results of Section III, the collision integrals are

$$I_{kl}(m_k) = I_{kl}(\mathscr{E}_k) = 0,$$

$$I_{kl}(\tfrac{1}{2}m_k w_k^2) = \frac{4n_k n_l}{\gamma^2}\left(2\zeta m_{kl}\,\Omega_{kl}^{1,1}(1) - \frac{(m_{kl})^2}{m_k}\,\Omega_{kl}^{2,0}(1)\right),$$

while

$$c_1^{uu} = c_1^{ur} = 0,$$

$$c_2^{uu} = -\tfrac{16}{3}m_{kl}\,\Omega_{kl}^{1,1}(1),$$

$$c_2^{ur} = \tfrac{32}{3}\gamma^2 m_{kl}(\Omega_{kl}^{1,1}(1) - \tfrac{2}{5}\Omega_{kl}^{1,1}(2)),$$

$$c_1^{pp} = \tfrac{64}{15}m_{kl}\,\zeta\Omega_{kl}^{1,1}(2) + \tfrac{16}{3}\frac{(m_{kl})^2}{m_k}\left(\tfrac{1}{5}\Omega_{kl}^{2,0}(2) - \tfrac{3}{5}\Omega_{kl}^{2,2}(2)\right),$$

$$c_2^{pp} = -\tfrac{32}{3}(\alpha/\beta^2)m_{kl}\,\Omega_{kl}^{1,1}(1),$$

with corresponding but somewhat more complicated expressions for the c^{qu} and c^{qr}. In these expressions the summation over $(k'l')$ is contained within the Ω's, these being defined by (cf. equation (40))

$$\Omega_{kl}^{\mu,\nu}(r) = \pi^{\frac{1}{2}}\int \exp(-y^2)\,y^{2r+2}\,\phi_{kl}(\mu,\nu)\,\mathrm{d}y,$$

with

$$\phi_{kl}(\mu,\nu) = \sum_{(k'l')}\phi_{kl}^{k'l'}(\mu,\nu) = \sum_{l'}\phi_{kl}^{kl'}(\mu,\nu),$$

and

$$\lambda^2_{kl,k'l'} = \lambda^2_{kl,kl'} = (1 - 2\Delta E_{kl,kl'}/m_{kl}g^2),$$

$$\Delta E_{kl,kl'} = \mathscr{E}_l - \mathscr{E}_{l'} - \delta E_{l'}.$$

In fact, for this case, a further notational simplification is possible. Redefining

$$\delta E \equiv \mathscr{E}_{l'} + \delta E_{l'},$$

the summation over l' may be implicitly contained within the cross section σ, using Dirac δ functions to account for discrete energies of excitation (including the purely elastic case) and step functions to account for the relevant continuum levels. Of course, at any level of description, σ also contains implicitly a step function of λ, since λ^2 must be greater than or equal to zero.

Finally, it should be noted that if, for instance, the above case corresponded to the inelastic scattering of electrons, then other integrals accounting for any ejected electron must also be evaluated in order to determine $I_e(\boldsymbol{\psi}_e)$. This particular case for electrons has been discussed in detail by Bydder (1967*b*).

V. REDUCTION OF EQUATIONS TO PRACTICAL FORMS

In this section the reduction of the equations of the preceding sections to more practical forms is briefly discussed. Such forms include transport relationships, conservation equations, the generalized Ohm's law, and equilibrium solutions.

The derivation of transport relationships is straightforward. These relationships are essentially "solutions" of equations (5), (8), and (9) for the $\boldsymbol{u}$, $\{\boldsymbol{p}\}$, and $\boldsymbol{q}$ (or $\boldsymbol{r}$) in terms of all other variables such as n, T (or p), $\boldsymbol{v}, \boldsymbol{f}, \ldots$. These solutions may be obtained by a method of successive approximation, being valid provided the collision or Larmor times and mean free paths or Larmor radii (or hybrids of these) are small compared with the characteristic times or dimensions of the system as a whole. Following the method of Herdan and Liley (1960), on using equations (15), (16), (17), and the expressions for $\boldsymbol{l}$, $\boldsymbol{h}$, and $\boldsymbol{H}$ given in Section II(*d*), equations (5), (8), and (9) may be written in the form

$$A_j(\boldsymbol{u}_j)+\frac{\partial p_j}{\partial \boldsymbol{x}}-\rho_j \boldsymbol{f}_j^0-\rho_j \boldsymbol{u}_j\times \boldsymbol{b}_j=\sum_s (c_{js}^{uu}\,\rho_s \boldsymbol{u}_s+c_{js}^{ur}\boldsymbol{r}_s)\,,$$

$$A_j(\{\boldsymbol{p}_j\})+2p_j\left\{\frac{\partial \boldsymbol{v}}{\partial \boldsymbol{x}}\right\}-2\rho_j\{\boldsymbol{f}_j^0\,\boldsymbol{u}_j\}-2\{\{\boldsymbol{p}_j\}\times \boldsymbol{b}_j\}=\sum_s c_{js}^{pp}\{\boldsymbol{p}_s\}\,,$$

$$A_j(\boldsymbol{q}_j)-\boldsymbol{f}_j^0.\{\boldsymbol{p}_j\}-\frac{5}{2}p_j \boldsymbol{f}_j^0+\frac{5}{2}\frac{\partial}{\partial \boldsymbol{x}}\left(\frac{kT_j}{m_j}p_j\right)-\boldsymbol{q}_j\times \boldsymbol{b}_j=\sum_s (c_{js}^{qu}\,\rho_s \boldsymbol{u}_s+c_{js}^{qr}\boldsymbol{r}_s)\,,$$

where

$$\boldsymbol{f}_j^0\equiv \boldsymbol{f}_j+\mathrm{d}\boldsymbol{v}/\mathrm{d}t=\boldsymbol{a}_j+\boldsymbol{v}\times \boldsymbol{b}_j\,.$$

The exact form of the A_j's may be determined by comparing these equations with those given in Section II(*b*), it being important to note, however, that they are primarily functions of the derivatives of $\boldsymbol{u}$, $\{\boldsymbol{p}\}$, and $\boldsymbol{q}$. A somewhat more convenient equation than that given for $\boldsymbol{q}$ is one for $\boldsymbol{r}$. This is obtained by subtracting $\frac{5}{2}kT_j/m_j$ times equation (3) from equation (5), leading to

$$A_j(\boldsymbol{r}_j)-\boldsymbol{f}_j^0.\{\boldsymbol{p}_j\}+\frac{5}{2}\frac{kp_j}{m_j}\frac{\partial T_j}{\partial \boldsymbol{x}}-\boldsymbol{r}_j\times \boldsymbol{b}_j=\sum_s (c_{js}^{ru}\,\rho_s \boldsymbol{u}_s+c_{js}^{rr}\boldsymbol{r}_s)\,,$$

where

$$c^{r\alpha}=c^{q\alpha}-\tfrac{5}{2}(kT/m)c^{u\alpha}\,.$$

On neglecting the A_j's these equations determine the first approximations for the $\boldsymbol{u}$'s, $\{\boldsymbol{p}\}$'s, and $\boldsymbol{r}$'s (or $\boldsymbol{q}$'s). Using these first approximations to obtain first approximations for the A_j's and on retaining these latter terms, the equations then yield second approximations for the $\boldsymbol{u}$'s, $\{\boldsymbol{p}\}$'s, and $\boldsymbol{r}$'s. This process is repeated until the desired degree of accuracy is achieved. In practice, however, there is little value in proceeding beyond the first approximation since the higher order expressions are usually so complex that they are analytically unusable. Therefore, if the first approximations should be inadequate a different method of approximation from that described must be sought.

Coupled with the transport relationships are the continuity (n_j) and the energy (p_j or T_j and U_j) equations and an equation for $\boldsymbol{v}$. If $\boldsymbol{v}$ is equivalent to $\boldsymbol{v}_0$, the mean mass velocity of the mixture, then an equation for this variable is readily obtained. On summing equations (5) over all j, the usual momentum conservation equation is derived, namely,

$$\frac{\partial \rho \boldsymbol{v}_0}{\partial t} = \rho \boldsymbol{g} + \sigma \boldsymbol{E} + \boldsymbol{j} \times \boldsymbol{B} - \frac{\partial}{\partial \boldsymbol{x}} \cdot (\boldsymbol{p} + \rho \boldsymbol{v}_0 \boldsymbol{v}_0),$$

where $\boldsymbol{j}$ is the current density and σ the charge density, given by

$$\boldsymbol{j} = \sum_j n_j e_j (\boldsymbol{u}_j + \boldsymbol{v}_0), \qquad \sigma = \sum_j n_j e_j,$$

while

$$\rho = \sum_j \rho_j, \qquad \boldsymbol{p} = \sum_j \boldsymbol{p}_j.$$

Similarly, a conservation equation for ρ may be obtained by summing equations (4), the result being

$$\frac{\partial \rho}{\partial t} + \frac{\partial}{\partial \boldsymbol{x}} \cdot \rho \boldsymbol{v}_0 = 0.$$

On the other hand, on summing equations (6) and (7), a true conservation equation is not obtained since radiation losses (and gains) have to be taken into account. It is, however, possible to establish a continuity equation for the radiation energy density D, this being of the form

$$\frac{\partial D}{\partial t} + \frac{\partial}{\partial \boldsymbol{x}} \cdot \boldsymbol{R} = -\sum_j \left(I_j(\mathscr{E}_j) + I_j(\tfrac{1}{2} m_j w_j^2) \right),$$

$\boldsymbol{R}$ being the radiation flux vector. (The absorption of radiation etc. is discussed in Section VI.) On summing over all j and adding the three types of energy equations the following equation is obtained

$$\frac{\partial(\frac{3}{2}p + U + D)}{\partial t} + \frac{\partial}{\partial \boldsymbol{x}} \cdot \left((\tfrac{3}{2}p + U)\boldsymbol{v}_0 + \boldsymbol{Q} + \boldsymbol{R} \right) + \boldsymbol{p} : \frac{\partial \boldsymbol{v}_0}{\partial \boldsymbol{x}} = \boldsymbol{E} . \boldsymbol{j},$$

where

$$p = \sum_j p_j, \qquad U = \sum_j U_j, \qquad \boldsymbol{Q} = \sum_j (\boldsymbol{q}_j + U_j \boldsymbol{u}_j),$$

$\boldsymbol{Q}$ being the total thermal flux vector.

The final basic equation for the system is the generalized Ohm's law. This is obtained by multiplying equations (5) throughout by e_j/m_j and summing over all j. However, due to differences in mass this equation is basically nothing more than an equation for the electrons. Furthermore, for $\boldsymbol{v} = \boldsymbol{v}_0$,

$$\boldsymbol{u}_j \ll \boldsymbol{u}_\mathrm{e} \quad (j \neq \mathrm{e}) \qquad \text{and} \qquad \boldsymbol{j} \simeq n_\mathrm{e} e_\mathrm{e} \boldsymbol{u}_\mathrm{e}.$$

Therefore, from equations (5), (16), and (47) the Ohm's law for the mixture is

$$\frac{m_e}{n_e e^2}\left(\frac{\partial \boldsymbol{j}}{\partial t}+\frac{\partial}{\partial \boldsymbol{x}}\cdot(\boldsymbol{v}_0\,\boldsymbol{j})+\boldsymbol{j}\cdot\frac{\partial \boldsymbol{v}_0}{\partial \boldsymbol{x}}\right)-\frac{1}{n_e e}\frac{\partial}{\partial \boldsymbol{x}}\cdot\boldsymbol{p}_e$$
$$+(n_e e)^{-1}\boldsymbol{j}\times\boldsymbol{B}-(\boldsymbol{E}+\boldsymbol{v}_0\times\boldsymbol{B}) = -\eta\boldsymbol{j}-\alpha\boldsymbol{r}_e\,,$$

where

$$\eta = -(n_e e^2)^{-1}\sum_k n_k c^{uu}_{e,ke}(\alpha_e)\,, \qquad \alpha = (n_e e m_e)^{-1}\sum_k n_k c^{ur}_{e,ke}(\alpha_e)\,,$$

and $e = |e_e|$. Again, due to mass differences the $c_{e,ke}$ coefficients may be reduced to relatively simple forms (e.g. see Bydder 1967*b*).

Without considering specific cases it is not possible to reduce these basic equations further. It would, of course, be convenient to define gross coefficients of thermal conductivity and viscosity. In general, however, this is not practicable. On adding together, say, the $\boldsymbol{q}_j$'s, terms other than a simple temperature gradient are involved, while the problem is further complicated by the fact that the various components of the mixture may have different temperatures. Again, since $\boldsymbol{Q}$ involves $U_j\boldsymbol{u}_j$ it is obvious that a density gradient could perhaps be of equal importance. However, in certain particular cases various simplifications should be possible. For instance, in a polyatomic gas mixture it should be possible to relate U to $\frac{3}{2}p$ by the introduction of the ratio of specific heats. In fact, it should even be possible to define a temperature characteristic of the internal energy of a particle and express the appropriate collision terms in such a manner that they exhibit the relaxation of energy between internal and translational degrees of freedom. Results of this nature have been obtained by Wang-Chang and Uhlenbeck (1951) using a Chapman–Enskog approach to the inelastic collision problem. So far, of course, the possibility of a number of internal degrees of freedom has been avoided, a particle being characterized solely by its total internal energy $\mathscr{E}_j$. To adequately account for this possibility the notation must be modified. One way of doing this is to put the subscript

$$j \equiv j_1+j_2+j_3+\ldots,$$

leading to

$$\mathscr{E}_j = \mathscr{E}_{j_1}+\mathscr{E}_{j_2}+\mathscr{E}_{j_3}+\ldots,$$

where $j_1, j_2, j_3, \ldots$ characterize the internal degrees of freedom. In general, this notational modification in no way alters the results of the preceding sections. However, for specific problems it can introduce additional notational complexity, since implicit within the summations over j, k, l, etc. there are also summations over $j_1, j_2, \ldots, k_1, k_2, \ldots$, etc.

Finally, referring to the equilibrium solutions, in the absence of spatial gradients and applied forces these are determined by

$$I_j(\psi_j) = 0\,, \qquad \text{for all} \quad \psi_j\,.$$

From (16), (17), and (18) these equations immediately yield

$$\boldsymbol{u}_j = \{\boldsymbol{p}_j\} = \boldsymbol{q}_j = \boldsymbol{r}_j = 0\,,$$

and the distribution functions become Maxwellian. On the other hand, the solutions of

$$I_j(m_j) = 0\,, \qquad I_j(\mathscr{E}_j) = 0\,, \qquad I_j(\tfrac{1}{2}m_j w_j^2) = 0$$

are not so obvious. In the absence of radiation it is to be expected that the appropriate solutions will be of the form

$$T_j = T\,, \qquad n_j \propto \exp(-\mathscr{E}_j/kT)\,, \qquad \text{for all } j\,.$$

However, this has not been proved and the problem of finding the correct equilibrium solutions has still to be solved.

VI. DISCUSSION

Inevitably, this paper has been primarily mathematical in character and little of the physics associated with the results has been discussed. In particular, it has not been possible to discuss the various effects implied by the collision integrals. For instance, it is interesting to note the coupling between the momentum and thermal (or heat) flux equations. In the case of simple monatomic gases such coupling leads to thermal diffusion effects, anisotropic diffusion and resistivity coefficients, and other effects. These are well known and in general well understood. However, what is interesting is the implication that such effects are a peculiarity of particle type and not simply particle mass. That is, for instance, it is possible that these effects (thermal diffusion in particular) associated with inelastic collisions could lead to spatial separation of excited states of the same atom. Only an exact evaluation of the relevant coefficients involved, however, will prove or disprove this conjecture. Another interesting observation concerns the energy integrals. Even if the collision is inelastic there is still an "elastic" exchange of energy. On reflection this is an obvious result, but it is particularly well emphasized by the exact form of the energy integrals.

As already remarked, with one notable omission, all important collision phenomena in a relatively dilute gas have been accounted for. The omission concerns the direct interaction of radiation with the gas particles. The various emission processes such as bound–bound (excitation and natural decay), free–bound (recombination and natural decay), and free–free (bremsstrahlung, via the δE term) have all been included. On the other hand, absorption, stimulated emission, photo-ionization, and Compton scattering have been ignored. However, on regarding a photon as a particular particle type, these processes are analogous to recombination, ionization, a general inelastic collision, and a general inelastic collision respectively. In one sense, therefore, the physics of these processes has also been dealt with in the preceding sections. In fact, because of this, it is interesting to speculate on whether or not the results of this paper may also be applied to such direct photon interactions.

A photon of frequency ν is equivalent to a particle of mass $h\nu/c^2$. If in addition the energy of the photon is divided into a translational component of $\frac{1}{2}h\nu$ ($= \frac{1}{2}mc^2$) and an internal energy of $\frac{1}{2}h\nu$, then on ignoring relativistic effects the basic dynamics of a collision between a photon and a gas particle are the same as for any other two particles. Therefore, on associating a velocity distribution function $f_\nu(\boldsymbol{x}, \boldsymbol{w}, t)$ with photons of frequency ν, these may be regarded as a particular particle type characterized by a mass m_ν, internal energy $\mathscr{E}_\nu$, and charge e_ν, where

$$m_\nu = h\nu/c^2\,, \qquad \mathscr{E}_\nu = \tfrac{1}{2}h\nu\,, \qquad e_\nu = 0\,.$$

It follows that an effective kinetic temperature T_ν may be defined by

$$\tfrac{3}{2}kT_\nu = \tfrac{1}{2}h\nu,$$

leading, in particular, to an α_ν given by

$$\alpha_\nu \equiv m_\nu/2kT_\nu = 3/2c^2\,,$$

c being, of course, the speed of light. Thus all parameters such as β, γ, and ζ that were introduced in Section III are well-defined functions. On the other hand, the final form for the collision integrals given in Section III(d) depended on using the expressions (14) for the distribution functions. Obviously these functions as such cannot be used directly to describe the velocity distribution of photons. However, for a given speed $\boldsymbol{w}$ they do specify the angular distribution in velocity space. Therefore, for $f \equiv f_\nu$, on replacing f^0 in equations (14) by

$$f^0 \equiv f^0_\nu N\,\delta(c-g)\,,$$

where $\delta(c-g)$ is a *Dirac* delta function, g being any relevant relative or "peculiar" speed, these functions may also be used to describe the photon velocity distributions, with

$$f^0_\nu = n_\nu(\alpha_\nu/\pi)^{3/2}\exp(\alpha_\nu w^2)$$

and N defined by

$$\int \boldsymbol{w}\, f_\nu\, \mathrm{d}\boldsymbol{w} = n_\nu\,.$$

n_ν is the number density per unit frequency range for photons of frequency ν and N is a dimensional normalizing factor. Using the previously determined value for α_ν it may be confirmed that

$$N = (\tfrac{2}{3}\pi c^2)^{3/2}\exp(\tfrac{3}{2})/4\pi c^2 \simeq c\,.$$

It then follows that provided the term

$$N\,\delta(c-g) \equiv N\,\delta(\gamma c - y)$$

is included within the Ω's, the results of Section III(d) can be applied directly to photon–particle interactions. Of course, in general the inclusion of photons introduces a continuum of particle types (i.e. a continuum of ν or m_ν) and hence various of the summations over k, l, and $(k'l')$ must be replaced by integrations over ν. Again, various equations of change for the photons must be developed in order to determine, in particular, the n_ν. With $\boldsymbol{\nu}$ set equal to zero this poses no problem since such equations will be the same as those given in Section II(b). However, for $\boldsymbol{\nu}$ equal to say ν_0, the relevant equations may be somewhat more complex since it is possible that a relativistic-like summation of velocities may be involved. This particular aspect has not been pursued. Again, no rigorous confirmation or proof of the various statements and conjectures made in this discussion has been sought. Nevertheless, even if some or all of these statements and conjectures should ultimately prove to be false, it is clear that it should be possible to arrive at a kinetic theory for the photons which is perfectly consistent with the analysis of the preceding sections.

VII. References

Bydder, E. L. (1967*a*).—Australian National University Dept. Engineering Physics Rep. No. RR 17.

Bydder, E. L. (1967*b*).—Ph.D. Thesis, Australian National University.

Bydder, E. L., and Liley, B. S. (1967).—Australian National University Dept. Engineering Physics Rep. No. RR 15.

Chapman, S., and Cowling, T. G. (1952).—"The Mathematical Theory of Non-uniform Gases." 2nd Ed. (Cambridge Univ. Press.)

Engelhardt, A. G., and Phelps, A. V. (1963).—*Phys. Rev.* **131**, 2115.

Grad, H. (1949).—*Communs pure appl. Math.* **2**, 331.

Herdan, R., and Liley, B. S. (1960).—*Rev. mod. Phys.* **32**, 731.

Hirschfelder, J. O., Curtiss, C. F., and Bird, R. B. (1954).—"Molecular Theory of Gases and Liquids." (Wiley: New York.)

Kolodner, I. I. (1950).—Doctoral Dissertation, New York University.

Liley, B. S. (1963).—Ph.D. Thesis, University of Reading.

Wang-Chang, C. S., and Uhlenbeck, G. E. (1951).—University of Michigan, Rep. No. CM-681.

ELECTRON DRIFT AND DIFFUSION IN PARAHYDROGEN AT 77°K

By R. W. CROMPTON* and A. I. McINTOSH*†

[*Manuscript received April* 10, 1968]

Summary

This paper reports a series of experiments to measure electron diffusion and drift in pure parahydrogen at 77°K. Tables of data are given for the electron drift velocity W in the range $1\cdot2\times10^{-19} \leqslant E/N \leqslant 9\cdot5\times10^{-17}$ V cm² and for the ratio of diffusion coefficient to mobility D/μ for $2\times10^{-20} \leqslant E/N \leqslant 6\times10^{-17}$ V cm². As expected, these data are indistinguishable from the data for normal hydrogen in the thermal region and at the higher values of E/N where vibrational excitation is the dominant process controlling the electron energy distribution. However, at intermediate values of E/N, the values of W and D/μ differ by more than 10 and 20% respectively from the corresponding values in normal hydrogen, demonstrating the influence of the difference in the statistical weights of the rotational levels in the two gases.

I. INTRODUCTION

Measurements of the transport coefficients of a swarm of electrons drifting and diffusing through a gas under the influence of a uniform electric field can be used to determine the energy dependence of the cross sections for the elastic and inelastic collisions between the electrons and the gas molecules (Frost and Phelps 1962; Engelhardt and Phelps 1963; Crompton, Elford, and Jory 1967). In a previous paper (Crompton, Elford, and McIntosh 1968) it was pointed out that, although the momentum transfer cross section can be deduced with adequate precision in the inert gases at energies below the first excitation threshold (see, e.g. Crompton, Elford, and Jory 1967), the results obtained in the molecular gases have been less satisfactory. Although this situation is partly due to the spread in some of the experimental data, it is largely the result of the difficulties in obtaining a unique set of elastic and inelastic cross sections.

The first of the limitations described above has been largely removed for hydrogen and deuterium by recent determinations of the drift velocity W and the ratio D/μ of diffusion coefficient to mobility (Lowke 1963; Crompton, Elford, and McIntosh 1968) but the second limitation remains. Thus, although it is now possible to determine unambiguously whether a particular set of cross sections is consistent with the experimental data, the more fundamental difficulty associated with the necessity to determine the cross sections for three or more processes from measured values of only two transport coefficients has not been overcome. For this reason we have measured electron transport coefficients in parahydrogen at 77°K. At this temperature, provided the mean energy of electrons in the swarm is not much greater

---

* Ion Diffusion Unit, Australian National University, P.O. Box 4, Canberra, A.C.T. 2600.

† Present address: Department of Pure and Applied Physics, The Queen's University of Belfast, Northern Ireland.

Aust. J. Phys., 1968, **21**, 637–47

than the mean molecular energy, energy transfer between electrons and gas molecules can occur only through elastic collisions or by the excitation of the $J = 0 \rightarrow 2$ rotational transition. Thus, in analysing the transport data, cross sections for only these two processes need be considered and it should be possible to make a unique determination of their energy dependence in this special case.

A preliminary account of the work described in this paper has been given elsewhere (Crompton and McIntosh 1967).

II. APPARATUS AND EXPERIMENTAL TECHNIQUES

The measurements of the electron drift velocity W were made using the Bradbury–Nielsen time-of-flight technique, while the measurements of D/μ, the ratio of diffusion coefficient to mobility, were made using the Townsend–Huxley lateral diffusion method. The experimental techniques and the apparatuses used have been described previously (Crompton and Jory 1962; Lowke 1963; Crompton, Elford, and Gascoigne 1965; Crompton, Elford, and McIntosh 1968) and the present description is therefore restricted to those features peculiar to the parahydrogen experiments.

Although parahydrogen is commonly prepared in liquid form, it is difficult to prepare gas that contains almost 100% of the para-modification and that has the degree of purity required for the D/μ measurements at 77°K, where the oxygen concentration must be less than one part in 10^9 (Crompton, Elford, and McIntosh 1968). The techniques used to prepare the gas samples and to test their parahydrogen content are described in detail in the Appendix. The gas samples used were of a purity comparable with that of the normal hydrogen and deuterium used by Crompton, Elford, and McIntosh and were shown to contain not less than 98% of the para-form. The possible 2% of unconverted gas would not significantly alter the values of either W or D/μ.

In previous measurements of the electron transport coefficients, thermionic emission from platinum filaments was used as the source of electrons. However, initial tests of the stability of the parahydrogen samples when in contact with a heated filament showed that reconversion to normal hydrogen (25% para, 75% ortho at 77°K) occurred very rapidly. On the other hand, when the filament was replaced by a silver-coated foil of americium 241 to provide electrons by volume ionization of the gas, the parahydrogen samples remained stable over a period of several days.

The use of the radioactive source introduced a difficulty into the D/μ measurements that was not present in the work described previously. It was now possible for some electrons to be present within the diffusion chamber that had not entered through the source hole. These electrons, which would falsify the distribution of current at the anode, could be produced either by α-particles entering the chamber through the source hole or by the accompanying weak γ-radiation. The first possibility was eliminated by the suitable design of the source itself. The foil was formed into a cylinder that fitted within a supporting copper cylinder mounted in place of the filament normally used and a series of annular baffle plates was then fitted within the cylinder to prevent the incidence of α-particles on the hole.

Since the entry of the γ-rays into the diffusion chamber could not be prevented, compensation had to be made for the small background currents which they caused. Since these currents were a function of the gas pressure and the electric field, the compensation had to be adjusted for each determination of a current ratio. At the highest gas pressures the background current to the annular electrode was a few per cent of the current to be measured, while that to the disk, which had only a small fraction of the area, was almost negligible. Compensation was effected by means of a high resistor (10^{13} ohms) and variable potential connected to each of the electrometers. After applying a field in the reverse direction in the region above the source hole, the compensating devices were adjusted to ensure negligible drift of the electrometers during the 50 sec integrating cycle. The smallness of the currents and their stability were such that no difficulty was experienced in annulling them. Since the current-measuring technique is based on an integrating null method, the shunting effect of the high resistors was negligible, the time constants of the electrometers being still of the order of 300 sec.

In both the W and D/μ experiments, the values of E/N, the ratios of electric field strength to gas number density, were found from the known values of the electric field strength and accurate measurements of the gas temperature T and pressure p. All the experimental parameters were measured in the manner described by Crompton, Elford, and McIntosh (1968).

III. Results

(a) Drift Velocity

As in previous work, values of the drift velocity were determined at a series of E/N values, using several gas pressures for each value. In each determination, the characteristic frequency f_0 was found by measuring the frequencies corresponding to the first two maxima in the graph of transmitted current as a function of frequency (see, e.g. Elford 1966). The pairs of values of f_0 found in this way were in agreement to within $0\cdot2\%$ for all the measurements used to calculate the measured drift velocities W' shown in Table 1. Errors from contact potential differences were kept below $0\cdot25\%$ by including only those data for which the electric field strength was $5\cdot0$ V cm^{-1} or greater.

Two experimental runs in parahydrogen were made, one covering the pressure range $10 \leqslant p \leqslant 250$ torr and the other the range $10 \leqslant p \leqslant 350$ torr. At the pressures common to the two runs the agreement between the sets of data was always better than $0\cdot3\%$. This suggests that the single set of data taken at pressures of 300 and 350 torr can also be considered reliable.

The mean temperature (77·0°K) at which the results were recorded for pressures greater than 100 torr has been taken as the gas temperature to which all the measurements refer. For $p \geqslant 100$ torr, fluctuations about this temperature were less than 0·2 degK. At pressures less than 100 torr somewhat larger temperature variations (but still less than 0·5 degK) were observed. However, the lower pressures were required only for the measurements at higher values of E/N where the energy distribution, and hence the value of W, is substantially independent of the temperature; consequently, provided the correct temperature is used to calculate the value of the number density from the pressure, no significant error is made in assuming all the results to apply to 77·0°K.

TABLE 1

EXPERIMENTAL VALUES OF DRIFT VELOCITY FOR ELECTRONS IN PARAHYDROGEN AT 77·0°K

The number in square brackets following a value is the power of 10 by which this and subsequent values are to be multiplied: 1·195[−19] means $1 \cdot 195 \times 10^{-19}$

E/N (V cm^2)	W' (cm sec^{-1})							Best Estimate, W (cm sec^{-1})
	p = 350	300	250	200	100	50	20 torr	
1·195 [−19]	3·78 [4]							
1·435	4·40	4·41 [4]						
1·594	4·80	4·80	4·80 [4]					
1·992	5·73	5·73	5·73	5·72 [4]				
2·391	6·58	6·58	6·58	6·57				
3·188	8·14	8·14	8·14	8·13				
3·985	9·57	9·58	9·59	9·58	9·57 [4]			
4·782	1·094 [5]	1·094 [5]	1·096 [5]	1·095 [5]	1·095 [5]			
5·579	1·226	1·227	1·230	1·229	1·230			
6·376	1·356	1·357	1·359	1·360	1·362			
7·173	1·483	1·485	1·487	1·487	1·491			
7·970	1·606	1·608	1·611	1·612	1·615	1·614 [5]		
9·564	1·846	1·848	1·850	1·852	1·857	1·858		
1·195 [−18]	2·18(3)	2·18(8)	2·19(0)	2·19(2)	2·19(7)	2·20(1)		
1·435	2·49(8)	2·50(2)	2·50(6)	2·50(8)	2·51(5)	2·52(1)		
1·594	2·69(6)	2·70(1)	2·70(5)	2·70(7)	2·71(4)	2·71(8)		
1·992	3·15	3·16	3·16	3·16	3·17	3·18	3·17 [5]	
2·391	3·56	3·57	3·57	3·57	3·58	3·59	3·58	
3·188		4·26	4·27	4·27	4·28	4·29	4·28	
	p = 300	250	200	100	50	20	10 torr	
3·985 [−18]		4·84 [5]	4·85 [5]	4·85 [5]	4·86 [5]	4·86 [5]		4·84 [5]
4·782			5·33	5·33	5·33	5·33		5·33
5·579				5·73	5·73	5·73		5·73
6·376				6·07	6·08	6·07		6·07
7·173				6·37	6·38	6·37		6·37
7·970				6·64	6·65	6·64		6·64
9·564				7·09	7·10	7·09		7·09
1·195 [−17]					7·64	7·64		7·64
1·435					8·09	8·09		8·09
1·594					8·36	8·36		8·36
1·992					8·96	8·97		8·96
2·391						9·53	9·54 [5]	9·52
3·188						1·064 [6]	1·066 [6]	1·063 [6]
3·985						1·174	1·178	1·173
4·782						1·282	1·286	1·281
5·579							1·389	1·387
6·376							1·487	1·485
7·173							1·582	1·580
7·970							1·675	1·673
9·564							1·850	1·848

Values of W'. are shown in Table 1 for the range $1 \cdot 2 \times 10^{-19} \leqslant E/N \leqslant 9 \cdot 5 \times 10^{-17}$ V cm^2. The "best estimate" values of the drift velocity W have been found by correcting the values of W' for the influence of diffusion using the procedure described previously (Lowke 1963; Crompton, Elford, and Jory 1967; Crompton, Elford, and McIntosh 1968). The corrections made to the values of W' were very small, the greatest difference between the values of W' and W being 0·15% at $E/N = 5\cdot579\times10^{-17}$ V cm². An error limit of ±2% is placed on the best estimate values of W in Table 1.

Below $E/N = 3\cdot985\times10^{-18}$ V cm² no best estimate values of W are given because, as in nitrogen (Lowke 1963) and deuterium (Crompton, Elford, and McIntosh 1968), the values of W' increase more rapidly as p is lowered than can be accounted for by the effects of diffusion. The differences not accountable for by diffusion are about 0·5% for values of E/N of the order of 10^{-18} V cm² where it was possible to take the results over the widest range of pressures. If account is taken of the departure of hydrogen from a perfect gas, this difference can be decreased by, at most, 0·1%. The discrepancies are very small but are considered significant when compared with the experimental scatter which was no more than ±0·15%.

TABLE 2

EXPERIMENTAL VALUES OF D/μ FOR ELECTRONS IN PARAHYDROGEN AT 77·3°K

E/N (V cm²)	D/μ (V)	E/N (V cm²)	D/μ (V)	E/N (V cm²)	D/μ (V)	E/N (V cm²)	D/μ (V)
		$1\cdot0\times10^{-19}$	0·00795	$1\cdot0\times10^{-18}$	0·0181(4)	$1\cdot0\times10^{-17}$	0·0786
		1·2	0·00830	1·2	0·0194(1)	1·2	0·0935
		1·4	0·00866	1·4	0·0206	1·4	0·107(7)
		1·6	0·00904	1·6	0·0219	1·6	0·124(0)
		1·8	0·00944	1·8	0·0231	1·8	0·139(0)
$2\cdot0\times10^{-20}$	0·00683	2·0	0·00983	2·0	0·0243	2·0	0·153(9)
2·5	0·00689	2·5	0·0106(8)	2·5	0·0273	2·5	0·189(1)
3·0	0·00695	3·0	0·0114(8)	3·0	0·0303	3·0	0·220
3·5	0·00699	3·5	0·0122(3)	3·5	0·0333	3·5	0·250
4·0	0·00705	4·0	0·0129(0)	4·0	0·0364	4·0	0·276
4·5	0·00710	4·5	0·0135(4)	4·5	0·0395	4·5	0·300
5·0	0·00716	5·0	0·0141(0)	5·0	0·0428	5·0	0·323
6·0	0·00730	6·0	0·0150(7)	6·0	0·0496	6·0	0·365
7·0	0·00745	7·0	0·0159(3)	7·0	0·0565		
8·0	0·00761	8·0	0·0167(3)	8·0	0·0638		
9·0	0·00778	9·0	0·0174(6)	9·0	0·0710		

(b) *Ratio of Diffusion Coefficient to Mobility*

Each experimental observation resulted in a value of E/N and a corresponding value of D/μ. All of the results for parahydrogen were plotted on a graph with scales sufficiently large to allow the values of D/μ to be read off at the required intervals of E/N with an error of no more than 0·3%.

Crompton, Elford, and McIntosh (1968) reported a number of sources of error which caused them to reject some of the data they obtained for H_2 and D_2 at 77°K when the field strength was less than 5·0 V cm⁻¹. In the present experiments the greater difficulties in preparing samples of pure parahydrogen made it impracticable to take results with many samples of gas, and therefore all the measured values of D/μ, including all those taken with field strengths of less than 5·0 V cm⁻¹, were used in the final graphs of the data.

Three experimental runs were made in parahydrogen. Above $E/N = 4\times10^{-18}$ V cm^2 all the data were obtained with field strengths of $5\cdot0$ V cm^{-1} or greater. Excellent agreement was obtained in this range, all of the 60 data points from the three runs lying within ±1% of the line of best fit. For many of the values of E/N below this limit, field strengths of $5\cdot0$ V cm^{-1} or greater could still be used, at least at the higher pressures, but the lower values called for the use of progressively smaller field strengths until, at the lowest values, field strengths of only $1\cdot0$ or $2\cdot0$ V cm^{-1} could be used. Although, as is to be expected, the results show more scatter in this region ($E/N < 4\times10^{-18}$ V cm^2), the data from two of the experimental runs were in satisfactory agreement. The third set of data showed evidence of a systematic error that resulted in the majority of points lying above this line. Subsequently, evidence was found that the voltage divider chain feeding the guard electrodes could possibly have been slightly defective during the low E/N portion of the third experimental run. The final curve from which the tabulated data were derived was therefore biased towards the results of the first two runs, but, nevertheless, all the data lay within 2% of the final curve. About 130 data points were measured and plotted in this range.

The values of D/μ in parahydrogen at $77\cdot3$°K were read from the graphs described above and are listed in Table 2. The error limit placed on the data is ±2% for $4\times10^{-18} \leqslant E/N \leqslant 6\times10^{-17}$ V cm^2 and ±3% for $E/N < 4\times10^{-18}$ V cm^2.

IV. Discussion

There have been no previous measurements of electron transport coefficients in parahydrogen. Comparisons of the present values of W and D/μ with similar data taken in normal hydrogen are shown in Figures 1 and 2. The values of D/μ and W in normal hydrogen are taken from the data of Crompton, Elford, and McIntosh (1968) and Lowke (1963) respectively.

The accuracy of the data is sufficient to show the small differences in the transport coefficients that result from the differences in the statistical weights of the rotational levels in the two gases. At low values of E/N the electrons are almost in thermal equilibrium with the gas molecules and, since the momentum transfer cross section is identical in normal and parahydrogen, the values of W and D/μ are the same in both gases. As the value of E/N is increased the electrons obtain sufficient energy to cause rotational excitation of the molecules and, as is shown in the figures, there is also a significant divergence between the data for the two gases. In parahydrogen at 77°K, $99\cdot5$% of the molecules occupy the $J = 0$ rotational state. Since the cross section for the transition $J = 0 \rightarrow 4$ is negligibly small compared with that for $J = 0 \rightarrow 2$, and since the electron currents are too small to raise significantly the population of molecules with $J = 2$, excitation of the $J = 0 \rightarrow 2$ transition is the only rotational excitation process that contributes significantly to the energy loss of the swarm. On the other hand, in normal hydrogen at this temperature 75% of the molecules occupy the $J = 1$ level and only 25% occupy the $J = 0$ level, the populations of higher levels being negligibly small (Farkas 1935). Since the cross sections for the $J = 0 \rightarrow 2$ and $J = 1 \rightarrow 3$ transitions are different (e.g. thresholds of $0\cdot045$ and $0\cdot075$ eV respectively) it follows that rotational energy losses in normal hydrogen differ from those in parahydrogen, causing the observed divergences in the transport data in this region. When the mean electron energy approaches 0·5 eV the majority of the electrons in the swarm have sufficient energy to cause vibrational excitation (for which the threshold is 0·516 eV; Herzberg 1950). Because the cross section for vibrational excitation is so much larger than those for rotational excitation (Engelhardt and Phelps 1963) and is the same for both gases, the differences in the rotational levels become unimportant and the two curves merge again.

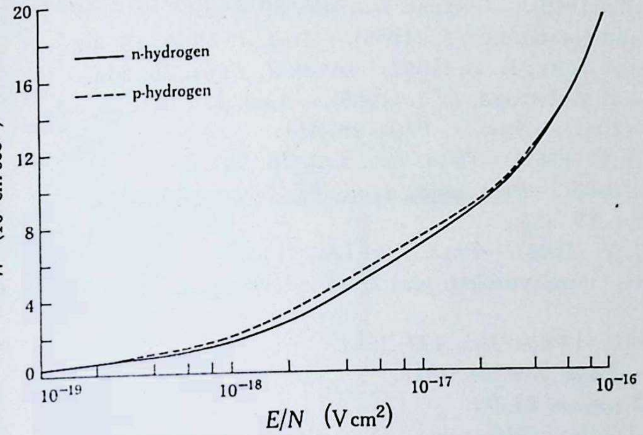

Fig. 1.—Electron drift velocities in parahydrogen at 77°K with the results in normal hydrogen shown for comparison.

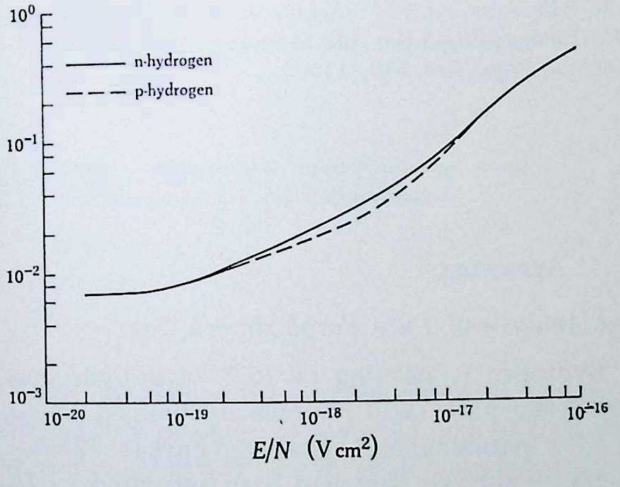

Fig. 2.—Experimental values of D/μ in parahydrogen at 77°K with the results in normal hydrogen shown for comparison.

Various theoretical forms of the cross section for rotational excitation (Gerjuoy and Stein 1955; Dalgarno and Moffett 1963; Sampson and Mjolsness 1965; Takayanagi and Geltman 1965; Lane and Geltman 1967) have been proposed. An analysis is in progress to determine which of them is most consistent with the present experimental data.

V. ACKNOWLEDGMENTS

The authors would like to thank Professor Sir Leonard Huxley for initiating this investigation. They also wish to express their gratitude to Mr. W. R. G. Kemp of the Division of Physics, CSIRO, Sydney, for his helpful advice on the design of the parahydrogen converter and for making the independent check of the ortho–para ratio. The technical assistance received from Mr. J. Gascoigne and the useful discussions with Dr. M. T. Elford are also gratefully acknowledged.

One of us (A. I. McI.) wishes to acknowledge the financial assistance from an Australian National University Research Scholarship.

VI. REFERENCES

BARRICK, P. L., WEITZEL, D. H., and CONNOLLY, T. W. (1954).—*Adv. cryogen. Engng* **1**, 285.
CROMPTON, R. W., and ELFORD, M. T. (1962).—*J. scient. Instrum.* **39**, 480.
CROMPTON, R. W., ELFORD, M. T., and GASCOIGNE, J. (1965).—*Aust. J. Phys.* **18**, 409.
CROMPTON, R. W., ELFORD, M. T., and JORY, R. L. (1967).—*Aust. J. Phys.* **20**, 369.
CROMPTON, R. W., ELFORD, M. T., and MCINTOSH, A. I. (1968).—*Aust. J. Phys.* **21**, 43.
CROMPTON, R. W., and JORY, R. L. (1962).—*Aust. J. Phys.* **15**, 451.
CROMPTON, R. W., and MCINTOSH, A. I. (1967).—*Phys. Rev. Lett.* **18**, 527.
DALGARNO, A., and MOFFETT, R. J. (1963).—*Proc. natn. Acad. Sci. India* **A33**, 511.
ELFORD, M. T. (1966).—*Aust. J. Phys.* **19**, 805.
ENGELHARDT, A. G., and PHELPS, A. V. (1963).—*Phys. Rev.* **131**, 2115.
FARKAS, A. (1935).—"Orthohydrogen, Parahydrogen and Heavy Hydrogen." (Cambridge Univ. Press.)
FROST, L. S., and PHELPS, A. V. (1962).—*Phys. Rev.* **127**, 1621.
GERJUOY, E., and STEIN, S. (1955).—*Phys. Rev.* **98**, 1848.
GRILLY, E. R. (1953).—*Rev. scient. Instrum.* **24**, 72.
HERZBERG, G. (1950).—"Spectra of Diatomic Molecules." (Van Nostrand: Princeton.)
LANE, N. F., and GELTMAN, S. (1967).—*Phys. Rev.* **160**, 53.
LOWKE, J. J. (1963).—*Aust. J. Phys.* **16**, 115.
SAMPSON, D. H., and MJOLSNESS, R. C. (1965).—*Phys. Rev.* **140**, A1466.
TAKAYANAGI, K., and GELTMAN, S. (1965).—*Phys. Rev.* **138**, A1003.

APPENDIX

The Preparation and Analysis of Pure Parahydrogen Gas

When a sample of normal hydrogen (consisting of 75% orthohydrogen and 25% parahydrogen) is cooled, the ortho–para ratio remains unchanged unless the cooling is done in the presence of a paramagnetic catalyst (Farkas 1935). The catalyst used in the present work was iron oxide that had been activated by baking at 140°C for 24 hr at a pressure of 10–20 μHg (Barrick, Weitzel, and Connolly 1954).

Although liquid parahydrogen is commonly prepared, it is more difficult to prepare gaseous parahydrogen having a low concentration of the ortho-modification and free of other impurities, especially oxygen (see Crompton, Elford, and McIntosh 1968). In order to meet the second requirement it is necessary for the conversion apparatus and storage tank to form a closed system with a low outgassing rate, and therefore special precautions are required to ensure that the content of the para-modification in the converted gas samples is very nearly 100%.

A block diagram of the experimental arrangement is shown in Figure 3. Details of the construction of the conversion chamber are shown in Figure 4. The gas reservoir was a stainless steel tank of 15 litres capacity fitted with a Granville–Phillips high pressure UHV valve. The heat exchanger consisted of 24 ft of $\frac{1}{16}$ in. internal diameter copper tubing closely wound into a 1 in. diameter coil. The conversion chamber, containing the heat exchanger and catalyst, and the reservoir were leak tested and thoroughly outgassed before the commencement of the experiment. The reservoir was then filled with high purity normal hydrogen to a pressure of about two atmospheres, using the silver–palladium alloy osmosis tubes described by Crompton and Elford (1962).

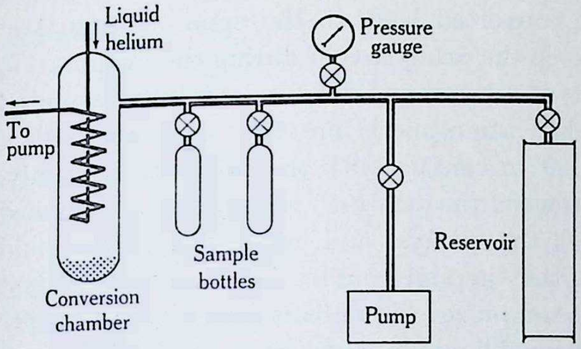
Liquid helium
Pressure gauge
To pump
Sample bottles
Reservoir
Conversion chamber
Pump

Fig. 3 (*above*).—Schematic diagram of the apparatus used for the preparation of pure parahydrogen gas.

Fig. 4 (*right*).—Schematic section of the parahydrogen conversion chamber.

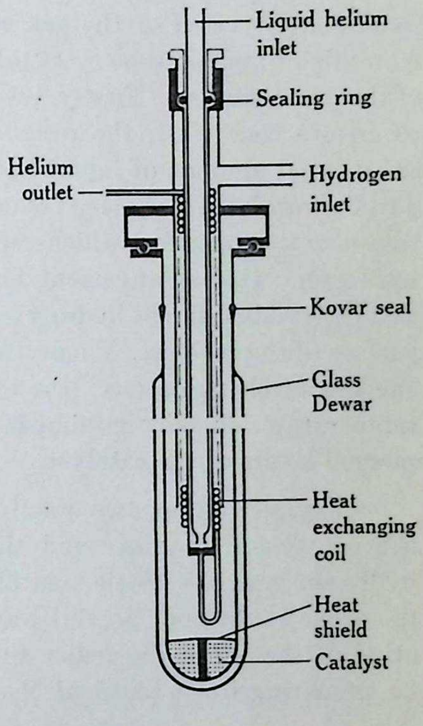
Liquid helium inlet
Sealing ring
Helium outlet
Hydrogen inlet
Kovar seal
Glass Dewar
Heat exchanging coil
Heat shield
Catalyst

To commence the conversion cycle, hydrogen was admitted to the conversion chamber to a pressure of several hundred torr while at the same time liquid helium was drawn through the heat-exchanging coil. The temperature of the system decreased until hydrogen condensed on the copper coil and dripped to the bottom of the chamber where it came into intimate contact with the catalyst. The supply of hydrogen to the conversion chamber was maintained from the reservoir and the cooling continued until the pressure throughout the system (conversion chamber+reservoir) corresponded to the triple point (~ 14°K, 50 torr). Further cooling resulted in the formation of solid hydrogen and reduced the pressure still further, thereby reducing the amount of unconverted normal hydrogen remaining in the reservoir. At this point the chamber was isolated and the reservoir evacuated. The conversion chamber was also pumped for a short period to remove as much as possible of the unconverted gaseous hydrogen without undue wastage of parahydrogen by evaporation from the solid state. With the pump isolated and the reservoir connected to the conversion chamber, evaporation was allowed to continue for some time before the system was cooled again to convert most of the hydrogen back to the solid state. The cycle was repeated several times to ensure that all the hydrogen in the chamber had been in contact at some time with the cold catalyst and the system was finally allowed to warm slightly. The solid and liquid parahydrogen then partially evaporated until the reservoir was filled to atmospheric pressure.

Since the parahydrogen must be made in a closed system, the catalyst remains in the conversion chamber during the warm-up cycle and it is therefore necessary to ensure that the temperature of the catalyst does not rise to a point at which a significant fraction of the gas could be converted back to the ortho-modification. A number of precautions were taken to keep the catalyst cold during the evaporation of the parahydrogen. Firstly, the amounts of catalyst and gas were carefully regulated to ensure that when the reservoir reached atmospheric pressure there was still a substantial amount of liquid hydrogen left in contact with the catalyst. Secondly, a radiation shield was placed over the surface of the catalyst; the shield was attached to a heavy copper rod which ran through the catalyst and into the residual liquid hydrogen. This arrangement improved the thermal contact between the catalyst and the residual liquid hydrogen and also minimized the radiant heating of the upper surface of the catalyst. Finally, a small flow of liquid helium was maintained through the heat-exchanging coil; the effect of this flow was to maintain the coil at a low temperature, thereby minimizing the transfer of heat by radiation to the unsubmerged layers of the catalyst.

Figure 3 shows two small glass sample bottles connected to the line between the conversion chamber and the reservoir. During the preparation of the parahydrogen gas, one bottle was filled at the beginning of the evaporation cycle and the other at the end. In this way samples of gas were obtained that were representative of the gas made under the most favourable and least favourable conditions for preparing 100% parahydrogen.

Analysis of the ortho–para ratios for the samples relies on the difference in thermal conductivity of the two forms (Farkas 1935). For our work a simple analyser based on the design of Grilly (1953) was used. A pair of Sylvania Pirani tubes matched in resistance to within 0·01 Ω formed two arms of a Wheatstone bridge network, the remaining arms being a pair of resistance boxes variable to 0·001 Ω. The tubes were immersed in a liquid nitrogen bath to obtain greater sensitivity. Hydrogen at a pressure of 40 torr was admitted to both the Pirani tubes and balance of the bridge obtained by adjusting the resistance boxes. One of the Pirani tubes was then isolated while the other was evacuated and then filled to a pressure of 40 torr with the gas to be analysed; the out-of-balance current in the bridge circuit was then a measure of the parahydrogen content of the gas sample. The current to the bridge was supplied by a stabilized d.c. supply and was adjusted so that 100% parahydrogen produced full-scale deflection on the meter which measured the out-of-balance current.

The device was calibrated with a sample of parahydrogen collected under the most favourable conditions for its preparation. It was assumed, therefore, that this sample contained 100% of the para-modification.* The sensitivity was found by preparing a 90% parahydrogen sample from a mixture of this gas and normal hydrogen. The resolution was such that a 0·5% change in the parahydrogen concentration could be detected.

The gas sample obtained at the end of the evaporation cycle was indistinguishable from the 100% sample. Similarly, gas samples taken from the stainless steel reservoirs and from the drift velocity apparatus at the end of an experimental run were also indistinguishable from the 100% sample. The parahydrogen content of all the samples used is claimed to be greater than 98%.

---

* The para–ortho ratio was checked at the Division of Physics, CSIRO, Sydney, using a Gow-Mac Instrument Co. Ortho–parahydrogen Analyzer. Within the limits of detection of the instrument, which were of the order of 1%, no orthohydrogen could be detected in the sample.

DIRECTIONAL CORRELATIONS OF GAMMA RAYS IN THE DECAY OF 36 hr ^{82}Br

By S. L. Gupta* and M. M. Bajaj*

[*Manuscript received May 14, 1968*]

Summary

Coincidence and gamma–gamma directional correlation measurements are made for the 10 cascades of ^{82}Kr: 1648–777, 1008–1044, 1317–777, 619–1475, 555–1317, 555–619, 828–1044, 828–(1044)–777, 698–777, and 619–698 keV, of which the cascade 1008–1044 keV has been attempted for the first time. The results permit a unique spin assignment of 5 for the 2829 keV level from the directional correlation of the 1008–1044 keV cascade and a spin of 3 to the level at 2425 keV from that of the 1648–777 keV cascade. Multipole character and admixture are determined for the transitions 1648, 1475, 1044, 1008, 555, 828, 698, 619, and 1317 keV. Computed E2 partial half-lives for the last two transitions are compared with the predictions of the single-particle estimate and the nonaxial rotor model.

I. Introduction

The 36 hr β-decay of ^{82}Br and the positron decay of ^{82}Rb^{m} into ^{82}Kr have been the subject of many investigations since 1941. Even the earlier results showed a rather complicated disintegration scheme and a high multiplicity of the cascades in the level structure of ^{82}Kr. Recent studies on the γ-transitions in ^{82}Kr using more refined techniques (Gfirtner, Reiser, and Schneider 1965; Kenney and Raman 1965; Koch *et al.* 1965; Mo, Hsu, and Wu 1965; Nieschmidt, Mandeville, and Ellsworth 1965; Reidy and Wiedenbeck 1965; Beard 1966; Etherton and Kelly 1966; Raman 1967) helped to construct an acceptable level scheme of ^{82}Kr (Fig. 3), which could also account for some of the earlier data. Some uncertainties, however, still exist. Etherton and Kelly (1966) using a permanent magnet electron spectrometer investigated the decay scheme of ^{82}Br and assigned three possible spin values 2, 3, or 4 to the 2425 keV level. On the other hand, Koch *et al.* (1965) had put forward a spin value of 3 for the same level from the study of the directional correlation of the 1648–777 keV gamma–gamma cascade. Recent correlation measurements of Hsu and Wu (1967) on the same cascade, however, favour a spin value of 3 or 4. In view of these uncertainties, a redetermination of the directional correlation of this cascade with sufficient accuracy is considered necessary for fixing the spin value of the 2425 keV level. The work of Etherton and Kelly (1966) also gave three possible spin values 4, 5, or 6 for the 2829 keV level. No unique spin assignment for this level is possible from the presently available data. An attempt is therefore made from the present directional

---

* Department of Physics and Astrophysics, University of Delhi, Delhi-7, India.

Aust. J. Phys., 1968, **21**, 649–60

correlation measurement of the 1008–1044 keV cascade to assign a spin to this level uniquely. The quadrupole admixture in the 1008 keV transition is also determined.

The internal conversion coefficient of γ1648 has not been measured so far and therefore the multipolarity of the transition is not definitely known. Koch *et al.* (1965) reported a predominantly dipole character for γ1648 from the directional correlation study of the 1648–777 keV cascade. As γ1648 is an extremely weak transition, further investigation of the directional correlation of the above cascade appears to be worth while. Again, Waddell and Jensen (1956), Simons *et al.* (1963), and Simons, Bergström, and Anttila (1964) measured the directional correlation of the 555–619 keV cascade. The coincidence rate observed for this cascade is strongly influenced by the Compton contributions of the neighbouring high energy γ-rays. Simons *et al.* (1963) estimated the percentage of the interfering coincidences, but did not apply the necessary correction to their correlation function. Waddell and Jensen (1956), on the other hand, seem to have neglected the interfering effects on their correlation function. Reinvestigation of the directional correlation of the 555–619 keV cascade, taking into account the contribution of the interfering cascades, is therefore considered desirable.

In addition to the above-mentioned cascades, seven other interfering cascades have also been re-examined here in order to make cross-checks on the multipole admixtures of the γ-transitions involved. Finally the partial lifetimes of the 619 and 1317 keV transitions obtained from the experimental data are compared with the single-particle Weisskopf estimates as well as with the nonaxial rotor model, as this may help in understanding the origin of the low-lying excited states of ^{82}Kr.

II. Experimental Procedure

(*a*) *Source Preparation and Details of Procedure*

The ^{82}Br (36 hr) source was produced by the irradiation of natural bromine (50·5% ^{79}Br and 49·5% ^{81}Br) in the form of NaBr with the pile neutrons in the Apsara Reactor of the Bhabha Atomic Research Centre, Bombay. As ^{80}Br^{m}, with a half-life of 4·5 hr, was produced together with the 36 hr ^{82}Br, the source was allowed to decay for several hours to reduce the ^{80}Br^{m} activity to a very low level.

All coincidence and directional correlation measurements were carried out using a fast–slow coincidence scintillation spectrometer having an effective resolving time of about 30 nsec. In coincidence measurements both the detectors were shielded from each other with anti-Compton graded cones and the spectra were analysed using standard line shapes. The coincidence counting rates were measured in 30° increments from 90° to 270°. The total number of coincidences collected at each angular position was about 15 000. The singles counting rates in the movable and fixed detectors and the coincidences were recorded simultaneously in all the runs at each angle. The ratio of true to chance coincidences was about 100 : 1. The singles counting rate at different angular positions was constant to within 1%. In the directional correlation measurements, the data were corrected for the source decay, chance coincidences, geometry, and the interfering cascades.

(*b*) *Gamma Ray Spectrum and Coincidence Measurements*

The observed γ-ray scintillation spectrum of ^{82}Br is reproduced in Figure 1. It does not indicate the presence of any impurity activity in the source.

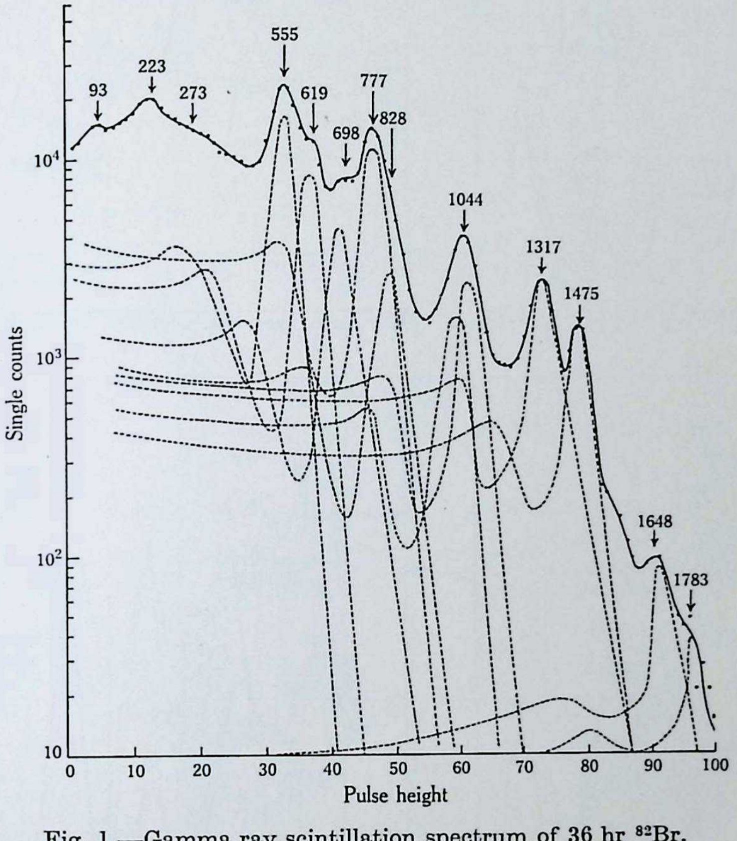

Fig. 1.—Gamma ray scintillation spectrum of 36 hr ^{82}Br.

Figures 2(*a*)–2(*i*) show the coincidence spectra recorded by setting one of the spectrometers successively around the 555, 619, 698, 777, 1044 (with and without conical shielding), 1317, 1475, and 1648 keV energy regions. Results confirm the earlier conclusions (Etherton and Kelly 1966) regarding the coincidence relationships between the various γ-rays. The results of the spectra have been used in correcting the directional correlation data of several cascades for interfering effects of neighbouring cascades.

All the correlation functions reported below, were obtained by fitting the experimental data by a least-squares method, following the treatment given by Breitenberger (1956), and were corrected for the finite geometry of the crystal using the correction factors given by Yates (1965).

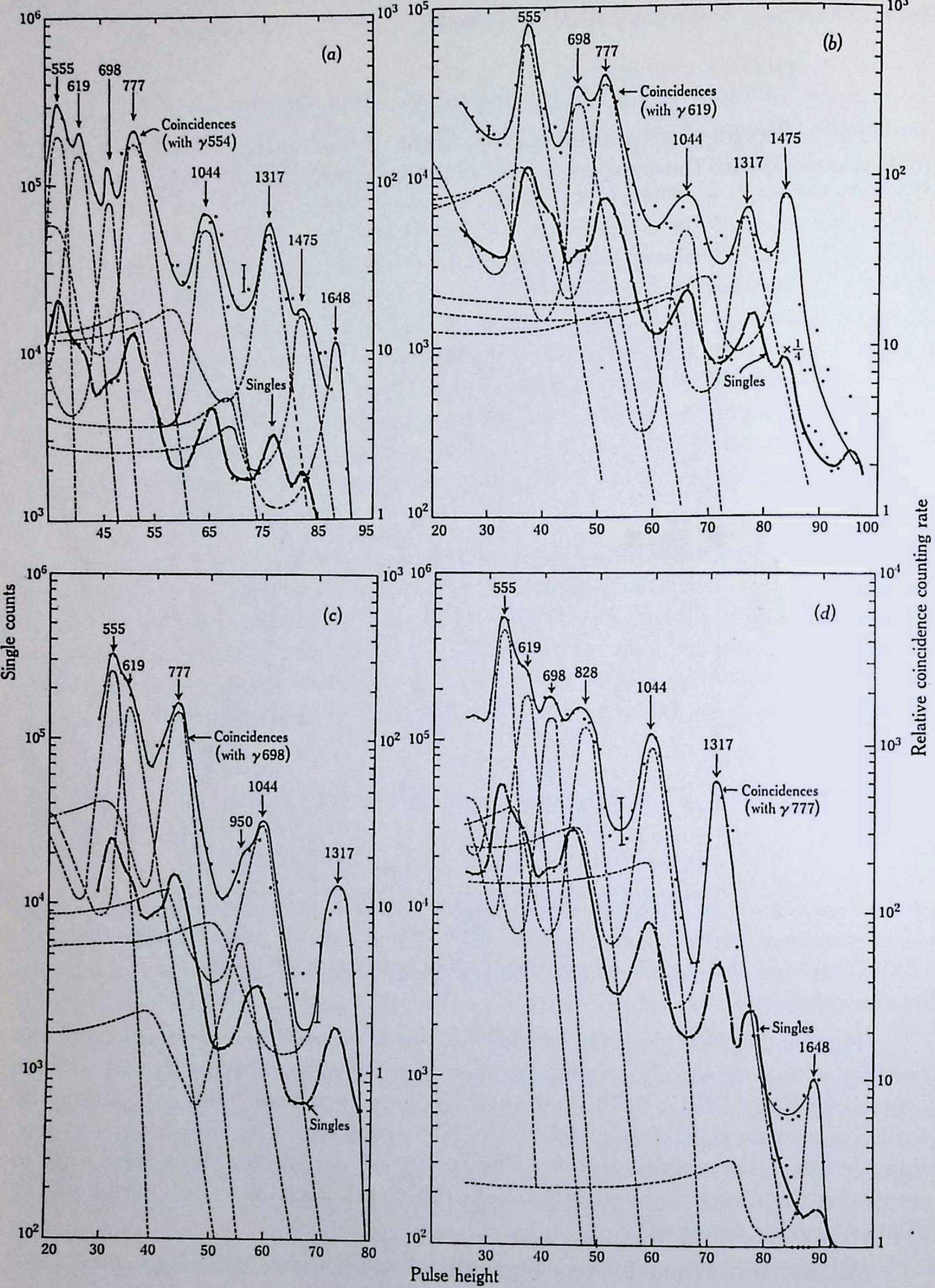

Figs. 2(*a*)–2(*i*).—Gamma ray spectra in coincidence with (*a*) 555 keV photopeak; (*b*) 619 keV region; (*c*) 698 keV region; (*d*) 777 keV photopeak; (*e*) 1044 keV region, recorded without conical shielding; (*f*) 1044 keV region, with conical shielding; (*g*) 1317 keV photopeak; (*h*) 1475 keV photopeak; and (*i*) 1648 keV region.

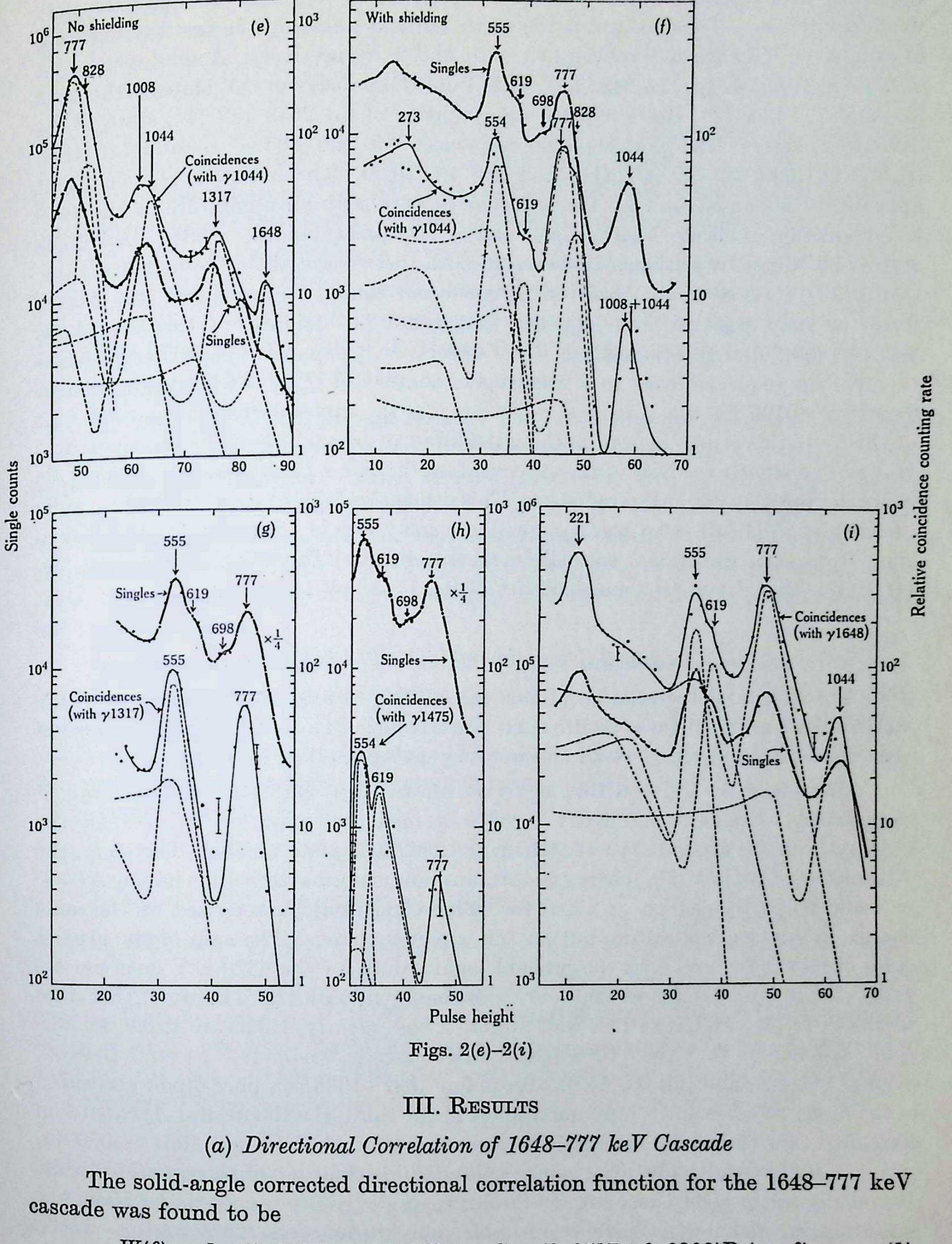

Figs. 2(*e*)–2(*i*)

III. Results

(*a*) *Directional Correlation of 1648–777 keV Cascade*

The solid-angle corrected directional correlation function for the 1648–777 keV cascade was found to be

$$W(\theta) = 1+(0\cdot0427\pm0\cdot0152)P_2(\cos\theta) -(0\cdot0517\pm0\cdot0308)P_4(\cos\theta)\,. \qquad (1)$$

This cascade has also been studied by Koch *et al.* (1965) and Hsu and Wu (1967). It is practically free from all interfering contributions. The reason is that the high energy γ-ray of energy 1783 keV also cascading with $\gamma777$ is extremely weak in intensity. The spin and parity of the ground state and the first excited state of even–even ^{82}Kr are well established as 0^+ and 2^+ respectively. A spin assignment of 2, 3, or 4 follows for the 2425 keV state from the γ-decay of this state to the 1475 (2^+) and 777 keV (2^+) states and the de-excitation of the 2649 keV (4^-) state to the 2425 keV state. The possible spin sequences for the above cascade are then (i) $2(D,Q)2(Q)0$, (ii) $3(D,Q)2(Q)0$, and (iii) $4(Q)2(Q)0$. The observed A_2 coefficient appears to be consistent with the sequence (i) only with an admixture in the 1648 keV transition of either $\sim 93\%$ dipole and $\sim 7\%$ quadrupole or $\sim 98\%$ quadrupole and $\sim 2\%$ dipole radiations. However, in both these cases, the finite negative value ($-0{\cdot}0517 \pm 0{\cdot}0308$) of the observed A_4 coefficient cannot be accounted for. Therefore, the only possible spin sequence that could be assigned to this cascade is $3(D,Q)2(Q)0$. Mixing ratio analysis of the observed A_2 expansion coefficient in terms of this spin sequence leads to a quadrupole content of $Q_{1648} = 0{\cdot}0210 \pm 0{\cdot}0035$ or $0{\cdot}9025 \pm 0{\cdot}0125$ for the 1648 keV radiation. As the internal conversion coefficient of this radiation is not known, nothing definite can be said about its multipolarity. However, a similar analysis of the A_4 coefficient favours a predominantly quadrupole character for the 1648 keV γ-radiation. This conclusion is in contrast with the results of Koch *et al.* (1965), who prefer a predominantly dipole character for this transition from their directional correlation measurements. The work of Hsu and Wu (1967) does not discuss the multipolarity of the 1648 keV transition.

(*b*) *Directional Correlation of 1008–1044 keV Cascade*

The directional correlation of this cascade appears to be isotropic within the statistical accuracy of the measurement. Interference due to neighbouring cascades was found to be extremely small and was therefore not taken into account.

Orbitals of the 777 and 1821 keV levels have been established to be 2^+ and 4^+ respectively. Etherton and Kelly (1966) obtained the value $\log ft = 5{\cdot}7$ for the β-decay from the ground state of ^{82}Br to the 2829 keV state in ^{82}Kr. Therefore, the β-transition of 264 keV (3%) energy is either an allowed normal transition having $\Delta I = 0$ or 1 and no parity change, or a first forbidden transition characterized by the same change in angular momentum but having a parity change. The spin of the ground state of ^{82}Br is 5^-, and thus the probable spin values for the 2829 keV level are 4^-, 4^+, 5^-, 5^+, 6^-, or 6^+. These values are also consistent with the γ-decay of this state to the 2649 (4^-) and 1821 (4^+) keV states. Consequently, there are three possible spin sequences for the 1008–1044 keV cascade, namely, (i) $4(D,Q)4(Q)2$, (ii) $5(D,Q)4(Q)2$, and (iii) $6(Q)4(Q)2$. Assuming that $\gamma1008$ is a pure dipole transition in the first two cases and a pure quadrupole in the third, the theoretical A_2 expansion coefficients for the above three spin sequences are found to be $+0{\cdot}1964$, $-0{\cdot}0714$, and $+0{\cdot}1021$ respectively. The spin sequence (iii) is thus out of the question, while (i) and (ii) can possibly account for the isotropic distribution only if the 1008 keV transition is assumed to have quadrupole admixtures of $\sim 23\%$ and $\sim 1{\cdot}1\%$ respectively. The spin sequence (ii) appears to be more sensitive to multipole mixing and we therefore conclude that the spin of the 2829 keV level is 5. As the conversion coefficient measurements have not been carried out so far for the 1008 keV transition, nothing can be decided about its multipole character or about the parity of the 2829 keV level.

(c) *Directional Correlations of 1317–777, 619–1475, and 555–1317 keV Cascades*

The measurement on the 1317–777 keV cascade is affected by the interfering contribution of the 1648–777 keV cascade. The interference due to the latter cascade has been estimated to be $\leqslant 2\cdot 5\%$ from a careful analysis of the singles and coincidence spectra. As this is quite negligible, we have made no correction for it.

In the case of the 619–1475 keV cascade, both the γ-rays were gated on their high energy sides to minimize interfering effects. With the channel settings and energy windows used, the contribution of each of the four interfering cascades 555–(619)–1475, 555–1317, 1317–777, and 1648–777 keV to the investigated one has been estimated to be $\leqslant 2\%$ and can be neglected.

In the 555–1317 keV cascade, with the gates fixed around the 555 and 1317 keV energy regions, the interfering coincidences are recorded in particular between (i) γ1317 and the Compton electrons of γ777, (ii) the Compton electrons of γ1475 and those of γ619, (iii) the Compton electrons of γ1648 and those of γ777, and (iv) γ555 and the Compton electrons of γ1475 (through the unobserved intermediate radiation γ619). Contributions due to (i) and (ii) are found to be $21\%\pm4\%$ and $6\%\pm4\%$ respectively (Figs. 1 and 2(*a*)); the percentage of interference due to (iii) and (iv) has been estimated to be quite negligible.

True correlation functions for these three cascades and the conclusions derived from them about the multipolarities of the γ-transitions 1317, 619, and 555 keV are given in Table 1. The results obtained are in excellent agreement with those reported by other authors (Benczer-Koller 1958; Simons *et al.* 1963; Simons, Bergström, and Anttila 1964; Etherton and Kelly 1966).

(*d*) *Directional Correlation of 555–619 keV Cascade*

Evaluation of the experimental data yields

$$W(\theta) = 1-(0\cdot0663\pm0\cdot0029)\mathrm{P}_2(\cos\theta)+(0\cdot0110\pm0\cdot0059)\mathrm{P}_4(\cos\theta)\,. \qquad (2)$$

This cascade is influenced by all other high energy cascades and needs further correction. Waddell and Jensen (1956), Simons *et al.* (1963), and Simons, Bergström, and Anttila (1964) have made directional correlation measurements on this cascade and have reported the correlation functions without taking into account the interfering contributions. Their uncorrected functions compare well with our equation (2).

The major contributions in this cascade are from the 1317–777, 1044–777, and 555–1317 keV cascades, which are estimated to be $12\cdot2\%\pm4\cdot0\%$, $4\cdot4\%\pm4\cdot0\%$, and $24\cdot3\%\pm4\cdot0\%$ respectively (Figs. 1 and 2(*a*)). As we did not measure the correlation function for the 1044–777 keV cascade, the expansion coefficients for this cascade were taken from the work of Etherton and Kelly (1966) and were used in applying the correction to the 555–619 keV cascade. Corrections for the interfering contributions from the 1317–777 and 555–1317 keV cascades were applied by using

TABLE 1

CASCADE DATA

Cascade (keV)	A_2	A_4	Possible Spin Sequence	Multipole Mixing in γ-transitions (%)
1317–777	$-0\cdot0301\pm0\cdot0069$	$-0\cdot0452\pm0\cdot0140$	$3(D,Q)2(Q)0$	γ1317: $95\cdot5\ \pm0\cdot5$ E2, $4\cdot5\ \pm0\cdot5$ M1
619–1475	$-0\cdot0992\pm0\cdot0029$	$-0\cdot0022\pm0\cdot0061$	$3(D,Q)2(Q)0$	γ 619: $84\cdot5\ \pm0\cdot5$ E2, $15\cdot5\ \pm0\cdot5$ M1
555–1317	$-0\cdot0915\pm0\cdot0084$	$+0\cdot0500\pm0\cdot0123$	$4(D,Q)3(D,Q)2$	γ1317: $90\cdot5\ \pm2\cdot5$ E2, $9\cdot5\ \pm2\cdot5$ M1 γ 555: pure E1 and γ 555: $99\cdot95\pm0\cdot05$ E1, $0\cdot05\pm0\cdot05$ M2 γ1317: $95\cdot5\ \pm0\cdot5$ E2
828–1044	$+0\cdot2005\pm0\cdot0295$	$-0\cdot0074\pm0\cdot0667$	4(E1)4(E2)2	γ 828: pure E1 γ1044: pure E1
828–(1044)–777	$+0\cdot1244\pm0\cdot0253$	$-0\cdot0162\pm0\cdot0436$	4(E1)4(E2)2(E2)0	γ 828: pure E1 γ1044: pure E2 γ 777: pure E2
698–777	$-0\cdot247\ \pm0\cdot066$	$+0\cdot191\ \pm0\cdot064$	2(E2, M1)2(E2)0	γ 698: 86 ± 11 E2
619–698	$+0\cdot0688\pm0\cdot0206$	$+0\cdot0975\pm0\cdot0464$	3(E2, M1)2(E2, M1)2	γ 698: 82 ± 8 E2

the results given in Section III(*c*). The contributions due to the cascades 698–777, 828–1044, 1008–1044, 555–(619)–1475, 555–(619)–698, 619–1475, 619–698, and 1648–777 keV were estimated to be negligible. The true correlation function for the 555–619 keV cascade then turns out to be

$$W(\theta) = 1-(0\cdot1370\pm0\cdot0142)\mathrm{P}_2(\cos\theta)+(0\cdot0050\pm0\cdot0072)\mathrm{P}_4(\cos\theta)\,. \tag{3}$$

From considerations based on the level structure of ^{82}Kr (Simons *et al.* 1963; Koch *et al.* 1965; Etherton and Kelly 1966) the levels concerned here are 1475(2^+), 2094(3^+), and 2649(4^-) keV. Equation (3) was therefore analysed in terms of the spin sequence $4(D,Q)3(D,Q)2$. Using the result (0·155 M1 +0·845 E2) for the multipolarity of γ619 from Table 1, the mixing ratio analysis shows that the 555 keV transition is predominantly E1 having a very small M2 admixture ($Q_{555} = 0\cdot0005\pm0\cdot0005$).

This cascade provides another check on the multipole character of the 555 keV radiation and supports the results for the cascade 555–1317 keV given in Section III(*c*).

(*e*) *Directional Correlations of 828–1044, 828–(1044)–777, 698–777, and 619–698 keV Cascades*

The true correlation functions for these four cascades, after applying all corrections, are also given in Table 1.

The importance of the triple cascade 828–(1044)–777, with the intermediate radiation being unobserved, lies in deciding the placement of the 828 and 1044 keV transitions. If we regard the 828 keV transition to be the first and the 1044 keV transition to be the second, the measured correlation function between the 828 and 777 keV transitions will correspond to the triple cascade 828–(1044)–777 keV. If, however, we reverse this order then it will correspond to the simple gamma–gamma cascade 828–777 keV.

In the first case, we may explain the measured correlation function in terms of the spin sequence 4(E1)4(E2)2(E2)0. The theoretical A_2 coefficient for this spin sequence is $+0\cdot0994$, which agrees fairly well with the experimental A_2 expansion coefficient ($+0\cdot1244\pm0\cdot0253$). In the second case, the measured correlation function will have to be considered as that for the 828–777 keV gamma–gamma cascade. Mixing ratio analysis for the A_2 expansion coefficient ($+0\cdot1244\pm0\cdot0253$) in terms of the spin sequence 2(1, 2)2(2)0 shows that the quadrupole content in γ828 is $0\cdot0115+0\cdot0035$ ($\delta_{828} = -0\cdot108\pm0\cdot017$). If the same expansion coefficient is analysed in terms of the spin sequence 3(1, 2)2(2)0, the quadrupole content in γ828 becomes $0\cdot075\pm0\cdot025$ ($\delta_{828} = -0\cdot285\pm0\cdot051$). Both these values of Q_{828} are, however, inconsistent with the conclusions drawn from the analysis of the 828–1044 keV cascade discussed above and that of the 1044–777 keV cascade reported by Etherton and Kelly (1966). We therefore conclude that the successive placement of the transitions is 828–1044–777 keV (Fig. 3). This conclusion strongly favours the analysis reported by Etherton and Kelly.

The multipole admixture of the 698 keV transition has been calculated from both the cascades 698–777 keV and 619–698 keV. The two results, as shown in Table 1, agree well within the experimental error.

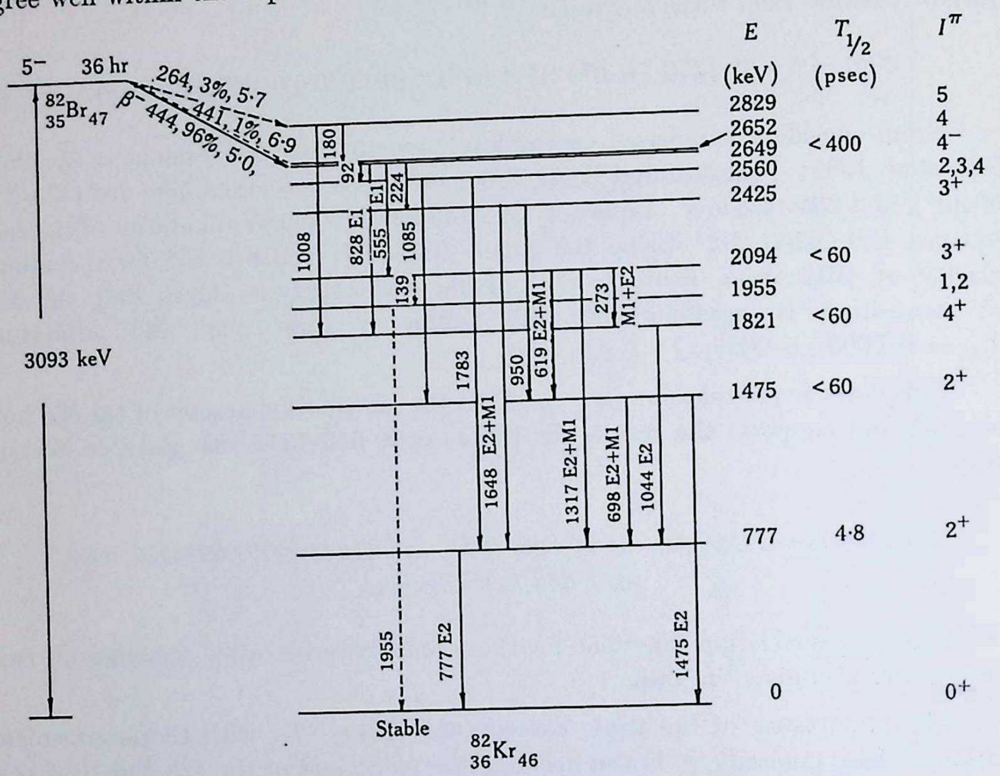
5⁻
36 hr
$^{82}_{35}Br_{47}$
β^-
264, 3%, 5·7
441, 1%, 6·9
444, 96%, 5·0,
3093 keV
E (keV)
$T_{1/2}$ (psec)
I^π
2829 5
2652 4
2649 <400 4⁻
2560 2,3,4
2425 3⁺
2094 <60 3⁺
1955 1,2
1821 <60 4⁺
1475 <60 2⁺
777 4·8 2⁺
0 0⁺
180
92
E1
224
1008
828 E1
555
1085
139
273
M1+E2
1783
950
619 E2+M1
1648 E2+M1
1317 E2+M1
698 E2+M1
1044 E2
1955
777 E2
1475 E2
Stable
$^{82}_{36}Kr_{46}$

Fig. 3.—Decay scheme of ^{82}Br based on the results of earlier workers and on those obtained in the present investigation.

IV. Discussion

The 180 keV radiation originating from the 2829 keV level feeds the level at 2649 keV, which is populated by the 444 keV extremely intense beta group. The 2649 keV level decays to 2425, 2094, and 1821 keV states with the emission of 224, 555, and 828 keV γ-radiations. The level at 2652 keV, which is populated by an extremely weak ($\sim 1\%$) beta group of 441 keV energy, decays to a 2560 keV state with the emission of an extremely weak ($\sim 1\%$) γ-radiation of 92 keV. There is no evidence for any other γ-ray that originates from or feeds this level. The possible existence of the 2652 keV level therefore does not interfere with the gamma–gamma cascades under consideration.

We have computed the E2 lifetimes, τ_γ, for the 619 and 1317 keV γ-transitions, using the measured values of δ^2, the experimental $T_{\frac{1}{2}}$ values, and the known α_K values and they are given in Table 2. The E2 component in the case of γ619 appears to be enhanced by a factor of about 2, whereas in the case of γ1317 it is retarded by a factor of about 10 with respect to corresponding single-particle estimates. The E2 lifetime values seem to follow the order of the single-particle values and thus do not reflect the many-body collective behaviour of even–even nuclei.

As has been pointed out by Etherton and Kelly (1966), the nonaxial rotor model of Davydov and co-workers (Davydov and Filippov 1959; Davydov and Chaban 1960) predicts more or less correctly the ordering and spacing of the strongly excited states of ^{82}Kr, and, further, that the rotation–vibrational interaction does not affect the reduced E2 transition probabilities of even–even nuclei, provided the nonadiabaticity parameter $\mu \leqslant 0\cdot5$. Using our computed values of τ_γ(E2) for γ619 and γ1317 we have evaluated the ratio of the reduced E2 transition probabilities for the transitions from the 2094 keV (3^+) state to the 1475 keV (2^+) and 777 keV (2^+) states. The resulting ratio is

TABLE 2

E2 LIFETIMES FOR 619 AND 1317 keV γ-TRANSITIONS

Energy of Transition (keV)	Mixing Ratio δ	*A* $\tau_\gamma(\mathrm{E2})_{\mathrm{expt}}$ (10^{-11} sec)	*B* $\tau_\gamma(\mathrm{E2})_{\mathrm{w}}$ (10^{-11} sec)	E2 Enhancement (*B*/*A*)
619	$-2\cdot34\pm0\cdot05$	$<23\cdot52$	$41\cdot67$	$\geqslant1\cdot8$
1317	$-4\cdot61\pm0\cdot26$	$<11\cdot22$	$0\cdot96$	$\geqslant0\cdot09$

$$B(\mathrm{E2};619)/B(\mathrm{E2};1317) = 0\cdot011\,,$$

which corresponds to the nonaxiality parameter $\gamma = 27\cdot9°$. This is in good agreement with the corresponding value ($\gamma = 29\cdot0°$) reported by Klema, Mallmann, and Day (1961) on the basis of energy considerations.

V. ACKNOWLEDGMENTS

The authors wish to express their sincere thanks to Professor F. C. Auluck, Head of the Department of Physics and Astrophysics, University of Delhi, for providing facilities for this work. Thanks are also due to Professor N. K. Saha for his guidance throughout the course of the work. One of the authors (M.M.B.) is indebted to the Council of Scientific and Industrial Research, India, for financial support.

VI. REFERENCES

BEARD, G. B. (1966).—*Phys. Rev.* **145**, 862.
BENCZER-KOLLER, N. (1958).—Univ. California Rep. No. CU–177.
BREITENBERGER, E. (1956).—*Proc. phys. Soc.* A **69**, 489.
DAVYDOV, A. F., and CHABAN, A. A. (1960).—*Nucl. Phys.* **20**, 499.
DAVYDOV, A. F., and FILIPPOV, G. F. (1959).—*Soviet Phys. JETP* **8**, 303, 488.
ETHERTON, R. C., and KELLY, W. H. (1966).—*Nucl. Phys.* **84**, 129.
GFIRTNER, H., REISER, W., and SCHNEIDER, H. (1965).—*Z. Naturf.* **20a**, 1727.
HSU, F. H. H., and WU, C. S. (1967).—*Nucl. Phys.* A **94**, 205.
KENNEY, E. S., and RAMAN, S. (1965).—*Bull. Am. phys. Soc.* **10**, 588.
KLEMA, E. D., MALLMANN, C. A., and DAY, P. (1961).—*Nucl. Phys.* **25**, 266.

Koch, J., Münnich, F., Schaare, W., Fischer, K., and Fricke, K. (1965).—*Z. Naturf.* **20a**, 845.

Mo, L., Hsu, F., and Wu, C. S. (1965).—*Bull. Am. phys. Soc.* **10**, 81.

Nieschmidt, E. B., Mandeville, C. E., and Ellsworth, L. D. (1965).—*Bull. Am. phys. Soc.* **10**, 129.

Raman, S. (1967).—*Nucl. Phys.* A **90**, 508.

Reidy, J., and Wiedenbeck, M. L. (1965).—*Bull. Am. phys. Soc.* **10**, 1131.

Simons, L., Bergström, S., and Anttila, A. (1964).—*Nucl. Phys.* **54**, 683.

Simons, L., Nystén, K. E., Holmberg, P., Junger, H., Anttila, A., Bergström, S., and Hagebø, E. (1963).—*Acta polytech. scand.* **Ph 22**.

Waddell, R. C., and Jensen, E. N. (1956).—*Phys. Rev.* **102**, 816.

Yates, M. J. L. (1965).—*In* "Alpha-, Beta- and Gamma-ray Spectroscopy". (Ed. K. Siegbahn.) p. 1691. (North-Holland: Amsterdam.)

DIFFRACTION BY A SLIT APERTURE FORMED BY TWO INCLINED SURFACES

By H. S. Tan*

[*Manuscript received April* 1, 1968]

Summary

The problem of diffraction by a slit aperture in a nonplanar screen formed by two inclined half-planes is formulated in terms of integral equations by means of the Lebedev transform. A convenient iterative solution of these equations is presented, based on a theorem by Karp and Zitron and its interpretations. The diffracted field is computed and compared with experimental measurements, and is found to contain a reflection interaction effect due to the nonplanar screen geometry.

I. Introduction

Studies in aperture diffraction theory have almost entirely been confined to apertures in plane screens. Out of the considerable literature on the subject, only a very few papers have been concerned with apertures in nonplanar screens. The reason for this may be that planar diffraction problems are far from being exhausted, and that a nonplanar screen introduces new difficulties in the mathematical analysis. However, a study of the problem of diffraction by an aperture in a nonplanar screen would be useful for comparison with diffraction by an identical aperture in a plane screen and for testing various approximate theories that have been used fairly successfully in planar problems. The planar problem possesses a plane of symmetry that results in certain simple properties of the diffracted field, e.g. the Babinet principle, and the property of an unperturbed tangential magnetic field and a normal electric field in the aperture plane. Without such a plane of symmetry, a nonplanar screen may have other characteristic properties not evident in the planar case.

The simplest nonplanar problem is that of a slit aperture formed by two inclined half-planes. Skalskaya (1963) has suggested an approximate solution of the integral equations for the induced currents on the screens for E-polarized plane wave incidence. His method was to assume that the slit width is large enough for the kernel to be suitably approximated so that an iterative solution can be computed. The purpose of the present paper is to formulate the more general problem of diffraction by a cylindrical wave, using an approach similar to Skalskaya. For the case of plane wave incidence, we show how a convenient iterative scheme may be used. Its interpretation in terms of interactions between the screens is discussed. The diffracted electric field intensity is also computed and compared with experiment.

---

* Department of Physics, University of Malaya, Kuala Lumpur, Malaysia.

Aust. J. Phys., 1968, **21**, 661–70

II. DIFFRACTION BY AN INCIDENT CYLINDRICAL WAVE

For Dirichlet boundary conditions on the screens A and B with an incident cylindrical wave from a line source S, the induced screen currents j_A and j_B are given by the equations

$$\int_0^\infty j_A(\rho)\,H_0^{(2)}(k\,|r-\rho|)\,d\rho = -H_0^{(2)}(kS_A) - \int_0^\infty j_B(\rho)\,H_0^{(2)}(kR)\,d\rho\,, \tag{1}$$

$$\int_0^\infty j_B(\rho)\,H_0^{(2)}(k\,|r-\rho|)\,d\rho = -H_0^{(2)}(kS_B) - \int_0^\infty j_A(\rho)\,H_0^{(2)}(kR)\,d\rho\,, \tag{2}$$

where the notation is defined in Figure 1. The equation

$$\int_0^\infty j_{A0}(\rho)\,H_0^{(2)}(k\,|r-\rho|)\,d\rho = -H_0^{(2)}(kS_A)\,, \tag{3}$$

which describes the half-plane diffraction problem with cylindrical wave incidence, will be solved first, since the results will be used in the solution of (1) and (2).

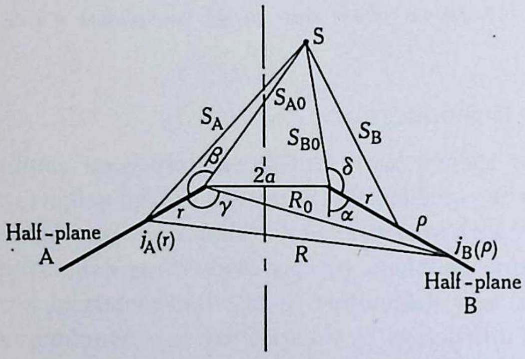

Fig. 1.—Diagram for diffraction by a cylindrical wave from S.

The Kontorovich–Lebedev transform and its inverse for a function $\phi(r)$ are defined as (Kontorovich and Lebedev 1938; Jones 1964)

$$\bar{\phi}(t) = \int_0^\infty r^{-1}\,\phi(r)\,e^{\frac{1}{2}\pi t}\,H_{it}^{(2)}(kr)\,dr\,, \tag{4}$$

$$\phi(r) = -\tfrac{1}{2}\int_0^\infty t\sinh(\pi t)\,\bar{\phi}(t)\,e^{\frac{1}{2}\pi t}\,H_{it}^{(2)}(kr)\,dt\,. \tag{5}$$

Applying this transform to (3), we have

$$\begin{aligned}\int_0^\infty j_{A0}(\rho)\,d\rho\int_0^\infty e^{\frac{1}{2}\pi t}\,H_{it}^{(2)}(kr)\,\frac{1}{r}\Big(H_0^{(2)}(k\,|r-\rho|) - e^{-ikr}\,H_0^{(2)}(k\rho)\Big)\,dr \\ = -\int_0^\infty e^{\frac{1}{2}\pi t}\,H_{it}^{(2)}(kr)\,\frac{1}{r}\Big(H_0^{(2)}(kS_A) - e^{-ikr}\,H_0^{(2)}(kS_{A0})\Big)\,dr\,.\end{aligned} \tag{6}$$

The left-hand side of (6) becomes

$$-\frac{2}{it\sinh(\pi t)}\Big(H_0^{(2)}(kS_{A0}) - \cosh(\pi t)\,\overline{(\rho j_{A0})}\Big)\,,$$

where we have used the relation

$$\int_0^\infty j_{\mathrm{A}0}(\rho)\,\mathrm{H}_0^{(2)}(k\rho)\,\mathrm{d}\rho = -\mathrm{H}_0^{(2)}(kS_{\mathrm{A}0}) \tag{7}$$

derived from (3) by putting $r = 0$.

The integral on the right-hand side of (6) can be evaluated to give (Oberhettinger and Higgins 1961)

$$\frac{2\mathrm{i}}{t\sinh(\pi t)}\left(-\mathrm{e}^{\frac{1}{2}\pi t}\,\mathrm{H}_{\mathrm{i}t}^{(2)}(kS_{\mathrm{A}0})\cosh(\pi-\beta)t + \mathrm{H}_0^{(2)}(kS_{\mathrm{A}0})\right),$$

so that equation (6) can now be written as

$$\overline{(\rho j_{\mathrm{A}0})} = -\mathrm{e}^{\frac{1}{2}\pi t}\,\mathrm{H}_{\mathrm{i}t}^{(2)}(kS_{\mathrm{A}0})\,\{\cosh(\pi-\beta)t\}/\cosh(\pi t)\,. \tag{8}$$

On inverting the transform, we have

$$j_{\mathrm{A}0}(r) = \frac{1}{2r}\int_0^\infty t\,\mathrm{e}^{\pi t}\cosh(\pi-\beta)t\tanh(\pi t)\,\mathrm{H}_{\mathrm{i}t}^{(2)}(kr)\,\mathrm{H}_{\mathrm{i}t}^{(2)}(kS_{\mathrm{A}0})\,\mathrm{d}t\,. \tag{9}$$

To evaluate this integral, it is convenient to rewrite the integrand in terms of modified Bessel functions and to assume temporarily that the wave number k is purely imaginary. Using

$$\mathrm{K}_\mu(z) = -\tfrac{1}{2}\mathrm{i}\pi\mathrm{e}^{-\mathrm{i}\frac{1}{2}\pi\mu}\,\mathrm{H}_\mu^{(2)}(z\mathrm{e}^{-\mathrm{i}\frac{1}{2}\pi}), \qquad k = -\mathrm{i}\kappa,$$

equation (9) becomes

$$j_{\mathrm{A}0}(r) = -\frac{2}{\pi^2 r}\int_0^\infty t\,\mathrm{K}_{\mathrm{i}t}(\kappa r)\,\mathrm{K}_{\mathrm{i}t}(\kappa S_{\mathrm{A}0})\cosh(\pi-\beta)t\tanh(\pi t)\,\mathrm{d}t\,, \tag{10}$$

which can be written as an integral along the entire real axis of t by use of the relation

$$\mathrm{K}_\mu(z) = \tfrac{1}{2}\pi\{\mathrm{I}_{-\mu}(z) - \mathrm{I}_\mu(z)\}/\sin(\mu\pi)\,. \tag{11}$$

Thus

$$j_{\mathrm{A}0}(r) = \frac{\mathrm{i}}{\pi r}\int_{-\infty}^\infty t\,\mathrm{K}_{\mathrm{i}t}(\kappa S_{\mathrm{A}0})\,\mathrm{I}_{-\mathrm{i}t}(\kappa r)\,\frac{\cosh(\pi-\beta)t}{\cosh(\pi t)}\,\mathrm{d}t\,, \qquad r < S_{\mathrm{A}0}\,. \tag{12}$$

The path of integration is now closed by a semicircle in the upper half-plane, and Cauchy's theorem then yields

$$j_{\mathrm{A}0}(r) = \frac{\mathrm{i}}{2r}\sum_{n=0}^\infty (2n+1)\mathrm{H}_{n+\frac{1}{2}}^{(2)}(kS_{\mathrm{A}0})\,\mathrm{J}_{n+\frac{1}{2}}(kr)\sin(n+\tfrac{1}{2})\beta\,, \qquad r < S_{\mathrm{A}0}\,. \tag{13}$$

For $r > S_{\mathrm{A}0}$, the arguments of $\mathrm{H}_{n+\frac{1}{2}}^{(2)}$ and $\mathrm{J}_{n+\frac{1}{2}}$ must be interchanged.

The solution of an equation of the type

$$\int_0^\infty j'_{\mathrm{A}}(\rho)\,\mathrm{H}_0^{(2)}(k|r-\rho|)\,\mathrm{d}\rho = -\int_0^\infty j_{\mathrm{B}}(\rho)\,\mathrm{H}_0^{(2)}(kR)\,\mathrm{d}\rho\,, \tag{14}$$

where only the second term on the right-hand side of (1) or (2) is present, is given by the same procedure from (6) to (13). Thus

$$j'_{\mathrm{A}}(r) = \int_0^\infty j_{\mathrm{B}}(\rho)\, j_0(r, R_0, \gamma)\, \mathrm{d}\rho\,,$$

where, from (13),

$$j_0(r, R_0, \gamma) = \frac{\mathrm{i}}{2r} \sum_{n=0}^{\infty} (2n+1) \mathrm{H}^{(2)}_{n+\frac{1}{2}}(kR_0)\, \mathrm{J}_{n+\frac{1}{2}}(kr) \sin(n+\tfrac{1}{2})\gamma\,, \qquad r < R_0\,, \tag{15}$$

is the current induced at r on half-plane A due to unit line current at ρ on half-plane B. Equations (1) and (2) have now been transformed into the Fredholm equations

$$j_{\mathrm{A}}(r) = j_0(r, S_{\mathrm{A0}}, \beta) + \int_0^\infty j_{\mathrm{B}}(\rho)\, j_0(r, R_0, \gamma)\, \mathrm{d}\rho\,, \tag{16a}$$

$$j_{\mathrm{B}}(r) = j_0(r, S_{\mathrm{B0}}, \delta) + \int_0^\infty j_{\mathrm{A}}(\rho)\, j_0(r, R_0, \gamma)\, \mathrm{d}\rho\,. \tag{16b}$$

III. DIFFRACTION BY AN INCIDENT PLANE WAVE

For an E-polarized plane wave incident on the screens in Figure 1, equation (1), for example, is modified to

$$\int_0^\infty g_{\mathrm{A}}(\rho)\, \mathrm{H}_0^{(2)}(k\,|\,r-\rho\,|)\, \mathrm{d}\rho = (c/\pi k)\exp(-\mathrm{i}kr\cos\theta) - \int_0^\infty g_{\mathrm{B}}(\rho)\, \mathrm{H}_0^{(2)}(kR)\, \mathrm{d}\rho\,, \tag{17}$$

where we have assumed that the incident wave makes an angle θ with the half-plane A. The solution of the equation

$$\int_0^\infty g_{\mathrm{A0}}(\rho)\, \mathrm{H}_0^{(2)}(k\,|\,r-\rho\,|)\, \mathrm{d}\rho = (c/\pi k)\exp(-\mathrm{i}kr\cos\theta) \tag{18}$$

is again obtained from the Kontorovich–Lebedev transform. The left-hand side of (18) becomes

$$\frac{2}{\mathrm{i}t\sinh(\pi t)}\left(\frac{c}{\pi k} - \cosh(\pi t)\,\overline{(\rho g_{\mathrm{A0}})}\right),$$

while the right-hand side gives

$$\frac{c}{\pi k}\frac{2\mathrm{i}}{t\sinh(\pi t)}\Big(\cosh(\theta t) - 1\Big)\,.$$

Inverting the transform,

$$g_{\mathrm{A0}}(r) = -\frac{c}{\pi k}\frac{1}{2r}\int_0^\infty t\,\mathrm{e}^{\frac{1}{2}\pi t}\tanh(\pi t)\cosh(\theta t)\,\mathrm{H}^{(2)}_{\mathrm{i}t}(kr)\,\mathrm{d}t\,, \tag{19}$$

from which,

$$g_{\mathrm{A0}}(r) = -\frac{c}{\pi k}\frac{\mathrm{i}}{2r}\sum_{n=0}^{\infty}(2n+1)\mathrm{J}_{n+\frac{1}{2}}(kr)\,\mathrm{i}^{n+\frac{1}{2}}\sin(n+\tfrac{1}{2})\theta\,. \tag{20}$$

The solution of (17) with only the second term on the right-hand side present is given by (15), so that (17) now becomes

$$g_{\mathrm{A}}(r) = g_{\mathrm{A}0}(r,\theta) + \int_0^\infty g_{\mathrm{B}}(\rho)\, j_0(r, R_0, \gamma)\, \mathrm{d}\rho \tag{21}$$

with a similar equation for $g_{\mathrm{B}}(r)$.

IV. Solution of Integral Equation

An approximate iterative solution of the integral equations (16) and (21) can be obtained by the procedure used in Tan (1968), where the plane slit aperture was considered. Each of the line currents $g_{\mathrm{B}}(\rho)$ in (21), for example, is considered to be radiating a cylindrical wave that can be expanded in terms of plane waves and derivatives of plane waves with respect to their angles of incidence (Karp and Zitron 1964). The currents induced on half-plane A by $g_{\mathrm{B}}(\rho)$ are therefore equivalent to those induced by a series of plane waves and their derivatives. We thus write

$$j_0(r, R_0, \gamma) = \mathrm{H}_{\mathrm{op}}(\rho, \mathrm{d}/\mathrm{d}\theta)\, g_{\mathrm{A}0}(r,\theta)\,, \tag{22}$$

where the operator $\mathrm{H}_{\mathrm{op}}(\rho, \mathrm{d}/\mathrm{d}\theta)$ contains the series of plane waves and their derivatives. By using

$$\begin{aligned} \mathrm{H}^{(2)}_{n+\frac{1}{2}}(kR_0) &= (2/\pi kR_0)^{\frac{1}{2}} \exp\{-\mathrm{i}kR_0 + \mathrm{i}\tfrac{1}{4}\pi + \tfrac{1}{2}(n+\tfrac{1}{2})\pi\} \\ &\quad \times \sum_{m=0}^{\infty} \frac{\{1+4\,\mathrm{d}^2/\mathrm{d}\theta^2\}\{9+4\,\mathrm{d}^2/\mathrm{d}\theta^2\}\dots\{(2m-1)+4\,\mathrm{d}^2/\mathrm{d}\theta^2\}}{(-8\mathrm{i}kR_0)^m\, m!} \end{aligned} \tag{23}$$

in equation (15) and comparing with $g_{\mathrm{A}0}$ in (20), we have

$$\begin{aligned} \mathrm{H}_{0\mathrm{p}}(\rho, \mathrm{d}/\mathrm{d}\theta) &= (2/\pi kR_0)^{\frac{1}{2}} \exp(-\mathrm{i}kR_0 + \mathrm{i}\tfrac{1}{4}\pi) \\ &\quad \times \left(1 + \mathrm{i}\,\frac{1+4\,\mathrm{d}^2/\mathrm{d}\theta^2}{8kR_0} - \frac{9+40\,\mathrm{d}^2/\mathrm{d}\theta^2 + 16\,\mathrm{d}^4/\mathrm{d}\theta^4}{128k^2R_0^2} + \dots\right). \end{aligned} \tag{24}$$

Equation (21) then becomes

$$g_{\mathrm{A}}(r) = g_{\mathrm{A}0}(r,\theta) + \left\{\int_0^\infty g_{\mathrm{B}}(\rho)\, \mathrm{H}_{\mathrm{op}}\left(\rho, \frac{\mathrm{d}}{\mathrm{d}\gamma}\right) \mathrm{d}\rho\right\} g_{\mathrm{A}0}(r,\gamma)\,, \tag{25}$$

where $g(r,\gamma)$ has been taken outside the integral because γ is assumed to be a slowly varying function of ρ. This approximation assumes that the main contribution of the interaction between the two screens comes from the induced currents near the edges, where $\gamma \simeq \frac{1}{2}\pi + \alpha$. The iteration procedure for solving (25) is now simple, since each iteration yields essentially the same integral. For the plane slit aperture γ is independent of ρ, and this procedure has been shown to give excellent results compared with the rigorous solution in terms of Mathieu functions. The iterative solution has the simple interpretation that it represents a series of successive interactions between the two screens.

V. CALCULATION OF DIFFRACTED FIELD

To calculate the diffracted field of screen A, for example, we write from equation (21) and Figure 2

$$E_{\mathrm{A}}(\mathrm{P}) = -\frac{\pi k}{c}\int_0^\infty g_{\mathrm{A}0}(r,\theta)\,\mathrm{H}_0^{(2)}(kr_{\mathrm{A}})\,\mathrm{d}r$$
$$-\frac{\pi k}{c}\int_0^\infty g_{\mathrm{B}}(\rho)\,\mathrm{d}\rho\int_0^\infty j_0(r,R_0,\gamma)\,\mathrm{H}_0^{(2)}(kr_{\mathrm{A}})\,\mathrm{d}r\,. \tag{26}$$

The first term on the right-hand side of (26), E_1, is obviously the half-plane diffracted field of the incident plane wave, while the second term E_2 is the diffracted field of the half-plane A due to a line source at ρ on the half-plane B. These fields are given by (Born and Wolf 1965)

2

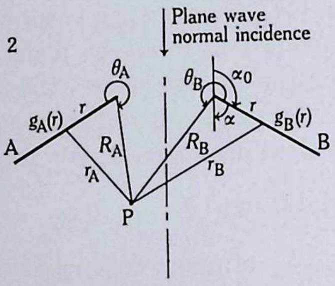
Plane wave
normal incidence
θ_A
θ_B
α_0
r
$g_A(r)$
A
R_A
r_A
R_B
r_B
α
r
$g_B(r)$
B
P

3

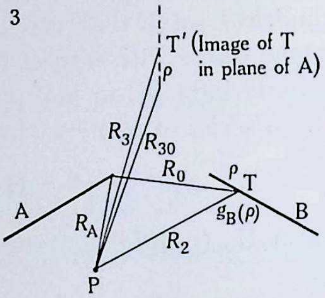
T′ (Image of T in plane of A)
ρ
R_3
R_{30}
R_0
ρ
T
A
R_A
$g_B(\rho)$
B
R_2
P

Fig. 2 (*above*).—Diagram for diffraction by a normally incident plane wave.

Fig. 3 (*above right*).—Diagram for field from source T and its image T′.

Fig. 4 (*right*).—Diagram for reflection interaction between screens.

4

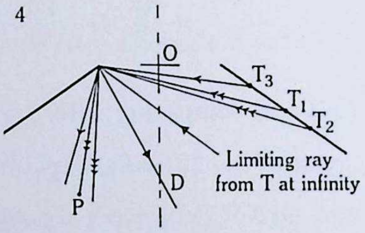
O
T_3
T_1
T_2
Limiting ray
from T at infinity
D
P

$$E_1 = -\pi^{-\frac{1}{2}}\exp(\mathrm{i}\tfrac{1}{4}\pi)\big[\exp\{\mathrm{i}kR_{\mathrm{A}}\cos(\theta_{\mathrm{A}}-\alpha_0)\}F\{(2kR_{\mathrm{A}})^{\frac{1}{2}}\cos\tfrac{1}{2}(\theta_{\mathrm{A}}-\alpha_0)\}$$
$$+\exp\{\mathrm{i}kR_{\mathrm{A}}\cos(\theta_{\mathrm{A}}+\alpha_0)\}F\{-(2kR_{\mathrm{A}})^{\frac{1}{2}}\cos\tfrac{1}{2}(\theta_{\mathrm{A}}+\alpha_0)\}\big]\,, \tag{27}$$

where, referring to Figure 3,

$$E_2 = \left.\begin{array}{ll} E_0+(\pi k/c)\mathrm{H}_0^{(2)}(kR_3)\,, & 0 \leqslant 2\pi-\theta_{\mathrm{A}} \leqslant \pi-\gamma\,, \\ E_0\,, & \pi-\gamma < 2\pi-\theta_{\mathrm{A}} < \pi+\gamma\,, \end{array}\right\} \tag{28}$$

and

$$E_0 = \frac{2\mathrm{i}k}{c}\bigg(\exp(-\mathrm{i}kR_3)\int_{[k(R_1-R_3)]^{\frac{1}{2}}}^{\infty}\frac{\exp(-\mathrm{i}\mu^2)}{(\mu^2+2kR_3)^{\frac{1}{2}}}\,\mathrm{d}\mu$$
$$+\exp(-\mathrm{i}kR_2)\int_{[k(R_1-R_2)]^{\frac{1}{2}}}^{\infty}\frac{\exp(-\mathrm{i}\mu^2)}{(\mu^2+2kR_2)^{\frac{1}{2}}}\,\mathrm{d}\mu\bigg)\,. \tag{29}$$

The two integrals in E_0 can be approximated by Fresnel integrals to a degree of accuracy that is inadequate only if both the source T and the point of observation P are well within a wavelength of the diffracting edge of A. This approximation is done by replacing μ in the non-exponential part of the integrand by the lower limit of the integral (Clemmow 1950), giving

$$\left.\begin{aligned} E_0 &\simeq \frac{2ik}{c}\left(\frac{\exp(-ikR_3)}{\{k(R_1+R_3)\}^{\frac{1}{2}}}F(\{k(R_1-R_3)\}^{\frac{1}{2}})+\frac{\exp(-ikR_2)}{\{k(R_1+R_2)\}^{\frac{1}{2}}}F(\{k(R_1-R_2)\}^{\frac{1}{2}})\right), \\ F(V) &= \int_V^\infty \exp(-i\mu^2)\,d\mu, \qquad R_1 = R_0+R_A. \end{aligned}\right\} \tag{30}$$

If P lies in the region $0 \leqslant 2\pi-\theta_A \leqslant \pi-\gamma$, the additional term $(\pi k/c)H_0^{(2)}(kR_3)$ in (28) represents the reflected wave of the line source T, which appears to be radiated by an image source at T′. It is these reflected waves of the line sources between the two screens that account for the reflection interaction effect measured in certain parts of the diffracted field. This effect has been discussed in Tan (1967*a*, 1967*b*).

The point P does not necessarily receive the reflected waves of all the line sources on half-plane B. For example, in Figure 4, P will see the reflected waves of only those line sources on B for which $\rho > \rho_0$. A source T_2 will include P in its region of reflected waves, while a source T_3 will not. In general, the diffracted field from half-plane A will be, from (26),

$$E_A(P) = E_1 + \int_0^\infty g_B(\rho)\,E_0\,d\rho + \frac{\pi k}{c}\int_{\rho_0}^\infty g_B(\rho)\,H_0^{(2)}(kR_3)\,d\rho. \tag{31}$$

The iteration scheme can now be applied by successively substituting for the unknown g_B the values of the iterations g_{B0} etc. from (25). For all but the smallest slit widths (e.g. slit widths of half a wavelength or smaller), only one or two iterations will give results of sufficient accuracy, a fact borne out by comparison with experimental measurements of electric field intensity and phase (Tan 1967*b*).

With one iteration, the second term in (31) gives

$$\int_0^\infty g_{B0}(\rho)\,E_0\,d\rho \simeq \frac{\sin\frac{1}{2}\alpha_0}{\pi}\left(\frac{\exp(-ikR_{30})}{\{k(R_A+2a+R_{30})\}^{\frac{1}{2}}}F(\{k(R_A+2a-R_{30})\}^{\frac{1}{2}}) + \frac{\exp(-ikR_B)}{\{k(R_A+2a+R_B)\}^{\frac{1}{2}}}F(\{k(R_A+2a-R_B)\}^{\frac{1}{2}})\right), \tag{32}$$

where we have made the approximations

$$\left.\begin{aligned} g_{B0}(\rho) = g_{A0}(\rho) &\simeq c\pi^{-3/2}\sin\tfrac{1}{2}\alpha_0\,(2ik\rho)^{-\frac{1}{2}}\exp(-ik\rho), \\ R_3 \simeq R_{30}+\rho, &\qquad R_2 \simeq R_B+\rho, \end{aligned}\right\} \tag{33}$$

and have assumed the case of normal plane wave incidence. The approximations (33) are justifiable in that only the current to the edge (ρ small) contributes appreciably to this term.

To evaluate the last term in (31), we replace the Hankel function by the first term of its asymptotic series. However, here we must include the line sources on the entire screen and not just those near the screen edge. Writing

$$g_{\mathrm{B0}}(\rho) = \frac{c}{\pi^{3/2}}\left(\frac{\exp(-\mathrm{i}k\rho)}{(2\mathrm{i}k\rho)^{\frac{1}{2}}}\sin\tfrac{1}{2}\alpha_0 + \exp(\mathrm{i}\tfrac{1}{4}\pi)\sin\alpha_0\exp(\mathrm{i}k\rho\cos\alpha_0)\right.$$
$$\left.\times\int_0^{(2k\rho)^{\frac{1}{2}}\cos\frac{1}{2}\alpha_0}\exp(-\mathrm{i}\mu^2)\,\mathrm{d}\mu\right), \tag{34a}$$

$$\mathrm{H}_0^{(2)}(kR_3) = \{k(R_{30}+\rho)\}^{-\frac{1}{2}}(2/\pi)^{\frac{1}{2}}\exp(\mathrm{i}\tfrac{1}{4}\pi)\exp\{-\mathrm{i}k(R_{30}+\rho)\}, \tag{34b}$$

the two integrals for this reflection effect are

$$\frac{\pi k}{c}\int_{\rho_0}^{\infty}\frac{c}{\pi^{3/2}}\frac{\exp(-\mathrm{i}k\rho)}{(2\mathrm{i}k\rho)^{\frac{1}{2}}}\sin\tfrac{1}{2}\alpha_0\left(\frac{2}{\pi}\right)^{\frac{1}{2}}\exp(\mathrm{i}\tfrac{1}{4}\pi)\frac{\exp(-\mathrm{i}kR_3)}{(kR_3)^{\frac{1}{2}}}\,\mathrm{d}\rho$$
$$\simeq\frac{2^{\frac{1}{2}}}{\pi}\sin\tfrac{1}{2}\alpha_0\frac{\exp(-\mathrm{i}kR_{30})}{\{k(R_{30}+\rho_0)\}^{\frac{1}{2}}}F\big((2k\rho_0)^{\frac{1}{2}}\big) \tag{35}$$

and

$$\frac{\pi k}{c}\int_{\rho_0}^{\infty}\left(\frac{c}{\pi^{3/2}}\exp(\mathrm{i}\tfrac{1}{4}\pi)\sin\alpha_0\exp(\mathrm{i}k\rho\cos\alpha_0)\int_0^{(2k\rho)^{\frac{1}{2}}\cos\frac{1}{2}\alpha_0}\exp(-\mathrm{i}\mu^2)\,\mathrm{d}\mu\right)$$
$$\times\left(\frac{2}{\pi}\right)^{\frac{1}{2}}\exp(\mathrm{i}\tfrac{1}{4}\pi)\frac{\exp(-\mathrm{i}kR_3)}{(kR_3)^{\frac{1}{2}}}\,\mathrm{d}\rho$$
$$\simeq\frac{2^{\frac{1}{2}}}{\pi}\left(\frac{\sin\alpha_0}{1-\cos\alpha_0}\frac{\exp(-\mathrm{i}kR_{30})}{\{k(R_{30}+\rho_0)\}^{\frac{1}{2}}}\right)\left(\exp\{-\mathrm{i}k\rho_0(1-\cos\alpha_0)\}\int_0^{(2k\rho_0)^{\frac{1}{2}}\cos\frac{1}{2}\alpha_0}\exp(-\mathrm{i}\mu^2)\,\mathrm{d}\mu\right.$$
$$\left.+\cos\tfrac{1}{2}\alpha_0F\big((2k\rho_0)^{\frac{1}{2}}\big)\right). \tag{36}$$

Combining (35) and (36), we have that

$$\frac{\pi k}{c}\int_{\rho_0}^{\infty}j_{\mathrm{B0}}(\rho)\,\mathrm{H}_0^{(2)}(kR_3)\,\mathrm{d}\rho$$
$$\simeq\frac{2^{\frac{1}{2}}}{\pi}\frac{\exp(-\mathrm{i}kR_{30})}{\{k(R_{30}+\rho_0)\}^{\frac{1}{2}}}\left(\frac{F\big((2k\rho_0)^{\frac{1}{2}}\big)}{\sin\frac{1}{2}\alpha_0}+\frac{\sin\alpha_0}{1-\cos\alpha_0}\exp\{-\mathrm{i}k\rho_0(1-\cos\alpha_0)\}\right.$$
$$\left.\times\int_0^{(2\rho_0)^{\frac{1}{2}}\cos\frac{1}{2}\alpha_0}\exp(-\mathrm{i}\mu\ )^2\mathrm{d}\mu\right). \tag{37}$$

Finally, the total electric field at P is given by

$$E = E^{\mathrm{t}} + E_{\mathrm{A}}(R_{\mathrm{A}},\theta_{\mathrm{A}}) + E_{\mathrm{B}}(R_{\mathrm{B}},\theta_{\mathrm{B}}), \tag{38}$$

where E_{A} is given by (31), (32), and (37), and E_{B} is similar to E_{A} except for obvious modifications.

From Figure 4, it is seen that the reflection term given by (37) will be present in the illuminated region behind the aperture (in the geometrical optics sense) only for screen inclination angle $\alpha < \frac{1}{3}\pi$. This is because for $\alpha > \frac{1}{3}\pi$ the reflected waves of all the current sources on both screens are confined to the two shadow regions near the screens. In particular the axial field is free from this reflection effect for such cases. When $\alpha < \frac{1}{3}\pi$ this reflection term occurs along the axis for $\rho >$ OD, where D is the intersection on the axis of the reflected ray from sources very far from the edge of B. Near the point D, this reflection would be small since ρ_0 in (31) is large. On the other hand, this term is also small when z is large because, although ρ_0 is now small, the distance from the virtual image sources from which the reflections appear to radiate, R_3, is very large. Thus we expect that the magnitude of this reflection term on the axis increases with z for $z >$ OD, and then begins to decrease as z becomes large. In any case it is a small effect, but its significance lies in the fact that it is essentially due to the two half-planes not being coplanar, and gives one of the main differences between planar and nonplanar diffraction problems. Whereas the planar problem can usually be discussed in terms of edge interactions, the nonplanar case has screen interactions as well.

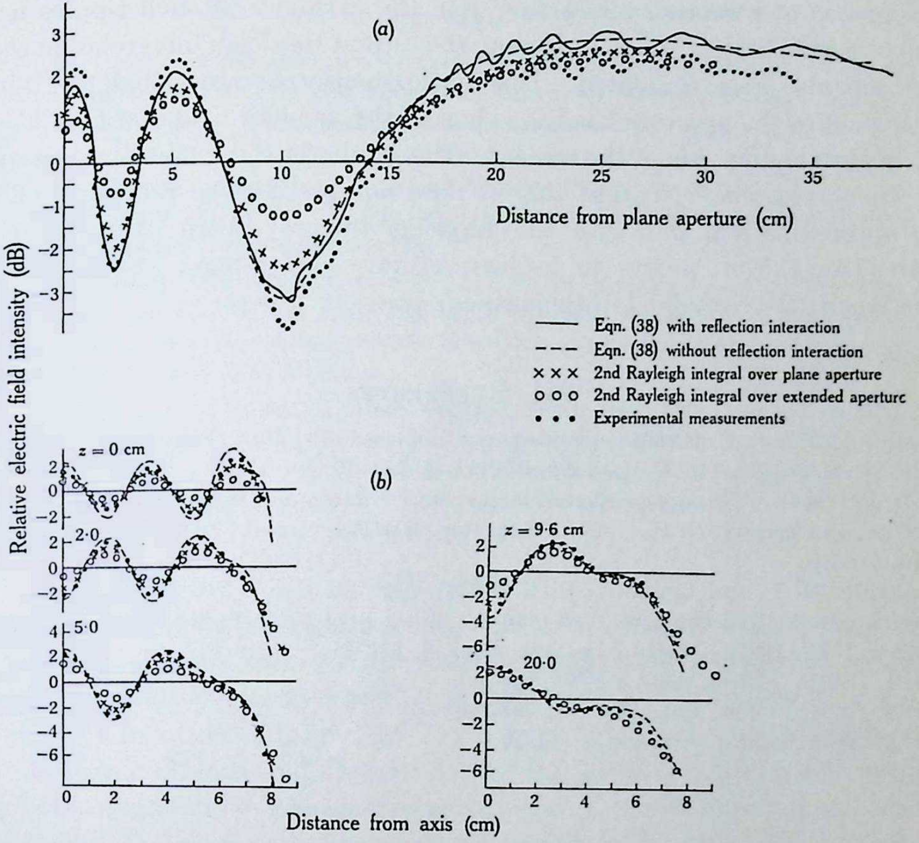

Fig. 5.—Comparison of theoretical and measured values of the electric field intensity (*a*) along and (*b*) transverse to the axis of a slit aperture, with $ka = 5\pi$, $\alpha = \frac{1}{4}\pi$, and $\lambda = 3 \cdot 2$ cm.

VI. Results and Discussion

Figure 5(*a*) shows a comparison of theory with measured values of the electric field intensity along the axis of a 5λ slit aperture with $\alpha = \frac{1}{4}\pi$ and $\lambda = 3\cdot 2$ cm. The reflection effect appears to be observed as ripples about three wavelengths behind the aperture. Figure 5(*b*) presents five transverse scans of the same slit aperture.

The computed curves show significant differences between the results obtained with and without reflection interaction. In particular, a characteristic ripple appears in consequence of reflection interaction, and the existence of such ripples has been detected experimentally. For comparison, the second Rayleigh integral over the plane aperture has also been computed. This approximation assumes that the tangential magnetic field in the aperture has the values of the incident field and that it is negligible over the shadow side of the screens. The results in Figure 5 show this approximation to be reasonable, except that it does not predict the reflection effect. A similar approximation, but with the Rayleigh integral taken over the extended aperture (Tan 1967*b*), proves to be less accurate everywhere. Fuller discussions of these results are contained in the author's previous reports.

VII. References

BORN, M., and WOLF, E. (1965).—"Principles of Optics." 3rd Ed. (Pergamon Press: Oxford.)

CLEMMOW, P. C. (1950).—*Q. Jl Mech. appl. Math.* **3**, 241–56.

JONES, D. S. (1964).—"Theory of Electromagnetism." (Pergamon Press: Oxford.)

KARP, S. N., and ZITRON, N. R. (1964).—Res. Rep. EM-199, Courant Inst. Math. Sci., New York University.

KONTOROVICH, M. I., and LEBEDEV, N. N. (1938).—*Zh. éksp. teor. Fiz.* **8**, 1192–206.

OBERHETTINGER, F., and HIGGINS, T. P. (1961).—Math. Note No. 246, Boeing Scientific Res. Lab.

SKALSKAYA, I. P. (1963).—*Soviet Phys. tech. Phys.* **8**, 179–81.

TAN, H. S. (1967*a*).—*Proc. phys. Soc.* **91**, 248–53.

TAN, H. S. (1967*b*).—*Proc. phys. Soc.* **91**, 768–73.

TAN, H. S. (1968).—*Aust. J. Phys.* **21**, 35–41.

THE ORIGIN AND PROPAGATION OF ACOUSTIC–GRAVITY WAVES DUCTED IN THE THERMOSPHERE

By A. F. Wickersham*

[*Manuscript received March* 13, 1968]

Summary

The theory of acoustic-gravity waves in a thermoclinal atmosphere shows that damping decreases as the thermal gradient increases. If the thermal gradient is large enough it offsets the increase in amplitude caused by upward propagation into a region of decreasing ambient density and the motion is completely undamped, neglecting viscosity. Thus it appears that long distance propagation can occur in the principal duct at 150 km altitude, where the thermal gradient is almost large enough to eliminate nonviscous damping.

It is shown that thermal perturbation of the principal duct by the long winter-solstice sunrise in the polar regions is a source of ducted gravity waves consistent with the seasonal variations in directions of travelling ionospheric disturbances (TID's) observed in Australia.

The observed tilts of TID's are compared with theory and can be used to determine the period of a disturbance. The effect of ionospheric charge equilibration is discussed briefly, and a leaky-duct gravity wave model is proposed which reconciles the observations of tilted wave fronts and long distance propagation.

I. Introduction

Naturally occurring travelling ionospheric disturbances (TID's) have been detected for many decades, and several writers have suggested that they are propagating atmospheric acoustic-gravity waves (e.g. Martyn 1950; Hines 1960). For more than 10 years it has been known that TID's have fronts that are inclined in the direction of travel. Munro and Heisler (1956*b*) measured the tilt in 430 naturally occurring TID's and found it to be 65°, measured from the horizontal, for disturbances travelling in the direction of the geomagnetic meridian; however, they found that disturbances travelling at right angles to such direction also have tilted fronts, the tilt being about 54°. This probably means that the tilt is in the neutral disturbance itself and is not principally a result of charged particle interaction with the geomagnetic field. Other work by Munro and Heisler (1956*a*) shows that such tilted-front TID's propagate horizontally over large distances, and Munro (1958) has measured the seasonal variation in number and direction of such naturally occurring disturbances.

In the past few years it has been shown that there is quantitative agreement between the observed speed distributions of TID's and those expected theoretically for ducted gravity waves; also, there is agreement between the theoretical speeds expected for various ducted modes and the observed speeds of disturbances caused

---

* Radio Physics Laboratory, Stanford Research Institute, Menlo Park, California 94025, U.S.A.

by a nuclear detonation at Novaya Zemla (Wickersham 1964, 1965*b*, 1966). The theoretical speeds used for comparison with observations are the numerical results of Pfeffer and Zarichny (1963) and are based on a realistic atmosphere.

It is the present purpose to further examine the theory of acoustic-gravity waves in a thermoclinal atmosphere in order to attempt additional comparisons with observations. We shall see, from an approximate form of the equations of motion, that a principal duct exists in the thermosphere where minimal damping occurs because of the large thermal gradient. By analysing the consequences of a thermal perturbation of the duct in the thermosphere we find that winter sunrise in the polar regions is a source of ducted acoustic-gravity waves consistent with the seasonal changes in direction observed by Munro.

From the equations of motion appropriate for a thermoclinal atmosphere we can find an expression for the tilt of a gravity wave disturbance. If we assume that the duct in the thermosphere is leaky and that some energy flows up into the ionosphere, we can compare theoretical and observed tilts to determine the period of the portion of the disturbance that appears in the ionosphere. The leaky-duct hypothesis reconciles tilted fronts and horizontal ducting.

II. DISPERSION EQUATIONS FOR AN ATMOSPHERE WITH A LINEAR THERMOCLINE

For an atmosphere with a linear gradient in the scale height $H = H_0(1+\alpha z)$, the equation satisfied by the hydrodynamical divergence χ is

$$\chi''+(H'-1)H^{-1}\chi'+(\omega^2/c^2-K_x^2+K_x^2\,\omega_B^2/\omega^2)\chi = 0 \tag{1}$$

(Lamb 1945; Martyn 1950). In this notation ω is the frequency, c the local speed of sound, K_x the horizontal wave number, which may be complex ($K_x = k_x+\mathrm{i}\beta_x$, $K_x^2 \approx k_x^2+\mathrm{i}2k_x\beta_x$), ω_B the angular Brünt frequency, and primes denote differentiation with respect to z, the vertical coordinate. The reciprocal of the Brünt frequency is sometimes called the thermobaric period,

$$\tau_B = 2\pi(H/g)^{\frac{1}{2}}\{(\gamma-1)/\gamma+H'\}^{-\frac{1}{2}}\,. \tag{2}$$

A graph of thermobaric period based on the 1961 CIRA standard atmosphere is shown in Figure 1.

In the present discussion we shall use an approximate form of equation (1) obtained by replacing H^{-1} by H_0^{-1} in the second term. With the understanding that the equation of motion now is approximately valid only in a region $z_0\pm\Delta z$, such that $\Delta z\,\mathrm{d}H/\mathrm{d}z \ll H_0$, we can seek solutions of the form $\chi_0\exp(-\mathrm{i}K_z z)$, where K_z is complex, $K_z = k_z+\mathrm{i}\beta_z$. With the assumption that β_z is small, so that $K_z^2 \approx k_z^2+\mathrm{i}2k_z\beta_z$, we obtain the dispersion equations

$$\omega^4/c^2-\omega^2[k^2-\beta_z(\alpha-H_0^{-1})]+k_x^2\,\omega_B^2 = 0\,, \tag{3}$$

$$\beta_x = \frac{\tau_B^2}{\tau^2-\tau_B^2}\frac{k_z}{k_x}\left(\beta_z+\tfrac{1}{2}\alpha-\tfrac{1}{2}H_0^{-1}\right), \tag{4}$$

where $k^2 = k_x^2 + k_z^2$. Introducing $\cot\phi = k_z/k_x$ into (3), we find a useful expression for the angle ϕ that a wave front makes with the horizontal, namely,

$$\cot^2\phi = \frac{\tau^2 - \tau_B^2}{\tau_B^2} + \frac{\lambda_x^2}{c^2\tau^2}\left(1 + \frac{\beta_z c^2 \tau^2}{4\pi^2}(\alpha - H_0^{-1})\right), \tag{5}$$

where λ_x is the horizontal wavelength. We also can use equation (3) to compute the direction of energy flow, $-\partial k_x/\partial k_z$, and find that it is given by the same angle ϕ. In other words, the direction of energy flow is in the plane of the phase front, a result pointed out by Hines (1960) for an isothermal model atmosphere.

We see from equation (4) that if the conditions $\alpha = H_0^{-1}$ and $\beta_z = 0$ prevail then β_x vanishes and the motion is undamped. From the definition of linear variation of scale height, $H = H_0(1 + \alpha z)$, the first condition can be expressed as $\partial H/\partial z = 1$. On examining these conditions, we shall find that the first implies the second; further, the first is nearly satisfied in the normal atmosphere at about 150 km altitude.

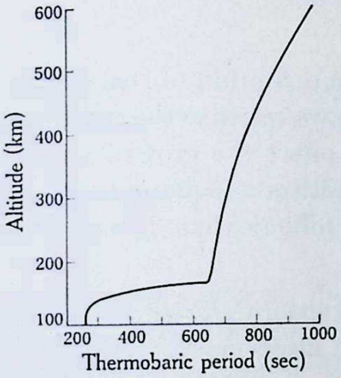

Fig. 1.—Thermobaric period for a COSPAR model atmosphere.

The energy in a gravity wave is partitioned equally into a kinetic form, $\frac{1}{2}\rho_0 u^2$, and a potential form, the latter being further partitioned into elastic energy, $\frac{1}{2}\rho_0 \xi_e^2 c^2$, where ξ_e is the condensation $\delta\rho_e/\rho$, and into thermobaric energy (e.g. Eckart 1960). The thermobaric energy is the product of the average thermobaric force during a quarter-cycle of the motion and the vertical displacement $W_t = \frac{1}{2}(-\rho\omega_B^2\,\delta z)\delta z$ (Eckart 1960). From the definition of scale height we can define a thermobaric condensation

$$\xi_t = -\frac{\delta z}{H}\left(\frac{\gamma - 1}{\gamma} + \frac{\partial H}{\partial z}\right),$$

so that the thermobaric energy can be written as

$$\tfrac{1}{2}\rho_0\,\omega_B^2\left(\frac{\gamma-1}{\gamma} + \frac{\partial H}{\partial z}\right)^{-2} H^2 \xi_t^2 .$$

With the help of equation (2) and the relation $c^2 = \gamma g H$, we obtain

$$W_t = \tfrac{1}{2}\rho_0 \frac{1}{\gamma}\left(\frac{\gamma-1}{\gamma} + \frac{\partial H}{\partial z}\right)^{-1} c^2 \xi_t^2 , \tag{6}$$

and the total energy in a gravity wave is

$$E = \tfrac{1}{2}\rho_0 u^2 + \tfrac{1}{2}\rho_0 c^2 \xi_{\mathrm{e}}^2 + \tfrac{1}{2}\rho_0 \frac{1}{\gamma}\left(\frac{\gamma-1}{\gamma}+\frac{\partial H}{\partial z}\right)^{-1} c^2 \xi_{\mathrm{t}}^2 . \tag{7}$$

Since $E = \rho_0 u^2$, we find from equation (7)

$$u = c\xi , \tag{8}$$

where

$$\xi^2 = \frac{1}{\gamma}\left(\frac{\gamma-1}{\gamma}+\frac{\partial H}{\partial z}\right)^{-1} \xi_{\mathrm{t}}^2 + \xi_{\mathrm{e}}^2 .$$

The energy carried across a unit area must be conserved; that is, $\rho u_z^2 c$ is constant or, by virtue of equation (8), $\rho c^2 |u_z| |\xi_z|$ is constant. If now we ask that the product of the kinetic and elastic amplitudes be constant or independent of altitude, then we must have $\partial(\rho c^2)/\partial z = 0$, or

$$\frac{1}{\rho}\frac{\partial \rho}{\partial z} + \frac{1}{c^2}\frac{\partial c^2}{\partial z} = 0 . \tag{9}$$

From equation (9), the perfect gas law, and the definition of scale height, it follows that $H^{-1} + H^{-1}\,\partial H/\partial z = 0$, or $\partial H/\partial z = 1$. Thus we see that the motion is undamped when the thermal gradient is large enough to offset the growth in amplitude that results from decrease in ambient density with altitude (equation (9)). If amplitude is independent of altitude, then $\beta_z = 0$ and it follows that $\beta_x = 0$ and the motion is undamped, neglecting viscosity.

The condition $\partial H/\partial z = 1$ is almost satisfied ($\partial H/\partial z \approx 0 \cdot 7$) from about 150 to 160 km altitude in the 1961 CIRA standard atmosphere. This altitude range is part of a gravity wave duct that has boundaries at about 100 and 165 km (Wickersham 1965*a*) and, because it is almost free of nonviscous damping, we conclude that this is a major duct for the long distance propagation of gravity waves that perturb the lower ionosphere.

III. A Source of Ducted Acoustic-gravity Waves

From Figure 1 we see that in the principal thermospheric duct the thermobaric period varies from 270 sec at the lower boundary near 100 km to 650 sec at the upper boundary near 160 km. Since gravity waves with short periods, say 270–430 sec, would be confined to the lower half of the duct and suffer nonviscous damping, we shall confine our attention to the upper portion of the duct, 150–160 km, where the period varies from $\tau_{\min} = 430$ sec to $\tau_{\max} = 650$ sec and has a mean or central value of about $\tau_0 = 540$ sec or 9 min. We shall regard this altitude region as an ensemble of thermobaric oscillators having an approximately uniform density in frequencies and subject to thermal perturbations varying in time. Beyond the altitude interval of interest we shall consider the thermobaric period to be constant, as indicated in the idealized distribution shown in Figure 2.

A major thermal perturbation must occur diurnally when dawn, first at 160 km and then down to 150 km, increases the temperature and local scale height, causing an atmospheric heave or vertical displacement. If z is the vertical displacement within the region, the corresponding thermobaric force is

$$-\rho\omega_{\mathrm{B}}^{2}z \sim -\rho\omega_{\mathrm{B}}(\partial z/\partial H)(\partial H/\partial t)\delta t\,,$$

the $\partial H/\partial t$ factor being proportional to the time rate of change in temperature. We shall neglect equilibration time lag and represent this perturbing force in time by a simple square pulse, starting at dawn at 160 km and ending at dawn at 150 km (Fig. 3). The width of the pulse varies from about 1·6 min in the equatorial regions to 1 hr 20 min for the winter solstice dawn nearest the pole.

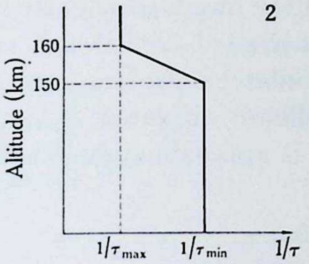

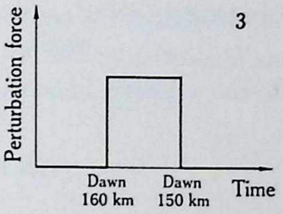

Fig. 2 (*left*).—Idealized distribution of thermobaric periods assumed for estimating the response of the 150–160 km altitude interval to a thermal impulse.

Fig. 3 (*right*).—An assumed form of the perturbation caused by sunrise in the 150–160 km altitude region.

The square pulse shown in Figure 3 can be regarded as a superposition of up and down Heaviside step functions. The second step function will excite an oscillator with a phase opposite to that of the first; therefore, maximum excitation occurs when the pulse width is equal to half the period of the oscillator. For the central oscillator this would be a pulse width of 4·5 min. A time difference of 4·5 min corresponds to 1·125° of rotation of the Earth. The segment between dawn lines at 160 and 150 km altitude that includes 1·125° of polar arc is shown in Figure 4, a projection of the dawn lines onto a plane tangent to the South Pole. The segment is about 6° north of the Antarctic Circle. A line drawn from the segment and normal

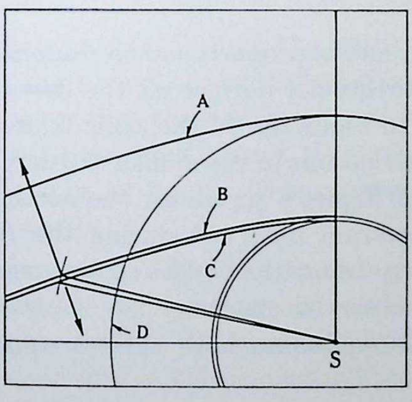

Fig. 4.—A projection of the polar region onto a tangent plane at the South Pole. Three approximately parallel lines indicate dawn at sea level (A), 150 km (B), and 160 km (C) altitude. Curve D is the Antarctic Circle.

to the dawn line indicates the most probable directions of propagation of disturbances excited in the duct. Extended on a great circle to Sydney, Australia, the line indicates a direction of arrival there of about 30° east of north.

We see that during the Australian winter, when the dawn line near the Antarctic Circle is at its closest approach to Australia, we should expect ducted gravity waves to arrive in Australia from the south-east. Conversely, during the Australian summer, disturbances should arrive from the north-west from the winter dawn line near the Arctic Circle. These indeed are the seasonal characteristics observed by Munro (1958, Fig. 11).

To obtain a quantitative prediction of the observed angular spectrum, we note that the amplitude, or response, of a pulse-excited oscillator is proportional to its bandwidth. The bandwidth of the central oscillator is the largest and is approximately $B_0 \approx \tau_0(\tau_{\max}-\tau_{\min})/\tau_{\max}\tau_{\min}$. For an oscillator displaced $\pm\Delta\tau$ sec in period from the central period, the relative bandwidth is approximately $B \approx B_0-2\Delta\tau/\tau_0$, from which we have

$$\Delta B \approx 2\Delta\tau/\tau_0 . \tag{10}$$

At points along the dawn line to the left or right of the 4·5 min dawn interval, there are dawn intervals shorter or longer than 4·5 min. These pulses will excite oscillators that have bandwidths less than that of the central oscillator; thus, their response will be less than that of the central oscillator. According to equation (10), the response decreases linearly as the time interval becomes less than or greater than τ_0.

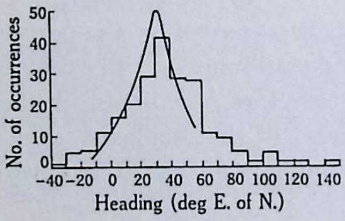

Fig. 5.—A comparison of the angular spectrum of TID's observed by Munro (1958) with a spectrum derived heuristically by postulating a thermal source of gravity waves in the antarctic region.

If we assume that probability of occurrence is proportional to response, we can associate a relative probability with each directional normal on the dawn line and obtain the relative angular spectrum shown in Figure 5. In the same figure we show a histogram of Munro's 5-year average of observations in the month of June. The two spectra are in agreement. A mirror image of Figure 4 serves for the northern hemisphere and can be used to predict the spectrum observed during the Australian summer; however, the source in this case is now more than twice as far removed from Australia, and, as might be expected, the observed spectrum has somewhat more angular spread than predicted. During the equinoxes both spectra appear to be observed.

IV. The Tilt and Period of TID's

The morphology of TID's as deduced from ionosonde data by Munro and Heisler appears to be confirmed by the incoherent scattering measurements recently presented by Thome (1964). The electron density perturbation caused by a disturbance as measured by Thome is reproduced here in Figure 6. Unfortunately, Thome did not report the speed of the disturbance but gave only a range of 50–100 m/sec as typical of most disturbances. If we assume a horizontal speed of 57 m/sec we obtain the isodensity contours in spatial coordinates, as shown in Figure 7. We shall consider this to be a representative TID since the 45° slope near the centre is almost as large as the mean values of 51° to 65° observed by Munro and Heisler.

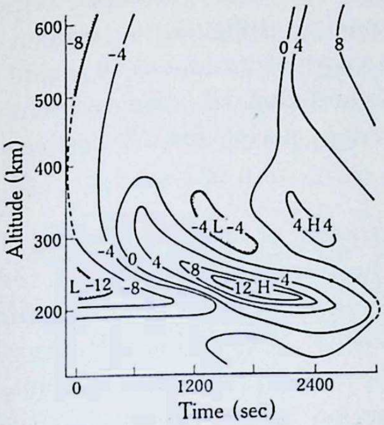

Fig. 6.—Charge density contours associated with a TID detected by the incoherent scattering technique (from Thome 1964).

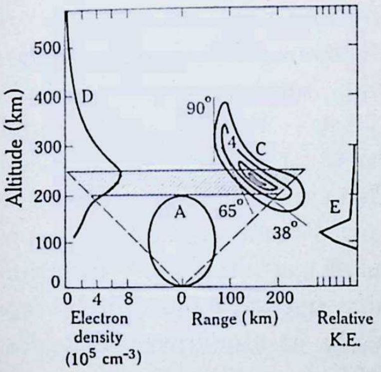

Fig. 7.—Charge density contours (C), associated with the TID observed by Thome (1964), transformed to spatial coordinates by assuming a horizontal propagation speed of 57 m/sec. Ambient electron density (D), from Thome, is shown at left; an energy density profile (E) for a ducted gravity wave, from Pfeffer and Zarichny (1963), is shown at right. At bottom centre there is an assumed cosine-squared antenna radiation pattern (A).

From equation (5), since the last term is small, we see that when the wave front is vertical the period of the disturbance must be $\tau \approx \tau_B$. From either Figure 6 or Figure 7 we see that the leading edge of the disturbance is vertical just above 300 km altitude, and thus from Figure 1 we conclude that the period of the disturbance is about 705 sec or 11·7 min. This conclusion is independent of the speed assumed for the disturbance.

At the centre of the disturbance, near 225 km, the slope of an 11·7 min gravity wave should be, by equation (5), about 74°. This is somewhat greater than the average upper limit of 65° measured by Munro and Heisler and considerably greater than the slope of the TID shown in Figure 7. The slope near the centre of the TID shown in Figure 7 is, of course, dependent on the speed assumed for the disturbance. We can obtain agreement with Munro and Heisler's upper value of 65° if we assume β_z small and $\lambda_x = 200$ km. To obtain agreement with the centre slope of the TID in Figure 3 we should have to assume $\lambda_x \geqslant 445$ km. So large a value of horizontal wavelength would be difficult to reconcile with our first determination of an 11·7 min period and the theoretical and observed propagation speeds of TID's. The difficulty increases at still lower altitudes. Even with a horizontal wavelength as large as 445 km we cannot reconcile theory and observation at 160 km altitude. From equation (5) we should predict a slope of 38° where the observed slope is zero. It is possible that the observed slope is zero at 160 km because the disturbance does not extend to lower altitudes. However, if this were so, then the disturbance would consist of an oblique rising of energy from no apparent source at 160 km altitude to an ultimate dissipation at 300 km altitude, an interpretation difficult to reconcile with long-range horizontal propagation. We find a more satisfactory model by assuming that the neutral disturbance extends to lower levels and that the disagreements between theoretical and observed slopes at the lower edges derive from the effects of ionospheric chemistry.

It is possible that the trailing edge of the disturbance is more a measure of ionospheric chemical equilibration time rather than the duration or width of the neutral wave. We note that above 180 km altitude the ionospheric electron reservoir is controlled by the charge-exchange reaction $O^+ + N_2 \rightarrow NO^+ + N$. Using the atmospheric model and reaction-rate compilation of Ferguson *et al.* (1965), and assuming a linear, positive temperature dependence for the reaction rate, we find that the effective time constant for the above reaction is about 500 sec at 270 km altitude. This is also the time interval between the 6% or half-amplitude levels at 270 km altitude for the TID shown in Figures 6 and 7. Just below 170 km altitude the reaction $NO^+ + e^- \rightarrow N + O$ controls the electron reservoir; however, at this altitude both reactions have effective time constants less than 20 sec. Because of the rapid equilibration, the charge density no longer reflects the neutral particle perturbation and the TID is almost unobservable by radio means. This expectation appears to be confirmed by the data shown in Figure 6 as well as by other data shown by Thome. If chemical equilibration time determines the duration of the charge perturbation caused by a TID then the slope of the electron density perturbation will be less than that of the neutral density perturbation, especially at the lower altitudes, and at 170 km the almost zero slope may be a result of fast equilibration.

From the above brief consideration we see a difficulty in determining the period from the slope; a difficulty, however, that may ultimately prove useful in studying ionospheric chemistry. We shall see also that it is difficult to determine the period on the basis of the time during which the charge perturbation interacts with radio equipment.

Curve E of Figure 7 shows the relative kinetic energy profile for a 13 min period, fully ducted, third-order gravity mode computed by Pfeffer and Zarichny. This profile is typical of many of the gravity modes in that some energy appears in the *F* region but the centroid is between 100 and 165 km altitude. Curve D of this figure shows the ambient electron density measured by Thome at about the time of the TID. We see that the charge density perturbation can be expected to be considerably higher than the maximum disturbance in the neutral particles; thus, it is possible that an observed *F* region charge perturbation is only the wake of a stronger disturbance in a lower region.

In Figure 7 we also show a cosine-squared radiation pattern (A) which is typical of many sweep-frequency ionosondes. The half-power points of such radiation patterns are at 45°, and these are shown as broken lines in the figure. With such sounders one can detect disturbances up to the maximum in the electron density profile (~ 250 km altitude). The sensitivity of most vertical incidence sounders is greatest in the shaded region shown in the figure. The average charged particle perturbation caused by TID's, as measured by Munro and Heisler, is 20% of equilibrium, with maximum perturbations as large as 30%. A TID that causes a 20% charge perturbation possibly could affect the edge of the antenna radiation pattern and continue to do so as it moves through the shaded region. A disturbance similar to that shown in Figure 7, moving at a speed of 57 m/sec, would interact with the sounder for 130 min. It is possible that the first half of such an interaction could be observed and a "period" ascribed to the disturbance of about 65 min. Some observers, however, would take the time interval between this disturbance and the next one to be the period. We see that interaction times might be longer than the periods we have discussed earlier and should not necessarily be taken as a measure of the period of a TID.

V. A Leaky-duct Model of TID's

We now have a large number of theoretical and experimental restrictions and can attempt to construct a gravity wave model of TID's. A model should be consistent with all of the following information.

1. TID's have fronts inclined in the direction of travel.
2. The slopes of TID's are nearly independent of the direction of the geomagnetic field.
3. TID's propagate large distances with little attenuation.
4. The speed distributions of TID's agree with those predicted theoretically for ducted acoustic-gravity waves.
5. The effective time constant of the reaction $O^+ + N_2 \rightarrow NO^+ + N$ corresponds to the observed half-width of a TID observed by Thome.
6. Most of the centroids of the energy profiles of ionospheric, long-period, ducted gravity waves, as computed numerically by Pfeffer and Zarichny, lie in the strong thermoclinal channel between 100 and 165 km altitude.
7. Fast chemical equilibration in the 100–165 km altitude region would prevent observation of long-period neutral particle disturbances by means of radio detection of charged particle perturbations.
8. Fast equilibration in the lower ionosphere appears to be consistent with the fact that observed slopes of TID's are less than can be predicted by gravity wave theory.

To obtain a model consistent with the above information we turn to a leaky-duct model somewhat similar to one suggested originally by Hines (1960). We assume a model in which a wave packet, or pulse, of gravity waves is ducted in the thermoclinal channel between 100 and 165 km altitude. The longer period components of the wave packet leak through the upper boundary of the channel—the knee in the thermobaric period profile of Figure 1—to provide detectable perturbations of the upper ionospheric charge density.

This model is analagous to the bow wave caused by a ship. To an observer in a nearby rowboat, the bow wave appears to move normal to its wave front. To an observer in an aeroplane, the wake of the bow wave has an apparent velocity equal to and in the direction of that of the ship. Thus the horizontal speed of an unseen disturbance, ducted in the channel at 100–165 km altitude, can be determined from measurements of the wake detectable in the upper ionosphere; however, the wake itself has neither the morphology nor direction of motion of a ducted disturbance. A principal difference between the model and the analogy is the forward slope of the energy leaking through the top of the duct, as contrasted with the backward slope of a ship's bow wave. This effect is peculiar to gravity waves. Energy propagates upward in the plane of the downward-sloping wave front.

Note added in proof. The conditions under which a plane wave solution is appropriate to the equation of motion are more general than stated in the text. If the nonviscous damping is small as a result of the condition $\partial H/\partial z \approx 1$ being satisfied, then the coefficient of the second term of the equation of motion, equation (1), vanishes and plane wave solutions are valid for the remaining equation.

If $\partial H/\partial z < 1$, there is nonviscous damping as a result of amplitude increase with increasing altitude. In this case the amplitude increase is due to decreasing ambient density. If $\partial H/\partial z > 1$, there is nonviscous damping as a result of amplitude increase with decreasing altitude. In this case the amplitude increase is due to decreasing sound speed, or temperature, in the ambient medium. The condition $\partial H/\partial z > 1$ is not an instability condition for a horizontally growing wave.

VI. REFERENCES

ECKART, C. (1960).—"Hydrodynamics of Oceans and Atmospheres." (Pergamon Press: New York.)

FERGUSON, E. E., FEHSENFELD, F. C., GOLDEN, P. D., and SCHMELTEKOPF, A. L. (1965).—*J. geophys. Res.* **70**, 4323.

HINES, C. O. (1960).—*Can. J. Phys.* **38**, 1441.

LAMB, H. (1945).—"Hydrodynamics." 6th Ed. Sec. 312. (Dover: New York.)

MARTYN, D. F. (1950).—*Proc. R. Soc.* **201**, 216.

MUNRO, G. H. (1958).—*Aust. J. Phys.* **11**, 91.

MUNRO, G. H., and HEISLER, L. H. (1956*a*).—*Aust. J. Phys.* **9**, 343.

MUNRO, G. H., and HEISLER, L. H. (1956*b*).—*Aust. J. Phys.* **9**, 359.

PFEFFER, R. L., and ZARICHNY, J. (1963).—*Geofis. pura appl.* **55**, 175.

THOME, G. D. (1964).—*J. geophys. Res.* **69**, 4047.

WICKERSHAM, A. F., JR. (1964).—*J. geophys. Res.* **69**, 457.

WICKERSHAM, A. F., JR. (1965*a*).—*J. geophys. Res.* **70**, 1729.

WICKERSHAM, A. F., JR. (1965*b*).—*J. geophys. Res.* **70**, 4875.

WICKERSHAM, A. F., JR. (1966).—*J. geophys. Res.* **71**, 4551.

PROPAGATION OF SHOCK WAVES IN A POLYTROPE WITH A POLOIDAL MAGNETIC FIELD

By Narendra K. Sinha*

[*Manuscript received February* 13, 1968]

Summary

The propagation of a spherically developed shock wave in a polytrope with a poloidal magnetic field has been studied using a generalization of Whitham's method. The effect of the magnetic field on the geometry of the front as well as on the effects brought about by the shock has been discussed.

I. Introduction

The propagation of shock waves in nonuniform compressible media with or without magnetic fields has been considered by a number of authors (Kopal 1954; Rogers 1956; Mackie and Weir 1960; Ôno, Sakashita, and Yamazaki 1960*a*, 1960*b*; and others). In most cases, even though attention has been confined to problems in which physical variables depend upon one spatial coordinate and time, recourse has had to be made to various approximate methods, one of the most useful of which is that first described explicitly by Whitham (1958). Whitham first writes the equation of motion in characteristic form and then applies the differential relation that must be satisfied by flow quantities along a certain characteristic to these flow quantities just behind the shock. When the shock relations are used, a differential equation results for the propagation of the shock. If the appropriate characteristic is chosen, the method gives accurate results for a wide class of problems and shock strengths. Sakashita and Tanaka (1962), Bird (1964), Bhatnagar and Sachdev (1966), and other authors have applied Whitham's method to study the propagation of shock in stellar media with a view to explaining certain astrophysical phenomena.

However, very few investigations have been made on the propagation of a shock in a stellar model with a magnetic field. A magnetic field is known to exist in stellar bodies and a shock wave propagates in a much more complicated way in the presence of a magnetic field. Together with other novel features, there is in general an anisotropy involved in this case. The difficulties inherent in the solution of problems of shock propagation in nonuniform regions are thus sharply accentuated. Even in the simple case when there is only a poloidal magnetic field present the flow quantities are functions of three independent variables.

In the present paper Whitham's rule has been generalized in order to be able to deal with such problems. As in Whitham's method the differential equations are written in characteristic form. However, there is an important difference involved here, in that Whitham's characteristic equations are ordinary differential equations whereas in the present case the equations for the characteristic manifolds are first-order partial differential equations. The approximation used here is to assume that

---

* Department of Mathematics, Monash University, Clayton, Vic. 3168.

Aust. J. Phys., 1968, **21**, 681–93

the motion of the shock is identical with the motion of the fast outward magneto-acoustic wave. The partial differential equations involved are solved by using the method of bicharacteristics. A detailed discussion of this method can be found in Jeffrey and Taniuti (1964).

The problem of finding suitable stellar models with magnetic fields is still under investigation and detailed results are not available. Studies on the structure of magnetic fields in a polytrope have been made, however, as a first step towards the solution of the problem of magnetic fields in real stars. In the absence of such a solution, we use the polytropic solutions to illustrate a method of dealing with shock waves in magnetic stars. Roxburgh (1966) has discussed the poloidal magnetic field structure in polytropes without any internal motion. We take his solution (Section III) as our equilibrium solution of the polytropic star and illustrate the propagation of shock waves in this medium.

We have not discussed the mechanism of the generation of shock waves in the stellar interiors, but its possibility cannot be ruled out. For example, any rapid expansion of the core brought about by nuclear reactions may induce a shock wave. In fact, shock waves are at present associated with some interesting astrophysical phenomena like novae and supernovae explosions, gas motions in the chromosphere, etc. Ôno and Sakashita (1961) have quantitatively used shock waves to explain the mechanism of supernovae explosions.

II. BASIC EQUATIONS

Since we are only considering poloidal magnetic fields here, the magnetic induction $\boldsymbol{B}$ and the fluid velocity $\boldsymbol{v}$ may be written as

$$\boldsymbol{B} = \boldsymbol{e}_r B_r + \boldsymbol{e}_z B_z , \qquad \text{and} \qquad \boldsymbol{v} = \boldsymbol{e}_r u_r + \boldsymbol{e}_z u_z ,$$

where r, ϕ, z are cylindrical coordinates and $\boldsymbol{e}_r, \boldsymbol{e}_\phi, \boldsymbol{e}_z$ the corresponding unit vectors. The origin of the coordinates has been supposed to be at the centre of the polytrope and the z axis along the axis of symmetry. Furthermore, it is clear that, with poloidal fields, $\boldsymbol{v}$ and $\boldsymbol{B}$ as well as the density ρ and the pressure p will depend only upon r, z, and t. Then assuming that the viscosity is negligible, the conductivity infinite, and the medium a perfect fluid, the Lundquist equations (Jeffrey and Taniuti 1964) reduce to the following system of quasi-linear hyperbolic partial differential equations:

$$\frac{\partial \rho}{\partial t} + u_r \frac{\partial \rho}{\partial r} + u_z \frac{\partial \rho}{\partial z} + \rho \frac{\partial u_r}{\partial r} + \rho \frac{\partial u_z}{\partial z} + \rho \frac{u_r}{r} = 0 , \tag{1}$$

$$\rho \frac{\partial u_r}{\partial t} + \rho u_r \frac{\partial u_r}{\partial r} + \rho u_z \frac{\partial u_r}{\partial z} + \frac{\partial p}{\partial r} + \frac{B_z}{\mu} \frac{\partial B_z}{\partial r} - \frac{B_z}{\mu} \frac{\partial B_r}{\partial z} = -\rho \frac{\partial \Psi}{\partial r} , \tag{2}$$

$$\rho \frac{\partial u_z}{\partial t} + \rho u_r \frac{\partial u_z}{\partial r} + \rho u_z \frac{\partial u_z}{\partial z} + \frac{\partial p}{\partial z} + \frac{B_r}{\mu} \frac{\partial B_r}{\partial z} - \frac{B_r}{\mu} \frac{\partial B_z}{\partial r} = -\rho \frac{\partial \Psi}{\partial z} , \tag{3}$$

$$\frac{\partial B_r}{\partial t} + u_r \frac{\partial B_r}{\partial r} + u_z \frac{\partial B_r}{\partial z} - B_z \frac{\partial u_r}{\partial z} + B_r \frac{\partial u_z}{\partial z} + \frac{B_r u_r}{r} = 0 , \tag{4}$$

$$\frac{\partial B_z}{\partial t} + u_r \frac{\partial B_z}{\partial r} + u_z \frac{\partial B_z}{\partial z} - B_r \frac{\partial u_z}{\partial r} + B_z \frac{\partial u_r}{\partial r} + \frac{B_z u_r}{r} = 0 , \tag{5}$$

$$\rho\frac{\partial p}{\partial t}+\rho u_r\frac{\partial p}{\partial r}+\rho u_z\frac{\partial p}{\partial z}-\gamma p\frac{\partial \rho}{\partial t}-\gamma p u_r\frac{\partial \rho}{\partial r}-\gamma p u_z\frac{\partial \rho}{\partial z}=0\,, \tag{6}$$

where Ψ is the gravitational potential. The entropy relation $S = S_0+C_v\ln(p\rho^{-\gamma})$ has been assumed. Further Ψ satisfies Poisson's equation

$$\frac{\partial^2\Psi}{\partial r^2}+\frac{1}{r}\frac{\partial\Psi}{\partial r}+\frac{\partial^2\Psi}{\partial z^2}=4\pi G\rho\,. \tag{7}$$

Since the motion is axisymmetrical, we discuss the motion in an azimuthal plane only.

III. EQUILIBRIUM SOLUTION

Roxburgh (1966) has considered dipole solutions $\bar{S}(R,\theta) = A(R)\sin^2\theta$, expressing the field as

$$\boldsymbol{B}\equiv\left(\frac{2A\cos\theta}{R^2},-\frac{\mathrm{d}A}{\mathrm{d}R}\frac{\sin\theta}{R},0\right), \tag{8}$$

in the spherical coordinates (R,θ,ϕ), θ being the angle made with the z axis. $\bar{S}$ = constant are the field lines of $\boldsymbol{B}$. The equation determining A comes out to be

$$\frac{\mathrm{d}^2A}{\mathrm{d}R^2}-\frac{2A}{R^2}+D\rho R^2=0\,, \tag{9}$$

where D is a constant. Using the transformations

$$\left.\begin{aligned} R&=a\xi\,, & A&=D\rho_{\mathrm{c}}a^4\bar{\gamma}\,,\\ \rho_0&=\rho_{\mathrm{c}}\,\theta_0^n\,, & a&=\left\{K(n+1)\rho_{\mathrm{c}}^{n^{-1}-1}/4\pi G\right\}^{\frac{1}{2}}, \end{aligned}\right\} \tag{10}$$

where the symbols have their usual meanings, equation (9) reduces to

$$\frac{\mathrm{d}^2\bar{\gamma}}{\mathrm{d}\xi^2}-\frac{2\bar{\gamma}}{\xi^2}=-\theta_0^n\,\xi^2\,. \tag{11}$$

For the polytrope $n = 1$, $\theta_0 = (\sin\xi)/\xi$ and therefore $\xi = \pi$ defines the surface of the polytrope. With the boundary conditions

$$\bar{\gamma}=\mathrm{d}\bar{\gamma}/\mathrm{d}\xi=0 \qquad \text{at} \qquad \xi=0$$

and

$$\xi\,\mathrm{d}\bar{\gamma}/\mathrm{d}\xi+\bar{\gamma}=0 \qquad \text{at} \qquad \xi=\pi,$$

equation (11) is found to have the solution

$$\bar{\gamma}=\tfrac{1}{3}\xi^2+\xi\sin\xi+2\cos\xi-(2\sin\xi)/\xi\,,$$

which is not in agreement with the solution given by Roxburgh (equation (29) in his paper; the variable $\bar{\gamma}$ here is the same as γ of Roxburgh).

The structure of the magnetic field in the polytrope is now known. The resolutes of $\boldsymbol{B}$ corresponding to the field (8) are

$$B_r=\frac{Jrz(3Q-1-\cos\xi)}{r^2+z^2}, \qquad B_z=\frac{J\{(2z^2-r^2)Q+(1+\cos\xi)r^2\}}{r^2+z^2}, \tag{12}$$

where

$$Q = \frac{1}{3} + \frac{\sin\xi}{\xi} + \frac{2\cos\xi}{\xi^2} - \frac{2\sin\xi}{\xi^3},$$

and

$$J = \rho_c a^2 D$$

is a constant that is proportional to the strength of the magnetic field. The null point of the field is located at $\xi = 2\cdot4035$ approximately on the r axis. The field lines form closed loops about the null point, in the clockwise sense, in an azimuthal plane. On $\xi =$ constant the magnitude of the field (Fig. 1), as well as its inclination with the r axis, decreases as θ increases. Moreover, $B_r = 0$ when either $r = 0$ or $z = 0$, so that at points on the axes the field is parallel to the z axis.

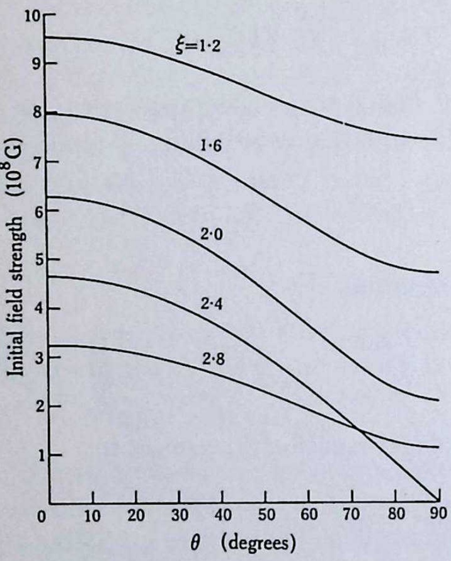

Fig. 1.—Initial distribution of field strength on curves $\xi =$ constant in the upper half of the azimuthal plane; $\mathscr{S}_0 = 0\cdot707$ (Section VI).

Furthermore, p and ρ, which are spherically symmetric to the first approximation, are given by

$$p = k\rho^2, \qquad \rho = \rho_c(\sin\xi)/\xi,$$

where ξ is expressed as

$$\xi = (r^2+z^2)^{\frac{1}{2}}/a.$$

IV. Shock Relations

Equations (1)–(6), being a system of quasi-linear hyperbolic partial differential equations, admit of weak solutions in which the values of the physical quantities p, ρ, $\boldsymbol{v}$, and $\boldsymbol{B}$ may be discontinuous across certain surfaces called shock fronts. (Since the gravitational potential Ψ satisfies the elliptic equation (7), it will be analytic throughout the whole region.) The equations connecting the values of the physical quantities on each side of the shock front are obtained by writing the equations (1)–(6) in conservation form (Jeffrey and Taniuti 1964), and in the present case they are

$$U(\rho-\rho_0) = \rho u_{\mathrm{n}}\,, \tag{13a}$$

$$U(B_{\mathrm{e}}-B_{\mathrm{e}0}) = B_{\mathrm{e}}\,u_{\mathrm{n}}-B_{\mathrm{n}}\,u_{\mathrm{e}}\,, \tag{13b}$$

$$B_{\mathrm{n}} = B_{\mathrm{n}0}\,, \tag{13c}$$

$$U\rho u_{\mathrm{n}} = \rho u_{\mathrm{n}}^2+(p-p_0)+(1/2\mu)(B^2-B_0^2)\,, \tag{13d}$$

$$U\rho u_{\mathrm{e}} = \rho u_{\mathrm{e}}\,u_{\mathrm{n}}-(1/\mu)(B_{\mathrm{e}}-B_{\mathrm{e}0})B_{\mathrm{n}}\,, \tag{13e}$$

$$U\left(\tfrac{1}{2}\rho u^2+\frac{p-p_0}{\gamma-1}+\frac{1}{2\mu}(B^2-B_0^2)\right) = u_{\mathrm{n}}\left(\tfrac{1}{2}\rho u^2+\frac{\gamma p}{\gamma-1}+\frac{B^2}{\mu}\right)-\frac{B_{\mathrm{n}}}{\mu}\left(B_{\mathrm{n}}\,u_{\mathrm{n}}+B_{\mathrm{e}}\,u_e\right), \tag{13f}$$

where U is the absolute normal velocity of the shock front. The subscript 0 refers to the region at rest ahead of the shock and variables without it refer to the shocked region. Further, the subscripts n and e give the components normal and tangential to the shock front respectively in the azimuthal plane. The values of the physical quantities behind the shock may now be expressed in terms of those ahead of the shock and the shock strength λ as

$$\rho = \lambda\rho_0\,, \tag{14a}$$

$$u_{\mathrm{n}} = (1-1/\lambda)U\,, \tag{14b}$$

$$u_{\mathrm{e}} = (1-\lambda)B_{\mathrm{n}}\,B_{\mathrm{e}0}\,U/(U^2\mu\rho_0-\lambda B_{\mathrm{n}}^2)\,, \tag{14c}$$

$$B_{\mathrm{n}} = B_{\mathrm{n}0}\,, \tag{14d}$$

$$B_{\mathrm{e}} = (U^2\mu\rho_0-B_{\mathrm{n}}^2)\lambda B_{\mathrm{e}0}/(U^2\mu\rho_0-\lambda B_{\mathrm{n}}^2)\,, \tag{14e}$$

$$p = p_0+\left(1-\frac{1}{\lambda}\right)U^2\rho_0-\left(U^2\mu\rho_0-\lambda B_{\mathrm{n}}^2+\lambda(U^2\mu\rho_0-B_{\mathrm{n}}^2)\right)\frac{(\lambda-1)U^2B_{\mathrm{e}0}^2\,\rho_0}{2(U^2\mu\rho_0-\lambda B_{\mathrm{n}}^2)^2}, \tag{14f}$$

where U itself is given by the equations

$$U = 0\,, \qquad \text{or} \qquad U^6-E_1\,U^4+E_2\,U^2-E_3 = 0\,, \tag{15}$$

E_1, E_2, and E_3 being known functions of the physical quantities ahead of the shock. The r and z components of the physical quantities behind the shock are easily obtained from equations (14) by the transformations

$$F_r = \frac{h_r\,F_{\mathrm{n}}-h_z\,F_{\mathrm{e}}}{(h_r^2+h_z^2)^{\frac{1}{2}}} \qquad \text{and} \qquad F_z = \frac{h_z\,F_{\mathrm{n}}+h_r\,F_{\mathrm{e}}}{(h_r^2+h_z^2)^{\frac{1}{2}}}.$$

The speeds U of propagation given by (15) correspond to the various discontinuities that exist in a magnetohydrodynamic medium. The case $U = 0$ corresponds to a contact discontinuity and is immediately ruled out. The second equation in (15) is a cubic in U^2 and gives the speeds of the fast, slow, and intermediate shocks. This equation may be rewritten as

$$E^{\mathrm{I}}\lambda^3-E^{\mathrm{II}}\lambda^2+E^{\mathrm{III}}\lambda-E^{\mathrm{IV}} = 0\,, \tag{16}$$

where

$$E^{\mathrm{I}} = \{(\gamma-1)\mu U^2 B_0^2\,\rho_0 + 2\gamma\mu B_{\mathrm{n}}^2 p_0\} B_{\mathrm{n}}^2\,,$$

$$E^{\mathrm{II}} = \{(\gamma+1)B_0^2 + 4\gamma\mu p_0\}\mu U^2 B_{\mathrm{n}}^2\,\rho_0 - \{(2-\gamma)B_0^2 - \gamma B_{\mathrm{n}}^2\}\mu^2 U^4 \rho_0^2\,,$$

$$E^{\mathrm{III}} = \{(\gamma-1)\mu U^2 \rho_0 + 2\gamma\mu p_0 + (\gamma+2)B_{\mathrm{n}}^2 + \gamma B_0^2\} U^4 \mu^2 \rho_0^2\,,$$

$$E^{\mathrm{IV}} = (\gamma+1)\mu^3 U^6 \rho_0^3\,.$$

The equation (16) is a cubic in λ and gives the strength of the fast, slow, and intermediate shocks that correspond to a given speed U of propagation. To find the root λ_{f}, corresponding to the fast shock, the evolutionary conditions for a physically relevant shock are invoked. The intermediate shock is noncompressive and therefore the corresponding λ is less than or equal to unity. Such a root is discarded. Furthermore, we note that a fast shock brings about an increase in the magnitude of the tangential component of the magnetic field, whereas the latter is decreased on the passage of a slow shock. We use this property to isolate λ_{f}. However, when $B_{\mathrm{n}} = 0$, perpendicular shock locally, equation (16) reduces to the quadratic equation in λ

$$(2-\gamma)b_0^2\,\lambda^2 + \{(\gamma-1)U^2 + 2c_0^2 + \gamma b_0^2\}\lambda - (\gamma+1)U^2 = 0\,, \tag{17}$$

where $c^2 = \gamma p/\rho$ is the square of the sound speed and $\boldsymbol{b} = (\mu\rho)^{-\frac{1}{2}}\boldsymbol{B}$ is the Alfven velocity vector. One of the roots of equation (17) is positive and the other is negative. Since U^2 is greater than $c_0^2 + b_0^2$, the positive root is greater than unity and gives λ_{f} in this case. Similarly, when $\gamma = 2$ the only remaining root is greater than unity and corresponds to λ_{f}.

Thus U and the state ahead of the shock being known, the value of λ_{f} can be obtained and then the values of the physical quantities behind the shock can be determined with the help of equations (14).

V. GENERALIZED WHITHAM'S METHOD USING CHARACTERISTIC MANIFOLDS

If $h(r,z,t) = 0$ is the equation of a characteristic manifold, across which there may be discontinuities in the derivatives of p, ρ, $\boldsymbol{v}$, and $\boldsymbol{B}$, then we get the equation (Courant and Friedrichs 1948)

$$\left(\frac{\mathrm{d}h}{\mathrm{d}t}\right)^2\left\{\left(\frac{\mathrm{d}h}{\mathrm{d}t}\right)^4 - (c^2+b^2)(h_r^2+h_z^2)\left(\frac{\mathrm{d}h}{\mathrm{d}t}\right)^2 + c^2(h_r^2+h_z^2)\frac{(B_r h_r + B_z h_z)^2}{\mu\rho}\right\} = 0 \tag{18}$$

for the characteristic manifolds, where

$$\frac{\mathrm{d}}{\mathrm{d}t} \equiv \frac{\partial}{\partial t} + u_r\frac{\partial}{\partial r} + u_z\frac{\partial}{\partial z}\,,$$

and the subscripts on h indicate partial derivatives. The equation (18) shows the existence of the following three real characteristic manifolds.

$$\mathrm{d}h/\mathrm{d}t = 0\,, \tag{19}$$

$$(\mathrm{d}h/\mathrm{d}t)^2 - \tfrac{1}{2}(h_r^2+h_z^2)(c^2+b^2+\eta) = 0\,, \tag{20}$$

$$(\mathrm{d}h/\mathrm{d}t)^2 - \tfrac{1}{2}(h_r^2+h_z^2)(c^2+b^2-\eta) = 0\,, \tag{21}$$

where

$$\eta = +\{(c^2+b^2)^2-\nu\}^{\frac{1}{2}}, \qquad \text{with} \qquad \nu = \frac{4c^2}{\mu\rho}\frac{(B_r h_r+B_z h_z)^2}{(h_r^2+h_z^2)}.$$

Equation (19) simply means that the particle paths are bicharacteristics, i.e. they generate a characteristic manifold. The characteristic manifolds given by equations (20) and (21) are the fast and slow magnetoacoustic wave fronts respectively.

The equation for the outward moving fast magnetoacoustic wave $h(r,z,t)=0$ is obtained as

$$h_t+u_r h_r+u_z h_z+\{\tfrac{1}{2}(h_r^2+h_z^2)(c^2+b^2+\eta)\}^{\frac{1}{2}}=0. \tag{22}$$

The characteristic rays in this case are given by the following system of differential equations.

$$\frac{\mathrm{d}r}{\mathrm{d}t} = u_r+\frac{1}{\eta_3}\left(\eta_2 h_r-\frac{2\eta_1 c^2 h_z}{\eta}\right), \tag{23}$$

$$\frac{\mathrm{d}z}{\mathrm{d}t} = u_z+\frac{1}{\eta_3}\left(\eta_2 h_z+\frac{2\eta_1 c^2 h_r}{\eta}\right), \tag{24}$$

$$\frac{\mathrm{d}h_r}{\mathrm{d}t} = -h_r\frac{\partial u_r}{\partial r}-h_z\frac{\partial u_z}{\partial r}+\eta_4\frac{\partial p}{\partial r}+\eta_5\frac{\partial \rho}{\partial r}+\eta_6\frac{\partial B_r}{\partial r}+\eta_7\frac{\partial B_z}{\partial r}, \tag{25}$$

$$\frac{\mathrm{d}h_z}{\mathrm{d}t} = -h_r\frac{\partial u_r}{\partial z}-h_z\frac{\partial u_z}{\partial z}+\eta_4\frac{\partial p}{\partial z}+\eta_5\frac{\partial \rho}{\partial z}+\eta_6\frac{\partial B_r}{\partial z}+\eta_7\frac{\partial B_z}{\partial z}, \tag{26}$$

$$\frac{\mathrm{d}h_t}{\mathrm{d}t} = -h_r\frac{\partial u_r}{\partial t}-h_z\frac{\partial u_z}{\partial t}+\eta_4\frac{\partial p}{\partial t}+\eta_5\frac{\partial \rho}{\partial t}+\eta_6\frac{\partial B_r}{\partial t}+\eta_7\frac{\partial B_z}{\partial t}, \tag{27}$$

where

$$\eta_1 = (B_r h_r+B_z h_z)(B_r h_z-B_z h_r)/(h_r^2+h_z^2)\mu\rho,$$

$$\eta_2 = c^2+b^2+\eta,$$

$$\eta_3 = +2\{\tfrac{1}{2}(h_r^2+h_z^2)\eta_2\}^{\frac{1}{2}},$$

$$\eta_4 = (h_r^2+h_z^2)(\nu-2c^2\eta_2)/4p\eta\eta_3,$$

$$\eta_5 = (h_r^2+h_z^2)(c^2\eta_2+b^2\eta_2-\nu)/2\rho\eta\eta_3,$$

$$\eta_6 = \left(h_r^2+h_z^2\right)\left(\frac{\nu h_r}{2(B_r h_r+B_z h_z)\eta\eta_3}-\frac{\eta_2 B_r}{\mu\rho\eta\eta_3}\right),$$

$$\eta_7 = \left(h_r^2+h_z^2\right)\left(\frac{\nu h_z}{2(B_r h_r+B_z h_z)\eta\eta_3}-\frac{\eta_2 B_z}{\mu\rho\eta\eta_3}\right).$$

The position and orientation of the wave front are thus known if the system of equations (23)–(26) can be solved. An exact solution is not possible and, in general, numerical integration has to be employed. The method to determine the motion of the shock wave is to assume that the motion of the shock wave is identical with the motion of the outward moving fast magnetoacoustic wave with which the shock originally coincided. In this case the various physical quantities occurring in the second members of the equations (23)–(26) are related to the physical quantities ahead of the shock by the shock relations (13). Since the medium ahead of the shock is independent of time, it follows from equation (27) that h_t is constant.

The speed U of the wave front is given by

$$U = -h_t/(h_r^2+h_z^2)^{\frac{1}{2}},$$

where h_t is now constant. If the initial values of h_r and h_z are chosen so that $h_r^2+h_z^2 = 1$, then $-h_t = U_0$, the initial value of U, and we get

$$U = U_0/(h_r^2+h_z^2)^{\frac{1}{2}}. \tag{28}$$

The shock is moving in an inhomogeneous medium and in a nonuniform magnetic field. Consequently, the orientation of the shock front as well as its velocity will be changing as it moves onwards. Equation (28) serves to give the value of the normal velocity of the wave front at any time at any point.

VI. NUMERICAL INTEGRATION

The central density and the radius of the polytrope under consideration ($n = 1$), which are independent of each other in this case, have been assumed to be identical with the solar values, so that

$$\rho_c = 75\cdot858 \qquad \text{and} \qquad \bar{R} = 6\cdot951\times10^{10},$$

(in CGS units) where $\bar{R}$ is the radius. (We use CGS units throughout the calculation.) From equations (10) it is then found that

$$a = 2\cdot212\times10^{10} \qquad \text{and} \qquad K = 2\cdot052\times10^{14}.$$

The shock is assumed to develop and start spherically outwards at the surface $\xi = 1$. On this surface it is found that $J \simeq 1\cdot26\times10^9\,\mathscr{S}_0$, where $\mathscr{S} = b/c$ is a nondimensional parameter. Shocks of different initial intensity, corresponding to Mach number $M_{s,i}$ ($\equiv U_0/C_0$) $= 1\cdot25$, 2, 3, and 5 have been considered and the propagation of each of them studied for different strengths of the field (12). The magnetic field encountered in astrophysical problems is generally weak and hence it has been chosen to correspond to the values $0\cdot3$, $0\cdot5$, and $0\cdot707$ of $\mathscr{S}_0$ at $\xi = 1$. For these characteristic values the field is about 10^8 G, which agrees well with its estimated value in the stellar interiors. $M_{s,i}$ is limited to 5 because we have confined studies here to nonrelativistic and physically realistic phenomena. Knowledge of $M_{s,i}$ helps to obtain the value of U_0, and that of $\mathscr{S}_0$ at $\xi = 1$ helps to determine J. When J is known the poloidal field (12) is specified completely.

With these initial and other relevant data equations (23)–(26) have been integrated in conjunction with equation (28) using the Runge–Kutta method on a CDC 3200 computer, with time steps $\Delta t = 0\cdot1$. After every 100 steps of integration the values of the physical quantities just behind the shock were computed with the help of equations (14). Since the magnetic field is dipole in nature, the values of the physical quantities must be symmetrical about the r axis. This follows also from the fact that the set of equations (1)–(6) is invariant under the transformation ($z \to -z, u_z \to -u_z, B_r \to -B_r$). Therefore the computation has been carried out only in the upper half of the azimuthal plane (r–z quadrant), carrying it nearly as far out as the surface. Furthermore, the initial shock position now becomes a quadrant of the circle $\xi = 1$.

The results of the foregoing integration give the characteristic rays through any prescribed values of r, z, h_r, and h_z, considering this set as the initial values. The integration has been done for 19 different points on the initial shock position at 5° intervals of θ, unfolding the characteristic ray in each case. The position of the front, at any subsequent time t, in the quadrant is obtained as the locus of the positions at time t on the different rays. The front is, in general, not circular and we have expressed the different radial distances obtained for the front at any particular time t as the series

$$R_0(t) + R_2(t)\,\mathrm{T}_2(\cos\theta) + R_4(t)\,\mathrm{T}_4(\cos\theta) + \ldots,$$

where $\mathrm{T}_n(\omega) = \cos(n\cos^{-1}\omega)$ are the Chebyshev polynomials. Owing to the symmetry of the problem about the r axis and the parity property of these polynomials, only even terms appear in the expansion. The first term $R_0(t)$ gives the mean radius of the front at time t, whereas each of the remaining terms introduces a nonspherical distortion. Similarly, the density ratio λ, pressure ratio Π, and ratio β of the magnetic field across the front, as well as the shock Mach number M_s at different times t have also been expressed as the respective series

$$\lambda_0(t) + \lambda_2(t)\,\mathrm{T}_2(\cos\theta) + \lambda_4(t)\,\mathrm{T}_4(\cos\theta) + \ldots,$$

$$\Pi_0(t) + \Pi_2(t)\,\mathrm{T}_2(\cos\theta) + \Pi_4(t)\,\mathrm{T}_4(\cos\theta) + \ldots,$$

$$\beta_0(t) + \beta_2(t)\,\mathrm{T}_2(\cos\theta) + \beta_4(t)\,\mathrm{T}_4(\cos\theta) + \ldots,$$

and

$$M_0(t) + M_2(t)\,\mathrm{T}_2(\cos\theta) + M_4(t)\,\mathrm{T}_4(\cos\theta) + \ldots.$$

As above, the first term in each case gives the mean value of the function over the front at time t whereas the remaining terms introduce the nonspherically symmetric variations in these quantities.

VII. RESULTS AND DISCUSSION

As indicated in Section VI, shock waves with different initial parameters have been studied. The physical values recorded in some of the cases are depicted in the figures. The different curves, as also the corresponding cases, are referred according to the following scheme of initial parameters:

Curve/Case	1	2	3	4	5	6
$M_{s,i}$	1·25	1·25	1·25	2·0	3·0	5·0
$\mathscr{S}_0$	0·3	0·5	0·707	0·707	0·707	0·707

The following results about the shock front and the changes in physical variables brought about by the passage of the shock front as it propagates outwards in the polytrope follow from the investigations.

(i) *Behaviour of Π*

The variations of Π_0 and Π_2 with $\bar{R}_0$, where $\bar{R}_0 = R_0/\bar{R}$, are shown in Figures 2(*a*) and 2(*b*) respectively. Π_2 is small and brings only a small change in Π_0 at different points on the front. This change decreases with decreasing $\mathscr{S}_0$. This is the pure gas-dynamical limit. In the pure gas-dynamical limit ($\mathscr{S}_0 \to 0$) the ratio of the values of any physical variable across the front is uniform over the front. Π_0, and hence Π, continuously amplifies, the amplification being more pronounced with increasing $M_{\mathrm{s},i}$ and less sensitive to small changes in field strength (FS). However, it does not increase without limit and even for the case (6), Π_0 and Π_2 are only 430·9 and 4·8 at $0\cdot94\,\bar{R}_0$. These values are small compared with those obtained by earlier workers in the absence of a magnetic field, for example, Π_0 and Π_2 are only 54 and $-0\cdot35$ at $\bar{R}_0 = 0\cdot835$ for the case (5) compared with the Π values of 102 and 281 obtained by Bhatnagar and Sachdev (1966) for different models, taking the impoverishment of Π due to radiation into account but excluding any magnetic field. The relatively small growth of Π in the present case is due to the presence of a magnetic field which always inhibits the growth of Π, as can be seen from equations (14).

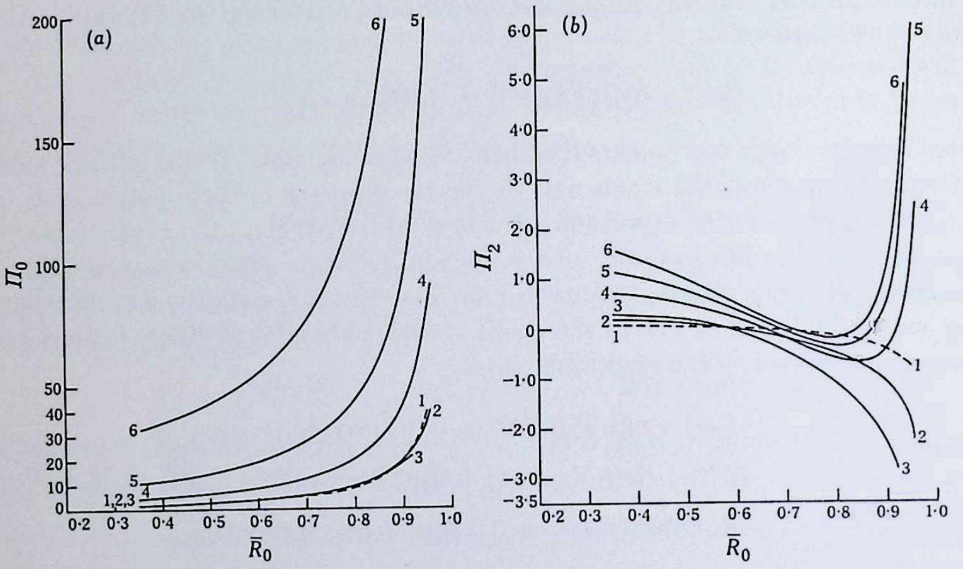

Fig. 2.—Variation of (*a*) Π_0 and (*b*) Π_2 as functions of $\bar{R}_0$ for different initial characteristics.

(ii) *Behaviour of λ*

λ also increases continuously (Fig. 3), but as expected (as $1 < \lambda < (\gamma+1)/(\gamma-1)$) is always less than 3. λ_2 is small compared with λ_0 and becomes vanishingly small as $\mathscr{S}_0$ becomes small, which is the gas-dynamical limit. The results near the surface of the polytrope may be illusory because radiation effects, which are always significant there, have not been included in this paper. The effect of $M_{\mathrm{s},i}$ on λ is more pronounced than that of $\mathscr{S}_0$. Increasing $M_{\mathrm{s},i}$ leads to increasing compression of the matter in the medium, but the gradient is sharper for lower $M_{\mathrm{s},i}$. The change in

FS does not alter λ appreciably. In the early stages, λ is greater for weaker FS but in this case there exist two critical $\bar{R}_0$ values, one at $0 \cdot 575\, \bar{R}_0$ and the other at $0 \cdot 835\, \bar{R}_0$ for $M_{\mathrm{s},i} = 1 \cdot 25$, and λ changes its behaviour after each of these values.

(iii) *Behaviour of* β

The effect of the second term, β_2, is more significant (Fig. 4) in the case of the ratio of the magnetic field. This is due to the nonuniform and anisotropic nature of the poloidal magnetic field. FS, as expected, always increases after the passage of the shock. Taking the contribution of β_2 into account, it is found that β is not very sensitive to the weak changes in $\mathscr{S}_0$. However, β does increase, though not appreciably, with increasing $M_{\mathrm{s},i}$. The compression of the matter in the medium is basically responsible for the increase in the magnetic field and this explains the above behaviour of β. The null point exists at $0 \cdot 765\, \bar{R}_0$ on the equatorial plane, which explains why all the curves behave critically near this point.

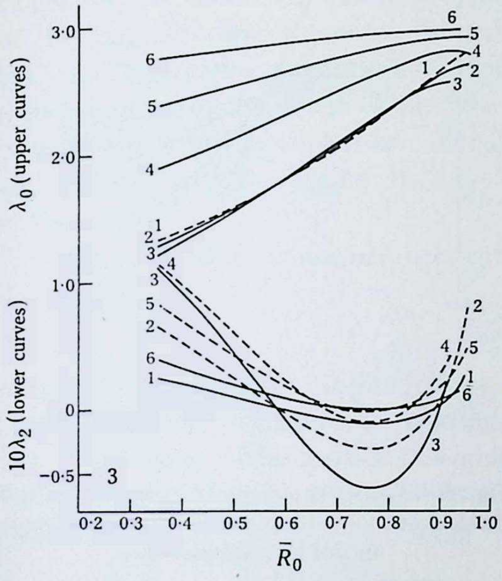

Fig. 3.—Profiles illustrating the density ratio as a function of $\bar{R}_0$ for different initial characteristics.

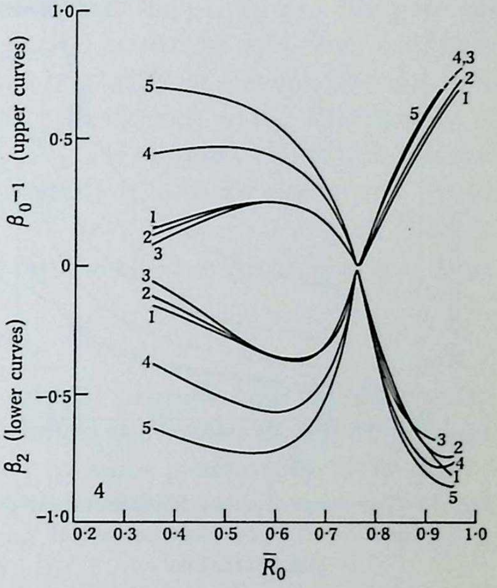

Fig. 4.—Profiles illustrating the field strength ratio as a function of $\bar{R}_0$ for different initial characteristics.

(iv) *Behaviour of* M_{s}

The shock Mach number M_{s} also continuously increases (Fig. 5) and does so more and more rapidly as $M_{\mathrm{s},i}$ increases. This agrees with the results of Masani (1963) and Bhatnagar and Sachdev (1966). However, M_{s} is also not very sensitive to small changes in $\mathscr{S}_0$, but this picture of the shock may be illusory, because the shock moves out in a medium in which the material density is continuously decreasing. In fact, the shock velocity, though always increasing, does so only slightly; for example, the shock velocity changes from $2 \cdot 024$ at $\xi = 1$ to a maximum of only $2 \cdot 29$ in case (1), $2 \cdot 33$ in case (2), and $2 \cdot 4$ in case (4) (in 10^8 units) near the surface. Even in case (6) the shock velocity changes from $8 \cdot 09$ at $\xi = 1$ to only $8 \cdot 13$ near the surface. In fact, it appears that the greater the initial shock velocity (ISV) the less the shock velocity increases towards the surface. This behaviour is in marked contrast to the changes in the shock velocity obtained in the absence of a magnetic field. For example, Ôno, Sakashita, and Yamazaki (1960*a*) have found that in the Eddington model ($M = 1\,M_{\odot}$, $\bar{R} = 0 \cdot 1\,R_{\odot}$) the shock velocity increases from an initial value of $2 \cdot 1 \times 10^8$ at $0 \cdot 125\,x$ to $5 \cdot 1 \times 10^9$ near the surface ($x = 0 \cdot 87$). Thus the magnetic field restrains the growth of the shock velocity.

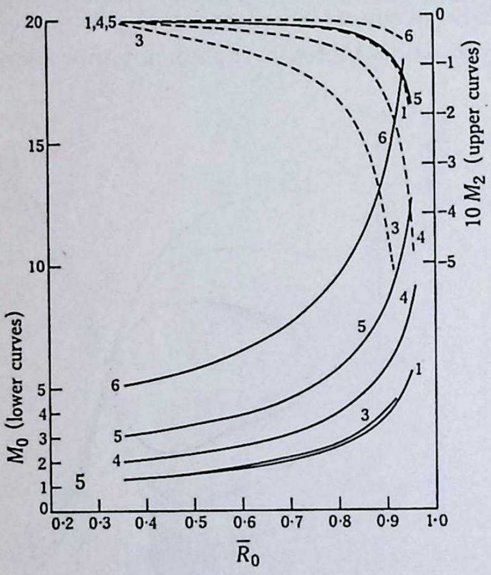

Fig. 5.—Variation of shock Mach numbers as a function of $\bar{R}_0$ for different initial characteristics.

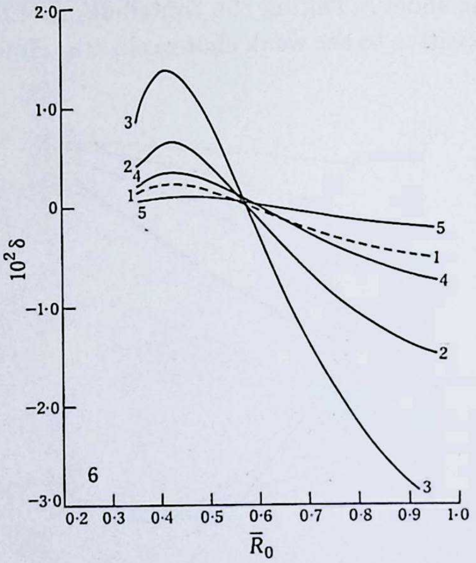

Fig. 6.—Variation of the oblateness of the shock front as a function of $\bar{R}_0$ for different initial characteristics.

(v) *Geometry of the Front*

The coefficients R_{2j} ($j = 1, 2, 3, \ldots$) decrease rapidly so that to a first approximation

$$R = R_0 + R_2\,\mathrm{T}_2(\cos\theta)\,,$$

showing that the front is elliptical. Since the value of $\mathrm{T}_2(\cos\theta)$ is $+1$ along the axis and -1 at the equator, the oblateness δ of the front is given by

$$\delta = 2R_2/R_0\,.$$

The variation of δ with $\bar{R}_0$ has been shown in Figure 6. Both the FS and ISV strongly influence the behaviour of δ. In the early stage of propagation δ increases but soon after it starts to decrease steadily and becomes negative in the outer layers of the polytrope. This behaviour may be attributed to the structure of the magnetic field. The change from positive to negative takes place at the same R_0 for different FS but the same ISV. This critical R_0 differs, though only slightly, for different ISV. Decreasing FS decreases δ, which would vanish in the pure gas-dynamical limit when FS $\rightarrow 0$. For a given FS, however, δ decreases with increasing $M_{s,i}$, showing that fronts moving in a given magnetic field are less distorted for more intense shocks.

In other words, the less intense the shock the greater is the time lag of the front in reaching the equator and in reaching successively the points on the surface of the polytrope with increasing latitudes up to the poles. For example, in case (1) it takes 165·9 sec to move to $0 \cdot 97 \bar{R}_0$ along the axis whereas 158·7 sec only to traverse the same distance in the equatorial plane.

As a result of increasing shock velocity the particle velocity behind the shock also increases as the front propagates outwards. The escape velocity at the surface is given by

$$u_{\text{esc}} = (2GM/R)^{\frac{1}{2}} = 6 \cdot 2 \times 10^7 \text{ cm sec}^{-1}.$$

This velocity is always attained, in the present case, even for $M_{s,i} = 1 \cdot 25$, so that in general the shock will cause an ejection of mass from the polytrope. The presence of the magnetic field increases the particle velocity, as can be seen from equations (14), and hence the magnetic field increases the possibility of ejection of mass from a stellar body in the event of the generation of a shock wave in it. This may be of importance in novae explosions. For large $M_{s,i}$, u_{esc} is attained well within the star and, in fact, with increasing $M_{s,i}$ the escape velocity is attained nearer and nearer to the centre.

The rise in temperature brought about by the shock may be obtained from the relation

$$T/T_0 = \Pi/\lambda,$$

where T is temperature, and it follows that a poloidal magnetic field inhibits the rise in temperature, i.e. the intense heating of the medium that occurs during the passage of a shock wave. The growth of higher nuclear reactions in the stellar body due to a shock is thus slowed and supernovae explosions are inhibited by the presence of the magnetic field.

VIII. ACKNOWLEDGMENT

The author wishes to thank Dr. E. D. Fackerell for suggesting the problem and for valuable discussions during the progress of this work.

IX. REFERENCES

BHATNAGAR, P. L., and SACHDEV, P. L. (1966).—*Nuovo Cim.* **44**, 15.

BIRD, G. A. (1964).—*Astrophys. J.* **139**, 675.

COURANT, R., and FRIEDRICHS, K. O. (1948).—"Supersonic Flow and Shock Waves." (Interscience: New York.)

JEFFREY, A., and TANIUTI, T. (1964).—"Non-linear Wave Propagation." (Academic Press: New York.)

KOPAL, Z. (1954).—*Astrophys. J.* **120**, 159.

MACKIE, A. G., and WEIR, D. G. (1960).—*Proc. Camb. phil. Soc.* **56**, 64.

MASANI, A. (1963).—*Nuovo Cim.* **29**, 224.

ÔNO, Y., and SAKASHITA, S. (1961).—*Publs astr. Soc. Japan* **13**, 146.

ÔNO, Y., SAKASHITA, S., and YAMAZAKI, H. (1960*a*).—*Prog. theor. Phys., Kyoto* **23**, 294.

ÔNO, Y., SAKASHITA, S., and YAMAZAKI, H. (1960*b*).—*Prog. theor. Phys., Kyoto* **24**, 155.

ROGERS, M. H. (1956).—*Proc. R. Soc.* A. **235**, 120.

ROXBURGH, I. W. (1966).—*Mon. Not. R. astr. Soc.* **132**, 347.

SAKASHITA, S., and TANAKA, Y. (1962).—*Prog. theor. Phys., Kyoto* **27**, 127.

WHITHAM, G. B. (1958).—*J. Fluid Mech.* **4**, 337.

THE NATURE OF SPREAD-F IRREGULARITIES IN ANTARCTICA

By G. G. Bowman*

[*Manuscript received June* 6, 1968]

Summary

Some characteristics of spread-F ionograms from the Antarctic region are discussed. Very disturbed periods, such as when magnetic storms are in progress, have been neglected in this analysis. Two important characteristics are the frequent occurrence of resolved as well as diffuse traces, and the appearance from time to time of an enhanced trace which seems to be produced by signals that arrive from directions close to the magnetic field direction. Two independent sets of spread-F traces are reported. Several possible models are examined and some ray tracing performed. The analysis favours a model that incorporates kinking of the contours of equal ionization density to produce "wavelengths" in the ionospheric structure of some tens of kilometres. Because of the similarities at mid and high latitude regions, it is suggested that similar mechanisms are operating at both regions to produce spread-F.

I. Introduction

The precise nature of the irregularities responsible for spread-F signals has concerned workers in the field for many years. For mid and high latitude regions the most favoured theory in the past has been one that regarded the irregularities as relatively small-scale columns of enhanced ionization lying along the direction of the magnetic field. Calculated dimensions for these irregularities are of the order of 1 km (Yeh and Swenson 1964). Signals scattered from such irregularities should produce a diffuse record. Since a significant percentage of mid and high latitude ionograms show spread-F as diffuse echoes, this appeared to be a satisfactory model. In a recent summary article on spread-F, Herman (1966) discusses this and other theories.

Results by Klemperer (1963) appear significant because they show that high latitude spread-F signals have a high specular component, which does not support the scattering theory. Some of the more recent work has suggested various waveguide mechanisms. For example, perhaps signals that propagate in a waveguide mode between field-aligned columns of enhanced ionization are responsible for spread-F (Booker 1961; Pitteway 1962); or perhaps these extra traces on ionograms result from waveguide propagation between field-aligned sheets of ionization, as has been suggested for some topside reflections (Muldrew 1963).

In the present paper the nature of the spread-F irregularities over a high latitude region (Antarctica) is considered. This follows an examination of many ionograms from this region which show the phenomenon. Several aspects of the phenomenon will be illustrated and discussed in Section II. Any theory that attempts to describe the nature of these irregularities must be consistent with the experimental observations treated in Section II.

---

* On leave to Space Systems Division, AVCO Corporation, Lowell, Massachusetts, U.S.A., from present address: Department of Physics, University of Queensland, St. Lucia, Brisbane, Qld. 4067.

Aust. J. Phys., 1968, **21**, 695–714

It must be stressed that the appearance of ionograms in Antarctica, when additional echoes (spread-F echoes) are present, can show a variety of forms. The reason for this seems to be the dynamic character of the ionosphere in this region. Topside soundings by artificial Earth satellites (Warren 1963; Sharp, Crother, and Gilbreth 1964; Titheridge 1966) show that the electron density distribution in high latitude regions can change radically as the satellite moves from one place to another. Because of this, and the fact that the direction of arrival of spread-F signals can be off-vertical by as much as 60° (Bowman 1968*a*), it is not surprising that relatively large-scale disturbances, which affect the background ionization distribution, can produce additional complications in the appearance of the traces from the spread-F irregularities.

During times of magnetic storms, apart from blackout conditions, drastic changes can occur in the electron density profile of the F_2 layer. Additional low-lying ionization in the D and E regions is common at these times leading to further retardation effects, especially on the off-vertical traces that traverse these regions obliquely. The appearance of spread-F traces at these times is considerably different from that at quiet times.

When all observable aspects of the phenomenon are considered, spread-F traces can be seen in many different forms, more than can be illustrated or discussed adequately here. Contrast, for example, Figures 1(*a*), 1(*d*), and 1(*f*) for some idea of the differences in appearance that can occur. Therefore, the phenomenon of high latitude spread-F cannot be represented by a single ionogram, or even by a restricted group of ionograms.

Although disturbances of some kind or other producing changes in the electron density distribution of the layer seem to be nearly always present, periods when pronounced changes occur, such as when magnetic storms are in progress, have been avoided in the present analysis. Only those aspects of the phenomenon that occur regularly and can be identified in an ionosphere that appears to have a relatively stable background will be considered. Multilayer conditions which occur in the daytime have also been neglected. Spread-F conditions during the occurrence of large-scale disturbances require additional study. In any case, the presence of these large-scale disturbances only complicates attempts to decide upon the nature of the spread-F irregularities.

In Section III a number of possible mechanisms are discussed and certain calculations made. When ray tracing through model ionospheres is performed, the effect of the magnetic field will be neglected. In view of the considerable differences in the nature of the various models that are proposed, this approximation seems justified. Its use cannot be expected to influence the choice of a particular model. It will be shown that some of these models are inconsistent with experimental observations. Discussion on, and conclusions from, this analysis are treated in Sections IV and V respectively.

Fig. 1.—A selection of ionograms showing spread-F characteristics in Antarctica. Most of the records are from Ellsworth. The South Pole and Wilkes records are labelled. All records were taken in 1958 and local times are used.

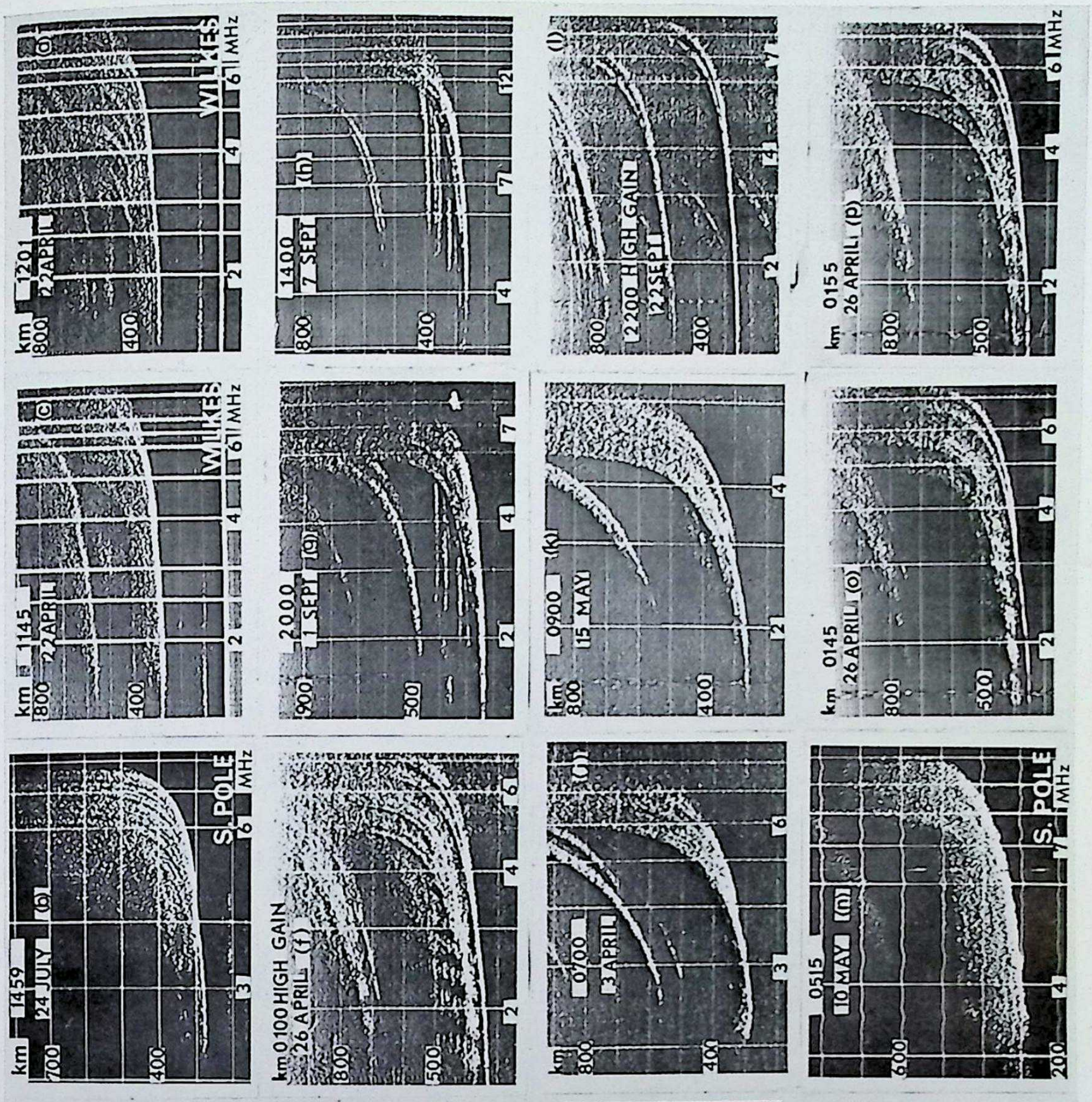
1455 24 JULY (a) S. POLE
1459 24 JULY (b) S. POLE
1145 22 APRIL (c) WILKES
1201 22 APRIL (d) WILKES
0030 26 APRIL (e)
0100 HIGH GAIN 26 APRIL (f)
2000 1 SEPT (g)
1400 7 SEPT (h)
2030 22 SEPT (i)
0700 3 APRIL (j)
0900 15 MAY (k)
2200 HIGH GAIN 22 SEPT (l)
0500 10 MAY (m) S. POLE
0515 10 MAY (n) S. POLE
0145 26 APRIL (o)
0155 26 APRIL (p)
km
MHz

In this paper the term "satellite" refers to the additional traces on ionograms which are satellites of the main trace. The term should not be taken as referring to information from orbiting Earth satellites. The subdivisions "range spreading" and "frequency spreading" of the spread-*F* phenomenon are defined by Bowman (1960).

Some 25 station-months of ionosonde records taken during the equinoctial and winter months of sunspot-maximum years (1957–1958) have been examined for this analysis. In addition, 20 station-months for 1961 have also been inspected for the same periods of the year. The stations used were located in Antarctica and were: Ellsworth (dip 66°), Byrd (dip 75°), South Pole (dip 75°), Little America (dip 80°), and Wilkes (dip 82°). Although the phenomena discussed in Section II are common to all stations, ionograms illustrating these effects are shown from only Ellsworth, South Pole, and Wilkes.

II. SOME CHARACTERISTICS OF SPREAD-*F* IONOGRAMS AT HIGH LATITUDES

In this section certain easily recognized characteristics of spread-*F* ionograms that are recorded in the Antarctic region will be considered.

(*a*) *Off-vertical Angles of Arrival*

Ionograms taken at the Ellsworth station show a system of nulls, equally spaced in frequency on certain sections of the main and satellite traces. The Ellsworth station is located on the Filchner iceshelf of the Antarctic continent at a geographic position several hundreds of kilometres outside the night-time auroral zone. The nulls result from the interference between the ray travelling upwards from the antenna and the ray that travels first to the bottom of the iceshelf before being reflected upwards. Because of the systematic shift with range of the frequency of the nulls for diffuse sporadic-*E* reflections, it has been possible to calibrate the system so that the off-vertical angles of arrival of signals reflected from any level can be determined with reasonable accuracy. Bowman (1968*a*) has shown that when spread-*F* traces are present, whether they be diffuse or resolved, the measured angles of arrival suggest that, at least for range spreading at the low frequency end of the ionograms, the satellite signals are reflected from approximately the same level as the signals at the same frequency that travel vertically to produce the main trace. The extra range of the traces produced by these signals is a consequence of the ray paths to and from the spread-*F* irregularities being off-vertical. Figures 1(*e*) and 1(*f*) illustrate the shift in frequency of the nulls for spread-*F* satellite traces. Even when a certain amount of the excess range appears to result from retardation effects, significant off-vertical angles are measured. This suggests that the reflection levels for all frequencies of the satellite traces are close to the reflection levels of the corresponding frequencies of the main trace. Klemperer (1963) has obtained results that indicate a semi-angle of 13° for the cone embracing the returning spread-*F* signals. It is not known if these measurements apply to frequency spreading or range spreading. The iceshelf measurements show that when range spreading is present, irrespective of whether or not there is a spread in critical frequency, large off-vertical angles (up to 60°) are common. These results would seem to be important when considering the nature of the spread-*F* irregularities.

(*b*) *Diffuse and Resolved Traces*

One of the most striking aspects of high latitude spread-F traces is the fact that the spreading from the main trace in range and/or frequency on the ionogram often appears diffuse. However, what is probably of equal importance is that, on just as many occasions, structure is revealed in the form of resolved traces. Inspection of all the ionograms shown in Figure 1 shows the nature of the resolved traces that are often seen. On most of the occasions when structure is present only part of the ionogram is resolved while the rest of the ionogram is diffuse. However, ionograms can be found when the satellite traces are all resolved. The change from complete diffuseness to partial resolution (or vice versa) can occur over a short interval of time. Compare, for example, Figures 1(*a*) and 1(*b*) showing ionograms (from South Pole) taken 4 min apart. At 16 min later the ionogram appears diffuse again as in Figure 1(*a*). Compare also Figures 1(*c*) and 1(*d*) showing ionograms (from Wilkes) taken 16 min apart. Again in this case, 14 min later the ionogram is completely diffuse.

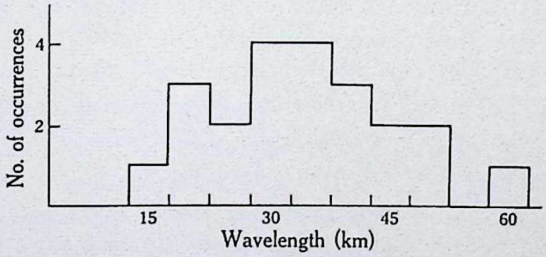

Fig. 2.—Distribution of irregularity spacings deduced from a small sample of Antarctic ionograms.

In both cases the first ionogram is almost completely diffuse and yet in several minutes changes to an ionogram that has a certain amount of structure. It does not seem likely that the nature of the irregularities changes over these small intervals of time to give different records. Thus the ionospheric structure that produces the resolved traces is, in all probability, also responsible for the diffuse traces. As relatively small height changes are always taking place for the F_2 layer, it is possible that changes in the orientation of the background layer, relative to the horizontal plane, are effective in allowing structure to be seen more clearly at some times than at others. It seems important that both aspects (diffuseness and resolution) be considered when investigating models to explain Antarctic spread-F.

Using certain simplifying assumptions, estimates can be made of the horizontal spacings (wavelengths) between individual components of the irregularities that produce resolved range spreading. Figure 12 of Bowman (1968*a*) illustrates the method. Figure 2 in the present paper shows the distribution of wavelengths determined from a small sample of ionograms from Antarctica which showed satellite traces. Wavelengths of some tens of kilometres are found.

(*c*) *Two Sets of Satellite Traces*

Examination of the structure in Antarctic spread-F ionograms reveals that two independent sets of satellites can be recognized fairly frequently. The predominant set (set 1) consists of satellite traces which appear as replicas of the main trace, except that their critical frequencies are usually lower. A particular trace shows a smooth change in curvature, free of kinks of any kind, over the range of frequencies it records. Figures 1(*b*), 1(*e*), and 1(*f*) show examples of set 1. The other set (set 2) consists of traces that have shapes showing less retardation effects than the main trace. The critical frequencies of these traces are obviously greater than that of the main trace, although the high frequency end of the traces is missing on most occasions. They can be distinguished from set 1 because they appear to cut across the traces of set 1 at a particular frequency range. They are seen up to ranges in excess of the main trace of several hundreds of kilometres and seem to favour occurrence at the higher ranges. Figure 3 illustrates the two sets. Set 1 is often present when set 2 is not. Figures 1(*g*) and 1(*h*) show examples where set 2 can be clearly distinguished from set 1. A careful inspection of the other ionograms of Figure 1 will show that even though it is sometimes difficult to distinguish between the two sets, they are nevertheless present quite often (see e.g. Fig. 1(*k*)). Figure 1(*m*) indicates that even when the ionograms show a certain degree of diffuseness, the two sets can sometimes be distinguished. Set 2 seems to be resolved more often than set 1. Another distinguishing feature between the sets is that set 1 can be seen on the higher traces (e.g. second- and third-hop traces) whereas this does not occur for set 2.

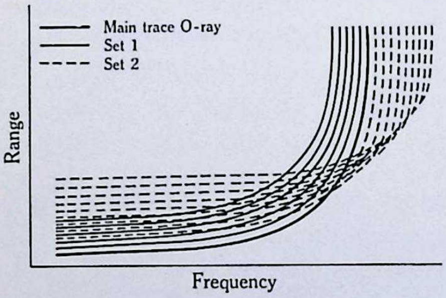

Fig. 3.—Illustration of two sets of spread-F traces for the O-ray mode.

When the traces are resolved for set 1 there is a smooth progression between an increase in range at the low frequency end and a decrease in critical frequency for corresponding traces at the high frequency end. Direction-of-arrival information on spread-F at Ellsworth (Bowman 1968*a*) has shown that the increase in range at low frequencies really represents an increase in off-vertical angle of the spread-F signals. The fact that the shapes of the satellite traces of this set closely resemble the shape of the main trace suggests that, whatever forms the spread-F irregularities take, they should be relatively simple distortions of the background ionization. In some cases, the discrete traces can be followed from high frequencies near the critical frequency to the frequency of the lower limit of the ionosonde indicating that, on these occasions, the individual irregularities can be identified from the lowest levels right up to the maximum of the F_2 layer.

Any model that satisfies these observations must allow for a variation in the electron density distribution along various off-vertical paths, which is somewhat similar to the variation in the vertical direction; otherwise, trace shapes similar to the shape of the main trace would not be produced. It seems likely that the spread in frequency is produced by a horizontal gradient in f_0F_2. The f_0F_2 value of the satellite traces would then change as signals with different off-vertical angles reach the maximum of the layer at different horizontal displacements from the zenith position. It has been shown by Sato and Rourke (1964) that a positive gradient of f_0F_2 exists in a direction towards the magnetic pole in Antarctica at night.

(*d*) *Enhanced Satellite Traces*

When the satellite traces are resolved, the high frequency end of the traces close to the critical frequency is often missing. Although this is pronounced for set 2, it is also true to a lesser degree for set 1. When the main trace can be distinguished from the satellite traces of the spread-F phenomenon, it is often weak or missing for frequencies close to the critical frequency.

However, there is sometimes one particular trace among the satellite traces that appears to be produced by signals that are relatively strong at all frequencies right up to the critical frequency. At times this trace can be identified from an otherwise diffuse record because of its greater signal strength. At Ellsworth the measured off-vertical angle of arrival of this trace, from examples where the null system is well defined, is approximately 24°. This is consistent with a direction of arrival along or close to the magnetic field direction for this station, which has a magnetic inclination (dip) of 66°. If the range in excess of the main-trace range at the low frequency end is regarded as a true increase in range produced by the signal direction being off-vertical, then the observed enhanced traces at South Pole and Wilkes also suggest propagation close to the magnetic field direction. An enhanced trace from South Pole is illustrated by Figure 1(m). Enhanced traces for Ellsworth are shown in Figures 1(e), 1(f), and 1(p). It should be noted how well the critical frequencies of these traces are defined compared with the corresponding main-trace critical frequencies.

When ionograms are taken at 15 min intervals, it is unusual for two consecutive ionograms to show the enhanced trace. Figure 1(m) shows an ionogram with an enhanced trace prominent in an otherwise diffuse record. Five minutes previously (at 0455 hr) the record is almost completely diffuse as it is 15 min later (illustrated by Fig. 1(n)). Figures 1(o) and 1(p) show another pair of ionograms taken 10 min apart. The first shows no enhanced trace while it is clearly observable in the second record.

(*e*) *Low Frequency Retardation of Satellite Traces*

It might be thought when the satellite traces show a spread in frequency near the critical frequency of the main trace but not a spread in range at the lower frequencies (frequency spreading) that the irregularities are confined to the region of the F_2 layer just below the maximum of ionization density. However, on some occasions when frequency spreading exists, the low-lying ionization in the D and/or E regions is large enough to produce retardation at the low frequency end of the X-ray trace which is greater than usual. Similar retardation effects are seen, although less frequently, for the O-ray trace. If the satellite traces that produce frequency spreading are off-vertical, they will suffer greater retardation effects than the main trace since the path through the retarding region is longer. This seems to be the case in the examples shown here (Figs. 1(i) and 1(j)) since the increased retardation of the satellite traces at the low frequency end is sufficient to distinguish them from the main trace. Satellite traces are not observed at medium frequencies on the ionograms illustrated by Figures 1(i) and 1(j). Figure 1(i) shows a single satellite trace giving resolved frequency spreading near the critical frequency. The single satellite trace can also be seen near the X-ray "tail". Figure 1(j) shows unresolved frequency spreading near the critical frequency and resolved range spreading near the O-ray "tail". This aspect of frequency spreading suggests that the irregularities that produce these effects extend through the layer from the lowest levels up to at least the level of maximum electron density. The irregularities are not apparently confined to any particular region of the layer. In these cases, the real increase in range of the off-vertical satellite traces is probably not great enough for them to be observed at medium frequencies where retardation effects are at a minimum.

(*f*) *Spreading on Multiple-hop Traces*

During equinoctial months, there are occasions when the first-hop main trace is clear of satellite traces. However, when this occurs it does not necessarily mean that the multiple-hop traces (e.g. second- or third-hop trace) are also free of satellite traces. Figure 1(l) is an example of this aspect of the spread-F phenomenon. The range spreading present on the third trace consists of off-vertical signals. The displacement of nulls in Figure 1(l) gives 30°, 40°, and 43° respectively as the off-vertical angles of arrival of the three well-defined traces (Bowman 1968*a*). Also, this ionogram shows the tenth-, eleventh-, and twelfth-hop traces with some spreading associated with these traces. The positions of nulls on these high multiple traces indicate a vertical direction of arrival for their main traces. These results suggest that irregularities are present, but that they have certain features that prevent detection for one-hop reflections but allow it for multiple hops. A possible model is proposed in Section III(e).

(*g*) *Similarity to Mid Latitude Spread-*F *Traces*

The observations reported in the previous subsections deal with conditions when the ionosphere, although at times markedly disturbed by the spread-F irregularities, was nevertheless relatively free from the larger-scale disturbances. The results reported in this section are similar in nearly all respects to those reported by the author for a mid latitude station (Bowman 1960, 1968*b*).

Night-time D-region effects are negligible at mid latitudes so the observation of retardation effects at low frequencies for satellite traces (Subsection (e) above) is not made at mid latitudes. Also, set 2 of the satellite traces is not observed at mid latitudes. The observation of this set may be related to the slope of the magnetic field at a particular station. Apart from the ionograms illustrated in Figure 1 and the spread-F characteristics at high latitudes which are discussed in this section, the general impression gained as the Antarctic records were examined was that the phenomenon was the same at both latitudes. Of course, spread-F conditions, when the high latitude ionosphere is otherwise greatly disturbed by large-scale disturbances, have been disregarded for this assessment.

The enhanced trace (Subsection (*d*) above) which is so pronounced at the high latitude regions (Ellsworth, dip 66°; South Pole, dip 74°) has been reported by Bowman (1957, 1960) from Brisbane (dip 57°) and Townsville (dip 45°) for both *E*- and *F*-region reflections.

III. Spread-*F* Theories for High Latitude Regions

In this section a number of mechanisms or models that could possibly be responsible for the production of spread-*F* traces will be considered.

(*a*) *Scattering from Columns of Enhanced Ionization or Other Discontinuities*

As discussed in the Introduction, this seems to be ruled out as a possibility for high latitude regions following the measurement by Klemperer (1963) of a high specular component in spread-*F* echoes. In any case, the frequent appearance of resolved satellite traces on Antarctic spread-*F* ionograms is inconsistent with a scattering mechanism. Inspection of the various ionograms shown in Figure 1 suggests that relatively large ionospheric structures which give resolved traces under certain circumstances must be considered when spread-*F* models are being proposed.

(*b*) *"Blobs" or "Holes" in the Background Electron Density Distribution*

When spread-*F* is present, whether or not range spreading forms part of the phenomenon, the satellite traces will show a spread in critical frequency. It might be thought that measurement of the spread in critical frequency would give a measure of the increase or decrease over the background ionization of the electron density at the centre of the irregularities. In this case the irregularities would be regarded as having the form of "blobs" or "holes". The range of critical frequency Δf represents a change in electron density ΔN, and so the proportional change in electron density $\Delta N/N$ can be calculated. Here N represents the background electron density.

In frequency spreading, the spread-*F* signals seem to originate from near-vertical propagation because of the limited range spreading at these times. The background electron density distribution shown in Figure 4 has been derived from the main trace of the ionogram shown in Figure 1(*k*). An electron density profile, determined from this record by an $N(h)$ analysis (Ventrice and Schmerling 1958) was subsequently adjusted empirically so that a calculation of the shape of the main trace from the profile produced a trace shape reasonably close to the observed main trace. Only the top portion of the electron density profile is shown in Figure 4. This figure also shows three localized irregularities in the electron density, (*a*) a hole, and (*b*) and (*c*) blobs. If the effect of the magnetic field is neglected, the group paths to various reflection levels can be calculated for vertical propagation along lines that pass through the centres of these irregularities by evaluating the integral

$$\int 1/\mu \, \mathrm{d}s \, .$$

The refractive index is μ and $\mathrm{d}s$ is the increment in the vertical path. These calculations can be used to derive satellite traces. The calculated satellite traces for the irregularities (*a*), (*b*), and (*c*) of Figure 4 are shown in Figures 5(*a*), 5(*b*), and 5(*c*) respectively.

The shapes of the satellite traces are noticeably different from that of the main trace as would be expected because the electron density profiles in a vertical direction through the irregularities are different from that of the undisturbed ionosphere. Observations on frequency spreading show that the satellite traces merge gradually with the main trace, but for these models the satellite traces come out of the main trace somewhat abruptly at a particular frequency.

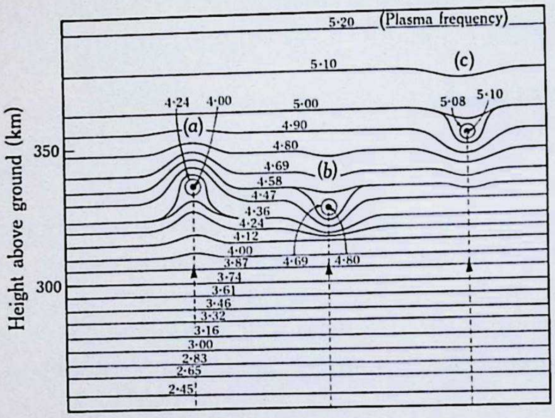
5·20
(Plasma frequency)
5·10
(c)
4·24
4·00
5·00
5·08
5·10
(a)
4·90
4·80
4·69
(b)
4·58
4·47
4·36
4·24
4·12
4·00
3·87
4·69
4·80
3·74
3·61
3·46
3·32
3·16
3·00
2·83
2·65
2·45
350
300
Height above ground (km)

Fig. 4.—Model of spread-*F* irregularities incorporating localized enhancements and reductions in electron density concentration. All frequencies are in megahertz.

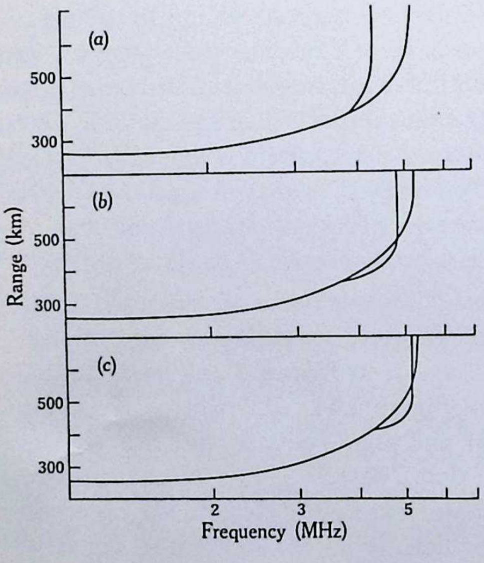

Fig. 5.—Calculated satellite-trace shapes for the irregularities (*a*), (*b*), and (*c*) illustrated in Figure 4.

The range-spreading traces of set 1, which are resolved or partially resolved, also follow the main trace in shape. If off-vertical reflections from blobs or holes occur to produce range spreading then satellite-trace shapes similar to that of the main trace will not be expected in view of the frequency-spreading results given in Figure 5.

The evidence presented in this subsection suggests that the irregularities do not have the form of blobs or holes. Figure 2 of Booker (1961) shows the distorted nature of satellite traces resulting from a hole in the ionosphere produced by the transit of a missile.

(c) *Specular Reflection from Columns of Enhanced Ionization*

Aspect-sensitive reflections at frequencies greater than the critical frequency of the F_2 layer are regularly observable (Peterson *et al.* 1955; Swenson 1964).

There seems little doubt that the irregularities responsible for these reflections are field-aligned columns of enhanced ionization. The observed ranges to these irregularities for azimuths slightly displaced from the direction of the magnetic pole strongly suggest this type of irregularity. It is possible that, for the frequencies which are normally reflected from the F_2 layer, aspect-sensitive reflections occur after suitable refraction has turned the ray so that it is perpendicular to the magnetic field direction.

In a layer where the electron density varies linearly with height, in a vertical direction, calculations can be made for the ray paths through the layer for any particular angle of incidence. In these calculations the effect of the Earth's magnetic field has been neglected. For such a layer we can write $N = \alpha^2 z$, where z is the height measured from the base of the layer, N is the electron density content, and α is a constant. For the particular model used here α^2 can be calculated. Also, since the square of the plasma frequency at any height is proportional to the electron density, we can write $f_{\mathrm{p}}^2 = K^2 N$, where K is a known constant and f_{p} is the plasma frequency. For a particular angle of incidence of upgoing radiation, θ_0, the horizontal distance D travelled by the ray before it reaches the ground again is given by

$$D = 4(f^2/\alpha^2 K^2)\sin\theta_0\cos\theta_0 + 2h_0\tan\theta_0\,,$$

where f is the operating frequency and h_0 is the height of the base of the layer. The horizontal displacement of the position of the maximum height reached by the ray is therefore given by $\frac{1}{2}D$. An additional calculation of the maximum height in the layer, z_{r}, reached by this ray will give the precise position (point E in Fig. 6) in the layer for the maximum vertical excursion of the ray

$$z_{\mathrm{r}} = (f^2\cos^2\theta_0)/\alpha^2 K^2\,.$$

The equations used in the foregoing discussion in this subsection are given by Kelso (1964). The path in the layer (HDEJ in Fig. 6) is a parabola and is given by

$$x = x_{\max}(1 - z^2/z_{\max}^2)\,,$$

where x is the horizontal distance measured from point L in Figure 6 and z is the vertical displacement of the ray from the base of the layer HLJ. Using this relationship, enough points were determined to allow the ray path for any particular angle of incidence and operating frequency to be determined with reasonable accuracy. Figure 7 has been drawn to indicate some of the ray paths calculated in this subsection, for an angle of incidence in this case of 20°. Point D (Figs. 6 and 7) was determined by finding the position where the tangent to the curve was perpendicular to the direction of the magnetic field at Ellsworth (24° from a vertical direction). The group path for the ray that travels a path AHD is given by the straight line AB (Fig. 6; see also Fig. 7) by Breit and Tuve's theorem (Budden 1961). Two cases are considered.

If the ray originates at point A (Fig. 6) and travels south in the magnetic meridian plane (southern hemisphere) to be reflected at perpendicular incidence with the field-aligned irregularity, the group path is given by AB (that is, AC—BC). If the ray starts at G (Fig. 6) and travels north in the magnetic meridian plane (southern hemisphere) for a similar reflection situation, the group path is given by AC+BC since Figure 6 is symmetrical about CL. In this way calculations were made for a number of angles of incidence and of frequencies. It has been assumed that the proposed irregularities are capable of reflecting rays that are incident perpendicular to their orientation from any location in the layer. The maximum density of the model layer used restricted the frequencies that could be reflected in this manner. The model was calculated from the ionogram taken at Ellsworth at 0315 hr (local time), April 26, 1958. Figure 1(p) shows an ionogram taken 1 hr 20 min earlier than the one used for the model. It is similar in appearance. An $N(h)$ analysis of the main trace of the ionogram taken at 0315 hr produced an electron density distribution given by the points in Figure 8. It will be seen that there is a linear variation of density from a base height of 305 km to a maximum for the layer of 410 km. The termination of the layer at 410 km was determined from the value of f_0F_2 (7 MHz).

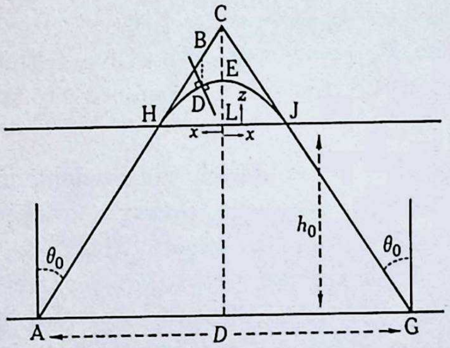

Fig. 6.—Illustration of a ray path through an ionosphere where the electron density varies linearly with height.

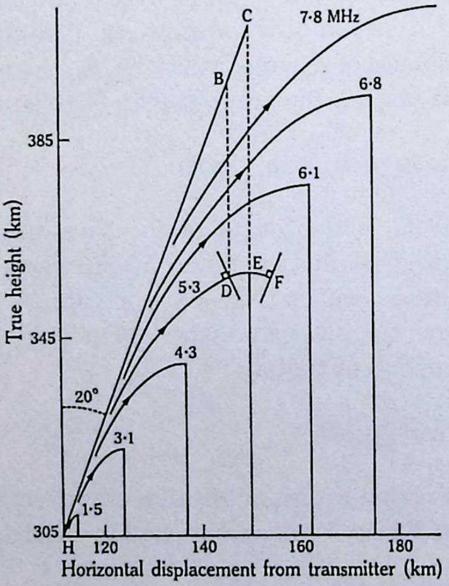

Fig. 7.—Ray paths for various frequencies through a "linear" ionosphere for an angle of incidence of 20°.

The group paths for signals arriving from the same directions in the magnetic meridian plane (10°, 25°, 35°, 40°, and 45° off-vertical) are shown by Figures 9(*a*) and 9(*b*) for the two cases described in the previous paragraph. Group-path positions for a constant angle of incidence have been joined to give a trace over the range of frequencies which will be reflected for each angle. The plots have been made in this way for convenience in presentation. It does not imply that traces of this kind can be expected. If the ionosphere has field-aligned irregularities at evenly distributed positions, capable of reflecting all frequencies that are refracted to be perpendicular to the orientation of the irregularities, the plots in Figure 9 will give some indication

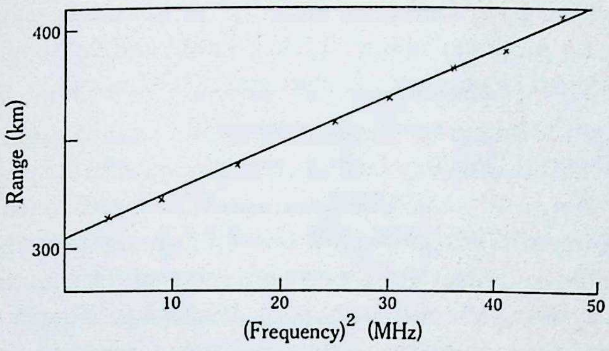

Fig. 8.—Electron density (proportional to frequency squared) profile calculated from the main trace of an Ellsworth ionogram at 0315 hr local time on April 26, 1958.

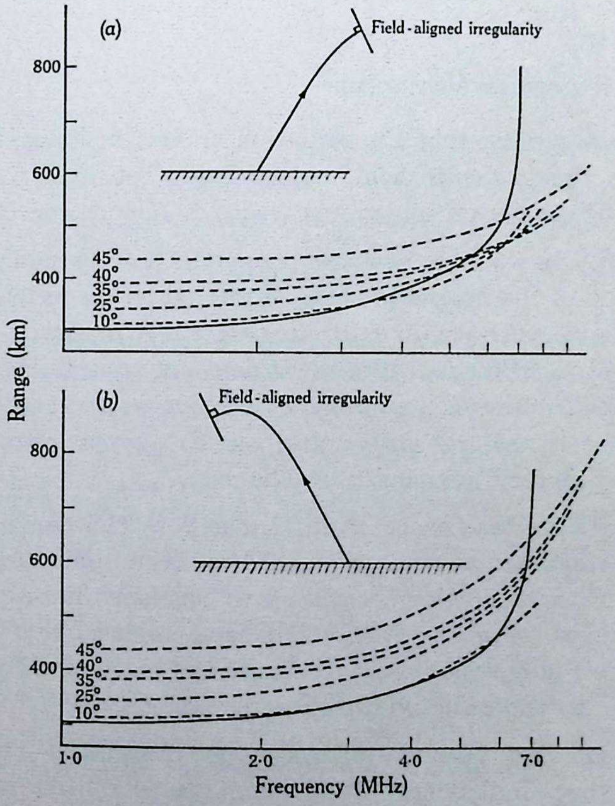

Fig. 9.—Calculated group ranges for

(*a*) energy refracted in the model ionosphere and reflected at perpendicular incidence to field-aligned irregularities, and

(*b*) energy initially reflected from the layer at oblique incidence and subsequently reflected at perpendicular incidence to field-aligned irregularities.

of the envelope of the spread-F signals. It is only this envelope that should be compared with the observed characteristics of the phenomenon, particularly with those features observed in the ionogram shown by Figure 1(p). The results shown by Figure 9 were made assuming the same electron density distribution for horizontal displacements from the transmitter. The geometry is such that perpendicular incidence is possible for propagation outside the magnetic meridian plane. In this case each trace shown in Figure 9 can be imagined as widened in range to allow for these extra rays.

The predominant spreading in the ionogram used for the model is that described as set 1 in Section II. Set 2 is present but can only be detected by a careful inspection of the negative of this ionogram. Figure 1(f) is a high-gain record taken 2 hr 15 min earlier. It shows set 2 clearly. The results given in Figure 9, for propagation that is returned to the transmitter after being reflected at perpendicular incidence to the field-aligned irregularities, do not appear to represent the set 1 traces in Figure 1(p). For both Figures 9(a) and 9(b) the envelope of the satellite signals crosses the main trace giving spread-F signals at frequencies higher than the critical frequency of the main trace. It is conceivable that set 2 of the spread-F traces as illustrated in Figure 1(f) is related to the mode of propagation being investigated in this subsection, since the locations on the ionogram of the satellite signals are similar for both cases. This is discussed in Section IV.

(d) *Waveguide Mechanisms*

A number of authors have suggested that the radiation travels in ionospheric waveguides, oriented parallel to the magnetic field, before being returned to the transmitter site to form spread-F signals on ionograms (see e.g. Klemperer 1963).

For this type of mechanism, one would expect the energy to be returned from directions centred on the direction of the magnetic field. Resolved traces extending over about the same frequency range as the main trace are sometimes observed with off-vertical angles between 50° and 60° (Bowman 1968a). It does not seem likely that in Antarctica, where the magnetic field direction approaches a direction perpendicular to the surface of the Earth, that these large off-vertical angles for the returning energy are consistent with the proposed waveguide mechanism.

When resolution of the satellite traces occurs in Antarctica, the horizontal distance in which the structure appears to repeat itself has been estimated at distances around 30 km (Fig. 2). This separation is too large to consider the propagation as being of the waveguide type. Further, it should be remembered that even when the traces appear diffuse this may result simply because the traces from these structures are a finite width due to the pulse width of transmissions.

It has been shown in Section II(g) that the phenomenon of spread-F at mid latitudes and high latitudes is very similar, suggesting similar mechanisms in the production. At mid latitudes (Bowman 1968b) the azimuths of arrival of spread-F signals are, on practically all occasions, well away (some tens of degrees) from the magnetic azimuth direction. This experimental observation is inconsistent with the concept of spread-F signals returning after propagation in field-aligned waveguides.

(*e*) *Kinking of Contours of Equal Electron Density in the* F_2 *Region*

Since the phenomenon of spread-*F* seems to be the same at mid and high latitudes, a model similar to that used to explain mid latitude spread-*F* will be investigated here for observations at high latitudes. At times, records from topside sounders suggest reflections from structures that are somewhat similar to those given by this model (Muldrew 1963). The model will be based on some of the features of a particular ionogram showing spread-*F*. Figure 1(*k*) shows the ionogram that calculations from the model seek to reproduce with some degree of accuracy. The electron density distribution for a vertical direction from the station was the same as that calculated in Subsection (*b*) above. An ionogram taken 15 min before that shown in Figure 1(*k*) showed an enhanced trace with an off-vertical angle (determined from null displacements) consistent with propagation close to the magnetic field direction. An $N(h)$ analysis of this enhanced trace therefore gave an electron density distribution for the proposed model in a direction 24° off-vertical. From these two distributions a model was built up with a horizontal gradient of f_0F_2 which can be seen from Figure 10 to be continuous from one side of the transmitter to the other. A certain degree of resolution occurs on the ionogram shown in Figure 1(*k*) and the ionograms either side of it in time. From this an estimate of 35 km has been made for the horizontal distance in which the irregularity pattern repeats itself. Examination of Figure 10 will reveal the pattern of kinking that has been devised with the aid of the information derived from the ionograms. It is assumed that the cross section of the irregularities shown by Figure 10 is the same along a front several hundreds of kilometres in extent. The presence of the enhanced trace during the period suggests that the fronts extend in an east–west direction. However, this need not necessarily be precisely perpendicular to the plane containing the magnetic meridian. As in the model used for mid latitudes, the positions of kinks in the electron density contours have been made to change monotonically with height so that the irregularities have fronts sloping in directions close to the magnetic field direction.

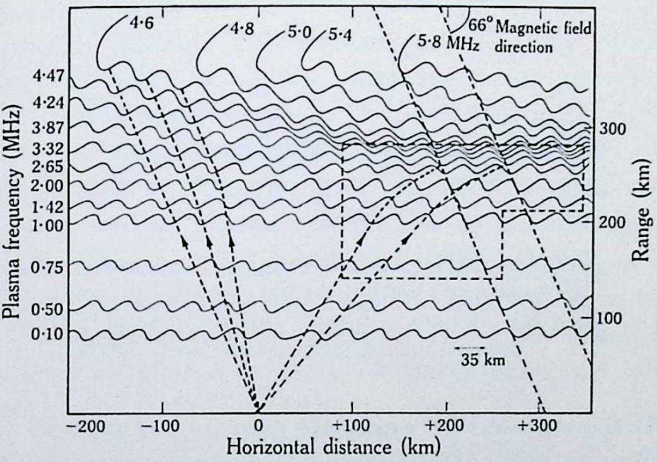

Fig. 10.—Model ionosphere involving kinking of ionization contours deduced by using information from Figure 1(*k*) (Ellsworth, 0900 hr local time, May 15, 1958). Some ray tracing is shown.

Ray-tracing methods have been used to the left of the transmitter (see Fig. 10) to determine satellite traces which this structure might give. The effect of the magnetic field has been neglected and Snell's law has been used in the ray tracing. It can be seen that a model such as this presents to radiation, travelling in the direction of the magnetic field, contours of equal ionization that are parallel to one another, similar to that encountered by radiation travelling vertically through a quiet horizontally stratified ionosphere. For this model, rays travelling in directions close to the magnetic field direction will produce echoes with greater signal strengths than from any other direction, because the kinking of the contours will be effective in dispersing radiation travelling in these other directions (vertical incidence included). Thus the model gives results consistent with the enhanced traces reported in Section II(d).

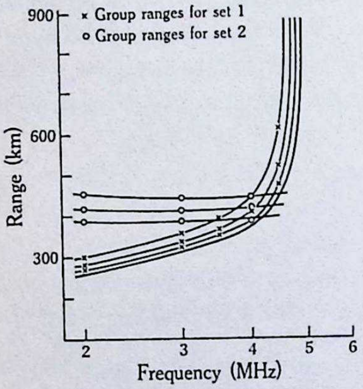

Fig. 11.—Reconstructed satellite traces using the model in Figure 10 for propagation to left and right of the transmitter.

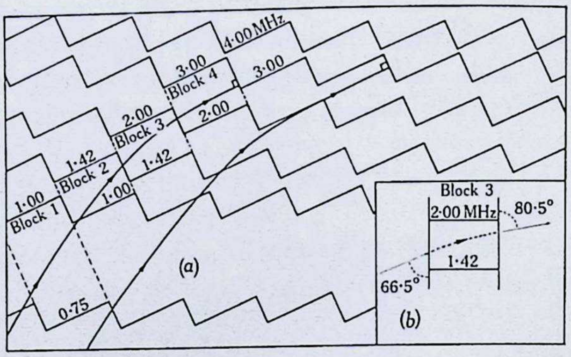

Fig. 12.—Idealized section (a) of the model in Figure 10 to allow calculations to the right of the transmitter; two ray paths are shown. (b) is an example showing the calculation for propagation in block 3.

The ray paths to the left of the transmitter which are drawn on Figure 10 are for a frequency of 4·58 MHz. Similar paths for other frequencies have been determined and the group paths calculated by evaluating $\int 1/\mu \, ds$ along each path. Results are shown by the three satellite traces (Fig. 11) drawn through the calculated group paths indicated by crosses.

Because of the nature of the kinking used in the model it was more difficult to use Snell's law with any degree of accuracy for ray tracing to the right of the transmitter. Here a different method was used to get some indication of possible ray paths. The kinking was idealized so that the contours of equal electron density were alternatively perpendicular to the magnetic field lines and parallel to them. Figure 12 shows that portion of Figure 10 (enclosed by a dashed line) which has been treated in this way. The ionization has been divided into blocks. Within each block, the plasma frequencies terminating the upper and lower boundaries are determined from the model shown in Figure 10. Starting from the first block, the position of entry into the block and the direction of travel of radiation is known. It is assumed that between the upper and lower boundaries of each block the electron density varies linearly. Because of this assumption, by using equations given by Kelso (1964) for propagation in a linear layer (see Subsection (c) above) it has been possible to calculate for each block the position and direction of travel for radiation leaving the block. Calculations made from block to block eventually gave the angle between the direction of travel of the radiation and the field-aligned ionization contour that can be expected to reflect the radiation for perpendicular incidence. Trial and error methods were used until an initial ray-path direction was found which terminated perpendicular to this electron density contour. Figure 12(a) shows two ray paths determined in this way. Figure 12(b) illustrates the calculation of the position and direction of travel of the emerging radiation for a particular block. Once the ray paths were determined the group path was calculated by using the expression $\int 1/\mu \, ds$ along the path. Evaluation of this integral for the paths illustrated and also for paths at other frequencies has allowed the satellite traces shown in Figure 11 to be obtained (the open circles are the calculated points). It is realized that because, for the calculations just made, the nature of the kinking has been idealized the positions of these satellite traces will not be exact. Nevertheless, they do give some indication of the traces to be expected from the returning radiation that is initially propagated to the right of the transmitter in Figure 10.

The overall result shown by Figure 11, which was obtained by using ray-tracing methods in the model of Figure 10, appears to be promising. Two sets of traces can be expected. Further, the shapes of each set of satellite traces are consistent with observations (Section II(c)). The model also gives an explanation for the enhanced trace from a direction close to the magnetic field direction. The results from the model are also consistent with direction-of-arrival results (Bowman 1968a), which suggest that the reflection levels for the off-vertical satellite traces are approximately the same as the reflection levels for the same frequencies at vertical incidence.

It is possible to give a reasonably satisfactory explanation of the appearance of satellite traces that occur on multiple-hop main traces but that do not occur on the first-hop main trace (Section II(f)), by using a similar model with shallow oscillations. If it is assumed that the oscillation of the contours of equal electron density is so shallow that the maximum angle the orientation of the contours makes with the horizontal direction is 15°, the maximum possible ranges for ray paths for first-, second-, and third-hop satellite traces are shown in Figure 13(a). Retardation is neglected and a low frequency that would be reflected near the base of the layer is used. The details of these calculations are given below.

	Main Trace Range (km)	Maximum Possible Satellite Range (km)	Maximum Excess Range (km)
First hop	260	269	9
Second hop	520	560	40
Third hop	780	906	126

Because of the finite width of the traces, it is not possible to detect first-hop satellite traces (maximum excess range 9 km) with this model. It is possible for the second-hop and more likely for the third-hop satellite traces.

Figure 13(b) shows a model for the baseline of the layer incorporating a "shallow sine wave" variation with a maximum angle of 15° for the orientation of the baseline relative to the horizontal direction. Figure 13(b) seeks to show how this model can explain the resolved third-hop satellite traces shown in Figure 1(l) for a frequency of 2 MHz. The estimated ranges of 835, 860, and 885 km are relatively close to those observed (820, 860, and 880 km respectively). To get these ranges it has been necessary to use ray paths that leave and return to the transmitter with off-vertical angles of 32°, 38°, and 44° respectively.

Using the system of nulls, the calculated off-vertical angles of arrival for these traces are 30°, 40°, and 43° respectively. The spacing used between the oscillations, which could be considered as the wavelengths of the structures, is 45 km. Only specular reflections have been used. All factors considered, this seems to be a good model for the multiple-hop satellite traces.

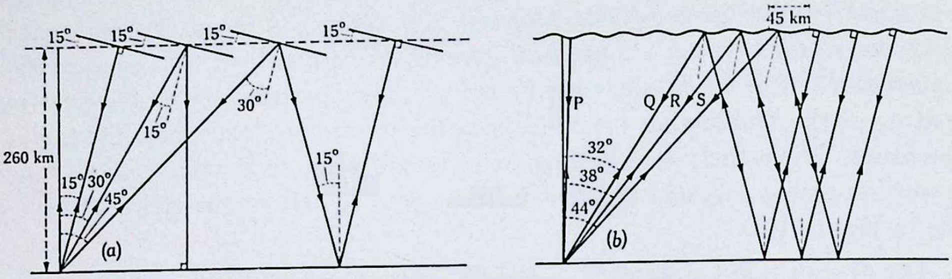

Fig. 13.—Illustrations of (*a*) maximum ray paths for first-, second-, and third-hop satellite traces for ionospheric irregularities with maximum slopes of 15°; and (*b*) model and ray paths to explain third-hop satellite traces shown in Figure 1(*l*) (Ellsworth, 2200 hr local time, September 22, 1958):

	Angle Calculated from Null Position	Range (km)
P	—	258
Q	30°	835
R	40°	860
S	43°	885

IV. Discussion

Of all the models proposed in Section III the one that seems, at least, to be consistent with all the experimental evidence presented in Section II is that involving kinking of the ionization contours. Ray tracing in the model (Fig. 10) derived from the ionograms shown in Figure 1(*k*) has produced Figure 11, which has characteristics similar to those of this particular ionogram and to spread-*F* ionograms generally.

The irregularities are probably the same type of phenomenon as the field-aligned sheets deduced by Muldrew (1963) from topside soundings, even though the orientation of the spread-*F* fronts can presumably vary. Muldrew estimates the structure size at several kilometres, an order of magnitude less than the irregularity spacings obtained here by using satellite-trace spacings (Fig. 2).

The nature of any particular trace of set 2 on Figure 11 is similar to that for a trace expected for aspect-sensitive reflections from the same off-vertical angle (see Fig. 9(*a*)). It is possible that, instead of these traces resulting from reflection from sharply steeped contours of electron density, as was originally proposed, they are produced by aspect-sensitive reflections, after refraction in the layer, from field-aligned columns. In this case, the columns would be located at the positions in the layer where the kinking is most pronounced.

High latitude, mid latitude, and low latitude measurements (Klemperer 1963; Bowman 1960; Roy and Verma 1953) suggest specular reflection from relatively large-scale structures for spread-*F* traces. The frequent occurrence of resolved traces on Antarctic records indicates structures of this type for polar regions.

Since radio-star scintillations were first recorded, associations have been found between these, or similar scintillations from Earth satellite transmissions, and spread-F (see e.g. Klemperer 1963; Beynon and Jones 1964). There seems little doubt that a relationship exists between these phenomena. Early work has concentrated on the irregular fast fluctuations of radio-signal amplitude, which were ascribed to diffraction effects from an irregular screen (Hewish 1951). The irregularities producing the diffraction were later described as field-aligned columns of enhanced ionization (see e.g. Yeh and Swenson 1964). However, particularly as a result of the use of swept-frequency interferometers (Wild and Roberts 1956; Singleton 1964; Warwick 1964) scintillations of a different type have also been reported. Because these scintillations show systematic features that vary with frequency, workers were led to the suggestion that refraction effects from "lens-like", "prism-like", or "wave-like" irregularities in the F_2 region with dimensions of the order of 10 km were responsible for these scintillations. The diffraction screen cannot be expected to give these frequency-dependent effects. Dagg (1957) reported particular types of scintillations at fixed frequency which he ascribed also to lens-like structures. Yeh and Swenson (1964) differentiated between the two types of scintillations, while Singleton (1964) has shown that the type of scintillation recorded seems to depend on the method of recording; he gives one example where both types are present simultaneously. Both Wild and Roberts (1956) and Singleton (1964) find associations between the second type of scintillations (associated with lens-like structures) and spread-F.

Thus, the explanation of the association between scintillations and spread-F does not appear to be as simple as at first thought. It does not seem likely that small-scale field-aligned irregularities are alone responsible for both scintillations and all types of spread-F. Rather it appears from the foregoing that possibly two classes of ionospheric irregularities exist simultaneously. The same disturbance may be responsible for the creation of both the lens-like structures and the field-aligned columns. These irregularities would then be responsible for the different types of scintillations that are recorded.

In terms of the favoured results of this analysis the lens-like structure can be identified with the kinking of the ionization contours, and the columns of enhanced ionization may possibly exist at particular positions in this kinking structure. It has been suggested here that the traces most often seen in the spread-F phenomenon (set 1) result from specular reflection from the relatively large-scale structure while possibly set 2 is produced by aspect-sensitive reflections from the field-aligned columns associated with the kinking.

V. CONCLUSIONS

For reasons that have already been discussed, the model for the irregularities that produce spread-F, which is favoured in this paper, consists of a simple kinking of the F_2-layer contours of equal electron density. This kinking produces quasi-sinusoidal shapes in these contours with wavelengths of some tens of kilometres. The position of the kinking in the layer is displaced monotonically with height in a way that is related to the orientation of the magnetic field (see Bowman 1960).

The orientation of the fronts along which the kinking occurs is not necessarily perpendicular to the magnetic-meridian plane since mid latitude results have shown that these fronts are often 30° or more away from this direction (Bowman 1960; Clarke 1965; Bowman 1968*b*). However, because of the frequent occurrence of the enhanced satellite trace on Antarctic ionograms it seems likely that the fronts here are often close to being magnetically east–west.

In the past, theoretical work on F_2-layer irregularities has concentrated on explaining local enhancements or reductions in electron density. If, as this paper suggests, kinking of the ionization contours plays a dominant role in the production of spread-*F*, it may be profitable to investigate disturbances that might possibly explain this aspect of the phenomenon.

VI. Acknowledgments

The author would like to thank Professor H. C. Webster, Dr. R. B. Penndorf, and Mr. G. F. Rourke for helpful assistance in the preparation of this paper. He is also grateful to Miss B. Willey, Miss E. Gistis, and Mr. S. H. Rosen, who made most of the calculations. The research was supported by the National Science Foundation under Contract NSF–C403.

VII. References

Beynon, W. J. G., and Jones, E. S. O. (1964).—*J. atmos. terr. Phys.* **26**, 1175.
Booker, H. G. (1961).—*J. geophys. Res.* **66**, 1073.
Bowman, G. G. (1957).—M.Sc. Thesis, University of Queensland.
Bowman, G. G. (1960).—*Planet. Space Sci.* **2**, 133.
Bowman, G. G. (1968*a*).—*J. atmos. terr. Phys.* **30**, 1115.
Bowman, G. G. (1968*b*).—*J. atmos. terr. Phys.* **30**, 721.
Budden, K. G. (1961).—"Radio Waves in the Ionosphere." pp. 186–7. (Cambridge Univ. Press.)
Clarke, R. H. (1965).—M.Sc. Thesis, University of Queensland.
Dagg, M. (1957).—*J. atmos. terr. Phys.* **11**, 118.
Herman, J. R. (1966).—*Rev. Geophys.* **4**, 255.
Hewish, A. (1951).—*Proc. R. Soc.* A **209**, 81.
Kelso, J. M. (1964).—"Radio Ray Propagation in the Ionosphere." Ch. 5. (McGraw-Hill: New York.)
Klemperer, W. K. (1963).—*J. geophys. Res.* **68**, 3191.
Muldrew, D. B. (1963).—*J. geophys. Res.* **68**, 5355.
Peterson, A. M., Villard, O. G., Jr., Leadabrand, R. L., and Gallagher, P. B. (1955).—*J. geophys. Res.* **60**, 497.
Pitteway, M. L. V. (1962).—*J. geophys. Res.* **67**, 5107.
Roy, R., and Verma, J. K. D. (1953).—*J. geophys. Res.* **58**, 473.
Sato, T., and Rourke, G. F. (1964).—*J. geophys. Res.* **69**, 4591.
Sharp, G. W., Crother, T. J., and Gilbreth, C. W. (1964).—*Trans. Am. geophys. Un.* **45**, 87.
Singleton, D. G. (1964).—*J. Res. natn. Bur. Stand.* **68D**, 867.
Swenson, E. M. (1964).—*Aust. J. Phys.* **17**, 490.
Titheridge, J. E. (1966).—*Polar Rec.* **13**, 7.
Ventrice, C. A., and Schmerling, E. R. (1958).—Penn. State Univ. Sci. Rep. No. 106.
Warren, E. S. (1963).—*Nature, Lond.* **197**, 636.
Warwick, J. W. (1964).—*J. Res. natn. Bur. Stand.* **68D**, 179.
Wild, J. P., and Roberts, J. A. (1956).—*J. atmos. terr. Phys.* **8**, 55.
Yeh, K. C., and Swenson, G. W., Jr. (1964).—*J. Res. natn. Bur. Stand.* **68D**, 881.

OBSERVATIONS OF CEN XR–2, SCO XR–1, AND TERRESTRIAL X–RAYS

By J. R. Harries* and R. J. Francey†

[*Manuscript received May* 21, 1968]

Summary

Two identical X-ray experiments were flown on Skylark rockets from Woomera, Australia, during April 1967. Sco XR-1 and Cen XR-2 were observed on both flights. The Cen XR-2 flux was $(1\cdot5\pm0\cdot1)\times10^{-7}$ erg cm^{-2} sec^{-1} (2–8 keV) when first observed but had decreased to $(1\cdot0\pm0\cdot1)\times10^{-7}$ erg cm^{-2} sec^{-1} and had become softer by the second flight. An X-ray flux from the Earth was observed and found to be due to solar X-rays reflected in the atmosphere.

I. Introduction

This paper presents the celestial X-ray results obtained from two identical experiments which were flown on Skylark rockets launched from Woomera, Australia (136°·5 E., 30°·9 S.), at 0032 U.T. on April 4, 1967 (flight I) and 2236 U.T. on April 20, 1967 (flight II). Both flights surveyed essentially the same area of the southern sky including the region around the south celestial pole. The most significant result was the discovery of a strong X-ray source in the constellation Centaurus (Harries *et al.* 1967) referred to as Cen XR-2, which was found to be variable (Chodil *et al.* 1967; Cooke *et al.* 1967; Francey *et al.* 1967).

The X-rays were detected by beryllium-window proportional counters, filled with a 90% xenon and 10% methane mixture at 1 atm pressure and with a depth of 2 in. The individual window thicknesses were measured on the recovered experiments and were found to be typically 14 mg cm^{-2}. The four counters on each rocket were mounted in pairs to form two independent detection systems, each having an effective area of 22 cm^2 and facing in diametrically opposite directions in a plane normal to the spin axis. Slit collimators mounted in front of the proportional counters defined a 10°·5 by 35° full width at half-maximum field of view, with the long axis parallel to the spin axis.

The pulses from a detection system were amplified and fed into a two-channel pulse height analyser, with channels corresponding to 2–5 and 5–8 keV energy deposited in the counter. The count rates observed in these channels will be referred to as S_1 (2–5 keV) and S_2 (5–8 keV) for the first detection system and S_3 (2–5 keV) and S_4 (5–8 keV) for the second system. The channels were calibrated immediately prior to launching using the 5·9 keV X-rays from a ^{55}Fe source.

---

* Physics Department, University of Adelaide, P.O. Box 498D, Adelaide, S.A. 5001.
† Physics Department, University of Tasmania, P.O. Box 252C, Hobart, Tas. 7001.

Aust. J. Phys., 1968, 21, 715–23

The sensitivity of each detection system to a point source of galactic X-rays was dependent on the background count rate, which was due to charged particles and the diffuse celestial X-ray flux. Approximately 75% of the high energy charged particles were rejected by the pulse height analyser because they deposited more than 8 keV in the counter gas. A source with an X-ray flux of approximately 1 photon $\mathrm{cm}^{-2}\,\mathrm{sec}^{-1}$ in the energy range 2–8 keV would give a response with a significance of three standard deviations for one scan over the source.

The attitudes of the rockets throughout the part of the flight above 60 km altitude were determined from data provided by the standard Skylark sunslits, magnetometers, and rate gyroscopes. Independent attitude solutions were also obtained from the British Aircraft Corporation, Bristol, U.K. The final solutions, used to obtain the position of Cen XR-2, gave correct positions for Sco XR-1 (Gursky *et al.* 1966) and the Sun to an accuracy of better than 2°. The spin period of both rockets was about 11 sec and the spin axis described a slow flat precession cone, with a half-angle of about 64° and period of about 400 sec. This motion was ideal for the survey as it allowed almost the whole sky to be scanned in an orderly manner. Although the parameters of the motion were similar on the two flights, the orientations of the precession cones were very different.

II. Analysis Procedures

A marked increase in the proportional counter count rates was observed as the rocket altitude increased from 70 to 90 km. This increase was caused by the detection of celestial X-rays which can penetrate to this altitude in the atmosphere. Between the altitudes of 40 and 70 km, the count rate was due to energetic charged particles and photons and the detection of secondary particles produced in the rocket. The counts due to these processes were approximately equally distributed between the two energy channels and were present throughout the flight.

Although a low energy electron flux could contribute to the count-rate increase between 70 and 90 km, this was considered unlikely owing to the lack of a pitch angle distribution about the geomagnetic field and to the distribution of the increase between the two energy channels. Electrons of about 80 keV could penetrate the window, but they would produce about twice as many counts in the higher energy channel. The observed increase was four times greater in the low energy channel than in the high energy channel.

Above 90 km the count rate due to discrete X-ray sources was superimposed on a diffuse celestial X-ray flux and a constant energetic charged-particle background. The main discrete X-ray sources observed were the Sun, Sco XR-1, and Cen XR-2. X-rays were also observed from the sources near the galactic centre with intensities consistent with the results of Friedman, Byram, and Chubb (1967), but the angular resolution and small detector area precluded any detailed analysis. Although the X-ray count rate observed from the Sun saturated the system, an estimate of the solar flux was obtained by considering the X-rays reflected from the atmosphere. This albedo flux is discussed in Section V.

X-rays from Sco XR-1 or Cen XR-2 were detected on at least seven consecutive scans by each detection system on both flights and so an accurate position and flux could be obtained which were not subject to errors in the correction for collimator response. For each individual scan of the source a triangular collimator response, whose base was related directly to the spin period, was fitted to the observed count rate by the least-squares technique. This gave the position of maximum response along the scan and the corresponding count rate due to the source. The response curve from scan to scan, i.e. across the long axis of the collimator, depended on the attitude solution but it was found that for source positions within 5° of each other the shapes of the response curves were almost identical. Hence, using a preliminary source position a theoretical response curve was obtained and fitted to the count rates from the different scans, again by the least-squares method. This gave the position of the source relative to the scan paths and also the count rate corresponding to normal incidence.

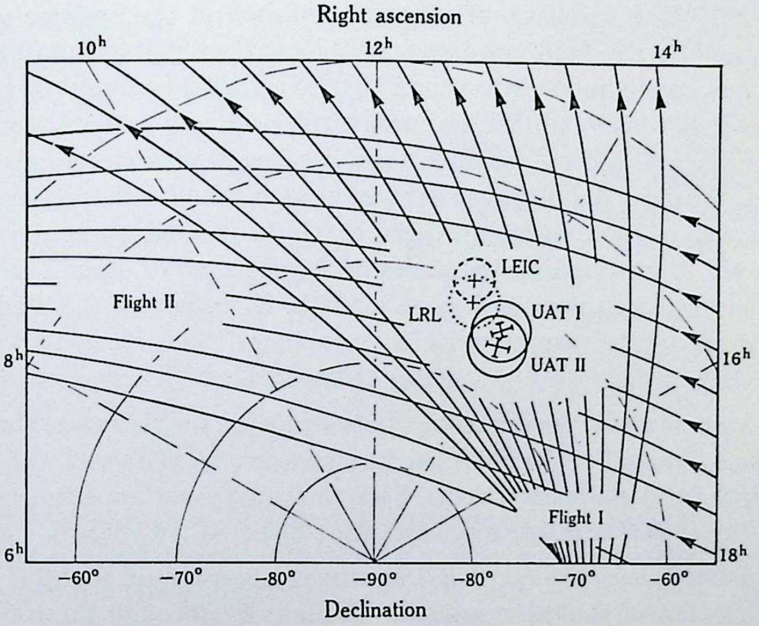

Fig. 1.—Scan paths on flight I and flight II during which Cen XR-2 was detected. The resultant UAT positions are indicated (mean position R.A. $13^{h}\cdot 9$, Dec. $-64°$); error bars show the statistical uncertainty in the maximum of the count rate data while the circles combine the statistical error with the 2° accuracy of the attitude solutions. The LRL (Chodil *et al.* 1967) and LEIC (Cooke *et al.* 1967) positions are also shown, together with their claimed accuracies.

The resultant position for Cen XR-2 is shown in Figure 1, together with the scans on which it was observed. The crossed error bars represent the statistical errors given by the fitting process, while the error circles include an estimated 2° uncertainty due to systematic errors in the attitude solution. The positions for Sco XR-1 and the Sun obtained by the same method were accurate to within 2°. The position of Cen XR-2 from this analysis was $13\cdot 9\pm 0\cdot 4$ hr right ascension and $-64°\pm 3°$ declination ($l^{\mathrm{II}} = -2°\pm 3°$, $b^{\mathrm{II}} = 310°\pm 3°$). An optical search of most of the region about this position for Cen XR-2 by Dr. G. Lynga and Dr. L. Searle of Mt. Stromlo Observatory (personal communication) found about 80 violet stars down to 16th magnitude. A search for nova-like characteristics in both optical and radio emissions is being undertaken.

III. Spectra

In order to obtain the incident X-ray spectra corresponding to the observed counting rates of the two-channel pulse height analyser it was necessary to understand the manner in which the detection system would modify the X-ray spectrum.

Initially the incoming X-rays were assumed to have the exponential spectrum

$$\mathrm{d}N/\mathrm{d}E = J_0 E^{-1}\exp(-E/T) \quad \text{photons}\,\mathrm{cm}^{-2}\,\mathrm{sec}^{-1}\,\mathrm{keV}^{-1}. \tag{1}$$

This type of spectrum is consistent with bremsstrahlung radiation from a thin hot plasma of temperature T.

The above spectrum was corrected for the proportional counter efficiency using the measured beryllium-window thickness and the mass absorption coefficients of Victoreen (1949). The spectrum of photons absorbed in the counter gas was then modified to allow for the finite resolution of the counter. The resolution of most of the counters was considerably worse than that of an ideal counter. For calculation, the resolution (full width at half maximum expressed as a percentage of the mean pulse height) was assumed to consist of ideal resolution plus an energy-independent factor to bring it up to the observed resolution at 5·9 keV. Corrections were made for the end effects of the counters of flight II which affected approximately 30% of the window area. Field-forming electrodes in the counters of flight I eliminated this problem; however, corrections had to be made to S_3 and S_4 of this flight for a gain decrease observed and measured prior to launching. These calculations gave the spectrum of output pulses corresponding to an incident X-ray spectrum.

Taking into account the effective window area of the detector, the count rates expected in each channel of the pulse height analyser were obtained. The ratio of the count rates in the two channels (that is, S_2/S_1 or S_4/S_3) was then a function of T, and for a given T the total number of counts (S_1+S_2 or S_3+S_4) was a function of J_0.

As discussed below, the Sco XR-1 spectrum observed on flight II was in close agreement with that of the other groups. In flight I, although the total number of counts from Sco XR-1 was in agreement with the flight II result, the ratio was inconsistent with the predicted value. Furthermore, it was found that the ratios for the other known sources were inconsistent with the predicted values and that the ratio for the energetic charged-particle background differed from unity. These factors could be explained only by assuming that the centre bias level of the pulse height analyser had changed during launching. Measurements on the recovered round predicted that for flight I the channels should be 2–4·5 and 4·5–8 keV, and these were also the channels necessary for the Sco XR-1 spectra to agree on both flights.

The incident X-ray spectra from Sco XR-1 observed by the two UAT flights (Universities of Adelaide and Tasmania) agreed with the results of Gorenstein, Giacconi, and Gursky (1967) in October 1966, Cooke *et al.* (1967) (the University of Leicester (LEIC) group) in April 1967, and Chodil *et al.* (1967) (the Lawrence Radiation Laboratory (LRL) group) in May 1967. These spectra were a factor of two less than some early proportional counter measurements (Chodil *et al.* 1965; Grader *et al.* 1966; Hayakawa, Matsuoka, and Yamashita 1966) but were consistent with the less accurate flux measurements made by other early experimenters (Bowyer *et al.* 1964; Giacconi, Gursky, and Waters 1965). Manley (1967) has suggested that the discrepancy was instrumental in origin and did not represent a real variation. Even if such a variation did occur the agreement between the Sco XR-1 spectra during April–May 1967 could be used as a common reference for the comparison of the different measurements of Cen XR-2.

The spectra of Cen XR-2, calculated on the assumption of an exponential spectrum, are given in Figure 2 and show the effects observed in the raw data, namely, the source was decreasing in intensity and becoming softer with time.

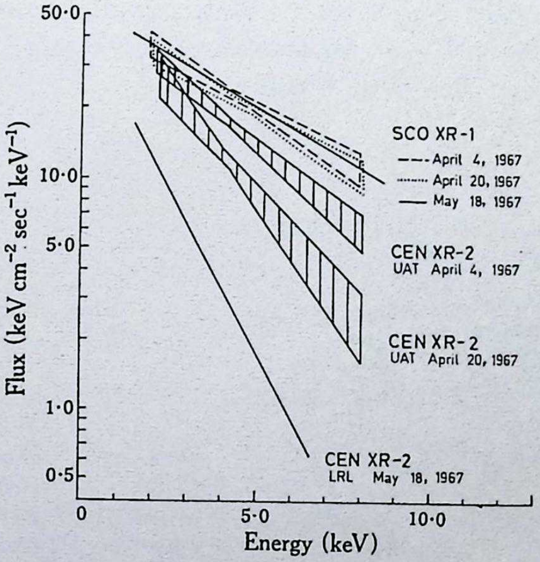

Fig. 2.—Variations in the Cen XR-2 spectra as observed on the present flights and the LRL flight (Chodil *et al.* 1967). The good agreement obtained for Sco XR-1 serves as a reference between the different experiments.

The bremsstrahlung from a thin hot plasma as represented by equation (1) is only one of three likely mechanisms for the generation of celestial X-rays. A black body would give a Planck distribution,

$$\frac{\mathrm{d}N}{\mathrm{d}E} = \frac{AE^2}{\exp(E/T_\mathrm{b})-1} \quad \text{photons cm}^{-2}\,\text{sec}^{-1}\,\text{keV}^{-1}, \tag{2}$$

while a synchrotron (magnetic bremsstrahlung) emitter would give

$$\mathrm{d}N/\mathrm{d}E = AE^{-\alpha} \quad \text{photons cm}^{-2}\,\text{sec}^{-1}\,\text{keV}^{-1}. \tag{3}$$

Clearly, two-channel pulse height analysis cannot distinguish between these various two-parameter spectra, and so spectra of Cen XR-2 were also calculated on the assumption of both the black-body and the power law spectra using the same method as for the exponential spectrum. The results for the three types of spectra are shown in Table 1. The total 2–8 keV flux for the UAT experiments is the same for all three types of spectra within the errors shown. The April 10 flux was obtained by the University of Leicester (Cooke *et al.* 1967) in the range 2–5 keV; nevertheless their flux is greater than the flux measured over the larger range 2–8 keV on April 4 or April 20 and suggests that Cen XR-2 might have passed through a maximum.

All three types of spectra could be fitted to the Cen XR-2 results of the LRL group. The black-body temperature was obtained on the assumption of a body of constant dimensions as determined by the UAT flights. Chodil *et al.* (1968), from a flight on September 28, 1967, found that Cen XR-2 was too weak to be observed. The results for all these flights are given in Table 1.

The count rates observed when the counters were not looking at any discrete X-ray sources or at the atmosphere were analysed to obtain the diffuse celestial X-ray flux. The count rate was corrected for the high energy charged-particle background by subtracting the count rate observed below an altitude of 70 km. A power law spectrum (equation (3)) was assumed and the background spectrum calculated from the count rates using the method previously discussed for the exponential spectrum. The incident diffuse flux was found to be $2\cdot8\pm0\cdot6$ photons $\text{cm}^{-2}\,\text{sec}^{-1}\,\text{sr}^{-1}\,\text{keV}^{-1}$ at 3 keV and $0\cdot8\pm0\cdot5$ photons $\text{cm}^{-2}\,\text{sec}^{-1}\,\text{sr}^{-1}\,\text{keV}^{-1}$ at 6 keV.

TABLE 1

VARIATIONS OF THE CEN XR-2 SPECTRUM

Group	Date	Exponential Temperature (keV)	Black-body Temperature (keV)	Synchrotron Index α	Flux ($\text{erg cm}^{-2}\,\text{sec}^{-1}$)	
LRL	Oct. 28, 1965				$<2\times10^{-9}$	(2–8 keV)
UAT	Apr. 4, 1967	$3\cdot6\pm0\cdot5$	$1\cdot21\pm0\cdot07$	$2\cdot15\pm0\cdot15$	$(1\cdot5\pm0\cdot1)\times10^{-7}$	(2–8 keV)
LEIC	Apr. 10, 1967				$1\cdot6\times10^{-7}$	(2–5 keV)
UAT	Apr. 20, 1967	$2\cdot4\pm0\cdot4$	$1\cdot10\pm0\cdot07$	$2\cdot75\pm0\cdot25$	$(1\cdot0\pm0\cdot1)\times10^{-7}$	(2–8 keV)
LRL	May 18, 1967	$1\cdot5$	$0\cdot73$	$3\cdot8$	$2\cdot8\times10^{-8}$	(2–8 keV)
LRL	Sept. 28, 1967				$<3\times10^{-9}$	(2–5 keV)

IV. ALBEDO X-RAYS FROM THE EARTH

A flux of X-rays was observed from the direction of the Earth in the 2–5 keV energy interval, which was comparable to the celestial diffuse X-ray flux. The albedo flux in the 5–8 keV channel was at least an order of magnitude less than that in the 2–5 keV channel, indicating a very soft spectrum.

The solar X-ray flux, observed directly, saturated the telemetry system and a lower limit of only 2000 photons $\text{cm}^{-2}\,\text{sec}^{-1}$ greater than 2 keV could be obtained. In fact, the solar flux would be expected to be considerably higher and to have a soft spectrum (Mandelstam 1965). Although most of these photons will be absorbed at about 80 km altitude in the atmosphere by the photoelectric effect, some of them will be scattered by the electrons in the gas molecules of the atmosphere. The calculation of the scattering differential cross section for oxygen, nitrogen, and argon takes into account the coherent scattering of a photon by all of the electrons in the molecule using the method of Compton and Allison (1935). This was an important effect as it caused the cross section to increase rapidly at small scattering angles producing the peak in the albedo flux at the X-ray horizon nearest the Sun (Fig. 3).

When corrections are made for the attenuation of the incident and scattered X-rays in the atmosphere and for the geometric factor of the collimator, the flux $\mathrm{d}N_{\mathrm{S}}/\mathrm{d}E$ of X-rays entering the counter window is

$$\frac{\mathrm{d}N_{\mathrm{S}}}{\mathrm{d}E} = 2\cdot 08\times 10^{22}\,\frac{\omega}{\mu(E)\,(1+\cos\psi/\cos\theta)}\,\frac{\mathrm{d}\sigma}{\mathrm{d}\Omega}(E,\phi)\,\frac{\mathrm{d}N_0}{\mathrm{d}E}\quad \text{photons cm}^{-2}\,\text{sec}^{-1}\,\text{keV}^{-1}, \qquad (4)$$

where $\mathrm{d}N_0/\mathrm{d}E$ is the differential solar X-ray flux, $\mu(E)$ is the atmospheric attenuation at energy E keV (Victoreen 1949), $\mathrm{d}\sigma/\mathrm{d}\Omega$ is the scattering differential cross section at angle ϕ, θ and ψ are the Sun and rocket zenith angles measured from the scattering volume, and ω is the collimator solid angle.

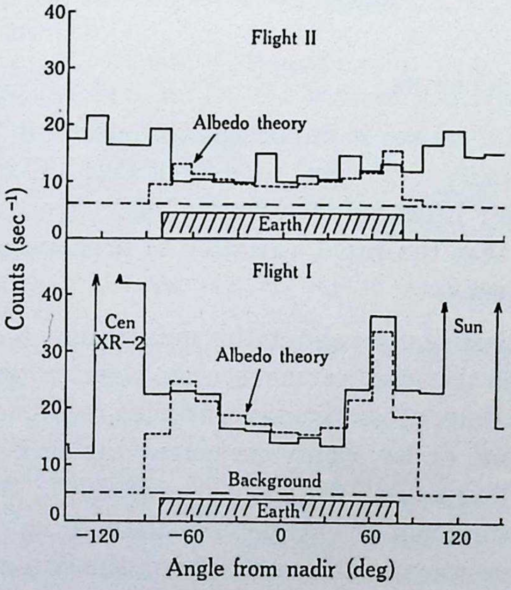

Fig. 3.—Averages of five (flight II) and four (flight I) scans through the nadir showing the X-rays observed from the Earth. The flight II scans are normal to the Sun zenith line while the flight I scans pass through the Sun and show the peak albedo flux at the horizon closest to the Sun. The horizontal dashed lines indicate the charged-particle background.

Another small fraction of the incident solar X-ray flux will undergo photoelectric absorption in argon. Photons with energies greater than 3·2 keV can eject a K electron, which will be followed in 12% of the cases (Fink *et al.* 1966) by the emission of a K X-ray of energy 2·94 keV. These X-rays will be emitted in all directions and those reaching the rocket will be detected in the lower energy channel. When corrections are made for the absorption of the fluorescent X-rays in the atmosphere, the flux reaching the detector window is found to be

$$N_{\mathrm{F}}(2\cdot 94\,\mathrm{keV}) = 1\cdot 14\times 10^{-3}\int_{3\cdot 2}^{\infty}\frac{\omega}{\mu(2\cdot 94)/\mu(E)+\cos\psi/\cos\theta}\,\frac{\mathrm{d}N_0}{\mathrm{d}E}\,\mathrm{d}E \quad \text{photons cm}^{-2}\,\text{sec}^{-1}.$$

Since the scattered and fluorescent components constitute only a small proportion of the incident solar flux, the total albedo flux is the sum of the two effects. The solar X-ray spectrum was assumed to be exponential (equation (1)) and to be absorbed in a thin layer at 80 km altitude. The angles θ, ψ, and ϕ could then be determined from the direction of arrival of the X-rays at the rocket and the altitude of the rocket.

The albedo flux was calculated for various values of the effective plasma temperature T, and the expected count rate of the pulse height analyser channels was obtained. The variation of the albedo flux with the nadir angle was found to be almost independent of plasma temperature in the range $0 \cdot 2$–$0 \cdot 5$ keV. The value of J_0 was varied by the least-squares method to fit the observed data. The theoretical albedo is shown in Figure 2 for a solar spectrum with an effective plasma temperature of $0 \cdot 4$ keV ($4 \cdot 6 \times 10^6$ °K) for some averaged scans from both flights. The solar flux required to give these fits was about 9×10^4 photons cm^{-2} sec^{-1} above 2 keV, and was very similar (within 20%) on both flights. The difference in the magnitude of the albedo between the flights was mainly caused by the difference in the Sun zenith angle, which was 49° for flight I and 74° for flight II. These fluxes were in very good agreement with the satellite measurements at the time (Solar Geophysical Data 1967).

V. CONCLUSIONS

The observed variability of Cen XR-2 makes it important to determine if the other known sources are varying to any extent. Several models of Cen XR-2 have been proposed (Manley 1967; Edwards 1968; Edwards and Harries 1968; Prendergast and Burbidge 1968) and would indicate that the rapid variation is perhaps only a transient stage in the life of an X-ray object.

The existence of the albedo flux raises doubts about the measurement of the diffuse X-ray flux by the difference between the count rates when the counter looks up and when it looks down. Fortunately, to date, most experiments with results on the diffuse flux have been made at night-time, or have only measured the flux above about 5 keV (Hayakawa, Matsuoka, and Yamashita 1966; Cooke *et al.* 1967; Seward *et al.* 1967). However, any daytime measurement at energies less than 10 keV must be suspect unless it can be shown that there was no X-ray activity on the Sun at that time.

Note added in proof. Lewin, Clark, and Smith (1868*a*, 1968*b*) have observed X-rays above 20 keV on October 15 and 24, 1967 from a source in the vicinity of Cen XR-2 and whose intensity decreased by 35 ± 17% between the two flights. If this source is Cen XR-2 then its observable life is much longer than is suggested by a simple extrapolation of the 2–8 keV observations discussed in the present paper.

VI. ACKNOWLEDGMENTS

The initial X-ray detector hardware was constructed at the Southwest Center for Advanced Studies, Dallas, Texas, under NASA contract NASr-198. We gratefully acknowledge the discussions and assistance of Professor K. G. McCracken and Dr. A. G. Fenton and the support provided by CSIRO (J.R.H.) and Commonwealth (R.J.F.) Post-graduate Scholarships. We thank the Science Research Council of the United Kingdom for providing the opportunity to make these flights, and the personnel of the British Aircraft Corporation, Filton, U.K., and of the Weapons Research Establishment, Salisbury, Australia, for their invaluable help.

VII. References

Bowyer, S., Byram, E. T., Chubb, T. A., and Friedman, H. (1964).—*Nature, Lond.* **201**, 1307.

Chodil, G., Jopson, R. C., Mark, H., Seward, F., and Swift, C. D. (1965).—*Phys. Rev. Lett.* **15**, 605.

Chodil, G., *et al.* (1967).—*Phys. Rev. Lett.* **19**, 681.

Chodil, G., Mark, H., Rodrigues, R., and Swift, C. D. (1968).—*Astrophys. J.* **152**, L45.

Compton, A. H., and Allison, S. K. (1935).—"X-rays in Theory and Experiment." (MacMillan: London.)

Cooke, B. A., Pounds, K. A., Stewardson, E. A., and Adams, D. J. (1967).—*Astrophys. J.* **150**, 189.

Edwards, P. J. (1968).—*Nature, Lond.* **217**, 43.

Edwards, P. J., and Harries, J. R. (1968).—*Proc. astr. Soc. Aust.* **1**, 109.

Fink, R. W., Jopson, R. C., Mark, H., and Swift, C. D. (1966).—*Rev. mod. Phys.* **38**, 513.

Francey, R. J., Fenton, A. G., Harries, J. R., and McCracken, K. G. (1967).—*Nature, Lond.* **216**, 773.

Friedman, H., Byram, E. T., and Chubb, T. A. (1967).—*Science* **156**, 374.

Giacconi, R., Gursky, H., and Waters, J. R. (1965).—*Nature, Lond.* **207**, 572.

Gorenstein, P., Giacconi, R., and Gursky, H. (1967).—*Astrophys. J.* **150**, L85.

Grader, R. J., Hill, R. W., Seward, F. D., and Toor, A. (1966).—*Science* **152**, 1499.

Gursky, H., *et al.* (1966).—*Astrophys. J.* **146**, 310.

Harries, J. R., McCracken, K. G., Francey, R. J., and Fenton, A. G. (1967).—*Nature, Lond.* **215**, 38.

Hayakawa, S., Matsuoka, M., and Yamashita, K. (1966).—*Rep. Ionosph. Space Res. Japan* **20**, 480.

Lewin, W. H. G., Clark, G. W., and Smith, W. B. (1968*a*).—*Astrophys. J.* **152**, L49.

Lewin, W. H. G., Clark, G. W., and Smith, W. B. (1968*b*).—Decrease in the high energy X-ray flux from Cen XR-2. *Astrophys. J.* (in press).

Mandelstam, S. L. (1965).—*Space Sci. Rev.* **4**, 587.

Manley, O. P. (1967).—*Phys. Rev. Lett.* **19**, 1144.

Prendergast, K. H., and Burbidge, G. R. (1968).—*Astrophys. J.* **151**, L83.

Seward, F., *et al.* (1967).—*Astrophys. J.* **150**, 845.

Solar Geophysical Data (1967).—Environmental Science Administration, IER-FB-278, 279.

Victoreen, J. A. (1949).—*J. appl. Phys.* **20**, 1141.

OPTICAL AND RADIO OBSERVATIONS OF THE FLARE STAR UV CETI IN AUSTRALASIA DURING SEPTEMBER–OCTOBER 1967

By C. S. Higgins,* L. H. Solomon,† and F. M. Bateson‡

[*Manuscript received May* 17, 1968]

Summary

This paper presents the results of a joint radio-optical programme of observations in Australasia on the flare star UV Ceti during an observing period in September–October 1967 organized by Commission 27 of the International Astronomical Union.

Eight of the 21 optical events were recorded by more than one observatory and are regarded as certain flares. Six of the verified flares were also monitored at radio frequencies and 5 of these were accompanied by radio emission. Two bright flares were recorded within a time interval of 2 hr on October 3, 1967.

On existing evidence, it is suggested that if a flare period does exist, it is probably shorter than 0·1821 day (Chugainov, preprint 1967).

Over the range $80 < f < 2650$ MHz, the average spectrum of radio bursts from UV Ceti decreases with increasing frequency. The exponent of an assumed power law variation is less than -1 below 240 MHz and steeper at higher frequencies.

I. Introduction

Commission 27 of the International Astronomical Union has recently formed a working group which has initiated a programme of worldwide observation of certain well-known flare stars. One of the main objects of this investigation is to establish a continuous monitor of these stars over a time interval of the order of a fortnight, using optical and radio observatories in different countries. The present paper describes the optical and radio observations carried out in Australia and New Zealand during the first of these programmes on UV Ceti for the interval September 26 to October 10, 1967.

During the observations 8 flares were certainly detected, and in addition there is less conclusive evidence for the occurrence of another 13 outbursts from this star.

II. Observations

Fortunately, we were able to make use of a reasonably extensive network of optical telescopes which were operated by both professional and amateur organizations; this cooperative effort (Slee, Higgins, and Patston 1963; Slee, Solomon, and Patston 1963) has been fostered over the past eight years primarily for the purpose of providing optical evidence for the occurrence of flares at times corresponding to the reception of bursts of radio emission.

---

* Division of Radiophysics, CSIRO, P.O. Box 76, Epping, N.S.W. 2121.
† Smithsonian Astrophysical Observatory, Cambridge, Massachusetts, U.S.A.
‡ Mt. John University Observatory, Lake Tekapo, New Zealand.

Aust. J. Phys., 1968, **21**, 725–34

During the latter half of the programme, from October 2 to October 9, radio observations were also conducted with the 64 m telescope at Parkes, N.S.W., on frequencies of 150 and 2650 MHz, and with the recently commissioned radioheliograph at Culgoora, N.S.W., on a frequency of 80 MHz.

TABLE 1

COOPERATING OBSERVATORIES

Location	Operating Authority	Instrument	Type of Observation
Belfield, N.S.W.	Astronomical Society of New South Wales	25 cm reflector	Visual
Brisbane, Qld.	Page Observatory	30 cm Schmidt camera	Photographic
Brisbane, Qld.	Balmoral Observatory	30 cm reflector	Visual
Brisbane, Qld.	Roscom Astronomical Society	15 cm reflector	Visual
Bundaberg, Qld.	Amateur Astronomical Club of Bundaberg	49 cm reflector	Visual
Lithgow, N.S.W.	Lithgow Observatory	20 cm reflector	Visual
Moe, Vic.	Latrobe Valley Astronomical Society	20 cm reflector	Visual
Yallourn, Vic.	Latrobe Valley Astronomical Society	32 cm reflector	Visual
Auckland, N.Z.	Astronomical Society of Auckland	51 cm reflector	Visual
Nelson, N.Z.	Royal Astronomical Society of New Zealand	32 cm reflector	Visual
Lake Tekapo, N.Z.	Mt. John University Observatory	20 cm refractor	Visual
Lake Tekapo, N.Z.	Mt. John University Observatory	41 cm reflector	Photoelectric
Mt. Stromlo, A.C.T.	University of Uppsala, Sweden	66 cm Schmidt camera	Photographic
Woomera, S.A.	Smithsonian Institution	50 cm Baker–Nunn Schmidt camera	Photographic
Culgoora, N.S.W.	CSIRO	3 km heliograph	Radio (chart recorder)
Parkes, N.S.W.	CSIRO	64 m reflector	Radio (chart and digital recorder)

The observatories that contributed to these observations are listed in Table 1, which also briefly describes the telescopes and the type of observation made with each instrument. The methods used by the various observing groups are described briefly below.

(a) *Amateur Visual Observations*

These were carried out by nine groups of amateurs, each group consisting of two or three observers, who took turns to man the telescope. During each observer's turn at the telescope, estimates were made at intervals of 30 sec of the flare star's brightness relative to preselected comparison stars in the same field; these results were recorded by one of the members of the group. The accuracy of such visual determinations is hard to assess and obviously varies with the competence and experience of the particular observer and the seeing conditions. However, even experienced observers record a peak-to-peak fluctuation level of about $0^m{\cdot}5$ over an observing interval of 1 hr, so that it does not appear legitimate to attach much significance to brightness increases of $< 0^m{\cdot}5$ unless there is some independent confirmatory observation.

(b) *Amateur Photographic Measurements*

The Schmidt camera located at Brisbane made use of plates, with a fast panchromatic emulsion, which were exposed for intervals of 4–6 min. Up to four or five exposures were made on each plate by laterally shifting the plate holder so that the stellar images were displaced a few seconds of arc. The time interval between the end of one exposure and the start of the next was only a few seconds, except when the plate was changed, when a break of about 5 min occurred. The smallest detectable brightness increase appears to be about $0^m{\cdot}2$.

(c) *Baker–Nunn Schmidt Camera*

The observations conducted at Woomera also made use of multiple displaced images, each exposure being of a few seconds duration with an interruption of about 20 sec between exposures. The 55 mm Extended-Red Royal-X Pan Recording film can be quickly transported through the camera, so that no appreciable interruption occurs between exposures on different frames. The minimum detectable brightness increase is about $0^m{\cdot}3$.

(d) *Uppsala Schmidt Camera*

This equipment made use of the displaced-image technique, exposure times being $3{\cdot}5$ min on Kodak I-N emulsion through a Schott RG2 filter. Observations were conducted on one night only for $1^h 14^m$, during which a brightness increase of $\sim 0^m{\cdot}2$ would have been detected.

(e) *Lake Tekapo, Visual Observations*

These observations have been described in some detail elsewhere (Bateson and Kohler 1968) and it is not proposed to repeat the description here. An inspection of the variability of the brightness estimates suggests that it would be difficult to detect a flare of magnitude $< 0^m{\cdot}5$ unless there is independent confirmatory evidence.

Bateson and Kohler suggest that some of the fast brightness fluctuations may be intrinsic in the star, although their conclusions are yet to be confirmed.

(f) *Lake Tekapo, Photoelectric Observations*

The 41 cm reflector at the Mt. John University Observatory was used with a photomultiplier RCA 1P21, observations being made in integrated light without a filter. In addition to the normal pen-recorder, a General Electric integrating voltmeter, with an integration time of 1 min, was used. This gave an accuracy approaching $0^m{\cdot}01$.

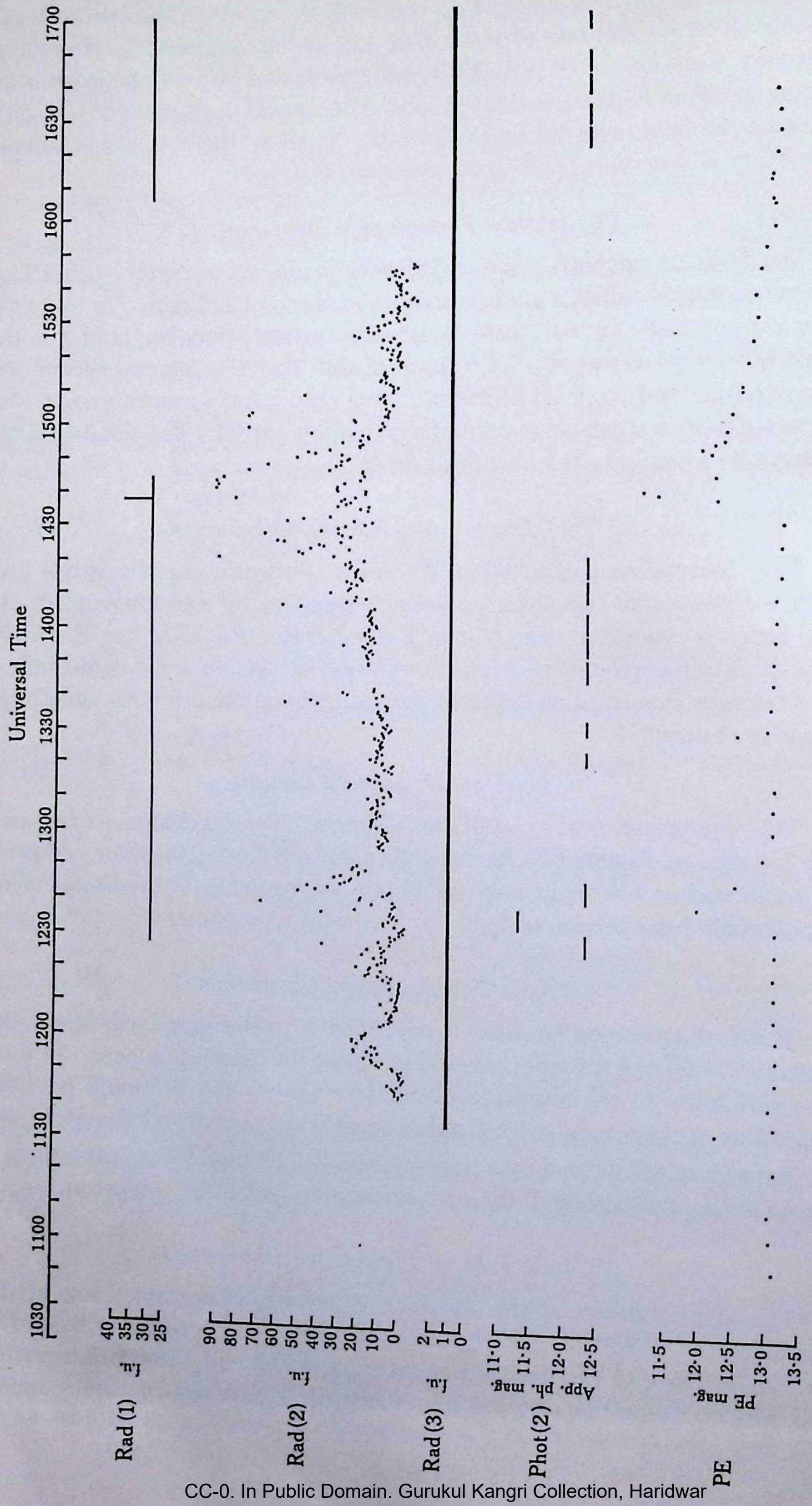
Universal Time
1030
1100
1130
1200
1230
1300
1330
1400
1430
1500
1530
1600
1630
1700
Rad (1)
f.u.
40
35
30
25
Rad (2)
f.u.
90
80
70
60
50
40
30
20
10
0
Rad (3)
f.u.
2
1
0
Phot (2)
App. ph. mag.
11·0
11·5
12·0
12·5
PE
PE mag.
11·5
12·0
12·5
13·0
13·5

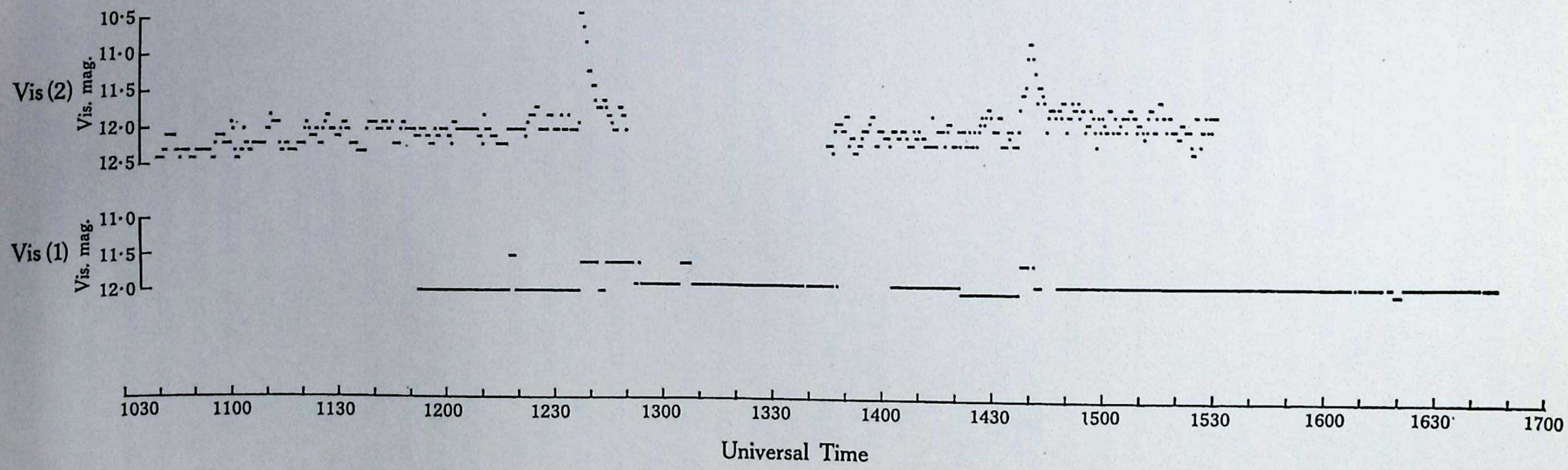

Fig. 1.—The two major flares of October 3, 1967 recorded by radio, photographic, photoelectric, and visual observers. Gaps in the plots denote the absence of good records.

Rad(1), Culgoora (radio, 80 MHz): the horizontal line denotes the upper limit of flux density detected. The minimum detectable peak flux density was 28 f.u. A single burst of a few seconds duration, recorded during the second major flare, is shown as a vertical line.
Rad(2), Parkes (radio, 150 MHz): values of flux density are plotted at intervals of 30 sec.
Rad(3), Parkes (radio, 2650 MHz): the upper limit of flux density is plotted as a horizontal line.
Phot(2), Brisbane (photographic): each exposure is shown as a short horizontal line.
PE, Lake Tekapo (photoelectric): readings are plotted at intervals of several minutes.
Vis(2) and Vis(1), Lake Tekapo and Bundaberg respectively (visual): observations are shown at intervals of 30 sec.

(*g*) *Radio Observations*

The 64 m reflector at Parkes, N.S.W., was equipped with feeds and receivers for frequencies of 150 and 2650 MHz. With the telescope tracking the flare star, continuous chart readings (time constant ~ 2 sec) were obtained at both frequencies; in addition, during possible flare-star activity the output of the 150 MHz receiver was digitized, a facility which is useful for plotting out the recorded radio amplitude to the same time scale as any possible optical activity. The limiting detectable peak flux densities were 3 and 0·4 f.u. at 150 and 2650 MHz respectively (1 flux unit $= 10^{-26}\,\mathrm{W\,m^{-2}\,Hz^{-1}}$).

At Culgoora, N.S.W., the radioheliograph operates at 80 MHz and has a diameter of 3 km. By means of the appropriate interconnection between the 96 aerials forming the heliograph, the equipment produces 48 circular beams with half-power widths of ~ 4 min of arc, the beams being spaced at intervals of 2·1 min of arc along the north–south direction. In this experiment, the radiation received in the six central beams, one of which was placed on the flare star, was recorded on a six-channel chart recorder. The flare star was tracked for an interval of 4·5 hr centred on upper transit. The full sensitivity of the equipment had not been realized at the time of these observations and the minimum detectable peak flux density was 28 f.u.

III. RESULTS

The detailed results of the optical and radio observations have been plotted in the form of curves of light intensity and radio flux density. All known observations have been included in the plots, a set of curves being constructed for each night of the programme. An example is shown in Figure 1, which depicts the behaviour of UV Ceti on the most active night (October 3, 1967) when two major flares were observed within an interval of 2 hr.

Table 2 lists most of the important information which we believe is contained in the light curves. It is apparent that 8 flares were almost certainly recorded, as shown in section (*a*) of the table. The 13 possible flares listed in section (*b*) should be regarded with some caution, since they were recorded by only one optical observatory.

Six of the verified flares were monitored at radio frequencies, and for five of these optical–radio correlations were obtained. Two major flares were observed, both on October 3 and only 2 hr apart. In both cases there is strong evidence that radiation was received at 150 MHz, although care must be exercised in accepting this conclusion without reservation because of the occasionally high level of interference at this frequency. Figure 1 shows that the radio result is more convincing for the flare which commenced at 1237 U.T.; some interference may have been present before the second optical flare, which commenced at 1436. At 80 MHz no radiation was detected during the first flare (peak flux density < 28 f.u.) and a single burst of a few seconds duration (peak flux density ~ 37 f.u.) occurred near the start of the second flare. No emission was detected at 2650 MHz during either event.

Radio observations were also conducted during six of the unconfirmed optical events listed in Table 2(*b*). None of these were accompanied by detectable radio emission except that of October 8 at 1341 U.T., when a pulse of radio emission lasting about

3 sec was recorded at 2650 MHz. Some significance should be attached to this apparent correlation, because the remainder of the 2650 MHz record was singularly free of similar deflections.

TABLE 2

OPTICAL AND RADIO EVENTS

October 2, 4, 5, 9, and 10 were days of no flare activity

Date (1967)	Time* (U.T.)	Equipment†	Maximum Brightness Change‡ Δm	Peak Radio Flux Density (f.u.)		
				80	150	2650 MHz
			(a) Confirmed Flares			
Sept. 29	1409–1417	Phot(2), Vis(4)	0·3, 0·7	—	—	—
30	1604–1610	Phot(1), Phot(2)	0·5, ?	—	—	—
Oct. 3	1237–1250	PE, Phot(2) Vis(1), Vis(2)	2·0, 1·0 0·4, 1·6	<28·0	20·0	<1·0
3	1436–1455	PE, Vis(1), Vis(2)	2·0, 1·0 2·0	37·0	25·0	<1·0
6	1612	Phot(1), Vis(4)	0·4, 0·3	—	7·0	—
6	1622	Phot(1), Vis(4)	0·4, 0·4	—	4·5	—
8	1230–1234	PE, Vis(2)	0·6, 0·4	<28·0	<3·0	<0·4
8	1433–1450	PE, Vis(2)	0·4, 0·4	<28·0	4·0	<0·4
			(b) Unconfirmed Flares			
Sept. 26	1539–1543	Phot(2)	0·2	—	—	—
27	1131	Phot(1)	0·4	—	—	—
28	1523	Phot(1)	0·3	—	—	—
29	1433	Phot(1)	0·3	—	—	—
Oct. 1	1151–?	Vis(3)	1·0	—	—	—
1	1403	Phot(1)	0·4	—	—	—
3	1134	PE	0·8	<28·0	—	—
3	1330	PE	0·6	<28·0	<3·5	<1·0
3	1601	PE	0·5	—	—	<1·0
4	1008	Vis(2)	0·5	—	—	—
8	1341	Vis(2)	0·5	<28·0	—	1·2 (short pulse)
8	1344·5	Vis(2)	0·6	<28·0	—	<0·5
9	1356·0	Vis(2)	0·5	<28·0	—	<0·4

* Where a single time is given for Baker–Nunn Schmidt observations it refers to the time of maximum brightness; for the photoelectric observations it denotes a short outburst lasting only a few seconds.

† Phot(1) = Baker–Nunn Schmidt, Woomera; Phot(2) = Page Schmidt, Brisbane; Vis(1) = Bundaberg; Vis(2) = Lake Tekapo; Vis(3) = Belfield; Vis(4) = Auckland; PE = photoelectric, Lake Tekapo.

‡ For the photographic observations Phot(2) this value is averaged over the exposure time of 4–6 min.

IV. DISCUSSION

The extensive monitoring of UV Ceti described here was initiated mainly to check a possible periodic tendency for the flares to erupt. It has been suggested by Andrews (1966*a*, 1966*b*) that the flares on YZ Canis Minoris and V1216 Sagittarii tend to recur at 2-day intervals; recently Chugainov (preprint 1967) has proposed that the flares on UV Ceti may follow a similar tendency, but interprets this behaviour in terms of a much shorter basic period of occurrence of 0·1821 day. On this interpretation, the apparent 2-day recurrence cycle is brought about by the limited observing time at any one site.

The optical events outlined in Table 2 are not sufficiently numerous to enable us to search for periodicities; this must await an assessment of the worldwide results by the Working Committee of Commission 27 of the International Astronomical Union. However, the limited results published here permit us to question seriously the period of 0·1821 day proposed by Chugainov. For example, it appears unlikely that the two major flares of October 3, 1967 would occur within 2 hr if a regular period of this order existed.

The data which Chugainov has gathered from various observations and which he uses to deduce the proposed period may indicate shorter intervals between flares. On five nights during August–October 1965 pairs of flares were recorded within time intervals ranging from 34^{m} to $1^{h}57^{m}$. Hence we conclude that if a basic flare period does exist, it is much shorter than 0·1821 day and, on the existing evidence, probably shorter than 1 hr.

One of the more interesting features of the optical results is the realization that two catastrophic releases of energy, each of $\sim 10^{25}$ J, can occur from the same star within a time interval of 2 hr. The rate at which the flare energy is released is approximately equal to the rate of total energy radiation by the quiescent star, yet the star appears to suffer no permanent alteration to its brightness.

The present observations can be used to deduce some rather limited, but nevertheless useful, information on the radio spectra of the flares from UV Ceti. Lovell, Whipple, and Solomon (1963) and Lovell and Solomon (1966) have given average values of peak flux density at 240 MHz, resulting from flares with a maximum brightness increase of one magnitude in the photographic region of the spectrum. These values range from 4·6 to 7·1 f.u. For the five cases in Table 2(*a*) for which radio emission appears to have been detected at 150 MHz the average peak radio flux density is 9·1 f.u. for a brightness change of one magnitude; the individual flares give values varying between 7·0 and 12·9 f.u. Hence, if it is a valid procedure to compare average values of this quantity recorded in different intervals of time, it appears that the average radio flux density in the range 150–240 MHz is falling at a rate which is not as steep as a $(\text{frequency})^{-1}$ law.

The one positive result recorded at 80 MHz, during one of the more intense flares on October 3, indicates a spectrum of $(\text{frequency})^{-0\cdot6}$; the negative result obtained during the second bright flare on the same date places an upper limit of $-0\cdot5$ on the exponent. It thus appears that the 150 and 80 MHz results during the present programme are consistent with the spectrum deduced from a comparison of the average results at 240 and 150 MHz as described in the preceding paragraph.

At the high frequency end of the radio spectrum, the lack of detectable radio emission at 2650 MHz during any of the confirmed flares shows conclusively that the flux density continues to fall at frequencies above 240 MHz. In the case of the two bright flares on October 3, 1967 the average exponent of an assumed power law variation between frequencies of 150 and 2650 MHz is greater than −1. Hence, the average spectrum of radio bursts from UV Ceti appears to decrease with increasing frequency over the range $80 < f < 2650$ MHz, with the exponent of an assumed power law variation being less than −1 below 240 MHz and steeper at higher frequencies.

From the existing meagre information on the radio spectra of UV Ceti flares, it appears that the most profitable range of frequencies for flare-star work, especially for detailed spectral observations, is 150–250 MHz. At the low frequency end of this band the receiver sensitivity is limited by the cosmic background temperature, which is increasing as $\sim \lambda^{2\cdot5}$. On the high frequency side of this band, the combination of a flare spectrum that decreases as $(\text{frequency})^{-1}$ or steeper, and a receiver noise temperature that is not easily reduced below 300°K, will ensure a progressively decreasing signal-to-noise ratio as the frequency is increased.

It appears to be of some importance in future radio observations of flare stars to determine the state of polarization of the emission so that the characteristics of these eruptions can be compared with solar flares. There is now reasonable spectroscopic evidence (Gershberg 1967) that the UV Ceti type flare is, like its solar counterpart, restricted to a small volume in the well-developed chromosphere or corona of a red dwarf star. If this is so, it may be possible to observe the types of polarization seen in radio bursts associated with solar flares. A first attempt should be made to record the dynamic spectra of some of these bursts, although a fast sweeping spectrograph of the type used for solar observations would not possess the required sensitivity. It appears that the best that can be achieved in this important field in the immediate future is to obtain recordings of the outputs of several receivers each of bandwidth, say, 1 MHz and separated in centre frequency by several MHz. The observation of time delays between the arrival of bursts in the separated channels would be rather conclusive evidence for the existence of solar-type flare phenomena. In addition, if plasma oscillations are shown to be responsible for the production of the radio emission, some useful information on electron densities in the atmospheres of these stars may be obtained.

V. ACKNOWLEDGMENTS

The authors wish to thank Mr. O. B. Slee, who carried out the observations at Culgoora and provided helpful discussion in the preparation of this paper.

Thanks are also due to Mr. U. Kohler of the RemeisSternwarte, Bamberg, who, during an observing period at the Mount John University Observatory, New Zealand, made photoelectric measurements of the flare star, and to Dr. G. Lynga of Mount Stromlo Observatory for photographic observations.

The authors are indebted to the amateur astronomical groups who participated in the programme and provided data used in the investigations: Mr. G. E. Patston, director of the Belfield Observatory and his large group of observers; Mr. and Mrs. A. Page, Page Observatory, Brisbane; Mr. J. van Vegchel and Mr. M. van Vegchel, Balmoral Observatory, Brisbane; the Amateur Astronomical Club of Bundaberg,

under the leadership of Mr. G. Fielding; Mr. D. Batcheldor and Mr. K. Batcheldor, Lithgow; Mr. G. Manley, Moe; Mr. T. B. Tregaskis and Mr. K. Bryant, Latrobe Valley Astronomical Society, Victoria; Mr. A. Jones of Nelson, New Zealand; and members of the Astronomical Society of Auckland, New Zealand.

VI. References

Andrews, A. D. (1966*a*).—*Publs astr. Soc. Pacif.* **78,** 324.

Andrews, A. D. (1966*b*).—*Publs astr. Soc. Pacif.* **78,** 542.

Bateson, F. M., and Kohler, U. (1968).—*Sth. Stars* **22,** 118.

Gershberg, R. E. (1967).—*Usp. Fiz. Nauk* **92,** 65.

Lovell, A. C. B., and Solomon, L. H. (1966).—*Observatory* **86,** 16.

Lovell, A. C. B., Whipple, F. L., and Solomon, L. H. (1963).—*Nature, Lond.* **198,** 228.

Slee, O. B., Higgins, C. S., and Patston, G. E. (1963).—*Sky Telesc.* **25,** 83.

Slee, O. B., Solomon, L. H., and Patston, G. E. (1963).—*Nature, Lond.* **199,** 991.

A CONTINUUM SURVEY OF THE SOUTHERN MILKY WAY AT 1410 MHz

By E. R. Hill*

[*Manuscript received March* 22, 1968]

Summary

This paper presents a contour map of the Southern Milky Way at 1410 MHz obtained using the 210 ft radio telescope at Parkes.

I. Introduction

Shortly after the commissioning of the 210 ft radio telescope at Parkes, simultaneous surveys of the Southern Milky Way at frequencies of 408 and 1410 MHz were commenced. The results of the 408 MHz survey have already been described by Komesaroff (1966), and the present paper describes in part the results of the 1410 MHz survey.

The survey described here was intended to fulfil two objectives. Firstly, the beamwidth of 14 min of arc at 1410 MHz was more than a factor of three smaller than that used in the previous surveys of the region by Hill, Slee, and Mills (1958) and by Mathewson, Healey, and Rome (1962). Accordingly, the higher resolution study could be expected to reveal considerably more structural detail in the distribution of galactic radio emission. The second reason for the survey was that it provided an opportunity to obtain experience with the newly installed digital recording system designed by M. Beard, as well as with digital computer processing of radio astronomical data.

This paper presents the contour map of the aerial temperature distribution derived from the observations. A subsequent paper will list radio data concerning the sources found and enumerate optical identifications and, where possible, provide contour maps of the individual sources.

II. Observations

The observations were carried out in March–April, June–July, and September 1962, with the assistance of M. M. Komesaroff and M. Beard. The area surveyed was between new galactic longitudes 281° and 356° and latitudes of about ±5° or ±6°. Scans were made in declination using drive rates of between 2 and $2\cdot5$ deg/min. The spacing between scans was about $3'\cdot5$ arc; this corresponds to about one-quarter beamwidth, which theoretically (see Bracewell and Roberts 1954) means that there is much redundancy in the observations. However, the theory makes no allowance for the occurrence in real data of receiver drifts, or other forms of equipment instability, or for the presence of interference. To enable the detection of these effects, the redundancy was thought worth while. The usefulness of the redundancy was enhanced by scanning an area of sky on one night with half-beamwidth spacing,

---

* Division of Radiophysics, CSIRO, P.O. Box 76, Epping, N.S.W. 2121.

Aust. J. Phys., 1968, 21, 735–7

and then on another night making a further series of scans of the same area at the same spacing but positioned midway between the previous set of scans.

The feed rotator at present installed on the telescope was not available at the time of these observations and this made it impossible to maintain constant position angle over the whole area surveyed during the time available for the survey.

Two receiver front-ends were used for these observations. During the first observing period March–April 1962, a crystal-mixer system described briefly by Cooper (1963) was used. In the two subsequent periods the parametric receiver built by Gardner and Milne (1963) was used. In all observations the time constant was 1 sec. At all times the receiver output was recorded digitally on paper tape and monitored with analogue recordings. Subsequently, all the processing was done using the digital records, the analogue records being used primarily to select which digital records to process.

In addition to the survey scans in declination, a series of zenith-angle scans and another series of reference scans were made. The zenith-angle scans were made in regions of the sky well away from the galactic plane. Here the variation of cosmic radiation is negligible so that observed variations measure the change with zenith angle of ground radiation entering the system. Two sets of reference scans were made, both sets running roughly parallel to the galactic plane, one set near the northern declination limit of the survey, the other near the southern limit. Every survey scan was thus intersected twice by these reference scans. The purpose of these scans was to provide two points for the baseline of each survey scan. Temperatures were determined along the reference scans relative to the south celestial pole and the effects of zenith angle were removed on the basis of the information derived from the zenith-angle scans. Since the survey scans were made at zenith angles where this effect was linear, this reduction procedure removed the effects of varying zenith angle along each survey scan and, incidentally, the effects of any other disturbances (such as receiver drifts) that varied linearly along the scans.

The observing procedure during each night included, in addition to survey scanning, frequent gain calibrations by recording the output of a noise source which was itself checked against a reference radio source.

III. ANALYSIS

The reduction procedure adopted for this part of the work is identical with that developed in conjunction with M. Beard and outlined by Beard (1966) and need not be repeated here. The only difference is that the present results are expressed as aerial temperatures rather than brightness temperatures. The temperature scale used is based on a value of 53°K for the source 13S6A provided by B. F. C. Cooper.

IV. CONTOUR MAP

Contours plotted in Figure 1 are those of aerial temperature referred to the south celestial pole as 0°K. Generally the levels plotted are

2, 3, 4, 6, 8, ... 20, 25, 30, ... 50, 75, 100, ... °K.

In some regions, however, where such contours crowd together too much, only a selection of these levels has been plotted. The coordinates are new galactic, l^{II}, b^{II}.

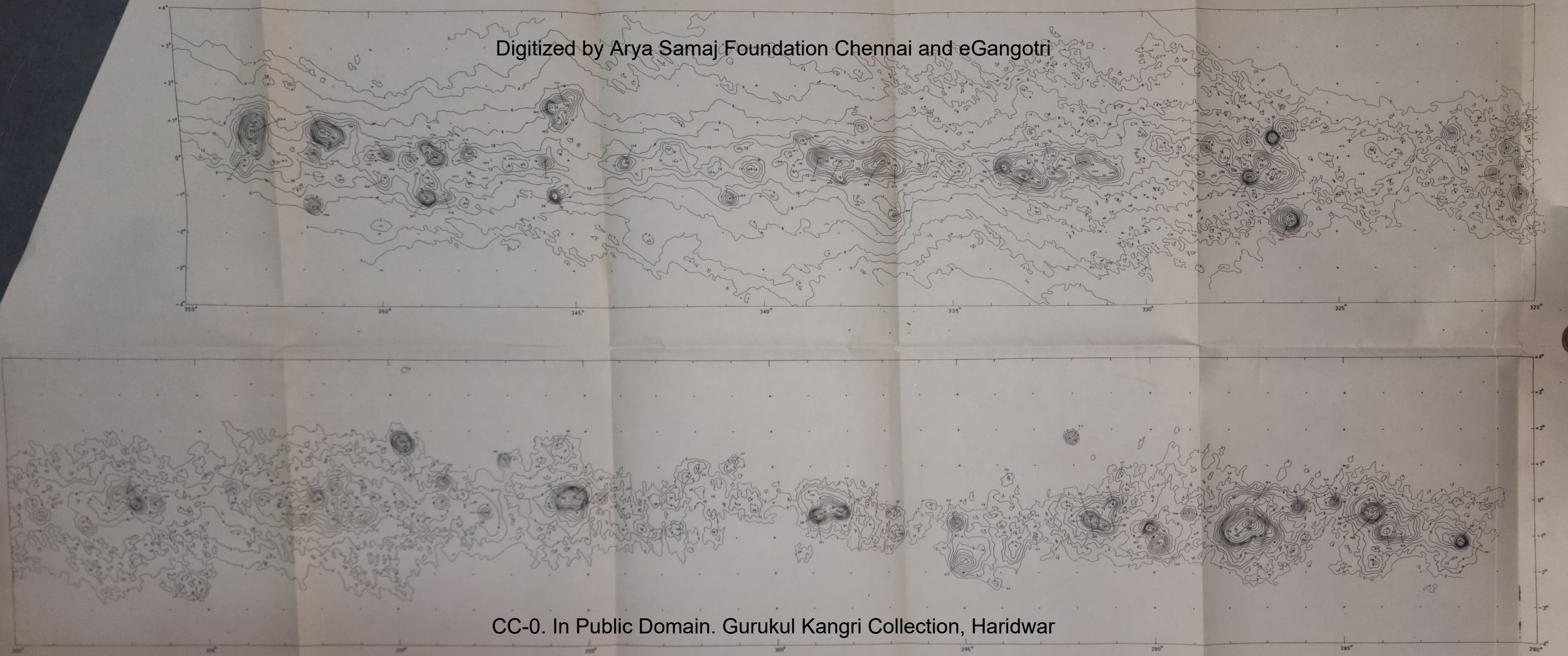
+4°
+3°
+2°
+1°
0°
-1°
-2°
-3°
-4°
355°
350°
345°
340°
335°
330°
325°
320°
320°
315°
310°
305°
300°
295°
290°
285°
280°

Fig. 1.—Contour map of aerial temperature distribution at 1410 MHz over the Southern Milky Way obtained using the Parkes 210 ft radio telescope. The coordinates are l^{II}, b^{II}.

The error in the temperatures quoted on the contour map is considered to be in the vicinity of 10–15%. This error arises principally from the assumed aerial temperature of the reference source and variations in the gain and linearity of the receiving system. The failure to maintain constant position angle for the aerial feed during the observations is expected, on the basis of available polarization measurements in this part of the sky, to introduce only small errors.

V. ACKNOWLEDGMENTS

Thanks are due to Mr. M. M. Komesaroff and Mr. M. Beard, who helped obtain the observations. Mr. Beard and Miss J. Spells also helped greatly with the processing of the observations.

VI. REFERENCES

BEARD, M. (1966).—*Aust. J. Phys.* **19**, 141.
BRACEWELL, R. N., and ROBERTS, J. A. (1954).—*Aust. J. Phys.* **7**, 615.
COOPER, B. F. C. (1963).—*Proc. Instn Radio Engrs Aust.* **24**, 113.
GARDNER, F. F., and MILNE, D. K. (1963).—*Proc. Instn Radio Engrs Aust.* **24**, 127.
HILL, E. R., SLEE, O. B., and MILLS, B. Y. (1958).—*Aust. J. Phys.* **11**, 530.
KOMESAROFF, M. M. (1966).—*Aust. J. Phys.* **19**, 75.
MATHEWSON, D. S., HEALEY, J. R., and ROME, J. M. (1962).—*Aust. J. Phys.* **15**, 354.

SUPERNOVA REMNANTS AS RADIO SOURCES

By M. J. L. Kesteven*

[*Manuscript received May* 20, 1968]

Summary

The results of a survey with the 1 mile Molonglo cross-type radio telescope of nonthermal galactic sources are discussed in terms of supernova remnant theories. The contour maps obtained indicate that most sources are consistent with a portion of a shell of emission. The results suggest that a remnant's spectral index is independent of its age. A supernova remnant evolutionary path is also derived, and compared with the path predicted by the various theories.

I. Introduction

Surveys of the galactic plane at radio frequencies reveal sources of two types, the basis for classification being the spectral index. On various grounds, the sources with a nonthermal index are generally thought to be remnants of supernova outbursts. For example, sources have been found at the sites of three observed supernovae: Taurus A, Tycho's nova, and Kepler's nova. Further, gas filaments consistent with a supernova outburst have been found at the positions of some radio sources: Cassiopeia A, Cygnus Loop, IC 443 (Minkowski 1959), and RCW 86 (Westerlund and Mathewson 1966). Several theories have been proposed relating a radio source to the gaseous remnant (Shklovskii 1960*a*; Van der Laan 1962). There have been few opportunities, however, for testing these theories: the most direct tests require that the distance to the source be known. This is so for a small number of sources only. Statistical tests have been of little use as each of the low resolution surveys available contained too few sources, and the ensemble of surveys failed to form a statistically homogeneous sample. It was hoped that the catalogue described in a previous paper (Kesteven 1968) would permit a fresh approach to the problem. Four questions are tackled in the present paper. The first relates to the type of supernova; it will be shown that the distribution of the sources is similar to the distribution of population I objects, suggesting that the sources are remnants of type II supernovae. Secondly, the morphology of the sources is examined; it will be shown that few sources have the circularly symmetric structure characteristic of the complete shell of emission assumed by the theories. The majority of the sources are consistent, however, with a fraction of a shell. Thirdly, the evolution of the radiation spectral index is examined. Analyses of the loss mechanisms that affect the radiation spectrum indicate that the spectral index should be independent of the age of the source. The present results confirm this, in contrast to the findings of Harris (1962) and Pskovskii (1963). Finally, the evolution of the radiated power is examined. This could be a sensitive test of the various theories, but the errors associated with the present set of observations are too large for the conclusions to be of great significance.

---

* Cornell–Sydney University Astronomy Centre, School of Physics, University of Sydney, N.S.W. 2006.

Aust. J. Phys., **1968, 21, 739–54**

II. Galactic Distribution of the Sources

The galactic distribution of the sources of the catalogue indicates that they are associated with population I objects; both the thermal and nonthermal sources lie close to the galactic plane. The mean absolute latitude of 0°·8 is consistent with the value noted by other observers: Large, Mathewson, and Haslam (1961), for example, found $|b^{\mathrm{II}}| = 0°\cdot 3$. The distribution in longitude is equally consistent with a population I distribution, as the sources show a "bunching" suggesting a spiral arm structure. The number of sources is too small to determine the location of the arms with precision, but the peaks in the source distribution agree with the "tangential points" noted by other observers (Mills 1959; Elsasser and Haug 1960; Kerr 1962; Mathewson, Healey, and Rome 1962). The source distribution is shown in Figure 1 along with the tangential points of Mills.

It appears then that the nonthermal sources are remnants of type II supernovae (if indeed they are supernova remnants).

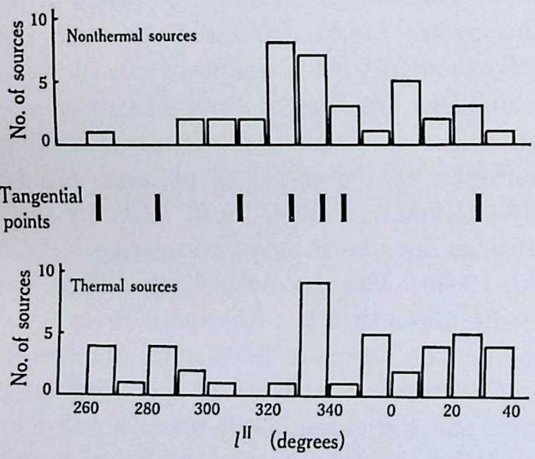

Fig. 1.—Distribution in galactic longitude l^{II} of the sources of the catalogue.

III. Source Contour Diagrams

Both theories of the supernova remnant assume the radio source to be associated with an expanding shell of plasma ejected by the outburst. In Shklovskii's theory the source is embedded in the shell; in Van der Laan's theory the source is situated in the region between the shell and the associated shock front. In addition, both theories assume the shell to be complete. Nineteen of the nonthermal sources are large enough to be resolved by the pencil beam of the cross-type telescope of the Molonglo Observatory. It could be hoped that an examination of the contours might decide between these two theories. Further, it should be possible to determine from the contours the nature of the shell, in the manner described by Hill (1967).

Figs. 2(*a*)–2(*r*).—The 408 MHz isophotes of the 19 largest nonthermal sources of the catalogue. In each figure the contour interval (c.i.) is shown and the solid circle is an estimate of the outer radius of the supernova shell.

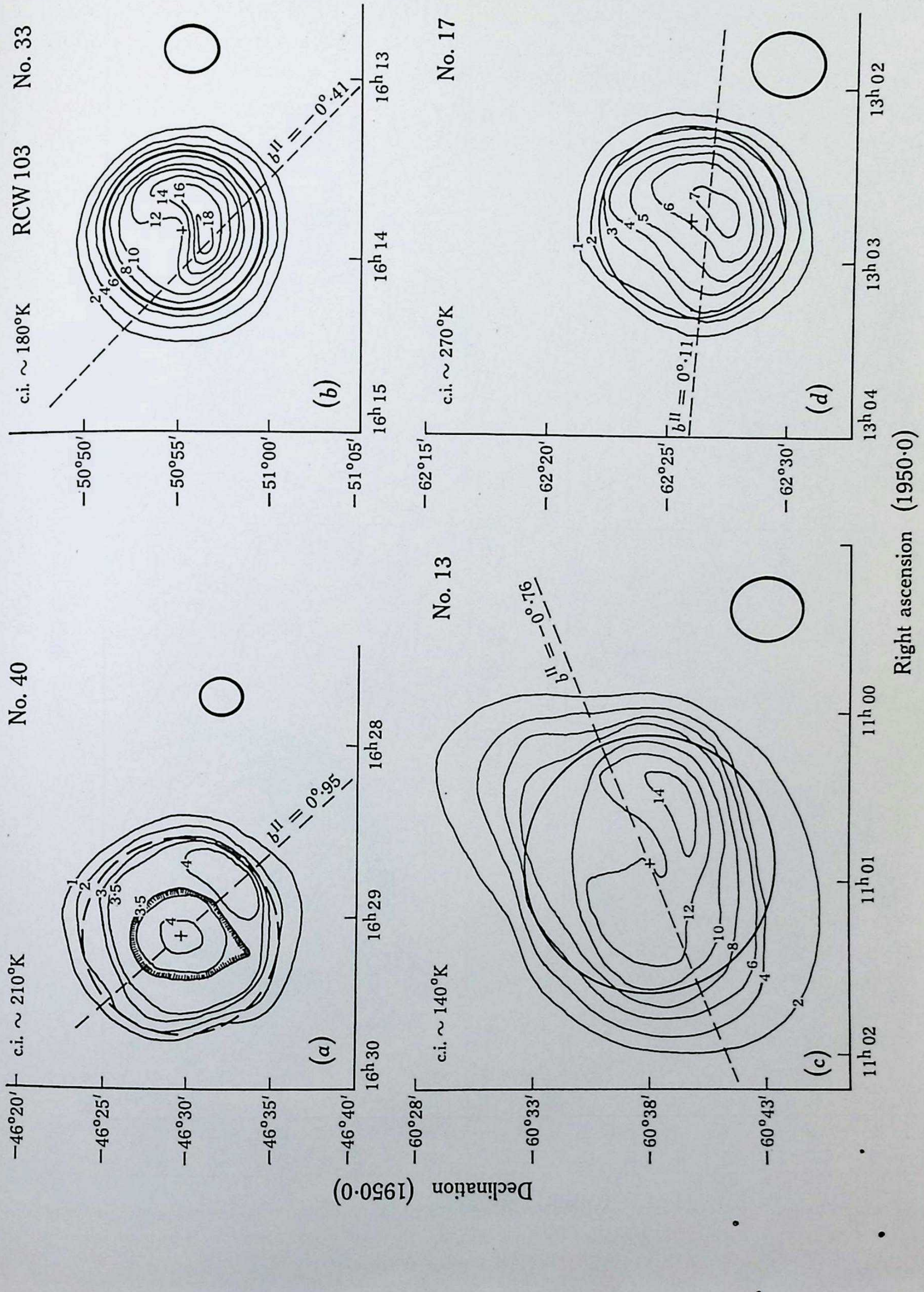
c.i. ~ 210°K
No. 40
(a)
$b^{II} = 0°.95$
1
2
3
3·5
3·5
4
4
−46°20′
−46°25′
−46°30′
−46°35′
−46°40′
16h30
16h29
16h28
c.i. ~ 180°K
RCW 103
No. 33
(b)
$b^{II} = -0°.41$
2
4
6
8
10
12
14
16
18
−50°50′
−50°55′
−51°00′
−51°05′
16h15
16h14
16h13
c.i. ~ 140°K
No. 13
(c)
$b^{II} = -0°.76$
2
4
6
8
10
12
14
−60°28′
−60°33′
−60°38′
−60°43′
11h02
11h01
11h00
c.i. ~ 270°K
No. 17
(d)
$b^{II} = 0°.11$
1
2
3
4
5
6
7
−62°15′
−62°20′
−62°25′
−62°30′
13h04
13h03
13h02
Declination (1950·0)
Right ascension (1950·0)

Figs. 2(*a*)–2(*d*)

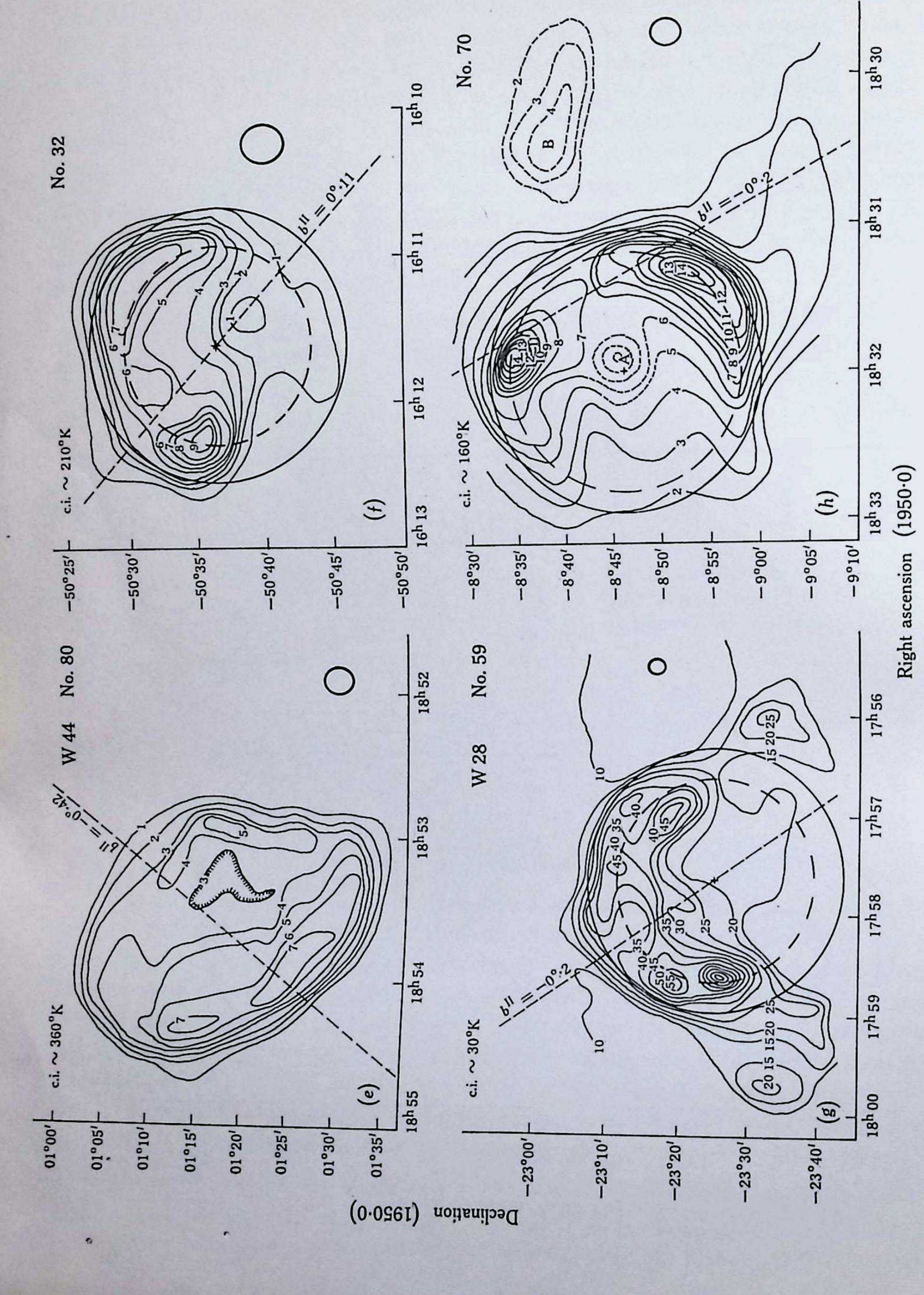
W 44 No. 80
c.i. ~ 360°K
(e)
$b^{II} = -0°.42$
No. 32
c.i. ~ 210°K
(f)
$b^{II} = 0°.11$
W 28 No. 59
c.i. ~ 30°K
(g)
$b^{II} = -0°.2$
No. 70
c.i. ~ 160°K
(h)
$b^{II} = -0°.2$
A
B
01°00′
01°05′
01°10′
01°15′
01°20′
01°25′
01°30′
01°35′
18h 55
18h 54
18h 53
18h 52
−50°25′
−50°30′
−50°35′
−50°40′
−50°45′
−50°50′
16h 13
16h 12
16h 11
16h 10
−23°00′
−23°10′
−23°20′
−23°30′
−23°40′
18h 00
17h 59
17h 58
17h 57
17h 56
−8°30′
−8°35′
−8°40′
−8°45′
−8°50′
−8°55′
−9°00′
−9°05′
−9°10′
18h 33
18h 32
18h 31
18h 30
Declination (1950·0)
Right ascension (1950·0)

Figs. 2(e)–2(h)

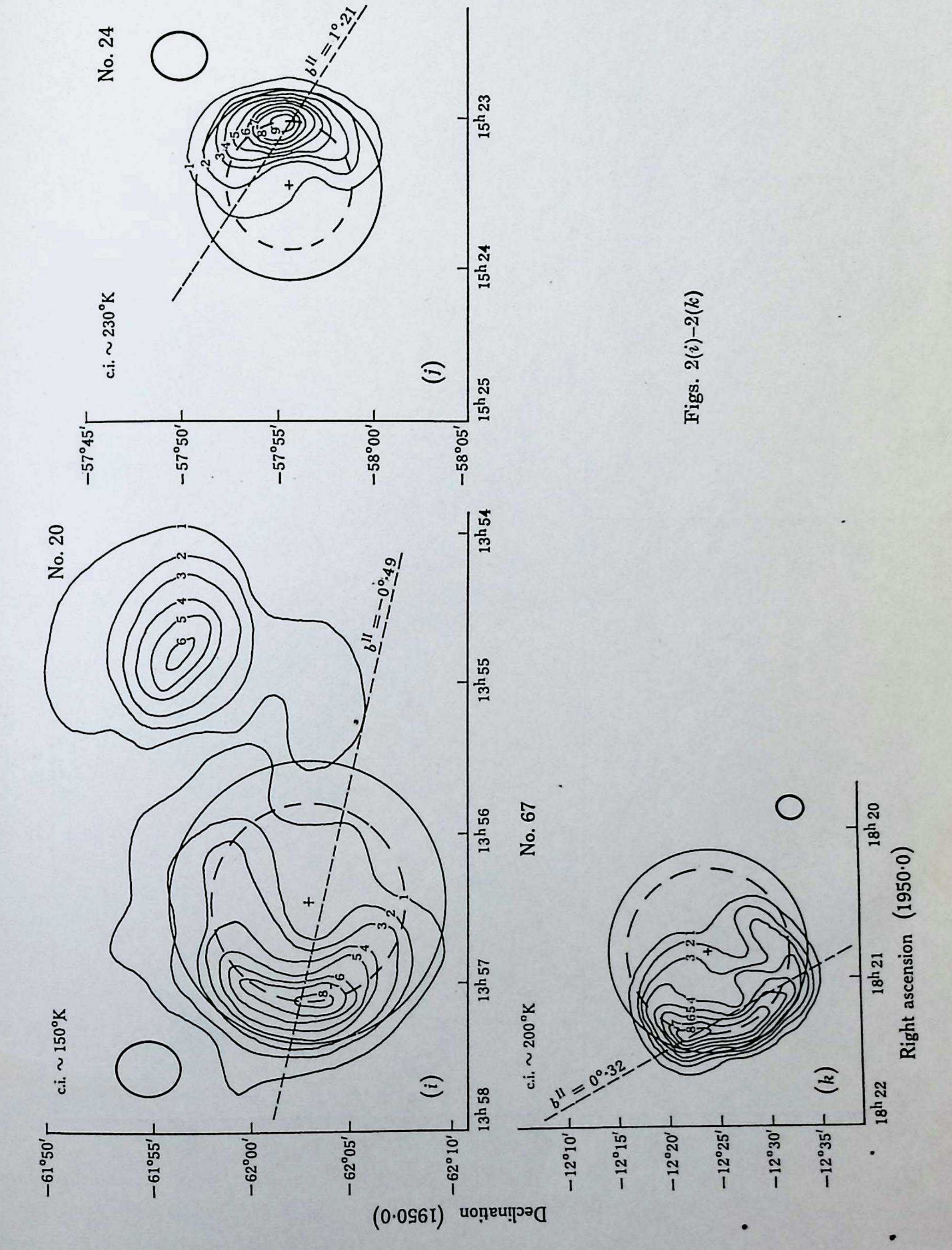
c.i. ~ 150°K
No. 20
$b^{II} = -0°.49$
(i)
c.i. ~ 230°K
No. 24
$b^{II} = 1°.21$
(j)
c.i. ~ 200°K
No. 67
$b^{II} = 0°.32$
(k)
−61°50′
−61°55′
−62°00′
−62°05′
−62°10′
13h58
13h57
13h56
13h55
13h54
−57°45′
−57°50′
−57°55′
−58°00′
−58°05′
15h25
15h24
15h23
−12°10′
−12°15′
−12°20′
−12°25′
−12°30′
−12°35′
18h22
18h21
18h20
Declination (1950·0)
Right ascension (1950·0)

Figs. 2(i)–2(k)

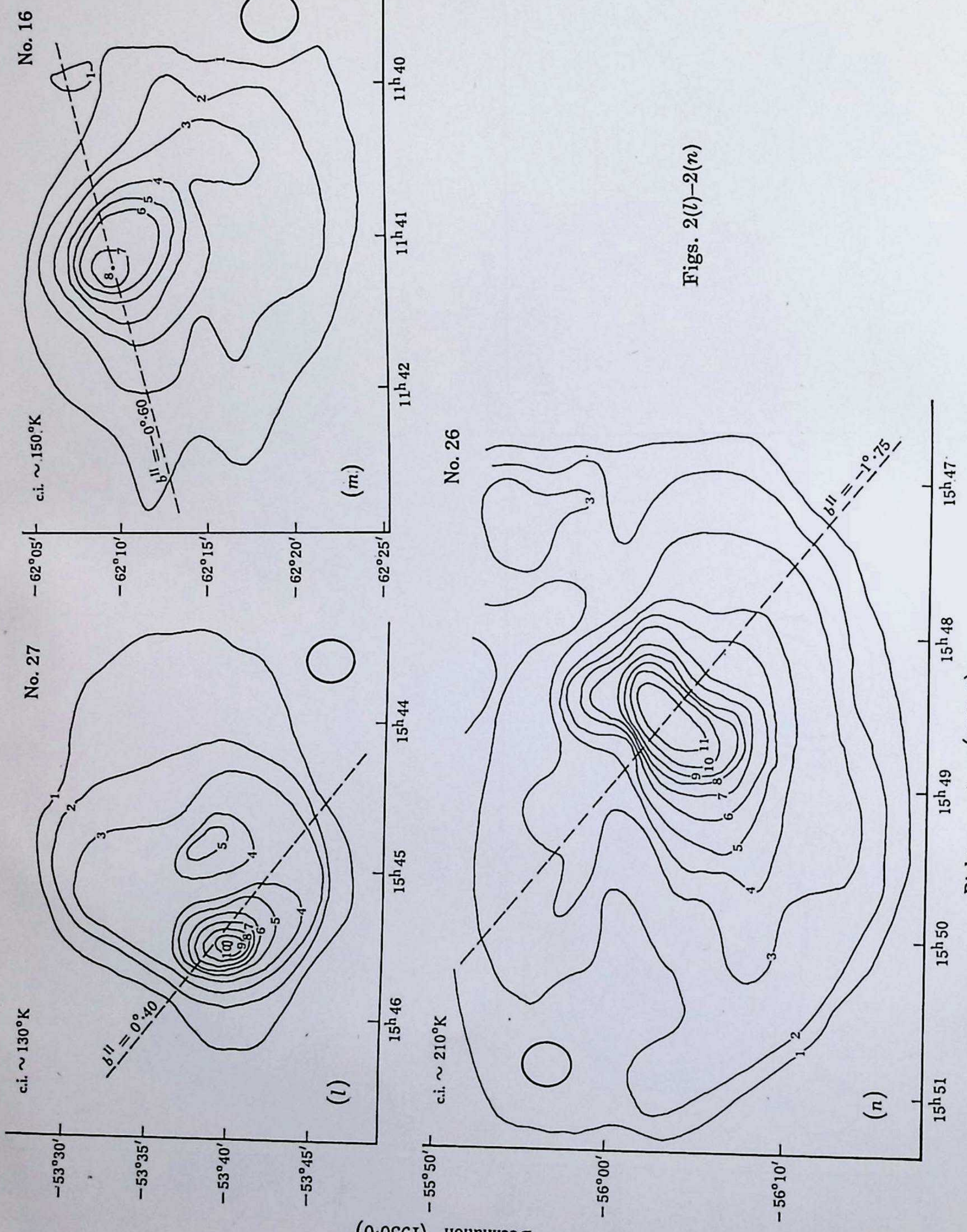
No. 27
c.i. ∼ 130°K
$b^{II} = 0°·40$
(l)
−53°30′
−53°35′
−53°40′
−53°45′
15h44
15h45
15h46
No. 16
c.i. ∼ 150°K
$b^{II} = -0°·60$
(m)
−62°05′
−62°10′
−62°15′
−62°20′
−62°25′
11h40
11h41
11h42
No. 26
c.i. ∼ 210°K
$b^{II} = -1°·75$
(n)
−55°50′
−56°00′
−56°10′
15h47
15h48
15h49
15h50
15h51
Right ascension (1950·0)
Declination (1950·0)
1
2
3
4
5
6
7
8
9
10
11

Figs. 2(l)–2(n)

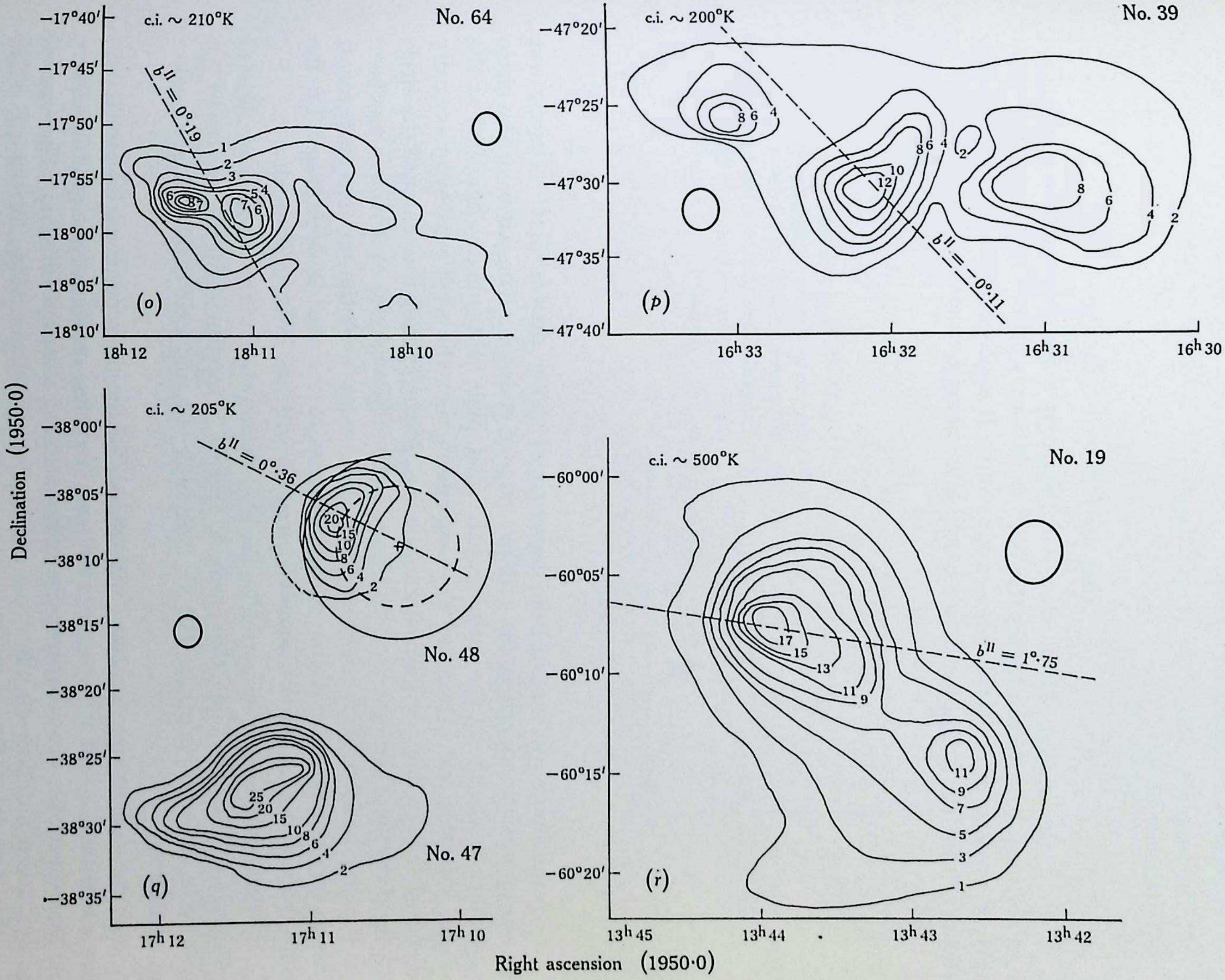
c.i. ~ 210°K
No. 64
$b^{II} = 0°.19$
(o)
c.i. ~ 200°K
No. 39
$b^{II} = -0°.11$
(p)
c.i. ~ 205°K
$b^{II} = 0°.36$
No. 48
No. 47
(q)
c.i. ~ 500°K
No. 19
$b^{II} = 1°.75$
(r)
−17°40′
−17°45′
−17°50′
−17°55′
−18°00′
−18°05′
−18°10′
18h12
18h11
18h10
−47°20′
−47°25′
−47°30′
−47°35′
−47°40′
16h33
16h32
16h31
16h30
−38°00′
−38°05′
−38°10′
−38°15′
−38°20′
−38°25′
−38°30′
−38°35′
17h12
17h11
17h10
−60°00′
−60°05′
−60°10′
−60°15′
−60°20′
13h45
13h44
13h43
13h42
Declination (1950·0)
Right ascension (1950·0)

Figs. 2(o)–2(r)

The contours are shown in Figures 2(*a*)–2(*r*). It is clear that few sources can be described as shells of emission. Two classes of sources can be distinguished:

(*a*) The sources of this group (Figs. 2(*a*)–2(*k*)) are consistent with a shell of emission, or at least a fraction of a shell.

(*b*) The sources of this group (Figs. 2(*l*)–2(*r*)) are amorphous masses, about which little can be said.

Class (*a*) *Sources*

Since the majority of the sources of this group show only a fraction of a shell, it is pertinent to enquire whether this is an evolutionary effect. Although there is no way, at present, of measuring the age of a source, it appears (on the basis of the two theories) that the brightness is a reasonable measure.

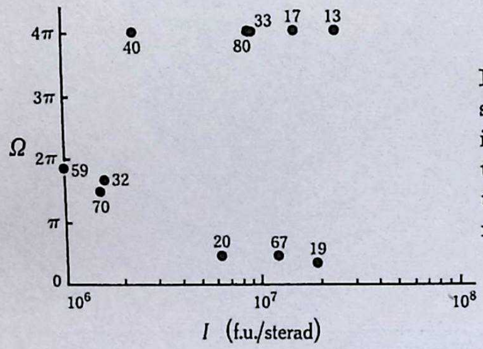

Fig. 3.—Plot of the class (*a*) sources of the catalogue, showing source brightness I versus the solid angle Ω subtended (at the site of the outburst) by the region of emission.

An estimate was made of the degree to which the shell is filled. A circle was drawn approximately concentric with the ridge of emission. The centre of the circle was taken as the site of the outburst. The solid angle subtended by the shell at the centre was then calculated, on the assumption that the shell was symmetrically disposed about a line, perpendicular to the line of sight, joining the centre of the circle to the centroid of the emission. In Figure 3 the solid angle for each source has been plotted as a function of its brightness. It is clear that no evolutionary trend is present, which suggests that the degree of completeness of the shell is determined by the outburst and not by the subsequent interaction with the interstellar medium.

This conclusion is supported by the observation that, of the previously reported complete shell sources, one, Cassiopeia A, exceeds in brightness all the sources of the catalogue, whilst three others, HB 21, PKS 1439−62, and PKS 0902−38, are weaker in brightness.

Four sources were analysed with the aid of the table prepared by Hill (1967) to determine the shell parameters; the aerial response measured along a radius was compared with the predicted response of the aerial to a shell of emission. The sources analysed are numbers 40, 33, 13, and 17 of the catalogue (Figs. 2(*a*)–2(*d*)). The results are shown in Figure 4. In each case there is reasonable agreement between the predicted and the observed responses. The analysis indicates that for source number 13 the emission occurs in two shells; but since the observed response is in fact an average taken around the source, the particular values for the emissivity should be treated with caution. This source could have been analysed as an ellipsoid, in the manner described by Crowther (1966), but it is doubtful whether a significantly better fit to the observations would have been achieved.

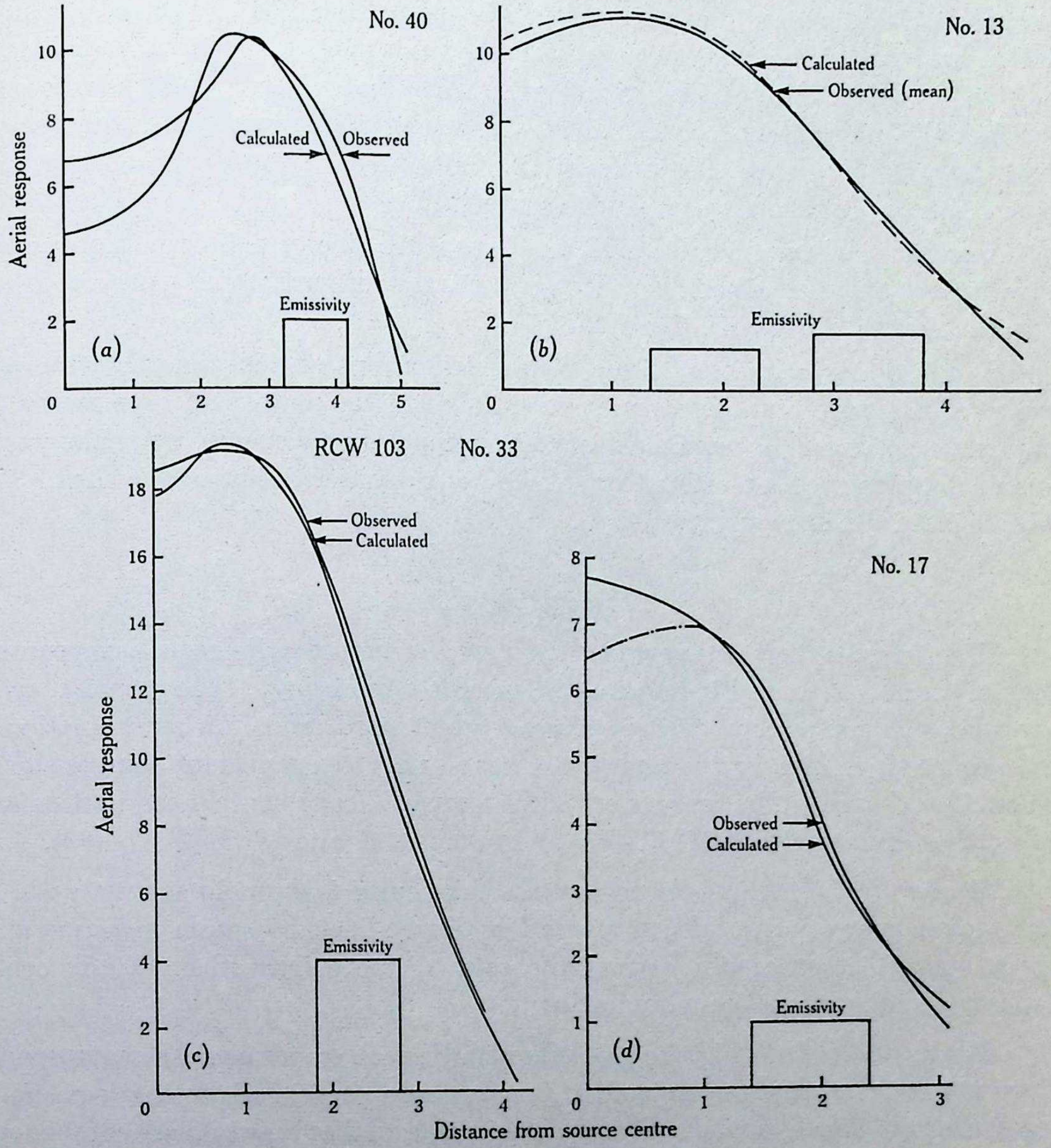

Figs. 4(*a*)–4(*d*).—Calculated radial response of the aerial to a shell of emission compared with the observed response. The unit of distance is half the half-power beamwidth. The radial dependence of the volume emissivity is also shown.

It will be noted that in the case of number 40, the central response is substantially less than the predicted value. (The analysis was in terms of shells of emission whose thicknesses were half the half-power beamwidth; analysis with shells of smaller thickness will not significantly alter this result.) Since this source has a fair degree of circular symmetry, it is pertinent to enquire whether an explanation for the low central value can be found which is independent of the line of sight. Absorption in the interior of the source would give a low central value, but this is unlikely to be the explanation for No. 40; the temperature of the gas ejected by the outburst would have to be less than 10^3 °K, the brightness temperature of the radiation. A low central value would result if the radiation were emitted preferentially tangentially to the surface of the shell. On the assumption that the radiation is due to the synchrotron mechanism, this would indicate a radial magnetic field, which implies a magnetic monopole. In this context, however, it is of interest to note that Mayer and Hollinger (1967) found polarization in Cassiopeia A that is consistent with a radial field. However, the magnitude of the polarization is small ($\sim 4 \cdot 5\%$) and would be inadequate to explain the observations of number 40. High resolution polarization observations would clearly be of great value in elucidating this source. It appears, however, that the symmetry requirements will have to be relaxed.

A partial shell symmetrically disposed about the line of sight would give a low central value. In view of the relatively large number of partial shells observed, this seems the most likely explanation.

W44 is clearly consistent with a shell emission, but no analysis was attempted in view of the large east–west asymmetry. For similar reasons of asymmetry, no analysis was made on the remaining sources of group (*a*). However, by analogy with the analysis presented, an estimate was made of the outer radius of the shell. This radius is indicated in Figures 2(*a*)–2(*k*).

Class (*b*) *Sources*

These sources show little evidence of a shell structure; the general appearance is one of a peak embedded in a broad region of low brightness. The question arises as to whether perhaps some of these sources are extragalactic. An extrapolation of source counts from high latitude surveys indicates that 3 extragalactic sources should be found by chance in the present set of 19 sources. Three sources are particularly noteworthy: number 19 (MSH 13−6*2*) and numbers 47 and 48 (MSH 17−6*3*).

Number 19 (Fig. 2(*r*)).—In appearance this source is strongly suggestive of an extragalactic source. In addition, neutral hydrogen-line absorption measurements suggest that this source lies beyond the solar distance from the galactic centre (Radhakrishnan, personal communication).

Numbers 47 and 48 (Fig. 2(*q*)).—Individually, each source could be a supernova remnant, but the close proximity of the two brightest sources of the catalogue must suggest that the sources are in some way associated, and that they also are components of an extragalactic source.

Search for Optical Features

A search was made of the optical fields of the 19 sources. Only in 1 case were optical features found. As indicated by Beard (1966) number 33 is in good agreement with the object RCW 103. The field, from an enlargement of an Uppsala Schmidt plate provided by Dr. G. Lynga, is shown in Figure 5. It will be noted that the filaments are in good agreement with the projection of the shell determined from the isophotes.

In addition to a search for gas filaments, a particular effort was made in the case of the sources 19, 47, and 48. A search along the major axis failed to reveal, in either case, any object of note. In particular, there was no evidence of a galaxy in the field. This was not unexpected, however, in view of the obscuration in the plane of the galactic disk.

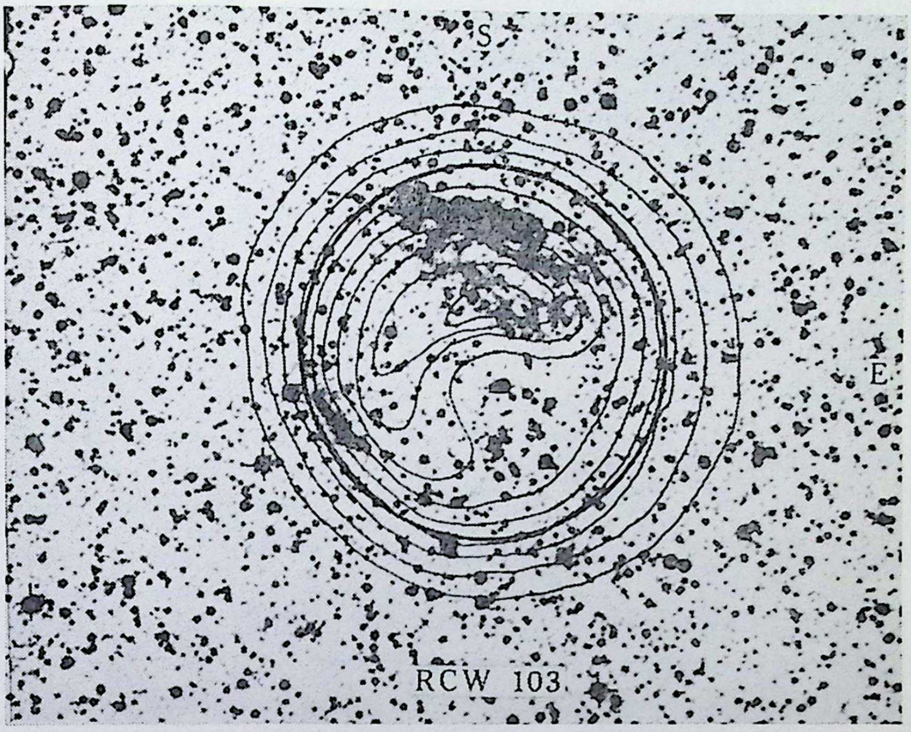

Fig. 5.—Field of the source RCW 103 (number 33 of the catalogue). The radio isophotes are also shown.

IV. Evolution of Spectral Index

Analyses by Kardashev (1963) and by de la Beaujardière (1966) of the loss mechanisms likely to be present in a supernova remnant indicate that the spectral index of the radiation is unlikely to evolve. Under some extreme conditions, however, the spectral index could steepen, in the sense of becoming more nonthermal. This result is in direct contrast to the findings of Harris (1962) and Pskovskii (1963), which indicate that the index flattens as the source ages. If this latter result were confirmed, it would indicate that either the conditions in the remnant differ substantially from the current estimates, or that the sources are not supernova remnants. In view of these consequences, the question was re-examined.

Estimates of the spectral index are available for 30 nonthermal sources of the catalogue. In addition, data have been published on a further 28. In Figure 6 the indices have been plotted as a function of the source brightness. There is little indication of an evolutionary trend. The mean of the low brightness sources is $-0\cdot44\pm0\cdot04$, and that of the high brightness sources is $-0\cdot52\pm0\cdot05$. The means lie just within their standard deviations, suggesting that the evolutionary trend, if present, is very slight. The spectral indices are centred on a value of $-0\cdot5$ with an r.m.s. scatter of about $0\cdot3$.

V. Evolution of Radiated Power

The two theories that have received most attention in the literature are due to Shklovskii (1960*a*) and Van der Laan (1962). According to Shklovskii's hypothesis, both the field and the particles are generated by the outburst and are situated within the expanding plasma shell. The assumption is then made that the expansion of the shell is adiabatic; a relation can then be determined between the source radius and the radiated flux. This can be expressed in the form

$$P \propto R^{-2\gamma}, \tag{1}$$

where P is the power per unit bandwidth radiated over all directions at the observing frequency, R the shell radius, and γ the exponent of the relativistic electron energy spectrum:

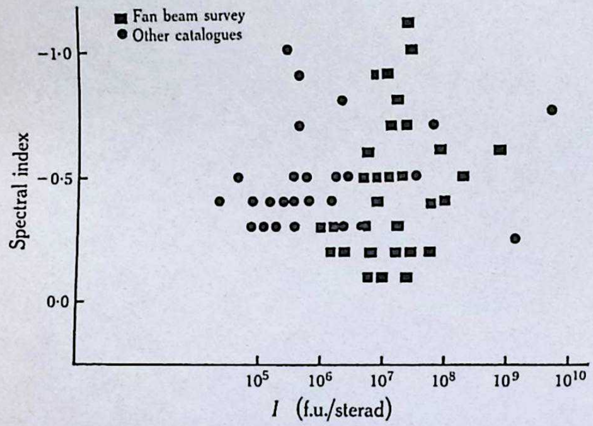

Fig. 6.—Plot of the distribution of the source spectral index as a function of its brightness I.

$$N(E)\,\mathrm{d}E = KE^{-\gamma}\,\mathrm{d}E\,.$$

Here γ is related to the radiation spectral index α by the expression

$$\alpha = -\tfrac{1}{2}(\gamma-1)\,.$$

Equation (1) was derived on the assumption that the source was a spherical mass rather than a shell. The same expression is obtained if the source is a shell whose thickness is a constant fraction of the radius.

The rate at which the shell thickness increases is determined by the gas and the magnetic pressures. (Essentially, the problem is that of expansion into a vacuum.) Thus, if the magnetic field is weak, the ratio of the shell thickness to the shell radius may decrease during the initial stages of the remnant's evolution. The limiting case is where the shell thickness is constant, and the evolution equation becomes

$$P \propto R^{-\frac{1}{2}(3\gamma-1)}\,. \tag{2}$$

Van der Laan's theory assumes the relativistic particles to be generated by the outburst, and to be trapped in the region between the expanding shell and the shock generated by the expansion. The magnetic field is due to a compression of the galactic medium. The evolution in this model, once the mass of the interstellar gas swept up by the shell exceeds the mass of the shell, is given approximately by the form

$$P \propto R^{-3\gamma}\,. \tag{3}$$

There are few ways in which these theories can be tested. There is no clear evidence to indicate whether the radio source lies within the expanding plasma shell or in the shocked region. This is because of the small number of cases where optical filaments have been found at the site of a radio source, the difficulty in defining the position of the plasma shell, and the insufficient resolution of the radio observations. The lack of evolution in the spectral index indicates that the current estimates of the conditions within the shell are plausible, without deciding between the two theories. However, the differences between the models in the predicted evolution of the radiated power are substantial and should provide a reasonable basis for testing.

The secular decrease in the flux density can be calculated if the expansion rate of the shell is known. This is the basis of the prediction made in 1960 by Shklovskii (1960*b*) for Cassiopeia A. The observed value of $\sim 2\%$ is consistent with equations (1) and (2). The value from equation (3) seems rather higher than can be accounted for with the observational errors.

An evolutionary path can be reconstructed if the distances are known to a number of sources which are assumed to have similar evolutionary paths. There are five sources at known distances: Cassiopeia A and the Cygnus Loop in the Milky Way (Minkowski 1959) and N49, N63A, and N132D in the Large Magellanic Cloud (Westerlund and Mathewson 1966). The possible evolutionary paths are shown in Figure 7, along with the points corresponding to the five sources. It is clear from equations (1), (2), and (3) that an allowance ought to be made for the different spectral indices. Such correction is not warranted (at present) in view of the uncertainties in the observed parameters. The models are based on a spectral index of $-0\cdot5$, the mean of all the nonthermal sources.

Each model is of the form

$$P = AR^{-g}\,.$$

The constant A was determined from the curve of index $-g$ which best fits the data.

Equation (2) seems the best fit, although the observations cannot exclude the other two models.

Since the distance is not known for the sources of the catalogue, a statistical method was tried. Let the frequency of occurrence of the supernova outbursts be f, and assume (for the moment) that all supernova remnants of given brightness are detected. The number of remnants brighter than a given value I is

$$N(\geqslant I) = f_0\, t(I)\,, \tag{4}$$

where $t(I)$ is the age of a remnant whose brightness is I and f_0 is the frequency of supernovae outbursts in the longitude range $180° < l^{\mathrm{II}} < 40°$. On the assumption that the outbursts all occur within 10 kpc of the galactic centre, f_0 can be related to the frequency f for the whole galaxy by

$$f \sim 1{\cdot}2 f_0 .$$

Equations (1), (2), and (3) can be reformulated in terms of brightness I,

$$I = S/\Omega = P/4\pi^2R^2 = (A/4\pi^2)R^{-g-2},$$

where S is the integrated flux density and Ω the solid angle subtended by the source (derived from the observed half-power dimensions).

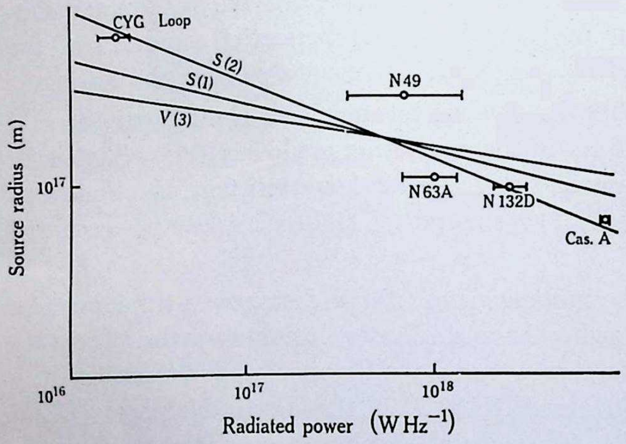

Fig. 7.—Evolutionary relation between the radius of a remnant and its radiated power, calculated on the basis of the three models of a supernova remnant: S(1), Shklovskii (equation (1)); S(2), Shklovskii (equation (2)); V(3), Van der Laan (equation (3)). Points corresponding to the five sources are also plotted.

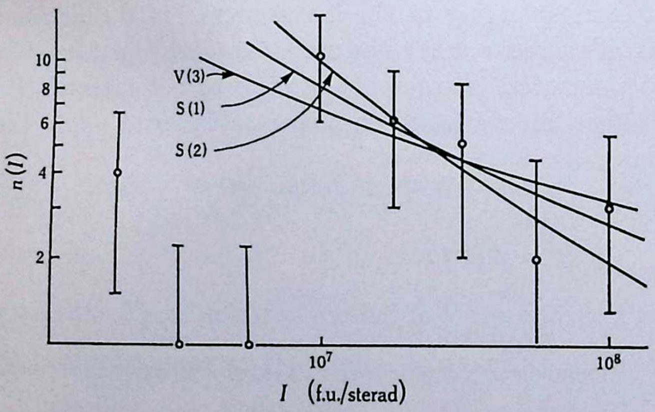

Fig. 8.—Differential number brightness distribution $n(I)$ calculated for the three models, $n(I) = N(\geqslant 0{\cdot}56\,I) - N(\geqslant I)$.

An analysis of the expansion of the plasma shell yields a relation between the shell radius and its age:

$$t = \frac{R}{V_0}\left(1+\frac{\pi\rho}{3M_0}(\alpha R)^3\right), \tag{5}$$

where ρ is the density of the interstellar medium ($\sim 0{\cdot}5$ hydrogen atom/cm), M_0 the mass of the shell ($\simeq 10\ M_\odot$), and V_0 the initial velocity of the shell (~ 7000 km/sec). This expression is derived on the assumption that there is no energy input after the initial explosion, and no interaction between different parts of the shell. The constant

α (~ 1) accounts for the difference between the radius of the shell and the radius of the shock front. The precise value is of little importance, in view of the uncertainty in ρ and M_0. Thus

$$t(I) = \left(\frac{A}{4\pi^2 I}\right)^{1/(g+2)} \frac{1}{V_0}\left\{1+\frac{\pi\rho\alpha^3}{3M_0}\left(\frac{A}{4\pi^2 I}\right)^{3/(g+2)}\right\}. \tag{6}$$

In Figure 8 the function $n(I) = N(\geqslant 0\cdot 56\,I) - N(\geqslant I)$ has been plotted. This function, rather than $N(\geqslant I)$, was chosen in order to minimize the contaminating effect of the class II sources included by chance in the catalogue. The 32 sources in this figure are drawn from the catalogue and refer to the longitude range $180° < l^{\mathrm{II}} < 40°$. A number of these sources are small relative to the aerial beamwidth and no contours have been produced. No estimate of the spectral index is available for some of the sources; they are therefore not included in Figure 2. Also shown in Figure 8 are the functions $n(I)$ calculated from equations (1), (2), and (3). The scale factor of the calculated functions is the frequency of occurrence f. Since this is not known, the curves have been drawn in the position of best fit. The frequency corresponding to these curves is given in Table 1. The values are in good agreement with estimates made by other observers.

TABLE 1

FREQUENCY OF SUPERNOVA OUTBURSTS

Technique	$\tau = 1/f$ (yr)	Reference
Supernova remnants	$50\pm30\%$	Present paper (equation (1))
	90	Present paper (equation (2))
	40	Aizu and Tabara (1967)
	30–60	Shklovskii (1955)
	50	Minkowski (1964)
Search for supernovae in external galaxies	450	Zwicky (1965)
	60	Bertaud (1961)
Cosmic ray density*	100	Kaplon and Skadron (1966)
	$10^{2\pm0\cdot5}$	Rosen and Milford (1966)
	50	Ginzburg and Syrovatskii (1964)

* In this method the supernova outbursts are assumed to be the sites of cosmic ray production. Subject then to the assumed efficiency of the generation process, an estimate can be made of the frequency of the outbursts from the cosmic ray density.

Because of the nature of the instrument used in the primary survey, the limiting condition governing the inclusion of a source in the catalogue is a complex function of the integrated flux density and the angular size. The function $n(I)$ is therefore affected in the low brightness region. No attempt has been made to calculate $n(I)$ in this region, as the function depends critically on the distribution of supernovae in the Galaxy. The brightness corresponding to the maximum of $n(I)$ has been estimated, on the assumption that the distribution is uniform out to 10 kpc. The maximum occurs in the interval $10^7 < I < 1\cdot 8\times 10^7$, which is reasonably consistent with Figure 8.

These various tests suggest that Van der Laan's theory is a poor fit to the data, and that either variant of Shklovskii's theory is plausible. The present statistical method indicates that the remnants do have a common evolutionary path but, due to the uncertainties of the technique, this path is not yet well defined. It is likely that the evolutionary path could be recovered if the distance were known to a number of sources. The neutral hydrogen absorption measurements may be of particular value in this context, even though the errors in their results may be large.

VI. ACKNOWLEDGMENTS

This work was supported by grants from the U.S. National Science Foundation and the Australian Research Grants Committee. I should like to thank Professor B. Y. Mills for his helpful suggestions and I am indebted to Dr. G. Lynga for providing photographic plates of the galactic plane taken with the Uppsala Schmidt camera. I gratefully acknowledge a CSIRO Studentship and a General Motors–Holden Scholarship.

VII. REFERENCES

AIZU, H., and TABARA, H. (1967).—*Prog. theor. Phys., Osaka* **37**, 296.
BEARD, M. (1966).—*Aust. J. Phys.* **19**, 141.
DE LA BEAUJARDIÈRE, O. (1966).—*Annls Astrophys.* **29**, 345.
BERTAUD, C. (1961).—*Annls Astrophys.* **24**, 516.
CROWTHER, H. A. (1966).—*Observatory* **85**, 110.
ELSASSER, H., and HAUG, V. (1960).—*Z. Astrophys.* **50**, 121.
GINZBURG, V. L., and SYROVATSKII, S. I. (1964).—"Origin of Cosmic Rays." (Pergamon: Oxford.)
HARRIS, D. (1962).—*Astrophys. J.* **135**, 661.
HILL, E. R. (1967).—*Aust. J. Phys.* **20**, 297.
KAPLON, M. F., and SKADRON, G. (1966).—*Rev. Geophys.* **4**, 177.
KARDASHEV, N. S. (1963).—*Soviet Astr.* **7**, 740.
KERR, F. J. (1962).—*Mon. Not. R. astr. Soc.* **126**, 327.
KESTEVEN, M. J. L. (1968).—*Aust. J. Phys.* **21**, 369.
LARGE, M. I., MATHEWSON, D. S., and HASLAM, C. S. T. (1961).—*Mon. Not. R. astr. Soc.* **123**, 113.
MATHEWSON, D. S., HEALEY, J. R., and ROME, J. M. (1962).—*Aust. J. Phys.* **15**, 354.
MAYER, C. H., and HOLLINGER, J. P. (1967).—*Astr. J.* **72**, 815.
MILLS, B. Y. (1959).—Symp. IAU No. 9 (Paris 1958) p. 431.
MINKOWSKI, R. (1959).—Symp. IAU No. 9 (Paris 1958) p. 315.
MINKOWSKI, R. (1964).—*A. Rev. Astr. Astrophys.* **2**, 247.
PSKOVSKII, Y. P. (1963).—*Soviet Astr.* **7**, 17.
ROSEN, S., and MILFORD, S. N. (1966).—*Astr. J.* **71**, 385.
SHKLOVSKII, I. S. (1955).—"Cosmic Radio Waves." (Harvard Univ. Press.)
SHKLOVSKII, I. S. (1960*a*).—*Soviet Astr.* **4**, 243.
SHKLOVSKII, I. S. (1960*b*).—*Soviet Astr.* **4**, 355.
VAN DER LAAN, H. (1962).—*Mon. Not. R. astr. Soc.* **124**, 179.
WESTERLUND, B. E., and MATHEWSON, D. S. (1966).—*Mon. Not. R. astr. Soc.* **131**, 371.
ZWICKY, F. (1965).—"Stars and Stellar Systems." Vol. 8. (Univ. Chicago Press.)

SHORT COMMUNICATIONS

COSMIC RAY INTENSITY INCREASE ON JANUARY 28, 1967*†

By L. V. Sud‡

During the present solar cycle, which started in October 1964, the ground-based cosmic ray detectors have so far recorded two increases in the intensity of cosmic rays. The first one was observed on July 7, 1966 and the other on January 28, 1967. Both these events were somewhat unusual in their characteristics.

The July 7, 1966 increase was the smallest ever recorded and was associated with a visible solar flare in the most northerly location so far known to produce an increase of cosmic ray intensity in ground-level detectors (Ahluwalia, Sud, and Schreier 1967).

The January 28, 1967 increase was a moderate one with a maximum amplitude of $\gtrsim 24\cdot1\%$ recorded at Sulphur Mt. and a minimum amplitude of $\sim 1\cdot4\%$ recorded at Dallas. The increase was isotropic throughout. The rigidity spectrum of the increase was rather flat with $\gamma = -1\cdot7$ and this value remained constant from the time of the maximum through the intensity decay. The decay was slow with a characteristic decay time of $\sim 5\cdot2$ hr.

In Figure 1 are plotted the pressure-corrected hourly data from 23 stations for January 28, 1967. Table 1 summarizes the information about the observing stations and their detectors, whose data have been used for this analysis. From Figure 1 the following features can be easily seen.

(1) The increase had a large rise time ($\sim$ 3–4 hr).

(2) Stations having a vertical cutoff rigidity of $> 4\cdot35$ GV did not observe the increase.

(3) The largest increase was recorded by the Sulphur Mt. super-neutron monitor and the smallest by the Dallas monitor.

(4) None of the meson monitors registered the increase.

In Figure 2 are plotted pressure-corrected 5 min neutron monitor data from Churchill, Alert, Resolute, Goose Bay, Inuvik, and Deep River. Onset times have been indicated by arrows at points O and are given in the caption to the figure. There is a spread of about 20 min in the onset times. In view of the fact that there are large statistical errors ($\sim 0\cdot4\%$) associated with these data, we are led to believe that the additional flux was isotropic even at the outset. The time at which

---

* This research was supported in part by the U.S. Air Force Office of Scientific Research under grant No. AF-AFOSR-319-66.

† Manuscript received April 5, 1968.

‡ Laboratorio de Física Cósmica, Universidad Mayor de san Andres, La Paz, Bolivia, South America.

Aust. J. Phys., 1968, **21**, 755–9

maximum flux was recorded at different stations together with the magnitude of the increase, determined from hourly data (except for College), have also been listed in Table 1.

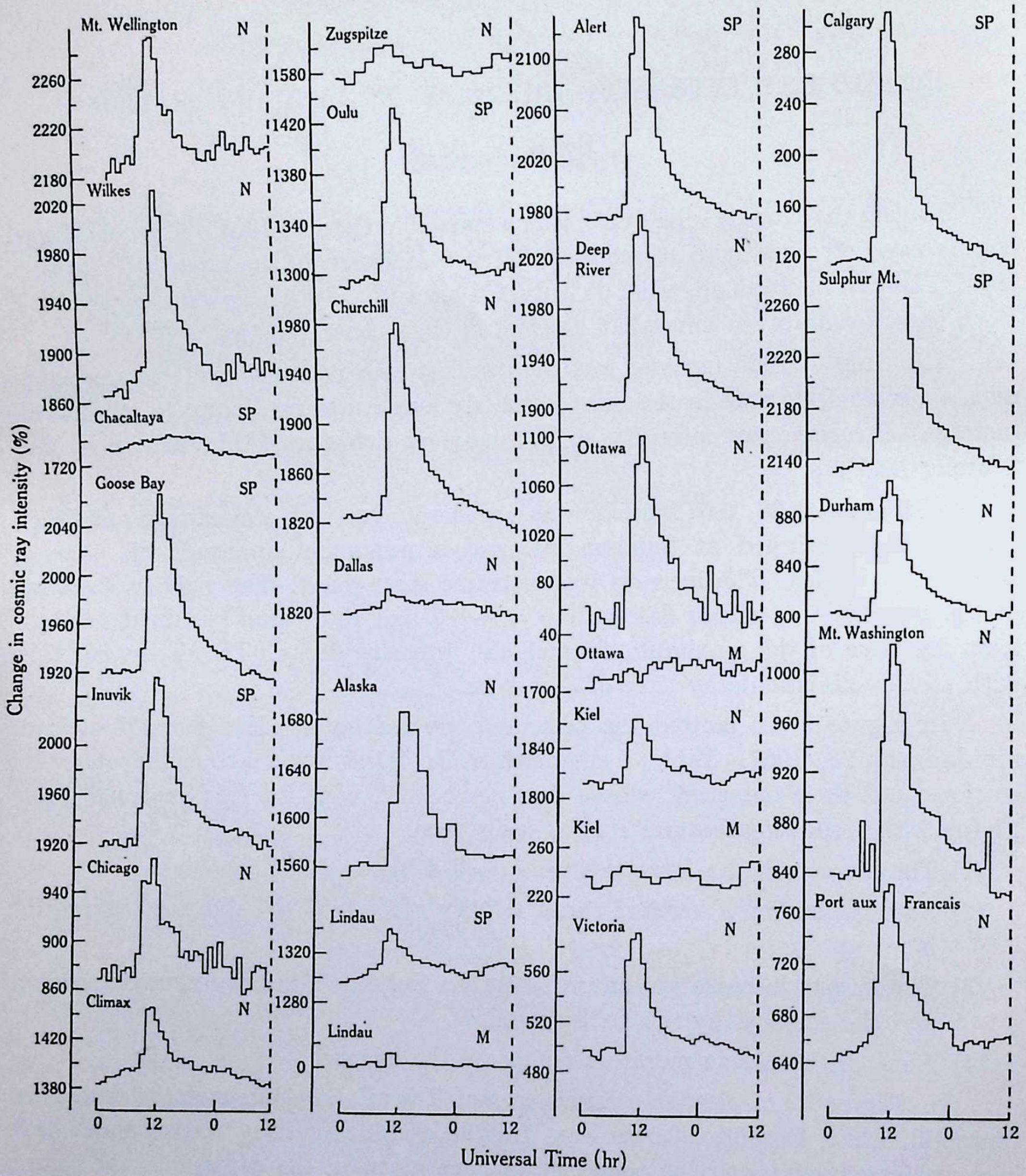

Fig. 1.—Pressure-corrected hourly data from 23 stations for the cosmic ray intensity increase on January 28, 1967 (N, neutron detector; M, meson detector; SP, super-neutron detector).

We find that the rigidity spectrum for the event, starting from the maximum phase, remains constant throughout the decay. The value of the exponents is 1·7±0·2. Kodama (1967) has obtained a similar value for γ from the multiplicity measurements during the flare period. This value is very small compared with that for other cosmic ray increases. Its constancy throughout the event suggests a complete isotropy of the additional flux.

Following McCracken (1962), Figure 3 shows the dependence of cosmic ray flux upon direction at 1400 U.T. on January 28, 1967. The distribution of points and the corresponding flux magnitudes around the position of the Sun confirm that there were no preferred directions of arrival for this event and that the flux was more or less isotropic.

Table 1

OBSERVING STATIONS AND COSMIC RAY INCREASE DATA

N = neutron monitor, M = meson monitor, n.o. = increase not observed

Station	Vertical Cutoff (GV)	Detector	Time of Increase (hr U.T.)		Magnitude of Increase* (%)	
			N	M	N	M
Calgary	1·09	N	11·5±0·5	—	19·4	—
Sulphur Mt.†	1·14	N		—	> 24·1	—
Churchill	0·21	N	11·5±0·5	—	15·4	—
Durham	1·41	N	11·5±0·5	—	11·2	—
Mt. Washington	1·24	N	12·5±0·5	—	18·2	—
Port aux Francais	1·19	N	12·5±0·5	—	13·4	—
Victoria	1·86	N	11·5±0·5	—	9·7	—
Ottawa	1·08	N, M	11·5±0·5	n.o.	15·6	n.o.
Lindau	3·00	N, M	10·5±0·5	n.o.	4·3	n.o.
Kiel	2·29	N, M	11·0±0·5	n.o.	5·1	n.o.
Deep River	1·02	N	11·5±0·5	—	14·9	—
College‡	0·54	N	11·0±1·0	—	12·3	—
Chacaltaya	13·10	N	n.o.	—	n.o.	n.o.
Alert	< 0·5	N	11·5±0·5	—	15·7	—
Goose Bay	0·52	N	11·5±0·5	—	14·7	—
Inuvik	< 0·18	N	11·5±0·5	—	13·8	—
Dallas	4·35	N	9·5±0·5	—	1·5	—
Chicago	1·72	N	11·5±0·5	—	9·7	—
Climax	3·03	N	11·5±0·5	—	5·2	—
Zugspitze	4·24	N	11·0±1·0	—	3·0	—
Oulu	0·81	N	11·5±0·5	—	13·2	—
Wilkes	< 0·05	N	11·5±0·5	—	15·3	—
Mt. Wellington	0·05	N	11·5±0·5	—	10·1	—

* Measured from the point where monotonic increase began.

† A break in the data from this station prevented determination of the time of increase.

‡ Only bihourly data were available from this station.

The decay of intensity followed an exponential law. Mathews and Wilson (1967) found that the characteristic decay time was $\sim 5{\cdot}2$ hr. This implies a somewhat slower decay than for most of the other increases.

Wilson, Mathews, and Johnson (1967) found the absorption length of the additional flux to be 103 ± 3 g cm^{-2}, which is in agreement with the value for solar flux and suggests that the additional flux was of solar origin.

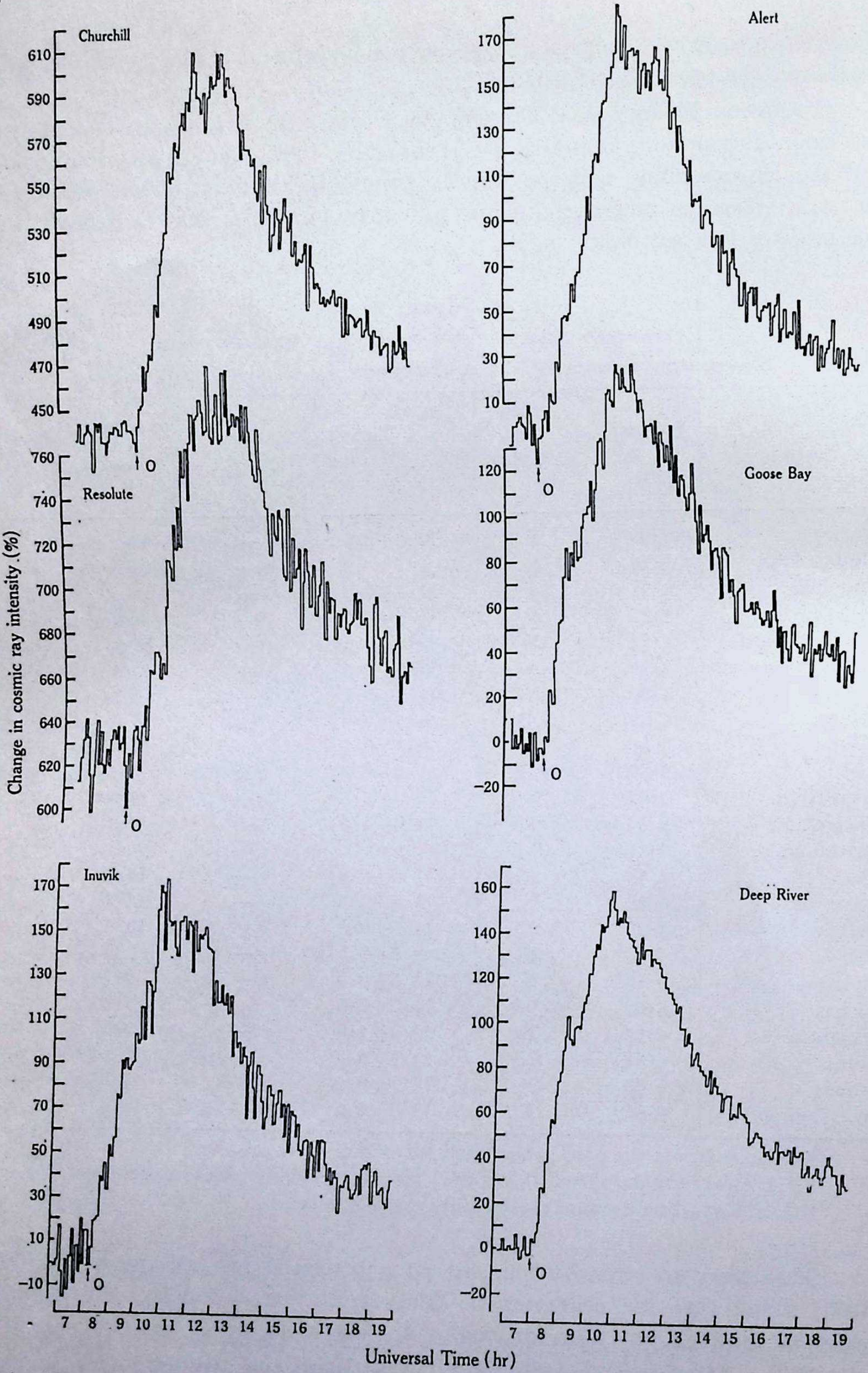

Fig. 2.—Pressure-corrected 5 min neutron data from 6 stations for the cosmic ray intensity increase on January 28, 1967. Arrows at the points O indicate the onset times: Churchill 8·40±0·04, Alert 8·08±0·04, Resolute 8·40±0·04, Goose Bay 8·33±0·04, Inuvik 8·40±0·04, Deep River 8·25±0·04 hr U.T.

The most unusual feature of the January 28, 1967 increase is that it is not possible to associate it with any flare on the visible side of the Sun. There is no magnetic storm a week before or after the event. The other associated phenomena, such as PCA or ionospheric disturbances, that are normally expected with an increase of this magnitude were not observed. This leads to the possibility that fairly large increases in intensity of cosmic rays, of solar origin, may occur without any association with a visible solar flare.

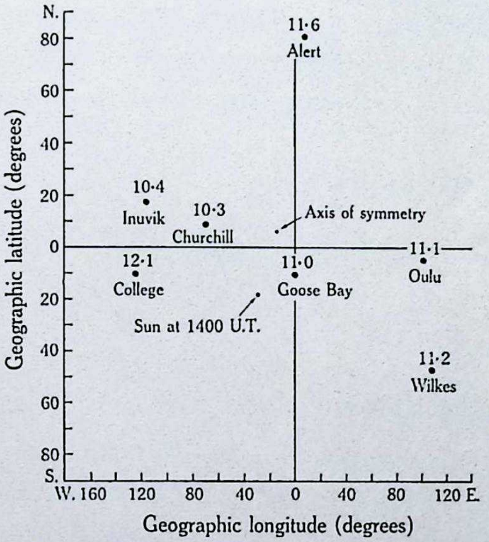

Fig. 3.—Dependence of cosmic ray flux of solar origin on direction at 1400 U.T. on January 28, 1967.

The author is grateful to Dr. H. S. Ahluwalia for his interest in the work, and to the investigators whose data have been used for this analysis. Computational assistance from Mr. A. Carrasco is also gratefully acknowledged.

References

Ahluwalia, H. S., Sud, L. V., and Schreier, M. (1967).—The increase in the low energy cosmic ray intensity on July 7, 1966. *Ann. IQSY* (in press).
Kodama, M. (1967).—10th Int. Conf. on Cosmic Rays, Calgary, 1967.
McCracken, K. G. (1962).—*J. geophys. Res.* **67**, 423.
Mathews, T., and Wilson, B. G. (1967).—10th Int. Conf. on Cosmic Rays, Calgary, 1967.
Wilson, B. G., Mathews, T., and Johnson, R. H. (1967).—*Phys. Rev. Lett.* **18**, 675.

THE PROPERTIES OF A DRIFTING AND DIFFUSING PULSE OF ELECTRONS AND TOWNSEND'S COEFFICIENT OF IONIZATION α_T†

By L. G. H. Huxley‡

When diffusion is active in an ionizing stream of electrons the experimental Townsend coefficient of ionization α_T is not simply the ratio ν_i/W of ν_i, the average rate of volume ionization per electron, to the drift speed W of the electrons, as was implied by Townsend's interpretation of α_T, but is given by the formula (Huxley 1959)

$$\alpha_T = \lambda - \mu = \lambda\{1-(1-2\alpha_i/\lambda)^{\frac{1}{2}}\}, \tag{1}$$

in which $2\lambda = W/D$, where D is the coefficient of diffusion in the gas, $\alpha_i = \nu_i/W$, and $\mu = (\lambda^2 - 2\lambda\alpha_i)^{\frac{1}{2}}$. Also

$$\text{as} \quad D\to 0, \qquad \lambda\to\infty \quad \text{and} \quad \alpha_T\to\alpha_i = \nu_i/W, \tag{2}$$

in conformity with Townsend's interpretation of α_T.

These matters have been discussed recently in the literature (see Crompton 1967), and the theory of steady currents in gases has been given (Burch and Huxley 1967) in which the effects both of diffusion and of the electrodes are incorporated.

In what follows the properties of an ionizing and travelling pulse of electrons, spreading by diffusion as it advances through the gas, are examined, and a measure of insight into the physical basis of formula (1) is thus achieved.

It is assumed throughout that D and W are constant and thus independent of the spatial coordinates (x, y, z) and of the time t.

Equation of Continuity

The analysis is based on the equation of continuity, which here is

$$\mathrm{d}n/\mathrm{d}t = D\,.\,\nabla^2 n - \overline{W}\,.\,\mathrm{grad}\,n + \nu_i\, n, \tag{3}$$

in which $n \equiv n(x, y, z, t)$ is the number density of the electrons. When $|W| = W_z = W$, then $\overline{W}\,.\,\mathrm{grad}\,n = W\,\partial n/\partial z$. It is therefore assumed without loss of generality that $\overline{W}$ is parallel to the axis $+0z$.

The one-dimensional number density is

$$q(z,t) = \int_{-\infty}^{\infty}\int_{-\infty}^{\infty} n\,\mathrm{d}x\,\mathrm{d}y\,,$$

and $q(z,t)\,\mathrm{d}z$ is the number of electrons contained between the planes z = constant and $z+\mathrm{d}z$ = constant. It is assumed that the stream is of finite lateral extent such that n and $\mathrm{grad}\,n$ are zero when $|x|$ and $|y|$ are large.

---

† Manuscript received June 24, 1968.

‡ 19 Glasgow Place, Hughes, Canberra, A.C.T. 2605.

Aust. J. Phys., 1968, **21**, 761–4

Apply the operator $\int_{-\infty}^{\infty}\int_{-\infty}^{\infty} \mathrm{d}x\,\mathrm{d}y$ to all terms of equation (3) to obtain

$$\frac{1}{D}\frac{\mathrm{d}q}{\mathrm{d}t} = \frac{\partial^2 q}{\partial z^2} - 2\lambda\frac{\partial q}{\partial z} + 2\lambda\alpha_{\mathrm{i}}\,q\,, \tag{4}$$

with

$$2\lambda = W/D\,, \qquad \alpha_{\mathrm{i}} = \nu_{\mathrm{i}}/W\,, \qquad q \equiv q(z,t)\,.$$

The flux F of particles across a plane $z =$ constant is (in unit time)

$$F = (W - D\,\partial/\partial z)\,q(z,t)\,.$$

Growth and Progress of a Pulse

Consider the following solution of equation (4)

$$q(z,t) = \tfrac{1}{2}N(\pi Dt)^{-\frac{1}{2}}\exp(\alpha_{\mathrm{i}}\,Wt)\exp\{-(z-Wt)^2/4Dt\}\,, \tag{5}$$

which represents a moving and diffusing pulse that begins from the plane $z = 0$ at $t = 0$ as a δ-function containing N particles.

Note that:

(1) The total population of the pulse at time t is

$$\int_{-\infty}^{\infty}\int_{-\infty}^{\infty} q(z,t)\,\mathrm{d}z = N\exp(\alpha_{\mathrm{i}}\,Wt)\;;$$

its growth factor is $\exp(\alpha_{\mathrm{i}}\,Wt) = \exp(\nu_{\mathrm{i}}\,t)$.

(2) The relative distribution of particles in the pulse is the same as that when $\nu_{\mathrm{i}} = 0$; that is to say, the "shape" of the pulse is unaffected by the process of ionization by collision when D, W, and ν_{i} are independent of position, as has been assumed.

(3) The distance z_{max} at which $q = q_{\mathrm{max}}$, its greatest value at a given time t, is $z = z_{\mathrm{max}} = Wt$; thus the "crest" of the pulse, which is also its centroid, progresses at speed W. Conversely, the time $t = t_{\mathrm{max}}$ at which the crest crosses the plane $z =$ constant is $t_{\mathrm{max}} = z/W$. Consequently, the pulse travels in the same manner as a pulse in which $\nu_{\mathrm{i}} = 0$, apart from the overall growth factor $\exp(\nu_{\mathrm{i}}\,t)$.

The solution of equation (3) that is adopted in equation (5) was used by Lucas (1964) to interpret the growth of continuous currents between plane electrodes in terms of a succession of pulses and their images.

Total Number of Particles that cross the Geometrical Plane $z =$ constant

This number is

$$T(z) = \int_0^{\infty} (W - D\,\partial/\partial z)\,q(z,t)\mathrm{d}t\,. \tag{6}$$

The number is not $N\exp(\alpha_{\mathrm{i}}z_{\mathrm{max}})$ except in the absence of diffusion, when the pulse travels as a δ-function whose growth factor is the same for all its particles, namely, $\exp(\alpha_{\mathrm{i}}z_{\mathrm{max}}) = \exp(\alpha_{\mathrm{T}}z)$. In a pulse that spreads by diffusion as it travels, particles cross the fixed geometrical plane at different times t, and those that cross ahead of the crest do so with smaller values of the growth factor than the values of those that cross after the crest. There is no *a priori* reason why the mean value of these growth factors should have the value of the growth factor of the centroid. In fact, as shown below, the growth factor of $T(z)$ in equation (6) is indeed $\exp\{(\lambda-\mu)z\}$ in agreement with equation (1).

Consider

$$I(z) = \int_0^\infty q(z,t)\,\mathrm{d}t = \frac{N}{2\pi^{\frac{1}{2}}}\int_0^\infty \exp(\nu_{\mathrm{i}}t)\,\frac{\exp\{-(z-Wt)^2/4Dt\}}{(Dt)^{\frac{1}{2}}}\,\mathrm{d}t\,.$$

Put $s = Dt$, $\mu = (\lambda^2-2\lambda\alpha_{\mathrm{i}})^{\frac{1}{2}}$, and expand and regroup the terms of the exponent to obtain

$$I(z) = \frac{N\exp(\lambda z)}{2\pi^{\frac{1}{2}}D}\int_0^\infty \exp(-\mu s)\,\frac{\exp(-z^2/4s)}{s^{\frac{1}{2}}}\,\mathrm{d}s\,.$$

But (Watson 1944)

$$\int_0^\infty \exp(-ps)\,\frac{\exp(-z^2/4s)}{s^{\nu+1}}\,\mathrm{d}s = 2^{\nu+1}\frac{p^{\frac{1}{2}\nu}}{z^\nu}K_\nu(p^{\frac{1}{2}}z)\,.$$

Put $\nu = -\frac{1}{2}$; $p = \mu$ to find

$$I(z) = (N/2D)\,\mu^{-1}\exp\{(\lambda-\mu)z\}\,,$$

and from equation (6)

$$T(z) = (W-D\,\mathrm{d}/\mathrm{d}z)\,I(z) = N\{(\lambda+\mu)/2\mu\}\exp\{(\lambda-\mu)z\}\,. \tag{7}$$

Steady Current

The emission of particles at a uniform rate $\bar{i}$ at the plane $z = 0$ can be considered as a sequence of pulses of content $\bar{i}\,\mathrm{d}t$ emitted at short intervals $\mathrm{d}t$. Thus if in equation (7) N is replaced by $\bar{i}\,\mathrm{d}t$ and the summation is made over an interval of time t, the total number of particles crossing the plane $z =$ constant in this time is

$$it = Nt\{(\lambda+\mu)/2\mu\}\exp\{(\lambda-\mu)z\}\,,$$

and consequently the current across the plane is

$$i = N\{(\lambda+\mu)/2\mu\}\exp\{(\lambda-\mu)z\} = i_0\exp(\alpha_{\mathrm{T}}z)\,, \tag{8}$$

where

$$i_0 = N(\lambda+\mu)/2\mu \qquad \text{and} \qquad \alpha_{\mathrm{T}} = \lambda-\mu = \lambda\{1-(1-2\alpha_{\mathrm{i}}/\lambda)^{\frac{1}{2}}\}\,.$$

The same formula (8) is obtained by summing the instantaneous fluxes of particles across the plane $z =$ constant, contributed by pulses $\bar{i}\,\mathrm{d}t$ that have travelled for times ranging from $t = 0$ to $t = \infty$.

Direct Method

Equation (8) is, of course, more readily derived from the steady state form of equation (4) ($\mathrm{d}q/\mathrm{d}t = 0$), namely,

$$\mathrm{d}^2q/\mathrm{d}z^2 - 2\lambda\,\mathrm{d}q/\mathrm{d}z + 2\lambda\alpha_{\mathrm{i}}\,q = 0\,,$$

the general solution of which is

$$q = A\exp\{(\lambda-\mu)z\} + B\exp\{(\lambda+\mu)z\}\,.$$

The solution appropriate to a stream proceeding to $z = \infty$ is that with $B = 0$. Consequently

$$i = (W - D\,\mathrm{d}/\mathrm{d}z)\,q(z) = A(\lambda+\mu)\exp\{(\lambda-\mu)z\}\,.$$

Let i_0 be the value of i given by this formula when $z = 0$. It follows that

$$i = i_0\exp\{(\lambda-\mu)z\} = i_0\exp(\alpha_{\mathrm{T}}z)\,.$$

Evidently the relationship $\alpha_{\mathrm{T}} = \lambda-\mu = \lambda\{1-(1-2\alpha_{\mathrm{i}}/\lambda)^{\frac{1}{2}}\}$ is a property of the stream and is not to be attributed to the influence of the electrodes.

Acknowledgment

I am greatly indebted to Dr. R. W. Crompton for discussions on the subject.

References

Burch, D. S., and Huxley, L. G. H. (1967).—*Aust. J. Phys.* **20**, 625.

Crompton, R. W. (1967).—*J. appl. Phys.* **38**, 4093.

Huxley, L. G. H. (1959).—*Aust. J. Phys.* **12**, 174.

Lucas, J. (1964).—*J. Electron. Control* **17**, 43.

Watson, G. N. (1944).—"Theory of Bessel Functions." 2nd Ed. Sec. 6.23, Eqn. (15). (Cambridge Univ. Press.)

THE (γ, p) AND (γ, n) REACTIONS IN MOLYBDENUM*

By R. W. Gellie†

Measurements have been made of the cross sections for some of the (γ, p) and (γ, n) reactions in molybdenum using the technique of residual activation analysis. The gross structure of these cross sections is compared with previous measurements and the results are interpreted as evidence for the isospin splitting of the giant dipole resonance in medium weight nuclei.

The results of the present work are shown in Figure 1 together with other measurements (Duffield, Hsiao, and Sloth 1950; Ferrero *et al.* 1957; Mutsuro *et al.* 1959; Costa *et al.* 1965). No special effort was taken in the present experiment to define the peak positions accurately and the results from other laboratories which are shown in these figures have been adjusted in energy and (with the exception of the ^{100}Mo (γ, p) cross section) normalized to the peak cross sections measured in the present work.

Fallieros, Goulard, and Venter (1965) and Morinaga (1965) have suggested that the observed appearance of the peak in the (γ, p) cross section at a higher energy than that of the (γ, n) cross section in medium and heavy nuclei arises from an isospin splitting of the giant dipole resonance. This interpretation has been applied to recent measurements for zirconium (Fallieros, Goulard, and Venter 1965; Balashov and Yadrovsky 1966; Berman *et al.* 1967). Owing to the action of the isospin selection rules and the Coulomb barrier, it is expected in the simple picture of isospin splitting of the dipole states that the T-lower $(T_<)$ states should decay by neutron emission and the T-upper $(T_>)$ states by proton emission, thus leading to (γ, n) and (γ, p) cross sections with single resonances peaked at about 15 and 20 MeV respectively. Macfarlane (1966) shows that when the (γ, p) reaction is identified with the photoabsorption to the higher $(T_>)$ dipole states and the neutrons are emitted entirely from the decay of the lower $(T_<)$ dipole states the expected ratio of the two cross sections is $(T_> - T_<)/T_<$.

The molybdenum (γ, n) and (γ, p) cross sections as shown in Figure 1 indeed show the main resonances to lie at the energies predicted by the isospin splitting theory. To compare the ratio of the experimental (γ, p) and (γ, n) cross sections with the theoretical prediction, the results shown in Figures 1(*b*) and 1(*c*) can be used to determine the integrated cross sections for the (γ, n) and (γ, p) reactions in ^{100}Mo. The cross section shown in Figure 1(*b*) is the sum of the ^{100}Mo (γ, n) and (γ, p) reactions; the measurement of the cross section for the (γ, n) reaction by Duffield, Hsiao, and

---

* Manuscript received July 15, 1968.

† School of Physics, University of Melbourne, Parkville, Vic. 3052; present address: Department of Natural Philosophy, University of Glasgow, Scotland.

Aust. J. Phys., 1968, **21**, 765–8

Sloth (1950) suggests that the cross section above about 18 MeV arises entirely from the (γ, p) reaction. Making this assumption the integrated cross section for the ^{100}Mo (γ, n) reaction is found to be 1000 MeV mb and from the results of Ferrero *et al.* (1957) shown in Figure 1(*c*) the integrated cross section for the ^{100}Mo (γ, p) reaction is 100 MeV mb, so that the ratio of the photoproton to photoneutron cross section is 10%. Since for ^{100}Mo $T_{>} = 9$ and $T_{<} = 8$, the above theory would predict a ratio of the two cross sections of 12·5%, which is in fair agreement with the experimental result.

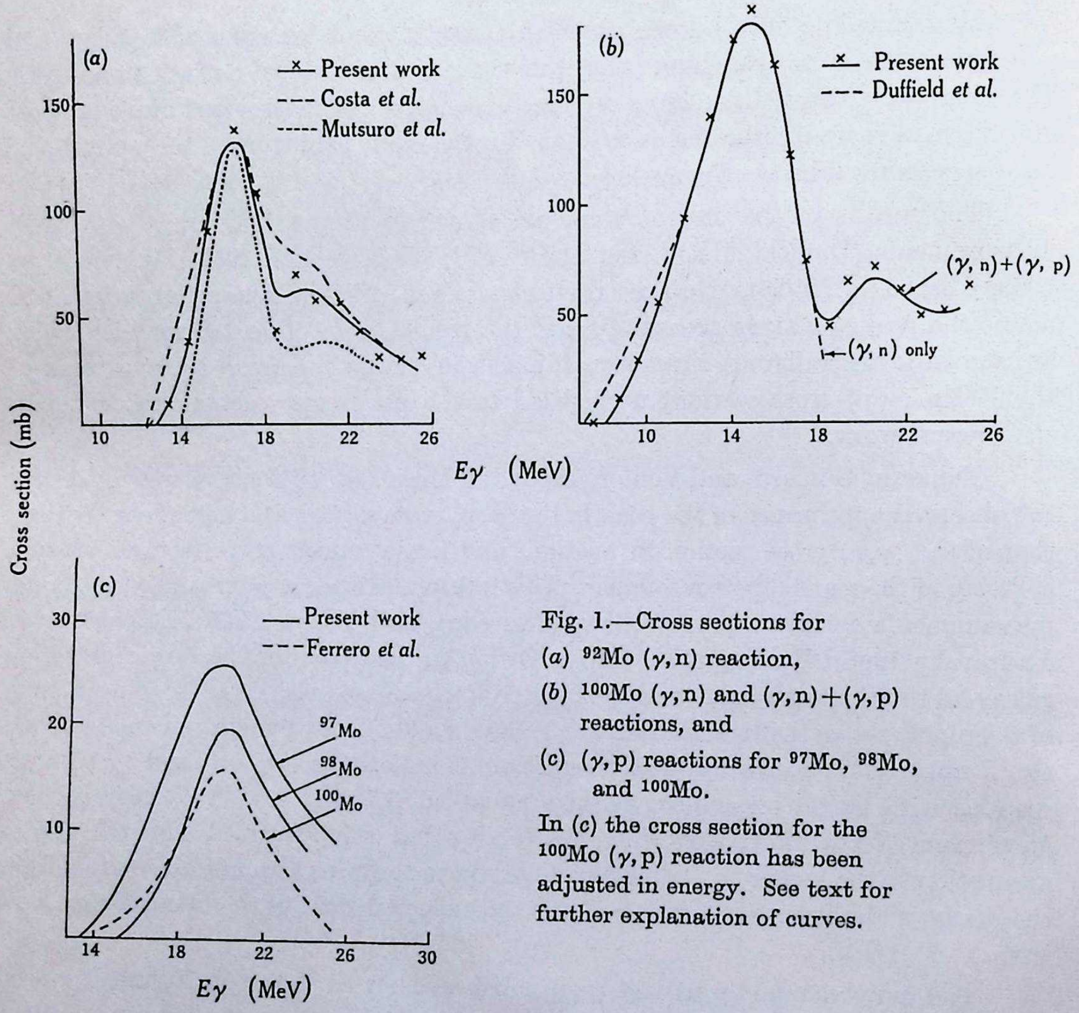

Fig. 1.—Cross sections for
(*a*) ^{92}Mo (γ, n) reaction,
(*b*) ^{100}Mo (γ, n) and $(\gamma, n)+(\gamma, p)$ reactions, and
(*c*) (γ, p) reactions for ^{97}Mo, ^{98}Mo, and ^{100}Mo.
In (*c*) the cross section for the ^{100}Mo (γ, p) reaction has been adjusted in energy. See text for further explanation of curves.

The simple picture of isospin splitting of the giant dipole states seems to successfully predict some of the important features of the cross sections; however, as shown in Figure 1(*a*), the ^{92}Mo (γ, n) cross section has a subsidiary peak in the region of 22 MeV (i.e. at the same energy as the peak in the (γ, p) cross sections). This peak appears not only in the present work but is seen also in the previous measurements shown in Figure 1(*a*).

Three possible reasons have been suggested (Spicer 1968) for the appearance of a peak in the (γ, n) cross section in the energy region of the (γ, p) giant resonance. Firstly, it could arise from isospin mixing in the dipole states, which would allow decay by neutron emission of the higher dipole state ($T_{>} = 5$ for ^{92}Mo), through its $T_{<} = 4$ impurity, to low lying states of ^{91}Mo. A second explanation is that the 22 MeV peak in the ^{92}Mo (γ, n) cross section is a component of the electric quadrupole giant resonance. The third possible explanation is that the ^{92}Mo (γ, n) reaction may proceed through the upper dipole states leaving the residual nucleus ^{91}Mo in its higher excited state; in particular those states that have $T = \frac{9}{2}$ for which the process is not forbidden by the isospin selection rules.

The measured (γ, p) and (γ, n) cross sections indicate that the maximum of the subsidiary peak in the (γ, n) cross section and the peak value of the (γ, p) cross section are approximately the same. It would thus appear that, if the observed cross section in the subsidiary peak of the (γ, n) reaction were attributed to neutron emission from the upper dipole states to low lying states of ^{91}Mo, essentially complete mixing of the isospin states would be required; or, in other words, that isospin is not a good quantum number for the dipole states. Also, measurements of the angular distributions of photoprotons from the ^{92}Mo (γ, p) reaction by Butler and Almy (1953) using $22 \cdot 5$ MeV bremsstrahlung showed that the protons were strongly anisotropic at all energies with a symmetry of the angular distribution about 90°, indicating that the photo-absorption in this energy region is electric dipole in character.

This evidence seems to rule out the first two possible mechanisms and it remains to examine the suggestion that the upper dipole states of ^{92}Mo decay by neutron emission to $T = \frac{9}{2}$ states in ^{91}Mo.

Costa *et al.* (1965) have measured the ^{92}Mo (γ, n) reaction leading to the isomeric state in ^{91}Mo. Their results show that although about 30% of the (γ, n) yield in the energy region between 15 and 20 MeV does not lead to the isomeric state, almost all the (γ, n) decay in the peak near 22 MeV leads to ^{91}Mo$^{\mathrm{m}}$. This indicates that the neutron emission from photon absorption in the region of the main peak leads to different states in the residual nucleus than the decay corresponding to the subsidiary peak. Further, the measurement of the ^{100}Mo (γ, n) cross section by Duffield, Hsiao, and Sloth (1950), shown in Figure 1(*b*), indicates that there is no secondary photoneutron resonance in the case of the ^{100}Mo isotope in the region near 22 MeV. Calculation of the energies involved shows that, whereas there is energy available for decay of the ^{92}Mo dipole states by neutron emission to $T = \frac{9}{2}$ states in ^{91}Mo, this process is certainly not energetically possible for ^{100}Mo decay to the $T = \frac{17}{2}$ states of ^{99}Mo.

It is concluded that the isospin splitting of the giant dipole resonance states is observed in the photodisintegration of molybdenum and that the subsidiary photoneutron resonance in the ^{92}Mo (γ, n) reaction arises from decay by neutron emission of the upper dipole states in ^{92}Mo to $T = \frac{9}{2}$ states in ^{91}Mo. Further experiments with this element and in particular an investigation of the energy spectra for neutrons emitted from the (γ, n) reactions in ^{92}Mo and ^{100}Mo could provide valuable evidence to test these conclusions.

Financial assistance from a CSIRO Post-graduate Studentship held during the course of this work is gratefully acknowledged.

References

Balashov, V. V., and Yadrovsky, E. L. (1966).—*Phys. Lett.* **22**, 509.

Berman, B. L., Caldwell, J. T., Harvey, R. R., Kelly, M. A., Bramblett, R. L., and Fultz, S. C. (1967).—*Phys. Rev.* **162**, 1098.

Butler, W. A., and Almy, G. M. (1953).—*Phys. Rev.* **91**, 58.

Costa, S., Ferrero, F., Ferroni, S., Pasqualini, L., and Silva, E. (1965).—*Nucl. Phys.* **72**, 158.

Duffield, R. B., Hsiao, L., and Sloth, E. N. (1950).—*Phys. Rev.* **79**, 1011.

Fallieros, S., Goulard, B., and Venter, R. H. (1965).—*Phys. Lett.* **19**, 398.

Ferrero, F., Hanson, A. O., Malvano, R., and Tribuno, C. (1957).—*Nuovo Cim.* **6**, 585.

Macfarlane, M. H. (1966).—*In* "Isobaric Spin in Nuclear Physics". (Eds. J. D. Fox and D. Robson.) p. 383. (Academic Press: New York.)

Morinaga, H. (1965).—*Z. Phys.* **188**, 182.

Mutsuro, N., Ohnuki, Y., Sato, K., and Kimura, M. (1959).—*J. phys. Soc. Japan* **14**, 1649.

Spicer, B. M. (1968).—The giant dipole resonance. *In* "Advance in Physics". Vol. 2. (Plenum Press: New York.) (In press.)

APPLICATION OF REACTION MATRIX THEORY TO MESON PROCESSES

By J. L. Cook*

[*Manuscript received May* 21, 1968]

Summary

The possible application of reaction matrix theory to pion–nucleon processes is discussed. It is found that suitable boundary conditions can remove the effects of the nucleon–pion cloud, leading to the conventional R-matrix formalism. A simple dynamical channel-coupling scheme is proposed which permits full analysis of experiments.

I. Introduction

The reaction matrix theory of nuclear interaction processes has proved highly satisfactory in explaining many features of nucleon–nuclear collisions, despite the great complexity of the intermediate compound nucleus states. Even though the Wigner and Eisenbud (1947) theory does not, for example, predict the energy eigenvalues at which resonances occur, it does display specifically how the cross sections should be parameterized, and lends physical meaning to the parameters.

A similar if not wholly analogous situation exists today with meson–nucleon interactions. There is no many-body theory of the complex forces involved and, owing to the large magnitude of the pion–nucleon coupling constant (Bethe and de Hoffman 1955), the perturbation theory developed by Feynman (1949) failed to give useful answers. On the other hand, dispersion theory (recently reviewed by Hamilton 1967) has made great progress towards an understanding of the intermediate processes and the relationship between two-body channels (Mandelstam 1958), but seems to lack one essential feature: it does not predict exactly how the contributions from various states should be parameterized. Donnachie and Hamilton (1964) came closest to a derivation from first principles with variational calculations, achieving considerable success using Layson's (1961) form for the P33 phase shift, unitarity, and dispersion relations. They obtained mutually consistent sets of phase shifts.

Let us consider how reaction matrix theory might be made compatible with current theories of high energy processes. Presumably, if the perturbation series with all conceivable intermediate states could be summed, one would then have a type of wave equation, such as the Bethe and Salpeter (1951) equation, which has appropriate interaction terms derived from field theory and whose solutions possess eigenvalues in energy corresponding to resonant states. Such a task has not been carried out fully, owing to the prohibitive number of intermediate processes that require consideration and an uncertainty about the eventual convergence of the perturbation series.

---

* Physics Division, Australian Atomic Energy Commission, Research Establishment, Private Mail Bag, Sutherland, N.S.W. 2232.

Aust. J. Phys., 1968, **21**, 769–77

The only successful field theoretical model to date is the static theory of Chew and Low (1956), which fits the P33 low energy behaviour quite adequately but fails to predict most of the other phase shifts correctly. Jackson's (1958) presentation of this theory exhibits the close connection with conventional quantum mechanics, and we shall assume that a meaningful wave equation exists for the problem in its entirety, although Jackson assumes the pion to be a conventional quantum mechanical particle and treats the nucleon as a quantized field.

It is shown in the present paper that, under very general assumptions, the source terms in such an equation still provide a simple form for the reaction matrix, although mixtures of states can contribute to a given resonance level, and the energies corresponding to the poles in the R-matrix do not necessarily correspond to eigenvalues of the wave equation. The effect of variations in the radial channel parameter is investigated.

II. GREEN'S THEOREM AND DISTRIBUTION OF EIGENVALUES

We assume that the wave function of the compound pion–nucleon system satisfies an equation of the Bethe–Salpeter type, and that the basic amplitude for the two-body state has the character of a spinor with the following properties.

(i) In the region of interaction the amplitude satisfies the two equations

$$(\gamma.\mathbf{P}+M)\Psi = \Lambda_1 \tag{1a}$$

and

$$(\Box^2-\mu^2)\Psi = \Lambda_2\,, \tag{1b}$$

where Λ_1 and Λ_2 are source terms describing the quantized field effects, the γ's are conventional Dirac matrices, $\mathbf{P}$ is the four-momentum of the nucleon, M is the mass of the nucleon, μ is the mass of the meson, and each equation becomes the free-particle equation under the conditions

$$\Lambda_1 \to 0\,,\quad \Lambda_2 \to 0 \qquad \text{as} \qquad |\mathbf{r}_1-\mathbf{r}_2| \to \infty\,,$$

where $\mathbf{r}_1 = (r_1, t_1)$ are the nucleon four-vector coordinates and $\mathbf{r}_2 = (r_2, t_2)$ the pion four-vector coordinates, t_2, t_1 being the time coordinates of the pion and nucleon respectively.

(ii) It is assumed that the spinor $\Psi(\mathbf{r}_1, \mathbf{r}_2)$ is factorizable in the above asymptotic region and in the interaction region as

$$\Psi(\mathbf{r}_1,\mathbf{r}_2) = \phi\big((M\mathbf{r}_1+\mu\mathbf{r}_2)/(M+\mu)\big)\,\Psi_R(\mathbf{r}_1-\mathbf{r}_2)\,, \tag{2}$$

a property found by Cutkosky (1954) and Wick (1954).

(iii) In the centre-of-mass system, the time derivatives in the wave equation of the two-body system can be separated in such a way that the spinor Ψ_R of equation (2) satisfies

$$(\nabla_R^2+k^2)\,\Psi_R(\mathbf{R},\mathbf{k}) = \rho(\mathbf{R},\mathbf{k})\,, \tag{3}$$

where $\mathbf{R} = \mathbf{r}_1-\mathbf{r}_2$, $\mathbf{k} = (k, ik_0)$, ρ is the pion field source, and $\eta = M\mu/(M+\mu)$.

(iv) Should many multiparticle channels be involved, we assume that the amplitude Ψ still obeys an equation with the structure

$$\left(\sum_i \frac{\mathbf{P}_i^2}{2M_i} - \tfrac{1}{2}\sum_i M_i\right)\Psi = \Lambda,$$

where $\mathbf{P}_i$ is the particle four-momentum and M_i is the particle mass, which is such that a separation of the relative time derivatives yields an equation

$$\sum_c \left(\frac{\nabla_{Rc}^2}{2\eta_c} + \frac{k_c^2}{2\eta_c}\right)\Psi_R = \sum_c \frac{\rho_c}{\eta_c} = \frac{\rho}{\eta}, \tag{4}$$

η_c being the reduced mass in channel c.

(v) The wave functions X_λ representing the eigenfunctions in the region of interaction obey

$$\left(\sum_c \frac{\nabla_{Rc}^2}{2\eta_c} + \frac{k_\lambda^2}{2\eta}\right)X_\lambda = \frac{\rho_\lambda}{\eta}, \qquad \frac{1}{\eta} = \sum_i \frac{1}{M_i}, \tag{5}$$

where

$$\sum_c (k_{\lambda c}^2/\eta_c) = k_\lambda^2/\eta \qquad \text{and} \qquad \sum_c (k_c^2/\eta_c) = k^2/\eta,$$

for each state X_λ for which there is an eigenvalue λ.

The Ψ_R and X_λ are chosen with the relative time coordinate put equal to zero to define a series of completely space-like surfaces in the centre-of-mass system. One expects from this non-invariant separation that the source terms ρ_λ will involve recoil corrections.

(vi) If the superposition principle is to hold everywhere we must have

$$\Psi_R(\boldsymbol{r}, \boldsymbol{k}) = \sum_\lambda A_\lambda(\boldsymbol{k})\, X_\lambda(\boldsymbol{r}, \boldsymbol{k}) \tag{6a}$$

and

$$\rho(\boldsymbol{r}, \boldsymbol{k}) = \sum_\lambda A_\lambda(\boldsymbol{k})\, \rho_\lambda(\boldsymbol{r}, \boldsymbol{k}). \tag{6b}$$

Now the appropriate boundary conditions involve the value of the logarithmic derivatives of the radial wave functions in each channel c (Preston 1962) and partition α, which is defined at each channel radius a_c as

$$\psi_{\lambda c}(a_c) = \int \overset{*}{\Phi_c}\, X_\lambda \,\mathrm{d}s, \tag{7}$$

where

$$\Phi_c = r_\alpha^{-1}\, \mathrm{i}^l\, \mathrm{Y}_l^m(\omega)\, \psi_{\alpha s_\mu},$$

$\mathrm{Y}_l^m(\omega)$ is the conventional spherical harmonic, the integral is taken over the surface defined by a sphere of radius a_c, and $\psi_{\alpha s_\mu}$ is a normalization constant.

Proceeding in the standard way from (5), it follows that

$$\begin{aligned}\int d\tau \left(\sum_c (\overset{*}{X}_\lambda \nabla^2_{Rc}\Psi_R - \Psi_R \nabla^2_{Rc}\overset{*}{X}_\lambda)\eta/\eta_c\right) + (k^2-k_\lambda^2)\int d\tau\, \overset{*}{X}_\lambda \Psi_R \\ = \int d\tau\, (\overset{*}{X}_\lambda \rho - \Psi_R \overset{*}{\rho}_\lambda) \\ = \sum_\mu A_\mu \int d\tau\, (\overset{*}{X}_\lambda \rho_\mu - X_\mu \overset{*}{\rho}_\lambda) \\ = \sum_\mu G_{\lambda\mu} A_\mu, \qquad (8)\end{aligned}$$

the integral being taken over the volume of the region of interaction of the finite range forces. Usually X_λ and ρ_λ are real functions and so $G_{\lambda\mu}$ is an antisymmetric real matrix. More generally,

$$G_{\lambda\mu} = -\overset{*}{G}_{\mu\lambda}. \qquad (9)$$

The components of **G** are related to transition matrix elements for processes involving field sources. Notice that for purely lamellar interactions of the form

$$\rho_\lambda = V(R) X_\lambda, \qquad (10)$$

where V is a scalar potential function, equations (8) lead to a null matrix **G**, showing the absence of the field source type of transition.

It is shown in Section VI that, if the X_λ are normalized in such a way that

$$\int d\tau\, \overset{*}{X}_\lambda X_\mu = \delta_{\lambda\mu} \qquad \text{and} \qquad A_\lambda = \int d\tau\, \overset{*}{X}_\lambda \Psi_R, \qquad (11)$$

then $G_{\lambda\mu}$ also becomes a null matrix if the derivatives of the internal radial wave functions vanish at the channel radii.

Using Green's theorem in equations (8), we get

$$\sum_c \left(\overset{*}{\psi}_{\lambda c}\Psi'_{Rc} - \Psi_{Rc}\overset{*}{\psi}{}'_{\lambda c}\right)_{a_c} \frac{\eta}{\eta_c} + (k^2-k_\lambda^2) A_\lambda = \sum_\mu G_{\lambda\mu} A_\mu, \qquad (12)$$

where the $\psi_{\lambda c}$ are the radial wave functions in channel c with eigenvalues k_λ and the primes denote differentiation with respect to r_c, Ψ_{Rc} being the appropriate channel wave function.

By using boundary condition matrices B_c (Preston 1962) one can solve (12) for A_λ to obtain

$$A_\mu = \sum_\lambda (C_{\lambda\mu})^{-1} \sum_c \left(\overset{*}{\psi}_{\lambda c}\Psi'_{Rc} - \frac{B_c}{a_c}\overset{*}{\psi}_{\lambda c}\Psi_{Rc}\right)_{a_c} \frac{\eta}{\eta_c}, \qquad (13)$$

where

$$a_c \psi'_{\lambda c} = B_c \psi_{\lambda c}, \qquad \text{and} \qquad C_{\lambda\mu} = \delta_{\lambda\mu}(k_\lambda^2 - k^2) + G_{\lambda\mu}. \qquad (14)$$

The inverse of $C_{\lambda\mu}$ becomes diagonal in the case of lamellar forces.

In terms of equations (6) and (13) the wave function in channel c becomes

$$\Psi_{Rc}(r_c) = \sum_{c'} \left(\Psi'_{Rc'}(a_{c'}) - \frac{B_{c'}}{a_{c'}}\Psi_{Rc'}(a_{c'})\right) \sum_{\lambda} \sum_{\mu} \overset{*}{\psi}_{\lambda c'}(a_{c'})\, \psi_{\mu c}(r_c) \frac{\eta}{\eta_c} (C_{\lambda\mu})^{-1}. \qquad (15)$$

III. Reaction Matrix

The reaction matrix is defined as the relationship between the wave functions and their derivatives at the channel radii a_c, according to

$$(\eta_c a_c)^{-\frac{1}{2}}\, \Psi_c(a_c) = \sum_{c'} R_{cc'}\, (\eta_{c'} a_{c'})^{-\frac{1}{2}} (a_{c'} \Psi'_{c'} - B_{c'} \Psi_{c'})_{a_{c'}}. \qquad (16)$$

Here η_c is the reduced mass in channel c and the suffix R has been omitted for convenience. Evaluating $\Psi_c(r_c)$ at a_c in (15), we find by comparison with (16) that

$$R_{cc'} = \sum_{\lambda} \sum_{\mu} \overset{*}{\gamma}_{\lambda c'}\, \gamma_{\mu c}\, (C_{\lambda\mu})^{-1}, \qquad (17)$$

where

$$\gamma_{\lambda c} = \hbar(\eta/\eta_c a_c)^{\frac{1}{2}}\, \psi_{\lambda c}(a_c).$$

Equation (17) is the expression for the reaction matrix in the presence of source terms. To illustrate how it differs from the conventional form, let **C** be a 2×2 matrix denoting the existence of two eigenvalues to the field equation (5):

$$\mathbf{C} = \begin{pmatrix} E_1 - E & G \\ -\overset{*}{G} & E_2 - E \end{pmatrix}, \qquad E_\lambda = k_\lambda^2, \qquad G = G_{12} = -\overset{*}{G}_{21}.$$

We shall assume that there is no diagonal component coming from **G**. Hence

$$\mathbf{C}^{-1} = \frac{1}{(E_1 - E)(E_2 - E) + |G|^2} \begin{pmatrix} E_2 - E & -G \\ \overset{*}{G} & E_1 - E \end{pmatrix}. \qquad (18)$$

Let $C' = C = 1$ denote the elastic scattering channel, giving, for real G,

$$R_{11} = \frac{\gamma_{11}^2}{E_1 - E + |G|^2/(E_1 - E)} + \frac{\gamma_{21}^2}{E_2 - E + |G|^2/(E_2 - E)}. \qquad (19)$$

The conventional expression for R_{11} is obtained by putting $|G|^2$ equal to zero.

IV. Way of Reducing to Conventional Form

It is probable that the off-diagonal elements of **C** may be impossible to isolate from the experimental data. This is because they occur as part of a scalar product in $R_{cc'}$ and not as separate terms. For a large number of eigenvalues, we can write

$$R_{cc'} = (1/D(E))(\gamma_{1c}\gamma_{1c'} N_{11} + \gamma_{1c}\gamma_{2c'} N_{12} + \ldots),$$

where the N_{ij} are the appropriate cofactors of each element of **C** and

$$D(E) = \det \mathbf{C}. \qquad (20)$$

The resonances occur when $D(E)$ vanishes, so let E'_λ be the q roots of $D(E) = 0$. By the well-known theorem of partial fractions (Gradshteyn and Ryzhik 1965) we can write

$$(C_{ij})^{-1} = \frac{N_{ij}}{D(E)} = \frac{A_{ij}}{E'_1 - E} + \frac{B_{ij}}{E'_2 - E} + \dots ,$$

where

$$A_{ij} = N_{ij}(E'_1)/D'(E'_1), \quad B_{ij} = N_{ij}(E'_2)/D'(E'_2), \quad \dots$$

and

$$D'(E) = \mathrm{d}D(E)/\mathrm{d}E .$$

Thus

$$R_{cc'} = \sum_{ij} \gamma_{ic}\gamma_{jc'} \frac{N_{ij}(E'_\lambda)}{D'(E'_\lambda)} \frac{1}{E'_\lambda - E} \tag{21}$$

is a form exhibiting the poles and residues of $R_{cc'}$. It only remains to redefine the partial widths such that

$$\gamma'_{\lambda c}\gamma'_{\lambda c'} = \sum_{ij} \gamma_{ic}\gamma_{jc'} N_{ij}(E'_\lambda)/D'(E'_\lambda) , \tag{22}$$

to yield the conventional form for $R_{cc'}$ of

$$R_{cc'} = \sum_{\lambda} \gamma'_{\lambda c}\gamma'_{\lambda c'}/(E'_\lambda - E) \tag{23}$$

given first by Wigner and Eisenbud (1947).

This result shows that we can admit a wider class of wave equations than the Schrödinger equation with lamellar potentials without changing the structure of reaction matrix theory. However, the poles of the R-matrix no longer correspond to the eigenvalues of the wave equations in the interior region, even after taking account of the usual level shifts.

V. BOUNDARY CONDITION MATRIX

Consider Green's theorem for two of the eigenfunctions X_λ, and an interaction of the type in equation (4),

$$\begin{aligned}\int \mathrm{d}s \left(\overset{*}{X}_\lambda \frac{\partial X_\mu}{\partial r} - X_\mu \frac{\partial \overset{*}{X}_\lambda}{\partial r} \right)_{r=a} &= G_{\lambda\mu} + (k_\mu^2 - k_\lambda^2) \int \overset{*}{X}_\lambda X_\mu \,\mathrm{d}\tau \\ &= \sum_c \left(\overset{*}{\psi}_{\lambda c} \frac{\partial \psi_{\mu c}}{\partial r} - \psi_{\mu c} \frac{\partial \overset{*}{\psi}_{\lambda c}}{\partial r} \right)_{r=a} . \end{aligned} \tag{24}$$

When the X_λ are orthogonal, equation (24) yields a relation connecting $G_{\lambda\mu}$ to the derivatives at the channel radii. By adopting the boundary condition (13) the matrix elements can be made to vanish, and this leads to the condition from (8) that

$$\int \overset{*}{X}_\lambda \rho_\mu \,\mathrm{d}\tau = \int X_\mu \overset{*}{\rho}_\lambda \,\mathrm{d}\tau . \tag{25}$$

An inspection of Jackson's P-wave equation in the static model reveals that condition (25) is indeed satisfied by the source terms. As well as taking account of such effects as the diffusiveness of the nucleon surface, the boundary condition matrices can diagonalize $C_{\lambda\mu}$, showing that the Wigner–Eisenbud reaction matrix takes into account meson field sources when applied to nuclear problems.

As an alternative, if such general boundary conditions cannot be found, one may work with the derivatives themselves as parameters. In general, one will have

$$A_{\mu} = \sum_{\lambda} \sum_{c} (C_{\lambda\mu})^{-1} (\overset{*}{\psi}_{\lambda c} \psi'_{c} - \psi_{c} \overset{*}{\psi}{}'_{\lambda c}) \eta / \eta_{c} ,$$

whence

$$\psi_{c} = \sum_{c'} \sum_{\lambda} \sum_{\mu} (C_{\lambda\mu})^{-1} (\overset{*}{\psi}_{\lambda c'} \psi'_{c'} - \psi_{c'} \overset{*}{\psi}{}'_{\lambda c'}) \psi_{\mu c'} \eta / \eta_{c} ,$$

which yields

$$\begin{aligned} \psi_{c} \hbar \left(\frac{\eta}{\eta_{c} a_{c}} \right)^{\frac{1}{2}} &= \sum_{c''} \psi'_{c''} \left\{ \left(\sum_{\lambda} \sum_{\mu} (C_{\lambda\mu})^{-1} \frac{\hbar^{2} \eta}{(\eta_{c} \eta_{c'} a_{c} a_{c'})^{\frac{1}{2}}} \overset{*}{\psi}_{\lambda c} \psi_{\mu c'} \right) \left(\delta_{cc'} + F_{cc'} \right)^{-1} \right\} \\ &= \sum_{c''} R_{cc''} \hbar (\eta / \eta_{c''} a_{c''})^{\frac{1}{2}} \psi'_{c''} , \end{aligned} \tag{26}$$

where $\delta_{cc'}$ is the Kronecker delta function. Hence

$$R_{cc''} = \sum_{\lambda} \sum_{\mu} \sum_{c'} (C_{\lambda\mu})^{-1} \gamma_{\lambda c''} \gamma_{\mu c'} (\delta_{cc'} + F_{cc'})^{-1} ,$$

where

$$F_{cc'} = \hbar^{2} \sum_{\lambda} \sum_{\mu} (C_{\lambda\mu})^{-1} \overset{*}{\psi}{}'_{\lambda c'} \psi_{\mu c} . \tag{27}$$

The derivatives appear as parameters in $F_{cc'}$, and this is the most general form for $R_{cc'}$, without the greatly simplifying assumption of the boundary conditions (13). In applications to experiment we have used this assumption with satisfactory results.

VI. Coupling Assumptions

To examine the question of the effect of unitarity upon phase shifts for multiparticle processes, Cook (1967) assumed that the partial wave transition amplitudes in all channels had the same phase. This assumption is a far too restrictive dynamical condition to be of much practical use, but can be broadened a little by observing that, in low energy neutron nuclear collisions, the inverse R-matrix always has very much larger elements than the R-matrix itself and that, where single-level fits are adequate, the inverse R-matrix can be considered to be singular. That is

$$\det(R_{cc'}) \simeq 0 . \tag{28}$$

In fact, every 2×2 minor of $\mathbf{R}$ can be considered to be zero. This is essentially a dynamical constraint connecting the asymptotic behaviour of the various channel wave functions and implies that the reduced widths for each channel are in approximately constant ratio, or that one particular term in $R_{cc'}$ is dominant. It is a most useful assumption in multichannel analysis, as it allows us to connect all inelastic channels to the real and imaginary parts of the scattering phase shift. If we write

$$\text{(i)}\ \mathbf{Q} = (1/\mathrm{i})(\mathbf{1}+\mathbf{S}_1)^{-1}(\mathbf{S}_1-\mathbf{1})\,, \qquad \mathbf{S}_1 = \mathbf{\Omega}^{-1}\mathbf{P}^{-\frac{1}{2}}\mathbf{S}\mathbf{P}^{\frac{1}{2}}\mathbf{\Omega}^{-1}\,,$$

and

$$\text{(ii)}\ \mathbf{R} = \mathbf{Q}(\mathbf{s}\mathbf{Q}+\mathbf{P})^{-1}\,, \tag{29}$$

where $\mathbf{\Omega}$ is the hard sphere phase matrix, $\mathbf{P}$ the penetration factor matrix, and $\mathbf{s}$ the level shift matrix, these quantities being diagonal matrices (as defined by Preston 1962), we get

$$\det\mathbf{Q} = \det(\mathbf{S}_1-\mathbf{1}) \simeq 0\,. \tag{30}$$

From this condition we obtain

$$\mathbf{S}_1-\mathbf{1} \simeq (2\mathrm{i}/\Delta)\mathbf{Q} = 2\mathrm{i}\mathbf{T}_1\,,$$

where $\mathbf{T}_1$ is the reduced transition matrix and

$$\det\mathbf{S} = \Delta^*/\Delta\,, \qquad \Delta = \det(\mathbf{1}-\mathrm{i}\mathbf{Q})\,.$$

For example, in the two-channel case we can parameterize $\mathbf{S}_1$ as

$$\mathbf{S}_1 = \begin{pmatrix} \eta e^{2i\delta} & (1-\eta^2)^{\frac{1}{2}}e^{2i\phi} \\ (1-\eta^2)^{\frac{1}{2}}e^{2i\phi} & -\eta e^{2i(2\phi-\delta)} \end{pmatrix}, \tag{31}$$

where η is the absorption coefficient, δ the scattering phase shift, and ϕ the production phase shift. Hence

$$-\det\mathbf{S}_1 \simeq e^{4i\phi} \simeq (1-\eta e^{2i\delta})/(1-\eta e^{-2i\delta})\,, \tag{32}$$

from which the phase shift for production can be determined. This assumption was tested and found to give no contradiction with experiment.

VII. CONCLUSIONS

Some complications that might arise when applying *R*-matrix theory to pion field interactions have been investigated. It has been found that Lorentz invariance imposes minor modifications of underlying concepts, and that boundary condition matrices can remove off-diagonal elements of the *R*-matrix in the space of eigenfunctions. Finally, a simple dynamical coupling assumption has been proposed which simplifies analysis of multichannel experiments.

VIII. ACKNOWLEDGMENTS

The author thanks Professor D. C. Peaslee, Mr. B. Clancy, and Dr. R. Garnsworthy for informative discussions.

IX. REFERENCES

BETHE, H. A., and DE HOFFMAN, F. (1955).—"Mesons and Fields." Vol. 2. (Row, Peterson & Co.: New York.)

BETHE, H. A., and SALPETER, E. E. (1951).—*Phys. Rev.* **84**, 1232.

CHEW, G. F., and LOW, F. E. (1956).—*Phys. Rev.* **101**, 1570.

COOK, J. L. (1967).—*Aust. J. Phys.* **20**, 347.

CUTKOSKY, R. E. (1954).—*Phys. Rev.* **96**, 1135.

DONNACHIE, A., and HAMILTON, J. (1964).—*Phys. Rev.* **133B**, 1053.

FEYNMAN, R. P. (1949).—*Rev. mod. Phys.* **20**, 367.

GRADSHTEYN, I. S., and RYZHIK, I. M. (1965).—"Tables of Integrals, Series and Products." p. 56. (Academic Press: New York.)

HAMILTON, J. (1967).—*In* "High Energy Physics". (Ed. E. H. S. Burhop.) p. 193. (Academic Press: New York.)

JACKSON, J. D. (1958).—"The Physics of Elementary Particles." (Princeton Univ. Press.)

LAYSON, W. M. (1961).—*Nuovo Cim.* **20**, 1207.

MANDELSTAM, S. (1958).—*Phys. Rev.* **112**, 1344.

PRESTON, M. A. (1962).—"Physics of the Nucleus." (Addison–Wesley: Massachusetts.)

WICK, G. C. (1954).—*Phys. Rev.* **96**, 1124.

WIGNER, E. P., and EISENBUD, L. (1947).—*Phys. Rev.* **72**, 29.

ON THE PROBLEM OF UNRESOLVED RESONANCES IN NEUTRON SPECTROSCOPY

By A. R. de L. Musgrove*

[*Manuscript received June* 21, 1968]

Summary

A direct method of calculating the probability for missing levels in slow neutron spectroscopy is described. The method gives a criterion for missing levels based on the Breit–Wigner resonance profile between adjacent levels and does not depend on correcting an observed distribution of resonance parameters to the theoretically expected one.

I. Introduction

In neutron cross section measurements, statistical errors in the accumulated counts and the finite instrumental resolution impose a practical limit on the ability to detect weak resonances. In addition, when overlapping between levels occurs, quite large resonances may remain unresolved. The probability of missing levels below the detectability limit depends only on the incident neutron energy while the overlapping probability depends primarily on the ratio of average level width $\langle \Gamma \rangle$ to average level spacing $\langle D \rangle$. When calculating average parameters such as the s-wave strength function and the average level spacing, an important correction must be applied to the raw data for these unresolved levels.

Fuketa and Harvey (1965) have described a method of calculating the proportion of levels lying below the detectability limit, based on the Porter–Thomas distribution of the reduced neutron widths. The experimental resolution limit is proportional to a power of the neutron energy, and integration of the Porter–Thomas distribution up to this limit over the energy range considered yields the relative probability of missing the weak levels. This method does not take into account the levels that are missed by overlapping since these may have reduced neutron widths in excess of the detectability limit.

The Fuketa and Harvey method is not rigorously correct (Wilkins 1967) even for the calculation of the probability of missing weak levels, since it is assumed that resonances are randomly distributed on the energy axis instead of obeying a distribution such as that proposed by Wigner (1957), where small spacings are rare for levels of the same spin sequence. The effect of the assumption about the random placement of levels is to overestimate the number of levels missed in the energy range.

---

* Australian Atomic Energy Commission Research Establishment, Private Mail Bag, Sutherland, N.S.W. 2232.

Aust. J. Phys., 1968, **21**, 779–92

In fissile nuclei, where the ratio $\langle\Gamma\rangle/\langle D\rangle$ is large, overlapping of levels cannot be ignored and Musgrove (1967) developed a method of calculating the number of levels missed in these nuclei. The method in effect corrected the observed distribution of resonance peak heights and, since it was insensitive to the precise experimental resolution limit, it was expected to contain a contribution from overlapping levels. A calculation performed on ^{233}U, which has the largest known value of $\langle\Gamma\rangle/\langle D\rangle$, indicated that approximately 30% of the levels in that nucleus were undetected.

The correction method described here is an improvement over those outlined above since it no longer depends on correcting an experimental distribution of parameters, but gives the total probability for missing levels directly. Both classes of missed resonances are treated identically and weak levels are assumed to be missed owing to "overlapping", no matter what the inter-resonance spacing.

II. METHOD OF CORRECTION FOR NONFISSILE NUCLIDES

The Doppler-broadened capture cross section at an energy E between two adjacent resonance levels at energies E_1 and E_2 is given approximately by the sum of two Breit–Wigner terms and a contribution from distant levels:

$$\sigma_{\mathrm{c}}(E) = 4\pi\lambdabar^2\left(\frac{g_1\Gamma_{\mathrm{n}1}\Gamma_{\gamma1}}{\Gamma_1^2}\psi(x_1,t_1)+\frac{g_2\Gamma_{\mathrm{n}2}\Gamma_{\gamma2}}{\Gamma_2^2}\psi(x_2,t_2)\right)+\sigma_{\mathrm{dist}}, \tag{1}$$

where Γ_{n}, Γ_γ, and Γ are respectively the neutron, radiation, and total widths of a level, $\lambdabar$ is the neutron wavelength, and g is the appropriate spin weight factor. Also

$$\psi(x,t) = \tfrac{1}{2}(\pi t)^{-\frac{1}{2}}\int_{-\infty}^{\infty}(1+y^2)^{-1}\exp\{-(x-y)^2/4t\}\,\mathrm{d}y$$

is the usual Voigt profile with arguments defined by

$$x = 2(E-E_{\mathrm{r}})/\Gamma, \qquad t = 4\mu E_{\mathrm{r}}T/\Gamma^2,$$

where μ is the mass ratio and T the temperature of the absorber atom in energy units.

Radiation widths vary little from level to level since radiative decay proceeds through a large number of independent channels, and it is usual to assume that the neutron decay widths are negligible in comparison. Under this assumption the total widths are approximately constant and equal to the radiation width, and equation (1) can be written as

$$\sigma_{\mathrm{c}} \simeq \mathrm{const}\{\psi(x,t)+R\psi(x-a,t)\}+\sigma_{\mathrm{dist}}, \tag{2}$$

where $a = 2(E_2-E_1)/\Gamma$, $R = \Gamma^0_{\mathrm{n}2}/\Gamma^0_{\mathrm{n}1}$ is the ratio of the peak heights, and we have further assumed for simplicity that $g_1 = g_2$ and $t_1 = t_2$. When $R = 0$, the second resonance is missed for all values of a, but, for a particular nonzero value of R, a limiting separation exists, say $a_{\mathrm{L}}(R,t)$, where the two levels are just resolved. We adopt the criterion that the resonances are just resolved at the first formation of a "shoulder" between them, i.e. when two points of inflexion first occur in the resonance profile of equation (2) in the interval $0 < x < a$. Using the expression for $\partial^2\psi/\partial x^2$

given by Clancy and Keane (1964), the second derivative of the cross section with respect to x can be written as

$$\begin{aligned} \mathrm{d}^2\sigma/\mathrm{d}x^2 = \mathrm{const}\big[&1-(1+x^2+2t)\psi(x)-2x\big(x\psi(x)-\phi(x)\big) \\ &+R\big\{1-\big(1+(x-a)^2+2t\big)\psi(x-a)-2(x-a)\big((x-a)\psi(x-a)-\phi(x-a)\big)\big\}\big] \\ &+\mathrm{d}^2\sigma_{\mathrm{dist}}/\mathrm{d}x^2, \end{aligned} \tag{3}$$

where

$$\phi(x,t)=\tfrac{1}{2}(\pi t)^{-\frac{1}{2}}\int_{-\infty}^{\infty} y(1+y^2)^{-1}\exp\{-(x-y)^2/4t\}\,\mathrm{d}y,$$

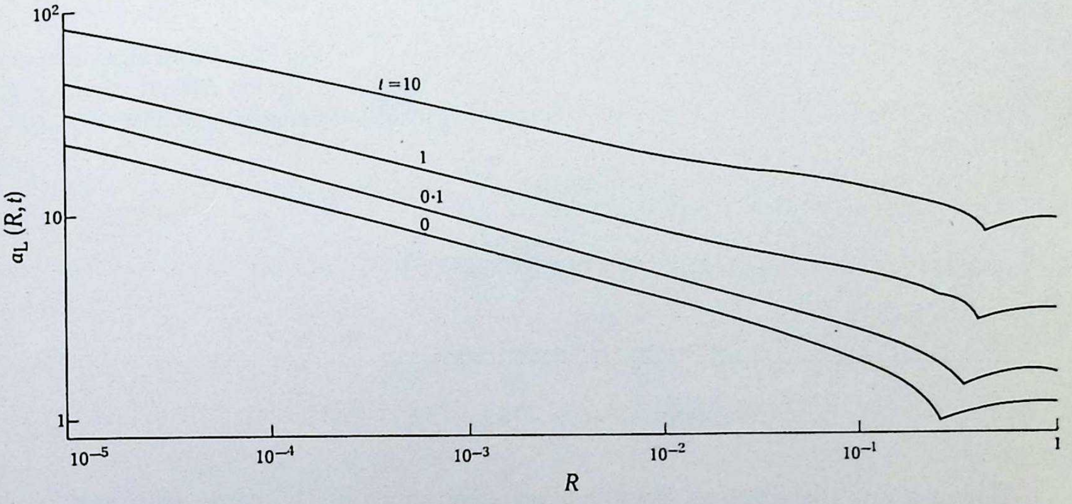

Fig. 1.—Limiting separation of two resonances $a_L(R,t)$ (in units of half the level width) for which the levels are just resolved plotted against the peak height ratio R.

and the argument t has been suppressed in $\psi(x,t)$ and $\phi(x,t)$. If it is now assumed that σ_{dist} is a slowly varying quantity between the resonances and consequently that $\mathrm{d}^2\sigma_{\mathrm{dist}}/\mathrm{d}x^2 \simeq 0$, the positions of the zeros of the $\mathrm{d}^2\sigma/\mathrm{d}x^2$ can be found numerically. The limiting separation of the two resonances $a_L(R,t)$ for which less than two points of inflexion occur in $0 < x < a$ is shown in Figure 1 plotted against R for four values of t. For small values of R ($\leqslant 10^{-2}$) it is seen that $a_L(R,t)$ is proportional to a power of R, the exact dependence being given by

$$\left.\begin{aligned} a_L(R,0) &= 1\cdot213\,R^{-0\cdot257}, &\qquad a_L(R,0\cdot1) &= 1\cdot546\,R^{-0\cdot257}, \\ a_L(R,1) &= 2\cdot266\,R^{-0\cdot257}, &\qquad a_L(R,10) &= 7\cdot482\,R^{-0\cdot208}. \end{aligned}\right\} \tag{4}$$

The total probability of failing to resolve the two levels is the product of the probability for finding a relative peak height R and a level separation less than $\frac{1}{2}\Gamma a_L(R,t)$, integrated over all R. The two distributions are readily obtained for a nonfissile nucleus that forms two level sequences when bombarded with slow neutrons.

The frequency function for the peak height ratio R is given simply by the F distribution with (1, 1) degrees of freedom, since reduced neutron widths are distributed about their mean as χ^2 variables with one degree of freedom:

$$R(r)\,\mathrm{d}r = \left\{r^{-\frac{1}{2}}/\pi(1+r)\right\}\mathrm{d}r\,. \tag{5}$$

This function is plotted against the ratio $r = \Gamma_{\mathrm{n}2}/\Gamma_{\mathrm{n}1}$ in Figure 2.

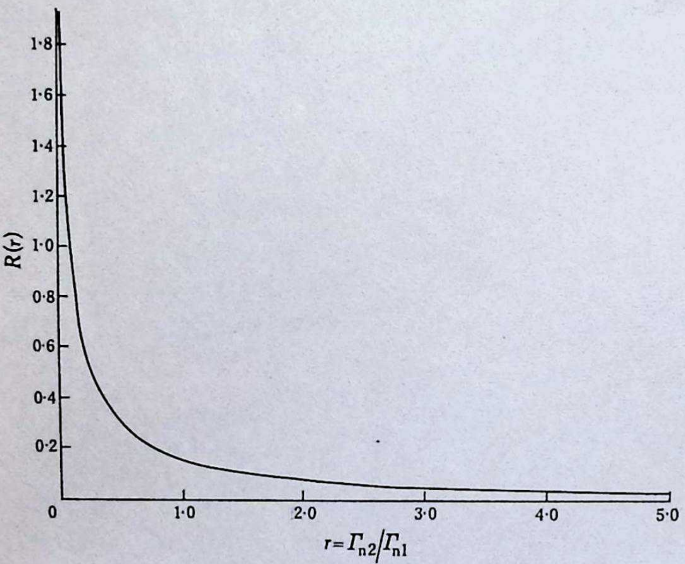

Fig. 2.—Probability density function $R(r)$ in equation (5) versus the ratio $r = \Gamma_{\mathrm{n}2}/\Gamma_{\mathrm{n}1}$.

The spacing distribution law for a level sequence of the same spin and parity and average level spacing $\langle D\rangle$ is given to a good approximation by the surmise of Wigner (1957)

$$p_1(x)\,\mathrm{d}x = \tfrac{1}{2}\pi x\exp(-\tfrac{1}{4}\pi x^2)\,\mathrm{d}x\,, \tag{6}$$

where $x = D/\langle D\rangle$. Owing to the level repulsion effect, overlapping between levels of the same spin sequence is negligible and the correction technique of Fuketa and Harvey (1965) is adequate. However, since the spacing distributions for different spin states are independent, the probability of overlapping becomes appreciable when two spin states are superimposed. The probability density of spacings resulting from the random superposition of two level sequences both having equal average level spacings $\langle D\rangle$ and spacing distributions given by equation (6) is given by (e.g. Mehta 1967)

$$q_1(x) = \tfrac{1}{2}\pi x\exp(-\tfrac{1}{4}\pi x^2)\,\mathrm{erfc}(\tfrac{1}{2}\pi^{\frac{1}{2}}x) + \exp(\tfrac{1}{2}\pi x^2)\,, \tag{7}$$

where $x = D/\langle D\rangle$; and finally the distribution function for such a sequence is

$$P(y \leqslant x) = 1-\exp(-\tfrac{1}{4}\pi x^2)\,\mathrm{erfc}(\tfrac{1}{2}\pi^{\frac{1}{2}}x)\,, \tag{8}$$

where

$$\mathrm{erfc}\,z = 2\pi^{-\frac{1}{2}}\int_z^\infty \exp(-t^2)\,\mathrm{d}t\,.$$

The frequency and distribution functions for the spacings of two superimposed level sequences given by equations (7) and (8) are shown in Figure 3.

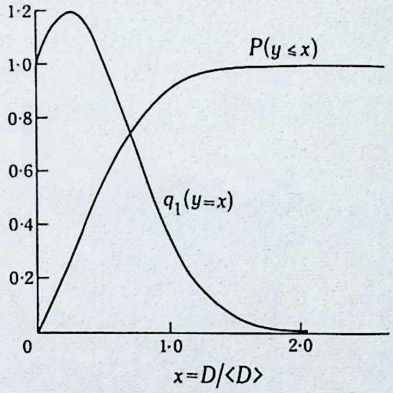

Fig. 3.—Probability density function $q_1(y = x)$ and distribution function $P(y \leqslant x)$ for spacings of two superimposed level sequences versus $x = D/\langle D\rangle$. $\langle D\rangle$ is the average level spacing per spin state, assumed the same for each sequence.

The total probability for failing to resolve the two levels can now be written as

$$P_1(\text{overlap}) = \int_0^\infty R(r)\, P\big(x \leqslant x_\text{L}(r)\big)\, \mathrm{d}r\,, \tag{9}$$

where $x_\text{L}(r) = \Gamma a_\text{L}(r)/2\langle D\rangle$. The integration is performed numerically and Figure 4

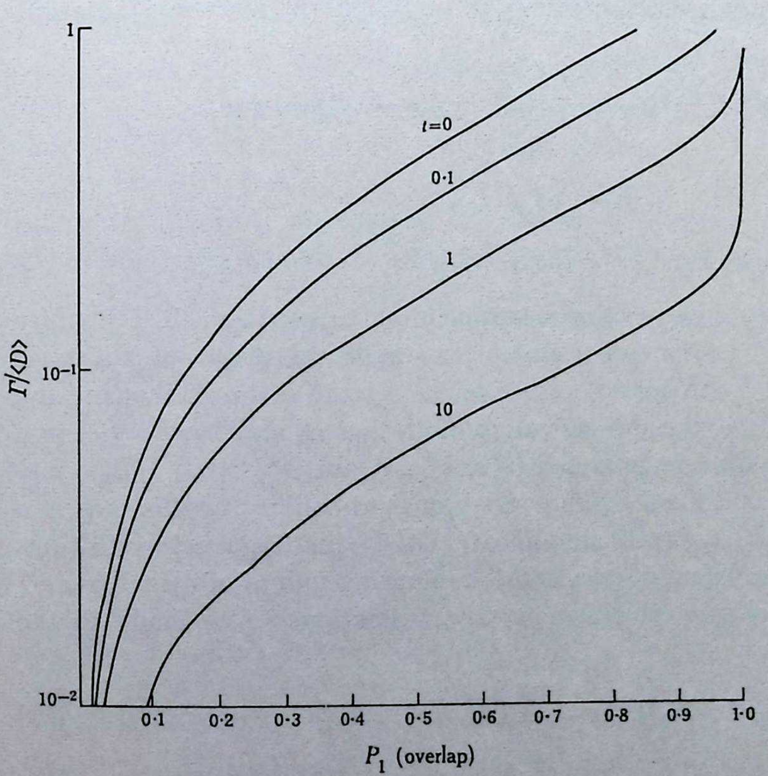

Fig. 4.—Probability of two levels overlapping P_1(overlap) in nonfissile nuclei versus the ratio $\Gamma/\langle D\rangle$.

shows the overlapping probability versus the ratio $\Gamma/\langle D\rangle$ for four values of t. There are further small corrections to be applied to the missing probability of equation (9) from multiple overlapping of levels. The contribution from levels overlapping three at a time can be calculated as for the two-level case, but since this will be found to be small no higher order corrections will be attempted.

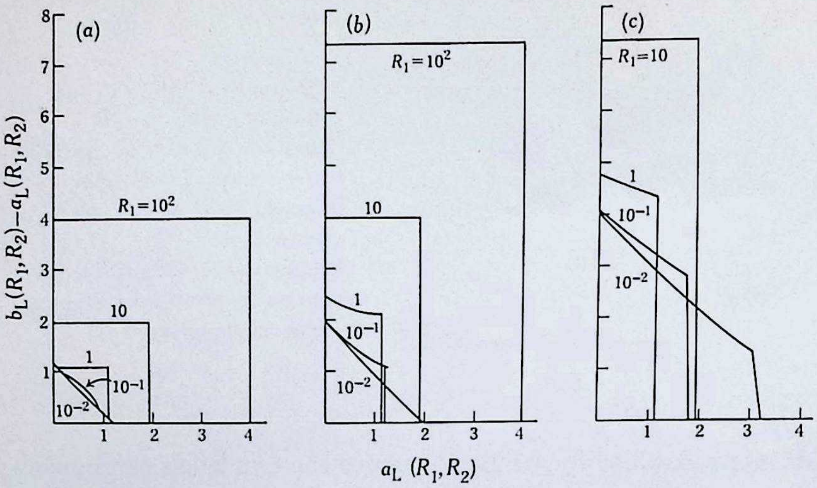

Fig. 5.—Limiting separations of three adjacent levels $a_L(R_1,R_2,t)$ and $b_L(R_1,R_2,t)-a_L(R_1,R_2,t)$ shown for $t=0$, various values of R_1, and (a) $R_2=1$, (b) $R_2=0\cdot1$, and (c) $R_2=0\cdot01$.

III. Correction for Triple Overlapping of Levels

The capture cross section corresponding to equation (2) for three adjacent levels can be written as

$$\sigma_c \simeq \text{const}\{\psi(x,t)+R_1\psi(x-a,t)+R_2\psi(x-b,t)\}+\sigma_{\text{dist}}, \tag{10}$$

where

$$R_1=\Gamma^0_{n2}/\Gamma^0_{n1}; \qquad R_2=\Gamma^0_{n3}/\Gamma^0_{n1},$$

$$a=2(E_2-E_1)/\Gamma, \qquad b=2(E_3-E_1)/\Gamma, \qquad 0\leqslant a\leqslant b.$$

The second derivative of the cross section corresponding to equation (3) is readily found and again the limiting values of a and b for which less than two points of inflexion occur in $0<x<b$ are found numerically. Figure 5 shows the limiting values $a_L(R_1,R_2)$ and $b_L(R_1,R_2)$ for several values of R_1 and R_2 and $t=0$. Because of the symmetry between the configurations $(1,R_1,R_2)$ and $(1,R_1/R_2,1/R_2)$ only values of $R_2\leqslant1$ need be considered. The overlapping probability in this case is a double integral over R_1 and R_2 and some simplification of the limiting level separations is desirable for computation. Comparison with the limiting values of a in Figure 1 for the two-level problem allows the following approximations to be made to the limiting three-level separations:

$$R_1\geqslant1,\ R_2\leqslant1 \qquad a_L(R_1,R_2)\simeq a_L(R_1), \quad b_L(R_1,R_2)\simeq a_L(R_1)+a_L(R_1/R_2), \tag{11}$$

$$R_1\leqslant1,\ R_2\leqslant1,\ R_1>R_2 \quad a_L(R_1,R_2)\simeq a_L(R_1), \quad b_L(R_1,R_2)\simeq a_L(R_2), \tag{12}$$

$$R_1\leqslant1,\ R_2\leqslant1,\ R_2>R_1 \quad a_L(R_1,R_2)\simeq a_L(R_2), \quad b_L(R_1,R_2)\simeq a_L(R_2), \tag{13}$$

where the argument t has been suppressed. Owing to symmetry, the three regions of R_1,R_2 above are sufficient to include all possible configurations of three levels.

To proceed further, we require the probability that if a resonance occurs at E, which is taken to be the origin, then the second level occurs within an interval $x_1 \leqslant a$ and the next level occurs within an interval $x_2 \leqslant b$. The two level sequences are assumed to have equal average level spacings, and without loss of generality the resonance at E is assumed to belong to the first sequence. The probability that the third resonance occurs in $x, x+\mathrm{d}x$, conditional upon the second having occurred at $x_1 = k$, can be written as (Wilkins and Musgrove, to be published)

$$\begin{aligned} P(x \mid x_1 = k)\,\mathrm{d}x = h_1(k)\Big\{&p_1(x-k)\int_x^\infty \exp(-\tfrac{1}{4}\pi y^2)\,\mathrm{d}y\left(\int_k^\infty \exp(-\tfrac{1}{4}\pi y^2)\,\mathrm{d}y\right)^{-1} \\ &+\exp(-\tfrac{1}{4}\pi x^2)\left(\int_k^\infty \exp(-\tfrac{1}{4}\pi y^2)\,\mathrm{d}y\right)^{-1}\int_x^\infty p_1(y-k)\,\mathrm{d}y\Big\}\,\mathrm{d}x \\ +h_2(k)\Big\{&p_1(x-k)\int_x^\infty p_1(y)\,\mathrm{d}y\left(\int_k^\infty p_1(y)\,\mathrm{d}y\right)^{-1} \\ &+p_1(x)\left(\int_k^\infty p_1(y)\,\mathrm{d}y\right)^{-1}\int_x^\infty p_1(y-k)\,\mathrm{d}y\Big\}\,\mathrm{d}x, \end{aligned} \tag{14}$$

where $p_1(x)$ is the Wigner distribution in equation (6) and $h_i(k)$ is the probability that the resonance at k is of the ith sequence and

$$\left.\begin{aligned} h_1(k) &= \tfrac{1}{2}\pi k\exp(-\tfrac{1}{4}\pi k^2)\,\mathrm{erfc}(\tfrac{1}{2}\pi^{\frac{1}{2}}k)/q_1(k), \\ h_2(k) &= \exp(-\tfrac{1}{2}\pi k^2)/q_1(k), \end{aligned}\right\} \tag{15}$$

with $q_1(k)$ given by equation (7). The probability that the third resonance occurs anywhere in the interval $k \leqslant x_2 \leqslant b$ can then be written as

$$\begin{aligned} P(x_2 \leqslant b \mid x_1 = k) &= \int_k^b P(x \mid x_1 = k)\,\mathrm{d}x \\ &= \tfrac{1}{2}\pi k\frac{\exp(-\frac{1}{4}\pi k^2)}{q_1(k)}\Big(\mathrm{erfc}(\tfrac{1}{2}\pi^{\frac{1}{2}}k) - \exp\big(-\tfrac{1}{4}\pi(b-k)^2\big)\,\mathrm{erfc}(\tfrac{1}{2}\pi^{\frac{1}{2}}b)\Big) \\ &\quad+\frac{\exp(-\frac{3}{8}\pi k^2)}{q_1(k)}\Big(\exp(-\tfrac{1}{8}\pi k^2) - \exp\big(-\tfrac{1}{2}\pi(b-\tfrac{1}{2}k)^2\big)\Big), \end{aligned} \tag{16}$$

and the required distribution is

$$P(x_2 \leqslant b, x_1 \leqslant a) = \int_0^k q_1(k)\,P(x_2 \leqslant b \mid x_1 = k)\,\mathrm{d}k, \tag{17}$$

where $a \leqslant b$. Figure 6 shows the slightly different distribution function $P(x_2 \leqslant (b-a), x_1 \leqslant a)$ versus x_1 and x_2, where in this case x_2 is the spacing between the second and third levels. The integration of equation (17) was performed numerically.

Since R_1 and R_2 are dependent variables, the probability element in their joint distribution is required. The distribution of reduced neutron widths about their mean is given by

$$P(x) = (2\pi x)^{-\frac{1}{2}} \exp(-\tfrac{1}{2}x)\,,$$

and putting $x_i = \Gamma^0_{\mathrm{n}i}/\langle\Gamma^0_{\mathrm{n}}\rangle$, $i = 1,2,3$, the joint element for x_1, x_2, and x_3 can be written as

$$P(x_1,x_2,x_3)\,\mathrm{d}x_1\,\mathrm{d}x_2\,\mathrm{d}x_3 = \prod_{i=1}^{3} (2\pi x_i)^{-\frac{1}{2}} \exp(-\tfrac{1}{2}x_i)\,\mathrm{d}x_i\,. \tag{18}$$

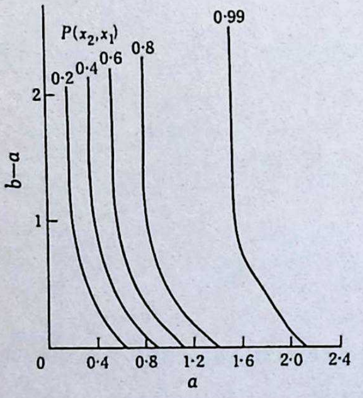

Fig. 6.—Distribution function $P(x_2 \leqslant (b-a),\, x_1 \leqslant a)$ shown for first resonance spacing x_1 and second resonance spacing x_2 for a superposition of two simple sequences having equal average level spacings.

The required element is obtained by substituting $r_1 = x_2/x_1$ and $r_2 = x_3/x_1$ in equation (18) and integrating over x_1 to obtain

$$R(r_1,r_2)\,\mathrm{d}r_1\,\mathrm{d}r_2 = \big\{2\pi(r_1 r_2)^{\frac{1}{2}}(1+r_1+r_2)^{3/2}\big\}^{-1}. \tag{19}$$

The probability of failing to resolve the three levels is therefore

$$P_2(\text{overlap}) = \int_0^\infty \mathrm{d}r_1 \int_0^\infty R(r_1,r_2)\, P\big(x_2 \leqslant x_{2\mathrm{L}}(r_1,r_2),\, x_1 \leqslant x_{1\mathrm{L}}(r_1,r_2)\big)\,\mathrm{d}r_2\,, \tag{20}$$

where

$$x_{1\mathrm{L}} = \Gamma a_{\mathrm{L}}(r_1,r_2)/2\langle D\rangle \qquad \text{and} \qquad x_{2\mathrm{L}} = \Gamma b_{\mathrm{L}}(r_1,r_2)/2\langle D\rangle\,.$$

When the appropriate values for a_{L} and b_{L} are inserted from equations (11), (12), and (13) the integration can be carried out, and Figure 7 shows the probability for triple overlapping versus $\Gamma/\langle D\rangle$ for four values of t. For most nuclei the correction can be ignored for small energies; however, in ^{233}U for which $\langle\Gamma\rangle/\langle D\rangle \simeq 0\cdot2$ the correction amounts to approximately 2%.

IV. METHOD OF CORRECTION FOR FISSILE NUCLIDES

In fissile nuclides the calculation of the correction for missed levels is complicated by the fact that the fission widths, and hence the total widths, fluctuate from level to level and the peak height ratio of two resonances is no longer given by the ratio of two reduced neutron widths. The fission cross section between two adjacent levels is given in the single-level Breit–Wigner approximation by

$$\sigma_{\mathrm{f}}(E) = 4\pi\lambda\!\!\!^{-2}\left(\frac{g_1\,\Gamma_{\mathrm{n1}}\,\Gamma_{\mathrm{f1}}}{\Gamma_1^2}\psi(x,t)+\frac{g_2\,\Gamma_{\mathrm{n2}}\,\Gamma_{\mathrm{f2}}}{\Gamma_2^2}\psi(x-a,t)\right)+\sigma_{\mathrm{dist}}\,, \tag{21}$$

where Γ_{f} is the fission width of the level and all other symbols have been defined previously. Multilevel effects have been ignored in equation (21) since, owing to the level repulsion effect, overlapping is much more probable for levels of opposite spin than for levels of the same spin and parity. In any case, it is expected that the limiting separation at which two levels with peak height ratio R are just resolved will, at least on *average*, be given by the $a_{\mathrm{L}}(R)$ found in the nonfissile case. In analogy with equation (2), the fission cross section can be written as

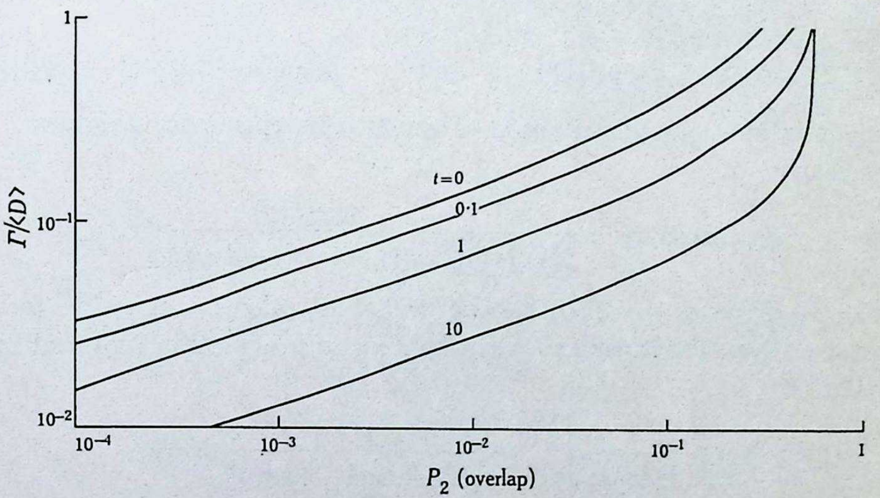

Fig. 7.—Probability of three levels overlapping P_2(overlap) versus the ratio $\Gamma/\langle D\rangle$ for four values of t.

$$\sigma_{\mathrm{f}} \simeq \mathrm{const}\{\psi(x,t)+RS\psi(x-a,t)\}+\sigma_{\mathrm{dist}}\,, \tag{22}$$

where

$$R = \Gamma^0_{\mathrm{n2}}/\Gamma^0_{\mathrm{n1}} \qquad \text{and} \qquad S = (\Gamma_{\mathrm{f2}}/\Gamma_2^2) \div (\Gamma_{\mathrm{f1}}/\Gamma_1^2)\,.$$

The fission process proceeds through a small number of open channels and the distribution of fission widths about their mean is usually represented by a chi-squared distribution with n degrees of freedom, where n usually lies between 2 and 4:

$$P(z) = \left(n^{\frac{1}{2}n}/\{2^{\frac{1}{2}n}\,\Gamma(\tfrac{1}{2}n)\}\right)\exp(-\tfrac{1}{2}nz)\,z^{\frac{1}{2}n-1}\,, \tag{23}$$

with $z = \Gamma_{\mathrm{f}}/\langle\Gamma_{\mathrm{f}}\rangle$. It should be noted that it is purely a matter of convenience to represent this distribution by a member of the χ^2 family since the fission process typically proceeds through a different number of channels from each spin state and the average fission widths for each spin state are usually different.

To obtain the probability element for the variate $\Gamma_{\mathfrak{f}}/\Gamma^2$, the substitution $y = z/(z+c)^2$ is made in equation (23). Thus

$$c = \Gamma_\gamma/\langle\Gamma_{\mathfrak{f}}\rangle \quad \text{is constant,} \qquad z = \left\{1-2cy\pm(1-4cy)^{\frac{1}{2}}\right\}/2y\,,$$

and

$$P(y)\,\mathrm{d}y = \frac{n^{\frac{1}{2}n}}{2^{\frac{1}{2}n}\,\Gamma(\frac{1}{2}n)}\,\frac{f(y)}{y(1-4cy)^{\frac{1}{2}}}\,\mathrm{d}y\,, \qquad 0 \leqslant y \leqslant 1/4c\,, \tag{24}$$

where

$$f(y) = \exp(-\tfrac{1}{2}n\zeta_1)\,\zeta_1^{\frac{1}{2}n} + \exp(-\tfrac{1}{2}n\zeta_2)\,\zeta_2^{\frac{1}{2}n}\,,$$

with

$$\zeta_1 = \left\{1-2cy+(1-4cy)^{\frac{1}{2}}\right\}/2y \qquad \text{and} \qquad \zeta_2 = \left\{1-2cy-(1-4cy)^{\frac{1}{2}}\right\}/2y\,.$$

The element in the joint distribution of the two independent variables $\Gamma_{\mathfrak{f}1}/\Gamma_1^2$ and $\Gamma_{\mathfrak{f}2}/\Gamma_2^2$ is clearly

$$P(x,y)\,\mathrm{d}x\,\mathrm{d}y = \frac{n^n}{2^n(\Gamma(\frac{1}{2}n))^2}\,\frac{f(x)f(y)}{xy\{(1-4cx)(1-4cy)\}^{\frac{1}{2}}}\,\mathrm{d}x\,\mathrm{d}y\,, \tag{25}$$

where $x = \Gamma_{\mathfrak{f}1}/\Gamma_1^2$ and $y = \Gamma_{\mathfrak{f}2}/\Gamma_2^2$. The probability density function for the ratio x/y is obtained by substituting $u = x/y$ and $v = y$ in equation (25) and integrating over v. Thus

$$P(u)\,\mathrm{d}u = \frac{n^n}{2^n(\Gamma(\frac{1}{2}n))^2}\int_0^{1/4c}\frac{f(uv)f(v)}{uv\{(1-4cv)(1-4cuv)\}^{\frac{1}{2}}}\,\mathrm{d}v\,\mathrm{d}u\,, \qquad u<1\,, \tag{26a}$$

$$= \frac{n^n}{2^n(\Gamma(\frac{1}{2}n))^2}\int_0^{1/4cu}\frac{f(uv)f(v)}{uv\{(1-4cv)(1-4cuv)\}^{\frac{1}{2}}}\,\mathrm{d}v\,\mathrm{d}u\,, \qquad u>1\,. \tag{26b}$$

Putting $v = \sin^2\theta/4c$ in equation (26a) and $v = \sin^2\theta/4cu$ in (26b) we obtain

$$P(u)\,\mathrm{d}u = \frac{K}{u}\int_0^{\frac{1}{2}\pi}\frac{f(\sin^2\theta/4c)\,f(u\sin^2\theta/4c)}{\sin\theta\,(1-u\sin^2\theta)^{\frac{1}{2}}}\,\mathrm{d}\theta\,\mathrm{d}u\,, \qquad u<1\,, \tag{27a}$$

$$= \frac{K}{u^{\frac{1}{2}}}\int_0^{\frac{1}{2}\pi}\frac{f(\sin^2\theta/4c)\,f(u\sin^2\theta/4c)}{\sin\theta\,(u-\sin^2\theta)^{\frac{1}{2}}}\,\mathrm{d}\theta\,\mathrm{d}u\,, \qquad u>1\,, \tag{27b}$$

where

$$K = n^n/2^{n-1}(\Gamma(\tfrac{1}{2}n))^2\,.$$

The joint probability element in the distribution of $S = (\Gamma_{\mathfrak{f}1}/\Gamma_1^2) \div (\Gamma_{\mathfrak{f}2}/\Gamma_2^2)$ and $R = \Gamma_{\mathrm{n}1}^0/\Gamma_{\mathrm{n}2}^0$ is now

$$P(r,u)\,\mathrm{d}u\,\mathrm{d}r = \left\{r^{-\frac{1}{2}}P(u)/\pi(1+r)\right\}\mathrm{d}u\,\mathrm{d}r\,,$$

and the element for the product ur is obtained by substituting $x = ur$ and $y = u$ and integrating over y. Thus

$$Q(x) = K\int_0^1\frac{(x/y)^{-\frac{1}{2}}P(y)}{\pi(x+y)}\,\mathrm{d}y + K\int_1^\infty\frac{(x/y)^{-\frac{1}{2}}P(y)}{\pi(x+y)}\,\mathrm{d}y \tag{28}$$

and ultimately the required probability element in the distribution of $x = RS$ becomes

$$Q(x)\,\mathrm{d}x = \frac{K}{\pi}\int_0^1 \frac{1}{(xy)^{\frac{1}{2}}}\left(\frac{1}{x+y}+\frac{1}{xy+1}\right)\mathrm{d}y\int_0^{\frac{1}{2}\pi}\frac{f(\sin^2\theta/4c)\,f(y\sin^2\theta/4c)}{\sin\theta\,(1-y\sin^2\theta)^{\frac{1}{2}}}\,\mathrm{d}\theta\,\mathrm{d}x\,, \qquad (29)$$

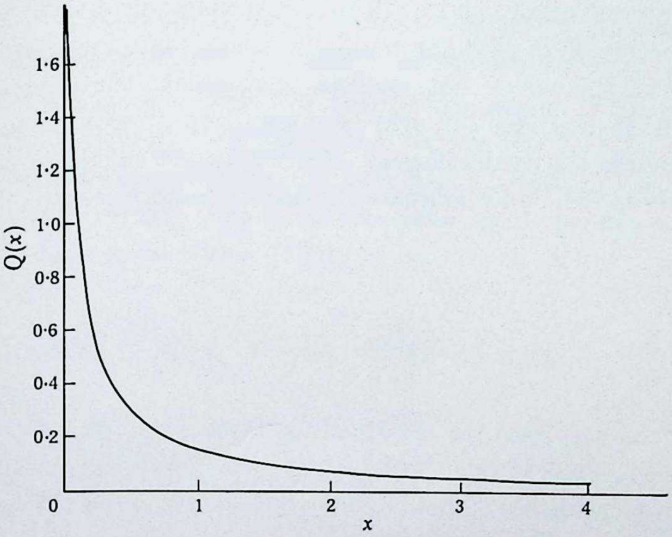

Fig. 8.—Probability density function $Q(x)$ in equation (29) versus $x = (\Gamma^0_{\mathrm{n}2}\Gamma_{\mathrm{f}2}/\Gamma^2_2) \div (\Gamma^0_{\mathrm{n}1}\Gamma_{\mathrm{f}1}/\Gamma^2_1)$ for $c = 0\cdot 1$ and $n = 3$.

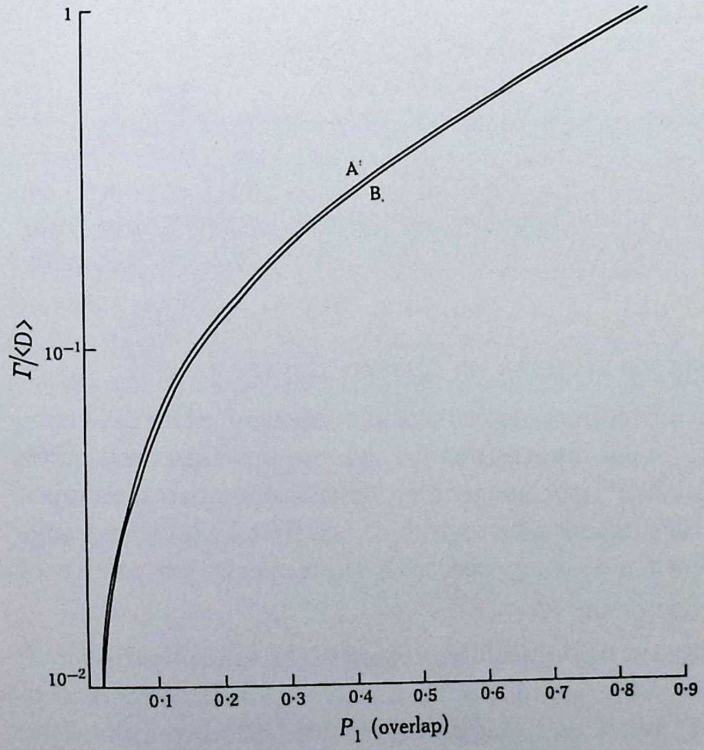

Fig. 9.—Probability of two-level overlap versus the ratio $\Gamma/\langle D\rangle$ for $t = 0$ in (A) nonfissile nuclides, and (B) fissile nuclides.

upon manipulating the second integral in equation (28). Figure 8 gives $Q(x)$ versus x for $c = 0\cdot 1$ and an assumed value of $n = 3$ for the number of degrees of freedom in the fission width distribution. The total probability for missing either of two adjacent levels in fissile nuclei can now be obtained by replacing the R distribution by Q in equation (9):

$$P_1(\text{overlap}) = \int_0^\infty Q(r)\,P(x \leqslant x_{\text{L}}(r))\,\mathrm{d}r\,. \tag{30}$$

The overlapping probability is shown in Figure 9 against $\Gamma/\langle D\rangle$ for $t = 0$ and is compared with that found for the nonfissile nuclides. The overlapping probability for fissile nuclei is at most 5% greater than that for nonfissile nuclei and for most purposes can be ignored. Because of this we do not attempt to calculate the three-level overlapping probability for fissile nuclides but will be content to approximate it by the correction already calculated in the nonfissile case. We now give a calculation of the probability for missing levels in ^{233}U and compare it with an earlier result of Musgrove (1967).

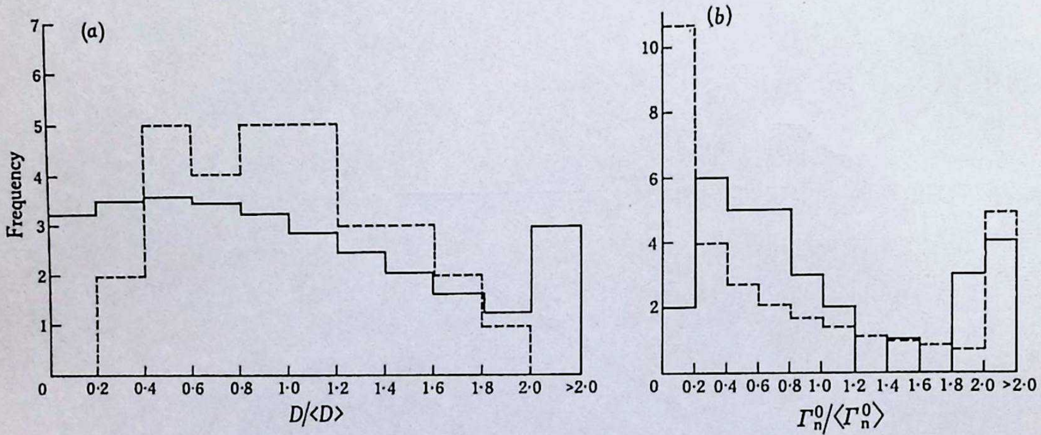

Fig. 10.—Histograms for ^{233}U of (*a*) first 30 level spacings compared with the expectation values (dashed lines) from equation (7) and (*b*) 31 values of $\Gamma_{\text{n}}^0/\langle\Gamma_{\text{n}}^0\rangle$ compared with the expectation values.

V. CALCULATION OF PROBABLE NUMBER OF MISSED LEVELS IN ^{233}U

There is a considerable body of indirect experimental evidence for the existence of undetected resonances in ^{233}U. Small inter-resonance spacings are observed much less frequently than is expected when two independent level sequences are superimposed. This is seen in Figure 10(*a*) where a histogram of the first 30 level spacings (normalized to unit mean) is shown and compared with the expectation values of equation (7).

In the experimental distribution of reduced neutron widths, once again, small values are lacking as is seen in the histogram plotted in Figure 10(*b*) with expectation values. In fact, Nifenecker (1964) found that this distribution is fitted quite well by a χ^2 distribution with four degrees of freedom instead of the expected one degree of freedom. Since there is no reason to believe that ^{233}U has other than a single neutron decay channel, or that the distributions of resonances of different spin states are not independent in that nucleus, it appears that unresolved levels may cause the discrepancies.

In order to calculate the probable number of levels missed for ^{233}U, care must be taken to select an "unbiased" sample of observed levels. Our criterion for failing to resolve two levels with peak height ratio R is that the levels are separated by less than $a_L(R)\langle\Gamma\rangle/2\langle D\rangle$. In fissile nuclei where Γ fluctuates considerably from level to level it is possible for two levels to be resolved experimentally with separations less than the limit (e.g. when $\frac{1}{2}(\Gamma_1+\Gamma_2) \leqslant \langle\Gamma\rangle$). In ^{233}U, the levels reported by Nifenecker (1964) at 7·65, 16·82, 18·75, and 26·50 eV fall into this category and are therefore omitted from the "observed" resonances for this calculation.

Suppose that N_0 levels are detected experimentally in an energy range $E_1 \leqslant E \leqslant E_n$, where E_1 and E_n are the energies of the first and last levels in the sequence, and further suppose that ν levels with average total width $\langle\Gamma\rangle'$ are missed in this range. The actual average level spacing per spin state $\langle D\rangle$ and the actual average total width $\langle\Gamma\rangle$ may be written as

$$\langle D\rangle = 2(E_n-E_1)(N_0+\nu-1)^{-1}, \qquad \langle\Gamma\rangle = \left(\sum_{i=1}^{n_0}\Gamma_i + \nu\langle\Gamma\rangle'\right)(N_0+\nu)^{-1}, \tag{31}$$

where Γ_i is the total width of the ith level and we have assumed equal average level spacings in each spin state. For this calculation it will be assumed that the missed levels have the same average total width as the observed levels. The expected number of levels missed in ^{233}U can now be obtained by iteration. Thus

$$\nu^{(m)} = (N_0+\nu^{(m-1)})\{P_1(\gamma^{(m-1)})+P_2(\gamma^{(m-1)})\}, \tag{32}$$

where m is the order of the iteration, γ is the ratio $\langle\Gamma\rangle/\langle D\rangle$, and P_1 and P_2 are respectively the probabilities for two- and three-level overlap given in equations (9) and (20). The parameters used in the present calculation were taken from Nifenecker (1964), where 31 levels are reported with average total width 0·38 eV between energies 1·799 and 29·51 eV. Since four of these levels are "unresolved" by our criterion, we solve equation (32) for ν using $N_0 = 27$. The probable number of levels missed in the range was found to be 16·8 after 12 iterations. The positions of 4 of these are known already, but the remaining 13 levels are undetected. This value agrees very well with the earlier result of Musgrove (1967) where 11 ± 2 was the expected number of levels missed for the Nifenecker data in a slightly smaller energy range. The corrected average level spacing of ^{233}U for the present calculation is 0·64 eV compared with the earlier corrected value of 0·65 eV.

VI. CONCLUSIONS

In the direct method of calculating the probability for missing levels in slow neutron spectroscopy as described above, the probability depends only on the observed ratio $\langle\Gamma\rangle/\langle D\rangle$, unlike earlier methods which require the (unknown) average reduced neutron width of the missed levels as a parameter. The present method treats overlapping levels and weak levels identically and it has been shown that for practical purposes only two-level overlapping contributes to the total probability for missing levels. For nonfissile nuclides the correction is small ($\lesssim 10\%$) at low energies but a calculation of the number of missed levels in ^{233}U indicates that approximately 30% of the levels in that nucleus are undetected. This value agrees quite well with that reported by Musgrove (1967).

VII. REFERENCES

CLANCY, B. E., and KEANE, A. (1964).—Australian Atomic Energy Commission Rep. No. AAEC/E117.

FUKETA, T., and HARVEY, J. A. (1965).—*Nucl. Instrum. Meth.* **33**, 107.

MEHTA, M. L. (1967).—"Random Matrices." p. 216. (Academic Press: New York.)

MUSGROVE, A. R. (1967).—*Aust. J. Phys.* **20**, 617.

NIFENECKER, H. (1964).—*J. Physique* **25**, 877.

WIGNER, E. P. (1957).—Oak Ridge National Lab. Rep. No. ORNL 2309, p. 59.

WILKINS, C. A. (1967).—*J. nucl. Sci. Technol.* **4**, 37.

CHARGE EXCHANGE COLLISIONS INVOLVING MULTIELECTRON ATOMS (LITHIUM AND SODIUM)

By J. G. Lodge* and R. M. May*

[*Manuscript received August* 19, 1968]

Summary

The cross section for forming both ground state and excited state hydrogen atoms by charge exchange between protons and lithium or sodium atoms is calculated. These calculations are performed using the Brinkman–Kramers approximation along with a multiplicative correction factor; the target lithium and sodium atoms are first described by simple "effective-Z" wavefunctions, and then the lithium case is treated more accurately both by including the inner electrons and by using a more accurate numerical lithium wavefunction.

The results are in satisfactory agreement with the experiments of Il'in *et al.* (Both theory and experiment pertain to incident proton energies of around 10–100 keV.)

I. Introduction

The charge exchange collision has been a subject of some interest over the past 15 years, stimulated by an interest in producing beams of excited neutral particles for injection into plasma devices such as ALICE, PHOENIX, and OGRA II, which are described in articles by Futch *et al.* (1966), Bernstein *et al.* (1966), and Artemenkov *et al.* (1966).

The method of production is to inject fast protons into a neutral gas, resulting in excited neutral atoms formed by charge exchange. An essential parameter for this process is the charge exchange cross section which, as is well known, is difficult to calculate exactly. In the present case this will not be attempted, but rather several stages of approximation will be considered and the results compared with the experimental results of Il'in *et al.* (1965).

The problem is usually formulated in one of two ways, one being the impact-parameter method as described by Wu and Ohmura (1962), and the other, the wave treatment as given by Mott and Massey (1965); a Born approximation is then generally applied in either case. (In the present work we will employ the wave treatment.) In either of the methods used there are two points to consider. Firstly the change in momentum of the exchanged electron must be fully described, allowing for the change in the centre of mass of the two heavy particle systems. The second point concerns the choice of interaction potential for the collision.

There has been considerable controversy over the appropriate interaction potential to be used in treating this collision in Born approximation. The usual Born treatment leads to a matrix element $\langle\psi_i|V|\psi_f\rangle$, where ψ_i and ψ_f are the initial and final wavefunctions of the electron and V is the interaction potential. The ψ_i, ψ_f are

---

* Theoretical Physics Department, School of Physics, University of Sydney, Sydney, N.S.W. 2006.

Aust. J. Phys., 1968, **21**, 793–801

taken as products of the bound state wavefunction of the electron and a plane wave representing the momentum between the colliding systems. It is in the choice of V that the trouble arises.

The original Brinkman–Kramers (BK) assumption is that the interaction V should consist wholly of the interaction between the electron and the incoming proton since it is unlikely that the repulsive nucleus–nucleus interaction should influence the transfer of an electron from one nucleus to the other.

It is well known that the cross sections calculated in this BK approximation are too large particularly at resonance (~ 25 keV) but also at high energy. The nucleus–nucleus term was therefore included by Bates and Dalgarno (1952) and Jackson and Schiff (1953) to obtain much better results. However, in the Jackson–Schiff paper an added note by Wick suggests that the nucleus–nucleus contribution should be less by an order of m/M than the value of the electron–nucleus term. Also Jackson (1956) has shown that for the proton–hydrogen charge exchange a term in the second Born approximation cancels most of the nucleus–nucleus term if it is included in the first Born approximation.

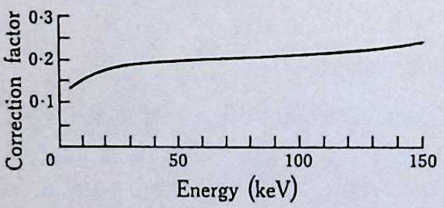

Fig. 1.—Average correction factor evaluated using hydrogen and helium.

More recently Bates (1958) and Bassel and Gerjouy (1960) have independently sought to account for the lack of orthogonality between the initial and final wavefunctions (a feature of exchange collisions). In both cases the resulting effective interaction potentials contained a term resembling the nucleus–nucleus term of Bates and Dalgarno and of Jackson and Schiff. So although it may be shown that the nucleus–nucleus term should contribute only an order m/M (e.g. May 1964*a*), when lack of orthogonality is included the Jackson–Schiff-type term is justified.

Therefore it appears to be necessary to use the nuclear term or the more complex interaction of Bates or Bassel and Gerjouy. However, Jackson and Schiff (1953) have observed for hydrogen that although the BK cross sections are too large for the reaction $H^{+}+H \rightarrow H(nl)+H^{+}$, the ratios of the BK cross sections for different n agree quite well with those obtained using more exact formulae. That is, for hydrogen the BK cross sections may be used and multiplied by a correction factor (energy dependent but independent of n) to obtain the cross sections for hydrogen.

This situation has been investigated by Mapleton (1962) for helium using both BK and corrected potentials and he has found a similar situation, namely, that the ratios between BK cross sections are preserved. In particular by choosing the "average correction factor" given in Figure 1 both the hydrogen and helium cross sections fit to within 12% over the range of energies used by Mapleton. These values for the hydrogen cross section compare well with the experimental values of Gilbody and Ryding (1966).

We will therefore make the simple assumption that the situation described above for hydrogen and helium remains satisfactory for the case of lithium and sodium. The BK approximation will therefore be used to calculate cross sections of charge exchange for protons on lithium and sodium gas targets. The same average correction factor of Figure 1 will be used for these cases. The results of this will then be compared with the experimental results of Il'in *et al.* (1965) to determine (1) if the correction factor is satisfactory, and (2) if the ratios between excited states are still predicted by the BK approximation.

II. Cross Section Formula

We consider now the charge exchange reaction in which a proton of speed v passes a complex atom M_B of N electrons and captures the jth electron. The distance between the nuclei is $\boldsymbol{t}$ and between the centres of mass of the two initial and final systems is $\boldsymbol{\rho}$ and $\boldsymbol{\sigma}$ respectively.

The initial and final wavefunctions are

$$\psi_{\mathrm{i}} = \phi_{M_B}(\ldots \boldsymbol{r}_i \ldots)\exp(\mathrm{i}\boldsymbol{k}_0 . \boldsymbol{\rho})\exp(-\mathrm{i}E_0 t/\hbar),$$

$$\psi_{\mathrm{f}} = \phi_{M_B^*}(\ldots \boldsymbol{r}_i(i \neq j) \ldots)\exp(\mathrm{i}\boldsymbol{k}_{\mathrm{f}} . \boldsymbol{\sigma})\exp(-\mathrm{i}E_n t/\hbar),$$

and the interaction potential in the prior case is

$$V = e^2 \sum_i |\boldsymbol{t}+\boldsymbol{r}_i|^{-1}.$$

For the type of reaction considered here the wavefunction of a complex atom may be replaced by a product of single-particle wavefunctions. (Mapleton (1962) has verified the validity of this for helium by using both post and prior interactions.)

The situation then reduces to a form dealt with by May (1964*b*) and May and Lodge (1965) and yields

$$\sigma_n^{\mathrm{e}} = \frac{(\mathrm{con})^2}{(2\pi p)^2}\iint \mathrm{d}k'_x\,\mathrm{d}k'_y\,|\langle\phi_{\mathrm{H}}(\boldsymbol{t})\,t^{-1}\exp(\mathrm{i}\boldsymbol{K}_1 . \boldsymbol{t})\rangle\langle\phi_{M_{Bj}}(\boldsymbol{r}_j)\exp(\mathrm{i}\boldsymbol{K}_2 . \boldsymbol{r}_j)\rangle|^2, \qquad (1)$$

where

$$\boldsymbol{K}_1 = (k'_x, k'_y, (2a_0)^{-1}\{p+(Z_B^2/n_B^2-1/n^2)/p\}),$$

$$\boldsymbol{K}_2 = (k'_x, k'_y, (2a_0)^{-1}\{p-(Z_B^2/n_B^2-1/n^2)/p\}),$$

$$\mathrm{con} = \left|\prod_{i\neq j}\langle\phi_{M_{Bi}}(\boldsymbol{r}_i)\,\phi_{M^*_{Bi}}(\boldsymbol{r}_i)\rangle\right|,$$

$-Z_B^2/2n_B^2$ is the potential energy of the jth electron, a_0 is the radius of the Bohr orbit, and $p = \hbar v/e^2$ (kinetic energy $= 25p^2$ keV). In the above $\phi_{M^*_{Bi}}(\boldsymbol{r}_i)$ denotes the orbital wave function of the ith electron after the jth electron has been removed.

Clearly when the jth electron is an outer electron the orbits are not greatly disturbed and so $(\mathrm{con})^2 \sim 1$. But when an inner electron is removed this may not be so. However, since this unusual type of wavefunction is not known and since it is expected that the effect will not be large, we take $(\mathrm{con})^2 = 1$, observing that it is at least an upper limit. This general form will now be used to evaluate the cross sections where both inner and outer electrons are involved.

III. Particular Cases

Initially the two exchange media (lithium and sodium) will be treated using simple effective-Z hydrogenic wavefunctions in which only the outer electron is included. Then lithium will be treated more accurately firstly by including the inner electrons in the effective-Z treatment and lastly by using accurate wavefunctions derived by Roothaan, Sachs, and Weiss (1960).

(a) *Effective-Z Cases*

The formula for the cross section (1) may be rewritten in terms of the functions g and f given by May and Lodge (1965):

$$\sigma^{\mathrm{e}}_{n_2} = \frac{1}{(2\pi p)^2}\iint \mathrm{d}k'_x\,\mathrm{d}k'_y\,|g(\boldsymbol{K}_1)\,f_{M_B}(\boldsymbol{K}_2)|^2\,, \tag{2}$$

$$\boldsymbol{K}_1 = \left(k'_x, k'_y, (2a_0)^{-1}\{p+(Z_1^2/n_1^2-1/n_2^2)/p\}\right),$$

and

$$\boldsymbol{K}_2 = \left(k'_x, k'_y, (2a_0)^{-1}\{p-(Z_1^2/n_1^2-1/n_2^2)/p\}\right),$$

which give

$$a_0^2 K_1^2+1/n_2^2 = a_0^2 K_2^2+Z_1^2/n_1^2 = a_0^2(k_x'^2+k_y'^2)+Z_1^2\beta\,,$$

$$\beta = (4p^2Z_1^2)^{-1}\{p^4+2p^2(Z_1^2/n_1^2+1/n_2^2)+(Z_1^2/n_1^2-1/n_2^2)^2\}\,,$$

$$g_{\mathrm{H}}(\boldsymbol{K}_1) = \int \phi_{\mathrm{H}}(\boldsymbol{r})\,r^{-1}\exp(\mathrm{i}\boldsymbol{K}_1.\boldsymbol{r})\,\mathrm{d}\boldsymbol{r}\,,\qquad f_{M_B}(\boldsymbol{K}_2) = \int \phi_{M_B}(\boldsymbol{r})\exp(\mathrm{i}\boldsymbol{K}_2.\boldsymbol{r})\,\mathrm{d}\boldsymbol{r}\,,$$

and

$$\sum_{lm}|g_{\mathrm{H}}(\boldsymbol{K}_1)|^2 = (2^4\pi a_0/n_2^3)(a_0^2K_1^2+1/n_2^2)^{-2}\,.$$

The second term in the integral (2) involves the wavefunction of the atom M_B which may be a complex atom. However, for this case a simple hydrogenic effective-Z wavefunction will be used. The type of wavefunction we use is actually quite restricted. In the above the K_1 dependence of $\Sigma\,|g|^2$ is in terms of the function $a_0^2K_1^2+1/n_2^2$, which was shown to be equal to a similar term in K_2. This equality came originally from energy considerations, but the term $a_0^2K_2^2+Z_1^2/n_1^2$, which will occur in $\Sigma\,|f(K_2)|^2$, comes from the wavefunction. This means that, for a simple result, a single effective Z must be chosen for both energy and wavefunction. When this is done the result reduces to

$$\sigma^{\mathrm{e}}_{n_2} = \pi a_0^2(p^2n_2^3Z_{\mathrm{eff}}^5)^{-1}F(n_1,l_1,\beta)\,,$$

as given by May and Lodge (1965) in which the quantum number m of the initial state is averaged over, and the quantum numbers l_2, m_2 of the final state are summed over. This type of situation has also been investigated by Nikolaev (1967), who has described the electron by a different effective Z for energy and for wavefunction. The resultant expression is more complex in this situation and of course still requires the wavefunction to be hydrogenic. Bearing this in mind and considering the simple result obtained in Section III(b) below, in which a much more flexible wavefunction is allowed, we take the view that if the one-parameter restriction is relaxed then it is no more difficult (with a computer) to use an accurate wavefunction (parameterized in the manner of Roothaan, Sachs, and Weiss 1960) than it is to use a two-parameter description. Thus in the following a single effective Z will be used.

In the cases of interest the initial atom is in the 1S, 2S, or 3S state and for these the F functions are

$$n=1, \qquad F_{1\mathrm{S}}=\frac{2^8}{5\beta^5},$$

$$n=2, \qquad F_{2\mathrm{S}}=\frac{2^5}{5\beta^5}\left(1-\frac{5}{6\beta}+\frac{5}{28\beta^2}\right),$$

$$n=3, \qquad F_{3\mathrm{S}}=\frac{2^8}{135\beta^5}\left(1-\frac{80}{81\beta}+\frac{1760}{5103\beta^2}-\frac{320}{6561\beta^3}+\frac{1280}{531\,441\beta^4}\right).$$

These formulae were used to obtain cross sections for $n_2=1,\ldots,5$ and also the limit highly excited form $\lim_{n_2\to\infty} n_2^3\sigma_{n_2}^{\mathrm{e}}$. Only the total and highly excited cross sections will be presented here.

The range of values of p was $0\cdot5$–$2\cdot5$, that is, an energy range of 6 to 150 keV.

The effective Z for lithium was chosen to give the correct electron energy and, using values given by Slater (1960), yielded (1) inner electron $Z=2\cdot16$, and (2) outer electron $Z=1\cdot25$. The results for the effective Z for lithium when the inner electrons are included and when they are not are compared for the highly excited case in Figure 2. We see from this that for the lithium effective Z the inner electrons contribute a term equally important with the outer ones when $p\sim1\cdot6$, and when $p\sim2\cdot5$ the inner contribution is about five times as large as the outer. These results are compared with the experimental results of Il'in *et al.* (1965) in Figure 3. The correction factor used is the average factor given in Figure 1. The comparison with experiment for lithium is surprisingly good considering the crude effective-Z wavefunctions and the simple correction to the BK cross sections. Of more significance is the relationship between Figures 3(*a*) and 3(*b*), where we note that total cross sections and the highly excited cross sections are consistent, which indicates that the BK ratios are still yielding good predictions of the actual ratios as mentioned in the Introduction.

For sodium, again the electron energy (Slater 1960) was used to choose the effective Z. However, for sodium the full calculation with inner electrons included has not been done, so that the results are meaningful only at low energy. For these results we have used $Z=1\cdot85$ and p has been restricted to $1\cdot7$.

The results are compared with experimental values of Il'in *et al.* (1965) in Figure 4, again using the correction factor given in Figure 1. The total cross section (Fig. 4(*a*)) compares quite well but the highly excited cross section (Fig. 4(*b*)) does not compare so well. However, by altering the effective Z a better fit could undoubtedly be obtained. We see then that the BK approximation is now not giving such good ratios between cross sections as before, but is still quite good considering the crude wavefunction used for sodium. Also the calibration curve of Figure 1 calculated from hydrogen and helium cross sections is still apparently largely unchanged.

(*b*) *Accurate Lithium Case*

In the previous subsection the lithium wavefunction was set up using a crude effective-Z function. We now use a more accurate function given by Roothaan,

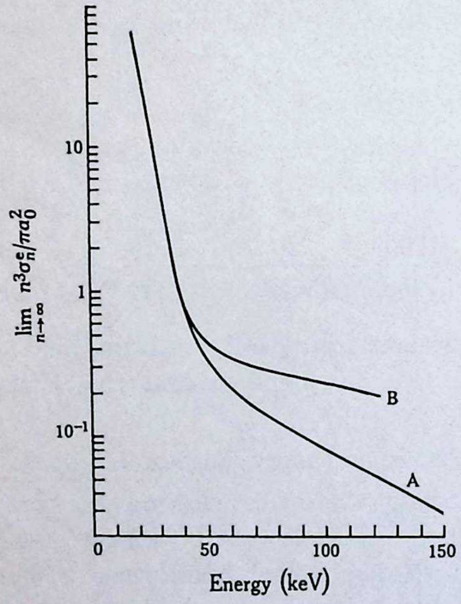

Fig. 2.—Highly excited charge exchange cross sections for lithium in the effective-Z approximation:

A, outer electron only;

B, both inner and outer electrons.

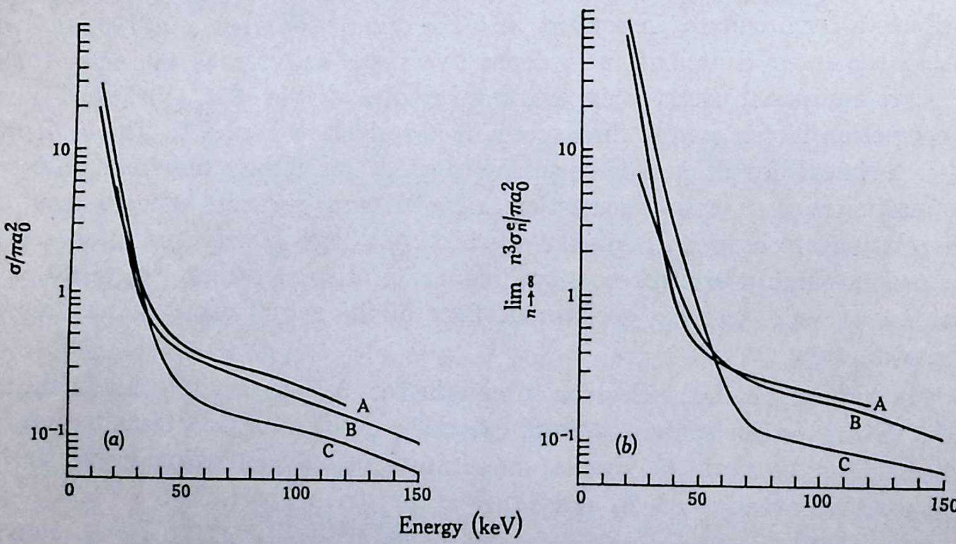

Fig. 3.—Total (*a*) and highly excited (*b*) charge exchange cross sections for lithium: A, experimental results of Il'in *et al.* (1965); B, results using the effective-Z wavefunction; C, results using the accurate wavefunction.

Sachs, and Weiss (1960) for lithium. This has already been done by Hiskes (1965), but in his calculation he failed to include the inner electrons, which are the major contributors above 40 keV.

Referring to equation (2) in Subsection (*a*), we have the expression for f

$$f_{M_B}(\boldsymbol{K}_2) = \int \phi_{M_B}(\boldsymbol{r}) \exp(\mathrm{i}\boldsymbol{K}_2 . \boldsymbol{r})\, \mathrm{d}\boldsymbol{r},$$

where $\phi_{M_B}(\boldsymbol{r})$ is now a function defined by Roothaan, Sachs, and Weiss (1960) as

$$\phi_{M_B}(\boldsymbol{r}) = (4\pi)^{-\frac{1}{2}} \sum \left\{(2a_{0i}\,\zeta_i^{3/2} + (2/\sqrt{3})a_{1i}\,\zeta_i^{5/2} r) \exp(-\zeta_i r)\right\},$$

the constants ζ_i, a_{0i}, and a_{1i} being tabulated by them.

The energy of the electron involved is also needed for the term $(Z_B^2/n_B^2 - 1/n^2)$ which occurs in the expressions for $\boldsymbol{K}_1$ and $\boldsymbol{K}_2$. Roothaan, Sachs, and Weiss give a value for the difference in energy of a lithium atom with two and with three electrons, which yields this energy when the outer electron is captured. However, the situation in which there is one electron in the 1S level and one in the 2S level is not considered.

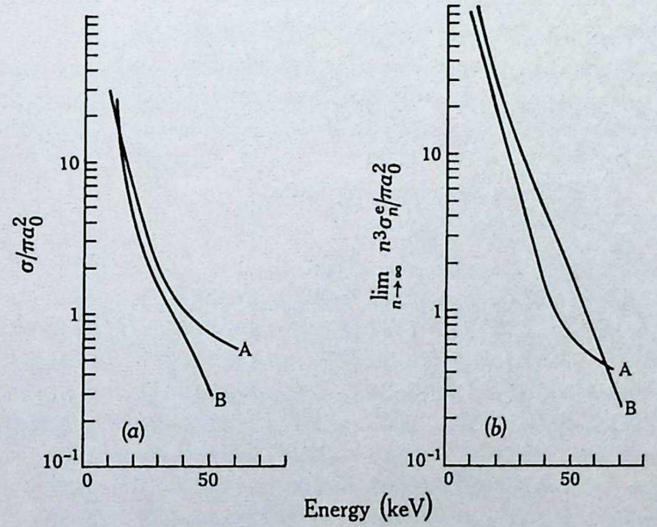

Fig. 4.—Total (*a*) and highly excited (*b*) charge exchange cross sections for sodium:

A, experimental results of Il'in *et al.* (1965);

B, effective-Z results with only outer electron included.

The energy for this was obtained from the wavelengths of Li$^+$ transitions given in Circular No. 467 of the United States National Bureau of Standards. In this regard we have two choices: the transitions $1\mathrm{S}^2 \rightarrow 1\mathrm{S}\,2\mathrm{S}$, $J = 1$, and $1\mathrm{S}^2 \rightarrow 1\mathrm{S}\,2\mathrm{S}$, $J = 0$. The resultant energies are not very different and, since the cross section is found to be insensitive to small changes in Z_B^2/n_B^2 (in this case), we take the average value, namely $Z_B^2/n_B^2 = 4{\cdot}7$. The result for the cross section then reduces to

$$\sigma_{n_2}^{\mathrm{e}} = \frac{2^6}{p^2 n_2^3 \beta^5} \int_0^1 y^4\, \mathrm{d}y \left| \sum_j \left(\frac{\overset{*}{a}_{0j}}{(1+c_j y)^2} + \frac{a_{1j}\{(\alpha_j - c_j)y - 1\}}{(1+c_j y)^3} \right) \right|^2 \pi a_0^2, \tag{3}$$

where

$$\beta = \tfrac{1}{4}p^4 + \tfrac{1}{4}p^{-2}(Z_B^2/n_B^2 - 1/n_2^2) + \tfrac{1}{2}(Z_B^2/n_B^2 + 1/n_2^2)^2,$$

$$c_j = (\zeta_j^2 - Z_B^2/n_B^2)/\beta, \qquad \alpha_j = 4\zeta_j^2/\beta,$$

$$\overset{*}{a}_{0j} = 2a_{0j}\,\zeta_j^{5/2}, \qquad \overset{*}{a}_{1j} = (2/\sqrt{3})a_{1j}\,\zeta_j^{5/2}.$$

The integral (3) could have been taken further analytically but it was judged to be simpler to proceed numerically from this point.

The results are given in Figure 3 and the BK cross sections (without correction factor) are presented in Table 1. In both cases the inner and outer electrons are included. From Figure 3 we see that the results are not as good as the effective-Z case. However, the trend is the same for both the highly excited case and the total cross sections, and thus we may say that the BK cross sections still give the correct ratios between states but the correction factor may not be appropriate for lithium, particularly in the region in which the inner electrons contribute.

It is apparent from the figures that crude effective-Z cross sections can approximate the results. This is not always the case. For lithium the largest cross section is for $n = 2$, and for this and all higher n cross sections there is reasonable agreement between effective-Z and Roothaan, Sachs, and Weiss cross sections. However, for the $n = 1$ cross section (not given) the effective-Z treatment grossly overestimates the Roothaan, Sachs, and Weiss wavefunction result. Thus it cannot always be assumed that a simple effective-Z result fitted to the electron energy will produce a satisfactory estimate of the cross section (nor could changing the effective Z to any other value help the fit).

Table 1

BK CHARGE EXCHANGE CROSS SECTIONS FOR PROTON–LITHIUM COLLISION IN WHICH LITHIUM IS DESCRIBED BY A ROOTHAAN, SACHS, AND WEISS WAVEFUNCTION

The correction factor of Figure 1 is not included. The table is for values of normalized velocity p against final states $n = 1(1)5$ and also the highly excited limit. The numbers in square brackets are the powers of 10 by which each value is to be multiplied: 6·74 [−1] means $6 \cdot 74 \times 10^{-1}$

	BK Cross Sections (πa_0^2 units)					
$p = \frac{\hbar v}{e^2}$	$n = 1$	2	3	4	5	$\lim_{n \to \infty} n^3 \sigma_n^c$
0·7	6·74 [−1]	8·04 [+1]	4·69 [+1]	2·33 [+1]	1·27 [+1]	1·73 [+3]
0·9	6·33 [−1]	1·47 [+1]	9·62 [0]	5·19 [0]	2·96 [0]	4·44 [+2]
1·0	6·3 [−1]	5·96 [0]	3·98 [0]	2·18 [0]	1·25 [0]	1·91 [+2]
1·2	6·66 [−1]	9·45 [−1]	6·16 [−1]	3·38 [−1]	1·95 [−1]	3·02 [+1]
1·4	5·85 [−1]	1·76 [−1]	9·53 [−2]	5·06 [−1]	2·88 [−2]	4·37 [0]
1·7	5·84 [−1]	6·71 [−2]	2·06 [−2]	8·93 [−3]	4·64 [−3]	6·02 [−1]
2·0	4·31 [−1]	5·48 [−2]	1·62 [−2]	6·81 [−3]	3·48 [−3]	4·33 [−1]
2·5	1·26 [−1]	3·08 [−2]	9·34 [−3]	3·97 [−3]	2·04 [−3]	2·56 [−1]

IV. Conclusions

From the comparison between the present theoretical calculations and the experimental results of Il'in *et al.* (1965), we conclude the following.

(1) At high incident proton energies the target's inner electrons must be included in the calculation.

(2) When the inner electrons are included, the theoretical prediction as to the ratio between the cross section for producing highly excited hydrogen atoms and the total cross section is in agreement with experiment. (This extends to lithium and sodium targets the remarks made by Jackson and Schiff (1953) that the BK approximation predicts correct *ratios*.)

(3) The present results for the total charge exchange cross section, and for the individual cross sections for particular final states, are also in agreement with experiment. This extends the conjectures of Nikolaev (1967) and tends to justify the use of the multiplicative correction factor for the individual cross sections.

(4) With respect to the choice of wavefunction for the target atom, lithium exchange was evaluated both using a crude effective-Z wavefunction and a Roothaan, Sachs, and Weiss (1960) wavefunction. The result of this was that for exchange to excited states below the quasi-symmetric state the approximate results were badly in error, but for all other cases both the accurate and crude wavefunctions gave comparable results.

V. ACKNOWLEDGMENTS

Our thanks are due to Professor S. T. Butler for several helpful discussions, to Professor H. Messel, Director of the Nuclear Research Foundation, for the facilities provided, and also to CSIRO for a Senior Post-graduate Studentship which one of us (J.G.L.) held.

VI. REFERENCES

ARTEMENKOV, L. I., *et al.* (1966).—Proc. IAEA Conf. on Plasma Physics and Controlled Nuclear Fusion Research, Culham, Vienna. Vol. 2, p. 45.

BASSEL, R. H., and GERJOUY, E. (1960).—*Phys. Rev.* **117**, 749.

BATES, D. R. (1958).—*Proc. R. Soc.* A **247**, 294.

BATES, D. R., and DALGARNO, A. (1952).—*Proc. phys. Soc.* A **65**, 919.

BERNSTEIN, W., *et al.* (1966).—Proc. IAEA Conf. on Plasma Physics and Controlled Nuclear Fusion Research, Culham, Vienna. Vol. 2, p. 23.

FUTCH, A. H., *et al.* (1966).—Proc. IAEA Conf. on Plasma Physics and Controlled Nuclear Fusion Research, Culham, Vienna. Vol. 2, p. 3.

GILBODY, H. B., and RYDING, G. (1966).—*Proc. R. Soc.* A **291**, 441.

HISKES, J. R. (1965).—*Phys. Lett.* **15**, 42.

IL'IN, R. N., OPARIN, V. A., SOLOVYOV, E. S., and FEDORENKO, N. V. (1965).—Proc. 4th Int. Conf. on Physics of Electronic and Atomic Collisions, Quebec. p. 315.

JACKSON, J. D. (1956).—*Proc. phys. Soc.* A **70**, 26.

JACKSON, J. D., and SCHIFF, H. (1953).—*Phys. Rev.* **89**, 359.

MAPLETON, R. A. (1962).—*Phys. Rev.* **126**, 1477.

MAY, R. M. (1964*a*).—*Phys. Lett.* **7**, 26.

MAY, R. M. (1964*b*).—*Phys. Rev.* A **136**, 669.

MAY, R. M., and LODGE, J. G. (1965).—*Phys. Rev.* A **137**, 699.

MOTT, N. F., and MASSEY, H. S. W. (1965).—"Theory of Atomic Collisions." 3rd Ed. Ch. 15, Part 2; Ch. 19, Parts 2 and 3. (Oxford Univ. Press.)

NIKOLAEV, V. S. (1967).—*Soviet Phys. JETP* **24**, 847.

ROOTHAAN, C. C. J., SACHS, L. M., and WEISS, A. W. (1960).—*Rev. mod. Phys.* **32**, 186.

SLATER, J. C. (1960).—"Quantum Theory of Atomic Structure." Vol. 1, p. 206. (McGraw-Hill: New York.)

WU, T. Y., and OHMURA, T. (1962).—"Quantum Theory of Scattering." p. 224. (Prentice Hall: New Jersey.)

STATES IN ^{27}Al AND ^{89}Y USING HIGH RESOLUTION SURFACE BARRIER COUNTERS

By G. M. CRAWLEY,* D. L. POWELL,* and B. V. NARASIMHA RAO*

[*Manuscript received July* 15, 1968]

Summary

The resolution of a solid state detector was investigated and a best value of about 16 keV was obtained after cooling. The energy levels of ^{89}Y and ^{27}Al were measured with this detector. New states were observed at around 3·0 and 3·7 MeV in ^{89}Y and over 20 new levels were noted in ^{27}Al.

I. INTRODUCTION

A number of recent papers have discussed the use of semiconductor counters with very good resolution over a range of incident proton energies up to 40 MeV (McCarthy and Crawley 1966; Andersson-Lindstroem 1967; Goulding, Landis, and Pehl 1967; Gruhn *et al.* 1968). Solid state counters have many advantages for charged particle detection, particularly the wide energy range of particles accepted and the immediate availability of the data for on-line appraisal and computer analysis. While the ultimate resolution of a solid state counter is probably not as good as that of a large magnet analysis system, there are situations where the intrinsic resolution of the magnet is not used. For example, when the counting rate is low the resolution is often limited by target thickness or kinematic broadening.

One application for a counter with very good resolution is the determination of nuclear energy levels especially when the spacing is small. Thus the energy levels of ^{89}Y have been the subject of a number of investigations (Awaya 1966; Shafroth *et al.* 1967; Stautberg, Krausharr, and Ridley 1967), but there still remain inconsistencies in the region up to 4 MeV of excitation. It was therefore decided to measure these energy levels with a solid state counter of good resolution.

The various factors contributing to the resolution of a surface barrier counter were studied using a thin gold target on a carbon backing to attempt to reproduce the excellent resolution reported previously by Andersson-Lindstroem (1967).

A resolution of 16 keV full width at half maximum height (FWHM) was obtained for 10 MeV protons entering a cooled 1000 μ surface barrier detector. The main residual contribution at this point was the intrinsic detector noise.

In studying the ^{89}Y levels up to 4 MeV, a ^{27}Al target was used to calibrate the energy scale. From the calibration runs information on levels in ^{27}Al was obtained which confirmed the presence of some doubtful levels in the region 6–8 MeV and revealed a number of levels previously unreported.

---

* Department of Nuclear Physics, Australian National University, G.P.O. Box 4, Canberra, A.C.T. 2600.

Aust. J. Phys., **1968, 21, 803–10**

II. DETECTOR TESTS

The factors affecting the total energy resolution in a charged particle experiment are (1) statistics of the electron–hole production process; (2) energy resolution of the beam; (3) target thickness; (4) kinematic broadening, either from the angle subtended by the counter slits or from variation in the angle of the incoming beam; (5) electronic noise from the preamplifier and amplifier system, including the effect of cable and detector capacitance at the input to the preamplifier; (6) detector noise from reverse current in the diode and the surface barrier junction; (7) pile-up, both of positively charged particles and also of low energy electrons stripped from atoms in the target; (8) charge collection effects in the detector; and (9) stability of the electronics.

The first of these factors is seldom a limitation since the energy required to form an electron–hole pair in silicon is 3·66 eV and the Fano factor is about 0·15 (Goulding, Landis, and Pehl 1967). Thus, for a 10 MeV proton, the statistical limit on the resolution is less than 6 keV.

The effects (2), (3), and (4) are controllable in principle although, in any real experiment, counting-rate considerations may mean that one or other of them actually limits the resolution.

The test runs were made with an Ortec surface barrier counter (Model SBCJ-050-1000) with a specified noise of 14 keV FWHM. The 10 MeV proton beam from the Australian National University tandem accelerator was used to bombard a thin gold target on a carbon backing. The gold–carbon separation acted as an internal calibration and the resolution was then measured from the width of the gold peak. A pulser connected at the input of the preamplifier monitored the electronic noise. All slits were kept small enough to eliminate kinematic broadening. Cabling to the preamplifier, both inside and outside the chamber, was kept as short as possible to reduce the effect of stray capacitance on the electronic noise. An Ortec 109 FET preamplifier was coupled to an Ortec 410 main amplifier and the signals were passed through a biased amplifier and pulse stretcher before being analysed in an Intertechnique CA13 analogue to digital converter and stored in the IBM 1800 computer. The resolution both of a pulser peak and the gold peak was found to improve quite rapidly when the time constants of the 410 amplifier were increased to about 1 μsec, and then more slowly as they were further increased. A time constant of 1 μsec was chosen for all the following experiments.

Pile-up of high energy charged particles in the detector can be improved by reducing the beam intensity or by the use of more sophisticated electronics. It was found that for the thin targets used in the present experiments this was unnecessary. However, another source of pile-up, which is not always recognized, is the large number of atomic electrons stripped off the target atoms, which produce low energy pulses in the detector and affect the resolution. Perhaps the most dramatic improvement in the resolution was obtained by the addition of a small (500 gauss) magnetic field in front of the antiscattering slit (Fig. 1) to prevent the low energy electrons from reaching the detector. This reduced the resolution from about 50 keV to 24 keV FWHM.

Both the resolution and the peak to valley ratio were improved when the detector was overbiased and, in general, it was run at 300 V bias rather than the 225 V required for full depletion. This presumably reflects the importance of higher charge collection efficiency in obtaining best resolution.

In order to reduce the intrinsic noise the detector was cooled to about −70°C using a dry ice and alcohol eutectic mixture. The counter was mounted in a brass block thermally insulated by Lucite and cooled alcohol was circulated through the block. This gave rapid and efficient cooling of the detector, reducing the detector current from about 0·9 μA to less than 0·05 μA in about 5 min. The detector resolution decreased from a previous best value of 24 keV to 16 keV FWHM. At this stage, the electronic noise was measured as 7 keV. The cooling system has worked satisfactorily for up to eight detectors simultaneously. It also allows rapid warmup of the detectors since warm air or water can also be circulated through the block before opening the scattering chamber to air.

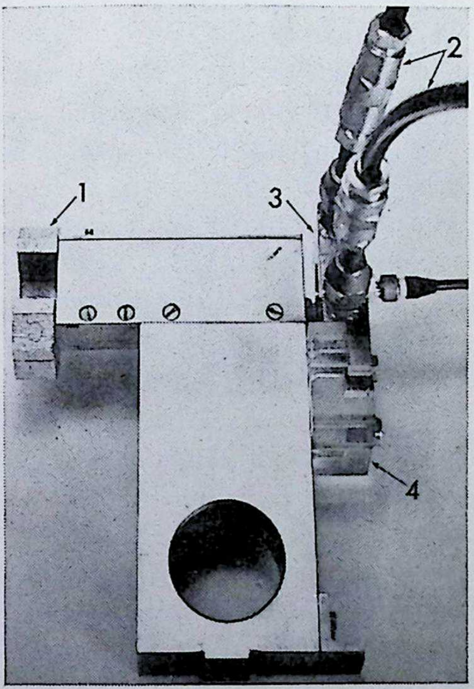

Fig. 1.—Experimental apparatus showing:
1, small magnet to deflect electrons
2, coolant tubes
3, brass detector block
4, Lucite insulating block

III. CALIBRATION: LEVELS IN ^{27}Al

In order to determine the positions of the levels in ^{89}Y with accuracy, it was necessary to calibrate the energy scale. Protons scattered from a thin ^{27}Al target provided such a calibration since the energies of the low lying levels of this nucleus are known to better than 1 keV. Spectra from the ^{27}Al target were taken before each ^{89}Y run at incident proton energies of 10 and 12 MeV.

All the spectra were analysed using a programme MIKIMAUS 4,* which makes a least squares fit of a cubic curve to the background, subtracts the background, and finds the centroid of each peak. The programme then generates both a linear and a

---

* MIKIMAUS 4 is derived from MIKIMAUS 3, which was made available by G. Berzins and J. Kolota of the Cyclotron Laboratory, Michigan State University, U.S.A.

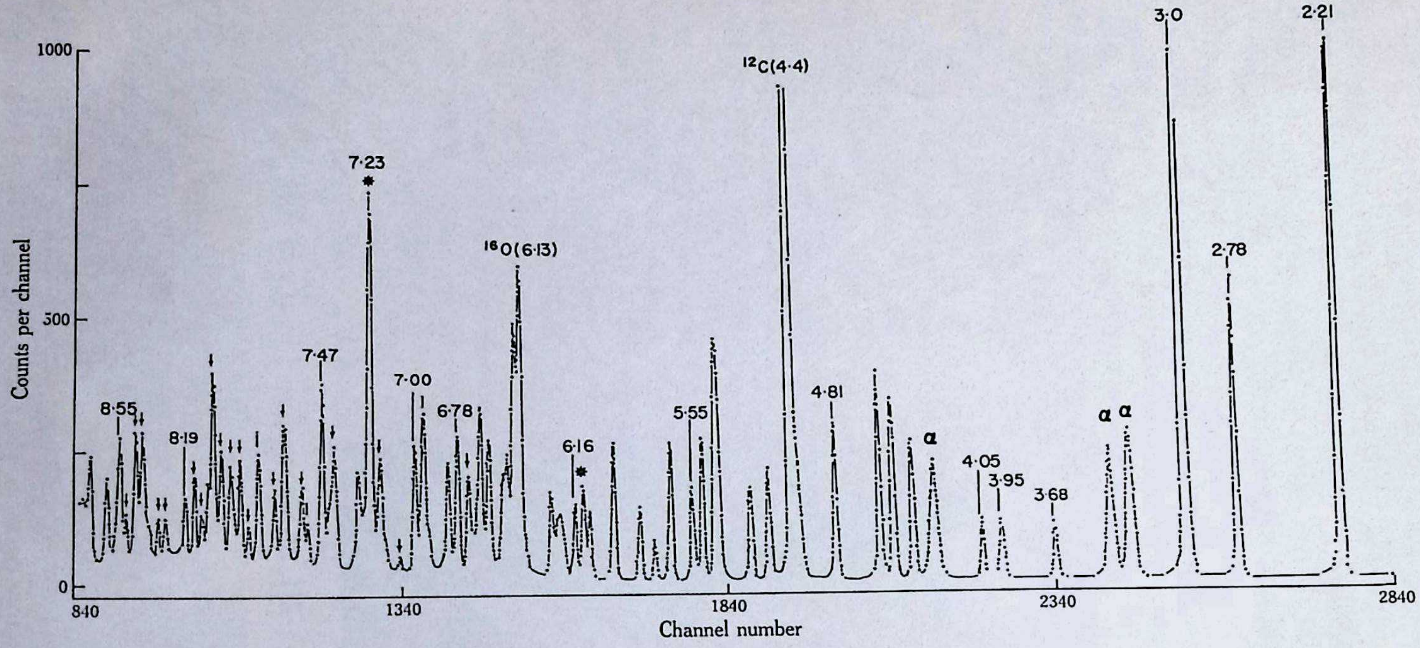

Fig. 2.—Spectrum of 12 MeV protons scattered at 70° from a thin aluminium target. The broader states marked **α** are from the ^{27}Al(p, α)^{24}Mg reaction. The levels marked with arrows have not been previously observed; those marked with an asterisk were previously uncertain. All energies shown are in MeV.

quadratic calibration curve from known peaks and calculates the Q value corresponding to any number of "unknown" peaks in this or following spectra.

Examination of the calibration spectra indicated a number of new levels especially in the region between 7·5 and 8·5 MeV. A spectrum of protons from ^{27}Al is shown in Figure 2. Only the levels above 2 MeV are shown so as to allow greater expansion of the region containing the unknown levels. Levels previously suspected and confirmed in this experiment are indicated by an asterisk while the new levels are marked by arrows.

The spectrum also contains peaks corresponding to α-particles from the ^{27}Al(p, α)^{24}Mg reaction but these were easily identified by their greater width and the kinematic shift that they show with change of angle.

The energy calibration below 7·5 MeV of excitation was readily obtained using levels in ^{27}Al whose energies are well determined. The levels used for the calibration are given in Table 1. In order to determine the energies of levels above 7·5 MeV the calibration was first extrapolated to a region above the ^{26}Mg plus proton threshold (8·271 MeV). A number of resonances have been observed in the ^{26}Mg(p, γ) reaction (Endt and Van der Leun 1967) and two of these at 292 and 338 keV were close to the energies of three levels in the inelastic spectrum obtained from the extrapolated calibration. Although one of the levels was consistently within about 25 keV of an energy corresponding to the 292 keV resonance, each of the three levels was matched to each of the two resonances and a complete new calibration was determined. The standard deviations for both a linear and a quadratic calibration curve were always smaller if one of the levels was set equal to 8·552 MeV corresponding to the 292 keV resonance.

Now it is possible that the (p, γ) reaction and the inelastic scattering process excite different states in ^{27}Al. In fact, the resonance at 392 keV does not appear to correspond to any strong level excited in (p, p′). Therefore, the matching of the level in the (p, p′) spectrum with the 292 keV resonance in ^{26}Mg(p, γ) may be accidental. There is thus the possibility of a systematic error in the energies of the levels above 7·5 MeV which increases with excitation energy and in the worst case is estimated to be about 30 keV. One check which suggests that such a systematic effect is not present is the agreement of the level observed at 8·194 MeV with a previously observed level at 8·200 MeV (Endt and Van der Leun 1967), although no error is assigned to this latter energy.

The average energies of levels above 4 MeV obtained from about six different angles are shown in Table 1, together with the mean deviation. The previously known levels from Endt and Van der Leun are given for comparison. In all cases, except for unresolved doublets, the energies match within the quoted errors. It should also be noted that six of the levels marked as "new" in Table 1 between 6·5 and 8 MeV are within 30 keV of levels observed recently in inelastic scattering at 17·5 MeV (Crawley and Garvey 1968). The lowest lying new level is the lower member of a close doublet at about 6·5 MeV with an energy of 6·514 MeV ±5 keV. There is also evidence from the consistent broadening of the level at 7·674 MeV that this is also a close doublet with a separation of less than 20 keV. The previously suspected states at 6·119 and 7·231 MeV show up clearly at all angles and, in fact, the 7·231 MeV state is one of the levels above 3 MeV most strongly excited in this reaction (Fig. 2).

TABLE 1

STATES IN ^{27}Al FROM ^{27}Al(p, p′)^{27}Al

All energies are in keV

Present Experiment	Error	Endt and Van der Leun (1967)	Error
Calibration		3955·9	1·3
4058·1	2·8	4054·8	1·4
4409·9	2·0	4409·0	2·0
4511·6	1·6	4508	5
4582·6	1·7	4580	2
Calibration	—	4811	2
5154·3	1·3	5155	3
5247·3	1·8	5246	2
5431·8	2·5	5410 5434	6 2
5499·3	2·9	5491	6
Calibration	—	5550	2
5665·9	2·0	5659	6
5751·9	2·3	5752	4
5826·7	1·5	5825	6
5962·1	1·2	5955	6
6083·9	0·7	6082	2
6118·6	1·0	(6114)	4
Calibration	—	6160	2
6287·5	3·8	6284	5
6480·1	1·7	6466 6477	3 3
6534·4‡	—	6547	12
6612·1	3·2	6606	3
6658·1	1·6	6653	3
6719·6	2·6	New	
Calibration	—	6778	3
6825·5	1·5	6815 6821	2 2

Present Experiment	Error	Endt and Van der Leun (1967)	Error
6955·5	1·5	New*	
Calibration	—	6997	3
7079·1	3·3	New	
7178·8	1·3	New	
7231·0	1·3	(7226)*	3
7291·4	1·1	7285	3
7411·5	1·6	New*	
Calibration	—	7471	3
7548·3	2·0	New	
7577·4	1·1	New	
7673·5†	—	New*	
7724·7	2·0	New	
7807·5	1·7	New*	
7865·9	1·9	New	
7909·1	2·0	New	
7954·1	0·7	New	
8006·4	2·0	New*	
8057·9	1·6	New	
8109·2	0·5	New	
8148·1	1·8	New	
8194·4	2·5	8200	
8302·2	2·6	New	
8345·6	1·3	New	
8424·1	2·4	New	
8470·8	2·5	New	
8509·0	11·4	New	
Calibration	—	8552·0	1

* Levels observed by Crawley and Garvey (1968) at 6·94, 7·23, 7·44, 7·66, 7·79, and 7·99 MeV.

† Probably close doublet with about 20 keV separation.

‡ Probably doublet with energies 6514 and 6547 keV.

IV. STATES IN ^{89}Y

The yttrium target was prepared by vacuum evaporation of the metal (100% ^{89}Y) onto a carbon backing to obtain a thickness of 100 μg cm^{-2} of metal. The main impurities in the target were carbon, oxygen, and fluorine. This last impurity has excited states in the region of interest which can be identified by their kinematic shift with angle.

Spectra were obtained at 10 MeV and later 12 MeV at about six angles from 40° to 140°. A spectrum at 85° is shown in Figure 3. The states at 1·5 and 0·91 MeV are obscured by impurity peaks, indicating the necessity of running at a large number of angles. The energy levels up to 4 MeV are given in Table 2 together with previously published values. Again the errors in the present results reflect the standard deviation of the mean of the energies obtained at different angles. In

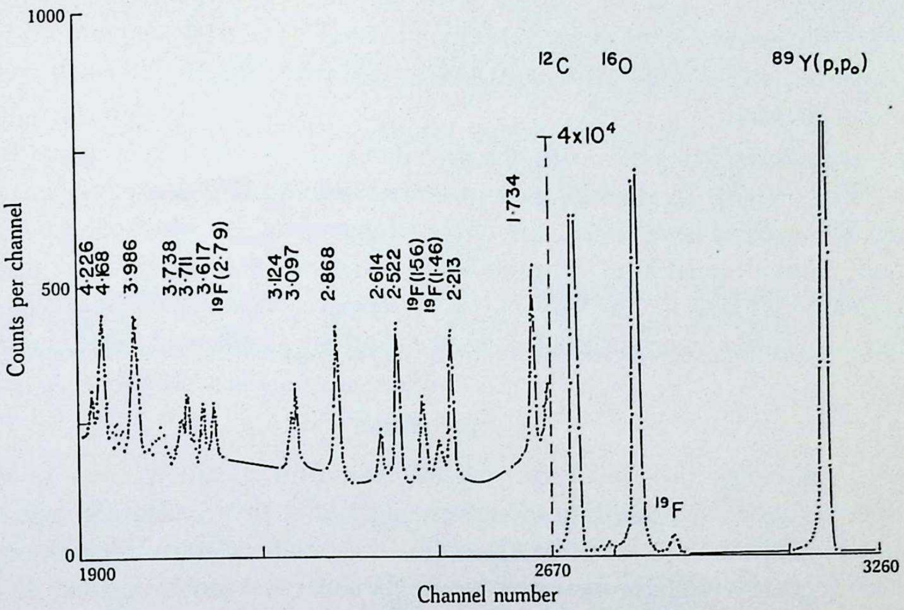

Fig. 3.—Spectrum of 12 MeV protons scattered at 85° from ^{89}Y. Protons scattered from the ^{19}F impurity target are also seen in this spectrum. All energies shown are in MeV.

Table 2

ENERGY LEVELS OF ^{89}Y

All energies are in keV

Awaya (1966)	Stautberg, Krausharr, and Ridley (1967)	Long and Fox (1968)	Present Work
0	0	0	0
$894\pm^{20}_{10}$	910	897 ± 8	$910\cdot4\pm3\cdot8$
1502 ± 12	1490	1499 ± 8	$1503\cdot5\pm3\cdot5$
1730 ± 12	1740	1736 ± 8	$1733\cdot9\pm1\cdot6$
2207 ± 15	2220	2219 ± 8	$2212\cdot6\pm4\cdot6$
2518 ± 13	2520		$2522\cdot0\pm3\cdot4$
2605 ± 15			$2613\cdot8\pm3\cdot5$
2862 ± 11	2870		$2868\cdot3\pm2\cdot7$
			$3096\cdot7\pm1\cdot0$
3115 ± 12	3120		$3123\cdot8\pm1\cdot5$
3622 ± 13	3620		$3616\cdot7\pm1\cdot3$
3719 ± 12			$3711\cdot4\pm2\cdot5$
	3750		$3737\cdot9\pm2\cdot6$
			$(3851\ \ \pm5)$
3992 ± 12	3990		$3986\cdot0\pm2\cdot4$
4163 ± 13	4180		$4167\cdot8\pm1\cdot1$
			$(4226\ \ \pm5)$

addition to these random errors in determining the peak position, a small systematic error is possible because of the uncertainty in the laboratory angle of the counter. Using the ^{27}Al states as a calibration therefore involves an error because of the different masses of ^{27}Al and ^{89}Y. In the worst case this may introduce an uncertainty of about 5 keV into the level position. Since this effect is angle dependent it should lead to a systematic change of excitation energy with angle. No such systematic effects were observed.

The present values agree with the recent results on the levels up to 2 MeV of Long and Fox (1968). A doublet was observed near to 3·0 MeV but no evidence was found for a third level near this energy referred to by Shafroth *et al.* (1967). The second, close, doublet seen at around 3·7 MeV has not been reported previously. The levels at 3·851 and 4·226 MeV indicated in parentheses were observed at only a few angles and with poor statistics, and their energy is not well determined.

V. CONCLUSIONS

Care in reducing pile-up effects and electronic noise and the use of a simple cooling system allows a resolution of less than 20 keV to be obtained with a solid state counter. This has proved to be a useful technique for determining the positions of nuclear energy levels. The energy levels of ^{89}Y have been investigated up to 4 MeV and some new levels have been found. Many new levels in ^{27}Al have been observed up to the region of the proton threshold.

VI. ACKNOWLEDGMENT

One of the authors (G.M.C.) would like to acknowledge financial assistance from the Queen Elizabeth II Fellowships Committee during this work.

VII. REFERENCES

ANDERSSON-LINDSTROEM, G. (1967).—*Nucl. Instrum. Meth.* **56**, 309.

AWAYA, Y. (1966).—*Phys. Lett.* **21**, 75.

CRAWLEY, G. M., and GARVEY, G. T. (1968).—*Phys. Rev.* **167**, 1070.

ENDT, P. M., and VAN DER LEUN, C. (1967).—*Nucl. Phys.* A **105**, 1.

GOULDING, F. S., LANDIS, D. A., and PEHL, R. H. (1967).—Univ. California Radiation Lab. Rep. No. UCRL 17556.

GRUHN, C. R., KUO, T., MAGGIORE, C., PREEDOM, B., SAMUELSON, L., and CHANDER, J. (1968).—Lithium drifted germanium for charged particle spectroscopy. *IEEE Trans. nucl. Sci.* (in press).

LONG, D. D., and FOX, J. D. (1968).—*Phys. Rev.* **167**, 1131.

McCARTHY, A. L., and CRAWLEY, G. M. (1966).—*Phys. Rev.* **150**, 935.

SHAFROTH, S. M., AINRICHSEN, P. F., HOROSHKO, R. N., and VAN PATTER, D. M. (1967).—*Bull. Am. phys. Soc.* **11**, 511.

STAUTBERG, M. M., KRAUSHARR, J. J., and RIDLEY, B. W. (1967).—*Phys. Rev.* **157**, 977.

THE CHARACTERISTIC LOSS SPECTRA OF THE SECOND AND THIRD SERIES TRANSITION METALS*

By M. J. Lynch† and J. B. Swan†

[*Manuscript received June 4, 1968*]

Summary

Characteristic electron energy loss spectra are presented for the second and third series transition metals Y, Zr, Nb, Mo, Rh, Pd, Ag, and Hf, Ta, W, Re, Ir, Pt, Au. An identification of most of the spectral features in terms of collective and individual particle excitations is made.

Introduction

The simple theory of plasmon oscillations in solids (Bohm and Pines 1953) considers collective longitudinal oscillation of the nearly-free electrons and assumes a sharp distinction between these electrons and those tightly bound in the atomic core. This theory has had considerable success when applied to experimental observations of the characteristic electron energy loss spectra of numerous elements; a sharp peak in the spectrum is observed at an energy loss closely corresponding to the plasmon excitation energy. In many other cases, however, modification of the theory is required in order to obtain satisfactory agreement with experiment. This modification may be in the form of a correction in which the polarizability of the inner electrons is allowed for because their binding energy is not large relative to the plasmon energy, or it may take into account the shift in plasmon energy occasioned by single-particle excitations at nearby energies (Nozières and Pines 1958, 1959).

The situation arises for the transition metals in particular, in which there is no obvious distinct separation between the two groups of electrons, the nearly free and the tightly bound. Earlier experiments on the characteristic loss spectra of the first group of transition metals (Robins and Swan 1960) indicated that for elements occurring early in the group the electrons in both the s and d bands must be considered to be free, but that for the elements of higher atomic number some electrons at least in these bands are more tightly bound, as shown by a decrease in plasmon energy below the value given by the simple theory. While such a decrease is predicted theoretically (Nozières and Pines 1958, 1959), no support was found for the prediction that in the first few elements the energy loss would be greater than the value calculated on the assumption that all s and d electrons are essentially free.

It was considered that similar studies of the second and third group of transition metals would be of interest, and accordingly measurements of the characteristic loss spectra of Y, Zr, Nb, Mo, Rh, Pd, Ag, and Hf, Ta, W, Re, Ir, Pt, Au have been made.

---

* This work was supported by the U.S. Army Research Office and the University of Western Australia.

† Physics Department, University of Western Australia, Nedlands, W.A. 6009.

Aust. J. Phys., 1968, **21**, 811–16

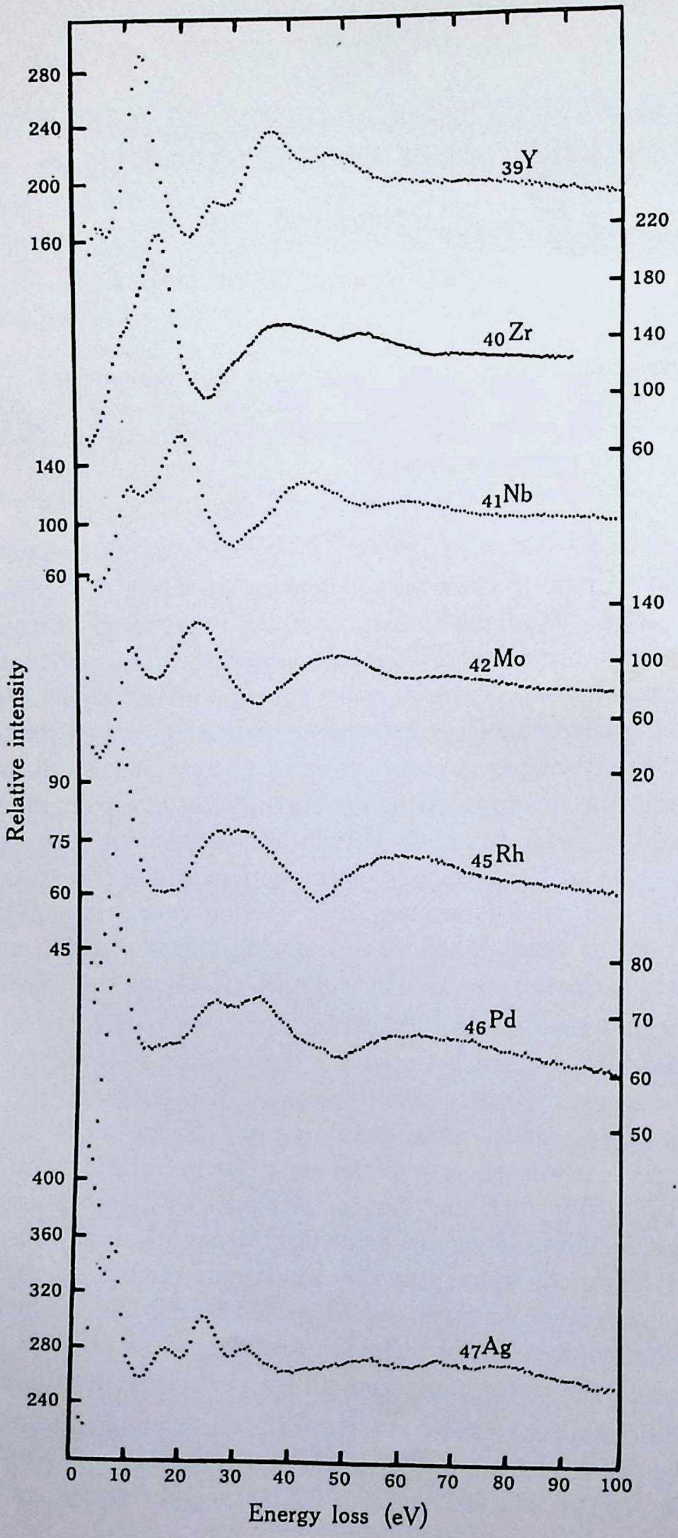

Fig. 1(*a*).—Typical spectra of elements of the second transition group.

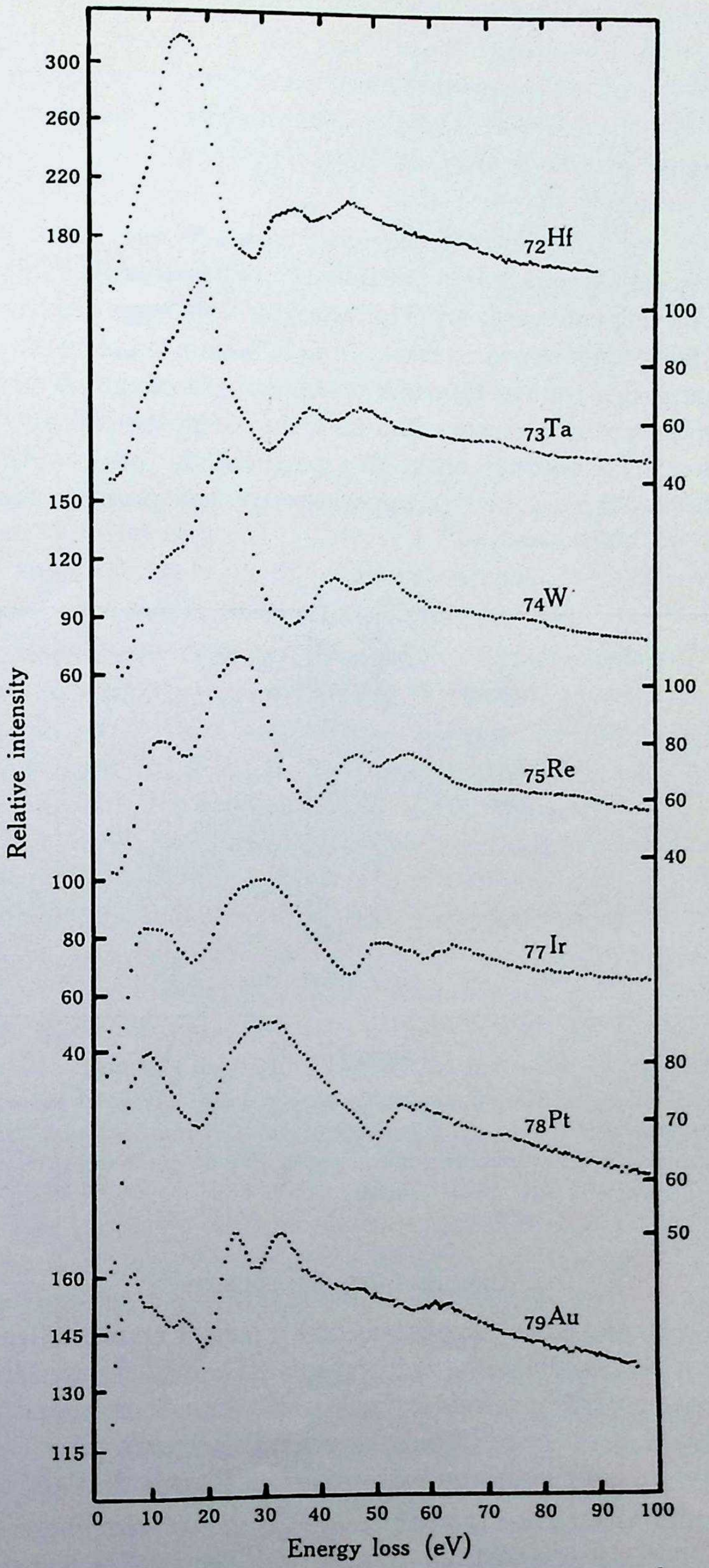

Fig. 1(*b*).—Typical spectra of elements of the third transition group

APPARATUS AND PROCEDURE

The apparatus used in this work (Swan 1964) and the method of data processing (Hartley and Swan 1966) have been described previously. Briefly, the energy spectrum of a beam of monoenergetic electrons after scattering through 90° in the target material is obtained and stored in a multichannel analyser, and these data are processed by a computer to yield the energy loss value of each peak in the spectrum to an accuracy of ±0·1 eV.

The target was composed of the material under investigation, and a clean surface was maintained either by continuous evaporation (in suitable cases), by scraping, or by having the target as a thin wire and heating it electrically (Hagstrum and D'Amico 1960). Numerous runs were made with each element, operating over a range of primary electron energies and a range of recorded loss energies, to ensure that all observable peaks corresponding to losses of up to 100 eV were measured. The resolution of neighbouring peaks depended on the peak widths and relative intensities and was limited in the apparatus by the primary energy spread of approximately 0·5 eV.

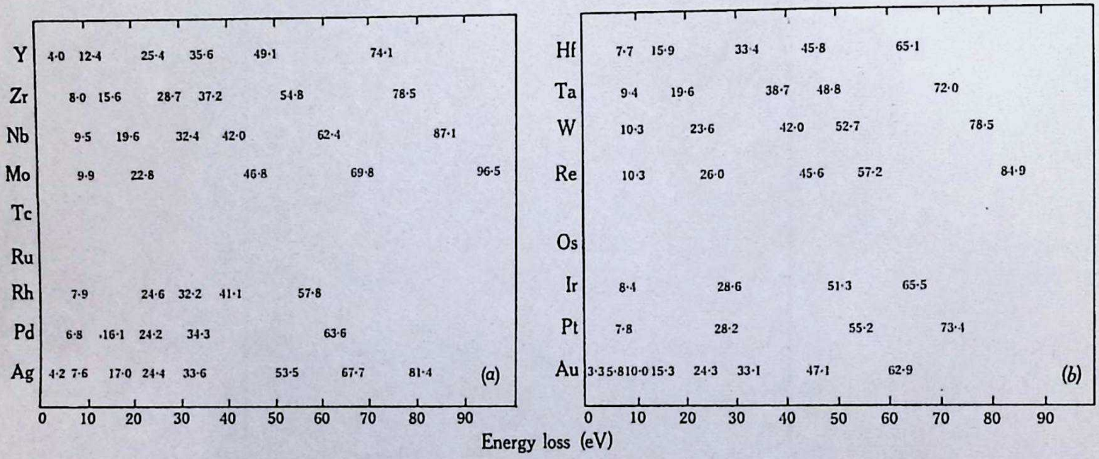

Fig. 2.—Numerical values of the characteristic energy losses observed in elements of (*a*) the second transition group and (*b*) the third transition group. Groupings and trends in values are apparent and comparisons in appearances of the peaks may be made with the aid of Figures 1(*a*) and 1(*b*).

RESULTS AND DISCUSSION

Typical spectra observed for the second group of transition metals Y–Ag are shown in Figure 1(*a*), and for the third group Hf–Au in Figure 1(*b*). Remarkable similarities are immediately obvious, as are the trends in shape and energy on progressing through each series. The energy trends are even more clearly illustrated in the scale diagrams of the energy losses given in Figures 2(*a*) and 2(*b*).

Reference to the second transition series shows that the measured energy losses of 12·4, 15·6, 19·6, and 22·8 eV in Y, Zr, Nb, and Mo respectively compare favourably with the theoretical values, $\hbar\omega_p$ (where $\omega_p^2 = 4\pi ne^2/m$, e being the electronic charge, m the electronic mass, and n the calculated free electron density of the metal assuming all outer s and d electrons are free), of 12·5, 15·3, 19·4, and 23·0 eV, assuming 3, 4, 5, and 6 free s and d electrons respectively.

For the third series of transition metals the loss peaks at 15·9, 19·6, 23·6, and 26·0 eV in Hf, Ta, W, and Re are in good agreement with the theoretical $\hbar\omega_p$ values of 15·7, 19·5, 22·9, and 25·7 eV, assuming 4, 5, 6, and 7 free s and d electrons respectively.

Thus identification of the plasmon loss is obvious for the first four elements of each group, for which the volume loss peak is relatively sharp and intense and occurs at an energy in excellent agreement with the theoretical value. Recent electron energy loss studies (Creuzburg 1966; Daniels 1967) correlated with optical studies indicate that the energy loss peaks observed at 4·2 and 3·3 eV in the Ag and Au spectra respectively are the unresolved surface and volume plasmon losses. The plasmon losses in the remaining two elements of each series are identified, on the basis of appearance and the trends in energy throughout the series, as the 24·6, 24·2, 28·6, and 28·2 eV losses in Rh, Pd, Ir, and Pt respectively. The loss energies in these elements, however, lie below the theoretical values of 30·1, 30·6, 29·5, and 30·2 eV, assuming all s and d electrons effectively free.

Other loss peaks can be identified by appearance and energy also. In particular, the peaks at 49·1, 54·8, 62·4, and 69·8 eV in Y, Zr, Nb, and Mo are in reasonable agreement with the N_1 ionization energies of these elements, while $N_{2,3}$-level ionization in Y, Zr, Nb, Mo, Rh, Pd, and Ag is probably responsible for the losses of 25·4, 28·7, 32·4, 46·8, 57·8, 63·6, and 67·7 eV. The peaks at 65·1, 72·0, 78·5, and 84·9 eV in Hf, Ta, W, and Re are almost certainly due to O_1-level ionization and those at 33·4, 38·7, 42·0, 45·6, 51·3, 55·2, and 62·9 eV in Hf, Ta, W, Re, Ir, Pt, and Au are probably O_3-level ionization. The above interpretation of loss peaks in terms of ionization processes has been supported by measurements made to the point of inflexion of the ionization loss edge rather than to the intensity maxima (Lynch and Swan 1967). The low intensity peaks at 74·1, 78·5, 87·1, and 96·5 eV in Y, Zr, Nb, and Mo resemble ionization peaks, and are possibly also due to ionization processes.

A peak belonging to a distinct set, and being the smallest observed discrete energy loss, is observed in each element except in the Ag and Au spectra where it has not been resolved from the volume plasmon loss. These peaks are interpreted as arising from the surface plasmon excitation. While they do not bear the simple energy ratio to the volume plasmon of $1/\sqrt{2}$, this does not of itself negate the interpretation. The peaks are quite narrow and symmetrical in those elements where they appear with intensities sufficient to enable estimates of widths to be made, and this indicates that they are not due to ionization processes. Their change in relative intensity with changing energy of the primary electrons, together with their sensitive intensity dependence on surface cleanliness, supports the interpretation. The trend of increasing intensity on progressing through the members of each group of transition metals is very similar to the behaviour observed in the first transition group (Robins and Swan 1960).

In several of the elements a relatively intense peak is observed. The energies of these peaks cannot be identified with known ionization processes; however, the similarities in appearance and trends in energy from element to element suggest a common origin. Peaks of this kind, termed "G" peaks, have been described previously (Robins and Swan 1960; Best 1962), and in the present work have energies of 35·6 (Y), 37·2 (Zr), 42·0 (Nb), 45·8 (Hf), 48·8 (Ta), 52·7 (W), 57·2 (Re), 65·5 (Ir), and 73·4 eV (Pt). A hypothesis concerning the origin of these G peaks has been published (Robins and Best 1962), though an alternative interpretation has been recently advanced by Hartley (1968).

CONCLUSIONS

From this study of the energy loss spectra of seven elements in each of the second and third groups of transition metals, one peak in the spectrum of each element has been identified with confidence as arising from volume plasmon excitation and another peak has been ascribed to surface plasmon excitation. On the basis of reasonable energy agreement and appearance, other peaks have been associated with ionization occurring in identifiable atomic subshells. A set of broad intense peaks in each group of transition metals has been assigned a common but unidentified origin. In addition several peaks, in the spectra of Ag and Au in particular, have not been considered here in any detail but presumably arise from interband transitions of some kind.

REFERENCES

BEST, P. E. (1962).—*Proc. phys. Soc.* **79**, 133.

BOHM, D., and PINES, D. (1953).—*Phys. Rev.* **92**, 609.

CREUZBURG, M. (1966).—*Z. Phys.* **196**, 433.

DANIELS, J. (1967).—*Z. Phys.* **203**, 235.

HAGSTRUM, H. D., and D'AMICO, C. (1960).—*J. appl. Phys.* **31**, 715.

HARTLEY, B. M. (1968).—Ph.D. Thesis, University of Western Australia.

HARTLEY, B. M., and SWAN, J. B. (1966).—*Phys. Rev.* **144**, 295.

LYNCH, M. J., and SWAN, J. B. (1967).—*Aust. J. Phys.* **20**, 345.

NOZIÈRES, P., and PINES, D. (1958).—*Phys. Rev.* **109**, 1062.

NOZIÈRES, P., and PINES, D. (1959).—*Phys. Rev.* **113**, 1254.

ROBINS, J. L., and BEST, P. E. (1962).—*Proc. phys. Soc.* **79**, 110.

ROBINS, J. L., and SWAN, J. B. (1960).—*Proc. phys. Soc.* **76**, 857.

SWAN, J. B. (1964).—*Phys. Rev.* **135**, A1467.

THE POTENTIAL DUE TO TWO POINT CHARGES EACH AT THE CENTRE OF A SPHERICAL CAVITY AND EMBEDDED IN A DIELECTRIC MEDIUM

By D. K. Ross*

[*Manuscript received April* 16, 1968]

Summary

A method is found for determining the electrostatic potential due to two separated spherical cavities each containing a point charge with the whole system embedded in a continuous dielectric medium. The potential is obtained as a sum involving Legendre polynomials and it is shown that the coefficients of this series can be expanded as a convergent power series in the reciprocal of the distance between the centres of the cavities. This solution is suitable for numerical calculations because there is a simple relationship between successive terms in the series and because this series is convergent even at contact separation.

I. Introduction

Ever since Bernal and Fowler (1933) discussed the nature of ions in an aqueous solution there has been a growing interest in spherical and ellipsoidal cavity models which are used to represent ions and their attached water molecules. For example, Onsager (1936), Kirkwood and Westheimer (1938, 1939), Hill (1944), Scholte (1949), Ross and Sack (1950), Abbott and Bolton (1952), Linderstrøm-Lang (1953), Buckley and Maryott (1954), Buckingham (1957), and Kober and Fitts (1966) have placed charges in an isolated cavity at appropriate points and have solved the electrostatic problem in order to develop a theory of polar liquids. Now to discuss the interaction of an ion pair in an aqueous medium we can use, as a very crude mathematical model, a pair of nonoverlapping spherical cavities each containing a point charge at its centre. Rosenthal (1967) discussed some of the applications of a two-sphere model where both cavities have the same radius but opposite charge, but he did not consider the validity of the expansions nor did he find an expression for successive terms in the series.

To date a number of problems involving separated conducting spheres have been solved by making use of spherical polar coordinates. Thus, Kottler (1927) and Mitra (1944) found a functional equation whose solution leads to a determination of the capacity of two spheres, assumed to be exterior to each other. On the other hand, Hobson (1931) and Lebedev (1965) obtained a much simpler solution for the potential in terms of dipolar coordinates. Davis (1964) extended this work to take into account the influence of a field that is uniform at infinity. The latter approach was not found useful in solving the problem under consideration here because it leads to a set of four simultaneous difference equations for which there is no known solution. Instead, we shall use two spherical polar coordinate systems and apply Hobson's

---

* Department of Mathematics, University of Melbourne, Parkville, Vic. 3052.

Aust. J. Phys., 1968, **21**, 817–22

method of transforming solid harmonics in order to satisfy the boundary conditions on the two surfaces.

Similar problems related to the present one are treated by Shail (1962), who extended Mitra's method to find a harmonic function that takes prescribed values on two nonintersecting spheres, and Snow (1949), who considered the case of overlapping conducting spheres in great detail. There are also a number of papers on inviscid flow near toroids, lenses, and overlapping spheres which are related to the problem at hand (see Stimson and Jeffrey 1926; Payne and Pell 1960; Pell and Payne 1960*a*, 1960*b*; Collins 1963; Ranger 1965).

II. Expansions for the Potential

Consider two spherical cavities S_1 and S_2 which do not overlap and which are at separation $R = O_1 O_2$ where O_1 and O_2 are the centres of the cavities containing the point charges e_1 and e_2 respectively. Let P be a typical point in the vicinity such that $O_i P = r_i$, for $i = 1$ or 2, and let θ_1 and θ_2 be the angles PO_1O_2 and PO_2O_1. (In what follows the suffix $i = 1$ or 2 will be used to refer to the first and second cavity respectively.) These coordinates are so defined that $r_1 = r_2$ and $\theta_1 = \theta_2$ for any point P on the median plane. The spherical cavities are taken to have radius a_i and the whole system is embedded in a continuous medium of dielectric constant ϵ.

An expansion for the potential at P inside S_i can be obtained by applying Green's theorem. Now the potential inside the cavity S_i may be written

$$V_i(P) = e_i/r_i + U_i(P)\,, \tag{1}$$

where $U_i(P)$ is harmonic inside S_i. Let Q_i be any point on the boundary of S_i with coordinates $(a_i, \theta_i^*, \phi_i^*)$ then

$$U_i(P) = \frac{1}{4\pi}\int\left\{U(Q_i)\frac{\partial}{\partial n}\left(\frac{1}{\rho_i}\right) - \frac{1}{\rho_i}\frac{\partial U(Q_i)}{\partial n}\right\}\mathrm{d}S_i\,, \tag{2}$$

where $\rho_i = PQ_i$, $U(Q_i)$ is the potential on the boundary of S_i, and $\partial/\partial n$ denotes differentiation along the outward normal $\boldsymbol{n}$. An expression for $U_i(P)$ can then be found by integrating the above equation with respect to ϕ_i^*, remembering that the potential is independent of the azimuthal angle, and using the identities

$$\rho_i^2 = a_i^2 + r_i^2 - 2a_i r_i \cos\gamma_i \tag{3}$$

and

$$\cos\gamma_i = \cos\theta_i \cos\overset{*}{\theta_i} + \sin\theta_i \sin\overset{*}{\theta_i} \cos(\phi_i - \overset{*}{\phi_i})\,, \tag{4}$$

together with the addition formula

$$\mathrm{P}_n(\cos\gamma_i) = \mathrm{P}_n(\cos\theta_i)\,\mathrm{P}_n(\cos\overset{*}{\theta_i}) + 2\sum_{m=1}^{n}\frac{(n-m)!}{(n+m)!}\mathrm{P}_n^m(\cos\theta_i)\,\mathrm{P}_n^m(\cos\overset{*}{\theta_i})\cos\{m(\phi_i - \overset{*}{\phi_i})\}\,, \tag{5}$$

where the $\mathrm{P}_n^m(x)$ are the associated Legendre functions as defined in Hobson (1931).

Finally, we obtain

$$V_i(\mathrm{P}) = e_i/r_i + (e_i/a_i) \sum_{s=0}^{\infty} d_s^i (r_i/a_i)^s \, \mathrm{P}_s(\cos\theta_i)\,, \tag{6}$$

where the unknown coefficients d_s^i will be determined from the boundary conditions and

$$d_s^i = -(a_i/2e_i) \int_0^{\pi} W(\mathrm{Q}_i)\, \mathrm{P}_s(\cos \overset{*}{\theta}_i) \sin \overset{*}{\theta}_i \, \mathrm{d}\overset{*}{\theta}_i\,, \tag{7}$$

with

$$W(\mathrm{Q}_i) = a_i\, \partial U(\mathrm{Q}_i)/\partial n + (s+1) U(\mathrm{Q}_i)\,. \tag{8}$$

By Schwarz's inequality (Titchmarsh 1950) it follows that

$$\begin{aligned}(d_s^i)^2 &\leqslant (a_i/2e_i)^2 \int_0^{\pi} W^2(\mathrm{Q}_i) \sin \overset{*}{\theta}_i \, \mathrm{d}\overset{*}{\theta}_i \int_0^{\pi} \mathrm{P}_s^2(\cos \overset{*}{\theta}_i) \sin \overset{*}{\theta}_i \, \mathrm{d}\overset{*}{\theta}_i \\ &= \{a_i^2/2e_i(2s+1)\} \int_0^{\pi} W^2(\mathrm{Q}_i) \sin \overset{*}{\theta}_i \, \mathrm{d}\overset{*}{\theta}_i\,. \end{aligned} \tag{9}$$

From equations (7) and (8) and the integrability of the potential and its gradient normal to the boundary S_i we obtain the result that $|s^{-\frac{1}{2}} d_s^i|$ is bounded for all s. Thus the series in (6) is absolutely and uniformly convergent within S_i and convergent on the boundary of S_i, except perhaps at the points $\theta_i = 0$ or π (see Hobson 1931).

In much the same way we can find an expression for the potential outside the two cavities. Thus,

$$\begin{aligned} V_0(\mathrm{P}) = {} & \frac{1}{\epsilon}\left(\frac{e_1}{r_1} + \frac{e_2}{r_2}\right) \\ & + \frac{1}{\epsilon} \sum_{s=1}^{\infty} \left\{ \frac{e_1}{a_1} g_s^1 \left(\frac{a_1}{r_1}\right)^{s+1} \mathrm{P}_s(\cos\theta_1) + \frac{e_2}{a_2} g_s^2 \left(\frac{a_2}{r_2}\right)^{s+1} \mathrm{P}_s(\cos\theta_2) \right\}, \end{aligned} \tag{10}$$

where

$$g_s^i = (\epsilon a_i/2e_i) \int_0^{\pi} X(\mathrm{Q}_i)\, \mathrm{P}_s(\cos \overset{*}{\theta}_i) \sin \overset{*}{\theta}_i \, \mathrm{d}\overset{*}{\theta}_i \tag{11}$$

and

$$X(\mathrm{Q}_i) = a_i\, \partial U(\mathrm{Q}_i)/\partial n - sU(\mathrm{Q}_i)\,. \tag{12}$$

In this way we find that the series in (10) are absolutely and uniformly convergent outside the two cavities and convergent on the boundaries, except possibly at the points where $\theta = 0$ or π.

III. FORMULATION OF DIFFERENCE EQUATION

The boundary conditions that must be satisfied at the surfaces of the two spheres $r_i = a_i$ are

$$V_i = V_0\,, \qquad \partial V_i/\partial r_i = \epsilon\, \partial V_0/\partial r_i \tag{13}$$

and these will be used to obtain two difference equations for the coefficients g_s^i.

In what follows we shall use the formula of zonal harmonics

$$\frac{\mathrm{P}_n(\cos\theta_2)}{r_2^{n+1}} = \frac{1}{R^{n+1}} \sum_{m=0}^{\infty} \binom{m+n}{n} \left(\frac{r_1}{R}\right)^m \mathrm{P}_m(\cos\theta_1)\,, \tag{14}$$

when $|r_1| < R$ and a similar expression with the suffixes 1 and 2 interchanged. These formulae were obtained by Hobson (1931) but he defined the angles θ_i in a slightly different way.

To begin, both boundary conditions will be applied on the surface $r_1 = a_1$ and then an interchange of the suffixes will give the equations appropriate to the surface $r_2 = a_2$. From the first of the conditions in (13) we obtain, after substituting (14) into (10), rearranging the absolutely (and uniformly) convergent series, multiplying by $\mathrm{P}_s(\cos\theta_i)\sin\theta_i$, and integrating from 0 to π,

$$\frac{e_1}{a_1} d_0^1 = -\frac{e_1}{a_1}\left(1 - \frac{1}{\epsilon}\right) + \frac{e_2}{\epsilon R}\left(1 + \sum_{m=1}^{\infty} g_m^2 t_2^m\right) \tag{15}$$

and

$$\frac{e_1}{a_1} d_n^1 = -\frac{e_1}{\epsilon a_1} g_n^1 + \frac{e_2}{\epsilon R}\left(1 + \sum_{m=1}^{\infty} \tbinom{m+n}{n} g_m^2 t_2^m\right) t_1^n\,, \tag{16}$$

for $n = 1, 2, 3, \ldots$, where $t_i = a_i/R$. Similarly, the second boundary condition in (13) leads to

$$\frac{e_1}{\epsilon a_1} d_n^1 = -\frac{e_1}{\epsilon a_1}\left(1 + \frac{1}{n}\right) g_n^1 + \frac{e_2}{\epsilon R}\left(1 + \sum_{m=1}^{\infty} \tbinom{m+n}{n} g_m^2 t_2^m\right) t_1^n\,, \tag{17}$$

for $n = 1, 2, 3, \ldots$. Since the last terms in (16) and (17) are identical it follows that

$$n(\epsilon - 1) d_n^1 = (2n+1) g_n^1 \tag{18}$$

and hence, on substituting back into (16) or (17), we get

$$(e_2/e_1)\alpha_n t_1^{n+1} t_2 = g_n^1 t_2 - (e_2/e_1) \sum_{m=1}^{\infty} \alpha_n P_{n,m} g_m^2\,, \tag{19}$$

for $n = 1, 2, 3, \ldots$, where

$$P_{n,m} = \tbinom{m+n}{n} t_2^{m+1} t_1^{n+1} \tag{20}$$

and

$$\alpha_n = (\epsilon - 1)/\{\epsilon(1 + 1/n) + 1\}\,. \tag{21}$$

The two boundary conditions are now applied on the second surface $r_2 = a_2$ in which case we obtain the relation

$$(e_1/e_2)\alpha_n t_2^{n+1} t_1 = g_n^2 t_1 - (e_1/e_2) \sum_{m=1}^{\infty} \alpha_n P_{m,n} g_m^1\,, \tag{22}$$

for $n = 1, 2, 3, \ldots$.

IV. Existence and Uniqueness of Solution

The problem that remains is to solve equations (19) and (22) for the sets of coefficients g_n^i. Since this involves an infinite number of equations it is important to determine the condition under which a solution exists and then to devise a method of finding it.

The sum by rows and columns of the matrix $P_{n,m}$ are given by

$$R_n = \sum_{m=1}^{\infty} P_{n,m} = t_2\left[\{t_1/(1-t_2)\}^{n+1} - t_1^{n+1}\right] \tag{23}$$

and

$$C_m = \sum_{n=1}^{\infty} P_{n,m} = t_1\left[\{t_2/(1-t_1)\}^{m+1} - t_2^{m+1}\right]. \tag{24}$$

Clearly both R_n and C_m are bounded functions since, for nonoverlapping cavities, we have $0 \leqslant t_1+t_2 < 1$. Hence

$$0 < R_n < t_2 \qquad \text{and} \qquad 0 < C_m < t_1. \tag{25}$$

If we now eliminate g_n^2 between equations (19) and (22) we obtain

$$(e_2/e_1)\alpha_n t_1^{n+1} + \sum_{m=1}^{\infty} \alpha_m \alpha_n P_{n,m} t_2^m = \sum_{s=1}^{\infty} (\delta_{n,s} - Q_{n,s}) g_s^1, \tag{26}$$

where $\delta_{n,s}$ is the Kronecker delta and

$$Q_{n,s} = \sum_{m=1}^{\infty} \alpha_n \alpha_m P_{n,m} P_{s,m}/(t_1 t_2). \tag{27}$$

Since $0 < \alpha_k < 1$ the inequalities in (25) imply that $Q_{n,s}$ has row and column bounds less than unity and hence, from theorem 2.4.I on page 30 of Cooke (1950), it follows that $(\delta_{n,s} - Q_{n,s})$ has the unique and two-sided reciprocal

$$\mathbf{I} + \sum_{p=1}^{\infty} \mathbf{Q}^p, \tag{28}$$

where $\mathbf{Q} = (Q_{n,s})$ and $\mathbf{I}$ is the unit matrix. The coefficients g_s^i can therefore be expressed as a double power series in t_1 and t_2 provided that $0 \leqslant t_1+t_2 < 1$.

V. Iterative Solution

The double power series expansion for the unknown coefficients can be obtained more easily by a direct substitution into equations (19) and (22). Let

$$g_n^i = \alpha_n t_i^{n+1} \sum_{r=0}^{\infty} \sum_{s=0}^{\infty} a_n^i(r,s)\, t_i^r t_{(3-i)}^s, \qquad i = 1 \text{ or } 2, \tag{29}$$

and substitute into equations (19) and (22). On equating the coefficients of powers of t_1 and t_2 we obtain

$$a_n^i(0,0) = 1\,, \qquad a_n^i(r,s) = \sum_{m=1}^{[\frac{1}{2}(s-1)]} \binom{m+n}{n} \alpha_m\, a_m^{(3-i)}(r, s-2m-1)\,, \tag{30}$$

if r and s are not both zero. This is a difference equation from which it is a straightforward matter to calculate successive values of $a_n^i(r,s)$. Thus, after a considerable amount of algebra, we find that

$$\begin{aligned} g_n^1 = \alpha_n t_1^{n+1}\biggl\{1 &+ \left(\frac{e_2}{e_1}\right)\binom{n+1}{1}\alpha_1 t_2^3 + \left(\frac{e_2}{e_1}\right)\binom{n+2}{2}\alpha_2 t_2^5 + 2\binom{n+1}{1}\alpha_1^2 t_1^3 t_2^3 \\ &+ \left(\frac{e_2}{e_1}\right)\binom{n+3}{3}\alpha_3 t_2^7 + 3\binom{n+2}{2}\alpha_1\alpha_2 t_1^3 t_2^5 + 2\binom{n+1}{1}\alpha_1^2 t_1^5 t_2^3 + \ldots\biggr\}\,, \end{aligned} \tag{31}$$

with a similar expression for g_n^2. The above equation is consistent with the result given by Rosenthal (1967), who was concerned only with the case $e_1 = -e_2$ and $t_1 = t_2$.

This method of determining an expansion for the coefficients g_n^i is very easily carried out and is particularly suitable for numerical computations, some of which were carried out in an earlier paper (see Rosenthal 1967 for further discussion).

VI. REFERENCES

ABBOTT, J. A., and BOLTON, H. C. (1952).—*Trans. Faraday Soc.* **48**, 422.

BERNAL, J. D., and FOWLER, R. H. (1933).—*J. chem. Phys.* **1**, 515.

BUCKINGHAM, A. D. (1957).—*Discuss. Faraday Soc.* **24**, 151.

BUCKLEY, F., and MARYOTT, A. A. (1954).—*J. Res. natn. Bur. Stand.* **53**, 229.

COLLINS, W. D. (1963).—*Mathematika* **10**, 72.

COOKE, R. G. (1950).—"Infinite Matrices and Sequence Spaces." (MacMillan: London.)

DAVIS. M. H. (1964).—*Q. Jl Mech. appl. Math.* **27**, 499.

HILL, T. L. (1944).—*J. chem. Phys.* **12**, 147.

HOBSON, E. W. (1931).—"Spherical and Ellipsoidal Harmonics." (Cambridge Univ. Press.)

KIRKWOOD, J. G., and WESTHEIMER, F. H. (1938).—*J. chem. Phys.* **6**, 506, 513.

KIRKWOOD, J. G., and WESTHEIMER, F. H. (1939).—*J. chem. Phys.* **7**, 437.

KOBER, F. P., and FITTS, D. D. (1966).—*Electrochim. Acta* **11**, 641.

KOTTLER, F. (1927).—*In* "Handbuch der Physik". Vol. 12, p. 443. (Springer-Verlag: Berlin.)

LEBEDEV, N. N. (1965).—"Special Functions and their Applications." (Prentice Hall: New Jersey.)

LINDERSTRØM-LANG, K. (1953).—*C.r. Trav. Lab. Carlsberg* **28**, 281.

MITRA, S. K. (1944).—*Bull. Calcutta math. Soc.* **36**, 31.

ONSAGER, L. (1936).—*J. Am. chem. Soc.* **58**, 1486.

PAYNE, L. E., and PELL, W. H. (1960).—*J. Fluid Mech.* **7**, 529.

PELL, W. H., and PAYNE, L. E. (1960*a*).—*Mathematika* **7**, 78.

PELL, W. H., and PAYNE, L. E. (1960*b*).—*Q. appl. Math.* **18**, 257.

RANGER, K. B. (1965).—*Proc. Camb. phil. Soc.* **61**, 271.

ROSENTHAL, D. K. (1967).—Ph.D. Thesis, Manchester University.

ROSS, I. G., and SACK, R. A. (1950).—*Proc. R. Soc.* B **63**, 893.

SCHOLTE, TH. G. (1949).—*Physica* **15**, 437, 450.

SHAIL, R. (1962).—*Mathematika* **9**, 57.

SNOW, C. (1949).—*J. Res. natn. Bur. Stand.* **43**, 377.

STIMSON, M., and JEFFREY, G. B. (1926).—*Proc. R. Soc.* A **111**, 110.

TITCHMARSH, E. C. (1950).—"The Theory of Functions." (Cambridge Univ. Press.)

THE SHAPE AND ENERGY OF A REVOLVING LIQUID MASS HELD TOGETHER BY SURFACE TENSION

By D. K. Ross*

[*Manuscript received June* 27, 1968]

Summary

The shape of a drop of incompressible fluid held together by the action of surface tension and made to rotate about an axis is determined, the effect of gravity being neglected. Two distinct problems are investigated. In the first an isolated drop of liquid in the form of a surface of revolution is considered. At zero angular speed the drop is spherical and with increasing angular momentum the oblateness increases until a maximum angular speed is reached (where the total mechanical potential is a minimum) beyond which a new linear series of equilibrium forms emerges. A solution in the form of a toroid is also found.

In the second problem the drop is rotating together with a denser medium. It is shown that the drop tends to become a cylindrical thread with increasing angular speed and that there is a critical angular speed at which the angular momentum is a maximum and the total energy is a minimum.

I. Introduction

The equilibrium of a revolving isolated finite mass of fluid under the action of capillary force was considered by Lord Rayleigh (1914). He found a solution in which the liquid drop is a surface of revolution that meets the axis of the rotation provided that the angular speed is sufficiently small. At a certain critical speed this drop collapses onto its equator and, for a finite range of speeds, two equilibrium configurations are mathematically possible; for low speeds one meets the axis of the rotation and the other has the form of a toroid, but for higher speeds both meet the axis of the rotation. Lord Rayleigh used a graphical technique to determine the angular speed corresponding to collapse but did not point out the difficulties associated with reaching this stage, nor the non-uniqueness of the configurations as a function of the angular speed.

When a drop of liquid rotates rigidly with a denser surrounding medium the drop tends to become a cylindrical thread as the angular speed tends to infinity. Rosenthal (1962) obtained this result but failed to show that the angular momentum of the system has a maximum where the total energy is a minimum.

It is the purpose of the present paper to compute the potential and kinetic energies of the systems since, according to Orr (1906, 1907), Lyttleton (1953), and Pozharitiskii (1964), these quantities may be related to a discussion of the stability of rigid body rotation. Such a discussion appears in the following paper (present issue, pp. 837–44).

---

* Department of Mathematics, University of Melbourne, Parkville, Vic. 3052.

Aust. J. Phys., 1968, **21**, 823–35

II. Equilibrium Forms of Surfaces of Revolution

It is rather difficult to consider cases in which the liquid does not form a surface of revolution because the expression for the total curvature at a point on a general surface is very complicated. The possible existence of other configurations is suggested from an analogous problem to do with self-gravitating masses. For these it is known (Lichtenstein 1933) that for a rotating system the plane through the mass centre perpendicular to the axis of the rotation must be a plane of symmetry of an equilibrium form and that ellipsoids having three unequal axes are admissible provided that the angular momentum has the appropriate value. Of course not all these forms are stable to small disturbances. Poincaré (1902) was even able to show that "pear-shaped figures" existed which are not axially symmetrical around the longest axis.

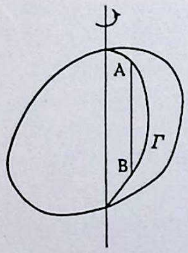

Fig. 1.—Typical rotating liquid mass showing cylindrical element AB parallel to the axis of rotation.

For a rotating liquid held together by the action of the capillary force we do not have such a simple theorem relating to symmetrical forms. At best we can argue as follows. Suppose that the mass of liquid is simply connected and that it is divided up into elementary cylindrical columns parallel to the axis of the rotation and with infinitesimal cross section. Let Γ be the curve which lies at the intersection of the liquid mass with a plane through the axis of the rotation and which contains the typical cylindrical element AB (see Fig. 1). Then it is apparent that the pressure differences at the boundary points A and B are equal, because the contributions from the centrifugal force are the same. Since we do not take into account variations in the coefficient of surface tension over the surface it follows that the total curvature of the surface at A and B must be equal. This, by itself, does not imply geometrical symmetry, although it does show that the rate of change of total curvature with arc length measured along the curve Γ must be zero at the point on Γ that is furthermost from the axis of the rotation. Whether or not this criterion can be used to limit more general configurations to a very much narrower class has still to be examined.

For a viscous fluid not acted upon by forces other than those in the interface it is known that no steady motion can exist unless the fluid rotates as a rigid body. So we shall assume that the angular speed ω is constant. It is then found convenient to make use of the cylindrical polar coordinates (r, θ, z) with the z axis as the axis of rotation and to take as the equation of the interface, say, $r = f(z)$.

To begin we shall suppose that $r = f(z)$ is a single-valued function, for then one way of determining the equilibrium configuration at a given angular speed is to apply a variational principle to the liquid drop of density ρ_1 and its surroundings of density ρ_2. Lyttleton (1953) used Lagrange's equations of motion to show that for a dynamical system of particles rotating with constant angular velocity the positions of relative equilibrium are obtained by finding stationary values of the Lagrangian L of the motion. Thus, if L is calculated from the kinetic energy due to the rigid body rotation and from the energy associated with the capillary force in the interface then the problem becomes one of finding the function $f = f(z)$ for which

$$L = T_1 + T - U\,, \tag{1}$$

with

$$T = \tfrac{1}{2}\pi \int (\rho_1 - \rho_2)\omega^2 f^4 \, \mathrm{d}z \qquad \text{and} \qquad U = 4\pi \int \alpha f (1 + f'^2)^{\frac{1}{2}} \, \mathrm{d}z\,, \tag{1a}$$

is stationary but subject to the restriction that the volume

$$V = 2\pi \int f^2 \, \mathrm{d}z \tag{2}$$

is known beforehand. Here T_1 is the kinetic energy that the system would have if the liquid drop had the same density as its surroundings and is independent of the shape of the interface although it depends on the angular speed, T is the kinetic energy of the drop minus the kinetic energy that the drop would have if it had the same density as its surroundings, and U is the energy stored in the interface. The coefficient of surface tension α is taken to be constant in time and over the whole interface, and the prime denotes differentiation with respect to z. Actually the quantity U may be interpreted as a potential energy, for work is done by the capillary force when the surface of separation undergoes an infinitesimal displacement which reduces the total surface area. It is also to be noted that T is negative when $\rho_1 < \rho_2$. The reason for choosing this derivation of the equation lies in the connection between the energy integral in (1a) and the stability criteria to be discussed in the following paper. This technique is also discussed by Landau and Lifshitz (1959), who used a variational principle to derive similar equilibrium conditions.

In reality the two media are separated by a narrow transitional layer, but this is so thin that it may be neglected as a first approximation. The existence of this layer and the consequent phenomena associated with it, which are neglected here, are discussed at length by Hirschfelder, Curtiss, and Bird (1954). The most important omissions concern the variation in the coefficient of surface tension due to surface contamination or the existence of a temperature gradient and the neglect of the gravitational forces. The latter omission is justified for small drops of fluid that are not too small for the transition layer to be dominant provided that the characteristic length g/ω^2 (where g is the acceleration due to gravity) is small and that the capillary length, defined by $\{2\alpha/(|\rho_1 - \rho_2|g)\}^{\frac{1}{2}}$, is large compared with the dimensions of the drop.

Now the extremal problem can be solved by using a first integral of the Euler–Lagrange equation, namely

$$F - f'\,\partial F/\partial f' = \text{constant}\,, \qquad F = T - U - 2\pi\beta \int f^2 \, \mathrm{d}z\,, \tag{3}$$

because (1) has no term in z. This then leads to the differential equation

$$\pm(1 + f'^2)^{-\frac{1}{2}} = \beta f/2\alpha + (\rho_1 - \rho_2)\omega^2 f^3/8\alpha - A/f\,, \tag{4}$$

where $2\pi\beta$ is the usual Lagrange multiplier and A is a constant of integration that has the value zero if the liquid intersects the axis of the rotation.

Actually a solution to this problem exists for which $r = f(z)$ is not single valued. In this case we may imagine that the interface is divided into two parts, for example, $r = f_1(z)$ and $r = f_2(z)$, with $f_1(z) \geqslant f_2(z)$ for all z, and where the equal sign applies only at the point z_0 where $\mathrm{d}z/\mathrm{d}f_1 = \mathrm{d}z/\mathrm{d}f_2 = 0$. We now alter the equations for T, U, and V by changing the variable of integration from z to f since we are then dealing with single-valued functions and in this way we obtain equation (4) once again. The plus and minus signs in equation (4) thus refer respectively to the upper curve $f_1(z)$ and the lower curve $f_2(z)$. However, the constant A may now be different for each curve, but we shall follow Lord Rayleigh (1914) and examine only those configurations for which A is the same.

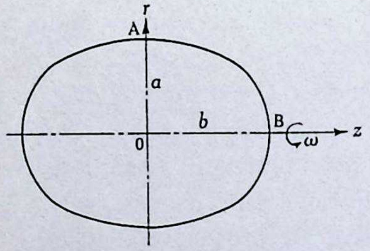

Fig. 2.—Plane section through the axis 0z of the liquid drop.

III. Case 1: Drops that Intersect the Axis of Rotation

Firstly we consider the case when the liquid meets the axis of rotation (see Fig. 2) so that we can write (4) in the form

$$\pm(1+f'^2)^{-\frac{1}{2}} = \beta f/2\alpha + \omega^{*2} f^3/d^3, \qquad \text{with} \qquad \omega^{*2} = (\rho_1-\rho_2)\omega^2 d^3/8\alpha, \tag{5}$$

where β is a constant to be determined from the condition that the enclosed volume is given the value V, and d is the mean radius of the drop defined by the relation

$$V = 4\pi d^3/3. \tag{6}$$

Clearly the quantity $|\omega^*|$ will serve as a nondimensional angular speed (note that $\omega^{*2} \leqslant 0$ whenever $\rho_1 < \rho_2$). Now the magnitude of the total curvature at a point on the surface is given by

$$J = \frac{1}{f}\frac{\mathrm{d}}{\mathrm{d}f}\left(f(1+f'^2)^{-\frac{1}{2}}\right) = \frac{\beta}{\alpha} + \frac{4\omega^{*2} f^2}{d^3} \tag{7}$$

and hence we can identify β as the pressure difference $\Delta p = p_1 - p_2$ on the axis of rotation at the poles.

When the angular speed is zero the drop is under the influence of the capillary force alone and so the liquid surface must be spherical; therefore, at small angular speeds ω^*, $\Delta p > 0$ and the drop has width $2a$ corresponding to the curve on the surface for which $f' = 0$. On combining this condition with equation (5) it appears that

$$\Delta p = 2\alpha(1-e)/a, \qquad \text{with} \qquad e = (\rho_1-\rho_2)\omega^2 a^3/8\alpha, \tag{8}$$

and so $\Delta p \geqslant 0$ as long as the parameter $e \leqslant 1$. However, the curvature K of a plane section through the axis of the drop is given by

$$K = -\frac{\mathrm{d}}{\mathrm{d}f}\left((1+f'^2)^{-\frac{1}{2}}\right) = -\frac{1-e}{a} - \frac{3ef^2}{a^3} \tag{9}$$

and this remains negative as long as $-\frac{1}{2} < e \leqslant 1$. Here the term $(1-e)/a$ can be interpreted as the curvature of the plane section at the poles.

If we now define a function $\phi(f)$ by the relation

$$\phi = \phi(f) = (1-e)f/a + e(f/a)^3 \tag{10}$$

then equation (5) takes on the form

$$\mathrm{d}z/\mathrm{d}f = -\phi(1-\phi^2)^{-\frac{1}{2}}, \tag{11}$$

since it is sufficient to take $\mathrm{d}z/\mathrm{d}f \leqslant 0$ when f is small. If $\Delta p \geqslant 0$ then, as f/a increases from zero, ϕ increases to its maximum value 1 and, at this point, $\mathrm{d}f/\mathrm{d}z = 0$. For further decrease in z we set

$$\mathrm{d}z/\mathrm{d}f = +\phi(1-\phi^2)^{-\frac{1}{2}} \tag{12}$$

and this leads to a closed section in which f has only the one turning value at $f/a = 1$.

If $e < 0$ then the density of the liquid is less than that of its surroundings. For $e < -\frac{1}{2}$, $\phi = 1$ has one positive zero less than a which means that equation (11) takes on complex values; for $e = -\frac{1}{2}$ the left-hand side of (11) has a first-order pole at $f/a = 1$ and, since the volume of the drop is finite, this leads to the conclusion that the length of the drop tends to infinity as $e \to -\frac{1}{2}+0$. If we now use equations (5) and (8) then this condition shows that

$$\omega^{*2} = e(a/d)^{-3} \to -\infty \qquad \text{as} \qquad e \to -\tfrac{1}{2}+0. \tag{13}$$

This result was obtained by Rosenthal (1962), who showed that the drop is always convex and that it becomes threadlike as the angular speed tends to infinity. If we look at the angular momentum H of the drop (see Figs. 3 and 4) then it is clear that it is not a monotonically increasing function of the angular speed because the moment of intertia of an infinitely thin thread must be zero. (A formal proof is given in equation (36).) It follows that the angular speed is the fundamental quantity to be considered in this case.

Table 1 makes clear the following points.

(1) There exists a surface of revolution corresponding to each angular speed.

(2) The maximum angular momentum occurs when the sum of the kinetic and potential energies is least and is given by $H_{\max} = 0{\cdot}6609\,\pi\{2(\rho_2-\rho_1)\alpha d^7\}^{\frac{1}{2}}$, where the angular speed $\omega = 1{\cdot}2851\{8\alpha/(\rho_2-\rho_1)d^3\}^{\frac{1}{2}}$ and $e = 0{\cdot}4859$.

(3) For each value of the angular momentum less than the maximum there are two possible surfaces of revolution.

(4) The angular speed increases monotonically and indefinitely as the parameter e decreases from 0 to $-\frac{1}{2}$ so that, for a given angular speed, there exists only one surface of revolution.

(5) The potential energy of the interface increases from the value $4\pi\alpha d^2$, when the drop is spherical, to infinity when the drop is an infinitely long thread; while the kinetic energy associated with the system increases from zero to infinity.

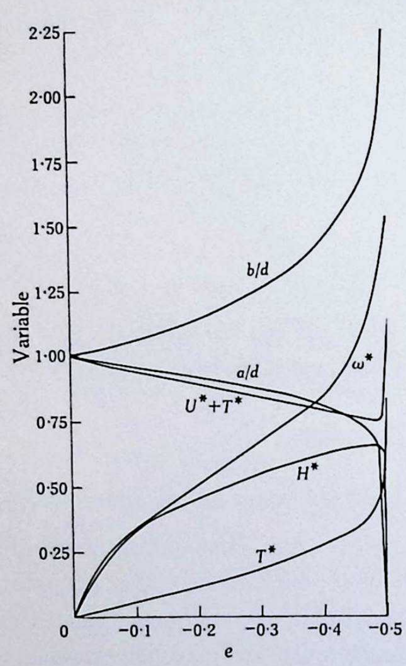

Fig. 3.—Changes in the physical variables with the parameter e for a drop rotating in a denser medium. Here $\omega^* = \omega\{(\rho_2-\rho_1)d^3/8\alpha\}^{\frac{1}{2}}$.

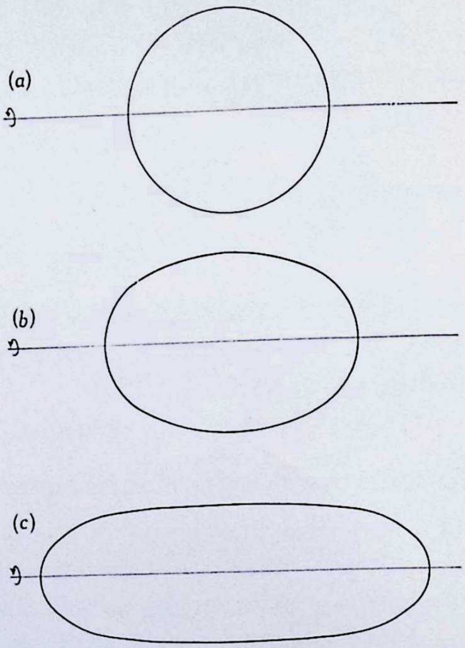

Fig. 4.—Shapes of the drop rotating at angular speeds of (a) 0, (b) 0·6713, and (c) 1·2851. The last configuration corresponds to the form of bifurcation of the linear series.

For $0 \leqslant e < 1$, $\phi(f)$ has only one real zero and so the drop is again convex; however, for $e > 1$ this function has two possible zeros at $f/a = \{(e-1)/e\}^{\frac{1}{2}}$ and $f/a = 1$. In the latter case equilibrium forms exist which are partly concave and for these shapes the angular speed is such that the pressure difference at the poles is negative. It follows that there is then a tendency for the liquid to collapse onto its equator.

Table 1

PHYSICAL QUANTITIES CORRESPONDING TO DROP OF LIQUID THAT ROTATES WITH DENSER MEDIUM

e	$\omega\{(\rho_2-\rho_1)d^3/8\alpha\}^{\frac{1}{2}}$	$H/\pi\{2(\rho_2-\rho_1)\alpha d^7\}^{\frac{1}{2}}$	$T/4\pi\alpha d^2$	$(U+T)/4\pi\alpha d^2$	a/d	b/d
0	0	0	0	1	1	1
−0·1	0·3338	0·3316	−0·0553	0·9466	0·9646	1·0723
−0·2	0·5038	0·4605	−0·1160	0·8931	0·9237	1·1604
−0·3	0·6713	0·5528	−0·1856	0·8394	0·8731	1·2771
−0·4	0·8813	0·6230	−0·2745	0·7857	0·8016	1·4619
−0·4859	1·2851	0·6609	−0·4247	0·7478	0·6651	1·9261
−0·5	∞	0	−∞	∞	0	∞

If we now replace the variables f by f/a and z by z/a then the volume of the drop becomes

$$V = -2\pi a^3 \int_0^1 f^2 \,\mathrm{d}z/\mathrm{d}f \,\mathrm{d}f \tag{14}$$

and so, on using the expression (11) for $\mathrm{d}z/\mathrm{d}f$ and integrating in a suitable manner, we find that the above equation reduces to the form

$$V = 2\pi a^3\{1-(1-e)b/a\}/3e\,, \tag{15}$$

where

$$b/a = \int_0^1 \phi(1-\phi^2)^{-\frac{1}{2}}\,\mathrm{d}f \tag{16}$$

and $b = \mathrm{OB}$ (Fig. 2) is half the distance from pole to pole. If we express the volume in terms of the mean radius and use the definition of angular speed ω^* given in (5) then (15) becomes

$$2\omega^{*2} = 1-(1-e)b/a \tag{17}$$

and so it is seen that collapse corresponds to $2\omega^{*2} = 1$, where

$$\omega = \{16\pi\alpha/3(\rho_1-\rho_2)V\}^{\frac{1}{2}}\,. \tag{18}$$

This verifies that the action of surface tension is to try to prevent collapse and that smaller drops are less prone to this kind of "instability". Again, for $e > 1$ we have $\mathrm{d}z/\mathrm{d}f = 0$ only where $f = 0$ or $f = \{(e-1)/e\}^{\frac{1}{2}}$ and so if we allow e to increase from one then the point of collapse must occur before e has a value that allows the interface to have a second point at which $\mathrm{d}f/\mathrm{d}z = 0$. That is, there can be no positive root of the equation $\phi = -1$. A simple calculation shows that this critical value must be less than four. In fact it is the positive root of the transcendental equation

$$\int_0^1 \phi(1-\phi^2)^{-\frac{1}{2}}\,\mathrm{d}f = 0 \tag{19}$$

and has the value $2\cdot3291$. Of course, whether collapse can be realized in practice has still to be investigated. Lord Rayleigh (1914) did not consider this question at all but used a graphical technique to estimate the value of the parameter e at collapse. He obtained the value $2\cdot4$.

If we look at equation (17) (also Fig. 5) then it is clear that $2\omega^{*2} = 1$ for one other value of the parameter e, namely, $e = 1$, which corresponds to the case where the pressure reversal just begins. This shows that ω^* does not increase monotonically with the parameter e as one might have suspected from the fact that the ratio b/a diminishes monotonically with e. This latter statement comes from the inequality

$$\frac{\mathrm{d}(b/a)}{\mathrm{d}e} = -\int_0^1 \frac{f(1-f^2)}{(1-\phi^2)^{3/2}}\,\mathrm{d}f < 0\,. \tag{20}$$

Actually ω^* has one maximum at $\omega^* = \omega_{\max} = 0\cdot7540$ where $e = 1\cdot6608$. Thus in order to make the liquid collapse onto its equator it is necessary to increase the angular speed of the drop up to its maximum value $\omega_{\max}$ and then to decrease it to the value $0\cdot7071$. At this stage the drop ought to have collapsed. Clearly it is necessary that changes in the angular speed be very gradual so that no instabilities are introduced from the source of angular momentum.

Now it might appear as if an increase in the angular speed followed by a decrease, as described above, would ultimately lead back to the spherical form, but this is not so if we can ensure that the angular momentum of the liquid increases throughout the change. Figure 6 shows the variations in the typical drop geometry with angular speed.

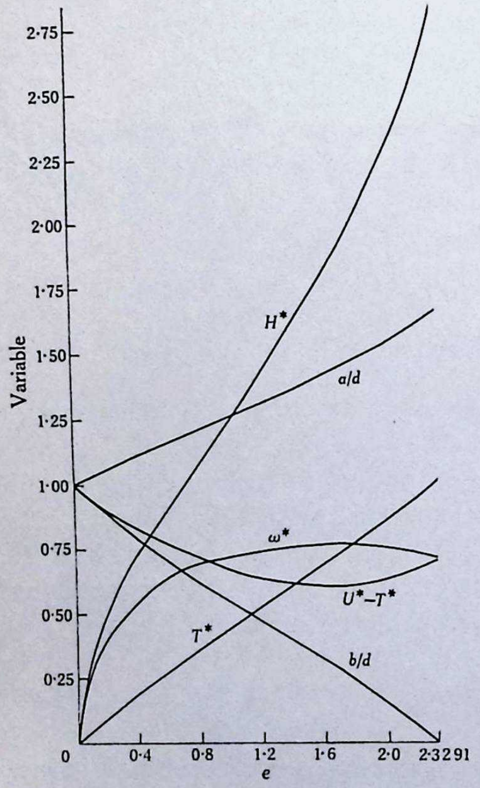

Fig. 5.—Changes in the physical variables with the parameter *e* for an isolated drop.

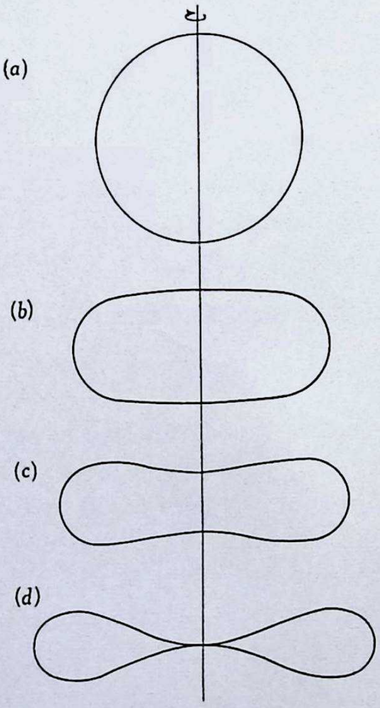

Fig. 6.—Shapes of isolated drops rotating at angular speeds of (*a*) 0, (*b*) 0·7071, (*c*) 0·7540, and (*d*) 0·7071, which are respectively the drop at rest, the last of the convex forms, the stage beyond which the drop becomes unstable, and the collapse configuration.

Table 2 makes clear the following points.

(1) There exists a surface of revolution for each value of the angular momentum $H \leqslant H_{\max} = 2\cdot8506\,\pi\{2(\rho_1-\rho_2)\alpha d^7\}^{\frac{1}{2}}$.

(2) The maximum angular speed occurs when the difference between the potential and kinetic energies is least and is given by $\omega_{\max} = 0\cdot7540\{8\alpha/(\rho_1-\rho_2)d^3\}^{\frac{1}{2}}$ when $e = 1\cdot6608$.

(3) For each value of the angular speed less than the maximum but greater than $0\cdot25\pi\{(\rho_1-\rho_2)d^3/\alpha\}^{\frac{1}{2}}$ two possible surfaces of revolution exist.

(4) The angular momentum increases monotonically to the finite value $H_{\max}$ as e increases from 0 to 2·3291 so that for a given angular momentum less than this only one surface of revolution can exist.

(5) The potential energy of the interface increases from the value $4\pi\alpha d^2$, when the drop is spherical, to the finite value $1{\cdot}7238 \times 4\pi\alpha d^2$ when the drop collapses; while the kinetic energy associated with the drop increases from 0 to $1{\cdot}0079 \times 4\pi\alpha d^2$.

Table 2

PHYSICAL QUANTITIES CORRESPONDING TO ISOLATED DROP

e	$\omega\{(\rho_1-\rho_2)d^3/8\alpha\}^{\frac{1}{2}}$	$H/\pi\{2(\rho_1-\rho_2)\alpha d^7\}^{\frac{1}{2}}$	$T/4\pi\alpha d^2$	$(U-T)/4\pi\alpha d^2$	a/d	b/d
0	0	0	0	1	1	1
0·5	0·5810	0·8173	0·2374	0·7948	1·1399	0·7404
1·0	0·7071	1·2591	0·4452	0·6677	1·2599	0·5433
1·5	0·7514	1·7130	0·6436	0·6044	1·3850	0·3580
1·6608	0·7540	1·8780	0·7080	0·5998	1·4295	0·2965
2·0	0·7424	2·2905	0·8503	0·6246	1·5367	0·1573
2·3291	0·7071	2·8506	1·0079	0·7159	1·6701	0

In order to interpret the occurrence of a maximum angular speed (see Pozharitiskii (1964), who related this to the stability of the liquid) we shall begin by relating the kinetic and potential energies to the angular speed and the corresponding angular momentum. We define the energies as fractions of the potential energy that the drop would have at rest, i.e. in units of $4\pi\alpha d^2$. With this definition the nondimensional kinetic and potential energies become respectively

$$T^* = (a/d)^2 \int_0^1 ef^4\phi(1-\phi^2)^{-\frac{1}{2}}\,\mathrm{d}f \tag{21}$$

and

$$U^* = (a/d)^2 \int_0^1 f(1-\phi^2)^{-\frac{1}{2}}\,\mathrm{d}f. \tag{22}$$

The asterisk indicates that the quantity is expressed as a fraction of $4\pi\alpha d^2$.

If we start with the identity

$$ef^4\phi = f - f(1-\phi^2) - (1-e)f^2\phi \tag{23}$$

and then combine it with equations (14), (16), (21), and (22), we get

$$T^* - U^* = \frac{2(e-1)}{3(a/d)} - (a/d)^2 \int_0^1 f(1-\phi^2)^{\frac{1}{2}}\,\mathrm{d}f, \tag{24}$$

which, on integrating the last term by parts, leads to

$$5T^* - 2U^* = 2(e-1)/(a/d). \tag{25}$$

This is a rather surprising result in view of the complexity of the defining relations and it has been used as a check on the numerical calculations.

If we now make T^* and U^* the subjects of equations (24) and (25) then we find that

$$T^* = \frac{2(e-1)}{9(a/d)} + \tfrac{2}{3}(a/d)^2 \int_0^1 f(1-\phi^2)^{\frac{1}{2}}\,\mathrm{d}f \tag{26}$$

and

$$U^* = -\frac{4(e-1)}{9(a/d)} + \tfrac{5}{3}(a/d)^2 \int_0^1 f(1-\phi^2)^{\frac{1}{2}}\,\mathrm{d}f, \tag{27}$$

and since

$$\left|\int_0^1 f(1-\phi^2)\,\mathrm{d}f\right| < \tfrac{1}{2} \qquad \text{for all} \qquad e \geqslant -\tfrac{1}{2} \tag{28}$$

it follows that $U^* \to +\infty$ and $T^* \to -\infty$ as $e \to -\frac{1}{2}+0$, while they tend to finite values as $e \to 2\cdot 3291$. These results are shown in Tables 1 and 2.

The next step is to examine the condition under which the angular speed has a stationary value with respect to the parameter e. To investigate this situation we can differentiate (24) with respect to e and then, after a considerable amount of algebra which involves using the identity (25), we find that

$$\mathrm{d}(U^*-T^*)/\mathrm{d}(\omega^{*2}) = -T^*/\omega^{*2} \leqslant 0\,. \tag{29}$$

The quantity U^*-T^* is known as the total mechanical potential and this has an absolute minimum where the angular speed is greatest. Lyttleton (1953) showed that this criterion corresponds to "secular stability". This is discussed in the following paper.

In order to understand the physics of this problem more clearly it is found useful to determine the angular momentum of the liquid and how it varies with the parameter e. Since the drop rotates rigidly in an equilibrium configuration, we can express the angular momentum H in terms of the kinetic energy by means of the relation

$$H = 8\pi T^* \alpha d^2/\omega\,; \tag{30}$$

this can then be expressed in units of $\pi\{2(\rho_1-\rho_2)\alpha d^7\}^{\frac{1}{2}}$, in which case we may write

$$H^* = H/\pi\{2(\rho_1-\rho_2)\alpha d^7\}^{\frac{1}{2}} = 2T^*/\omega^*\,. \tag{31}$$

On differentiating this equation with respect to e we obtain

$$\omega^* \frac{\mathrm{d}H^*}{\mathrm{d}e} = -\frac{T^*}{\omega^{*2}}\frac{\mathrm{d}\omega^{*2}}{\mathrm{d}e} + \frac{2\mathrm{d}T^*}{\mathrm{d}e} \tag{32}$$

and then by applying (29) we have

$$\omega^* = \mathrm{d}(U^*+T^*)/\mathrm{d}H^* \tag{33}$$

and

$$H^* = -\,\mathrm{d}(U^*-T^*)/\mathrm{d}\omega^*\,. \tag{34}$$

The configuration of the drop and hence the potential and kinetic energies depend only on a single parameter and so, at various stages in the above derivation, we regard them as functions of either the parameter e, the angular speed, or the angular momentum, as the case may be. Equation (33) shows that the angular momentum increases with the "total energy" U^*+T^* whilst equation (34) verifies that the angular speed is a maximum when the total mechanical potential U^*-T^* is a minimum.

When the outer medium is the denser it is clear that there is a value of e for which the angular momentum is a maximum. This result is indicated by the fact that at high angular speeds the interface is approximated by a cylindrical surface with small corrections at the ends, and so the angular momentum is given by

$$H \simeq \tfrac{1}{2}Ma^2\omega\,, \tag{35}$$

where M is the mass of the drop of liquid and is finite. If we now apply condition (13) then we see that $H \to 0$ as $|\omega| \to \infty$. The existence of a maximum follows from the fact that H is a continuous function of e and that it is zero when $\omega = 0$. A formal proof of this can be obtained by using the fact that $e \to -\frac{1}{2}$ as $|\omega^*| \to \infty$ and then applying this condition in equations (26) and (27). Thus

$$H^* = \frac{2T^*}{\omega^*} = \frac{4(e-1)}{9\omega^*(a/d)} + \frac{4(a/d)^2}{3\omega^*}\int_0^1 f(1-\phi^2)^{\frac{1}{2}}\,\mathrm{d}f \to 0 \qquad \text{as} \qquad |\omega^*| \to \infty\,, \tag{36}$$

because of the inequality (28). Similarly

$$U^*/\omega^* \to 0 \qquad \text{as} \qquad |\omega^*| \to \infty\,. \tag{37}$$

IV. CASE 2: DROPS OF LIQUID IN THE FORM OF AN ANNULUS

When the liquid does not meet the axis of rotation the constant of integration A that appears in equation (4) has to be retained. Hence, if the liquid is to form a closed surface it is necessary that $f' = 0$ for two positive values of f, namely $f = a_0$ and $f = a$, with $a > a_0$, say. The differential equation describing the surface then becomes

$$\pm f(1+f'^2)^{-\frac{1}{2}} = \omega^{*2}(f^2-a_0^2)(f^2-a^2)/d^3 + (f^2-aa_0)/(a-a_0)\,, \tag{38}$$

where the plus and minus signs have the same meaning as in equation (4). If we again replace f by f/a and z by z/a and then define a function $w(f)$ by the relation

$$w = w(f) = e(f^2-1)(f^2-a_1^2) + (f^2-a_1)/(1-a_1)\,, \tag{39}$$

where $a_1 = a_0/a$, equation (38) takes on the alternative form

$$\mathrm{d}z/\mathrm{d}f = -w(f^2-w^2)^{-\frac{1}{2}}\,, \tag{40}$$

so that we can get a closed drop only if the parameters e and a_1 are so related that

$$I(e, a_1) \equiv \int_{a_1}^{1} w(f^2-w^2)^{-\frac{1}{2}}\,\mathrm{d}f = 0\,. \tag{41}$$

Actually these parameters must satisfy the inequality

$$e(1-a_1)(1+a_1)^2 < 4\,, \tag{42}$$

which is the condition that $\mathrm{d}z/\mathrm{d}f$ remain finite in the open interval $a_1 < f < 1$. This result serves as a guide to the numerical computation of the roots of the transcendental equation (41).

By a simple differentiation we find that

$$\frac{\partial I(e,a_1)}{\partial e} = -\int_{a_1}^{1} \frac{f^2(1-f^2)(f^2-a_1^2)}{(f^2-w^2)^{3/2}}\,\mathrm{d}f \leqslant 0, \tag{43}$$

and so it follows that to each value of $a_1 > 0$ there corresponds one positive value for the parameter e. It should be mentioned that if a_1 is set equal to zero then we obtain the differential equation that corresponds to case 1; so we see that a_1 is zero for all shapes that meet the axis of the rotation and that a_1 is positive for the ring-shaped surfaces, vanishing only at the point of collapse. Also the volume of the closed drop is

$$V = -2\pi a^3 \int_{a_1}^{1} f^2 w (f^2-w^2)^{-\frac{1}{2}}\,\mathrm{d}f, \tag{44}$$

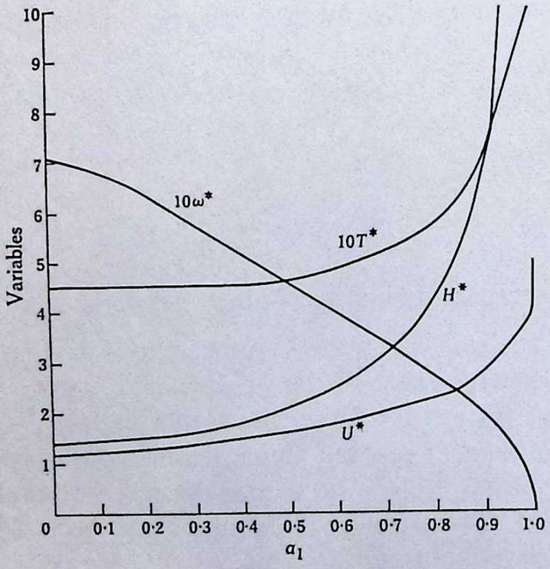

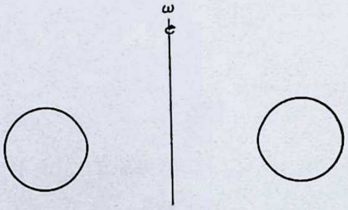

Fig. 7 (*left*).—Changes in the physical variables with the parameter a_1 for a toroidal drop.

Fig. 8 (*above*).—Typical toroidal drop at an angular speed $\omega^* = 0\cdot4460$ where $a_1 = \frac{1}{2}$.

where, for a given e, we choose a_1 to satisfy (41). Then, the kinetic and potential energies will be given by

$$T^* = (a/d)^2 \int_{a_1}^{1} e f^4 w (f^2-w^2)^{-\frac{1}{2}}\,\mathrm{d}f \tag{45}$$

and

$$U^* = (a/d)^2 \int_{a_1}^{1} f^2 (f^2-w^2)^{-\frac{1}{2}}\,\mathrm{d}f, \tag{46}$$

and, in a manner analogous to case 1, we can prove that

$$5T^* - 2U^* = 2\{e(1+a_1^2) - (1-a_1)^{-1}\}/(a/d) \tag{47}$$

and hence that

$$\omega^* = \mathrm{d}(U^*+T^*)/\mathrm{d}H^* \tag{48}$$

and

$$H^* = -\,\mathrm{d}(U^*-T^*)/d\omega^*. \tag{49}$$

Now it happens that $I(e, a_1)$ is a small quantity for a wide range of values of e and hence that it is not practical to solve equation (41) directly. Instead it is better to use the formulae for the kinetic and potential energies which are analogous to those given in equations (26) and (27) and then to find the value of e for which these equations are consistent with (45) and (46). In this case the relevant physical quantities are given in Table 3 and their variations with a_1 are illustrated in Figure 7.

Lord Rayleigh (1914) assumed that the toroidal form tends to a circular cross section as $a_1 \rightarrow 1-0$ and used a perturbation method to determine the shape at small angular speeds. The validity of this assumption is confirmed by the calculations and is illustrated in Figure 8.

TABLE 3

PHYSICAL QUANTITIES CORRESPONDING TO TOROIDAL DROP

a_1	e	$\omega\{(\rho_1-\rho_2)d^3/8\alpha\}^{\frac{1}{2}}$	$H/\pi\{2(\rho_1-\rho_2)\alpha d^7\}^{\frac{1}{2}}$	$T/4\pi\alpha d^2$	$U/4\pi\alpha d^2$
0·90	2·81	0·20	7·43	0·65	2·62
0·70	1·10	0·32	2·94	0·47	1·90
0·50	0·95	0·45	2·06	0·46	1·63
0·30	0·98	0·57	1·62	0·46	1·39
0·10	1·11	0·69	1·45	0·46	1·23
0·05	1·00	0·69	1·29	0·46	1·14
0·01	0·90	0·70	1·25	0·44	1·11

So far we have examined the shapes of rigidly rotating isolated drops corresponding to surfaces of revolution; however, it is most likely that other forms exist at angular speeds greater than $\omega_{\max}$. Two possibilities present themselves: either there are equilibrium forms that are not surfaces of revolution or else the fluid inside the drop ceases to rotate as a rigid body, in which case no steady-state configuration exists. A complete study of these problems is very difficult and is not attempted here.

V. REFERENCES

HIRSCHFELDER, J. O., CURTISS, C. F., and BIRD, R. B. (1954).—"Molecular Theory of Gases and Liquids." (Wiley: New York.)

LANDAU, L. D., and LIFSHITZ, E. M. (1959).—"Fluid Mechanics." (Pergamon Press: Oxford.)

LICHTENSTEIN, I. (1933).—"Gleichgewichtsfigüren Rotierender Flüssigkeiten." (Springer-Verlag: Berlin.)

LYTTLETON, R. A. (1953).—"The Stability of Rotating Liquid Masses." (Cambridge Univ. Press.)

ORR, W. McF. (1906).—*Proc. R. Ir. Acad.* A **27**, 9.

ORR, W. McF. (1907).—*Proc. R. Ir. Acad.* A **27**, 69.

POINCARÉ, H. (1902).—"Figures d'Equilibre d'une Masse Fluide." (G. Carré: Paris.)

POZHARITISKII, G. K. (1964).—*J. appl. Math. Mech.* **28**, 67.

RAYLEIGH, LORD (1914).—*Phil. Mag.* **28**, 161.

ROSENTHAL, D. K. (1962).—*J. Fluid Mech.* **12**, 358.

THE STABILITY OF A ROTATING LIQUID MASS HELD TOGETHER BY SURFACE TENSION

By D. K. Ross*

[*Manuscript received July* 19, 1968]

Summary

The stability of a drop of incompressible fluid held together by the action of surface tension and made to rotate rigidly about an axis is determined, the effect of gravity being neglected. Two distinct problems are investigated. In the first is considered an isolated drop in the form of a surface of revolution and the manner in which its stability changes with angular speed is investigated. At zero angular speed, where the drop is spherical, infinitesimal disturbances are shown to be stable and beyond a certain critical angular speed a new linear series of equilibrium forms emerges, the original series becoming unstable.

In the second problem the drop is rotating together with a denser medium. It appears that the drop tends to become a cylindrical thread with increasing angular speed and that it is stable to infinitesimal disturbances at high and low angular speeds. This suggests that the drop is stable at intermediate angular speeds as well.

I. INTRODUCTION

In recent years the behaviour of rotating liquid masses has attracted much attention because of their application to a number of practical problems including (1) the electromagnetic levitation of liquid metals, as discussed by Polonis, Butters, and Parr (1954), Comenetz and Salatka (1958), and Laithwaite (1965), (2) the study of the equilibrium configurations of fission barriers for liquid drop nuclei (see Bohr and Wheeler 1939; Sperber 1963), and (3) the measurement of the dynamic coefficient of surface tension, as suggested by Rosenthal (1962*a*) and carried out by Princen, Zia, and Mason (1967). In each of these problems the surface tension of the liquid is known to be a contributing factor but the details of the phenomena have only been worked out in the last case.

One question that is still open is the stability of the equilibrium configurations. Chandrasekhar (1965*a*), who was concerned with the stability of an isolated rotating liquid drop held together by surface tension, was the first to relate this problem to the stability analysis of self-gravitating liquids. He used a new technique involving an extension of the method of the tensor virial that he had developed earlier (Chandrasekhar 1960, 1961). This method has since been extended in a series of papers by Rosenkilde (1967*a*, 1967*b*, 1967*c*, 1967*d*), but this approach does not predict the

---

* Department of Mathematics, University of Melbourne, Parkville, Vic. 3052.

existence of a point of bifurcation of the linear series of equilibrium forms. This fact is first mentioned in the preceding paper (pp. 823–35 of the present issue), where it is shown that a new series of equilibrium forms emerges when the angular speed increases from zero at a point where the angular speed is a maximum. With further increase in angular momentum the isolated drop tends to collapse onto its equator and the angular speed decreases until the drop finally breaks away from the axis of the rotation. Sperber (1963) suggested, incorrectly (at least, according to Chandrasekhar 1965*a*), that the point where collapse begins is the point at which the linear series of equilibrium forms becomes unstable. It is one of the purposes of the present paper to use some of the results of Basset (1888, 1892) and Lyttleton (1953) to show that the isolated drop is stable to certain types of small disturbance.

One of the major difficulties in this type of stability analysis is the fact that the equilibrium surfaces are so complicated that even infinitesimal perturbation theory is hard to apply. For isolated drops of rotating liquid held together by the action of surface tension Lord Rayleigh (1914) developed an approximate method for finding the equilibrium forms, while in the preceding paper it is shown that a solution in elliptic integrals is feasible; however, there a numerical method is used to describe the shape of the free surface. For a drop of liquid rotating with a denser medium and held together by surface tension the equilibrium forms have been obtained by Vonnegut (1942), Rosenthal (1962*a*), and in the preceding paper. Again, only the last paper shows that there is a point of bifurcation of the linear series of forms which emerges when the angular speed increases from zero. In fact, there is an angular speed at which the angular momentum of the liquid drop is a maximum. The existence of points of bifurcation for self-gravitating liquids has been known for some time (see Basset 1888, 1892; and the most recent papers of Chandrasekhar 1965*b*, 1966 for an up to date review of the subject).

As pointed out by Lyttleton (1953) the existence of a point of bifurcation does not, in itself, ensure that there is a loss of stability of the original series of equilibrium forms, as is so often assumed. Certainly what happens at such a point should be examined in detail. One possibility is that the free surface ceases to be a surface of revolution. This is precisely what happens to the self-gravitating liquid when the angular momentum is sufficiently high. In that case, Poincaré (1895) and Jeans (1919) showed that a "pear-shaped" series could emerge. On the other hand, Basset (1888) showed that the rotation also ceased to be a rigid one. This is a point that seems to have been overlooked in the literature.

Now according to Lyttleton (1953), Schwarzchild (1897) was the first to show that an equilibrium form may be unstable when the angular speed is constant, yet may be stable when the angular momentum remains constant. It is with this point in mind that the present paper examines the stability of rotating liquid drops held together by surface tension. Essentially the method employed here makes use of the potential and kinetic energies of the drops since, according to Orr (1906, 1907), Lyttleton (1953), and Pozharitiskii (1964), these quantities may be related to a discussion of the stability of rigid body rotations.

II. The Isolated Drop

It is well known that an isolated spherical drop held together by the action of the capillary force is stable to infinitesimal disturbances that depend exponentially upon time. Landau and Lifshitz (1959) expressed the most general small disturbance of this kind as a Fourier series in the azimuthal angle and so were able to define a perturbation from the equilibrium configuration in terms of the stream function

$$\Psi = \sum_{(m,n)} A_{m,n} r^n \mathrm{P}_n^m(\cos\theta) \exp\{\mathrm{i}(\sigma_{m,n} t + m\phi)\},$$

where (r, θ, ϕ) are the spherical polar coordinates, $\sigma_{m,n}$ is the complex frequency of the appropriate normal mode, $\mathrm{P}_n^m(\cos\theta)$ are the associated Legendre polynomials, and $A_{m,n}$ are the complex amplitude factors that are indeterminate in this linearized stability analysis. Landau and Lifshitz showed that such disturbances are stable and that in fact the frequency of the normal modes is given by

$$\sigma_{m,n}^2 = \alpha n(n-1)(n+2)/\rho_1 d^3, \tag{1}$$

where n is a positive integer. We see that to each value of n there correspond $2n+1$ different modes; for $n = 0$ the oscillations must be radial but, if the liquid is assumed to be incompressible, then their amplitudes must vanish; for $n = 1$ the motion is a translation of the liquid as a whole and so the smallest possible frequency of oscillation corresponds to $n = 2$ in which case

$$\sigma_{\min}^2 = 8\alpha/\rho_1 d^3.$$

This result is not unexpected because any disturbance of the surface must lead to an increase in the total surface area and hence to an increase in the potential energy. Now in any motion for which the sum of the kinetic and potential energies is constant, the potential energy cannot exceed the initial value of this sum and so any small disturbances must be stable. Of course this system may oscillate finitely, but in a real fluid this motion would be damped by the action of the viscous stresses.

When the liquid is made to rotate the situation is much more complicated as the surface is no longer spherical and it may happen that a small disturbance will lead to a reduction in the surface area and hence to an initial decrease in the potential energy U. Alternatively, the disturbance may extract energy from the source of the angular momentum and so be maintained.

Lyttleton (1953) showed that the positions of relative equilibrium, for a fluid rotating with constant angular speed ω, are obtained by finding stationary values of the total mechanical potential $U - \frac{1}{2}I\omega^2$, where I is the moment of inertia of the system about the axis of rotation. Thus, in order to obtain the equilibrium configurations we may proceed as follows.

Consider a drop of fluid of density ρ_1 which rotates, at constant angular speed ω, together with a fluid of density ρ_2. If we introduce the cylindrical polar coordinates (r, θ, z) with the z axis as the axis of rotation and assume that the interface is the surface of revolution $r = f(z)$, then the equilibrium configurations are given by finding the functions $f = f(z)$ for which

$$L = U - T, \tag{2}$$

with

$$U = 4\pi \int \alpha f(1+f'^2)^{\frac{1}{2}}\,\mathrm{d}z, \qquad \text{and} \qquad T = \tfrac{1}{2}\pi \int (\rho_1 - \rho_2)\omega^2 f^3\,\mathrm{d}z, \tag{2a}$$

is stationary but subject to the restriction that the volume

$$V = 2\pi \int f^2\,\mathrm{d}z$$

is known beforehand. Here α is the coefficient of surface tension appropriate to the two fluids, and the prime denotes differentiation with respect to z. This is an interesting result for we may now apply the Legendre test (see Fox 1950) to the integrands of equations (2a). We find that $\partial L/\partial f' < 0$ and hence that the quantity L is a minimum with respect to all neighbouring configurations rotating with the same angular speed ω and having the same volume $V = 4\pi d^3/3$, say.

Now the extremal problem can be solved by using a first integral of the Euler–Lagrange equation. Thus, for a drop of liquid that meets the axis of rotation it is shown in the preceding paper that the equation of the interface is given by

$$\pm(1+f'^2)^{-\frac{1}{2}} = (1-e)f/a + e(f/a)^3, \tag{3}$$

where

$$e = \omega^{*2}(a/d)^3, \qquad \text{with} \qquad \omega^{*2} = (\rho_1 - \rho_2)\omega^2 d^3/8\alpha, \tag{4}$$

and $2a$ is the width of the drop corresponding to the curve on the surface for which $f' = 0$. For $e \geqslant 0$ equations (3) and (4) correspond to the isolated drop of density ρ_1 (with $\rho_2 = 0$) but, for $-\frac{1}{2} < e \leqslant 0$, these equations describe the interface between the drop of density ρ_1 and the order medium of density ρ_2 ($\rho_2 > \rho_1$) with which it rigidly rotates.

Now Lyttleton (1953) proved that, when there are no external forces other than the couple maintaining the constant rotation, the energy of this system is

$$T_{\mathrm{R}} + U - \tfrac{1}{2}I\omega^2 = \text{constant},$$

where T_{R} is the kinetic energy of the liquid relative to the rotating axes. Thus, if the equilibrium configuration is such that $U - \frac{1}{2}I\omega^2$ is an absolute minimum and since $T_{\mathrm{R}} \geqslant 0$, it follows that $U - \frac{1}{2}I\omega^2$ cannot increase indefinitely and that it remains small if the initial disturbance is infinitesimal. In the absence of frictional forces, the drop must therefore oscillate in the neighbourhood of the equilibrium position, but if there is friction proportional to the relative velocities, as there must always be to some extent in a natural system, then these oscillations die away. Under these conditions the equilibrium configuration is secularly stable.

In order to discuss the stability of the isolated drop it is necessary to evaluate the change in the potential energy U and the moment of inertia I for a general deformation of the surface. Clearly this is difficult and moreover the rotation can then no longer be assumed to remain rigid; however, if we restrict the displacements to those for which the free surface is an equilibrium form corresponding to a neighbouring value of the parameter e then the two energy terms U and $\frac{1}{2}I\omega^2$ are given by the expressions we already have. Of course, this method can only be used to show instability, for a general displacement may be assumed to contain contributions from all possible types of deformation. At zero angular speed the drop is spherical and hence stable to infinitesimal disturbances. Now it was shown in the preceding paper that

$$\mathrm{d}(U-T)/\mathrm{d}e < 0 \qquad \text{for} \qquad 0 < \omega^* \leqslant \omega_{\max},$$

where

$$\omega_{\max} = 0\cdot 7540\{8\alpha/(\rho_1-\rho_2)d^3\}^{\frac{1}{2}},$$

and this suggests that the drop is stable at angular speeds less than $\omega_{\max}$ and that it becomes unstable for greater values for which a new equilibrium or linear series of forms emerges. At $\omega_{\max}$ there must therefore be a loss of stability of the original linear series. Of course, for $\omega < \omega_{\max}$, any displacement of the drop from the axis of rotation results in an interchange of denser fluid near the axis with less dense fluid away from the axis. This lowers the potential energy of the rotation and leads to instability. This kind of argument was also developed by Orr (1906, 1907) and Pozharitiskii (1964), who showed that, for a system with a finite number of degrees of freedom, there is a close relation between the energy of the disturbance and the frequencies of the normal modes into which it can be resolved.

III. A Drop at the Axis of a Rotating Body of Liquid

The shape of a drop of liquid that is less dense than its surroundings was investigated by Rosenthal (1962*a*). He was able to show that the liquid takes on a form that differs very little from an ellipse when the angular speed is such that the parameter e is small, and that it tends to become a cylindrical thread as $e \leqslant -\frac{1}{2}$. Actually, in this case, the spherical form is stable, as can easily be verified by using the method of Landau and Lifshitz described earlier. In fact the frequencies of the normal modes can be obtained from equation (1) by replacing n by $-n-1$ and ρ_1 by $-\rho_2$.

As a preliminary investigation into the stability of these rather complicated surfaces we can examine the growth or decay of disturbances on an infinitely long column of liquid that rotates as a rigid body together with its denser surroundings. Here we neglect the effect of the ends when the drop is sufficiently long since they are more likely to have a stabilizing rather than a destabilizing influence. To carry out this analysis we may divide infinitesimal disturbances into three kinds: (1) plane disturbances that are confined to cross sectional planes and are the same in all such parallel planes, (2) axisymmetrical disturbances for which the varicosity is of a given wavelength, and (3) axisymmetrical disturbances in the form of torsional oscillations. Investigations along such lines have been carried out by numerous authors. Thus, Hocking and Michael (1959) carried out an analysis on an inviscid column of liquid and found that it is stable to plane disturbances of wave number S if the coefficient of surface tension satisfies

$$\alpha \geqslant (\rho_1-\rho_2)\omega^2\bar{a}^3/S(S+1), \tag{5}$$

where $\bar{a}$ is the mean radius of the column, which differs from the undisturbed radius a by a term of the second order in the perturbation amplitudes. This fact was mentioned by Lord Rayleigh (1879). Thus, when we take into account the denser outer liquid it is clear that we have $(\rho_1-\rho_2) < 0$ so that condition (5) is satisfied for all wave numbers S. Therefore in the present problem we can infer that the column is stable to infinitesimal plane disturbances. This is not surprising for it is clear that any plane disturbance must increase the length of the boundary of the plane section of the column and hence produce an increase in the surface energy, and, moreover, the effect of rotation is stabilizing.

Hocking (1960) examined the influence of viscosity on the stability of the column and showed that, at high and low viscosities, it is stable to plane disturbances for which

$$\alpha \geqslant (\rho_1-\rho_2)\omega^2\bar{a}^3/(S^2-1). \tag{6}$$

This criterion differs from the inviscid case although it does not involve the viscosity explicitly. It follows from (5) and (6) that, when account is taken of a small but finite viscosity, a previously neutral disturbance can become unstable, i.e. viscosity induces a measure of instability. The curiosity lies in the fact that the inviscid liquid should be stable for all wave numbers satisfying (5) but not (6). Hocking explains this as due to the fact that the disturbed part of the pressure at the surface is exactly 180° out of phase with the increase in the radius of the column, so that it can provide the necessary inward force to balance the difference between the capillary and the centrifugal forces. This balance is upset once criterion (5) fails and then instabilities arise. Gillis (1961) used a computational method to obtain (6) at intermediate values of the viscosity, while Gillis and Suh (1962) came to the same conclusion although they included the effects of a rotating concentric solid core. In the present problem $\rho_1-\rho_2 < 0$ and so we can infer stability.

Hocking (1960) also considered the case of axisymmetric disturbances with varicosity of wave number k and found that, at zero or high viscosity, infinitesimal oscillations are stable whenever

$$\alpha \geqslant (\rho_1-\rho_2)\omega^2\bar{a}^3/(k^2\bar{a}^2-1).$$

Again, Gillis and Kaufman (1961) showed that this criterion is valid at all viscosities. If we now write the above inequality in the form

$$k^2\bar{a}^2-8e(\bar{a}/a)^3 \geqslant 1,$$

then this condition is satisfied for all wave numbers k when the thread of liquid is long because $e \to -\frac{1}{2}$; so the drop of liquid is stable to all disturbances of varicosity k if $e < -\frac{1}{8}$, provided that the ends do not have a destabilizing influence on the drop.

The work of Pekeris (1948) on laminar flow in a circular pipe suggests that axisymmetric infinitesimal disturbances can be of two types which are not coupled when there is no rotation or when the Reynolds number is sufficiently small. In the one case motion is in concentric circles in planes perpendicular to the axis of the column (torsional) and in the other the motion is in planes passing through the axis (meridional). For the case of flow in a pipe he shows that torsional oscillations are stable at all Reynolds numbers directly from the differential equation. The problem with which we are concerned is to determine the effect on the stability of having a fluid interface in place of a rigid boundary but with no mean flow. Hocking (1960) showed that, for an isolated column of liquid at zero viscosity, the torsional and meridional oscillations are proportional and hence that these two types of infinitesimal disturbances have exactly the same stability characteristics; while at high viscosities there can be no interaction between the disturbances to the rotation and the motion in the meridian planes. In this special case the torsional oscillations satisfy a Bessel-type differential equation for which it is easily shown that the eigenvalues are such that the disturbances do not make the column unstable. When the effect of an outer medium is considered there again exists a simple solution which implies stability to torsional oscillations when both media have high viscosities. This is proved by Rosenthal (1962*b*) but does not seem to occur in any earlier literature.

The above arguments suggest that infinitesimal disturbances of the rigid rotation of a column of less dense liquid are stable at all Reynolds numbers because of the stabilizing effect of the rigid rotation of the outer medium. These results are in agreement with those of Ponstein (1959) and Pedley (1967), who considered a similar problem and found that the column is unstable when the outer medium has the smaller density. In fact they were able to show that the most unstable modes are not necessarily axisymmetric, although for a nonrotating column it is known that only the axially symmetric disturbances can be unstable.

So far we have only considered the stability of two limiting forms. Thus, a drop of less dense liquid is stable when there is no rotation and when the angular speed is sufficiently large. This suggests that the drop is stable at all angular speeds since it is unlikely that there are two or more critical speeds at which there is an exchange of stability.

A discussion of the stability of intermediate configurations can be given in terms of the energy of the system. Let U_0 denote the potential energy that the drop would have if there were no rotation (that is, $U_0 = 4\pi\alpha d^2$) then the quantity $E = U - U_0 + \frac{1}{2}H^2/I$ measures the capacity of the drop to do work on itself. Thus, if the system is assumed to rotate freely with constant angular momentum then its capacity to do work on itself is least when E is a minimum and in this case the drop will be in stable equilibrium. Suppose that the interface is slightly disturbed so that E is increased. Then the system will tend to return to its relative equilibrium position and may oscillate although the action of frictional forces will be to dampen this motion. This criterion was obtained by Basset (1888, 1892) in relation to self-gravitating masses but it works equally well in this context. Again for a freely rotating system Lyttleton (1953) proved that

$$T_{\mathrm{R}} + U + \tfrac{1}{2}H^2/I = \text{constant}$$

and hence that any coordinate measured relative to the equilibrium position remains bounded by a small quantity related to the initial infinitesimal disturbance. He thereby arrived at the same criterion.

If we apply this result here then the above suggests that the drop may become secularly unstable where $d(U+T)/de = 0$, i.e. at the point of bifurcation where the angular momentum is a maximum. However, as Basset pointed out, a surface of bifurcation does not necessarily involve an exchange of stabilities. We conclude that this drop of liquid is always stable to infinitesimal disturbances.

IV. REFERENCES

BASSET, A. B. (1888).—"A Treatise of Hydrodynamics." Vol. 2, p. 95. (Cambridge Univ. Press.)

BASSET, A. B. (1892).—*Proc. Camb. phil. Soc.* **8**, 23.

BOHR, N., and WHEELER, J. A. (1939).—*Phys. Rev.* **56**, 426.

CHANDRASEKHAR, S. (1960).—*J. math. Analysis Applic.* **1**, 240.

CHANDRASEKHAR, S. (1961).—"Hydrodynamics and Hydromagnetic Stability." (Cambridge Univ. Press.)

CHANDRASEKHAR, S. (1965*a*).—*Proc. R. Soc.* A **286**, 1.

CHANDRASEKHAR, S. (1965*b*).—*Astrophys. J.* **142**, 890.

CHANDRASEKHAR, S. (1966).—*Astrophys. J.* **145**, 842.

COMENETZ, G., and SALATKA, J. W. (1958).—*J. electrochem. Soc.* **105**, 221.

FOX, C. (1950).—"An Introduction to the Calculus of Variations." (Oxford Univ. Press.)

GILLIS, J. (1961).—*Proc. Camb. phil. Soc.* **57**, 152.

GILLIS, J., and KAUFMAN, B. (1961).—*Q. appl. Math.* **19**, 301.

GILLIS, J., and SUH, K. S. (1962).—*Phys. Fluids* **5**, 1149.

HOCKING, L. M. (1960).—*Mathematika* **7**, 1.

HOCKING, L. M., and MICHAEL, D. H. (1959).—*Mathematika* **6**, 25.

JEANS, J. H. (1919).—"Problems of Cosmogony and Stellar Dynamics." (Oxford Univ. Press.)

LAITHWAITE, E. R. (1965).—*Proc. Instn elect. Engrs* **112**, 2361.

LANDAU, L. D., and LIFSHITZ, E. M. (1959).—"Fluid Mechanics." (Pergamon Press: Oxford.)

LYTTLETON, R. A. (1953).—"The Stability of Rotating Liquid Masses." (Cambridge Univ. Press.)

ORR, W. McF. (1906).—*Proc. R. Ir. Acad.* A **27**, 9.

ORR, W. McF. (1907).—*Proc. R. Ir. Acad.* A **27**, 69.

PEDLEY, T. J. (1967).—*J. Fluid Mech.* **30**, 127.

PEKERIS, C. L. (1948).—*Proc. natn. Acad. Sci. U.S.A.* **34**, 285.

POINCARÉ, H. (1895).—*In* "Capillarité". (Ed. G. Carré.) (Gauthier–Villars: Paris.)

POLONIS, D. H., BUTTERS, R. G., and PARR, J. G. (1954).—*Research Lond.* **7**, 272.

PONSTEIN, J. (1959).—*Appl. scient. Res.* **8**, 425.

POZHARITISKII, G. K. (1964).—*J. appl. Math. Mech.* **28**, 67.

PRINCEN, H. M., ZIA, I. Y. Z., and MASON, S. C. (1967).—*J. Colloid Interface Sci.* **23**, 99.

RAYLEIGH, LORD (1879).—*Proc. R. Soc.* A **29**, 71.

RAYLEIGH, LORD (1914).—*Phil. Mag.* **28**, 161.

ROSENKILDE, C. E. (1967*a*).—*J. math. Phys.* **8**, 84.

ROSENKILDE, C. E. (1967*b*).—*J. math. Phys.* **8**, 88.

ROSENKILDE, C. E. (1967*c*).—*J. math. Phys.* **8**, 98.

ROSENKILDE, C. E. (1967*d*).—*Astrophys. J.* **148**, 825.

ROSENTHAL, D. K. (1962*a*).—*J. Fluid Mech.* **12**, 358.

ROSENTHAL, D. K. (1962*b*).—M.A. Thesis, University of Melbourne.

SCHWARZCHILD, N. (1897).—*Ann. Munchener Sternwante* **3**, 233.

SPERBER, D. (1963).—*Phys. Rev.* **130**, 468.

VONNEGUT, B. (1942).—*Rev. scient. Instrum.* **13**, 6.

ON THE RELATIONSHIP BETWEEN RECENT MEASUREMENTS OF COSMIC RAY ELECTRONS, NONTHERMAL RADIO EMISSION FROM THE GALAXY, AND THE SOLAR MODULATION OF COSMIC RAYS*

By W. R. Webber†

[*Manuscript received April* 30, 1968]

Summary

Utilizing recent measurements of the cosmic ray electron spectrum at the Earth and the effects of solar modulation on this spectrum, possible limits on the local interstellar electron spectrum have been determined. Synchrotron emission from these interstellar electrons is then compared with the local (disk) volume emissivity of nonthermal radio emission as deduced from a study of radio intensity profiles along the galactic equator. The detailed spectrum and magnitude of radio emissivity can be reproduced from the electron spectrum only for very stringent conditions on the magnitude of the local interstellar magnetic field, and the amount of solar modulation of cosmic rays. Specifically it is found that $B_\perp \approx 7\ \mu\mathrm{G}$, and the residual modulation parameter $K_\mathrm{R} \approx 0\cdot75$ GV. If solar modulation effects on the cosmic ray electron component are negligible then an implausibly high local field of $\approx 20\ \mu\mathrm{G}$ is required.

If the local interstellar electron spectrum that best reproduces the spectrum of local radio emissivity is compared with the electrons expected as secondaries from cosmic ray collisions in the Galaxy, it is found that most electrons $\lesssim 300$ MeV may originate via the secondary mechanism rather than be directly accelerated as are the the higher energy electrons.

Adaption of this local interstellar electron spectrum which is quite different from that at the Earth also greatly modifies the interpretation of the effects of interstellar absorption by ionized hydrogen on the low frequency end of the radio spectrum. Emission measures of $< 0\cdot5$, 20, and $10^3\ \mathrm{cm}^{-6}$ pc are found in the polar, anticentre, and galactic centre directions respectively. These values are substantially below earlier estimates and would seem to rule out the existence of a large HII region about the Sun, for example.

Finally it is noted that the interstellar intensity of cosmic ray nuclei above 30 MeV deduced using a residual modulation constant of $0\cdot75$ GV is inadequate by two orders of magnitude to produce the required heating of interstellar HII clouds. If this heating is produced by cosmic rays it must be caused by a low energy component with a very steep spectrum. It is argued that such a component might arise from cosmic ray emission from solar-type stars in the Galaxy.

---

* Research supported by NASA Grant NSG-281-62, January 1968.

† On leave to the Department of Physics, University of Adelaide, G.P.O. Box 498D, Adelaide, S.A. 5001, from present address: School of Physics and Astronomy, University of Minnesota, Minneapolis, Minnesota 55455.

Aust. J. Phys., 1968, **21**, 845–70

INTRODUCTION

In this paper we propose to re-examine the familiar comparison between data on primary cosmic ray electrons and nonthermal radio emission from the Galaxy. This study is made in the light of recent measurements of the extraterrestrial electron intensity near the Earth in the energy range 15–200 MeV (Jokipii, L'Heureux, and Meyer 1967; Webber 1968), which indicate a much lower intensity than previously assumed. In addition, the first measurements of solar modulation effects on the electron component have recently been carried out (Webber 1967*a*; L'Heureux *et al.* 1968). These measurements enable useful limits on the electron spectrum in the local region of interstellar space to be deduced from the spectrum observed near the Earth.

The significance of this extrapolation lies in the fact that the interstellar electron spectrum can then be related via the synchrotron process to the nonthermal radio emissivity of nearby space. In this approach the present study differs importantly from most earlier attempts, which have compared the measured electron spectrum at Earth (usually without any consideration of solar modulation effects) with the radio emission that is assumed to emanate from the galactic halo, inferring a characteristic halo magnetic field in the process. It is clear that a comparison with the local radio emissivity is much more relevant and this comparison is greatly facilitated by significant new measurements of the features of nonthermal radio emission from the Galaxy. In order to determine the local radio emissivity it is necessary to utilize both high and low resolution radio measurements to determine the relative importance of emission from the galactic disk, the halo, and from outside the Galaxy. Satellite and ground-based observations have now defined the polar radio spectrum in the 1–10 MHz range, and measurements of the Hobart group have defined the disk component for all but the lowest frequencies. At higher frequencies the work of the Cambridge group has been completely revised and extended.

The comparison between the primary electron spectrum and the nonthermal radio spectrum has important consequences with regard to the solar modulation of cosmic rays. It is generally accepted that even at the time of minimum solar activity there remains an appreciable residual solar modulation for the nucleonic components of the cosmic radiation. Even though there is much more accurate information on the solar modulation of nuclei than for electrons it is not possible at the present time to determine the magnitude of the residual modulation from these studies. As a result, differences of a factor of 1000 exist in the extrapolated intensities of cosmic ray nuclei (compare Durgaprasad, Fichtel, and Guss 1967 and Balasubrahmanyan *et al.* 1968).

On the other hand, the comparison between the primary electron spectrum and the nonthermal radio spectrum provides important constraints on the magnitude of the electron modulation. This, in turn, may be used to set limits on the modulation of nuclei. A comparison of the modulation experienced by electrons and by nuclei will allow one to distinguish between contributions due to rigidity- and velocity-dependent modulation and hence lead to definitive conclusions regarding the mechanism and magnitude of the solar modulation.

We now summarize the approach to be used in this paper.

(1) The electron spectrum measured at the Earth in 1966 is presented. This spectrum is now quite accurately known between about 5 MeV and 6 GeV energy.

(2) The effects of solar modulation on this spectrum are discussed. Although major uncertainties still exist in our knowledge of the magnitude and energy dependence of this modulation, sufficiently accurate limits on the interstellar electron spectrum can be set to enable a useful comparison with the nonthermal radio emission.

(3) The demodulated (interstellar) electron spectrum is then related to:
(*a*) The calculations of "secondary" electrons produced by cosmic ray nuclei moving in the Galaxy. An attempt will be made to separate the so-called "primary" and "secondary" components of electrons as a function of energy.
(*b*) The observations of nonthermal radio emission as deduced for the local region of the disk. Crucial to this comparison is the strength of the local galactic magnetic field. Certain limits as to the strength of this field are obtained.

PRIMARY ELECTRON SPECTRUM

The measurements on the primary electron spectrum appropriate to 1966 are summarized in Figure 1. Our measurements (Beedle and Webber 1968) and those of L'Heureux (1967) are seen to be in excellent agreement for the energy range 200–6 GeV, over which range the electron spectrum can be represented by

$$\frac{\mathrm{d}j}{\mathrm{d}E}=\frac{(10\pm2)\times10^2}{E^{1\cdot55\pm0\cdot1}}\qquad\left(\frac{\text{electrons}}{\mathrm{m^2\,sr\,sec\,MeV}}\right).$$

Similarly our work and that of Cline, Ludwig, and McDonald (1964) in the energy range < 20 MeV are consistent. In this energy range there is considerably more uncertainty regarding the spectrum, however. A spectrum embracing all measurements can be represented by

$$\frac{\mathrm{d}j}{\mathrm{d}E}=\frac{(5\pm2)\times10^2}{E^{1\cdot8\pm0\cdot2}}\qquad\left(\frac{\text{electrons}}{\mathrm{m^2\,sr\,sec\,MeV}}\right).$$

The derivation of the spectrum in the 20–200 MeV range has been discussed in two recent publications (Jokipii, L'Heureux, and Meyer 1967; Webber 1968). It is in this energy range that a significant kink in the electron spectrum occurs. This kink is apparent in both measurements. It plays a crucial role in the subsequent comparison of the electron spectrum with the nonthermal radio emission.

At least three measurements of the electron spectrum above 10 GeV presently exist (Daniel and Stephens 1967; Bleeker *et al*. 1968; Danjo *et al*. 1968). We regard the integral measurement of Daniel and Stephens above 16 GeV as the most reliable—since the energy is defined accurately by the well-known geomagnetic cutoff. Assuming a differential spectrum $j(E) = K_e/E^{2\cdot4}$ above 16 GeV allows us to plot the Daniel and Stephens point, as shown in Figure 1(*b*). The measurement of L'Heureux (1967) does not give an integral flux above the highest differential energy interval; however, Beedle and Webber (1968) obtain a flux of $4 \cdot 5 \pm 0 \cdot 5$ electrons $m^{-2}\,sr^{-1}\,sec^{-1}$ above 6 GeV. Comparing this integral value with the integral value obtained by Daniel and Stephens at the equator allows us to obtain the differential flux in the 6–16 GeV interval, as shown in Figure 1(*b*). It is evident that a simple extension of the spectrum measured below 6 GeV will not fit the data at higher energies. The dashed line in Figure 1(*b*) is the best estimate of the spectrum between about 6 and 25 GeV. Thus it appears that there is a change of slope in the primary electron spectrum at ~ 6 GeV, and, between 6 and 25 GeV,

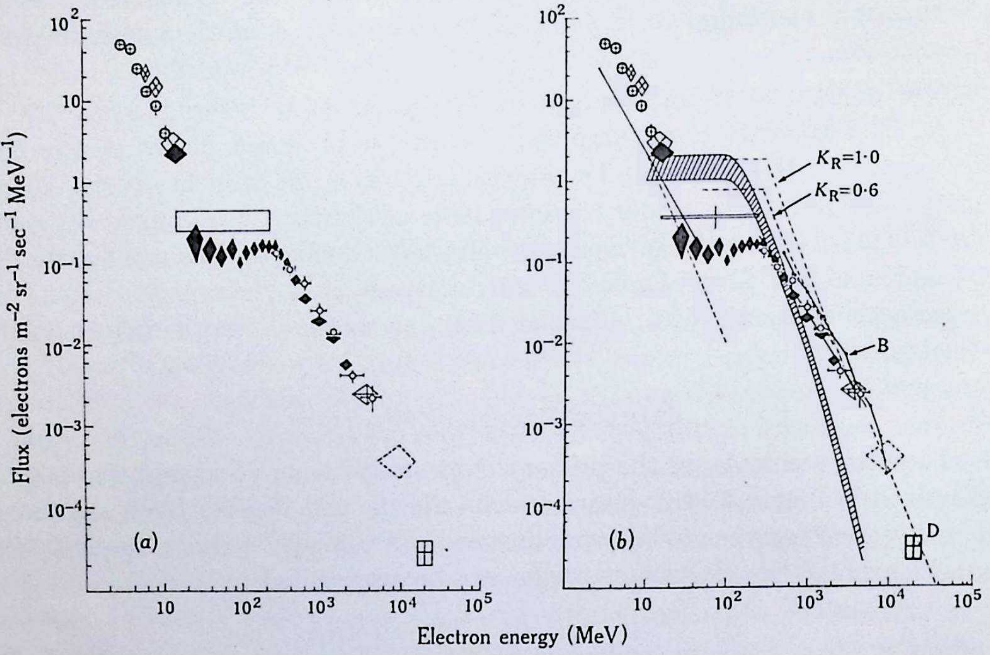

Fig. 1.—Extraterrestrial electron spectrum in 1966:

⊗, Cline, Ludwig, and McDonald (1964);
◆, ◇, Beedle and Webber (1968) and Webber (1968);
□, Jokipii, L'Heureux, and Meyer (1967);
○, L'Heureux (1967).

In (*b*) additional measurements of Bleeker *et al.* (1968) are shown as the (smoothed) beaded line (B), and Daniel and Stephens (1967) as the rectangle (D). The expected flux of secondary electrons arising from nuclear interactions of cosmic ray nuclei in the Galaxy is shown as the shaded area for passage of these nuclei through limits of 3 and 6 g cm^{-2} of hydrogen. The interstellar electron spectra obtained using solar demodulation constants of 0·6 and 1·0 GV are shown by the dashed lines.

$$\frac{dj}{dE} = \frac{1 \cdot 6 \times 10^5}{E^{2 \cdot 4}} \qquad \left(\frac{\text{electrons}}{\text{m}^2\,\text{sr}\,\text{sec}\,\text{MeV}}\right).$$

The occurrence of such a break, arising as a result of the degradation of the high energy part of the electron spectrum through the interaction with the cosmic 3° black-body radiation has been the subject of much discussion since the original observations of Daniel and Stephens (1967). It is not the purpose here to add further speculation to this question. As will be seen later the radio evidence for such a break is at least partially obscured by radio emission from this 3° radiation itself above 1000 MHz. A best estimate of the high energy part of the electron spectrum is presented so that the effects of solar modulation on the spectrum at low energies may be more fully appreciated.

Solar Modulation of Electrons and Interstellar Electron Spectrum

In order to gain some insight into the problem of the solar modulation of electrons let us briefly summarize the current situation with regard to the modulation of cosmic ray protons. For these particles the generally recognized form for the modulation may be written (Nagashima, Duggal, and Pomerantz 1966)

$$n(r_0)/n(\infty) = \exp(-K_R/D),$$

where $n(r_0)$ and $n(\infty)$ are the densities of cosmic rays at the Earth and in interstellar space (outside the region of solar modulation) respectively. The quantity D is the diffusion coefficient describing the motion of the particles in the solar magnetic fields that permeate interplanetary space; K_R is a quantity related most directly to the bulk outward velocity of the solar plasma (the solar wind) and to the extent of the region of modulation about the Sun. D is dependent on the rigidity and species of particle in question but K_R is independent of these parameters. D can, and has been, accurately evaluated over a wide range of rigidities by studying the rigidity dependence of the proton and helium variations. The experimental results and theoretical predictions are in reasonable accord on most points (Webber 1967*b*). It has not yet been possible to evaluate the absolute value of K_R experimentally (and therefore the total modulation existing between the Earth and interstellar space); although various limits can be set on the basis of theoretical models (e.g. Quenby 1967). Generally the values of K_R obtained in this way are $\sim 0 \cdot 5$ GV. It is also possible to estimate K_R by making certain assumptions regarding the similarity of the demodulated (interstellar) proton and helium spectra. Values of K_R obtained in this way have ranged from $< 0 \cdot 5$ to as large as $2 \cdot 5$ GV (Balasubrahmanyan *et al.* 1968).

Consider particles with an "effective rigidity" of $0 \cdot 2$ GV $\equiv D$ (200 MeV electrons, 22 MeV protons). Then if we accept residual modulation parameters K_R as large as 2 GV, the intensity of particles of this particular rigidity in interstellar space is e^{10} or 2×10^4 times that at Earth. It is evident that uncertainties in the value taken for K_R lead to even greater uncertainties in the interstellar cosmic ray flux. Recently Gloeckler and Jokipii (1967) summarized all evidence and introduced arguments of their own to suggest that the best value for K_R is $0 \cdot 9$ GV, with it extremely unlikely that K_R is greater than $1 \cdot 2$ GV.

To actually perform the corresponding demodulation of the electron spectrum we require a knowledge of the rigidity dependence of the electron modulation itself, i.e. the effective diffusion coefficient for electrons. Two rather sharply divergent measurements of the electron modulation presently exist. Our measurements (Webber 1967*a*) covering the rigidity range $0 \cdot 3$–2 GV, give an electron modulation that is of the same order as that for protons at the same rigidity. Below $0 \cdot 3$ GV we have suggested that the effective electron modulation is independent of energy, in keeping with a changeover to a purely velocity-dependent modulation, which has been observed for protons of these rigidities (Ormes and Webber 1968). L'Heureux *et al.* (1968) found no evidence for solar modulation effects on the electron component and as a result set an upper limit of $\sim 0 \cdot 2$ for the ratio of the electron–proton modulation at the same rigidity in the range 0·3–1 GV.

In Figure 1(*b*) we show the extrapolated interstellar electron intensities using our measurements of the solar modulation effects and values of $K_{\mathrm{R}} = 0 \cdot 6$ and 1·0 GV. If the modulation measurements of L'Heureux *et al.* (1968) are used then the interstellar electron intensity is virtually the same as that measured near the Earth in 1966, even for residual modulation parameters as large as 1 GV.

As a result, there exist two rather clear-cut limits on the possible interstellar electron spectrum, depending on which modulation is assumed for the electrons.

COMPARISON OF ELECTRON SPECTRA WITH CALCULATIONS OF "SECONDARY" ELECTRONS PRODUCED IN THE GALAXY

Two possible mechanisms have been proposed for the source of the energetic electrons that are observed near the Earth: (1) collisions of cosmic ray nuclei with interstellar material and the subsequent production of π mesons and decay muons and electrons, and (2) direct acceleration, presumably, although not necessarily, in the source regions that also accelerate the cosmic ray nuclei. The intensity of electrons from the first mechanism, known as secondary electrons, can and has been calculated using data on the cross sections and multiplicities for π-meson production and independent estimates of the amount of interstellar material that the cosmic ray nuclei have traversed. An analysis of this problem using contemporary estimates of the relevant quantities has been carried out by Ramaty and Lingenfelter (1966). Their estimates of this secondary electron spectrum for the limits that the energetic cosmic ray nuclei have passed through 3 and 6 $\mathrm{g\,cm^{-2}}$ of material are shown in Figure 1(*b*). A comparison of these calculations with the electron spectrum measured at Earth and that estimated to exist in interstellar space is illuminating. Firstly we observe that the commonly referenced situation wherein the observed electron intensity is much greater than the predicted secondary flux, thus suggesting another source for these particles, is certainly evident above 1 GeV. However, below 500 MeV the measured intensity of electrons at Earth is actually less than the secondary source. Between 30 and 150 MeV this deficiency is a factor of five.

If the calculated secondary intensities are now compared with those deduced for interstellar space we find that the two are comparable at energies < 200 MeV, if the electron modulation measured by Webber (1967*a*) is used.

If the electron modulation measurements of L'Heureux *et al.* (1968) are taken then the interstellar electron flux in the 30–200 MeV is inadequate by a factor of at least three to account for the expected secondary electron intensity. It would be necessary to assume that energetic (> 1 GeV nucleon^{-1}) cosmic ray protons have travelled through $\sim 1\ \mathrm{g\,cm^{-2}}$ of interstellar material in order that the calculated secondary intensity agree with the extrapolated interstellar electron intensity. The best value for energetic (> 1 GeV nucleon^{-1}) heavier cosmic ray nuclei, obtained using measurements of the abundance of lithium, beryllium, and boron nuclei, is

$4 \cdot 5 \pm 1$ g cm^{-2} (Shapiro and Silberberg 1968). We believe that it is reasonable to assume that the amount of material traversed by protons and heavier nuclei is the same and that a substantial amount of solar modulation is affecting the low energy electrons observed at the Earth.

We will see that a comparison of the low energy interstellar electron intensity and the local low frequency radio emission also suggests that substantial modulation of the low energy electrons must be occurring.

Relation between Electron Spectrum and Nonthermal Radio Spectrum

The synchrotron mechanism is generally considered to be responsible for most of the nonthermal radiation from our Galaxy. Several authors (Schwinger 1949; Oort and Walraven 1956) have discussed the theory of synchrotron radiation and have presented the necessary formulae. They are presented here only insofar as they are relevant to the present analysis.

A relativistic electron gyrating in a magnetic field generates synchrotron radiation at a rate

$$P_{\mathrm{tot}} = 6 \times 10^{-28} E^2 B_{\perp}^2 \qquad \mathrm{erg\,sec^{-1}},$$

where E is in million electron-volts and $B_{\perp}$, the perpendicular component of the magnetic field, is in microgauss. The spectral distribution of this radiation is characterized by a frequency

$$\nu_{\mathrm{c}}\,(\mathrm{MHz}) = 1 \cdot 6 \times 10^{-5} \{E\,(\mathrm{MeV})\}^2 B_{\perp}\,(\mu\mathrm{G})\,.$$

The actual spectral distribution of power emitted by a single electron is given by

$$\mathrm{d}P/\mathrm{d}\nu = 2 \cdot 3 \times 10^{-29} F(\alpha)\, B_{\perp} \qquad \mathrm{erg\,sec^{-1}\,MHz^{-1}},$$

with $\alpha = \nu/\nu_{\mathrm{c}}$. $F(\alpha)$ has been tabulated (Westfold 1959) and is found to have a maximum at $\alpha_{\mathrm{m}} \sim 0 \cdot 5$ decreasing as $(\nu/\nu_{\mathrm{c}})^{\frac{1}{3}}$ for $(\nu/\nu_{\mathrm{c}}) \ll 1$, and exponentially for $\nu/\nu_{\mathrm{c}} \gg 1$. In actual fact the frequency at which maximum power is emitted ν_{m} is about $\frac{1}{2}\nu_{\mathrm{c}}$.

Suppose now there exists a differential spectrum of electrons given by

$$j(E)\,\mathrm{d}E = K_{\mathrm{e}}/E^m\,,$$

then the volume emissivity of synchrotron emission per unit frequency interval is given by

$$\epsilon(\nu) = \frac{\mathrm{d}P_\nu}{\mathrm{d}\nu\,\mathrm{d}\tau} = \int \mathrm{d}\Omega \int_E^\infty \frac{\mathrm{d}P}{\mathrm{d}\nu}\, n(E)\,\mathrm{d}E\,,$$

where $n(E)\,\mathrm{d}E$ is the density of electrons in the energy interval E to $E + \mathrm{d}E$. The intensity of synchrotron emission along a particular line of sight is

$$I(\nu) = \int_0^R \epsilon(\nu)\,\mathrm{d}r\,,$$

where the extent of the radiating region is given by R.

Usually to obtain $I(\nu)$ a number of assumptions are made: (1) the electron distribution is isotropic and $n(E)$ is constant over the region of integration; (2) the magnetic field is disordered or chaotic. It is also frequently assumed that all the emission takes place at the characteristic frequency ν_c. In this instance the spectral form of the emission takes the particularly simple form

$$I(\nu) \sim \nu^{\gamma},$$

where γ is related to the electron spectral exponent by $\gamma = \frac{1}{2}(1-m)$ (for $\nu > \nu_c$). The intensity of emission at a particular frequency is related to the magnetic field strength $B_\perp$ through the electron spectrum by

$$I(\nu) \sim B_\perp^{\frac{1}{2}(m+1)}.$$

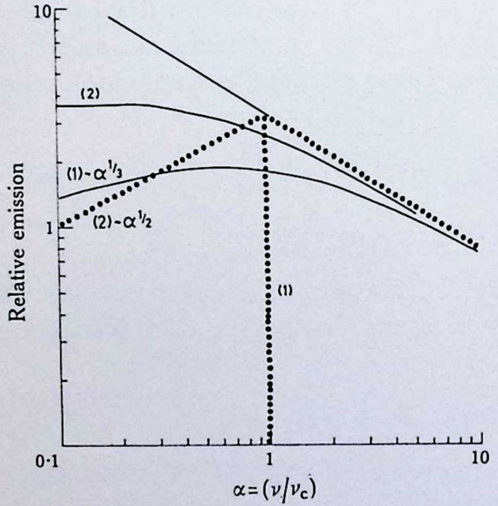

Fig. 2.—Radio synchrotron spectra as a function of $\alpha = (\nu/\nu_c)$ obtained for an electron spectrum given by $j(E)\,\mathrm{d}E = K_e/E^{2\cdot 2}$ for $E > E_1 \equiv \nu_{c1}$ and (1) $j(E)\,\mathrm{d}E = 0$, $E < E_1$; (2) $j(E)\,\mathrm{d}E =$ constant, $E < E_1$. The δ-function approximation is shown by the dotted lines.

This so-called δ-function approximation is particularly useful for relating an electron spectrum of constant spectral index to the spectrum of radio emission. If the electron spectral index is changing with energy or has a discontinuity then the δ-function approximation is inadequate, particularly for obtaining the low frequency part of the radio emission spectrum.

Consider the following examples. The electron spectrum is given by $j(E)\,\mathrm{d}E = K_e/E^{2\cdot 2}$ above some energy E_1 corresponding to the characteristic frequency ν_{c1}. Below this energy the electron spectrum is given by (1) $j(E)\,\mathrm{d}E = 0$; and (2) $j(E)\,\mathrm{d}E =$ constant. Figure 2 shows the relative radio emission as a function of frequency calculated for these electron spectra using the δ-function approximation and also by actually carrying out the required integration using the explicit values for the function $F(\alpha)$ as tabulated by Westfold (1959). The large difference in the two calculations at low frequencies is due mainly to the long low frequency tail on the function $F(\alpha)$. Even for an electron spectrum that becomes zero below some energy E_1 the synchrotron emission spectrum falls off no faster than $(\nu/\nu_c)^{\frac{1}{3}}$ at low frequencies. For a differential electron spectrum that becomes constant, the synchrotron spectrum becomes almost flat at low frequencies and shows a gradual flattening at $\sim 2\nu_c$ even though the change in the electron spectrum is abrupt (c.f. discussion of Turtle 1963).

In a plot such as Figure 2, the shape of the emission spectrum from different regions should be similar as long as we assume that the electron *spectrum* in these regions is also similar; however, this curve will be displaced along the $\log \nu$ axis by a constant amount depending on the ratio of the field strengths in the two regions (and also on any change in the absolute intensity of the electrons themselves).

Considerations regarding the actual distribution of field strength and direction along a line of sight and deviations of the electron distribution from isotropy may modify the above arguments slightly. We do not believe that the added complication introduced by considering these effects is justified at the present stage of analysis.

NONTHERMAL RADIO EMISSION PROFILES

The objective in this section is to derive the local interstellar volume emissivity of radio emission characterizing a region $\sim 0 \cdot 5$ kpc in diameter centred on the Sun. This emissivity will then be related to the interstellar electron spectrum. This approach differs from most of the previous approaches (e.g. Felton 1966) wherein the electron measurements near the Earth are related directly to radio emission from the galactic halo.

For the derivation of the local interstellar radio emission it shall be convenient to consider two regions of the radiofrequency spectrum.

(1) Frequencies $\gtrsim 30$ MHz where interstellar absorption by free electrons (HII regions) is not important.

(2) Frequencies < 30 MHz and extending down to ~ 1 MHz where interstellar absorption effects are becoming progressively more important, particularly in the direction of the galactic centre.

Eventually at the lowest frequencies the optical depth is ~ 1 at distances of less than 1 kpc in some directions and indeed we are seeing only the synchrotron emission from "local" electrons.

In both frequency ranges the radio emission as a function of frequency will be derived in four directions: the galactic centre, the anticentre, the north polar region, and the direction of minimum radio brightness (R.A. ~ 10 hr, Dec. $\sim 40°$). Then by a process of subtraction we shall derive the local radio emissivity spectrum.

In the case of the spectra in the directions of the galactic centre and anticentre it is necessary to use surveys with sufficiently narrow beamwidths (e.g. $\sim 1°$) to resolve the galactic disk. In some instances for measurements in the anticentre direction, we have utilized surveys of medium resolution ($\sim 10°$) at frequencies > 10 MHz to substantiate the narrow beam data when it is felt that they contribute a higher level of absolute accuracy (principally the recent measurements of the Cambridge group). For the present purposes the anticentre is defined as the region $b^{\mathrm{II}} = \pm 2°$, $l^{\mathrm{II}} = 175°$–$185°$; and the centre as $b^{\mathrm{II}} = \pm 2°$, $l^{\mathrm{II}} = 350°$–$10°$ (omitting the strong source Sgr A located at the origin of the new galactic coordinate system). The narrow and medium resolution surveys are synthesized to the anticentre region using the narrow beam survey of Blythe (1957) at 38 MHz.

In the cases of the spectra in the north polar region and the direction of minimum radio brightness both medium resolution and low resolution ($\sim 30°$)

studies have been used. It should be pointed out that the brightness in these directions does depend to some extent on the resolution of the instrument involved. Since at frequencies above 10 MHz the brightness is lowest in the polar direction, the better the resolution the lower the brightness (this can be clearly seen in the work of Bridle 1967). We have attempted to adjust all measurements in these two directions to a common aperture of $\sim 15°$ by $15°$ using the higher resolution measurements of Bridle (1967).

In no instance has the published brightness been modified by more than 30% by these adjustments; however, we believe that truer representations of the actual spectra are obtained.

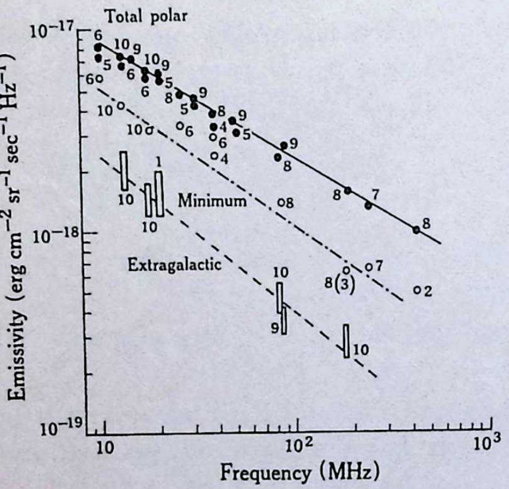

Fig. 3.—Radio brightness spectra in the direction of the north galactic pole and the direction of minimum brightness. The extragalactic component deduced by a number of observers is also shown:

1, Shain, Komesaroff, and Higgins (1961)
2, Pauliny-Toth and Shakeshaft (1962)
3, Turtle and Baldwin (1962)
4, Kenderdine (1963)
5, Parthasarathy and Lerfeld (1965)
6, Andrew (1966)
7, Large, Quigley, and Haslam (1966)
8, Purton (1966)
9, Yates and Wielebinski (1966)
10, Bridle (1967)

The spectra above 10 MHz for the polar direction and the direction of the minimum brightness are shown in Figure 3. (The spectra below 10 MHz for the polar region are presented in Figure 9.) The numbers beside each point indicate the authors responsible for the measurement. Measurements of the total polar emission lean heavily on the most recent work of the Cambridge group (e.g. Andrew 1966; Purton 1966; Bridle 1967), which has updated and extended the earlier work of Turtle *et al.* (1962), Turtle and Baldwin (1962), Turtle (1963), and others. It should be pointed out that the emissivity in the southern polar region, as illustrated by the measurements of Yates and Wielebinski (1966), is identical to within 20% with that in the northern polar region. The solid line in Figure 3 represents a simple spectrum of the form

$$I(\nu) = 3\cdot4\times10^{-16}\nu^{-0\cdot60} \qquad \mathrm{erg\,cm^{-2}\,sr^{-1}\,sec^{-1}\,MHz^{-1}}.$$

There is some evidence that the spectrum is becoming flatter at the lower frequencies although it is difficult to see how a spectral exponent much greater than $0\cdot7$ can be taken at frequencies > 50 MHz. It should be noted that Anand, Daniel, and Stephens (1968), using much the same data, have drawn a smoothly varying curve through the data. Their curve, which gives a spectral exponent $\sim 0\cdot4$ at the lowest frequencies, is certainly an alternative fit to our data points. Individual authors have also tried to fit their own data points and arrived at essentially the same conclusion. For example, Andrew (1966), Purton (1966), and Bridle (1967) all found that an exponent $\sim 0 \cdot 4$ was most suitable in the range 10–100 MHz, whereas above this frequency they supported an exponent $\sim 0 \cdot 9$. Yates and Wielebinski (1966) found an exponent $\sim 0 \cdot 5$ at 85 MHz slowly decreasing to $0 \cdot 3$ at the low frequency end of their range. Above 85 MHz they favoured an exponent $\sim 0 \cdot 6$.

The emission in the direction of minimum brightness is about 50% of that in the polar region. The spectrum in this direction is not as well defined but appears to be very similar to that in the polar direction.

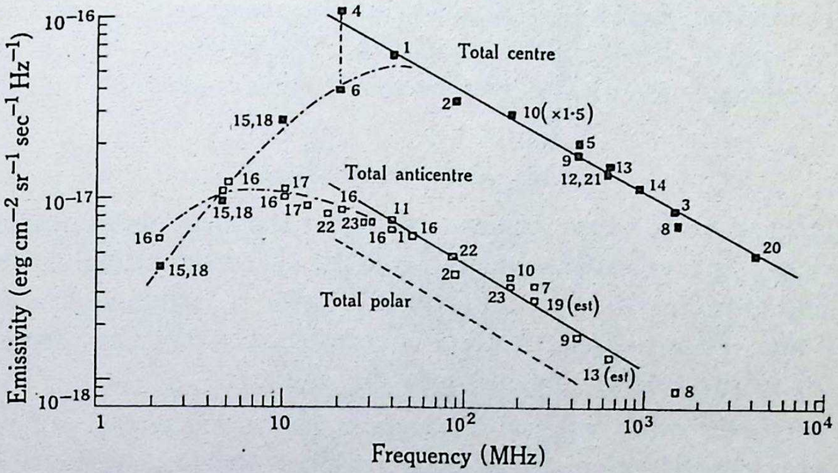

Fig. 4.—Radio brightness spectra in the direction of the galactic centre and anticentre (as defined in the text). The total polar spectrum is shown as a reference: 1, Blythe (1957); 2, Hill, Slee, and Mills (1958); 3, Westerhout (1958); 4, Komesaroff (1961); 5, Large, Mathewson, and Haslam (1961); 6, Shain, Komesaroff, and Higgins (1961); 7, Davies and Hazard (1962); 8, Mathewson, Healey, and Rome (1962); 9, Pauliny-Toth and Shakeshaft (1962); 10, Turtle and Baldwin (1962); 11, Kenderdine (1963); 12, Turtle (1963); 13, Moran (1964); 14, Davies (1965); 15, Ellis (1965); 16, Parthasarathy and Lerfeld (1965); 17, Andrew (1966); 18, Ellis and Hamilton (1966); 19, Large, Quigley, and Haslam (1966); 20, Penzias and Wilson (1966); 21, Purton (1966); 22, Bridle (1967); 23, Parthasarathy (1967).

From observations of the variation of brightness and spectral index across the sky, a number of observers have attempted to determine the percentage of the radio emission that could be extragalactic. It is assumed that this extragalactic emission is isotropic and has a different (steeper) spectral index than that coming from the various regions of the Galaxy. The estimates of this extragalactic component are shown in Figure 3. They seem to define a spectrum of slope $\sim 0 \cdot 8$ and of magnitude $\sim 30\%$ of the total polar emission at ~ 10 MHz. If indeed the extragalactic component has such a steep spectrum and extends to lower frequencies then it may dominate the flattening total polar spectrum at frequencies of 1–2 MHz. This interesting possibility has been discussed in some detail by Smith (1965).

The situation in the galactic centre and anticentre directions is shown in Figure 4. At frequencies below ~ 38 MHz there is a lack of high resolution data for the anticentre region. For this reason we have used medium and low resolution measurements, synthesizing the emissivities found in these lower resolution studies to the standard anticentre direction using the high resolution measurements of Blythe

(1957) at 38 MHz. These adjustments amount to multiplying the given low resolution radio intensities by factors of from 1·1 to 1·3.

The dramatic decrease in the spectra below 20 MHz in the centre and anticentre directions due to absorption by ionized hydrogen is clearly evident. Above about 30 MHz, however, both spectra follow very closely the solid lines that are drawn for spectral indices of $-0\cdot6$. The magnitude of the anticentre emission is about twice that in the polar direction whereas the emission in the direction of the galactic centre is about 10 times that in the anticentre direction. The characteristics of the spectrum above 10 MHz in the anticentre region are in fact not noticeably different to the spectrum in the polar direction, a point that is in agreement with the conclusions of Andrew (1966), Purton (1966), and Bridle (1967). The index of $-0\cdot6$ in the direction of the galactic centre is identical with that found by Komesaroff (1961).

LOCAL DISK EMISSIVITY

To derive from these measurements a value for the local disk emissivity we must first consider a simple geometrical model for the galactic disk and halo. This would be a spherical halo of radius 15 kpc, and a flat disk also of radius 15 kpc and of semi-thickness 0·4 kpc. In this model the Sun is at a distance of 10 kpc from the centre, approximately on the galactic equator (see Fig. 6(*a*)).

If the emissivity were uniform throughout the disk the ratio of intensities in the centre–anticentre direction would be 5 : 1. The observed ratio of about 10 : 1 indicates that the average emissivity must increase as one moves towards the centre of the Galaxy. To examine this behaviour more closely we have utilized the results of six surveys of nonthermal radio emission with sufficiently narrow beamwidths to resolve the galactic disk. For $b^{\mathrm{II}} = 0$ (galactic equator) the longitudinal variation of the nonthermal component of radio emission is plotted in Figure 5. The data are normalized in the anticentre direction using a $\nu^{-0\cdot6}$ dependence for the emission.

The galactic profile is very similar from each of these studies and shows an increasing wealth of detail with increasing resolution (related to spiral arm structure etc). The intensity profile to be expected if the emissivity is uniform throughout the disk is shown as curve A. The fact that the observed intensity profiles follow this curve for all directions except within 50° of the galactic centre indicates that the emissivity must be almost independent of radius at distances $\gtrsim 10$ kpc from the galactic centre. This leads us to consider a very simple form for emissivity as a function of distance out to 8 kpc from the galactic centre,

$$\epsilon(r) = \epsilon_{\mathrm{S}}(5\cdot8-0\cdot6r)\,,$$

where r is the distance (kpc) and ϵ_{S} is the emissivity near the Sun. Beyond 8 kpc the emissivity remains constant out to the boundary of the disk at 15 kpc. The corresponding galactic disk intensity profile is given by curve B in Figure 5. Approximately as good a fit to the observed profile would be obtained if

$$\epsilon(r) = \epsilon_{\mathrm{S}}(-1\cdot6r/r_{\mathrm{S}})$$

(c.f., for example, Okuda and Tanaka 1968), the biggest difference being in the continued decrease in emissivity beyond 10 kpc, which is not evident in the galactic disk intensity profiles.

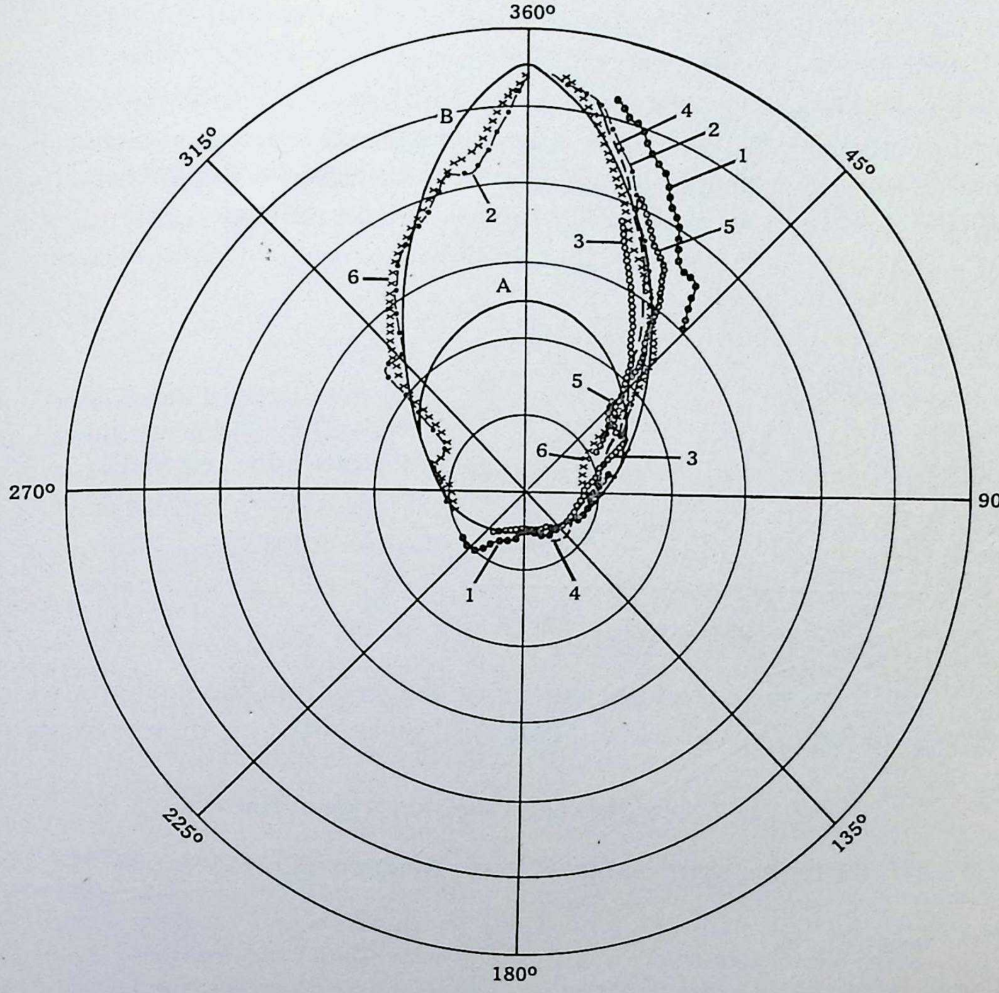

Fig. 5.—Polar diagram of radio emission measured along the galactic plane with high resolution surveys. Data at six frequencies are shown (normalized in the anticentre direction): 1, 38 MHz (Blythe 1957); 2, 85 MHz (Hill, Slee, and Mills 1958); 3, 178 MHz (Turtle and Baldwin 1962); 4, 404 MHz (Pauliny-Toth and Shakeshaft 1962); 5, 610 MHz (Moran 1964); 6, 1440 MHz (Mathewson, Healey, and Rome 1962). Curve A represents the polar diagram to be expected if the radio emission is uniform throughout the disk. Curve B is obtained for the radial profile of emissivity given in Figure 6(*b*).

To obtain the emissivity per unit volume in the disk near the Sun it is only necessary to divide the intensity of radio emission in the anticentre direction by $(4\pi) \times 5$ kpc, the assumed distance over which this emission is coming. This procedure neglects the extragalactic component, which is $\sim 10\%$ of the total emission in the anticentre direction. It also neglects the fact that the emission is probably not uniformly distributed over the 5 kpc distance to the boundary but is concentrated in the spiral arms. Since the Sun is located in an arm (at the edge of the Orion arm), a consideration of this nonuniformity would tend to enhance the values for the local emissivity.

If one were to take the exponential decrease of emissivity illustrated in Figure 6, the local emissivity would need to be $\sim 1\cdot 4$ times greater.

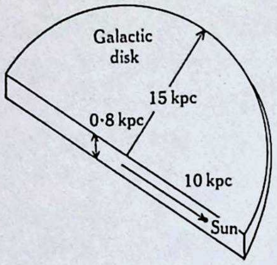

Fig. 6(*a*).—Schematic representation of galactic disk and halo.

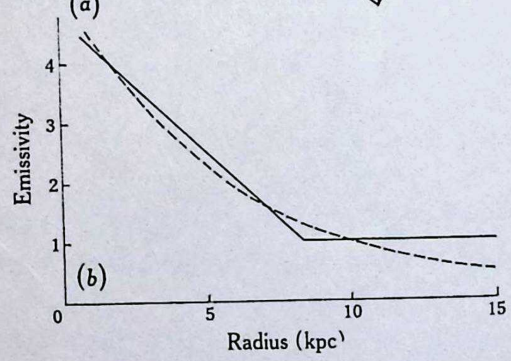

Fig. 6(*b*).—Radial dependence of emissivity (arbitrary units) in galactic disk required to produce profile B in Figure 5.

In Figure 7 we show the local emissivity deduced from the model in which the emissivity is uniform beyond 8 kpc. This local emissivity can be represented by a form

$$\epsilon(\nu) = 5\times 10^{-38}\,\nu^{-0\cdot 6} \qquad \mathrm{erg\,cm^{-3}\,sec^{-1}\,Hz^{-1}}$$

above 20 MHz, flattening appreciably at lower frequencies.

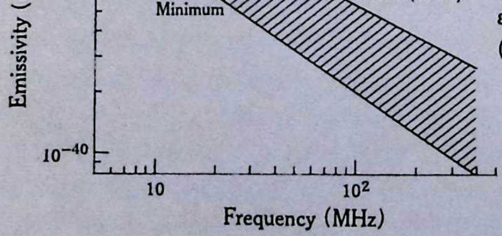

Fig. 7.—Local spectrum of radio emissivity from the galactic disk. The maximum and minimum allowable emissivity for a uniform halo are also shown, as is the halo emissivity at 81 MHz deduced by Felton (1966).

Before comparing this directly with the electron spectrum, let us attempt, using the above spectrum for the local emissivity, to derive a characteristic emissivity spectrum for the halo. Now as one looks out in the polar direction and the direction of minimum nonthermal radio emission, contributions will occur from radio emission in the disk and the halo as well as the extragalactic component. The spectrum from the extragalactic component has already been derived, and using the above local emissivity and assuming a disk semithickness of 400 pc (Baldwin 1966) we can estimate that part of the emission spectrum from the disk. This turns out to be ≈ 20% of the total polar emission, or comparable to the extragalactic component.

If the remaining emission is to be ascribed to a spherical halo, then calling this remainder in the polar direction the maximum halo, and in the direction of minimum radio emission the minimum halo, we have the halo emissivities per unit volume given in Figure 7. (Note that the recent estimate of halo emissivity at 81 MHz by Felton (1966) lies almost on top of our maximum halo spectrum.)

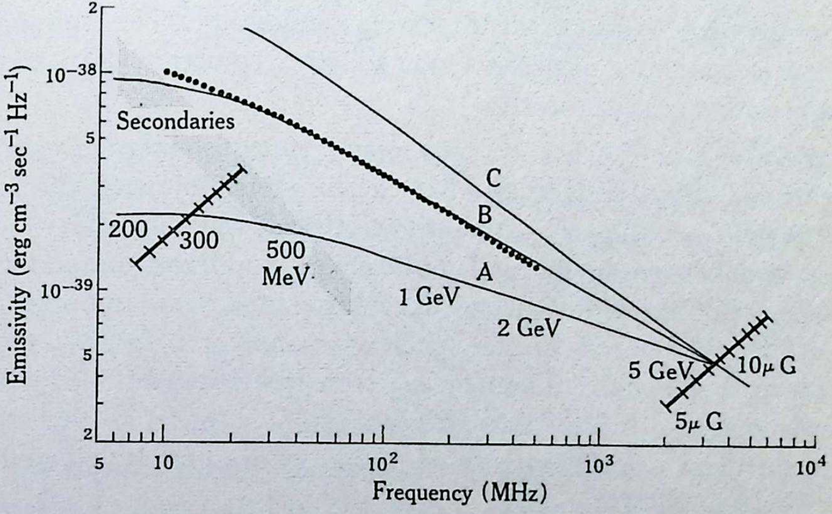

Fig. 8.—Comparison of local disk emissivity (●) with the emissivity to be expected from secondary electrons and (A) electron spectrum measured at Earth in 1966, (B) interstellar electron spectrum obtained with a residual modulation parameter of 0·6 GV, and (C) interstellar electron spectrum with a residual modulation parameter of 1·0 GV. The manner in which the curves A, B, and C must be displaced for different galactic disk magnetic field strengths is shown, as are the equivalent electron energies.

The characteristic halo emissivity is an order of magnitude less than the local disk emissivity and if one takes the minimum halo emissivity then the halo is a very weak radio emitter indeed and it becomes reasonable to ask whether there is a halo at all. Of course more sophisticated models of the halo and disk distributions can be taken (e.g. Mills 1959) but it seems that the central problem concerns the magnitude and uniformity of the disk component. If there is considerable structure to the disk, in the form of loops and spurs in addition to a more regular component of semithickness ~400 pc then the minimum halo emissivity that we have derived is probably the most realistic one.

Turning now to a comparison of the previously derived spectrum of local emissivity with that to be anticipated from the interstellar electron spectrum, the situation is summarized in Figure 8. The manner in which this emissivity spectrum varies with the magnetic field strength is given in nomogram fashion in the figure. The emissivities deduced from the electron spectra are illustrated for an interstellar magnetic field $B_\perp = 8\ \mu$G. This magnetic field strength provides an excellent fit for the interstellar electron spectrum obtained with a residual modulation parameter of 0·6 GV. Even the low frequency flattening of the radio spectrum is reproduced as a result of the flattening of the electron spectrum below 300 MeV.

If the emissivity from the interstellar electron spectrum, derived using a residual modulation parameter of 1·0 GV, is compared with that deduced from the radio measurements, a weaker magnetic field ($\sim 5\ \mu$G) is required to produce an approximate agreement. In this instance, however, the emissivity obtained from the electron spectrum has a notably steeper spectrum than that deduced from the radio measurements.

If, in turn, the interstellar electron spectrum is essentially that measured at the Earth in 1966, then the local interstellar magnetic field must be at least 18 μG to even approximately reproduce the deduced radio emissivity. The emissivity obtained from this electron spectrum also has a much flatter spectrum than any reasonable limitation on the measured emissivity.

An interstellar field of this magnitude seems much too large in view of all of the other observational evidence (Davies 1965). This difficulty with the magnitude of the interstellar field is enhanced when we recall that the emissivity deduced from the radio measurements probably tends to be slightly underestimated for the reasons discussed earlier. We therefore believe that this comparison supports the idea of a large modulation for electrons in the solar environment. Indeed, the agreement between emissivities when an interstellar electron spectrum obtained with a residual modulation parameter of 0·6 GV is used gives strong support to the argument that the energy dependence of the solar modulation is reasonably given by the form measured by Webber (1967*a*).

A further observation concerns the comparison of the emissivity to be expected from the spectrum of secondary electrons only and the emissivity deduced from the radio measurements. The limits on the emissivity from the secondary spectra calculated by Ramaty and Lingenfelter (1966) for passage of cosmic ray nuclei through 3 and 6 g cm^{-2} of material are shown in Figure 8. If the radio emission from these secondary electrons were to exceed the measured emission, this would be suggestive that one of the arguments relating to the comparison was incorrect (e.g. the interstellar magnetic field $> 8\ \mu$G, or the path length for cosmic ray nuclei < 3 g cm^{-2}).

However, the situation is such that the radio emission from secondary electrons alone does not exceed the measured emission, although it is becoming an increasingly greater fraction of it as one goes to lower frequencies.

RADIO SPECTRUM BELOW 10 MHz AND INTERSTELLAR ELECTRON SPECTRUM AT LOW ENERGIES

The interpretation of the galactic radio spectrum below 10 MHz is treated separately from the high frequency part of the spectrum for two reasons. Firstly, the uncertainties in the measured radio emission are much larger at these frequencies, particularly in the polar direction. Secondly, the effects of absorption by ionized hydrogen in the disk of the Galaxy become important at these frequencies and tend to influence the interpretation of the results.

The experimental situation below 10 MHz in the centre, anticentre, and polar directions is summarized in Figure 9. The intensity versus frequency profiles for the centre and anticentre directions are taken from Figure 4. The data below 10 MHz in these directions are almost entirely due to Ellis and co-workers at Hobart.

The situation in the polar directions is unfortunately not decisive from the point of view of trying to determine a radio spectrum. The obvious differences in the measurements do not seem to be clearly related to whether the measurements are made from the ground, where ionospheric absorption could play an important role, or from satellites, where calibration difficulties are encountered. For example, the polar intensities measured from the ground by Ellis (1965) and Parthasarathy (1967) differ by a factor of more than two at 5 and 10 MHz and have quite a different slope at the lower frequencies. There is some evidence from satellite observations (Hartz 1964) that emission from the south polar regions is greater than from the north polar region at low frequencies. This might account for some of the difference between the two ground-based observations, although it should be recalled that no difference between south polar and north polar radio intensities is noticed above 10 MHz. The reader is referred to a more thorough discussion of the possible north–south differences by Andrew (1966).

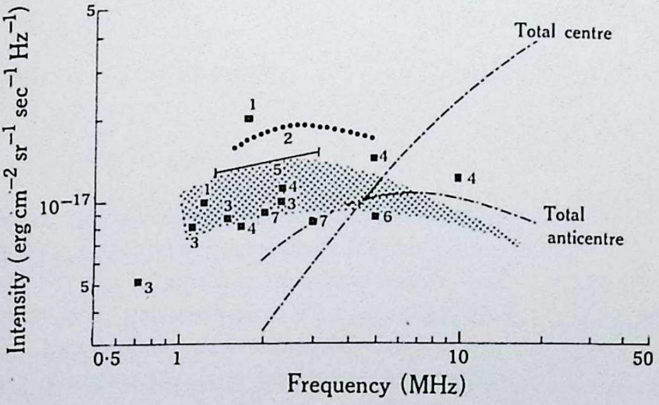

Fig. 9.—Measurements of radio brightness below 10 MHz in the direction of the galactic pole. The total brightness in the centre and anticentre directions is also shown.
1, Walsh, Haddock, and Schulte (1963)
2, Hartz (1964)
3, Benediktov *et al.* (1965)
4, Ellis (1965)
5, Hugill and Smith (1965)
6, Parthasarathy and Lerfeld (1965)
7, Parthasarathy (1967)

The situation regarding the agreement between the individual satellite measurements below 5 MHz is equally uncertain. It is not the present purpose to attempt to resolve these differences but mainly to try and determine an applicable spectrum of radio emission in the polar direction. To be realistic such a spectrum must encompass the shaded region in Figure 9, and is well determined above 10 MHz by the data already presented in Figure 3.

The polar spectrum that we shall adapt is a smooth curve drawn through the centre of the shaded region in Figure 9. This polar spectrum is shown again in Figure 10 along with the spectra in the directions of the galactic centre and anticentre. It should be pointed out that the uncertainty in the polar spectrum is reflected in the subsequent comparison of the spectra as presented in Figure 10.

It is obvious nevertheless that the spectra in the centre and anticentre directions are turning over at low frequencies as a result of absorption in interstellar ionized hydrogen. The same effect may also be occurring in the spectrum in the polar direction but it is much less evident. In fact, as has been emphasized earlier, this flattening could be directly related to the flattening of the low energy electron spectrum.

It is convenient at this point to introduce the concept of a "projected" radio intensity or brightness. This intensity is defined as that to be expected in a particular direction in the absence of absorption by ionized hydrogen. As a result it is directly related to true local emissivity in that direction. Two possibilities for the spectrum of projected intensity (emissivity) will be considered.

(1) For the first model (I) we shall utilize the fact that the spectra in both the centre and anticentre directions are $\sim \nu^{-0\cdot 6}$ at higher frequencies where absorption effects are negligible and write for the projected intensity

$$\mathscr{I}(\nu) = (\nu/\nu_0)^{-0\cdot 6}\, I(\nu_0),$$

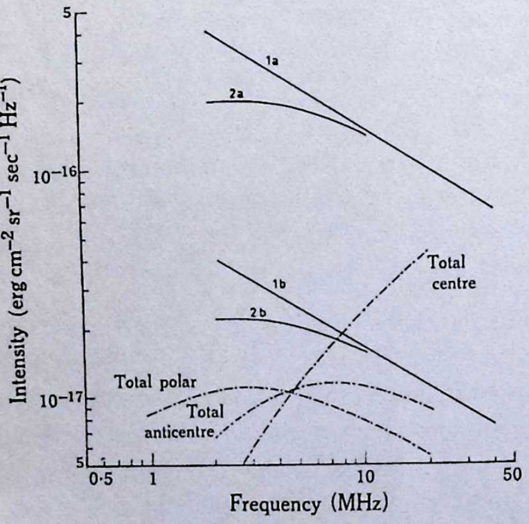

Fig. 10.—Comparison of radio brightness at low frequencies in the polar, anticentre, and centre directions. Curves 1a and 1b represent the projected brightness in the centre and anticentre directions under the circumstances of no absorption by ionized hydrogen and a volume emissivity $\epsilon(\nu) \sim \nu^{-0\cdot 6}$. Curves 2a and 2b are the same except that the volume emissivities are taken to have the same spectrum as the total polar brightness.

where ν_0 is a frequency where absorption effects are negligible. Projected intensity spectra according to this relation are shown in Figure 10, in the centre and anticentre directions. Komesaroff (1961) has introduced a similar concept to examine the effects of absorption in the direction of the galactic centre, and has used an identical spectral index for the projected intensity.

(2) For the second model (II) we shall assume that above 2 MHz absorption effects in the polar direction are in fact negligible and let the measured spectrum above this frequency be the projected intensity spectrum as well. In other words, we shall make an important departure from earlier work and allow the intrinsic emissivity spectrum itself to flatten at low frequencies. The justification for this is, of course, the indication that the electron spectrum may also flatten at low energies. The corresponding projected spectra in the centre and anticentre directions are shown as curves 2a and 2b in Figure 10.

Let us now consider in some detail the effects of absorption by ionized hydrogen. The coefficient of interstellar absorption by the free–free process in the radio region is (Ginzburg 1961)

$$K_\nu = \frac{1\cdot 38 \times 10^{-14}}{T_{\mathrm{e}}^{3/2}}\left(\frac{N_{\mathrm{e}}^2}{\nu^2}\right) g\,,$$

where ν is in megahertz, N_{e} is the electron density in CGS units, and g is a quantity given by

$$g = \{17\cdot 7 + \ln(T^{3/2}/\nu)\}\,.$$

For frequencies ≈ 1 MHz and effective temperatures between 10^3 and 10^4 °K, g is ≈ 18. The electron temperature associated with the ionized hydrogen is usually taken to be 10^4 °K, so that

$$K_\nu = 2\cdot 5 \times 10^{-19}(N_{\mathrm{e}}^2/\nu^2)\,.$$

The optical depth is

$$\tau = \int K_\nu \,\mathrm{d}r\,.$$

For the usual case where K_ν is taken not to vary with distance and integrating over a distance of 1 pc (with L in pc),

$$\tau = K_\nu r = 0\cdot 75(N_{\mathrm{e}}^2/\nu^2)L\,.$$

Defining a quantity called the emission measure $E = N_{\mathrm{e}}^2 L$,

$$\tau = 0\cdot 75\, E/\nu^2 \qquad \mathrm{cm}^{-6}\,\mathrm{pc}\,.$$

For examining the effects of absorption we may consider two simplified galactic models. In the first instance it is assumed that all of the HII lies between the observer and the nonthermal region. In this case

$$I(\nu) = \mathscr{I}(\nu)\exp(-0\cdot 75\, E/\nu^2)\,.$$

Figure 11 shows the ratios of $I(\nu)/\mathscr{I}(\nu)$ in the centre and anticentre directions deduced from the measured values of $I(\nu)$ and for the two assumptions regarding the spectrum of the projected emission $\mathscr{I}(\nu)$. The values for $I(\nu)/\mathscr{I}(\nu)$ expected on the basis of model I are also shown in the figure, normalized at values of $\tau = 1$. Model I gives a very poor fit to the data, predicting a much more rapid cutoff of $I(\nu)$ than is actually observed.

Model I may be more reasonably applied to the data in the polar direction if it is assumed that most of the emission in this direction comes from beyond the disk. The crucial question is: what is the spectrum $\mathscr{I}(\nu)$ in this direction? If it is taken to be a simple extension of the spectrum $I(\nu) \sim \nu^{-0\cdot 6}$ measured at higher energies, τ is comparatively large, being $\sim 1\cdot 5$ at 1 MHz (e.g. Hoyle and Ellis 1963). The corresponding emission measure is then ~ 2 cm^{-6} pc.* The implications of this emission measure in the polar directions have been discussed by Ellis and Hamilton (1966), who attribute it to absorption in interstellar HII, and by Lencheck (1964) and Alexander and Stone (1965), who have attributed this absorption to the solar HII region.

---

* From a detailed study of low frequency brightness profiles Ellis and Hamilton (1966) have derived an emission measure of 8 cm^{-6} pc, for $b^{\mathrm{II}} = 60°$.

The observed turnover of the total polar spectrum at low frequencies is totally unlike that to be expected on the basis of model I. In fact, down to ~ 2 MHz it follows exactly the form to be expected if the spectrum of electrons producing the emission is itself turning over. Only below ~ 2 MHz may the suggested fall-off of the total polar spectrum begin to indicate the effects of HII absorption between the emission and the source. If one assumes that this flattened spectrum does in fact resemble $\mathscr{I}(\nu)$, as we have earlier, then τ cannot be greater than about $0 \cdot 3$ at 1 MHz. The corresponding emission measure is $\sim 0 \cdot 4$ cm^{-6} pc, which is an order of magnitude less than previously assumed.

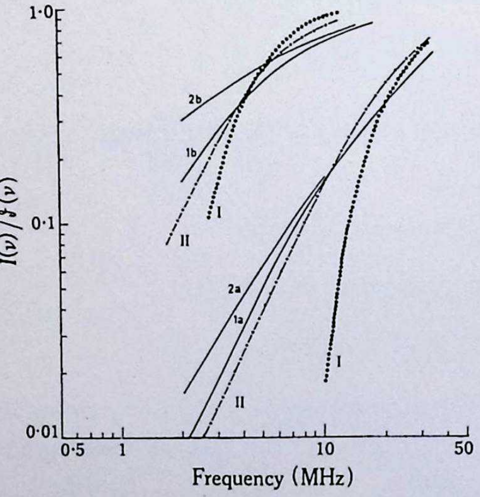

Fig. 11.—Ratio of measured brightness $I(\nu)$ to projected brightness $\mathscr{I}(\nu)$ as a function of frequency. The curves 1a, 1b, 2a, and 2b, have the same meaning as in Figure 10. The curves are also given for the ratios to be expected if models I and II for absorption and emission apply.

In model II we shall consider that nonthermal emission and absorption by interstellar HII occur continuously along the line of sight and that the ratio of these two quantities and the quantities themselves are constant. This more closely approximates conditions in the galactic disk, although it is still a very simplified picture. We know from our earlier discussion that $\epsilon(\nu)$ is certainly a function of distance at least within 10 kpc of the galactic centre. Further, it might be expected that regions of high absorption would be related to the regions of high emission (e.g. Fig. 2 of Smith 1965), although a strict constancy of the ratio of these quantities should not be expected. At any rate under the simplified assumptions of model II we have

$$I(\nu) = \mathscr{I}(\nu)\{\tau_\nu{}^{-1}(1-\mathrm{e}^{-\tau_\nu})\}.$$

Note that for $\tau_\nu \equiv K_\nu L \gg 1$, $I(\nu)/\mathscr{I}(\nu) \approx \nu^2$.

The calculated ratios $I(\nu)/\mathscr{I}(\nu)$ for $\tau = 600$ at 1 MHz in the direction of the galactic centre and $\tau = 40$ at 1 MHz in the direction of the anticentre are shown in Figure 11. These curves provide a much better fit to the data although there is evidence that the real $I(\nu)$ is decreasing somewhat less rapidly with frequency than expected on the basis of model II.

The calculated ratios correspond to emission measures 800 and 53 cm^{-6} pc respectively.* If the analysis in these two directions is to be consistent the ratio of emission measures should be approximately 10 : 1 (corresponding to the fact that the total path length L is five times longer in the direction of the galactic centre and the average emissivity in this direction is a factor of two larger, i.e. more simply the ratio I_ν (centre)/I_ν (anticentre) at high frequencies). The ratio of ~ 15 obtained above is indeed reasonable within the accuracy of the $I(\nu)/\mathscr{I}(\nu)$ curves, particularly since a close inspection of Figure 11 reveals that the calculated curves may be adjusted to give the expected ratio of 10 and still provide a reasonable fit to the measured data. The important point to note here is that a radial dependence of $\epsilon(\nu)$, which surely exists, will not affect the *shape* of the separate $I(\nu)/\mathscr{I}(\nu)$ curves but will only enter into the ratio of the emission measures calculated in the centre and anticentre directions as long as the ratio $\epsilon(\nu)/K_\nu$ remains constant. The only way the shape of the $I(\nu)/\mathscr{I}(\nu)$ curves themselves can be varied is to assume that $\epsilon(\nu)/K_\nu$ varies with distance. A comparison of the $I(\nu)/\mathscr{I}(\nu)$ curves calculated on the basis of model II and those deduced from the measurements reveals that $\epsilon(\nu)/K_\nu$ must vary in such a way that $\epsilon(\nu)/K_\nu$ becomes larger near the Sun. That is to say radio emission from electrons is relatively more important than absorption effects from interstellar HII in the local environment, as compared with the average along a line of sight in either the centre or anticentre directions. Obviously by choosing the proper variation of the ratio of $\epsilon(\nu)/K_\nu$ it is possible to reproduce either curves 1 or 2 in Figure 11. As a result this comparison is unable to provide a separate indication as to the actual form of $\epsilon(\nu)$ at low frequencies. To do this we must compare $\epsilon(\nu)$ with the various possible interstellar electron spectra, as will be done in the following section.

This approach does emphasize, however, how importantly our conclusions regarding the typical electron densities in the HII regions depend on the assumed shape of the projected brightness spectrum at low frequencies. For example, the values of emission measure in the centre and anticentre directions indicate an average electron density $\sim 0{\cdot}10\ \mathrm{cm}^{-3}$ in interstellar space near the Sun. The emission measure of 2 cm^{-6} pc obtained earlier in the polar direction when taken with this electron density gives a disk semithickness of ≈ 200 pc, whereas if the smaller polar emission measure of $0{\cdot}5\ \mathrm{cm}^{-6}$ pc is taken the disk semithickness is effectively only 40 pc (the absorption is assumed to be interstellar rather than from a solar HII region). From the point of view of radio emission, the characteristic semithickness of the disk is usually taken to be ~ 300–400 pc. Conversely, taking this semithickness as the region in which absorption occurs gives electron densities of $0{\cdot}05$ and $0{\cdot}01\ \mathrm{cm}^{-3}$ respectively for the two values of emission measure. These two viewpoints can be interpreted in terms of a paucity of absorption relative to emission and may reflect the point we have deduced already from the $I(\nu)/\mathscr{I}(\nu)$ curves, namely that the Sun is in a region of relatively low radio absorption.

---

* Komesaroff (1961) has typically obtained values of $\tau \approx 10$ at 20 MHz corresponding to ~ 4000 at 1 MHz in the direction of the galactic centre, which is a factor of 10 larger than we obtain. However, our results represent an average over a band $\pm 2°$ on either side of the galactic equator. The value obtained by Komesaroff applies within $\pm 0{\cdot}5°$ of the equator and he finds a decrease of an order of magnitude in the optical depth only 3°–4° off the equator. The two results are in fact in reasonable accord as is the value of 165 cm^{-6} pc for $b^{\mathrm{II}} = 5°$ obtained by Ellis and Hamilton (1966).

Let us now see what a comparison of the interstellar electron spectrum with the low frequency radio emissivity tells us. The low frequency radio emissivity is obtained in exactly the same manner as before and using the same dependence of $\epsilon(\nu)$ on r as at higher frequencies, except that we now have the possibility of using two curves for the projected intensity $\mathscr{I}(\nu)$ which is used in calculating $\epsilon(\nu)$. These are the curves 1 and 2 in Figure 10. The corresponding low frequency emissivity profiles are shown in Figure 12, and are simply an extension of the profile presented in Figure 8. The expected emissivity for various interstellar electron spectra is also shown in Figure 12 again for a local magnetic field of 8 μG. The manner in which this emissivity scales with $B_\perp$, and the corresponding electron energies, are also shown in the figure. It is seen that the expected emissivity from the low energy electron spectrum measured near the Earth in 1966 is almost an order of magnitude less than actually deduced. In order to provide sufficient emissivity from such a low intensity of electrons the local magnetic field is required to exceed 20 μG. Since a field as large as this is highly unlikely, solar modulation effects must be depressing the low energy electron spectrum near the Earth. Emissivities based on interstellar electron spectra obtained using demodulation constants of 0·6 and 1·0 GV are in much better accord with the deduced emissivities. The best agreement is obtained for $K_{\mathrm{R}} = 0{\cdot}75$ GV and $B_\perp = 6\ \mu$G. If $K_{\mathrm{R}} = 0{\cdot}6$ GV then $B_\perp$ must be $\sim 9\ \mu$G, whereas if $K_{\mathrm{R}} = 1{\cdot}0$ GV then $B_\perp \sim 4\ \mu$G.

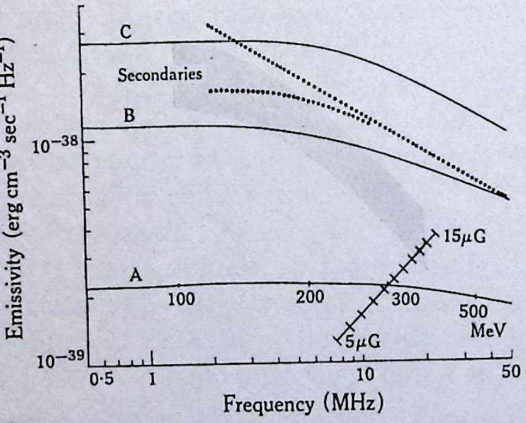

Fig. 12.—Comparison of local disk emissivity deduced at low frequencies (dotted curves) with the emissivity to be expected from:
A, electron spectrum measured at Earth in 1966,
B, interstellar electron spectrum obtained with a residual parameter of 0·6 GV, and
C, interstellar electron spectrum obtained with a residual parameter of 1·0 GV.
The manner in which the curves A, B, and C must be displaced for different galactic magnetic field strengths is also shown. The shaded area is the range of expected emission from secondary electrons.

The correspondence between the shapes of the emissivity spectra at low frequencies sets very severe restraints on the characteristics of the electron modulation at low energies. Using the energy dependence of the modulation given by Webber (1967*a*) the emission from the interstellar electron spectrum almost exactly reproduces the emission profile based on a projected intensity profile that flattens at low frequencies. This does not prove that such a profile is correct and the projected intensity profile based on an extension of the $\nu^{-0\cdot 6}$ spectrum measured at higher frequencies will also be suitable, provided we assume a different electron modulation at lower energies. The limits on the interstellar electron spectrum are rather clearly defined by the above comparison, however.

The question of the radio emission at these low frequencies from the secondary electrons is also relevant. As is evidenced in Figure 1(*b*) as well as Figure 13, if the calculations of the secondary electron intensity are correct, then most of the observed low energy electrons must be of secondary origin if the cosmic ray nuclei have passed through $\gtrsim 3\ \mathrm{g\,cm^{-2}}$ of matter. The deduced emissivity at low frequencies sets a very positive upper limit of $< 6\ \mathrm{g\,cm^{-2}}$ of material if *all* of the low energy electrons are secondaries.

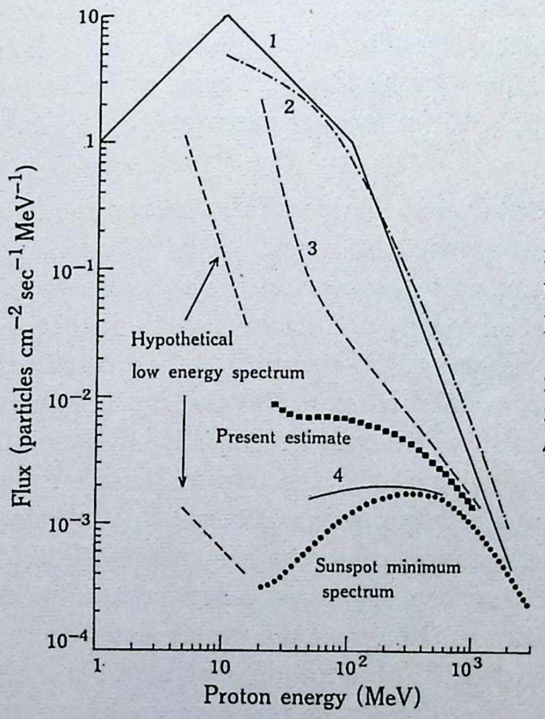

Fig. 13.—Interstellar cosmic ray proton spectrum obtained using a residual modulation parameter of 0·75 GV:
1, Hayakawa (1964)
2, Balasubrahmanyan *et al.* (1968)
3, Gloeckler and Jokipii (1967)
4, Durgaprasad, Fichtel, and Guss (1967)

Interstellar Proton Spectrum

Utilizing the residual modulation constant of 0·75 GV derived from the electron data we may attempt to determine the interstellar proton spectrum. As noted earlier, the rigidity dependence of the proton modulation has been more completely measured (above 50 MeV ≡ 0·3 GV rigidity) than for electrons; however, there is no *direct* method available to estimate the residual solar modulation of these particles from the data on protons alone—hence the huge differences in the estimates of the unmodulated (interstellar) proton spectrum. A summary of various estimates is given in Figure 13. Here the sunspot minimum spectrum is taken from the work of Gloeckler and Jokipii (1967). Curves 1, 2, 3, and 4 represent various estimates of the interstellar proton spectrum by Hayakawa (1964), Balasubrahmanyan *et al.* (1968), Gloeckler and Jokipii (1967), and Durgaprasad, Fichtel, and Guss (1967) respectively. Estimates 1 and 2 are based principally on the requirement that the rate of energy loss by ionization of these cosmic ray protons is sufficient to maintain the heating of interstellar HI clouds (see Balasubrahmanyan *et al.* for a discussion of this problem).

However, these spectra contain an energy density of cosmic rays ~ 5–$10\ \mathrm{eV\,cm^{-3}}$ as compared with an energy density $\sim 0{\cdot}5\ \mathrm{eV\,cm^{-3}}$ for the sunspot minimum spectrum near the Earth. This interstellar energy density is equivalent to that contained in a magnetic field $\sim 20\ \mu$G, and according to Parker (1966) an energy density $\gtrsim 2\ \mathrm{eV\,cm^{-3}}$ for cosmic rays leads to difficulties in holding together the combined magnetic-field–cosmic-ray system in the spiral arms by gravity.

The curve 3 is actually obtained using a residual modulation constant K_{R} of $0{\cdot}9$ GV and gives a more reasonable cosmic ray energy density $\sim 1\ \mathrm{eV\,cm^{-3}}$ in interstellar space. This spectrum is also sufficient to produce the required heating of interstellar HI clouds, according to Balasubrahmanyan *et al.* (1968).

Our estimate differs from that of Gloeckler and Jokipii (curve 3) in that (1) we have used a slightly smaller demodulation constant as suggested by the data on electrons, and (2) we have used a modulation $\sim 1/\beta$ at low energies as indicated by the work of Ormes and Webber (1968) instead of a steeper function more like $1/\beta P$ used by Gloeckler and Jokipii (1967).

Below 20 MeV no reliable measurements are available on the proton modulation and there are very few data on the proton spectrum itself. Fan, Gloeckler, and Simpson (1965) give some evidence that the proton spectrum near the Earth begins to turn up at energies < 20 MeV, as represented by the dashed curve in Figure 13. It is not clear whether these protons are of solar origin or are merely a continuation of the higher energy part of the spectrum reaching us from the Galaxy. Suppose we take the latter point of view and suppose also we assume that the $1/\beta$ dependence of the modulation measured by Ormes and Webber (1968) for protons at intermediate energies extends to lower energies. This latter assumption is supported by the previously discussed measurements of a $1/\beta$ dependence for the electron modulation at equivalent rigidities (Webber 1967*a*). The low energy interstellar proton spectrum obtained by the resulting solar demodulation is shown as the upper dashed curve in Figure 13. This spectrum supplies a comparable amount of heating to interstellar HI regions as do spectra 1, 2, and 3, albeit from lower energy protons losing energy by ionization at a greater rate.

The demodulation effectively transforms a proton spectrum $\sim 1/E$ near the Earth to an interstellar spectrum $\sim 1/E^3$, one that is very similar to that actually observed for solar cosmic rays near the Earth. It is therefore tempting to ask whether such a low energy component of interstellar cosmic rays could be produced by solar type stars in the Galaxy. The answer, based on order-of-magnitude estimates of the number of particles emitted and the energy spectra involved, is yes. Consider the Sun. Estimates of the number of particles emitted during solar cosmic ray events can be made on a number of grounds (e.g. Webber 1963) and lead to an average rate of emission $\sim 10^{30}$–10^{31} particles $\mathrm{sec^{-1}}$ above a few million electron-volts averaged over the last 10 years. Now it is not clear what fraction of these actually escape into interstellar space; however, we may suppose that it is comparable to the number emitted. If the value of 10^{11} main sequence stars similar to the Sun is taken for our Galaxy, we have a total emission of low energy cosmic rays of $\sim 10^{41}$–$10^{42}\ \mathrm{sec^{-1}}$ from such sources. The lifetime of these cosmic rays is short ($\sim 3\times10^{13}$ sec for $n_{\mathrm{H}} \sim 1\ \mathrm{cm^{-3}}$) as they rapidly lose energy by ionization loss. The total number in the

Galaxy at any one time is thus $\sim 3\times10^{54}$–3×10^{55} particles. Presumably these particles will not travel far from their source of origin, but will diffuse mainly in the disk of the Galaxy. The volume in which they reside is thus $\sim 10^{66}$–10^{67} cm^3, depending on how closely they are confined to the spiral arms themselves. The density ρ that could be supplied by solar-type stars thus works out to be $\sim 3\times10^{-11}$–3×10^{-13} particles cm^{-3}. The density required by the spectrum in Figure 13 is $\sim 3\times10^{-11}$ particles cm^{-3} above 5 MeV.

The near equality of these numbers suggests the plausibility of such a source for providing a prominent galactic spectrum of low energy particles.

ACKNOWLEDGMENTS

The author wishes to thank Professor K. G. McCracken for the kind hospitality of his laboratory, and for moral and financial support, the latter through AFOSR contract No. AF-AFOSR-1183-67.

REFERENCES

ALEXANDER, J. K., and STONE, R. G. (1965).—*Astrophys. J.* **142**, 1327.

ANAND, K. C., DANIEL, R. R., and STEPHENS, S. A. (1968).—*Proc. Ind. Acad. Sci.* **67**, 267.

ANDREW, B. H. (1966).—*Mon. Not. R. astr. Soc.* **132**, 79.

BALASUBRAHMANYAN, V. K., BOLDT, E., PALMEIRA, R. A. R., and SANDRI, G. (1968).—Proc. 10th Int. Conf. on Cosmic Rays, Calgary. *Can. J. Phys.* **46**, S633.

BALDWIN, J. E. (1966).—IAU Symp. No. 31, Noordwijk.

BEEDLE, R. E., and WEBBER, W. R. (1968).—Proc. 10th Int. Conf. on Cosmic Rays, Calgary. *Can. J. Phys.* **46**, S1014.

BENEDIKTOV, E. A., GETMANTSER, G. G., MITJAKOV, N. A., RAPOPORT, V. O., SAZONOV, J. A., and TARASOV, A. F. (1965).—*Space Research* **6**, 110.

BLEEKER, J. A. M., BURGER, J. J., DEEMENBERG, J. M., SCHEEPMAKER, A., SWANENBURG, B. N., and TANAKA, Y. (1968).—Proc. 10th Int. Conf. on Cosmic Rays, Calgary. *Can. J. Phys.* **46**, S522.

BLYTHE, J. H. (1957).—*Mon. Not. R. astr. Soc.* **117**, 652.

BRIDLE, A. H. (1967).—*Mon. Not. R. astr. Soc.* **136**, 219.

CLINE, T. L., LUDWIG, G. H., and MCDONALD, F. B. (1964).—*Phys. Rev. Lett.* **13**, 786.

DANIEL, R. R., and STEPHENS, S. A. (1967).—*Proc. Ind. Acad. Sci.* **65**, 319.

DANJO, A., HAYAKAWA, S., MAKINO, F., and TANAKA, Y. (1968).—Proc. 10th Int. Conf. on Cosmic Rays, Calgary. *Can. J. Phys.* **46** S530.

DAVIES, R. D. (1965).—Proc. 9th Int. Conf. on Cosmic Rays, London. Vol. 1, p. 35.

DAVIES, R. D., and HAZARD, C. (1962).—*Mon. Not. R. astr. Soc.* **124**, 147.

DURGAPRASAD, N., FICHTEL, C. E., and GUSS, D. E. (1967).—*J. geophys. Res.* **72**, 2765.

ELLIS, G. R. A. (1965).—*Mon. Not. R. astr. Soc.* **130**, 429.

ELLIS, G. R. A., and HAMILTON, P. A. (1966).—*Astrophys. J.* **146**, 78.

FAN, C. Y., GLOECKLER, G., and SIMPSON, J. A. (1965).—Proc. 9th Int. Conf. on Cosmic Rays, London. Vol. 1, p. 105.

FELTON, J. E. (1966).—*Astrophys. J.* **145**, 589.

GINZBURG, V. L. (1961).—"Propagation of Electromagnetic Waves in Plasma." (Gordon & Breach: New York.)

GLOECKLER, G., and JOKIPII, J. R. (1967).—*Astrophys. J.* **148**, 141.

HARTZ, T. R. (1964).—*Annls Astrophys.* **27**, 823.

HAYAKAWA, S. (1964).—Brandeis Summer Institute in Theoretical Physics, Vol. 2.

HILL, E. R., SLEE, O. B., and MILLS, B. Y. (1958).—*Aust. J. Phys.* **11**, 530.

HOYLE, F., and ELLIS, G. R. A. (1963).—*Aust. J. Phys.* **16**, 1.

HUGILL, J., and SMITH, F. G. (1965).—*Mon. Not. R. astr. Soc.* **131**, 137.

JOKIPII, J. R., L'HEUREUX, J., and MEYER, P. (1967).—*J. geophys. Res.* **72**, 4375.

KENDERDINE, S. (1963).—*Mon. Not. R. astr. Soc.* **126**, 41.

KOMESAROFF, M. M. (1961).—*Aust. J. Phys.* **14**, 515.

LARGE, M. I., MATHEWSON, D. S., and HASLAM, C. G. T. (1961).—*Mon. Not. R. astr. Soc.* **123**, 113.

LARGE, M. I., QUIGLEY, M. J. S., and HASLAM, C. G. T. (1966).—*Mon. Not. R. astr. Soc.* **131**, 335.

LENCHECK, A. M. (1964).—*Annls Astrophys.* **27**, 219.

L'HEUREUX, J. (1967).—*Astrophys. J.* **148**, 399.

L'HEUREUX, J., MEYER, P., VERMA, S. D., and VOGT, R. (1968).—Proc. 10th Int. Conf. on Cosmic Rays, Calgary. *Can. J. Phys.* **46**, S896.

MATHEWSON, D. S., HEALEY, J. R., and ROME, J. M. (1962).—*Aust. J. Phys.* **15**, 369.

MILLS, B. Y. (1959).—*Publs astr. Soc. Pacif.* **71**, 267.

MORAN, M. (1964).—*Mon. Not. R. astr. Soc.* **129**, 447.

NAGASHIMA, K., DUGGAL, S. P., and POMERANTZ, M. A. (1966).—*Planet Space Sci.* **14**, 177.

OKUDA, H., and TANAKA, Y. (1968).—Proc. 10th Int. Conf. on Cosmic Rays, Calgary. *Can. J. Phys.* **46**, S642.

OORT, J. H., and WALRAVEN, T. (1956).—*Bull. astr. Insts Neth.* **12**, 285.

ORMES, J. F., and WEBBER, W. R. (1968).—*J. geophys. Res.* (in press).

PARKER, E. N. (1966).—*Astrophys. J.* **145**, 811.

PARTHASARATHY, R. (1967).—*Proc. astr. Soc. Aust.* **1**(3), 94.

PARTHASARATHY, R., and LERFELD, G. M. (1965).—*Mon. Not. R. astr. Soc.* **129**, 395.

PAULINY-TOTH, I. I. K., and SHAKESHAFT, J. R. (1962).—*Mon. Not. R. astr. Soc.* **124**, 61.

PENZIAS, A. A., and WILSON, R. W. (1966).—*Astrophys. J.* **146**, 666.

PURTON, C. R. (1966).—*Mon. Not. R. astr. Soc.* **133**, 463.

QUENBY, J. J. (1967).—*Planet Space Sci.* **15**, 257.

RAMATY, R. R., and LINGENFELTER, R. E. (1966).—*J. geophys. Res.* **71**, 3687.

SCHWINGER, J. (1949).—*Phys. Rev.* **75**, 1912.

SHAIN, C. A., KOMESAROFF, M. M., and HIGGINS, C. S. (1961).—*Aust. J. Phys.* **14**, 508.

SHAPIRO, M. M., and SILBERBERG, R. (1968).—Proc. 10th Int. Conf. on Cosmic Rays, Calgary. *Can. J. Phys.* **46**, S561.

SMITH, F. G. (1965).—*Mon. Not. R. astr. Soc.* **131**, 145.

TURTLE, A. J. (1963).—*Mon. Not. R. astr. Soc.* **126**, 405.

TURTLE, A. J., and BALDWIN, J. E. (1962).—*Mon. Not. R. astr. Soc.* **124**, 459.

TURTLE, A. J., PUGH, J. E., KENDERDINE, S., and PAULINY-TOTH, I. I. K. (1962).—*Mon. Not. R. astr. Soc.* **124**, 297.

WALSH, D., HADDOCK, F. T., and SCHULTE, H. F. (1963).—*Space Research* **IV** (VII), 935.

WEBBER, W. R. (1963).—Proc. NASA–AAS Symp. on Solar Flares. p. 215.

WEBBER, W. R. (1967*a*).—*J. geophys. Res.* **72**, 5949.

WEBBER, W. R. (1967*b*).—Proc. 10th Int. Conf. on Cosmic Rays, Calgary. Invited paper (unpublished).

WEBBER, W. R. (1968).—*J. geophys. Res.* **73**, 4905.

WESTERHOUT, G. (1958).—*Bull. astr. Insts Neth.* **14**, 215.

WESTFOLD, K. C. (1959).—*Astrophys. J.* **130**, 241.

YATES, K. W., and WIELEBINSKI, R. (1966).—*Aust. J. Phys.* **19**, 389.

STUDY OF A COMPLETE SAMPLE OF COSMIC RADIO SOURCES

By W. Davidson*

[*Manuscript received June* 27, 1968]

Summary

An examination is made of the redshifts and intrinsic powers of the identified radio sources in a complete sample taken from the Cambridge 3C Revised catalogue. The sample consists of the 89 sources of the catalogue having flux density $S_{178} \geqslant 15 \times 10^{-26}\ \mathrm{W\,m^{-2}\,Hz^{-1}}$ and $|b^{\mathrm{II}}| > 15°$, of which 71 are now identified. The subset of the sources having $S_{178} \geqslant 30 \times 10^{-26}\ \mathrm{W\,m^{-2}\,Hz^{-1}}$, in which there are 23 sources with 22 identified, is also considered. Where redshifts for the radio sources were not available (in 16 cases out of the 71 identified) these were calculated from the observed visual apparent magnitudes using the Einstein–de Sitter cosmology, and alternatively the Milne cosmology.

The intrinsic powers of the sources at 178 MHz were calculated for the same two universes, using the given flux density and redshift with an assumed power spectrum common to all sources.

The resulting information presents new evidence on the nature of the local luminosity distribution and the local luminosity function of the sources. In addition, observed distributions of redshift and luminosity such as are found here are likely to be of critical importance in future testing of evolutionary schemes designed to interpret the radio source counts.

I. Introduction

The object of the present paper is to make use of the recently accumulated identifications of radio sources in order to derive new evidence regarding the distribution of the sources in space and in luminosity.

The distribution of the radio sources with regard to redshift and intrinsic power will be of cardinal importance in further attempts to fit cosmological schemes to the radio source counts. Previous efforts in this direction (Davidson and Davies 1964*a*, 1964*b*, 1966; Longair 1966) have shown that the actual number count curve of the sources can be fitted by at least two hypotheses regarding the collective evolution of the sources. There is also, as far as fitting the actual count curve is concerned, a considerable latitude in the choice of the median value in the local luminosity distribution. Therefore, information such as we find here will be necessary to discriminate between these otherwise satisfactory models. This consideration has been the main inspiration of the present paper.

No attempt is made here to set up a new definitive local luminosity distribution or luminosity function of the sources, although the implication of our results for these is indicated. Rather, the properties of a particular sample of sources, chosen in a region of the sky away from the galactic plane and yielding 71 identifications out of 89, is examined for the evidence it can supply in its own right.

---

* University of Otago, Dunedin, New Zealand.

Aust. J. Phys., 1968, **21**, 871–80

II. Analysis of the Sample

The sample consists of the 89 sources of the 3C R catalogue (Bennett 1962) that have flux density $S_{178} \geqslant 15$ f.u.* and $|b^{\rm II}| > 15°$. The sample occupies $5 \cdot 11$ sr of the sky and so the mean sky density is approximately $17 \cdot 4$ sr^{-1}. This is in good statistical agreement with the published mean count over the whole sky for $S_{178} \geqslant 15$ f.u. which is 18 ± 2 sr^{-1} (Gower 1966). Accordingly, since 71 of the 89 sources are now identified, the information that the sample provides is likely to be of valuable significance for cosmology.

The 71 identifications are made up of 55 radio galaxies and 16 quasars. The great majority are those sources in the specified area which have been presented by Wyndham (1966) as identifications falling into the categories 1, 2, or 3 defined by him to be "certain", "highly probable", or "probable" respectively. Several of the sources in categories 2 and 3 have been independently identified by the Parkes radio astronomers (Bolton and Ekers 1966*a*, 1966*b*; Clarke, Bolton, and Shimmins 1966). With regard to the "possible" identifications by Wyndham (category 4) only one has been used here, namely the source 3C 313 which has received independent identification by the Parkes group (Bolton and Ekers 1966*a*). Account has also been taken of more recent identifications which have appeared in notices of redshift measurements, and in the case of quasars reference was made to the comprehensive list provided by Burbidge (1967*a*).

Of the 71 identifications, redshifts are available for 55, which include 41 radio galaxies (Maltby, Matthews, and Moffet 1963; Matthews, Morgan, and Schmidt 1964; Schmidt 1965; Sandage 1966; Burbidge 1967*b*) and 14 quasars (Burbidge 1967*a*). Redshifts for the remaining 16 identified sources (14 radio galaxies and 2 quasars) were estimated from the visual apparent magnitudes given in the reports of identifications.

Calculation of the 16 redshifts was performed for two cosmological models, the Einstein–de Sitter model and the Milne model. In the case of the radio galaxies an adequate formula was found to be

$$m_{\rm V} - K_{\rm V} - A_{\rm V} = 21 \cdot 03 + 5 \log_{10} z + (1-q)z, \tag{1}$$

where z is the redshift, $K_{\rm V}$ is the K correction for visual magnitudes, $A_{\rm V}$ allows for visual absorption in the Galaxy, and q is the deceleration parameter of the model. $K_{\rm V}$ was taken to be $3z$ (Humason, Mayall, and Sandage 1956; Sandage 1964) and $A_{\rm V}$ as $0 \cdot 2 \operatorname{cosec} |b^{\rm II}|$. The constant $21 \cdot 03$ results from taking the Hubble time H^{-1} to be 10^{10} yr and adopting a mean absolute visual magnitude $M_{\rm V}$ for radio galaxies of $-21 \cdot 4$. The latter value was found to be the best fit for the sources whose redshifts are already known, and is very close to the value implied in a recent paper by Sandage (1967). The formula (1) was solved by iteration for z.

The highest redshift calculated for a radio galaxy in this way was $0 \cdot 33$, and in no case did the two values for the cosmological models differ by more than $0 \cdot 02$. Accordingly, no distinction between the two values was made for these sources in presenting the data in Tables 1 and 2, the value corresponding to $q = 0 \cdot 5$ being adopted.

---

* 1 flux unit $= 10^{-26}$ W m^{-2} Hz^{-1}.

For the z calculation in the case of the two quasars a value for M_V of -26 was chosen. This appeared to be the best mean value calculated for the quasars of known z, assuming big-bang models ranging between the Einstein–de Sitter and Milne cases (cf. McVittie and Stabell 1967). There is a wide scatter about this value and for this reason it was not thought worth while to include the K_V correction for quasars; in fact K_V is known (Sandage 1965) to be quite small for quasars having $z < 4$. The m_V versus z relation for quasars in the Einstein–de Sitter model was therefore taken to be

$$m_V - A_V = 16\cdot43 + 5\log_{10}\big(2(1+z)^{\frac{1}{2}}\{(1+z)^{\frac{1}{2}}-1\}\big)\,, \tag{2}$$

and in the Milne model

$$m_V - A_V = 16\cdot43 + 5\log_{10}\big(z(1+\tfrac{1}{2}z)\big)\,. \tag{3}$$

TABLE 1

DISTRIBUTION OF REDSHIFT FOR 22 SOURCES HAVING $S_{178} \geqslant 30$ F.U.

Redshift z	Radio Galaxies	Quasars	Total	N (sr^{-1})
0–0·1	12	0	12	2·35
0·1–0·4	4	2	6	1·17
0·4–∞	1	3	4	0·78

For the two quasars in question, namely 3C 216 and 3C 230, equations (2) and (3) gave respectively the values $z = 1\cdot79$ and $1\cdot34$ for 3C 216, and $z = 1\cdot16$ and $0\cdot95$ for 3C 230.* For the purpose of simply but significantly demonstrating the distribution of the sources having $S_{178} \geqslant 15$ f.u. in Table 2, it was considered adequate to tabulate for each of the two sources the average z arising from the two cosmological models. The values $z = 1\cdot57$ and $z = 1\cdot06$ were therefore adopted for 3C 216 and 3C 230 respectively. As only two quasars were involved, this procedure has negligible effect on the distribution of redshift for $S_{178} \geqslant 15$ f.u. In the case of the subset of sources having $S_{178} \geqslant 30$ f.u., all redshifts were as directly measured.

Table 1 shows the distribution of redshift for the 22 identified sources of the complete subset of 23 that have $S_{178} \geqslant 30$ f.u. and lie in the chosen area of the sky. Only one source is missing, namely 3C 363·1, which is so far unidentified. The table shows a breakdown of the totals into radio galaxies and quasars in each range of redshift. Also shown is the total number N of identified sources per steradian in each range of redshift. This information will be valuable for future testing of cosmological schemes designed to fit the counts of the sources, bearing in mind that 1 source in 23 or 0·196 source per steradian is missing.

---

* A referee has pointed out that the identification of 3C 230 with a quasar is now doubtful. If it is preferred to exclude this source from the analysis, then the necessary minor modification of the results can easily be calculated. For example, the effect on Table 2 would be to reduce the number of sources identified in the range $0\cdot8 < z < 1\cdot4$ by one and to reduce N (sr^{-1}) for this range by 0·20.

Table 2 shows the distribution of redshift for the 71 identified sources, 55 radio galaxies and 16 quasars, having $S_{178} \geqslant 15$ f.u. For each total, the number of sources whose redshifts have been calculated is shown in parentheses. It is to be emphasized that this distribution was found to be essentially independent of the geometry of the cosmological model assumed for these calculations. What is likely to be found of far greater significance is the explanation of the observed distribution in terms of an evolutionary scheme of source density and intrinsic power within a given cosmological model. In this connection it is to be borne in mind that 18 sources of the complete sample of 89 are missing, so far unidentified. Nevertheless these results will be valuable for testing evolutionary schemes, since they show the lower limit of source number per steradian in each range of redshift that any satisfactory theory must predict.

TABLE 2

DISTRIBUTION OF REDSHIFT FOR 71 SOURCES HAVING $S_{178} \geqslant 15$ F.U.

Redshift z	Radio Galaxies	Quasars	Total*	N (sr^{-1})
0–0·1	29	0	29(2)	5·67
0·1–0·2	13	1	14(6)	2·74
0·2–0·3	10	0	10(5)	1·96
0·3–0·8	3	5	8(1)	1·56
0·8–1·4	0	7	7(1)	1·37
1·4–∞	0	3	3(1)	0·59

* The number of sources whose redshifts have been calculated is shown in parentheses.

The distribution of intrinsic power of the 22 sources identified in the range $S_{178} \geqslant 30$ f.u., and that of the 71 sources identified in the range $S_{178} \geqslant 15$ f.u., are shown in Figure 1. The emission powers P_{178} (W sr^{-1} Hz^{-1}) are based on an assumed spectrum $P(\nu) \propto \nu^{-\alpha}$, where the value of α is taken to be 0·8. The results shown are calculated for an Einstein–de Sitter cosmology in which the relation between flux density S_{178} and redshift z for a source of intrinsic power P_{178} is

$$S = P/4c^2T^2(1+z)^\alpha\{(1+z)^{\frac{1}{2}}-1\}^2\,, \tag{4}$$

in which $T\ (= H^{-1})$ is the Hubble time.

The luminosity distribution was also calculated for the Milne model, for which the corresponding relation is

$$S = P(1+z)^{1-\alpha}/c^2T^2z^2(1+\tfrac{1}{2}z)^2\,. \tag{5}$$

However, although the intrinsic powers in this case were systematically higher, the difference was small and the resulting change in the luminosity distribution insignificant. Thus it can be safely asserted that the histograms of Figure 1, just as Tables 1 and 2, are independent of the geometry and kinematics of the cosmological model assumed. This of course may not be the case for flux densities lower than 15 f.u.

Once again, however, a satisfactory explanation of these distributions within a given cosmological model is likely to be critically dependent on the evolutionary scheme assumed for the sources. Consequently, such data provide another valuable means of testing such schemes. For this purpose the number of sources identified per steradian in each histogram power range are listed in Table 3 for $S_{178} \geqslant 30$ f.u. and for $S_{178} \geqslant 15$ f.u. An adequate theory of the collective evolution of the sources must predict numbers in close agreement with the list for $S_{178} \geqslant 30$ f.u. (allowing for one source missing in 5·11 sr), and must be greater than or equal to those listed for $S_{178} \geqslant 15$ f.u. (18 sources missing in 5·11 sr).

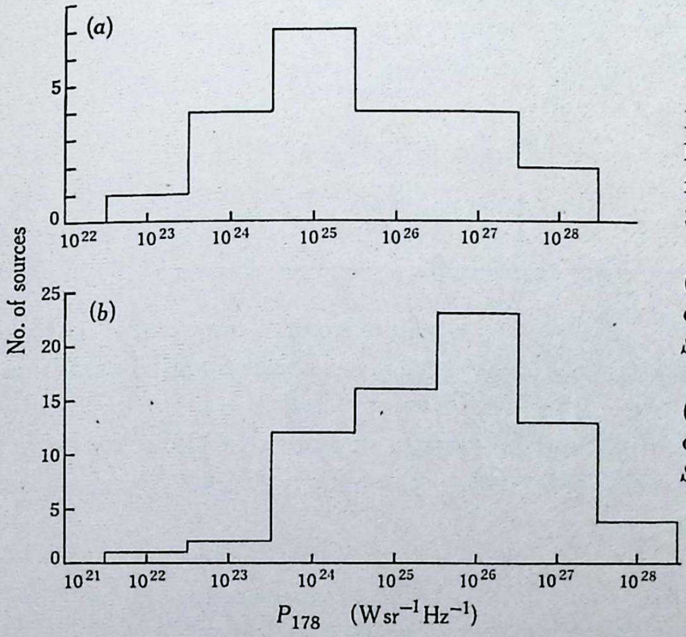

Fig. 1.—Distribution of emission luminosity, normalized to 178 MHz, for the following sources in the 3C R catalogue:

(*a*) the 22 sources identified out of the total sample of 23 having $S_{178} \geqslant 30$ f.u. and $|b^{\mathrm{II}}| > 15°$;

(*b*) the 71 sources identified out of the total sample of 89 having $S_{178} \geqslant 15$ f.u. and $|b^{\mathrm{II}}| > 15°$.

The 18 unidentified sources in this sample from the 3C R catalogue are those in the chosen area of the sky which have been classified by Wyndham (1966) as "unidentified" (his categories I–IV) or else of only "possible" identification with an extragalactic object (category 4). Exceptions to this remark arise for a few of Wyndham's sources which have been identified since his paper was published. The 18 sources (having $S_{178} \geqslant 15$ f.u. and $|b^{\mathrm{II}}| > 15°$) are 3C 6·1, 55, 65, 68·1, 105, 225, 228, 249, 265, 268·1, 274·1, 280, 327·1, 330, 337, 363·1, 427·1, and 437·1.

III. Some Interpretations of the Data

(*a*) *Luminosity Distributions*

The luminosity distribution shown in Figure 1(*a*) may be taken as nearly representative of that expected in any region of the sky for $S_{178} \geqslant 30$ f.u., since only 1 source in the total sample of 23 is missing. The statistics are of course necessarily meagre for $S_{178} \geqslant 30$ f.u., but an area of 5·11 sr away from the galactic plane must be regarded as the best available until a similar investigation is undertaken for radio sources in the southern sky. Detailed analysis of the luminosity calculations shows that the median power for the 22 sources is 3×10^{25} W sr^{-1} Hz^{-1} and the mode is at 10^{25} W sr^{-1} Hz^{-1}.

Since 18 of the 89 sources are missing, Figure 1(*b*) cannot be taken as completely representative of the luminosity distribution for $S_{178} \geqslant 15$ f.u. However, it is interesting to split up the calculated intrinsic powers of the sample in greater detail as shown in Figure 2. A possibility then becomes apparent, because of the unfilled depressions in this detailed histogram, that several of the 18 unidentified sources may have $P_{178} < 10^{26}$ W sr^{-1} Hz^{-1}. Moreover, a smooth envelope curve through the highest ordinates of the histogram would leave sufficient room for all 18 unidentified sources to be contained within it. This would imply that the resulting median and mode of the complete sample would not be greatly in excess of those found here for the 71 identified sources, namely $5 \cdot 5 \times 10^{25}$ W sr^{-1} Hz^{-1} for the median and 7×10^{25} W sr^{-1} Hz^{-1} for the mode.

TABLE 3

LUMINOSITY DISTRIBUTIONS FOR $S_{178} \geqslant 30$ F.U. AND $S_{178} \geqslant 15$ F.U.

P_{178} (W sr^{-1} Hz^{-1})	No. of Sources per Steradian $S_{178} \geqslant 30$ f.u.	$S_{178} \geqslant 15$ f.u.
$3 \cdot 16 \times 10^{21}$–$3 \cdot 16 \times 10^{22}$	0	0·20
$3 \cdot 16 \times 10^{22}$–$3 \cdot 16 \times 10^{23}$	0·20	0·39
$3 \cdot 16 \times 10^{23}$–$3 \cdot 16 \times 10^{24}$	0·78	2·35
$3 \cdot 16 \times 10^{24}$–$3 \cdot 16 \times 10^{25}$	1·37	3·13
$3 \cdot 16 \times 10^{25}$–$3 \cdot 16 \times 10^{26}$	0·78	4·51
$3 \cdot 16 \times 10^{26}$–$3 \cdot 16 \times 10^{27}$	0·78	2·55
$3 \cdot 16 \times 10^{27}$–$3 \cdot 16 \times 10^{28}$	0·39	0·78

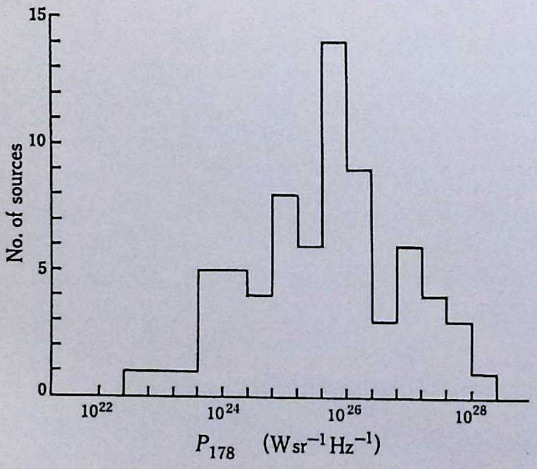

Fig. 2.—More detailed histogram of the emission luminosity at 178 MHz for the 71 sources described in Figure 1(*b*). The median power is at $5 \cdot 5 \times 10^{25}$ W sr^{-1} Hz^{-1} and the mode at 7×10^{25} W sr^{-1} Hz^{-1}.

To have $S_{178} \geqslant 15$ f.u., a radio galaxy of $P_{178} < 10^{26}$ W sr^{-1} Hz^{-1} must have $z < 0 \cdot 27$ according to equation (4) or (5). Taking $M_V = -21 \cdot 4$, as before, this would imply an uncorrected visual magnitude $m_V < 19 \cdot 4$ according to (1), setting $q = 0 \cdot 5$, say. It would not be altogether surprising that such sources had eluded identification so far. A galaxy of redshift $z > 0 \cdot 20$ and $m_V \sim 19$ could be quite difficult to identify with a radio source if the latter were located at a distance several hundred kiloparsecs from it, as would be likely in an "old" radio source. Indeed the sources 3C 6·1, 55, 225, 268·1, 274·1, 330, 337, and 437·1 are all known to be double or more complex in radio structure (Macdonald, Kenderdine, and Neville 1968).

From the appearance of Figure 2 it can be said with somewhat greater probability that a substantial proportion of the 18 missing sources may have $P_{178} < 2 \cdot 5 \times 10^{26}$ W sr^{-1} Hz^{-1}, and therefore $z < 0 \cdot 4$. Such sources are unlikely to be quasars, as the great optical brightness of the latter would have led to identification in this range of redshift (a radio galaxy having $z \sim 0 \cdot 4$ would have $m_{\mathrm{V}} \sim 20$). Therefore it is possible that several of these sources may yet be identified in the range $0 \cdot 20 < z < 0 \cdot 4$ (cf. 3C 295 at $z \sim 0 \cdot 42$). It may be significant that 4 of the missing sources, namely 3C 68·1, 265, 274·1, and 327·1 have been assigned "possible" identifications with galaxies (Wyndham 1966). Using our formulae and the given values of S_{178} and m_{V} these 4 sources would all have $P_{178} < 2 \times 10^{26}$ W sr^{-1} Hz^{-1} and $z < 0 \cdot 33$.

Nevertheless, the possibility cannot yet be entirely excluded that the majority of the missing sources are powerful radio galaxies or quasars beyond their respective optical limits. In their earlier examination of the optical identifications, Longair and Scott (1965) assessed the median and mode of the distribution for $S_{178} \geqslant 15$ f.u. to be at 8×10^{25} W sr^{-1} Hz^{-1}. However, a considerably smaller number of identifications was then available and a very precarious estimate had to be made of the contribution of galaxies and quasars having $P_{178} > 3 \times 10^{26}$ W sr^{-1} Hz^{-1}. It is also relevant to point out that the contribution in the range

$$3 \cdot 16 \times 10^{23} < P_{178} < 3 \cdot 16 \times 10^{24} \qquad \mathrm{W\,sr^{-1}\,Hz^{-1}}$$

shown for our present sample in Figures 1(*b*) and 2 and in Table 3 is significantly greater, by a factor of at least 1·5, than that estimated by Longair and Scott. A revision of the Longair–Scott distribution in this respect would tend to lower their calculated median luminosity.

For the present sample it can be stated that if all 18 unidentified sources have $P_{178} > 10^{26}$ W sr^{-1} Hz^{-1} then the median of the complete distribution for $S_{178} \geqslant 15$ f.u. will be slightly in excess of 10^{26} W sr^{-1} Hz^{-1}, and the mode presumably higher.

(*b*) "*Local*" *Luminosity Distribution*

Whatever the final median power for $S_{178} \geqslant 15$ f.u. turns out to be, the present investigation supports a recent contention by the author (Davidson 1967) that the "local" luminosity distribution has a median value no higher than 4×10^{25} W sr^{-1} Hz^{-1}.

The local luminosity distribution $n_0(P)$ is theoretically associated with the limit $S \to \infty$, and is related to $\rho_0(P)$ the local space density frequency of the sources (the so-called "luminosity function") in accordance with the Euclidean formula

$$n_0(P) \propto P^{3/2} \rho_0(P) \,. \tag{6}$$

As shown previously (Davidson and Davies 1964*a*, 1966), for an ideally smooth distribution of sources in an isotropic world model this relation between the luminosity distribution and the luminosity function would in fact be realized as $S \to \infty$.

In practice one may approach this limit only as far as the discrete distribution of radio sources will permit an adequate count of sources within a sufficiently small local region of space.

However, if $\rho_0(P)$ is established from the identifications of all sources in a suitable region of space local to the observer, one may determine the theoretical local luminosity distribution $n_0(P)$ by using relation (6) with suitable normalization. Then the actually observed luminosity distribution should approach $n_0(P)$ as S is taken at successively higher values. The limitation of statistically adequate samples will tend to prevent complete coincidence being reached.

The author has previously (Davidson 1967) used the $\rho_0(P)$ function provided at 178 MHz by Caswell and Wills (1967) to calculate the associated $n_0(P)$ function defined by (6). This distribution turned out to be roughly Gaussian in log P_{178}, with standard deviation $\sigma \sim 1$. The median was located at about $3\cdot16\times10^{25}$ W sr^{-1} Hz^{-1} and the mode at $1\cdot5\times10^{25}$ W sr^{-1} Hz^{-1}.

Consider now the evidence of the present samples for $S_{178} \geqslant 15$ f.u. and $S_{178} \geqslant 30$ f.u. As already stated in Subsection (*a*), detailed analysis yields for the median luminosity at $S_{178} \geqslant 15$ f.u. the value $5\cdot5\times10^{25}$ W sr^{-1} Hz^{-1}, with mode at 7×10^{25} W sr^{-1} Hz^{-1}. It seems unlikely that the identification of the complete sample will lower these values. On the other hand, the median power for $S_{178} \geqslant 30$ f.u., for 22 sources out of 23, was found to be 3×10^{25} W sr^{-1} Hz^{-1} with a mode of 10^{25} W sr^{-1} Hz^{-1}. The close agreement of the results for the $n_0(P)$ distribution with those for $S_{178} \geqslant 30$ f.u., and their disparity with those for $S_{178} \geqslant 15$ f.u., strongly support two points of the author's earlier argument (Davidson 1967):

(i) The median power of the local luminosity distribution $n_0(P)$ probably lies between 10^{25} and 4×10^{25} W sr^{-1} Hz^{-1} at 178 MHz.

(ii) The more distant, more powerful, sources that appear in the luminosity distribution for $S_{178} \geqslant 15$ f.u., and even at the higher end of that for $S_{178} \geqslant 30$ f.u., have to be regarded as part of a cosmic evolutionary trend (into the past) away from the local luminosity distribution.

Point (ii) is pertinent since only a sufficiently local region of space can serve to define the local luminosity function $\rho_0(P)$ and the associated distribution $n_0(P)$. This is because the lifetime of the majority of individual radio sources is confined to between 10^6 and 10^7 yr (Ryle and Longair 1967). Hence the observed properties of radio sources seen at redshifts exceeding $0\cdot1$ will belong to an epoch at least 10^9 yr into the past, and so would have shared in any general collective evolutionary trend operating on the radio sources. Fortunately the $\rho_0(P)$ function on which $n_0(P)$ depends was established by Caswell and Wills (1967) up to $P_{178} \sim 3\times10^{25}$ W sr^{-1} Hz^{-1}, mainly from the region $z < 0\cdot1$. It is impossible, however, to obtain adequate statistics for $P_{178} > 3\times10^{25}$ W sr^{-1} Hz^{-1} without considering sources having $z > 0\cdot1$ (cf. Tables 1 and 2), and so some uncertainty must remain for $\rho_0(P)$ and $n_0(P)$ for $P_{178} > 3\times10^{25}$ W sr^{-1} Hz^{-1}. The tendency will be to exaggerate the importance of this region of the $n_0(P)$ distribution, since the information is drawn from more distant space where the radio source counts indicate that sources occur either in greater numbers or with greater intrinsic power.

The significant result established here is that when S_{178} is raised to 30 f.u., at which distant powerful sources still contribute, the median power is no higher than 3×10^{25} W sr^{-1} Hz^{-1} and the mode no higher than 10^{25} W sr^{-1} Hz^{-1}.

(c) *Criteria for Testing Cosmological Models*

Tables 1, 2, and 3 together set a stiff test to be passed by any cosmological model that purports to explain the counts of radio sources. Even allowing for the fact that 18 sources of the representative sample for $S_{178} \geqslant 15$ f.u. are missing it is not difficult to imagine that many otherwise plausible cosmological models will fail to pass this test. The most common reasons for their elimination are likely to be (1) a failure to give the correct luminosity distribution for a given flux density and (2) allowing the main weight of the luminosity distribution to fall in the wrong redshift region.

These considerations are likely to have particular relevance to both the assumed median power of the local luminosity distribution $n_0(P)$ and the assumed evolutionary character of the model. Because so many sources of relatively low power have to appear in the range $z < 0\cdot1$, a fact responsible for the low median and mode of the luminosity distribution for $S_{178} \geqslant 30$ f.u., the assumption of a median power of $n_0(P)$ in excess of 4×10^{25} W sr^{-1} Hz^{-1} is unlikely to provide agreement with Tables 1, 2, and 3. Indeed, considering the range $S_{178} \geqslant 15$ f.u., a further breakdown of the results displayed in Table 2 shows that only 5 of the 29 identified sources in the region $z \leqslant 0\cdot1$ have $P_{178} > 1\cdot5\times10^{25}$ W sr^{-1} Hz^{-1}. Yet all sources in our chosen region of the sky that have $z \leqslant 0\cdot1$ and $P_{178} > 1\cdot5\times10^{25}$ W sr^{-1} Hz^{-1} should have $S_{178} > 15$ f.u. and belong to our sample. Again, only 8 of the 43 sources in Table 2 that have $z \leqslant 0\cdot2$ have also $P_{178} > 5\cdot7\times10^{25}$ W sr^{-1} Hz^{-1}, but all such sources should have $S_{178} > 15$ f.u. and in principle be identified in our present sample. This demonstrates clearly the paucity of high-powered sources in local space. Moreover, whether the fit of the radio source counts relies mainly on evolution of source density, or alternatively on evolution of mean source power, is likely to require different distributions in P and z, for which Tables 1, 2, and 3 provide a gauge.

Finally, and this may not be independent of the above considerations, any model in which the limiting redshift z (beyond which no radio sources are assumed to have existed) is set too high is again unlikely to agree with Tables 1 and 2. For such a model would necessarily imply that an unduly large contribution to the count at a given flux density would arise from very distant sources.

IV. ACKNOWLEDGMENTS

I am indebted to Dr. B. G. Cox, Director of the Computing Centre, University of Otago, for his help in computing the intrinsic powers of the sources. I also thank Sir Martin Ryle, F.R.S., for helpful comments during the preparation of the paper.

V. REFERENCES

BENNETT, A. S. (1962).—*Mem. R. astr. Soc.* **68**, 163.
BOLTON, J. G., and EKERS, JENNIFER (1966*a*).—*Aust. J. Phys.* **19**, 471.

BOLTON, J. G., and EKERS, JENNIFER (1966*b*).—*Aust. J. Phys.* **19**, 559.
BURBIDGE, E. M. (1967*a*).—*A. Rev. Astr. Astrophys.* **5**, 399.
BURBIDGE, E. M. (1967*b*).—*Astrophys. J.* **149**, L51.
CASWELL, J. L., and WILLS, D. (1967).—*Mon. Not. R. astr. Soc.* **135**, 231.
CLARKE, MARGARET E., BOLTON, J. G., and SHIMMINS, A. J. (1966).—*Aust. J. Phys.* **19**, 375.
DAVIDSON, W. (1967).—*Nature, Lond.* **216**, 1076.
DAVIDSON, W., and DAVIES, M. (1964*a*).—*Mon. Not. R. astr. Soc.* **127**, 241.
DAVIDSON, W., and DAVIES, M. (1964*b*).—*Mon. Not R. astr. Soc.* **128**, 363.
DAVIDSON, W., and DAVIES, M. (1966).—*Mon. Not. R. astr. Soc.* **134**, 405.
GOWER, J. F. R. (1966).—*Mon. Not. R. astr. Soc.* **133**, 151.
HUMASON, M. L., MAYALL, N. U., and SANDAGE, A. R. (1956).—*Astr. J.* **61**, 97.
LONGAIR, M. S. (1966).—*Mon. Not. R. astr. Soc.* **133**, 421.
LONGAIR, M. S., and SCOTT, P. F. (1965).—*Mon. Not. R. astr. Soc.* **130**, 379.
MACDONALD, G. H., KENDERDINE, S., and NEVILLE, A. C. (1968).—*Mon. Not. R. astr. Soc.* **138**, 259.
MCVITTIE, G. C., and STABELL, R. (1967).—*Nature, Lond.* **213**, 133.
MALTBY, P., MATTHEWS, T. A., and MOFFET, A. T. (1963).—*Astrophys. J.* **137**, 153.
MATTHEWS, T. A., MORGAN, W. M., and SCHMIDT, M. (1964).—*Astrophys. J.* **140**, 35.
RYLE, M., and LONGAIR, M. S. (1967).—*Mon. Not. R. astr. Soc.* **136**, 123.
SANDAGE, A. R. (1964).—Proc. Padua Symp. Extragalactic Res. p. 104.
SANDAGE, A. R. (1965).—*Astrophys. J.* **141**, 1560.
SANDAGE, A. R. (1966).—*Astrophys. J.* **145**, 1.
SANDAGE, A. R. (1967).—*Astrophys. J.* **150**, L9.
SCHMIDT, M. (1965).—*Astrophys. J.* **141**, 1.
WYNDHAM, J. D. (1966).—*Astrophys. J.* **144**, 459.

5 GHz CONTINUUM RADIATION FROM SOUTHERN HEMISPHERE GALACTIC HII REGIONS

By F. F. GARDNER* and M. MORIMOTO†

[*Manuscript received March* 12, 1968]

Summary

The continuum radiation from about 36 southern thermal radio sources has been surveyed at 6 cm wavelength with a beamwidth of 4′·2 arc, and maps are shown for 28 of these. The positional accuracy is better than 1′ arc.

All the sources are resolved to some extent. Peak temperatures, half-intensity widths, and peak emission measures are given for each.

I. INTRODUCTION

The 6 cm continuum survey described in the present paper was undertaken mainly to supplement observations currently in progress at the Australian National Radio Astronomy Observatory at Parkes of recombination lines and OH- and H-line emission and absorption. The wavelength is the same as that used in a similar survey by Mezger and Henderson (1967) in the northern hemisphere, but the beamwidth is 50% narrower (4′·2 arc compared with 6′·4 arc). While the emphasis was on the strongest thermal sources‡ in the southern sky, there are 10 sources in common with Mezger and Henderson. As in the latter survey, the interest has been in the brightest concentrations for which peak antenna temperatures are measured and (to a lesser degree of accuracy) the brightness temperatures, fluxes, and emission measures derived. Distance estimates for the HII regions are not considered in the present paper.

II. TELESCOPE AND EQUIPMENT

The observations were made in May 1967 with the Parkes 210 ft telescope. The reflecting surface consists of an inner 55 ft of solid surface surrounded by 1380 mesh panels. With the aid of a special survey instrument these panels were set so that the shape was optimum near zenith angle 30° (Minnett, Yabsley, and Puttock 1967). This minimized the variation in performance over the normal range of zenith angle, and in fact point source measurements with fixed focus showed that the gain, including extinction, exceeded 95% of its peak value in the range 20° to 55°, where practically all observations in the present paper were made. In practice, the gain variation was less than this, as the focus was adjusted to the value appropriate to the mean zenith angle for each source.

The feed system consisted of a dual-mode circular horn similar to one used previously at 18 cm wavelength (Gardner, McGee, and Robinson 1967). This pro-

---

* Division of Radiophysics, CSIRO, P.O. Box 76, Epping, N.S.W. 2121.

† This work was performed during the tenure of a CSIRO fellowship at the Division of Radiophysics, CSIRO, P.O. Box 76, Epping, N.S.W. 2121. Present address: Tokyo Astronomical Observatory, Tokyo, Japan.

‡ Listed by Westerhout (1958) and Mathewson, Healey, and Rome (1962).

Aust. J. Phys., 1968, **21**, 881–94

duced a circular feed beam with low spillover and, within the accuracy of measurement, a circular secondary beam. The illumination taper was somewhat greater than in the preliminary 6 cm observations (Broten *et al.* 1965) and as a result the half-intensity beamwidth of 4′·2 arc was slightly greater than before.

The radiometer was switched at 40 Hz between the feed and a liquid-nitrogen-cooled termination. Approximate noise balance was achieved by adding noise to the signal side. The receiver consisted of a tunnel diode input stage followed by a double-sideband mixer with an intermediate-frequency band from 5 to 100 MHz. The input bandwidth was twice this, covering 4·9–5·1 GHz. The overall noise temperature was around 800°K.

The 10°K calibration used in the observations was obtained from a noise lamp through an adjustable attenuator and a directional coupler. It was set by reference to a thermal calibration in which the load temperature was changed from 0°C to 50°C.

The brightness temperature scale was determined from measurements of the beam shape for small diameter sources and from a measurement of the ratio of the peak response (mean of two orthogonal polarizations) to the calibration for the quasi-stellar source 3C 273 (assuming that the flux of 3C 273 at the time of observation, mid May 1967, was 41 f.u.). On the same scale Hydra A and M 87 had peak flux values of 13 and 69 f.u. respectively.

For a Gaussian beamshape with half-intensity width B, an extended region of brightness temperature T_b will give the same radiometer output as a point source of flux S if

$$T_\mathrm{b}/S = 3\cdot 77\times 10^3(\lambda/B)^2 = 0\cdot 77$$

in our case, with λ in metres and B in minutes of arc. The corresponding antenna temperature T_a for a 210 ft paraboloid with aperture efficiency η_a is

$$T_\mathrm{a}/S = 1\cdot 165\eta_\mathrm{a} \qquad \text{or} \qquad T_\mathrm{b}/T_\mathrm{a} = 0\cdot 66/\eta_\mathrm{a}\,.$$

With T_a derived from the thermal calibration, as outlined earlier, $T_\mathrm{b}/T_\mathrm{a} \simeq 2\cdot 0$ and correspondingly $\eta_\mathrm{a} = 0\cdot 33$. This includes atmospheric extinction under good conditions at a zenith angle of $\sim 35°$.

III. OBSERVATIONAL METHOD

The main observations were generally drift scans at declination intervals of 2′·0 arc. At least two scans were made and averaged for each declination and if there was any obvious difference between them a third scan was made. Forward and reverse scans in declination at 0·25 deg/min were made through the source peak position and also as tie-in scans at right ascensions away from steep gradients in intensity. At declinations below −50° the right ascension scans were made with the telescope driving at about $+0\cdot 25\sec\delta$ deg/min. The time constant of 1 sec was allowed for in the reduction, which was done from the analogue charts. The sensitivity was generally governed by receiver drifts and fluctuations in sky background rather than by receiver noise. Extinction corrections for "good-seeing" conditions are included in the calibration.

In all cases the accuracy of pointing of the telescope was better than 1′ arc. Average refraction is compensated for in the error detection system (Bolton, Gardner, and Mackey 1964).

IV. Results

The results of the survey are presented in Figures 1(*a*)–1(*w*) and Table 1. Column (1) of the table gives the source name. If available, the optical number is given precedence—Messier, NGC, or RCW (Rodgers, Campbell, and Whiteoak 1960); otherwise the Westerhout (W) number or a coordinate number as used in the Parkes catalogue (Bolton, Gardner, and Mackey 1964) is used. Columns (2) and (3) give the source peak position in celestial and galactic coordinates. Column (4) gives the observed widths θ'_α and θ'_δ in minutes of arc and column (5) gives the derived widths θ_α and θ_δ of the components under the assumption of Gaussian source and beam. Column (6) gives antenna temperature T_a, column (7) the flux S, column (8) the central brightness temperature T_b derived for a Gaussian model, and column (9) the corresponding central emission measure.

The conversion from θ'_α to θ_α is through the formula

$$(\theta'_\alpha)^2 = \theta_\alpha^2+(4\cdot2)^2 .$$

The flux S is given by

$$S = S_{\max}\,\theta'_\alpha\,\theta'_\delta/(4\cdot2)^2 ,$$

and the central brightness temperature T_b for a Gaussian model by

$$T_\mathrm{b} = T_{\mathrm{b,max}}\,\theta'_\alpha\,\theta'_\delta/\,\theta_\alpha\,\theta_\delta \simeq 2T_\mathrm{a}\,\theta'_\alpha\,\theta'_\delta/\,\theta_\alpha\,\theta_\delta .$$

Here $T_{\mathrm{b,max}}$ is the peak chart deflection measured in terms of the full-beam brightness temperature scale.

The formula of Scheuer (1960) or equation (5) of Mezger and Henderson (1967) relates T_b and emission measure E.M. in pc cm^{-6}. For 5·0 GHz

$$T_\mathrm{b} = (\mathrm{E.M.})\times1\cdot10\times10^{-4} .$$

For a number of multiple-component sources the individual components cannot be clearly separated from the surrounding background, and the fluxes derived will depend on the beamwidth and on assumptions about the underlying background.

V. Discussion

When a comparison is made with the results of Mezger and Henderson (1967) for the sources in common, it is found that most of our values of flux are lower and emission measures higher for the central components. This is probably just the result of the 50% greater resolution, and it is likely that the trend would continue with further increase in resolution, as was found by Mezger, Schraml, and Terzian (1967) to be the case for W 49.

Six of the sources shown in Figures 1(*a*)–1(*w*) are associated with strong OH emission, namely PKS 1308−62, PKS 1608−51, PKS 1617−50, NGC 6334, W 49,

TABLE 1

PARTICULARS OF CONTINUUM SOURCES AT 6 CM

(1)	(2)		(3)		(4)		(5)		(6)	(7)	(8)	(9)	(10)
Source	Position (1950·0)		Galactic Coordinates		Observed Widths		Source Widths		Antenna Temp-erature T_a	S	Central Brightness Temp-erature T_b	Emission Measure	Remarks
	R.A.	Dec.	l^{II}	b^{II}	R.A. θ'_α	Dec. θ'_δ	R.A. θ_α	Dec. θ_δ					
	h m s	° ′	°	°	′	′	′	′	(°K)	(f.u.)	(°K)	(10^5 pc cm^{-6})	
Orion A	05 32 50	−05 25·4	209·0	−19·4	5·33	5·43	3·28	3·45	80·8	344	414	37·6	
NGC 2024	05 39 09	−01 56·1	206·5	−16·4	5·36	5·00	3·3	2·7	13·8	57·5	82	7·4	
RCW 38	08 57 18	−47 19·2	267·9	− 1·1	4·75	4·82	2·2	2·35	54·5	183	482	43·7	
RCW 36	08 57 35	−43 33·9	265·1	+ 1·4	5·05	5·00	2·8	2·7	6·9	26·6	46	4·2	
RCW 46	10 04 52	−56 57·7	282·0	− 1·2	4·84	4·80	2·4	2·4	8·2	28·0	66	6·0	
RCW 49	10 22 18	−57 32·1	284·3	− 0·3	6·76	7·9	5·3	6·7	24·2	190	73	6·6	
Carina nebula	10 41 32	−59 19·7	287·3	− 0·6	7·0	9·0	5·6	8·0	13·5	125	38	3·4	
	10 42 48	−59 23·7	287·8	— 0·6	9·7	5·8	8·7	4·0	12·4	103	40	3·6	
RCW 57	11 09 41	−61 02·3	291·3	− 0·7	4·56	4·72	1·8	2·2	31·6	100	343	31·1	
	11 12 46	−60 59·2	291·6	− 0·5	6·09	7·75	4·4	6·5	24·1	167	79	7·1	
PKS 1207−62	12 07 19	−62 33·4	298·2	− 0·3	4·72	4·5	2·2	1·6	8·5	26·5	102	9·2	
PKS 1308−62	13 08 10	−62 29·5	305·2	+ 0·0	7	7	5·6	5·6	3·5	25·2	11	1·0	RCW 74
	13 08 15	−62 18·9	305·2	+ 0·2	6·5	7	5·0	5·6	5·5	36·6	18	1·6	
	13 09 16	−62 18·8	305·3	+ 0·2	6	5	4·3	2·7	9·2	40·6	47	4·3	
	13 11 04	−62 29·1	305·5	+ 0·0	~6	5·5	4·3	3·5	1·6	7·8	7	0·6	
PKS 1441−59	14 41 29	−59 37·0	316·8	− 0·05	5·1	5·0	2·9	2·7	9·4	34·1	61	5·5	
PKS 1442−59	14 42 00	−59 12·5	317·0	+ 0·3	~10	~8·5			1·4	~17·5	~3	~0·3	
PKS 1540−54	15 40 47	−53 57·2	326·7	+ 0·6	5·0	6·3	2·7	4·7	8·8	40·7	44	4·0	Contains smaller core
PKS 1549−54	15 49 12	−54 26·3	327·3	− 0·5	4·79	4·40	2·3	1·3	15	48·1	220	19·9	Core only; broad ext. to S. and W.
PKS 1608−51	16 08 19	−51 19·2	331·5	− 0·1	5·03	4·74 4·98*	2·8	2·2 2·7*	9·1	31·8 33·6	70	6·3	

Norma sources	16 15 55	−50 56·1	332·6	− 0·6	5·0	5·0	2·7	2·7	4·3	15·8	29	2·6	
	16 16 19	−50 48·7	332·8	− 0·5	6	7	4·3	5·6	3·0	18·5	10	0·9	
	16 16 51	−50 32·9	333·0	− 0·5	5·5	4·5	3·6	1·6	6·8	24·7	58	5·2	
	16 17 13	−50 30·4	333·1	− 0·5	5·5	5·5	3·6	3·6	8·3	36·8	39	3·5	
	16 17 43	−50 20·5	333·3	− 0·4	4·8	5·0	2·4	2·7	10·0	35·2	74	6·7	
	16 18 23	−49 59·5	333·6	− 0·2	4·75	4·5	2·2	1·6	25·7	80·9	313	28·3	
PKS 1630−47	16 30 48	−47 30·0	336·8	+ 0·1	10·9	8·4	10·0	7·4	4·6	61·9	11	1·0	Another component at R.A. $16^{h} 33^{m} 20^{s}$
PKS 1636−46	16 36 27	−46 16·2	338·4	+ 0·2	6·0	7·5	4·3	6·2	3·9	25·8	13	1·2	
	16 37 07	−46 17·5	338·4	+ 0·1	7·2	9·5	5·8	8·5	5·2	52·3	14	1·3	
PKS 1716−38	17 16 38	−38 55·1	348·7	− 1·0	4·95	4·9	2·6	2·5	11	39·3	82	7·4	
NGC 6334	17 16 26	−36 03·0	351·0	+ 0·7	7·6	7·8	6·3	6·6	4·7	40·9	13	1·2	
	17 17 18	−35 47·1	351·3	+ 0·7	—	—			14·2		>40	>3·6	Ridge of small diam. sources at $b^{II} = 0°·7$
	17 17 31	−36 01·1	351·2	+ 0·5	5·8	4·5	4·0	1·6	3·9	14·9	31	2·8	
NGC 6357	17 21 24	−34 08·1	353·2	+ 0·9	7·0	5·2	5·6	3·1	22·5	120	94	8·5	
	17 22 15	−34 20·1	353·1	+ 0·6	9·2	8·0	8·2	6·8	16	67·5	42	3·8	
	17 23 21	−34 31·1	353·1	+ 0·4					3·6		10	0·9	
M 8	18 00 38	−24 23·0	6·0	− 1·2	5·5	5·5	3·6	3·6	10	44·5	47	4·3	Ext. component removed
W 31	18 06 04	−20 04·2	10·3	− 0·1	5·0	6·0	2·7	4·3	5·1	22·4	27	2·4	
	18 06 28	−20 19·8	10·2	− 0·4	5·47	4·5	3·5	1·6	14·0	50·9	123	11·1	
	18 07 34	−19 56·8	10·6	− 0·4	5·8	5·0	4·0	2·7	2·3	9·8	12	1·1	
M 16	18 15 38	−13 44·2	17·0	+ 0·9	10	10	9·1	9·1	2·9	42·6	7	0·6	
	18 16 09	−13 51·6	16·9	+ 0·7	9	10	8·0	9·1	3·4	45·0	9	0·8	
M 17	18 17 40	−16 13·0	15·0	− 0·7	5·9	7·5	4·15	6·2	66	430	227	20·6	Ext. component removed
W 43	18 45 02	−01 58·9	30·8	− 0·0	6·1	6·4	4·4	4·8	16	91·7	65	5·9	Ext. component removed
W 49	19 07 52	+09 00·7	43·2	+ 0·0	5·26	4·50	3·2	1·6	15·7	54·7	145	13·1	
	19 08 44	+09 00·5	43·3	− 0·2	5·73	5·13	3·9	2·7	4·9	21·2	26		
W 51*	19 20 04	+13 58·4	48·9	− 0·3	7·5	11	6·2	10·1	4·8	58·3	13	1·2	
	19 20 37	+14 02·0	49·1	− 0·4					3·9		10	0·9	
	19 20 44	+14 09·5	49·2	− 0·4	5·7	5·0	3·9	2·7	6	25·2	32	2·9	
	19 20 55	+14 20·8	49·4	− 0·3	5·4	5·0	3·4	2·7	7	27·8	41	3·7	
	19 21 25	+14 24·2	49·5	− 0·4	5·3	5·0	3·2	2·7	28	109	168	15·2	

---

* Background not subtracted.

and W 51. For five of these, the OH positions (Gardner, McGee, and Robinson 1967; McGee, Gardner, and Robinson 1967; Weaver *et al.* 1968) are displaced to the edge of the thermal source—in most cases to a distance where the emission (when corrected for beam broadening) would be below one-quarter of the central intensity. That is, the OH emission is from near the edge of the HII region, as expected for the simple model discussed by Gardner, McGee, and Robinson in connection with NGC 6334. For W 49, our resolution is inadequate for any meaningful comment, but Mezger, Schraml, and Terzian (1967) find that only one of the two OH components is near the periphery of the source. For the source IC 1795, which is not visible from Parkes, Rogers *et al.* (1967) have found that the OH emission is again from the outer edge of the intense HII region, but Mezger *et al.* (1967) have found a weak source in approximate coincidence with the OH-emission position. Our resolution is insufficient to rule out the possibility of similar weak continuum sources coincident with the OH positions for the other sources listed above.

The map of the Carina nebula shows two components separated by some 10′ arc along a line of constant galactic latitude. The similarity in peak intensity and angular size of the two components suggests that they are parts of the same object. However, 126α and 127α hydrogen recombination line profiles observed by McGee and Gardner (1968) are very different for the two components. The western component has a normal line-to-continuum ratio and width, and its central velocity of -20 km sec^{-1} is that expected from the galactic rotation model. However, the eastern component, nearer to the peculiar star η Carinae, has a lower line-to-continuum ratio and the profile is very broad and appears to be composed of two components with mean velocities of 0 and -40 km sec^{-1}. Future high resolution recombination line mapping of the nebula should be very useful for revealing the details of these large internal motions.

VI. Conclusions

Twenty-eight HII regions have been mapped with a $4'\cdot 2$ arc beam and individual components with angular diameter down to $1'\cdot 5$ have been found. It is quite likely that finer detail would emerge with more resolution. To this extent the peak emission measures quoted should be considered only as lower limits.

A comparison between positions of OH and continuum features indicates that in five out of six cases the OH emission originates from the periphery of the HII region. For these five cases higher resolution mapping would be required to reveal the presence of weak continuum features coincident with the OH-emission position.

VII. Acknowledgments

The authors are indebted to Miss J. Milton and Miss M. Adams for their assistance with the data reduction, and to Mr. F. Tonking who was responsible for the design and construction of the radiometer.

Figs. 1(*a*)–1(*w*).—Contour maps of galactic radio sources at $\lambda = 6$ cm. The scale is shown for each map and asterisks indicate OH-emission positions.

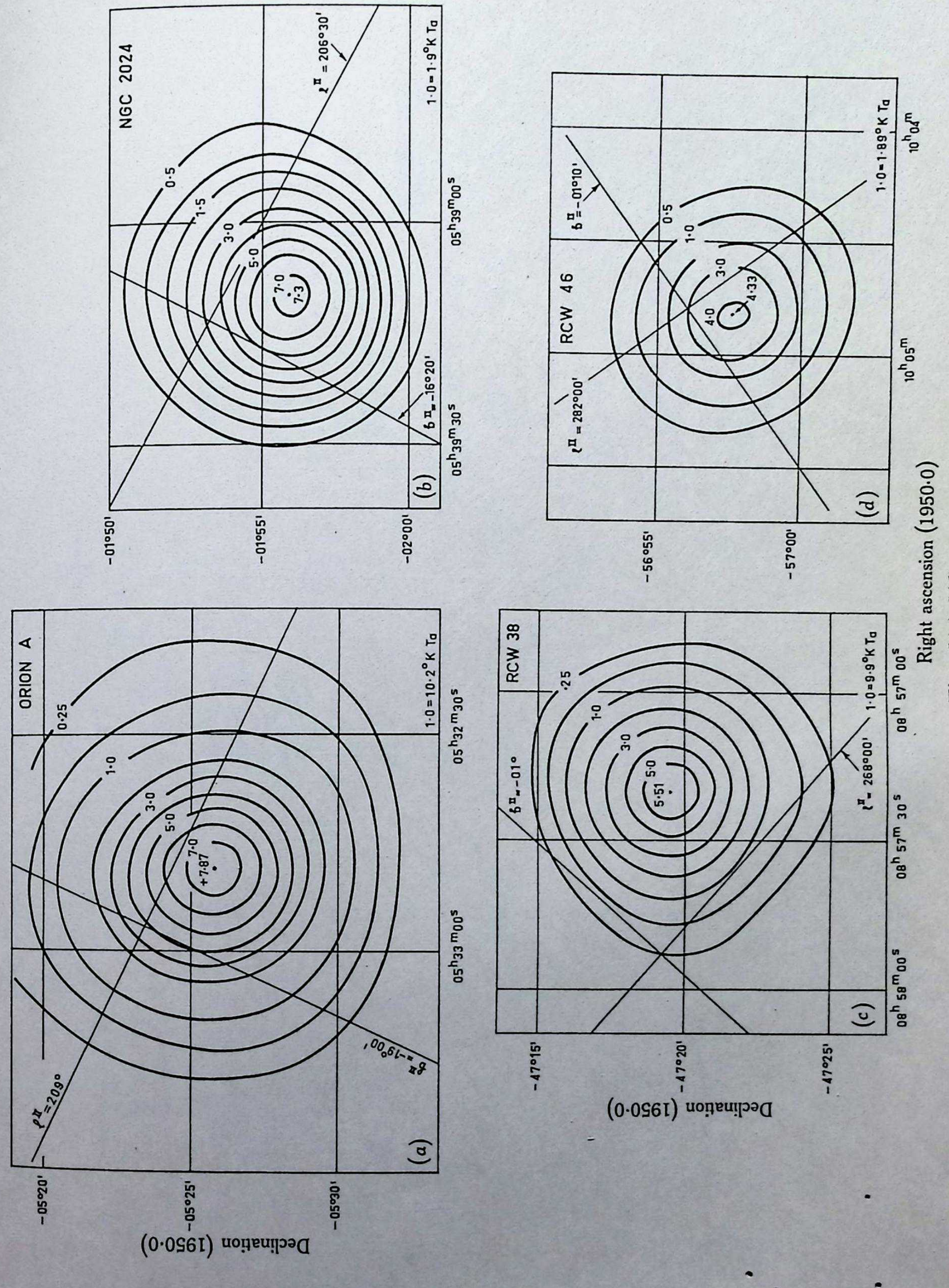
ORION A
0·25
1·0
3·0
5·0
7·0
+7·87
l^{II}=209°
b^{II}=-19°00'
1·0=10·2°K Ta
(a)
−05°20'
−05°25'
−05°30'
Declination (1950·0)
05h33m00s
05h32m30s
NGC 2024
0·5
1·5
3·0
5·0
7·0
7·3
l^{II} = 206°30'
b^{II}=-16°20'
1·0=1·9°K Ta
(b)
−01°50'
−01°55'
−02°00'
05h39m30s
05h39m00s
RCW 38
·25
1·0
3·0
5·0
5·51
b^{II}=-01°
l^{II}= 268°00'
1·0=9·9°K Ta
(c)
−47°15'
−47°20'
−47°25'
Declination (1950·0)
08h58m00s
08h57m30s
08h57m00s
RCW 46
0·5
1·0
3·0
4·0
4·33
l^{II}= 282°00'
b^{II}=-01°10'
1·0=1·89°K Ta
(d)
−56°55'
−57°00'
10h05m
10h04m
Right ascension (1950·0)

Figs. 1(a)–1(d)

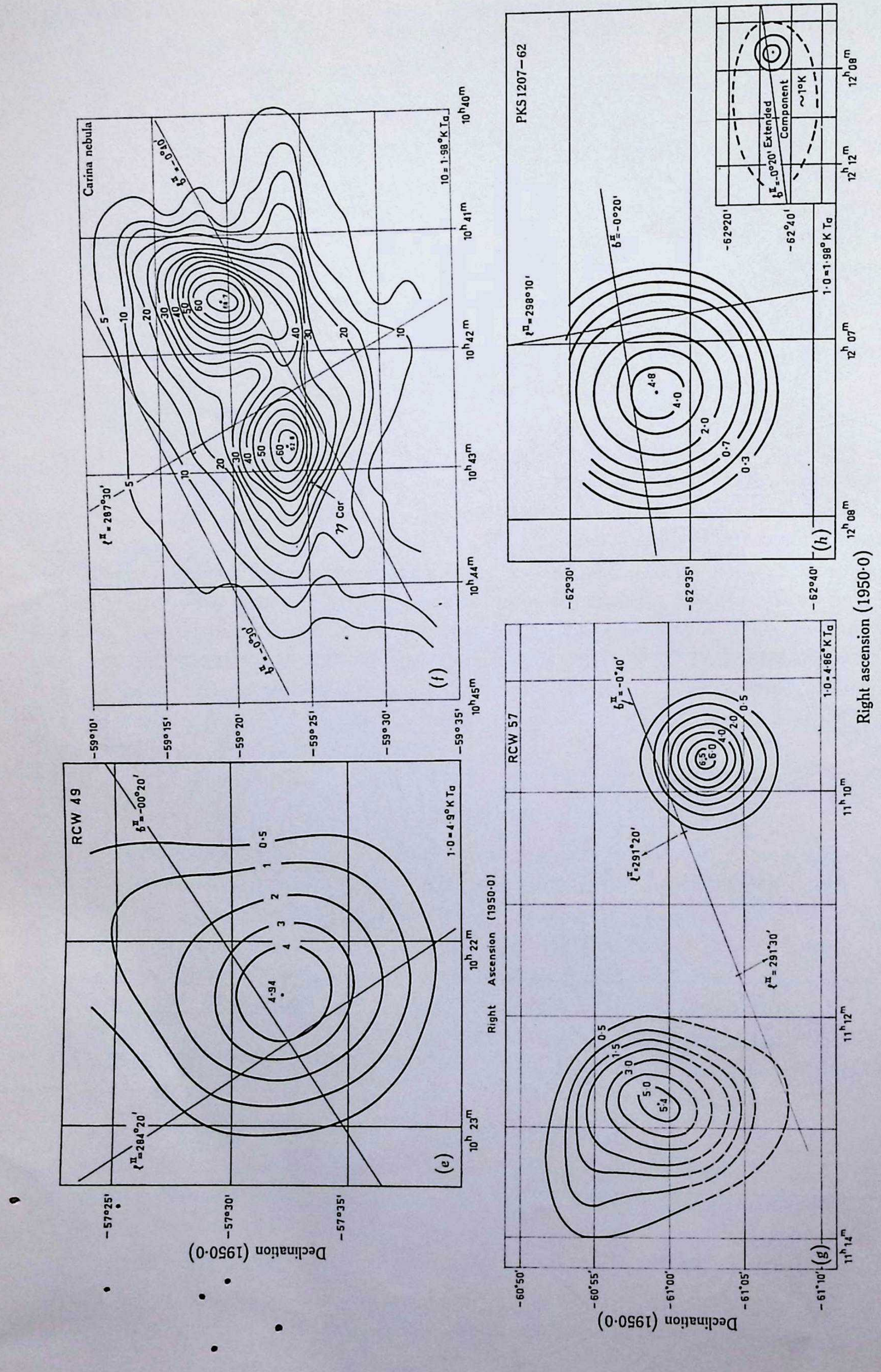
RCW 49
(e)
$b^{II}=-00°20'$
$l^{II}=284°20'$
4·94
1·0 = 4·9° K Ta
$10^h 23^m$
$10^h 22^m$
Right Ascension (1950·0)
−57°25'
−57°30'
−57°35'
Declination (1950·0)
Carina nebula
(f)
$b^{II}=-0°10'$
$b^{II}=-0°30'$
$l^{II}=287°30'$
η Car
10 = 1·98° K Ta
$10^h 45^m$
$10^h 44^m$
$10^h 43^m$
$10^h 42^m$
$10^h 41^m$
$10^h 40^m$
−59°10'
−59°15'
−59°20'
−59°25'
−59°30'
−59°35'
RCW 57
(g)
$b^{II}=-0°40'$
$l^{II}=291°20'$
$l^{II}=291°30'$
1·0 = 4·86° K Ta
$11^h 14^m$
$11^h 12^m$
$11^h 10^m$
−60°50'
−60°55'
−61°00'
−61°05'
−61°10'
Declination (1950·0)
PKS 1207−62
(h)
$l^{II}=298°10'$
$b^{II}=-0°20'$
$b^{II}=-0°20'$ Extended Component
~1°K
1·0 = 1·98° K Ta
$12^h 08^m$
$12^h 07^m$
$12^h 12^m$
$12^h 08^m$
−62°30'
−62°35'
−62°40'
−62°20'
−62°40'
Right ascension (1950·0)

Figs. 1(e)–1(h)

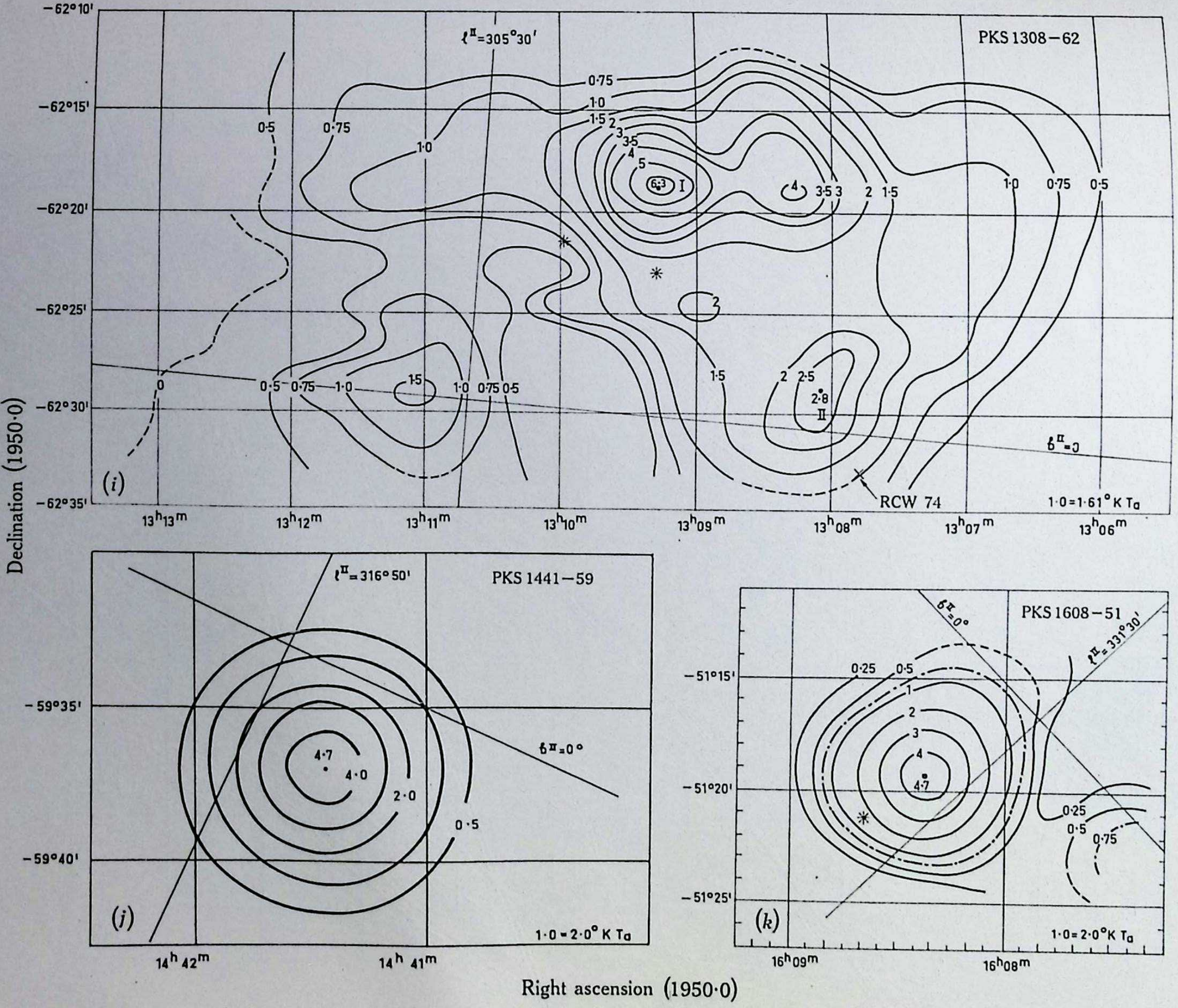

Figs. 1(*i*)–1(*k*).—The asterisks in (*i*) and (*k*) indicate OH emission.

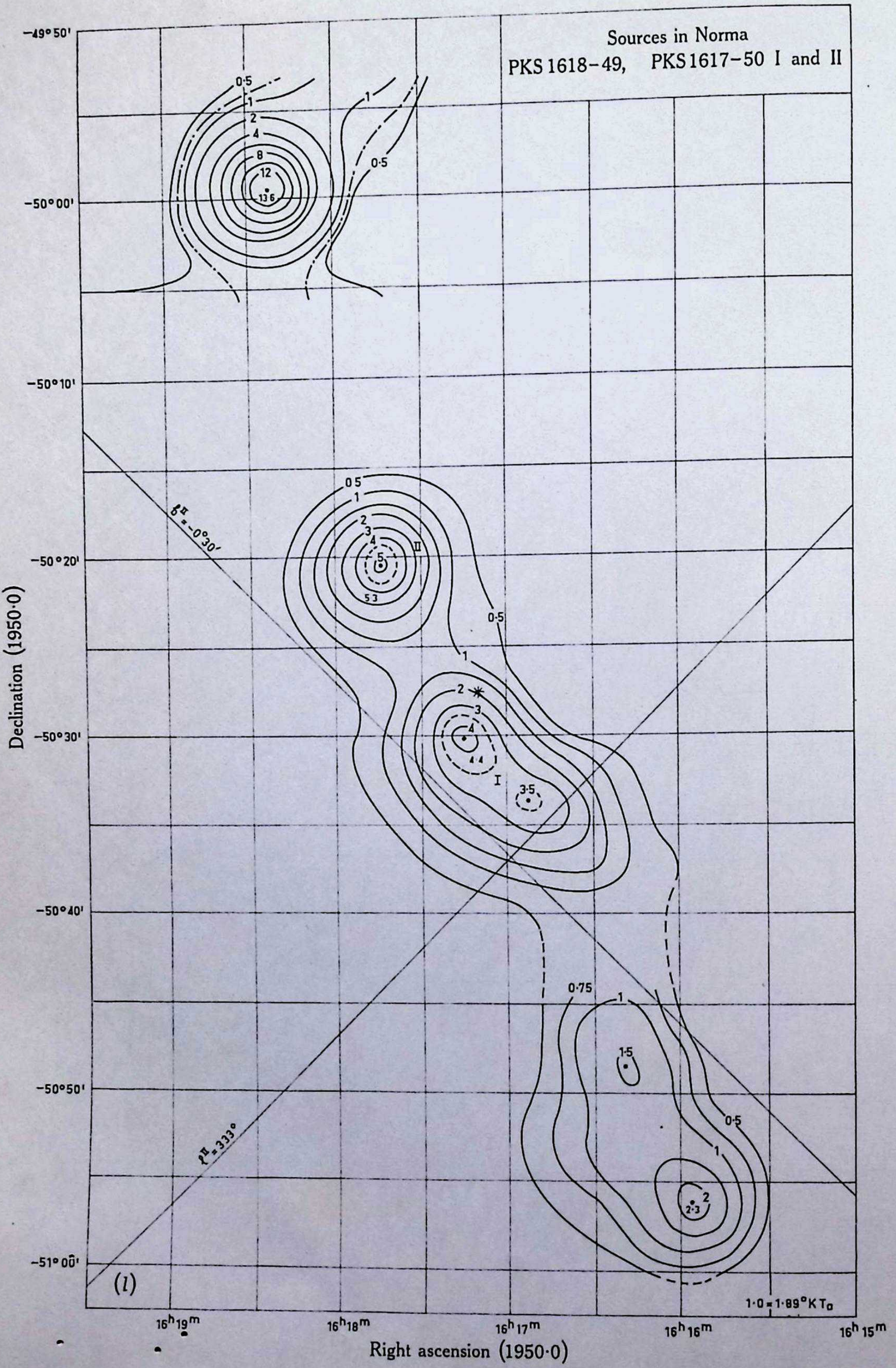

Fig. 1(*l*).—The asterisk indicates OH emission.

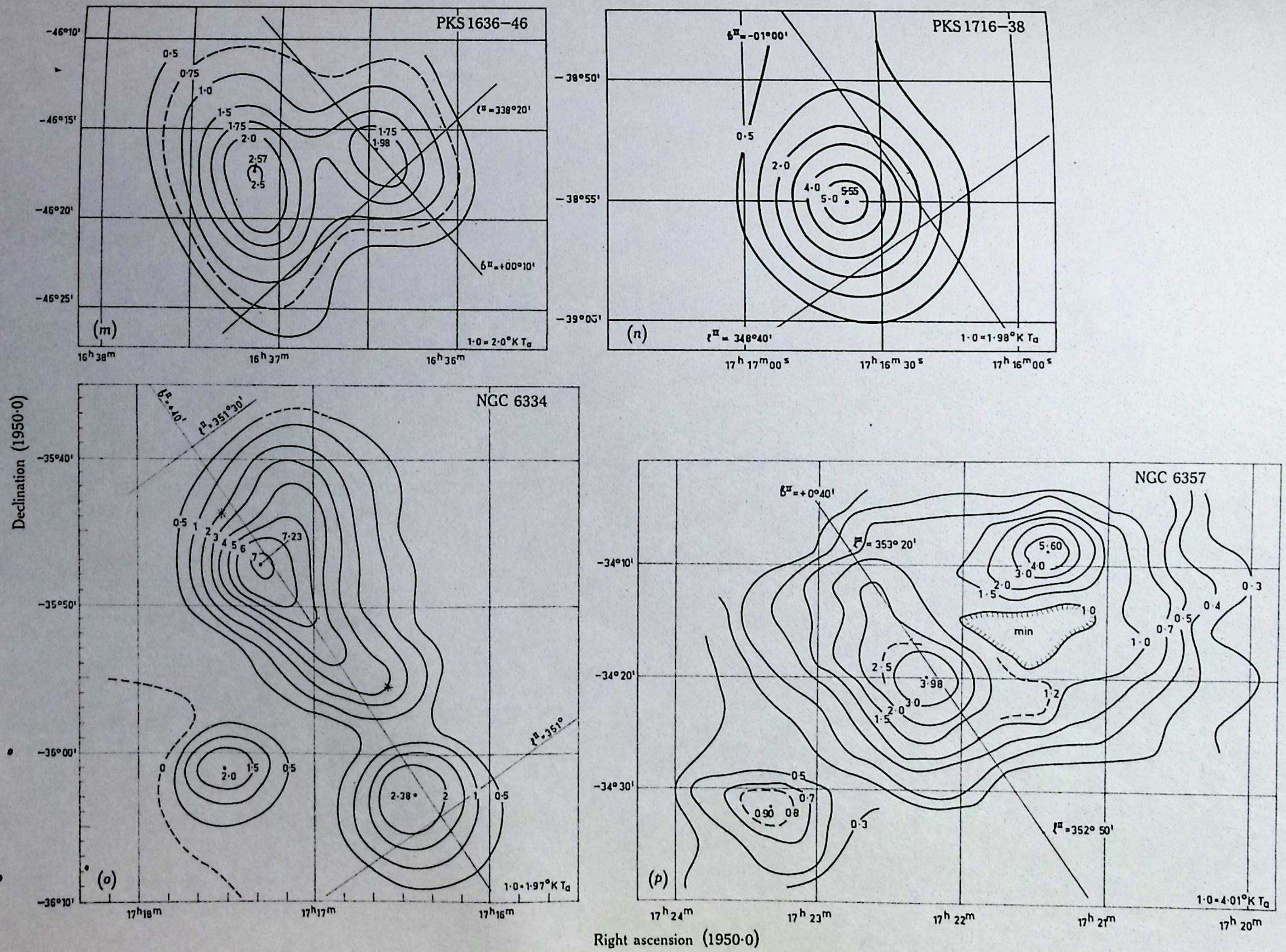

Figs. 1(*m*)–1(*p*).—The asterisks in (*o*) indicate OH emission.

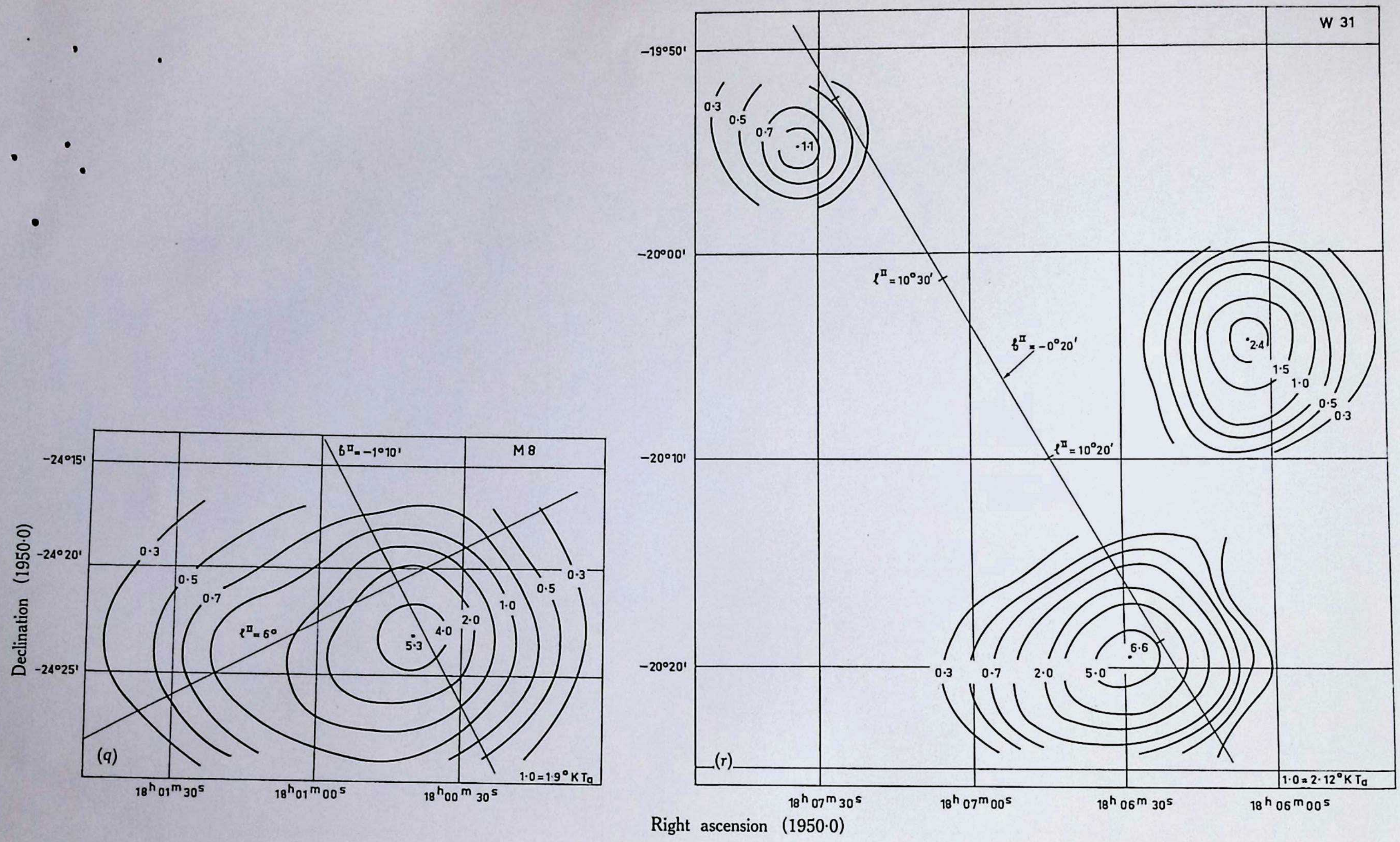

Figs. 1(*q*) and 1(*r*)

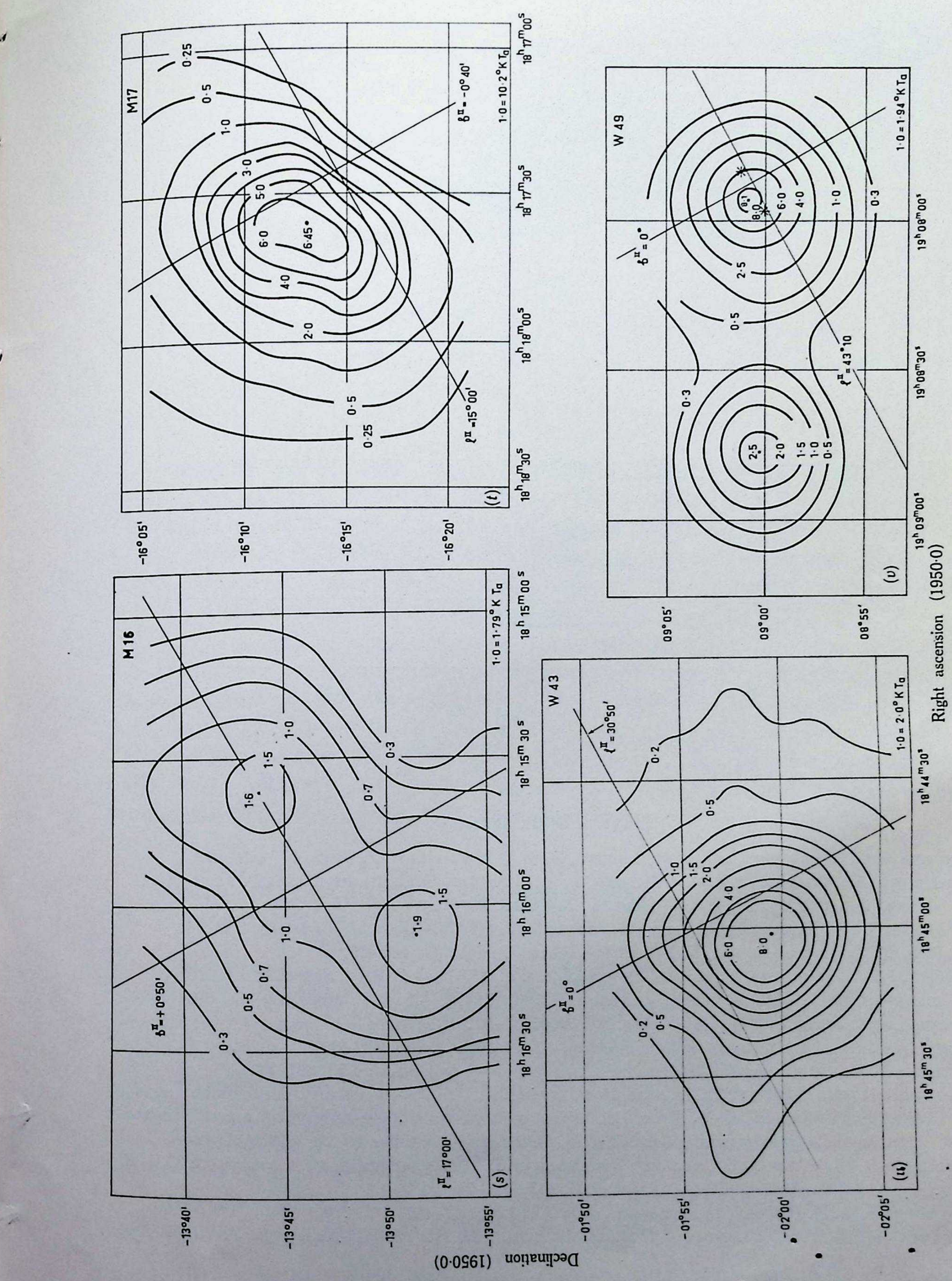

Figs. 1(s)–1(v).—The asterisks in (v) indicate OH emission.

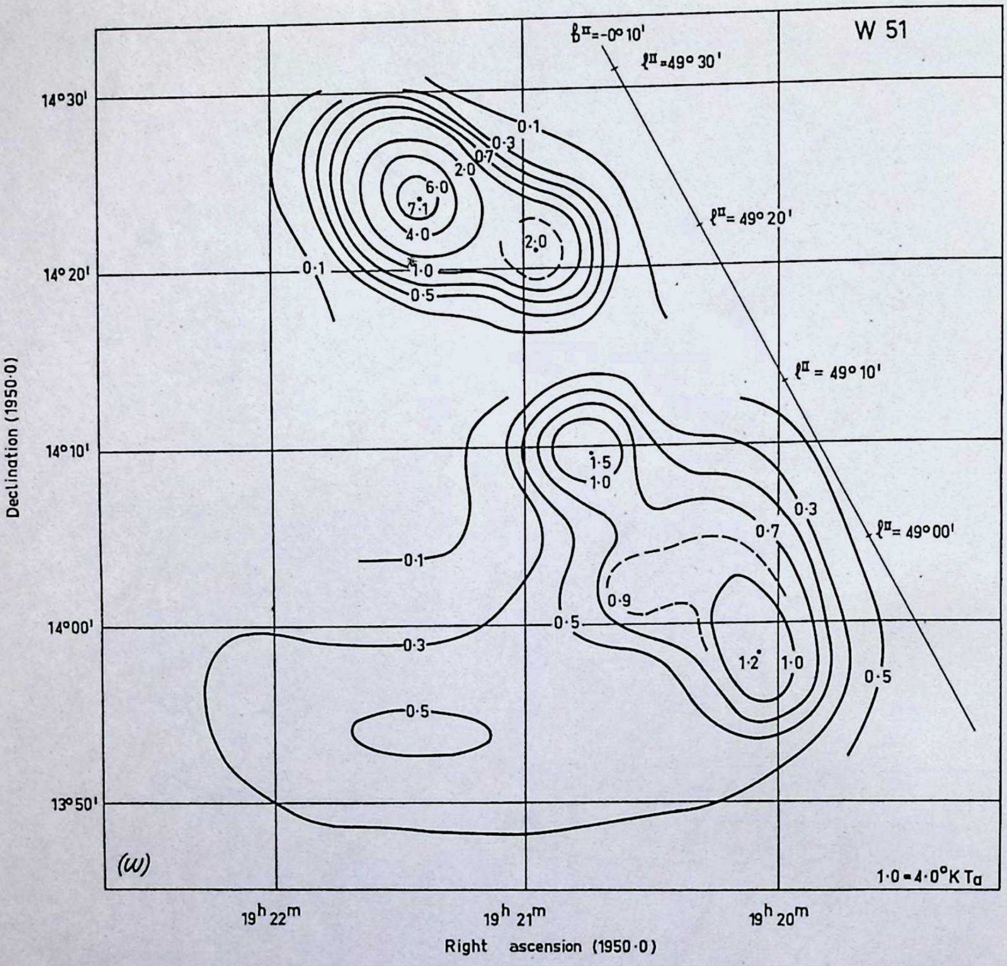

Fig. 1(*w*).—The asterisk indicates OH emission.

VIII. References

Bolton, J. G., Gardner, F. F., and Mackey, M. B. (1964).—*Aust. J. Phys.* **17**, 340–72.

Broten, N. W., Cooper, B. F. C., Gardner, F. F., Minnett, H. C., Price, R. M., Tonking, F. G., and Yabsley, D. E. (1965).—*Aust. J. Phys.* **18**, 85–90.

Gardner, F. F., McGee, R. X., and Robinson, B. J. (1967).—*Aust. J. Phys.* **20**, 309–24.

McGee, R. X., and Gardner, F. F. (1968).—*Aust. J. Phys.* **21**, 149–66.

McGee, R. X., Gardner, F. F., and Robinson, B. J. (1967).—*Aust. J. Phys.* **20**, 407–20.

Mathewson, D. S., Healey, J. R., and Romé, J. M. (1962).—*Aust. J. Phys.* **15**, 354–68.

Mezger, P. G., *et al.* (1967).—*Astrophys. J.* **150**, L157–66.

Mezger, P. G., and Henderson, A. P. (1967).—*Astrophys. J.* **147**, 471–89.

Mezger, P. G., Schraml, J., and Terzian, Y. (1967).—*Astrophys. J.* **150**, 807–23.

Minnett, H. C., Yabsley, D. E., and Puttock, M. J. (1967).—Structural performance of the Parkes 210-ft paraboloid. Proc. Int. Symp. on Structures Technology for Large Radio and Radar Telescope Systems, Mass. Inst. of Technology, October 18–20, 1967 (in press).

Rodgers, A. W., Campbell, C. T., and Whiteoak, J. B. (1960).—*Mon. Not. R. astr. Soc.* **120**, 1–8.

Rogers, A. E. E., *et al.* (1967).—*Astrophys. J.* **147**, 369–76.

Scheuer, P. A. G. (1960).—*Mon. Not. R. astr. Soc.* **120**, 231–41.

Weaver, H., Dieter, Nannielou H., and Williams, D. R. (1968).—*Astrophys. J. Suppl. Ser.* **16**, No. 146.

Westerhout, G. (1958).—*Bull. astr. Insts Neth.* **14**, 215–60.

OBSERVATIONS OF THE SOUTHERN SKY AT 10·02 MHz

By P. A. Hamilton* and R. F. Haynes*

[*Manuscript received August* 16, 1968]

Summary

The brightness distribution of cosmic radio noise has been surveyed at 10·02 MHz between declinations −2° and −65° with an aerial beam of 4° by 5°. The galactic plane appears as a region of low brightness. Spectra of sources observed are discussed.

I. Introduction

Recent low frequency surveys of the sky have shown the galactic plane in absorption as a region of low brightness. The results to date are consistent with the existence of a general ionized atmosphere within the galactic disk with an r.m.s. electron density of 0·1–0·2 cm^{-3}. While this conclusion is not inconsistent with other astronomical measurements, it may represent the first positive evidence on the nature of the interstellar intercloud medium.

It is therefore of some interest to obtain high resolution maps of sky brightness at a number of low frequencies in order to map the distribution of ionized hydrogen. A programme of such observations has been in operation in Tasmania since 1962 at frequencies of 2·1 MHz (Reber 1968), 4·7 MHz (Ellis and Hamilton 1966*a*), and 10·02 MHz reported here. Construction of a new radio telescope for the range 7–20 MHz has commenced and a higher frequency reference survey at 153 MHz has been completed (Hamilton and Haynes, in preparation).

II. Observations

(*a*) *Aerial System and Receiver*

The antenna consisted of a plane rectangular array of 24 by 15 half-wave dipoles at a height of a quarter-wave above the ground. The resulting beam to the half-power points was 4° by 5°. A plan of the array and the computed aerial space factors are given in Figure 1. The aerial system was situated at latitude 42·9° S. and longitude 147·0° E.

The receiver was a mutichannel instrument, using a variable intermediate frequency and delay cables to give six simultaneous beams. A detailed description of the receiver is given elsewhere (Hamilton 1968).

Considerable difficulty was experienced in finding channels free from transmitting-station interference, and the observing technique that has become standard

---

* Department of Physics, University of Tasmania, G.P.O. Box 252 C, Hobart, Tas. 7001.

Aust. J. Phys., 1968, **21**, 895–902

in Tasmania for low frequency measurements was adopted: The receiver centre frequency is swept over a frequency range of five to six times the passband. A transmitting station within this range then appears as a periodic impulse at the second detector. If the second detector is followed by a minimum reading d.c. amplifier (Ellis 1960), this impulse is ignored and the final record is free from the interference. This permits continuous automatic operation of the telescope without re-tuning as other stations appear. The success of this method depends on the separation of stations being greater than the receiver bandwidth, and a careful choice of sweep rate and second-detector time constant. The final i.f. bandwidth of the receiver was 2·1 kHz (−6 dB) and the receiver centre frequency was swept through 10 kHz five times a second. Approximately two-thirds of the records were reasonably clear of transmitting-station interference.

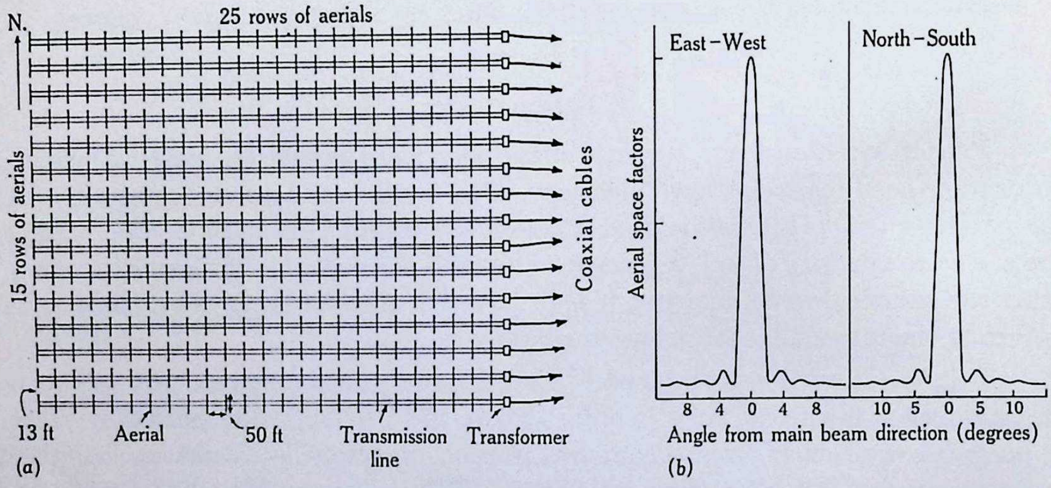

Fig. 1.—Details of the receiving system showing (*a*) a plan of the dipole array and feeds and (*b*) computed aerial space power factors (normalized).

(*b*) *Operation of Equipment*

The aerial phasing system required that all the r.f. amplifiers be adjusted to have identical phase shifts and gains, and so the whole receiver was re-aligned weekly, although the tests made on these occasions indicated that this was unnecessarily often. The gain of the system was held constant to within 5% by this method.

The telescope was operated in 1965 and 1966; observations were terminated prematurely in February 1967 when the array was destroyed in a bush fire.

(*c*) *Results*

Final records were chosen from night-time observations only, when ionospheric effects were negligible (Ellis 1965; Ellis and Hamilton 1966*a*). Sample records at eight declinations are given in Figure 2. The best records at each declination were selected for smoothness of trace, reproducibility, and absence of transmitting-station interference. Final profiles were then obtained by the method of Ellis and Hamilton, which assists the rejection of ionospheric effects.

The distribution of sky brightness is given in Figure 3 in galactic coordinates. The contour interval is chosen to bring the temperature of the featureless region in the vicinity of the south galactic pole into agreement with low resolution observations of the same region. We have taken the temperature of this region to be $6 \cdot 3 \times 10^5$ °K, as obtained by Higgins and Shain (1954) and independently by Ellis (1965). This makes the contour interval equal to 2×10^5 degK.

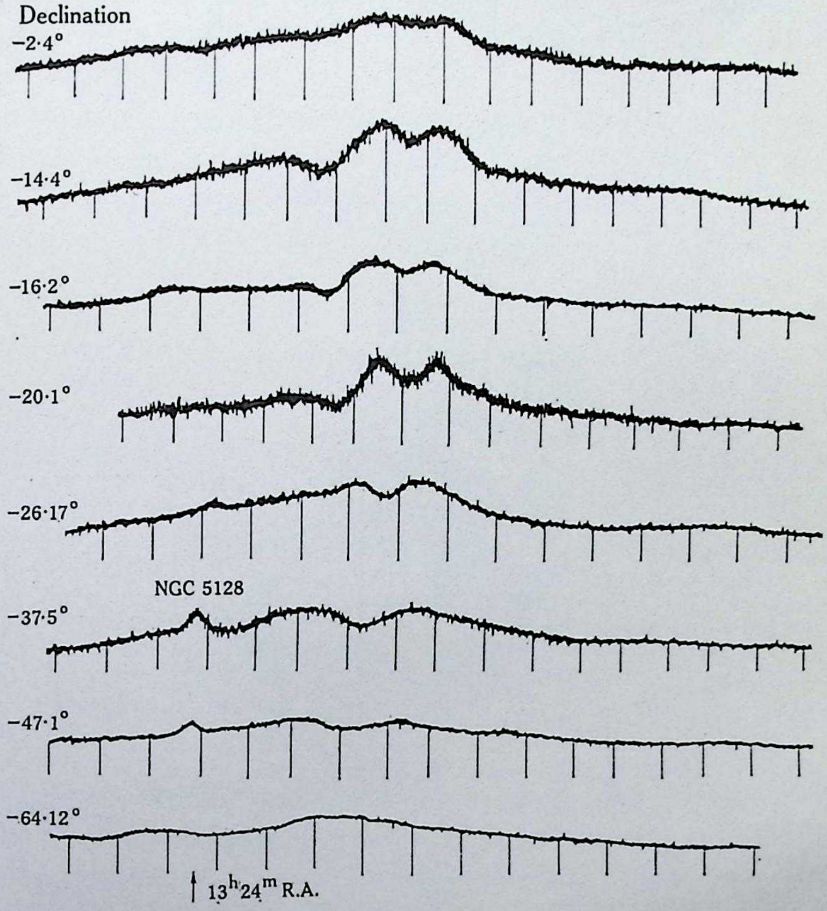

Fig. 2.—Sample records at eight declinations.

III. Discussion of Results

(a) *Background Survey*

The striking feature of all sky surveys at frequencies below 20 MHz is the band of low brightness lying along the galactic plane, reaching a minimum at the galactic centre. A preliminary analysis of low frequency surveys (Ellis and Hamilton 1964) has suggested that the Sun is embedded in a region of ionized hydrogen that is uniform to an angular scale of 1° as seen from the Earth. The absorption coefficient τ is given by

$$\tau \simeq 0 \cdot 2 E / T^{3/2} f^2,$$

where T is the electron temperature, f the wave frequency, and the emission measure

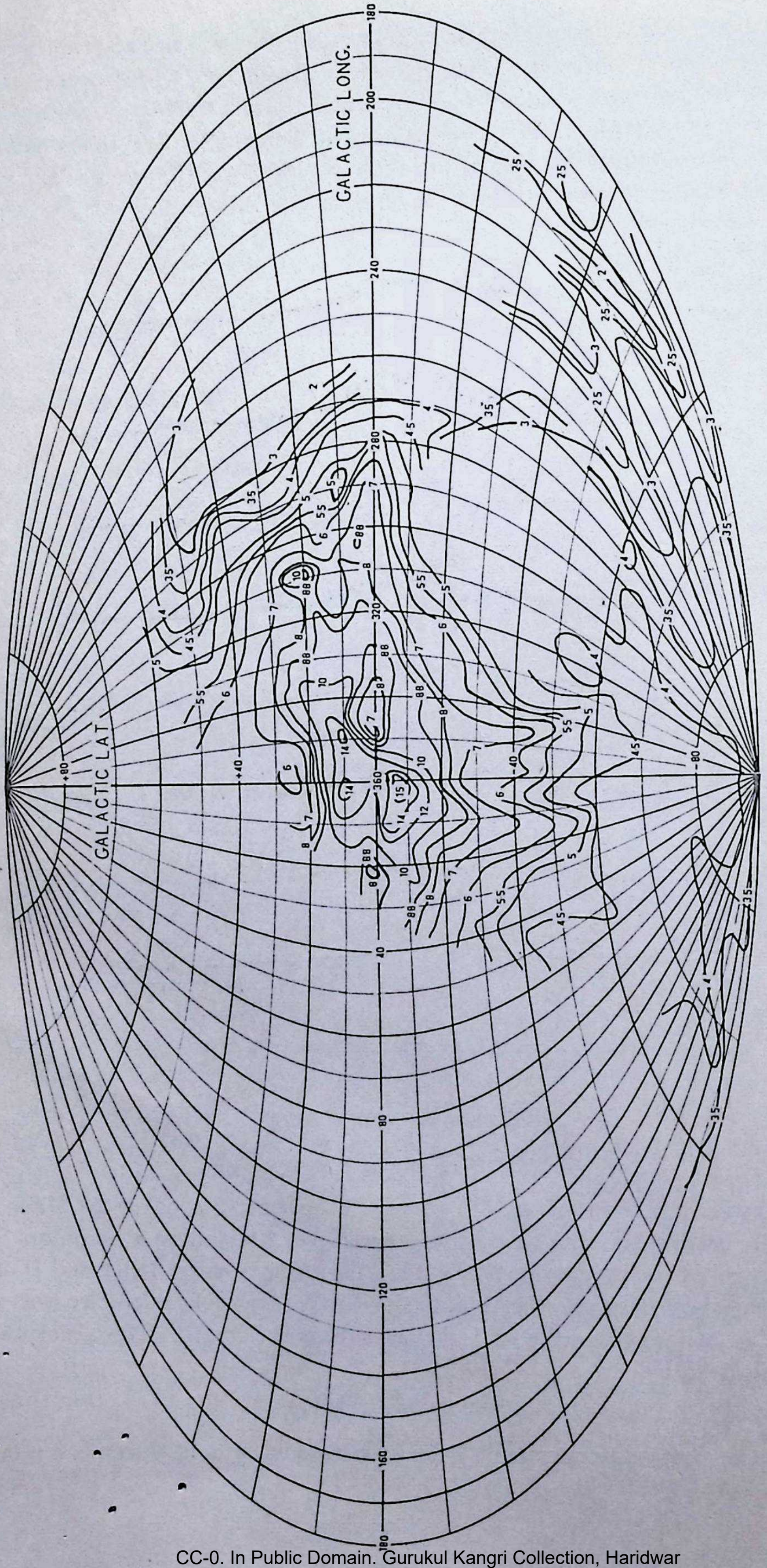
GALACTIC LONG.
180
200
240
280
320
360
40
80
120
160
180
GALACTIC LAT.
+80
+40
-40
-80

Fig. 3.—Background survey at 10·02 MHz (contour intervals of 2×10^5 degK).

E is given by

$$E=\int_0^L N^2\,\mathrm{d}l\,,$$

with N the electron density, and L the path length in the absorber. A single scan at declination $-37°$ has been analysed in detail (Ellis and Hamilton 1966*b*) for a model in which the observed radiation is the sum of the radiation from distant sources that has passed through this absorption together with radiation from within the ionized hydrogen region itself. Electron densities in the range $0{\cdot}1$–$0{\cdot}2\ \mathrm{cm}^{-3}$ were obtained for this model.

At low frequencies the absorption coefficient is a rapid function of frequency. Comparison of the present survey with other low frequency surveys would not therefore be expected to give good agreement. In fact only the broad features agree with those seen at 19·7 MHz (Shain, Komesaroff, and Higgins 1961) and 4·7 MHz (Ellis and Hamilton 1966*a*), and agreement is poor with the survey at 2·1 MHz (Reber 1968). At frequencies above 20 MHz the absorbing region becomes transparent and a resolution of 1° or better at 30 MHz is required before the galactic plane can be seen in absorption. The surveys at 30 MHz (Mathewson, Broten, and Cole 1965) and 85 MHz (Yates, Wielebinski, and Landecker 1967) were made with resolutions too low to enable direct comparison with the 10 MHz survey. However, these surveys can be used in an analysis of the type made by Ellis and Hamilton (1966*b*), and such a detailed analysis of the low frequency maps is in progress.

TABLE 1

FLUX DENSITIES OF SOURCES

PKS Catalogue Number	Position (1950·0) R.A. h m s	Dec. ° ′	Flux Density (f.u.) $S_{4\cdot7}$	$S_{10\cdot02}$	$S_{85\cdot5}$	S_{408}	S_{1410}	Remarks
0821 − 43			3600	2800	690			Puppis A not resolved
0834 − 46					1100			
1322 − 42	13 22 24	− 42 45·0	51000	43000	8700			Centaurus A
1343 − 60	13 43 19	− 60 10·0		1500	795	242	130	IAU 13S6A
1549 − 56	15 49 01	− 56 01·0	2000	1400	270	144	130	Nonthermal
1648 + 05	16 48 42	+ 05 04·5		7800	890	161	46·0	Herc. A
1711 − 38	17 11 18	− 38 24·0	1500	1600	300	196	77	Nonthermal

(*b*) *Discrete Sources*

(i) *Measurements*

Problems of transmitting-station interference mentioned earlier led to the combination of narrow bandwidth and short second-detector time constant. The resulting fluctuation in record levels was therefore rather high, making measurement of discrete sources difficult. The smallest observable flux density was calculated to be in the range 800–1400 f.u.,* depending on the background. The minimum reading d.c. amplifier caused further difficulty if the source was scintillating due to ionospheric irregularities.

---

* 1 flux unit $= 10^{-26}\,\mathrm{W\,m^{-2}\,Hz^{-1}}$.

The flux densities of those sources whose records reproduced accurately a sufficient number of times are given in Table 1, together with their flux densities at 4·7 MHz (Ellis and Hamilton 1966*a*), 85·5 MHz (Mills, Slee, and Hill 1960), and 408 and 1410 MHz (Parkes catalogue: Bolton, Gardner, and Mackey 1964; Price and Milne 1965; Day *et al.* 1966; Shimmins *et al.* 1966).

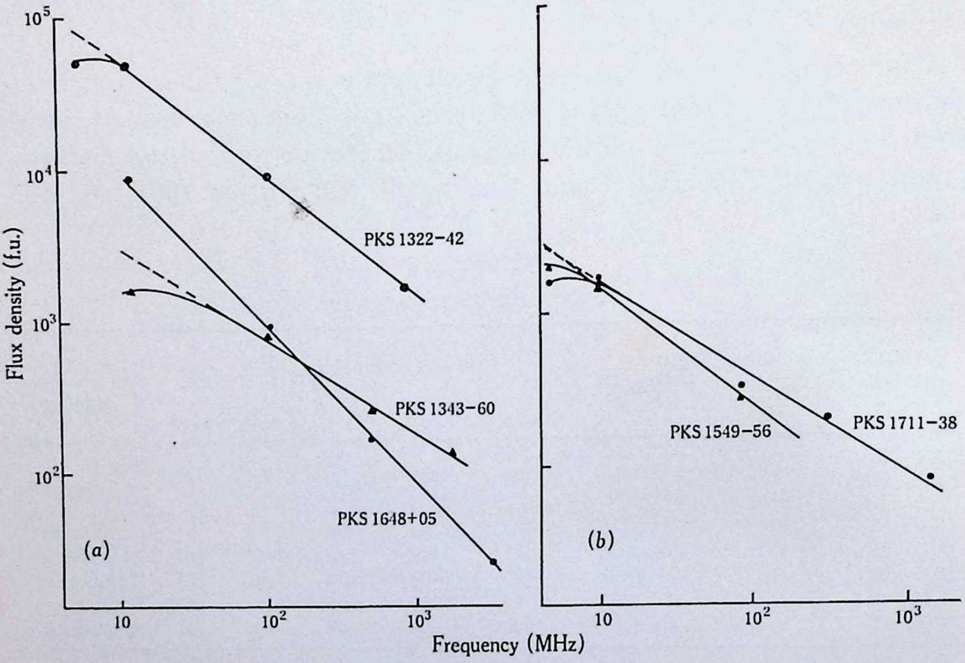

Fig. 4.—Spectra of sources measured at 10·02 MHz.

(ii) *Discussion*

Comparing the results at 10·02 MHz with the other observations given in Table 1 (see Fig. 4), it can be seen that none of the measured sources show any increase in spectral index at low frequency. (The spectral index α is defined by the relation $S = Af^{-\alpha}$, where S is the source flux density, f the frequency, and A a constant.)

Four of the sources (PKS 1322−42, 1343−60, 1549−56, and 1711−38) show definite curvature at low frequencies, some of which is due to absorption within the galactic disk. The preliminary work of Ellis and Hamilton (1966*b*) suggests that the low frequency absorption results from a layer of ionized hydrogen within the disk. The observed flux density S is then related to the emitted flux density S_0 by

$$S = S_0 \exp(-\zeta E/T^{3/2}f^2),$$

where T is the electron temperature within the absorber, f is the wave frequency, E is the emission measure along the line of sight within the absorber, and ζ is a factor that $\simeq 0·2$ at these frequencies (Ginzburg 1964). Ellis and Hamilton found that the emission measure was approximately proportional to cosec b (where b is the galactic latitude) for $30° \leqslant b \leqslant 90°$, while it increased at a somewhat faster rate as $b \to 0$. They obtained emission measures of $8 \cdot 1$ cm^{-6} pc for $b = 60°$ and 165 cm^{-6} pc for $b = 5°$.

Taking these results it is possible to obtain the spectrum for PKS 1322−42 as seen outside the galactic disk, since for $b \simeq 21°$ we would expect the emission measure along the line of sight to be ~ 30 cm^{-6} pc. This spectrum is shown as the dashed line in Figure 4(a), and it is apparent that the emission spectrum of the source is linear down to 4·7 MHz. The emission is consistent with synchrotron radiation from a region with an electron energy distribution of the form

$$N(E)\,\mathrm{d}E = KE^{-\gamma}.$$

The spectral index of 0·7 gives $\gamma = 2 \cdot 4$.

The three remaining sources showing curvature in their spectra are all at galactic latitudes of 2° or less. Ellis and Hamilton were unable to give emission measures at such low galactic latitudes because of the limited resolution of the surveys on which their calculations were based. However, it can be asserted that the emission measures along these three lines of sight to the edge of the galactic disk are all well in excess of the value of 165 cm^{-6} pc given for $b = 5°$. If we assume that the emission spectra of these sources are linear to 10 MHz and that the observed curvature is the result of interstellar absorption, we can calculate the emission measures required to produce this absorption, and these results are given below.

Source	Coordinates l^{II}	b^{II}	Emission Measure (N^2L cm^{-6} pc)	L for $N = 0 \cdot 2$ cm^{-3} (pc)
PKS 1343−60	309·8	2·1	93	2300
PKS 1549−56	326·3	−1·7	31	760
PKS 1711−38	349·2	0·6	49	1240

The emission measures obtained indicate that either the sources are galactic objects or the emission spectra have sharp increases in spectral index at low frequencies. If the emission measures are correct and the sources are galactic, we can estimate the distances from these sources to the Sun. Taking $N = 0 \cdot 2$ cm^{-3} (Ellis and Hamilton 1966b), we obtain the distances shown above. The source PKS 1343−60 (IAU 1356A) has been identified by Shlovsky as a supernova remnant but no distance estimate has been made from optical measurements. The other sources have not been identified with optical objects.

IV. ACKNOWLEDGMENTS

We wish to acknowledge advice and assistance from Professor G. R. A. Ellis throughout this survey. One of us (R.F.H.) is indebted to CSIRO for support in the form of a Senior Post-graduate Scholarship. The radiophysics group within the Department of Physics, University of Tasmania, is supported financially by grants from the Australian Research Grants Committee and the Radio Research Board.

V. References

Bolton, J. G., Gardner, F. F., and Mackey, M. B. (1964).—*Aust. J. Phys.* **17**, 340.

Day, G. A., Shimmins, A. J., Ekers, R. D., and Cole, D. J. (1966).—*Aust. J. Phys.* **19**, 35.

Ellis, G. R. A. (1960).—*Proc. Instn Radio Engrs Aust.* **48**, 1950.

Ellis, G. R. A. (1965).—*Mon. Not. R. astr. Soc.* **130**, 429.

Ellis, G. R. A., and Hamilton, P. A. (1964).—*Nature, Lond.* **204**, 272.

Ellis, G. R. A., and Hamilton, P. A. (1966*a*).—*Astrophys. J.* **143**, 227.

Ellis, G. R. A., and Hamilton, P. A. (1966*b*).—*Astrophys. J.* **146**, 78.

Ginzburg, V. L. (1964).—"Propagation of Electromagnetic Waves in a Plasma." (Pergamon Press: Oxford.)

Hamilton, P. A. (1968).—*Proc. Instn Radio Engrs Aust.* **29**, 56.

Higgins, C. S., and Shain, C. A. (1954).—*Aust. J. Phys.* **7**, 460.

Mathewson, D. S., Broten, N. W., and Cole, D. J. (1965).—*Aust. J. Phys.* **18**, 665.

Mills, B. Y., Slee, O. B., and Hill, E. R. (1960).—*Aust. J. Phys.* **13**, 676.

Price, R. M., and Milne, D. K. (1965).—*Aust. J. Phys.* **18**, 329.

Reber, G. (1968).—*J. Franklin Inst.* **285**, 1.

Shain, C. A., Komesaroff, M. M., and Higgins, C. S. (1961).—*Aust. J. Phys.* **14**, 508.

Shimmins, A. J., Day, G. A., Ekers, R. D., and Cole, D. J. (1966).—*Aust. J. Phys.* **19**, 837.

Yates, K. W., Wielebinski, R., and Landecker, T. L. (1967).—*Aust. J. Phys.* **20**, 597.

ACCURATE POSITIONS AND IDENTIFICATIONS OF 75 RADIO SOURCES BETWEEN DECLINATIONS +20° AND +27°

By Jeannette K. Merkelijn*

[*Manuscript received June* 17, 1968]

Summary

Accurate positions have been obtained for 75 sources between declinations +20° and +27°. For most sources the estimated error is less than 15″ arc in each coordinate. Identifications are suggested for 27 sources from inspection of the Palomar Sky survey prints near the new positions. Fourteen of the suggested identifications are galaxies and 13 are quasi-stellar objects.

I. Introduction

Bolton, Shimmins, and Merkelijn (1968) and Merkelijn, Shimmins, and Bolton (1968) have recently reported a number of identifications using transit positions of sources from the +20° to +27° Parkes catalogue (Shimmins and Day 1968). Additional accurate position measurements have now been made of the remainder of the catalogue sources in this region for which identifications appeared likely on the basis of their catalogue positions. In contrast to the previous accurate position measurements, which were done at transit, the present observations were made within a fairly wide range of hour angle. This was possible because of a recent improvement in the pointing of the 210 ft telescope.

The work described in this paper is part of a programme in which more precise positions are being determined for all sources in the Parkes catalogue for which identifications have been suggested or appear possible from their catalogue positions.

II. Equipment

The 210 ft telescope at Parkes was used for the position measurements. Considerable improvement has been made to the pointing accuracy of this instrument by isolating the central tower on which the master equatorial is mounted from the floors of the main tower on which the telescope is supported. Although such isolation was envisaged in the design of the instrument it was not in fact achieved in the construction, as compression and partial penetration by concrete of the isolating material occurred during pouring of the floors. Further links were inadvertently provided by some pipes and conduits which were buried beneath the final concrete surface. A clear air gap has now been achieved at all floor levels. Subsequent observations of calibrator sources showed that the effects of diurnal temperature and wind loads transmitted from the main tower to the master equatorial column had been greatly reduced and it was possible to determine fairly accurately a pointing error in azimuth as a function of zenith angle. Compensation has been introduced into the control system for this error, which amounts to 24″ arc at 60°

---

* Division of Radiophysics, CSIRO, P.O. Box 76, Epping, N.S.W. 2121.

zenith angle. It had previously been difficult to determine this error because it was masked by the thermal and wind effects. It is believed that the modification permits measurements to be made north of —33° at any hour angle with an accuracy comparable to that reached in the old transit measurements.

The observations were made at 2700 MHz using a broad band hybrid-junction radiometer. The radiometer is equipped with a dual feed system. One of the feeds coincides with the optical axis of the telescope; the second feed is offset by 18′·5 arc. The receiver effectively records the difference between the signals received at the two feeds. The result is that a source in the on-axis beam appears as a positive deflection on the recorder chart, while a source in the offset beam appears as a negative deflection.

The receiver has an i.f. bandwidth of 200 MHz and a system noise temperature of 80°K. With a 2 sec output time constant the peak-to-peak noise fluctuations are approximately 0·06 degK (0·11 f.u.*) and short-term receiver instabilities are of the same order.

A full description of the radiometer and feed system is given by Batchelor, Brooks, and Cooper (1968). The beam shape was approximately Gaussian with a width of 7′·6 arc at half-intensity points. A typical record is given by Merkelijn, Shimmins, and Bolton (1968, Fig. 1).

III. OBSERVATIONS

The observations were made between January 12 and January 17, 1968. All sources were observed between hour angles $22^h 30^m$ and $0^h 30^m$. Calibrator sources in or near the +20° to +27° zone were observed at approximately two-hourly intervals throughout the observations. The sensitivity of the receiver was calibrated at the end of each position observation by injecting a 1°K noise signal. The same method was used for measuring both right ascension and declination. The telescope was set on one coordinate and several scans in the other coordinate were made through the source in both directions at a rate of 0·5 deg/min. The receiver output was recorded on a paper chart run at 80 mm/min. Markers were recorded on the same trace at every 5′ arc in declination or 20^s in right ascension.

The feed system was set at position angle 0° for the right ascension scans and 90° for the declination scans; in this way any marked polarization could be seen, and the average was used for the determination of the flux density. In the few cases where there was a confusing source in the offset reference beam, additional measurements were made at other position angles of the feed to eliminate or reduce the confusion effect.

IV. ANALYSIS OF OBSERVATIONS

The records were all analysed by hand. For most sources the apparent right ascensions or declinations were determined from the centre of symmetry of the scans. For those observations where there was evidence of a confusing source or second component an attempt was generally made to determine the position of the second source; in such cases the nearby sources are listed in the results (Table 2). Where it was not possible, the presence of a confusing source is noted in the table. A correction for the receiver time constant was applied to each scan, after which the average of each set of scans was determined. The averaged values were calibrated by the procedure described in Section V. All observed right ascensions and declinations were then precessed to epoch 1950·0.

---

* 1 flux unit = 10^{-26} W m^{-2} Hz^{-1}.

The flux density of each source was determined by measuring for each coordinate the peak amplitude of the smoothed record relative to the baseline, applying a correction for any error in the set coordinate, and averaging the resultant values. No attempt was made to determine the integrated flux for extended sources; the values given in Table 2 are peak flux densities.

TABLE 1

POSITION CALIBRATORS, DECLINATIONS +20° TO +27°

PKS Catalogue Number	Position (1950·0) R.A. h m s	Dec. ° ′ ″	Flux Density (f.u.) S_{21}	S_{11}	References‡	Other Catalogue Numbers
0017+15	00 17 49·83	+15 24 16·5	2·1	1·1	3	3C 9
0229+13	02 29 02·35	+13 09 41·0	1·2	1·4	6	
0316+16*	03 16 09·1	+16 17 41·2	8·2	5·27	2	CTA 21
0518+16†	05 18 16·51	+16 35 26·2	9·3	6·25	3	3C 138
0725+14	07 25 20·10	+14 43 47·3	2·1	1·1	6	3C 181
0903+16	09 03 44·15	+16 58 15·7	1·4	0·8	3	3C 215
1040+12†	10 40 06·03	+12 19 15·0	3·0	2·10	6	3C 245
1116+12	11 16 20·79	+12 51 06·3	1·9	1·7	1	4C 12·39
1241+16	12 41 27·68	+16 39 18·7	2·9	1·5	3	3C 275·1
1328+25A	13 28 16·12	+25 24 37·1	7·0	5·5	4	3C 287
1510−08†	15 10 08·90	−08 54 48·0	3·4	3·2	6	
1622+23	16 22 32·45	+23 52 00·7	2·7	1·5	3	3C 336
2120+16	21 20 25·64	+16 51 46·0	1·7	0·7	5	3C 432
2249+18	22 49 59·56	+18 38 30·3	2·4	1·2	5	3C 454
2251+15	22 51 29·46	+15 52 53·6	12·8	10·0	6	3C 454·3
2354+14	23 54 44·70	+14 29 26·0	1·4	0·5	7	4C 14·85

* Flux calibrator, occultation.

† Flux calibrators.

‡ References to positions used are: 1, Bolton *et al.* (1965); 2, Clarke and Batchelor (1965); 3, Sandage, Véron, and Wyndham (1965); 4, Véron (1965); 5, Véron (1966); 6, Bolton (1968); 7, Kinman (personal communication).

V. CALIBRATION AND ERRORS

(*a*) *Calibration Procedure*

The measured positions were corrected for time constant, hour-angle, and diurnal pointing errors by using observations of the calibrators in Table 1. The value of the time-constant correction was calculated by averaging scans in opposite direction for the position calibrators. The hour-angle pointing correction was determined by plotting the differences between observed and true positions of the calibrators against hour angle. The results are given in Figure 1.

After removing the hour-angle error, the position errors for the calibrators were plotted against sidereal time. There was no clear diurnal effect for the days on which the observations were made. Corrections for the short-term time-dependent error were made with respect to adjacent calibrators.

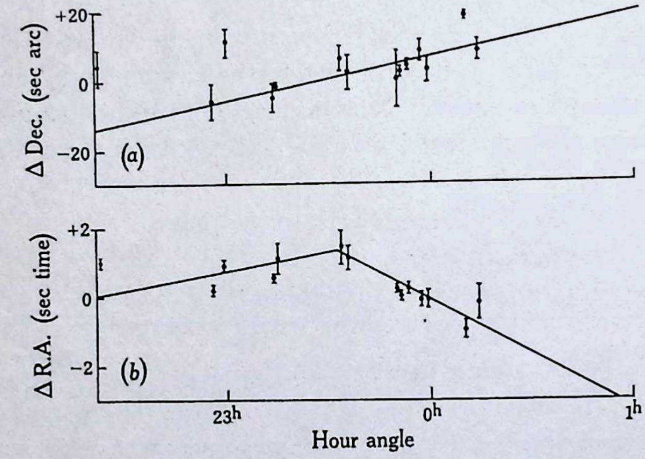

Fig. 1.—Differences between calibrator positions and observed radio positions, plotted against hour angle, for (*a*) declination, and (*b*) right ascension.

(*b*) *Errors*

The r.m.s. errors per scan e_s for a sample of sources were calculated from

$$e_s = \{\Delta(x_a - x_s)^2/(n-1)\}^{\frac{1}{2}},$$

where x_a is the position averaged over n scans, x_s the position obtained from a single scan (corrected for time constant), and n the number of scans per coordinate. The expression $\Delta(x_a - x_s)^2$ represents the errors in the determination of the centre of the scan due to receiver noise.

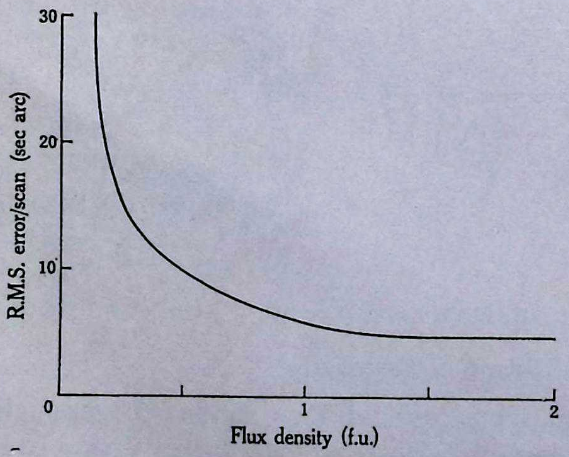

Fig. 2.—R.M.S. receiver noise error per scan plotted against flux density at 2700 MHz.

The r.m.s. errors per scan plotted against flux density are given in Figure 2. The errors seem to be slightly larger than in the previously published transit observations (Merkelijn, Shimmins, and Bolton 1968). This is probably due to higher

TABLE 2

POSITIONS OF RADIO SOURCES, DECLINATIONS +20° TO +27°

(1)	(2)	(3)	(4)	(5)	(6)	(7)	(8)	(9)	(10)	(11)	(12)	(13)	(14)	(15)	(16)	(17)
PKS Catalogue Number	Radio Position (1950·0) R.A. h m s	Dec. ° ′ ″	No. of Scans R.A.	Dec.	R.M.S. Error R.A. ″	Dec. ″	Optical Posn. relative to Radio Source R.A. s	Dec. ′	Ident.	Mag.	S_{11}	S.I.	Remarks	Galactic Coords. l^{II} °	b^{II} °	Other Catalogue Numbers
0035+23	00 35 19·2	+23 50 41	2	2	8	9	0·2 p.	0	QSO?	19	0·70	0·5		119	−39	CTD 5
0039+21	00 39 04·6	+21 07 09	4	2	8	12			III		0·41	0·7	Faint gals. 0′·5 n.p.	120	−41	4C 21·5
0044+23	00 44 06·0	+23 55 43	4	4	11	12			III		0·25	1·0	Blue object 0′·7 p.	122	−39	4C 23·3
0055+26	00 55 41·5	+26 35 34	2	2	7	8	0·5 p.	0·1 N.	E2	14·5	1·07	0·6		125	−36	4C 26·3 CTD 7
0117+22	01 17 48·3	+22 40 31	2	4	11	8			III		0·44	0·7		132	−39	NPC
0123+25	01 23 56·9	+25 43 04	4	4	8	8	1·0 f.	0·2 N.	QSO	18	0·54	C	$z = 2{\cdot}36$ (Schmidt, personal comm.); weak source 10′ S.	133	−36	4C 25·5
0124+22	01 24 23·5	+22 57 58	6	4	11	16	1·5 p.	0·2 S.	g	19·5	0·18	1·3		133	−39	4C 23·5
0130+24	01 30 39·5	+24 12 31	3	4	9	8	0·2 p.	0·2 S.	QSO	17	0·44	0·9	Schmidt (personal comm.)	135	−37	4C 24·2
0149+21	01 49 28·5	+21 52 06	2	3	7	7			III		1·22	0·6		141	−39	NPC
0152+24	01 52 08·6	+24 11 49	4	4	10	12			III		0·27	1·0	Blank field	141	−36	4C 24·3
0222+26	02 22 24·2	+26 39 28	4	4	9	10	0·2 f.	0·2 S.	g	20	0·35	1·0		148	−31	4C 26·8
0248+21	02 48 04·8	+21 08 54	4	4	8	8			III		0·46	0·6		157	−34	4C 21·10
0327+24	03 27 02·2	+24 06 18	4	4	9	10			III		0·32	1·0		163	−26	4C 24·7
0340+20	03 40 02·4	+20 51 23	4	4	9	9			III		0·38	0·9	Possible blue object 0′·4 n.f.	168	−26	4C 20·12
0349+21	03 49 44·4	+21 17 28	4	4	9	9	0·2 f.	0·2 S.	E2–3	18	0·37	0·7		170	−25	4C 21·13
0350+23	03 50 00·4	+23 07 15	4	4	10	11			III		0·30	0·8		168	−23	4C 23·7
0403+20	04 03 23·4	+20 48 26	4	4	8	8			III		0·44	0·9		172	−23	4C 20·13
0418+23	04 18 20·0	+23 42 03	4	4	10	11			III–IV		0·30	0·9		173	−18	4C 23·8
0421+21	04 21 17·3	+21 19 34	2	2	9	9			III–IV		0·64	0·8	Faint gals. within 1′ of posn.	175	−19	4C 21·16
0425+21	04 25 47·1	+21 27 13	2	2	8	8			III–IV		0·79	0·5		176	−18	4C 21·17
0428+20	04 28 05·3	+20 31 21	2	2	7	8			III		3·18	C		177	−19	NPC
0452+23	04 52 21·8	+23 05 34	4	4	8	9			III		0·41	0·8		178	−13	4C 23·12
0600+21	06 00 50·8	+21 59 55	2	2	8	8			III–IV		0·75	0·6		188	0	4C 22·12
0623+2[illegible]	06 23 48·9	+26 24 59	2	4	8	7	0·9 p.	0·1 N.	g	19·5	1·00	0·5		187	7	4C 26·22 CTD 44 3C 160 NRAO 235

TABLE 2 (*Continued*)

(1)	(2)	(3)	(4)	(5)	(6)	(7)	(8)	(9)	(10)	(11)	(12)	(13)	(14)	(15)	(16)	(17)
PKS Catalogue Number	Radio Position (1950·0) R.A. h m s	Dec. ° ′ ″	No. of Scans R.A.	Dec.	R.M.S. Error R.A. ″	Dec. ″	Optical Posn. relative to Radio Source R.A. s	Dec. ′	Ident.	Mag.	S_{11}	S.I.	Remarks	Galactic Coords. l^{II} °	b^{II} °	Other Catalogue Numbers
0628+25	06 28 19·2	+25 03 11	4	4	7	7	1·5 p.	0	E1	17	0·58	0·9		188	7	4C 25·18 CTD 45 3C 162 NRAO 237
0825+23	08 25 50·4	+23 29 52	6	6	11	14			III		0·16			201	31	NPC
0832+26	08 32 11·8	+26 44 55	6	6	9	10			III		0·27	2·0		198	34	CTD 56
0934+25	09 34 16·7	+25 34 23	4	4	11	13			III		0·23	1·0	19^{m}·5 gal. 0′·5 n.p.	204	47	4C 25·27
0951+21	09 51 19·3	+21 36 48	2	2	10	10	1·1 f.	0·2 N.	QSO?	20	0·54	0·7		211	49	4C 21·26
1000+20	10 00 11·4	+20 06 40	2	2	8	9	0·2 p.	0·2 S.	g	19·5	0·71	0·7		214	51	4C 20·20
1002+22	10 01 56·5	+22 40 03	4	4	9	10	1·5 f.	0·3 S.	QSO?	18	0·35	1·0		211	52	4C 22·26
1019+25	10 19 20·9	+25 38 32	3	3	9	10	1·1 f.	0·1 S.	QSO?	18	0·42	0·8		207	57	4C 25·32
1022+20	10 22 36·5	+20 25 27	2	2	9	9			III		0·62	0·8	Blue object in field is K star (Bolton and Kinman, personal comm.)	217	56	4C 20·22
1049+21	10 49 06·9	+21 35 55	2	2	7	8	1·0 f.	0·1 N.	QSO?	19	1·40	0·2		218	62	4C 21·28
1055+20	10 55 36·9	+20 08 20	2	2	7	8	1·0 f.	0·3 S.	QSO	18·5	1·65	0·6	$z = 1 \cdot 11$ (Bolton and Kinman, personal comm.)	222	63	4C 20·24
1119+21	11 19 52·7	+21 42 02	3	3	10	10	1·0 p.	0·1 S.	E0	19	0·38	1·3	Brightest gal. in cluster	224	69	NPC
1123+20A	11 23 16·7	+20 08 38	2	3	9	8			III		0·58	—		229	69	4C 20·25
1123+20B	11 23 22·8	+20 22 19	3	3	12	14	1·0 p.	0·1 S.	N	18	0·25	—		228	69	NPC
1125+26	11 25 27·5	+26 02 15	4	4	12	14			III		0·22	1·0	Faint gal. 1′ S. Ext. or conf. to N. (10′)	212	71	4C 25·35
1134+26	11 34 53·3	+26 36 06	4	4	12	14			III		0·22	1·0	Blue object 0′·5 f.	211	73	4C 26·33
1139+23A	11 38 56·9	+23 26 05	4	3	11	15			III		0·24	1·5	Nearest gal. of cluster 0′·5 f.	223	74	4C 23·28
1150+26	11 50 12·5	+26 30 48	4	4	12	14			III		0·21	1·1		213	77	4C 26·34
1150+22	11 50 34·0	+22 46 01	4	4	21	24			III		0·12	1·2		229	76	4C 22·32
1151+22	11 51 38·0	+22 46 01	4	4	23	25			III		0·11	1·1		229	76	NPC
1201+24	12 01 05·7	+24 00 30	4	4	12	14			III		0·22	1·4		228	79	NPC
1202+26	12 02 50·2	+26 51 05	4	4	12	14			III		0·22	1·0	Faint gals. within 1′. Faint source 10′ S.	213	80	4C 26·36

1210+24	12 10 14·6	+24 14 29	4	4	14	18			III		0·15	1·2		231	81	4C 24·25
1215+25	12 15 24·4	+25 46 02	2	2	11	12	1·0 f.	0	QSO?	18	0·44	0·9		223	82	4C 25·39 3C 269 NRAO 394
1216+20	12 16 28·5	+20 12 33	4	4	7	7	1·1 f.	0·3 S.	g	20·5	0·58	0·8		255	80	4C 20·28
1257+23	12 57 51·7	+23 45 03	4	6	13	14			III		0·16	1·1		332	86	4C 23·34
1323+24	13 23 29·6	+24 48 16	4	4	18	22			III		0·13	1·3		16	82	NPC
1328+25B	13 28 57·0	+25 06 17	4	4	9	10			III		0·32	1·2	Ext. or conf. to N. (~ 7′). Near PKS 1328+25A (3C 287)	21	81	4C 25·44
1422+26	14 22 25·4	+26 51 02	4	4	8	8	0·8 f.	0·1 S.	E2	15	0·54	0·9		37	69	CTD 86
1437+22	14 37 38·6	+22 03 55	4	4	10	11	0·1 p.	0·1 S.	N	19·5	0·29	0·8		27	65	4C 22·42
1444+21	14 44 34·3	+21 44 13	4	4	9	10	0·1 p.	0·1 N.	QSO?	19	0·33	0·9	N.f. object of pair	27	63	4C 21·42
1446+20	14 46 32·7	+20 38 07	6	6	7	7			III		0·54	0·9		25	62	4C 20·34 3C 304 NRAO 454
1459+21A	14 59 13·2	+21 46 31	4	4	12	15	0·8 p.	0·2 S.	g	20	0·20	—	Member of cluster	29	60	4C 21·44
1553+24	15 53 44·5	+24 14 55	3	4	13	14			III		0·22	1·0	Cluster of faint gals. in field	39	49	4C 24·35
1601+21	16 01 19·7	+21 35 11	6	7	9	9			III		0·28	1·3		36	46	NPC
1607+26	16 07 08·9	+26 49 22	2	2	7	8	1·1 f.	0·2 S.	QSO?	19	3·04	C	Gal. 0′·5 s.p. Flux variable	44	46	CTD 93
1619+24	16 19 49·1	+24 42 40	6	4	8	10			III		0·32	1·1		42	43	4C 24·37
1623+26	16 23 11·8	+26 57 40	6	2	7	11	0·2 p.	0·2 S.	QSO	18	0·48	0·9	Gal. 0′·2 n.f. (Schmidt, personal comm.)	46	43	4C 26·48
1729+21	17 29 09·1	+21 07 34	4	4	9	10			III		0·34	0·7		44	27	4C 21·50
1735+24	17 35 33·7	+24 02 36	6	4	6	7	0	0·1 N.	QSO?		1·02	0·8	Wills (1968) gives blue object 0′·6 N. as ident.	48	26	4C 24·42 CTD 101
1737+20	17 37 27·5	+20 29 34	4	4	13	16	0·5 p.	0·2 N.	g	20	0·18	—	Various objects in field might be blue. Very ext. in Dec. (~ 15′). Slightly ext. in R.A.	44	25	NPC
1744+20	17 44 18·1	+20 10 33	4	4	7	8			III		0·55	0·6	Blue object 0′·4 S.	45	23	4C 20·43
1803+20	18 03 34·0	+20 28 01	4	4	8	8			III		0·46	0·8	Various objects in field might be blue	47	19	4C 20·44
[illegible]+23	18 04 51·8	+23 32 31	4	4	8	8	1·2 f.	0·1 S.	QSO?	19	0·46	1·0		50	20	4C 23·47 NRAO 544
2137+20	21 37 28·6	+20 57 56	4	4	7	7			III		0·78	0·6		74	−23	NPC
2147+24	21 47 11·8	+24 53 43	5	4	8	9			III		0·37	1·0		79	−22	4C 24·56
2203+2[illegible]	22 02 58·3	+24 00 16	5	4	10	13			III		0·24	0·9	Slightly ext.	81	−25	4C 24·57
2227+2[illegible]	22 27 13·5	+26 04 07	4	4	9	10			III		0·32	0·8	Flux variable?	87	−27	4C 26·62
2245[illegible]	22 45 13·3	+23 11 15	6	4	7	8			III		0·46	1·0		89	−31	NPC
2246+20	22 46 51·1	+20 32 40	5	4	10	12			III		0·25	1·0		88	−34	4C 20·55
2318+20	23 18 25·3	+20 33 35	4	4	10	12			III		0·27	1·4		96	−37	4C 20·56

peak-to-peak noise fluctuations in the present series of observations. The r.m.s. error in right ascension and declination for each source was calculated from

$$e = (e_s^2/n + \sigma_{\mathrm{cal}}^2)^{\frac{1}{2}},$$

where σ_{cal} is the r.m.s. error due to calibration of the measurements and e_s is read off Figure 2 for each source. Owing to the calibration method, it is unfortunately difficult to determine σ_{cal} accurately; however, it is unlikely to be larger than the value from the transit observations of 6″ arc.

No allowance has been made for confusion; confusion only occurred in a few cases and in most of these the nearby source was almost wholly resolved. Notes are given in Table 2 in cases where a source is extended (ext.) or confused (conf.); for those sources the r.m.s. error might be slightly larger than the value given.

VI. Optical Identification

An extensive description of the identification procedure is given by Clarke, Bolton, and Shimmins (1966); a short description follows here.

The prints of the 48 in. Palomar Sky Survey have been examined near the position of all radio sources in the survey. The coordinates of each source, a 2′ arc square field centred on the position of the source, and the relative positions of 10 comparison stars on the scale of the Sky Survey prints were marked on transparent plotting paper, which was then used to search the prints. The results of the search are given in columns 10 and 11 of Table 2.

The results were:

13 fields contained blue stars that might be quasi-stellar objects, and of these objects 4 have been confirmed by spectroscopy (see references in remarks column of Table 2);
14 fields contained galaxies;
5 fields contained objects that might be blue or were blue and within 1′ arc of the source position;
7 fields contained faint galaxies within 1′ arc of the source position;
35 fields contained stars of normal colour;
1 field was blank.

Included in the fields containing normal stars is one case where an identification with a possible quasi-stellar object has been previously published. This is the source PKS 1022+20 (Bolton, Shimmins, and Merkelijn 1968). The source position in the present survey is only negligibly different from the old position but its identification is not supported by spectroscopy (Bolton and Kinman, personal communication).

Figs. 3– —Finding charts for the identifications. The scale is 5 mm = 1′ arc. North-east is at the top left-hand corner of each chart.

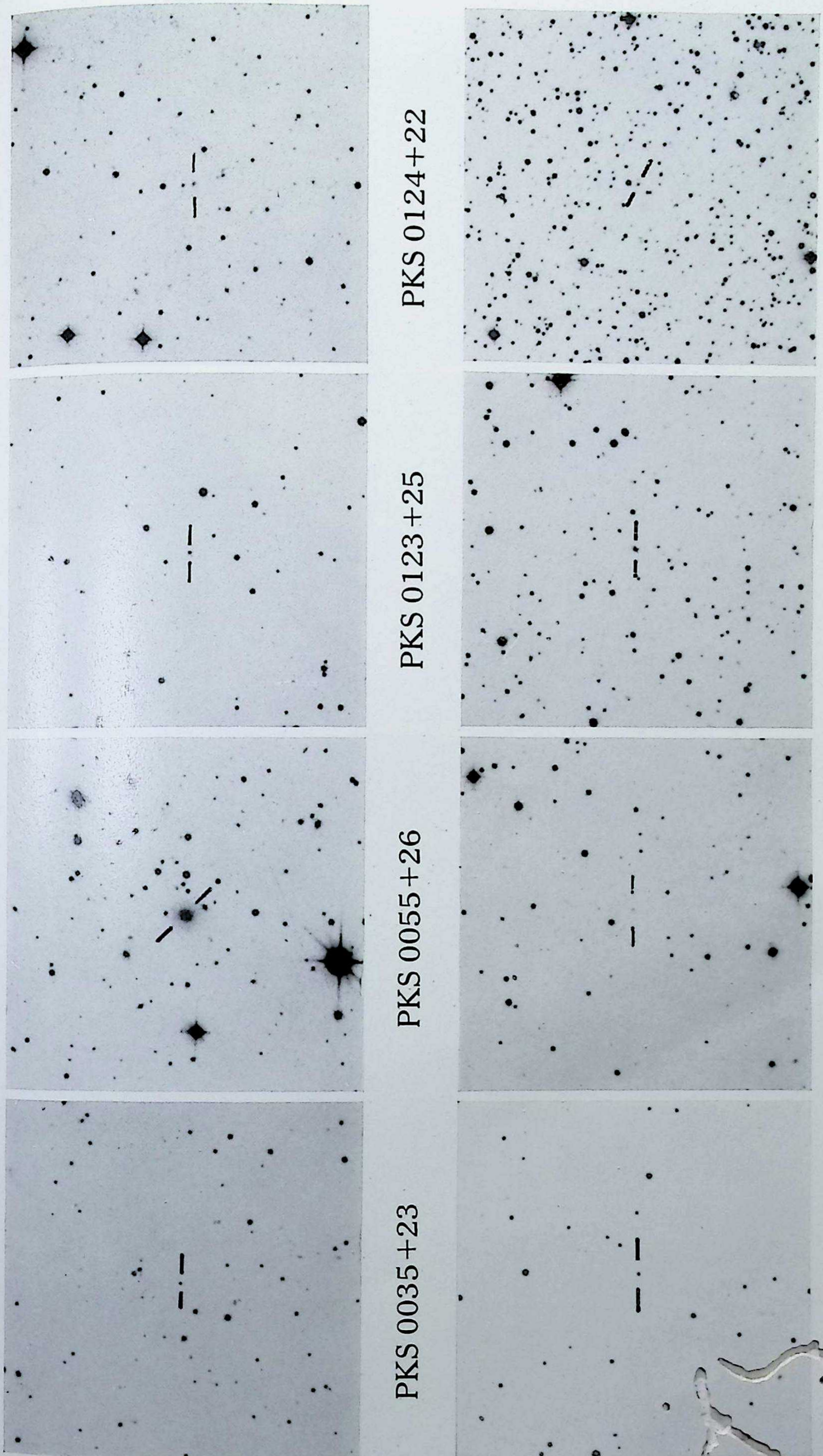
PKS 0035+23
PKS 0055+26
PKS 0123+25
PKS 0124+22
PKS 0130+24
PKS 0222+26
PKS 0349+21
PKS 0623+26

Fig. 3

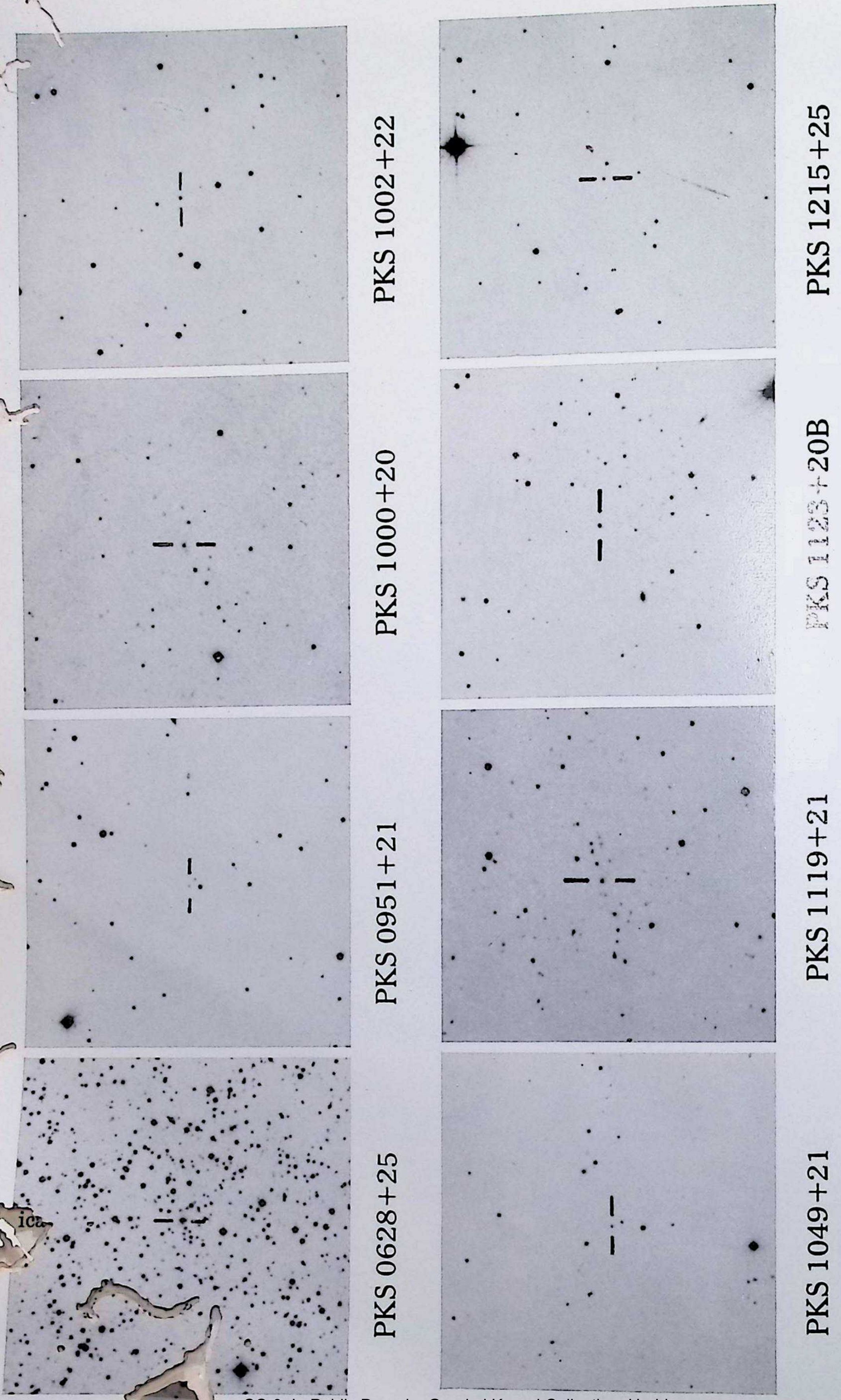

PKS 0628+25

PKS 0951+21

PKS 1000+20

PKS 1002+22

PKS 1049+21

PKS 1119+21

PKS 1123+20B

PKS 1215+25

Fig. 4

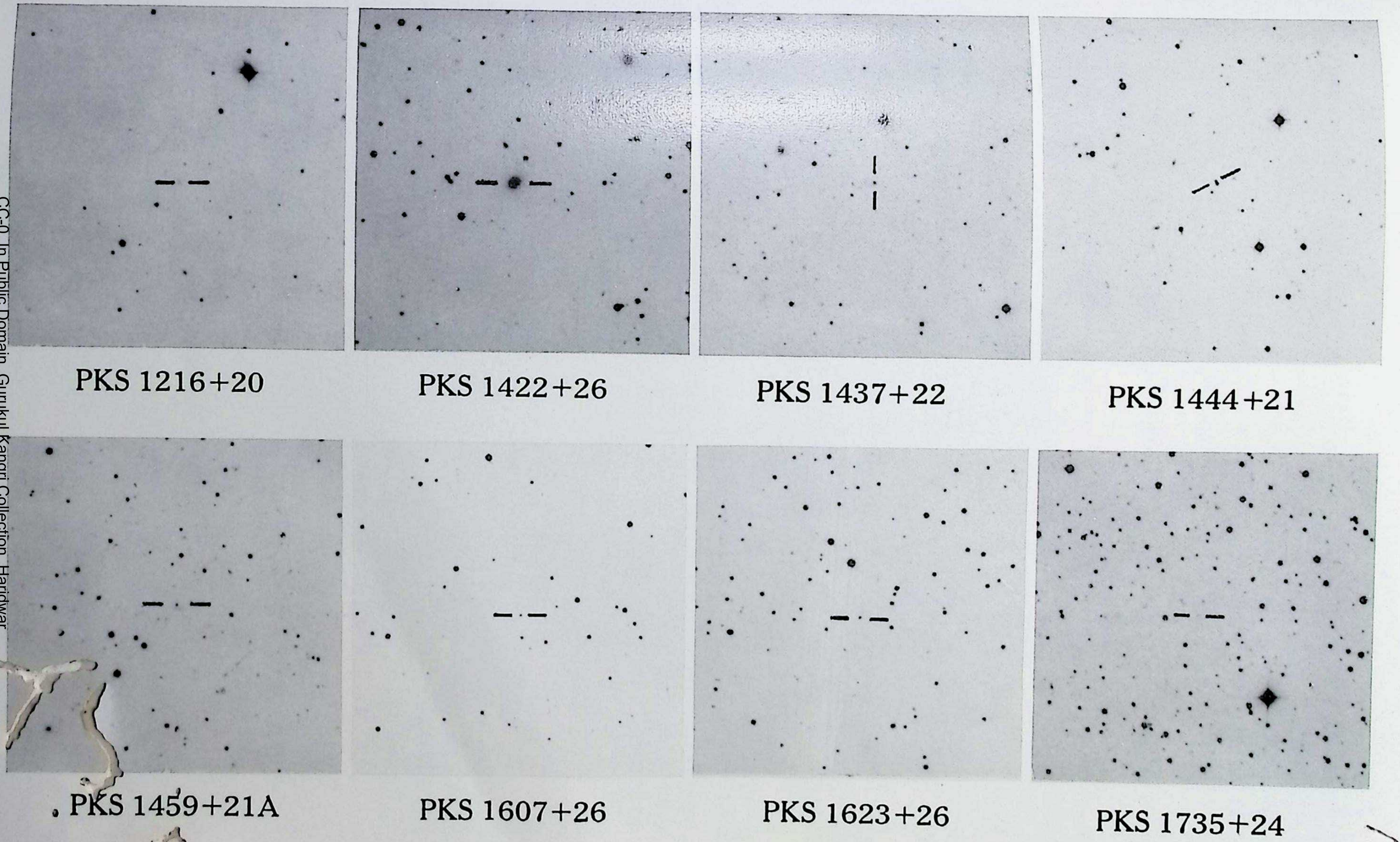
PKS 1216+20
PKS 1422+26
PKS 1437+22
PKS 1444+21
PKS 1459+21A
PKS 1607+26
PKS 1623+26
PKS 1735+24

Fig. 5

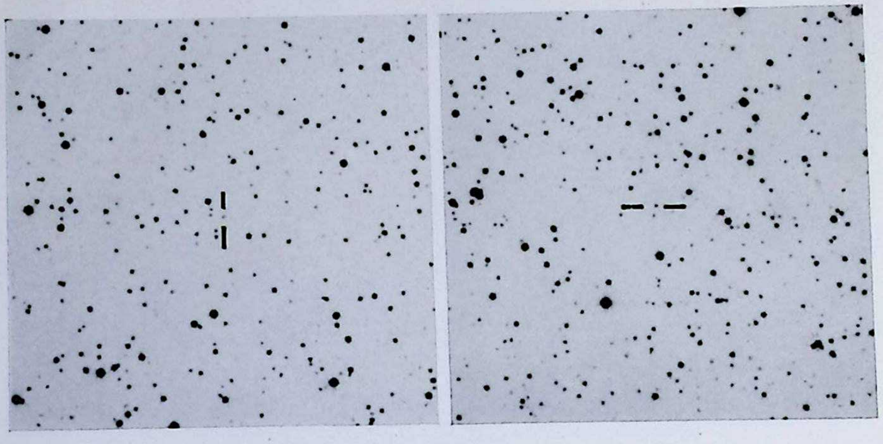

PKS 1737+20

PKS 1804+23

Fig. 6

VII. SOURCE TABLE

The results of the present observations are given in Table 2.

Column 1 gives the Parkes catalogue number. Where the source has been previously listed in the 3C catalogue (Edge *et al.* 1959), the 4C catalogue (Pilkington and Scott 1965), the CTD catalogue (Kellermann and Read 1965), or the NRAO catalogue (Pauliny-Toth, Wade, and Heeschen 1966), the appropriate catalogue number is given in column 17.

Columns 2 and 3 contain the radio position of the source from the present observations.

Columns 4 and 5 give the number of scans in right ascension and declination for each of the sources, and the r.m.s. errors in right ascension and declination are given in columns 6 and 7.

Columns 8 and 9 give the difference between the position of the optical identification and the radio position measured from the 48 in. prints to $0^{s}\cdot 1$ in right ascension and to $0'\cdot 1$ arc in declination. The error in the optical determination is unlikely to be greater than $0'\cdot 2$ arc.

Column 10 gives the type of identification, as follows: QSO?, blue star, possible quasi-stellar object; QSO, quasi-stellar object confirmed by its optical spectrum; E, elliptical galaxy; N, compact galaxy; g, galaxy, too faint for classification; III, stars only, normal colours; III–IV, reddened stars only.

Column 11 gives the photographic magnitude of the identification as estimated from the Sky Survey print; the values for galaxies have been estimated from the red prints and for possible quasi-stellar objects from the blue prints. Columns 12 and 13 give the flux density at 2700 MHz and the spectral index. Column 14 contains notes on additional points of interest and references for the optical confirmations. Columns 15 and 16 give the galactic coordinates.

VIII. FINDING CHARTS

The finding charts for the identified objects are given in Figures 3–6. They were prepared from the Sky Survey prints, and contrast has been increased over that of the original prints. For quasi-stellar objects the blue or "O" print has been used and for galaxies the red or "E" print, except for PKS 1216+20, where the galaxy was too faint on the red print.

IX. ACKNOWLEDGMENTS

I wish to thank Mr. J. G. Bolton for assistance with the observations and inspection of the Palomar Sky Survey prints, and Mr. A. J. Shimmins and Mr. J. V. Wall for their assistance with the observations.

X. REFERENCES

BATCHELOR, R. A., BROOKS, J. W., and COOPER, B.F.C. (1968).—*IEEE Trans. Antennas Propag.* **AP16**, 228.

BOLTON, J. G. (1968).—*Publs astr. Soc. Pacif.* **80**, 5.

BOLTON, J. G., CLARKE, MARGARET, E., SANDAGE, A., and VÉRON, P. (1965).—*Astrophys. J.* **142**, 1290.

Bolton, J. G., Shimmins, A. J., and Merkelijn, Jeannette K. (1968).—*Aust. J. Phys.* **21**, 81.

Clarke, Margaret E., Bolton, J. G., and Shimmins, A. J. (1966).—*Aust. J. Phys.* **19**, 375.

Clarke, R. W., and Batchelor, R. A. (1965).—*Nature, Lond.* **207**, 511.

Edge, D. O., Shakeshaft, J. R., McAdam, W. B., Baldwin, J. E., and Archer, S. (1959).—*Mem. R. astr. Soc.* **68**, 37.

Kellermann, K. I., and Read, R. B. (1965).—*Publs Owens Valley Radio Observ.* **1**, No. 2.

Merkelijn, Jeannette K., Shimmins, A. J., and Bolton, J. G. (1968).—*Aust. J. Phys.* **21**, 523.

Pauliny-Toth, I. I. K., Wade, C. M., and Heeschen, D. S. (1966).—*Astrophys. J. Suppl. Ser.* **13**, 65.

Pilkington, J. D., and Scott, P. F. (1965).—*Mem. R. astr. Soc.* **69**, 183.

Sandage, A., Véron, P., and Wyndham, J. D. (1965).—*Astrophys. J.* **142**, 1307.

Shimmins, A. J., and Day, G. A. (1968).—*Aust. J. Phys.* **21**, 377.

Véron, P. (1965).—*Astrophys. J.* **141**, 332.

Véron, P. (1966).—*Astrophys. J.* **144**, **861**.

Wills, D. (1968).—*Mon. Not. R. astr. Soc.* **135**, 337.

EFFECT OF HORIZONTAL AND VERTICAL MAGNETIC FIELDS ON KELVIN–HELMHOLTZ INSTABILITY

By R. C. Sharma* and K. M. Srivastava*

[*Manuscript received April* 9, 1968]

Summary

This paper discusses the effect of a general oblique magnetic field on the stability of two superposed fluids in relative horizontal motion. The stable and unstable cases at the interface ($z = 0$) between two uniform fluids with constant densities and velocities of streaming are separately discussed. The combined effect of horizontal and vertical magnetic fields is to increase the wavelength at which the Kelvin–Helmholtz instability sets in.

I. Introduction

Michael (1955) has discussed the stability of a combined current and vortex sheet in a perfectly conducting fluid, while the effect on the Kelvin–Helmholtz instability of a magnetic field transverse to the direction of streaming has been considered by Northrop (1956). In the present note we study the effect of both horizontal and vertical magnetic fields on the Kelvin–Helmholtz instability. A general equation formulating this effect is first obtained. We then suppose that the two uniform fluids, of densities ρ_1 and ρ_2 and velocities of streaming U_1 and U_2, are separated by a horizontal boundary at $z = 0$. The stable and unstable cases are then separately discussed.

II. Basic Equations

The fluid is considered to be heterogeneous, inviscid, and of zero resistivity. We also suppose that the streaming takes place in the x direction with a velocity U.

The equations of motion and continuity are

$$\rho . \mathrm{d}\boldsymbol{q}/\mathrm{d}t = -\nabla p - \rho \boldsymbol{g} + \mu \boldsymbol{j} \times \boldsymbol{H}; \tag{1}$$

where $\boldsymbol{q}$ is the velocity vector, p the pressure, μ the magnetic permeability, and $\boldsymbol{g}$ the acceleration due to gravity; and

$$\nabla . \boldsymbol{q} = 0 , \tag{2}$$

as the fluid is considered to be incompressible.

Since the density of a particle moving with the fluid remains constant,

$$\partial\rho/\partial t + (\boldsymbol{q} . \nabla)\rho = 0 . \tag{3}$$

Using Maxwell's equations for a perfect conductor ($\eta = 0$)

$$\partial H/\partial t = \nabla \times (\boldsymbol{q} \times \boldsymbol{H}) . \tag{4}$$

---

* Department of Mathematics, University of Jodhpur, Jodhpur, India.

Aust. J. Phys., **1968, 21, 917–21**

Let the actual density at any point due to a disturbance be $\rho+\delta\rho$ and let δp denote the corresponding increment in pressure. Also let the components of velocity in the perturbed state be $U+u$, v, and w. Further, if $H_\perp$ and $H_\parallel$ denote the vertical and horizontal magnetic fields respectively and $\boldsymbol{h} = (h_x, h_y, h_z)$ is the perturbation in H, we have

$$\rho\left(\frac{\partial u}{\partial t}+U\frac{\partial u}{\partial x}+w\frac{\mathrm{d}U}{\mathrm{d}z}\right)+\frac{\mu H_\perp}{4\pi}\left(\frac{\partial h_y}{\partial x}-\frac{\partial h_x}{\partial y}\right) = -\frac{\partial}{\partial x}.\delta p\,, \tag{5}$$

$$\rho\left(\frac{\partial v}{\partial t}+U\frac{\partial v}{\partial x}\right)-\frac{\mu H_\parallel}{4\pi}\left(\frac{\partial h_y}{\partial x}-\frac{\partial h_x}{\partial y}\right) = -\frac{\partial}{\partial y}.\delta p\,, \tag{6}$$

$$\rho\left(\frac{\partial w}{\partial t}+U\frac{\partial w}{\partial x}\right)-\frac{\mu H_\parallel}{4\pi}\left(\frac{\partial h_z}{\partial x}-\frac{\partial h_x}{\partial z}\right)-\frac{\mu H_\perp}{4\pi}\left(\frac{\partial h_z}{\partial y}-\frac{\partial h_y}{\partial z}\right) = -\frac{\partial}{\partial z}.\delta p-g.\delta\rho\,, \tag{7}$$

$$\frac{\partial u}{\partial x}+\frac{\partial v}{\partial y}+\frac{\partial w}{\partial z}=0\,, \tag{8}$$

$$\frac{\partial}{\partial t}.\delta\rho+U\frac{\partial}{\partial x}.\delta\rho = -w.\frac{\mathrm{d}\rho}{\mathrm{d}z}, \tag{9}$$

and

$$\left(\frac{\partial}{\partial t}+U\frac{\partial}{\partial x}\right)\boldsymbol{h} = \left(\frac{\partial}{\partial x}.H_\parallel+\frac{\partial}{\partial y}.H_\perp\right)\boldsymbol{q}+h_z.\mathrm{D}U\,. \tag{10}$$

Analysing the disturbances into normal modes, we seek solutions whose dependence on x, y, and t is given by

$$\exp\{\mathrm{i}(k_x.x+k_y.y+n.t)\}\,, \tag{11}$$

where k_x, k_y, and n are constants; k_x is the wave number along the x direction, k_y the wave number along the y direction, and k the resultant wave number. Using the above perturbation, equations (5)–(10) become

$$\mathrm{i}\rho(n+k_xU)u+\rho(\mathrm{D}U)w+(\mu H_\perp/4\pi)(\mathrm{i}k_x.h_y-\mathrm{i}k_y.h_x) = -\mathrm{i}k_x.\delta p\,, \tag{12}$$

$$\mathrm{i}\rho(n+k_xU)v-(\mu H_\parallel/4\pi)(\mathrm{i}k_x.h_y-\mathrm{i}k_y.h_x) = -\mathrm{i}k_y.\delta p\,, \tag{13}$$

$$\mathrm{i}\rho(n+k_xU)w+(\mu H_\parallel/4\pi)(\mathrm{D}h_x-\mathrm{i}k_x.h_z)+(\mu H_\perp/4\pi)(\mathrm{D}h_y-\mathrm{i}k_y.h_z) = -\mathrm{D}.\delta p-g.\delta\rho\,, \tag{14}$$

$$\mathrm{i}k_x.u+\mathrm{i}k_y.v+\mathrm{D}w=0\,, \tag{15}$$

$$\mathrm{i}(n+k_xU).\delta\rho = -w.\mathrm{D}\rho\,, \tag{16}$$

$$h_x = \frac{k_xH_\parallel+k_yH_\perp}{n+k_xU}\left(u-\frac{\mathrm{i}\,\mathrm{D}U}{n+k_xU}w\right), \tag{17a}$$

and

$$h_y = \frac{k_xH_\parallel+k_yH_\perp}{n+k_xU}v\,, \qquad h_z = \frac{k_xH_\parallel+k_yH_\perp}{n+k_xU}w\,. \tag{17b}$$

Multiplying equations (12) and (13) by $-\mathrm{i}k_x$ and $-\mathrm{i}k_y$ respectively and adding, and substituting the values of h_x and h_y, we get

$$\rho(n+k_xU)\mathrm{D}w-k_x\rho(\mathrm{D}U)w = \mathrm{i}k^2.\delta p\,. \tag{18}$$

Multiplying equations (12) and (13) by $-ik_y$ and $+ik_x$ respectively and adding, we obtain the z component of vorticity ζ as

$$\zeta = ik_x v - ik_y u = \{k_y(DU)/(n+k_x U)\}w . \tag{19}$$

Also

$$ik^2 u = -(k_x Dw + k_y \zeta) = -[k_x Dw + \{k_y^2 DU/(n+k_x U)\}w] \tag{20a}$$

and

$$ik^2 v = (k_x \zeta - k_y Dw) = [\{k_x k_y (DU)/(n+k_x U)\}w - k_y Dw] . \tag{20b}$$

Eliminating δp between equations (14) and (18) and using (9), (19), and (20), we get finally

$$\begin{aligned} D(\rho(n+k_x U)Dw - \rho k_x(DU)w) &= k^2\rho(n+k_x U)w + gk^2 \frac{D\rho}{n+k_x U} w \\ &+ k_x^2 \frac{\mu H_\parallel^2}{4\pi}\left\{D\left(\frac{Dw}{n+k_x U}\right) - \frac{k^2 w}{n+k_x U}\right\} - k_x^3 \frac{\mu H_\parallel^2}{4\pi} D\left(\frac{DU}{(n+k_x U)^2} w\right) \\ &+ k_y^2 \frac{\mu H_\perp^2}{4\pi}\left\{D\left(\frac{Dw}{n+k_x U}\right) - \frac{k^2 w}{n+k_x U}\right\} - k_x k_y^2 \frac{\mu H_\perp^2}{4\pi} D\left(\frac{DU}{(n+k_x U)^2} w\right) \\ &+ k_x k_y \frac{\mu H_\parallel H_\perp}{2\pi}\left\{D\left(\frac{Dw}{n+k_x U}\right) - \frac{k^2 w}{n+k_x U}\right\} - k_x^2 k_y \frac{\mu H_\parallel H_\perp}{2\pi} D\left(\frac{DU}{(n+k_x U)^2} w\right) . \end{aligned} \tag{21}$$

Equation (21) is thus a general equation formulating the effects of both horizontal and vertical magnetic fields on the Kelvin–Helmholtz instability. The particular cases of horizontal and vertical fields (cf. Chandrasekhar 1961, pp. 510 and 512) can be derived in the limit of vanishing $H_\perp$ and $H_\parallel$ respectively.

III. TWO UNIFORM FLUIDS IN RELATIVE MOTION SEPARATED BY A HORIZONTAL BOUNDARY

The two uniform fluids of densities ρ_1 and ρ_2 and velocities of streaming U_1 and U_2 are supposed to be separated by a horizontal boundary at $z = 0$. Then, in the two regions of constant ρ and U, equations (19) and (21) give

$$\zeta = 0 , \tag{22}$$

and

$$\left(\rho(n+k_x U) - \frac{k_x^2}{n+k_x U}\frac{\mu H_\parallel^2}{4\pi} - \frac{k_y^2}{n+k_x U}\frac{\mu H_\perp^2}{4\pi} - \frac{k_x k_y}{n+k_x U}\frac{\mu H_\parallel H_\perp}{2\pi}\right)\left(D^2 - k^2\right) w = 0 . \tag{23}$$

Since w must be bounded both when $z \to +\infty$ (in the upper fluid) and $z \to -\infty$ (in the lower fluid), the solutions of equation (23) can be written as

$$w_1 = A(n+k_x U_1)e^{+kz} , \qquad z < 0 , \tag{24a}$$

$$w_2 = A(n+k_x U_2)e^{-kz} , \qquad z > 0 , \tag{24b}$$

$w/(n+k_x U)$ being continuous at the interface.

Integrating equation (23) across the interface at $z = 0$, we get

$$\Delta_0\{\rho(n+k_x U)\mathrm{D}w\} = k_x^2\frac{\mu H_\parallel^2}{4\pi}\Delta_0\left(\frac{\mathrm{D}w}{n+k_x U}\right)+k_y^2\frac{\mu H_\perp^2}{4\pi}\Delta_0\left(\frac{\mathrm{D}w}{n+k_x U}\right)$$

$$+k_x k_y\frac{\mu H_\parallel H_\perp}{2\pi}\Delta_0\left(\frac{\mathrm{D}w}{n+k_x U}\right)+gk^2\Delta_0(\rho)\left(\frac{w}{n+k_x U}\right)_0, \qquad (25)$$

where $\Delta_0(f)$ is the change that a quantity f experiences at $z = 0$, and $(w/(n+k_x U))_0$ is the unique value that this quantity has at $z = 0$.

Substituting the values of w_1 and w_2 from equations (24) in (25), we obtain the characteristic equation

$$\rho_2(n+k_x U_2)^2+\rho_1(n+k_x U_1)^2 = gk(\rho_1-\rho_2)+k_x^2(\mu H_\parallel^2/2\pi)+k_y^2(\mu H_\perp^2/2\pi)+k_x k_y(\mu H_\parallel H_\perp/\pi). \qquad (26)$$

Letting $\alpha_1 = \rho_1/(\rho_1+\rho_2)$ and $\alpha_2 = \rho_2/(\rho_1+\rho_2)$, the roots of equation (26) are

$$n = -k_x(\alpha_1 U_1+\alpha_2 U_2) \pm \left(gk(\alpha_1-\alpha_2)+k_x^2\frac{\mu H_\parallel^2}{2\pi(\rho_1+\rho_2)}+k_y^2\frac{\mu H_\perp^2}{2\pi(\rho_1+\rho_2)}\right.$$

$$\left.+k_x k_y\frac{\mu H_\parallel H_\perp}{\pi(\rho_1+\rho_2)}-k_x^2\alpha_1\alpha_2(U_1-U_2)^2\right)^{\frac{1}{2}}. \qquad (27)$$

The Kelvin–Helmholtz instability occurs only if n contains a negative imaginary part.

(a) *Stable Case*

In this case $\alpha_1 > \alpha_2$. It is observed from equation (27) that the combined effect of horizontal and vertical magnetic fields is to suppress the Kelvin–Helmholtz instability if

$$k_x^2\alpha_1\alpha_2(U_1-U_2)^2 \leqslant F, \qquad (28a)$$

where

$$F = gk(\alpha_1-\alpha_2)+k_x^2\frac{\mu H_\parallel^2}{2\pi(\rho_1+\rho_2)}+k_y^2\frac{\mu H_\perp^2}{2\pi(\rho_1+\rho_2)}+k_x k_y\frac{\mu H_\parallel H_\perp}{\pi(\rho_1+\rho_2)}. \qquad (28b)$$

In any direction, instability occurs when

$$k_x^2\alpha_1\alpha_2(U_1-U_2)^2 > F. \qquad (29)$$

Hence for a given difference in velocity U_1-U_2 and a given direction of the wave vector k, instability occurs for all wave numbers

$$k > g(\alpha_1-\alpha_2)\left(\alpha_1\alpha_2(U_1-U_2)^2\cos^2\theta-\frac{\mu H_\parallel^2}{2\pi(\rho_1+\rho_2)}\cos^2\theta-\frac{\mu H_\perp^2}{2\pi(\rho_1+\rho_2)}\sin^2\theta\right.$$

$$\left.-\frac{\mu H_\parallel H_\perp}{\pi(\rho_1+\rho_2)}\sin\theta\cos\theta\right)^{-1}, \qquad (30)$$

where θ is the angle between the directions of k and U. The minimum wave number

$k_{\min}$ is given by

$$k_{\min} = 2g(\alpha_1-\alpha_2)[\{v_A^2-\alpha_1\alpha_2(U_1-U_2)^2-v_B^2\}^2+4v_A^2v_B^2]^{\frac{1}{2}}$$
$$\times(\{\alpha_1\alpha_2(U_1-U_2)^2-v_A^2+v_B^2\}^2+4v_A^2v_B^2+\{\alpha_1\alpha_2(U_1-U_2)^2-v_A^2-v_B^2\}$$
$$[\{v_A^2-\alpha_1\alpha_2(U_1-U_2)^2-v_B^2\}^2+4v_A^2v_B^2]^{\frac{1}{2}})^{-1}, \qquad (31)$$

and occurs when θ is given by

$$2\theta = n\pi+\tan^{-1}[2v_Av_B/\{v_A^2-v_B^2-\alpha_1\alpha_2(U_1-U_2)^2\}], \qquad (32)$$

where

$$v_A^2 = \mu H_{\parallel}^2/2\pi(\rho_1+\rho_2) \qquad \text{and} \qquad v_B^2 = \mu H_{\perp}^2/2\pi(\rho_1+\rho_2)\,.$$

The minimum wave number occurs for odd n. Thus it is clear that for a given U_1-U_2, instability occurs for the least wave number given by equation (31), when k is inclined at an angle θ given by equation (32) with the direction of U for odd n. We will have instability for $k > k_{\min}$.

(*b*) *Unstable Case*

In this case $\alpha_2 > \alpha_1$. It is clear from equation (27) that the combined effect of horizontal and vertical magnetic fields will suppress the Kelvin–Helmholtz instability if

$$k_x^2\alpha_1\alpha_2(U_1-U_2)^2 < F\,. \qquad (33)$$

Also, if

$$k_x^2\alpha_1\alpha_2(U_1-U_2)^2 = F\,,$$

then

$$n = -k_x(\alpha_1U_1+\alpha_2U_2)\,, \qquad (34)$$

which leads to stability.

In any direction, instability occurs under the condition (29). Here $k_{\min}$ occurs for even n and is given by

$$k_{\min} = 2g(\alpha_2-\alpha_1)[\{v_A^2-\alpha_1\alpha_2(U_1-U_2)^2-v_B^2\}^2+4v_A^2v_B^2]^{\frac{1}{2}}$$
$$\times(\{\alpha_1\alpha_2(U_1-U_2)^2-v_A^2-v_B^2\}^2+4v_A^2v_B^2+\{v_A^2+v_B^2-\alpha_1\alpha_2(U_1-U_2)^2\}$$
$$\times[\{v_A^2-\alpha_1\alpha_2(U_1-U_2)^2-v_B^2\}^2+4v_A^2v_B^2]^{\frac{1}{2}})^{-1}, \qquad (35)$$

for the same value of θ given by equation (32). We will have instability for $k > k_{\min}$.

IV. REFERENCES

CHANDRASEKHAR, S. (1961).—"Hydrodynamic and Hydromagnetic Stability." pp. 510–12. (Clarendon Press: Oxford.)

MICHAEL, D. H. (1955).—*Proc. Camb. phil. Soc.* **51**, 528–32.

NORTHROP, T. G. (1956).—*Phys. Rev.* **103**, 1150–4.

EFFECT OF HORIZONTAL AND VERTICAL MAGNETIC FIELDS ON RAYLEIGH–TAYLOR INSTABILITY

By R. C. Sharma* and K. M. Srivastava*

[*Manuscript received April* 1, 1968]

Summary

A general equation studying the combined effect of horizontal and vertical magnetic fields on the stability of two superposed fluids has been obtained. The unstable and stable cases at the interface ($z = 0$) between two uniform fluids, with both the possibilities of real and complex n, have been separately dealt with. Some new results are obtained. In the unstable case with real n, the perturbations are damped or unstable according as $2(k^2-k_x^2L^2)-(\alpha_2-\alpha_1)k$ is $>$ or <0 under the physical situation (35). In the stable case, the perturbations are stable or unstable according as $2(k^2-k_x^2L^2)+(\alpha_1-\alpha_2)k$ is $>$ or <0 under the same physical situation (35). The perturbations become unstable if $H_{\parallel}/H_{\perp}$ ($= L$) is large. Both the cases are also discussed with imaginary n.

I. Introduction

Hide (1955) considered the effect of a vertical magnetic field on the stability of two superposed fluids, while the effect of a horizontal magnetic field on the Rayleigh–Taylor instability was considered by Kruskal and Schwarzschild (1954). The object of the present paper is to study the combined effect of horizontal and vertical magnetic fields on the Rayleigh–Taylor instability.

After obtaining an equation that describes the effect of the magnetic fields we then suppose that two uniform fluids, of densities ρ_1 and ρ_2, are separated by a horizontal boundary at $z = 0$. The unstable and stable cases for both real and imaginary n are then separately dealt with and discussed.

II. Basic Equations

The fluid is considered to be heterogeneous, inviscid, and of zero resistivity. The equations of motion and continuity are

$$\rho\,\mathrm{d}\boldsymbol{q}/\mathrm{d}t = -\nabla p-\rho\boldsymbol{g}+\mu\boldsymbol{j}\times\boldsymbol{H}\,; \tag{1}$$

where $\boldsymbol{q} = (u,v,w)$ is the velocity vector, p the pressure, μ the magnetic permeability, and $\boldsymbol{g}$ the acceleration due to gravity; and

$$\nabla.\boldsymbol{q} = 0\,, \tag{2}$$

as the fluid is considered to be incompressible.

Since the density of a particle moving with the fluid remains constant,

$$\partial\rho/\partial t+(\boldsymbol{q}.\nabla)\rho = 0\,. \tag{3}$$

---

* Department of Mathematics, University of Jodhpur, Jodhpur, India.

Using Maxwell's equations for a perfect conductor ($\eta = 0$),

$$\partial H/\partial t = \nabla \times (\boldsymbol{q} \times \boldsymbol{H}) . \tag{4}$$

Let the actual density at any point due to a disturbance be $\rho + \delta\rho$ and let δp denote the corresponding increment in pressure. Further, if $H_\perp$ and $H_\parallel$ denote the vertical and horizontal magnetic fields respectively and $\boldsymbol{h} = (h_x, h_y, h_z)$ is the perturbation in H, we have

$$\rho \frac{\partial u}{\partial t} - \frac{\mu H_\perp}{4\pi}\left(\frac{\partial h_x}{\partial z} - \frac{\partial h_z}{\partial x}\right) = -\frac{\partial}{\partial x} . \delta p , \tag{5}$$

$$\rho \frac{\partial v}{\partial t} - \frac{\mu H_\perp}{4\pi}\left(\frac{\partial h_y}{\partial z} - \frac{\partial h_z}{\partial y}\right) - \frac{\mu H_\parallel}{4\pi}\left(\frac{\partial h_y}{\partial x} - \frac{\partial h_x}{\partial y}\right) = -\frac{\partial}{\partial y} . \delta p , \tag{6}$$

$$\rho \frac{\partial w}{\partial t} + \frac{\mu H_\parallel}{4\pi}\left(\frac{\partial h_x}{\partial z} - \frac{\partial h_z}{\partial x}\right) = -\frac{\partial}{\partial z} . \delta p - g . \delta\rho , \tag{7}$$

$$\frac{\partial u}{\partial x} + \frac{\partial v}{\partial y} + \frac{\partial w}{\partial z} = 0 , \qquad \frac{\partial h_x}{\partial x} + \frac{\partial h_y}{\partial y} + \frac{\partial h_z}{\partial z} = 0 , \tag{8}$$

$$\frac{\partial}{\partial t} . \delta\rho = -w \frac{\mathrm{d}\rho}{\mathrm{d}z} , \tag{9}$$

and

$$\frac{\partial h}{\partial t} = \left(H_\parallel . \frac{\partial}{\partial x} + H_\perp . \frac{\partial}{\partial z}\right) \boldsymbol{q} . \tag{10}$$

Analysing the disturbances into normal modes, we seek solutions whose dependence on x, y, and t is given by

$$\exp(\mathrm{i}k_x . x + \mathrm{i}k_y . y + n . t) , \tag{11}$$

where k_x, k_y, and n are constants, k_x being the wave number along the x direction, k_y the wave number along the y direction, and k the resultant wave number. Using this perturbation, equations (5)–(10) become

$$\rho n u - (\mu H_\perp/4\pi)(\mathrm{D}h_x - \mathrm{i}k_x . h_z) = -\mathrm{i}k_x . \delta p , \tag{12}$$

$$\rho n v - (\mu \mathrm{H}_\perp/4\pi)(\mathrm{D}h_y - \mathrm{i}k_y . h_z) - (\mu H_\parallel/4\pi)(ik_x . h_y - \mathrm{i}k_y . h_x) = -\mathrm{i}k_y . \delta p , \tag{13}$$

$$\rho n w + (\mu H_\parallel/4\pi)(\mathrm{D}h_x - ik_x . h_z) = -\mathrm{D} . \delta p + (g/n)(\mathrm{D}\rho) w \tag{14}$$

(on substituting for $\delta\rho$ from (9)),

$$\mathrm{i}k_x . u + \mathrm{i}k_y . v = -\mathrm{D}w , \qquad \mathrm{i}k_x . h_x + \mathrm{i}k_y . h_y = -\mathrm{D}h_z , \tag{15}$$

and

$$h_x = (H_\perp/n)\mathrm{D}u + (H_\parallel/n)\mathrm{i}k_x . u , \tag{16a}$$

$$h_y = (H_\perp/n)\mathrm{D}v + (H_\parallel/n)\mathrm{i}k_x . v , \tag{16b}$$

$$h_z = (H_\perp/n)\mathrm{D}w + (H_\parallel/n)\mathrm{i}k_x . w . \tag{16c}$$

Multiplying (12) by $-\mathrm{i}k_x$ and (13) by $-\mathrm{i}k_y$ and adding, we get

$$\rho \mathrm{D}w - \frac{\mu H_\perp}{4\pi n}(\mathrm{D}^2 - k^2)h_z + \frac{\mu H_\parallel}{4\pi n} k_y(k_y . h_x - k_x . h_y) = -\frac{k^2}{n}\delta p . \tag{17}$$

Substituting the values of h_x, h_y, and h_z, equation (17) becomes

$$\rho \mathrm{D}w + \mathrm{i}\frac{\mu H_\parallel H_\perp}{4\pi n^2}\Big(k_y . \mathrm{D}\zeta - k_x(\mathrm{D}^2 - k^2)w\Big) - \frac{\mu H_\perp^2}{4\pi n^2}(\mathrm{D}^2 - k^2)\mathrm{D}w - \frac{\mu H_\parallel^2}{4\pi n^2}k_x k_y \zeta = -\frac{k^2}{n}\delta p\,, \qquad (18)$$

where ζ, the z component of vorticity, is given by

$$\zeta = \partial v/\partial x - \partial u/\partial y = \mathrm{i}k_x . v - \mathrm{i}k_y . u\,. \qquad (19)$$

Since equation (19) and $-\mathrm{D}w = \mathrm{i}k_x . u + \mathrm{i}k_y . v$ hold,

$$u = k^{-2}(\mathrm{i}k_y . \zeta + \mathrm{i}k_x . \mathrm{D}w)\,.$$

Again, from equation (16a)

$$h_x = \Big(\frac{H_\perp}{n}\mathrm{D} + \frac{\mathrm{i}k_x}{n}H_\parallel\Big)u,$$

so that

$$\mathrm{D}h_x = \frac{D}{k^2}\Big(\frac{H_\perp}{n}\mathrm{D} + \frac{\mathrm{i}k_x}{n}H_\parallel\Big)\Big(\mathrm{i}k_y . \zeta + \mathrm{i}k_x . \mathrm{D}w\Big)\,, \qquad (20)$$

which is obtained on substituting the value of u. Eliminating δp between (14) and (18), we obtain

$$\{\mathrm{D}(\rho \mathrm{D}w) - k^2\rho w\} - 2\mathrm{i}k_x . \frac{\mu H_\parallel H_\perp}{4\pi n^2}(\mathrm{D}^2 - k^2)\mathrm{D}w - \frac{\mu H_\perp^2}{4\pi n^2}(\mathrm{D}^2 - k^2)\mathrm{D}^2 w + \frac{\mu H_\parallel^2 . k_x^2}{4\pi n^2}(\mathrm{D}^2 - k^2)w = -\frac{gk^2}{n^2}(\mathrm{D}\rho)w\,. \qquad (21)$$

Equation (21) is thus a general equation formulating the effects of both the horizontal and vertical magnetic fields on the Rayleigh–Taylor instability. If we put $H_\parallel = 0$ in (21) we get an equation that is the same as the corresponding equation in the presence of a vertical magnetic field, as given in Chandrasekhar (1961, p. 458). Also, if we put $H_\perp = 0$ in (21) we get the corresponding equation in the presence of a horizontal magnetic field (Chandrasekhar 1961, p. 465).

III. Boundary Conditions

We suppose that the two uniform and perfectly conducting fluids are separated by a horizontal boundary at $z = 0$. Then, at the interface,

$$w \quad \text{and} \quad h_z \quad \text{are continuous}\,, \qquad (22)$$

and from equation (16c), the continuities of w and h_z imply that

$$\mathrm{D}w \quad \text{is continuous}\,. \qquad (23)$$

Also at the interface between two uniform fluids $e^{\pm kz}$ is a solution of equation (21). Since w and $\mathrm{D}w$ are continuous at the interface, we infer from equation (21) that

$$\mathrm{D}^2 w \quad \text{is also continuous}\,. \qquad (24)$$

Integrating equation (21) across the interface, a further boundary condition can be obtained, namely

$$\Delta_{\mathrm{s}}\left(\rho\,\mathrm{D}w-\frac{\mu H_{\perp}^{2}}{4\pi n^{2}}(\mathrm{D}^{2}-k^{2})\mathrm{D}w+\frac{\mu H_{\parallel}^{2}\,.\,k_{x}^{2}}{4\pi n^{2}}\mathrm{D}w-2\mathrm{i}k_{x}\,.\,\frac{\mu H_{\perp}H_{\parallel}}{4\pi n^{2}}(\mathrm{D}^{2}-k^{2})w\right)$$

$$=-\frac{gk^{2}}{n^{2}}\Delta_{\mathrm{s}}(\rho)\,w_{\mathrm{s}}\,. \tag{25}$$

IV. At the Interface between Two Uniform Fluids

We suppose that the two uniform fluids of densities ρ_1 and ρ_2 are separated by a horizontal boundary at $z=0$ and define a dimensionless parameter $L=H_{\parallel}/H_{\perp}$, so that equation (21) reduces to

$$(\mathrm{D}^{2}-k^{2})\mathrm{D}^{2}w+2\mathrm{i}k_{x}\,.\,L(\mathrm{D}^{2}-k^{2})\mathrm{D}w-(4\pi\rho n^{2}/\mu H_{\perp}^{2}+k_{x}^{2}L^{2})(\mathrm{D}^{2}-k^{2})w=0\,. \tag{26}$$

The solution of (26) is a linear combination of $\mathrm{e}^{\pm kz}$ and $\mathrm{e}^{\pm qz}$, where

$$(q+\mathrm{i}k_{x}L)^{2}=4\pi\rho n^{2}/\mu H_{\perp}^{2}\,.$$

We now consider the unstable and stable cases separately.

(a) *Unstable Case*

If n is real then the unstable case requires $n^2>0$, and if n is complex it is supposed that the real part of n^2 is positive. Further we assume that

$$q=-\mathrm{i}k_{x}L+n(4\pi\rho/\mu H_{\perp}^{2})^{\frac{1}{2}}\qquad\text{and}\qquad \mathrm{Re}(n)>0\,.$$

Since w must be bounded when $z\to+\infty$ (in the upper fluid) and $z\to-\infty$ (in the lower fluid), the solutions of equation (26) can be written as

$$w_{1}=A_{1}\exp(+kz)+B_{1}\exp(+q_{1}z)\,,\qquad z<0\,, \tag{27a}$$

$$w_{2}=A_{2}\exp(-kz)+B_{2}\exp(-q_{2}z)\qquad z>0\,, \tag{27b}$$

where A_1, B_1, A_2, and B_2 are constants of integration,

$$q_{1}+\mathrm{i}k_{x}L=n(4\pi\rho_{1}/\mu H_{\perp}^{2})^{\frac{1}{2}}\,,\qquad\text{and}\qquad q_{2}+\mathrm{i}k_{x}L=n(4\pi\rho_{2}/\mu H_{\perp}^{2})^{\frac{1}{2}}\,. \tag{28}$$

In writing the solutions for w in the two regions $z<0$ and $z>0$ in the manner (27), we have assumed that q_1 and q_2 are so defined that their real parts are positive.

Using the boundary conditions (22)–(25) and substituting for w_1 and w_2 from (27), at the interface $z=0$ we get an equation in q_1 and q_2 of the form

$$\Delta(q_{1},q_{2})=\begin{vmatrix}1 & 1 & -1 & -1\\ k & q_{1} & +k & +q_{2}\\ k^{2} & q_{1}^{2} & -k^{2} & -q_{2}^{2}\\ C & D & E & F\end{vmatrix}=0\,,$$

where

$$C = \tfrac{1}{2}R-\alpha_1-\alpha_1 k_x^2 L^2/(q_1+\mathrm{i}k_x L)^2,$$

$$D = \tfrac{1}{2}R-\alpha_1(q_1/k)+\frac{\alpha_1(q_1/k)(q_1^2-k_1)}{(q_1+\mathrm{i}k_x L)^2}-\frac{\alpha_1(q_1/k)k_x^2 L^2}{(q_1+\mathrm{i}k_x L)^2}+\frac{\alpha_1 2\mathrm{i}k_x L(q_1^2-k^2)/k}{(q_1+\mathrm{i}k_x L)^2},$$

$$E = \tfrac{1}{2}R-\alpha_2-\alpha_2 k_x^2 L^2/(q_2+\mathrm{i}k_x L)^2,$$

$$F = \tfrac{1}{2}R-\alpha_2(q_2/k)+\frac{\alpha_2(q_2/k)(q_2^2-k^2)}{(q_2+\mathrm{i}k_x L)^2}-\frac{\alpha_2(q_2/k)k_x^2 L^2}{(q_2+\mathrm{i}k_x L)^2}-\frac{\alpha_2 2\mathrm{i}k_x L(q_2^2-k^2)/k}{(q_2+\mathrm{i}k_x L)^2},$$

with

$$\alpha_1 = \frac{\rho_1}{\rho_1+\rho_2}, \qquad \alpha_2 = \frac{\rho_2}{\rho_1+\rho_2}, \qquad \text{and} \qquad R = \frac{gk}{n^2}(\alpha_2-\alpha_1).$$

The determinant is solved by removing the factors q_1-k and q_2-k (since these become identically zero on substitution of the functions w_1 and w_2, giving the characteristic roots $q_1 = k$ and $q_2 = k$) and expanding the remaining determinant to obtain

$$\left\{R-1-L^2k_x^2\left(\frac{\alpha_1}{(q_1+\mathrm{i}k_x L)^2}+\frac{\alpha_2}{(q_2+\mathrm{i}k_x L)^2}\right)\right\}\left(q_1+q_2+2k\right)$$
$$= 2k\left(\frac{\alpha_1 q_1+2\mathrm{i}k_x L\alpha_1}{(q_1+\mathrm{i}k_x L)^2}(q_2+k)+\frac{\alpha_2 q_2-2\mathrm{i}k_x L(\alpha_2/k)(2q_2+k)}{(q_2+\mathrm{i}k_x L)^2}(q_1+k)\right). \quad (29)$$

We define the Alfven velocity $V_{\mathrm{A}} = \{\mu H_\perp^2/4\pi(\rho_1+\rho_2)\}^{\frac{1}{2}}$, so that

$$q_1 = -\mathrm{i}k_x L+(n/V_{\mathrm{A}})\alpha_1^{\frac{1}{2}} \qquad \text{and} \qquad q_2 = -\,\mathrm{i}k_x L+(n/V_{\mathrm{A}})\alpha_2^{\frac{1}{2}}.$$

Substituting for q_1, q_2, and R we obtain

$$\frac{gk}{n^2}\left(\alpha_2-\alpha_1\right)\left(\frac{n}{kV_{\mathrm{A}}}+\frac{2}{\alpha_1^{\frac{1}{2}}+\alpha_2^{\frac{1}{2}}}\right) = \frac{n}{kV_{\mathrm{A}}}+2(\alpha_1^{\frac{1}{2}}+\alpha_2^{\frac{1}{2}})+\frac{2kV_{\mathrm{A}}}{n}+\frac{2}{k}k_x^2 L^2\frac{V_{\mathrm{A}}}{n}-4\mathrm{i}k_x L\frac{V_{\mathrm{A}}}{n}$$
$$-\frac{2\mathrm{i}k_x L}{k(\alpha_1^{\frac{1}{2}}+\alpha_2^{\frac{1}{2}})}-\frac{4\mathrm{i}k_x L(k^2+k_x^2 L^2)}{k(\alpha_1^{\frac{1}{2}}+\alpha_2^{\frac{1}{2}})}\frac{V_{\mathrm{A}}^2}{n^2}+\frac{2\mathrm{i}k_x L}{k(\alpha_1^{\frac{1}{2}}+\alpha_2^{\frac{1}{2}})}\frac{gk}{n^2}(\alpha_2-\alpha_1)-4\mathrm{i}k_x L\frac{V_{\mathrm{A}}}{n}\frac{\alpha_1^{\frac{1}{2}}-\alpha_2^{\frac{1}{2}}}{\alpha_1^{\frac{1}{2}}+\alpha_2^{\frac{1}{2}}}$$
$$+\frac{8\mathrm{i}k_x L}{k(\alpha_1^{\frac{1}{2}}+\alpha_2^{\frac{1}{2}})}\left(\frac{k_x^2 V_{\mathrm{A}}^2 L^2}{n^2}+\mathrm{i}k_x L(\alpha_1^{\frac{1}{2}}+\alpha_2^{\frac{1}{2}})\frac{V_{\mathrm{A}}}{n}-\alpha_1^{\frac{1}{2}}\alpha_2^{\frac{1}{2}}+\mathrm{i}k_x Lk\frac{V_{\mathrm{A}}^2}{n^2}-k\alpha_2^{\frac{1}{2}}\frac{V_{\mathrm{A}}}{n}\right), \quad (30)$$

measuring n and k in the units $(g/V_{\mathrm{A}})\,\mathrm{sec}^{-1}$ and $(g/V_{\mathrm{A}}^2)\,\mathrm{cm}^{-1}$ respectively.

Equation (30) in nondimensional form reduces to

$$n^3+\left(2k(\alpha_1^{\frac{1}{2}}+\alpha_2^{\frac{1}{2}})-\frac{2\mathrm{i}k_x L}{\alpha_1^{\frac{1}{2}}+\alpha_2^{\frac{1}{2}}}(1+4\alpha_1^{\frac{1}{2}}\alpha_2^{\frac{1}{2}})\right)n^2+k\left(2k+\alpha_1-\alpha_2-\frac{6}{k}k_x^2 L^2-8\mathrm{i}k_x L\right)n$$
$$+2k^2(\alpha_1^{\frac{1}{2}}-\alpha_2^{\frac{1}{2}})-\frac{4\mathrm{i}k_x L(k^2+k_x^2 L^2)}{\alpha_1^{\frac{1}{2}}+\alpha_2^{\frac{1}{2}}}-2\mathrm{i}k_x L(\alpha_1^{\frac{1}{2}}-\alpha_2^{\frac{1}{2}})k$$
$$+\frac{8\mathrm{i}k_x L}{\alpha_1^{\frac{1}{2}}+\alpha_2^{\frac{1}{2}}}(k_x^2 L^2+\mathrm{i}k_x Lk) = 0. \quad (31)$$

This is the general equation for combined horizontal and vertical magnetic fields.

(i) *Real n*

In this case $\alpha_2 > \alpha_1$. If n is real then separating real and imaginary parts of equation (31) we get

$$n^3+2k(\alpha_1^{\frac{1}{2}}+\alpha_2^{\frac{1}{2}})n^2+k\left(2k+\alpha_1-\alpha_2-\frac{6}{k}k_x^2L^2\right)n-\frac{8k_x^2L^2k}{\alpha_1^{\frac{1}{2}}+\alpha_2^{\frac{1}{2}}}+2k^2(\alpha_1^{\frac{1}{2}}-\alpha_2^{\frac{1}{2}})=0, \quad (32)$$

and

$$(1+4\alpha_1^{\frac{1}{2}}\alpha_2^{\frac{1}{2}})n^2+4k(\alpha_1^{\frac{1}{2}}+\alpha_2^{\frac{1}{2}})n+\{2(k^2-k_x^2L^2)+(\alpha_1-\alpha_2)k\}=0. \quad (33)$$

On solving equation (33) we get

$$n=-2k(\alpha_1^{\frac{1}{2}}+\alpha_2^{\frac{1}{2}})\pm[4k^2(\alpha_1^{\frac{1}{2}}+\alpha_2^{\frac{1}{2}})^2-(1+4\alpha_1^{\frac{1}{2}}\alpha_2^{\frac{1}{2}})\{2(k^2-k_x^2L^2)+(\alpha_1-\alpha_2)k\}]^{\frac{1}{2}}. \quad (34)$$

If the term in square brackets is denoted by T then equation (34) gives the characteristic value of n under the condition

$$f(k)\equiv\pm T^{3/2}-4k(\alpha_1^{\frac{1}{2}}+\alpha_2^{\frac{1}{2}})T\pm\{4k^2(\alpha_1^{\frac{1}{2}}+\alpha_2^{\frac{1}{2}})^2+2k^2+k(\alpha_1-\alpha_2)-6k_x^2L^2\}T^{\frac{1}{2}}$$
$$-\left\{2k^2(\alpha_1^{\frac{1}{2}}+\alpha_2^{\frac{1}{2}})\left(2k+\alpha_1-\alpha_2-\frac{6}{k}k_x^2L^2\right)-2k^2(\alpha_1^{\frac{1}{2}}-\alpha_2^{\frac{1}{2}})+\frac{8k_x^2L^2k}{\alpha_1^{\frac{1}{2}}+\alpha_2^{\frac{1}{2}}}\right\}=0. \quad (35)$$

For n to be real

$$4k^2(\alpha_1^{\frac{1}{2}}+\alpha_2^{\frac{1}{2}})^2-(1+4\alpha_1^{\frac{1}{2}}\alpha_2^{\frac{1}{2}})\{2(k^2-k_x^2L^2)-(\alpha_2-\alpha_1)k\}$$

must be positive. The perturbations are damped or unstable according as

$$2(k^2-k_x^2L^2)-(\alpha_2-\alpha_1)k \quad \text{is} \quad > \quad \text{or} \quad < 0$$

under the condition (35).

(ii) *Complex n*

We suppose that $n=\alpha\pm i\beta$, where α and β are real. Substituting for n in equation (31) and equating real and imaginary parts we obtain,

$$(\alpha^3-3\alpha\beta^2)+\left(2k(\alpha_1^{\frac{1}{2}}+\alpha_2^{\frac{1}{2}})(\alpha^2-\beta^2)+\frac{4k_xL(1+4\alpha_1^{\frac{1}{2}}\alpha_2^{\frac{1}{2}})}{\alpha_1^{\frac{1}{2}}+\alpha_2^{\frac{1}{2}}}\alpha\beta\right)$$
$$+k\left(2k+\alpha_1-\alpha_2-\frac{6}{k}k_x^2L^2+8k_xLk\beta\right)+2k^2(\alpha_1^{\frac{1}{2}}-\alpha_2^{\frac{1}{2}})-\frac{8k_x^2L^2k}{\alpha_1^{\frac{1}{2}}+\alpha_2^{\frac{1}{2}}}=0 \quad (36)$$

and

$$(3\alpha^2\beta-\beta^3)+\left(2k(\alpha_1^{\frac{1}{2}}+\alpha_2^{\frac{1}{2}})2\alpha\beta+\frac{2k_xL}{\alpha_1^{\frac{1}{2}}+\alpha_2^{\frac{1}{2}}}(\beta^2-\alpha^2)(1+4\alpha_1^{\frac{1}{2}}\alpha_2^{\frac{1}{2}})\right)+\left\{k\beta\left(2k+\alpha_1-\alpha_2-\frac{6}{k}k_x^2L^2\right)\right.$$
$$\left.-8k_xLk\alpha\right\}-\frac{4k_xL}{\alpha_1^{\frac{1}{2}}+\alpha_2^{\frac{1}{2}}}(k^2+k_x^2L^2)-2k_xLk(\alpha_1^{\frac{1}{2}}-\alpha_2^{\frac{1}{2}})+\frac{8k_xL}{\alpha_1^{\frac{1}{2}}+\alpha_2^{\frac{1}{2}}}k_x^2L^2=0. \quad (37)$$

Considering the cases $\alpha >, =,$ or $< \sqrt{3}\beta$, since $\alpha_2 > \alpha_1$ we conclude that, however α and β are related, equation (36) must allow at least one change of sign and hence one positive root, showing that the equilibrium is unstable.

(b) *Stable Case*

(i) *Real n*

In this case $\alpha_2 < \alpha_1$. Again we consider equations (34) and (35). Here the perturbations are stable or unstable according as

$$2(k^2 - k_x^2 L^2) + (\alpha_1 - \alpha_2)k \quad \text{is} \quad > \text{ or } < 0$$

under the physical situation (35). The perturbations become unstable if $H_\parallel / H_\perp = L$ is large.

(ii) *Complex n*

Consider the three cases $\alpha >, =,$ or $< \sqrt{3}\,\beta$ in equation (36). If $\alpha \geqslant \sqrt{3}\,\beta$, equation (36) does not possess any change of sign and hence the equilibrium is stable. Thus $\alpha \geqslant \sqrt{3}\,\beta$ is the condition for stable equilibrium.

V. REFERENCES

CHANDRASEKHAR, S. (1961).—"Hydrodynamic and Hydromagnetic Stability." pp. 457–65. (Clarendon Press: Oxford.)

HIDE, R. (1955).—*Proc. R. Soc.* A **233**, 376–96.

KRUSKAL, M., and SCHWARZSCHILD, M. (1954).—*Proc. R. Soc.* A **223**, 348–60.

SHORT COMMUNICATIONS

STUDY OF COMBINED EFFECT OF KELVIN–HELMHOLTZ INSTABILITY AND GRAVITATIONAL INSTABILITY ON A SELF-GRAVITATING FLUID LAYER*

By C. Uberoi† and R. Jayakaran Isaac‡

The instability of a self-gravitating fluid layer of finite thickness surrounded by another fluid of different density has been studied recently by Uberoi (1963) and Tassoul (1967) § under varying conditions. Now the condition can arise when the fluid inside the layer and the surrounding material are in relative horizontal motion. It is interesting to study the combined effects of the Kelvin–Helmholtz (KH) instability associated with short wavelengths and the gravitational instability associated with long wavelengths on this layer.

We consider a homogeneous distribution of gravitating ideally conducting fluid mass with constant density ρ in the form of a plane layer of thickness $2h$. The XOY plane is taken to coincide with the unperturbed middle level of the layer and the positive z axis in the upward direction normal to the unperturbed fluid surfaces. This layer is surrounded by a nonconducting fluid of uniform density ρ_0. In the equilibrium state we assume that the system is pervaded by a uniform magnetic field H_1 in the conducting layer and H_2 in the nonconducting fluid, both directed in the x direction. We further assume that initially the conducting and nonconducting fluids are moving with velocities V_1 and V_2 respectively in the x direction. As the disturbances along the direction of the streaming velocities of the fluids and the magnetic field are most sensitive to the KH instability (Chandrasekhar 1961), we shall consider the wave propagation in the x direction only. Hence, we assume that the perturbed quantities depend on time t and spatial coordinate x as $\exp\{\mathrm{i}(\omega t+kx)\}$. As the mathematical procedure is well known (e.g. Uberoi 1963; Tassoul 1967), we shall not give the details here. Following the procedure given in Uberoi (1963), we obtain the dispersion relation, which factorizes into the following two factors corresponding to the asymmetric and symmetric perturbations:

$$\{(\omega+kV_1)^2-k^2V_{\mathrm{A}}^2\}\tanh\theta+\tau\{(\omega+kV_2)^2-k^2V_{\mathrm{B}}^2\}+4\pi G\rho(1-\tau)\left(-1+\frac{1-\tau}{1+\coth\theta}\right)=0 \tag{1}$$

---

* Manuscript received June 14, 1968.

† On leave to Harvard College Observatory, Cambridge, Massachusetts, U.S.A., from present address: Department of Applied Mathematics, Indian Institute of Science, Bangalore-12, India.

‡ Department of Applied Mathematics, Indian Institute of Science, Bangalore-12, India.

§ In Chakraborty (1964, quoted from Tassoul 1967) the presence of surrounding material of density ρ_0 is taken into account in deriving the dispersion relation but is discussed only for the case $\rho_0 = 0$.

Aust. J. Phys., 1968, **21**, 931–7

and

$$\{(\omega+kV_1)^2-k^2V_{\mathrm{A}}^2\}\coth\theta+\tau\{(\omega+kV_2)^2-k^2V_{\mathrm{B}}^2\}+4\pi G\rho(1-\tau)\left(-1+\frac{1-\tau}{1+\tanh\theta}\right)=0\,, \tag{2}$$

where

$$\tau=\rho_0/\rho\,,\qquad \theta=kh\,,\qquad V_{\mathrm{A}}^2=\frac{\mu_0H_1^2}{4\pi\rho}\frac{1}{4\pi G\rho h^2}\,,\qquad V_{\mathrm{B}}^2=\frac{\mu_0H_2^2}{4\pi\rho_0}\frac{1}{4\pi G\rho h^2}\,.$$

In the following analysis we shall assume $\tau<1$ and finally point out some important results that appear due to the presence of relative motion in the case $\tau>1$.

Symmetric Perturbations

(i) $H_1=H_2=0$

The dispersion relation (2) in this case, gives

$$\omega=-k\frac{V_1+V_2\tau\tanh\theta}{1+\tau\tanh\theta}\pm\frac{(4\pi G\rho\tanh\theta)^{\frac{1}{2}}\varDelta^{\frac{1}{2}}}{1+\tau\tanh\theta}\,, \tag{3}$$

where

$$\varDelta=\{(1-\tau)(1+\tau\tanh\theta)G(\theta)-\theta^2\tau U^2\}\,,$$

$$G(\theta)=\left(\theta-\frac{1-\tau}{1+\tanh\theta}\right),\qquad U^2=\frac{(V_2-V_1)^2}{4\pi G\rho h^2}\,.$$

When $U=0$, and if θ' denotes the root of the equation $G(\theta)=0$, then the system is stable for $\theta>\theta'$ and unstable for $\theta<\theta'$ (Uberoi 1963), the instability arising due to self-gravitational force. Considering the case when $U\neq 0$, we find that the presence of the relative streaming velocities of the fluids, however small, alter the stability criterion as seen below.

From (3) we note that $\varDelta$ is negative for all values of $\theta\leqslant\theta'$. For $\theta>\theta'$ the function $G(\theta)$ is a positive monotonically increasing function, increasing as θ. As $\tau U^2\theta^2$ increases as θ^2, $\varDelta$ is negative for large θ. Hence, depending on the value of τU^2 either $\varDelta$ will be negative for all θ or it will have two roots θ_1,θ_2 such that $\varDelta$ is positive for $\theta_1<\theta<\theta_2$ and negative for all other values of θ. Thus, for fixed τ, depending on the value of U^2 either the system is overstable for all wavelengths or there exists a range of values of wave numbers $\theta_1\leqslant\theta\leqslant\theta_2$ for which the system is stable. We note that as U^2 increases, i.e. as the kinetic energy due to the relative motion of the two fluids increases in comparison to the gravitational energy, this range of stability decreases. The range of instability is $0<\theta<\theta_1$ and $\theta>\theta_2$, which shows that the waves are either very long or very short to be stabilized. Here we point out that the instability of long waves is due to self-gravitational force and of small waves is due to the relative motion of the fluid layers.

Table 1 gives critical values θ_1, $\theta_{1\mathrm{m}}$, $\omega_{\mathrm{m}}(\theta=\theta_{1\mathrm{m}})$, and θ_2 for various values of τ and U^2. We note the following points: (1) As U^2 and τ increase, the range of stability decreases until this range becomes zero and the system becomes overstable for all θ. (2) As U^2 increases, the critical wavelength $\lambda^*=(2\pi h/\theta_1)$ associated with the long wavelength instability decreases. Hence, the presence of the relative speed $(V_2 - V_1)$ enhances the instability mainly arising from self-gravitational forces. (3) The maximum wavelength $\lambda^* = (2\pi h/\theta_2)$, associated with the short wavelength KH instability, increases as the value of U^2 and τ is increased. (4) For the case of long wavelength instability due to self-gravitational force, the wave number $\theta_{1\mathrm{m}}$ associated with the maximum mode of instability and the characteristic frequency ω_{m} at $\theta_{1\mathrm{m}}$ increase with the increase in U^2. Hence, the dimensions of the fragments into which the layer tends to break up gravitationally and the characteristic time $t = (2\pi/\omega_{\mathrm{m}})$ of this breakup are decreased by the presence of the relative motion.

TABLE 1

θ_1, $\theta_{1\mathrm{m}}$, ω_{m}, AND θ_2 AS FUNCTIONS OF τ AND U^2 FOR SYMMETRIC CASE IN ABSENCE OF MAGNETIC FIELD

θ_1 and $\theta_{1\mathrm{m}}$ are the wave numbers at which the instability occurs and at which it is a maximum, ω_{m} is the frequency at $\theta_{1\mathrm{m}}$, and θ_2 is the minimum wave number at which the KH instability sets in

U^2	$\tau = 0{\cdot}1$				$\tau = 0{\cdot}3$			
	θ_1	$\theta_{1\mathrm{m}}$	$\omega_{\mathrm{m}}(4\pi G\rho)^{-\frac{1}{2}}$	θ_2	θ_1	$\theta_{1\mathrm{m}}$	$\omega_{\mathrm{m}}(4\pi G\rho)^{-\frac{1}{2}}$	θ_2
0	0·58801	0·27001	0·31974	—	0·48401	0·22201	0·22491	—
0·2	0·59400	0·27201	0·32031	49·04595	0·49800	0·22601	0·22619	14·80799
0·5	0·60401	0·27401	0·32119	19·33999	0·52400	0·23401	0·22825	5·69400
1	0·62001	0·27801	0·32270	9·42800	0·58601	0·24801	0·23209	2·62000
2	0·66201	0·29001	0·32592	4·45001	—	—	—	—
5	—	—	—	—	—	—	—	—
	$\tau = 0{\cdot}5$				$\tau = 0{\cdot}7$			
0	0·37001	0·17201	0·14153	—	0·24201	0·11601	0·07002	—
0·2	0·39200	0·17801	0·14309	7·23999	0·26800	0·12201	0·07141	3·48599
0·5	0·43400	0·19001	0·14573	2·71599	0·33200	0·14001	0·07405	1·15600
1	0·63601	0·22001	0·15141	0·96801	—	—	—	—
2	—	—	—	—	—	—	—	—
5	—	—	—	—	—	—	—	—

(ii) $H_1 \neq 0,\ H_2 \neq 0$

From the dispersion relation (2) we obtain

$$\omega = -k\frac{(V_1 \coth\theta + V_2\tau)}{\tau + \coth\theta} \pm \frac{(4\pi G\rho)^{\frac{1}{2}}(\tanh\theta)^{\frac{1}{2}}\Delta^{\frac{1}{2}}}{\tau\tanh\theta + 1}, \tag{4}$$

where

$$\Delta = \theta^2\Phi + G(\theta), \tag{5}$$

$$\Phi = \coth\theta\,[V_{\mathrm{B}}^2\tau^2\tanh^2\theta - \{U^2 - (V_{\mathrm{A}}^2 + V_{\mathrm{B}}^2)\}\tau\tanh\theta + V_{\mathrm{A}}^2],$$

$$G(\theta) = (1-\tau)(\tau\tanh\theta + 1)\left(\theta - \frac{1-\tau}{1+\tanh\theta}\right).$$

As Φ is quadratic in $\tanh\theta$, it is easy to show that when $U^2 < (V_{\rm A}+V_{\rm B})^2$, Φ is positive for all positive values of θ; when

$$(V_{\rm A}+V_{\rm B})^2 < U^2 < U^{*2} \equiv (\tau+1)/\tau(V_{\rm A}^2+\tau V_{\rm B}^2), \qquad \text{and} \qquad \tau > V_{\rm A}/V_{\rm B},$$

Φ is positive for $\theta < \theta_1$ and $\theta > \theta_2$, while it is negative when $\theta_1 < \theta < \theta_2$; when

$$(V_{\rm A}+V_{\rm B})^2 < U^2 < U^{*2}, \qquad \text{but} \qquad \tau < V_{\rm A}/V_{\rm B},$$

Φ is positive for all θ; when $U^2 > U^{*2}$, Φ is positive if $\theta < \theta_1$ and negative if $\theta > \theta_1$, where θ_1 and θ_2 are given by

$$\tanh\theta_{1,2} = (2V_{\rm B}^2\tau)^{-1}[\{U^2-(V_{\rm A}^2+V_{\rm B}^2)\}\mp\{U^2-(V_{\rm A}-V_{\rm B})^2\}^{\frac{1}{2}}\{U^2-(V_{\rm A}+V_{\rm B})^2\}^{\frac{1}{2}}].$$

TABLE 2

θ', $\theta'_{\rm m}$, $\omega_{\rm m}$, AND θ'' AS FUNCTIONS OF τ, U^2, $V_{\rm A}^2$, AND $V_{\rm B}^2$ FOR SYMMETRIC CASE IN PRESENCE OF MAGNETIC FIELD

θ' and $\theta'_{\rm m}$ are the wave numbers at which the instability occurs and at which it is a maximum, $\omega_{\rm m}$ is the frequency at $\theta'_{\rm m}$, and θ'' is the minimum wave number at which the KH instability sets in

U^2	$\tau = 0\cdot5$				$\tau = 0\cdot7$			
	θ'	$\theta'_{\rm m}$	$\omega_{\rm m}(4\pi G\rho)^{-\frac{1}{2}}$	θ''	θ'	$\theta'_{\rm m}$	$\omega_{\rm m}(4\pi G\rho)^{-\frac{1}{2}}$	θ''
				$V_{\rm A}^2 = 0\cdot5,\ V_{\rm B}^2 = 2$				
0	0·18001	0·09001	0·10616	—	0·09001	0·04601	0·04539	—
2	0·20401	0·10001	0·10967	—	0·10001	0·05001	0·04691	—
4	0·24601	0·11401	0·11441	—	0·12201	0·05801	0·04892	—
4·7	0·27401	0·12201	0·11657	7·24200	0·13601	0·06001	0·04985	8·34800
4·9	0·28601	0·12401	0·11726	3·47800	0·14001	0·06201	0·05014	2·23600
5·0	0·29201	0·12601	0·11762	2·71600	0·14401	0·06201	0·05030	1·28601
5·2	0·30601	0·12801	0·11838	1·81600	0·15201	0·06401	0·05062	0·65201
5·4	0·32601	0·13201	0·11918	1·29001	0·16001	0·06601	0·05096	0·47401
				$V_{\rm A}^2 = 2,\ V_{\rm B}^2 = 1$				
0	0·09001	0·04401	0·07434	—	0·03801	0·01801	0·02884	—
2	0·09201	0·04601	0·07493	—	0·03801	0·01801	0·02897	—
4	0·09601	0·04601	0·07555	—	0·03801	0·02001	0·02914	—
6	0·10001	0·04801	0·07624	—	0·04001	0·02001	0·02933	—
8	0·10401	0·05001	0·07696	2·86199	0·04201	0·02001	0·02951	0·92601
10	0·11001	0·05201	0·07775	0·89001	0·04201	0·02001	0·02969	0·51801
12	0·11801	0·05401	0·07862	0·56401	0·04401	0·02001	0·02988	0·36401
14	0·12801	0·05601	0·07460	0·40001	0·04601	0·02201	0·03009	0·27801

The analytical behaviour of the function Φ and the numerical estimates of $\Phi(\theta)$ and $G(\theta)$, for a few chosen values of $V_{\rm A}^2$, $V_{\rm B}^2$, and τ, show that for $0 < U^2 < U^{*2}$ there exists a critical wave number $\theta_{\rm c}$ such that $\Delta(\theta)$ is negative for $\theta > \theta_{\rm c}$. Hence, from (5) we note that the system is stable for wavelengths $\lambda < \lambda_{\rm c}$ $(= 2\pi h/\theta_{\rm c})$ and is overstable for wavelengths greater than $\lambda_{\rm c}$.

When $U^2 > U^{*2}$, we find that there exists a range of wave numbers, say $\theta' < \theta < \theta''$ for which $\Delta(\theta)$ is positive and is negative for all other values. But as U^2 is increased, the range of wave numbers for which $\Delta(\theta)$ is positive decreases and for higher values of U it becomes negative for all θ. Hence, depending on the values of U^2, the system is either stable for $\theta' < \theta < \theta''$ and overstable for $\theta < \theta'$ and $\theta > \theta''$ or is overstable for all values of θ. Once again we find that the waves are very long or very short to be stabilized.

TABLE 3

MINIMUM WAVE NUMBER θ_c AT WHICH INSTABILITY SETS IN AS FUNCTION OF τ AND U^2 FOR ASYMMETRIC CASE IN ABSENCE OF MAGNETIC FIELD

U^2	θ_c				
	$\tau = 0{\cdot}1$	$0{\cdot}2$	$0{\cdot}4$	$0{\cdot}6$	$0{\cdot}8$
0·2	49·04595	23·59397	10·18999	5·12599	2·17199
0·5	19·33999	9·18200	3·87601	1·94800	0·94801
1	9·42800	4·36001	1·78600	0·98801	0·56401
2	4·45001	1·92600	0·84201	0·55401	0·35801
5	1·39801	0·58401	0·36801	0·29001	0·20601

Hence, we find that the presence of a magnetic field suppresses the instability associated with short wavelengths when $U^2 < U^{*2}$, but due to self-gravitational forces the instability at long wavelengths persists. When the relative speed exceeds the critical speed U^*, the short wavelength instability sets in and we again have two ranges of instability for very short and very long wavelengths. As U is increased, the range of wave numbers for which the system is stable decreases till the system is overstable for all wavelengths. We note from equations (3) and (4) that the real frequency of oscillation is not affected by the magnetic field. Table 2 gives the critical values θ', θ'_m, $\omega_m(\theta = \theta'_m)$, and θ'' for various values of τ, U^2, V_A^2, and V_B^2. We note that the increase in relative motion decreases the dimensions of the fragments, into which the layer tends to break due to gravitational instability, and also the characteristic time associated with this breakup, whereas the increase in total magnetic

TABLE 4

MINIMUM WAVE NUMBER θ_c AT WHICH INSTABILITY SETS IN AS A FUNCTION OF τ, U^2, V_A^2, AND V_B^2 FOR ASYMMETRIC CASE IN PRESENCE OF MAGNETIC FIELD

U^2	θ_c			
	$\tau = 0{\cdot}5$	$0{\cdot}7$	$0{\cdot}5$	$0{\cdot}7$
	$V_A^2 = 0{\cdot}5$, $V_B^2 = 2$		$V_A^2 = 2$, $V_B^2 = 1$	
0	—	—	—	—
4	—	—	—	—
6	0·93001	0·80601	—	—
8	0·49801	0·46201	2·46000	0·43601
10	0·36601	0·34401	0·37201	0·30001
12	0·29601	0·28001	0·28401	0·24201
14	0·25401	0·24001	0·23801	0·20601
16	0·22401	0·21201	0·20801	0·18201

pressure has the tendency to increase the value of λ_{m} and $t = (2\pi/\omega_{\mathrm{m}})$. We also note that for values of U^2 very close to U^{*2} the maximum wavelength $(= 2\pi h/\theta'')$ for which the system is unstable due to KH instability has a very small value.

TABLE 5

θ_{c}, θ_{m}, AND ω_{m} AS FUNCTIONS OF τ, U^2, V_{A}^2, AND V_{B}^2

(a) Symmetric Case

U^2	$\tau = 2$			$\tau = 4$		
	θ_{c}	θ_{m}	$\omega_{\mathrm{m}}(4\pi G\rho)^{-\frac{1}{2}}$	θ_{c}	θ_{m}	$\omega_{\mathrm{m}}(4\pi G\rho)^{-\frac{1}{2}}$
			$V_{\mathrm{A}}^2 = 0·5$, $V_{\mathrm{B}}^2 = 2$			
0	0·44201	0·25801	0·33231	0·99601	0·30601	0·97123
2	0·61401	0·35801	0·37940	1·15601	0·40601	1·00795
4	1·07201	0·55801	0·47755	1·35601	0·50601	1·04908
6	2·53801	1·05601	0·71090	1·70601	0·60601	1·10692
8	—	—	—	2·41001	0·80601	1·19082
10	—	—	—	7·30601	2·20601	1·37074
12	—	—	—	—	—	—
			$V_{\mathrm{A}}^2 = 2$, $V_{\mathrm{B}}^2 = 1$			
0	0·38801	0·15401	0·27868	1·10601	0·40601	0·99548
2	0·55401	0·25401	0·31017	1·40601	0·40601	1·00925
4	1·06401	0·55401	0·39105	1·90601	0·60601	1·06945
6	—	—	—	3·59000	1·10601	1·18304
8	—	—	—	—	—	—
10	—	—	—	—	—	—
12	—	—	—	—	—	—

(b) Asymmetric Case

U^2	θ_{c}	θ_{m}	$\omega_{\mathrm{m}}(4\pi G\rho)^{-\frac{1}{2}}$	θ_{c}	θ_{m}	$\omega_{\mathrm{m}}(4\pi G\rho)^{-\frac{1}{2}}$
			$V_{\mathrm{A}}^2 = 0·5$, $V_{\mathrm{B}}^2 = 2$			
0	0·40201	0·15801	0·29811	0·90601	0·40601	0·73512
2	0·47001	0·25801	0·30876	1·00601	0·40601	0·75287
4	0·61801	0·25801	0·32951	1·10601	0·50601	0·77781
6	2·21801	1·25601	0·36544	1·50601	0·60601	0·81170
8	—	—	—	2·30601	0·90601	0·87634
10	—	—	—	7·20601	3·30601	1·32504
12	—	—	—	—	—	—
			$V_{\mathrm{A}}^2 = 2$, $V_{\mathrm{B}}^2 = 1$			
0	0·54001	0·25401	0·36037	1·13601	0·50601	0·83563
2	0·69401	0·35401	0·38380	1·39000	0·60601	0·87318
4	1·07401	0·45401	0·43263	1·89000	0·80601	0·93047
6	—	—	—	3·50601	1·50601	1·07484
8	—	—	—	—	—	—
10	—	—	—	—	—	—
12	—	—	—	—	—	—

Asymmetric Perturbations

We do not wish to present the detailed mathematical analysis for asymmetric perturbations as the results follow from physical interpretation. As seen in the symmetric case, the KH instability and the gravitational instability both act independently. Hence, as the layer in the case $U = 0$ is gravitationally stable for asymmetric perturbations (Uberoi 1963), the only instability that appears when $U \neq 0$ is the short wavelength KH instability. The results, which are similar to those of Chandrasekhar (1961) are as follows.

In the absence of a magnetic field we have a critical wave number θ_c such that for $\theta < \theta_c$ the system is stable, while for $\theta > \theta_c$ the system is overstable. Table 3 gives the values of θ_c for various values of τ and U^2. We note that as U^2 increases the range of stable wave numbers decreases, i.e. the maximum wavelength for which the system is unstable increases with U. Increase in τ also increases the maximum wavelength of instability. In the presence of a magnetic field we conclude that when $0 \leqslant U^2 < U^{*2}$, the system is stable for all wave numbers but, when $U^2 > U^{*2}$, it is stable for all wave numbers $\theta < \theta_c$ and overstable for $\theta > \theta_c$. Hence, the magnetic field is able to suppress the KH instability when

$$(V_2 - V_1)^2 < (\rho_0 + \rho)(H_1^2 + H_2^2)/4\pi\rho_0\,\rho\,.$$

Table 4 gives the values of θ_c for various values of V_A, V_B, τ, and U^2.

Considering the case $\tau > 1$ in the presence of a magnetic field, we find both for symmetric and asymmetric perturbations that when $U^2 < U^{*2}$, the system is overstable for θ less than a certain θ_c but, when $U^2 > U^{*2}$, the system becomes overstable for all wavelengths. Thus, when the surrounding material is denser we do not have two ranges of instability for any value of U. The magnetic field suppresses the short wavelength instability for $U^2 < U^{*2}$ and makes the potentially unstable equilibrium arrangement stable for wavelengths $\lambda < \lambda_c$; but as the relative speed between the two fluid layers increases, the system acquiring the extra source of kinetic energy becomes overstable. We note that for $\tau > 1$ the system behaves alike both in the presence of symmetric and asymmetric perturbations. Table 5 gives the values of θ_c and θ_m and ω_m, the wave number and characteristic frequency at θ_m associated with the maximum mode of instability, for various values of V_A, V_B, $\tau > 1$, and U^2. We note that the wavelength $\lambda_m = 2\pi h/\theta_m$ and the characteristic time $t = 2\pi/\omega_m$ decrease as the relative motion is increased, and as the value of U^2 approaches the critical value U^{*2} the values of λ_m and t become strikingly small.

We wish to acknowledge helpful discussions with Professor P. L. Bhatnagar. Our particular thanks are due to Dr. G. F. Anderson for help in the numerical calculations. One of us (C.U.) is grateful to the Donald H. Menzel Fellowship for support in this work.

References

CHANDRASEKHAR, S. (1961).—"Hydrodynamic and Hydromagnetic Stability." (Clarendon Press: Oxford.)

TASSOUL, J. L. (1967).—*Mon. Not. R. astr. Soc.* **137**, 1.

UBEROI, C. (1963).—*J. Indian Inst. Sci.* **46**, 11.

THE TEMPERATURE AT 120 KM ALTITUDE IN APRIL–MAY 1965*

By L. M. Sheppard†

Grenade glow clouds were observed at Woomera in April–May 1965 following the firing of five Skylark sounding rockets. The glow cloud experiments formed part of the British programme for upper atmosphere wind measurement. Special observations of the glow clouds were made by the Baker–Nunn camera station at Woomera.

This paper gives new data on the variability of temperature near 120 km altitude using results obtained from observations of 10 grenade glow clouds between 118 and 174 km altitude. Molecular diffusion coefficients are calculated and the atmospheric temperature and density determined using the methods described by Lloyd and Sheppard (1966). The results are compared with those given in the CIRA (1965) model atmosphere. Details of the calculations are given by Sheppard (1968).

Table 1

ATMOSPHERIC TEMPERATURE

Altitude (km)	T (°K) October 1963*	T (°K) April–May 1965	T (°K) CIRA (1965)†
120	—	463	355
130	—	558	477
140	600	605	573
150	670	626	652
160	728	638	721
170	768	647	784
180	795	653	840
190	816	—	890
200	832	—	934

* Lloyd and Sheppard (1966). † Mean model.

The variation of molecular diffusion coefficient with altitude is described by a diffusion scale height H_D. The method given by Lloyd and Sheppard (1966) enables temperature to be calculated over the altitude range for which H_D is known. For the present results, this method was modified because the temperature at the altitude of the highest glow cloud had been determined by Low (1967) from observations of aluminium monoxide spectra. Consequently an ordinary first-order differential equation for the temperature T was integrated downwards from $T = 650 \pm 50$°K at 175 km altitude.

---

* Manuscript received August 2, 1968.

† Australian Defence Scientific Service, Department of Supply, Weapons Research Establishment, Salisbury, S.A. 5108.

Aust. J. Phys., 1968, **21**, 939–40

Errors in the temperature result arise from two main sources. The error in Low's (1967) measurement is ±50°K and there are errors in the measurement of H_D, arising from errors in the molecular diffusion coefficients. It is found that the latter source of error dominates at 120 km altitude, where the maximum error is ±50°K. The results are given in Table 1.

The table shows that the temperature at 120 km altitude was 460±50°K, much greater than the value of 355°K predicted by CIRA (1965). It seems that conditions at 120 km altitude are variable, not constant as was assumed in constructing the CIRA (1965) model atmospheres.

The density was calculated using the temperature results given above; near 170 km altitude it was found to be higher than that predicted by the CIRA (1965) model atmosphere but very similar to that measured previously at Woomera in October 1963. The density at 120 km altitude was a little less than that predicted by the CIRA (1965) model atmosphere.

References

CIRA (1965).—Cospar International Reference Atmosphere 1965. (North-Holland: Amsterdam.)

Lloyd, K. H., and Sheppard, L. M. (1966).—*Aust. J. Phys.* **19**, 323–42.

Low, C. H. (1967).—*Planet. Space Sci.* **15**, 199–200.

Sheppard, L. M. (1968).—Weapons Research Establishment Tech. Note No. HSA 131.

THE DETERMINATION OF STACKING FAULT ENERGY BY THE TETRAHEDRON METHOD*

By P. HUMBLE† and C. T. FORWOOD†

At present there are three methods for obtaining values of the stacking fault energy γ of face-centred cubic (f.c.c.) materials by direct observation of dislocation–stacking fault configurations in the electron microscope. These are based on measurements of extended three-fold dislocation nodes (e.g. Whelan 1958; Brown and Thölen 1964), faulted dipole configurations (e.g. Häussermann and Wilkens 1966; Steeds 1967), and triangular Frank dislocation loops and stacking fault tetrahedra (e.g. Silcox and Hirsch 1959; Loretto, Clarebrough, and Segall 1965). The main advantages of the third method over the other two are that it is applicable to materials of a very wide range of stacking fault energy and involves only simple length measurements of defects that are easily recognized. However, it has suffered from the disadvantage that the values of γ deduced from these measurements relied on an incomplete theory. The present authors have reconsidered this problem and, subject to the limitations of isotropic linear elasticity, have taken into account the major variables that may affect the values of γ. It is the purpose of this note to present the results of this theory in a form in which values of γ may easily be obtained from measurements of Frank dislocation loops and stacking fault tetrahedra without the resources of a large digital computer.

Loretto, Clarebrough, and Segall (1965) have shown that triangular Frank dislocation loops and stacking fault tetrahedra are formed in f.c.c. metals and alloys when these are plastically deformed. Their experiments indicated that a dislocation mechanism was responsible for the formation of the triangular Frank loops and that all the stacking fault tetrahedra were formed by the dissociation of these in the manner originally suggested by Silcox and Hirsch (1959). Thus, by observing the size of the largest tetrahedron and the smallest Frank loop in a given plastically deformed material, it is possible to determine the critical edge length l_c above which the transformation of loops to tetrahedra is energetically unfavourable.

Several authors (Czjzek, Seeger, and Mader 1962; Jøssang and Hirth 1966; Humble, Segall, and Head 1967) have computed the energy balance between triangular Frank loops and stacking fault tetrahedra as a function of defect size, but they have considered only the terms in the dislocation interaction energy and stacking fault energy. We have recently reformulated the problem considering the total energy of the defect (Humble and Forwood 1968). This formulation includes terms such as the kinetic energy of the moving Shockley dislocations T, the energy dissipated to the crystal lattice μ, and the work done by the stress W, as well as terms in the interaction energy E_{td} and fault energy $E_{t\gamma}$. The potential energy of a crystal containing the defect $E_{td}+E_{t\gamma}-W$ was plotted as a function of dissociation,

---

* Manuscript received August 21, 1968.

† Division of Tribophysics, CSIRO, University of Melbourne, Parkville, Vic. 3052.

Aust. J. Phys., 1968, **21**, 941–4

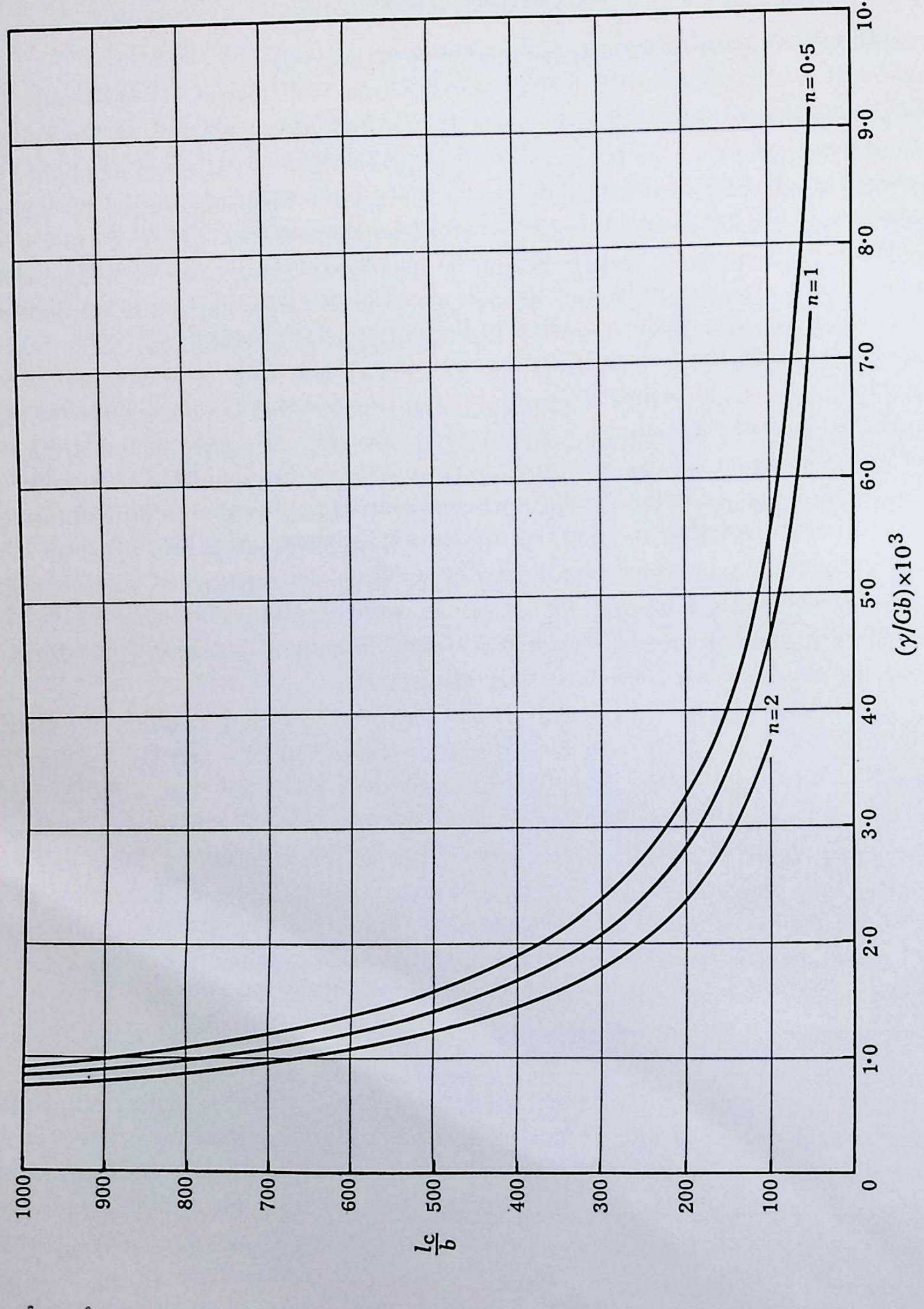

Fig. 1.—Curves of the critical defect edge length l_c/b versus the stacking fault energy γ/Gb along which triangular Frank dislocation loops just transform to stacking fault tetrahedra. See text for full details.

and any decrease in the potential energy from its value at zero dissociation (the Frank loop) corresponds to an equivalent increase in $T+\mu$. By considering the maximum kinetic energy available to the Shockley dislocations for the cases of copper, silver, and gold, it was possible to estimate their maximum velocity and thus show that very little energy is lost to the crystal lattice. It is possible, therefore, to consider the transformation to be conservative.

For a given critical size of defect l_c, the stacking fault energy was determined by finding that value of γ at which the total drop in potential energy from the value for the undissociated Frank loop, A, to the minimum in the curve, B, was equal to the increase from B to a maximum at C, which took place during the later stages of dissociation. This procedure for determining stacking fault energy by equating the potential energy at A to that at C was shown to be reliable, since, within the limitations of the model, these two points are independent of the exact detail involved in the dynamics of the transformation.

On the basis of these considerations, curves of stacking fault energy γ/Gb (where G is the shear modulus and b the interatomic distance) have been calculated as a function of the critical edge length l_c/b. Three such curves are shown in Figure 1. They were calculated on the basis of a three-parameter model for the way in which triangular Frank loops dissociate (Humble, Segall, and Head) and on the assumption that all the kinetic energy of the moving dislocation is conserved.

In calculating the curves in Figure 1, the inner cutoff radius ϵ for a particular dislocation has been taken to be directly proportional to the Burgers vector **B** of that dislocation, that is, $\epsilon = n\,|\mathbf{B}|$. The three curves in Figure 1 correspond to values of $n = 0{\cdot}5$, 1, and 2.

The value of the shear stress used in the calculations was $1{\cdot}57\times10^{-5}G$. This corresponds to a tensile stress σ of $0{\cdot}5\times10^{-3}G$ in the metal acting normal to the plane of the Frank loop. This is of the order of the flow stress for most metals. To indicate the variation in the value of γ with variation in stress, the values of γ/Gb for three values of l_c/b at tensile stresses of 0, $0{\cdot}5$, and $1{\cdot}0\ \times10^{-3}G$ for $n = 1$ are given in Table 1.

TABLE 1

VARIATION OF γ WITH VARIATION IN STRESS FOR $n = 1$

	$(\gamma/Gb)\times10^3$ at:		
l_c/b	$\sigma = 0$	$\sigma = 0{\cdot}5\times10^{-3}G$	$\sigma = 1{\cdot}0\times10^{-3}G$
100	4·54	4·63	4·72
400	1·58	1·67	1·76
1000	0·75	0·84	0·93

The value of Poisson's ratio ν used throughout the calculations was $0{\cdot}4$. To within 1%, the l_c versus γ curves for other values of ν may be obtained from the curves in Figure 1 by multiplying the values of γ/Gb for a particular l_c by the factor $(1-0{\cdot}4)/(1-\nu)$.

It may be seen from Table 1 that the values of γ/Gb show a different dependence on l_c from that deduced using previous theories. For example, the values deduced on the theory of Humble, Segall and Head (1967) using the same model as that used here with the energy criterion of Czjzek, Seeger, and Mader (1962) for values of l_c equal to $100b$, $400b$, and $1000b$ are $4\cdot37\times10^{-3}$, $1\cdot33\times10^{-3}$, and $0\cdot60\times10^{-3}$ respectively.

The curves given in Figure 1, together with the variations indicated above, provide a means of estimating the stacking fault energy of a wide range of f.c.c. metals under varying conditions whenever the determination of a critical edge length for the transformation of triangular Frank loops to stacking fault tetrahedra is possible.

References

Brown, L. M., and Thölen, A. R. (1964).—*Discuss. Faraday Soc.* **38**, 35.

Czjzek, G., Seeger, A., and Mader, S. (1962).—*Phys. Status Solidi* **2**, 558.

Häussermann, F., and Wilkens, M. (1966).—*Phys. Status Solidi* **18**, 609.

Humble, P., and Forwood, C. T. (1968).—*Phys. Status Solidi* **29**, 99.

Humble, P., Segall, R. L., and Head, A. K. (1967).—*Phil. Mag.* **15**, 281.

Jøssang, T., and Hirth, J. P. (1966).—*Phil. Mag.* **13**, 657.

Loretto, M. H., Clarebrough, L. M., and Segall, R. L. (1965).—*Phil. Mag.* **11**, 459

Silcox, J., and Hirsch, P. B. (1959).—*Phil. Mag.* **4**, 72.

Steeds, J. W. (1967).—*Phil. Mag.* **16**, 785.

Whelan, M. J. (1958).—*Proc. R. Soc.* A **249**, 114.

CORRIGENDUM

VOLUME 21, NUMBER 2

"Inelastic scattering of deuterons from ^{56}Fe." By A. R. Majumder and H. M. Sen Gupta. pp. 235–7

Throughout the paper *replace* 2·077 MeV *by* 2·081 MeV for the energy of the second level.

INDEX

PAGE
Aluminium, energy levels in 803
Aluminium: study of 3·00 MeV level of $^{27}\mathrm{Al}$ via $^{24}\mathrm{Mg}(\alpha, p\gamma)^{27}\mathrm{Al}$ 405
Andrews, M., Bertram, W. K., and Tassie, L. J.—
  The behaviour of DWBA stripping amplitudes near the Butler pole .. 423
Antarctica, spread-*F* irregularities in .. 695
Astronomy
  Observations of flare star UV Ceti .. 725
  Optical spectrum of Vela X 501
  Rectangular coordinates of galactic plane positions on the Palomar Sky Atlas .. .. APS* 5
  See also Astrophysics; Identifications, astronomical; Radiofrequency radiation, cosmic
Astrophysics
  Consequences of existence of charged intermediate vector bosons .. 139
  Equilibrium poloidal magnetic fields in rotating stars 293
  Nonlinear adiabatic pulsations of massive stars 465
  Propagation of shock waves in polytrope with poloidal magnetic field 681
  Structure of polytropes with purely toroidal magnetic fields 283

Bajaj, M. M.—
  See Gupta, S. L. 649
Bajaj, M. M., Gupta, S. L., and Saha, N. K.—
  Directional correlation of gamma rays in the decay of 2·3 d $^{115}\mathrm{Cd}$ 317
Barker, A. A.—
  A quantum mechanical calculation of the radial distribution function for a plasma 121
Barker, F. C., and Fitzpatrick, B. M.—
  R-matrix fit to $^{9}\mathrm{Be}(\gamma, n)^{8}\mathrm{Be}$ cross section near threshold 415
Barker, F. C., Hay, H. J., and Treacy, P. B.—
  0^{+} states of $^{8}\mathrm{Be}$ 239

PAGE
Bassett, I. M.—
  Trial of a numerical method for solving the Schrödinger wave equation in several variables 113
Bateson, F. M.—
  See Higgins, C. S. 725
Baxter, R. J.—
  Ornstein–Zernike relation for a disordered fluid 563
Bennett, J. A.—
  The ray theory of Doppler frequency shifts 259
Bertram, W. K.—
  See Andrews, M. 423
Beryllium: 0^{+} states of $^{8}\mathrm{Be}$ 239
Beryllium: *R*-matrix fit to $^{9}\mathrm{Be}(\gamma, n)^{8}\mathrm{Be}$ cross section 415
Bolton, J. G.—
  See Merkelijn, Jeannette K. 523
Bolton, J. G., Shimmins, A. J., and Merkelijn, Jeannette—
  Identification of radio sources between declinations +27° and −30° .. 81
Boltzmann equation, exact solution of, for rigid sphere gas 543
Bowman, G. G.—
  The nature of spread-*F* irregularities in Antarctica 695
Bromine: γ-rays in decay of 36 hr $^{82}\mathrm{Br}$ 649
Brooker, P. I., and Green, H. S.—
  An exact solution of Boltzmann's equation for a rigid sphere gas .. 543
Butler pole, behaviour of DWBA stripping amplitudes near 423
Bydder, E. L., and Liley, B. S.—
  The formal nonequilibrium theory of partially ionized and/or nonuniform gas mixtures 609

Cadmium: directional correlation of γ-rays in 2·3 d $^{115}\mathrm{Cd}$ decay 317
Campbell, J. A.—
  Astrophysical consequences of the existence of charged intermediate vector bosons 139
Cole, T.—
  Finite sample correlations of quantized Gaussians 273

* APS 5 = Astrophysical Supplement No. 5.

PAGE

Cook, J. L.—
Application of reaction matrix theory to meson processes 769
Cosmic rays: sudden intensity increases 755
Crawley, G. M., Powell, D. L., and Narasimha Rao, B. V.—
States in ^{27}Al and ^{89}Y using high resolution surface barrier counters .. 803
Crompton, R. W., Elford, M. T., and McIntosh, A. I.—
Electron transport coefficients in hydrogen and deuterium 43
Crompton, R. W., and McIntosh, A. I.—
Electron drift and diffusion in parahydrogen at 77°K 637
Cross, R. C., and Lehane, J. A.—
Compressional Alfvén wave propagation below ion cyclotron frequency .. 129

Davidson, W.—
Study of a complete sample of cosmic radio sources 871
Davies, G. F.—
Equilibrium poloidal magnetic fields in rotating stars 293
Day, G. A.—
See Shimmins, A. J. 377
Delves, L. M., and Kalotas, T.—
The ground state of the (p–μ–p)$^+$ molecule ion 1
Variational calculations for three-body S-states with Coulomb interactions .. 431
Deuterium, electron transport coefficients in 43
Deuterons, APB model analysis for elastic scattering of 7
Deuterons inelastically scattered from ^{56}Fe 235, 944
Doppler frequency shifts, ray theory of 259
Dyne, R. J.—
See Parsons, R. W. 13

Electrons
Drift and diffusion in parahydrogen at 77°K 637
Energy loss spectra for second and third series transition metals .. 811
Possible limits on local interstellar spectrum 845
Properties of drifting and diffusing pulse 761
Transport coefficients in hydrogen and deuterium 43

PAGE

Elford, M. T.—
See Crompton, R. W. 43
Elliott, R. V.—
See Kean, D. C. 405

Fitzpatrick, B. M.—
See Barker, F. C. 415
Forwood, C. T.—
See Humble, P. 941
Francey, R. J.—
See Harries, J. R. 715

Gardner, F. F.—
See McGee, R. X. 149
Gardner, F. F., and Morimoto, M.—
5 GHz continuum radiation from southern hemisphere galactic HII regions 881
Garzón Cárdenas, X.—
See Wielebinski, R. 185
Gaseous electronics
Electron drift and diffusion in parahydrogen at 77°K 637
Electron transport coefficients in hydrogen and deuterium 43
Formal nonequilibrium theory of partially ionized and/or nonuniform gas mixtures 609
Properties of drifting and diffusing pulse of electrons and Townsend's coefficient of ionization 761
Gellie, R. W.—
The (γ, p) and (γ, n) reactions in molybdenum 765
Geomagnetism: multipole analysis theory and geomagnetic multipoles 1965·0 .. 455
Gold, electron energy loss spectrum for 811
Goss, M.—
Rectangular coordinates of galactic plane positions on the Palomar Sky Atlas .. .. APS 5
Green, H. S.—
See Brooker, P. I. 543
Gupta, S. L.—
See Bajaj, M. M. 317
Gupta, S. L., and Bajaj, M. M.—
Directional correlations of gamma rays in the decay of 36 hr ^{82}Br 649

Hafnium, electron energy loss spectrum 811
Hamilton, P. A.—
See Haynes, R. F. 87, 539

PAGE

Hamilton, P. A., and Haynes, R. F.—
Observations of the southern sky at $10 \cdot 02$ MHz 895
Harries, J. R., and Francey, R. J.—
Observations of Cen XR-2, Sco XR-1, and terrestrial X-rays 715
Harvey, P. J.—
A search for a $5 \cdot 5$ MeV level in ^{7}Li .. 103
Hay, H. J.—
See Barker, F. C. 239
Haynes, R. F.—
See Hamilton, P. A. 895
Haynes, R. F., and Hamilton, P. A.—
Observations of 31 radio sources between 40 and 130 MHz 87
Haynes, R. F., Hamilton, P. A., and McCulloch, P. M.—
Observations of 11 radio sources near 55 MHz 539
Higgins, C. S.—
See Slee, O. B. 341
Higgins, C. S., Solomon, L. H., and Bateson, F. M.—
Optical and radio observations of the flare star UV Ceti in Australasia during September–October 1967 725
Hill, E. R.—
A continuum survey of the Southern Milky Way at 1410 MHz 735
Humble, P.—
Computed electron micrographs for tilted foils containing dislocations and stacking faults 325
Humble, P., and Forwood, C. T.—
The determination of stacking fault energy by the tetrahedron method .. 941
Huxley, L. G. H.—
The properties of a drifting and diffusing pulse of electrons and Townsend's coefficient of ionization α_T 761
Hydrodynamics
Combined effect of Kelvin–Helmholtz instability and gravitational instability on a self-gravitating fluid layer 931
Effect of horizontal and vertical magnetic fields on Kelvin–Helmholtz instability 917
Effect of horizontal and vertical magnetic fields on Rayleigh–Taylor instability 923
Shape and energy of revolving liquid mass held together by surface tension 823
Stability of revolving liquid mass held together by surface tension 837

PAGE

Hydrogen
Continuum radiation, 5 GHz, from southern hemisphere galactic HII regions 881
Electron drift and diffusion in parahydrogen at 77°K 637
Electron transport coefficients in hydrogen 43
Excited atomic H lines 126α and 127α in HII regions 149

Identifications, astronomical
Radio sources between declinations $+20°$ and $+27°$ 523, 903
Radio sources between declinations $+27°$ and $-30°$ 81
Ion, isolated monovalent, interaction energy of 597
Ion pair with overlapping hydration shells, interaction energy of .. 571, 587
Ionosphere
Nature of spread-*F* irregularities in Antarctica 695
Ray theory of Doppler frequency shifts 259
Ions: potential due to two point charges each at the centre of a spherical cavity and embedded in a dielectric medium 817
Iridium, electron energy loss spectrum for 811

James, R. W.—
Multipole analysis. I. Theory, and geomagnetic multipoles $1965 \cdot 0$ .. 455
Jayakaran Isaac, R.—
See Uberoi, C. 931
Jupiter
Decametric radio emission and the solar wind 341
Interpretation of radio rotation period in terms of the cyclotron theory .. 409
Linear polarization of radiation at 6 cm wavelength 337

Kalotas, T.—
See Delves, L. M. 1, 431
Kean, D. C., Elliott, R. V., and Spear, R. H.—
A study of the $3 \cdot 00$ MeV level of ^{27}Al via ^{24}Mg(α, pγ)^{27}Al 405
Kelvin–Helmholtz instability, effect of horizontal and vertical magnetic fields 917
Kelvin–Helmholtz instability, effect on self-gravitating fluid layer of 931

PAGE

Kesteven, M. J. L.—
  A catalogue of galactic radio sources 369
  Supernova remnants as radio sources 739
Khan, A. H.—
  See Rahman, M. 7

Lehane, J. A.—
  See Cross, R. C. 129
Levine, S.—
  See Ross, D. K. 571
Liley, B. S.—
  See Bydder, E. L. 609
Lithium: search for 5·5 MeV level in ^{7}Li 103
Lithium atoms, charge exchange collisions between protons and 793
Lodge, J. G., and May, R. M.—
  Charge exchange collisions involving multielectron atoms (lithium and sodium) 793
Lynch, M. J., and Swan, J. B.—
  The characteristic loss spectra of the second and third series transition metals 811

McCulloch, P. M.—
  Interpretation of the radio rotation period of Jupiter in terms of the cyclotron theory 409
  See also Haynes, R. F. 539
McGee, R. X., and Gardner, F. F.—
  The excited atomic hydrogen lines 126α and 127α in HII regions 149
McIntosh, A. I.—
  See Crompton, R. W. 43, 637
Majumder, A. R., and Sen Gupta, H. M.—
  Inelastic scattering of deuterons from ^{56}Fe 235, 944
May, R. M.—
  See Lodge, J. G. 793
Merkelijn, Jeannette K.—
  Accurate positions and identifications of 75 radio sources between declinations +20° and +27° 903
  See also Bolton, J. G. 81
Merkelijn, Jeannette K., Shimmins, A. J., and Bolton, J. G.—
  Accurate positions and some optical identifications for 67 radio sources between declinations +20° and +27° 523
Meson processes, application of *R*-matrix theory to 769
Metchnik, V. I.—
  See Parsons, R. W. 13
Microwave spectroscopy: collision broadening of spectral lines 13

PAGE

Milky Way, Southern, continuum survey 735
Mills, B. Y., and Shaver, P. A.—
  High resolution observations of the Orion Nebula at 408 MHz 95
Mills, B. Y., Shobbrook, R. R., and Stewart-Richardson, D.—
  Radio sources in clusters of galaxies 511
Milne, D. K.—
  Radio emission from the supernova remnant Vela X 201
  The optical spectrum of Vela X 501
Molybdenum, electron energy loss spectrum for 811
Molybdenum, (γ, p) and (γ, n) reactions in 765
Morimoto, M.—
  See Gardner, F. F. 881
Morris, D., and Whiteoak, J. B.—
  The distribution of linear polarization over 13 extended sources at 21·2 cm wavelength 475
  Observations of the linear polarization of radio sources at 6 cm wavelength 493
Morris, D., Whiteoak, J. B., and Tonking, F.—
  The linear polarization of radiation from Jupiter at 6 cm wavelength 337
Murphy, J. O.—
  Nonlinear adiabatic pulsations of massive stars 465
Musgrove, A. R. de L.—
  On the problem of unresolved resonances in neutron spectroscopy 779

Narasimha Rao, B. V.—
  See Crawley, G. M. 803
Nicholas, J. F.—
  Calculation of surface energy as a function of orientation for cubic crystals 21
Niobium, electron energy loss spectrum 811
Nuclear physics
  Angular distributions in the giant resonance of ^{16}O 107
  APB model analysis for elastic scattering of deuterons 7
  Application of *R*-matrix theory to meson processes 769
  Behaviour of DWBA stripping amplitudes near the Butler pole 423
  Directional correlations of γ-rays in decay of 36 hr ^{82}Br 649
  Directional correlations of γ-rays in decay of 2·3 d ^{115}Cd 317

PAGE

- (γ, p) and (γ, n) reactions in molybdenum 765
- Gamma radiation from $^{20}Ne(\alpha, \alpha'\gamma_{1\cdot63})^{20}Ne$ and $^{20}Ne(\alpha, p\gamma_{0\cdot44})^{23}Na$ 307
- Ground state of the $(p\text{–}\mu\text{–}p)^+$ molecule ion 1
- Inelastic scattering of deuterons from ^{56}Fe 235
- 0^+ states of ^8Be 239
- R-matrix fit to $^9Be(\gamma, n)^8Be$ cross section near threshold 415
- Search for 5·5 MeV level in ^7Li .. 103
- States in ^{27}Al and ^{89}Y using high resolution surface barrier counters .. 803
- Study of 3·00 MeV level of ^{27}Al via $^{24}Mg(\alpha, p\gamma)^{27}Al$ 405
- Unresolved resonances in neutron spectroscopy 779
- Variational calculations for three-body S-states with Coulomb interactions 431

Oitmaa, J.—
- Dielectric saturation in ionic crystals. II. Deformable ions 439

Optics
- Diffraction by E-polarized plane slit aperture 35
- Diffraction by slit aperture formed by two inclined surfaces 661

Orion Nebula, high resolution observations of 95

Ornstein–Zernike relation for disordered fluid 563

Oxygen: angular distributions in the giant resonance of ^{16}O 107

Palladium, electron energy loss spectrum 811

Parkes catalogue of radio sources, declination zone +20° to +27° 377

Parsons, R. W., Metchnik, V. I., and Dyne, R. J.—
- The collision broadening of spectral lines 13

Plasma
- Charge exchange collisions involving multielectron atoms (lithium and sodium) 793
- Compressional Alfvén wave propagation below ion cyclotron frequency 129
- Quantum mechanical calculation of radial distribution function 121

Platinum, electron energy loss spectrum 811

Powell, D. L.—
- *See* Crawley, G. M. 803

PAGE

Quantum theory: exact solution of Boltzmann equation for rigid sphere gas 543

Radiofrequency radiation, cosmic
- Accurate positions and some optical identifications for 67 sources between declinations +20° and +27° .. 523
- Accurate positions of 75 sources between declinations +20° and +27° .. 903
- Accurate positions of 210 radio sources 65
- Accurate right ascensions of selected southern sources 221
- Catalogue of galactic sources 369
- Continuum radiation, 5 GHz, from southern hemisphere galactic HII regions 881
- Continuum survey of Southern Milky Way at 1410 MHz 735
- Distribution of linear polarization over 13 extended sources at 21·2 cm .. 475
- Emission from supernova remnant Vela X 201
- Emissions from 158 galaxies 193
- Excited atomic H lines 126α and 127α in HII regions 149
- High resolution observations of Orion Nebula at 408 MHz 95
- Identification of radio sources between declinations +27° and −30° .. 81
- Interpretation of distribution of metre wavelength emission 167
- Interpretation of radio rotation period of Jupiter in terms of cyclotron theory 409
- Linear polarization of Jovian radiation at 6 cm 337
- Nonthermal emission from the Galaxy and local interstellar electron spectrum 845
- Observations of 11 radio sources near 55 MHz 539
- Observations of flare star UV Ceti .. 725
- Observations of linear polarization at 6 cm 493
- Observations of southern sky at 10·02 MHz 895
- Observations of 31 radio sources between 40 and 130 MHz 87
- Parkes catalogue of radio sources, declination zone +20° to +27° .. 377
- Solar wind and Jovian decametric radio emission 341
- Sources in clusters of galaxies .. 511

PAGE

- Study of complete sample of sources 871
- Supernova remnants as sources .. 739
- Survey of galactic plane at 85 and 150 MHz 185

Rahman, M., Khan, A. H., and Sen Gupta, H. M.—
- The Akhieser–Pomeranchuk–Blair model analysis for elastic scattering of deuterons 7

Rayleigh–Taylor instability, effect of horizontal and vertical magnetic fields 923

Rhenium, electron energy loss spectrum 811

Rhodium, electron energy loss spectrum 811

Ross, D. K.—
- The interaction energy of an ion pair with overlapping hydration shells. II. A spheroidal cavity model .. 587
- The interaction energy of an isolated monovalent ion 597
- The potential due to two point charges each at the centre of a spherical cavity and embedded in a dielectric medium 817
- The shape and energy of a revolving liquid mass held together by surface tension 823
- The stability of a rotating liquid mass held together by surface tension .. 837

Ross, D. K., and Levine, S.—
- The interaction energy of an ion pair with overlapping hydration shells. I. A truncated spheres model .. 571

Saha, N. K.—
- *See* Bajaj, M. M. 317

Sen Gupta, H. M.—
- *See* Majumder, A. R. 235, 944
  - Rahman, M. 7

Sharma, R. C., and Srivastava, K. M.—
- Effect of horizontal and vertical magnetic fields on Kelvin–Helmholtz instability 917
- Effect of horizontal and vertical magnetic fields on Rayleigh–Taylor instability 923

Shaver, P. A.—
- *See* Mills, B. Y. 95

Sheppard, L. M.—
- The temperature at 120 km altitude in April–May 1965 939

Shimmins, A. J.—
- Accurate positions of 210 radio sources 65
- *See also* Bolton, J. G. 81
  - Merkelijn, Jeannette K. .. 523

PAGE

Shimmins, A. J., and Day, G. A.—
- The Parkes catalogue of radio sources, declination zone +20° to +27° .. 377

Shobbrook, R. R.—
- *See* Mills, B. Y. 511

Silver, electron energy loss spectrum for 811

Sinha, Narendra K.—
- Propagation of shock waves in a polytrope with a poloidal magnetic field 681
- Structure of polytropes with purely toroidal magnetic fields 283

Slater determinants employed in a numerical method for solving Schrödinger wave equation 113

Slee, O. B., and Higgins, C. S.—
- The solar wind and Jovian decametric radio emission 341

Smith, D. H.—
- *See* Wielebinski, R. 185

Sodium atoms, charge exchange collisions between protons and 793

Solid state physics
- Computed electron micrographs for tilted foils containing dislocations and stacking faults 325
- Crystals, ionic, dielectric saturation in 439
- Determination of stacking fault energy by tetrahedron method 941
- Surface energy as a function of orientation for cubic crystals 21

Solomon, L. H.—
- *See* Higgins, C. S. 725

Spear, R. H.—
- *See* Kean, D. C. 405

Spear, R. H., and Wright, I. F.—
- Gamma radiation from the reactions $^{20}\mathrm{Ne}(\alpha, \alpha'\gamma_{1\cdot63})^{20}\mathrm{Ne}$ and $^{20}\mathrm{Ne}(\alpha, p\gamma_{0\cdot44})^{23}\mathrm{Na}$ 307

Srivastava, K. M.—
- *See* Sharma, R. C. 917, 923

Stewart, R. J. J.—
- Angular distributions in the giant resonance of $^{16}\mathrm{O}$ 107

Stewart-Richardson, D.—
- *See* Mills, B. Y. 511

Sud, L. V.—
- Cosmic ray intensity increase on January 28, 1967 755

Sun: solar wind and Jovian decametric radio emission 341

Sutton, J. M.—
- Accurate right ascensions of selected southern radio sources 221

PAGE

Swan, J. B.—
See Lynch, M. J. 811

Tan, H. S.—
Diffraction by a slit aperture formed by two inclined surfaces 661
Electromagnetic diffraction by a plane slit aperture 35
Tantalum, electron energy loss spectrum 811
Tassie, L. J.—
See Andrews, M. 423
Tonking, F.—
See Morris, D. 337
Tovmassian, H. M.— ..
Radio emission of 158 galaxies .. 193
Treacy, P. B.—
See Barker, F. C. 239
Tungsten, electron energy loss spectrum 811

Uberoi, C., and Jayakaran Isaac, R.—
Study of Kelvin–Helmholtz instability and gravitational instability on a self-gravitating fluid layer 931
Upper atmosphere
Acoustic-gravity waves ducted in the thermosphere 671
Temperature at 120 km in April–May 1965 939

Vela X, optical spectrum of 501
Vela X, Y, and Z, radio emission from .. 201

PAGE

Webber, W. R.—
On the relationship between recent measurements of cosmic ray electrons, nonthermal radio emission from the Galaxy, and the solar modulation of cosmic rays 845
Whiteoak, J. B.—
See Morris, D. 337, 475, 493
Wickersham, A. F.—
The origin and propagation of acoustic-gravity waves ducted in the thermosphere 671
Wielebinski, R., Smith, D. H., and Garzón Cárdenas, X.—
A survey of the galactic plane at 85 and 150 MHz 185
Wright, I. F.—
See Spear, R. H. 307

X-rays: observations of Cen XR-2, Sco XR-1, and terrestrial X-rays 715

Yates, K. W.—
An interpretation of the distribution of metre wavelength radio emission .. 167
Yttrium, electron energy loss spectrum 811
Yttrium, energy levels in 803

Zirconium, electron energy loss spectrum 811

AUSTRALIAN JOURNAL
OF PHYSICS

VOLUME 21

MELBOURNE
1968

AUSTRALIAN JOURNAL OF PHYSICS

Published by the Commonwealth Scientific and Industrial Research Organization. Issued six times a year, $A4 per annum.

BOARD OF STANDARDS

The Board of Standards for this Journal is appointed by the Commonwealth Scientific and Industrial Research Organization and the Australian Academy of Science and consists of Professor J. S. Turner (Chairman), Mr. A. E. Scott (Editor-in-Chief), Professor C. W. Emmens, Dr. S. D. Hamann, Professor C. B. O. Mohr, and Professor G. H. Satchell.

ADVISORY COMMITTEE

Acceptance of papers for this Journal is in the hands of an Advisory Committee appointed by the Board of Standards in consultation with the Australian Institute of Physics and consisting of Mr. A. E. Scott (Editor-in-Chief and Chairman), Professor A. J. F. Boyle, Dr. J. L. Farrands, Dr. C. H. B. Priestley, Professor R. Street, and Dr. J. P. Wild.

◆

All enquiries and manuscripts should be forwarded to:
The Editor-in-Chief,
Editorial and Publications Section, CSIRO,
Sixth Floor,
372 Albert Street,
East Melbourne, Victoria 3002

CONTENTS

Number 1, February 1968

PAGE

The ground state of the $(p\text{–}\mu\text{–}p)^+$ molecule ion. By L. M. Delves and T. Kalotas 1

The Akhieser–Pomeranchuk–Blair model analysis for elastic scattering of deuterons. By M. Rahman, A. H. Khan, and H. M. Sen Gupta .. 7

The collision broadening of spectral lines. By R. W. Parsons, V. I. Metchnik, and R. J. Dyne 13

Calculation of surface energy as a function of orientation for cubic crystals. By J. F. Nicholas 21

Electromagnetic diffraction by a plane slit aperture. By H. S. Tan 35

Electron transport coefficients in hydrogen and deuterium. By R. W. Crompton, M. T. Elford, and A. I. McIntosh 43

Accurate positions of 210 radio sources. By A. J. Shimmins 65

Identification of radio sources between declinations +27° and −30°. By J. G. Bolton, A. J. Shimmins, and Jeannette Merkelijn 81

Observations of 31 radio sources between 40 and 130 MHz. By R. F. Haynes and P. A. Hamilton 87

High resolution observations of the Orion Nebula at 408 MHz. By B. Y. Mills and P. A. Shaver 95

Short Communications

A search for a 5·5 MeV level in ^{7}Li. By P. J. Harvey 103

Number 2, April 1968

Angular distributions in the giant resonance of ^{16}O. By R. J. J. Stewart .. 107

Trial of a numerical method for solving the Schrödinger wave equation in several variables. By I. M. Bassett 113

A quantum mechanical calculation of the radial distribution function for a plasma. By A. A. Barker 121

Compressional Alfvén wave propagation below ion cyclotron frequency. By R. C. Cross and J. A. Lehane 129

NUMBER 2, APRIL 1968 (*Continued*)

PAGE

Astrophysical consequences of the existence of charged intermediate vector bosons. By J. A. Campbell 139

The excited atomic hydrogen lines 126α and 127α in HII regions. By R. X. McGee and F. F. Gardner 149

An interpretation of the distribution of metre wavelength radio emission. By K. W. Yates 167

A survey of the galactic plane at 85 and 150 MHz. By R. Wielebinski, D. H. Smith, and X. Garzón Cárdenas 185

Radio emission of 158 galaxies. By H. M. Tovmassian 193

Radio emission from the supernova remnant Vela-X. By D. K. Milne .. 201

Accurate right ascensions of selected southern radio sources. By J. M. Sutton 221

Short Communications

Inelastic scattering of deuterons from ^{56}Fe. By A. R. Majumder and H. M. Sen Gupta 235

NUMBER 3, JUNE 1968

0^+ states of ^{8}Be. By F. C. Barker, H. J. Hay, and P. B. Treacy 239

The ray theory of Doppler frequency shifts. By J. A. Bennett 259

Finite sample correlations of quantized Gaussians. By T. Cole 273

Structure of polytropes with purely toroidal magnetic fields. By Narendra K. Sinha 283

Equilibrium poloidal magnetic fields in rotating stars. By G. F. Davies .. 293

Gamma radiation from the reactions ^{20}Ne(α,$\alpha'\gamma_{1\cdot63}$)^{20}Ne and ^{20}Ne(α,p$\gamma_{0\cdot44}$)^{23}Na. By R. H. Spear and I. F. Wright 307

Directional correlation of gamma rays in the decay of 2·3 d ^{115}Cd. By M. M. Bajaj, S. L. Gupta, and N. K. Saha 317

Computed electron micrographs for tilted foils containing dislocations and stacking faults. By P. Humble 325

The linear polarization of radiation from Jupiter at 6 cm wavelength. By D. Morris, J. B. Whiteoak, and F. Tonking 337

The solar wind and Jovian decametric radio emission. By O. B. Slee and C. S. Higgins 341

Number 3, June 1968 (*Continued*)

PAGE

A catalogue of galactic radio sources. By M. J. L. Kesteven 369

The Parkes catalogue of radio sources, declination zone +20° to +27°. By A. J. Shimmins and G. A. Day 377

Short Communications

A study of the $3\cdot00$ MeV level of ^{27}Al via $^{24}\mathrm{Mg}(\alpha,\mathrm{p}\gamma)^{27}\mathrm{Al}$. By D. C. Kean, R. V. Elliott, and R. H. Spear 405

Interpretation of the radio rotation period of Jupiter in terms of the cyclotron theory. By P. M. McCulloch 409

Number 4, August 1968

R-matrix fit to $^{9}\mathrm{Be}(\gamma,\mathrm{n})^{8}\mathrm{Be}$ cross section near threshold. By F. C. Barker and B. M. Fitzpatrick 415

The behaviour of DWBA stripping amplitudes near the Butler pole. By M. Andrews, W. K. Bertram, and L. J. Tassie 423

Variational calculations for three-body S-states with Coulomb interactions. By L. M. Delves and T. Kalotas 431

Dielectric saturation in ionic crystals. II. Deformable ions. By J. Oitmaa .. 439

Multipole analysis. I. Theory, and geomagnetic multipoles $1965\cdot0$. By R. W. James 455

Nonlinear adiabatic pulsations of massive stars. By J. O. Murphy 465

The distribution of linear polarization over 13 extended sources at $21\cdot2$ cm wavelength. By D. Morris and J. B. Whiteoak 475

Observations of the linear polarization of radio sources at 6 cm wavelength. By D. Morris and J. B. Whiteoak 493

The optical spectrum of Vela X. By D. K. Milne 501

Radio sources in clusters of galaxies. By B. Y. Mills, R. R. Shobbrook, and D. Stewart-Richardson 511

Accurate positions and some optical identifications for 67 radio sources between declinations +20° and +27°. By Jeannette K. Merkelijn, A. J. Shimmins, and J. G. Bolton 523

Short Communications

Observations of 11 radio sources near 55 MHz. By R. F. Haynes, P. A. Hamilton and P. M. McCulloch 539

NUMBER 5, OCTOBER 1968

PAGE

An exact solution of Boltzmann's equation for a rigid sphere gas. By P. I. Brooker and H. S. Green 543

Ornstein–Zernike relation for a disordered fluid. By R. J. Baxter 563

The interaction energy of an ion pair with overlapping hydration shells. I. A truncated spheres model. By D. K. Ross and S. Levine 571

The interaction energy of an ion pair with overlapping hydration shells. II. A spheroidal cavity model. By D. K. Ross 587

The interaction energy of an isolated monovalent ion. By D. K. Ross .. 597

The formal nonequilibrium theory of partially ionized and/or nonuniform gas mixtures. By E. L. Bydder and B. S. Liley 609

Electron drift and diffusion in parahydrogen at 77°K. By R. W. Crompton and A. I. McIntosh 637

Directional correlations of gamma rays in the decay of 36 hr ^{82}Br. By S. L. Gupta and M. M. Bajaj 649

Diffraction by a slit aperture formed by two inclined surfaces. By H. S. Tan 661

The origin and propagation of acoustic-gravity waves ducted in the thermosphere. By A. F. Wickersham 671

Propagation of shock waves in a polytrope with a poloidal magnetic field. By Narendra K. Sinha 681

The nature of spread-F irregularities in Antarctica. By G. G. Bowman .. 695

Observations of Cen XR-2, Sco XR-1, and terrestrial X-rays. By J. R. Harries and R. J. Francey 715

Optical and radio observations of the flare star UV Ceti in Australasia during September–October 1967. By C. S. Higgins, L. H. Solomon, and F. M. Bateson 725

A continuum survey of the Southern Milky Way at 1410 MHz. By E. R. Hill 735

Supernova remnants as radio sources. By M. J. L. Kesteven 739

7794

Short Communications

Cosmic ray intensity increase on January 28, 1967. By L. V. Sud 755

The properties of a drifting and diffusing pulse of electrons and Townsend's coefficient of ionization α_T. By L. G. H. Huxley 761

The (γ, p) and (γ, n) reactions in molybdenum. By R. W. Gellie 765

NUMBER 6, DECEMBER 1968

PAGE

Application of reaction matrix theory to meson processes. By J. L. Cook .. 769

On the problem of unresolved resonances in neutron spectroscopy. By A. R. de L. Musgrove 779

Charge exchange collisions involving multielectron atoms (lithium and sodium). By J. G. Lodge and R. M. May 793

States in ^{27}Al and ^{89}Y using high resolution surface barrier counters. By G. M. Crawley, D. L. Powell, and B. V. Narasimha Rao 803

The characteristic loss spectra of the second and third series transition metals. By M. J. Lynch and J. B. Swan 811

The potential due to two point charges each at the centre of a spherical cavity and embedded in a dielectric medium. By D. K. Ross 817

The shape and energy of a revolving liquid mass held together by surface tension. By D. K. Ross 823

The stability of a rotating liquid mass held together by surface tension. By D. K. Ross 837

On the relationship between recent measurements of cosmic ray electrons, nonthermal radio emission from the Galaxy, and the solar modulation of cosmic rays. By W. R. Webber 845

Study of a complete sample of cosmic radio sources. By W. Davidson .. 871

5 GHz continuum radiation from southern hemisphere galactic HII regions. By F. F. Gardner and M. Morimoto 881

Observations of the southern sky at 10·02 MHz. By P. A. Hamilton and R. F. Haynes 895

Accurate positions and identifications of 75 radio sources between declinations +20° and +27°. By Jeannette K. Merkelijn 903

Effect of horizontal and vertical magnetic fields on Kelvin–Helmholtz instability. By R. C. Sharma and K. M. Srivastava 917

Effect of horizontal and vertical magnetic fields on Rayleigh–Taylor instability. By R. C. Sharma and K. M. Srivastava 923

Short Communications

Study of combined effect of Kelvin–Helmholtz instability and gravitational instability on a self-gravitating fluid layer. By C. Uberoi and R. Jayakaran Isaac 931

The temperature at 120 km altitude in April–May 1965. By L. M. Sheppard 939

The determination of stacking fault energy by the tetrahedron method. By P. Humble and C. T. Forwood 941

Corrigendum 944

Index to Volume 21 945

पुस्तकालय
गुरुकुल कांगड़ी विश्वविद्यालय

Compiled
1999-2000

सन्दर्भ ग्रन्थ
REFERENCE BOOK

यह पुस्तक वितरित न की जाय
NOT TO BE ISSUED